

Spencer Sherwin
Peter Schmid
Xuesong Wu *Editors*

IUTAM Laminar- Turbulent Transition

9th IUTAM Symposium, London, UK,
September 2–6, 2019

IUTAM Bookseries

Volume 38

The IUTAM Bookseries publishes the refereed proceedings of symposia organised by the International Union of Theoretical and Applied Mechanics (IUTAM).

Every two years the IUTAM General Assembly decides on the list of IUTAM Symposia. The Assembly calls upon the advice of the Symposia panels. Proposals for Symposia are made through the Assembly members, the Adhering Organizations, and the Affiliated Organizations, and are submitted online when a call is launched on the IUTAM website.

The IUTAM Symposia are reserved to invited participants. Those wishing to participate in an IUTAM Symposium are therefore advised to contact the Chairman of the Scientific Committee in due time in advance of the meeting. From 1996 to 2010, Kluwer Academic Publishers, now Springer, was the preferred publisher of the refereed proceedings of the IUTAM Symposia. Proceedings have also been published as special issues of appropriate journals. From 2018, this bookseries is again recommended by IUTAM for publication of Symposia proceedings.

Indexed in Ei Compendex and Scopus.

More information about this series at <http://www.springer.com/series/7695>

Spencer Sherwin · Peter Schmid · Xuesong Wu
Editors

IUTAM Laminar-Turbulent Transition

9th IUTAM Symposium, London, UK,
September 2–6, 2019



Springer

Editors

Spencer Sherwin
Imperial College London
London, UK

Peter Schmid
Imperial College London
London, UK

Xuesong Wu
Imperial College London
London, UK

ISSN 1875-3507 ISSN 1875-3493 (electronic)

IUTAM Bookseries

ISBN 978-3-030-67901-9

ISBN 978-3-030-67902-6 (eBook)

<https://doi.org/10.1007/978-3-030-67902-6>

© The Editor(s) (if applicable) and The Author(s), under exclusive license to Springer Nature Switzerland AG 2022

This work is subject to copyright. All rights are solely and exclusively licensed by the Publisher, whether the whole or part of the material is concerned, specifically the rights of translation, reprinting, reuse of illustrations, recitation, broadcasting, reproduction on microfilms or in any other physical way, and transmission or information storage and retrieval, electronic adaptation, computer software, or by similar or dissimilar methodology now known or hereafter developed.

The use of general descriptive names, registered names, trademarks, service marks, etc. in this publication does not imply, even in the absence of a specific statement, that such names are exempt from the relevant protective laws and regulations and therefore free for general use.

The publisher, the authors and the editors are safe to assume that the advice and information in this book are believed to be true and accurate at the date of publication. Neither the publisher nor the authors or the editors give a warranty, expressed or implied, with respect to the material contained herein or for any errors or omissions that may have been made. The publisher remains neutral with regard to jurisdictional claims in published maps and institutional affiliations.

This Springer imprint is published by the registered company Springer Nature Switzerland AG
The registered company address is: Gewerbestrasse 11, 6330 Cham, Switzerland

Preface

This Special Volume contains 72 papers of presentations delivered during an IUTAM Symposium on Laminar-Turbulent Transition 2019 held on 2–6 September 2019 at Imperial College London, UK. IUTAM Transition 2019 was the ninth symposia in the series which started in Stuttgart in 1979. Although there have been two other European symposia in France (1989) and Sweden (2009), this is the first time that there has been a symposium in the UK.

The recent decades have witnessed significant developments in fundamental and applied aspects of stability and laminar-turbulent transition in complex flows at all speed regimes. The papers in this volume, are amongst the oral and paper presentations contributed to this Symposium, and reflect recent achievements in the following topics:

- Global analysis of instabilities and receptivities for complex configurations;
- Nonlinear dynamical systems approaches to minimal seeds and transition to turbulence;
- Influence of multi-physics phenomena on transition: reactive flows, non-Newtonian material behaviour, interfacial flows, flows with interacting structures;
- Novel experimental measurement and evaluation techniques for transition in complex flows;
- Roughness-induced transition; transition from steps, gaps, junctions and other geometric imperfections;
- Transition in hypersonic flows; prediction of thermal loads.
- Active and passive control of flows undergoing transition; transition delay;
- Transition mechanisms in natural and controlled environments; receptivity techniques and studies;
- Late stages of transition and breakdown to fully developed turbulence;
- Transient growth problems and bypass mechanisms and their role in the transition process;

The papers were peer-reviewed by the following Committee members: Chris Atkin (City University London), Mike Gaster (City University London) Yongyun Hwang (Imperial College London), Jonathan Morrison (Imperial College London), Neil Sandham (University of Southampton), Vassilis Theofilis (University of Liverpool), Peter Schmid (Imperial College London), Spencer Sherwin (Imperial College London), Xuesong Wu (Imperial College London).

The IUTAM Transition 2019 have received unprecedented interest with nearly 200 submitted abstracts and 175 registered delegates from 15 countries: Australia, Belgium, Brazil, China, France, Germany, India, Italy, Israel, Japan, the Netherlands, Poland, Sweden, the USA and the UK. Moreover, the Symposium was well attended by early career academics, postgraduate students (40% of all participants), industry representatives, senior members of the community and invited guests.

The scientific programme covered a range of fundamental topic areas and comprised plenary sessions, individual talks and poster networking sessions. Nine of the internationally renowned, invited plenary and keynote speakers were: Stefania Cherubini (Politecnico di Bari, Italy), Jeffrey Crouch (The Boeing Company, USA), Mujeeb Malik (NASA Langley Research Center, USA), Tom Mullin (Oxford University, UK), Helen Reed (Texas A&M University, USA), Tamer Zaki (Johns Hopkins University, USA), Andre Cavalieri (Instituto Tecnologico de Aeronautica, Brazil), Xiaolin Zhong (University of California, Los Angeles, USA), Maksim Ustinov (TsAGI Central Aerohydrodynamic Institute, Russia). Further more, the conference included 67 contributing talks and 78 poster presentations.

The Scientific Committee appointed by the IUTAM Bureau consisted of Carlo Cossu (LHEEA - CNRS, Nantes, France), Jeffery Crouch (The Boeing Corporation, USA), Rama Govindarajan (International Centre for Theoretical Sciences, India), Dan Henningson (Royal Institute of Technology (KTH), Sweden), Yury Kachanov (Institute of Theoretical and Applied Mechanics, Russia), Marcello Medeiros (Universidade de Sao Paolo, Brazil), Tim Pedley (IUTAM Representative, Cambridge University, UK), William Saric (Texas A & M University, USA).

Overall, we hope the event has fulfilled its objectives to present and discuss novel developments in fundamental and applied aspects of stability and laminar-turbulent transition in complex flows, at all speed regimes, and to provide a forum for the free exchange of ideas for their implementation in an industrial setting. Further, the symposium aimed at bringing together leading scientists and industrial practitioners in transition research from Europe, Asia and the Americas to consider and evaluate future directions and demands.

Last but not least, the Local Organising Committee would like to acknowledge the financial and in-kind support received from several sources: Air Force Office of Scientific Research—for providing funds to cover the cost of the main plenary lectures; EPSRC Grant (EP/R029423/1)—PRISM: Platform for Research In Simulation Methods—for an administrative time contribution; Imperial College London—for offering the conference venue at a competitive rate. Finally, we are very indebted

for the time, energy and enthusiasm provided by Anna Radomska. Without her assistance, we would not have been able to make the symposium so successful.

London, UK

Local Organising Committee

Spencer Sherwin

Peter Schmid

Xuesong Wu

Contents

Invited Papers

Unraveling Transition and Turbulence Using Nonlinear Optimization	3
Stefania Cherubini	
Predicting Laminar-Turbulent Transition Influenced by Surface-Induced Flow Distortions	19
J. D. Crouch	
40 Years of Transition Research at NASA: A Personal Perspective	33
Mujeeb R. Malik	
Progress in Stability and Transition Research	55
Helen L. Reed	
Progress in Development of Amplitude Method of Transition Prediction on Swept Wing	71
Maksim V. Ustinov	
Coherent Structures, Dynamical Systems, Edge States	
Nonlinear Optimal Disturbances in Compressible Shear Flows	87
Zhu Huang, Tim Flint, and M. J. Philipp Hack	
On Subharmonic Resonance and Other Nonlinear Mechanisms in Wavepackets in Boundary Layers	97
A. G Martinez, F. H. T Himeno, M. S. Mathias, and M. A. F. Medeiros	
Numerical Simulation of Gas Injection Effect on Boundary Layer Instability for Space Vehicles	107
Ivan Egorov, Anton Obraz, Natalia Palchekovskaya, and Alexander Fedorov	
Two-Dimensional Self-Sustaining Processes Involving Critical Layer/Wall Layer Interaction	117
Rishi Kumar and Andrew Walton	

Study of Transition to Turbulence Using Discrete Directed Percolation Model	127
Kouta Watanabe, Hideki Shiiba, and Yoshio Ishii	
Nonlinear Evolution of Multiple Helical Modes in the Near-Nozzle Region of Subsonic Circular Jets: A Weakly Nonlinear Critical-Layer Theory	137
Zhongyu Zhang and Xuesong Wu	
Experiments	
Investigation of Distributed Roughness Element System Based on Dielectric Barrier Discharge for the Suppression of Stationary Cross-Flow Vortices on the Swept Wing	151
Sergey Baranov, Ivan Moralev, Dmitry Sboev, Stepan Tolkachev, and Maxim Ustinov	
Bump-Induced Transition in Compressible High Reynolds Number Flow: Experimental Results and Correlation with Linear Stability Analysis	159
Marco Costantini, Stefan Hein, Steffen Risius, Stefan Koch, and Christian Klein	
Experimental Analysis of the Effect of Suction and Step Height on Boundary-Layer Transition	171
Benjamin Dimond, Marco Costantini, and Christian Klein	
On the Interaction of Freestream Turbulence and Attachment-Line Boundary Layer	181
Isabella Fumarola, Michael Gaster, and Chris J. Atkin	
Isolated Roughness and Tollmien-Schlichting Waves in Boundary-Layer Transition	193
Shumpei Hara, Santhosh B. Mamidala, and Jens H. M. Fransson	
Instabilities and Transition on a Rotating Cone—Old Problems and New Challenges	203
K. Kato, A. Segalini, P. H. Alfredsson, and R. J. Lingwood	
An Experimental Investigation of the Effects of Wires and Forward-Facing Steps on the Laminar-Turbulent Transition of a Sucked Boundary Layer	215
Jeanne Methel, Maxime Forte, Olivier Vermeersch, and Grégoire Casalis	
Control of Unsteady Görtler Instability Modes by Steady Görtler Vortices	227
D. A. Mischenko, V. I. Borodulin, A. V. Ivanov, and Y. S. Kachanov	

Transitional Intermittency in a Flat Plate Boundary Layer Subjected to Elevated Free-Stream Turbulence	233
Nguyen Thanh Tung and Dmitry Sboev	
Response of NLF Airfoils to Small Scale Turbulence	243
Jonas Romblad, Duncan Ohno, Amandine Guissart, Werner Würz, and Ewald Krämer	
Disturbances in a Three Dimensional Boundary Layer at Elevated Free Stream Turbulence	255
Dmitry Sboev and Stepan Tolkachev	
 Flow Control	
Experimental Investigation of Spanwise-Periodic Surface Heating for Control of Crossflow-Dominated Laminar-Turbulent Transition	267
Hans Peter Barth and Stefan Hein	
Nonlinear Optimal Control Using Deep Reinforcement Learning	279
Michele Alessandro Bucci, Onofrio Semeraro, Alexandre Allauzen, Laurent Cordier, and Lionel Mathelin	
Linear Impulse Response of a Plasma Jet	291
S. Demange, U. Ali Qadri, and F. Pinna	
Control of Travelling Crossflow Vortices Using Volume Forcing	301
Zhengfei Guo, Philipp C. Dörr, and Markus J. Kloker	
Experimental Attenuation of a Trailing Vortex Inspired by Stability Analysis	313
Ross Richardson, Brian Eckert, Yang Zhang, Louis N. Cattafesta III, Adam Edstrand, Yiyang Sun, Peter Schmid, and Kunihiko Taira	
 General Stability Analysis	
Distributed Excitation of Crossflow Waves Due to Scattering of Freestream Vortices by Surface Waviness	327
V. I. Borodulin, A. V. Ivanov, and Y. S. Kachanov	
Overview of the AFT Model for Transition Prediction in Complex Aerodynamic Flows	337
James G. Coder	
BiGlobal Stability Analysis of Swept-Wing Boundary Layers with Forward and Backward Facing Steps	347
Thibaut Appel, Emma Cooke, Shahid Mughal, and Richard Ashworth	
Effect of Discrete Widely Spaced Suction on a Transitioning Flow at High Suction Rates	359
B. Crowley and C. Atkin	

Global Stability Analysis and DNS of a Swept Airfoil Section in Subsonic Flow	369
N. De Tullio and N. D. Sandham	
Instability of Tilted Shear Flow in a Strongly Stratified and Viscous Medium	379
Lloyd Fung and Yongyun Hwang	
Towards Understanding of Natural Boundary-Layer Transition for Low-Speed Flows via Random Excitation	391
Shirzad Hosseinvandi and Hermann F. Fasel	
On the Propagation of Two Types of Disturbances Through a Laminar Boundary Layer Subjected to Separation and Transition	407
Thomas J. B. Irps and Vasudevan Kanjirakkad	
Stability and Control of the Flow in a Porous Channel	419
Ravi Kant, Narayanan Vinod, and Uddipta Ghosh	
Use of Instabilities for Optimal Laminar Separation Delay	439
Michael Karp and M. J. Philipp Hack	
Wave Packet Dispersion in Inflectional and Non-inflectional Flows	451
Kirthy K. Srinivas, Sourabh S. Diwan, and O. N. Ramesh	
Linearized Formulation for Fluid-Structure-Interaction for Rigid-Body Motion	459
Prabal S. Negi, Ardeshir Hanifi, and Dan S. Henningson	
Investigations of Laminar to Turbulent Transition in an Oscillating Airfoil Boundary Layer	469
Duncan Ohno, Jonas Romblad, Marwan Khaled, and Ulrich Rist	
Global Stability Analysis of JAXA H-II Transfer Vehicle Re-entry Capsule	479
Andrea Sansica, Atsushi Hashimoto, and Yuya Ohmichi	
Global Linear Stability and Sensitivity of Hypersonic Shock-Boundary Layer Interactions	489
G. S. Sidharth, A. Dwivedi, J. W. Nichols, M. Jovanović, and G. V. Candler	
On the Influence of Frequency and Spanwise Wavelength on the Formation of Görtler Vortices	499
Adriano Sueke Takata and Leandro Franco de Souza	
Non-modal Linear Stability Analysis of Ablation Flows Relative to Inertial Confinement Fusion	509
G. Varillon, J.-M. Clarisse, and A. Couairon	
Transition Due to Aerofoil-Wake Boundary Layer Interaction	521
Dhamotharan Veerasamy and Chris Atkin	

High Speed and Hypersonics

Roughness-Induced Laminar-Turbulent Transition in the Boundary Layer of a Capsule-Like Geometry at Mach 20 Including Non-equilibrium	531
Antonio Di Giovanni and Christian Stemmer	
The Role of Receptivity in Prediction of High-Speed Laminar-Turbulent Transition	541
I. V. Egorov, A. V. Fedorov, A. V. Novikov, and P. V. Chuvakhov	
Numerical Investigation of the Nonlinear Transition Stages in a High-Enthalpy Hypersonic Boundary Layer on a Right Cone	553
Michelle Bailey, Christoph Hader, and Hermann F. Fasel	
Direct Numerical Simulations (DNS) of Natural Transition in High-Speed Boundary Layers Using a Broadband Random Forcing Approach	565
Christoph Hader and Hermann F. Fasel	
Sensitivity of Boundary-Layer Stability and Transition to Thermochemical Modeling	575
H. L. Kline, C.-L. Chang, and F. Li	
Effects of Streaky Structures on the Instability of Supersonic Boundary Layers	587
Jianxin Liu, Elena Marenzi, and Xuesong Wu	
Sensitivity of Reacting Hypersonic Boundary Layers to n-periodic Surface Roughness	599
Athanassios T. Margaritis, Taraneh Sayadi, Olaf Marxen, and Peter J. Schmid	
Hypersonic Boundary Layer Instability and Control by Passive Porous Coatings	613
S. O. Morozov, S. V. Lukashevich, and A. N. Shiplyuk	
Numerical Study of Crossflow Jet Generated Instabilities in a High-Speed Boundary Layer	621
Andrey V. Novikov and Alexander V. Fedorov	
Influence of High-Temperature Effects on the Stability of the Wake Behind an Isolated Roughness Element in Hypersonic Flow	631
Iván Padilla Montero, Fernando Miró Miró, and Fabio Pinna	
Effect of the Single Roughness on Shock Wave/Laminar Boundary Layer Interaction	643
Pavel A. Polivanov and Andrey A. Sidorenko	
Linear Instability of Shock-Dominated Laminar Hypersonic Separated Flows	651
Saurabh S. Sawant, Ozgur Tumuklu, Vassilis Theofilis, and Deborah A. Levin	

Controlled Cross-Flow Mode Interaction in Mach 6 Boundary Layer	661
Alexander Arndt, Thomas Corke, Eric Matlis, and Michael Semper	
Stability Analyses of Hypersonic, Conical Flows with Transpiration Cooling	671
Viola Wartemann, Giannino Ponchio Camillo, Jens Neumann, Alexander Weber, and Alexander Wagner	
Nonlinear PSE Transition Predictions in Hypersonic Boundary Layers with Finite-Rate Chemical Reactions	691
L. Zanus, F. Miró Miró, and F. Pinna	
Roughness and Receptivity	
Investigation of a Sectioned Boundary Layer Suction System in Case of Failure of One of Its Sections in Application to the Three-Dimensional Boundary Layer Laminarization on the Swept Wing	705
Sergey Baranov, Andrey Kiselev, Dmitry Sboev, and Stepan Tolkachev	
Destabilisation of Stationary and Travelling Crossflow Disturbances Due to Forward and Backward Facing Steps over a Swept Wing	713
Emma E. Cooke, Shahid Mughal, Spencer Sherwin, Richard Ashworth, and Stephen Rolston	
Deep Learning Based Transition Prediction for Aeronautical Applications	725
Renato Cosin, Marcio T. Mendonca, Ardeshir Hanifi, Dan S. Henningson, and Gilberto G. Becker	
Numerical Studies on the Influence of Step-Like Surface Irregularities on the Development of Tollmien-Schlichting Waves	737
Juan Alberto Franco and Stefan Hein	
Receptivity to Surface Imperfections	749
Michael Gaster	
Influence of Cylindrical and Two-Dimensional Roughness Elements on the Laminar-Turbulent Transition on Flying Wing Model	757
A. M. Pavlenko, V. S. Kaprilevskaya, V. V. Kozlov, and S. N. Tolkachev	
On the Effects of Sound in Subsonic Boundary Layer Flows	769
Henrique Raposo, Shahid Mughal, and Richard Ashworth	
Receptivity of Unsteady Compressible Görtler Flows to Free-Stream Vortical Disturbances	781
Pierre Ricco and Samuele Viaro	

Leading-Edge Receptivity of Moderately Supersonic Boundary Layers to Free-Stream Disturbances	793
Pierre Ricco and M. E. Goldstein	
Direct Numerical Simulations of Tollmien-Schlichting Disturbances in the Presence of Surface Irregularities	805
Francesco Tocci, Guillaume Chauvat, Stefan Hein, and Ardeshir Hanifi	
Stability Analysis of Boundary Layer Flow with Rotating Cylindrical Surface Roughness Elements	815
Yongxiang Wu and Ulrich Rist	
Triadic Resonance Analysis of Distributed Roughness Effects on Crossflow Instability in Swept-Wing Boundary Layers	825
Jiakuan Xu, Jiyang He, and Xuesong Wu	

Invited Papers

Unraveling Transition and Turbulence Using Nonlinear Optimization



Stefania Cherubini

Abstract Subcritical transition in shear flows is due to both nonnormality and nonlinearity. Nonlinear optimization of perturbations of a given base flow is a powerful tool coupling nonnormality and nonlinearity, allowing to explore the phase space at a finite distance from the reference flow and study its nonlinear stability. This tool allows to compute: (i) minimal energy thresholds for transition, (ii) the most amplified coherent structures in transitional and turbulent flows, (iii) heteroclinic orbits connecting different invariant solutions of the Navier-Stokes equations, (iv) efficient ways for controlling transition to turbulence of finite-amplitude perturbations. The present work presents the nonlinear optimization framework and discusses its different applications to the study and control of transition and turbulence in shear flows.

1 Introduction

Non-modal stability theory [1] asserts that subcritical transition in shear flows is due to constructive interaction of non-orthogonal eigenmodes, leading to a transient energy amplification. The main argument for attributing subcritical transition to this purely linear amplification mechanism can be found in the Reynolds-Orr equation [2], showing the conservative nature of the nonlinear advection terms of the Navier-Stokes (NS) equations. Nonetheless, the crucial contribution of nonlinearity in subcritical transition can be illustrated by the following model equations [3]:

$$\frac{dx}{dt} = -\frac{x}{R} + y + xy, \quad \frac{dy}{dt} = -y - x^2. \quad (1)$$

S. Cherubini (✉)

Department of Mechanics, Mathematics and Management, Politecnico di Bari, Via Re David 200, Bari, Italy

e-mail: s.cherubini@gmail.com

This system shows some important features of the NS equations for asymptotically stable flows, namely, energy-conserving nonlinear terms, the presence of a stable node at the origin, and two non-trivial fixed points $x^\pm = \frac{1}{2}(-1 \pm \sqrt{\Delta})$ (a stable node and a saddle point), which arise with a saddle-node bifurcation at $\Delta = 1 - 4/R = 0$. Neglecting nonlinear terms, one can observe a transient growth of the kinetic energy $E = \frac{1}{2}(x^2 + y^2)$ for $\Delta > 0$, but the fixed point at the origin still remains a sink, and every initial perturbation leads to relaxation towards this solution. Considering nonlinear terms leads to the same initial transient growth, which can or not lead to the non-trivial state x^+ , depending on the initial perturbation. Crucial importance is assumed by the stable manifold of the saddle state x^- , which represents a separatrix between the basin of attractions of the trivial and non-trivial stable solutions. Notably, the point of minimal energy on this separatrix measures the minimal energy needed to reach the non-trivial state while perturbing the trivial one (which is the equivalent of passing from the laminar to the turbulent regime, in shear flows). In the linearized system, although the energy can transiently grow, transition to non-trivial states (namely, invariant solutions sustaining turbulence) is not possible and no such separatrix exists in phase space. Thus, one can conclude that nonnormality of the linearized operator is not itself responsible for subcritical transition, nonlinearity being an essential ingredient that one cannot neglect.

Despite that, before this decade, subcritical transition in shear flows has been studied using linearized approaches for computing the perturbations to the laminar solution able to induce the largest possible growth at a given target time, namely, the *linear optimal perturbations* [4]. These perturbations are found to reproduce very well flow structures typically found in bypass transition, such as streamwise streaks [5]. Nevertheless, linear approaches cannot provide any relevant information about the minimal energy for which a given (or any) perturbation may actually experience transition, and cannot give any hint about the mutual interaction between linear mechanisms such as, for instance, (nonmodal) transient growth of streaks and their secondary (modal) instability. Some efforts on including both nonnormal and non-linear effects into simple flow models [6] or in a simplified set of equations [7, 8] have been done before this decade. But only in recent years, the increase of available and affordable computational resources has pushed the development of numerical strategies allowing to optimize problems described by non-linear partial differential equations and constituted by a large number of degrees of freedom, such as the NS equations for fluid flows. The first non-linear optimization in shear flows have been conducted, almost at the same time, by two different research groups, for pipe [9] and boundary-layer [10] flows. In both cases, nonlinear optimal perturbations very different from linear ones have been found [11, 12], including already all the ingredients for optimally linking different linear energy growth mechanisms by means of nonlinearity. These perturbations have shown robustness with respect to different objective functions [13], and have been computed for different flows [14–18], even in turbulent conditions [19, 20], showing different shapes depending on the flow configuration. Different research groups have assessed the relevance of these optimal perturbations for the determination of minimal energy thresholds for transition in the case of different shear flows [21–23] and for different transition times [24]. The same

variational procedure has been successfully adapted to passive or active flow control [14, 25–27] and used for the computation of exact coherent states [28] and heteroclinic orbits [29]. A thorough review of nonlinear optimization of perturbations in shear flows can be found in Refs. [30, 31]. The present work aims at discussing how the variational mathematical framework used for nonlinear optimization can be easily adapted to different problems relevant to subcritical transition in shear flows and its control. Section 2 provides the optimization framework and a thorough discussion of many of its possible applications. Section 3 provides results of two applications of the presented algorithm. Section 4 concludes the paper.

2 Mathematical Framework

Let us define a base flow $\mathbf{Q} = (\mathbf{U}, P)^T$ (\mathbf{U} being the velocity vector, and P the pressure), which is a steady solution of the Navier-Stokes equations, representing a fixed point in the state space. A perturbation $\mathbf{q} = (\mathbf{u}, p)^T$ is added at $t = 0$ to the base flow, laying at a certain initial distance from this fixed point. While evolving in time, the perturbation can increase or decrease its distance from the fixed point, depending on linear stability, nonnormality and nonlinearity of the equations, as discussed in the Introduction. The aim of the present nonlinear optimization is to maximize, at a certain target time T , the distance of the perturbation from the base flow, expressed in the energy norm $E(T) = \|\mathbf{u}(T)\|_2^2$, defined with respect to the scalar product

$$\langle \mathbf{a}, \mathbf{b} \rangle = \frac{1}{V} \int_V (\mathbf{a} \cdot \mathbf{b}) dV, \quad (2)$$

V being the volume of the considered computational domain, and \mathbf{a}, \mathbf{b} two generic velocity fields in that domain. The objective function $\mathfrak{I} = E(T)$ is subject to partial differential constraints such as the initial energy shell E_0 around the base flow and the incompressible Navier-Stokes (NS) equations written in their perturbative formulation with respect to the considered base flow:

$$\begin{aligned} NS(\mathbf{u}, \mathbf{U}, p) = & \frac{\partial \mathbf{u}}{\partial t} + (\mathbf{u} \cdot \nabla) \mathbf{U} + (\mathbf{U} \cdot \nabla) \mathbf{u} + (\mathbf{u} \cdot \nabla) \mathbf{u} + \nabla p - \frac{1}{Re} \nabla^2 \mathbf{u} = 0 \\ & \nabla \cdot \mathbf{u} = 0. \end{aligned} \quad (3)$$

where $Re = U_c h / \nu$ is the Reynolds number, U_c being the reference velocity of the steady solution, h the reference length, and ν the kinematic viscosity. The constraints are added to the objective function via scalar product with the Lagrange multipliers (or adjoint variables) $(\mathbf{u}^\dagger, p^\dagger, E^\dagger)$, yielding the *augmented functional* $\mathcal{L}(\mathbf{u}, p, \mathbf{u}^\dagger, p^\dagger, \mathbf{u}(T), \mathbf{u}(0), E^\dagger)$:

$$\mathcal{L} = E(T) - \int_0^T \langle \mathbf{u}^\dagger, NS(\mathbf{u}, \mathbf{U}, p) \rangle dt - \int_0^T \langle p^\dagger, \nabla \cdot \mathbf{u} \rangle dt - E^\dagger (E(0) - E_0), \quad (4)$$

Integrating by parts and setting to zero the first variation of \mathcal{L} with respect to $(\mathbf{u}(t \in (0, T)), p)$ yields the adjoint equations

$$NS^\dagger(\mathbf{u}, \mathbf{u}^\dagger, \mathbf{U}, p^\dagger) = \frac{\partial \mathbf{u}^\dagger}{\partial t} + (\mathbf{U} + \mathbf{u}) \cdot \nabla \mathbf{u}^\dagger - \nabla(\mathbf{U} + \mathbf{u})^T \cdot \mathbf{u}^\dagger + \nabla p^\dagger + \frac{1}{Re} \nabla^2 \mathbf{u}^\dagger, \quad (5)$$

$$\nabla \cdot \mathbf{u}^\dagger = 0.$$

Whereas, setting to zero the first variation of \mathcal{L} with respect to $(\mathbf{u}(0), \mathbf{u}(T))$ yields the compatibility and the gradient conditions

$$\frac{\delta \mathcal{L}}{\delta \mathbf{u}(T)} = \mathbf{u}(T) - \mathbf{u}^\dagger(T) = 0; \quad \frac{\delta \mathcal{L}}{\delta \mathbf{u}(0)} = -E^\dagger \mathbf{u}(0) + \mathbf{u}^\dagger(0) = 0. \quad (6)$$

The former relates the direct to the adjoint variables at target time, whereas the latter must be nullified to attain the maximum of the constrained objective function. This is accomplished by the iterative procedure described in the following:

1. An initial guess is made for the initial condition, $\mathbf{q}(0)$, within the energy shell E_0 ;
2. The direct problem (3) is integrated up to $t = T$.
3. The adjoint variables, $\mathbf{q}^\dagger(T)$, are provided by the compatibility conditions (first equation in (6)).
4. The adjoint problem (5) is integrated backward in time from $t = T$ to $t = 0$.
5. At $t = 0$, the initial direct state is updated in a direction determined by the gradient.
6. The objective function $E(T)$ and/or its gradient are evaluated to determine the convergence of the algorithm. If convergence is not achieved, the procedure is continued from step 2, otherwise, the loop is stopped.

Different algorithms based on the gradient can be used for updating the initial perturbation at each iteration. Rather simple methods such as the steepest ascent [9] or the conjugate gradient [32] methods have been used with success, although their convergence efficiency depends on the choice of E^\dagger , the Lagrange multiplier enforcing the initial energy constraint. A better performance in terms of convergence are achieved using the gradient-rotation method [16, 33], which avoids direct determination of E^\dagger by projecting the perturbation on a hypersphere of energy E_0 . It should also be remarked that the algorithm suffers from a computational drawback, namely, the requirement of storing all the direct variables at each time step during the forward NS integration, for using them as advective terms in the backwards time-integration (see Eq. 5). This can lead to storage issues, which may be nonetheless avoided by using lighter storage alternatives such as the receding-horizon algorithm [26, 34]. As a final note, we remark that the presented looping procedure can be also used for computing optimal perturbations of invariant solutions of the NS equations different flow the laminar state, by simply defining the initial perturbation $\mathbf{u}(0)$ with respect to

a different base flow. For instance, optimal perturbations of a given travelling wave, have been recently computed for the plane Poiseuille flow [35].

2.1 Computation of the Minimal Seed

Reference [21] defines the disturbance of minimum amplitude capable of triggering turbulence in a given flow as its *minimal seed* for transition. This peculiar perturbation represents the energy minimum on the laminar-turbulent separatrix [36], and allows an accurate estimate of the minimal energy threshold (E_c) for turbulent transition at given flow conditions. The minimal seed can be easily computed using the iterative procedure described above, choosing a sufficiently large target time and initialising the optimization with two different initial guesses, one with sufficiently high energy to induce transition, the other with a small initial energy ensuring relaminarization. Once the nonlinear optimal perturbations have been computed for these two initial energies, a new value of E_0 is computed bisecting the previous ones, and the direct-adjoint looping is restarted, using the result of one of the two previous optimisations rescaled to the new value of E_0 . This procedure is continued until the initial energy is sufficiently low for inducing relaminarisation of the flow, leading to the determination of E_c . Notice that too large values of the initial energy lead to lack of convergence, thus some initial test runs may be necessary for choosing appropriate initial values of the energy shell. Following this algorithm, the minimal energy threshold for transition have been obtained for the pipe [21], Couette [22] and for the asymptotic suction boundary layer [23], although the method can be used for any type of flow and adapted to flow control [25].

2.2 Applications to Flow Control

The direct-adjoint looping procedure presented above can be esasily adapted also to control problems, may it be passive or active. Optimal passive control strategies can be designed using the presented fully nonlinear variational method in order to design more nonlinearly stable flows. For instance, one can manipulate the boundary conditions of a certain flow in order to increase the critical disturbance energy for the onset of turbulence, as done in Ref. [25] for the Couette flow. Optimal active control can be also designed using the same variational method. For instance, using an optimal suction and blowing at the wall, one can hamper the rapid growth of unsteady finite-amplitude perturbations [14], and/or delay transition to turbulence [27, 34]. The direct-adjoint looping strategy can be easily adapted to these kind of problems by minimising (instead of maximizing) the chosen objective function, which may be simply the kinetic energy of disturbances, or a different measure of turbulent transition, plus a weighted measure of the control cost. For instance, in the case of wall suction actuators placed in a boundary-layer flow, Ref. [14] minimized

the objective function

$$\mathfrak{J} = E(T) + \gamma^2 \int_0^T \int_{S_w} [v_w(t)]^2 dS_w, \quad (7)$$

$v_w(t)$ being the blowing-and-suction actuation law, characterised by a zero-mass condition and localized only in a given region of the wall S_w . This leads to the following two further constraints:

$$-\Phi \int_0^T \int_{S_w} (v - v_w) dt dS_w - \Lambda \int_0^T \left[\int_{S_w} v_w(t) dS_w - 0 \right] dt \quad (8)$$

which should be added to Eq. (4). Using the boundary conditions of the direct and adjoint problem one can find an expression for the Lagrange multiplier Φ which is used to determine an equation for the gradient of the functional with respect to v_w , namely:

$$\frac{\delta \mathcal{L}}{\delta v_w} = \gamma^2 v_w - \Phi \quad \text{with} \quad \Phi = -\Lambda - p^\dagger - \frac{v_y^\dagger}{Re}. \quad (9)$$

For minimizing the objective function, the initial state is updated in the steepest descent direction, namely the direction opposed to the gradient. This nonlinear optimal control strategy has been found able to suppress bypass transition due to large-amplitude optimal disturbances [14], which are almost insensitive to linear control. More recently, a similar procedure has been used to delay transition due to bimodal interactions for short [27] and long target times [34] (in this last case using a receding-horizon algorithm for avoiding instability of the adjoint equations), making it a very promising control strategy.

2.3 Computation of Heteroclinic Orbits

The previously presented direct-adjoint iterative procedure can be easily adapted for finding heteroclinic connections between invariant solutions of the NS equations, usually called Exact Coherent States (ECS) [37]. In such type of connection, the flow field leaves the initial ECS (\mathbf{U}_i) at $-\infty$ and approaches the final one (\mathbf{U}_f) at $+\infty$. Since integrating the NS equations for an infinite time is practically unachievable, we start our computation in a neighbourhood of the initial ECS to reach in a finite time T the neighbourhood of the final one. Therefore, we aim at finding the initial perturbation $\mathbf{u}(0)$, constrained in the energy shell E_{0_i} around the initial equilibrium, that minimizes, within a given threshold E_{0_f} , the distance to the final ECS at time $t = T$. Such a distance is measured using the energy norm, $E_h(T) = \|\mathbf{u}(T) + \mathbf{U}_i - \mathbf{U}_f\|_2^2$ where the perturbation \mathbf{u} is defined with respect to the initial ECS. Thus, the

augmented functional of the Lagrangian optimization reads as follow:

$$\mathcal{L} = E_h(T) - \int_0^T \langle \mathbf{u}^\dagger, NS(\mathbf{u}, \mathbf{U}_i, p) \rangle dt - \int_0^T \langle p^\dagger, \nabla \cdot \mathbf{u} \rangle dt - E^\dagger (E_h(0) - E_{0_i}), \quad (10)$$

Following the previously described procedure, one obtains the adjoint equations (5) with $\mathbf{U} = \mathbf{U}_i$, and the compatibility and gradient conditions that now read:

$$\frac{\delta \mathcal{L}}{\delta \mathbf{u}(T)} = -\mathbf{u}^\dagger(T) + \mathbf{u}(T) + \mathbf{U}_i - \mathbf{U}_f = 0 \quad (11)$$

$$\frac{\delta \mathcal{L}}{\delta \mathbf{u}(0)} = -E^\dagger(\mathbf{u}(0) + \mathbf{U}_i - \mathbf{U}_f) + \mathbf{u}^\dagger(0) = 0 \quad (12)$$

Minimizing the gradient of the functional with respect to $\mathbf{u}(0)$ and imposing a sufficiently long time horizon, the procedure will find any existing heteroclinic connection within the given energy shells. However, for an increasing optimization time, the chaotic behaviour of the NS equations will hinder the convergence of the algorithm. Thus, one should start the optimization with a short time horizon which is slowly increased until final convergence is achieved. For a given value of the target time, the direct-adjoint iteration is performed until the residual $\epsilon = ((E_h(T)^{n+1} - E_h(T)^n)/E_h(T)^n)$ becomes smaller than a given value ϵ_{cr} . At the end of these direct-adjoints iterations, if for the current value of the target time the perturbation does not approach the final state within the desidered energy threshold, E_{0_f} , T is increased and a new iteration cycle is started. The algorithm stops when the perturbation reaches a distance from the final ECS smaller than the chosen threshold E_{0_f} . This approach has been recently used for computing several new heteroclinic orbits in plane Couette flow [29].

2.4 Extention to Turbulent Conditions

The direct-adjoint nonlinear framework can be also easily extended to turbulent flow conditions. In fact, a transient growth approach in a nonlinear framework may be well suited to find the flow structures able to trigger rapid events with a strong energy growth in turbulent flows, such as for instance, bursting events [19]. For modeling the dynamics of perturbations, one can employ a Reynolds decomposition approach [38], where the instantaneous flow vector is decomposed into a mean flow component $\bar{\mathbf{Q}}(y) = [\bar{U}, 0, 0, \bar{P}]^T$ and a disturbance $\tilde{\mathbf{q}}(x, y, z, t) = [\tilde{u}, \tilde{v}, \tilde{w}, \tilde{p}]^T$. Injecting this decomposition in the NS equations and averaging over a long time, the following Reynolds-averaged-NS equations are obtained:

$$\bar{\mathbf{U}} \cdot \nabla \bar{\mathbf{U}} = -\nabla \bar{P} + \frac{1}{Re} \Delta \bar{\mathbf{U}} - \nabla \cdot \bar{\tilde{\mathbf{u}}} \bar{\tilde{\mathbf{u}}}, \quad (13)$$

• denoting long-time averaging. Subtracting the time-averaged equations (13) from the NS equations provides the dynamics of the disturbances that reads:

$$\begin{aligned} \widetilde{NS}(\tilde{\mathbf{u}}, \bar{\mathbf{U}}, \tilde{p}) &= \frac{\partial \tilde{\mathbf{u}}}{\partial t} + \tilde{\mathbf{u}} \cdot \nabla \tilde{\mathbf{u}} + \bar{\mathbf{U}} \cdot \nabla \tilde{\mathbf{u}} + \tilde{\mathbf{u}} \cdot \nabla \bar{\mathbf{U}} + \nabla \tilde{p} - \frac{1}{Re} \nabla^2 \tilde{\mathbf{u}} + \nabla \cdot \bar{\tilde{\mathbf{u}}} \bar{\tilde{\mathbf{u}}}, \\ \nabla \cdot \tilde{\mathbf{u}} &= 0. \end{aligned} \quad (14)$$

The last term of the momentum equation is the divergence of the Reynolds stress tensor $\tau = \bar{\tilde{\mathbf{u}}} \bar{\tilde{\mathbf{u}}}$ forcing the mean turbulent velocity profile (see Eq. (13)), which appears when the perturbative formulation employs a 'base' flow which is not a steady solution of the NS equations. Reynolds stresses need to be known, computed or modeled for closing the governing equations.

Using Eq. (14), one can look for perturbations capable of inducing a peak of kinetic energy in a finite time T . To do so, one should maximize the turbulent kinetic energy $E_t(T) = ||\tilde{\mathbf{u}}(T)||_2^2$ at time T using the Lagrange multiplier approach previously discussed. As in transitional conditions, one should impose as constraints the initial energy E_{t_0} , and Eq. (14), using the Lagrange multipliers or adjoint variables $(\tilde{\mathbf{u}}^\dagger, \tilde{p}^\dagger, E^\dagger)$, as follows:

$$\mathcal{L} = E_t(T) - \int_0^T \langle \tilde{\mathbf{u}}^\dagger, \widetilde{NS} \rangle dt - \int_0^T \langle \tilde{p}^\dagger, \nabla \cdot \tilde{\mathbf{u}} \rangle dt - E^\dagger (E_t(0) - E_{t_0}). \quad (15)$$

Deriving the functional \mathcal{L} with respect to the variables $\tilde{\mathbf{u}}, \tilde{p}$, one obtains adjoint equations identical to those in Eq. (5) with $\mathbf{u} = \tilde{\mathbf{u}}$ and $\mathbf{U} = \bar{\mathbf{U}}$, and compatibility and gradient conditions as in Eq. (6). Once again, the gradient of \mathcal{L} with respect to the initial disturbance is nullified by direct-adjoint iterations coupled with a gradient rotation algorithm [17, 33].

3 Results

In this section we present the results of the nonlinear optimization procedure described above, with particular focus to the plane Poiseuille flow. The optimization has been performed in laminar and turbulent conditions, as discussed below. In all the presented cases, no-slip boundary conditions for the three velocity components are imposed at the walls, whereas periodicity is prescribed in the streamwise and spanwise directions. Computations are performed using the spectral-element code NEK5000 [39], with Legendre polynomial reconstruction of degree 7 and second-order accurate Runge-Kutta time integration [40]. The iterative procedure is stopped when the relative variation between two successive direct-adjoint loops,

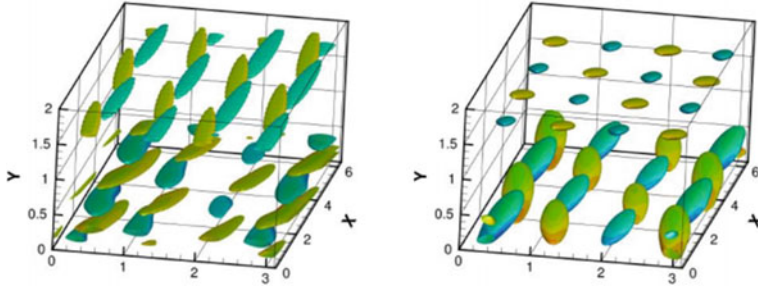


Fig. 1 Nonlinear optimal perturbation for $T = 10$ and $E_0 = 1 \times 10^{-6}$. Isosurfaces of Q-criterion coloured by the values of the streamwise vorticity: $Q = 0.000195$ at $t = 0$ (left) $Q = 0.011$ at $t = T$ (right)

$e = (E^n - E^{n-1})/E^n$ is smaller than 10^{-7} , n being the iteration number. Depending on the selected target time, 40 to 80 direct-adjoint iterations are needed for reaching convergence for one set of parameters, each optimization needing 60.000 to 800.000 CPU hours on an IBM cluster Intel ES 4650.

3.1 Optimal Perturbations in Transitional Flow

We consider the plane Poiseuille flow at $Re = U_c h / \nu = 4000$ (U_c being the centerline velocity and h the half-height of the channel) in a domain $l_x \times l_y \times l_z = 2\pi \times 2 \times \pi$, where y is the wall-normal direction, x and z are the streamwise and spanwise (periodic) directions. Nonlinear optimisations have been performed for several initial energies in the range $[10^{-7}, 10^{-5}]$, for a small target time, $T = 10$. For very low values of the initial energy, $10^{-7} < E_0 < 10^{-6}$, the perturbation is similar to that obtained by linear optimization, constituted by x -independent streamwise vortices at $t = 0$ and streamwise streaks at $t = T$. Increasing the value of the initial energy in the range $10^{-6} < E_0 < 1.25 \times 10^{-6}$, the structure of the optimal perturbation begins to change, being characterized by alternated vortices inclined with respect to the streamwise direction which lay on the flanks of a region of negative streamwise velocity disturbance, as provided in Fig. 1. The upstream tilting with respect to the wall-normal direction, which is observed also in the linear optimal case [32] is linked to the Orr mechanism. On the other hand, in the linear case, no inclination of the vortices in the spanwise direction is observed, meaning that it is a direct effect of nonlinear interactions. Notably, these optimal perturbations are constituted by a peculiar flow structure which is replicated in the three flow directions. This *building block*, which is very similar to those obtained for the Blasius and the asymptotic suction boundary layer flows [11, 23], is composed by spanwise-inclined streamwise vortices alternating in the spanwise direction and flanking a region of high negative streamwise disturbance. Slightly increasing the initial energy to $E_0 = 1.25 \times 10^{-6}$ does not

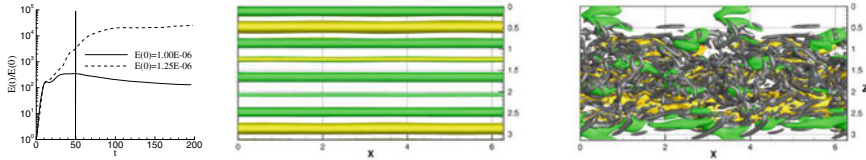


Fig. 2 Time evolution of the energy gain of nonlinear optimal perturbations computed for $T = 10$ and two different initial energies (left, see legend) and snapshot of the evolution of these optimal perturbation at $t = 50$ (indicated by a vertical line in the left frame) with $E_0 = 10^{-6}$ (middle), $E_0 = 1.25 \times 10^{-6}$ (right). Middle: Isosurface of streamwise velocity disturbance ($u = \pm 0.05$, yellow positive and green negative). Right: isosurfaces of the Q-criterion ($Q = 1$, grey) and streamwise velocity disturbance ($u = \pm 0.2$)

affect the main structure of the perturbation, but leads to a localization of the perturbation on one of the two walls, as already observed in other shear flows [11, 41]. Due to spatial localization, the initial amplitude of the disturbances considerably increases, enhancing the nonlinear effects allowing a growth of the initial energy larger than the linear one. The left frame of Fig. 2 shows the energy gain obtained by further marching in time the initial optimal perturbation found by the optimization procedure for $E_0 = 1 \times 10^{-6}$ and $E_0 = 1.25 \times 10^{-6}$. Although being characterized by a very similar structure, these two initial perturbations experience different dynamics. The one with lowest energy grows only transiently, creating elongated positive/negative streaks which saturate nonlinearly and eventually decay towards the laminar state. Whereas, the highest energy optimal disturbance experiences secondary instability of the streaks, finally leading the flow to turbulence (see Fig. 2 where we show, for the two considered cases, flow snapshots extracted at $t = 50$, namely, the time at which the energy gain recovered by long-time DNS peaks). Thus, it appears that this *weakly nonlinear* optimal overtakes the linear optimal growth by exploiting the mechanism of secondary instability of streaky structures. In particular, the three main ingredients of this scenario, which are also the main bricks of the self-sustained process theorized in Ref. [42] (namely, streaks, vortices and sinuous modulations of the streaks), are already contained in the initial perturbation, allowing the establishment of a cycle sustaining turbulence. Further increasing the initial energy within the range $1.25 \times 10^{-6} < E_0 < 10^{-5}$, the nonlinear optimal perturbation changes again its main structure, further localizing in the streamwise and spanwise direction as shown in Fig. 3. At initial time (left), we observe tubes of counter-rotating vorticity placed side by side and tilted against the base flow. This confirms the presence of linear energy growth mechanisms such as the Orr [43] and the lift-up [44]. Differently from the lower energy cases, the downstream tilting causes the merging of one extremity of the two counter-rotating vortices, creating a characteristic hairpin vortex structure at target time (right frame of Fig. 3). This basic structure observed in the top frames of the figure slightly extends in space for a further increase of the initial energy, although remaining confined on only one of the walls (at least for the values of initial energy considered here) and presenting a very similar flow structure.

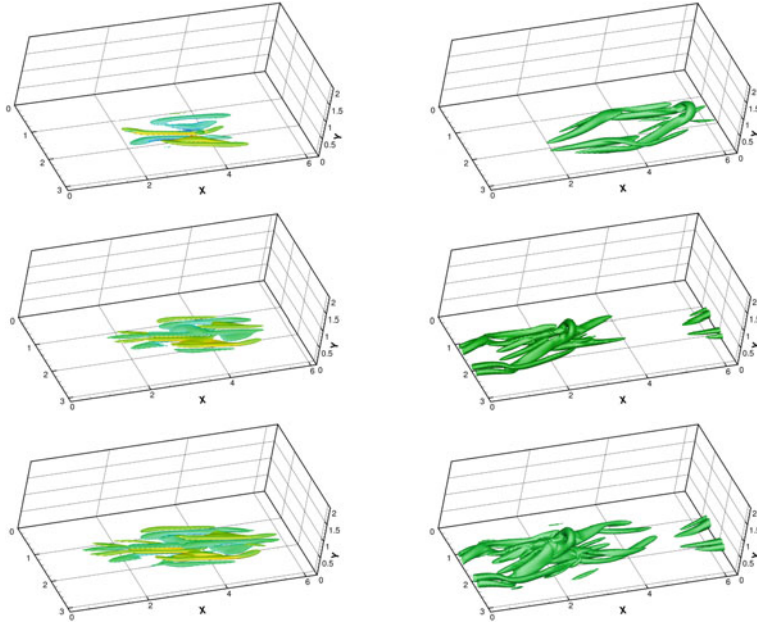


Fig. 3 Nonlinear optimal perturbations for $T = 10$ and (first row) $E_0 = 2 \times 10^{-6}$, (second row) $E_0 = 2.5 \times 10^{-6}$, (third row) $E_0 = 5 \times 10^{-6}$. Isosurfaces of the Q-criterion coloured by the streamwise vorticity: $Q = 0.01$ at $t = 0$ (left frames) and $Q = 0.2$ at $t = 10$ (right frames)

Notably, the optimal disturbance providing the highest energy growth is that obtained for $E_0 = 2 \times 10^{-6}$, namely, that constituted by a localized hairpin vortex structure. These results suggest that hairpin structures are highly energetic flow structures able to provide the maximum possible energy growth, much larger than that achievable under linearized conditions, exploiting nonlinear interactions of linear energy growth mechanisms. The fact that these peculiar flow structures may grow the most amongst many other ones present in a shear flow, may indicate the reason for the recurrence of hairpin vortices in transitional flow. In the remainder of the paper we carry out nonlinear optimization in a turbulent channel flow, aiming at investigating whether similar conclusions can be drawn also in the turbulent regime.

3.2 Optimal Perturbations in Turbulent Flow

We now consider a turbulent channel flow at friction Reynolds number $Re_\tau = u_\tau h/\nu = 180$; u_τ being the friction velocity. Since two scalings of the variables are employed, variables expressed in inner units (normalized using u_τ and viscous length scale, $\delta_v = \nu/u_\tau$) are indicated with the superscript $+$, whereas variables without any superscript are scaled in outer units (normalized using the centerline velocity

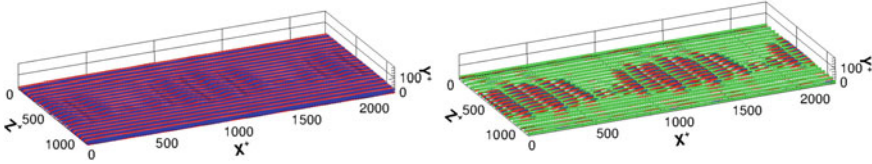


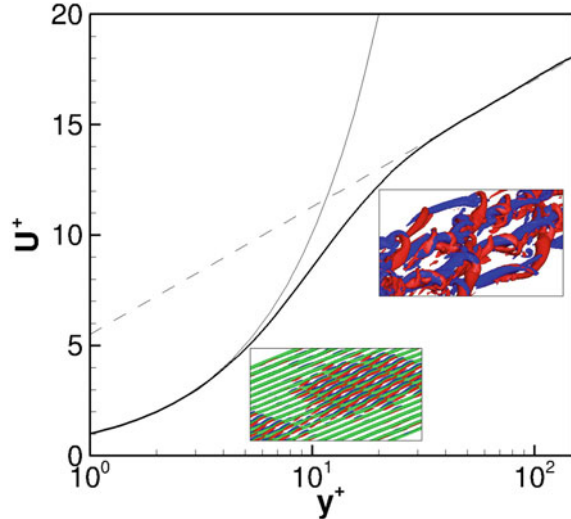
Fig. 4 Nonlinear optimal perturbation of the mean flow in a plane turbulent channel with $T^+ = 21.94$ and $E_0 = 10^{-2}$ at $t^+ = 0$ (left) and $t^+ = T^+$ (right). Left: red and blue isosurfaces for positive and negative streamwise vorticity. Right: green isosurfaces indicate negative streamwise velocity and blue/red ones represent the Q-criterion coloured by values of streamwise vorticity (blue for positive, red for negative)

U_c and h). A computational domain having streamwise, wall-normal, and spanwise dimensions equal to $l_x = 4\pi$, $l_y = 2$, $l_z = 2\pi$, respectively, is used. The numerical code and boundary conditions are the same as those used in the transitional case.

To integrate the Reynolds-Averaged NS equations we have first computed by DNS and validated the mean flow velocity $\bar{\mathbf{U}}$ and the Reynolds stress $\bar{\mathbf{u}}\bar{\mathbf{u}}$, which are then employed in Eq. (14) for the optimization. Figure 4 provides the nonlinear optimal perturbation of the mean flow in a plane turbulent channel with $T^+ = 21.94$ and $E_0 = 10^{-2}$. At $t^+ = 0$ (left), the perturbation is characterized by spanwise-alternated counter-rotating streamwise vortices, which present sinusoidal modulations in a localized region of the domain. These vortices are localized very close to the wall, which might be expected since the chosen target time corresponds to the eddy turnover time at $y^+ = 8$. At $t^+ = T^+$ (right frame of Fig. 4), the vortices create localized streaky structures alternated in the streamwise and spanwise directions, but localized in space and flanked by streamwise vortices. These structures are remnants of the wall-cycle theorized in Ref. [42].

Increasing the target time at values still linked to the eddy turnover time in the inner region, one obtains similar structures, as shown in the bottom inset of Fig. 5, providing the optimal perturbation for $T^+ = 80$ (corresponding to the eddy turnover time at $y^+ = 19$). Whereas, when the target time is increased to a time scale linked to the turnover time at the outer scale, the structure of the optimal perturbation dramatically changes, as shown in the top inset of Fig. 5, providing the optimal perturbation for $T^+ = 305$. For this target time, corresponding to the eddy turnover time at the centerline of the channel, a complex structure is observed, mostly composed of packets of hairpin vortices on top of highly oscillating streamwise streaks. Strong vortical structures with rather different length scales are observed. The small-scale ones, not bearing any spatial symmetry, placed on top of near-wall low-speed streaks with spanwise length close to that of turbulent streaky near-wall structures, $\lambda_z^+ \approx 100$ [45]. Whereas, the largest vortical structures have a spanwise-symmetric shape recalling that of hairpin vortices, with typical wavelengths $\lambda_z^+ \approx 2h$ and $\lambda_x^+ \approx 2.5h$, consistent with the observations of packets of hairpin vortices [46]. This perturbation able to optimize the energy growth in turbulent flows relying on large scale hairpin vortical structures, provides some hints to explain the onset of transient bursts on top

Fig. 5 Mean flow profile (bold solid line), linear law (thin solid line) and logarithmic one, shown together with the nonlinear optimal for $E_0 = 10^{-2}$, $T^+ = 21.94$ (bottom inset) and $E_0 = 10^{-2}$, $T^+ = 305$ (top inset). The green surfaces indicate negative streamwise velocity perturbation, the blue/red ones represent negative/positive streamwise vorticity



of long-living streaks. Bursting events are characterized by ejections and sweeps [46], which can be identified by a high probability density function (PDF) of streamwise and wall-normal velocity disturbances having opposite sign. Computing this PDF at different wall-normal positions for the optimal perturbation at $T^+ = 305$, we can see in Fig. 6 that it is mostly concentrated in the second and fourth quadrants of the $\tilde{u} - \tilde{v}$ plane, indicating the prevalence of ejection and sweep events, exactly as in bursting events. Moreover, this PDF compares very well with that extracted from the DNS of the turbulent flow no matter the y^+ , as shown in the bottom frames of the same figure. It must be also remarked that the PDF of the optimal perturbation computed for much smaller target times (not shown) is similar to the DNS one only at $y^+ = 10$, fading away while moving towards the center of the channel.

Thus, we can conclude that, while the nonlinear optimal disturbances computed for (small) target times typical of the inner flow structures, are representative of the self-sustained wall cycle, the ones computed for larger target times, typical of large-scale structures, are representative of bursting events, which dissipate the energy from the inner to the outer region. To further confirm this, we evaluate the energy exchange using the Reynolds-Orr equation following Ref. [47]. Integrating these equations in the wall-parallel directions one obtains an equation for the wall-normal transport of energy, where the wall-normal energy flux $\phi = \int_{L_x, L_z} \tilde{v} [\tilde{p} + (\tilde{u}^2 + \tilde{v}^2 + \tilde{w}^2)/2] dx dz$ is counter-balanced by the production and dissipation terms $P = \int_{L_x, L_z} -\tilde{u}_i \tilde{u}_j \partial_j \bar{U}_i dx dz$, $D = -\int_{L_x, L_z} \frac{1}{Re} (\partial_j \tilde{u}_i)^2 dx dz$. The time evolution of the net energy production $P(y^+) - D(y^+)$ is provided in Fig. 7 (left). As in fully developed turbulent flows at small values of Re_τ [47], the net energy production remains localized at the inner scale ($y^+ \approx 20$) for most of the time evolution, extending towards the outer layer only at a time slightly lower than the target time. The wall-normal energy flux provided in the right frame clearly indicates an

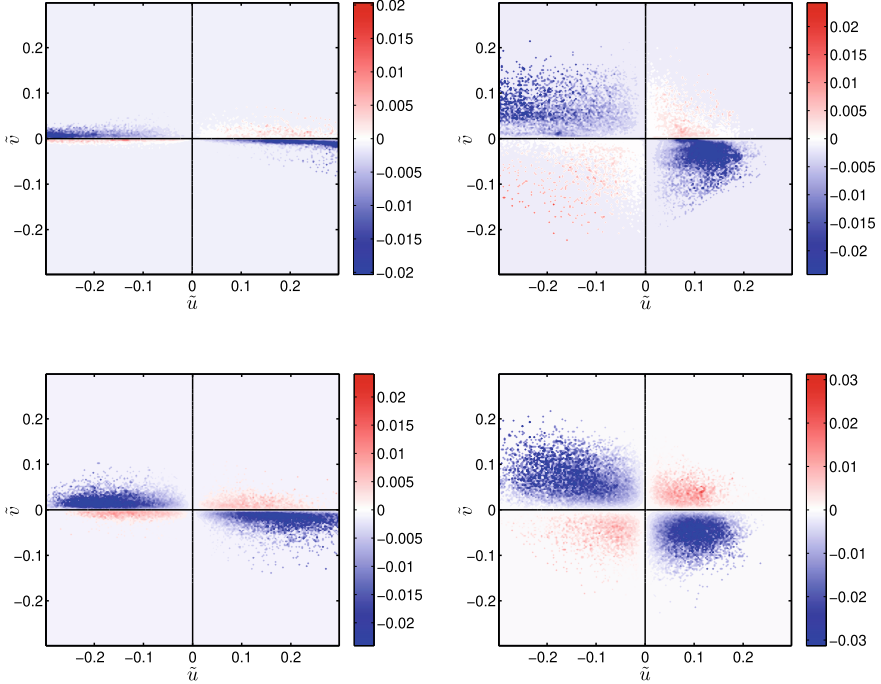


Fig. 6 Premultiplied PDF of the streamwise and wall normal velocities of the optimal structures for $t^+ = T^+ = 305$ (top) and for the fully turbulent flow (bottom) at different constant y^+ -planes: $y^+ = 10$ (left), $y^+ = 50$ (right)

outward flux of energy towards the center of the channel for $t^+ \approx T^+$ corresponding to the formation of the hairpin vortex. At the center of the channel, dissipation exceeds production, and the flux becomes negative. This indicates a transfer of energy from the wall, where energy is produced due to the self-sustained process, to the center of the channel, where energy is dissipated towards the creation of hairpin vortices and/or bursting events. Both these events are characterized by ejections and sweeps, and induce peaks of the kinetic energy. This scenario suggests that the most amplified coherent structures in fully turbulent flows are based on an inverse-cascade process [47], which is typically observed in turbulent flows at small values of Re_τ . Whereas, at larger values of Re_τ a (weaker) production peak is observed also at the outer scale, both in fully turbulent flows [48] and in the corresponding nonlinear optimal perturbations (see the results in Ref. [20] for $Re_\tau = 590$). Future works will aim at extending this analysis to larger values of Re_τ , for which a clear scale separation is observed in the spatial spectra and a second peak of energy production exists at the outer scale.

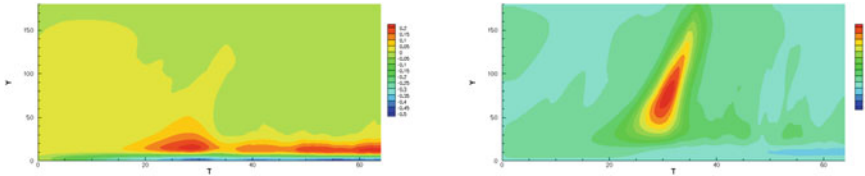


Fig. 7 Time evolution of the net local energy production (left) and of the wall-normal energy flux (right) at each y^+ for the nonlinear optimal disturbance for $T^+ = 305$

4 Conclusions

Subcritical transition in shear flows is due to nonnormality, allowing the transient growth of perturbations, but also to nonlinearity, leading to their breakdown to turbulence. Nonlinear optimization of perturbations of a given base flow is a powerful tool which couples both nonnormality and nonlinearity allowing to unravel: (i) the minimal energy thresholds for transition, (ii) the most amplified coherent structures in transitional and turbulent flows, (iii) heteroclinic orbits connecting different exact coherent states in the chaotic saddle, (iv) how to control transition to turbulence of finite-amplitude perturbations. Once presented the nonlinear optimization framework and reviewed many of its possible applications, this work presents an overview of optimally amplified coherent structures in transitional and turbulent channel flows. In both flow conditions, nonlinear optimal perturbations having the form of hairpin vortices and/or inclined streamwise vortices flanking bent streaks are found, which are recurrent coherent structures for these flows. Thus, in the same way as a linear transient growth analysis on a laminar or on a mean turbulent flow explains the linear growth of streaky structures in transitional turbulent flows [49], a nonlinear optimization approach is a suitable way for studying the most energetic events characterizing these kind of flows, such as bent streaks and hairpin vortices associated with bursting events.

Acknowledgements I would like to aknowledge M. Farano that performed most of the reported computations, J.-C. Robinet and P. De Palma who contributed to some of the reported works.

References

1. Trefethen, L., Trefethen, A., Reddy, S., Driscoll, T., et al.: *Science* **261**(5121), 578 (1993)
2. Schmid, P.J., Henningson, D.S.: *Stability and Transition in Shear Flows*, vol. 142. Springer, Berlin (2001)
3. Manneville, P.: *IUTAM Symposium on Laminar-Turbulent Transition and Finite Amplitude Solutions*, pp. 1–32. Springer, Berlin (2005)
4. Andersson, P., Berggren, M., Henningson, D.S.: *Phys. Fluids* **11**(1), 134 (1999)
5. Luchini, P.: *J. Fluid Mech.* **404**, 289 (2000)
6. Cossu, C.: *Comptes Rendus Mécanique* **333**(4), 331 (2005)

7. Zuccher, S., Luchini, P., Bottaro, A.: *J. Fluid Mech.* **513**, 135 (2004)
8. Zuccher, S., Bottaro, A., Luchini, P.: *Eur. J. Mech.-B/Fluids* **25**(1), 1 (2006)
9. Pringle, C.C.T., Kerswell, R.: *Phys. Rev. Lett.* **105**, 154502 (2010)
10. Cherubini, S., De Palma, P., Robinet, J.C., Bottaro, A.: *Phys. Rev. E* **82**(6), 066302 (2010)
11. Cherubini, S., De Palma, P., Robinet, J.C., Bottaro, A.: *J. Fluid Mech.* **689**, 221 (2011)
12. Rabin, S., Caulfield, C., Kerswell, R.: *J. Fluid Mech.* **712**, 244 (2012)
13. Monokrousos, A., Bottaro, A., Brandt, L., Di Vita, A., Henningson, D.S.: *Phys. Rev. Lett.* **106**, 134502 (2011)
14. Cherubini, S., Robinet, J.C., De Palma, P.: *J. Fluid Mech.* **737**, 440 (2013)
15. Pringle, C.C.T., Willis, A.P., Kerswell, R.R.: *Phys. Fluids* **27**(6), 064102 (2015)
16. Farano, M., Cherubini, S., Robinet, J.C., De Palma, P.: *J. Fluid Mech.* **775**, (2015)
17. Farano, M., Cherubini, S., Robinet, J.C., De Palma, P.: *Fluid Dyn. Res.* **48**, 061409 (2016)
18. Vermach, L., Caulfield, C.P.: *J. Fluid Mech.* **850**, 875 (2018)
19. Farano, M., Cherubini, S., Robinet, J.C., De Palma, P.: *J. Fluid Mech.* **817**, 35 (2017)
20. Farano, M., Cherubini, S., Palma, P.D., Robinet, J.C.: *Eur. J. Mech. - B/Fluids* **72**, 74 (2018)
21. Pringle, C.C., Willis, A.P., Kerswell, R.R.: *J. Fluid Mech.* **702**, 415 (2012)
22. Duguet, Y., Monokrousos, A., Brandt, L., Henningson, D.S.: *Phys. Fluids* **25**(8), 084103 (2013)
23. Cherubini, S., De Palma, P., Robinet, J.C.: *Phys. Fluids* **27**(3), 034108 (2015)
24. Cherubini, S., De Palma, P.: *J. Fluid Mech.* **764**, 572–598 (2015)
25. Rabin, S.M.E., Caulfield, C.P., Kerswell, R.R.: *J. Fluid Mech.* **738**, R1 (2014)
26. Passaggia, P., Ehrenstein, U.: *Eur. J. Mech.-B/Fluids* **41**, 169 (2013)
27. Xiao, D., Papadakis, G.: *Phys. Fluids* **29**(5), 054103 (2017)
28. Olvera, D., Kerswell, R.R.: *Phys. Rev. Fluids* **2**, 083902 (2017)
29. Farano, M., Cherubini, S., Robinet, J.C., De Palma, P., Schneider, T.M.: *J. Fluid Mech.* **858**, R3 (2019)
30. Kerswell, R.R., Pringle, C.C.T., Willis, A.P.: *Rep. Prog. Phys.* **77**, 085901 (2014)
31. Kerswell, R.: *Ann. Rev. Fluid Mech.* **50**(1), 319 (2018)
32. Cherubini, S., Robinet, J.C., Bottaro, A., De Palma, P.: *J. Fluid Mech.* **656**, 231 (2010)
33. Foures, D., Caulfield, C., Schmid, P.: *J. Fluid Mech.* **729**, 672 (2013)
34. Xiao, D., Papadakis, G.: *J. Fluid Mech.* **861**, 524 (2019)
35. Farano, M., Cherubini, S., Robinet, J.C., De Palma, P., Schneider, T.M.: *Phys. Rev. Lett.* submitted to (2019)
36. Schneider, T.M., Gibson, J.F., Lagha, M., De Lillo, F., Eckhardt, B.: *Phys. Rev. E* **78**, 037301 (2008)
37. Halcrow, J., Gibson, J.F., Cvitanović, P., Viswanath, D.: *J. Fluid Mech.* **621**, 365 (2009)
38. Eitel-Amor, G., Örlü, R., Schlatter, P., Flores, O.: *Phys. Fluids* **27**(2), 025108 (2015)
39. Fischer, P., Lottes, J., Kerkemeir S.: nek5000 Web pages (2008). <http://nek5000.mcs.anl.gov>
40. Deville, M.O., Fischer, P.F., Mund, E.H.: *High-Order Methods for Incompressible Fluid Flow*, vol. 9. Cambridge University Press, Cambridge (2002)
41. Cherubini, S., De Palma, P.: *J. Fluid Mech.* **716**, 251 (2013)
42. Hamilton, J.M., Kim, J., Waleffe, F.: *J. Fluid Mech.* **287**, 317 (1995)
43. Orr, W.M.: *Proceedings of the Royal Irish Academy*, pp. 69–138. Mathematical and Physical Sciences, Section A (1907)
44. Landahl, M.: *J. Fluid Mech.* **98**(02), 243 (1980)
45. Zhou, J., Adrian, R.J., Balachandar, S., Kendall, T.: *J. Fluid Mech.* **387**, 353 (1999)
46. Adrian, R.J.: *Phys. Fluids* (1994–present) **19**(4), 041301 (2007)
47. Jiménez, J.J., Pinelli, A.: *J. Fluid Mech.* **389**, 335 (1999)
48. Lee, M., Moser, R.D.: *J. Fluid Mech.* **774**, 395 (2015)
49. Pujals, G., García-Villalba, M., Cossu, C., Depardon, S.: *Phys. Fluids* **21**(1), 015109 (2009)

Predicting Laminar-Turbulent Transition Influenced by Surface-Induced Flow Distortions



J. D. Crouch

Abstract Approaches to transition prediction are considered within the context of applications to aircraft, where surface-induced distortions are an integral part of the boundary-layer flow. Different routes to transition are discussed as a function of the type and level of surface irregularity perturbing the flow. Amplitude methods offer the best potential for predicting the gradual movement of transition with increasing levels of flow distortion. Global stability analysis offers the potential for capturing abrupt transition near the source of the flow distortion (typically characterized as bypass transition). A semi-empirical amplitude method, based on a combination of stability theory and experiments, is considered for a-priori predictions to capture gradual changes to transition for realistic surface irregularities. This predictive framework is then used to characterize the different mechanisms and flow regimes responsible for boundary-layer transition in the presence of surface steps and gaps.

1 Introduction

Laminar-turbulent transition has long been a topic of fundamental interest in fluid mechanics, offering insights into the origins of complexity and the potential for better understandings of turbulence itself. Over the past several decades, much of the transition research has been motivated by potential applications to air vehicles (e.g. for laminar flow control to reduce airplane drag). However, even with a narrowly-focused target application, progress in the fundamental understanding of transition is essential for developing robust prediction methodologies that are critical enablers for air-vehicle applications.

Motivated by energy-availability concerns in the 1970s, significant investments were made in laminar-flow technology to reduce aircraft fuel burn [1]. This led to many advances in the fundamental understanding of transition, but no broad appli-

J. D. Crouch (✉)
The Boeing Company, Seattle, WA, USA
e-mail: jeffrey.d.crouch@boeing.com

cation of laminar flow control to transonic commercial aircraft. The last two decades have seen the first targeted applications of laminar flow control to large commercial transports and this has elevated interest in boundary-layer transition at low-speed and transonic-flow conditions [2, 3].

Laminar flow control requires a delicate balance between the aerodynamic design, the structural design and manufacture, and the in-service operability of the aircraft [2]. Of course the aerodynamic design is dependent on predictions for the extent of laminar flow under varied flow conditions, and this has been a key motivator for transition research and for high-fidelity transition modeling. Equally important to its role in establishing the nominal performance, transition modeling is essential to the development of requirements for build quality, and for assessing the robustness of the in-service performance. To this end, transition modeling must account for the influence of different surface irregularities (e.g. features such as protrusions or steps or gaps) that are a byproduct of the aircraft production or the in-service operation.

Surface irregularities introduce flow distortions to the idealized smooth-surface boundary layer. These flow distortions are an integral part of the boundary-layer flow, and must be incorporated in any airplane-level predictions.

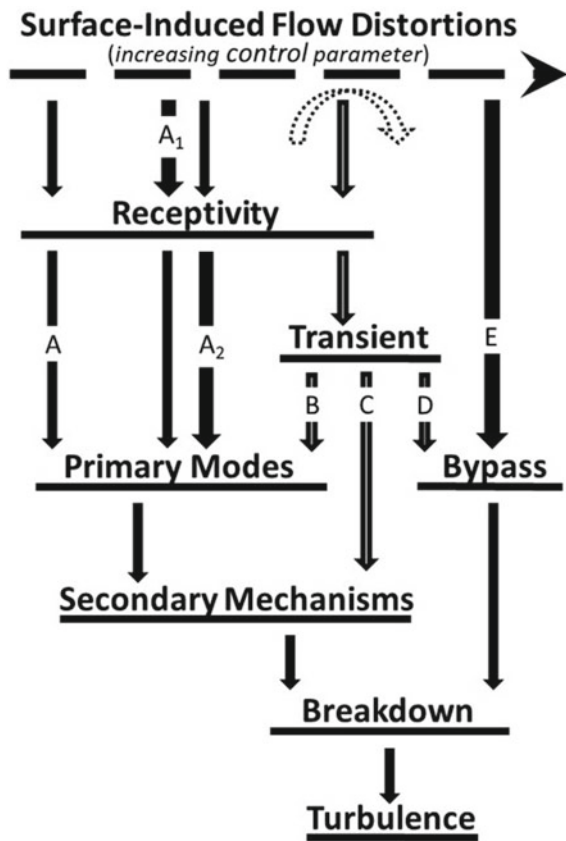
2 Paths to Transition

In order to establish a framework for transition modeling and prediction aimed at aircraft applications, we revisit the roadmap developed by Morkovin et al. describing the different paths to transition [4]. While they considered the more general case of transition in open flow systems, the focus here is on boundary-layer flows; and, rather than considering the full spectrum of potential environmental disturbances (including free-stream turbulence, noise, etc.), we focus on the influence of surface-induced flow distortions within a low free-stream-disturbance environment characteristic of flight. Figure 1 shows the different paths to transition, where the transition movement can be ‘gradual’ or ‘abrupt’ with an increasing control parameter such as step height or surface roughness level. The path to transition depends on the surface irregularity as well as the primary mode of instability (e.g. Tollmien-Schlichting waves, cross-flow vortices).

The path A is the primary-mode path for a smooth surface in a low-disturbance environment (just as described in [4]). With increasing levels of flow distortion, a few key distinctions are visible relative to the original—more general—diagram. The paths A_1 and A_2 signify enhanced receptivity and enhanced instability growth, respectively. The dashed arrow above B , C and D indicates that while transient mechanisms occur, they may not play a role in moving the transition location. The transition may jump from path A_1 or A_2 directly to path E . In the case of large flow distortions, bypass transition E does not require receptivity, but rather results from a local ‘oscillator’ or global flow instability.

An example of the A_1 path is cross-flow transition with increasing levels of surface roughness, as considered in the experiments of Radeztsky et al. [5] and Kachanov

Fig. 1 Diagram showing the paths to transition in boundary layers in low-disturbance environments with increasing level of surface-induced flow distortion (after the more general version of [4]). Example control parameters include step height, gap depth and width, and roughness level



et al. [6, 7]. As the level of roughness is increased, the transition resulting from stationary crossflow instability moves forward. The surface roughness has the ability to directly excite the stationary crossflow instabilities [8]. This behavior is very well captured by scaling the initial instability amplitude with the rms roughness level normalized by the boundary-layer thickness at the instability neutral point [7, 9].

An example of the A_2 path is transition due to Tollmien-Schlichting waves in the presence of a forward- or backward-facing step (e.g. [10–19]). As the step height is increased, the transition location moves forward until it ultimately reaches the step location. The transition movement has been linked to localized destabilization of the flow [10–14]. This linkage is further supported by the weak sensitivity of the transition position to the step location in relation to the branch-I neutral point. Transition movement as a result of enhanced receptivity would show a much greater effect for steps near branch-I.

Finally, an example that potentially involves the A_1 , A_2 , C and E paths is transition due to TS-waves in the presence of a 3D protuberance. As the protuberance height is increased, the transition moves forward in a narrow zone behind the protuberance

[20]. This transition movement can result from some combination of receptivity, modified growth, and/or mode interactions [21–23]. The 3D protuberance is also known to result in transient growth [24–26], but in this case the transient growth does not lead to a forward movement in the transition location [26]. Rather, the transition appears unaffected by the transient disturbance (or potentially stabilized [25]) with increasing protuberance height—ultimately jumping forward to the protuberance location. This abrupt movement in transition looks to be well captured by global instability analysis [27–29].

3 Approaches to Predicting Transition

In order to support the intended application to flight vehicles, transition-prediction methods must account for the various paths to transition with differing levels of surface-induced flow distortions. For abrupt transition at the source of the flow distortion, global instability analysis shows the potential for predicting this as a form of bypass as shown in Fig. 1. A range of potential methods for predicting the gradual movement of transition is presented in Fig. 2.

The simplest and oldest methods are based on correlations to a parameter characterizing key features of the boundary-layer flow that influence primary-instability growth (e.g. momentum-thickness Reynolds number). In practice, these methods have largely been supplanted by e^N methods, which calculate the primary-mode growth and correlate the growth factor to an observed transition location from a wind-tunnel or flight test. Amplitude methods link the transition onset to finite disturbances, which can be altered by changes to the receptivity or the instability growth. These methods offer the potential to account for changing environmental inputs, or

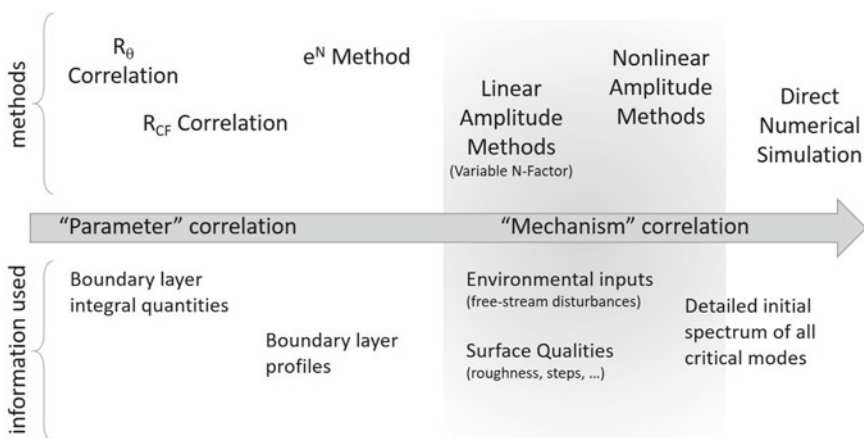


Fig. 2 Methods for predicting transition

alterations of the surface quality. Finally, direct simulation methods offer the potential for capturing all of the essential physics from receptivity to breakdown. However, to benefit from direct simulations a significant amount of information on the initial disturbance spectrum is required—and this may not be available. Thus, amplitude methods are the most promising for predicting the effects of various flow distortions in practice.

3.1 Nonlinear Amplitude Methods

The main elements of a nonlinear amplitude method are shown in the diagram of Fig. 3. The parabolized stability equations provide a good framework for efficiently capturing the linear growth and the nonlinear interactions for weakly-nonparallel boundary layers [30]. Different criteria can be used for defining the transition onset.

An early example of a nonlinear amplitude approach to predicting transition is given in Bertolotti and Crouch [31] for a flat plate with mild surface waviness in the presence of free-stream acoustic disturbances. The PSE are used to capture the entire process from receptivity to transition (based on the criteria of sustained growth). The primary mode of instability is TS waves, and the nonlinear stage includes secondary instabilities. The results show a strong sensitivity to the level of surface waviness for some parameter ranges, leading to large movements in the transition location. This highlights a difficulty of nonlinear methods where small changes in inputs can lead to large variations in the predictions. Typical uncertainties in characterizing the surface quality translate to significant uncertainties in the transition location—potentially offsetting the expected gains from the more complex modeling.

An example of nonlinear amplitude methods used for predicting transition due to crossflow instability is given by Malik et al. [32]. The analysis considered the conditions of the experiment of Reibert et al. [33] for transition resulting from a spanwise row of discrete roughness elements. Initial amplitudes were adjusted for the various modes to provide a good match to the measured amplitudes during the linear growth stage. Very good agreement with the experiments is also seen for the nonlinear-amplitude stage. However, the nonlinear PSE do not provide any obvious demarcation for the onset of transition. Using the nonlinear disturbance field, a sec-

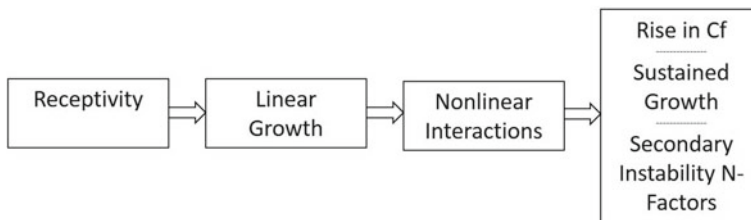


Fig. 3 Elements of a nonlinear amplitude method for transition prediction

ondary instability analysis was conducted. A good correlation was observed between the measured transition and calculated N-factors for the secondary instabilities. This example also shows difficulties that exist when trying to predict transition based on nonlinear amplitudes, which may not be sufficient in themselves.

3.2 Linear Amplitude Methods

The demands of nonlinear-amplitude methods for detailed initial values for the relevant modes, and the associated sensitivity of the transition location to these inputs, suggests that a linear amplitude correlation may provide an efficient alternative. A diagram showing the elements of a linear amplitude method is given in Fig. 4. Similar to the nonlinear amplitude method, the initial amplitudes of instabilities are captured in the receptivity process. However, in this case the transition criteria is based on a correlation to the linear primary-mode amplitude level without the need for information regarding other modes involved in the nonlinear development [34]. This reduces the demands and the sensitivity around the characterization of environmental inputs and surface qualities influencing the receptivity.

Application of this approach can be effective for capturing changes in the transition due to varied free-stream acoustics for transition due to TS waves (e.g. [35]). Application to crossflow transition is more complex. The receptivity and linear growth can be well captured [36], and the movement of transition can be estimated. However, there are some cases where increasing initial amplitudes of discrete modes leads to a downstream—rather than an upstream—movement in transition. This is the basis for using discrete roughness elements to delay transition, which is at odds with a linear amplitude prediction [33]. This mixed success for narrowband disturbances does not carry over to broadband disturbances, where the approach is expected to be more effective. For a broadband initial amplitude distribution $A_0(\omega, \beta)$, the downstream amplitude is given by

$$A(x; \omega, \beta) = A_0(\omega, \beta)e^{m(x; \omega, \beta)}, \quad (1)$$

and transition is predicted to occur when $A(x; \omega, \beta) \geq A_T$.

For general broadband disturbances (characterized by a uniform primary-mode spectrum at the neutral-point location), the linear-amplitude method can be recast in the form of a variable N-factor method. This implies a weak filtering due to receptivity, which is consistent with observed receptivity coefficients for both TS



Fig. 4 Elements of a linear amplitude method for transition prediction

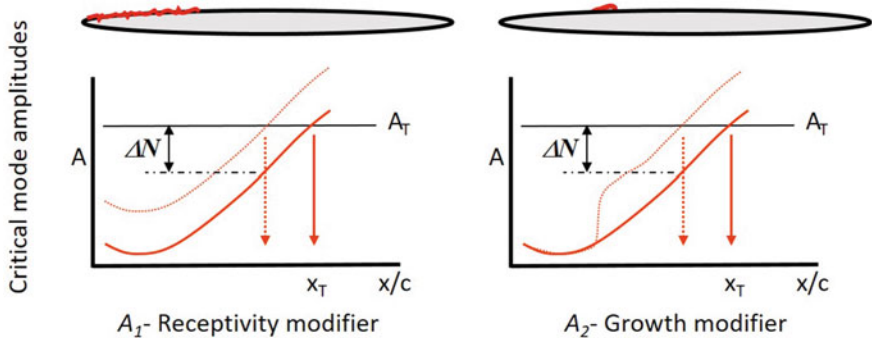


Fig. 5 Schematic showing linkage between a linear amplitude method and the variable N-factor approach

waves [8] and crossflow vortices [36, 37]. Using the envelope n of the physical-mode growth curves m , the amplitude threshold can be expressed as

$$n(x) = \max_{\omega} \max_{\beta} [m(x; \omega, \beta)] \geq N, \quad (2)$$

where $N \propto \ln(A_T/A_0)$. The value of N can be linked to a reference condition with $N = N_{ref} - \Delta N$, where ΔN captures changes to A_0 or to $\Delta m_{crit}(x_T)$. Figure 5 illustrates the linkage between ΔN and the linear amplitude for both paths A_1 and A_2 . The solid line in the figures corresponds to a critical mode causing transition for a given reference condition. The dashed line corresponds to a critical mode arising from enhanced receptivity or enhanced growth. In both cases, the forward movement of transition can be linked to a change in the transition N-factor ΔN .

The variable N-factor approach provides a method for a-priori predictions to account for varying surface-induced flow distortions. This method can also be used to interrogate experimental data sets to better understand potential mechanisms influencing transition movement.

4 Model Prediction as a Tool for Understanding

Combining linear stability theory for variable N-factor predictions with transition measurements, we can infer local effects on the primary modes resulting from the flow distortions. Inconsistencies with an otherwise robust prediction model provide evidence for some form of bypass to the primary-mode transition (e.g. transition along path E). Focusing on nominally 2D boundary-layer flows with TS waves as the primary mode causing transition, we revisit the effects of steps and gaps on transition.

4.1 Revisiting Step Effects on TS-Dominated Transition

Two earlier studies on step effects show that the transition movement can be linked to the step height through a change in the transition N-factor [15, 16]. A predictive model for the step effects is given in Crouch et al. [16] for both forward-facing steps (FFS) and backward-facing steps (BFS),

$$\text{FFS} : \quad \Delta N_{TS} = 1.6 \cdot h_{FFS}/\delta^*, \quad (3)$$

$$\text{BFS} : \quad \Delta N_{TS} = 4.4 \cdot h_{BFS}/\delta^*. \quad (4)$$

A more-recent study by Crouch and Kosorygin [19] examined the applicability of this model for capturing the effects of wide gaps or tape strips (rectangular protrusions) via superposition of two steps. Since Eqs. (3) and (4) show the BFS to have a much-greater influence than the FFS, the different surface irregularities were oriented such that the BFS is at the same streamwise position—as shown in Fig. 6a. Results for the isolated step, the tape and the gap are all shown in Fig. 6b. The ΔN_{TS} is plotted as a function of the BFS height nondimensionalized by the boundary-layer displacement thickness δ^* at the BFS location. The solid line is from Eq. (4). The isolated step and the gap are in good agreement with each other and with the prediction. This suggests that the downstream FFS in the gap does not play a significant role. The results for the tape, however, show a significantly greater effect than predicted by the BFS model.

The results of Fig. 6b are replotted in Fig. 7 as a function of the predicted $\Delta N_{TS} = 4.4h_{BFS}/\delta^* + 1.6h_{FFS}/\delta^*$, which includes a contribution from the FFS normalized by its local displacement thickness. The plot shows the measured tape results to

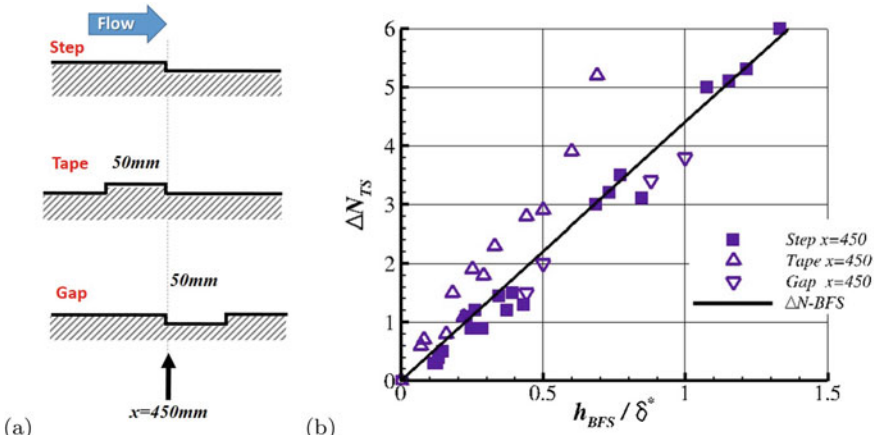
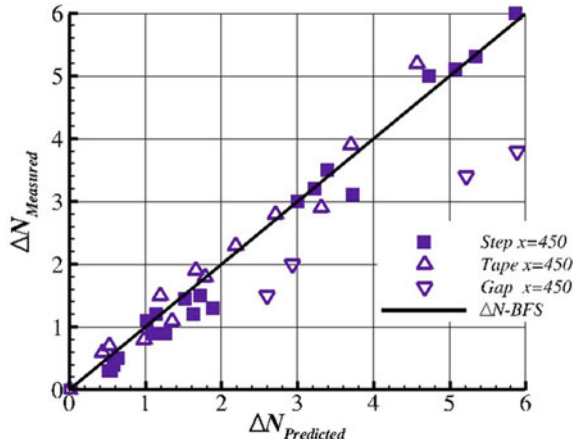


Fig. 6 **a** Schematic showing relative positions of step, tape and gap for assessing superposition of steps. **b** Variation of the TS-wave N-factor as a function of the BFS height. (from [19])

Fig. 7 Variation of the TS-wave N-factor as a function of the predicted value, including both the BFS and the FFS for the tape and the gap. (from [19])



be in very good agreement with the predictions, highlighting the importance of the FFS for the tape. In contrast, the inclusion of the FFS for the gap results in a significant overprediction of the effects. This further supports the observation that the downstream FFS in a wide gap does not play an important role in modifying the transition location.

Another question regarding the generalization of Eqs. (3) and (4) is how dependent the results are on the streamwise location of the steps. This was also considered in Crouch and Kosorygin [19]. Figure 8 shows a comparison between measured and predicted N-factor variations for steps at several positions between the instability neutral point and the smooth-surface transition location. For these predictions, the tape results include both the BFS and the FFS, but the gap results only include the BFS. The overall comparison looks very good, showing weak sensitivity to streamwise position. There does appear to be a small reduction in the ΔN_{TS} at the most downstream location, which has been linked to the level of instability growth between the step and the nominal transition location [19]. This is consistent with earlier observations of Costantini et al. [17], where they determined the ΔN_{TS} to be approximately 0.5 below the prediction from [16].

4.2 Gap Effects on TS-Dominated Transition

A recent investigation of Crouch et al. [38] follows a similar approach of combining a variable N-factor model with experimental data to study the effects of gaps on TS-wave transition. A large database was gathered over multiple wind-tunnel entries, including a wide range of gap characteristics. The high-level impact of the gaps on transition is shown in Fig. 9. The gap width w and depth d are nondimensionalized by the displacement thickness at the upstream edge of the gap. The different symbols

Fig. 8 Variation of the TS-wave N-factor as a function of the predicted value for steps at various streamwise positions. (from [19])

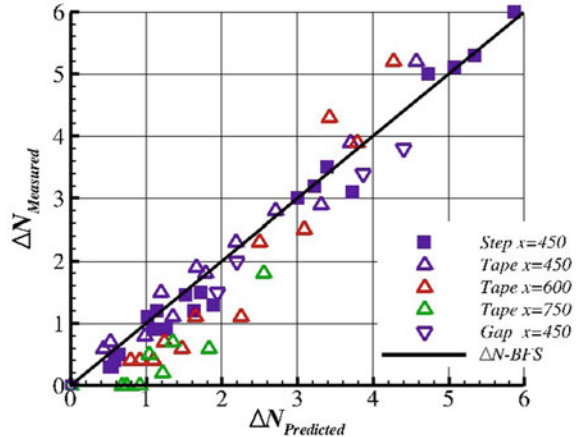
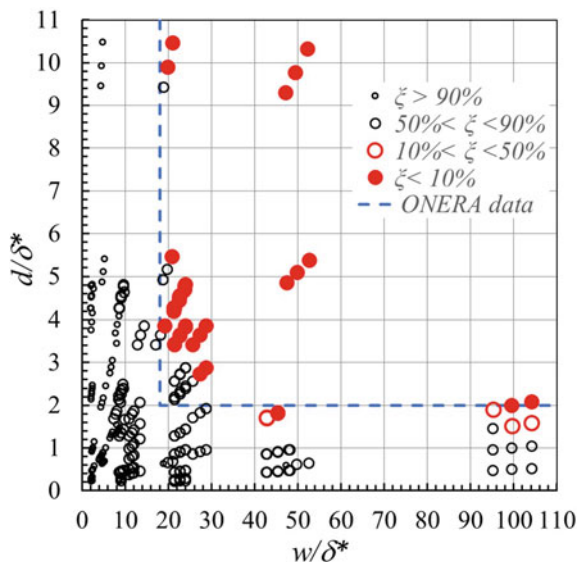


Fig. 9 Transition movement (characterized by ξ) for different combinations of gap width w and depth d . (from [38])



correspond to different values of the normalized transition length ξ , defined by $\xi = (x_T - x_G)/(x_{T0} - x_G)$, where x_G is the streamwise position of the gap, x_T is the transition location in the presence of the gap, and x_{T0} is the transition location in the absence of the gap. The small open symbols correspond to $\xi > 0.9$, where the gap has a minimal effect on transition. The intermediate and large open symbols correspond to $0.5 < \xi < 0.9$ and $0.1 < \xi < 0.5$, respectively. The solid symbols correspond to $\xi < 0.1$, where transition is essentially at the gap location—potentially as a result of some form of bypass mechanism. The dashed line shows the boundary for gaps resulting in transition at the gap location from a series of experiments at ONERA [39], in good agreement with [38].

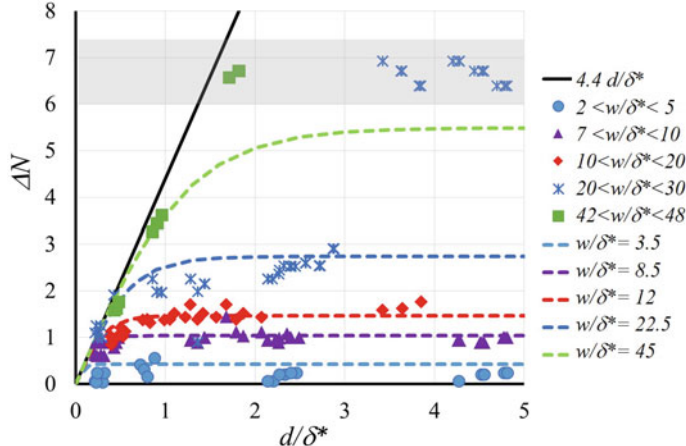


Fig. 10 Variation of the TS-wave N-factor as a function of gap depth for different values of the gap width. (from [38])

A subset of the data shown in Fig. 9 corresponding to gaps located in an adverse pressure gradient downstream of the instability neutral point is replotted in Fig. 10 in terms of the calculated ΔN_{TS} as a function of the gap depth. The different symbols correspond to experimental data at different gap widths. The solid line shows the predicted ΔN_{TS} based on a BFS of height d , and the shaded region around $\Delta N_{TS} \approx 7$ corresponds to the N-factor range that would result in transition at the gap location. A detailed examination of the results shows that the gap effects on TS-wave transition show two distinct trends: one for shallow gaps, and one for deep gaps [38].

Shallow gaps behave like a BFS, as discussed in Sect. 4.1. The ΔN_{TS} varies with the gap depth, but is independent of the gap width. For deep gaps, the ΔN_{TS} varies with width, but is independent of the gap depth. This leads to the N-factor variation model given by:

$$\Delta N_{TS} = 4.4 \cdot d/\delta^* \quad : \text{shallow gaps}, \quad (5)$$

$$\Delta N_{TS} = 0.12 \cdot w/\delta^* \quad : \text{deep gaps}. \quad (6)$$

The dashed lines in Fig. 10 are model predictions that capture the limiting behavior of Eqs. (5) and (6) with a demarcation between shallow and deep gaps at $w/d = 36$. This model appears to capture all but the most extreme movements in transition. Transition movements that are significantly out of line with this predicted TS-wave behavior can be linked to some form of bypass transition. Recent work has shown the existence of a global instability [40], which is likely responsible for this bypass behavior.

5 Conclusions

Transition prediction methods used to support aircraft applications must account for varying levels of surface irregularities. At low levels, these irregularities introduce steady flow distortions into the boundary layer. Depending on the level of the flow distortion, the transition to turbulence can follow different paths resulting in the forward movement of transition and a reduction in the extent of laminar flow. Any robust prediction must acknowledge and account for the different transition paths.

Amplitude methods, which attempt to predict the finite amplitudes of primary-instability modes, offer a viable framework for capturing the effects of flow distortions. Nonlinear amplitude methods have been shown to capture the critical physics leading to transition, but their application has been limited by their increase in complexity and their greater demands for (often unknown) environmental inputs. Linear amplitude methods forfeit details of the late-stage disturbance evolution in exchange for a less-demanding characterization of the environmental inputs.

For conditions where the initial spectrum of disturbances can be assumed to be nearly uniform, the linear amplitude approach can be simplified to a variable N-factor method. This approach is used to consider two typical sources of flow distortion: surface steps and surface gaps. Results show the variable N-factor approach provides an a-priori predictive capability, which can also be used to interrogate physical mechanisms causing transition.

Acknowledgements This paper has benefited from long-standing collaborations with Lian Ng and Mary Sutanto at The Boeing Company, and Vladimir Kosorygin at the Khristianovich Institute of Theoretical and Applied Mechanics, Novosibirsk.

References

1. Joslin, R.D.: Aircraft laminar flow control. *Ann. Rev. Fluid Mech.* **30**, 1–29 (1998)
2. Crouch, J.D.: Boundary-Layer Transition Prediction for Laminar Flow Control. AIAA Paper No 2015–2472 (2015)
3. Malik, M.R., Crouch, J.D., Saric, W.S., Lin, J.C., Whalen, E.A.: Application of drag reduction techniques to transport aircraft. In: *Encyclopedia of Aerospace Engineering*, Wiley, New York (2015)
4. Morkovin, M.V., Reshotko, E., Herbert, Th: Transition in open flow systems—a reassessment. *Bull. Am. Phys. Soc.* **39**, 1882 (1994)
5. Radeztsky, R.H., Reibert, M.S., Saric, W.S., Takagi, S.: Effect of micro-sized roughness on transition in swept-wing flows. AIAA Paper No 93-0076 (1993)
6. Borodulin, V.I., Ivanov, A.V., Kachanov, Y.S.: Scenarios of swept-wing boundary-layer transition in presence of various kinds of freestream turbulence and surface roughness. In: Medeiros, M. (ed.) *Procedia IUTAM*, vol. 14, pp. 283–294 (2015)
7. Crouch, J.D., Ng, L.L., Kachanov, Y.S., Borodulini, V.I., Ivanov, A.V.: Influence of surface roughness and free-stream turbulence on crossflow-instability transition. In: Medeiros, M. (ed.) *Procedia IUTAM*, vol. 14, pp. 295–302 (2015)
8. Crouch, J.D.: Theoretical studies on the receptivity of boundary layers. AIAA Paper No 94–2224 (1994)

9. Crouch, J.D., Ng, L.L.: Variable N-factor method for transition prediction in three-dimensional boundary layers. *AIAA J* **38**, 211–216 (2000)
10. Klebanoff, P.S., Tidstrom, K.D.: Mechanism by which a two-dimensional roughness element induces boundary-layer transition. *Phys. Fluids* **15**, 1173–1188 (1972)
11. Nayfeh, A.H.: Influence of two-dimensional imperfections on laminar flow. SAE Paper No 921990 (1992)
12. Parraud, J., Seraudie, A.: Effects of steps and gaps on 2-D and 3-D transition. *ECCOMAS 2000*, Barcelona (2000)
13. Wörner, A., Rist, U., Wagner, S.: Humps/steps influence on stability characteristics of two-dimensional laminar boundary layer. *AIAA J* **41**, 192–197 (2003)
14. Wu, X., Dong, M.: A local scattering theory for the effects of isolated roughness on boundary-layer instability and transition: transmission coefficient as an eigenvalue. *J. Fluid Mech.* **794**, 69–108 (2016)
15. Wang, Y.X., Gaster, M.: Effect of surface steps on boundary layer transition. *Exp. Fluids* **39**, 679–686 (2005)
16. Crouch, J.D., Kosorygin, V.S., Ng, L.L.: Modeling the effects of steps on boundary-layer transition. In: Govindarajan, R. (ed.) *IUTAM Symposium on Laminar-Turbulent Transition*, pp. 37–44 (2006)
17. Costantini, M., Risius, S., Klein, C.: Experimental investigation of the effect of forward-facing steps on boundary layer transition. In: Medeiros, M. (ed.) *Procedia IUTAM*, vol. 14, pp. 152–162 (2015)
18. Schrauf, G.: On allowable step heights: lessons learned from the F100 and ATTAS flight tests. *ECCM 6, ECFD 7*, Glasgow (2018)
19. Crouch, J.D., Kosorygin, V.S.: Surface-step effects on boundary-layer transition dominated by Tollmien-Schlichting Instability. *AIAA J*, **58**, 2943–2950 (2020). <https://doi.org/10.2514/1.J058518>
20. Kosorygin, V.S., Crouch, J.D., Ng, L.L.: Transition movement in the wake of protruding and recessed three-dimensional surface irregularities. In: Schlatter (ed.) *Seventh IUTAM Symposium on Laminar-Turbulent Transition*, pp. 213–218 (2010)
21. Crouch, J.D.: Excitation of secondary instabilities in boundary layers. *J. Fluid Mech.* **336**, 245–266 (1997)
22. Plogmann, B., Werner, W., Krämer, E.: Nonlinear mode interactions in the wake of a medium height roughness element In: Medeiros M (ed) *Procedia IUTAM*, vol. 14, pp. 423–432 (2015)
23. de Paula, I.B., Würz, W., Mendonça, M.T., Medeiros, M.A.F.: Interaction of instability waves and a three-dimensional roughness element in a boundary layer. *J. Fluid Mech.* **824**, 624–660 (2017)
24. White, E.B., Ergin, F.G.: Receptivity and transient growth of roughness-induced disturbances. *AIAA Paper No 2003-4243* (2003)
25. Fransson, J.H.M., Brandt, L., Talamelli, A., Cossu, C.: Experimental study of the stabilization of Tollmien-Schlichting waves by finite amplitude streaks. In: Govindarajan, R. (ed.) *IUTAM Symposium on Laminar-Turbulent Transition*, pp. 299–304 (2006)
26. Choudhari, M., Fischer, P.: Roughness-induced transient growth. *AIAA Paper No 2005-4765* (2005)
27. Loiseau, J.C.H., Robinet, J.C.H., Cherubini, S., Leriche, E.: Global stability analyses unravelling roughness-induced transition mechanisms. In: Medeiros, M. (ed.) *Procedia IUTAM*, vol. 14, pp. 182–191 (2015)
28. Citro, V., Luchini, P., Giannetti, F., Auteri, F.: Boundary-layer flows past an hemispherical roughness element: DNS, global stability and sensitivity analysis. In: Medeiros, M. (ed.) *Procedia IUTAM*, vol. 14, pp. 173–181 (2015)
29. Puckert, D.K., Rist, U.: Experiments on critical Reynolds number and global instability in roughness-induced laminar-turbulent transition. *J. Fluid Mech.* **844**, 878–904 (2018)
30. Herbert, Th: Parabolized stability equations. *Ann. Rev. Fluid Mech.* **29**, 245–283 (1997)
31. Bertolotti, F.P., Crouch, J.D.: Simulation of boundary-layer transition: receptivity to spike stage. In: Hirsch, C.H. (ed.) *Computational Fluid Dynamics 1992*, pp. 183–190 (1992)

32. Malik, M.R., Li, F., Choudhari, M.M., Chang, C.-L.: Secondary instability of crossflow vortices and swept-wing boundary-layer transition. *J. Fluid Mech.* **399**, 85–115 (1999)
33. Reibert, M.S., Saric, W.S., Carrillo, R.B., Chapman, K.L.: Experiments in nonlinear saturation of stationary crossflow vortices in a swept-wing boundary layer. AIAA Paper No 96-0184 (1996)
34. Mack, L.M.: Transition prediction and linear stability theory. In: Laminar-Turbulent Transition, AGARD CP 224:1/1-22 (1977)
35. Crouch, J.D.: Transition prediction and control for airplane applications. AIAA Paper No 97-1907 (1997)
36. Ng, L.L., Crouch, J.D.: Roughness-induced receptivity to crossflow vortices on a swept wing. *Phys. Fluids* **11**, 432–438 (1999)
37. Gaponenko, V.R., Ivanov, A.V., Kachanov, Y.S., Crouch, J.D.: Swept-wing boundary-layer receptivity to surface non-uniformities. *J. Fluid Mech.* **461**, 93–126 (2002)
38. Crouch, J.D., Kosorygin, V.S., Sutanto, M.I.: Modeling gap effects on transition dominated by Tollmien-Schlichting instability. AIAA Paper No 2020-3075 (2020)
39. Beguet, S., Perraud, J., Forte, M., Brazier, J-Ph: Modeling of transverse gaps effects on boundary-layer transition. *AIAA J. Aircraft* **54**, 794–801 (2017)
40. Mathias, M.S., Medeiros, M.A.F.: Global instability analysis of a boundary layer flow over a small cavity. AIAA Paper No 2019-3535 (2019)

40 Years of Transition Research at NASA: A Personal Perspective



Mujeeb R. Malik

Abstract An overview of the laminar-turbulent transition research conducted by the author and his colleagues at NASA during the past few decades is presented in this paper. This includes development of computational methods for compressible stability analysis, linear and nonlinear parabolized stability equations, development of quiet supersonic and hypersonic tunnels, supersonic and hypersonic boundary layer transition prediction including the effects of nose bluntness and gas chemistry, resolution of cone-to-flat plate transition controversy, instability and transition in rotating disk flow, secondary instability of Görtler and crossflow disturbances and instability of the attachment-line boundary layer. As a result of the computational and experimental research conducted at NASA, the understanding of transition mechanisms was greatly enhanced and prediction tools developed for across the speed regime. The research also provided the necessary foundation for additional developments by the transition community to solve this challenging problem in fluid dynamics.

1 Introduction

It has now been 50 years since Leslie Mack [1] published his landmark report on compressible boundary layer stability where he provided detailed numerical results for flat plate boundary layers at Mach numbers up to 10. These results have stood the test of time and continue to remain of fundamental significance for boundary layer transition, particularly for hypersonic flows where the second mode, first discovered by him, plays an important role in transition and have stimulated sustained computational and experimental research efforts even to this day.

There are two important modes of instability present in a two-dimensional (2D) or axisymmetric compressible boundary layer. The first mode is an extension to high speeds of the Tollmien-Schlichting (TS) instability present in incompressible flows, though for supersonic Mach numbers it differs in one aspect in that it is most amplified

M. R. Malik (✉)

NASA Langley Research Center, Hampton, VA 23681, USA

e-mail: m.r.malik@nasa.gov

when oblique. This mode represents viscous instability at low Mach numbers, but the inviscid nature of the instability begins to dominate when Mach number increases since 2D compressible boundary-layer profiles contain a generalized inflection point (i.e., $d/dy(\rho du/dy) = 0$ at some point in the boundary layer). This mode may be stabilized by wall cooling, suction and a favorable pressure gradient. The second mode is the result of an inviscid instability, which is present owing to a region of supersonic mean flow relative to the disturbance phase velocity. In fact, when this supersonic relative flow is present, there exist an infinite number of modes in the boundary layer. However, the first mode belonging to this family, commonly known as Mack's second mode, is most relevant, since it is known to have the highest growth rate. The second mode becomes important at Mach numbers above about 4 and has growth rates much higher than the first mode. The existence of both the first and second modes was established by the experiments of Kendall [2]. The second mode is different in character with respect to the first mode; it is most amplified when two-dimensional and is destabilized with wall cooling [3, 4]. It was found by Malik [5] that this mode can be stabilized with wall suction and a favorable pressure gradient. Fedorov et al. [6] showed that surface porosity could be used to control the mode growth owing to its acoustic nature. Fedorov and Khokholov [7] studied the role of slow and fast acoustic waves in initiating the instability modes and their subsequent development in hypersonic boundary layers.

Other boundary layer instability modes, relevant in both incompressible and compressible boundary layers, are Görtler and crossflow disturbances. Imbalance of centrifugal forces induces Görtler instability that manifests itself in the form of counterrotating streamwise vortices. The study of this instability is of practical significance in the presence of concavely curved walls or streamlines. Crossflow instability, relevant in three-dimensional (3D) boundary layers, often results in the formation of stationary corotating vortices commonly called crossflow vortices. This phenomenon is observed in swept-wing boundary layers, rotating disks, elliptic cones and other 3D flows, where inviscid streamlines are curved in the planes parallel to the solid surface. Associated with this streamline curvature is a pressure gradient that acts in a direction normal to the streamlines and introduces a secondary flow within the boundary layer. This secondary flow, commonly known as crossflow, is subject to inviscid instability due to the presence of an inflection point and is the reason for crossflow instability to exist.

Boundary layers act as amplifiers of the instability modes resulting in sufficiently large disturbances that lead to breakdown to turbulence. An empirical approach was devised by Smith and Gamberoni [8] and van Ingen [9] to correlate transition onset location with linear amplification of the relevant boundary layer disturbances. The disturbance amplification ratio, N is computed as $N = \int \sigma \cdot dx$, where σ is the disturbance growth rate, which is integrated along an appropriate direction x . By comparing against low speed experimental transition data, it was found that transition location could be correlated with an N value of about 9. This is the basis of the N factor method.

However, laminar-turbulent transition on aerodynamic surfaces occurs over a wide range of Reynolds number limits; the upper limit relevant in extremely

low-disturbance environments, and the lower limit being the “bypass transition”, Morkovin [10]. The N factor method for transition prediction is relevant only when transition occurs in low disturbance environment on smooth surfaces. Additional experimental information or direct numerical simulations are required to determine the departure from that limit and/or the lower bound. Computational tools (receptivity theory/linear Navier–Stokes, nonlinear parabolized stability equations, direct numerical simulation) are now available to estimate the departure from the upper limit due to factors such as surface roughness, free stream disturbances (acoustic, turbulence, etc.) and modern experimental techniques have helped validate these approaches and this process continues. There have been attempts at developing variable N factor methods to account for the effects of free stream turbulence and surface roughness (cf. Ref. [11, 12]).

I started working at the NASA Langley Research Center as a Research Associate almost 40 years ago. Although, I had no prior knowledge in stability theory, compressible or otherwise, my first task was to develop a compressible stability analysis code that could be routinely used in industry for laminar flow control studies by engineers who are not generally well-versed in the stability theory. This led to the development of the COSAL code [13], which was followed by additional computational developments and applications to a variety of flow configurations, and this paper is meant to provide a brief summary of those contributions.

It should be noted that boundary-layer transition is a complex subject that offers many challenges for a fluid dynamicist owing to multiple disturbance sources, receptivity mechanisms and vehicle surface conditions. The subject has drawn a great deal of attention in the past four decades because of its relevance to laminar flow control (LFC) technology and, particularly, due to its application to aerothermal design of hypersonic vehicles. This latter application stimulated heightened research activities about 30 years ago during the National Aero-Space Plane (NASP) Program, in which I was assigned a leading role to develop the relevant prediction technology. The second resurgence in hypersonic transition research in United States has been more recent under the sponsorship of the Department of Defense. This review is not meant to be exhaustive and mostly covers the work of the author, his colleagues, and that of other associates, but reference is made to other works where appropriate. Some early comprehensive reviews on the subject have been given by Reshotko [14], Arnal et al. [15], Reed et al. [16] and Malik et al. [17]. Recommendations for hypersonic flight transition experiments have been provided by Berry et al. [18].

2 Computational Methods for Compressible Stability Analysis

The governing, quasiparallel linear stability equations for compressible boundary layers can be written as a system of 5 ordinary differential equations, Malik and Orszag [19, 20]. Mack [1, 3] recast these as a system of 8 first-order equations

to obtain the numerical solution with an initial guess for the eigenvalue (complex frequency or wavenumber, given the other parameter). The numerical method that he used, and followed by others, was based on an initial value approach where the Runge–Kutta method was used and integration of the discretized equations started in the free stream and marched to the wall with the desired eigenvalue determined by an iterative procedure. To overcome the associated parasitic growth of the independent solutions, the method of Gram–Schmidt orthonormalization [21] was adopted. This approach, commonly known as the “shooting” method, was suitable for computer hardware available at the time as it required little computer memory; however, it generally required a very good guess of the eigenvalue that is not readily available for boundary layers over more complex configurations.

In Ref. [20], the original 5 ordinary differential equations were discretized using a finite-difference method. A boundary value approach for computing compressible boundary layer stability was devised, which consisted of two steps: (1) a global method that computed all the eigenvalues of the governing equation (i.e., the algebraic eigenvalue problem solved by the LR method), and (2) a local method used to refine the least stable eigenvalue using the inverse Rayleigh procedure [22]. The approach provided temporal eigenvalues and spatial growth rate was computed using Gaster’s group velocity transformation [23]. This procedure formed the basis of the author’s COSAL [13] code to compute disturbance N factors in three-dimensional compressible boundary layers, which was widely adopted in industry for laminar flow control studies. The method can be extended to solve the spatial eigenvalue problem by using a companion matrix method, which would increase the number of equations from 5 to 9. A similar approach was used by Khorrami et al. [24] for solving the spatial eigenvalue problem associated with swirling flows, where the incompressible governing equations were discretized using spectral collocation techniques.

An alternative approach, based on a fourth-order compact scheme [25], was later developed to solve the temporal or spatial local eigenvalue problem by rewriting the governing compressible stability equations as a system of 8 first-order equations. This more robust scheme for computing spatial eigenvalues was incorporated in the author’s e-Malik code [26] for hypersonic boundary stability studies and was also adopted by industrial participants of the NASP program.

In Ref. [27], a solution approach based on single and multidomain Chebyshev spectral methods was also developed for the generalized eigenvalue problem for compressible boundary layer stability studies. This approach is particularly suited for studying full eigenvalue spectrum for the compressible boundary layer stability problem (cf. Balakumar and Malik [28]). Note that the matrix size is $5N \times 5N$ for temporal stability and $9N \times 9N$ for spatial stability, where N is the number of wall-normal collocation points used for the solution. The cost of solving such a system varies as $(9N)^3$. In Ref. [27], an approximation was suggested to reduce the order of the matrix from 9 to 5 N when the generalized eigenvalue problem is solved only to obtain a guess for the spatial eigenvalue to be later refined by a local method.

3 2D Partial-Differential Eigenvalue Problem

There is a class of problems that are governed by homogeneous governing equations and boundary conditions but, since the mean flow varies strongly in two dimensions, the resulting eigenvalue problem is governed by a set of partial differential equations (PDEs). We call this a 2D eigenvalue problem, in contrast with the “1D” eigenvalue problem governed by a system of ordinary differential equations (e.g., the compressible stability equations referred to in Sect. 2 above). Examples of physical problems that require the use of 2D eigenvalue techniques include corner layers, the attachment-line boundary-layer and secondary instability studies. Since one must discretize the PDEs in two space variables, the order of the matrix eigenvalue problem becomes $9MN$ for spatial stability, where M and N are collocation points used in the two directions in which mean flow variation cannot be ignored. Direct solution of such a large eigenvalue problem can become prohibitively expensive. Therefore, iterative methods that exploit the bandwidth and sparsity of the matrix become attractive. One such method is Arnoldi’s subspace iteration method (cf. Saad [29]), which was used in some of the studies cited below.

4 Linearized Navier–Stokes

Linear stability equations referred to in Sect. 3 above involve certain approximations to simplify the problem. However, one could solve the linearized Navier–Stokes (LNS) without such approximations, albeit at a much higher computational cost, but the system of equations can be used to compute boundary layer receptivity (internalization of external disturbances) and the subsequent processing, including nonparallel effects. This approach was used by Streett [30] to simulate wavepackets in 3D boundary layers, and later by Guo et al. [31], for computation of instability waves in 2D and 3D boundary-layers. In both these studies, the harmonic form of the governing equations was used by assuming the solution to have only one prescribed frequency and, thus, the governing equations are rendered time-independent providing only a time-asymptotic solution. The alternative is to solve time-dependent version of LNS, which would allow computation of the transients and capture multiple frequency disturbances as long as an appropriate time integration step is used. The LNS approach can be used in receptivity studies (Choudhari and Streett [32]) and in flows that are rapidly varying or for tracking multiple instability modes. The linearized Navier–Stokes is of particular relevance in studying high Mach number flows at low Reynolds numbers, and such an attempt was made by Malik et al. [33] where they solved compressible linearized Navier–Stokes. In later studies, Mughal and Ashworth [34] used the LNS approach to compute receptivity of a swept-wing boundary layer to surface roughness.

5 Parabolized Stability Equations

Parabolized stability equations (PSE), which was an advancement of great consequence in the area of stability and transition, is the legacy of Thorwald Herbert [35]. Chang et al. [36] developed a compressible parabolized stability equation solver in primitive variables using a finite-difference method and were the first to observe that the marching procedure became unstable with a sufficiently small marching step size. Li and Malik [37] considered incompressible PSE to investigate the nature of the approximation and derived conditions for a stable marching solution. In Ref. [38], the case of compressible PSE was also considered, which results in less restrictive step size limitation. Recent work of Towne et al. [39] has further developed marching procedures for flows that involve multiple modes of instability.

The PSE approach is applicable to both linear and nonlinear development of disturbances in boundary and shear layers. Chang and Malik [40] were the first to apply the nonlinear PSE approach to the study of secondary instability and oblique mode interaction in supersonic boundary layers. The method captures quantitatively correct results compared to the Floquet analysis used for secondary instability studies (Herbert [41]), which only provides qualitative results due to the inherent shape-function assumption. Nonlinear PSE results generally agree well with direct numerical simulation (DNS) in early stages of transition development, with two orders of magnitude less computational time for the PSE. Therefore, PSE provides an attractive approach to generate initial conditions for DNS of transition to turbulence as, for example, used by Pruett and Chang [42].

Various boundary layer stability analysis and parabolized stability equations approaches developed at NASA, or those sponsored by NASA, have been encapsulated in the LASTRAC code (Langley Advanced Stability and Transition Analysis Code), see Chang et al. [43]. It is a general-purpose stability analysis and transition prediction suite of tools for shear layers, 2D/axisymmetric/infinite swept, and fully 3D boundary layers. It has perfect gas as well as thermochemical equilibrium or thermochemical nonequilibrium capability. Transition prediction approaches include N factors for primary (TS, Mack, Görtler, crossflow) disturbances, absolute amplitude criteria or N factors for secondary disturbances. A separate plane marching PSE capability is available for computing evolution of disturbances in boundary layers with strong spanwise variation.

6 Development of Quiet Tunnels

The dominant source of freestream disturbances in the nozzle test section of conventional supersonic nozzles is the acoustic radiation from eddies in the turbulent boundary layers on the nozzle walls. This noise is in the form of finite-strength wavelets that are propagated along Mach lines. Development of the supersonic quiet tunnels was one of the recommendations of the US Transition Study Group, led by Eli

Reshotko, almost 60 years ago. Ivan Beckwith of NASA Langley Research Center responded to the challenge and after a sustained research effort succeeded in the development of a Mach 3.5 low disturbance tunnel (see, Beckwith et al. [44]). Care was taken to treat the flow in the settling chamber and suction slots were provided ahead of the nozzle throat to remove the upstream turbulent boundary layer. A new laminar boundary layer developed starting from the lip of the converging–diverging nozzle, allowing development of extended laminar flow on the contoured walls of the rapid expansion rectangular nozzle resulting in a significantly long quiet test core. Experiments conducted on sharp cone models in this facility yielded transition Reynolds numbers about a factor of about 2 higher than those obtained in conventional tunnels, see Fig. 1.

Stability analysis of the nozzle wall boundary layers was conducted and transition was found to correlate well with amplification of Görtler vortices on the concavely curved walls [45]. The theory was then used to design new nozzles that promised longer runs of laminar flow. This new design included a straight radial flow region followed by a slow expansion nozzle (Fig. 2) and, when fabricated and tested, vali-

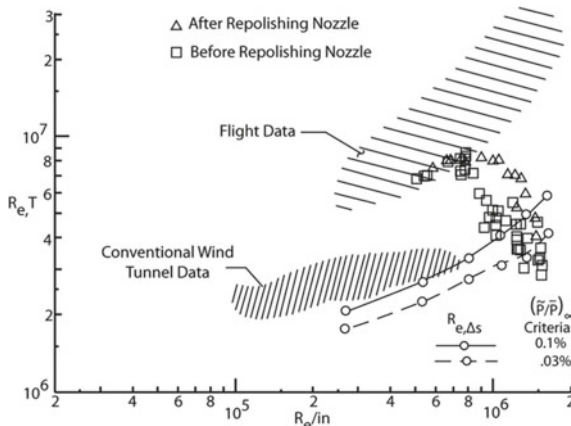


Fig. 1 Sharp cone boundary layer transition Reynolds number in Langley's Mach 3.5 tunnel compared to conventional supersonic tunnels (from Ref. [44])

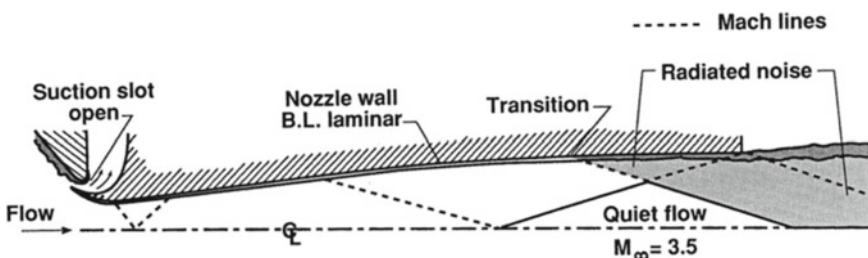


Fig. 2 Optimized Mach 3.5 nozzle (from [46])

dated the design [46, 47]. The same approach was used to design and build the world's first hypersonic (Mach 6) quiet tunnel [48–50]. A similar approach was subsequently used by Schneider [51, 52] to design a Mach 6 quiet flow Ludweig tube at Purdue University. Both these facilities (Langley's Mach 6 tunnel was later donated to Texas A&M University) have provided very valuable research data for hypersonic boundary layer transition on different configurations of practical interest. New higher Mach number (up to Mach 10) facilities are planned at US academic institutions under sponsorship of the Department of Defense.

7 Supersonic and Hypersonic Boundary Layer Transition

In supersonic wind-tunnel experiments, the significance of the freestream turbulence (vorticity) is greatly reduced with increasing Mach numbers due to large accelerations from the settling chamber to the test section. However, the sound field radiated by the turbulent tunnel-wall boundary layers in conventional tunnels constitutes a unique supersonic stream disturbance source, which influences the test model boundary layer and causes early transition. The work of Pate and Schueler [53] clearly showed the adverse effect of radiated noise on the transition Reynolds numbers. As a consequence, N factors at transition (i.e., disturbance amplification based on linear stability theory) were rather small due to initially large amplitudes present at the critical point (Mack [54]). The question remained that, if the external disturbances were very weak, would the compressible stability theory predict disturbance amplification (N factor) of the same order found in good low speed wind tunnels?

With the availability of supersonic flight transition data of Dougherty and Fisher [55] (see Fig. 3 for the installed cone) and that of the Langley Mach 3.5 quiet tunnel,

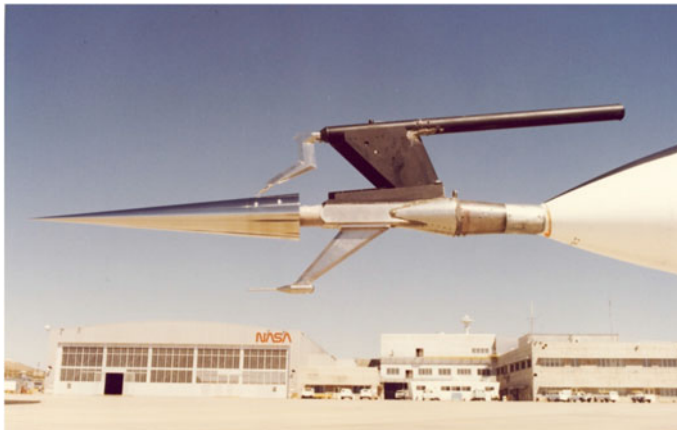


Fig. 3 Instrumented sharp cone installed at the nose of the aircraft used in Dougherty and Fisher [55] transition experiment

this question was answered. These data sets were first analyzed in Ref. [56] and it was shown that compressible linear stability theory correlated well with the same N factor values achieved earlier for low speed data from good quality tunnels. Later analysis also showed that compressible stability theory can also be used to predict transition in supersonic boundary layers over concave walls where Görtler vortices constitute the prime instability mechanism. Computations for sharp cones [4], using $N = 10$, showed that the first oblique mode is responsible for transition at adiabatic wall conditions for freestream Mach numbers up to about 7. For cold walls, the two-dimensional second mode dominates the transition process at lower hypersonic Mach numbers due to the well-known destabilizing effect of cooling on the second mode. These favorable correlations with the compressible stability theory-based N factor computations opened the door for many subsequent applications of the theory (whether using quasiparallel linear stability or PSE) to various other configurations.

Lachowicz et al. [57] conducted experiments on a flared cone model in Langley's Mach 6 quiet tunnel. Adverse pressure gradients present in the flare region enhanced the growth of second mode disturbances, in agreement with computational results of Balakumar and Malik [58]. Their results also showed that the adverse pressure gradient could prevent the growth of the boundary layer, allowing for sustained amplification of fixed frequency second mode disturbances for longer distances compared to a straight cone boundary layer. The flared cone model has also been tested in Langley's conventional Mach 6 tunnel and results from both tunnels have been reported by Horvath et al. [59], showing a significant difference in transition location, and hence N factors, see Fig. 4. Similar cone-flare model tests have been performed in Purdue's Mach 6 quite tunnel as well.

Pegasus swept-wing flight test (cf. Malik et al. [60]) was done to acquire flight data for crossflow-induced transition at a Mach number of about 4.5. Similar data were also obtained in the Mach 3.5 quiet tunnel over a delta wing configuration (Cattafesta et al. [61] and Cattafesta [62]). Compressible stability analysis for both

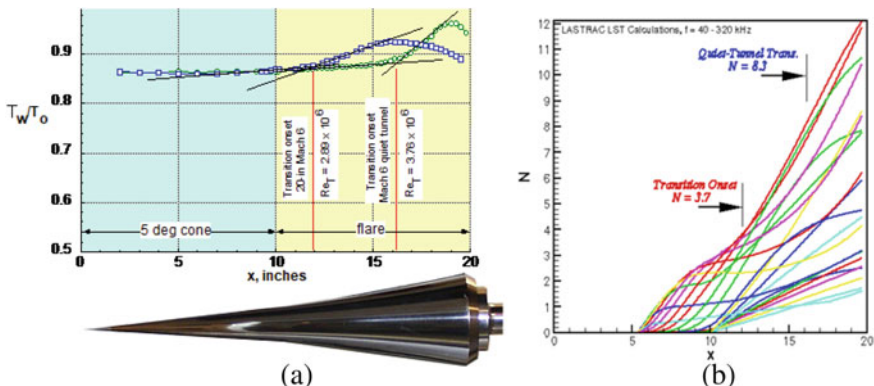


Fig. 4 **a** The flared cone and experimental locations of transition in Mach 6 conventional and quiet tunnels, **b** associated N factors [59]

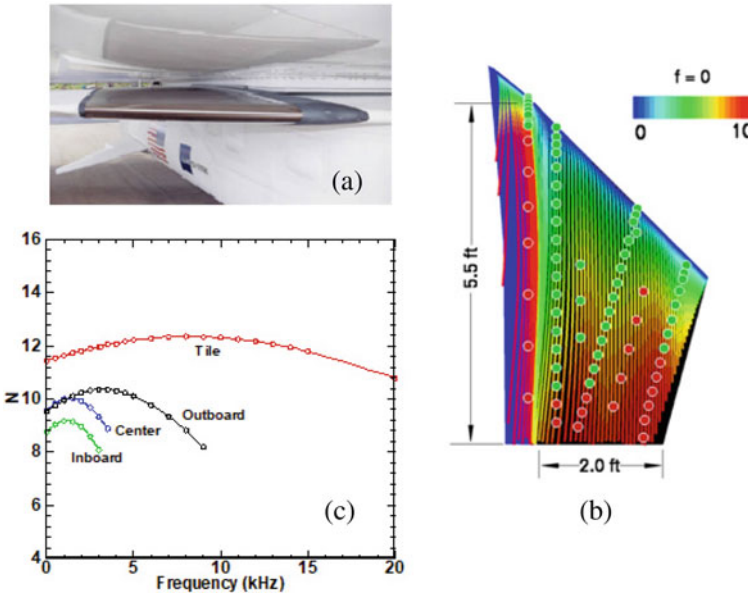


Fig. 5 Pegasus crossflow flight transition experiment [60]: **a** test article, **b** flow streamlines shaded with stationary crossflow N factor values, circles are thermocouple locations (green, laminar), **c** N factors for different frequency disturbances along different rows of thermocouples

these configurations yielded transition N factors in the range of 8 to 14 that contains the values computed for sharp cones above, where the instability mechanism constituted the first mode disturbances. Results for the Pegasus flight experiment are shown in Fig. 5. Analysis of the experiment showed that wall cooling had a stabilizing effect on crossflow instability. For the Mach 3.5 quiet tunnel experiment, constant N-factor contours for the delta wing configuration indicated that the transition front would be parallel to the leading-edge on one side and to the line of symmetry on the other, while inverting in the middle. Experiments using the thermocouple technique for transition detection did not support the calculations as it indicated that the transition front was not parallel to the line of symmetry, rather perpendicular to it. However, later measurements using the temperature sensitive paint technique were in agreement with the N factor prediction. Crossflow instability in the boundary layer over a cone at incidence was studied by King [63] experimentally in the Mach 3.5 quiet tunnel and computed by Malik and Balakumar [64]. All these results demonstrated applicability of compressible stability theory to the prediction of crossflow-induced transition, both in supersonic flight and quiet tunnel experiments.

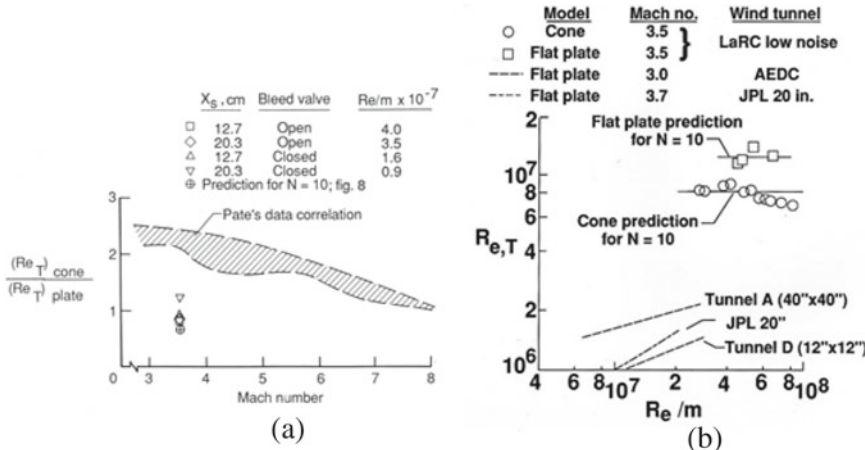


Fig. 6 **a** Ratio of cone to flat-plate transition Reynolds number, **b** flat plate transition Reynolds number and the associated N factors, [67]

8 Cone/Flat-Plate Transition Reynolds Number Controversy

There existed a longstanding controversy regarding the ratio of transition Reynolds numbers on cones to that on flat plates. Pate [65] had correlated end of transition data from five test facilities, which showed that the ratio of cone-to-flat-plate transition Reynolds numbers decreased from about 2.5 at Mach 3 to about 1 at Mach 8. However, there was no theoretical support that the transition Reynolds number for cones would be higher than that for flat plates (see, Mack [54, 66]). Mack used Mangler's transformation to transform flat plate boundary layer profiles to obtain mean flow for the cone and ignored transverse curvature in the stability analysis. Chen et al. [67] computed boundary layer profiles for the sharp cone and stability analysis included transverse curvature effects. N factor computations for Mach 3.5 flow using an N of 10 showed that the ratio of cone to flat plate transition Reynolds numbers was about 0.7 compared to 2.5 noted above. The experimental data used by Pate [65] were obtained from conventional supersonic/hypersonic wind tunnels. As noted above, the sharp cone transition Reynolds number in the Mach 3.5 quiet tunnel [44] was found to be higher by a factor of about 2 compared to similar experiments performed in conventional tunnels, and there was a similar expectation for the flat plate transition Reynolds number, which would not agree with the computed ratio of 0.7 noted above. However, when the experiment was performed in the Mach 3.5 quiet tunnel, it was found that the measured flat-plate transition Reynolds numbers were an order of magnitude higher than previous results obtained in conventional noisy supersonic wind tunnels [67].

The measured transition Reynolds number and the ratio of cone to flat-plate transition turned out to be in excellent agreement with the theoretical predictions based

on solving compressible stability equations (see, Fig. 6). Thus, this investigation resolved the discrepancy between the results of linear stability theory and the data from conventional supersonic wind tunnels regarding the ratio of cone-to-flat-plate transition Reynolds numbers. The established fact that transition Reynolds number for a flat-plate is higher than that for a cone influenced the change in the conceptual design of the forebody of the NASP from a conical to a somewhat flat design, which was also used for the subsequent X-43 scramjet demonstration flight [68].

9 Effect of Bluntness and Real Gas on Hypersonic Boundary Layer Transition

Accurate computation of boundary layer profiles as well as their wall-normal derivatives is a prerequisite for linear stability analysis and this requirement is readily met when the profiles are computed by solving boundary layer equations. However, there are numerous configurations where boundary layer equations do not capture the dominant physical effects (e.g., hypersonic flow past a blunt cone) and one must use Navier–Stokes, or at a minimum parabolized Navier–Stokes (PNS) equations, to obtain the mean flow. In one of the first studies of the effect of nose bluntness on boundary layer instability, Malik et al. [] used PNS to obtain mean flow for Mach 8 flow past a slightly blunted cone used in the experiment of Stetson et al. [], with initial conditions provided by solving full Navier–Stokes equations. This approach was made necessary to account for the variable entropy effects associated with the bow shock, while keeping computational cost commensurate with the available computers of the time. A ‘flat-plate test’ was devised to determine grid requirements for the PNS solution; in other words, the PNS grid was refined until the associated linear stability results matched those obtained based on the boundary layer equations within a prescribed tolerance.

Calculations were then performed for the conditions of the blunt cone experiment of Stetson et al. [70], who measured stability characteristics of Mach 8 flow in the presence of nose bluntness. Linear stability computations were also performed for the sharp cone experiments of Stetson et al. [71]. Comparison of the results revealed that, with a relatively small amount of bluntness, the critical Reynolds number for the onset of instability increased by an order of magnitude compared to the sharp cone value. The predicted transition Reynolds number also increased due to small bluntness, though the increase was relatively smaller compared to change in the critical Reynolds number, which was qualitatively in agreement with the experiment. The computed second mode frequencies were also in reasonable agreement with the experimental results. The computed N factor value at transition for the sharp cone was 5.5, because the experiment was conducted in a conventional tunnel because no hypersonic quiet tunnel existed at the time.

Nose bluntness introduces a new length scale into the problem and its stabilizing influence for a given set of flow conditions may be characterized by the nose Reynolds

number. This information was used in [69] to explain the effect of unit Reynolds number on transition present in the aeroballistic range data of Potter [72], which was later confirmed by direct numerical simulations performed by Kara et al. [73].

Transition data from two different classical hypersonic flight experiments were also analyzed using linear stability theory and parabolized stability equations [74, 75], including gas chemistry effects associated with high temperature boundary layers. The results suggested that transition in both these cases was caused by the amplification of second mode disturbances. The analysis showed that, consistent with previous findings for supersonic flows where first mode disturbances induce laminar-turbulent transition, N factors of between 9 and 11 correlated the transition onset locations from these two high Mach number (14 and 22) flight experiments. This provided confidence in the use of the N factor method for prediction of hypersonic flight transition. More recently, hypersonic transition experiments have been performed in the flight transition program (HIFiRE-1 and HIFiRE-5) sponsored by the US Air Force (see Kimmel et al. [76]). The test configuration for HIFiRE-1 was a slender cone, while the test article was an elliptic cone for HIFiRE-5. Li et al. [77] computed N factors for the sharp cone and found that transition correlated well with an N of about 13.5. The elliptic cone supports multiple instability mechanisms, including second mode, crossflow and shear flow instability, in different parts of the cone boundary layer. This flow field has also been analyzed both within and outside NASA.

10 Instability of Rotating Disk Flow

The three-dimensional rotating disk flow, which is subject to crossflow instability, had been investigated in several experiments, as well as theoretically, because it had been considered a model problem for technologically significant swept-wing boundary layer transition. Cebeci and Stewartson [78] solved the Orr-Sommerfeld equation and found the critical Reynolds number to be 175.6. They further found that transition onset location is correlated with an N factor of about 20, i.e., much higher than the values noted above for other flows. Malik et al. [79] derived a new 6th-order set of governing equations that included the effects of Coriolis forces and streamline curvature. The numerical results, obtained using Chebyshev polynomials, showed that the critical Reynolds number for establishment of stationary vortex flow is $R = 287$, which was later supported by the DNS of Spalart [80]. It was found in Ref. [79] that, due to the stabilizing effect of the Coriolis forces and streamline curvature on crossflow instability, N factor at transition onset is about 11, consistent with other values quoted above for a variety of flow configurations. Later computations [81] using PSE and a multiple-scale approach to account for nonparallel effects supported the results of [79].

Wilkinson and Malik [82] were the first to study experimentally the origin of crossflow vortices in rotating disk flow. Malik [83] obtained the neutral curve for stationary disturbances in rotating disk flow and found that the lower branch solution

behaves like R^{-1} , later confirmed by theoretical solution of Hall [84]. Traveling disturbances in rotating disk flow were investigated by Balakumar and Malik [85].

In the rotating disk experiment performed by Kohama [86], ring-like secondary instability riding on stationary crossflow vortices was observed. This was simulated by Balachandar et al. [87] using the Floquet approach. They found that secondary instability appeared when the primary crossflow amplitude was increased to about 10 percent, i.e., an order of magnitude higher than the amplitude of TS instability required for fundamental or subharmonic secondary disturbances [41] in a flat plate boundary layer. The assumption inherent in Floquet analysis becomes questionable at such large amplitudes. Therefore, in subsequent secondary instability analyses involving Görtler and crossflow vortices as primary instabilities, a new method based on nonlinear PSE was used.

11 Nonlinear Development of Görtler and Crossflow Vortices

Nonlinear development of stationary Görtler and crossflow vortices, in both incompressible and compressible boundary layers, leads to highly distorted mean flows where the streamwise velocity depends not only on the wall-normal but also the spanwise coordinate. This distorted boundary layer becomes subjected to inviscid instability, with odd and even modes related to spanwise and wall-normal shear, respectively. Parabolized stability equations provide an efficient tool to compute nonlinear development of Görtler and crossflow vortices. Instability of the distorted boundary layer can then be studied using the 2D partial-differential eigenvalue approach (see Sect. 3 above) with either inviscid or viscous analysis. This was done in a series of papers (cf. Malik et al. [88, 89], Li and Malik [90]). As an example, Fig. 7 shows a stationary nonlinear crossflow vortex, with the two modes of secondary instability present. In contrast, a Görtler vortex would exhibit a symmetric structure but essentially the same mechanism for secondary instabilities. In Ref. [89], it was shown that

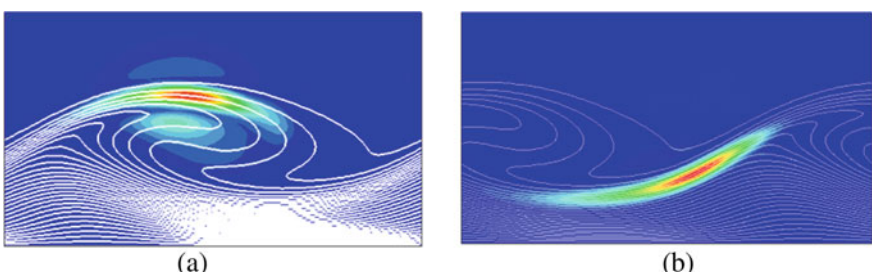


Fig. 7 Secondary instability modes associated with a crossflow vortex. White lines show a cross-section of the stationary vortex, and red/green colors reflect intensity of the instability modes: **a** Y-mode associated with wall-normal shear, **b** Z-mode associated with spanwise shear

a secondary N factor approach provides better prediction of transition onset than the use of an absolute amplitude criterion. Li and Choudhari [91] further improved the computational methodology and have applied it to a variety of configurations (e.g., swept-wing boundary layers, Mach 6 flared cone), where the same types of secondary instability mechanisms are present. It has also been found by Choudhari et al. [92] that the streaks behind roughness elements are also subject to the same types of instability, confirmed by carefully performed experiments in the Mach 3.5 quiet tunnel by Kegerise et al. [93].

12 The Attachment-Line Boundary Layer

The attachment-line boundary-layer on a swept-wing requires careful consideration since, in general, when this boundary-layer becomes turbulent, laminar flow is lost on the entire wing. It was found by Hall et al. [94] that the attachment-line is subject to small-amplitude traveling disturbances above a Reynolds number, \bar{R} , of 583. The frequencies of these viscous TS-like disturbances agreed well with the experimental results of Pfenninger and Bacon [95] and Poll [96, 97]. Later, Lin and Malik [98] used the 2D partial differential eigenvalue approach to solve for the attachment-line instability. Their results agreed with the most unstable mode found in Ref. [94], but this new approach allowed them to discover additional instability modes. Using a series expansion procedure, Theoflis et al. [99] solved the attachment line problem and recovered the results of Ref. [98], albeit with much reduced computational cost. Mack et al. [100] and Mack and Schmid [101] studied the attachment-line stability problem and connection to crossflow instability by solving compressible flow equations.

Experiments [95–97] have shown that the attachment-line boundary-layer can sustain turbulent flow at Reynolds numbers much below the critical value of 583 quoted above. Large amplitude disturbances are known to damp out only at $\bar{R} < 245$ (e.g., see [97]). Hall and Malik [102] used the weakly nonlinear theory, as well as direct numerical simulations, to show that the attachment-line boundary-layer is subject to subcritical instability, which allows large amplitude disturbances to amplify above a critical Reynolds number. The value of this critical Reynolds number was found to be about 535 below which all large disturbances pertaining to the mode found in Ref. [94] were damped. In other words, the results of Ref. [102] failed to explain the wide gap between the linear critical Reynolds of 583 and the minimum Reynolds number of 245 for sustenance of turbulence. On the other hand, DNS results of Spalart [103] showed that turbulence could not be sustained in the attachment-line boundary-layer below $\bar{R} < 245$, thus agreeing with the experiments. He was further able to show that the turbulent boundary-layer at $\bar{R} > 245$ could be laminarized with wall suction; this practically significant result has also been obtained experimentally by Poll and Danks [104]. Their experimental results showed that the boundary-layer could be laminarized up to \bar{R} of 600 with sufficient wall suction. For the design of natural laminar flow leading edges for swept-back wings, Poll's criterion of $\bar{R} < 245$ must be satisfied.

13 Epilogue

This paper has summarized a large body of computational and experimental work to enhance our understanding of instability mechanisms in 2D and 3D boundary layers across the speed regime, from subsonic to hypersonic. New computational tools were developed to provide this understanding and enable prediction of onset of transition in subsonic, supersonic and hypersonic boundary layers. Development of supersonic and hypersonic quiet tunnels was an important part of the research effort conducted at NASA. Physics-based transition prediction technology for supersonic and hypersonic flight was put on firm footings. Pioneering theoretical work on boundary layer receptivity to free stream disturbances was conducted by Goldstein [105]. The theoretical, computational and experimental research performed at NASA during the 1980s and 1990s provided a solid foundation for the greater transition community to build upon, as evidenced by construction of new quiet tunnels and computational tools in past two decades. The available transition prediction capability for practical configurations is much more advanced now, compared to 40 years ago, partly due to orders of magnitude improvement in computational infrastructure.

It is important to note that the N factor method is an empirical approach for transition prediction, whereby the value of N at transition depends upon the amplitude of the external forcing (free stream or surface condition). For example, it was shown in Fig. 4 that the N values were 3.7 and 8.3 when transition was detected in the Mach 6 conventional (noisy) and quiet (low disturbance) tunnels, respectively; on the other hand, the computed N value was 13.5 for the sharp cone used in the HIFIRE-1 flight experiment [77].

Transition is an initial boundary value problem and prescription of the external forcing (free stream disturbances) remains a challenge. What free stream forcing was there at high altitudes to induce second mode disturbances in, for example, Reentry-F [75] or HIFIRE-1 [76] cone boundary layers? Bushnell [106] hypothesized potential sources of such disturbances, including particulates interacting with vehicle bow shock. Fedorov [107] has considered supersonic boundary layer receptivity to solid particulates, while Fedorov and Tumin [108] considered the role of kinetic fluctuations as a source of disturbance. A lot remains to be done to predict boundary layer transition for configurations of interest from first principles. Specification of surface quality of flying vehicles is one such example, since surface condition has a first-order influence on transition.

References

1. Mack, L.M.: Boundary-Layer Stability Theory, Internal Document No. 900-277, Rev. A, Jet Propulsion Laboratory, Pasadena, CA (1969)
2. Kendall, J.: Wind tunnel experiments relating to supersonic and hypersonic boundary-layer transition. *AIAA J.* **13**, 24–299 (1975)
3. Mack, L.M.: Boundary-layer linear stability theory, Special Course on Stability and Transition of Laminar Flow, R. Michel (ed.), AGARD Report No. 709, pp. 3–1 to 3–81 (1984)

4. Mack, L.M.: Early history of compressible linear stability theory. In: Fasel, H.F., Saric, W.S. (eds.) IUTAM Symposium, Laminar Turbulent Transition, pp. 9–34. Sedona, AZ, Springer-Verlag (2000)
5. Malik, M.R.: Prediction and control of transition in supersonic and hypersonic boundary layers. *AIAA J.* **27**(11), 1487–1493 (1989)
6. Fedorov, A.V., Malmuth, N.D., Rasheed, A., Hornung, H.G.: Stabilization of hypersonic boundary layers by porous coatings. *AIAA J.* **39**(4), 605–610 (2001)
7. Fedorov, A.V., Khokholov, P.K.: Prehistory of instability in a hypersonic boundary layer. *Theoret. Comput. Fluid Dyn.* **14**(6), 359–375 (2001)
8. Smith, A.M.O., Gamberoni, N.: Transition, Pressure Gradient, and Stability Theory, p. 26388. Douglas Aircraft Company Inc., Report ES (1956)
9. Van Ingen, J.L.: A suggested semi-empirical method for the calculation of the boundary layer transition region, University of Technology, Department of Aerospace Engineering, Report UTH-74, Delft (1956)
10. Morkovin, M.: Bypass-transition research: issues and philosophy. In: Ashpis, Gatski and Hirsh (eds.) Instabilities and Turbulence in Engineering Flows, pp. 3–30, Kluwer (1993)
11. Mack, L.M.: Transition prediction and linear stability theory, AGARD CP-224, pp. 1–1 to 1–22 (1977)
12. Crouch, J.D., Ng, L.L.: Variable N-factor method for transition prediction in three-dimensional boundary layers. *AIAA J.* **38**(2), 211–216 (2000)
13. Malik, M.R.: COSAL—A black box compressible stability analysis code for transition prediction in three-dimensional boundary layers, NASA CR-165925 (1982)
14. Reshotko, E.: Boundary layer stability and transition. *Ann. Rev. Fluid Mech.* **8**, 311–349 (1976)
15. Arnal, D., Casalis, G., Juillen, J. C.: A survey of the transition prediction methods: from analytical criteria to PSE and DNS. In: Kobayashi, R. (ed.) Laminar Turbulent Transition, pp. 3–14. Sendai, Japan, Springer Verlag (1995)
16. Reed, H.L., Saric, W.S., Arnal, D.: Linear stability theory applied to boundary layers. *Ann. Rev. Fluid Mech.* **28**, 389–428 (1996)
17. Malik, M.R., Zang, T.A., Bushnell, D.M.: Boundary layer transition in hypersonic flows, AIAA 90-5232 (1990)
18. Berry, S.A., Kimmel, R., Reshotko, E.: Recommendations for hypersonic boundary layer transition flight testing, AIAA 2011-3415 (2011)
19. Malik, M.R., Orszag, S.A.: Efficient computation of the stability of three-dimensional compressible boundary layers, AIAA 1981-1277 (1981)
20. Malik, M.R., Orszag, S.A.: Linear stability analysis of three-dimensional compressible boundary layers. *J. Sci. Comput.* **2**(1), 77–97 (1987)
21. Mack, L.M.: Computation of the stability of the laminar boundary layers. In: Alder, B., Fernbach, S., Rotenberg, M. (eds.) Methods of Computational Physics, Vol. 4, pp. 247–299. Academic Press, NY (1965)
22. Wilkinson, J.H.: The Algebraic Eigenvalue Problem. Clarendon Press, Oxford (1965)
23. Gaster, M.: A note on the relation between temporally increasing and spatially increasing disturbances in hydrodynamic stability. *J. Fluid Mech.* **14**, 222–224 (1962)
24. Khorrami, M.R., Malik, M.R., Ash, R.L.: Application of spectral collocation techniques to the stability of swirling flows. *J. Comput. Phys.* **81**(1), 206–229 (1989)
25. Malik, M.R., Chuang, S., Hussaini, M.Y.: Accurate numerical solution of compressible, linear stability equations. *Zeitschrift fur angewandte Mathematik und Physik ZAMP* **33**(2), 189–201 (1982)
26. Malik, M.R.: eMalik: A new spatial stability analysis program for transition prediction using the e^N method, High Technology Report No. HTC-9203, High Technology Corporation, Hampton, VA (1992)
27. Malik, M.R.: Numerical methods for hypersonic boundary layer stability. *J. Comput. Phys.* **86**(2), 376–413 (1990)

28. Balakumar, P., Malik, M.R.: Discrete modes and continuous spectra in supersonic boundary layers. *J. Fluid Mech.* **239**, 631–656 (1992)
29. Saad, Y.: Variations on Arnoldi's method for computing eigenelements of large unsymmetric matrices. *Linear Algebra Appl.* **34**, 269–295 (1980)
30. Streett, C.L.: Direct harmonic linear Navier-Stokes methods for efficient simulation of wave packets, AIAA 98-0784 (1998)
31. Guo, Y., Malik, M.R., Chang, C.-L.: A solution adaptive approach for computation of linear waves. AIAA 97-2072 (1997)
32. Choudhari, M., Streett, C.L.: Theoretical prediction of boundary-layer receptivity. AIAA 94-2223 (1994)
33. Malik, M.R., Lin, R.S., Sengupta, R.: Computation of hypersonic boundary layer response to external disturbances. AIAA 99-0411 (1999)
34. Mughal, M.S., Ashworth, R.M.: Uncertainty quantification based receptivity modelling of crossflow instabilities induced by distributed surface roughness in swept wing boundary layers. AIAA 2013-3106 (2013)
35. Herbert, T.: Boundary-layer transition—Analysis and prediction revisited. AIAA 91-0737 (1991)
36. Chang, C.-L., Malik, M.R., Erlebacher, G., Hussaini, M.Y.: Compressible stability of growing boundary layers using parabolized stability equations. AIAA 91-1636 (1991)
37. Li, F., Malik, M.R.: On the nature of PSE approximation. *Theoret. Comput. Fluid Dyn.* **8**, 253–273 (1996)
38. Li, F., Malik, M.R.: Spectral analysis of parabolized stability equations. *Comput. Fluids* **26**(1), 279–297 (1997)
39. Towne, A., Rigas, G., Colonius, T.: A Critical assessment of the parabolized stability equations. *Theoret. Comput. Fluid Dyn.* **33**, 359–382 (2019)
40. Chang, C.-L., Malik, M.R.: Oblique-mode breakdown and secondary instability in supersonic boundary layers. *J. Fluid Mech.* **273**, 323–359 (1994)
41. Herbert, T.: Secondary instability of boundary layers. *Ann. Rev. Fluid Mech.* **20**, 487–526 (1988)
42. Pruett, C.D., Chang, C.-L.: Spatial direct numerical simulation of high-speed boundary-layer flows part II: transition on a cone in Mach 8 flow. *Theoret. Comput. Fluid Dyn.* **7**, 397–424 (1995)
43. Chang, C.-L., Kline, H., Li, F.: Effects of wall cooling on supersonic modes in high-enthalpy hypersonic boundary layers over a cone. AIAA 2019-2852 (2019)
44. Beckwith, I.E., Creel, T.R., Jr., Chen, F.-J., Kendall, J.M.: Free-stream noise and transition measurements on a cone in a Mach 3.5 pilot quiet tunnel, NASA TP-2180 (1983)
45. Chen, F.-J., Malik, M. R., Beckwith, I.E.: Instabilities and transition in the wall boundary layers of low-disturbance supersonic nozzles. AIAA 85-1573 (1985)
46. Chen, F.-J., Malik, M.R., Beckwith, I.E.: Advanced Mach 3.5 axisymmetric quiet nozzle. AIAA 90-1592 (1990)
47. Chen, F.-J., Malik, M.R., Beckwith, I.E.: Görtler instability and supersonic nozzle design. *AIAA J.* **30**(8), 2093–2094 (1992)
48. Chen, F.-J., Wilkinson, S.P., Beckwith, I.E.: Görtler instability and hypersonic quiet nozzle design. AIAA 91-1648 (1991)
49. Wilkinson, S.P.: A review of hypersonic boundary layer stability experiments in a quiet Mach 6 wind tunnel. AIAA 97-1819 (1997)
50. Blanchard, A.E., Lachowicz, J.T., Wilkinson, S.P.: NASA langley Mach 6 quiet wind-tunnel performance. *AIAA J.* **35**(1), 23–28 (1997)
51. Schneider, S.P.: Fabrication and testing of the purdue Mach 6 quiet-flow Ludweig tube. AIAA 2000-0295 (2000)
52. Schneider, S.P.: Development of hypersonic quiet tunnels. *J. Spacecr. Rockets* **45**(4), 641–664 (2008)
53. Pate, S.R., Schueler, C.J.: Radiated aerodynamic noise effects on boundary-layer transition in supersonic and hypersonic wind tunnels. *AIAA J.* **7**(3), 450–457 (1969)

54. Mack, L.M.: Linear stability theory and the problem of supersonic boundary-layer transition. *AIAA J.* **13**(3), 278–289 (1975)
55. Doughert, N.W., Jr., Fisher, D.F.: Boundary layer transition on a 10 deg cone: wind tunnel/flight data correlations, AIAA Paper 80-0154 (see also NASA TP 1971, 1982) (1980)
56. Malik, M.R.: Instability and transition in supersonic boundary layers. In: Uram, E.M., Weber, H.E. (eds.) *Laminar-Turbulent Boundary Layers, Proceedings of Energy Resources Technology Conference*, New Orleans, LA, February 12–16 (1984)
57. Lachowicz, J.T., Chokani, N., Wilkinson, S.P.: Boundary-layer stability measurements in a hypersonic quiet tunnel. *AIAA J.* **34**(12), 2496–2500 (1996)
58. Balakumar, P., Malik, M.R.: Effect of adverse pressure gradient and wall cooling on instability of hypersonic boundary layers. High Technology Corp. Report HTC-9404, Hampton, VA (1994)
59. Horwath, T.J., Berry, S.A., Hollis, B.R., Chang, C.-L., Singer, B.A.: Boundary layer transition on slender cones in conventional and low disturbance Mach 6 wind tunnels. *AIAA 2002-2743* (2002)
60. Malik, M.R., Li, F., Choudhari, M.: Analysis of crossflow transition flight experiment aboard the pegasus launch vehicle. *AIAA 2007-4487* (2007)
61. Cattafesta, L.N., Ill, Iyer, V., Masad, J.A., King, R.A., Dagenhart, J.R.: Three-dimensional boundary-layer transition on a swept wing at Mach 3.5. *AIAA 94-2375* (1994)
62. Cattafesta, L.N., Ill.: Swept-wing suction experiments in the supersonic low-disturbance tunnel, High Technology Corporation Report HTC-9605, Hampton, VA (1996)
63. King, R.A.: Three-dimensional boundary-layer transition on a cone at Mach 3.5. *Exp. Fluids* **13**, 305–314 (1992)
64. Malik, M.R., Balakumar, P.: Instability and transition in three-dimensional supersonic boundary layers. *AIAA 92-5049* (1992)
65. Pate, S.R.: Measurements and correlations of transition reynolds numbers on sharp slender cones at high speeds. *AIAA J.* **9**(6), 1082–1090 (1971)
66. Mack, L.M.: Boundary layer stability analysis for sharp cones at zero angle-of-attack. *AFWAL-TR-86-3022, A180610* (1986)
67. Chen, F.-J., Malik, M.R., Beckwith, I.E.: Boundary-layer transition on a cone and flat plate at Mach 3.5. *AIAA J.* **27**, 687–693 (1989)
68. Rausch, V.L., McClinton, C.R., Crawford, J.L.: HYPER-X: flight validation of hypersonic airbreathing technology. *ISABE 97-7024*, Sept (1997)
69. Malik, M.R., Spall, R.E., Chang, C.-L.: Effect of nose bluntness on boundary layer stability and transition. *AIAA 90-0112* (1990)
70. Stetson, K.F., Thompson, E.R., Donaldson, J.C., Siler, L.G.: Laminar boundary layer stability experiments on a cone at Mach 8, Part 2: Blunt Cone, *AIAA 84-0006* (1980)
71. Stetson, K. F., Thompson, E.R., Donaldson, J.C., Siler, L.G.: Laminar boundary layer stability experiments on a cone at Mach 8. Part 1: sharp cone. *AIAA 83-1761* (1983)
72. Potter, J.L.: The unit reynolds number effect on boundary layer transition. Ph.D. Thesis, Vanderbilt University (1974)
73. Kara, K., Balakumar, P., Kandil, O.A.: Effects of nose bluntness on hypersonic boundary-layer receptivity and stability over cones. *AIAA J.* **49**(12), 2593–2606 (2011)
74. Malik, M.R., Spall, R.E., Chang, C.-L.: Transition prediction in hypersonic boundary layers. In: Sixth National Aero-Space Plane Symposium, Wright-Patterson AFB, OH, April 1989, Paper 67 (1989)
75. Malik, M.R.: Hypersonic flight transition data analysis using parabolized stability equations with chemistry effects. *J. Spacecr. Rockets* **40**(3), 332–344 (2003)
76. Kimmel, R.L., Adamczak, D.W., Borg, M.P., Jewell, J.S., Juliano, T.J., Stanfield, S.A., Berger, K.T.: First and fifth hypersonic international flight research experimentation's flight and ground tests. *J. Spacecr. Rockets* **56**(2), 421–431 (2019)
77. Li, F., Choudhari, M., Chang, C.-L., Kimmel, R., Adamczak, D., Smith, M.: Transition analysis for the ascent phase of HIFIRE-1 flight experiment. *J. Spacecr. Rockets* **52**(5), 1283–1293 (2015)

78. Cebeci, T., Stewartson, K.: On stability and transition in three-dimensional flows. *AIAA J.* **18**(4), 398–405 (1980)
79. Malik, M.R., Wilkinson, S.P., Orszag, S.A.: Instability and transition in rotating disk flow. *AIAA J.* **19**, 1131–1138 (1981)
80. Spalart, P. R.: On the cross-flow instability near a rotating disk, boundary layer transition and control conference, Royal Aeronautical Society, Cambridge, UK (1991)
81. Malik, M.R., Balakumar, P.: Nonparallel stability of rotating disk flow using PSE, In: Hussaini, M.Y., Kumar, A., Streett, C.L. (eds) *Instability, Transition, and Turbulence*. ICASE NASA LaRC Series. Springer, New York, NY (1992)
82. Wilkinson, S.P., Malik, M.R.: Stability experiments in the flow over a rotating disk. *AIAA J.* **22**, 588–595 (1985)
83. Malik, M.R.: The neutral curve for stationary disturbances in rotating-disk flow. *J. Fluid Mech.* **164**, 275–287 (1986)
84. Hall, P.: An asymptotic investigation of the stationary modes of instability of the boundary layer on a rotating disc. *Proc. R. Soc. Lond. A* **406**, 93 (1986)
85. Balakumar, P., Malik, M.R.: Traveling disturbances in rotating-disk flow. *Theoret. Comput. Fluid Dyn.* **2**, 125–137 (1990)
86. Kohama, Y.: Study of boundary layer transition of a rotating disk. *Acta Mechanica* **50**, 193–199 (1984)
87. Balachandar, S., Streett, C.L., Malik, M.R.: Secondary instability in a rotating disk flow. *J. Fluid Mech.* **242**, 323–347 (1992)
88. Malik, M.R., Li, F., Chang, C.-L.: Crossflow disturbances in three-dimensional boundary layers: nonlinear development, wave interaction and secondary instability. *J. Fluid Mech.* **268**, 1–36 (1994)
89. Malik, M.R., Li, F., Choudhari, M.M., Chang, C.-L.: Secondary instability of crossflow vortices and swept-wing boundary-layer transition. *J. Fluid Mech.* **399**, 85–115 (1999)
90. Li, F., Malik, M.R.: Fundamental and subharmonic secondary instabilities of görler vortices. *J. Fluid Mech.* **297**, 77–100 (1995)
91. Li, F., Choudhari, M.M.: Spatially developing secondary instabilities in compressible swept airfoil boundary layers. *Theoret. Comput. Fluid Dyn.* **25**(1–4), 65–84 (2011)
92. Choudhari, M., Li, F., Edwards, J.: Stability analysis of roughness array wake in a high-speed boundary layer. *AIAA 2009-0170* (2009)
93. Kegerise, M.A., King, R.A., Choudhari, M., Li, F., Norris, A.T.: An experimental study of roughness-induced instabilities in a supersonic boundary layer. *AIAA 2014-2501* (2014)
94. Hall, P., Malik, M.R., Poll, D.I.A.: On the stability of an infinite swept attachment line boundary layer. *Proc. R. Soc. London, A* **395**, 229–245 (1984)
95. Pfenniger, W., Bacon, J. W.: Amplified laminar boundary layer oscillations and transition at the front attachment line of a 45° flat-nosed wing with and without boundary layer suction. In: Wells, C.S. (ed.) *Viscous Drag Reduction*, pp. 85–105. Plenum (1969)
96. Poll, D.I.A.: Transition in the infinite swept attachment line boundary layer. *Aeronaut. Quart.* **XXX**, 607 (1979)
97. Poll, D.I.A.: Three-dimensional boundary layer transition via the mechanisms of ‘attachment line contamination’ and ‘cross flow instability’. In: Eppeler, R., Fasel, H. (eds.) *IUTAM Symposium, Laminar-Turbulent Transition*, pp. 253–262. Stuttgart, Germany, Springer-Verlag (1980)
98. Lin, R.-S., Malik, M.R.: On the stability of attachment-line boundary layers. Part 1: the incompressible swept Hiemenz flow. *J. Fluid Mech.* **311**, 239–255 (1996)
99. Theofilis, V., Fedorov, A., Obrist, D., Dallmann, UCh.: The extended Görler-Hämmerlin model for linear instability of three-dimensional incompressible swept attachment-line boundary layer flow. *J. Fluid Mech.* **487**, 271–313 (2003)
100. Mack, C.J., Schmid, P.J., Sesterhenn, J.L.: Global stability of swept flow around a parabolic body: connecting attachment-line and crossflow modes. *J. Fluid Mech.* **611**, 205–214 (2008)
101. Mack, C.J., Schmid, P.J.: Global stability of swept flow around a parabolic body: the neutral curve. *J. Fluid Mech.* **678**, 589–599 (2011)

102. Hall, P., Malik, M.R.: On the instability of a three-dimensional boundary layer: weakly nonlinear theory and a numerical approach. *J. Fluid Mech.* **163**, 257–282 (1986)
103. Spalart, P.R.: Direct numerical study of leading-edge contamination, AGARD-CP-438, pp. 5.1–5.13 (1988)
104. Poll, D.I.A., Danks, M.: Relaminarisation of the swept wing attachment-line by surface suction. In: Kobayashi, R. (ed.) IUTAM Symposium, Laminar Turbulent Transition, pp. 137–144. Sendai, Japan, Springer Verlag (1995)
105. Goldsten, M.E.: The evolution of Tollmien-Schlichting waves near a leading edge. *J. Fluid Mech.* **127**, 59–81 (1983)
106. Bushnell, D.: Notes on initial disturbance fields for the transition problem. In: Hussaini, M.Y., Voigt, R.G. (eds.) Instability and Transition, vol. 1, pp. 217–232. Springer–Verlag, Berlin (1990)
107. Fedorov, A.V.: Receptivity of a supersonic boundary layer to solid particulates. *J. Fluid Mech.* **737**, 105–131 (2013)
108. Fedorov, A.V., Tumin, A.: Receptivity of high-speed boundary layers to kinetic fluctuations. *AIAA J.* **55**(7), 2335–2348 (2017)

Progress in Stability and Transition Research



Helen L. Reed

Abstract This paper provides an overview of the theoretical and computational boundary-layer receptivity, stability, and control research conducted by the author over the past four decades in collaboration with her colleagues and students. The overarching approach has been one of verification and validation, including working closely with experimentalists (both with ground facilities and flight platforms) to achieve closure between theory and experiment. She and her team have worked to identify instability mechanisms in complex three-dimensional (3-D) configurations, create and transfer physics-based models and tools, guidelines, and correlations including for surface features, and formulate effective control strategies.

1 Introduction

In boundary layers in external flows, the transition process can be qualitatively described using the roadmap of Morkovin et al. [1], and this paper relates to paths A and B. Receptivity is the first stage in all transition processes and defines how freestream disturbances enter the boundary-layer, interact with surface nonuniformities, and generate the initial disturbances responsible for the breakdown of laminar flow and ultimately the transition to turbulence (see also [2, 3]).

Path A is associated with weak freestream disturbances, and, in the absence of other effects such as roughness, is generally accepted as the appropriate path for the flight freestream environment. The initial growth of the disturbances in the boundary layer is described by linear theory of primary modes, including traditional mechanisms such as Tollmien-Schlichting (T-S), crossflow, Görtler, attachment-line, and others (including oblique first mode for supersonic flow and Mack mode). (1) For two-dimensional (2-D) flat or convex surfaces, the streamwise extent of linear growth is large compared to the nonlinear region. As the amplitude grows, 3-D and nonlinear

H. L. Reed (✉)
Texas A&M University, College Station, Texas 77843-3141, USA
e-mail: helen.reed@tamu.edu

interactions can occur in the form of subcritical subharmonic instabilities. Disturbance growth is very rapid in this stage (over a convective length scale) and breakdown occurs. Since linear stability behavior can be calculated and the extent of the laminar region is long compared to that of the nonlinear region, transition prediction schemes (such as linear stability theory [4]) often assume that transition follows path A and consider only the linear regime. However, since the initial conditions (receptivity) are not generally known, only correlations between two systems with similar environmental conditions are possible, or the methods can be used in a comparative sense. See [5, 6]. (2) For 3-D boundary layers (e.g. swept wings) and Görtler problems (concave surfaces), nonlinear distortions of the basic flow may occur early on due to the action of the primary instability (a stationary vortex). These flows are characterized by an extensive distance of nonlinear evolution with eventual saturation of the fundamental disturbance, leading to the strong amplification of very-high-frequency inflectional instabilities and breakdown [7, 8].

On Path B, both modal and transient growth are present - transient growth initially dominates and then modal. In transient growth, streamwise and wall-normal vorticity are important, and can lead to spanwise modulations of instabilities [9]. The early spanwise modulations observed by Klebanoff et al. [10] could have their origins in subcritical transient growth [11–14]. Also, Saric et al. [15] demonstrated that crossflow disturbances can be stabilized by micron-sized discrete roughness elements near the leading edge that nonlinearly distort the basic flow.

2 Personal Areas of Research

The author was very fortunate to have first been introduced to the field of stability and transition and Laminar Flow Control (LFC) through working under the direction of Dr. Werner Pfenninger at NASA Langley Research Center in 1977–78 on the design of supercritical LFC airfoils [16]. Please also see [17].

This work led to the author’s career path in an academic environment with an emphasis on the understanding, modeling, and control of the stability and transition process. In the development of aerospace systems from low speed to hypersonic, where transition occurs may critically drive system drag, thermal load, propulsive efficiency, and aerostability, and the development, validation, and introduction of physics-based approaches to accurate prediction will lead to more manageable uncertainties in design. Transition is highly dependent on operating conditions including freestream content, geometry, and surface conditions, and any prediction scheme must accurately account for the relevant physics.

Control may be applied for different reasons. (1) First is the desire to delay transition and extend laminar flow. This is termed Laminar Flow Control (LFC—as above) with benefits in fuel efficiency, aerodynamic heating load reduction, and long range and/or endurance—see [18] for a reference list. For example, that wall suction works is evidenced by the fact that the X-21 aircraft achieved laminar flow at transition Reynolds numbers of 27 million with a 20% decrease in overall drag [19].

(2) Second is the desire to encourage transition for enhanced mixing or separation delay, such as over control surfaces and at a propulsion system inlet. (3) Either way, the most effective strategy for control is to capitalize on the flow physics, identify the relevant instability mechanisms and what affects them, and modulate the most unstable disturbances as they are just beginning to grow.

Over four decades, the author and her team have conducted research in the following relevant areas:

- Surface suction and blowing related to LFC [20–22]
- Streamwise vorticity and its effect on the later stages of breakdown [23]
- 2-D leading-edge receptivity to sound/vorticity; curvature discontinuity [24–26]
- Crossflow instability, linear and nonlinear parabolized stability equations (LPSE and NPSE) related to swept wings [8, 27–38]
- Health monitoring systems for natural laminar flow applications [39]
- Saric discrete roughness element strategy for swept-wing LFC [15, 40–46]
- Legacy fleet roughness studies [47]
- Critical forward-facing steps in subsonic crossflow-dominated flow [48–50]
- Slotted LFC airfoils for ultra-efficient commercial vehicles [51]

The author and her team have also conducted research in the stability and transition of hypersonic chemically reacting boundary layers over many years [52]:

- Chemical nonequilibrium studies in stability analyses [53]
- Agreement between theory and experiments for Mack mode [54]
- Most unstable Mack mode not being 2-D in a 3-D boundary layer [30]
- Effect of transport models [55]
- Sensitivity of Mack mode to model misalignments in ground tests [56, 57]
- 3-D boundary layers—primary crossflow instability and secondary instabilities, crossflow vortex path and wavenumber prediction, transition onset prediction, co-existing instabilities, NPSE and spatial biglobal methods [27, 28, 34–38, 58]
- Complex flows/spatial biglobal methods [37, 38, 58, 59]
- Thermochemical nonequilibrium effects [60, 61]

Building upon this research, the author and her team have developed “EPIC” (Euonymous Parabolized Instability Code) [27, 28], a verified and validated 3-D NPSE [62] tool coupled with spatial bi-global analysis (BLAST; [58, 63]) to model the evolution of a variety of instabilities (primary, subcritical, and secondary) and interactions leading to transition on 2-D and 3-D configurations from subsonic to hypersonic. EPIC capability continues to be expanded, including receptivity.

3 Verification and Validation

Insights and lessons learned from years of verification and validation activities are provided. Verification means “am I solving the equations correctly” while validation means “am I solving the correct equations”. Per Roache [64], verification means

“confirming the accuracy and correctness of the code” (i.e., is the grid resolved, are there any programming errors in the codes, etc.). Validation requires verification of the code in addition to confirming the adequacy of the equations used to model the physical problem. Strictly speaking, a code can only be validated by comparison with documented, quality experimental data.

3.1 Verification

As outlined by Reed et al. [65], for stability problems, verification entails critiquing the grid architecture and resolution, the numerics (including dissipation effects), and so forth. The evolution of disturbances in the boundary layer is described by disturbance equations that are obtained by decomposing the total flow into a basic state plus a disturbance and assuming the basic state is a solution to the original equations of motion. In verification activities, the basic state can look converged, but the stability may not be. The acid test is to continue both systematic basic-state and stability formulation verification until the stability results do not change. The numerical accuracy of the basic state and boundary conditions must be very high because the stability and transition results will be very sensitive to small departures of the mean flow from its exact shape. See [66–68].

3.2 Validation

Computationalists and experimentalists should work together to advance the identification of relevant effects and mechanisms, prediction methods, and control [65, 69]. Transition is highly sensitive to operating conditions, and experiments provide validation of computations, and vice versa. The experimentalist can also benefit from learning what configuration and physics is actually being tested—see for example 3.2.1 (b) (i) below.

Provided in this section are some recommendations and example results from over the years:

3.2.1 Both groups must work with the same configurations, both geometrically and operationally, and confirm it.

- (a) Attention must be paid to coordinate systems. Computations are typically in a body-oriented frame whereas experiments are likely otherwise, and figuring out the coordinate transformations/rotations between the two frames is required.
 - (i) For example, the NLF(2)-0415 swept-wing stationary-crossflow NPSE computations of Haynes and Reed [33] were completed in body-oriented coordinates and required seven coordinate transformations to convert to wind-tunnel coordinates and single-hotwire measurements for successful

validation with the experiments of Reibert et al. [70]. Roache [71] cited this close collaboration as exemplary of validation and the results are shown on the cover of his book “Fundamentals of Computational Fluid Dynamics.”

- (b) Computationalists must solve for the flowfield *in situ*, including the model mounted in the wind tunnel or in its flight configuration. It is important to understand sensitivities, such as alignment, wall conditions, and so forth.

- (i) In hypersonic flow, wind-tunnel model alignment and freestream flow angularity were found to be important. Under the conditions of the Hofferth et al. [56] Mach 6 Quiet Tunnel experiments at Texas A&M on the Langley 93-10 flared cone at “0° yaw”, whereas the computations predicted a most unstable Mack mode frequency of 241 kHz at the end of the cone, initial experimental measurements showed a most unstable frequency $O(280 \text{ kHz})$. Because tightening mounting bolts or asymmetries in wind-tunnel flow can result in $O(0.1^\circ)$ offset in geometric-aerodynamic alignment [56] and studies have shown that disproportional heating will create a variation in nozzle boundary-layer thickness and thus create asymmetric flow [72], an LPSE study was done on the flared cone at different yaw angles [57]. For the most unstable frequency as a function of yaw, the computations predicted a slope $O(7.3 \text{ kHz per } 0.1^\circ)$, with the experiments showing similar effect. A misalignment creates a discrepancy in boundary-layer thickness on opposite sides of a symmetric model, resulting in different frequencies being most amplified. Differentially measuring this peak Mack mode frequency is now recommended for experiments to align models due to this sensitivity.
- (ii) The research team at Texas A&M conducted a closely coordinated series of flight/wind-tunnel/computational investigations into the interaction between crossflow-transition phenomena and a 2-D step excrescence in subsonic flow. Even judiciously designed LFC wings can fail to be laminar in an operational environment. Most aircraft have a 2-D spanwise step or gap from a leading-edge skin panel, high lift devices, anti-icing devices, and so forth.

A 30°-swept-wing model with adjustable step heights at 1% and 15% chord was mounted vertically under the port wing of the Flight Research Laboratory’s Cessna O-2A (operational environment with typical transport unit Reynolds numbers of ~ 5.5 million per meter) and in the Klebanoff-Saric (quiet) Wind Tunnel (KSWT). For the computations, it was necessary to model the test article, O-2A fuselage and wing, and all probes, struts, and other features influencing the stability results on the test article. Gridding was a challenge especially given the diverse range of spatial scales—from step heights $O(100 \mu\text{m})$ to boundary layer thicknesses $O(\text{mm})$ to the test model’s chord $O(\text{m})$ to the aircraft itself $O(10 \text{ m})$. Also time was spent systematically gridding and determining by computational testing which features (such as the propeller, horizontal

and vertical tail surfaces, and starboard features in this case) could be eliminated without affecting the stability results on the test article. Of note was the critical early effort to quantify the flow angularity due to the fuselage. The validation was first conducted by Rhodes et al. [73, 74] and then Tufts et al. [48] for a clean (no excrescences) model. This flight flowfield was then used to inform the boundary conditions for smaller (in spatial dimensions) grids surrounding the step excrescence [50]. Also, the test article was wall-mounted in the KSWT whose wall effects and fixture techniques (including the reference frame for pitching the model) were included in those computations.

In the subsequent study of forward-facing steps and crossflow, Tufts et al. [50] found that once a critical step height was exceeded, there was a sudden amplification of stationary modes with transition moving forward to the step. In a favorable pressure gradient, near the step, the lower half of the crossflow vortex tends to travel from tip to root, and the helical flow on top of the step travels from root to tip. Consequently, at low step heights, any interaction between the crossflow vortices and the helical flow on top of the step will be destructive, as the two flows oppose one another in terms of direction. However, once the step height is increased to be higher than the center of the crossflow vortex, it appears that interaction between the helical flow and crossflow vortex is now constructive as the two flows are moving in the same direction. Tufts et al. [50] reasoned that the height of the center of the crossflow vortex would roughly correspond to the critical forward-facing step height. This can be found from the location within the clean (no step) boundary layer of the maximum v (vertical velocity) perturbation of the stationary crossflow linear stability theory eigenmodes. This correlation agrees with the companion experimental results. The basic state accounts for the integrated picture of pressure gradients, curvature, sweep, wall conditions, operating conditions, and so forth. Given that laminar-flow wing designs will likely include performing at minimum a linear stability analysis, this seems an easily accessible criterion providing predictive tolerances.

3.2.2 Both groups must understand relevant receptivity mechanisms present (freestream conditions, interactions with geometry, ...). Transition is an initial-value problem, and a challenge for nonlinear stability methods such as NPSE and direct numerical simulations (DNS) is that the upstream conditions must be specified and one must assign the input modes and their amplitudes and phases. Working with an experiment with carefully documented conditions aids in this process.

- (a) What is the relevant freestream sound, vorticity ... content? It is not enough to quote “freestream turbulence level” for an experimental facility, rather one should separate amplitudes, frequencies, length scales, and orientations of both sound and vorticity components present in the freestream. Each instability mechanism responds differently—sometimes oppositely.

- (i) Within the Morkovin et al. [1] roadmap Path A, the unbounded growth of disturbances and the transition process are very sensitive to the details of the flow. Linear theories and weakly nonlinear theories fail after the instabilities achieve finite amplitude, and when various waves compete and grow simultaneously. Here, nonlinear 3-D effects become significant.
 A surprise from the analyses of Herbert [75] and other computations early on in a 2-D boundary layer, was that under amplitude conditions of the experimentally observed fundamental Klebanoff-type breakdown (K-type; [10]), the subharmonic Herbert-type breakdown (H-type) was still calculated to be the dominant breakdown mechanism instead of the fundamental mode. This was resolved by Singer et al. [23] who demonstrated that the upstream conditions for the computations were incomplete; when streamwise vorticity (as is present in facilities) is included, the result is the appearance of the fundamental mode and the ordered peak-valley K-type structure. In transient growth, streamwise and wall-normal vorticity can lead to spanwise modulations of instabilities (Path B in the roadmap; [9, 11–14]).
 - (ii) For 2-D basic states, the vortical parts of the freestream disturbances (turbulence) contribute to the 3-D aspects of breakdown [23, 76, 77]. On the other hand, the irrotational parts of the freestream disturbances (sound) contribute to the initial amplitudes of the 2-D T-S waves [78].
 - (iii) T-S (2-D) and crossflow (3-D) behave in opposite ways. T-S is more strongly influenced by freestream sound than by freestream vorticity within limits on freestream vorticity, with the opposite being true for crossflow.
- (b) Is the relevant transfer mechanism into the boundary layer included and well modeled in the computation?
- (i) External disturbances common to the flight environment are typically either acoustic or vortical (“natural” disturbances). These generally do not contain a wavelength that coincides with an instability amplified within the boundary layer. While frequency is generally conserved, a mechanism for transferring energy from a much longer wavelength wave to a relatively small wavelength instability wave must exist—this is receptivity. This includes: leading edge (radius and pressure gradients); distributed/discrete roughness, steps, gaps; curvature discontinuities; surface waviness; and so forth. Roughness and other surface nonuniformities can interact with freestream sound or vorticity to create streamwise and spanwise vorticity, and in a 3-D boundary layer they can create either stationary or traveling crossflow waves depending on the freestream content. These are part of receptivity.
 - (ii) Moreover, the picture for 3-D flows is expected to be different than that of 2-D flows. Within limits, T-S is destabilized by 2-D features, whereas crossflow and Görtler are destabilized by 3-D features.

- (iii) Spatial DNS was established as the framework needed to accurately model how the freestream relates to transition mechanisms observed in the boundary layer for 2-D leading-edge receptivity to sound and vorticity; see [24–26]. For each configuration, the integrated picture of geometry/nonuniformities, operating conditions/freestream environment, sweep, and associated pressure gradients must be included in any meaningful evaluation of receptivity.

For example, in studying 2-D leading-edge receptivity to freestream sound, with spatial DNS, finite curvature can be included in the leading-edge region. This feature was left out of some early unsuccessful receptivity models. Experimentally, a popular model geometry for receptivity had been the flat plate with an elliptic leading edge. Lin et al. [24] demonstrated computationally that as the aspect ratio of the elliptic nose on a flat plate is sharpened from 3 (blunt) to 9 to 40 (very thin), the vorticity tends to become singular. By stipulating the plate to have finite curvature at the leading edge, the singularity there is removed and a new length scale is introduced.

However, the curvature at the ellipse/flat-plate juncture is discontinuous and provides a source of receptivity [79, 80]. Lin et al. [24] introduced a new leading-edge geometry based on a modified super-ellipse (MSE) given by

$$[(a - x)/a]^{m(x)} + [y/b]^n = 1, \quad 0 < x < a, \quad m(x) = 2 + [x/a]^2 \quad \text{and} \quad n = 2$$

where $a = b * AR$, b is the plate half-thickness, and AR is the aspect ratio of the “elliptic” nose. For a usual super-ellipse, both m and n are constants. Curvature at the juncture will be continuous (zero) as long as $m > 2$ at $x/b = AR$. The MSE, with $m(x)$, has the further advantage of a nose radius and geometry (hence a pressure distribution) close to that of an ordinary ellipse.

Lin et al. [24] then simulated the receptivity to sound-like oscillations of the freestream streamwise velocity applied along the boundary of the computational domain and allowed to impinge on the body. They found: (1) T-S waves appearing in the boundary layer could be linked to sound present in the freestream. Receptivity occurred in the leading-edge region where rapid streamwise basic-flow adjustments occurred. (2) For plane freestream sound waves, T-S wave amplitude at Branch I decreased as the elliptic nose was sharpened. (3) When the discontinuity in curvature at the ellipse/flat-plate juncture was eliminated, the T-S wave amplitude at Branch I was cut in half.

A good recent reference is that of Shahriari et al. [81] who revisited leading-edge acoustic receptivity for the elliptic and MSE geometries and addressed contradictory results in the literature, both computational and experimental. Their results agree with those of Lin et al. [24] that Branch I receptivity decreases as the nose is sharpened, and their results

- agree with those of Fuciarelli et al. [26] for an MSE of aspect ratio of 6, but not for 20. (The present author believes the results of Shahriari et al. [81] are correct.)
- (iv) In a swept-wing flow, Rizzetta et al. [46] modeled leading-edge micron-sized roughness with a Navier-Stokes code, decomposed the flowfield into modes, amplitudes, and phases, and input these via linear stability theory eigenmodes as upstream conditions for the downstream-marching 3-D NPSE under crossflow-dominated conditions. A successful verification with DNS was shown, and related to available experiments and flight tests.

3.2.3 Have the computationalists included and well modeled the appropriate physics and effects in both the basic state and stability formulations? Are there multiple mechanisms at play?

- (a) Wall suction strips used for LFC were modeled by Reed & Nayfeh using triple deck theory [20]. Discrete wall suction provides a challenging boundary condition for a basic state, and this theory provided an efficient tool for configuration studies by allowing for superposition of solutions and including both the upstream and downstream influence of the strips on the boundary layer and on each other. An optimization process was developed for efficient strip placement to delay transition, and early suction (that is, near the Branch I neutral point) was found to be key to transition control in 2-D flows [21]. This was a successful validation with companion experiments by Reynolds and Saric [82] with hot-wire measurements quantitatively matching mode shapes and instability growth on the flat plate with suction strips. This was followed by a quantitative assessment of the effects of oversuction and blowing on transition [22].
- (b) Concerning crossflow, the past decades have seen international, close collaborations among theory, computation, experiment, and flight tests, with the identification of important factors for subsonic, transonic, and supersonic flows [8, 29]. Here the combination of sweep and streamwise pressure gradient produces curved streamlines and a 3-D boundary layer with inflection points leading to inviscid instability in the form of co-rotating essentially streamwise vortices. Swept wings, wing/fuselage/feature junctures, other 3-D configurations (for example, elliptic cone), and pitch/roll/yaw all create 3-D boundary layers. Recent efforts have shown that hypersonic 3-D applications display similarities in physics (related to primary crossflow and the secondary instabilities) as for the lower speed ranges, although the role of traveling crossflow and the Mack modes is under investigation (see for example [34–38]).

The following must be considered when modeling crossflow instability:

- (i) Unlike T-S instabilities, the crossflow instability exhibits stationary as well as traveling disturbances that are amplified. While linear theory predicts that traveling disturbances have higher growth rates [4], the interaction of surface roughness and freestream vorticity (receptivity) dictates whether stationary or traveling disturbances cause transition

- [83–85]. Stationary waves are more important in ultra-low-turbulence environments characteristic of flight, while traveling waves dominate in higher-turbulence environments. In the flight environment, the presence of micron-sized 3-D roughness at the leading edge (e.g. from a painted surface) establishes the stationary streamwise vortex. On the other hand, transition results from many wind tunnels may have no bearing on flight because quite low levels of freestream vorticity are sufficient to generate traveling-wave-dominated behavior, not what is observed in flight. One needs knowledge of the present relevant receptivity conditions to know what to model. This advice applies to any configuration and operating environment under consideration, whether 2-D or 3-D.
- (ii) Related to this, stationary and traveling instabilities can coexist in a boundary layer, and Moyes et al. [37] recently found that including both in an NPSE analysis matched quiet-tunnel experimental observations in hypersonics.
 - (iii) Haynes & Reed [33] demonstrated in their validation with Reibert et al. [70] that including convex curvature in stability formulations has a significant stabilizing effect. There may appear to be a very small effect on the metric coefficients, and this may compel the researcher to ignore curvature. However, even small changes in the metric coefficients can have a significant effect on development and growth. This has been found by others as well.
 - (iv) What marching path one chooses for stationary crossflow in stability formulations is important to accurately predict development and growth, and it should be in the group velocity direction. Kocian et al. [36] introduced and validated a method for the prediction of the stationary crossflow vortex direction based solely on the basic-state boundary layer profiles.
 - (v) Modeling the downstream evolution of the spanwise wavenumber is important, and Kocian et al. [36] introduced and validated a method based solely on the basic-state boundary layer profiles.
 - (vi) To model crossflow evolution requires a nonlinear analysis, such as NPSE or DNS. Nonlinear effects and modal interaction play an early role when stationary crossflow vortices dominate, such as is expected in flight. Since the wave fronts are fixed with respect to the model and the wavenumber vector is nearly perpendicular to the local inviscid streamline, the weak (v' , w') motion of the wave convects $O(1)$ streamwise momentum producing strong u' distortion in the streamwise boundary-layer profile. This integrated effect leads to basic-state modification and early development of nonlinear effects. See [8] for references—e.g., Haynes & Reed [33] demonstrated the inadequacy in using linear models and the accuracy of NPSE models.
 - (vii) The breakdown process for stationary crossflow is associated with the destabilization of high-frequency instabilities. The u' distortions above

are time-independent, resulting in spanwise modulation of the mean streamwise velocity profile. As the distortions grow, the boundary layer develops an alternating pattern of accelerated, decelerated, and doubly inflected profiles. The inflected profiles are inviscidly unstable and are subject to highly amplified, high-frequency secondary instabilities that lead to rapid local breakdown [34, 58, 86, 87, 88]. Transition develops locally with a front that is nonuniform in span and characterized by a saw-tooth pattern of turbulent wedges.

- (viii) For hypersonic flow, Moyes et al. [35, 37, 38] demonstrated that transition onset can be predicted by the deviation (from laminar) of the skin friction or heat transfer rate as predicted by the combination of the basic state plus the mean flow distortion from the NPSE solution. This point is also the neutral point for the high-frequency secondary instabilities described above.

3.2.4 Are the experiments well documented, high-quality, and meaningful with appropriate instrumentation, diagnostics, quantities measured, and uncertainties?

Guidelines for ground and flight testing are available for receptivity, stability, and transition research from resources such as Saric [89]. Both the experiments and computations have proven to require a lot of care to be done right.

4 Summary

Overall much progress has been made in understanding, modeling, control, and design. Challenges remain in (1) receptivity modeling including the characterization of conventional/quiet tunnel freestreams versus the flight freestream environment, and interactions with surface features (roughness and so forth), (2) complex geometries including the accurate modeling of the basic state, the in-depth understanding and modeling of relevant mechanisms, the development of lower-order models and tools for rapid parameter studies and design, an assessment of unsteadiness and off-design conditions along a flight path, and efficient control, (3) criteria for critical excrescences and tolerances, and (4) the need for validation experiments and flight tests, with flight tests being especially critical for crossflow.

From the author's personal experience, progress will occur when theoretical, computational, and experimental methods collaborate closely to address these important and sensitive problems.

Acknowledgements The author gratefully acknowledges support over the years from: Air Force Research Laboratory, Air Force Office of Scientific Research, Arnold Engineering Development Center, Defense Advanced Research Projects Agency, National Aeronautics and Space Administration, National Institute of Aerospace, Office of Naval Research, Texas A&M High Performance Research Computing Group, Texas Advanced Computing Center, Pointwise, Lockheed Martin, Northrop Grumman, and Boeing. She is also grateful to the many outstanding graduate and undergraduate students and other colleagues with whom she has had the privilege to collaborate.

References

1. Morkovin, M., Reshotko, E., Herbert, T.: Transition in open flow systems—a reassessment. *Bull. Am. Phys. Soc.* **39**(9), 1882 (1994)
2. Saric, W., Reed, H., Kerschen, E.: Boundary-layer receptivity to freestream disturbances. *Ann. Rev. Fluid Mech.* **34**, 291–319 (2002)
3. Reed, H., Reshotko, E., Saric, W.: Receptivity: the inspiration of Mark Morkovin. AIAA-2015-2471 (2015)
4. Mack, L.: Boundary-layer linear stability theory. AGARD Report 709: Special Course on Stability and Transition of Laminar Flow, 3.1–3.81 (1984)
5. Reed, H., Saric, W., Arnal, D.: Linear stability theory applied to boundary layers. *Ann. Rev. Fluid Mech.* **28**, 389–428 (1996)
6. Arnal, D., Casalis, G., Houdeville, R.: Practical transition prediction methods: subsonic and transonic flows. RTO-EN-AVT-151—Adv in Laminar-Turb Transition Modeling. VKI, 9–12 June (2008)
7. Saric, W.: Görtler vortices. *Ann. Rev. Fluid Mech.* **26**, 379–409 (1994)
8. Saric, W., Reed, H., White, E.: Stability of three-dimensional boundary layers. *Ann. Rev. Fluid Mech.* **35**, 413–442 (2003)
9. Schmid, P., Henningson, D.: Stability and Transition in Shear Flows. Springer-Verlag (2001)
10. Klebanoff, P., Tidstrom, K., Sargent, L.: The three-dimensional nature of boundary-layer instability. *J. Fluid Mech.* **12**(1), 1–34 (1962)
11. Andersson, P., Berggren, M., Henningson, D.: Optimal disturbances and bypass transition in boundary layers. *Phys. Fluids* **11**(1), 134–150 (1999)
12. Luchini, P.: Reynolds-number independent instability of the boundary layer over a flat surface: optimal perturbations. *J. Fluid Mech.* **404**, 289–309 (2000)
13. Andersson, P., Brandt, L., Bottaro, A., Henningson, D.: On the breakdown of boundary layer streaks. *J. Fluid Mech.* **428**, 29–60 (2001)
14. Tumin, A., Reshotko, E.: Spatial theory of optimal disturbances in boundary layers. *Phys. Fluids* **13**(7), 2097–2104 (2001)
15. Saric, W., Carrillo, R., Reibert, M.: Nonlinear stability and transition in 3-D boundary layers. *Mechanica* **33**(5), 469–487 (1998)
16. Pfenniger, W., Reed, H., Dagenhart, J.: Design considerations of advanced supercritical low drag suction airfoils. *Viscous Flow Drag Reduction, AIAA Prog in Astro and Aero Series* **72**, 249–271 (1980)
17. Pfenniger, W., Vemuru, C.: Design philosophy of long range LFC transports with advanced supercritical LFC airfoils. In: Barnwell, R., Hussaini, M. (eds.) *Natural Laminar Flow and Laminar Flow Control, ICASE/NASA LaRC Series*, pp. 177–221. Springer, New York, NY (1992)
18. Malik, M., Crouch, J., Saric, W., Lin, J., Whalen, E.: Application of drag reduction techniques to transport aircraft. In: Blockley, R., Shyy, W. (eds.) *Encyclopedia Aero Eng.* John Wiley: Chichester (2015)
19. Pfenniger, W.: Laminar flow control—laminarization. AGARD Report 654: special course on concepts for drag reduction, 3.1–3.75 (1977)
20. Nayfeh, A., Reed, H., Ragab, S.: Flow over plates with suction through porous strips. *AIAA J.* **20**(5), 587–588 (1982). May
21. Reed, H., Nayfeh, A.: Numerical-perturbation technique for stability of flat-plate boundary layers with suction. *AIAA J.* **24**(2), 208–214 (1986). Feb
22. Saric, W., Reed, H.: Effect of suction and weak mass injection on boundary-layer transition. *AIAA J.* **24**(3), 383–389 (1986). Mar
23. Singer, B., Reed, H., Ferziger, J.: The effects of streamwise vortices on transition in the plane channel. *Phys. Fluids A* **1**(12), 1960–1971 (1989). Dec
24. Lin, N., Reed, H., Saric, W.: Effect of leading-edge geometry on boundary-layer receptivity to freestream sound. In: Hussaini, M., Kumar, A., Streett, C. (eds.) *Instability, Transition, and Turbulence*, pp. 421–440. Springer-Verlag, New York, NY (1992)

25. Buter, T., Reed, H.: Boundary layer receptivity to freestream vorticity. *Phys. Fluids A* **6**(10), 3368–3379 (1994)
26. Fuciarelli, D., Reed, H., Lytle, I.: Direct numerical simulation of leading-edge receptivity to sound. *AIAA J.* **38**(7), 1159–1165 (2000). July
27. Oliviero, N., Kocian, T., Moyes, A., Reed, H.: EPIC: NPSE analysis of hypersonic crossflow instability on yawed straight circular cone. *AIAA-2015-2772* (2015)
28. Moyes, A., Beyak, E., Kocian, T., Reed, H.: Accurate and efficient modeling of boundary-layer instabilities. *AIAA-2019-1907* (2019)
29. Reed, H., Saric, W.: Stability of three-dimensional boundary layers. *Ann. Rev. Fluid Mech.* **21**, 235–284 (1989). Jan
30. Balakumar, P., Reed, H.: Stability of three-dimensional supersonic boundary layers. *Phys. Fluids A* **3**(4), 617–632 (1991). April
31. Lin, R., Reed, H.: Effect of curvature on stationary crossflow instability of a three-dimensional boundary layer. *AIAA J.* **31**(9), 1611–1617 (1993). Sep
32. Reed, H., Haynes, T.: Transition correlations in three-dimensional boundary layers. *AIAA J.* **32**(5), 923–929 (1994)
33. Haynes, T., Reed, H.: Simulation of swept-wing vortices using nonlinear parabolized stability equations. *J. Fluid Mech.* **305**, 325–349 (2000). Feb
34. Moyes, A., Paredes, P., Kocian, T., Reed, H.: Secondary instability analysis of crossflow on a hypersonic yawed straight circular cone. *J. Fluid Mech.* **812**, 370–397 (2017)
35. Moyes, A., Kocian, T., Mullen, D., Reed, H.: Boundary layer stability analysis of HIFiRE-5b flight geometry. Special Section on HIFiRE-5b. *J. Spacecr. Rockets* **55**(6), 1341–1355 (2018) Nov
36. Kocian, T., Moyes, A., Reed, H., Craig, A., Saric, W., Schneider, S., Edelman, J.: Hypersonic crossflow instability. Special Section on NATO/STO AVT 240 "Hypersonic Boundary-Layer Transition Prediction". *J. Spacecr. Rockets* **56**(2), 432–446 (2019) Mar
37. Moyes, A., Reed, H.: Nonlinear boundary-layer stability analysis of BOLT and HIFiRE-5. *AIAA-2019-2972* (2019)
38. Moyes, A., Reed, H.: Pre-flight boundary-layer stability analysis of BOLT geometry. Special Section on Boundary Layer Transition Flight Experiment (BOLT) - Pre-Flight Studies. *J. Spacecr. Rockets* **58**(1), 78–89 (2021) Jan
39. Mavris, D., Saric, W., Ran, H., Belisle, M., Woodruff, M., Reed, H.: Investigation of a health monitoring methodology for future natural laminar flow transport aircraft. In: ICAS_2010_193, 27th International Congress of the Aeronautical Sciences, September-October (2010)
40. Saric, W., Carpenter, A., Reed, H.: Passive control of transition with roughness in three-dimensional boundary layers. *Philosoph. Trans. Royal Soc. A* **369**(1940), 1352–1364 (2011). Apr
41. Saric, W., Reed, H.: Supersonic laminar flow control on swept wings using distributed roughness. *AIAA-2002-0147* (2002)
42. Saric, W., Reed, H., Banks, D.: Flight testing of laminar flow control in high-speed boundary layers. RTO-MP-AVT-111: Enhancement of NATO Military Flight Vehicle Performance by Management of Interacting Boundary Layer Transition and Separation, 30, Prague (2004)
43. Tufts, M., Reed, H., Saric, W.: Design of an infinite-swept-wing glove for an in-flight discrete-roughness-element experiment. *J. Aircr.* **51**(5), 1618–1631 (2014) Sep–Oct
44. Roberts, M., Reed, H., Saric, W.: Computational evaluation and linear stability of a transonic laminar-flow wing glove. *J. Aircr.* **52**(2), 595–608 (2015) Mar–Apr
45. Saric, W., West, D., Tufts, M., Reed, H.: Experiments on discrete roughness element technology for swept-wing laminar flow control. Special Section on Controls. *AIAA J.* **57**(2), 641–654 (2019) Feb
46. Rizzetta, D., Visbal, M., Reed, H., Saric, W.: Direct numerical simulation of discrete roughness on a swept wing leading edge. *AIAA J.* **48**(11), 2660–2673 (2010)
47. Moyes, A., Kostak, H., Cox, C., Kocian, T., Saric, W., Reed, H., Rivera, J., Dale, G.: Drag reduction initial conditions on various legacy fleet aircraft: surface roughness measurements. *AIAA-2017-0285* (2017)

48. Tufts, M., Duncan, G., Crawford, B., Reed, H., Saric, W.: Computational design of a test article to investigate 2-D surface excrescences on a swept laminar-flow wing. *Int. J. Eng. Syst. Modell. Simul.* **6**(3/4), 181–190 (2014)
49. Duncan, G., Crawford, B., Tufts, M., Saric, W., Reed, H.: Flight experiments on the effects of step excrescences on swept-wing transition. *Int. J. Eng. Syst. Modell. Simul.* **6**(3/4), 171–180 (2014)
50. Tufts, M., Reed, H., Crawford, B., Duncan, G., Saric, W.: Computational investigation of step excrescence sensitivity in a swept-wing boundary layer. *J. Aircr.* **54**(2), 602–626 (2017) Mar–Apr
51. Groot, K., Beyak, E., Heston, D., Reed, H.: Boundary-layer stability of a natural-laminar-flow airfoil at flight conditions. AIAA-2020-3052 (2020)
52. Reed, H., Kimmel, R., Schneider, S., Arnal, D.: Drag prediction and transition in hypersonics. AIAA-1997-1818 (1997)
53. Stuckert, G., Reed, H.: Linear disturbances in hypersonic, chemically reacting shock layers. *AIAA J.* **32**(7), 1384–1393 (1994)
54. Lytle, I., Reed, H., Shiplyuk, A., Maslov, A., Buntin, D., Schneider, S.: Numerical-experimental comparisons of second-mode behavior for blunted cones. *AIAA J.* **43**(8), 1734–1743 (2005). Aug
55. Lytle, I., Reed, H.: Sensitivity of second-mode linear stability to constitutive models within hypersonic flow. AIAA-2005-0889 (2005)
56. Hofferth, J., Saric, W., Kuehl, J., Perez, E., Kocian, T., Reed, H.: Boundary-layer instability and transition on a flared cone in a Mach 6 quiet wind tunnel. *Int. J. Eng. Syst. Modell. Simul.* **5**(1/2/3) 109–124 (2013)
57. Kocian, T., Perez, E., Oliviero, N., Kuehl, J., Reed, H.: Hypersonic stability analysis of a flared cone. AIAA-2013-0667 (2013)
58. Riha, A., Groot, K., Moyes, A., Reed, H.: Secondary-instability-mode identification in hypersonic crossflow-dominated boundary layers. AIAA-2020-2242 (2020)
59. Mullen, D., Moyes, A., Kocian, T., Beyak, E., Riha, A., Reed, H.: Parametric boundary-layer stability analysis on a hypersonic finned circular cone. AIAA-2018-3072 (2018)
60. Miró Miró, F., Beyak, E., Pinna, F., Reed, H.: Ionization and dissociation effects on boundary-layer stability. *J Fluid Mech.* **907**, A13 (2021)
61. Miró Miró, F., Beyak, E., Pinna, F., Reed, H.: High-enthalpy models for boundary-layer stability and transition. *Phys. Fluids* **31**(4), 044101 (2019) Apr
62. Herbert, T.: Parabolized stability equations. *Ann. Rev. Fluid Mech.* **29**, 245–283 (1997)
63. Theofilis, V.: Global linear instability. *Ann. Rev. Fluid Mech.* **43**, 319–352 (2011)
64. Roache, P.: Quantification of uncertainty in computational fluid dynamics. *Ann. Rev. Fluid Mech.* **29**, 123–160 (1997)
65. Reed, H., Perez, E., Kuehl, J., Kocian, T., Oliviero, N.: Verification and validation issues in hypersonic stability and transition prediction. Special Section on Numerical Simulation of Hypersonic Flows. *J. Spacecr. Rockets* **52**(1), 29–37 (2015) Jan
66. Arnal, D.: Boundary layer transition: predictions based on linear theory. AGARD Report 793: Special Course on Progress in Transition Modelling (1994)
67. Malik, M.: Numerical methods for hypersonic boundary layer stability. *J. Comput. Phys.* **86**(2), 376–413 (1990)
68. Groot, K., Miró Miró, F., Beyak, E., Moyes, A., Pinna, F., Reed, H.: DEKAF: spectral multi-regime basic-state solver for boundary layer stability. AIAA-2018-3380 (2018)
69. Reed, H., Kocian, T., Saric, W.: Interactive computations and experiments in stability and transition research. AIAA-2018-3320 (2018)
70. Reibert, M., Saric, W., Carrillo, R., Chapman, K.: Experiments in nonlinear saturation of stationary crossflow vortices in a swept-wing boundary layer. AIAA-1996-0184 (1996)
71. Roache, P., Fundamentals of Computational Fluid Dynamics (cover), Hermosa (1998)
72. Schneider, S.: Personal communication
73. Rhodes, R., Carpenter, A., Reed, H., Saric, W.: CFD analysis of flight-test configuration for LFC on swept wings. AIAA-2008-7336 (2008)

74. Rhodes, R., Reed, H., Saric, W., Carpenter, A., Neale, T.: Roughness receptivity in swept-wing boundary layers – computations. *Int. J. Eng. Syst. Model. Simul.* **2**(1/2), 139–148 (2010) Mar
75. Herbert, T.: Secondary instability of boundary layers. *Ann. Rev. Fluid Mech.* **20**, 487 (1988)
76. Kendall, J.: Experiments on the generation of Tollmien-Schlichting waves in a flat plate boundary layer by weak freestream turbulence. AIAA-1984-0011 (1984)
77. Kendall, J.: Experiments on boundary-layer receptivity to freestream turbulence. AIAA-1998-0530 (1998)
78. Kosorygin, V., Radeztsky, R., Saric, W.: Laminar boundary-layer, sound receptivity and control. In: Kobayashi, R. (eds.) *Laminar-Turbulent Transition IV*, pp. 517–524. IUTAM Symposia (International Union of Theoretical and Applied Mechanics) (Springer, Berlin, Heidelberg, 1995)
79. Goldstein, M.: Scattering of acoustic waves into Tollmien-Schlichting waves by small streamwise variations in surface geometry. *J. Fluid Mech.* **154**, 509–530 (1985)
80. Goldstein, M., Hultgren, L.: A note on the generation of Tollmien-Schlichting waves by sudden surface-curvature change. *J. Fluid Mech.* **181**, 519–525 (1987)
81. Shahriari, N., Bodony, D., Hanifi, A., Henningson, D.: Acoustic receptivity simulations of flow past a flat plate with elliptic leading edge. *J. Fluid Mech.* **800**, R2-1–R2-11 (2016)
82. Reynolds, G., Saric, W.: Experiments on the stability of a flat-plate boundary layer with suction. *AIAA J.* **24**(2), 202–207 (1986)
83. Deyhle, H., Bippes, H.: Disturbance growth in an unstable three-dimensional boundary layer and its dependence on initial conditions. *J. Fluid Mech.* **316**, 73–113 (1996)
84. Bippes, H.: Basic experiments on transition in three-dimensional boundary layers dominated by crossflow instability. *Prog. Aerosp. Sci.* **35**(4), 363–412 (1999)
85. White, E., Saric, W.: Secondary instability of crossflow vortices. *J. Fluid Mech.* **525**, 275–308 (2005)
86. Kohama, Y., Saric, W., Hoos, J.: A high-frequency secondary instability of crossflow vortices that leads to transition. In: Proceedings of the Royal Aeronautical Society: Boundary Layer Transition and Control, Cambridge, UK (1991)
87. Malik, M., Li, F., Chang, C.: Crossflow disturbances in three-dimensional boundary layers: nonlinear development, wave interaction and secondary instability. *J. Fluid Mech.* **268**, 1–36 (1994)
88. Craig, S., Saric, W.: Crossflow instability in a hypersonic boundary layer. *J. Fluid Mech.* **808**, 224–244 (2016)
89. Saric, W.: Boundary-layer stability and transition. In: Tropea, C., Yarin, A., Foss, J. (eds.) *Springer Handbook of Experimental Fluid Mechanics*, Chap.12, pp. 886–896 (Springer-Verlag, Berlin, Heidelberg, 2007)

Progress in Development of Amplitude Method of Transition Prediction on Swept Wing



Maksim V. Ustinov

Abstract An amplitude method of laminar-turbulent transition prediction in the boundary layer on a swept wing was developed and tested. It is based on findings of amplitudes and spectra of steady and traveling cross-flow instability modes and Tollmien-Schlichting waves generated by surface roughness or free-stream turbulence. Transition criterion is based on crucial values of maximal or local amplitudes of these perturbations found from experiments. Statistical methods describing intermittency in transition zone from this criterion are proposed.

1 Introduction

For small ambient disturbances laminar-turbulent transition is caused by instability of boundary layer to primary modes. It starts from generation of these modes by outer flow disturbances or surface roughness which is referred as boundary layer receptivity. Then linear amplification of these modes take place. When the amplitudes of primary perturbations become large enough the non-linear stage of transition starts. Recent transition prediction methods are based on evaluation of linear amplification factors of primary modes. All other physics such as variation of initial amplitude and non-linear effects are ignored or treated by empirical correlations for N-factors [1, 2]. Radical improvement of cross-flow dominated transition prediction may give an amplitude method proposed by Mack. It should be based on computation of r.m.s amplitudes of steady and traveling modes. Such a method includes three components: solution of receptivity problem, description of non-linear evolution of modes with continuous spectrum and random phases and criterion of transition to turbulence. Most of these were developed recently in the most part. Receptivity to roughness and FST can be evaluated by non-localized receptivity mechanism introduced by Crouch [3] and correctly formulated mathematically by Wu [4, 5]. Non-linear PSE method suitable for description of evolution of finite-amplitude disturbances was developed

M. V. Ustinov (✉)
Central Aerohydrodynamic Institute (TsAGI), Zhukovsky, Russia
e-mail: ustinov@tsagi.ru

in [6]. Combined amplitude criterion capable of predicting onset of secondary instability was proposed in [7]. The last thing should be done to finalize the amplitude method is adaptation of these approaches to random perturbations characteristic for “natural” transition. Amplitude method developed along this way is discussed.

2 Non-Linear PSE-Method for Random Perturbations

Consider the flow of incompressible viscose fluid in the boundary layer on an infinite-span swept wing of chord length L . Rectangular curvilinear coordinates x, y, z with x -axis directed along the upper surface perpendicular to leading edge, y -axis parallel to it and z -axis normal to the wing surface is used for flow description. Non-dimensional variables are introduced using the boundary layer thickness $\delta = (\nu L / u_\infty)^{1/2}$ and the oncoming flow velocity u_∞ as scales. The solution for velocity vector in the boundary layer \mathbf{V} is sought as a sum

$$\mathbf{V} = \mathbf{V}_0(x, z) + \mathbf{V}^s(x, y, z) + \mathbf{V}^{ns}(x, y, z, t) \quad (1)$$

The first term here represents averaged over span boundary layer, the second and third terms correspond to finite-amplitude steady and non-steady perturbations. The perturbations are assumed to be periodic in spanwise direction and time and they are presented as Fourier series

$$\mathbf{V}^s = \sum_{m=1}^M \mathbf{v}_{m0}^s(X, z) e^{i(\alpha_m^s(X)x + m\beta_h y)}; \quad \mathbf{V}^{ns} = \sum_{m=1}^M \sum_{n=-N}^N \mathbf{v}_{mn}^{ns}(X, z) e^{i(\alpha_{mn}^{ns}(X)x + m\beta_h y - n\omega_h t)} \quad (2)$$

Harmonics of steady perturbations describe steady cross-flow instability modes and non-steady disturbances represent traveling cross-flow instability modes or Tollmien-Schlichting waves. They are almost periodical functions of the chordwise coordinate. For this reason the amplitudes and streamwise wavenumbers are functions of the stretched variable $X = x/R$, $R = (u_\infty L / \nu)^{1/2}$. Expressions for perturbations may be treated as a discretization of continuous spectrum of disturbances observed in experiment. The amplitudes of harmonics in (2) are related with the spectral densities of steady S^s and non-steady disturbances S^{ns} as

$$\mathbf{V}_{m0}^s = S^s \sqrt{\beta_h}; \quad \mathbf{V}_{mn}^{ns} = S^{ns} \sqrt{\beta_h \omega_h}$$

For large M and N amplitudes of harmonics are small even for finite perturbations. Substitution of (1), (2) into Navier-Stokes equations and dropping $O(R^{-2})$ terms gives the set of parabolized stability equations for amplitudes of harmonics and the boundary layer equation for the averaged flow

$$\frac{\partial \mathbf{v}_{mn}}{\partial X} + \mathbf{L} \left(V(X), \frac{\partial V}{\partial X}, \alpha_{mn}(X), \beta, \omega \right) \circ \mathbf{v}_{mn} = 0$$

$$(\nabla \nabla, \mathbf{V}) = \mathbf{i} U_e \frac{d U_e}{d X} + \frac{\partial^2 \mathbf{V}}{\partial z^2} - < \mathbf{v}^s \nabla, \mathbf{v}^s > - < \mathbf{v}^{ns} \nabla, \mathbf{v}^{ns} >; \quad (\nabla, \mathbf{V}) = 0 \quad (3)$$

Distinct from non-linear PSE-method [6] for deterministic disturbances, the non-linear terms in equations for amplitudes of harmonics are omitted because of two reasons. First, amplitudes of harmonics are small. Second, initial disturbances are generated by random external fluctuations and solution should be independent from the phases of harmonics. Non-linear terms remain only in the equation for the averaged flow. They appear to be a sum of contributions of individual harmonics proportional to their amplitudes and do not depend on phases. For this reason solution is fully determined by spectra of steady and non-steady perturbations and becomes independent of the number of harmonics in (2) if M, N are large.

Initial conditions for the averaged flow were set in the point x_{00} located upstream of the neutral points of all harmonics. They correspond to solution of boundary layer equations without disturbances. Each harmonics of perturbations is assumed to be generated in the vicinity of its neutral point x_{0mn} . Before the neutral point its amplitude is set to be zero. At the neutral point wavenumber $\alpha_{mn}(x_0)$ is set to be equal to eigenvalue and amplitude is determined by eigenfunction in the neutral point with magnitude found from the solution of receptivity problem.

Criterion of transition was found from experiment [7] and deal with maximal amplitudes A_m defined as a maximal deviation of velocity from its averaged value. For transition caused by cross-flow instability it is proposed as

$$A_m^s + A_m^{ns} = a_c^{CF} = 0.3 \quad (4)$$

where A_m^s and A_m^{ns} are maximal amplitudes of steady and non-steady modes. Similar criterion $A_m^{ns} = a_c^{TS} = 0.03$ will be used for transition caused by TS waves.

Due to undetermined phases of harmonics simplified non-linear PSE method (3) gives only r.m.s amplitudes of steady and non-steady modes A_{rms}^s and A_{rms}^{ns} . Maximal amplitudes of random disturbances measured in experiment depend from the length or time interval where these maximums are found. Random function theory methods should be used for finding of exact relations between maximal and r.m.s. amplitudes of perturbations. Application of such approach to description of intermittency in the transitional zone is discussed in Sect. 4. However, this analysis now is completed only for two scenarios of transition excited by “pure” steady modes or T-S waves. For “miscellaneous” regimes with comparable magnitude of steady and non-steady modes criterion (4) with $A_m^s = s^s A_{rms}^s$, $A_m^{ns} = s^{ns} A_{rms}^{ns}$ and empirical coefficients $s^s = 2.12$, $s^{ns} = 2.2$ related maximal and r.m.s. amplitudes will be used to determine transition location.

3 Receptivity of Boundary Layer to Surface Roughness and FST

The shape of surface roughness z_w and the velocity perturbations in oncoming turbulent flow \mathbf{v} is presented as a superposition of elementary waves or Fourier integrals

$$z_w(x, y) = \int_{-\infty}^{+\infty} \int S_r(\alpha, \beta) e^{i(\alpha x + \beta y)} d\alpha d\beta;$$

$$\mathbf{v} = \int_{-\infty}^{+\infty} \int \int \mathbf{S}_v(\mathbf{k}, \omega) e^{i((\mathbf{k}, \mathbf{r}) - \omega t)} d\mathbf{k} d\omega$$

The response of the boundary layer to these ambient disturbances is sought in form of similar integral for the disturbances generated by elementary waves $z_e = \exp(i(\alpha x - \omega t))$ or $\mathbf{v}_e = \exp(i(\mathbf{k}, \mathbf{r} - \omega t))$. In accordance with the concept of non-localized receptivity mechanism [3–5], each eigenmode with spanwise wavenumber β and frequency ω is generated near its neutral point $x_0(\beta, \omega)$ via resonant interaction with ambient disturbances with the same ω, β and α in the close vicinity of eigenvalue α_0 in the neutral point. More precisely, resonant generation take place at interval $x - x_0 \sim R^{1/2}$ for the difference of wavenumbers $\alpha - \alpha_0 \sim R^{-1/2}$. It is described by solution of parabolized stability equation (3) linearized in X near the neutral point with the right part $\Phi(z)\exp(i(\alpha - \alpha_0)x)$. Its solution \mathbf{v}_r appears in the form of product of eigenfunction in neutral point \mathbf{v}_0 and slowly varying amplitude a

$$\mathbf{v}_r = R^{1/2} a(X_1) \mathbf{v}_0(z) + a_1(X_1) \mathbf{v}_1(X, z); \quad X_1 = R^{-1/2}(x - x_0)$$

Substitution of this to PSE equation with right part gives Orr-Sommerfeld equation with $\alpha = \alpha_0$ for \mathbf{v}_0 and the same inhomogeneous equation for \mathbf{v}_1 . The latter equation has solution if its right-hand side is normal to the eigenfunction of adjoint Orr-Sommerfeld operator \mathbf{v}_0^+ . This condition of resolvability gives the amplitude equation

$$\frac{da}{dX_1} - i\delta_1 X_1 a = r_e e^{i\delta_0 X}; \quad r_e = \frac{\|w_0^+, \Phi\|}{\left\|w_0^+, \frac{\partial \mathbf{L}_{oz}}{\partial \alpha} w_0\right\|}; \quad \delta_1 = R^{1/2} \frac{d\alpha_{CF}}{dX}|_{x=x_0};$$

$$\delta_0 = R^{1/2}(\alpha - \alpha_0)$$

Here r_e is receptivity coefficient to elementary wave, \mathbf{L}_{oz} —is Orr-Sommerfeld operator. The solution of this amplitude equation with zero initial condition for $X_1 = -\infty$ describes production of eigenmode with amplitude A_0 in neutral point given by

$$A_0 = R^{1/2} r_e \bar{A}_0; \quad \bar{A}_0 = \sqrt{\frac{\pi}{2\delta_1}} \exp\left(-\frac{\delta_0^2}{2|\delta_1|^2}\right) \quad (5)$$

This result shows that the resonant interaction results in excitation eigenmode of amplitude $\sim R^{1/2}$ in a narrow interval of wavenumber spectrum $\Delta\alpha \sim R^{-1/2}$. Similar amplitude equation describing the resonant generation of Tollmien-Schlichting wave in the vicinity of the neutral point was derived in [4] in the framework of the triple-deck asymptotic scheme. Amplitude of generated eigenmode found here $A_0 \sim R^{3/8}$ slightly differs from (5) because of asymptotical scaling for wavenumber $\alpha \sim R^{-1/4}$ in [4]. Square of the amplitude of eigenmode with fixed ω, β generated by a broadband spectrum of ambient perturbations is given by integral of A_0^2 over detuning parameter δ_0 . This gives the following relations between spectral densities of surface roughness and FST and steady and non-steady modes in the boundary layer

$$\begin{aligned} S^s(\beta) &= C_r(\beta) S_r(\alpha_0, \beta); \quad C_r = |r_e^s| I; \quad I^2 = R^{1/2} \int_{-\infty}^{+\infty} \bar{A}_0^2 d\delta_0 = \frac{\pi^{3/2}}{2} \sqrt{\frac{R}{\text{Im}(\delta_1)}} \\ S^{ns} &= Tu C_{Tu}(\omega, \beta); \quad C_{Tu}^{ns2} = \frac{1}{2\pi} L I^2 (\alpha_0^2 + \beta^2) (\omega - k_\tau)^2 \\ &\int_0^\infty S_{Tu}^2(k, (\omega - u_e k_\tau)) |r_e^{ns}(\omega, \mathbf{k})|^2 dk_z \end{aligned}$$

Here S_{Tu}^2 is energy spectrum of FST, k_τ and k_z are projections of \mathbf{k} on the outer flow velocity direction and z -axis, u_e is flow velocity above the boundary layer, C_r and C_{Tu} —receptivity coefficients to surface roughness and turbulence.

The spectrum of surface roughness was measured only in one experiment [8]. In all other works quality of surface is characterized by r.m.s. amplitude of roughness r_a . Simple model with constant spectral density

$$S_r(\alpha, \beta) = \frac{r_a l}{4\pi} \quad \text{for } |\alpha|, |\beta| < \frac{2\pi}{l}; \quad S_r(\alpha, \beta) = 0 \quad \text{for } |\alpha|, |\beta| > \frac{2\pi}{l} \quad (6)$$

was used in this case. Parameter l here is minimal length of humps or grooves in roughness profile. It is natural to suppose that profiles of technological roughness are self-similar, so this length is proportional to amplitude $l = Dr_a$. This assumption results in quadratic dependence of spectral density and initial amplitudes of steady modes in the boundary layer on the roughness amplitude.

In conventional model of frozen to flow turbulence the phase speed of all perturbations is equal to outer flow velocity u_e . This excludes the resonant excitation of eigenmodes by FST. However, phase velocities of perturbations in real turbulence deviate from u_e due to non-linear interaction of disturbances. This fact was taken into account by following model of energy spectrum of FST

$$S_{Tu}^2 = F(k)S(\mathbf{k}, \omega) ; \quad F(k) = \frac{55}{12\pi} \frac{(kL)^4}{(1 + (kL)^2)^{17/6}}; \quad S(\mathbf{k}, \omega^+) = \frac{L\tau}{\sqrt{\pi}} e^{-\tau\omega^+}$$

Here $F(k)$ is Von Karman spectrum, $S(\mathbf{k}, \omega^+)$ —is the frequency spectrum of perturbations in moving with flow velocity frame of reference, L —is integral scale of turbulence. Model of frequency spectrum includes correlation loss time τ which was found from experimental data in [9]. For large kL it takes form $\tau = (\lambda kLTu)^{-1}$ where $\lambda = 0.8$ is an empirical coefficient found from data of [10].

Because of velocity pulsations in FST are small one can conclude that the phase speed of elementary waves slightly deviate from the flow velocity. This is certainly valid for the major portion of disturbances, however spectrum of FST contains some perturbations of phase speed $O(1)$ in the moving frame of reference. Such elementary waves have large vertical component of wave-vector $k_z \sim 1/TuL$ but other its components k_x, k_y and frequency ω^+ are of order of unity. The longitudinal component of the phase speed of these waves is comparable with flow velocity, so they may generate eigenmodes via resonant forcing. Because of module of wave-vector $k \sim k_z$ is large, part of such high-frequency disturbances in the frequency spectrum $S(\mathbf{k}, \omega^+)$ is essential, and r.m.s. amplitude of these “generating” elementary waves is estimated as

$$a_g \sim Tu \left[\int_{1/TuL}^{\infty} F(k) dk \right]^{1/2} \sim Tu^{4/3}$$

For turbulence level $Tu \sim 10^{-3}$ characteristic for low-turbulence wind tunnels amplitude of such “generating” disturbances in the free stream is $\sim 10^{-4}$. If one percent of them with proper k_x, k_y and ω^+ generate Tollmien-Schlicsting waves with receptivity coefficient $r \sim 1$ initial amplitude of instability waves in the boundary layer will be $\sim 10^{-6}$. For amplification factor e^9 corresponding to this turbulence level the final amplitude of disturbances in the boundary layer will reach 1%. It is enough for transition. More accurate consideration based on asymptotics of Von Karman spectrum $F(k) \sim (kL)^{-5/3}$ and receptivity coefficient to elementary wave $r_e^{ns} \sim k^{-3/2}$ for $k \rightarrow \infty$ results in the following estimate of amplitude of the eigenmodes generated by turbulence $a_0 \sim Tu^{17/6} L^{-1/3}$ [11]. If the amplitude at transition point a_c is fixed, this gives expression for N-factor similar to Mack’s correlation $N_* = N_0 - (17/6) \ln(Tu) + (1/3) \ln L$. It should be noted that these results are valid if the wavenumbers of “generating” disturbances $k \sim 1/LTu$ fall into inertial interval of turbulence spectrum. Fulfillment of this condition in low-speed wind tunnels is not obvious. Approaches to evaluation of swept-wing boundary layer receptivity to surface roughness and FST used in the amplitude method of transition are described in more details in [12].

4 Statistical Description of Intermittency in Transition Zone

Theoretical description of transition induced solely by steady cross-flow instability modes or TS waves is considered here. These types of transition are characterized by development of disturbances along the streamlines of outer flow. For this reason a transversal coordinate y^* measured from some streamline of external flow will be used in this section (see Fig. 1).

We first consider transition induced by steady cross-flow instability modes. Because of selective amplification of modes with streamwise wavenumbers near β_m perturbations u' in transition zone are described by almost periodic function of y^*

$$u(x', y^*) = A(x', y^*) \sin(\beta_m y + \theta(y^*)) ; \quad A(x', y^*) = A_0(x, y^*) e^{\kappa(x' - x)}$$

Here amplitude A and phase θ slowly depend from y^* . We shall suppose that at the point where the amplitude exceeds threshold value a_c turbulent wedge appears. Let's find the probability to find turbulent flow at the reference point O located at distance x from the leading edge. This probability γ will be called intermittency coefficient for transition caused by steady modes. Flow in point O will be turbulent if at least one turbulent wedge appears in its area of influence Ω , which is a locus of tops of turbulent wedges containing the reference point. In the course of idea of Emmons [13] the following expression for probability of turbulent flow in this point may be derived

$$\gamma(x) = 1 - \exp(-F(\gamma)) ; \quad F(\gamma) = \iint_{\Omega} v_s(x') dS \quad (7)$$

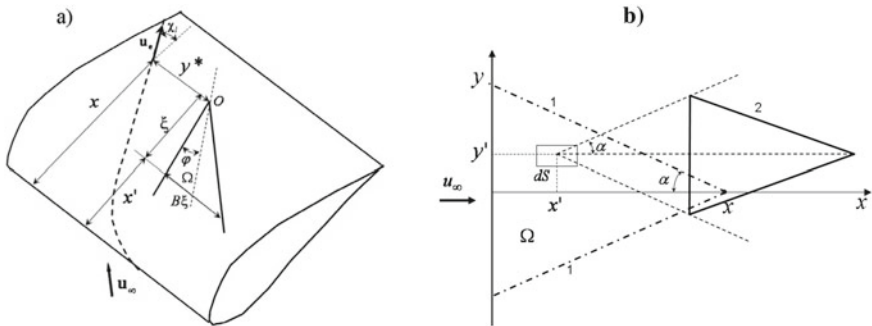


Fig. 1 Coordinates x, y^* , and influence domain for transition induced by steady CF modes (a); influence domain (1) and form of turbulent spot (2) used for computation of intermittency in transition caused by TS waves (b)

Here v_s is a probability of turbulent wedge origination per unit area at distance x' from leading edge. It may be found as a derivative of number of wedges per unit length along the span v_L with respect to x' . The number of verges per unit length v_L at the distance x' from leading edge equals to the frequency of overshoots of amplitude $A(x', y^*)$ over level a_c here. If the perturbations of velocity are normal random function of y^* with narrow spectrum its amplitude $A(y^*)$ has Reley's distribution and the frequency of its overshoots over a_c is expressed as

$$v_L = \frac{\Delta_\beta}{\sqrt{2\pi}} \frac{1}{a*} e^{-\frac{1}{2a^{*2}}}; \quad a* = \frac{A_{rms}^s(x')}{a_c}$$

where Δ_β is width of β -spectrum of steady modes. Its derivative with respect to x' found for constant Δ_β gives the probability of turbulent wedge appearance

$$v_s = \frac{\kappa \Delta_\beta}{\sqrt{2\pi}} \frac{1}{a*} \left(\frac{1}{a^{*2}} - 1 \right) e^{-\frac{1}{2a^{*2}}}$$

It is easy to see, that it has maximum for a definite value of normalized amplitude $A_{rms}/a_c = (2 + \sqrt{3})^{-1/2} \approx 0.51$. Integral (7) with this v_s can be found analytically but result is bulky. It can be simplified if smooth distribution $v_s(x')$ is replaced by Dirac's delta function placed in its maximum. This gives

$$\gamma_{CF} = 1 - \exp\left(-\frac{x - x_{tr}}{\Delta_{tr}^{CF}}\right); \quad \Delta_{tr}^{CF} = \frac{\sqrt{2\pi e}}{\Delta_\beta B_{CF}}$$

where B_{CF} is constant depending on the shape of turbulent wedge. It shows that the length of transition zone is inversely proportional to the width of spectrum Δ_β .

For transition excited by TS waves the intermittency coefficient γ is defined classically as a part of time when the flow is turbulent. In this case disturbances in transition zone are defined by amplitude $A(x', y^*, t)$ which is a random function of transversal coordinate y^* and time t . Turbulent spots of triangular form shown in Fig. 1b are generated if the amplitude exceeds threshold value. Intermittency coefficient is defined by (7) with v_s being replaced by the product of frequency of turbulent spots production and time of spot propagation through the reference point τ . Frequency of spots production is found similarly as a derivative with respect to x' of number of overshoots of random function $A(x', y^*, t)$ over level a_c per unit spanwise length and time. This results in the following expressions for frequency of turbulent spots production and γ

$$v_{st} = \frac{k \Delta_\beta \Delta_\omega}{\sqrt{2\pi^3}} \frac{1}{a*} \left(\frac{1}{a^{*2}} - 1 \right) e^{-\frac{1}{2a^{*2}}}; \quad \gamma_{TS} = 1 - \exp\left[-\left(\frac{x - x_{tr}}{\Delta_{tr}^{TS}}\right)^2\right]; \\ \Delta_{tr}^{TS} = \left(\frac{\sqrt{2\pi^3 e}}{\Delta_\beta \Delta_\omega B_{TS}}\right)^{1/2}$$

Here Δ_ω —is width of frequency spectrum of disturbances, B_{TS} is constant depending on shape of turbulent spot. Expression for intermittency for transition caused by TS waves is similar to the model by Narasimha [14], but statistical theory developed gives exact expression for the length of transition zone.

5 Comparison of Amplitude Method with Experiment

Most complete data for testing receptivity model and non-linear PSE-method describing disturbance growth were obtained in experiment [8] where comprehensive studies of influence of surface roughness amplitude and FST on cross-flow dominated transition were made. Measurements in this work were performed in the boundary layer on the flat plate with the swept leading edge. Necessary for cross-flow instability normal to the leading edge pressure gradient was induced by swept displacement body mounted above the plate. Artificial random roughnesses of different amplitudes with well-documented spectra were used to generate steady modes. Enhanced turbulence level was produced by a grid installed in the beginning of the test section and intensity and spectrum of FST were measured carefully. Place where secondary instability starts was treated as a transition point. Comparison of dependencies of maximal amplitudes of steady modes A_m^s measured in [8] on x with similar results of computations by amplitude method for low-turbulence regime ($Tu \sim 0.1\%$) is shown at Fig. 2a. Experimental maximal amplitudes A_m^s are found as $A_m^s = S^s A_{rms}^s$ with $S^s = 2.12$. Comparison of predicted transition location with experimental data is presented in Fig. 2b.

Similar results for r.m.s. amplitudes of non-steady modes and transition location for regimes with enhanced turbulence level are shown in Fig. 3. It should be mentioned that these results of computations were obtained for reduced turbulence level $Tu = 0.5\%$, compared with value $Tu = 0.74\%$ measured in experiment at these

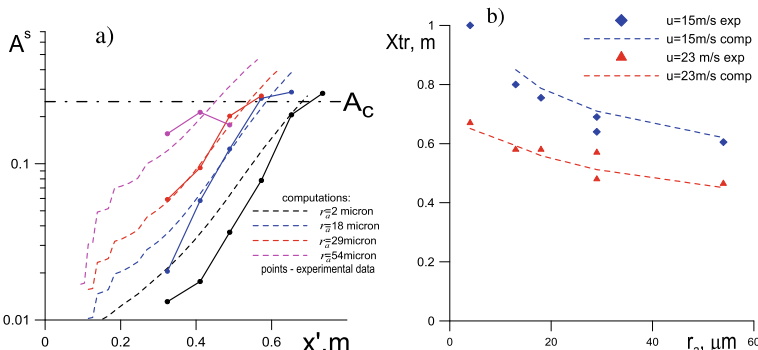


Fig. 2 Comparison of maximal amplitudes of steady modes (a) and transition location (b) measured in low-turbulence regime in [8] with results of computations

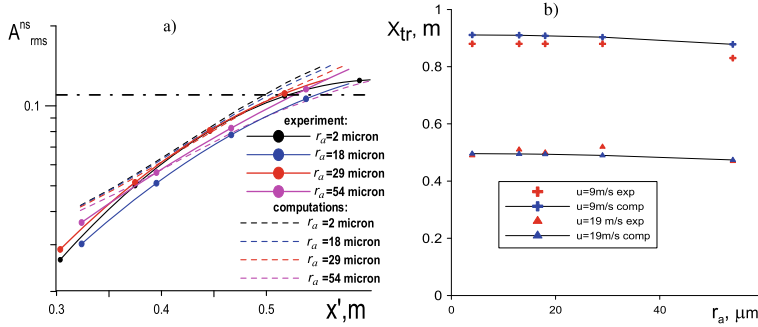


Fig. 3 Comparison of r.m.s. amplitudes of non-steady modes (a) and transition location (b) measured in regime with enhanced turbulence level in [8] with results of computations

regimes. Turbulence level was corrected because of large portion of low-frequency pulsations ($f < 10 \text{ Hz}$) were present in experimental turbulence spectra. After this correction, amplitude method well describes generation and subsequent evolution of steady and non-steady modes in conditions of experiment [8]. It also is capable of predicting the influence of surface roughness and enhanced turbulence level on the onset of transition or secondary instability origin.

Influence of amplitude of technological roughness on transition on large-scale swept-wing section of chord 1.2 m was investigated in experiments [15, 16]. Transition line in these experiments was found by method of naphthalene evaporation. This allows for use of these data for verification of intermittency model for transition caused by steady modes. Unfortunately, the spectra of surface roughnesses were not measured in [15], and a model of its spectrum (6) with empirical constant $D = 12$ was used in computations dealing with this experiment. Comparison of dependence of transition location on Reynolds number for different amplitudes of surface roughness found by amplitude method with similar experimental data is shown at Fig. 4. In most cases computations predict transition with accuracy near 5% of chord.

Figure 5a–c, shows comparison of model of intermittency for transition induced by steady modes with experimental data obtained in [16] for amplitude of roughness $3.3 \mu\text{m}$ and $\text{Re} = 2.4 \times 10^6$. Figure 5d, e shows comparison of computed intermittency coefficient with experimental data for transition induced by TS waves at the flat plate. Results of two experiments [10, 17] carried out at different facilities with sufficiently different turbulence level $Tu = 0.12\%$ and 0.05% are used for this purpose. Data for computation of intermittency coefficient in conditions of these experiments were obtained by the amplitude method with threshold amplitude $a_c = 3\%$. Figure 5 shows that the developed intermittency model with disturbances spectra found from amplitude method describes well intermittency distribution in different experimental conditions and regimes of transition.

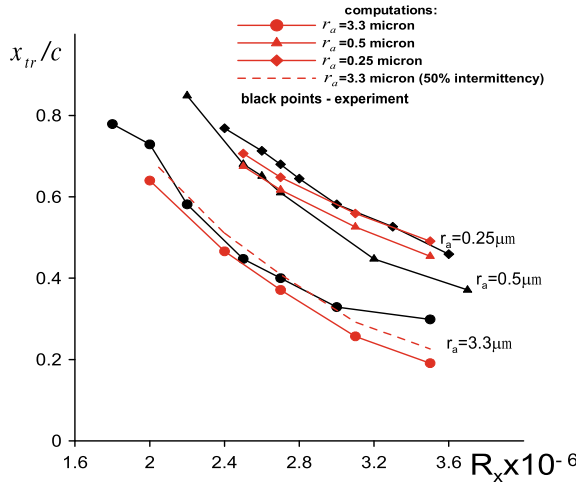


Fig. 4 Comparison of dependencies of transition location on Reynolds number measured in [15] for different surface roughness with predictions of amplitude method

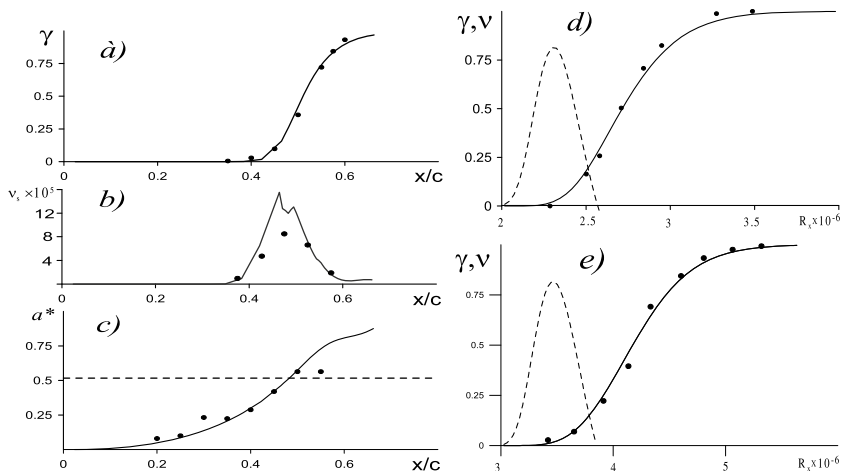


Fig. 5 Comparison of intermittency coefficient (a), number of turbulent wedges per unit square (b) and normalized amplitude of steady modes (c) found from data of [16] with computations. Intermittency coefficients and frequency of turbulent spots productions in conditions of experiments [10] (d) and [17] (e). Points—experiments, lines—computations

6 Conclusions

The amplitude method developed reproduces well influence of most important factors: turbulence level, amplitude of roughness, Reynolds number on laminar-turbulent transition caused by steady and traveling cross-flow instability modes on

the swept wing. It also gives distribution of intermittency coefficient in transition zone for transition excited by steady cross-flow instability modes and TS waves. In the course of development of this method three important theoretical results were obtained:

- Initial amplitude of eigenmodes generated by FST is proportional to $Tu^{17/6}$. This verifies theoretically well-known Mack's correlation for dependence of N factor for turbulence level
- The amplitude of steady cross-flow instability modes produced by random surface roughness depends quadratically on its amplitude
- The length of transitional zone is determined by the width of disturbances spectrum in the end of linear stage of their evolution

The amplitude method does not require large amount of computations and may be used in future as engineering tool instead of e^N method.

References

1. Mack, L.M.: Transition prediction and linear stability theory, AGARD Conf. proc. CP-224. p. 1/1–22 (1977)
2. Crouch, J.D., Ng, L.L.: Variable N-factor method for transition prediction in three-dimensional boundary layers. *AIAA J.* **38**(2), 211–215 (2000)
3. Crouch, J.D.: Non-localized receptivity of boundary layers, *J. Fluid Mech.* **244**, 567–581 (1992)
4. Wu, X.: Generation of Tollmien-Schlichting waves by convecting gusts interacting with sound. *J. Fluid Mech.* **397**, 285–316 (1999)
5. Wu, X.: Receptivity of boundary layers with distributed roughness to vortical and acoustic disturbances: a second-order asymptotic theory and comparison with experiments. *J. Fluid Mech.* **431**, 91–133 (2001)
6. Haynes, T.S., Reed, H.L.: Simulation of swept-wing vortices using nonlinear parabolized stability equations. *J. Fluid Mech.* **405**, 325–349 (2000)
7. Borodulin, V.I., Ivanov, A.V., Kachanov, Y.S., Crouch, J.D., Ng, L.L.: Criteria of swept-wing boundary-layer transition and variable N-factor methods of transition prediction. In: Fomin, V.M. (eds.) International Conference on Methods of Aerophysical Research. June 30–July 6, 2014. Proceedings. Novosibirsk: Inst. Theor & Appl. Mech., 2014, paper No 12, 10 p
8. Crouch, J.D., Ng, L.L., Kachanov, Y.S., Borodulin, V.I., Ivanov, A.V.: Influence of surface roughness and free-stream turbulence on crossflow-instability transition. In: Medeiros, M.A.F., Meneghinipp, J.R. (eds.) Procedia IUTAM, Vol. 14. IUTAM_ABCM Symposium on Laminar Turbulent Transition, pp. 295–302 (2015)
9. Comte-Bellot, G., Corrsin, S.: Simple Eulerian time correlations of full- and narrow-band velocity signals in grid generated “isotropic” turbulence. *J. Fluid Mech.* **48** Pt.2, 273–337 (1971)
10. Schubauer, G.B., Skramstad, H.K.: Laminar boundary layer oscillations and transition on a flat plate, NACA TN 909 (1948)
11. Ustinov, M.V.: Tollmien-Schlichting wave generation by flow turbulence. *Fluid Dyn.* **49**(4), 468–480 (2014)
12. Ustinov, M.V.: Amplitude method of prediction of laminar-turbulent transition on a swept wing. *Fluid Dyn.* **52**(1), 71–87 (2017)
13. Emmons H. W. The laminar-turbulent transition in a boundary layer-Pt I., *J. Aero. Sci.* 1951. v. 18. No 7. P. 490–498

14. Narasimha, R.: On the distribution of intermittency in the transition region of a boundary layer, *J. Aero. Sci* **24**(9), P.711–712 (1957)
15. Radetzky, R.H., Reibert, M.S., Saric, W.S.: Effect of micron-sized roughness on transition in swept-wing flows. *AIAA J.* **37**(11), 1370–1377 (1999)
16. Dagenhart, J.R., Saric, W.S.: Crossflow stability and transition experiments in swept-wing flow. *NASA TP-1999-209344* (1999)
17. Filippov, V.M.: Experimental study of pressure gradient influence on laminar-turbulent transition. *Uchonie Zapiski TsAGI* **6**(6), 114–118 (1975). (in Russian)

Coherent Structures, Dynamical Systems, Edge States

Nonlinear Optimal Disturbances in Compressible Shear Flows



Zhu Huang, Tim Flint, and M. J. Philipp Hack

Abstract We present a variational method for the computation and analysis of nonlinear optimal perturbations in compressible flows. The method is verified in parallel periodic pipe flow at $Re = 1750$ and $Ma = 0.20$. At low initial perturbation energy, the computed perturbations recover the results of linear transient growth analyses. At higher amplitudes, nonlinear effects become relevant, leading to higher energy gains which match the results for incompressible shear flows.

1 Introduction

Transition to turbulence has remained a problem of interest more than a century after the original experiment of Reynolds. Specifically, subcritical transition, that is, transition to turbulence in the absence of exponential instability [1] remains only partly understood in a range of canonical shear flows. For example, plane Couette flow is linearly stable for all Reynolds numbers [2], while turbulence has been observed experimentally at Reynolds numbers as low as 325 [3]. For plane Poiseuille flow, linear stability analysis predicts a critical Reynolds number of 5772 [4], while sustained turbulence can be observed at Reynolds numbers of about 1000 experimentally [5] and numerically [6].

The study of subcritical flow transition was greatly advanced by Refs. [7, 8], who, among others, noted that the linearized Navier-Stokes operator is non-orthogonal and thus allows a significant transient amplification of disturbances even in the absence of exponential instability. Thereafter, linear transient growth theory based on non-modal analysis was developed and applied to a variety of shear flows [9]. The underlying rationale of transient growth analysis is that finite-amplitude disturbances can amplify to amplitudes that are sufficiently high to evoke nonlinear interactions and trigger secondary instabilities.

Z. Huang · T. Flint · M. J. P. Hack (✉)

Center for Turbulence Research, Stanford University, Stanford, CA 94305, USA
e-mail: mjph@stanford.edu

For many parallel shear flows, the optimal disturbances that maximize transient disturbance growth are found to be streamwise independent [10] and to generate streamwise streaks by means of the lift-up mechanism [11]. If the base flow is non-parallel, the effectiveness of lift-up may be enhanced by interaction with the Orr mechanism [12], which describes the second pathway for the transient amplification of disturbances in shear flows and amplifies disturbances of finite streamwise wavelength by tilting via the mean shear. Comparison against data from direct simulations has shown that the streaks predicted by transient growth analysis match the conditionally sampled average of boundary layer streaks induced by broadband excitation in the free stream [13]. While their low frequency prevents the streaks from directly causing breakdown to turbulence, they modulate the flow and make it susceptible to secondary instabilities [14].

A variational approach has been used to identify the optimal disturbances for various shear flow configurations, such as plane Couette flow [15–17], pipe flow [18], boundary layers [19], and plane Poiseuille flow [20]. The variational method is typically implemented in terms of a Lagrange functional whose stationary points identify maxima of the objective functional. In this setting, the adjoint variables are formally introduced as Lagrange multipliers that enforce the Navier-Stokes equations as constraints. A variety of possible choices exist for the objective functional, including the disturbance kinetic energy at a given time horizon [21] and the time-averaged dissipation [15, 17].

Although the study of nonlinearly optimal disturbances has received considerable attention in recent years, these analyses have been limited to incompressible flows. Transition to turbulence is nonetheless of particular practical relevance in various flows with non-negligible compressibility effects. Our study therefore seeks to extend the analysis of nonlinearly optimal initial conditions for the first time to compressible flow. In this brief, we derive a variational framework based on the compressible Navier-Stokes equations in conserved variables. We verify the implementation of the algorithm in a simple test setting of periodic pipe flow.

2 Methodology

In the following, we present a framework for the identification of optimal disturbances based on the nonlinear compressible Navier-Stokes equations in conserved variables. The framework is generic and compatible with a wide range of objective functionals. For the pipe-flow setting considered herein, all flow quantities are non-dimensionalized by the centerline speed of sound, the centerline density, and the pipe diameter.

Without loss of generality, we can separate the flow variables into a steady base flow solution, marked by an overbar and a perturbation denoted by a prime, such that $m_i = \bar{m}_i + m'_i$. The governing equations are

$$\begin{aligned}
C0 : \quad & \frac{\partial \rho'}{\partial t} + \frac{\partial(\bar{m}_j + m'_j)}{\partial x_j} = 0, \\
Ci : \quad & \frac{\partial \bar{m} + m'_i}{\partial t} + \frac{\partial}{\partial x_j} \frac{(\bar{m}_j + m'_j)(\bar{m}_i + m'_i)}{(\bar{\rho} + \rho')} + \frac{\partial(\bar{p} + p')}{\partial x_i} \\
& - \frac{\partial}{\partial x_j} \frac{\mu}{Re} \left(\frac{\partial}{\partial x_j} \frac{(\bar{m}_i + m'_i)}{(\bar{\rho} + \rho')} + \frac{\partial}{\partial x_i} \frac{(\bar{m}_j + m'_j)}{(\bar{\rho} + \rho')} \right. \\
& \left. - \frac{2}{3} \frac{\partial}{\partial x_k} \frac{(\bar{m}_k + m'_k)}{(\bar{\rho} + \rho')} \delta_{ij} \right) = 0, \tag{1}
\end{aligned}$$

$$\begin{aligned}
C4 : \quad & \frac{\partial e'}{\partial t} + \frac{\partial}{\partial x_j} \frac{(\bar{e} + e' + \bar{p} + p')(\bar{m}_j + m'_j)}{(\bar{\rho} + \rho')} \\
& - \frac{\partial}{\partial x_j} \frac{\mu}{Re Pr} \frac{\partial(\bar{e} + e' - \frac{1}{2}(\bar{m}_i + m'_i)(\bar{m}_i + m'_i)/(\bar{\rho} + \rho'))}{\partial x_j} \frac{\gamma}{(\bar{\rho} + \rho')} \\
& - \frac{\partial}{\partial x_j} \frac{\mu}{Re} \left(\frac{(\bar{m}_k + m'_k)}{(\bar{\rho} + \rho')} \left(\frac{\partial}{\partial x_j} \frac{(\bar{m}_k + m'_k)}{(\bar{\rho} + \rho')} + \frac{\partial}{\partial x_k} \frac{(\bar{m}_j + m'_j)}{(\bar{\rho} + \rho')} \right) \right) \\
& - \frac{\partial}{\partial x_j} \frac{\mu}{Re} \left(\frac{(\bar{m}_k + m'_k)}{(\bar{\rho} + \rho')} \left(-\frac{2}{3} \frac{\partial}{\partial x_l} \frac{(\bar{m}_l + m'_l)}{(\bar{\rho} + \rho')} \delta_{jk} \right) \right) = 0, \tag{2}
\end{aligned}$$

where $i, j, k = \{1, 2, 3\}$, $m_j = \rho u_j$, $e = p/(\gamma - 1) + 1/2\rho u_i u_i$, ρ is density, u_i are the Cartesian components of the fluid velocity vector and p is pressure, μ is the viscosity, κ is heat conductivity, γ is the heat capacity ratio, Re is Reynolds number based on the speed of sound, $a = \sqrt{\gamma p/\rho}$, and Pr is the Prandtl number. We introduce a measure for the kinetic energy as

$$E(t) = \int_{\Omega} m'_i(t) m'_i(t) dV, \tag{3}$$

which can be equivalently expressed as

$$E(t) = \int_{\Omega} \mathbf{q}'^H(t) \mathbf{F}_E^H \mathbf{F}_E \mathbf{q}'(t) dV, \quad \text{with } \mathbf{F}_E = \begin{bmatrix} 0 & 0 & 0 & 0 & 0 \\ 0 & 1 & 0 & 0 & 0 \\ 0 & 0 & 1 & 0 & 0 \\ 0 & 0 & 0 & 1 & 0 \\ 0 & 0 & 0 & 0 & 0 \end{bmatrix}, \tag{4}$$

where $\mathbf{q}' = (\rho', m'_1, m'_2, m'_3, e')^T$ is the perturbation state vector and superscripts T and H denote the transpose and the complex conjugate transpose, respectively.

Our objective of capturing the initial perturbations that maximize the perturbation kinetic energy gain for a given magnitude of the perturbation vector at initial time is thus equivalent to maximizing the objective functional

$$\mathcal{J} = \frac{E(t_1)}{E(0)}, \quad (5)$$

which connects the energy norm at the end of the evolution interval, $t = t_1$, to the energy norm at the initial time, $t = 0$. We further require the computed perturbations to be solutions to the compressible Navier-Stokes equations. This constrained optimization problem may be written as the Lagrangian

$$\begin{aligned} \mathcal{L} = \mathcal{L}(\rho', m'_i, e', \rho^\dagger, m_i^\dagger, e^\dagger, \alpha; E_0, t_1) &= \mathcal{J} - \alpha(E(\mathbf{q}'(0)) - E_0) \\ &\quad - \int_0^{t_1} \langle \rho^\dagger, \mathbf{C0} \rangle dt - \int_0^{t_1} \langle m_i^\dagger, \mathbf{Ci} \rangle dt - \int_0^{t_1} \langle e^\dagger, \mathbf{C4} \rangle dt, \end{aligned} \quad (6)$$

whose stationary points identify the optimal solution. Here, $\rho^\dagger, m_i^\dagger, e^\dagger$, and α are Lagrange multipliers, and the angular brackets denote the integral inner product

$$\langle a, b \rangle = \int_{\Omega} a^H b \, dV, \quad (7)$$

In Eq. (6), the Lagrange multipliers $\mathbf{q}^\dagger = (\rho^\dagger, m_i^\dagger, e^\dagger)^T$ are the adjoint density, mass fluxes, and energy of the perturbations. We further introduce the supplementary multiplier α , which assigns the kinetic energy of the perturbation state vector at $t = 0$ to the scalar E_0 that, together with the length of the time interval t_1 , serves as a parameter of the optimization procedure. Taking the Lagrangian variation with respect to the adjoint variables \mathbf{q}^\dagger and α and setting them to zero, we recover the direct Navier-Stokes equations as well as the initial perturbations and kinetic energy. Setting the first variation of the Lagrangian with respect to perturbation variables to zero yields the following set of adjoint equations, which must be satisfied within the computational domain,

$$\begin{aligned} \frac{\delta \mathcal{L}}{\delta \rho'} &= \rho_t^\dagger + \frac{m_j}{\rho} \rho_{x_j}^\dagger + \frac{m_j}{\rho} (m_j^\dagger)_t + \frac{m_i m_j}{\rho^2} (m_i^\dagger)_{x_j} + \frac{e}{\rho} e_t^\dagger \\ &\quad + \left(e - \frac{1}{2} \frac{m_k m_k}{\rho} \right) \frac{\gamma - 1}{\rho} (m_j^\dagger)_{x_j} + \left[\frac{\gamma e}{\rho} + \frac{1}{2} \frac{m_k m_k}{\rho} \frac{(1 - \gamma)}{\rho} \right] \frac{m_j}{\rho} e_{x_j}^\dagger = 0, \end{aligned} \quad (8)$$

$$\begin{aligned} \frac{\delta \mathcal{L}}{\delta m'_i} &= (m_i^\dagger)_t + \rho_{x_i}^\dagger + \frac{m_j}{\rho} (m_i^\dagger)_{x_j} + \frac{m_j}{\rho} (m_j^\dagger)_{x_i} + \frac{m_i}{\rho} e_t^\dagger \\ &\quad + \frac{[\gamma e - 1/2(\gamma - 1)m_k m_k/\rho]}{\rho} e_{x_i}^\dagger + \frac{m_i m_j}{\rho^2} e_{x_j}^\dagger - \frac{1}{\rho Re} \left(e_{x_j}^\dagger \tau^{ij} \right) \\ &\quad + \frac{1}{\rho Re} \left[(m_i^\dagger)_{x_j} \mu \right]_{x_j} + \frac{1}{\rho Re} \left[(m_j^\dagger)_{x_i} \mu \right]_{x_j} - \frac{2}{3\rho Re} \left[(m_j^\dagger)_{x_j} \mu \right]_{x_i} \end{aligned}$$

$$+ \frac{1}{\rho Re} \left(e_{x_j}^\dagger \mu \frac{m_i}{\rho} \right)_{x_j} + \frac{1}{\rho Re} \left(e_{x_i}^\dagger \mu \frac{m_j}{\rho} \right)_{x_j} - \frac{2}{3} \frac{1}{\rho Re} \left(e_{x_j}^\dagger \mu \frac{m_j}{\rho} \right)_{x_i} = 0, \quad (9)$$

$$\frac{\delta \mathcal{L}}{\delta e'} = e_t^\dagger + m_{i,x_i}^\dagger (\gamma - 1) + \gamma e_{x_j}^\dagger \frac{m_j}{\rho} + \left(e_{x_j}^\dagger \frac{\mu}{Re Pr} \right)_{x_j} \frac{\gamma}{\rho} = 0. \quad (10)$$

Here, τ is the shear stress,

$$\tau_{ij} = \partial(m_i/\rho)/\partial x_j + \partial(m_j/\rho)/\partial x_i - 2/3 \partial(m_k/\rho)/\partial x_k \delta_{ij}. \quad (11)$$

Coupling conditions between the perturbation and adjoint state vector are derived by setting the first variation of the Lagrangian variation with respect to the perturbations at initial time $t = 0$ and the time horizon $t = t_1$ to zero,

$$\frac{\delta \mathcal{L}}{\delta \mathbf{q}'(0)} = \alpha \mathbf{F}_E \mathbf{q}'(0) - \mathbf{q}^\dagger(0) = 0, \quad (12)$$

$$\frac{\delta \mathcal{L}}{\delta \mathbf{q}'(t_1)} = \frac{\mathbf{F}_E \mathbf{q}'(t_1)}{N_0} - \mathbf{q}^\dagger(t_1) = 0. \quad (13)$$

The optimization procedure starts with a suitable initial guess of the optimal initial conditions, $\mathbf{q}'_{(0)}(0)$. In the absence of a solution from an earlier computation for similar parameters, a random field is chosen and normalized such that $E(0) \equiv E_0$. The initial condition is advanced to the target time t_1 by integrating the full Navier-Stokes equations, and the final state $\mathbf{q}'(t_1)$ is obtained. Subsequently, the adjoint state vector is initialized, as described in Eq. (13), $\mathbf{q}^\dagger(t_1) = \mathbf{q}'(t_1)/N_0$, followed by time marching of the adjoint governing equations from $t = t_1$ to the initial time $t = 0$. Equation (12) is satisfied if the value of $\mathbf{q}'_{(n)}(0)$ is optimal. Otherwise, it provides an estimate for the gradient $\mathbf{g} = \delta \mathcal{L} / \delta \mathbf{q}'_{(n)}(0)$. The iterative procedure has converged if \mathbf{g} is small, implying that $\mathbf{q}'_{(n+1)}(0)$ is close to $\mathbf{q}'_{(n)}(0)$.

The iterative optimization procedure based on time integration of the forward and adjoint equations has been implemented into a compressible flow solver. The solver supports complex geometries via a curvilinear formulation consistent with geometric conservation properties [22]. The spatial discretization employs fourth-order finite differences based on summation-by-parts operators [23]. Boundary conditions are weakly enforced via simultaneous approximation terms. Time integration is facilitated by a second-order explicit Runge-Kutta scheme, and checkpointing is used in the time integration of the adjoint governing equations. The solver is fully parallelized using the message-passing interface. For a more detailed description of the numerical implementation, the reader is referred to Ref. [24].

3 Results and Discussions

In the following, we present a brief verification of the implemented framework by applying it to the analysis of optimal disturbances in parallel periodic pipe flow at $Re = 1750$. The centerline convective speed is chosen to be one-fifth of the speed of sound. At the resulting Mach number, $Ma = 0.20$, compressibility effects are negligible and thus allow a comparison of the results to the literature on incompressible flows. The base flow is computed by supplementing the streamwise momentum and energy equations with forcing terms, $f_x = (16u_{max}\mu)/Re$.

In a first setting, we compare the disturbances identified with our framework to results from linear analysis. As shown in Ref. [21], nonlinear optimal disturbances converge to the results of classical linear transient growth analysis for an objective functional representing kinetic perturbation energy and sufficiently small initial perturbation energy, E_0 . Specifically, the scaling law in Ref. [25] predicts that for the present flow parameters, linear optimal perturbations attain their highest gain in kinetic energy, $E(t)/E(0) = 214.4$, after approximately $t_{lin,opt} = 21.35$ non-dimensional time units for an azimuthal wavenumber of one, which is chosen as the target time of the optimization with the initial perturbation energy set to $E_0 = 1 \times 10^{-8}$.

Figure 1 visualizes the convergence of the iterative procedure in terms of the evolution of the perturbation kinetic energy, $E(t)$, as a function of the iteration number. The initiation of the computational domain with random noise leads to a rapid decrease of $E(t)$ during the first iteration, followed by a gradual increase and an eventual leveling. Past the first iteration, the optimal initial perturbations are already largely converged to streamwise vortices, which drive the generation of streaks by

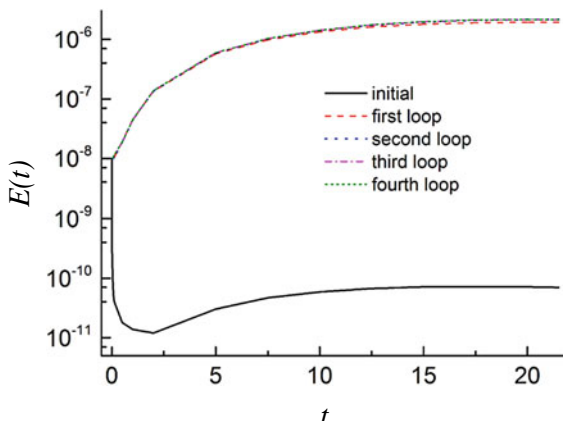


Fig. 1 The time variation of energy density with respect to time after several direct adjoint loops. The solid line shows the energy variation of random initial guess perturbations, while the dashed, dotted, dash-dotted, and short dotted lines show the energy variation of the initial perturbations with one, two, three, and four loops, respectively

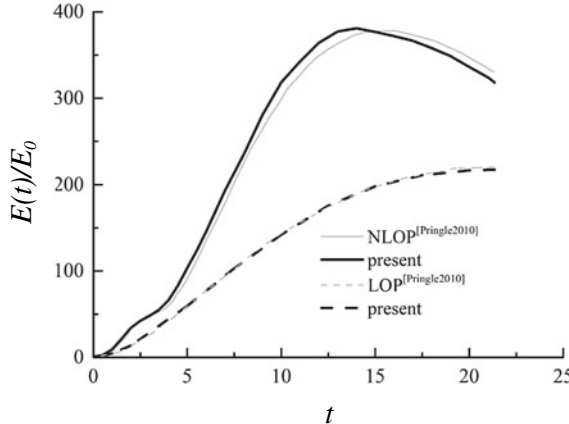


Fig. 2 The time variation of energy growth for linear optimal perturbations and nonlinear optimal perturbations. The bold dashed line denotes the present linear optimal perturbations; the gray dashed line denotes the linear optimal perturbations from the study by Ref. [21]. The bold solid line denotes the present nonlinear optimal perturbations; the gray line denotes the nonlinear optimal perturbations from Ref. [21]

means of lift-up. Only marginal changes are observed after the second iteration until the lines become virtually indistinguishable, indicating that the solution has converged.

We further verify our scheme by applying it in the identification of nonlinear optimal disturbances for the same flow parameters considered above. We trigger nonlinearity by increasing the initial energy of the perturbations to $E_0 = 2 \times 10^{-5}$. Figure 2 shows the computed evolution of the perturbation kinetic energy. For the purpose of comparison, the nonlinear results by Ref. [21] are also included in the figure. The two lines agree well, and show three distinct stages of amplification. During the first stage, the kinetic energy of the perturbations amplifies through the Orr mechanism via a tilting by the mean shear. The subsequent plateau at $t \approx 3$ is associated with nonlinear oblique interactions which lead to streamwise vortices. The vortices eventually give rise to highly energetic streaks by means of lift-up, leading to a peak at $t \approx 13$, followed by viscous decay.

The evolution of the streamwise component of the nonlinear optimal perturbations is presented in Figure 3 at several time instants. Initially, the localized perturbations are tilted against the mean shear, causing their reorientation and amplification via the Orr mechanism. The generated oblique structures interact nonlinearly to form streamwise vortices. Past this point, streamwise streaks are generated by the lift-up mechanism, resulting in further energy growth.

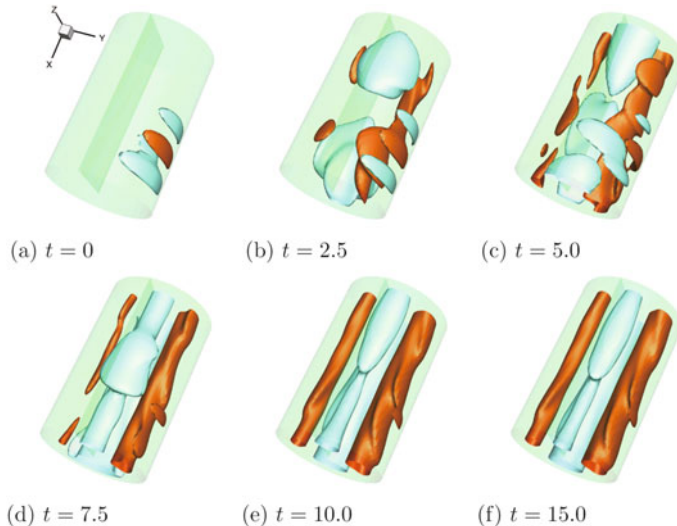


Fig. 3 Isosurfaces of streamwise perturbation velocity $u = \pm 0.5 \times \max(u)$ (dark or crimson for positive and light or light blue for negative) at the time instants $t = 0, 2.5, 5.0, 7.5, 10.0$, and 15 (a–f, respectively)

4 Conclusions

A variational framework based on the compressible Navier-Stokes equations has been presented. The approach allows for the first time the identification and analysis of nonlinear optimal disturbances in compressible flow. The underlying flow solver enables the efficient analysis of flows in complex geometries at high accuracy. The optimization algorithm was verified in parallel periodic pipe flow at low Mach numbers. In a first setting, linear optimal perturbations were accurately recovered after a small number of direct adjoint iterations. Subsequently, the framework was applied to identify nonlinear optimal perturbations. Comparison to the literature demonstrated good agreement with previous research in the same flow setting. An extension of the analysis to flows at higher Mach numbers is in progress.

Acknowledgements This investigation was funded by the Office of Naval Research under grant N00014-17-1-2341.

References

1. Hack, M.J.P., Moin, P.: *J. Fluid Mech.* **844**, 917 (2018)
 2. Romanov, V.A.: *Funct. Anal. Appl.* **7**, 137 (1973)
 3. Bottin, S., Chate, H.: *Eur. Phys. J. B* **6**, 143 (1998)
 4. Orszag, S.A.: *J. Fluid Mech.* **50**, 689 (1971)

5. Davis, S.J., White, C.M.: Proc. R. Soc. A **119**, 92 (1928)
6. Orszag, S.A., Kells, L.C.: J. Fluid Mech. **96**, 159 (1980)
7. Trefethen, L.N., Trefethen, A.E., Reddy, S.C., Driscoll, T.A.: Science **261**, 578 (1993)
8. Reddy, S.C., Schmid, P.J., Baggett, J.S., Henningson, D.S.: SIAM J. Appl. Math. **53**, 15 (1993)
9. Schmid, P.J.: Annu. Rev. Fluid Mech. **39**, 129 (2007)
10. Gustavsson, L.H.: J. Fluid Mech. **224**, 241 (1991)
11. Butler, K.M., Farrell, B.F.: Phys. Fluids A **4**, 1637 (1992)
12. Hack, M.J.P., Moin, P.: J. Fluid Mech. **829**, 112 (2017)
13. Hack, M.J.P., Zaki, T.A.: J. Fluid Mech. **778**, 389 (2015)
14. Hack, M.J.P., Zaki, T.A.: J. Fluid Mech. **741**, 280 (2014)
15. Monokrousos, S., Bottaro, A., Brandt, L., Vita, A.D., Henningson, D.S.: Phys. Rev. Lett. **106**, 134502 (2011)
16. Rabin, S.M.E., Caulfield, C.P., Kerswell, R.R.: J. Fluid Mech. **712**, 244 (2012)
17. Eaves, T.S., Caulfield, C.P.: J. Fluid Mech. **784**, 548 (2015)
18. Pringle, C.C.T., Willis, A.P., Kerswell, R.R.: J. Fluid Mech. **702**, 415 (2012)
19. Cherubini, S., Palma, P.D., Robinet, J.C., Bottaro, A.: J. Fluid Mech. **689**, 221 (2011)
20. Farano, M., Cherubini, S., Robinet, J.C., Palma, P.D.: Fluid Dyn. Res. **48**, 061409 (2015)
21. Pringle, C.C.T., Kerswell, R.R.: Phys. Rev. Lett. **105**, 154502 (2010)
22. Thomas, P.D., Lombard, C.K.: AIAA J. **17**, 1030 (1979)
23. Svärd, M., Nordström, J.: J. Comput. Phys. **39**, 129 (2014)
24. Huang, Z., Hack, M.J.P.: J. Fluid Mech. **894**, A5 (2020)
25. Schmid, P.J., Henningson, D.S.: J. Fluid Mech. **277**, 197 (1994)

On Subharmonic Resonance and Other Nonlinear Mechanisms in Wavepackets in Boundary Layers



A. G Martinez, F. H. T Himeno, M. S. Mathias, and M. A. F. Medeiros

Abstract On airplanes, transition often initiates from small and irregular disturbances introduced into the boundary layer. These disturbances produce TS waves which are modulated both in streamwise and spanwise directions. Such waves are well represented by wavepackets, whose most salient nonlinear feature is the growth of oblique low frequency waves. Experimental results, presented in the literature, additionally indicate the nonlinear growth of fundamental modes. Interestingly, DNS results presented here and in the literature, indicate the nonlinear subharmonic modes are well reproduced numerically but this is not observed for the fundamental modes. Our results also show the subharmonic resonance is substantially less active than previously thought.

1 Introduction

Wavepackets can reproduce most aspects of the natural transition that occurs under uncontrolled conditions in boundary layers, such as a wide spread frequency spectrum, wave modulation and production of turbulent spots constituting an interesting model for natural transition studies [1]. Moreover, several experimental observations of natural transition show that wavepackets play an important role in the transition process for a wide range of atmospheric turbulence levels [2]. These waves are modulated in streamwise and spanwise directions and evolve downstream generating

A. G. Martinez (✉) · F. H. T. Himeno · M. S. Mathias · M. A. F. Medeiros
Department of Aeronautical Engineering, University of São Paulo, João Dagnone Avenue 1100,
Sao Carlos, Sao Paulo 13563-120, Brazil
e-mail: german.andres.gaviria@gmail.com

F. H. T. Himeno
e-mail: fernando.himeno@usp.br

M. S. Mathias
e-mail: marlon.sproesser@usp.br

M. A. F. Medeiros
e-mail: marcello@sc.usp.br

vortical structures or short streaks before breakdown to turbulence [3]. Reeh and Tropea [4] also evidenced the presence of wavepackets for several flight conditions.

Early works on wavepackets established the main characteristics of its linear and nonlinear evolution in the streamwise direction in incompressible boundary layers [5, 6]. Later, these experiments were reproduced by DNS simulations [7–9]. Experiments further extended the results in the nonlinear regime [10, 11] and attribute the nonlinear activity of the wavepackets to subharmonic instabilities of either C-type or H-type. Here, we present the numerical reproduction of the experiment of Medeiros and Gaster [11] which is not found previously in the literature.

Cohen [12] also reports the presence of nonlinear fundamental modes in wavepackets despite the dominant subharmonic resonance. Similar nonlinear fundamental modes are also observed in experiment of Medeiros and Gaster [11]. Here, these aspects are investigated in detail.

The nonlinear interactions of random low amplitude three-dimensional waves are dominated by the subharmonic amplification. For higher amplitudes, a mixed mechanism route composed by the amplification of fundamental and subharmonic modes is observed [13]. These results indicate substantial similarities between the nonlinear evolutions of random disturbances and wavepackets.

2 DNS Code

The simulations were conducted using an in-house DNS (Direct Numerical Simulation) code that has been successfully used on other instability problems [14]. The code solves the non-conservative form of the Navier-Stokes equations for compressible flow. The equations can be written as

$$\frac{\partial \rho}{\partial t} = -\rho \frac{\partial u_i}{\partial x_i} - \frac{\partial \rho}{\partial x_i} u_i, \quad (1)$$

$$\frac{\partial u_j}{\partial t} = -\frac{\partial u_j}{\partial x_i} u_i - \frac{1}{\rho} \frac{\partial p}{\partial x_j} + \frac{1}{\rho} \frac{\partial \tau_{ij}}{\partial x_i}, \quad (2)$$

$$\frac{\partial e}{\partial t} = -\frac{\partial e}{\partial x_i} u_i - \frac{p}{\rho} \frac{\partial u_i}{\partial x_i} + \frac{1}{\rho} \tau_{ij} \frac{\partial u_j}{\partial x_i} - \frac{1}{\rho} \frac{\partial q_i}{\partial x_i}, \quad (3)$$

where ρ is density; u_i represents the flow velocity components; x_i , the direction vector aligned with the cartesian axis; p , is the pressure and e , the internal energy. The variables τ_{ij} and q_i are the viscous tensor and heat flux term defined by

$$\tau_{ij} = \frac{\mu(T)}{Re} \left[\frac{\partial u_i}{\partial x_j} + \frac{\partial u_j}{\partial x_i} - \frac{2}{3} \delta_{ij} \frac{\partial u_k}{\partial x_k} \right], \quad (4)$$

and

$$q_i = -\frac{\mu}{(\gamma - 1)RePrM_\infty^2} \frac{\partial T}{\partial x_i}, \quad (5)$$

where δ_{ij} is the unit tensor, μ_∞ , is the dynamic viscosity; c_p , the specific heat and γ , the heat capacity ratio.

The temperature, T, and the internal energy are related by

$$e = \frac{T}{(\gamma^2 - \gamma)M_\infty^2}. \quad (6)$$

To complete the set of equations required to solve the system, the ideal gas model is considered and the equation

$$p = (\gamma - 1)\rho e, \quad (7)$$

is used to relate the pressure, internal energy and density.

The viscosity was modeled by the Sutherland's law

$$\frac{\mu^*}{\mu_\infty} = \mu(T) = \frac{1 + C}{T + C} T^{\frac{3}{2}}, \quad (8)$$

with $C = \frac{110}{T_\infty^*}$ K and $T_\infty^* = 300$ K.

The variables are non-dimensionalized by the displacement thickness at the disturbance position, δ_0^* , the free-stream velocity U_∞^* and the density ρ_∞^* , where superscript * denotes a dimensional parameter.

The domain is a rectangular box domain. For the spatial discretization, a compact finite difference scheme, 4th-order accurate, is constructed with spectral like resolution as presented by Lele [15]. The time integration is performed with a standard 4th-order Runge-Kutta method. The grid domain in the stream- and spanwise directions are uniform and a grid stretching is applied in the direction normal to the wall.

At the inflow, the velocity components are imposed, with the streamwise velocity, $u = 1$, and null for the others directions whereas for the pressure a homogeneous boundary condition is imposed. At the outflow and the outerflow boundaries the pressure is fixed and the other flow variables are calculated using null second derivative. A buffer zone is also included at the outflow in order to avoid undesirable reflections into the integration domain. On the wall, a no-slip condition is applied to the velocity components except in a short region close to the inflow, where a free-slip wall condition is imposed to provide a more uniform pressure on the flow. The temperature is fixed on the wall and the density is calculated so that the pressure follows a homogeneous Neumann condition. Periodic boundary condition is applied in the spanwise direction.

A 10th-order lowpass filter [16] is also applied at each time iteration inside the physical domain in order to control high frequency spurious oscillations. In the

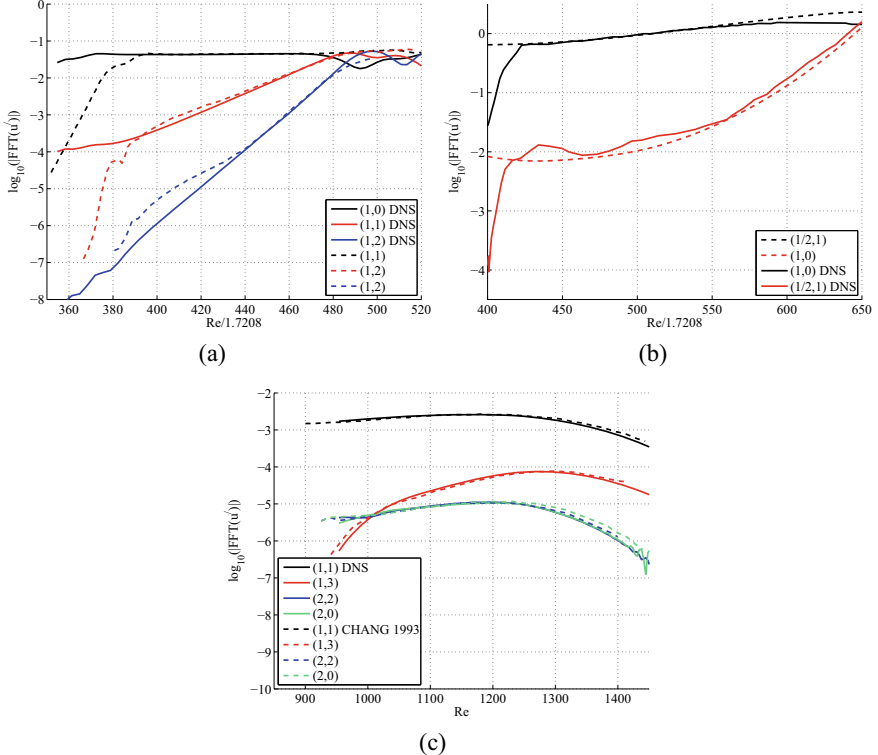


Fig. 1 **a** Comparison between amplification curves calculated with the current DNS and reference cases for (a) Fundamental resonance [17], **b** Subharmonic resonance [18], and **c** Oblique transition [19]

spanwise direction, a periodic compatible filter is used. The filtering levels are low and represent a condition with almost no filter.

3 Code Validation

The validation tests consisted of reproducing three nonlinear amplification mechanisms known for monochromatic Tollmien-Schilichting (T-S) waves, namely (a) fundamental, (b) subharmonic and (c) oblique transition. The base flow is perturbed via the wall normal velocity. Mach number is set to $M_\infty = 0.2$ which minimizes compressibility effects and allows considerable gains in the computational time.

Figure 1 shows good agreement between the DNS and the reference cases reproducing both linear and nonlinear amplifications of the two- and three-dimensional waves.

4 Nonlinear Stages of a Wavepacket

The current simulation nominally reproduces the experimental condition of Medeiros and Gaster [11]. In this experiment, the boundary layer developed on a 1.68 m long plate. The free-stream velocity was $U_\infty = 17.3$ m/s and the free-stream turbulence level was 0.008%, in the range of 0.001 to 5 kHz. The measurements of the streamwise velocity were carried out with a constant-temperature hot-wire anemometer. The results presented here are the ensemble average of 256 realizations. The flow perturbation was generated by a loudspeaker connected with the flow through a small hole of 0.3 mm, located at the plate centerline at $x_0^* = 203$ mm relative to leading edge. The signal driving the speaker was composed by the sum of $N_n = 80$ Fourier modes of identical amplitude with fundamental frequency $f_0^* = 5$ Hz which covered the entire linearly unstable frequency band. In the current study the same excitation time series was applied in the numerical simulations.

Figure 2 shows a comparison between the experimental and DNS results for the packet evolution along the centerline at a fixed y -position, $y = 0.6 \cdot \delta^*$. The packet has a very small amplitude, but displays nonlinear activity. In view of the small packet amplitude, the agreement in the linear regime is remarkable. At the late nonlinear regime the agreement is still good.

Figure 3 shows the agreement between numerical and experimental results is good over the whole spanwise domain. Figure 4 displays the evolution of the frequency vs. spanwise wavenumber spectrum. The dominant nonlinear activity is the so called subharmonic instability, which is well captured by the simulations.

Figure 5 shows the evolution of a typical subharmonic mode in the packet and its driving fundamental wave. The fundamental mode grows and decays according to the linear theory. This is associated with the fact that the boundary layer thickness grows and the dominant frequency in the packet reduces with the packet evolution. The subharmonic mode departs from linear regime early on, displays subharmonic instability for a short period and returns to linear. At the position where it reaches maximum amplitude, this mode behaves linearly, owing to the growth of the boundary layer thickness. This behaviour was typical of all subharmonic modes in the packet. These linear modes are unlikely to cause transition.

The experiments also showed nonlinear modes of fundamental frequency, which are not reproduced in the simulations. The experiment had a small, but measurable pressure gradient. Simulations with the same pressure gradient imposed shows the results are almost identical. The experiment also had an asymmetry at the source. The excitation in the numerical simulation calibrated to reproduce the same asymmetry also did not produce nonlinear fundamental modes. Similar fundamental modes were reported by Cohen [12] which were not observed in the corresponding simulations of Yeo et al. [9].

It is important to consider that the experiments are ensemble averaged over a large number of realizations, 256 in the case of Medeiros and Gaster [11]. This is intended to remove the uncorrelated noise present in the tunnel. However, this means that each individual packet had a higher spectral content compared to the ensemble aver-

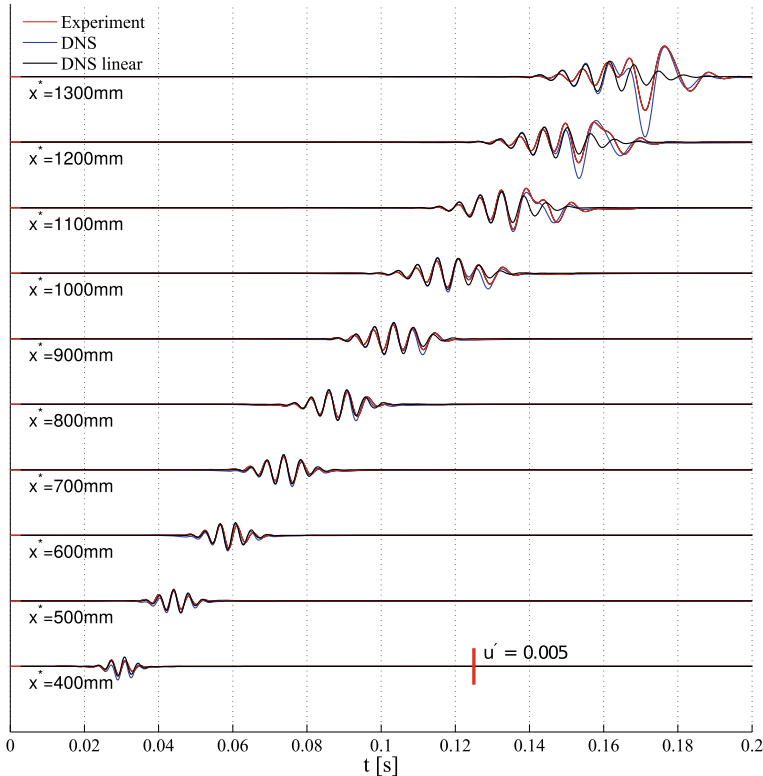


Fig. 2 Streamwise velocity fluctuation: experimental data from [11] and the DNS results for linear and nonlinear simulations at position $x = 1300$ mm and $y = 0.6\delta^*$

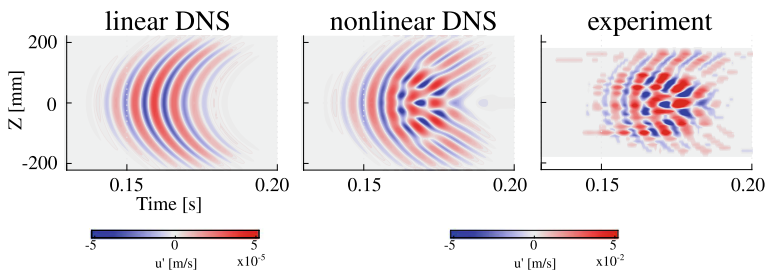


Fig. 3 Contour plot of physical space comparing the experimental data from [11] and the DNS results for linear and nonlinear simulations at $x = 1300$ mm and $y = 0.6\delta^*$

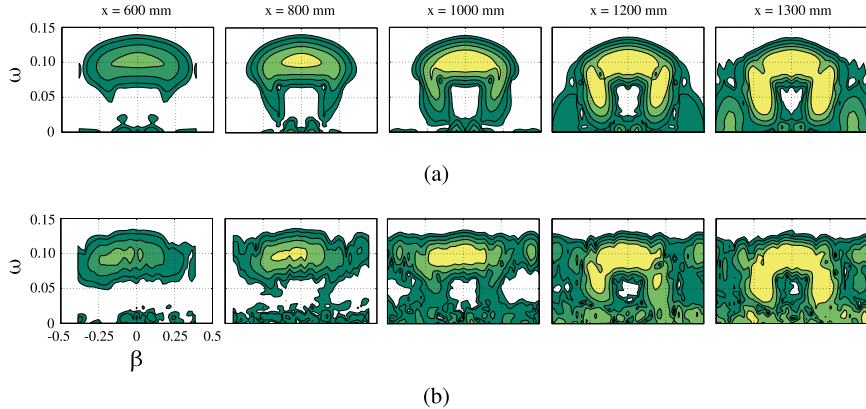


Fig. 4 Spectral evolution along plate for **a** DNS and **b** experiment

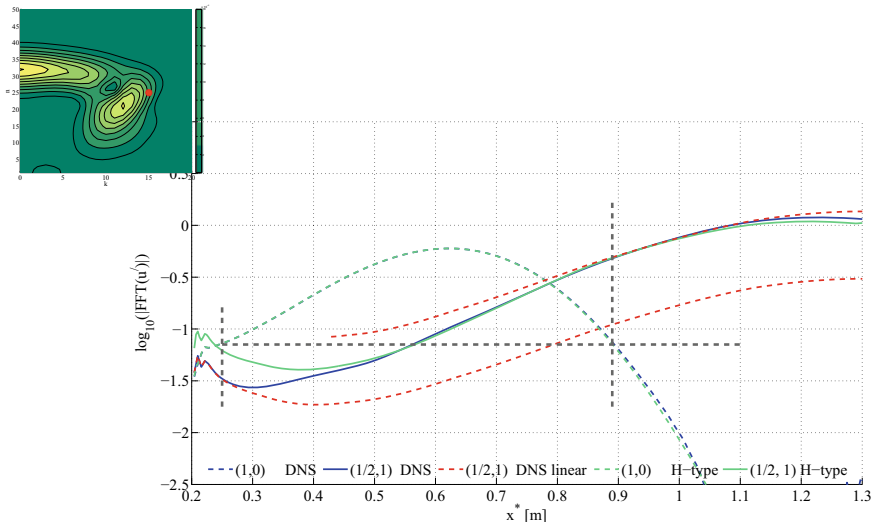


Fig. 5 Evolution of modes. Solid-green, controlled subharmonic instability. Solid-blue subharmonic mode in the packet. Dashed-red, subharmonic mode linear. Dashed-dashed blue, fundamental mode in the packet. Dashed-green fundamental mode in controlled subharmonic instability

aged one. Figure 6 shows the simulation results performed with the packet amplitude increased by 20%. This cases shows the nonlinear fundamental modes which resembles that observed in the experimental packet. The same approach produces a very similar outcome with regard to Cohen experiments [12]. This observation suggests a possible line to reconcile the experiments and the simulations and also provide a link to random noise experimental observation [13]. However, it also raises the question as to what caused transition in the experiment.

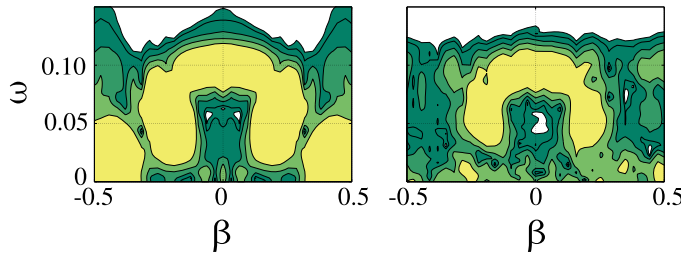


Fig. 6 Spectrum for a wave packet with disturbance amplitude increased 20% compared to experiment

5 Conclusions

In this work, we investigated the natural transition process modeled by wavepackets with experiments and DNS. The simulations reproduced the subharmonic stage observed in the experiment. They also showed that the subharmonic resonance is short lived and the so called subharmonic mode returns to linear regime. In fact it attains the maximum amplitude in the linear regime, after the subharmonic resonance. This is explained by the growth of the boundary layer thickness. It seems the subharmonic instability is less active than previously thought.

However, additionally to the subharmonic mode, the current and others experiments in the literature show the nonlinear growth of fundamental modes which are not reproduced numerically (neither here or in attempts at reproducing other experiments with wavepackets). It is suggested the disagreement is caused by the ensemble average process applied on experimental data. Since each experimental realization has a large spectral content this signal processing could lead to a stronger nonlinear activity. The implications of these findings to transition prediction are currently under further investigation.

Acknowledgements This work was funded U.S. Air Force Office of Scientific Research (AFOSR) under Grant No.FA9550-11-1-0354-P00002 with Dr. James Fillerup serving as program manager and Grant FA9550-18-1-0112 under Dr. Geoff Andersen. F. H. T. H., M. S. M and M. A. F. M. received funding from Sao Paulo Research Foundation (FAPESP/Brazil - grant #2018/02542-9 and #2018/04584-0), Coordination for the Improvement of Higher Education Personnel (CAPES/Brazil - grant #2018/04585-0) and CNPq/Brazil (grant # 304859/2016-8), respectively.

References

1. Yang, K.-S., Spalart, P.R., Ferziger, J.H.: Numerical studies of natural transition in a decelerating boundary layer. *J. Fluid Mech.* **240**, 433–468, 7 (1992)
2. Seitz, A., Horstmann, K.-H.: In flight investigations of tollmien schlichting waves. In: IUTAM Symposium on One Hundred Years of Boundary Layer Research, pp. 115–124. Springer, Berlin (2006)

3. Matsubara, M., Takaichi, K., Kenchi, T.: Experimental study of boundary layer transition subjected to weak free stream turbulence. In: Seventh IUTAM Symposium on Laminar-Turbulent Transition, pp. 277–282. Springer, Berlin (2010)
4. Reeh, A.D., Tropea, C.: Behaviour of a natural laminar flow aerofoil in flight through atmospheric turbulence. *J. Fluid Mech.* **767**, 394–429 (2015)
5. Vasudeva, B.R.: Boundary-layer instability experiment with localized disturbance. *J. Fluid Mech.* **29**, 745–763, 9 (1967)
6. Gaster, M., Grant, I.: An experimental investigation of the formation and development of a wavepacket in a laminar boundary layer. *Proc. R. Soc. Lond. A* **347**, 253–269 (1975)
7. Konzelmann, U., Fasel, H.: Numerical simulation of a three-dimensional wave packet in a growing flat plate boundary layer. In: Boundary layer Transition and Control, pp. 24.1–24.11, Cambridge, UK (1991). The Royal Aeronautical Society
8. Severin, M.: Direct numerical simulations of three-dimensional wavepackets in a flat-plate boundary-layer. Master's thesis, University of Arizona (2012)
9. Yeo, K.S., Zhao, X., Wang, Z.Y., Ng, K.C.: DNS of wavepacket evolution in a Blasius boundary layer. *J. Fluid Mech.* **652**, 333–372 (2010)
10. Cohen, J., Breuer, K.S., Haritonidis, J.H.: On the evolution of a wave packet in a laminar boundary layer. *J. Fluid Mech.* **225**, 575–606 (1991)
11. Medeiros, M.A.F., Gaster, M.: The production of sub-harmonic waves in the nonlinear evolution of wavepackets in boundary layers. *J. Fluid Mech.* **399**, 301–318 (1999)
12. Cohen, J.: The initial evolution of a wave packet in a boundary layer. *Phys. Fluids* **6**(3), 1133–1143 (1994)
13. Spalart, P.R., Yang, K.-S.: Numerical study of ribbon-induced transition in Blasius flow. *J. Fluid Mech.* **178**, 345–365 (1987)
14. Bergamo, L.F., Gennaro, E.M., Theofilis, V., Medeiros, M.A.F.: Compressible modes in a square lid-driven cavity. *Aerosp. Sci. Technol.* **44**, 125–134 (2015). Instability and Control of Massively Separated Flows
15. Lele, S.K.: Compact finite difference schemes with spectral-like resolution. *J. Comput. Phys.* **103**, 16–42 (1992)
16. Visbal, M.R., Gaitonde, D.V.: On the use of higher-order finite-difference schemes on curvilinear and deforming meshes. *J. Comput. Phys.* **181**(1), 155–185 (2002)
17. Rist, U., Fasel, H.: Direct numerical simulation of controlled transition in a flat plate boundary layer. *J. Fluid Mech.* **298**, 211–248 (1995)
18. Kachanov, YuS., Levchenko, V.Ya.: The resonant interaction of disturbances at laminar-turbulent transition in a boundary layer. *J. Fluid Mech.* **138**, 209–247 (1984)
19. Joslin, R.D., Streett, C.L., Chang, C.-L.: Spatial direct numerical simulation of boundary-layer transition mechanisms: Validation of pse theory. *Theor. Comput. Fluid Dyn.* **4**(6), 271–288 (1993)

Numerical Simulation of Gas Injection Effect on Boundary Layer Instability for Space Vehicles



Ivan Egorov, Anton Obraz, Natalia Palchekovskaya, and Alexander Fedorov

Abstract In this work effect of wall normal gas injection on boundary-layer stability is investigated for the high-speed flow over two models of space vehicles—the hemispherical model and the model of Exomars project. The mean flows are obtained using numerical solutions of the Navier-Stokes equations for laminar axisymmetric flow. It was shown that the transition onset, which was experimentally observed in the boundary layer with injection, is associated with relatively small integral amplification of instability. This indicates that in the experiment laminar-turbulent transition is governed by bypass mechanisms.

1 Introduction

Vehicles entering planetary atmospheres can be thermally protected by covering their surfaces with ablative heat shields. Ablation process can significantly reduce heat fluxes inside the vehicle wall. On the other hand, the ablation influences laminar-turbulent transition (LTT) processes in the boundary layer flow [1]: the boundary-layer stability is altered by the effective gas injection from the wall [2, 3] the body shape is changed and transition can be dominated by roughness [4]. The review of relevant experiments is presented in [5]. Recently, ablative heat shields have regained attention due to Mars exploration missions [6] and reentry vehicles [7].

In [8] the hypersonic flow past a cylinder with a hemispherical nose was treated experimentally. The nose wall was permeable and gas injection normal to the wall surface was used to simulate the ablation effect. The experiment was conducted in the wind tunnel at Mach number $M = 7.32$ in the range of unit Reynolds number $Re_1 = (0.64 \div 1.33) \times 10^7 \text{ m}^{-1}$. The calorimeter probes mounted on the nose were used to measure the heat fluxes. The boundary layer state was identified as laminar, transitional or turbulent by comparing the experimental heat-flux distributions with the

I. Egorov · A. Obraz · N. Palchekovskaya (✉) · A. Fedorov
Moscow Institute of Physics and Technology, 9 Institutsky Pereulok, Dolgoprudny, Moscow
Region, Russia
e-mail: natalie.palchekovskaya@gmail.com

corresponding analytical and/or computational distributions for laminar and turbulent flows. In the no injection case, the boundary-layer flow was fully laminar. As the injection rate was increased, the transitional region was detected on the nose and moved progressively toward the stagnation point. In the present work the configuration [8] is studied numerically with emphasis on: (1) the effect of distributed gas injection on the heat-flux distributions in the laminar flow regimes; (2) the effect of gas injection on stability and the transition onset in the transitional flow regimes. In this work model of descent vehicle of ExoMars project is studied at flow regimes with Mach number values $M = 5.15$ and $M = 7.7$ and Reynolds number $Re = 1.7 \times 10^6 \text{ m}^{-1}$. The laminar flow fields are obtained by solving the Navier-Stokes equations. Stability computations are performed using the local-parallel linear stability theory and the e^N method [9, 10]. These computations are verified by comparisons with the results [11], where the geometry and free stream conditions correspond the experiment [8] but the injection non-uniformity is neglected.

2 Numerical Simulation

2.1 Laminar Flow Over Hemispherical Model

Numerical simulations of axisymmetric laminar flow fields are performed using the in-house code HSFlow [12, 13], where the Navier-Stokes equations are discretized using Total Variation Diminishing (TVD) scheme of finite volume with the second-order approximation in space. A steady solution is obtained using the time relaxation method for solving the discretized system on structured multiblock grids. Computations were performed for air which is treated as perfect gas of specific heat ratio $\gamma = 1.4$ and Prandtl number $Pr = 0.72$. Flow parameters: $M_\infty = 7.32$, $Re_1 = (1.191 \div 1.331) \times 10^7$, $T_\infty = 63.84 \div 68$ K. The viscosity coefficient is calculated using the Sutherland law.

In the no injection case, the boundary conditions on the body surface are:

$$u_w = v_w = w_w = 0, T_w = 300 \text{ K}, (dp/dn)_w = 0$$

In the non-zero injection cases, the boundary conditions are modified in accord with the experiment [8], where the dimensionless mass flow rate of injected gas, $m = (\rho v)_w$, is given as a function of the longitudinal coordinate $s = R^* \theta$ (Fig. 1).

The function $m(s)$ is taken from [8] where the distributions $m(s)$ are provided in table form. These distributions are interpolated using third order polynomials.

For each distribution $m(s)$ the corresponding nominal value of the injection rate is determined as $m_* = m(s_*)$, where $s_* = R^* \pi/2$ is the point of juncture between hemispherical nose and cylindrical afterbody. A typical distribution of $m(s)$ is shown in Fig. 2 at the nominal value $m_* = 0.003$. Because the external wall pressure decreases with s , the mass flow rate monotonically increases versus θ and attains its maximum

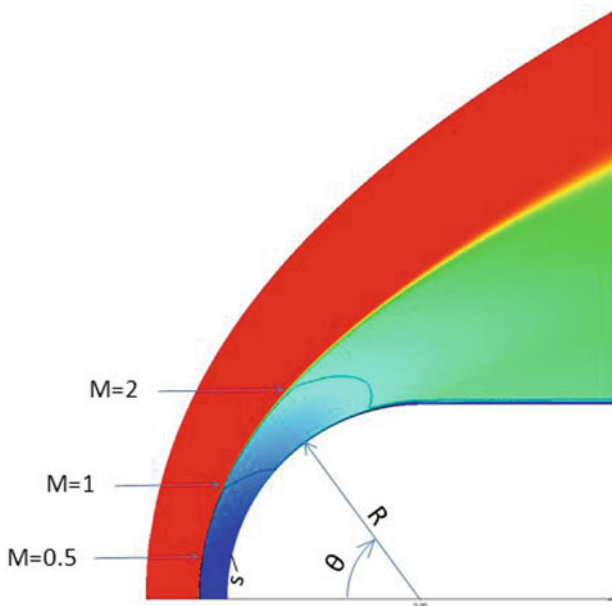
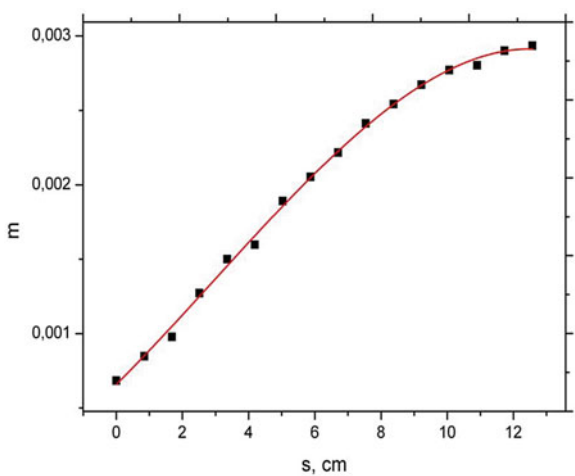


Fig. 1 Geometry of the model and the Mach number field

Fig. 2 Distribution of the mass flow rate at the nominal value. The black squares—experiment [8], red curve—approximation used in the present work



at $s = s^*$: $m_* = \max(m(s))$. The injected gas temperature is assumed equal to the wall temperature. The boundary conditions on the body surface are:

$$\rho_w v_w = m(s); u_w = w_w = 0; T_w^* = 300K$$

The boundary condition for pressure is obtained using the y-momentum conservation near the wall:

$$p_w + \rho_w v_w^2 = p_1 + \rho_1 v_1^2$$

For relatively small values of the nominal injection rate, $m_* < 0.1$, the approximate boundary condition is used:

$$\frac{\partial p}{\partial n} = 0$$

2.2 Laminar Flow Over ExoMars Vehicle Model

On the second stage of investigations flow over descent space vehicle model of ExoMars project with injection normal to the wall surface is studied. Front surface of the model is considered (Fig. 3) due to the fact that simulated ablation process takes place mostly on this part of the vehicle. Navier-Stokes equations in axisymmetric statement are chosen for the problem simulation. Perfect gas model is used with effective adiabatic exponent $\gamma = 1.3$. For calculations the regime is chosen with maximum Reynolds number on the descent trajectory $Re = 1.7 \cdot 10^6 \text{ m}^{-1}$ and Mach number values $M = 5.15$ and $M = 7.7$. For this regime intensities of normal injection are chosen $m = 0.01$ and $m = 0.013$, which are constant along the model surface. On the outer boundary of computational domain free stream boundary condition is set with Mach number $M = 5.15$ or $M = 7.7$ and temperature $T = 220 \text{ K}$, on the wall surface injection values $m = \rho V_n = \text{const}$ and radiation conditions are set.

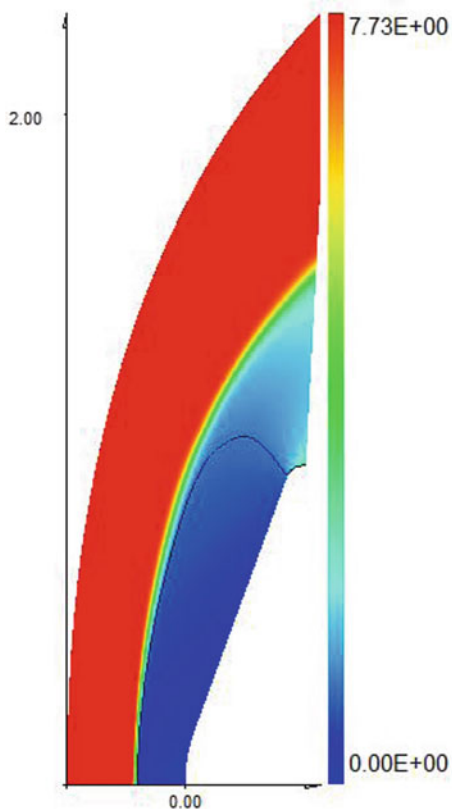
3 Stability Computations

Linear stability computations were performed using the stability module [14] of the HSFlow code. The spatial local-parallel stability problem is solved for disturbances of the convective wave form

$$\mathbf{q}'(s, y^*, z^*, t^*) = \hat{\mathbf{q}}(y^*) \exp \left(i \int_{s_0(\beta, \omega)}^s \alpha^*(\beta, \omega, s) ds + i\beta^* z^* - i\omega^* t^* \right)$$

Here $\mathbf{q}' = (u', v', w', p', T')^T$ and $\alpha^* = \alpha_r^* + i\alpha_i^*$ is a complex eigenvalue depending on angular frequency ω^* and transverse wave number β^* , $s_0(\beta^*, \omega^*)$ is the upstream neutral point.

Fig. 3 Geometry of front surface of ExoMars space vehicle model and computational grid



Without gas injection all modes of the discrete spectrum decay for both vehicle models; i.e. the boundary layer flow is stable on the nose. This is due to the favorable pressure gradient, which has a well-known stabilizing effect on the waves of Tollmien-Schlichting (TS) type. These findings agree with the experimental observations [8] and the stability computations [10] (Fig. 4).

At a certain nominal mass flow rate $m_{*,cr}$ the boundary layer becomes unstable. The point $s = s_{cr}$, where instability is observed for the first time, is called hereafter as a critical stability point. At $m_* = 0.007$ the boundary layer is still stable on the spherical nose, while at $m_* = 0.01$ the critical stability point is located near the sonic point: $s_{cr} \approx 6.5$ cm. Here the most unstable are plane waves of $\beta = 0$, and their eigenfunctions resemble those of TS-waves on a flat plate under similar flow conditions at the upper boundary-layer edge. Calculations show that upstream of the sonic point the most amplified are plane waves. Therefore, further stability computations were performed for plane waves of $\beta = 0$. Their downstream growth was modelled using the e^N method.

As shown in Fig. 5, the envelopes of amplification curves $N(s) = \max_{\omega^*} n(s, \omega^*)$ strongly depend on the nominal injection rate m_* . The critical point s_{cr} , where $N(s_{cr})$

Fig. 4 Comparison of tangential velocity profiles at constant value $m_* = 0.04$ along the surface. “PW”—results of the present work, “FC”—calculations [10]

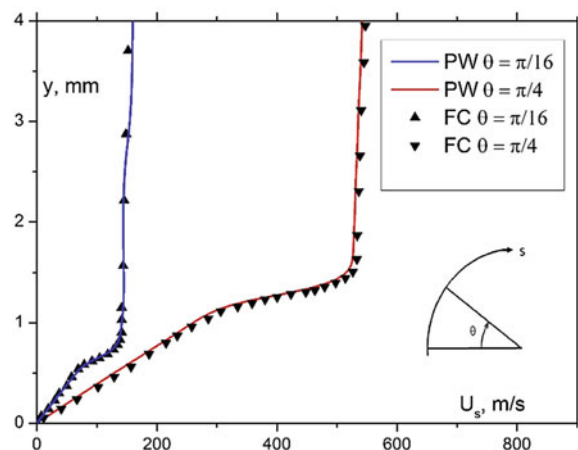
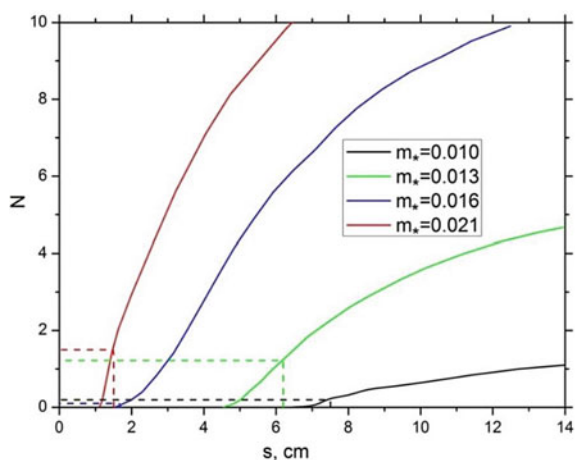


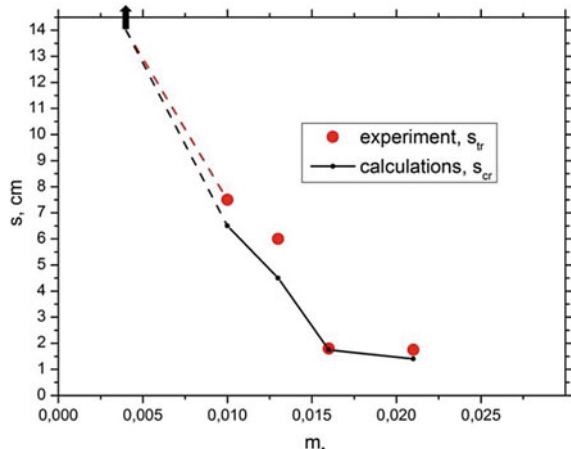
Fig. 5 The envelopes N (s) at various nominal injection rates m_* for hemisphere



$= 0$, rapidly moves upstream from: $s_{cr} \approx 6.5$ cm to $s_{cr} \approx 1.4$ cm as m_* increases from 0.01 to 0.021.

At the experimentally determined transition onset points the N -factors are small: $N(s_{tr}) < 1.5$ for all injection rates considered (see the dashed lines in Fig. 5). This indicates that the linear amplification stage of laminar-turbulent transition is bypassed in the wind-tunnel experiment [8]. Nevertheless, Fig. 6 shows that the critical points, predicted by the linear stability theory, correlate well with the empirical points of the transition onset. Thus, the nonlinear breakdown seems to be correlated with the linear instability mechanism. The assumption of whether this correlation has a physical basis can be checked by direct numerical simulations and/or detailed measurements of the controlled disturbances on the model tested in a quiet hypersonic wind tunnel.

Fig. 6 The correlation between the computed critical points $s_{cr}(m^*)$ (black line) and the transition onset points $s_{tr}(m^*)$ (red circles) measured in [8]



In Figs. 7 and 8 envelopes of N-factor are shown for two values of Mach number $M = 5.15$ and $M = 7.7$ for ExoMars model. Injection rates are constant along the vehicle surface. For typical value $N = 10$ [15] predicted LTT onset locations are shown. With increase of injection rate LTT onset location shifts to the model nose, but for the case $m = 0.01$ at $M = 7.7$ LTT is not observed.

This stability analysis shows that gas injection leads to destabilization of boundary layer on the front surface of the ExoMars model. At high injection rates LTT can be attributed to mass addition effect.

Fig. 7 The envelopes N at various injection rates at $M = 5.15$ for ExoMars model

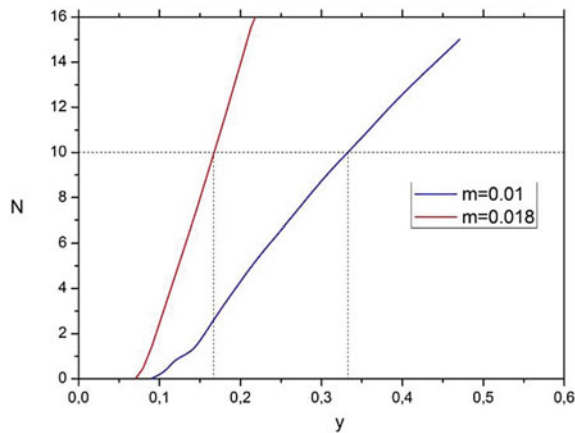
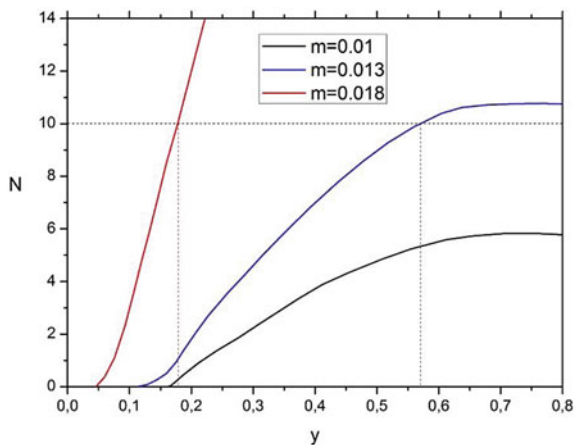


Fig. 8 The envelopes N at various injection rates at $M = 7.7$ for ExoMars model



4 Conclusion

The effect of normal gas injection on the boundary layer stability flow was investigated with the help of CFD solutions for the laminar (undisturbed) flow and the local-parallel linear stability theory. Nonuniform distributions of the injection mass flow rates were specified accurately using the experimental data. It was shown that the transition onset, which was experimentally observed in the boundary layer with injection, is associated with relatively small integral amplification of instability, $N(s_{tr}) < 1.5$. This indicates that in the experiment laminar-turbulent transition is governed by bypass mechanisms. Nevertheless, the empirical transition onset points correlate well with the critical stability points predicted by the linear stability theory.

This correlation might be useful for engineering estimations of the ablation rate at which laminar-turbulent transition is likely to occur on the nose of high-speed vehicle.

This work was performed at the Moscow Institute of Physics and Technology and supported by the Russian Foundation for Basic Research (project no. 17-08-00969) (calculations) and Russian Science Foundation (project no. 19-79-00184) (numerical technique development).

References

1. Morkovin, M.V.: Critical evaluation of transition from laminar to turbulent shear layers with emphasis on hypersonically traveling bodies. Air Force Flight Dynamics Laboratory. Technical Report AFFDL-TR-68-149, DTIC citation AD-686178 (1969)
2. Scott, C.J., Anderson, G.E.: Boundary-layer transition with gas injection. *J. Aerosp. Sci.* **25**, 791 (1958)
3. Pappas, C.C., Okuno: A. heat-transfer measurement for binary gas laminar boundary layers with high rates of injection. Ames Research Center. Technical Note TN-D-2473, NASA, Washington, D.C (1964)

4. Reda, D.C.: Review and synthesis of roughness-dominated transition correlations for reentry applications. *J. Spacecr. Rockets* **39**, 161–167 (2002)
5. Schneider, S.: Hypersonic boundary-layer transition with ablation and blowing. *J. Spacecr. Rockets* **47**, 225–237 (2010)
6. Merrifield, J.A., Gulhan, A., Neeb, D.: Rough wall heat flux augmentation analysis in the framework of the ExoMars project. AIAA Paper 2014–2817 (2014)
7. Johnston, C.O., Gnoffo, P.A., Mazaheri, A.: Study of ablation–flowfield coupling relevant to the Orion heat shield. *J. Thermophys. Heat Transf.* **26**, 213–221
8. Kaattari, G. E.: Effects of mass addition on blunt body boundary layer transition and heat transfer. NASA, TP-1139 (1978)
9. Smith, A.M.O., Gamberoni, N.: Transition, pressure gradient and stability theory, p. 26388. Douglas Aircraft Company, ES (1956)
10. Van Ingen, J.L.: A suggested semi-empirical method for the calculation of the boundary layer region. TU Delft. Technical Report VTH-74 (1956)
11. Li, F., Choudhari, M., Chang, C.L., White, J.: Effects of injection on the instability of boundary layers over hypersonic configurations. *Phys. Fluids* **25**, 1–16 (2013)
12. Palchekovskaya, N.V., Novikov, A.V., Egorov, I.V.: Numerical simulation of the flow over a segment-conical body on the basis of Reynolds equations. *Comput. Math. Math. Phys.* **58**, 118–129 (2018)
13. Novikov, A., Egorov, I., Fedorov, A.: Direct numerical simulation of wave packets in hypersonic compression-corner flow. *AIAA J.* **54**, 2034–2050 (2016)
14. Fedorov, A.V., Obraz, A.O.: The high-speed flow stability (HSFS) software package for stability analysis of compressible boundary layers. *TsAGI Sci. J.* **48**, 223–242 (2017)
15. Johnson H.B., Candler G.V.: Analysis of laminar-turbulent transition in hypersonic flight using PSE-Chem. AIAA paper 2006-3057 (2006)

Two-Dimensional Self-Sustaining Processes Involving Critical Layer/Wall Layer Interaction



Rishi Kumar and Andrew Walton

Abstract The nonlinear stability of plane Poiseuille-Couette flow is analyzed at large Reynolds number. An asymptotic self-sustaining structure is found which involves the interaction of two nonlinear critical layers with near-wall Stokes regions. A global property of the flow-field, involving the vorticity of the mean-flow distortion, is used to determine the amplitude dependence of the $O(1)$ wavenumber and phasespeed and it is found that solutions exist for values of wall sliding speed considerably in excess of the linear cut-off. In the situation where the phasespeed is almost equal to the wall sliding speed, a new nonlinear structure arises involving critical layer/shear layer interaction. The numerical results from this latter interaction are found to compare well with full solutions of the Navier-Stokes equations.

1 Introduction

In recent years a dynamical systems approach to transition has become fashionable in which equilibrium solutions of the Navier-Stokes equations play a key role in transitional and turbulent dynamics (see for example the review of [1]). The relevant equilibrium solutions are those in which there is a mutual interaction between a roll flow in the cross-stream plane, a streamwise streak and a wave propagating in the streamwise direction. This interaction is fundamentally three-dimensional in nature and has no obvious two-dimensional analogue. If we wish to consider Tollmien-Schlichting (TS) instabilities, which are inherently two-dimensional, then the roll/streak/wave theories are not directly applicable, even at high Reynolds num-

R. Kumar · A. Walton (✉)

Department of Mathematics, Imperial College London, London, UK
e-mail: a.walton@ic.ac.uk

R. Kumar
e-mail: r.kumar16@ic.ac.uk

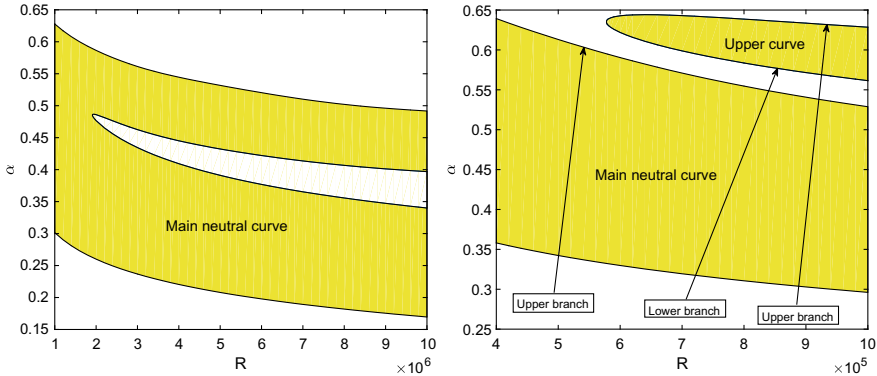


Fig. 1 Linear neutral curves for PCF. **a** $V = 0.017$; **b** $V = 0.019$

ber, unless a very specific spanwise variation is imposed. In this paper we investigate a form of self-sustaining process (SSP) that can operate in two dimensions and involves critical layer/wall layer interaction. We develop the theory under the assumption of an asymptotically large Reynolds number which allows us to identify the crucial scalings and regions where different physical balances dominate and to demonstrate the way in which those regions interact to ensure that the instability is maintained against viscous decay. We develop the theory here for the specific case of plane Poiseuille-Couette flow (PCF) which is well-known to support a TS form of instability provided the sliding speed is not too large, although the theory readily generalizes to other base flows.

We assume that the streamwise pressure gradient is fixed (the theory can be modified to accommodate a fixed mass flux instead), while the upper and lower walls move with the same prescribed constant streamwise speed but in opposite directions. The basic PCF can be written in the non-dimensional form

$$U_0 = 1 - y^2 + Vy, \quad (1)$$

where the channel walls are positioned at the scaled locations $y = \pm 1$ and V is the scaled wall speed. The Reynolds number R in operation here is based on the channel half-width and the maximum velocity of the Poiseuille component of the flow.

The linear stability properties of PCF, through the use of the Orr-Sommerfeld equation, were first studied by [2]. A single neutral curve was computed, demonstrating that for a given sliding speed V there exists a band of unstable wavelengths, provided the Reynolds number is above a critical value $R_c = R_c(V)$. Further, it was shown that this critical Reynolds number tends to infinity as $V \rightarrow V_c-$, with $V_c \simeq 0.34$ in terms of our non-dimensionalization. For $V > V_c$ the flow is linearly stable at all Reynolds numbers. Subsequently, a high Reynolds number asymptotic analysis by [3] suggested that the linear problem was considerably more complicated than originally thought and proposed that there may be multiple neutral curves

coexisting for $V < V_c$. This was confirmed in [4] and investigated in more detail in [5]. In Fig. 1a, for $V = 0.017$, we see the curve originally computed in [2] but also the existence of a stable intrusion at large Reynolds number. As V is increased this finger of stability extends to smaller R before slicing off a portion of the original neutral curve (Fig. 1b), thereby generating a second curve. With further increase in V this upper curve splits again. Eventually however, as $V \rightarrow V_c -$, all these regions of instability disappear, either by shrinking to a point or retreating to infinity. We will see later that, by comparing Navier-Stokes solutions with asymptotic theory, the nonlinear interaction formulated in this paper accurately describes solutions that bifurcate from one of these additional neutral curves.

2 Interaction Properties

The key idea underpinning the nonlinear self-sustaining interactions investigated in this paper concerns a property of the mean vorticity of the flow. First we define the quantity

$$\tau_M(y) = \frac{1}{2\pi} \frac{d}{dy} \int_0^{2\pi} (u - U_0) d\xi. \quad (2)$$

Here $\xi = \alpha(x - ct)$ is the travelling wave coordinate, $u(\xi, y)$ the streamwise velocity with the wavenumber α and phasespeed c both assumed real. It can be shown, by integration of the full two-dimensional Navier-Stokes equations, that τ_M must assume the same value at both walls, i.e.

$$\tau_M(1) = \tau_M(-1). \quad (3)$$

Since our theory assumes an asymptotically large value of R , the main effects of viscosity are confined to internal critical layers (where the basic flow is equal to the disturbance phasespeed) and thin layers adjacent to the channel walls, with the bulk of the flow-field subject to inviscid dynamics and satisfying a form of Rayleigh's equation. It follows from the property (3) that any jump in τ_M that occurs across the critical layer(s) in the flow must be exactly balanced by a similar jump across the wall layers, leading to an overall net jump of zero. This principle can be used to derive an amplitude equation for the nonlinear modes as we shall see in detail in the next section.

Another important property of these interactions concerns the behaviour of the solutions of Rayleigh's equation as the critical layers are approached from either side. The role of each critical layer is to smooth out the logarithmic singularity that arises in the streamwise velocity calculated from the Rayleigh solution. In the interaction we consider, these layers possess the properties first proposed by [6] in which the effects of viscosity only manifest themselves at relatively high order in the velocity

expansions. This means that as far as the Rayleigh solutions are concerned, we should impose a condition which ensures that the travelling waves do not undergo a phase shift at leading order as the critical layers are traversed. Mathematically this means that if a critical layer is situated at $y = y_c$ then, as far as the solution of the Rayleigh equation is concerned, terms of the form

$$\log(y - y_c) \text{ as } y \rightarrow y_c + \text{ are replaced by } \log(y_c - y) \text{ as } y \rightarrow y_c -. \quad (4)$$

Application of this connection formula across each critical layer allows us to formulate an eigenvalue problem to determine the dispersion relation $c = c(\alpha)$ for a prescribed sliding speed V .

We will consider two possible such interactions of this type in PCF. The first assumes that both the wall sliding speed V and the disturbance phasespeed c are $O(1)$ quantities, but are sufficiently distinct from one another that there exist two critical layers that reside an $O(1)$ distance from both walls, with viscous Stokes layers adjoining the boundaries. In the second scenario, the phasespeed is sufficiently close in value to the sliding speed of the upper wall that the upper critical layer and Stokes layer merge to form a viscous shear layer. In the final part of the paper we compare the results of this latter asymptotic theory with travelling wave computations of the full nonlinear two-dimensional Navier-Stokes equations.

3 A 2D SSP at Large R with Two Critical Layers

The relevant asymptotic structure consists of two critical layers embedded within an inviscid region with Stokes layers adjoining each wall with the scalings expressed in terms of the small quantity $\epsilon = R^{-1/6}$ as in a number of previous strongly nonlinear critical layer studies, e.g. [7]. We consider briefly each of the asymptotic regions: more detail on this structure can be found in [8].

An inviscid region extends across the majority of the channel. The appropriate velocity expansions here are

$$u = U_0(y) + \epsilon u_{1M}(y) + \epsilon^2 u_2(x, y, t) + \dots, \quad v = \epsilon^2 v_2(x, y, t) + \dots, \quad (5)$$

along with a corresponding expansion for the pressure, while the fundamental disturbances (u_2, v_2) take the form of travelling waves

$$A_0 (F_2(y) \cos \xi, G_2(y) \sin \xi), \quad (6)$$

where the amplitude A_0 (suitably normalized) is to be determined as part of the solution. The term with subscript M is a mean flow distortion induced by the critical layer dynamics and, as can be seen from the expansions (5), this quantity is significantly larger than the fundamental fluctuation throughout the bulk of the flow. As far as that fluctuation is concerned, substitution of (5), (6) into the Navier-Stokes equations

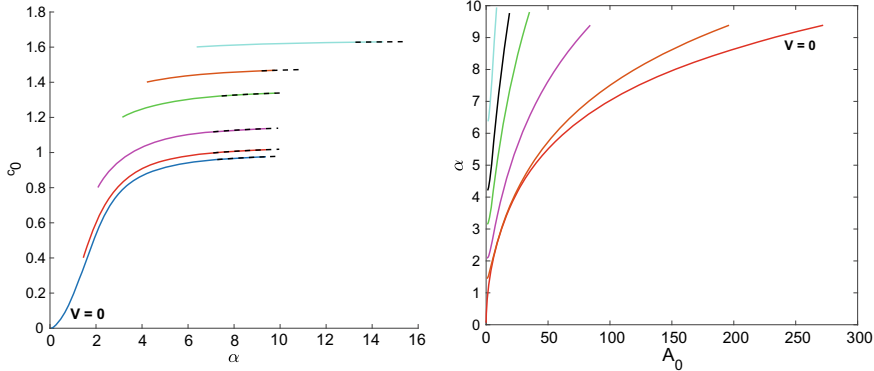


Fig. 2 Numerical results for the dual critical layer structure considered in Sect. 3 for (from bottom to top) $V = 0, 0.4, 0.8, 1.2, 1.4, 1.6$. **a** phasespeed $c_0(\alpha)$; **b** wavenumber α as a function of scaled amplitude A_0

leaves the normal velocity perturbations governed by the Rayleigh equation

$$(U_0 - c_0)(G_2'' - \alpha^2 G_2) = U_0'' G_2, \quad G_2(\pm 1) = 0, \quad (7)$$

where c_0 is the leading order term in the phasespeed expansion. The system (7) is solved subject to the connection formula (4) which holds at the locations $y_c \in \{y_1, y_2\}$ where $U_0 = c_0$. This problem can be solved numerically for a prescribed sliding speed to give $c_0(\alpha)$ as shown in Fig. 2a, where the dotted lines are large wavenumber asymptotic approximations. It can be seen that solutions exist for sliding velocities considerably in excess of the linear cut-off ($V_c \simeq 0.34$) referred to in Sect. 1.

The nonlinear critical layers each have thickness $O(\epsilon)$ with the disturbances here depending non-trivially on the travelling wave coordinate ξ in contrast to the leading-order monochromatic core flow solution evident in the expression (6). It turns out that J_{CL} , the net vorticity jump across both critical layers, is given by

$$J_{CL} = [\tau_M]_{y_1-}^{y_1+} + [\tau_M]_{y_2-}^{y_2+} = \epsilon \alpha^{-1/2} \sigma A_0^{1/2} \left\{ \left| \frac{\lambda_1}{b_1} \right|^{1/2} + \left| \frac{\lambda_2}{b_2} \right|^{1/2} \right\}, \quad (8)$$

where λ_1, λ_2 are constants determined from the solution of the Rayleigh problem and $b_i = (-1)^i(y_1 - y_2)$ measures the critical layer separation. The quantity $\sigma \simeq 5.516$ is a numerically-determined constant that has arisen in many previous critical layer studies (e.g. [7]).

In both wall layers the dominant balances are between the inertial term $\alpha(U_0 - c)$ and the viscous operator $R^{-1}\partial^2/\partial y^2$, implying a classical $O(R^{-1/2})$ thickness. If we first consider the layer near the upper wall, the appropriate velocity expansions are

$$u = V + \epsilon^2 \tilde{U}(\xi, Z_1) + \epsilon^4 \mathcal{F}_1(Z_1) + \dots, \quad v = \epsilon^2 R^{-1/2} \tilde{V}(\xi, Z_1) + \dots, \quad (9)$$

with $Z_1 = R^{1/2}(1 - y)$ of $O(1)$, where \mathcal{F}_1 is the mean-flow distortion. Again, as in the critical layer analysis, our main aim is to calculate the leading-order jump in mean vorticity, i.e. the quantity $J_{UW} = \epsilon [\mathcal{F}'_1(Z_1)]_\infty^0$. One can solve for the mean-flow distortion analytically here, and this allows us to deduce that

$$J_{UW} = -\epsilon 2^{-3/2} A_0^2 [G'_2(1)]^2 \alpha^{-3/2} (c_0 - V)^{-1/2}. \quad (10)$$

A similar analysis of the lower Stokes layer yields the result

$$J_{LW} = -\epsilon 2^{-3/2} A_0^2 [G'_2(-1)]^2 \alpha^{-3/2} (c_0 + V)^{-1/2}. \quad (11)$$

As remarked in Sect. 2, the flow structure is only self-consistent provided the total jump in mean flow distortion vorticity is zero: this implies $J_{CL} + J_{UW} + J_{LW} = 0$. Putting together the expressions (8), (10), (11) for the jumps leads us to the expression

$$A_0^{3/2} = 2^{3/2} \alpha \sigma \left(\left| \frac{\lambda_1}{b_1} \right|^{1/2} + \left| \frac{\lambda_2}{b_2} \right|^{1/2} \right) \left(\frac{[G'_2(1)]^2}{(c_0 - V)^{1/2}} + \frac{[G'_2(-1)]^2}{(c_0 + V)^{1/2}} \right)^{-1}, \quad (12)$$

determining explicitly the amplitude dependence of these nonlinear modes. The dependence on A_0 of wavenumber α is shown in Fig. 2b for various wall sliding speeds V . It can be seen that α increases monotonically with A_0 . The $A_0 \rightarrow \infty$ limit is investigated in [8] and it is found that the critical layers merge and a new shorter scale structure arises.

4 A 2D SSP at Large R with a Single Critical Layer

If the phasespeed of the travelling wave and the sliding speed of the upper wall are almost equal then the upper critical layer becomes embedded within the upper wall layer and a new structure emerges with a different set of Reynolds number scalings to those set out in Sect. 3. In particular we now have

$$c = V + R^{-1/3} c_1, \quad (13)$$

with c_1 to be determined in terms of the disturbance amplitude which we will denote by A_0 as in the previous section. We include only brief details here with the reader referred to [5] for more explanation of precisely how these scalings are deduced.

As before the bulk of the flow is governed by a Rayleigh equation, but now that $c = V$ to leading order we have

$$(U_0 - V)(G''_2 - \alpha^2 G_2) = U''_0 G_2, \quad G_2(\pm 1) = 0, \quad (14)$$

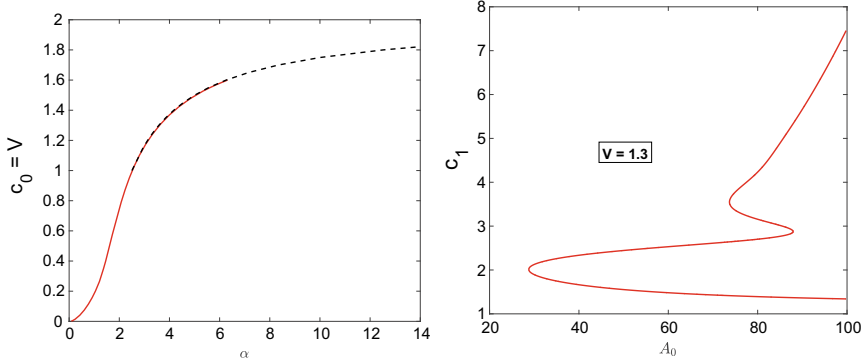


Fig. 3 Numerical results for the single critical layer structure considered in Sect. 4. **a** sliding speed V versus wavenumber α ; **b** phasespeed perturbation c_1 versus scaled amplitude A_0 for $V = 1.3$

replacing (7), but still subject to the jump condition (4) across the single critical layer located where $U_0 = V$. The numerical solution of this eigenvalue problem gives $\alpha = \alpha(V)$ and is shown in Fig. 3a, again indicating that solutions exist in excess of the linear cut-off. The fundamental disturbance in the core is still of size $O(\epsilon^2)$ as in (5), but now the Reynolds number dependence has changed so that $\epsilon = R^{-2/9}$ in this new regime. In order to derive a formula for the amplitude we again need to consider the vorticity jumps across the critical layer, the lower Stokes layer and the new shear region that forms near the upper wall in which the upper critical layer has coalesced with the upper Stokes layer. Despite the new scalings, the critical layer dynamics are virtually unchanged from those outlined in Sect. 3, except of course there is only one layer now, located at $y = y_c$ say. The jump across it, analogous to (8), is

$$J_{CL} = [\tau_M]_{y_c-}^{y_c+} = \epsilon \alpha^{-1/2} \sigma A_0^{1/2} |\mu_1/b_1|^{1/2}, \quad (15)$$

where μ_1 is a constant arising from the solution of the Rayleigh problem in the core, and the critical layer separation $b_1 = 2 - V$. In contrast to the previous case considered, it is found that the leading order vorticity jump across the Stokes layer is $o(\epsilon)$ and so this layer plays no role in determining the expression for the amplitude.

We now turn to the upper viscous shear layer. The crucial balance in this layer again arises from considering the sizes of the inertia term $\alpha(U_0 - c)$ and the viscous operator $R^{-1}\partial^2/\partial y^2$, but in contrast to the Stokes layers the quantity $U_0 - c$ is asymptotically small, given that the phasespeed and sliding velocity are related by (13) and hence coincide at leading order. Since $\alpha = O(1)$ in the current setting we therefore conclude that the thickness of this region is $O(\epsilon^{3/2})$. Letting $y = 1 - \epsilon^{3/2}Z_2$, the relevant flow expansions are (with $\lambda_0 = -U'_0(1)$):

$$u = V + \epsilon^{3/2} \lambda_0 Z_2 + \epsilon^2 \widehat{U}(\xi, Z_2) + \epsilon^{5/2} \mathcal{F}(Z_2) + \dots, \quad (16)$$

$$v = \epsilon^{7/2} \widehat{V}(\xi, Z_2) + \dots, \quad p = \epsilon^{7/2} \widehat{P}_2(\xi) + \dots, \quad (17)$$

alongside (13) for c . The resulting linear equations for $(\widehat{U}, \widehat{V}, \widehat{P}_2)$ now contain the influence of the basic flow shear. The leading order balances are

$$\alpha \widehat{U}_\xi + \widehat{V}_{Z_2} = 0, \quad \alpha(\lambda_0 Z_2 - c_1) \widehat{U}_\xi + \lambda_0 \widehat{V} = -\alpha \widehat{P}'_2(\xi) + \widehat{U}_{Z_2 Z_2}, \quad (18)$$

with the boundary conditions of no slip at the wall and matching to the core, so that $\widehat{U} = \widehat{V} = 0$ on $Z_2 = 0$, $\widehat{U} \rightarrow A_0 F_2(1) \cos \xi$ as $Z_2 \rightarrow \infty$. The explicit solution for the pressure is found to be

$$\overline{P}_2 = A_0 \alpha^{-1/3} \lambda_0^{2/3} F_2(1) \mathcal{G}(s), \quad \mathcal{G}(s) = i^{5/3} \text{Ai}'(\Theta)/\kappa(\Theta), \quad (19)$$

where \widehat{P}_2 is the real part of $\overline{P}_2 e^{i\xi}$. Here Ai is the Airy function, $\kappa(\Theta) = \int_\Theta^\infty \text{Ai}(q) dq$ and Θ is given in terms of the streamwise wavenumber, phasespeed correction and basic flow as

$$\Theta = -i^{1/3} s, \quad s = \alpha^{1/3} c_1 / \lambda_0^{2/3}. \quad (20)$$

It can be shown that the derivative of the mean flow distortion undergoes the jump

$$[\mathcal{F}'(Z_2)]_\infty^0 = \alpha A_0 F_2(1) \lambda_0^{-1} \text{Im}(\overline{P}_2)/2. \quad (21)$$

Substituting for \overline{P}_2 from (19) we see that the vorticity jump across the shear layer, J_{SL} , is therefore given by

$$J_{SL} = \epsilon \alpha^{2/3} A_0^2 [F_2(1)]^2 \lambda_0^{-1/3} \text{Im}(\mathcal{G}(s))/2. \quad (22)$$

Again we must ensure that the total jump in vorticity is zero, i.e. $J_{SL} + J_{CL} = 0$, and this leads to an amplitude equation of the form

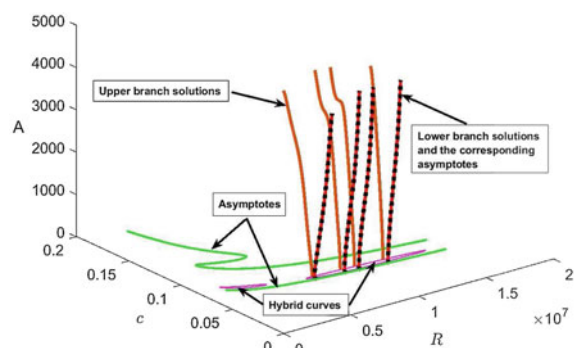
$$A_0^{3/2} = 2\sigma |\mu_1|^{1/2} \lambda_0^{-1/6} \alpha^{-7/6} [F_2(1)]^{-2} [\text{Im}(\mathcal{G}(s))]^{-1}. \quad (23)$$

The quantity $F_2(1)$ can be normalized to unity and then (14) can be solved for a given V to determine the quantities μ_1 and α . The expression (23) allows us to compute the wavespeed correction c_1 as a function of A_0 in view of the dependence of s on c_1 via (20). Sample numerical results are shown in Fig. 3b for $V = 1.3$. Note the existence of a critical amplitude below which no solutions exist. Above this value there are two solution branches with c_1 remaining finite as $A_0 \rightarrow \infty$ on the lower branch. On the upper branch c_1 increases without bound on this scale and in fact in the large amplitude limit we recover the dual critical layer structure investigated in Sect. 3.

5 Navier-Stokes Comparison

We now present some new computations of the Navier-Stokes equations and compare the results with those obtained from our asymptotic theory. For details of the numerical method employed (Chebyshev collocation in y , Fourier series expansion in ξ , together with Newton iteration) the reader is referred to [9]. We explicitly seek travelling wave solutions so that, for example, the normal velocity is expressed as the real part of $\sum_{n=1}^N \tilde{v}_n(y)e^{in\xi}$, with N taken suitably large. Previous numerical work on this flow (e.g. [10]) concentrated on solutions which bifurcate from the main neutral curve. Here we consider solutions which at vanishingly small amplitude lie on the additional neutral curve marked ‘upper curve’ on Fig. 1b. On this curve the phasespeed of the disturbance and the sliding velocity are of similar magnitudes and the asymptotic theory developed in Sect. 4 proves to be relevant in describing finite-amplitude solutions in the vicinity of this curve. In Fig. 4 we plot some Navier-Stokes solution trajectories for $V = 0.025$ at various large Reynolds numbers and the corresponding results from the asymptotic theory. The vertical axis represents a measure of the disturbance amplitude A defined by $A^2 = \sum_{n=1}^N R^2 |\tilde{v}_n|^2$. In the zero amplitude plane we plot the linear neutral curve and its asymptotic approximation. The solid paths projecting upwards out of the plane are the Navier-Stokes solutions emanating from particular positions on the linear neutral curve. For each value of R there are two Navier-Stokes solution trajectories: one bifurcating from the lower branch of the linear neutral curve and the other from the upper branch. The dots show the corresponding asymptotic predictions from the solution of the Rayleigh problem (14) and the amplitude equation (23). We see that there is excellent agreement with the Navier-Stokes solutions emanating from the lower branch. Numerical investigations are ongoing with the aim of also obtaining a comparison with the upper branch solutions.

Fig. 4 The solid lines are Navier-Stokes solutions at fixed Reynolds number that bifurcate from the upper linear neutral curve (denoted ‘hybrid curve’ here). The dots are asymptotic predictions arising from the theory of Sect. 4. The sliding speed is $V = 0.025$



6 Conclusion

We have seen that, by using high Reynolds number asymptotic analysis, it is possible to derive two distinct systems of equations which describe two-dimensional nonlinear travelling waves in plane Poiseuille-Couette flow. It is demonstrated that the solutions to one of these systems, in which the phasespeed and sliding speed are almost equal, is relevant to the bifurcation from a previously undetected linear neutral curve which splits from the main curve as the sliding speed increases. We have shown by comparing with finite Reynolds number Navier-Stokes solutions that the asymptotic theory accurately describes the nonlinear behaviour for a range of disturbance amplitudes. The comparison here was made for a value of V below the linear cut-off V_c , ensuring that a linear neutral curve exists. In future work we hope to use a continuation method to investigate nonlinear solutions for $V > V_c$ where the neutral surface is detached from the zero amplitude plane.

References

1. Kawahara, G., Uhlmann, M., van Veen, L.: The significance of simple invariant solutions in turbulent flows. *Ann. Rev. Fluid Mech.* **44**, 203–225 (2012)
2. Potter, M.C.: Stability of plane Poiseuille-Couette flow. *J. Fluid Mech.* **24**, 609–619 (1966)
3. Cowley, S.J., Smith, F.T.: On the stability of Poiseuille-Couette flow: a bifurcation from infinity. *J. Fluid Mech.* **156**, 83–100 (1985)
4. Dempsey L.J.: Nonlinear exact coherent structures in high Reynolds number shear flows. Ph.D. thesis, Imperial College London (2016)
5. Kumar, R., Walton, A.G.: Amplitude-dependent three-dimensional neutral modes in plane Poiseuille-Couette flow at large Reynolds number. *Q. J. Mech. Appl. Math.* **72**, 87–130 (2019)
6. Benney, D.J., Bergeron, R.F.: A new class of nonlinear waves in parallel flows. *Stud. Appl. Math.* **48**, 181–205 (1969)
7. Smith, F.T., Bodonyi, R.J.: Amplitude-dependent neutral modes in the Hagen-Poiseuille flow through a circular pipe. *Proc. R. Soc. Lond. A* **384**, 463–489 (1982)
8. Kumar, R., Walton, A.G.: Self-sustaining dual critical layer states in plane Poiseuille-Couette flow at large Reynolds number. *Proc R. Soc. Lond. A* **475**, 20180881 (2019)
9. Wong, A.W.H., Walton, A.G.: Axisymmetric travelling waves in annular Couette-Poiseuille flow. *Q. J. Mech. Appl. Math.* **65**, 293–311 (2012)
10. Balakumar, P.: Finite-amplitude equilibrium solutions for plane Poiseuille-Couette flow. *Theoret. Comput. Fluid Dyn.* **9**, 103–119 (1997)

Study of Transition to Turbulence Using Discrete Directed Percolation Model



Kouta Watanabe, Hideki Shiiba, and Yoshio Ishii

Abstract In this study, based on the Reynolds experiment (1883), the linear stabilization analysis, turbulence which are coherent structure or puff structure and Directed Percolation (DP), we have attempted to design and construct discrete DP models, recently, which is similar to Cellular Automaton. It has the characteristics that the variables of discrete DP model are all discrete. Moreover, we have attempted to design Ultradiscrete Burgers equation with Reynolds number. In previous studies, Reynolds number was not considered, for example traffic flow, so we have designed Ultradiscrete Burgers equation and discuss spatial patterns due to differences in initial conditions. The spatial state of traffic flow in previous studies changes depending on the initial density. Finally, we have discussed the effect of Reynolds number which is hold in a completely discrete system. On the transition to turbulent flow using Ultradiscrete Burgers equation model by numerical calculation and analysis.

Keywords Numerical method · Ultradiscretization · Navier-Stokes equations · Burgers equation · Partial differential and difference equation

1 Introduction

It is known that the laminar flow is maintained if the flow velocity is small and it becomes turbulent in the middle of the flow if the flow velocity is high by the Reynolds experiment (1883) [1]. Especially in the intermediate region, it has also been found that laminar flow and turbulence may occur intermittently. Existence of the region in which this turbulent and laminar flow coexist locally continued to be difficult to understand until recently. This is because the laminar flow is stable even at an

K. Watanabe · H. Shiiba
Information Systems Science, SOKA University, 1-236 Tangi-Machi, Hachioji-Shi, Tokyo
192-8577, Japan
e-mail: e19m5222@soka-u.jp

Y. Ishii (✉)
Faculty of Science and Engineering, SOKA University, 1-236 Tangi-Machi, Hachioji-Shi, Tokyo
192-8577, Japan
e-mail: chaos@soka.ac.jp

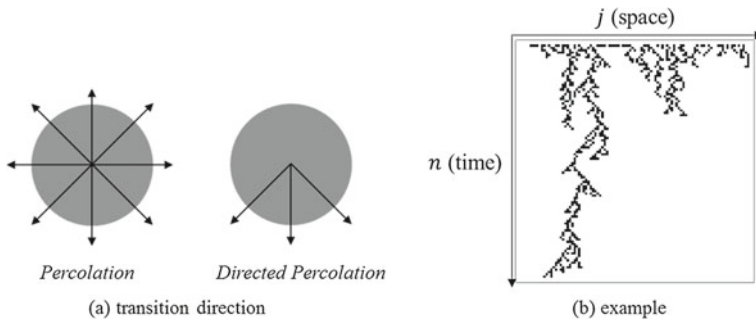


Fig. 1 Directed percolation

infinitely fast flow rate from the linear stabilization analysis [2], and experimentally, the laminar flow is sometimes maintained up to a relatively large flow velocity in some cases. In particular, it is also known that, when artificially disturbance of a nonlinear perturbation in the flow is given, there is a boundary of returning to laminar flow or turbulence. At that boundary, it appears an interesting localized interior structure in turbulence which are coherent structure or puff structure [3]. When this puff disappears, it returns to laminar flow, but recent studies have predicted that transition from laminar to turbulent flow is similar to Directed Percolation (DP) transition [4].

Directed Percolation [5] is percolation with a special direction along which the activity can only propagate one way but not the other, and describes a very generic universality class in the absorbing state phase transition. It is shown to Fig. 1.

In this study, based on these results, we have attempted to design discrete DP models. Representing the DP, recently, there is similar to Cellular Automata which is the most discrete model of which variables are all discrete. And we have attempted to design Ultradiscrete Burgers equation with Reynolds number (for discrete DP model). In previous studies [6], Reynolds number was not considered, for example traffic flow, so we have designed Ultradiscrete Burgers equation and discuss spatial patterns due to differences in initial conditions. The spatial state of traffic flow in previous studies changes depending on the initial density.

Finally, we have discussed the effect of Reynolds number which is hold in a completely discrete system. On the transition to turbulent flow using Ultradiscrete Burgers equation model by numerical calculation and analysis.

2 Navier-Stokes Equations and Burgers Equation

2.1 Navier-Stokes Equations

Navier-Stokes equations of fluid motion [7, 8] is nonlinear and partial differential equation. If the fluid is incompressible, viscosity be considered constant and there is

no external force, equation reduces to the following (1);

$$\frac{\partial \mathbf{u}}{\partial t} + u \frac{\partial \mathbf{u}}{\partial x} + v \frac{\partial \mathbf{u}}{\partial y} + w \frac{\partial \mathbf{u}}{\partial z} = -\frac{1}{\rho} \frac{\partial p}{\partial x} + \frac{1}{Re} \left(\frac{\partial^2 \mathbf{u}}{\partial x^2} + \frac{\partial^2 \mathbf{u}}{\partial y^2} + \frac{\partial^2 \mathbf{u}}{\partial z^2} \right) \quad (1)$$

The first term on the left-hand side is unsteady (if it is no change in time, steady flow, this term becomes zero), the second term is nonlinear, the first term on the right-hand side is pressure gradient and the second term is diffusion term. Nonlinear term on the left-hand side and diffusion term on the right-hand side are important in this equation. Where, u is the velocity of the fluid (m/s), p is the pressure of the fluid, t is time and Re is the Reynold number.

Reynolds number (Re) is an important dimensionless quantity in fluid dynamics. The Reynolds number is the ratio of inertial forces (nonlinear term) to viscous forces (diffusion term). The Reynolds number is defined as below (2),

$$Re = \frac{\rho U L}{\mu} \quad (2)$$

where, ρ is the density of the fluid (SI units: kg/m³), U is the velocity of the fluid with respect to the object (m/s), L is a characteristic linear dimension (m), μ is the dynamic viscosity of the fluid (Pa · s or N · s/m² or kg/m · s) and v is the kinematic viscosity of the fluid (m²/s).

At low Reynolds numbers, viscous forces (diffusion term) are dominant, and is characterized by smooth, constant fluid motion which occurs laminar flow, for example, Poiseuille flow, Stokes flow and so on. At high Reynolds numbers, fluid motion is dominated by inertial forces, which tend to produce chaotic eddies, vortices and other flow instabilities which turbulent flow occurs.

The state of flow (for example, laminar, turbulent and so on) changes according to Reynolds number.

2.2 Burgers Equation

In case of one dimension and there is no pressure gradient, Navier-Stokes Eq. (1) may be reduces to simple equation as below (3):

$$\frac{\partial \mathbf{u}}{\partial t} + u \frac{\partial \mathbf{u}}{\partial x} = \frac{1}{Re} \frac{\partial^2 \mathbf{u}}{\partial x^2} \quad (3)$$

This equation was proposed in 1948 by Burgers [9, 10], as a simple one-dimensional model from fundamental equations of fluid dynamics (Navier-Stokes Eq. (1)) to study turbulence phenomena which is a second order nonlinear partial differential equation. Here, first term in the left hand side of this equation is

represented unsteady, second is nonlinear, and right hand side is represented diffusion.

where, u is the flow velocity which is dependent variable and $\nu = 1/\text{Re}$ is the kinematic viscosity, which represents the stickiness of the fluid. This equation contains the fundamental features of the Navier-Stokes equations. In particular, the nonlinearity and diffusivity (dissipation \sim diffusion of momentum \sim viscosity) are important factors in turbulent flow characteristics.

3 Ultradiscretization

There is a technique to discretize dependent variable of differential equations. Using this technique [11, 12], we can obtain universal mathematical structure among differential equations, difference equations and digital equations called by max-plus equations. Method of transformations are as below (4); using variable transformation including parameter ε ,

$$a + b = c$$

$$a = e^{A/\varepsilon}, b = e^{B/\varepsilon}, c = e^{C/\varepsilon} \quad (4)$$

And taking a limit $\varepsilon \rightarrow +0$, we obtain the following equation (5).

$$C = \lim_{\varepsilon \rightarrow +0} \varepsilon \log \left(e^{A/\varepsilon} + e^{B/\varepsilon} \right) = \max(A, B) \quad (5)$$

Defined by the “max-plus” equation. The operation of obtaining a completely discrete equation as in (5) is called “Ultradiscretization”. As these results, every variable become independent.

Finally, we have described Ultradiscretized nonlinear and dissipation equations, for example, Ultradiscrete Burgers equation. Conventional numerical calculation performs numerical calculation by differentiating time and space variables of differential equations, however, Ultradiscretization system constructs complete differentiation equations of dependent variables. This is a method for systematically generating Cellular Automaton and its solution.

4 Discrete and Ultradiscrete Burgers Equation

4.1 Discrete Burgers Equation

Burgers equation is the second order partial differential equation of the nonlinear dissipative system. This equation can be linearized with Cole-Hopf Transformation. With this solution structure called linearizable, there are performed Ultradiscretization. Using the diffusion equation obtained by converting the Burgers equation into Cole-Hopf Transformation, the difference equation of the diffusion equation is as follows (6);

$$v_j^{n+1} = v_j^n \frac{\frac{1-2k}{\alpha k} + \frac{v_{j+1}^n}{\alpha^2} + \frac{1}{v_j^n}}{\frac{1-2k}{\alpha k} + \frac{v_j^n}{\alpha^2} + \frac{1}{v_{j-1}^n}} \quad (6)$$

where $k = \Delta t / (Re \cdot (\Delta x)^2)$, $\alpha = \Delta t / (Re \cdot \Delta x)$, Δt and Δx are the time and space difference. Here, there are various possibilities for differentiation. A flowchart of how to obtain these equations is shown in Fig. 2. Here, Ultradiscretization is performed using the following transformation (7) and (8);

$$\begin{cases} v_j^n = e^{V_j^n/\varepsilon} \\ \frac{1-2k}{\alpha k} = e^{-M/\varepsilon} \\ \alpha^2 = e^{L/\varepsilon} \end{cases} \quad (7)$$

$$V_n^{t+1} = V_n^t + \varepsilon \log \left(e^{\frac{-M}{\varepsilon}} + e^{\frac{V_{n+1}^t - L}{\varepsilon}} + e^{\frac{-V_n^t}{\varepsilon}} \right) - \varepsilon \log \left(e^{\frac{-M}{\varepsilon}} + e^{\frac{V_n^t - L}{\varepsilon}} + e^{\frac{-V_{n-1}^t}{\varepsilon}} \right) \quad (8)$$

The following equation (9) is obtained from (8);

$$V_j^{n+1} = V_j^n - \min(M, L - V_{j+1}^n, V_j^n) + \min(M, L - V_j^n, V_{j-1}^n) \quad (9)$$

This is an Ultradiscretization of differentiated Burgers equation. Incidentally, if we use $M = L = 1$ in this equation, all V take values of 0 or 1 and become Cellular Automaton of 3 neighborhood binary values. In this way, continuous system of Burgers Eq. (3) and discrete system of Cellular Automaton (9) are related. Continuous Burgers Eq. (3) has a shock wave solution as an analytical exact solution, but finds

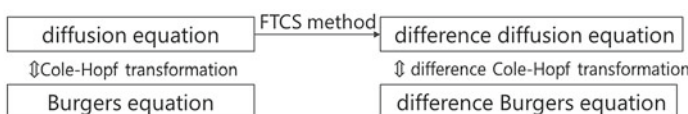


Fig. 2 Discretization procedure

a shock wave solution of a discrete Burgers equation and its Cellular Automaton coincides with an exact solution when an Ultradiscrete limit is taken.

4.2 *Cellular Automaton*

As in the past, approaches with differential equations may diverge the solutions when the equation is nonlinear. To avoid them, there are also Cellular Automaton models that reproduce complex phenomena in various fields. A system in which all independent and dependent variables of continuous differential equations are discretized is known as Cellular Automaton. For the values of three cells at time t , position $n, n - 1, n + 1$, the expression F of time evolution $t + 1$ is defined as follows (10);

$$u_j^{n+1} = F(u_{j-1}^n, u_j^n, u_{j+1}^n) \quad (10)$$

Here, u is a physical quantity (discretized value), and this formula is used to describe phenomena that is spatiotemporally developing such as fluid motion, wave phenomena and so on. It is considered that Cellular Automaton becomes a model of the discrete dynamical system and there is some relation with the continuous system of differential equation.

5 Results and Discussions

Using the numerical system designed and constructed in this studies, some significant results were obtained. We have considered the conventional results and the results obtained in this study and summarized below.

5.1 *Burgers Cellular Automaton*

We discuss the general Burgers Cellular Automaton using traffic flow ($Re = 1$). In the two states, 0 or 1, for Cellular Automaton, we apply general three neighborhoods j to advance time step n , which is update rule 184. When this numerical calculation was promoted, we have been obtained an interesting results.

As shown in Fig. 3, depending on the initial density, less than 50% or greater than 50%, property of shifting left and right. In more detail, Fig. 3a is spatial pattern when the density is less than 50%, and Fig. 3b is the density greater than 50%. The part where black continues is considered as a traffic jam area. In this results, traffic

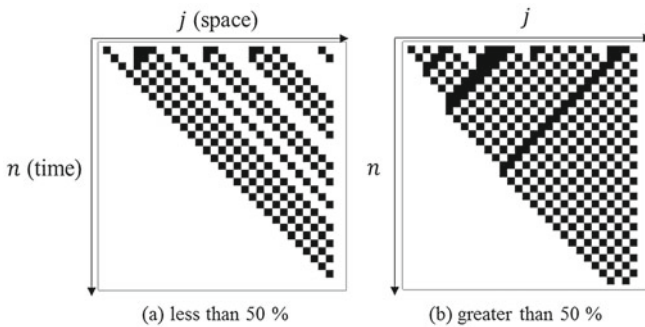


Fig. 3 Burgers Cellular Automaton

jams may or not occur depending on the initial density. It can be observed that the occurrence of a traffic jam area appears remarkably at 50%.

This phenomenon has been known for a long time, bit pattern analysis was used for the proof, the use of ultra-discretization has led to the discovery of a connection with differential difference, which has enabled a more analytical explanation. In this way, the relationship with the Burgers equation for perturbation propagation of traffic jam waves is clearly shown.

The Burgers equation is a model describing a one-dimensional shock wave, and represents a model of traffic jam when 0 is an opened space is 1 as a car. In this study, we have discussed the traffic jam and laminar to turbulence transition by introducing the Reynolds number parameter.

5.2 Effect of Reynolds Number

The results of Reynolds number changed are illustrated in Figs. 4 and 5, and shown in time space diagram from initial condition. Here, the vertical axis represents time

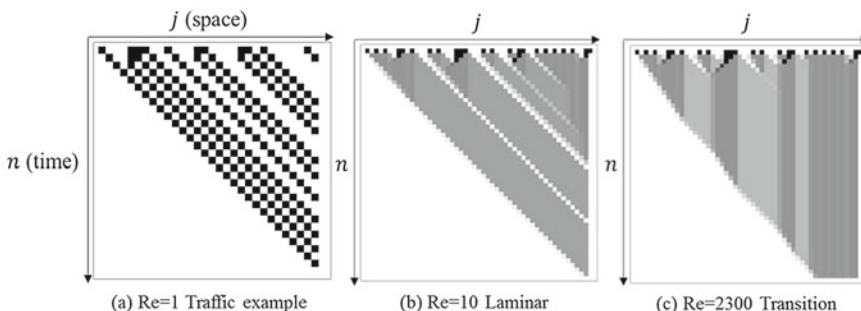


Fig. 4 Time-Space diagram from initial condition (less than 50%)

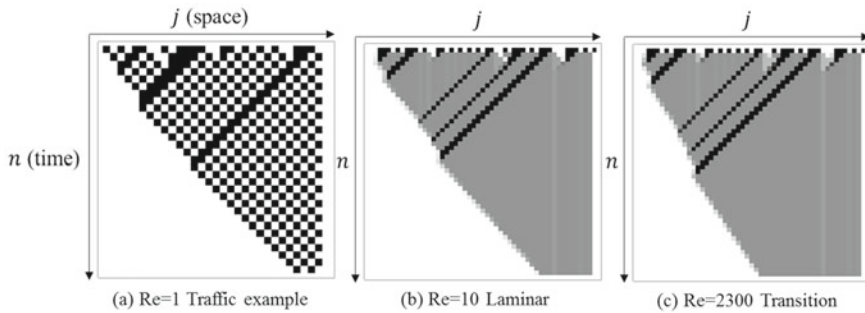


Fig. 5 Time-Space diagram from initial condition (greater than 50%)

, and the horizontal axis represents space one-dimensional . The simulation was performed in consideration of the Reynolds number.

As shown in Fig. 4, there are the same behavior as traffic flow results for cases below 50%. Here, in the case of $Re = 1$, the same thing as the previous result was obtained. When Re number was increased, characteristic results were obtained. Especially, when Reynolds number reaches the level of transition, the areas like traffic jams are observed. On the other hand, if it is high, there is traffic jam in the car, there is traffic jam area. In other words, this is considered as a transition from laminar flow to turbulent flow in terms of fluid dynamics. On the contrary, if it is low, there is no traffic jam area in the car as in the traffic flow, which is considered to be a laminar flow state in terms of fluid dynamics.

As shown in Fig. 5, initial density is greater than 50%. There is a traffic jam and shown similarity about in-viscidity (non-linearity) that is characteristic of the Navier-Stokes equations. If the density is high, increasing the Reynolds number will increase the amount of flow and lengthen the traffic. The effect of Reynolds number could be simulated with a completely discrete model. Comparing these results with (a) (b) (c) in Figs. 4 and 5, the effect of Reynolds number could be simulated with a completely discrete model.

From these results, this study compared the two traffic states of traffic jam, laminar flow and turbulent flow in the case of conventional traffic flow. The beginning of the laminar to turbulent transition has been found to be affected by the Reynolds number even in discrete systems. Furthermore, considering the initial conditions of the disturbance that gives the fluid the difference in the initial conditions, we have concluded that turbulence is likely to occur.

6 Conclusions

In conclusions, we have obtained the following from our studies;

- (1) It is possible to design an Ultradiscrete Burgers equation considered Reynolds number. This procedure has not been done before.
- (2) We have concluded the spatial patterns due to differences in initial conditions. From our results, depending on the density, it has converged to a right shift, left shift pattern, or static pattern.
- (3) we have considered the effect of Reynolds number that this effect was confirmed by Cellular Automaton.

Furthermore, we have considered the following; We have discussed study of the transition between traffic jams and non-traffic jams in the change of the conditions. About Numerical analysis, we will try to discretization and Ultradiscretization using implicit methods for without stability conditions. In addition, we will plan to make the vorticity equation of Ultradiscretization, which is two dimensional flow equation, because there is a vortex structure in turbulent flow.

References

1. Reynolds, O.: Phil. Trans. R. Soc. London **174**, P953 (1883)
2. Drazin, P.G., Reid, W.H.: Hydrodynamic Stability, Cambridge University Press (1981)
3. Hof, B., et al.: Science **305**, p1594 (2004)
4. Stauffer, D., Aharony, A.: Introduction to Percolation Theory. Taylor & Francis Ltd. (1991)
5. Sano, M., Tamai, K.: Nat. Phys. **12**, 249 (2016)
6. Nishinari, K., Takahashi, D.: J. Phys. A **31**, 54 (1998)
7. Navier, C.L.M.H.: Mémoire sur les lois du mouvement des fluides. Mémoires Acad. Roy. Sci. Inst. France **6**, 389–440 (1823)
8. Stokes, G.G.: On the theories of the internal friction of fluids in motion, and of the equilibrium and motion of elastic solids. Trans. Cambridge. Phil. Soc. **8**, 287–319 (1845)
9. Lighthill, M.J.: Viscosity effects in sound waves of finite amplitude. In: Batchelor, G.K., Davies, R.M. (eds.) Surveys in Mechanics, pp. 250–351. Cambridge University Press (1956)
10. Burgers, J.M.: Adv. Appl. Mech. **1**, 171–199 (1948)
11. Takahashi, D., Satsuma, J.: A soliton cellular automaton. J. Phys. Soc. Japan **59**, 3514–3519 (1990)
12. Tokihiro, T., Takahashi, D., Matsukidaira, J., Satsuma, J.: From soliton equations to integrable cellular automata through a limiting procedure. Phys. Rev. Lett. **76**, 3247–3250 (1996)

Nonlinear Evolution of Multiple Helical Modes in the Near-Nozzle Region of Subsonic Circular Jets: A Weakly Nonlinear Critical-Layer Theory



Zhongyu Zhang and Xuesong Wu

Abstract Helical modes in the near-nozzle region of a circular jet are weakly three-dimensional due to their much slower variation in the azimuthal direction than that in the radial and axial directions, and they are thus similar to near-planar oblique waves in planar shear layers discussed by Wu (1993, *J. Fluid Mech.*, vol. 256, pp. 685–715). These modes may enter nonlinear phase as they evolve downstream towards the end of the linearly unstable regime. Different from an axisymmetric, i.e. ring mode, whose evolution should be described by a strongly nonlinear theory, helical modes are governed by a weakly nonlinear one. When the ratio of the shear-layer thickness to the nozzle diameter is small, a nonlinear modulation equation that describes the interactions among an arbitrary finite number of helical modes together with a ring mode is derived by allowing the amplitude to be a function of the azimuthal variable. A significant feature of the modulation equation is that the nonlinear terms are history-dependent and involve derivatives with respect to the azimuthal variable. Moreover, the non-parallelism associated with the axially varying base flow is found to cause a translating-critical-layer effect. Numerical solutions of the modulation equation show that the nonlinear development depends crucially on the composition of initial components of the disturbance and exhibits complicated behaviours, which are broadly consistent with experimental measurements.

Z. Zhang

Department of Mechanics, Tianjin University, Tianjin 300072, P. R. China

e-mail: zyzhang_14@tju.edu.cn

X. Wu (✉)

Department of Mathematics, Imperial College London, 180 Queen's Gate,
London SW7 2AZ, UK

e-mail: x.wu@imperial.ac.uk

1 Introduction

Jets are typical inviscidly unstable flows due to the presence of a generalised inflection point on the base-flow profiles. There are different Rayleigh instability modes, including the axisymmetric ring mode and three-dimensional helical modes, in jets. Starting from the nozzle, the flow contains two different regions with correspondingly distinct dynamical features. A sharp shear layer appears near the nozzle where the exhaust flow starts to mix with the bypass stream. In this region, the three-dimensionality of the disturbances in the shear layer is weak due to the fact that the ratio of the shear-layer thickness to its central position (or the nozzle diameter), which is an index for three-dimensionality, is very small. Helical modes have nearly the same growth rates as that of the ring mode [4, 10] and they may co-exist and interact in this region [2]. As the shear layer spreads out, the inner nearly uniform core flow disappears, leading to a fully developed jet finally. In the course of this, the ring mode as well as helical modes with high azimuthal wavenumbers $\pm m$ would die out while helical modes with smaller m would survive [1]. Different theories are required to describe the dynamics of the disturbances in these regions respectively.

Fluctuations in the near-nozzle region are known to contribute substantial noise [9], and specifically the dynamics of the ring and helical modes has attracted much attention [6]. Earlier, experiments [8, 9] found that helical modes would interact nonlinearly with each other as well as with the ring mode to generate a significant azimuthally dependent mean-flow distortion, which modulates slowly in the axial direction and in general in time as well. According to the theoretical work of [13, 16], the temporal-spatial varying mean-flow distortion may be the main source of low-frequency noise. Furthermore, a first-principle theory for the emission of sound may be developed [15]. For that purpose, it is necessary as a first step to develop a nonlinear theory describing the nonlinear evolution of interacting helical modes.

Mathematically, critical-layer theory offers an appropriate and efficient tool to analyse the nonlinear interactions of near-neutral Rayleigh modes under the high-Reynolds-number assumption. The flow develops a double-layered structure consisting of the main shear layer, where the disturbance is inviscid and linear to the order of approximation, and a critical layer, where the viscous effect smoothes out the singularity in the main-layer solution, and more importantly nonlinear interactions take place. By analysing the disturbances in these two layers and matching the respective solutions, one derives the evolution system; a review of the subject was recently given by [12]. In the present case, all helical modes in the near-nozzle regime including the ring mode share the same critical layer and interact with each other.

The present study is to investigate the nonlinear interactions of an arbitrary number of helical/ring modes. We will derive a nonlinear modulation equation and solve it numerically to predict the ensuing nonlinear dynamics.

2 Asymptotic Theory: Weakly Nonlinear Critical Layer

2.1 Asymptotic Scaling and The Amplitude Equation

This paper focuses on a typical compressible circular jet, which forms between the exhaust flow from the nozzle and a coflow. The velocity and temperature of the former are denoted by U_1^* and T_1^* , while those of the latter by U_2^* and T_2^* . Typically, $U_1^* > U_2^*$; see Fig. 1. In order to describe the development of unstable modes in jets, we introduce the polar coordinates (x, r, θ) with x , r and θ being the coordinates in the axial, radial and azimuthal directions respectively, and the corresponding velocities are denoted by $\mathbf{u} \equiv (u, v, w)$. The reference length and velocity are taken to be a typical shear-layer thickness and $(U_1^* - U_2^*)/2$, respectively. The detail of the non-dimensionalization and the resulting dimensionless parameters, including Re , Ma and Pr , are given in [16].

We shall present a general mathematical formulation for the nonlinear evolution of multiple helical modes on an axisymmetric jet with the mean flow field $(\bar{\mathbf{U}}, \bar{T}, \bar{P}, \bar{\rho})$. The latter is perturbed by small disturbance $(\tilde{\mathbf{u}}, \tilde{T}, \tilde{p}, \tilde{\rho})$ so that the instantaneous field (\mathbf{u}, T, p, ρ) is decomposed as,

$$(\mathbf{u}, T, p, \rho) = (\bar{\mathbf{U}}, \bar{T}, \bar{P}, \bar{\rho}) + \epsilon(\tilde{\mathbf{u}}, \tilde{T}, \tilde{p}, \tilde{\rho}), \quad (1)$$

where $\epsilon \ll 1$ characterizes the initial amplitude of the disturbance.

Our focus will be on the instability in the near-nozzle region, where the thin shear layer is centred at non-dimensional position r_c , and since $r_c \gg 1$ it is rescaled as as $r_c^{-1} = l_\beta R_c^{-1}$ where $R_c = O(1)$ and $l_\beta \ll 1$ is a measure of three-dimensionality, whose distinguished scaling is to be determined.

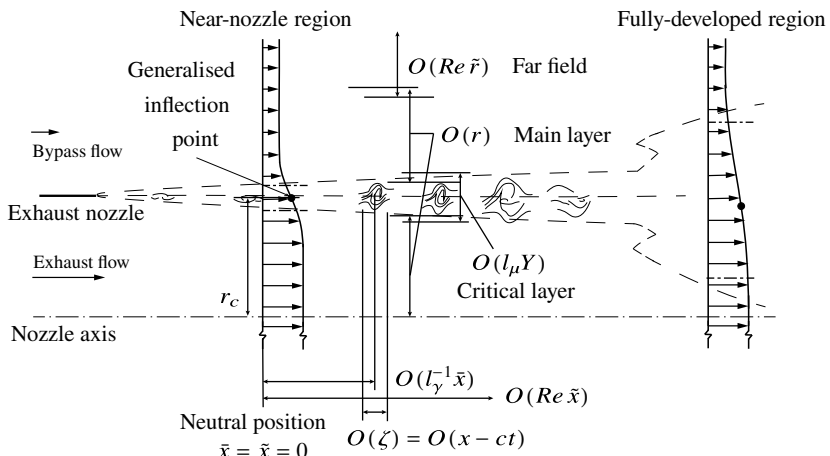


Fig. 1 Sketch of the flow structure and asymptotic scalings, where l_γ and l_μ are scales for temporal-spatial modulation and the critical-layer width respectively, and c is the phase speed of the modes

All ring and helical modes with (nearly) the same frequency but different azimuthal wavenumber $\pm m$ ($m = 0, 1, 2, \dots$) have, to leading-order approximation, the same phase speed, and hence share the same the critical level, which corresponds to the generalised inflection point. In order to analyse the nonlinear interactions among them, we introduce a local transverse variable or an inner variable as $Y = (r - r_c)/l_\mu$ with $l_\mu \ll 1$ characterising the critical-layer thickness, where the centre of the shear layer is taken to be the position of the generalised inflection point without losing generality.

A helical mode with azimuthal wavenumber m is analogous to an oblique mode with m/r_c playing the role of the spanwise wavenumber in the planar case. A disturbance consisting of all helical modes can be considered as a wavetrain modulated slowly in the azimuthal direction. Its amplitude is a function of θ , which plays the role of the slow spanwise variable in the planar case [11].

The wavetrain of nearly neutral modes evolves on a length scale $l_\gamma^{-1} \gg 1$, and it is also modulated slowly in time. As in [16], we introduce the slow axial and time variables, $\tilde{x} = l_\gamma x/c$ and $\tau = l_\gamma t$, with c being the common leading-order phase speed of the modes. The slow temporal and spatial evolutions give rise to the so-called non-equilibrium effect in the critical layer.

In order to identify the distinguished scalings, the nonlinear interactions and modulations of the disturbance are analysed here. The main nonlinear term in the momentum equation is $v\partial_y u$. The leading-order axial velocity of a helical mode exhibits a singularity of simple pole type, and acquires a magnitude $u^{(0)} = O(\epsilon l_\beta^2 l_\mu^{-1})$ in the critical layer. The quadratic interaction produces a forcing of $O(\epsilon^2 l_\beta^2 l_\mu^{-2})$, which drives a mean-flow distortion $u^{(1)} = O(\epsilon^2 l_\beta^2 l_\mu^{-3})$. At the cubic level, the fundamental mode interacts with the mean-flow distortion to regenerate a fundamental component $u^{(2)} = O(\epsilon^3 l_\beta^2 l_\mu^{-5})$. Matching this with the $O(\epsilon l_\gamma)$ solution in the main shear layer gives $\epsilon^3 l_\beta^2 l_\mu^{-5} = O(\epsilon l_\gamma)$. Detailed calculations following the above steps lead to the evolution equation.

The base flow $(\bar{U}, Re^{-1}\bar{V}, \bar{T}, \bar{P})$ depends on the slow axial variable $\tilde{x} = Re^{-1}x$ and the radial coordinate $y = r - r_c$. Its streamwise velocity and temperature in the critical layer near the neutral position $\tilde{x} = 0$, or $\bar{x} = 0$, can be Taylor expanded as,

$$\begin{bmatrix} \bar{U}(\tilde{x}, Y) \\ \bar{T}(\tilde{x}, Y) \end{bmatrix} = \begin{pmatrix} \bar{U}_c \\ \bar{T}_c \end{pmatrix} + \left[l_\mu \begin{pmatrix} \bar{U}'_c \\ \bar{T}'_c \end{pmatrix} Y + l_\gamma \begin{pmatrix} \bar{U}_{1,c} \\ \bar{T}_{1,c} \end{pmatrix} \tilde{x} \right] + \dots, \quad (2)$$

where $(\bar{U}_n, \bar{T}_n) = c^{-1} (\partial_{\tilde{x}^n} \bar{U}, \partial_{\tilde{x}^n} \bar{T})|_{\tilde{x}=0}$.

It is impossible to include the non-equilibrium and non-parallelism effects in the critical layer at the same order since the latter manifests itself over a asymptotically much longer length scale than the former does. However, both may be important factors for evolution in practice. Inspired by [13], it is possible to construct a composite theory by setting $Re^{-1} = O(l_\mu^3) = O(l_\gamma^2)$ and yet retaining the non-equilibrium effect. This brings in the translating-critical-layer effect (cf. [5]). Furthermore, inclusion of the azimuthal dependence requires $l_\beta = O(l_\gamma^2)$. It follows that we should set

$$l_\mu = O(\epsilon^{2/5}), \quad l_\gamma = O(\epsilon^{3/5}), \quad l_\beta = l_\gamma^{1/2} = O(\epsilon^{3/10}). \quad (3)$$

In the main part of the shear layer, the solution for the disturbance, which is a modulated travelling wavetrain, is expressed as

$$\tilde{q}(\tau, \bar{x}, y, \theta, \zeta) = \widehat{A}(\tau, \bar{x}, \theta) \hat{q}_0(y) e^{i\alpha\zeta} + \epsilon^{3/5} \hat{q}_1(y; \tau, \bar{x}, \theta) e^{i\alpha\zeta} \text{c.c.} + \dots, \quad (4)$$

where \tilde{q} stands for any quantity of the perturbation except \tilde{w} , which is proportional to \widehat{A}_θ and smaller by a factor of $O(l_\beta)$, and \widehat{A} is the amplitude function, whose evolution equation is to be derived. The eigenfunction \hat{q}_0 and the eigenvalue α are defined by the eigenvalue problem for the leading-order pressure \hat{p}_0 as

$$\frac{\partial^2 \hat{p}_0}{\partial y^2} + \left(\frac{\bar{T}'}{\bar{T}} - \frac{2\bar{U}'}{\bar{U} - c} \right) \frac{\partial \hat{p}_0}{\partial y} + \alpha^2 \left[\frac{Ma^2(\bar{U} - c)^2}{\bar{T}} - 1 \right] \hat{p}_0 = 0, \quad (5)$$

subject to the homogeneous boundary condition $\hat{p}_0 \rightarrow 0$ as $y \rightarrow \pm\infty$. Obviously, there is a critical level $y = 0$ or $r = r_c$ satisfying $\bar{U}(y = 0) = c$, where the outer expansion (4) ceases to be valid.

The second-order quantities in the outer expansion (4) can be expressed in terms of the pressure \hat{p}_1 , which is governed by an inhomogeneous Rayleigh equation satisfying again homogeneous boundary conditions. A solvability condition is required and can be derived to ensure the existence of \hat{p}_1 .

In the critical layer, the solution is sought via an inner expansion. The axial velocity of the regenerated fundamental component is calculated as described earlier. Matching it with \hat{u}_1 in the outer expansion (4) and making use of the solvability condition, we arrived at the modulation equation,

$$\frac{\partial \widehat{A}}{\partial \bar{x}} + \frac{1}{c_g} \frac{\partial \widehat{A}}{\partial \tau} - \frac{1}{c_h} \frac{\partial^2 \widehat{A}}{\partial \theta^2} = \sigma_s \bar{x} \widehat{A} + \mathcal{J}_{N,\Theta}(\widehat{A}; \tau, \bar{x}, \theta) + \mathcal{J}_{N,T}(\widehat{A}; \tau, \bar{x}, \theta), \quad (6)$$

where the nonlinear terms $\mathcal{J}_{N,\Theta}$, $\mathcal{J}_{N,T}$ are to be given below, and coefficients

$$\left. \begin{aligned} c_g &= \varsigma / \left[\frac{2iJ_2}{\alpha} - \frac{\pi\alpha j}{|\bar{U}'_c| \bar{T}_c} \right] \quad \text{with} \quad \varsigma = \frac{2i}{\alpha} \left(J_2 - \frac{J_1}{c} \right) - \frac{\pi\alpha j}{|\bar{U}'_c| \bar{T}_c}, \\ c_h &= \varsigma R_c^2 / J_h, \quad \sigma_s = [J_0 - \pi i \alpha^2 (\bar{U}_{1,c} - \bar{U}'_{c1}) / (|\bar{U}'_c| \bar{T}_c)] / \varsigma. \end{aligned} \right\} \quad (7)$$

The expressions for J_i ($i = 0, 1, 2$), j and j_1 are given [16], and $J_h = \int_{-\infty}^{\infty} \bar{T} \hat{p}_0^2$

$(\bar{U} - c)^{-2} dy$, which is, similar to J_i , a singular integral and should be interpreted as the Hadamard finite part. Here, c_g is the complex-valued group velocity [14], and σ_s characterizes the axial variation of the base flow. After defining the parameter characterising the drift of the critical level, $\chi = Re^{-1/6} \alpha \bar{U}_{1,c}$, and the scaled viscosity, $\lambda = (\epsilon^{6/5} Re)^{-1} \alpha^2 \bar{U}_c'^2 \bar{T}_c \mu_c$, the nonlinear terms can be written as,

$$\mathcal{J}_{N,\Theta} = -\frac{2\pi\alpha|\bar{U}'_c|Re^{1/3}}{\zeta\bar{T}_cR_c^2} \int_0^\infty \int_0^\infty K_\Theta(Re^{1/2}\lambda, Re^{1/3}\chi; \xi_1, \xi_2) \widehat{\mathcal{A}}_\Theta d\xi_1 d\xi_2, \quad (8)$$

$$\mathcal{J}_{N,T} = \frac{2i\pi\alpha^2\bar{U}'_c\bar{T}'_cRe^{1/3}}{|\bar{U}'_c|\zeta\bar{T}_c^2} \int_0^\infty \int_0^\infty K_T(Re^{1/2}\lambda, Re^{1/3}\chi; \xi_1, \xi_2) \widehat{\mathcal{A}}_N d\xi_1 d\xi_2, \quad (9)$$

in which the products of the amplitude functions are worked out as

$$\begin{aligned} \widehat{\mathcal{A}}_\Theta(\widehat{A}; \xi_1, \xi_2) &= \xi_1 \left[\widehat{A}^{\xi_1} \widehat{A}^{\xi_1 + \xi_2} \widehat{A}_\theta^{*2\xi_1 + \xi_2} \right]_\theta + \xi_1 \widehat{A}^{\xi_1} \widehat{A}^{\xi_1 + \xi_2} \widehat{A}_{\theta\theta}^{*2\xi_1 + \xi_2} \\ &\quad + \xi_2 \widehat{A}^{\xi_1} \left[\widehat{A}^{\xi_1 + \xi_2} \widehat{A}_\theta^{*2\xi_1 + \xi_2} \right]_\theta, \end{aligned} \quad (10)$$

$$\widehat{\mathcal{A}}_N(\widehat{A}; \xi_1, \xi_2) = \widehat{A}^{\xi_1} \widehat{A}^{\xi_1 + \xi_2} \widehat{A}^{*2\xi_1 + \xi_2}, \quad (11)$$

with the notation $\widehat{A}^\xi \equiv \widehat{A}(\tau - \xi, \bar{x} - \xi)$ and the kernels

$$K_\Theta(\lambda, \chi; \xi_1, \xi_2) = \xi_1^2 \exp[-2\lambda\xi_1^3/3 - \lambda\xi_1^2\xi_2 - i\chi(\xi_1^2 + \xi_1\xi_2)], \quad (12)$$

$$\begin{aligned} K_T(\lambda, \chi; \xi_1, \xi_2) &= \left\{ 1 + e^{\lambda(1-1/Pr)\xi_1^2\xi_2} \right. \\ &\quad \left. + \frac{1 - \bar{T}_c\mu'_c/\mu_c}{1 - 1/Pr} \left[e^{-\lambda(1-1/Pr)\xi_1^3/3} - e^{\lambda(1-1/Pr)(\xi_1^3/3 + \xi_1^2\xi_2)} \right] \right\} \\ &\quad \times \xi_1^2 \exp[-\lambda(1+1/Pr)\xi_1^3/3 - \lambda\xi_1^2\xi_2 - i\chi(\xi_1^2 + \xi_1\xi_2)]. \end{aligned} \quad (13)$$

This is a composite theory that contains the non-equilibrium-parallel regime in limit of $\lambda \rightarrow 0$ and the equilibrium-nonparallel regime in the limit of $\lambda \rightarrow \infty$; in the latter the nonlinear term is still non-local due to three-dimensionality, as was observed by [11]. Of the two nonlinear terms, $\mathcal{J}_{N,T}$ is proportional to R_c^{-2} and characterizes the effect of three-dimensionality, while $\mathcal{J}_{N,\Theta}$ is proportional to \bar{T}'_c and is contributed by compressibility.

2.2 Fourier Decomposition and Upstream Condition

For multiple helical modes, \widehat{A} can be decomposed as Fourier series respect to θ as

$$\widehat{A}(\tau, \bar{x}, \theta) = \sum_{m=-\infty}^{\infty} A_m(\tau, \bar{x}) e^{im\theta}, \quad (14)$$

where $m \in \mathbb{Z}$ is the azimuthal wavenumber with $m = 0$ denoting a ring mode and $m = \pm 1, \pm 2, \dots$ representing pairs of helical modes. The helical modes can be regarded as 'sideband' components of the ring mode and the nonlinear interactions are similar to 'sideband resonance'.

When $\bar{x} \rightarrow -\infty$, the amplitude is small that the nonlinear terms can be neglected. The solution of the resulting equation serves as the upstream condition for A_m ,

$$A_m(\tau, \bar{x}) \rightarrow a_m \exp \left[\sigma_s \bar{x}^2 / 2 + \kappa_m \bar{x} - i S_0 \tau \right] \quad \text{as} \quad \bar{x} \rightarrow -\infty, \quad (15)$$

where $\kappa_m = i S_0 / c_g - m^2 / c_h$ with its real part representing the scaled linear growth rate of each helical mode, and S_0 characterising the deviation of the disturbance frequency from that of the neutral mode, i.e. $\omega = \alpha c + \epsilon^{3/5} S_0$. The initial amplitude a_m of each mode may be specified independently. For the special case where the upstream condition is 'symmetric' ($a_{-m} = a_m$), the initial symmetry will be preserved during the evolution, that is, $A_{-m} = A_m$.

3 Numerical Solutions

The modulation equation is derived for a general base-flow profile. The coefficients in the equation will be evaluated for a base flow with the axial velocity

$$\bar{U}(\tilde{x}, y; \eta) = \frac{U_1^* + U_2^*}{U_1^* - U_2^*} - \tanh \eta(\tilde{x}, y) \quad \text{with} \quad \eta = \frac{y - y_0(\tilde{x})}{\delta(\tilde{x})}, \quad (16)$$

where η is a self-similar variable, y_0 and δ represent the centre position and thickness of the shear layer respectively, both being functions of \tilde{x} . The phase speed c of the neutral mode is given by $c = \bar{U}_c = \bar{U}\{\eta[0, y_0(0)]\}$. The mean-temperature profile is given by the Crocco-Busemann relation.

The non-parallelism enters through the variation of the base flow with respect to the slow axial variable \tilde{x} and the transverse drift of the critical level; the former is characterised by \bar{U}_1 and \bar{T}_1 , while the latter by χ . These quantities are all proportional to the growth rate of the shear-layer thickness $\partial_{\tilde{x}}\delta$ via

$$\partial_{\tilde{x}}y_0 = (\bar{U}_-/\bar{T}_-) [\mathcal{C}_0 / (\bar{U}_+ - \bar{U}_-) - \mathcal{C}_h] \partial_{\tilde{x}}\delta, \quad (17)$$

where $\bar{U}_{\pm} = (U_1^* + U_2^*)/(U_1^* - U_2^*) \mp 1$, $\bar{T}_- = 1$, $\bar{T}_+ = T_2^*/T_1^*$, and the mean-flow dependent constants, \mathcal{C}_0 and \mathcal{C}_h , are given in (6.22) and (6.24) of [16] respectively.

The modulation equation can describe the nonlinear interactions and development of an arbitrary finite number of helical modes. In order to focus on the effect of the composition of the seeded modes, we choose the initial amplitudes such that the 'overall amplitude' $\sum_m |a_m|^2 \equiv 1$. Other parameters are: the upstream velocity and temperature ratios $\bar{U}_2^*/\bar{U}_1^* = 1/9$ and $\bar{T}_2^*/\bar{T}_1^* = 7/8$, the exhaust Mach num-

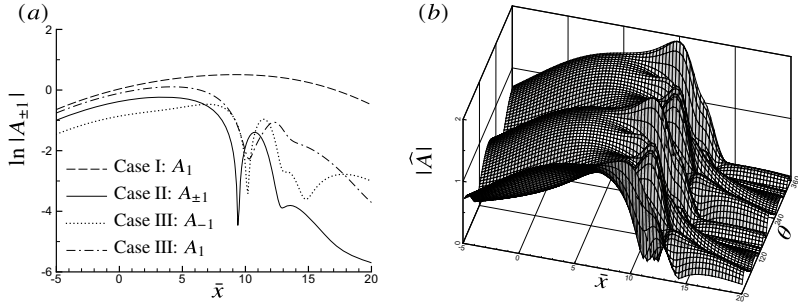


Fig. 2 (a) Amplitude evolution of $m = \pm 1$ modes when a single helical mode $m = 1$ (Case I), a pair of helical modes $m = \pm 1$ with the same initial amplitudes (Case II) and a pair of helical modes $m = \pm 1$ with initial-amplitude ratio $a_1/a_{-1} = 2$ (Case III) was seeded upstream; (b) Amplitude evolution against the axial and azimuthal variables for Case III

ber $Ma_1 = 0.6$, the Prandtl number $Pr = 0.7$, the Reynolds number $Re = 4500$, the dimensionless shear-layer centre position $r_c = 10$, and the spreading rate of the shear-layer thickness $\partial_{\bar{x}}\delta = 0.025$. We take $\epsilon = 0.05$, and S_0 is assigned a value such that the scaled linear growth rate of the ring mode $\kappa_0 = 0.1$.

Figure 2a shows the evolution when only helical modes are seeded upstream. The dashed line shows the case with only $m = 1$ mode seeded (Case I). For a single helical mode, no new mode is excited through nonlinear interactions, and moreover the nonlinear term associated with three-dimensionality vanishes, which is expected since a single oblique mode can be converted to a two-dimensional mode by Square's transformation [7]. The nonlinearity is solely associated with compressibility. The solid line shows the evolution of $m = \pm 1$ modes, both being seeded with equal initial amplitude $a_1 = a_{-1}$ (Case II). Compared with the single mode case, the evolution exhibits a more complex behaviour: after the first saturation following the linear stage, the amplitudes $A_{\pm 1}$ undergo amplification again and then the second saturation before the eventual decay. The nonlinear saturating pattern is broadly consistent with the measurement of [8], and it is due to the interactions between not only the two seeded modes but also among the excited modes ($m = \pm 3, \pm 5, \dots$). The dash-dotted line and the dotted line represent the evolution of A_1 and A_{-1} respectively, when the two modes are seeded together but with different initial amplitudes $a_1 = 2a_{-1}$ (Case III). The two modes interact with each other and evolve through the linear and nonlinear regimes sequentially, and the saturation exhibits a similar character to that in Case II. Modes with higher wavenumbers ($m = \pm 3, \pm 5, \dots$) are excited, and their evolution curves are similar to the dashed line in Case I. Figure 2b shows the overall evolution pattern in the axial and azimuthal directions. The shorter-scale azimuthal variation in the nonlinear stage signals the emergence of the nonlinearly excited modes ($m = \pm 3, \pm 5, \dots$).

Figure 3a shows the case with $m = 1, 2$ modes seeded upstream. In this case, not only the ‘mirror’ modes, $m = -1$ and $m = -2$, but also the ring mode $m = 0$ as well as higher-order helical modes are excited due to the interactions of the seeded

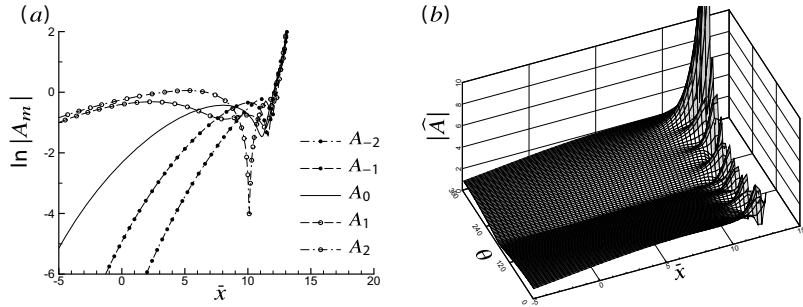


Fig. 3 (a) Amplitude evolution of multiple modes; (b) perspective plot of $|\hat{A}|$ against the axial and azimuthal variables with $m = 1, 2$ modes, $a_1 = a_2$, being seeded upstream

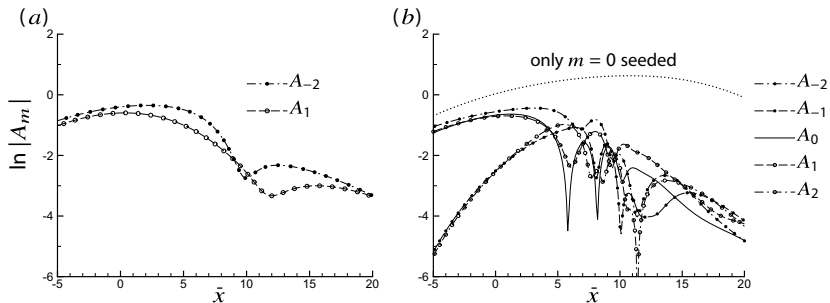


Fig. 4 Amplitude evolution for the cases (a) $m = 1, -2$ modes with $a_{-2} = a_1$, and (b) $m = -2, 0, 1$ modes with $a_{-2} = a_0 = a_1$, being seeded upstream

modes as well as the excited ones. The amplitudes appear to blow up in the form of a finite-distance singularity. The overall evolution is shown in Fig. 3b.

Figure 4a shows the amplitude evolution when $m = 1, -2$ modes are seeded. Interestingly and perhaps surprisingly, the behaviour is drastically different from that shown in Figure 3, despite the fact that only the seeded mode $m = -2$ replaced the $m = 2$ mode, and that the two helical modes with opposite azimuthal wavenumbers have many similar features. In the present case, the ring mode and the ‘mirror’ modes of the seeded ones cannot be excited, and instead higher-order modes, such as $m = -5, 4$, are excited by the nonlinear interactions. A_1 and A_{-2} undergo oscillatory saturation and eventually decay rather than blowing up.

Figure 4b shows the amplitude evolution when the ring mode $m = 0$ is also seeded together with $m = 1, -2$ modes. More modes, including the opposite modes $m = -1, 2$ and higher-order helical ones $m = \pm 3, \pm 4, \dots$, are excited and interact with each other, leading to a complex nonlinear features such as jittering. The dotted line in Fig. 4b shows the case with only $m = 0$ mode being seeded upstream, in which case the nonlinearity is only associated with compressibility. Though nonlinear effect is present, the quantity controlling the nonlinearity, \bar{T}'_c , is very small, and so the

evolution is nearly linear, and the 'saturation' is primarily due to the non-parallelism. It transpires that the present weakly nonlinear theory is inadequate for the ring mode, for which a strongly nonlinear theory is needed.

4 Conclusion

The present paper developed a weakly nonlinear theory which can characterise the interactions among an arbitrary finite number of helical modes together with the ring mode. An integro-differential equation for the disturbance amplitude was derived. This theory allows for spatial-temporal evolution, azimuthal dependence and the nonlinear effects, which are associated with three-dimensionality and compressibility. A composite approximation was adopted to include the effects of non-equilibrium and non-parallelism simultaneously. In this situation, we also found a translating critical-layer effect. Numerical solutions of the modulation equation showed that the nonlinear development depends crucially on the composition of the seeded modes, and exhibits complicated behaviours, which are in broad qualitative agreement with experimental data.

A few topics await for further study. Given that the nonlinearities in different regions of the jet are different, it is necessary to develop a unified or a composite theory in order to cover the present approach, the vary-near-nozzle region (the evolution in which requires a strongly nonlinear theory) and the fully developed region studied by [13]. Furthermore, unstable waves/wavepackets are recognized to be important sound sources, and so it is of interest to explain how wavepackets of helical modes radiate sound based on the first principles [15].

Acknowledgements This work is supported by the National Natural Science Foundation of China (Grant Nos. 91752116, 11472190).

References

1. Batchelor, G.K., Gill, A.: Analysis of instability of axisymmetric jet. *J. Fluid Mech.* **14**, 529–551 (1962)
2. Cohen, J., Wygnanski, I.: The evolution of instabilities in the axisymmetric jet. Part 1. The linear growth of disturbances near the nozzle. *J. Fluid Mech.* **176**, 191–219 (1987a)
3. Cohen, J., Wygnanski, I.: The evolution of instabilities in the axisymmetric jet. Part 2. The flow resulting from the interaction between two waves. *J. Fluid Mech.* **176**, 221–235 (1987b)
4. Churilov, S.M., Shukhman, I.G.: Nonlinear spatial evolution of helical disturbances to an axial jet. *J. Fluid Mech.* **281**, 371–402 (1994)
5. Cowley, S.J.: Pulsatile flow through distorted channels: low-Strouhal-number and translating-critical-layer effects. *Q. J. Mech. App. Math.* **38**(4), 589–619 (1985)
6. Davoust, S., Jacquin, L., Leclaire, B.: Dynamics of $m = 0$ and $m = 1$ modes and of streamwise vortices in a turbulent axisymmetric mixing layer. *J. Fluid Mech.* **709**, 408–444 (2012)
7. Leib, S.J.: Nonlinear evolution of subsonic and supersonic disturbances on a compressible free shear layer. *J. Fluid Mech.* **224**, 551–578 (1991)

8. Long, T.A., Petersen, R.A.: Controlled interactions in a forced axisymmetric jet. Part 1. The distortion of the mean flow. *J. Fluid Mech.* **235**, 37–55 (1992)
9. Narayanan, S., Barber, T.J., Polak, D.: High subsonic jet experiments: turbulence and noise generation studies. *AIAA J.* **40**(3), 430–437 (2002)
10. Strange, P.J.R., Crighton, D.G.: Spinning modes on axisymmetric jets. Part 1. *J. Fluid Mech.* **134**, 231–245 (1983)
11. Wu, X.: Nonlinear temporal-spatial modulation of near-planar Rayleigh waves in shear flows: formation of streamwise vortices. *J. Fluid Mech.* **256**, 685–719 (1993)
12. Wu, X.: Nonlinear theories for shear-flow instabilities: physical insights and practical implications. *Annu. Rev. Fluid Mech.* **51**, 421–485 (2019)
13. Wu, X., Huerre, P.: Low-frequency sound radiated by a nonlinear modulated wavepacket of helical modes on a subsonic circular jet. *J. Fluid Mech.* **637**, 173–211 (2009)
14. Wu, X., Tian, F.: Spectral broadening and flow randomization in free shear layers. *J. Fluid Mech.* **706**, 431–469 (2012)
15. Wu, X., Zhang, Z.: First-principle description of acoustic radiation of shear flows. *Phil. Trans. R. Soc. Lond. A.* **377**, 20190077 (2019)
16. Zhang, Z., Wu, X.: Nonlinear evolution and acoustic radiation of coherent structures in subsonic turbulent free shear layers. *J. Fluid Mech.* **884**, A10 (2020)

Experiments

Investigation of Distributed Roughness Element System Based on Dielectric Barrier Discharge for the Suppression of Stationary Cross-Flow Vortices on the Swept Wing



Sergey Baranov, Ivan Moralev, Dmitry Sboev, Stepan Tolkachev, and Maxim Ustinov

Abstract The distributed roughness element (DRE) conception based on dielectric barrier discharge (DBD) for the laminarization boundary layer of the swept wing was investigated. “Killer” mode was successfully excited and suppressed the development of the most unstable mode (“target” mode). But the DBD also excited travelling modes of crossflow instability, so the laminar-turbulent transition moved upstream.

Keywords Swept wing · Laminarization · Laminar-turbulent transition · Dielectric barrier discharge · Distributed roughness element · Stationary crossflow vortices · Crossflow instability

1 Introduction

Nowadays the laminarization is one of the advanced techniques for air drag reduction of airplane. On the most of modern planes swept wing are widely used, on which the cross-flow instability together with secondary instability mechanism cause the laminar-turbulent transition on the leading edge. There are several laminarization techniques, directed on suppression of these mechanisms: boundary layer suction; suppression of the most unstable modes using distributed roughness elements (DRE),

S. Baranov · D. Sboev · S. Tolkachev (✉) · M. Ustinov
Central Aerohydrodynamic Institute, Zhukovsky, Russia
e-mail: tolkachevst@gmail.com

S. Baranov
e-mail: baranov_sa@bk.ru

D. Sboev
e-mail: t124@inbox.ru

M. Ustinov
e-mail: ustinov@tsagi.ru

I. Moralev
Institute for High Temperatures RAS, Moscow, Russia
e-mail: morler@mail.ru

which was proposed by Saric [1, 2]; suppression of cross flow by dielectric barrier discharge (DBD) [3, 4]; riblets [5]. Each of them has pros and cons. The attractive sides of DBD for using on airplane are: comparatively simple integration to wing construction; could be used as a part of electrical ice-protection system; good controllability and quick response on control action.

The basis of laminarization technique, which was proposed Saric, is excitation of stationary mode (“killer”) by set of roughness elements, which grows fast on the leading edge, but decrease downstream, thus not lead to the transition. Modified structure of boundary layer become more stable to other stationary modes (“target” mode), so the laminar turbulent transition goes downstream in comparison to the surface without DRE. The extension of this idea is using of dielectric barrier discharge for creation of “killer” mode.

The use of DBD for exciting the “killer” mode requires significantly lower power in comparison to the method of suppressing the cross flow [3, 4], since the area of influence is smaller. In addition, it becomes possible to flexibly and quickly control the discharge parameters, which affects the amplitude of the introduced stationary vortices. Potentially, an actuator with a tunable step between the discharges can be developed, which allows one to choose the optimal discharge parameters for a wide range of flight conditions. Including, it is possible to control travelling modes of crossflow instability.

This work is dedicated to the application of DBD excitation of “killer” mode and its influence on the process of laminar-turbulent transition.

2 Experimental Setup

The study of the flow control by DBD was carried out in the test Sect. ($1000 \times 1000 \times 4000$ mm) of the low turbulent wind tunnel T-124 of Central Aerohydrodynamic Institute (TsAGI).

3D boundary layer was organized on a swept flat plate with curvilinear upper and side walls, imitating pressure gradient present on a swept wing (Fig. 1). The model with sweep angle 35° , 998 mm span, 2100 mm chord, 20 mm thickness was made of

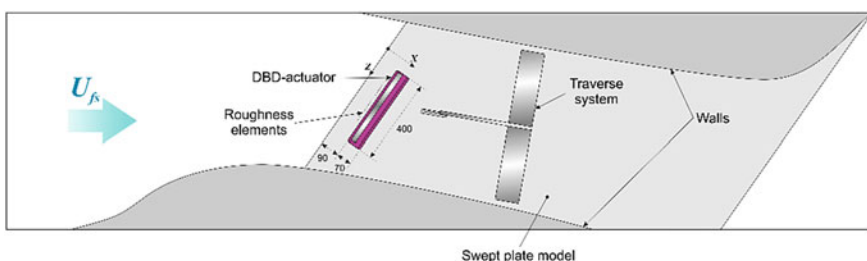


Fig. 1 Scheme of experiment

plexiglas. Leading edge of the model is ellipse shaped with a semi-major axis 80 mm. X distance is normal to the leading edge and counted from it. The curvilinear shape of the upper wall of the test section provides flow acceleration at the forward part of the plate till the distance 1000 mm from the leading edge. Its contour was chosen in order to provide almost linear growth of normal to leading edge velocity component with chordwise coordinate within the domain of measurements. The shape of side walls of test section repeats the form of near-plate streamlines of the flow in the virtual infinite-span channel formed by the plate and upper curvilinear wall. This experimental configuration was developed taking into account a preliminary analysis using the linear stability theory [6].

The freestream velocity in the experiment was chosen $U_{fs} = 30$ m/s. The freestream level of turbulence was 0.12%.

The investigation of the boundary layer structure was carried out by single wire constant temperature anemometry using the traverse system, which provides the accuracy of movement $\pm 3 \mu\text{m}$ in Y , Z directions. The accuracy of X -direction is ± 0.1 mm. To minimize drag of traverse system it was positioned to provide 10° between X -direction and longitudinal direction of traverse system X' . So, the coordinates of traverse system (X' , Y' , Z') were recalculated to the system coordinate of the model (X , Y , Z).

DBD actuator (Fig. 2), designed to create separate localized groups of microdischarges with a total span 390 mm was placed parallel to the leading edge 110 mm from it. According to preliminary calculation of boundary layer stability the pitch of microdischarge groups was chosen 5 mm on position $X = 125$ mm to create “killer” mode. Actuator was powered by sinusoidal voltage with amplitude of 2.5 kV and frequency 65 kHz. The selected frequency matches to the decaying travelling modes of crossflow instability.

To excite the “target” mode with a wavelength of 7.62 mm the set of cylindrical roughness elements $20 \mu\text{m} \times 1$ mm made of aluminium foil was placed on the leading edge at position $X = 75$ mm.

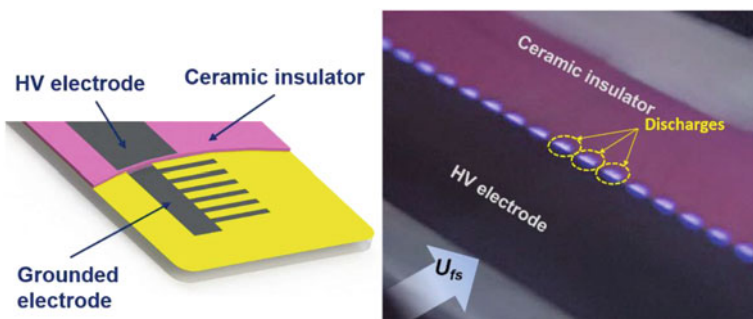


Fig. 2 The structure of DBD actuator (left picture); the view of DBD actuator at working state placed on the model (right picture)

3 Results

The wing model has 2 lines of 8 pressure taps. Typical distribution of pressure coefficient over the model for wide interval of freestream velocity presented on the Fig. 3. Accelerated flow is implemented and it creates favourable conditions for cross-flow instability on our swept plate model.

Using the pressure distribution Ustinov M. calculated the boundary layer structure and its stability properties relative to the stationary modes of cross-flow instability for the freestream velocity $U_{fs} = 25$ m/s. N-factors for the boundary layer are in Fig. 4. Basing on these results the wavelength 5 mm for “killer” mode was chosen—it has suitable growth rate near the leading edge up to $X = 200$ mm. For “target” mode the wavelength 7.62 mm was chosen – it should dominate after $X = 400$ mm and lead to transition.

Transversal distribution of stationary disturbance distribution in $X = 398$ mm is presented on Fig. 5. At the natural case the dominant mode has the wavelength $\lambda = 7.36$ mm, which was determined from spatial Fourier transform. The difference from the roughness step 7.62 mm seems to be caused by angle between stationary disturbance trajectory and longitudinal direction of traverse system. Activation of DBD-actuator lead to the appearance of $\lambda = 4.9$ mm mode. The positions of maximum velocity pulsations in this case are near the positions of inflection point of transversal velocity distribution, but it has only one maximum on one wavelength of stationary mode. Generally, the activation of DBD leads to the increase of velocity pulsations.

Fig. 3 The distribution of pressure coefficient on the model

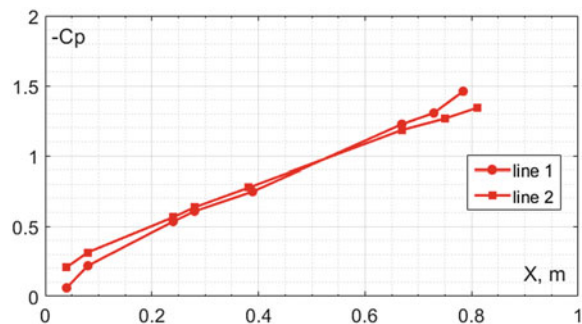


Fig. 4 N-factors of stationary cross-flow modes, calculated for the boundary layer on the model

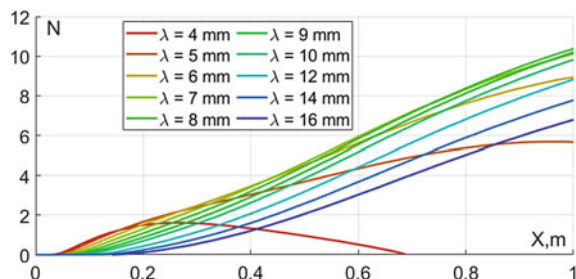
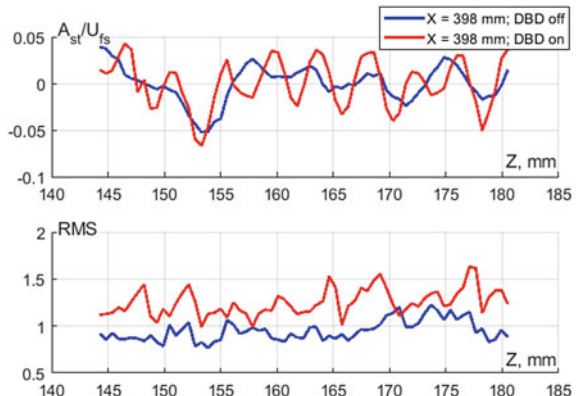


Fig. 5 Transversal distribution of stationary velocity disturbance (top figure); root mean squared of velocity pulsations (bottom figure)



The velocity pulsations spectra in the positions of maximum and minimum RMS are presented in Fig. 6. It is evidently, that DBD excites the disturbances in wide frequency interval up to 1 kHz in the same way whether in the position of maximum velocity pulsations or in minimum.

On the Fig. 7 the distribution of stationary disturbance in cases with and without DBD in $X = 512$ mm. The set of roughness elements excites periodical stationary disturbances with specific to cross-flow instability modes slope (right picture). The switching-on of DBD-actuator lead to the complication of flow pattern. The short-wave stationary disturbances (“killer” mode) overlap on the “target” mode (left picture).

Simultaneous development of the “killer” and “target” modes was studied in the region $X = 400$ – 650 mm. It was shown that a “killer” mode with an amplitude

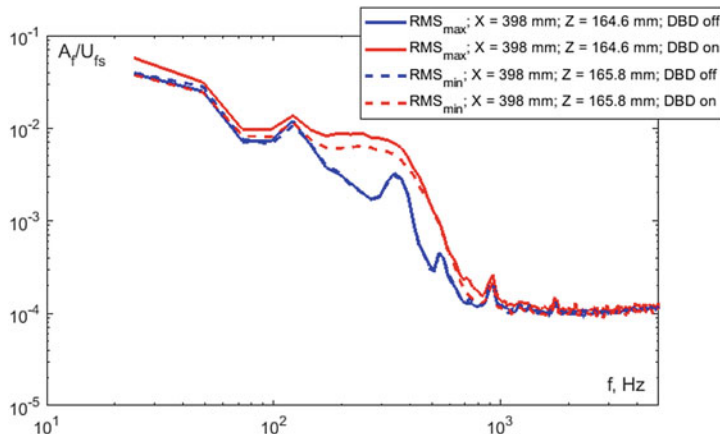


Fig. 6 Velocity pulsations spectra in positions of maximum (solid lines) and minimum (dashed lines) pulsations

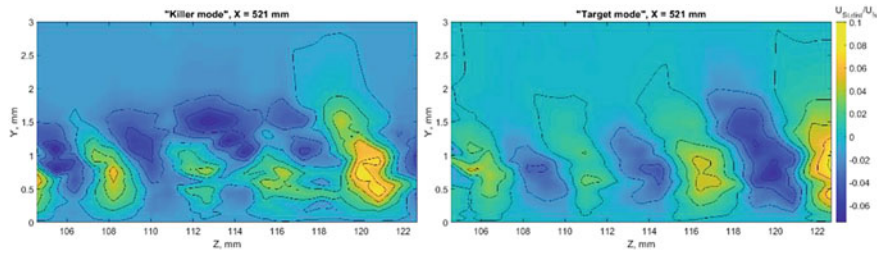


Fig. 7 The stationary velocity disturbance distribution in the cross-section of boundary layer for the excited by DBD case (left); excited only by set of roughness elements without DBD (right)

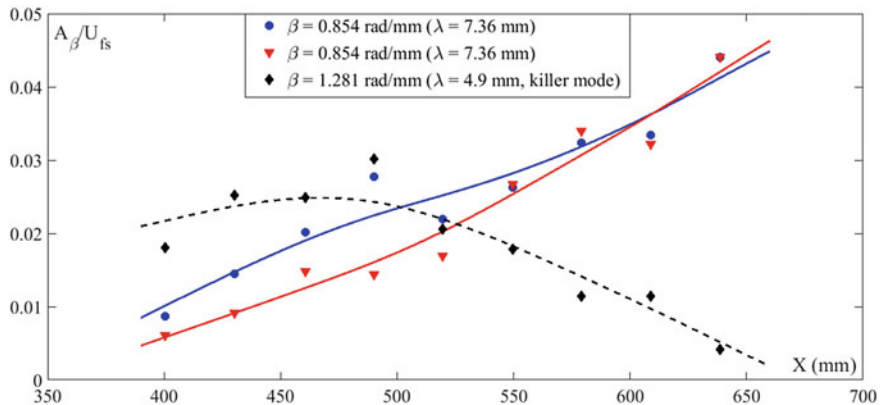


Fig. 8 The development of amplitude of stationary modes (“target” mode and “killer” mode) along the flow

more than 1% suppresses the development of “target” mode in the region $X = 400\text{--}550$ mm. Downstream from this region the amplitude of “target” mode for regime with DBD is nearly equals to the natural regime without DBD (Fig. 8).

Analysis of development of velocity pulsations spectra along the flow shows destabilizing effect of DBD on the flow (Fig. 9) in wide frequency band and it accelerates the laminar-turbulent transition.

The impact force of DRE-conception rises with the voltage supplied to the DBD-actuator (Fig. 10)—it leads to the increase of amplitude of “killer” mode and more intensive suppression of “target” mode.

However, the negative side of DBD reveals more distinctly—the non-stationary disturbances excite with an increase of voltage supplied to the actuator (Fig. 11).

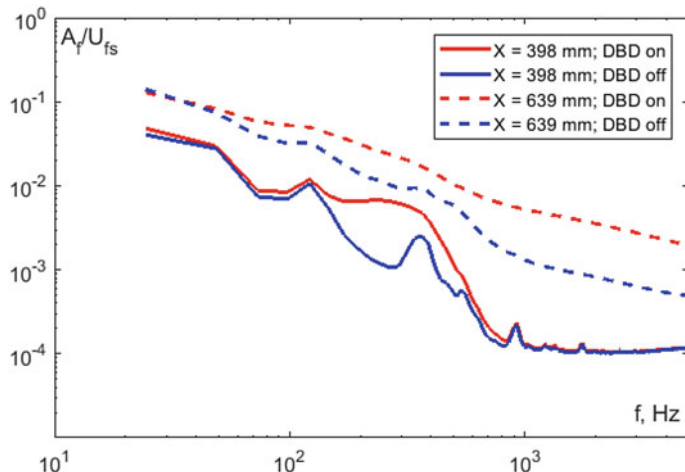


Fig. 9 Velocity pulsations spectra in positions $X = 398$ mm (solid lines) and $X = 639$ mm (dashed lines)

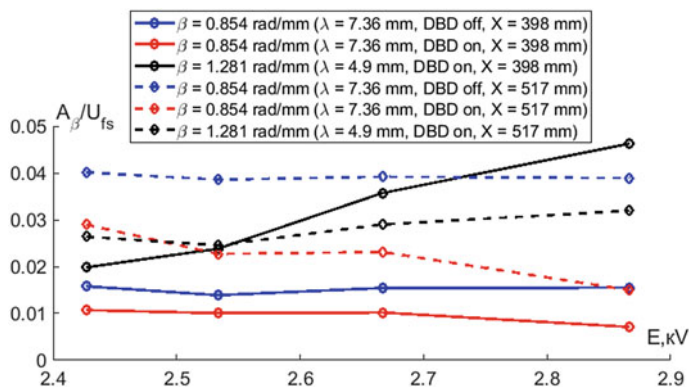
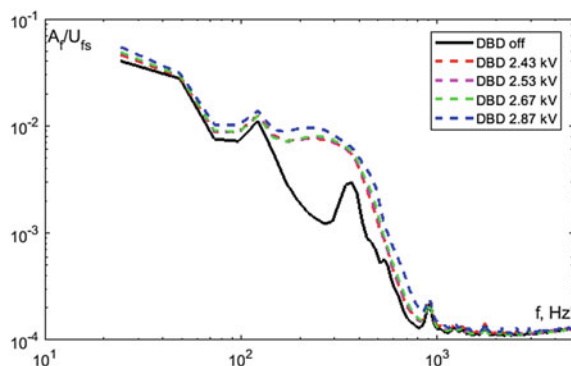


Fig. 10 The effect of voltage supplied to the actuator on the amplitude of “target” (blue—natural case; red—excited by DBD case) and “killer” (black) modes

4 Conclusion

Experiments in low-turbulent wind tunnel showed the possibility of excitation of “killer” mode by DBD-actuator. Generally, the conception of Saric’s laminarization technique works—the suppression effect of “killer” mode on the development of “target” mode was demonstrated. But variable physical nature of discharge leads to the powerful excitation of travelling modes of crossflow instability in wide frequency bandwidth—so this impact on the flow accelerates the laminar-turbulent transition. Similar results were obtained in [7].

Fig. 11 The effect of voltage supplied to the actuator on the velocity pulsations spectra



On the other hand, there are some possibilities for optimization of DBD construction: more accurate choice of “killer” mode wavelength, change of discharge area over each electrode. They could help to achieve better results in laminarization.

References

1. Saric, W., Carrillo, Jr., R., Reibert, M.: Leading-edge roughness as a transition control mechanism. In: 36th AIAA Aerospace Sciences Meeting and Exhibit. American Institute of Aeronautics and Astronautics, Reston, Virginia (1998)
2. White, E.B., Saric, W.S.: Application of variable leading-edge roughness for transition control on swept wings. In: 38th Aerospace Sciences Meeting and Exhibit (2000)
3. Chernyshev, S.L., Kuryachii, A.P., Manuilovich, S.V., Rusyanov, D.A., Skvortsov, V.V.: Attenuation of cross-flow-type instability in compressible boundary layer by means of plasma actuators. In: 51st AIAA Aerosp. Sci. Meet. Incl. New Horizons Forum Aerosp. Expo. (2013)
4. Yadala, S., Hehner, M.T., Serpieri, J., Benard, N., Dörr, P.C., Kloker, M.J., Kotsonis, M.: Experimental control of swept-wing transition through base-flow modification by plasma actuators (2018)
5. Grek, G.R., Kozlov, V.V., Titarenko, S.V., Klingmann, B.G.B.: The influence of riblets on a boundary layer with embedded streamwise vortices. Phys. Fluids (1995). <https://doi.org/10.1063/1.868694>
6. Ustinov, M.V., Kuriachii, A.P., Manuilovich, S.V.: Expected boundary layer characteristics and linear stability results for TsAGI T-124 experiment. BUTERFLI Deliverable 3.5, Feb. (2015)
7. Serpieri, J., Yadala Venkata, S., Kotsonis, M.: Conditioning of cross-flow instability modes using dielectric barrier discharge plasma actuators. J. Fluid Mech. (2017). <https://doi.org/10.1017/jfm.2017.707>

Bump-Induced Transition in Compressible High Reynolds Number Flow: Experimental Results and Correlation with Linear Stability Analysis



Marco Costantini · Stefan Hein · Steffen Risius · Stefan Koch ·
and Christian Klein

Abstract The effect of surface bumps on boundary-layer transition was systematically studied in this joint experimental and numerical work in combination with the influence of variations in streamwise (global) pressure gradient, freestream Mach number (up to 0.77) and chord Reynolds number (up to $10 \cdot 10^6$). The experiments were conducted in a (quasi-) two-dimensional flow in the Cryogenic Ludwieg-Tube Göttingen. Quasi-two-dimensional bumps, with a sinusoidal shape in the streamwise direction, fixed length and three different heights, were installed on a two-dimensional flat-plate model. The model was equipped with temperature-sensitive paint and pressure taps for the measurement of surface temperature and pressure distributions, respectively, which also served as inputs for laminar boundary-layer computations. The linear instability characteristics of the boundary layer were analyzed by both compressible local stability theory and parabolized stability equations. For the case of the small bump, over which the boundary layer did not undergo separation, the N-factors of Tollmien-Schlichting waves from local stability theory were also correlated with the experimental transition locations. This enabled to study the dependency of the transition N-factor on Mach number, Reynolds number and global pressure gradient in the presence of the bump.

1 Introduction

Drag reduction on aircraft surfaces with zero to moderate sweep angles can be achieved by means of Natural Laminar Flow (NLF) technology, as reported for example in Holmes and Obara [10], Wagner et al. [20] and Hansen [8]. However, NLF aircraft components can be affected by surface imperfections such as steps, gaps, bumps, waviness, incorrectly installed flush rivets, etc., the imperfections can induce the amplification of existing (or potentially existing) disturbances within the

M. Costantini · S. Hein · S. Risius · S. Koch · C. Klein
German Aerospace Center (DLR), Bunsenstrasse 10, 37073 Göttingen, Germany
e-mail: marco.costantini@dlr.de

laminar boundary layer and/or the generation of additional instabilities, thus leading to premature transition to turbulence (see Holmes and Obara [10] and (Masad and Iyer [12], among others). The present work focuses on surface bumps. As discussed in Wagner [20] and Hansen [8], bumps can occur at or between structural joints, ribs, and stringers, and also in the region of flush rivets. The effect of bumps (and waviness) on transition has been studied since the earlier experimental investigations reported in Fage [6] and Carmichael [2], which provided criteria for the determination of the “critical” imperfection size leading to premature transition. More recent numerical studies Masad and Iyer [12], Perraud et al. [14] and Franco et al. [7], among others) focused on the effect of bumps on the boundary-layer stability in terms of amplification of Tollmien-Schlichting (TS) waves. However, the influence of a variation in the global pressure gradient on boundary-layer stability and transition has not been systematically studied in previous research on surface bumps. This systematic investigation was carried out in this work, where boundary-layer stability and transition in the presence of surface bumps was examined for various streamwise pressure gradients in a compressible flow at high Reynolds numbers. The present work is based on and extends the experimental study presented in Costantini et al. [5] by a joint experimental and numerical effort. The effect of sinusoidal bumps on the stability and transition of the boundary layer developing over a flat-plate configuration was studied at freestream Mach numbers from 0.35 to 0.77, chord Reynolds numbers up to $10 \cdot 10^6$ and various streamwise pressure gradients relevant for NLF surfaces. The measurements were performed in a (quasi-) two-dimensional flow in the Cryogenic Ludwieg-Tube Göttingen by means of a Temperature-Sensitive Paint (TSP) and of pressure taps. As compared to the results presented in Costantini et al. [5], the experimental data were here further analyzed to provide the inputs for laminar boundary-layer computations. The obtained velocity and temperature profiles were examined according to compressible, linear stability theory, in order to determine the amplification factors (N-factors) of TS waves. Both the local approach (LST) and the Parabolized Stability Equations (PSE) were considered. The N-factor distributions calculated by means of LST were then correlated with the transition locations measured in the experiments, thus providing the transition N-factors for the examined range of test conditions.

2 Experimental and Numerical Setup

2.1 Experimental Setup

The experimental investigations were performed in the low-turbulence (momentum fluctuation level $Tu_{pu} \sim 0.06\%$ —see Koch [11]) Cryogenic Ludwieg-Tube Göttingen (DNW-KRG) on the *BuLASTra* two-dimensional flat plate, which is shown in Fig. 1a. Details on the DNW-KRG wind tunnel and its instrumentation are given in Rosemann [16], Koch [11] and Costantini et al. [4]. The *BuLASTra* model was designed for an

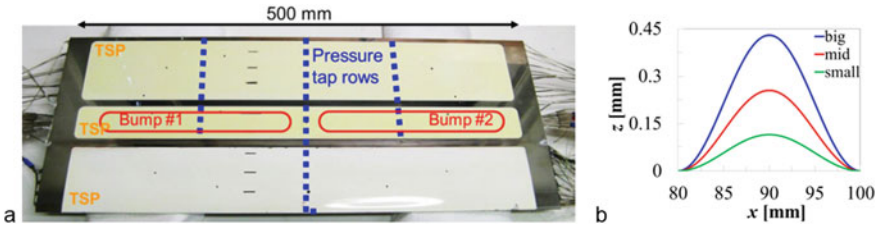


Fig. 1 **a** top view and instrumentation of the *BuLASTra* model with the leading edge at the bottom of the image (Costantini et al. [5]), **b** nominal contour of the examined bumps

essentially uniform global pressure gradient on the model upper side, which represented the surface of major interest in this work and on which exchangeable inserts can be installed. Surface bumps were manufactured on the inserts and had a sinusoidal shape in the streamwise direction x , given by the equation $z(\xi) = h/2 (\cos(2\pi\xi/a) + 1)$ for $-a/2 \leq \xi \leq a/2$. In this equation, a is the streamwise extent of the bumps, h the height of the bump crest, z the wall-normal coordinate and $\xi = x - x_b$ the streamwise coordinate relative to the bump crest location x_b . The streamwise extent of the bumps was $a = 20$ mm, i.e., 10% of the model chord $c = 200$ mm. The nominal contour of the examined bumps is shown in Fig. 1b. Start, crest and end of the bumps were located at $x/c = 40\%$, 45% and 50% , respectively. Three bumps with different height $h = 0.115$ mm (small bump), 0.255 mm (mid bump) and 0.430 mm (big bump) were examined. They were manufactured on two different inserts: the mid bump was manufactured on the port half of one insert, which starboard half was left clean (i.e., bump-free); the small and big bumps were manufactured on the port and starboard halves of the other insert, respectively. The bumps were essentially two-dimensional: as sketched in Fig. 1a, their spanwise extent was ten times larger than their streamwise extent, and their height was quasi-uniform in the spanwise direction (standard deviation within $\Delta h = \pm 0.005$ mm). Small steps and gaps were observed at the three junctions between the model parts, but their size was below the critical size which would have induced premature transition (see Costantini et al. [5]). As shown in Fig. 1a, the *BuLASTra* model was equipped with TSP for the global, non-intrusive measurement of the surface temperature distribution, thus enabling the detection of the laminar-turbulent transition (see, e.g., Tropea et al. [19] and Costantini [3]). Moreover, the model was instrumented with three rows of pressure taps to measure the surface pressure distribution. Details on the *BuLASTra* model, on the experimental setup and on the data processing are presented in Costantini et al. [5]. The current experimental setup enabled to decouple the effects on boundary-layer stability and transition of changes in Mach number, chord Reynolds number, streamwise pressure gradient and bump height.

2.2 Numerical Setup

The surface temperature and pressure distributions, measured via TSP and pressure taps, respectively, were used to conduct compressible boundary-layer calculations by means of the laminar boundary-layer solver COCO (Schrauf [17]). The other inputs for the boundary-layer computations on the model upper side were the freestream Mach number, the chord Reynolds number and the freestream static temperature. For the boundary-layer computations, the model surface was taken as an isothermal wall, with a representative value for the wall temperature chosen from the measured surface temperature distribution in the laminar flow region. Grid convergence was checked for both the laminar boundary layer and in the subsequent N-factor computations, for which two different stability-analysis tools were used: LILO (Schrauf [18]) and NOLOT (Hein et al. [9]). The N-factors of TS waves were calculated with both tools according to compressible, linear, local stability theory. Since the Mach number at the boundary-layer edge remained subsonic at all examined test conditions, only two-dimensional TS waves were considered. Moreover, the NOLOT code was also used to perform stability analyses based on compressible linear parabolized stability equations, which additionally take into account some effects neglected in LST, such as the growth of the boundary layer and the upstream history of the boundary-layer instability. As usual, surface curvature effects were neglected in all LST computations, whereas they were taken into account in the PSE computations based on the contour of the reference model setup, i.e., neglecting the minor changes in surface curvature due to the presence of the bumps. It should be noted here that the growth rate of two-dimensional TS waves in two-dimensional boundary layers is known to be quite insensitive to surface curvature effects anyway. Moreover, in the present setup most of the TS-disturbance growth occurs in regions where the model surface is represented by a flat plate. The N-factor data from the PSE computations discussed in the following were computed based on the total kinetic energy (see, e.g., Hein et al. [9]). When required due to the small step size in downstream direction, the stabilization technique of Andersson et al. [1] was applied to keep the PSE marching procedure numerically stable.

It should be emphasized here that the present approach is applicable only for cases without separation. As discussed in Costantini et al. [5], the laminar boundary layer was found to separate on the downstream side of the big bump; boundary-layer separation occurred very likely also on the downstream side of the mid bump, whereas separated flow regions were not seen in the small-bump cases examined in the experiments. Therefore, the numerical study and the correlation of the numerical results with the experimental data focused on the clean and small-bump configurations. Even for the small-bump cases, the laminar boundary-layer computations often stopped converging, indicating incipient boundary-layer separation due to a locally too strong bump-induced pressure rise. In these cases, however, even a slightly weaker local pressure gradient at this critical downstream position was sufficient to pass over this critical point. The local pressure gradient in the boundary-layer computations to some extent depends on the pre-processing details of the pressure tap data from the

experiment, e.g., the spline-type used. Therefore, a feature implemented in COCO that allows passing over such critical points by locally slightly modifying the local pressure gradient was activated, if necessary. Consequently, in the numerical analysis of the small-bump configuration always an attached boundary layer was considered.

3 Results

The investigations were performed at freestream Mach numbers from $M = U_\infty/a_\infty = 0.35$ to 0.77 and chord Reynolds numbers from $Re = U_\infty c/v_\infty = 3.5$ to $10 \cdot 10^6$, where U_∞ , a_∞ and v_∞ are the velocity, the speed of sound and the kinematic viscosity of the freestream, respectively. The Hartree parameter β_H of the self-similar solution of the boundary-layer equations (Falkner-Skan equation) was selected as the characteristic parameter for the global pressure distribution, as suggested, e.g., in Meyer and Kleiser [13]. As discussed in Costantini et al. [5], the experimental value of β_H was determined in the same manner as that presented in Costantini et al. [4] and Costantini [3], i.e., for the clean surface. The examined range of Hartree parameters was $-0.012 \leq \beta_H \leq 0.117$. Note here that, by virtue of the working principle of the DNW-KRG Ludwig-tube facility (see Koch [11] and Costantini et al. [4]), the ratio between surface and adiabatic-wall temperatures T_w/T_{aw} was larger than 1 in the experiments. For this reason, it was crucial to perform the boundary-layer computations with a non-adiabatic surface, as described in Sect. 2.2.

The experimental results have been already presented and discussed in detail in Costantini et al. [5]. Therefore, only the most relevant information is reported here. The effect of the surface bumps on boundary-layer transition is exemplarily presented in Fig. 2 in combination with the influence of a variation in the global pressure gradient. In this figure, TSP results obtained at $M = 0.77$, $Re = 6 \cdot 10^6$

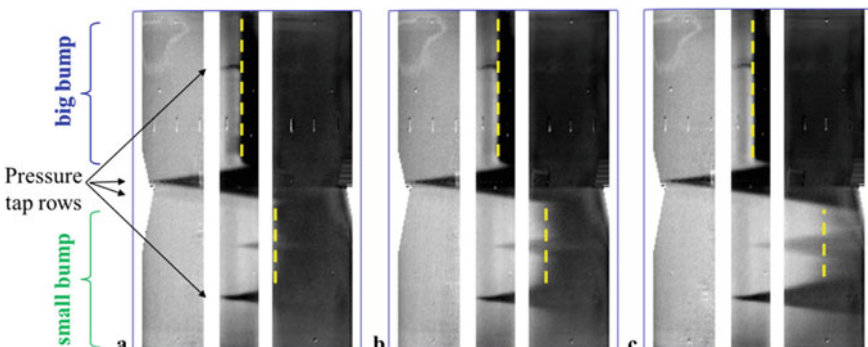
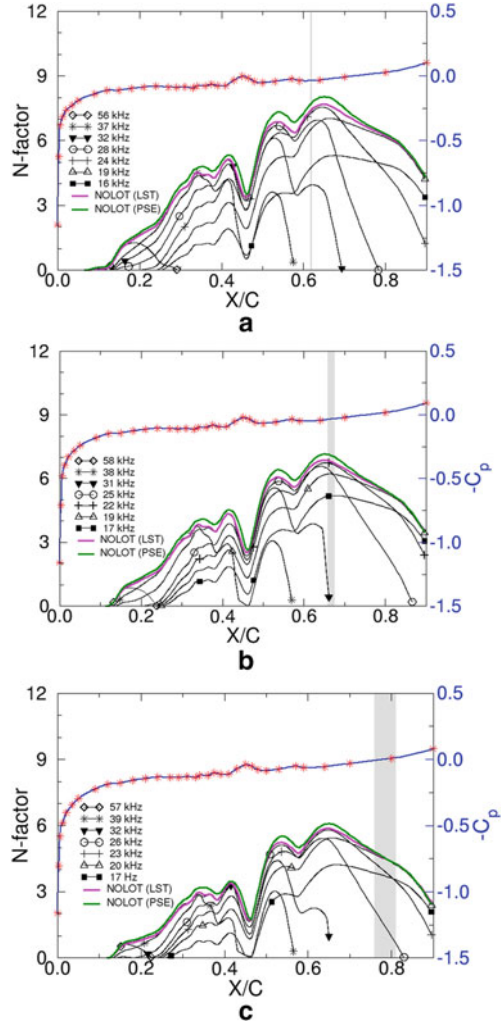


Fig. 2 TSP results for different global pressure gradients β_H obtained with the small ($h/a = 0.006$) and big ($h/a = 0.021$) bumps at $M = 0.77$ and $Re = 6 \cdot 10^6$. **a:** $\beta_H = 0.063$ ($x_T/c = 61.9 \pm 0.2\%$ vs. $x_T/c = 47.7 \pm 0.5\%$); **b:** $\beta_H = 0.076$ ($x_T/c = 66.7 \pm 0.9\%$ vs. $x_T/c = 48.4 \pm 0.1\%$); **c:** $\beta_H = 0.096$ ($x_T/c = 78.5 \pm 2.6\%$ vs. $x_T/c = 48.7 \pm 0.2\%$)

and three different global pressure gradients are shown for the model configuration with the small and big bumps. The flow is from the left; bright and dark regions correspond to areas of low and high wall heat flux, respectively, which is related to low and high wall shear stress. The detected locations of boundary-layer transition are indicated by yellow dashed lines. It should be noted here that boundary-layer transition was detected in the same manner as in Costantini et al. [5], i.e., at the location corresponding to the maximal temperature gradient, but in the current work the reported transition locations x_T/c were obtained as the averages of the values detected for a larger set of evaluation sections (10 for each bump configuration, instead of 5 as in Costantini et al. [5]). The evaluation sections were in regions sufficiently distant from the turbulent wedges arising from the pressure taps and from surface contamination (occurring during wind tunnel operation). As can be seen in Fig. 2, in spite of the turbulent wedges, natural transition was clearly shown to occur at a more upstream location for a higher bump. This finding was confirmed for the three examined global pressure gradients. In the presence of the small bump ($h/a = 0.006$), an increase in β_H (i.e., a more pronounced global flow acceleration) led to a significant shift of boundary-layer transition into a more downstream location: from $x_T/c = 61.9 \pm 0.2\%$ at $\beta_H = 0.063$ to $x_T/c = 78.5 \pm 2.6\%$ at $\beta_H = 0.096$. In contrast, a variation of the global pressure gradient was found to have no appreciable influence on boundary-layer transition in the presence of the big bump ($h/a = 0.021$); this was very likely due to the occurrence of transition over a laminar separation bubble induced by the marked adverse pressure gradient on the downstream side of the big bump, which was not affected significantly by a change in the global pressure gradient (see Costantini et al. [5]).

Example results of the numerical investigations are shown in Fig. 3, where the results of the linear stability analysis for the small-bump cases of Fig. 2 are presented. N-factor results computed with LILO for two-dimensional TS waves with selected frequencies relevant for the N-factor envelope are shown in Fig. 3 by black lines with different symbols, whereas only the overall envelope curve of the individual N-factor distributions computed using NOLOT is shown by a magenta line. The measured surface pressure distributions are shown by red symbols, while the interpolated pressure distributions used for the simulations are shown by blue lines. The vertical gray bars indicate the transition locations measured in the experiments with the related measurement uncertainty. As can be seen in Fig. 3, the LST-based N-factors computed by means of LILO and NOLOT were in good agreement. According to the expectations, the bump-induced pressure gradients had a strong influence on the N-factor evolution in the bump region. Moreover, more pronounced global flow acceleration (larger β_H) led to a reduction of the global positive gradient of the N-factor envelope curve in the region upstream of $x/c \sim 65\%$. Downstream of this location, the additional flow acceleration due to the adopted model cross-section (see Costantini et al. [4]) led to a negative slope of the N-factor envelope curve. At $\beta_H = 0.096$, transition was measured in this latter region, in contrast to the behavior expected according to the e^N methodology. It should be noted here that the uncertainty in the measured transition location was significantly larger in this case, as compared to the cases at $\beta_H = 0.063$ and 0.076; this behavior was observed also for other cases

Fig. 3 Results of linear stability analysis for the cases with the small-bump configuration ($h/a = 0.006$) presented in Fig. 2. N-factors of TS waves at $\beta_H = 0.063$ (a), $\beta_H = 0.076$ (b) and $\beta_H = 0.096$ (c). The vertical gray bars indicate the measured transition locations. The corresponding surface pressure distributions are also shown



where transition was found considerably downstream of the location corresponding to the maximal N-factor $x_{N\max}$, i.e., in the region with negative N-factor envelope slope. In order to evaluate the importance on the N-factor distributions of some of the effects neglected by LST (see Sect. 2.2), PSE computations were conducted via NOLOT; the resulting N-factor envelope curves are shown in Fig. 3 as green lines. As expected for two-dimensional TS waves in a two-dimensional boundary layer, the consideration of the boundary-layer growth and of the upstream history of the boundary-layer instability did not lead to major changes in the evolution of the N-factors. As compared to the N-factor envelope curves obtained via LST, a small ΔN was observed in the region at approx. $30\% < x/c < 75\%$. The aforementioned effects, included in the PSE-based computations, were thus not the major reason

for the disagreement between the expectations from linear stability theory and the experimental observations.

The results of the linear, local stability analysis were correlated with the transition locations determined in the experiments. Since the N-factors obtained via LILO and NOLOT were in good agreement, only the N-factors computed using LILO are considered for the correlation. The transition N-factors N_T obtained for the small-bump configuration are presented in Fig. 4 as a function of the Hartree parameter. Figure 4a, b and c correspond to the results obtained at the Mach numbers $M = 0.35, 0.50$ and 0.77 , respectively. Symbols with different colors correspond to data at different chord Reynolds numbers. The data points enclosed by circles indicate N-factors determined in regions considerably more downstream of $x_{N_{\max}}$, such as in the case presented in Fig. 3c. The experimental data were obtained in two different wind-tunnel entries, indicated by (I) and (II) in the figure legends. The corresponding transition N-factors were generally in agreement, except for cases where $x_T > x_{N_{\max}}$. The average transition location was found to be not well reproducible in these cases, thus leading to the observed variation in the N-factors. (However, as discussed above, the measurement uncertainty was also larger in these cases.) The solid horizontal

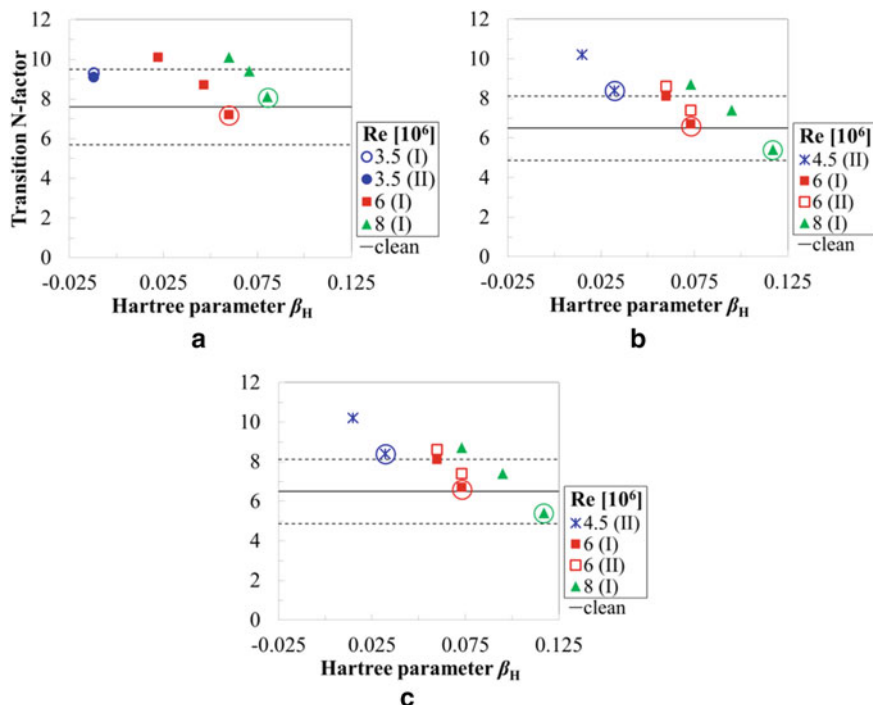


Fig. 4 Transition N-factors N_T obtained at $M = 0.35$ (a), 0.50 (b) and 0.77 (c) via linear stability computations. Data from different wind-tunnel entries are indicated by (I) and (II). Symbols enclosed by circles indicate data points where the transition location in experiment cannot be explained by an N-factor based transition prediction approach

lines in Fig. 4 indicate average transition N-factors $N_{T,0}$ for the clean configurations; these values of $N_{T,0}$ were taken from Costantini [3], since the bump-free surface had been investigated more extensively in that work with a less complex model configuration, and the results obtained with the two different model configurations were verified to be in agreement in Costantini et al. [5]. Dashed horizontal lines indicate a band of approximately $\pm 25\%$ about the corresponding average values of $N_{T,0}$, which was shown to be representative for the scatter of $N_{T,0}$ with the clean configuration (see Costantini et al. [4] and Costantini [3]). Interestingly, if the data points enclosed by the circles are excluded from the analysis, the present results for the small-bump configurations are generally around the upper bound of the data range reported for the clean configuration. Moreover, a variation in the chord Reynolds number appears to have no significant influence on the transition N-factors—at least for the considered range of parameters and with the available amount of data. At fixed Mach and Reynolds numbers, an increase in the Hartree parameter seems to lead to a reduction of N_T in some of the considered cases. It should be also noted here that the transition N-factors were generally lower at larger Mach numbers for both clean and small-bump configurations. Similarly to the cases discussed in Costantini [3] and Risius et al. [15] for the clean configuration, this effect was likely due to the increased level of external disturbances in DNW-KRG with increasing Mach number (see also Koch [11]), which is expected to lead to a decrease of N_T at larger Mach numbers also for the small-bump configuration.

4 Conclusions

The influence of sinusoidal bumps on the stability and transition of the (quasi-) two-dimensional boundary layer developing over a flat plate was systematically studied in this joint experimental and numerical work, focusing on the effect of variations in the streamwise (global) pressure gradient at freestream Mach numbers from 0.35 to 0.77 and chord Reynolds numbers from 3.5 to $10 \cdot 10^6$. Experimental and numerical results were generally in line with the expectations. In the experiments, boundary-layer transition—measured via temperature-sensitive paint—was shown to occur at a more upstream location with increasing bump height. Transition induced by the small bump was found to be dependent on streamwise pressure gradient, freestream Mach number and chord Reynolds number. In the case of higher bumps, however, the influence of the aforementioned parameters on bump-induced transition was significantly reduced. The results of compressible, linear stability analysis showed a weakening of the amplification of Tollmien-Schlichting waves with more pronounced global flow acceleration, and a marked effect of the bump-induced pressure gradients on the N-factors in the bump region. The N-factors computed with two different stability-analysis tools (LILO and NOLOT) according to local theory were shown to be in agreement. The results of the LST-based analysis were also correlated with the transition locations measured in the experiments. The transition N-factors for the small-bump configuration were generally found to be independent of the chord

Reynolds number, whereas they generally decreased at larger Mach numbers. These trends were in line with those observed for the clean configuration. In particular, the decrease of the transition N-factor observed at larger Mach numbers was likely related to the increased level of external disturbances in the wind tunnel with increasing Mach number. In some cases, the transition location in the experiments was found in a region downstream of the location corresponding to the maximal N-factor, where the streamwise gradient of the N-factor envelope curve was negative. In particular, this situation was observed as the global flow acceleration became more pronounced, while Mach and Reynolds numbers were kept fixed. The results of additional PSE-based stability computations showed that the boundary-layer growth and the upstream history of the boundary-layer instability were not the major reason for this behavior. Therefore, the observed transition locations could not be explained within an N-factor based transition prediction approach. A possible explanation for the observed behavior may be the increasing relative extent, with respect to the distance between model leading edge and transition location, of the non-linear phase of disturbance amplification, which was not covered by the used numerical tools. Further investigations are planned in future work to prove this conjecture and provide an explanation for the aforementioned behavior.

Acknowledgements The authors are grateful to the German Federal Ministry for Economic Affairs and Energy for the financial support to this work, which was conducted within the German Federal Aeronautical Research Programme LuFo V-1 “Low Drag Aircraft in Operation” [grant number 20A1302B]. Moreover, the authors would like to thank: C. Fuchs (DLR) for the accurate treatment of the TSP surface and for the constant support during the modifications of the model configuration; U. Gerhard (formerly DLR) for the support to the design of the wind-tunnel model; V. Ondrus (University of Hohenheim, now FH Münster) for the chemical development and synthesis of the used temperature-sensitive paint; U. Henne (DLR) for the support to the TSP data acquisition; L. Koop (DLR), H. Rosemann (formerly DLR), S. Schaber (Airbus, compound project partner in LuFo V-1) and W. Kühn (formerly Airbus) for the assistance to the LuFo V-1 Research Programme activities; and R. Kahle, M. Aschoff, A. Grimme (DNW) as well as S. Hucke (formerly DNW) for the support during the measurement campaign at DNW-KRG.

References

1. Andersson, P., et al.: On a stabilization procedure for the parabolic stability equations. *J. Eng. Math.* **33**(3), 311–332 (1998)
2. Carmichael, B.H.: Surface waviness criteria for swept and unswept laminar suction wings. Northrop Aircraft, Inc., Rep. NOR-59-438 (BLC-123) (1959)
3. Costantini, M. (2016) Experimental analysis of geometric, pressure gradient and surface temperature effects on boundary-layer transition in compressible high Reynolds number flows. PhD Thesis, RWTH Aachen
4. Costantini, M., et al.: Pressure gradient and non-adiabatic surface effects on boundary-layer transition. *AIAA J.* **54**(11), 3465–3480 (2016)
5. Costantini, M., et al.: Experimental study of bump effects on boundary-layer transition in compressible high Reynolds number flow. *Exp. Therm. Fluid Sci.* **106**, 234–256 (2019)
6. Fage, A. The smallest size of a spanwise surface corrugation which affects boundary-layer transition on an aerofoil. *ARC R&M 2120* (1943)

7. Franco, J.A. et al.: Effect of humps and indentations on boundary-layer transition of compressible flows using the AHLNS methodology. Proc. 6th ECCM – 7th ECFD, Paper 1821 (2018)
8. Hansen, H.: Laminar flow technology – the Airbus view. Proc. 27th ICAS: 453–461 (2010)
9. Hein, S., et al.: Linear nonlocal stability analysis – the linear NOLOT code. DLR-IB 223–94, A56 (1994)
10. Holmes, B.J., Obara, C.J.: Observations and implications of natural laminar flow on practical airplane surfaces. *J. Aircraft* **20**(12), 993–1006 (1983)
11. Koch, S.: Zeitliche und räumliche Turbulenzentwicklung in einem Rohrwindkanal und deren Einfluss auf die Transition an Profilmödellen. DLR FB 2004–19 (2004)
12. Masad, J.A., Iyer, V.: Transition prediction and control in subsonic flow over a hump. NASA CR 4543 (1993)
13. Meyer, F., Kleiser, L.: Numerical investigation of transition in 3D boundary layers. AGARD CP-438: 16–1 to 16–17 (1989)
14. Perraud, J., et al.: Laminar-turbulent transition on aerodynamic surfaces with imperfections. RTO-AVT-111: 14–1 to 14–14 (2004)
15. Risius, S., et al.: Unit Reynolds number, Mach number and pressure gradient effects on laminar-turbulent transition in two-dimensional boundary layers. *Exp. Fluids* **59**, 86 (2018)
16. Rosemann, H.: The cryogenic Ludwieg-tube tunnel at Göttingen. AGARD R-812: 8–1 to 8–13 (1997)
17. Schrauf, G.: COCO—A program to compute velocity and temperature profiles for local and nonlocal stability analysis of compressible, conical boundary layers with suction, ZARM technik report (1998)
18. Schrauf, G.: LILO 2.1—User's guide and tutorial. GSSC TR 6 (2006)
19. Tropea, C., et al.: Springer Handbook of Experimental Fluid Mechanics. Springer-Verlag, Berlin Heidelberg. Chap. 7.4: Transition-Detection by Temperature-Sensitive Paint (2007)
20. Wagner, R.D., et al.: Laminar flow—the past, present, and prospects. AIAA Paper 89–989 (1989)

Experimental Analysis of the Effect of Suction and Step Height on Boundary-Layer Transition



Benjamin Dimond, Marco Costantini, and Christian Klein

Abstract Laminar flow is challenging to maintain in the presence of surface imperfections such as steps and/or gaps, which can occur at structural joints. A substantial stream-wise delay of laminar-turbulent transition, however, can be achieved with boundary-layer suction. This work examines the delay of transition that can be obtained with slit suction. Imperfections such as forward-facing steps and backward-facing steps in combination with stream-wise gaps are studied. Systematic experimental investigations were performed in the low-turbulence Cryogenic Ludwieg-Tube Göttingen for large Reynolds numbers (chord Reynolds numbers up to $Re_c = 16 \cdot 10^6$), Mach numbers $0.35 \leq M \leq 0.77$ and various streamwise pressure gradients. Suction proves to delay transition significantly and even over-compensates the adverse effect of surface imperfections. With suction, transition locations for backward-facing steps were measured even further downstream than for similar sized forward-facing steps.

1 Introduction

Reducing fuel consumption on modern transport aircraft is becoming more and more important to limit the environmental impact of an ever growing industry. Laminar flow technology proves a promising way forward as it can significantly reduce wall shear stress and therefore fuel consumption. According to reference [16], almost 50% of all aerodynamic drag on conventional aircraft arises from friction of which a large part originates from the wings. Extending the regions of laminar boundary-layers, as opposed to turbulent boundary-layers predominant on most conventional wings, tails and nacelles, can yield a high possible saving. The benefits of suction for laminar

B. Dimond (✉) · M. Costantini · C. Klein
German Aerospace Center (DLR), Bunsenstrasse, 10 37073 Göttingen, Germany
e-mail: benjamin.dimond@dlr.de

M. Costantini
e-mail: marco.costantini@dlr.de

C. Klein
e-mail: christian.klein@dlr.de

flow has long been known and studied. Early studies date back to the 1940s to 1960s mainly investigating slit suction [3, 12]. More recent studies focus on suction through perforated panels as this enables a more uniform suction, thought to be more effective as described in [2, 9, 10]. Maintaining laminarity over surface imperfections such as steps and/or gaps proves to be especially challenging. Surface imperfections alone have been subject to many investigations. The goal of these investigations is mainly to identify critical design parameters, important for manufacturing tolerances [1]. The influence of suction in the presence of steps and gaps on boundary-layer transition however, has to our knowledge only been investigated in two groups of studies.

For low Mach numbers ($M < 0.1$), backward-facing steps upstream of suction slits have been investigated as stated in ref. [8].

More recently, numerical studies have been conducted where the effect of suction trough a gap directly upstream of a forward-facing step was investigated at $M = 0.6$. Both studies however only focus on limited parameter ranges. This study examines both forward- and backward-facing steps and two gap widths for Mach numbers from 0.35 to 0.77, chord Reynolds numbers ranging from $Re_c = 3.5 - 16 \cdot 10^6$ and various favourable and unfavourable streamwise pressure gradients. It is found, that backward-facing steps in combination with suction extends laminar regions further than similarly dimensioned forward-facing steps.

2 Experimental Setup

Figure 1 sketches the 2D wind tunnel model used for this investigation. In addition to its original design with front and main part and chord length $c = 200\text{ mm}$, an additional aft part was installed to reduce disturbances on the upper side of the model, thus extending the chord length to 240 mm. More details on the effect of this aft part can be found in ref. [15]. To be able to simply compare obtained results with those of previous measurements, the chord length will be stated as $c = 200\text{ mm}$ throughout this work, which is also the main area of focus in this work. The two-dimensional model with width $b = 500\text{ mm}$ is designed to maintain a large area of uniform streamwise pressure gradient on the upper side of the model. This surface of interest is coated with temperature-sensitive paint (TSP) for accurate, spatially resolved transition detection. Optical setup and paint composition is the same as in ref. [5].

The mid-span region of the model was equipped with pressure taps to obtain a stream-wise pressure distribution of the model. This enabled the calculation of a dimensionless pressure gradient parameter. For this work, the Hartree parameter β_H [14] was chosen and obtained from the pressure distribution between $x/c = 0.05$ and $x/c = 0.9$. A detailed description of the determination of this parameter is given in ref. [6].

Front and main part of the model were displaced by shims with varying thicknesses to retrieve well defined, sharp forward- and backward-facing steps at $x/c = 0.35$. Additional alignment pins enabled to displace the steps in spanwise direction by

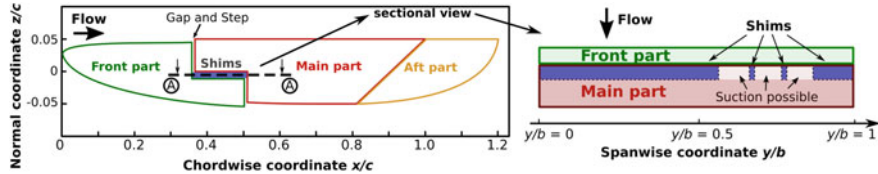


Fig. 1 Simplified sketch of the wind tunnel model (chord length $c = 200$ mm, width $b = 500$ mm). Shims enable a step and gap configuration at $x/c = 0.35$ with well defined dimensions. Left: side view of the whole model cross-section (axes not to scale). Right: sectional view in the A-A plane looking from the top. Shim sizes are in proportion, dimensions of gap and step are enlarged for better visibility

$d_{gap} = 200 \mu\text{m}$ and $d_{gap} = 100 \mu\text{m}$. The region directly upstream and downstream of the step and gap was not coated with TSP to ensure sharp edges. This results in a spanwise strip, where no TSP information can be obtained.

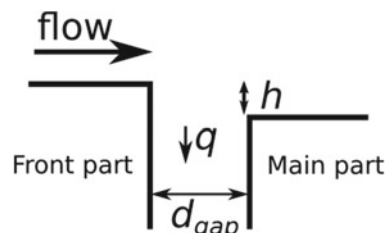
As can be seen in Fig. 1 right, the port side of the model was equipped with a long continuous shim, whereas the starboard side was equipped with narrow shims, which serve as placeholders. Over a large spanwise part, this allowed for a free channel from upper to lower side of the model. Because the pressure side with this particular model design is on the upper side of the model [4, 5, 15], an internal flow is induced through the gap. On the upper side of the model, where step and gap are installed, this internal flow acts as suction. No suction was possible on the port side because of the continuous shim. This allowed to separately examine the effect of surface imperfections with and without suction through the gap.

Figure 2 illustrates the step and gap with corresponding dimensions for a backward-facing step. The suction parameter q is defined as

$$q = \frac{v \cdot d_{gap}}{\delta^* \cdot U_\infty} \quad (1)$$

with average suction velocity v , gap width d_{gap} , freestream velocity U_∞ and displacement thickness δ^* . δ^* was determined with the laminar boundary-layer solver COCO [18] based on the measured temperature and pressure distribution and freestream parameters. Along the inside of the gap, pressure taps were installed to obtain a pres-

Fig. 2 Illustration of step (height: h) and gap (width: d_{gap}) at the junction between front part and main part of the model for a backward-facing step



sure distribution and calculate the average suction velocity v as described in detail in ref. [6].

Step height and gap width are quantified with step Reynolds number $Re_h = U_\infty h / v_\infty$ and gap Reynolds number $Re_{gap} = U_\infty d_{gap} / v_\infty$ with v_∞ being the freestream kinematic viscosity.

The experiments were conducted in the low-turbulence cryogenic Ludwieg-Tube Göttingen (DNW-KRG) ($Tu_{\mu u} \approx 0.06\%$ [11]). High Reynolds and Mach numbers are independently achievable in this facility by increasing pressure (up to 10 MPa) and/or decreasing temperature of the gas (down to 105 K). The test section is 0.35 m high, 0.4 m wide and 2 m long. Upper and lower walls of the test section are adaptable to allow interference-free measurements. Note here that because of the fast expansion of the test gas the temperature drops during a run. This leads to the model surface temperature being higher than the adiabatic wall temperature ($T_w / T_{aw} > 1$). Differing convective heat flows of laminar and turbulent boundary layers lead to a temperature change at the transition location, which can be detected using the temperature sensitive paint applied to the model.

3 Results and Discussion

Figure 3 shows a series of TSP result images for different dimensions of step height and gap width. Measurement conditions were $M = 0.6$, $Re_c = 10 \cdot 10^6$ and $\beta_H = 0.04$. Corresponding step and gap Reynolds numbers as well as suction parameter q and detected transition locations are listed in Table 1. Figure 3a depicts the result for the smooth configuration without step, gap and suction. Light areas correspond to laminar flow, dark areas correspond to turbulent flow. The two turbulent wedges in the center area of the model arise from the pressure taps installed in the leading edge region. The blue dashed lines indicate the detected, spanwise averaged transition location. Details on the automated transition detection algorithm are given in refs. [4, 6]. The white strip visible around the step and gap location is where no TSP was applied, which enabled to ensure sharp edges of the imperfection (see Sect. 2). Figure 3b includes a large forward-facing step ($h = 60 \mu\text{m}$, corresponding to step Reynolds number $Re_h \sim 2400$) and gap ($d_{gap} = 200 \mu\text{m}$, corresponding to gap Reynolds number $Re_{gap} \sim 8000$). Green and orange dashed lines correspond to the spanwise averaged transition location without and with suction, respectively. Compared to the smooth configuration, transition is detected further upstream without suction due to the surface imperfection. With suction, however, transition is detected considerably further downstream. For the examined suction rates, suction even over-compensates the adverse effect of step and gap, since transition was detected even further downstream as for the smooth configuration without suction.

In Fig. 3c a smaller step was implemented with step Reynolds number $Re_h \sim 1200$. Without suction, the smaller step height causes transition to occur on average 4% further downstream as compared to the configuration in Fig. 3b. With suction on the other hand, transition was detected at almost the same chordwise position (79%

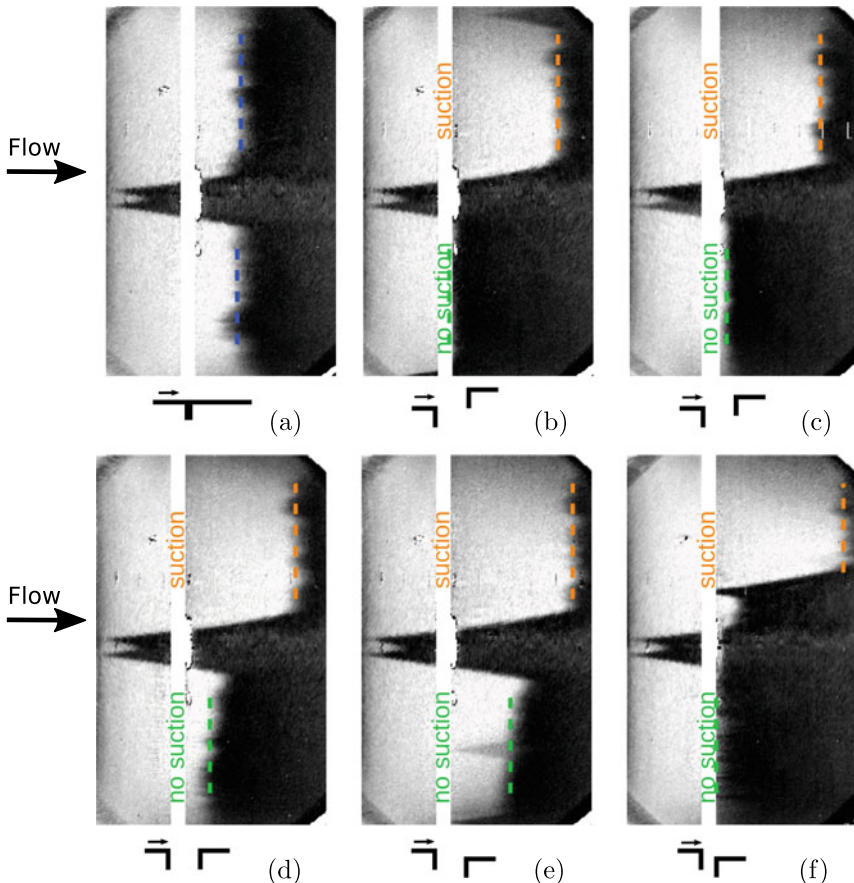


Fig. 3 Suction significantly delays laminar-turbulent transition for both forward- and backward-facing steps: TSP result images for $M = 0.6$, $Re_c = 8 \cdot 10^6$, $\beta_H = 0.04$ and different step and gap configurations. The dimensions of the imperfection (sketches here are not to scale) and detected transition locations are listed in Table 1

Table 1 Step and gap dimensions (forward-facing steps FFS and backward-facing steps BFS), suction rates q as well as transition locations for both port (no suction) and starboard side (suction) of the model for Fig. 3

	Re_{gap}	Re_h	q	x_T/c (p) (%)	x_T/c (sb) (%)
(a)	0	0	0	55	55
(b)	8000	2400 (FFS)	1.13	37	80
(c)	8000	1200 (FFS)	≈ 1	41	79
(d)	8000	0	0.96	48	82
(e)	8000	-1200 (BFS)	0.62	62	87
(f)	4000	-1200 (BFS)	0.27	38	89

compared to 80%). This is within the quantified uncertainty range of 1–2%, confirmed by reproduction measurements. Note here that the suction rate q for configuration (c) is an approximate value and could not be determined as precisely as for the other configurations.

Transition is also only marginally delayed for the gap-only configuration displayed in Fig. 3d, as transition is detected at 82% chord length. It changes significantly for a backward-facing step in (e), with laminar-turbulent transition now detected at $x_T/c = 87\%$. For this case the suction rate is also reduced by a large margin compared to the previous cases. This is very likely because the dynamic pressure at the gap inlet is not as pronounced for a backward-facing step compared to a forward-facing step.

This result is surprising as transition is detected further downstream despite the significantly reduced suction rate and because backward-facing steps are expected to have an even stronger influence on transition as forward-facing steps, due to the large separated area. Previous studies as those presented in ref. [7] for the same wind tunnel model showed that a small change in suction rate did not influence the transition location for the large forward-facing step configuration (with same gap width), suggesting a saturation effect in suction rate. Only a significantly reduced suction rate of less than half the original suction rate yielded a change in transition location.

For case (e) with small backward-facing step and no suction (starboard), the transition location is no longer 2D as for both forward-facing steps. Toward the center of the model, transition occurs further downstream than toward the side wall. This also occurs, although not as dominant, for the gap only configuration (d). Because of the geometry of the model presented in Figs. 1 and 2, there is a free path from port to starboard side of the model in its upper half. This is where a gap is present to obtain the desired surface imperfection before the large shim blocks the path. It is therefore possible for a spanwise flow to occur within the model, which will cause a light suction also on the port side of the model. The closer the spanwise position is to where no shims block the path to the lower side of the model, the more pronounced this suction will be, yielding the slanted transition line. For cases (d) and (e) the transition location on the port side must therefore be interpreted carefully, as most probably a small suction rate is also present here, especially in the region closer to the model centerline.

To overcome this problem, acrylic clay was placed inside the gap in the center region of the model for configuration (f) to prevent a spanwise flow for the same backward-facing step as in Fig. 3e. Additionally, a smaller gap width ($Re_{gap} \sim 4000$ instead of $Re_{gap} \sim 8000$) was chosen to reduce the suction rate. A turbulent wedge can be seen on the starboard side caused by the acrylic clay. For this case without suction, transition is detected close to the step and gap location in a similar area as for the forward-facing steps (b) and (c) with larger gap width $d_{gap} = 200 \mu\text{m}$.

Because the suction is passively driven by the pressure difference between upper and lower side of the model, the suction rate decreases dramatically by more than a factor 2 due to the smaller gap width. This once again leads to the transition location being detected even further downstream. It is unclear whether this is due to a reduced

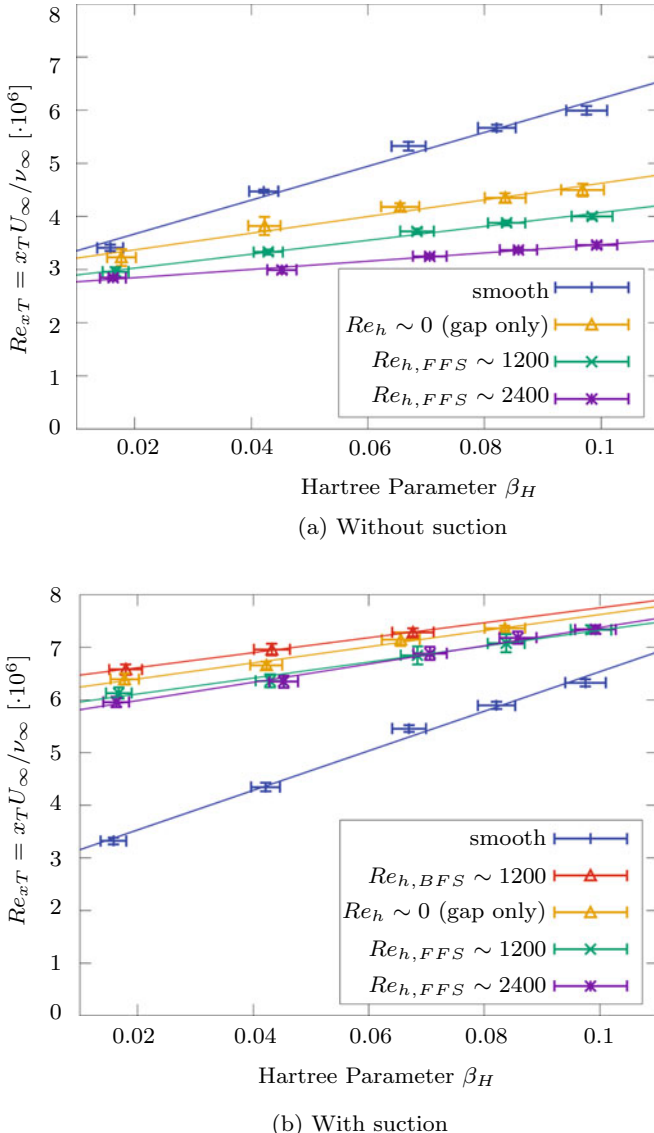


Fig. 4 Transition Reynolds number Re_{xT} increases for higher pressure gradient parameter β_H . Chord Reynolds number $Re_c = 8 \cdot 10^6$ and Mach number $M = 0.6$. Straight lines are to guide the eye. A gap is implemented in all step configurations. Without suction, the results for backward-facing steps are not shown due to the reasons stated in Chap. 3

gap width or the different suction rate or a combination of both, but demonstrates the significant effect of suction even for a comparably low suction rate.

Some research demonstrates the effect of oversuction for very high suction rates, when increasing suction rates causes earlier laminar-turbulent transition, as discussed for example in refs. [13, 17]. Often, oversuction is associated with suction through perforated plates because of 3D structures generated in the boundary-layer, but it can also be expected for slit suction for very high suction rates. No evidence of oversuction was found for the examined range of suction rates in ref. [7] which includes the suction rates presented in the current investigation. Yet it is thinkable, that a reduced suction rate has a positive impact on the backward-facing step configuration. The adopted experimental setup does not allow to fine tune the suction rate to a desired value without changing the geometry. This would be necessary to draw final conclusions on the difference of backward-facing steps and forward-facing steps for the same suction rate. The exemplary results presented above also hold true for the other Mach and Reynolds numbers investigated. This study therefore suggests, that suction has a more favourable effect on transition location for a backward-facing step as for a forward-facing step.

Figure 4 illustrates the change of detected transition location for different pressure gradient parameters β_H with and without suction. For $\beta_H \approx 0.04$, the underlying TSP result images are shown in Fig. 3. Higher β_H lead to transition occurring further downstream due to the accelerated, stabilizing boundary layer. This is confirmed also for the configurations with imperfections and with suction. Without suction, the difference in detected transition location for the varying step heights is much more pronounced than with suction. This is true for a large range of Hartree parameters.

4 Conclusions

For this study, experimental investigations were conducted in the Cryogenic Ludwieg-Tube Göttingen to analyse the effect of suction and step height on boundary-layer transition. Suction was achieved passively by exploiting the pressure difference between upper and lower side of the model. Mach numbers ranging from $M = 0.35$ to 0.77 , chord Reynolds numbers ranging from $Re_c = 3.5 \cdot 10^6$ to $16 \cdot 10^6$ and various pressure gradients were investigated, of which mainly the case for $M = 0.6$ and $Re_c = 8 \cdot 10^6$ was presented here. Varying step heights ($-30, 0, 30, 60 \mu\text{m}$) were examined in combination with a streamwise gap (mainly $200 \mu\text{m}$ but also $100 \mu\text{m}$). Additionally, a smooth reference configuration was also investigated.

Suction significantly delays transition and even overcompensates the adverse effect of step and gap for all examined test conditions. With suction, no significant difference in transition location could be determined for a $30 \mu\text{m}$ and $60 \mu\text{m}$ forward-facing step. For a backward-facing step, however, transition was detected further downstream compared to a forward-facing step, despite the significantly lower suction rate for the same gap width.

An additional configuration with reduced gap width, backward-facing step and acrylic clay was investigated to prevent suction on the starboard side of the model. In this case, even for a comparably low suction rate of $q \sim 0.27$, suction overcompens-

sated the adverse effect of gap and backward-facing step. It remains unclear, why the configurations with backward-facing steps delay transition further than those with forward-facing steps. Additional measurements need to be conducted to investigate the influence of suction rates and exclude the possibility of suction rates being in the regime of oversuction. Due to the more pronounced stagnation point for a forward-facing step compared to a backward-facing step, suction rates are higher. This could cause earlier laminar-turbulent transition if suction rates are in or close to the oversuction regime, where additional disturbances are coupled into the boundary-layer. Previous investigations however, showed no evidence that this is the case for the determined suction rates in this work. It therefore appears that backward-facing steps have a less negative effect on laminar-turbulent transition as compared to forward-facing steps for the examined measurement conditions with suction. The reason for this remains unclear and must be subject to future studies.

The results obtained for this investigation demonstrate that suction is a powerful tool to delay laminar-turbulent transition, even in the presence of surface imperfections as a combination of steps and gaps.

Acknowledgements The authors would like to thank M. Rein (DLR) for valuable advice during the measurement campaign and the discussion of the results, C. Fuchs and A. Kunis (DLR) for help with excellent model preparation, U. Henne (DLR) for support in the evaluation of TSP data and V. Ondrus for TSP synthesis and development. Additionally R. Kahle, M. Aschoff, A. Grimme and S. Hucke (DNW) are acknowledged for their support during the measurement campaign at DNW-KRG.

References

1. Arnal, D., Perraud, J., Séraudie, A.: Attachment line and surface imperfection problems. AGARD RTO-EN-AVT-151 pp. 9–1 to 9–20 (2009)
2. Braslow, A.L.: A History of Suction-Type Laminar-Flow Control with Emphasis on Flight Research, No. 13. Monographs in Aerospace History, No (1999)
3. Bushnell, D.M., Tuttle, M.H.: Survey and bibliography on attainment of laminar flow control in air using pressure gradient and suction. NASA RP 1035(1979)
4. Costantini, M.: Experimental analysis of geometric, pressure gradient and surface temperature effects on boundary-layer transition in compressible high reynolds number flows. Ph.D. thesis, RWTH Aachen (2016). <http://elib.dlr.de/117965>
5. Costantini M, Hein S, Henne U, Klein C, Koch S, Schojda L, Ondrus V, Schröder W (2016) Pressure gradient and nonadiabatic surface effects on boundary layer transition. AIAA Journal 54(11), 3465–3480, doi: 10.2514/1.J054583
6. Dimond, B., Costantini, M., Risius, S., Fuchs, C., Klein, C.: Experimental analysis of suction on step-induced boundary-layer transition. Exp. Thermal Fluid Sci. **109**(109842) (2019). <https://doi.org/10.1016/j.expthermflusci.2019.109842>, <http://www.sciencedirect.com/science/article/pii/S0894177718319794>
7. Dimond, B., Costantini, M., Risius, S., Klein, C., Rein, M.: Experimental investigation of the delay of step-induced transition by means of suction. New Results Numer. Exp. Fluid Mech. **XII**(16) (2020)
8. Hahn, M., Pfenninger, W.: Prevention of transition over a backward step by suction. Journal of Aircraft **10**(10), 618–622 (1973)

9. Hensch AK, Guntermann P, Longo R, Klein C, Risius S, Schaber S, Quest J, Okfen P (2019) Investigation of hybrid laminar flow control (HLFC) on a 2D-model in the cryogenic pilot european transonic windtunnel (PETW). In: AIAA Scitech 2019 Forum, 10.2514/6.2019-1181, <https://doi.org/10.2514/6.2019-1181>
10. Joslin, R.D.: Aircraft laminar flow control. *Ann. Rev. Fluid Mech.* **30**(1), 1–29 (1998). <https://doi.org/10.1146/annurev.fluid.30.1.1>
11. Koch, S.: Zeitliche und räumliche Turbulenzentwicklung in einem Rohrwindkanal und deren Einfluss auf die Transition an Profilmödellen. Ph.D. thesis, Georg-August-Universität, Göttingen (2004)
12. Kosin, R.E.: Laminar flow control by suction as applied to the X-21a airplane. *Journal of Aircraft* **2**(5), 384–390 (1965)
13. Messing, R., Kloker, M.J.: Investigation of suction for laminar flow control of three-dimensional boundary layers. *Journal of Fluid Mechanics* **658**, 117–147 (2010)
14. Meyer, F., Kleiser, L.: Numerical investigation of transition in 3D boundary layers. AGARD CP-**438** (16), 16–1 to 16–17 (1989)
15. Risius, S., Costantini, M., Koch, S., Hein, S., Klein, C.: Unit Reynolds number, Mach number and pressure gradient effects on laminar-turbulent transition in two-dimensional boundary layers. *Exp. Fluids* **59**(86) (2018). <https://doi.org/10.1007/s00348-018-2538-8>
16. Robert, J.: Drag reduction: an industrial challenge. AGARD-R-786, pp. 2–1 to 2–15 (1992)
17. Saric, W.S.: Laminar flow control with suction: theory and experiment. AGARD-R-**723** (3) (1985)
18. Schrauf, G.: COCO - a program to compute velocity and temperature profiles for local and non-local stability analysis of compressible, conical boundary layers with suction. ZARM Technik report (1998)

On the Interaction of Freestream Turbulence and Attachment-Line Boundary Layer



Isabella Fumarola, Michael Gaster, and Chris J. Atkin

Abstract One of the possible forcing mechanisms for inducing transition from laminar to turbulent flow is freestream turbulence. Among the different transition mechanisms, freestream turbulence influences the cross-flow instability which occurs on swept wings. In order to understand better the physical interaction between freestream turbulence and boundary layer, this work analyses how the turbulence is distorted approaching a leading edge and whether it is amplified approaching a swept leading edge. The paper contains a brief literature review of both the two-dimensional stagnation point and three-dimensional attachment-line flows. This reveals that freestream turbulence amplification has been investigated for two-dimensional leading edge flows, but there is a lack of research on the swept leading edge. In addition, the paper presents some experimental results on a circular cylinder at various sweep angles. The results show that the phenomenon observed at the two-dimensional stagnation point also occurs at a swept attachment-line, although some differences are identified.

1 Introduction

Laminar to turbulent transition is an active area of research and several open questions remain which need to be addressed. The overall view is that the flow instability is triggered by the disturbances (freestream turbulence, roughness, surface dishomogeneity, etc.) interacting with the boundary layer. Among those disturbances, freestream turbulence has an important influence on the instability mechanisms and, in particular, on cross-flow instability [1, 2]. Cross-flow instability arises from the combined effect of pressure gradient and sweep angle, as in the case of a swept wing or a rotating disk. In 1988, Bippes and Mueller investigated cross-flow instability on a swept flat plate under a displacement body [2]. The experiments were performed in different wind tunnels with different levels of turbulence intensity (from 0.08%

I. Fumarola (✉) · M. Gaster

City, University of London, Northampton Square, London EC1V0HB, UK
e-mail: isabella.fumarola.1@city.ac.uk

C. J. Atkin

School of Mathematics, University of East Anglia, Norwich NR4 7TJ, UK

up to 0.57%). In the lower turbulent intensity wind tunnel the transition process was dominated by stationary modes, while in the presence of higher turbulence level the transition process was dominated by travelling modes. Similar experiments [3–6] as well as DNS simulation [7] found similar results, investigating also the combined effect of freestream turbulence and roughness. The overall picture is that roughness establishes the initial conditions for stationary cross-flow modes, while freestream turbulence establishes the initial conditions for travelling cross-flow modes. In particular, when the freestream turbulence increases, the amplitude of the travelling cross-flow modes increases accordingly, while the stationary modes are damped. To provide a reference, when the turbulence level is in the range $Tu \leq 0.2\%$, the cross-flow instability on a swept wing is usually dominated by stationary modes [5].

Typical flight conditions present a level of turbulence much lower than that normally encountered in a wind tunnel test. It is, therefore, extremely important to understand the freestream turbulence and boundary layer interaction mechanisms to be able to interpret the experimental results. In addition, laminar to turbulent transition also has an important role in other applications where the oncoming flow has a higher level of turbulence. The importance of the leading edge region when considering receptivity mechanisms has already been ascertained by many researchers [8–10], while this paper focuses on the distortion and amplification of freestream turbulence as it approaches the boundary layer on a swept attachment-line.

In the first part of the paper, the freestream turbulence amplification mechanisms approaching a two-dimensional stagnation point are reviewed together with a few studies focusing on the attachment-line boundary layer. In the second part, an experimental investigation of both unswept and swept attachment-line flows is presented. The results show that velocity fluctuations approaching a swept attachment-line boundary layer are amplified in a similar way to those approaching a two-dimensional stagnation point flow.

2 Freestream Turbulence Approaching a Stagnation Point

The amplification of the velocity fluctuations approaching a leading edge was initially observed by Piercy and Richardson in 1928–1930 [11, 12]. A possible explanation was put forward by Sutera et al., known as *vorticity amplification theory* [13, 14]. The high level of velocity fluctuations was attributed to the oncoming freestream vorticity, which is stretched, and therefore amplified, approaching the leading edge of a two-dimensional body. The authors demonstrated that the amplification occurs only if the vorticity is oriented in the direction normal to the two dimensional section of the body and if the wavelength of the disturbance is greater than a threshold value. Experimentally, this theory was verified on different types of bodies (circular cylinder, vertical flat plate, aerofoil...) mainly using flow visualisation and single hot-wire anemometry. Typical experiments were carried out in environments with a high level of turbulence intensity. Flow visualisation experiments were carried out at low Reynolds number and were able to identify the presence of unsteady coher-

ent structures at the leading edge [15]. Hot-wire investigations could only employ single hot-wire anemometry, due to the proximity of the measurement domain to the wall, and, therefore, only one velocity component was measured. The velocity fluctuations were typically found to grow approaching the leading edge, with a maximum of amplification around the edge of the boundary layer. Although not always explicitly specified, the stagnation point boundary layer was turbulent in most of the experiments since they were carried out in the high freestream turbulence environment. Only Sadeh et al. published data in a low turbulence environment, where the boundary layer was clearly laminar [16]. At this time, the general interest was around the influence of freestream turbulence on heat transfer at the stagnation point, and not on laminar to turbulent transition.

The difficulty of carrying out measurements at the stagnation point is that the velocity field needs to be acquired very close to the surface with a good spatial resolution, since the laminar boundary layer is extremely thin. A recent investigation was carried out on a circular cylinder adopting a three-component Laser Doppler Anemometer (LDA) [18]. The fluctuations of the spanwise velocity component were found to be amplified as the flow approached the stagnation point with a maximum at the boundary layer edge. The work identified that the amplification is restricted to frequencies below 30 Hz. This paper will consider the same phenomenon for the swept attachment-line case.

3 Attachment-Line

When an aerofoil is mounted with a sweep angle, the flow at the leading edge is fully spanwise and, therefore, instead of a stagnation point the so-called *attachment-line* is defined.

The flow along the attachment-line was a focus of many researchers during the 60s, following flight tests and wind tunnel experiments by Pfeninger and Bacon [19], Anscombe and Illingworth [20] and Gaster [21], which demonstrated that the flow can already be turbulent at the attachment-line. Two important phenomena were found: attachment-line contamination and attachment-line instability. The first occurs due to disturbances propagating from the fuselage along the attachment-line of a swept-back wing. The second is due to a laminar boundary layer at the attachment-line becoming unstable at high Reynolds number. The attachment-line boundary layer flow was found to be well described by the Reynolds number based either on the attachment-line momentum thickness (Re_Θ) or on the velocity gradient ($Re = 0.4040 Re_\Theta$). According to Gaster [21] and Poll [22] on a sweptback wing, for $Re_\Theta < 100$, the disturbances coming from the fuselage decay naturally and the flow is laminar along the entire attachment-line, while, for $Re_\Theta \geq 100$, the flow is transitioning from laminar to turbulent and, for $Re \geq 300$, the flow is fully turbulent. The attachment-line instability was found to occur at much higher Reynolds number, $Re \leq 583.1$ according to the DNS by Spalart [23] and Hall and Malik [24]. A detail

review of theoretical and experimental work on attachment-line flow can be found in [25, 26].

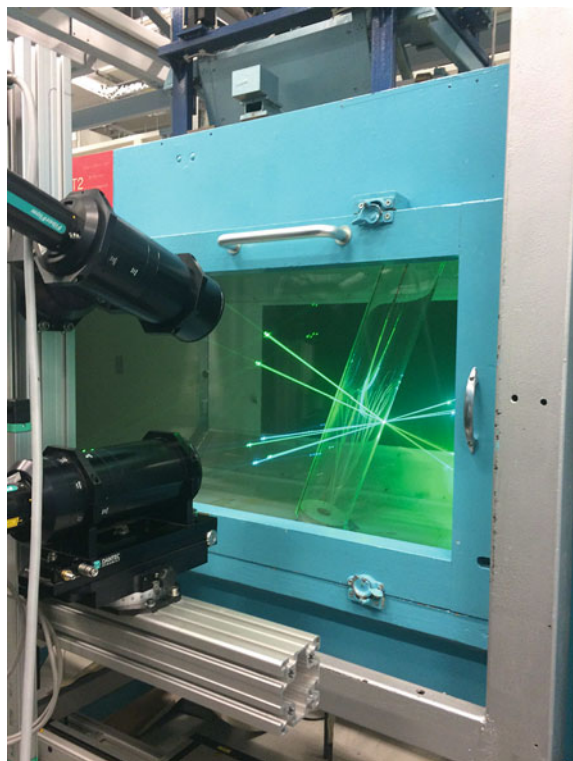
Despite the number of experimental and numerical studies available in the literature, there have been few, if any, investigations into the interaction between freestream turbulence and the attachment-line.

This experiment aims to contribute new measurements of the freestream velocity fluctuations approaching a swept, laminar attachment-line boundary layer.

4 Experimental Setup

The experiment was carried out in the T2 wind tunnel at City, University of London, using a hollow Perspex circular cylinder (radius $R = 75$ mm) mounted vertically in the wind tunnel at four sweep angles ($\Lambda = 0^\circ - 5^\circ - 10^\circ - 20^\circ - 30^\circ$). The freestream turbulence was around 1% without the model, rising to 1.4% with the model in all configurations (both measured at a distance of 220 mm from the leading edge). Detailed measurements of the turbulence level can be found in [17].

Fig. 1 LDA setup for a swept cylinder mounted in the wind tunnel (flow from right to left)



The flow measurements were taken using a Dantec Dynamics multi-component Laser Doppler Anemometer, as shown in Fig. 1. The system consists of six laser beams crossing at the same focal point and can acquire up to three velocity components in coincident mode. The LDA measurements used a probe volume of $0.12 \text{ mm} \times 0.12 \text{ mm} \times 2.60 \text{ mm}$ with a Bragg cell operating at a frequency of 40 MHz. The flow in the wind tunnel was seeded using olive oil particles of approximately $1 \mu\text{m}$ diameter.

Figure 2 shows the coordinate system on the model based on the model geometry: x chordwise, y perpendicular to the surface, z spanwise. The cylinder was equipped with 15 pressure taps which were used to align the attachment-line along the centre of the wind tunnel. The LDA beams were aligned with the attachment-line as well; minor adjustments were made by means of a velocity scan across the cylinder section. Further details for the methodology adopted for the experiment are available in [17]. The measurement domain extended from three radii upstream of the attachment-line down to the surface. The measurements were carried out in coincident mode. Only the spanwise and wall-normal velocity components are presented here, since the chordwise velocity component did not reveal any additional insight into the flow phenomena.

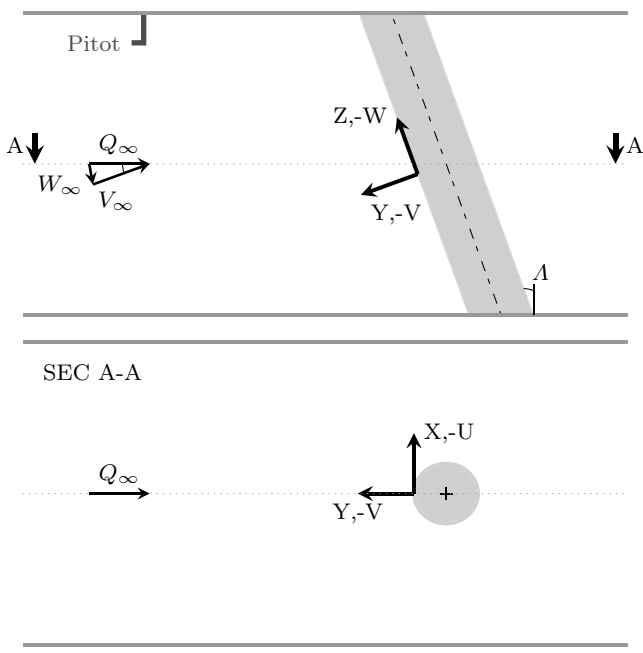


Fig. 2 Cylinder coordinate systems used

5 Results

The experiments were carried out at $Q_\infty = 6$ m/s with a maximum attachment-line Re_θ less than 32, hence much lower than the attachment-line contamination threshold.

The LDA data were processed considering the time taken by each particle to cross the probe volume (the transit time) as weighting factor. This technique, well established in turbulent flows, was found to be necessary to avoid bias error, although the flow was always in a laminar state [17].

Figure 3 shows the mean and the Root Mean Square (RMS) of the velocity components (V wall-normal and W spanwise) from the leading edge up to three times the radius of the cylinder. The mean flow agrees pretty well with potential flow theory, with the spanwise velocity being zero for the unswept case and uniform for the swept cases. The mean wall-normal velocity decreases linearly towards the wall for $Y/R \leq 0.01$. The velocity fluctuations (both components) remain almost constant for $Y/R \geq 1.3 R$ and then reduce more rapidly approaching the body. The trend is similar for all sweep cases. The most interesting behaviour is observed for the

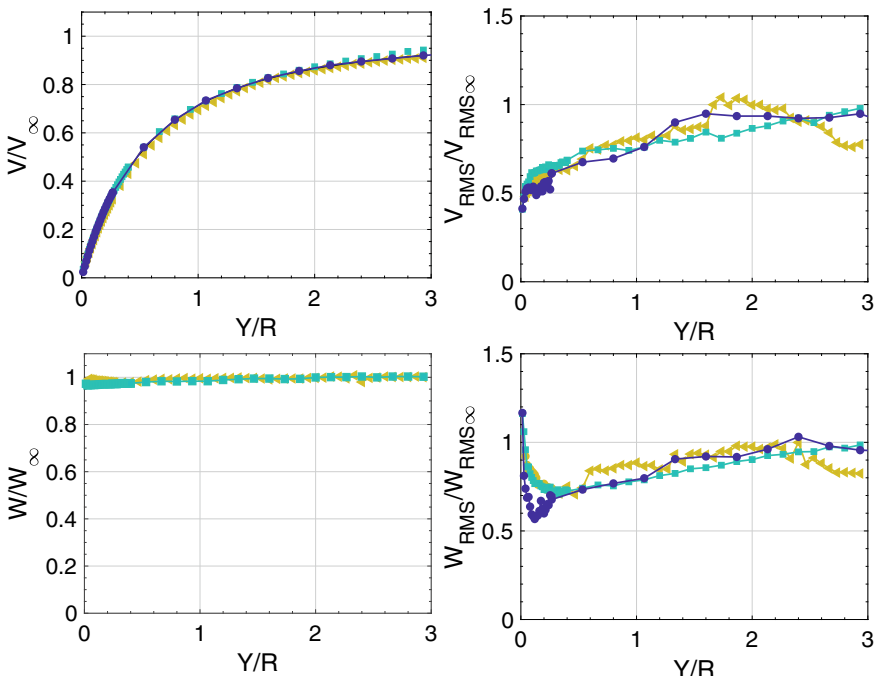


Fig. 3 Mean and RMS of the three velocity components approaching a swept cylinder: ● $\Lambda = 0^\circ$, ■ $\Lambda = 20^\circ$, ▲ $\Lambda = 30^\circ$. The black line in the V plot corresponds to the potential flow theory. The spanwise velocity for the unswept cylinder has not been plotted

spanwise velocity fluctuations, which reduce to a minimum and then increase quite rapidly close to the wall.

To understand better what happens close to the wall, Fig. 4 shows the velocity profiles in the boundary layer, expressed as function of the dimensionless coordinate η , with a higher spatial resolution. The mean flow is compared with the viscous Hiemenz flow results. The viscous effects induce a non linear region from around $Y/R \leq 0.005$ for the wall-normal velocity component. While, the mean of the spanwise velocity is constant up to $\eta > 5$, as predicted by the theory, and then develops a typical boundary layer; this represents the main difference from the unswept boundary layer case (see [18] for further details). The velocity fluctuations for the unswept and swept cases present many similarities: the wall-normal velocity fluctuations decrease up to a minimum very close to the surface, while the spanwise velocity fluctuations increase approaching the wall with a maximum around $\eta = 2$ for all the cases except $\Lambda = 30^\circ$. In the latter case, although the rate of amplification is similar to the other cases up to $\eta = 3$, the spanwise fluctuations increase rapidly close to the wall with no maximum recorded in the experimental domain.

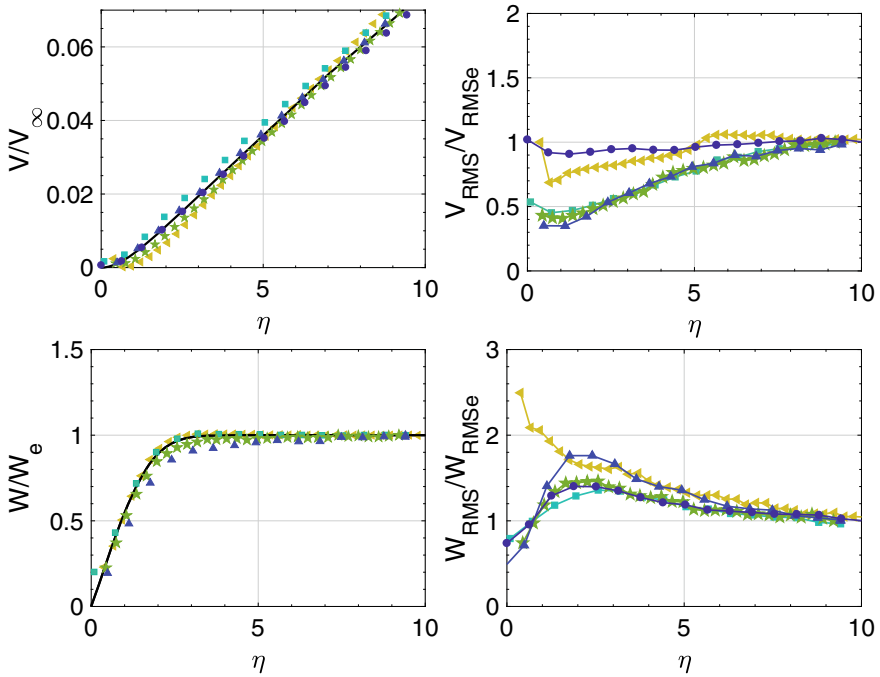


Fig. 4 Mean and RMS of the velocity components close to the leading edge, compared with the Falkner-Skan-Cooke numerical solution (black line), at different sweep angles: $\bullet \Lambda = 0^\circ$, $\blacktriangle \Lambda = 5^\circ$, $\star \Lambda = 10^\circ$, $\blacksquare \Lambda = 20^\circ$, $\blacktriangledown \Lambda = 30^\circ$. The mean spanwise velocity for $\Lambda = 0^\circ$ has not been plotted. $\eta = \sqrt{a/v} y$, $\eta = 10$ corresponds to $Y/R = 0.04$

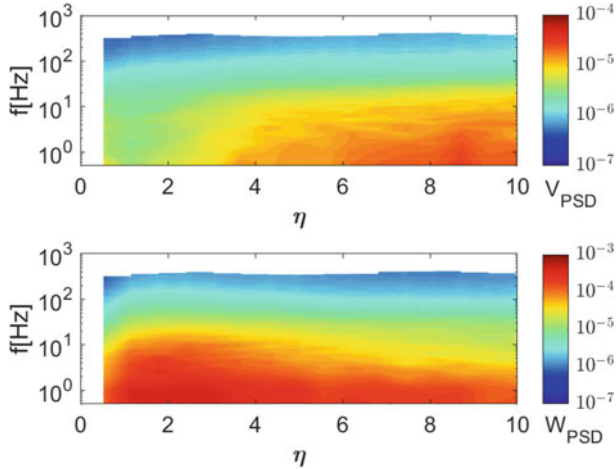


Fig. 5 Contour plot of the PSD ($\text{m}^2/\text{s}^2 \text{ Hz}$) for the V and the W velocity components for $\Lambda = 0^\circ$

To further analyse this behaviour, the Power Spectral Density (PSD) was evaluated from the auto-correlation function, which was obtained using the slotting technique [27]. Figures 5, 6 and 7 show the PSD for the wall-normal and spanwise velocity components for $\Lambda = 0^\circ$, $\Lambda = 20^\circ$ and $\Lambda = 30^\circ$. The amplification of the spanwise fluctuations is clearly associated with frequencies below 30 Hz; likewise the attenuation of the wall-normal velocity fluctuations. For the $\Lambda = 20^\circ$, the spectral analysis (Fig. 6) shows that the amplification is associated with a higher range of frequencies compared to the unswept case (Fig. 5).

For $\Lambda = 30^\circ$, the amplification, even very close to the wall, occurs at even higher frequencies, around 100 Hz. This shows that although the behaviour of the RMS signal at $\Lambda = 30^\circ$ shows a different trend compared to lower sweep angles with much higher velocity fluctuations close to the wall, the frequency trend is still consistent. This would be an interesting area for further investigations.

6 Conclusions

In the literature, the problem of freestream turbulence amplification approaching a leading edge has been studied for two-dimensional stagnation flow, but not for swept attachment-lines. The aim of this paper was, therefore, to explore the amplification of freestream turbulence approaching a laminar attachment-line boundary layer by comparing the flow over swept and unswept models.

The experiment, carried out on a cylinder mounted at four different sweep angles, demonstrates similar behaviour to that observed on the unswept model. For the highest sweep, a different behaviour was observed, where the amplification extended

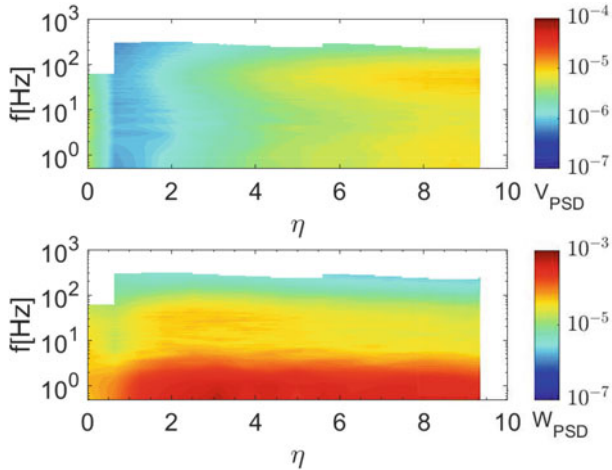


Fig. 6 Contour plot of the PSD ($\text{m}^2/\text{s}^2 \text{ Hz}$) for the V and the W velocity components for $\Lambda = 20^\circ$

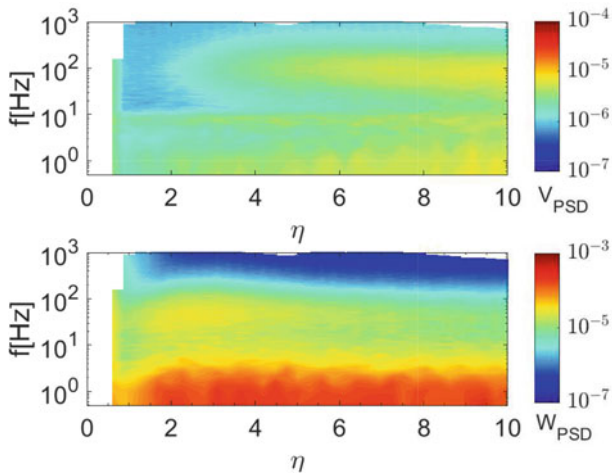


Fig. 7 Contour plot of the PSD ($\text{m}^2/\text{s}^2 \text{ Hz}$) for the V and the W velocity components for $\Lambda = 30^\circ$

much closer to the surface of the cylinder. Further investigations would be necessary to identify the exact sweep angle at which the trend changes. A consistent trend was also observed whereby increasing the sweep angle increased the frequency of the amplified disturbances. The experiment has, therefore, revealed two new and interesting sweep trends which could inform theoretical or computational analysis. Further experimental work to explore the sweep range 20° – 30° is also recommended to resolve the trends in greater detail.

Acknowledgements The authors would like to acknowledge the financial support of the Engineering and Physical Sciences Research Council under grant ref. EP L024888 1 UK National Wind Tunnel Facility, co-ordinated by Imperial College, and the support of InnovateUK under grant ref. 113024, Enhanced Fidelity Transonic Wing, led by Airbus.

References

1. Saric, W.S., Reed, H.L., White, E.B.: Stability and transition of three-dimensional boundary layers. *Annual Review of Fluid Mechanics* **35**, 413–440 (2003)
2. Bippes, H., Mueller, B.: Experiments on the laminar-turbulent transition on swept wings. *NASA STI/Recon Technical Report* **90**, 3–16 (1988)
3. White, E., Saric, W., Gladden, R., Gabet, P. (2001). Stages of swept-wing transition. *39th Aerospace Sciences Meeting and Exhibit*, p. 271
4. Downs, R.S., White, E.B.: Free-stream turbulence and the development of cross-flow disturbances. *Journal of Fluid Mechanics* **735**, 347–380 (2013)
5. Kurian, T., Fransson, J. H., Alfredsson, P. H. (2011). Boundary layer receptivity to free-stream turbulence and surface roughness over a swept flat plate. *Physics of Fluids*, 23
6. Borodulin, V.I., Ivanov, A.V., Kachanov, Y.S.: Swept-wing boundary-layer transition at various external perturbations: Scenarios, criteria, and problems of prediction. *Physics of Fluids* **29**(9), 094101 (2017)
7. Schrader, L. U. (2008). Receptivity of boundary layers under pressure gradient. PhD dissertation, KTH
8. Goldstein, M.E.: The evolution of Tollmien-Schlichting waves near a leading edge. *Journal of Fluid Mechanics*, Cambridge University Press **127**, 59–81 (1983)
9. Goldstein, M.E.: Scattering of acoustic waves into Tollmien-Schlichting waves by small streamwise variations in surface geometry. *Journal of Fluid Mechanics*, Cambridge University Press **154**, 509–529 (1985)
10. Hanson, R.E., Buckley, H.P., Lavoie, P.: Aerodynamic optimization of the flat-plate leading edge for experimental studies of laminar and transitional boundary layers. *Experiments in fluids*, Springer **53**, 863–871 (2012)
11. N. A. V. Piercy, E. G. Richardson, XCVI-The variation of velocity amplitude close to the surface of a cylinder moving through a viscous fluid, *The London, Edinburgh, and Dublin Philosophical Magazine and Journal of Science*, vol. 6-39, 970-977, Taylor & Francis (1928)
12. N. A. V. Piercy, E. G. Richardson, XCIV - The turbulence in front of a body moving through a viscous fluid, *The London, Edinburgh and Dublin Philosophical Magazine and Journal of Science*, vol. 9-60, 1038-1041, Taylor & Francis (1930)
13. S. P. Sutera, P. F. Maeder, J. Kestling, On the sensitivity of heat transfer in the stagnation point boundary layer to free stream vorticity, Cambridge Univ Press (1962)
14. S. P. Sutera, Vorticity amplification in stagnation-point flow and its effect on heat transfer, *Journal of Fluid Mechanics*, vol. 21-03, 513–534, Cambridge Univ Press (1965)
15. Sadeh, W.Z., Brauer, H.J., Garrison, J.A.: Visualization Study of Vorticity Amplification in Stagnation Flow. *Purdue Univ Lafayette Ind Project Squid* (1977). Headquarters
16. Sadeh, W.Z., Sutera, S.P., Maeder, P.F.: An investigation of vorticity amplification in stagnation flow. *Zeitschrift für angewandte Mathematik und Physik ZAMP*, Springer **21**, 177–742 (1970)
17. I. Fumarola, Effect of Freestream Turbulence on the Boundary Layer on a Swept Leading Edge. PhD Dissertation, City University of London (2019)
18. I. Fumarola, M. Gaster, C. Atkin (2019) Enhancement of the velocity fluctuations ahead of the stagnation region of a cylinder (under review)
19. Pfenniger, W., Bacon, J.W.: Amplified laminar boundary layer oscillations and transition at the front attachment line of a 45 swept flat-nosed wing with and without boundary layer suction, pp. 85–105. Plenum Press, *Viscous Drag Reduction proceedings* (1969)

20. Anscombe, A., Illingworth, L.N.: Wind-tunnel Observations of Boundary Layer Transition on a Wing at Various Angles of Sweepback. Aeronautical Research Council Great Britain, HM Stationery Office (1956)
21. Gaster, M.: On the flow along swept leading edges. *The Aeronautical Quarterly*, Cambridge University Press **18**, 165–184 (1967)
22. Poll, D. I. A. (1978). Some aspects of the flow near a swept attachment line with particular reference to boundary layer transition. PhD thesis, Cranfield Institute of Technology, College of Aeronautics
23. Spalart, P. R. (1988). Direct Numerical Study of Leading Edge Contamination. AGARD-CP, 438
24. Hall, P., Malik, M.R.: On the instability of a three-dimensional attachment-line boundary layer: weakly nonlinear theory and a numerical approach. *Journal of Fluid Mechanics*, Cambridge University Press **163**, 257–282 (1986)
25. Arnal, D., Casalis, G.: Laminar-turbulent transition prediction in three-dimensional flows. *Progress in Aerospace Sciences*, Elsevier **36**, 173–191 (2000)
26. Gowree, E. R. Influence of Attachment Line Flow on Form Drag. PhD Dissertation, City University of London (2014)
27. Gaster, M., Roberts, J.B.: The spectral analysis of randomly sampled records by a direct transform. *Proceedings of the Royal Society of London A: Mathematical, Physical and Engineering Sciences*, The Royal Society **354**, 27–85 (1977)

Isolated Roughness and Tollmien-Schlichting Waves in Boundary-Layer Transition



Shumpei Hara, Santhosh B. Mamidala, and Jens H. M. Fransson

Abstract An experimental investigation aimed at detecting the critical roughness Reynolds number ($Re_{kk,tr}$) both with and without Tollmien-Schlichting (T-S) waves is described in this paper. As a novel technique to examine $Re_{kk,tr}$ systematically, we employed isolated, cylindrical roughnesses with automatically adjustable height of micro-meter precision. The experiment was performed using hot-wire anemometry in flat-plate boundary layers developing under close to zero-pressure-gradient conditions in a low-turbulence level wind tunnel. The present data for $Re_{kk,tr}$ without T-S waves confirmed previous results and showed a strong correlation between the roughness aspect ratio and $\sqrt{Re_{kk,tr}}$. Controlling the roughness height while keeping the free-stream velocity fixed revealed noteworthy hysteresis for $Re_{kk,tr}$. As expected the critical roughness Reynolds number decreased with the presence of T-S waves. The necessary T-S wave amplitude needed for transition became smaller with increasing the roughness height with a sudden drop when approaching the critical roughness height without T-S waves.

1 Introduction

A deeper understanding of boundary-layer transition in different aerodynamic conditions would lead to improved transition to turbulence prediction methods as well as new control methods for skin-friction drag reduction. In the two-dimensional (2D) Blasius boundary layers with free-stream turbulence of low levels, Tollmien-Schlichting (T-S) waves [1] of spatial exponential growth are observed, and is well described by the modal linear stability theory. When the primary instability has

S. Hara (✉)
Doshisha University, Kyoto, Japan
e-mail: shhara@mail.doshisha.ac.jp

S. B. Mamidala · J. H. M. Fransson
KTH, Stockholm, Sweden
e-mail: mamidala@mech.kth.se

J. H. M. Fransson
e-mail: jensf@mech.kth.se

reached high enough amplitude and distorted the base flow Λ -vortices are formed in the streamwise direction, either aligned or in staggered patterns [2]. This is followed by breakdown to turbulent spots which leads to a fast transition to turbulence. In contrary, algebraic disturbance growth is observed in boundary layers when the free-stream turbulence intensity is about 1% [3], this transition scenario is characterized by the appearance of streaky structures consisting of alternating high- and low-speed regions inside the boundary layer with a spanwise scale given by the free-stream turbulence condition [4]. This phenomenon is explained by the transient disturbance amplification mechanism due to the non-orthogonality of eigenmodes [5].

Randomly distributed surface roughness is known to advance transition to turbulence. The actual flow disturbance by the roughness is determined by its geometrical shape, but its influence is still unclear, which has resulted in a long-lasting problem. Gregory and Walker [6] performed the first visualization of a steady horseshoe vortex from the spanwise distribution of the streamwise mean velocity behind a 3D roughness in the boundary layer. Simplified, 3D discrete roughness and its effect on transition are often characterized by its roughness Reynolds number (Re_{kk}), which is defined by the roughness height (k) and the corresponding local velocity (U_k) [7–11]. As to the relations between the instability and Re_{kk} , Puckert and Rist [12] observed a changeover of the instability from varicose to sinuous modes at the critical roughness Reynolds number ($Re_{kk,tr}$) for small diameter. They also confirmed the validity of their data in the transition diagram ($\sqrt{Re_{kk,tr}}$ versus the aspect ratio of the roughness η), proposed by von Doenhoff and Braslow (1961) [9], including various experimental results with different kinds of shapes of 3D roughness and arrays of roughness elements in the literature. Depending on Re_{kk} and the geometrical setting of the discrete roughness it has been shown that the transition can either be promoted or delayed [13].

The transition diagram published by von Doenhoff and Braslow in 1961 [9] shows a huge spread of the data because, in addition to the aforementioned roughness situation, the most restricted problem is the accuracy and repeatability of the data. When investigating the transition diagram, the installation of different roughnesses on different flat plates has been performed by different researchers in different flow facilities, and therefore it is difficult to qualitatively evaluate the differences. In addition, one has to be aware of the hysteresis of $Re_{kk,tr}$, which has been investigated by changing U_k for a three-dimensional roughness of a particular aspect ratio [12, 14], but, to our knowledge, no experimental study has focused on the the observed hysteresis by changing the roughness height continuously rather than U_∞ . Moreover, a lot of effort is needed for quantitative evaluation of laminar-turbulent transition originated from a combination of roughness disturbances and T-S waves, and then with a manual setting of the roughness it can lead to large errors in the results. Based on these points, we employ a cylindrical roughness with variable diameter and with automatically adjustable height of micro-meter precision, as a novel technique. The objective of the present study is to understand roughness induced-transition by reinforcing the transition diagram and to gain further insight into the interaction between roughness disturbances and T-S waves.

2 Experimental Setup

The experiment was performed in flat-plate boundary layers developing under zero-pressure-gradient conditions in a low-turbulence level wind tunnel at KTH, which has a test section of dimension $4.2 \times 0.5 \times 0.75$ m³ (length × width × height). The streamwise turbulence intensity is less than 0.04% of the free-stream velocity at the nominal speed of $U_\infty = 25$ m/s. We employed a 4 m long flat plate mounted vertically in the test section followed by a trailing edge flap to adjust the leading edge stagnation line. The localized roughness consists of a cylinder rod of interchangeable diameter, in the present study we used 3 and 6 mm rods. This roughness can move up and down continuously by a remote micrometer head RMH-13 (Opto Sigma) with micro-meter precision. The positional repeatability is 2 μm. The roughness is installed with a circular plug in the plate with its center located at 300 mm from the leading edge. T-S waves are generated by time-periodic suction and blowing at the wall. A slot in a plug for T-S waves mounted the plate is located at $x = 100$ mm from the leading edge. The periodic disturbance was generated using a signal generator connected to an audio amplifier driving a sealed loudspeaker to which flexible tubes are connected to the disturbance source. The amplitude of the loudspeaker was computer controlled allowing measurement runs with automated regulation of the T-S wave amplitude for a given frequency. The data acquisition was triggered by a reference signal in order to control the phase of the T-S wave. The free-stream velocity was measured at 300 mm from the leading edge with a Prandtl tube connected to a Furness FC0510. Measurements of the time-resolved streamwise velocity component were performed using hot-wire anemometry with a traversable probe with movement in three dimensions (x , y , and z axes directed along the streamwise, wall-normal, and spanwise direction, respectively). The origin is set on the centerline of the flat plate at the leading edge.

To confirm a close to zero-pressure-gradient condition over the flat plate the pressure coefficient ($C_p = 1 - (U/U_\infty)^2$) was measured for different U_∞ . The result is shown in Fig. 1, with error bars added corresponding to the standard deviation calculated from three measurement runs. The error bars are smaller than the symbols indicating that the base flow is stable. Downstream of the leading edge (from around $x = 150$ mm) the pressure gradients are close to zero with minor variations as U_∞ is changed, one may also conclude that the closest to zero-pressure gradient case is obtained for the lowest U_∞ .

In our experimental setup, there is no contamination from the plug where the roughness is mounted. In Fig. 2 the spanwise uniformity of the streamwise velocity profile in the wall-normal direction is elucidated. Here, the boundary layer scale δ corresponds to \sqrt{xv}/U_∞ . Spanwise locations are the centerline of the plate, $+2d$, and $-2d$, respectively, where d is equal to 3 mm in this figure.

Fig. 1 Pressure coefficient distribution versus the downstream distance for different U_∞

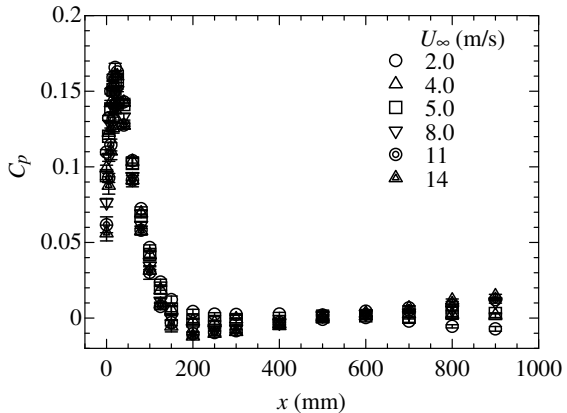
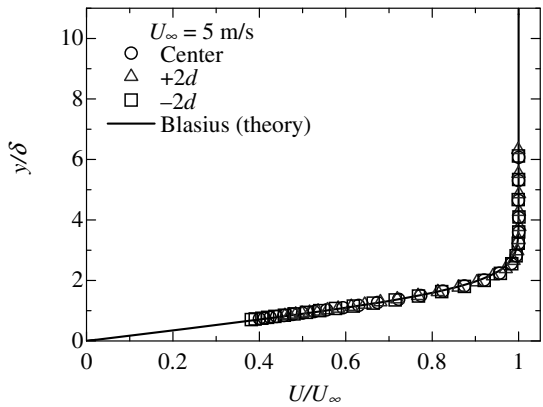


Fig. 2 Mean streamwise velocity profiles in the wall-normal direction for different spanwise directions



3 Roughness-Induced Transition With and Without T-S Waves

In the present study, the intermittency factor γ of the measured streamwise velocity signal is used to determine the critical roughness height k_{cr} for a given U_∞ needed to calculate the critical roughness Reynolds number $Re_{kk,tr}$. The intermittency factor was always measured on the roughness centerline and $50d$ downstream of the roughness. Figure 3 shows spanwise distributions of U inside the boundary layer at $x = 375, 450, 600$, and 900 mm for two roughness diameters. While a complicated disturbance is found in the region closest to the roughness, the decay phase of the streaks is shown downstream $x > 600$ mm. From the figure it is also clear that the traversing mechanism is not perfectly aligned in the streamwise direction of the air flow, since the wake centerline is shifted in the downstream direction.

To calculate the intermittency factor as a function of k we employ the procedure proposed in Ref. [15] with a high-pass filter from 240 Hz on the voltage-time signal

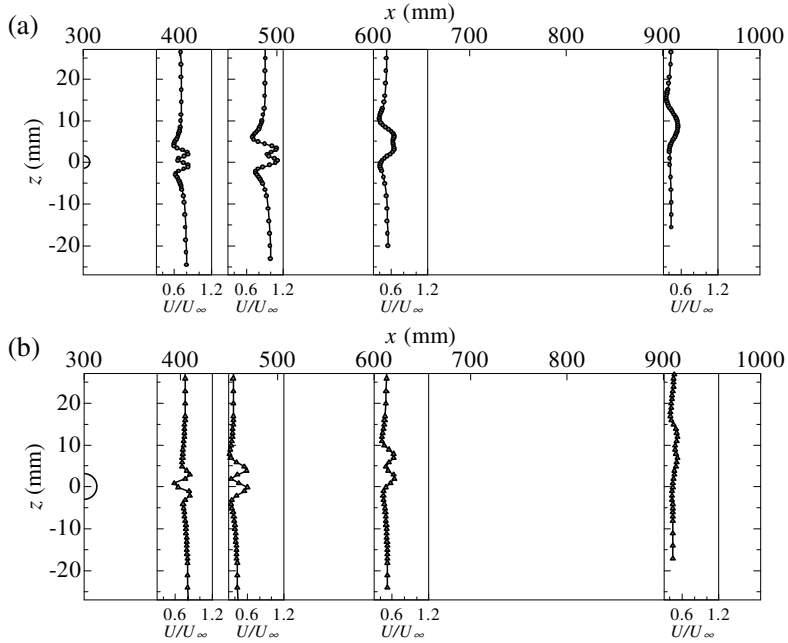


Fig. 3 Streamwise evolution of the spanwise mean velocity profiles taken at the wall-normal position for $k = 2$ mm. **a** $d = 3$ mm; **b** $d = 6$ mm

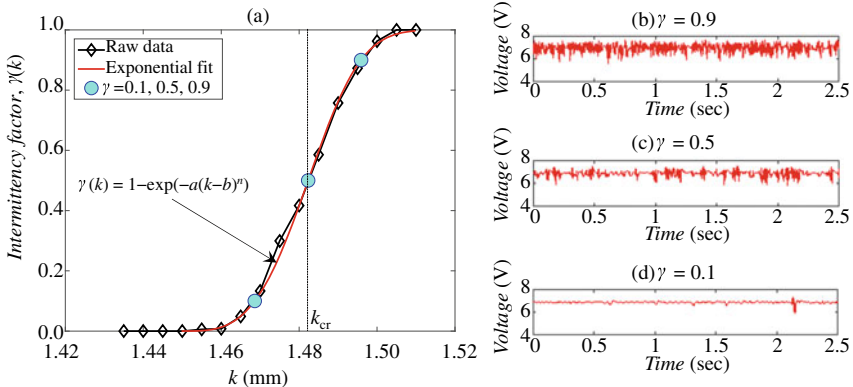
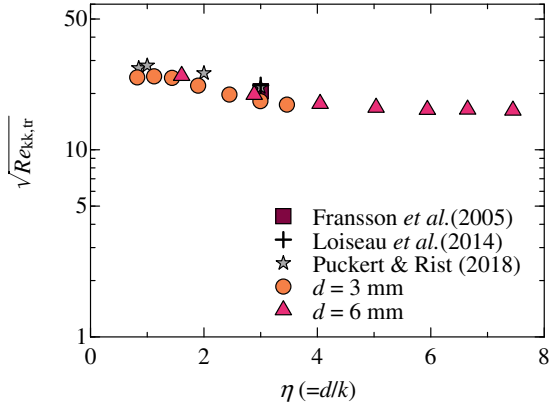


Fig. 4 Correspondence between the intermittency and time signal of voltage at $U_\infty = 3$ m/s as a typical case. **a** intermittency function versus k ; **b-d** time signal series for each γ

obtained from the hot-wire. Figure 4 shows the intermittency function for k with a sigmoid curve fitted to the data, including fitting parameters of a , b , and n , along with time voltage signals around $\gamma = 0.1$, 0.5 , and 0.9 . In the present study, k_{cr} is defined as the roughness height where $\gamma = 0.5$, i.e. half way through the transition

Fig. 5 Transition diagram for different roughness diameters in comparison with Refs. [12, 13, 16]



process. The relationship between γ and the time signal is elucidated in Fig. 4. The number of the spikes increases with γ and the calculated value of γ seems to resemble what may be estimated directly from visual inspection of the signal, and thus it is concluded that the intermittency detection method works with satisfaction. From this figure with $U_\infty = 3, the critical roughness height as an indicator for the roughness-induced transition can clearly be determined with the resolution of the remote micrometer head. Note that the transition takes place in the range of k from 1.46 mm to 1.50 mm. Furthermore, we confirmed that the accuracy to capture the k transition region was maintained for other experimental conditions.$

Here, we summarize the critical roughness Reynolds numbers obtained through the aforementioned procedure for all experimental results in this study together with some previous results into the transition diagram. While the transition diagram in [9] collects the result of different roughness shapes and roughness arrays our Fig. 5 only collects data of isolated cylindrical roughnesses, which makes the comparison more fair. If the reader is interested in a relative relationship with other conditions, please confer Ref. [12]. From the figure, it is found that the present results are in good agreement with the previous published results. The data show a clear dependence of η on $Re_{kk,tr}$, but seems to diminish for $\eta > 4$.

To gain insight to the roughness-induced transition with respect to the measurement location, the free-stream velocity, and the vertical blockage in terms of the roughness height to the boundary layer scale ratio, the data is replotted in Fig. 6. Here, $Re_{kk,tr}$ is divided by the streamwise Reynolds number $Re_x = U_\infty x / \nu$ and k_{cr} by the boundary layer scale $\delta_k = \sqrt{x_k \nu / U_\infty}$, where x_k is the streamwise distance of the roughness from the leading edge. The data show a linear behaviour up to $k_{cr}/\delta_k = 2.5$. Beyond this value it seems that $Re_{kk,tr}/Re_x$ grows somewhat faster.

To illustrate the hysteresis of $Re_{kk,tr}$ when changing k , the intermittency data for the flow configuration with $U_\infty = 9.0 at $d = 3\text{ mm}$ is shown in Fig. 7. In the figure, the red arrows mark the direction of successive change in k . Interestingly, there is a great difference in intermittency functions, which indicates a hysteresis phenomenon when changing k . This result is repeatable and the effect is clearly$

Fig. 6 Roughness Reynolds number divided by the streamwise Reynolds number versus the ratio of the roughness height to the boundary layer scale for different roughness diameters

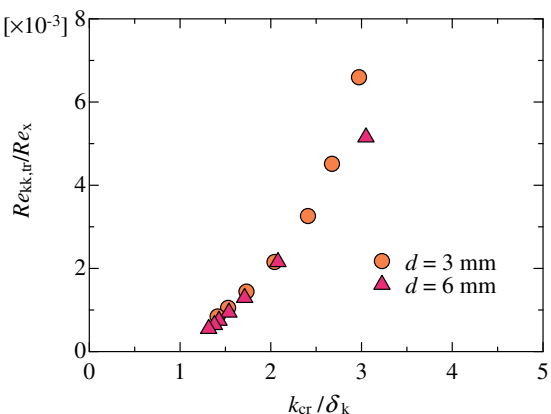


Fig. 7 Comparison of intermittency functions to the directional change in k for $U_\infty = 9.0$ m/s at $d = 3$ mm. Hysteresis region is described in gray

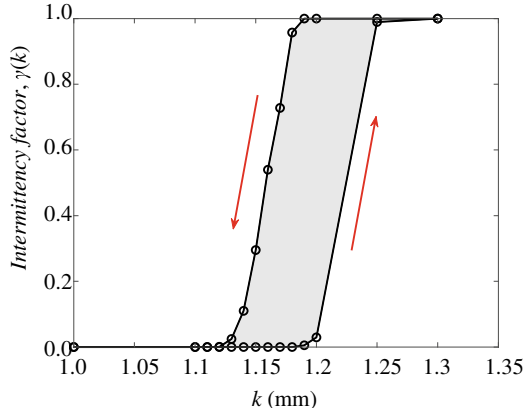
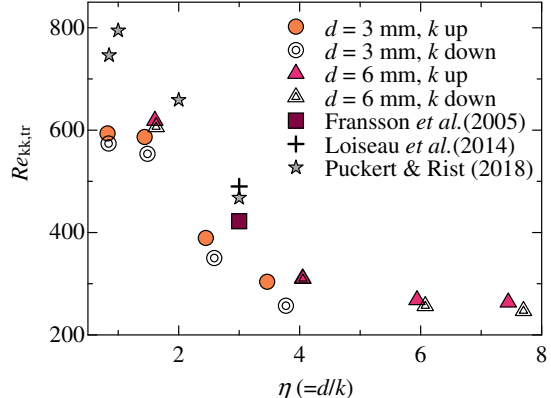


Fig. 8 Comparison of the critical roughness Reynolds number to the directional change in η (or k for a fixed d) for different U_∞ and roughness diameters



larger than the measurement accuracy of the roughness height movement. In Fig. 8 the hysteresis effect of $Re_{kk,tr}$ is shown for various aspect ratios, free-stream velocities and roughness diameters. It is found that there is noteworthy hysteresis, especially for lower d . In previous studies, [12, 14], the hysteresis of $Re_{kk,tr}$ was investigated by changing the free-stream velocity, but to the knowledge of the present authors nobody has reported the hysteresis effect when changing k .

Finally, the interaction between the roughness and T-S waves is quantitatively investigated for the condition of $U_\infty = 6$ m/s condition. Controlled T-S wave experiments were performed with roughness. The frequency f of the T-S waves was adjusted to be 65 Hz corresponding to $F = 170$, where F is the non-dimensional viscous frequency defined as $F = 2\pi f \nu / U_\infty^2 \times 10^6$. The hot-wire probe was placed at $x = 650$ mm from the leading edge in this experiment, i.e. close to the second branch of the neutral stability curve for this particular f and U_∞ . The T-S wave amplitude was measured at the wall-normal position corresponding to the disturbance inner peak. Here, the interaction is characterized by $Re_{kk,tr}$ and the amplitude of T-S wave A_{TS} . The amplitude of the 2D T-S wave was successively increased to detect $Re_{kk,tr}$ for fixed k condition, where k was systematically changed based on k_{cr} without T-S waves, i.e. from 0 to $0.9k_{cr}$ with a $0.1k_{cr}$ increment. In Fig. 9, the relationship between $Re_{kk,tr}$ and the amplitude of T-S waves are shown for the two diameters. From the figure it is quantitatively concluded that $Re_{kk,tr}$ decreases with the presence of T-S waves. Furthermore, the necessary T-S wave amplitude needed for transition becomes smaller with increasing k with a sudden drop when approaching k_{cr} . In Fig. 10 it is shown that with increasing aspect ratio, the amplitude of T-S waves increases drastically, but seems to saturate from $\eta = 10$ around $A_{TS}/U_\infty = 2.6\%$.

Fig. 9 The relation between the amplitude of T-S waves and critical roughness Reynolds number for different roughness diameters. Dashed and dash-dotted lines belong to the critical roughness Reynolds number for $d = 3$ and 6 mm without T-S waves, respectively

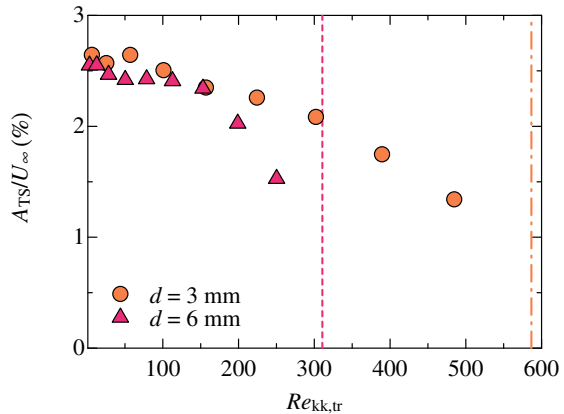
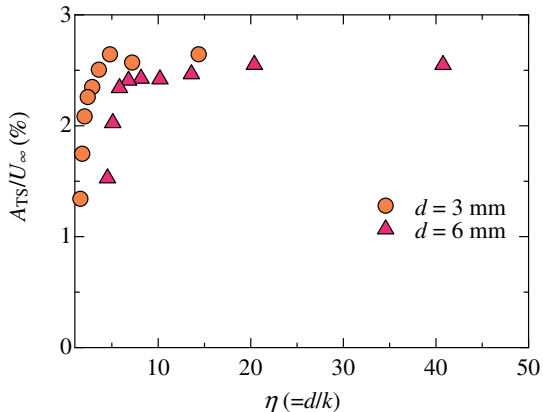


Fig. 10 The relation between the amplitude of T-S waves and aspect ratio for different roughness diameters



4 Conclusions

The present work reports the result obtained through a successful experimental setup with an isolated cylindrical roughness with adjustable height to detect the critical roughness Reynolds number $Re_{kk,tr}$ with and without T-S waves. The base flow is boundary layers developing over a flat plate under close to zero-pressure-gradient conditions in a low-turbulence level wind tunnel at KTH.

Roughness-induced transition is triggered when the roughness height passes over the wall-normal boundary layer scale at the roughness location. The critical roughness Reynolds number suddenly increases when the roughness height approaches two and a half times the boundary layer scale. From the transition diagram it is confirmed that there is a strong correlation between the aspect ratio and $\sqrt{Re_{kk,tr}}$. It is found that there is noteworthy hysteresis of $Re_{kk,tr}$ for different aspect ratios especially for the smaller of the two roughness diameters.

The quantitative evaluation for the interaction between the roughness and T-S waves reveals that $Re_{kk,tr}$ decreases with the presence of T-S waves. The necessary T-S waves amplitude needed for transition becomes smaller with increasing the roughness height with a sudden drop when approaching the critical roughness height without T-S waves. Furthermore, this amplitude increases with the aspect ratio until the ratio of the amplitude to the free-stream velocity is around 2.6%.

References

1. Schlichting, H.: *Boundary-layer theory*. McGraw-Hill, New York (2016)
2. Kachanov, Y.S.: Physical mechanisms of laminar-boundary-layer transition. *Annu. Rev. Fluid Mech.* **26**(1), 411–482 (1994)
3. Arnal, D., Juillen, J.C.: Contribution expérimentale à l'étude de la réceptivité d'une couche limite laminaire, à la turbulence de l'écoulement général. Rapport Technique 1/5018 AYD, ONERA (1978)

4. Fransson, J.H.M., Shahinfar, S.: On the effect of free-stream turbulence on boundary-layer transition. *J. Fluid Mech.* **899** (2020)
5. Schmid, P.J., Henningson, D.S.: *Stability and Transition in Shear Flows* Springer-Verlag (New York, 2001)
6. Gregory, N.T., Walker, W.S.: *The effect on transition of isolated surface excrescences in the boundary layer* (HM Stationery Office, 1956)
7. Klanfer, L., Owen, P.R.: The effect of isolated roughness on boundary layer transition. RAE (1953)
8. Klebanoff, P.S., Schubauer, G.B., Tidstrom, K.D.: Measurements of the effect of 2-dimensional and 3-dimensional roughness elements on boundary-layer transition. *J. Aeronaut. Sci.* **22**(11), 803–804 (1955)
9. von Doenhoff, A.E., Braslow, A.L.: The effect of distributed surface roughness on laminar flow. In: *Boundary layer and flow control* (Elsevier, 1961), pp. 657–681
10. Tani, I.: Effect of two-dimensional and isolated roughness on laminar flow. In *Boundary layer and flow control* (Elsevier, 1961), pp. 637–656
11. Tani, I., Komoda, H., Komatsu, Y., Iuchi, M.: *Boundary-layer transition by isolated roughness* (Aeronautical Research Institute, 1962)
12. Puckert, D.K., Rist, U.: Experiments on critical Reynolds number and global instability in roughness-induced laminar-turbulent transition. *J. Fluid Mech.* **844**, 878–904 (Cambridge University Press, 2018)
13. Fransson, J.H.M., Brandt, L., Talamelli, A., Cossu, C.: Experimental study of the stabilization of Tollmien-Schlichting waves by finite amplitude streaks. *Phys. Fluids* **17**(5), 054110 (AIP, 2005)
14. Klebanoff, P.S., Cleveland, W.G., Tidstrom, K.D.: On the evolution of a turbulent boundary layer induced by a three-dimensional roughness element. *J. Fluid Mech.* **237**, 101–187 (Cambridge University Press, 1992)
15. Fransson, J.H.M., Matsubara, M., Alfredsson, P.H.: Transition induced by free-stream turbulence. *J. Fluid Mech.* **527**, 1–25 (Cambridge University Press, 2005)
16. Loiseau, J.C., Robinet, J.C., Cherubini, S., Leriche, E.: Investigation of the roughness-induced transition: global stability analyses and direct numerical simulations. *J. Fluid Mech.* **760**, 175–211 (Cambridge University Press, 2014)

Instabilities and Transition on a Rotating Cone—Old Problems and New Challenges



K. Kato, A. Segalini, P. H. Alfredsson, and R. J. Lingwood

Abstract An experimental investigation of instabilities and transition in the boundary layer on a rotating broad (120° apex angle) cone through hot-wire measurements combined with local linear stability analysis (LLSA) has been undertaken. The rotating-cone flow is susceptible to both cross-flow and centrifugal instabilities. For broad cones, the cross-flow instability dominates over the centrifugal instability, and vice versa for slender cones. Although stationary vortical disturbances from the cross-flow instability are dominant on the broad cone (in this case 24–26 vortices develop), we have identified an initially slowly growing nonstationary mode with a much smaller wavenumber, which close to transition increases its growth rate dramatically. We report on a detailed process to identify the wavenumber of the measured nonstationary disturbance, as well as quantitative comparisons between experimental results and LLSA.

1 Introduction

Flows driven by a rotating cone or disk have been studied as a simplified model of three-dimensional boundary layers. The geometry is defined by the cone half-apex angle ψ shown in Fig. 1. Two main instabilities can be identified on a cone, a cross-

K. Kato (✉) · A. Segalini · P. H. Alfredsson · R. J. Lingwood
FLOW, Dept of Engineering Mechanics, KTH Royal Institute of Technology, SE-100 44
Stockholm, Sweden
e-mail: kentaro.kato@mech.kth.se

A. Segalini
e-mail: segalini@mech.kth.se

P. H. Alfredsson
e-mail: phal@mech.kth.se

R. J. Lingwood
e-mail: rebecca.lingwood@brunel.ac.uk

R. J. Lingwood
Department of Mechanical and Aerospace Engineering, Brunel University London,
UB8 3PH, London, UK

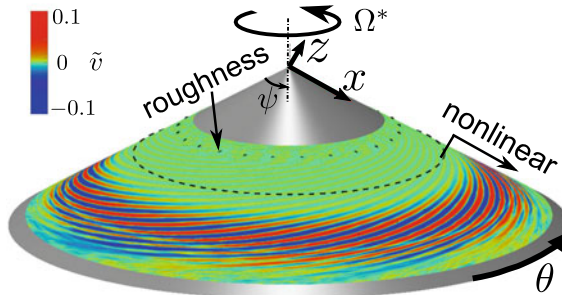


Fig. 1 The coordinate system (x, θ, z) on the rotating cone. The colour shows the phase-averaged azimuthal velocity component \tilde{v} (normalized by the local wall velocity) at $z = 1.2$. A pair of high- and low-speed regions shows the stationary vortex triggered by the surface roughness element

flow instability and a centrifugal instability. On a broad cone ($50^\circ < \psi \leq 90^\circ$), the cross-flow instability dominates [2], whereas on a slender cone ($\psi < 40^\circ$ including a cylinder with $\psi = 0^\circ$), the flow is susceptible to a centrifugal instability [3]. Thus, the rotating-cone flow is prone to two different instabilities, the dominant one depends on the cone apex angle [8]. However, the details of the switching between instabilities as well as the influences on transition have not yet been fully understood.

We consider the flow induced by a cone rotating at a rate Ω^* in a still fluid (* denotes a dimensional quantity). As shown in Fig. 1, we define an orthogonal coordinate system (x, θ, z) on the cone surface with the origin located at the apex; where x and z are the coordinates along the generating line of the cone and the wall-normal direction, respectively, and θ is the azimuthal coordinate. x and z are normalized by a viscous length, $\delta_\nu^* = \sqrt{\nu^*/(\Omega^* \sin \psi)}$, where ν^* is the kinematic viscosity of the fluid and $x = x^*/\delta_\nu^*$ is the square root of the Reynolds number. The mean flow on the cone has the same von Kármán similarity solution as the one on the disk when using δ_ν^* as the length scale [7, 10].

So far, most of experimental studies on broad cones including disks ($\psi = 90^\circ$) have reported the development of vortices fixed on the cone surface developing downstream of natural or artificial surface roughnesses. As x increases, these vortices increase in amplitude, develop nonlinearity, followed by secondary instability and collapse, finally leading to transition [1, 4]. However, the development of non-stationary large-scale disturbances has so far attracted little or no attention.

The present work aims to investigate instabilities and transition on a rotating cone with $\psi = 60^\circ$, which is expected to be similar to the rotating-disk flow [2, 8, 9] although there are some quantitative differences. For instance, in the natural case the disk typically develops 30–32 vortices whereas on a 60 degree cone 24–26 vortices are observed. The experimental data are the same as we used for our previous work [6, 7] however, in the present work, our analysis has identified a growing nonstationary mode from the measured data and thus has been compared with local linear stability analysis. We describe the details of the analysis and characterize the nonstationary disturbance.

2 Local Linear Stability Analysis

The local linear stability analysis (LLSA) is performed similarly to the analysis of Segalini & Camarri [10]. The linear perturbation equations in the laboratory frame of reference are solved in a parallel framework at several x -locations in the range $50 \leq x \leq 600$, where at each station the local mean velocity profile from the von Kármán profile is imposed (here denoted as $U_0(z)$, $V_0(z)$ and $W_0(z)$ for the meridian, azimuthal and wall-normal components, respectively). Modal analysis in the form $u \propto \hat{u}(z) \exp[i(\alpha x + n\theta - \omega t)]$ (and similarly for the other velocity components and pressure) is performed to transform the perturbation equations to a set of ordinary differential equations with the eigenfunctions and eigenvalue $\alpha = \alpha_r + i\alpha_i$ (the complex wavenumber) as unknowns (therefore a spatial formulation was followed for a given frequency value ω). This eigenvalue problem was solved at every x -location. n and ω are the azimuthal wavenumber and frequency (nondimensionalized by Ω^*), respectively. The perturbation equations in modal form are

$$\left(i\alpha + \frac{1}{x}\right)\hat{u} + \frac{i\beta}{\tilde{R}}\hat{v} + \frac{\partial\hat{w}}{\partial z} + \frac{1}{x}\cot\psi\hat{w} = 0, \quad (1)$$

$$[\mathcal{L} + U_0]\hat{u} - 2V_0\hat{v} + xU'_0\hat{w} + i\alpha\hat{p} = 0, \quad (2)$$

$$2V_0\hat{u} + [\mathcal{L} + U_0]\hat{v} + xV'_0\hat{w} + \cot\psi V_0\hat{w} + \frac{i\beta}{\tilde{R}}\hat{p} = 0, \quad (3)$$

$$-2\cot\psi V_0\hat{v} + [\mathcal{L} + W'_0]\hat{w} + \frac{\partial\hat{p}}{\partial z} = 0, \quad (4)$$

with the linear operator

$$\mathcal{L} = -\frac{i\omega}{\sin\psi} + i\alpha x U_0 + \frac{i\beta x V_0}{\tilde{R}} + W_0 \frac{\partial}{\partial z} + \alpha^2 + \frac{\beta^2}{\tilde{R}^2} - \frac{\partial^2}{\partial z^2} - \frac{1}{x\tilde{R}} \left(i\alpha + \cot\psi \frac{\partial}{\partial z} \right), \quad (5)$$

and $\tilde{R} = 1 + z \cot\psi/x$ with $\beta = n/(x \sin\psi)$. The primes in these equations indicate the derivative in z -direction for the undisturbed flow.

A Chebyshev collocation method with 100 points and a Gauss–Lobatto distribution was used to solve the stability equations (Eqs. 1–4). Stationary modes with respect to the rotating surface were characterized by the relationship $\omega = n$, while all the other disturbances that did not fulfil this requirement were considered as non-stationary modes. The wavenumber α and the eigenfunctions are determined at each x -location.

3 Experimental Set-Up

The experiments were made with a solid aluminium-alloy cone with a smooth surface finish (surface roughness of approx. $1 \mu\text{m}$). It is mounted on an air bearing to reduce vibrations and driven by an electrical motor; here all results are obtained with a rotation speed of 900 rpm. The azimuthal velocity component ($V + v$, where V is the averaged velocity and v is the deviation) was measured by a single hot-wire probe at fixed points in the laboratory frame. Further details of the measurement setup can be found in Refs. [6, 7].

To deterministically trigger the cross-flow instability 24 roughness elements were mounted uniformly in the θ -direction at $x^* = 115.7 \pm 0.5$ mm. Each roughness element has a circular shape with a diameter of 2 mm. The height was varied by layering one, two or four elements, giving $h^* \approx 4, 8$ and $17 \mu\text{m}$. Experiments without the roughness elements, denoted as the “clean cone” case, were also made.

4 Results and Discussions

First, we focus on the measurements at a constant wall height $z = 1.2$, which is close to the centre of the stationary vortices in the laminar boundary layer. In the following, the measured velocity was normalized by the local wall velocity $\Omega^* x^* \sin \psi$.

Figure 2 shows typical power-spectrum density distributions, where the left column shows data from the clean-cone case, and the right column the case with 24 roughness elements with $h^* = 8 \mu\text{m}$. The spectra of the total fluctuation v are shown in (a) and (b). The stationary component $\tilde{v}(\theta; x)$ was evaluated by phase averaging of the whole length of the sample record and the corresponding spectra are shown in (c) and (d). By subtracting the stationary modes from the total spectrum, we obtain the spectrum of the nonstationary component v' ((e) and (f)). Because n takes only integers in the physical case, ω (which, as a reminder, is defined in the laboratory frame, and is equal to the sum of n and ω in the rotating frame) of the stationary modes also takes only integer values whereas the nonstationary modes can take non-integer frequencies. Thus, Figs. 2c, d have peaks only at integer values of ω (other modes with non-integer frequencies are cancelled out after the phase averaging. The further details can be seen in Ref. [5]).

4.1 Old Problems: Stationary Modes

The stationary modes on the rotating cone are the main contributors to the fluctuations measured by the stationary hot wire. Initially, their growth in x agrees well with LLSA, i.e. disturbances grow only inside of the neutral curve, shown as a solid white line in Fig. 2c, d, below $x \approx 400$ ($20 \lesssim \omega \lesssim 28$). On the clean cone (the left column),

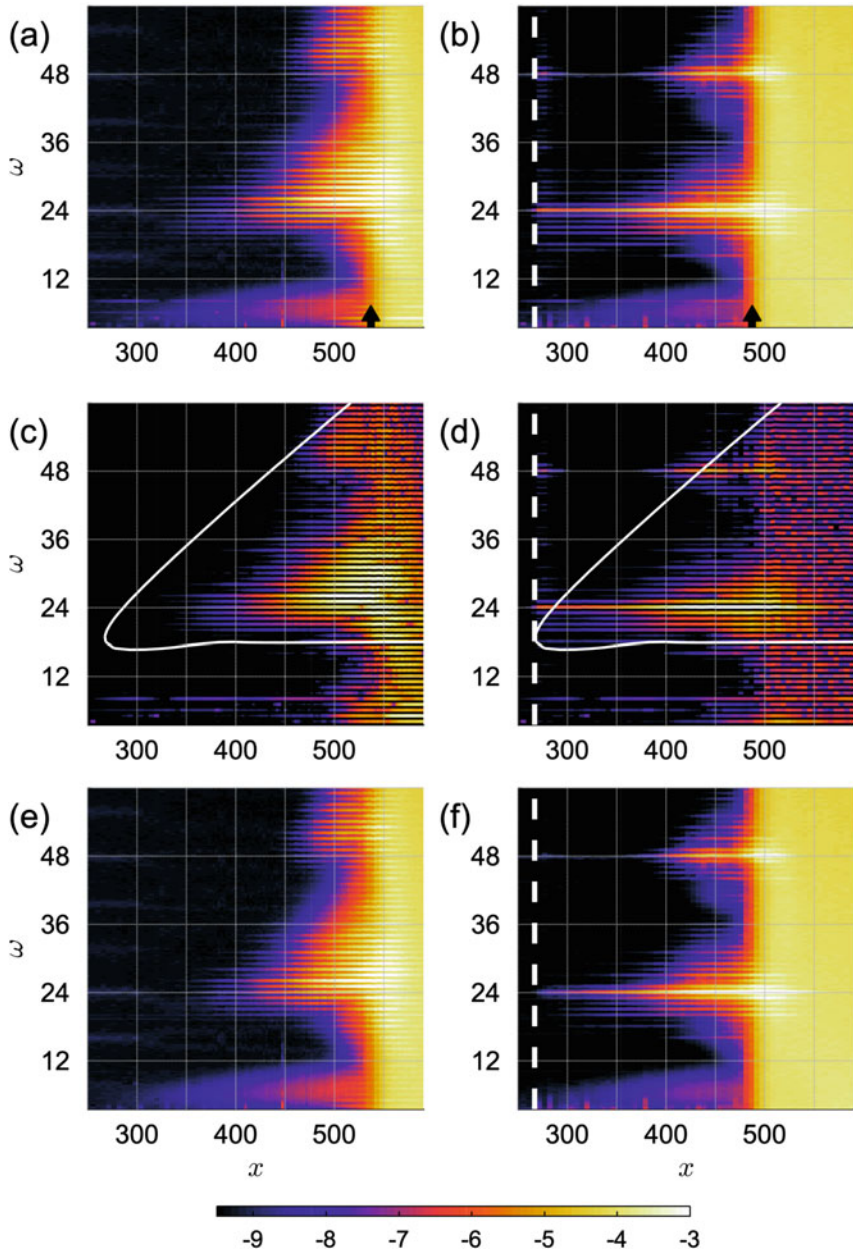


Fig. 2 Power-spectrum density distributions $\log(E)$ for the clean-cone case (left column) and cone with 24 roughness elements with a height of $h^* = 8 \mu\text{m}$ (right column): **a** and **b** total fluctuation v ; **c** and **d** stationary component \tilde{v} ; **e** and **f** non-stationary component v' . The solid white line in **(c)** and **(d)** shows the neutral curve for stationary disturbances obtained from LLSA. The dashed lines at $x = 267$ in the right column indicate the location of the roughness elements. The black arrow on the abscissa in **(a)** and **(b)** indicates the transition location [6]

the number of vortices is sensitive to random surface roughness and also changes with x . On the cone with roughness (the right column), in contrast, the roughness elements introduce the disturbance at a fixed frequency ($\omega = n = 24$) deterministically.

Further details can be seen in Fig. 3a; the rms of the stationary fundamental modes triggered by roughness of different heights as well as those of the clean case are shown as solid lines, where the fundamental frequencies are $\omega = 24$ and 26 for the cases with/without roughness elements, respectively. Only the amplitude of the stationary disturbance is affected by the roughness height and not the nonstationary one. Figure 3b shows that the measured spatial growth rates $-\alpha_i$ in the x -direction (thick lines) follow LLSA (thin lines) up to $x \approx 400$ and 450 where the fundamental mode reaches a certain magnitude ($\tilde{v}_{rms} \approx 10^{-2}$) for the cases with/without roughness.

In the range $430 \lesssim x \lesssim 525$, the fundamental mode appears to saturate in Fig. 3a when the magnitude reaches a certain amplitude ($\tilde{v}_{rms} \approx 0.05$). This is because the phase-average procedure does not take into account the vortex meandering; the high- and low-speed regions interact leading to a partial cancelling due to shift of the vortex location [7]. Just after the nonlinear saturation, the nonstationary components rapidly increase in the whole frequency range and fill up the spectra (Fig. 2). Here, we detect the rapid increases based on the spatial growth rates for each frequency. The location where the mean growth rate reaches its maximum is regarded as the transition location [6] and marked by the arrow at the bottom of Fig. 2a, b as well as Fig. 3a.

Thus, the transition process seems initially to be dominated by the amplitude of the stationary fundamental mode. The increase of roughness height shifts all processes upstream. Similar behaviours have been reported for the rotating-disk flow[1, 4].

4.2 New Challenges: Nonstationary Modes

We now focus on the growing nonstationary disturbance at $4 \lesssim \omega \lesssim 15$ in Fig. 2e, f. The disturbance develops exponentially in x (dotted lines in Fig. 3a). Also, the measured wall-normal profiles of the rms (Fig. 4) show that the nonstationary mode (open symbols) has a different wall-normal distribution as compared to the stationary mode (filled symbols).

These observations motivated further analysis. A challenge presented by our measurement technique is, however, that only the frequency ω is known; the azimuthal wavenumber n of the nonstationary mode is not known from the measurement alone.

To circumvent this problem we estimated n based on an error-minimization method compared with the growth rates obtained by LLSA. First, the spatial growth rate was calculated from the measurements using a five-point running average (applied twice) and central difference for a given frequency. An example is given in Fig. 3c; each symbol shows the measured growth rate of the nonstationary disturbance with $\omega = 7$ as a function of x for different roughness conditions. Then the growth rate was computed based on LLSA in a range of $0 \leq n \leq 20$. Among the calculated growth rates, the best fit curve that minimizes the deviation from each

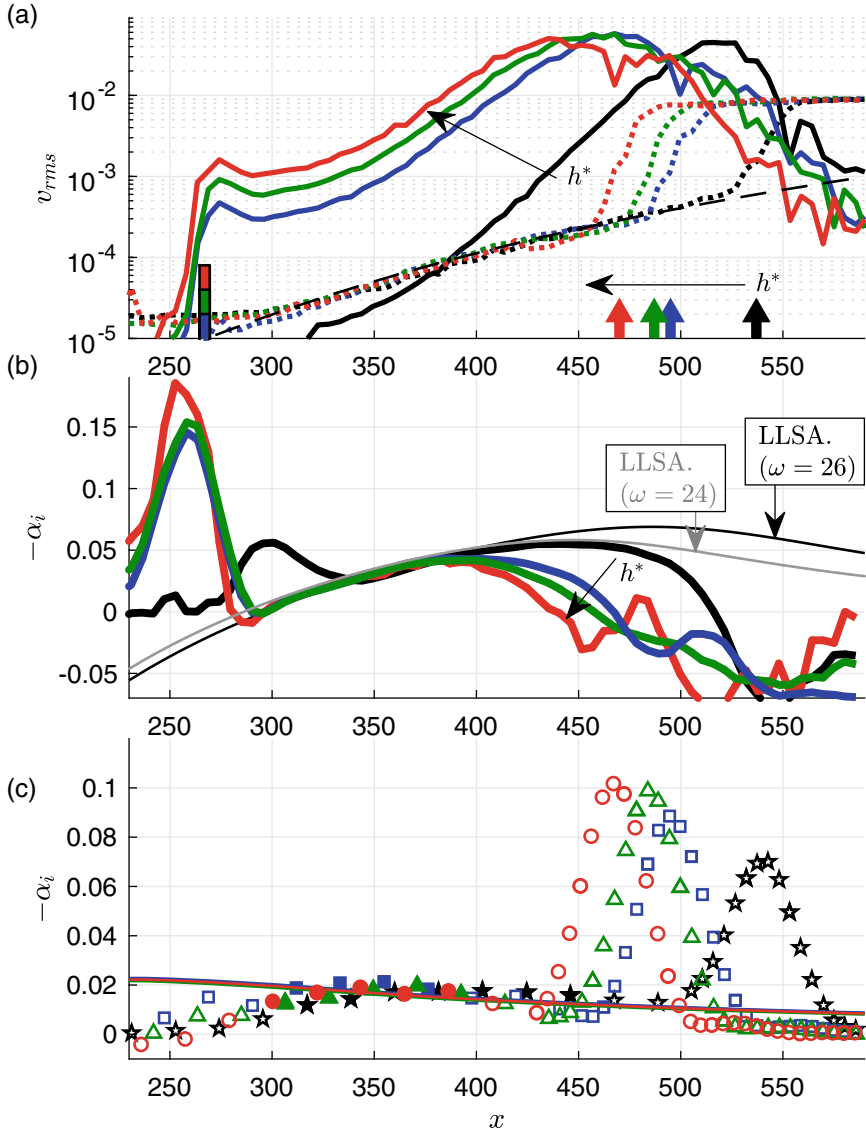


Fig. 3 **a** Root-mean square of the azimuthal velocity fluctuations of the stationary fundamental mode (solid lines) and the nonstationary mode ($\omega = 7$) (dotted lines), **b** spatial growth rate $-\alpha_i$ of the stationary fundamental mode, and **c** spatial growth rate $-\alpha_i$ of the nonstationary modes with $\omega = 7$: colour coding and symbols indicate different roughness heights: \star , clean cone; \square , $h^* = 4 \mu\text{m}$; \triangle , $h^* = 8 \mu\text{m}$; \circ , $h^* = 17 \mu\text{m}$. In **(a)** the rectangle at $x = 267$ indicates the roughness elements and the dashed line shows the estimated rms of the nonstationary mode based on LLSA ($\omega = 7$, $n = 0$). The arrows on the abscissa indicate the transition locations with different roughness heights, corresponding to the arrows in Fig. 2(a) and (b) [6]. The thin lines in **(b)** show the spatial growth rates for the stationary fundamental modes obtained by LLSA ($\omega = 24$: with roughness, $\omega = 26$: clean cone). The filled symbols in **(c)** show the data used for estimating the wavenumber n . The best fit curve from LLSA are shown by the line for each case. For all cases, the estimated n is around 0 (see the symbols at $\omega = 7$ in Fig. 5)

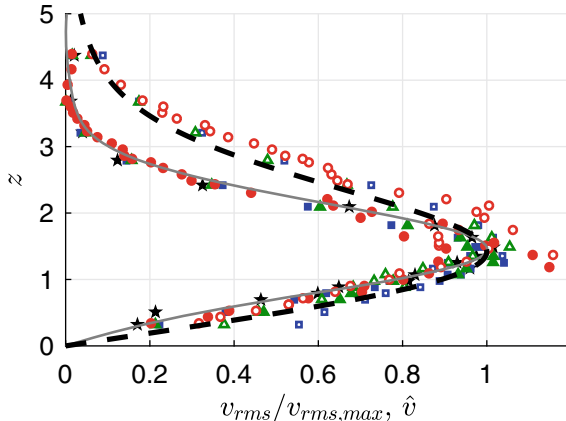


Fig. 4 Normalized rms profiles measured on the clean cone (symbols) and eigenfunctions \hat{v} of LLSA for stationary (solid line: $\omega = n = 26$) and nonstationary modes (dashed line: $\omega = 7, n = 0$): the filled and opened symbols indicate stationary and nonstationary modes at different x -locations: \star , $x = 330$; \square , $x = 386$; Δ , $x = 423$; \circ , $x = 461$. Rms is normalized by the local maximum $v_{rms,max}$, which was determined by a least square fit around the peak

measured growth rate was chosen and plotted as the line in Fig. 3c. n having the best fit growth rate was taken as the wavenumber of the nonstationary mode for the specified ω . For the fitting, we used only a limited range of the measured data (filled symbols) having a proper magnitude that is beyond resolution and noise limits but smaller than where nonlinear effects are apparent. For example, the nonstationary disturbance with $\omega = 7$ begins to have a measurable magnitude ($\approx 2 \times 10^{-5}$) at $x \approx 300$ as shown in Fig. 3a. Also, the nonlinearity appears at $x \approx 400$ and 450 for the cases with/without roughness as mentioned in Sect. 4.1. Thus, the data in the range $300 < x < 400$ and $300 < x < 450$ were used for the cases with/without roughness. The estimated growth rates (lines) agree with the measured values (filled symbols: in these regions, only every fourth measured point is shown for ease of visibility) and also collapse on to a single curve with different roughness conditions.

We repeated the above-mentioned process in the range $7 \leq \omega \leq 11$ and compare the estimated combinations of (n, ω) with LLSA. Figure 5 shows the spatial growth rate as a function of (n, ω) . The dotted line at $\omega = n$ indicates the stationary modes; The upper ($\omega > n$) and lower ($\omega < n$) regions indicate nonstationary modes travelling faster and slower than the cone surface, respectively. The neutral curve shown by the thick red line indicates that the flow first becomes unstable at $x \approx 100$, $n = 0$, and $\omega \approx 4 - 5$ in (a). As x increases, the unstable region extends and the most unstable frequency increases (for example, $\omega \approx 11$ at $n = 0$ in (f)). The estimated nonstationary modes are plotted with the same symbols as in Fig. 3c. They are mostly located in the unstable region in Fig. 5c–e. Especially, the estimated disturbance with $(n, \omega) = (0, 7)$ captures well the most unstable nonstationary mode in

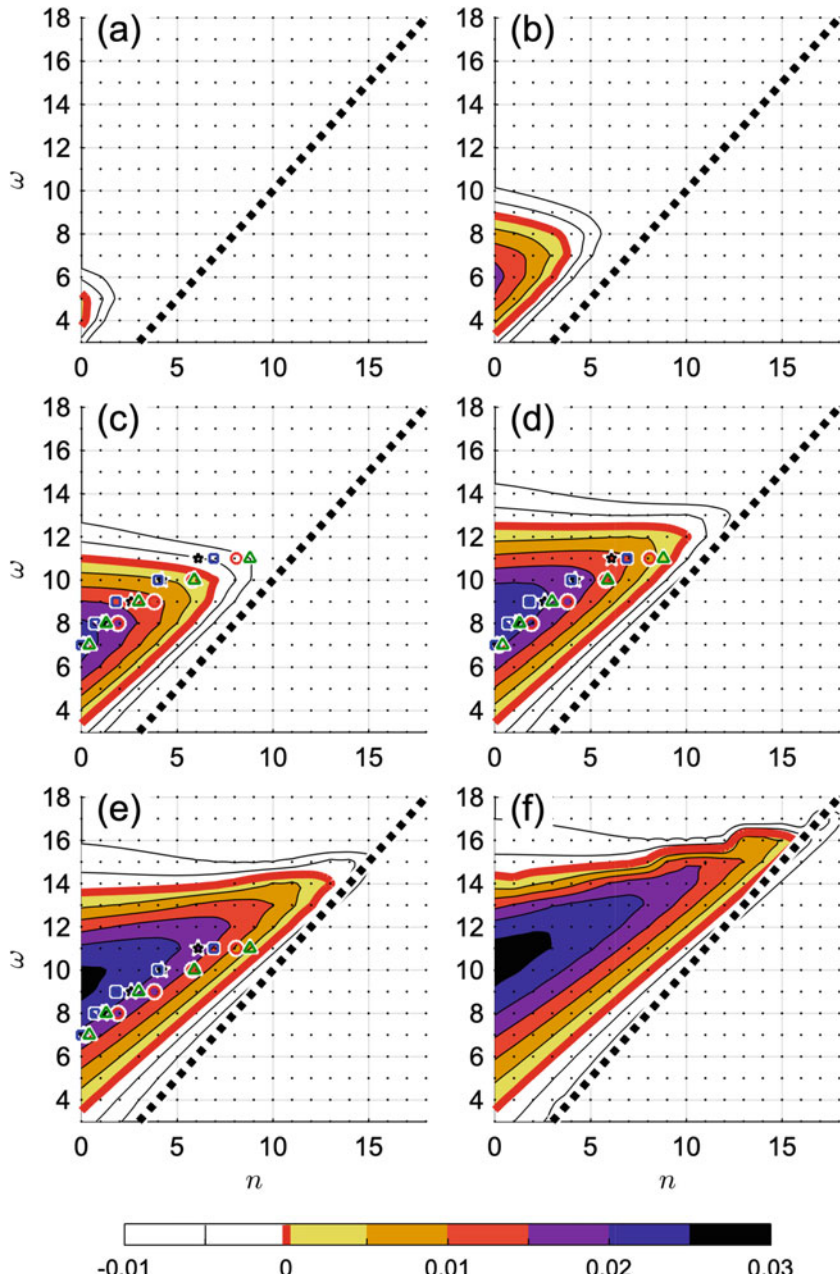


Fig. 5 Spatial growth rate at different x -locations: **a** $x = 106$, **b** $x = 161$, **c** $x = 217$, **d** $x = 272$, **e** $x = 328$, **f** $x = 383$. The thick red line indicates the neutral curve ($-\alpha_i=0$). The dotted line at $\omega = n$ indicates the stationary mode. The markers in (c), (d) and (e) show the nonstationary modes estimated from the measurements, corresponding to the lines similar to those in Fig. 3c. The symbols correspond to those in Fig. 3c. Small dots indicate the results of LLSA

Fig. 5c although the variation of estimated n among the different roughness conditions increases as ω increases (due to less measured data, restricted by the resolution/noise limits).

5 Summary and Discussion

We have reported results showing the growing stationary and nonstationary modes observed in hot-wire measurements on a broad rotating cone ($\psi = 60^\circ$). The stationary fundamental mode, triggered by surface roughness, develops according to LLSA until it reaches a certain magnitude. The saturation of the nonlinear development leads to vortex collapse and transition. Thus, transition seems to be triggered by the amplitude of the stationary fundamental mode (Fig. 3).

The observed nonstationary disturbances are evaluated through comparison with the growth rate obtained by LLSA. The azimuthal wavenumber n was estimated based on an error-minimization method. For frequencies where there are enough data points to make an accurate comparison of the growth rate such as $\omega = 7$, one obtains approximately the same n independently of the surface roughness height. The estimated combinations of (n, ω) agree with the unstable region (Fig. 5).

The estimated most unstable nonstationary mode $(n, \omega) = (0, 7)$ well explains the observed results; development (dashed line) in Fig. 3a as well as the eigenfunction (dashed line) in Fig. 4 show good agreement with measurements.

Figure 3a shows that the nonstationary mode develops according to LLSA up to its sudden growth at the transition point (marked by arrows and peaks in Fig. 3c), and seems to be little affected by the nonlinearity of the stationary mode and surface condition. In the present work, the nonstationary mode has much smaller amplitude near the transition than the stationary mode and the amplitudes are nearly the same for all surface conditions. The transition is dominated in large part by the amplitude of the stationary fundamental mode. However, it is not clear that would remain true if the nonstationary mode were preferentially excited to have larger amplitude. Also, further investigations are needed to clarify the relation between the nonstationary mode and ring-like vortex structure that is dominant on sharper cones due to the centrifugal instability [3, 8, 9] as well as how these nonstationary modes behave as ψ decreases.

Acknowledgements This work was supported by the Swedish Research Council through the ASTRID project (VR Contract No. 2013-5786).

References

1. Appelquist, E., Schlatter, P., Alfredsson, P.H., Lingwood, R.J.: Transition to turbulence in the rotating-disk boundary-layer flow with stationary vortices. *J. Fluid Mech.* **836**, 43–71 (2018)
2. Garrett, S.J., Hussain, Z., Stephen, S.O.: The cross-flow instability of the boundary layer on a rotating cone. *J. Fluid Mech.* **622**, 209–232 (2009)
3. Hussain, Z., Garrett, S.J., Stephen, S.O.: The centrifugal instability of the boundary-layer flow over slender rotating cones. *J. Fluid Mech.* **755**, 274–293 (2014)
4. Imayama, S., Alfredsson, P.H., Lingwood, R.J.: Experimental study of rotating-disk boundary-layer flow with surface roughness. *J. Fluid Mech.* **786**, 5–28 (2016)
5. Imayama, S., Alfredsson, P.H., Lingwood, R.J.: On the laminar-turbulent transition of the rotating-disk flow: the role of absolute instability. *J. Fluid Mech.* **745**, 132–163 (2014)
6. Kato, K., Alfredsson, P.H., Lingwood, R.J.: Boundary-layer transition over a rotating broad cone. *Phys. Rev. Fluids* **4**, 071902 (2019)
7. Kato, K., Kawata, T., Alfredsson, P.H., Lingwood, R.J.: Investigation of the structures in the unstable rotating-cone boundary layer. *Phys. Rev. Fluids* **4**, 053903 (2019)
8. Kobayashi, R.: Review: laminar-to-turbulent transition of three-dimensional boundary layers on rotating bodies. *ASME J. Fluids Eng.* **116**(2), 200–211 (1994)
9. Kobayashi, R., Izumi, H.: Boundary-layer transition on a rotating cone in still fluid. *J. Fluid Mech.* **127**, 353–364 (1983)
10. Segalini, A., Camarri, S.: Flow induced by a rotating cone: base flow and convective stability analysis. *Phys. Rev. Fluids* **4**, 084801 (2019)

An Experimental Investigation of the Effects of Wires and Forward-Facing Steps on the Laminar-Turbulent Transition of a Sucked Boundary Layer



Jeanne Methel, Maxime Forte, Olivier Vermeersch, and Grégoire Casalis

1 Introduction

While air traffic volume is projected to increase, the aviation industry is also faced with the need to reduce its fuel consumption for environmental sustainability, leading to a renewed interest in laminar flow control (LFC) research. One LFC technology consists in stabilizing the boundary layer using wall suction, most commonly through a micro-perforated suction panel or porous wall. Applying wall suction on a boundary layer increases its mean velocity profile curvature (and therefore its stability), and redistributes the disturbance energy closer to the wall where there is higher viscous dissipation. As a result, the growth of boundary layer instabilities is reduced and transition is delayed.

This technology has proven effectiveness as shown through numerous experimental investigations (Ref. [1, 2]) and numerical studies (Ref. [3–5]); however, attempts to develop a simple approach, such as the e^N method, on results from HLFC flight tests (Ref. [6]) were unsatisfactory in providing accurate transition prediction. Based on these studies, wall suction modeling still requires sophisticated numerical tools (Ref. [7]) that cannot easily be incorporated in the aircraft design cycle.

J. Methel (✉) · M. Forte · O. Vermeersch
ONERA/DMPE, Université de Toulouse, 31055 Toulouse, France
e-mail: Jeanne.Methel@onera.fr

M. Forte
e-mail: Maxime.Forte@onera.fr

O. Vermeersch
e-mail: Olivier.Vermeersch@onera.fr

G. Casalis
ISAE-Supaero, Université de Toulouse, 31055 Toulouse, France
e-mail: Gregoire.Casalis@isae-supapro.fr

In addition to this issue, current manufacturing techniques do not allow to conceive the implementation of a wall suction technology without introducing surface defects (e.g., gaps, forward- and backward-facing steps) at the junction between the porous and solid wall regions. Surface defects generally tend to destabilize the boundary layer either by modifying local receptivity, further amplifying existing instabilities or changing the mean flow stability by introducing inflection points in the mean velocity profile because of the small separation bubbles that can form around a defect. Transition criteria were also determined for surface defects such as gaps, forward- and backward-facing steps on “natural” boundary layers, i.e., without suction (Ref. [8, 9]). However, experimental data are currently not available in the open literature to determine whether or not a boundary layer with suction behaves similarly to one without suction in the presence of a surface defect. Additional investigations are therefore required to further understand the combined effects of wall suction and surface defects on boundary layer stability. With this additional information, transition prediction models can then be modified to account for this interaction more accurately.

The objective of the present study is therefore to perform an experimental characterization of the combined effects of surface defects (wires and forward-facing steps) and wall suction on the laminar-turbulent transition of a boundary layer in two-dimensional incompressible flow. First the experimental facility in which the present investigation was performed is presented, followed by a brief description of the stabilizing effects of wall suction in the smooth (no defect) case. Finally, the combined effects of surface defects and wall suction are characterized both experimentally and numerically.

2 Experimental Facility

This study was conducted in the ONERA TRIN 2 subsonic wind tunnel, shown in Fig. 1, operating at local atmospheric conditions. Test section speeds range from 20 m.s^{-1} to 50 m.s^{-1} , corresponding to equivalent unit Reynolds numbers between $1 \cdot 10^6 \text{ m}^{-1}$ and $3 \cdot 10^6 \text{ m}^{-1}$. In the present study, all measurements were performed at the single nominal unit Reynolds number of $2.6 \cdot 10^6 \text{ m}^{-1}$.

This facility is suited to laminar-turbulent transition experiments because the test section is decoupled from the driving fan located at the wind tunnel exhaust by a noise-reduction chamber (not shown in Fig. 1). The purpose of this chamber is to prevent pressure waves from the fan from propagating upstream into the test section. All the walls, floor and ceiling of the noise-reduction chamber are lined with foam and a partition obstructs the flow path between the diverging nozzle exit and the wind tunnel exhaust to create an additional obstacle to the upstream-travelling pressure waves from the fan. The resulting freestream turbulence levels, although dependent on test section speed, are consequently always below 0.18% (evaluated over frequencies ranging from 3 Hz to 10 kHz).

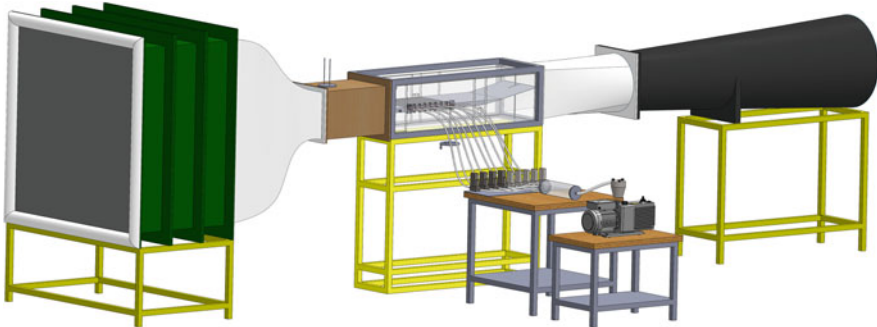


Fig. 1 Overview of the ONERA TRIN 2 subsonic wind tunnel facility

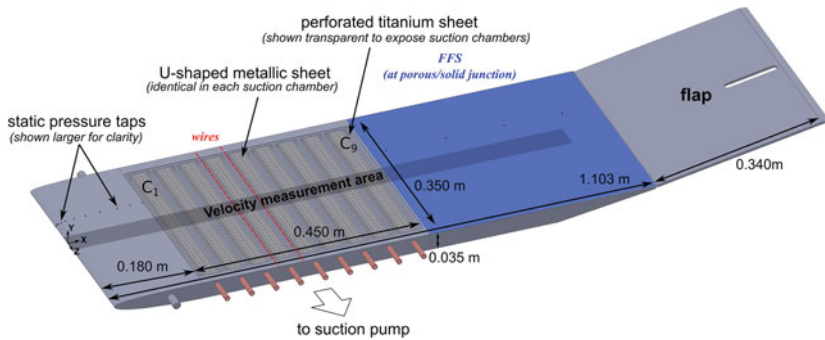
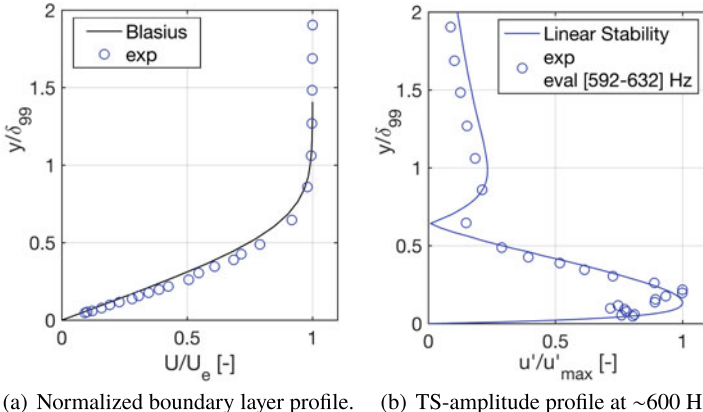


Fig. 2 Overview of the flat plate and flap with all wires positions and one FFS position

A flat plate model with a numerically-optimized leading edge was mounted, spanning the entire width of the test section (0.4 m) and with total length of 1.10 m. The suction region starts 0.18 m from the leading edge and is divided in nine suction chambers, each 0.048 m (x) long by 0.019 m (y) deep and separated by 0.002 m (x) stringers, totaling in a streamwise length of approximately 0.450 m. Additionally, the suction region is 0.350 m (z) in the spanwise direction. Chamber C1 is closest to the leading edge, while chamber C9 is furthest downstream. A general layout of the flat plate with the suction region and the coordinate system is given in Fig. 2. Further details about the facility and model can be found in Ref. [10].

The flat plate and flap angles of attack were set to have as close as possible to a zero pressure gradient over the entire plate's length (excluding the leading edge region) to obtain Blasius flow on the upper side. The presence of two-dimensional flow was also verified. The relatively low free-stream turbulence of the wind tunnel coupled to the flat plate with zero pressure gradient indicated that the traditional path to transition mainly driven by the linear amplification of primary modes, as defined by Ref. [11], would occur. Experimental verification confirmed that transition was indeed the result of the linear amplification of Tollmien-Schlichting (TS) waves, as



(a) Normalized boundary layer profile. (b) TS-amplitude profile at ~ 600 Hz.

Fig. 3 Boundary layer and TS profiles at $x = 558$ mm and $\delta_{99} = 2.43$ mm

shown on Fig. 3. In this figure, the profiles are acquired over the flat plate (with a solid panel over the suction region) at a streamwise position 558 mm from the leading edge. At this position, located upstream of the transition position (at x equal to 740 mm, corresponding to a transition Reynolds number of $1.92 \cdot 10^6$), the TS instabilities are amplified enough to be identified, as shown in Fig. 3a. The experimental profile (evaluated by integrating the velocity fluctuations spectrum over chosen frequencies) shows relatively good agreement with the eigenfunction of the streamwise velocity fluctuations, as calculated by Linear Stability Theory (LST).

3 Suction Parameters and Reference Smooth Configurations

In the present investigation, the nine chambers of the suction region are sealed with a 0.9 mm-thick micro-perforated titanium sheet. The perforations have a $90 \mu\text{m}$ diameter and are evenly spaced in a square pattern of dimensions 1.6 mm by 1.6 mm. The resulting porosity, defined as the ratio of the open area to the total surface of the sheet, is approximately 0.26%. Each suction chamber is connected to its corresponding mass flow meter-controller, and for all configurations the total suction mass flow rate was kept constant at 0.4 g.s^{-1} while only suction distribution changed.

Four suction configurations were chosen. The first one is *no suction*, where the boundary layer is simply in contact with the porous panel mounted over the chambers but the valves of all mass flow meters are closed. The next configurations with suction are C1/0.400, with all 0.4 g.s^{-1} are concentrated on chamber C1; C3,5/0.200, where suction is equally divided in 0.2 g.s^{-1} over chambers C3 and C5; and finally, *full suction* where suction is distributed over the entire suction region (equivalent to 0.044 g.s^{-1} per chamber).

Table 1 Transition positions for all suction cases with respect to the different panel porosities

	$p = 0.26\%$	$p = 0\%$
Suction case	Re_{xT} [-]	Re_{xT} [-]
No suction	$1.66 \cdot 10^6$	$1.92 \cdot 10^6$
C1/0.400	$2.20 \cdot 10^6$	N/A
C3,5/0.200	$2.30 \cdot 10^6$	N/A
Full suction	$2.30 \cdot 10^6$	N/A

For each of these suction configurations in the smooth case (no surface defect), the transition Reynolds number are given in Table 1. The transition position is defined as the location where streamwise velocity fluctuations start to increase past a threshold slope value, based on streamwise hot-wire traverses at a constant altitude from the flat plate surface. As expected, the results in the table show that wall suction effectively delays the onset of transition with respect to the *no suction* configuration. In agreement with results from Ref. [4], the suction distribution also influences transition position, with configuration C1/0.400 being slightly less effective than C3,5/0.200 and *full suction*. Since the boundary layer evolves spatially in the streamwise direction, the TS instabilities are also at different stages of development. Consequently, although the C1/0.400 case has the largest local suction velocity, suction here does not seem to be applied at the streamwise position that will most effectively influence the TS instabilities. Additionally, the presence of a porous wall without suction seems to destabilize the boundary layer since the *no suction* transition for the porous panel occurs upstream of that of the solid wall panel. This effect is related to the wall impedance and is discussed in more details in Ref. [12].

4 Combined Effect of Surface Defects and Suction on Transition

In this section, the effects of wall suction combined with either wires or FFS are first characterized experimentally, and then further discussed with a numerical analysis based on linear stability theory.

4.1 Experimental Characterization

The two types of positive surface defects that were tested were wires and FFS, which can both be characterized by their relative diameter or height h with respect to the local boundary layer thickness. Wires were tested first because of their ease of installation. Next, FFS with a rectangular edge were then mounted to investigate

Table 2 Local boundary layer displacement thickness and relative heights of selected wires

x_{SD} [mm]	Wire diameter, h [μm]	δ_1 [μm] at x_{SD} (from 3C3D)					No suction h/δ_1	\sim Mean (h/δ_1) (for ref)
		No suction	C1/ 0.400	C3,5/ 0.200	Full suction			
330	100	605	569	547	585	0.17	~0.2	
430	300	692	665	611	663	0.43	~0.5	

surface defects that were more representative of those found on aerodynamic surfaces. Although results from all the tested wires and FFS are discussed, Tables 2 and 3 give the local boundary layer displacement thickness (calculated using ONERA's in-house boundary layer code) at the defect location (x_{SD}) along with the corresponding relative height for selected wires and FFS, which are of particular interest. The general location of these selected defects is also shown on Fig. 2.

The transition Reynolds numbers Re_{xT} for each suction configuration and for all tested wires and FFS are summarized in Fig. 4a, b, respectively. For the wires, the data were compared to reference data by Ref. [13] and show relatively good agreement in terms of absolute values of the transition Reynolds with the *no suction* case. For the configurations with suction, regardless of the distribution, Re_{xT} is effectively delayed with respect to *no suction* for wires with relative heights below 0.4; however, past this threshold value, all configurations then collapse onto Tani's reference curve and transition actually occurs at the wire location. Regardless of whether or not suction was applied, the wire's critical relative height is therefore approximately equal to 0.4.

For the FFS, the experimental data from the present study are compared to data from Ref. [14]. In this case, no good agreement is found between the two studies, which can be attributed to two main reasons. The first is due to the difference in freestream turbulence levels between the two wind tunnel facilities used, as can be seen by the varying Re_{xT} in the smooth case ($h/\delta_1 = 0$) from the Wang and Gaster data and the *no suction* configuration in this study. The second is related to different various positions of the FFS on the flat plate models, as highlighted by the horizontal lines on Fig. 4b. Even in the framework of the present study, the data points from the FFS that were tested at two different streamwise positions (x equal to 430 mm and 640 mm from the leading edge) do not collapse.

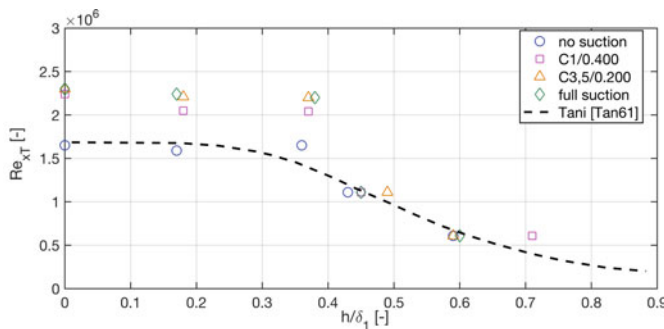
To enable comparisons between the different suction configurations to surface defects with similar values of h/δ_1 , a non-dimensional parameter Δ_{xT} was then introduced in Fig. 5 and is defined as:

$$\Delta_{xT} = \frac{Re_{xT,SD} - Re_{x,SD}}{Re_{xT,noSD} - Re_{x,SD}} = \frac{x_{T,SD} - x_{SD}}{x_{T,noSD} - x_{SD}}. \quad (1)$$

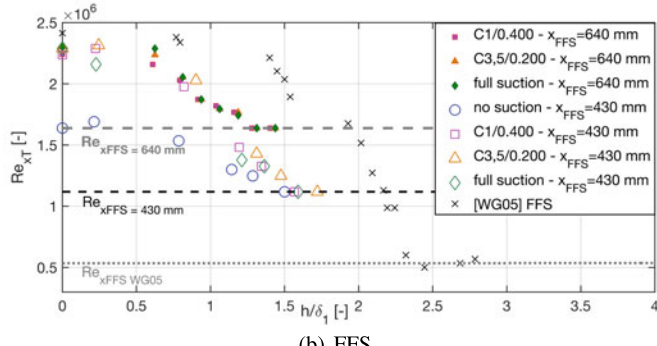
Since this parameter is used for both types of surface defects, the subscript "SD" is general and stands for "Surface Defect". For any given suction configuration

Table 3 Local boundary layer thickness and relative heights of selected FFS at $x_{FFS} = 640$ mm

	$x_{FFS} = 640$ mm				
	No suction	C1/0.400	C3,5/0.200	Full suction	
δ_1 (3C3D) [μm]	840	820	800	800	
FFS h [μm]	h/δ_1				\sim Rounded h/δ_1
500	0.60	0.61	0.63	0.63	\sim 0.6
850	1.01	1.04	1.06	1.06	\sim 1.0
1150	1.37	1.40	1.44	1.44	\sim 1.4



(a) Wires



(b) FFS

Fig. 4 Transition Reynolds Number as a function of h/δ_1 for wires and FFS

(and panel whenever indicated), variables $Re_{xT,SD}$ and $Re_{xT,noSD}$ correspond to the transition Reynolds number with and without a surface defect respectively, and $Re_{x,SD}$ corresponds to the location of the surface defect. The parameter Δ_{xT} can be used as an indicator of the relative change in transition position due to the presence of a surface defect, using the roughness element position as the reference. When

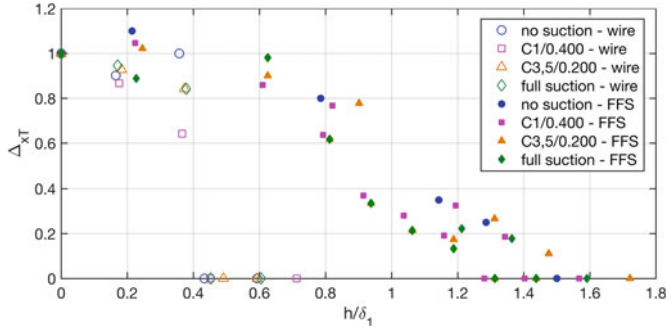


Fig. 5 Comparison of the Δ_{xT} parameter for all wires and FFS

Δ_{xT} is equal to 1, the surface defect has no effect on transition whereas when Δ_{xT} is equal to zero, transition occurs at the location of the surface defect.

Using the Δ_{xT} parameter on the wire data, the critical relative height of 0.4 is clearly identified. Additionally, the critical relative height for the FFS can now also be found and is approximately equal to 1.3, regardless of suction configuration and step location.

In order to understand the effect of each type of defect (both subcritical and critical), the power spectral densities (PSD) of the streamwise velocity fluctuations u' slightly upstream of the corresponding transition position, along with the mean velocity boundary layer profiles 1 mm downstream of the respective defect, are shown in Fig. 6.

In Fig. 6a, the Tollmien-Schlichting instabilities can be identified as the band of amplified frequencies between 400 Hz and 800 Hz in the *no suction smooth* configuration. Similarly, close to their respective transition position, the PSD for the subcritical wire and FFS exhibit the same band of amplified frequencies, indicating that transition is still the result of the linear amplification of Tollmien-Schlichting instabilities. Although in these subcritical cases, *full suction* effectively delays the transition position with respect to *no suction*, the transition mechanism is also unchanged. Immediately downstream of the subcritical defects, Fig. 6b shows that, for each type of defect, the profiles overlap well between the two suction configurations, which seems to indicate that at this location, the effect of the surface defect on the mean flow is larger than that of suction.

In contrast, in the critical case, the transition mechanism of each type of defect is different. In the case of the critical FFS (here $h/\delta_1 = 1.4$), the band of amplified frequencies between 400 Hz and 800 Hz that is characteristic to the Tollmien-Schlichting instabilities can be identified in the PSD of u' taken slightly upstream of the transition position, as shown in Fig. 6c. On the other hand, the PSD of u' for the critical wire only exhibits a band of amplified frequencies between 2 kHz and 3 kHz. Upon closer inspection of the mean velocity boundary layer profiles immediately downstream of the critical wire, a well-defined inflection point can be observed. In

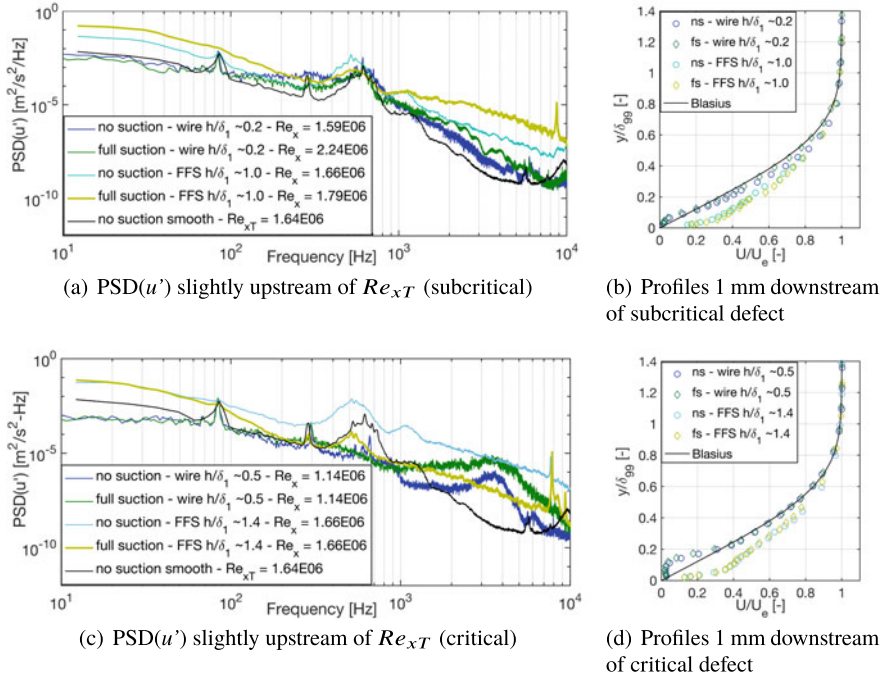


Fig. 6 Boundary layer profiles 1 mm downstream of defects and PSD(u') for subcritical and critical wires and FFS

this case, the transition mechanism has switched from being driven by viscosity to being an inflection-point instability.

4.2 Numerical Analysis

The fact that the transition mechanism for the FFS tested in this study remained unchanged and that the range of subcritical FFS h/δ_1 is between 0 and 1.3 warrants the use of the ΔN approach. The first step to determine the ΔN values for all experimental test cases is using LST, to evaluate the maximum N factor envelope curve for the smooth case and for each suction configuration. The N_T is then determined based on the experimental transition position, and is assumed to be constant for a given suction configuration. Next the N factor at the transition position with a surface defect, $N_{xT,FFS}$ is determined using the same maximum N factor envelope curve. The ΔN is then defined as:

$$\Delta N = N_{T,smooth} - N_{xT,FFS}. \quad (2)$$

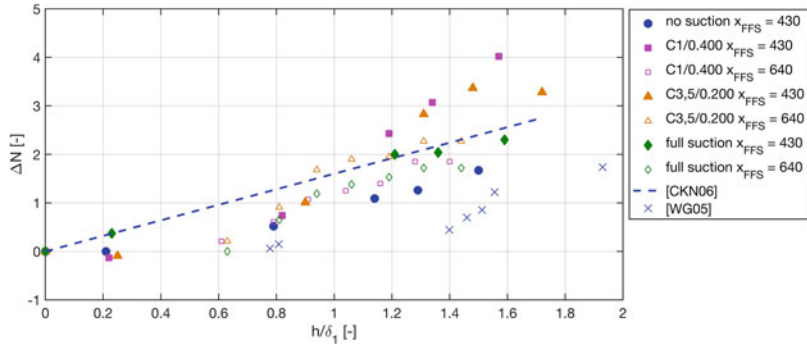


Fig. 7 All suction configurations with FFS compared with ΔN model for FFS from Ref. [15] and with measurements from Ref. [14]

The ΔN values from the present data are plotted and compared to data sets on solid panels (i.e., without suction), both experimental by Ref. [14] and numerical by Ref. [15], in Fig. 7. Good agreement is found between the data from the literature and *no suction*, which is the most comparable case. Data from the suction configurations with x_{FFS} at 640 mm seem to match the [CKN06] model relatively well. On the other hand, for the upstream FFS position, the suction configurations have ΔN values that significantly diverge from both of the curves labeled [WG05] (for Ref. [14]) and [CKN06] (for Ref. [15]).

5 Conclusion

An experimental investigation on the effects of wall suction combined to FFS and wires was carried out. For subcritical defect relative heights, wall suction was still found to be effective in delaying transition, albeit less effectively than in the smooth case configuration. However, the dimensions of the critical surface defects (where transition occurs at the defect location) were unchanged, regardless of whether or not suction was applied. The local change in boundary layer thickness under the influence of wall suction was therefore not significant enough to modify critical dimensions. Finally, existing ΔN model and data for FFS were in relatively good agreement with ΔN values from the present study, supporting the use of this approach for FFS both with and without suction.

References

1. Joslin, R.D.: Overview of laminar flow control. NASA/TP-1998-208705 (1999)
2. Braslow, A.L.: A history of suction-type laminar flow control with emphasis on flight research. Mon. in Aero. Hist. **13**, (1999)
3. Reed, H.L., Nayfeh, A.H.: Numerical-perturbation technique for stability of flat-plate boundary layers with suction. AIAA Journal **10**(2514/3), 9247 (1986)
4. Casalis, G., Copie, M.-L., Airiau, C., Arnal, D.: Nonlinear analysis with PSE approach. IUTAM Proc. (1996). https://doi.org/10.1007/978-94-009-1700-2_23
5. Zahn, J., Rist, U.: Study About Boundary-Layer Suction at a Juncture for Sustained Laminar Flow. New Res. in Num. and Exp. Fl. Mech. XI. (2018) https://doi.org/10.1007/978-3-319-64519-3_32
6. Schrauf, G.: Large-scale laminar flow tests evaluated with linear stability theory. Journal of Aircraft. **10**(2514/1), 9280 (2004)
7. Arnal, D., J. Reneaux, and G. Casalis: Numerical and experimental studies related to skin friction drag reduction problems. Proceedings of *Transitional Boundary Layers in Aeronautics* (1996)
8. Nenni, J.P., Gluyas, G.L.: Aerodynamic design and analysis of an LFC surface. Astronautics & Aeronautics **4**(7), (1966)
9. Béguet, S., Perraud, J., Forte, M., Brazier, J.-P.: Modeling of Transverse Gaps Effects on Boundary-Layer Transition. Journal of Aircraft **10**(2514/1), c033647 (2016)
10. Methel, J., Forte, M., Vermeersch, O., Casalis, G.: An experimental study on the effects of two-dimensional positive surface defects on the laminar-turbulent transition of a sucked boundary layer. Exp. in Fluids (2019). <https://doi.org/10.1007/s00348-019-2741-2>
11. Morkovin, M.V., Reshotko, E., Herbert, T.: Transition in open flow systems-a reassessment. Bull. Am. Phys. Soc. **39**, (1994)
12. Methel, J.: An experimental investigation on the effects of surface imperfections on the laminar-turbulent transition of a boundary layer undergoing wall suction. PhD Dissertation (2019)
13. Tani, I.: Effect of two-dimensional and isolated roughness on laminar flow. Bound. Layer and Flow Cont. (1961). <https://doi.org/10.1016/b978-1-4832-1323-1.50004-x>
14. Wang, Y.X., Gaster, M.: Effect of surface steps on boundary layer transition. Bound. Exp. in Fluids (2005). <https://doi.org/10.1007/s00348-005-1011-7>
15. Crouch, J.D., Kosorygin, V.S., Ng, L.L.: Modeling the effects of steps on boundary-layer transition. IUTAM Proc. (2006). https://doi.org/10.1007/1-4020-4159-4_4

Control of Unsteady Görtler Instability Modes by Steady Görtler Vortices



D. A. Mischenko, V. I. Borodulin, A. V. Ivanov, and Y. S. Kachanov

Abstract The paper presents the first results of an experimental study of a new effective control mechanism of evolution of fast-growing unsteady Görtler modes by modifying the base flow (the boundary layer on a concave surface) by means of quasi-steady (physically steady) Görtler vortices of finite amplitude. It is found that this mechanism is able to strongly suppress growth rates of the disturbances under control. The suppression efficiency depends on the phase relations between the control and controlled perturbations, but does not depend on amplitudes of the latter.

1 Introduction

The Görtler instability is widespread in various shear flows with curved streamlines at sub-, super-, and hypersonic speeds. The instability is caused by centrifugal force whose action is essentially nonuniform in the cross-flow direction due to presence of a strong cross-flow mean-velocity gradient. It leads to the appearance of specific streamwise oriented vortices (called Görtler vortices), which can grow downstream, significantly change the base-flow characteristics and also lead to premature flow turbulization. Recent experiments have shown that besides the traditionally considered and well known *steady* Görtler vortices, some *unsteady* Görtler modes may also exist in the flow and grow downstream [1]. It was found that these unsteady perturbations can be efficiently excited by surface vibrations [4] and by weak unsteady

D. A. Mischenko (✉) · V. I. Borodulin · A. V. Ivanov · Y. S. Kachanov
Khristianovich Institute of Theoretical and Applied Mechanics, Novosibirsk, Russian Federation
e-mail: misch2005@yandex.ru; D.A.Mischenko@itam.nsc.ru

V. I. Borodulin
e-mail: bo@itam.nsc.ru

A. V. Ivanov
e-mail: aniva101010@gmail.com

Y. S. Kachanov
e-mail: kachanov@itam.nsc.ru

blowing/suction [1], as well as by freestream low-frequency turbulence [2]. Recently attention has been drawn to the study of important fundamental and applied problem of the Görtler instability control. However, all present studies on control of steady [6] and unsteady [5] Görtler modes are purely theoretical. This work is devoted to the first experimental investigation of a new, not yet studied (neither experimentally nor theoretically) control mechanism of the streamwise evolution of unsteady Görtler modes through a modification of the boundary-layer flow developing over a concave wall by finite-amplitude stationary Görtler vortices. The experiments were carried out using a quasi-stationary approach similar to that developed in [1].

2 Experimental Setup

Experiments were carried out in a low-turbulence wind tunnel T-324 of ITAM SB RAS (Novosibirsk). Figure 1 shows the sketch of the high-precision experimental model with working surface of constant radius of curvature $R = 8.37$ m. The measurements in the boundary layer (which was Blasius-like, see [2]) were performed by a hot-wire probe at freestream velocity $U_e = 9.18$ m/s. The fully controlled unsteady (in general) perturbations were excited by the universal disturbance source VS-III (see below). The control mechanism under study was investigated in two independent experiments performed in years 2018 and 2019, referred to as the ‘preliminary’ and the ‘systematic’ one, correspondingly.

The preliminary experiment was devoted to the first experimental detection of the supposed control mechanism. The controlling quasi-steady Görtler vortices had dimensionless spanwise scale $\Lambda = (U_e \lambda_z / v) \cdot (\lambda_z / R)^{1/2} = 206$ and the frequency parameter $F = 2\pi f v / U_e \cdot 10^6 = 2.3$ (here $\lambda_z = 10$ mm is the dimensional spanwise wavelength, $f = 2$ Hz is the frequency and v is the kinematic air viscosity). Their amplitude at the end of the region of measurements was of about 20% of U_e .

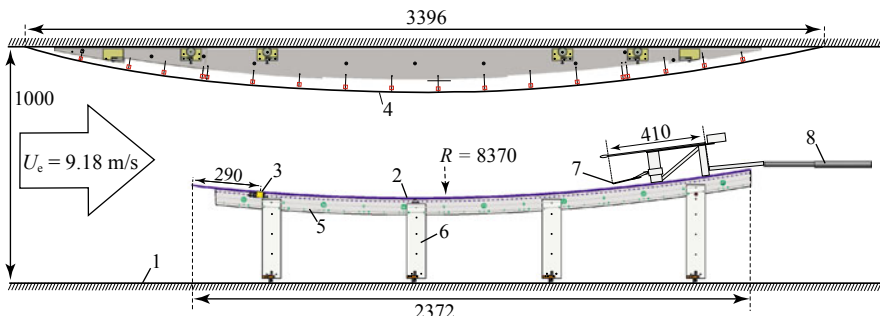


Fig. 1 Sketch of the experimental model: wind-tunnel test-section wall (1), concave surface of the experimental model (2), universal disturbance source VS-III (3), adjustable wall bump (4), frame of arch ribs (5), load-bearing members (6), hot-wire probe (7), and traversing mechanism (8). Dimensions are given in mm

Unsteady Görtler instability modes under control with $F = 5.75$ and 10.35 ($f = 5$ and 9 Hz respectively) had the same value of Λ , while their amplitudes were less than 0.5% of U_e . The measurements were carried out in paired regimes, in which unsteady Görtler instability modes developed at conditions of either *presence* (regimes ‘ON’) or *absence* (regimes ‘OFF’) of controlling quasi-steady (physically steady) Görtler vortices. Two most interesting cases of spanwise phase relationships between controlled and controlling perturbations were studied: (i) ‘in-phase’ case—when positions of amplitude maxima of the two types of disturbances coincided in the spanwise direction and (ii) ‘out-of-phase’ case—when they were shifted by 90 degrees.

Systematic experiment was devoted to a much more detailed study of the control mechanism found in the preliminary study. Nine paired (ON and OFF) *in-phase* regimes were investigated in these experiments, since the most efficient control mechanism was found to be in the in-phase case. In all studied regimes, the controlling disturbances had the same parameters: $\Lambda = 147$ ($\lambda_z = 8$ mm) and $F = 2.3$ ($f = 2$ Hz), while parameters of the disturbances under control varied and were: $\Lambda = 147, 270$, and 416 ($\lambda_z = 8, 12$ and 16 mm); $F = 5.75, 10.35$, and 14.95 ($f = 5, 9$, and 13 Hz). Relation between amplitudes of quasi-steady and essentially unsteady Görtler vortices was approximately the same as in the preliminary experiment.

Main measurements in both experiments were carried out in a range of curvilinear streamwise x -coordinate (which was directed along the concave wall) corresponding to Görtler numbers $G^* = (U_e \delta^*/\nu) \cdot (\delta^*/R)^{1/2} = 14.2\text{--}23.2$ (here δ^* is the boundary layer displacement thickness).

3 Disturbance Source

To excite the finite-amplitude controlling Görtler vortices in the boundary layer, a new disturbance source, VS-III, was created on a basis on a radical modification of the well-known disturbance source VS-II [3]. Its new electronic and software parts were developed based on the 8-channel, 16-bit DAC “R-Technology”, while the mechanical part was created using the original technology. This technology included three main stages: 1—development of a computer CAD-model of the mechanical part, 2—printing a thin shell of the source by high-quality SLS 3D-printer, and 3—filling the shell by epoxy resin. In this way the appropriate rigidity of the construction, as well as impermeability of the source body were achieved.

Two different mechanical parts of the disturbance sources were used. In the preliminary experiment, the source represented two long spanwise-oriented slits (of 1 mm width and of 1 mm depth) with a number of thin channels distributed at their bottoms with a step of 5 mm (Fig. 2a, b). The channels were connected to a block of 8 loudspeakers (placed outside the wind tunnel test section and closed with covers) by plastic tubes (of 5 m long)—pneumolines. At driving the loudspeakers by electronic part of the source, the mechanical part excited relatively weak blowing/suction fluctuations in the boundary layer, which were spanwise periodic and had a fixed desired frequency. During the experiment the two slits worked simultaneously and

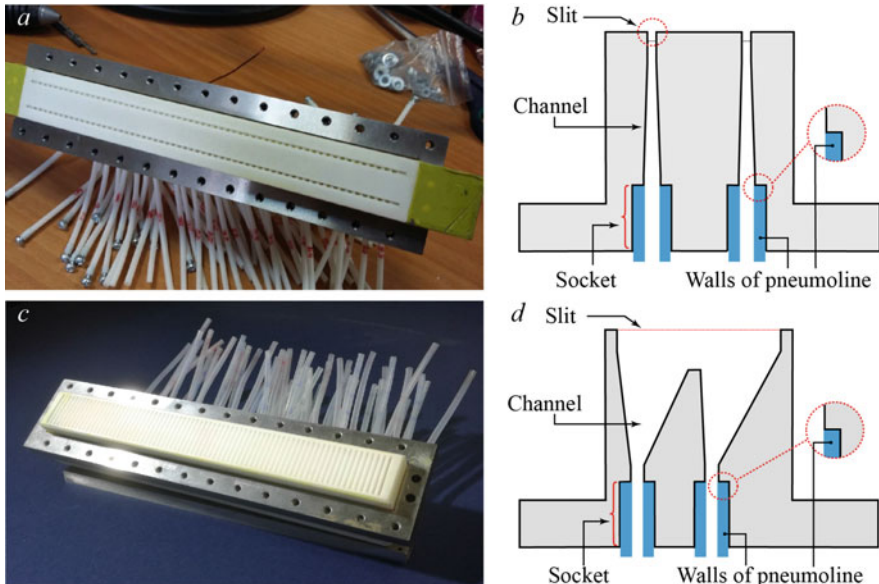


Fig. 2 **a, c**—photos of used mechanical parts of VS-III source in metal frames prepared to installation into the experimental model. **b, d**—sketches of their cross-sectional views

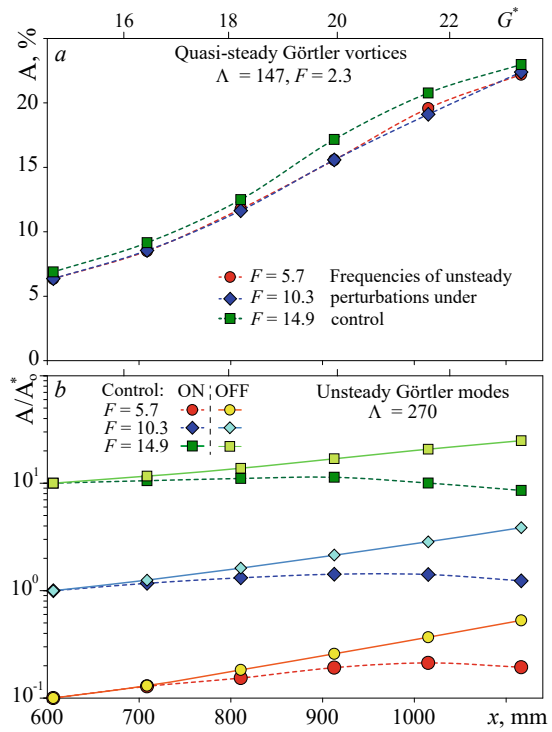
were driven by the same signals. In the systematic experiment the source worked in a similar way, but the mechanical part of the source represented a set of parallel, streamwise oriented slits with a width of 0.9 mm and a length of 16 mm, arranged in the spanwise direction with a step of 2 mm (Fig. 2c). A sketch of the source inner structure (Fig. 2d) shows, that each slit represented a uniformly narrowing channel, connected to a pair of pneumolines.

Hot-wire measurements have shown that the two new sources are capable of generating both high-amplitude (more than 10% of U_e) and low-amplitude (tenths and hundredths of a percent of U_e) *high-quality* boundary layer perturbations, which represent unsteady (in general) Görtler vortices in the disturbance source far field. As a whole, the sources are able to excite Görtler modes in a broad range of their parameters: amplitudes, frequencies and spanwise scales.

4 Main Results

Experiments showed that despite a rather high amplitudes of controlling quasi-steady perturbations and nonlinear distortion of the wall-normal profiles of the unsteady Görtler modes under control, the position of their amplitude maximum in wall-normal profiles remains at a distance to the wall corresponding approximately to $U/U_e = 0.6$ of the undisturbed boundary layer (here U is the local streamwise mean

Fig. 3 Amplification curves of controlling quasi-steady Görtler vortices (**a**) and unsteady Görtler modes under control (**b**) in presence (ON) and in absence (OFF) of controlling perturbations. Curves in plot (**b**) are normalized by some “initial” amplitudes. Systematic experiment



flow velocity). Fourier processing of the sets of spanwise amplitude and phase distributions of controlling and controlled disturbances, measured at various distances from the model leading edge in the source far field, at wall normal distance corresponding to $U/U_e = 0.6$, allowed us to obtain the amplification curves of quasi-steady and unsteady Görtler vortices in ‘ON’ and ‘OFF’ regimes (Fig. 3a, b). It is found that the presence of finite-amplitude quasi-steady perturbations leads to a strong suppression of unsteady Görtler modes’ growth rates in all in-phase regimes studied. However, it is found that the suppression effect depends on the phase relation between the controlling and controlled disturbances. In the case of equal spanwise scales of quasi-steady and unsteady Görtler vortices, the suppression effect disappears at all in the out-of-phase regimes. At the same time, it has been found that the effect of suppression of unsteady Görtler modes could be present also in case when the ratio of spanwise wavelengths of controlling and controlled disturbances is not integer. The studied control mechanism is found do not depend on the amplitude of unsteady Görtler vortices (at least in examined amplitude range).

Acknowledgements This work is supported by the Russian Science Foundation (project No. 17-71-10179).

References

1. Boiko, A.V., Ivanov, A.V., Kachanov, Y.S., Mischenko, D.A.: Steady and unsteady Görtler boundary-layer instability on concave wall. *Eur. J. Mech. B. Fluids* **29**, 61–83 (2010). <https://doi.org/10.1016/j.euromechflu.2009.11.001>
2. Borodulin, V.I., Ivanov, A.V., Kachanov, Y.S., Mischenko, D.A.: Systematic study of distributed excitation of unsteady Görtler modes by freestream vortices. *Eur. J. Mech. B. Fluids* **68**, 167–183 (2018). <https://doi.org/10.1016/j.euromechflu.2017.11.008>
3. Borodulin, V.I., Kachanov, Y.S., Koptsev, D.B.: Experimental study of resonant interactions of instability waves in self-similar boundary layer with an adverse pressure gradient: I. Tuned resonances. *J. Turbul.* **3**, 1–38 (2002). <https://doi.org/10.1088/1468-5248/3/1/062>
4. Ivanov, A.V., Kachanov, Y.S., Mischenko, D.A.: Generation of nonstationary Görtler vortices by localized surface nonuniformities. Receptivity coefficients. *Thermophys. Aeromech.* **19**(4), 523–540 (2012). <https://doi.org/10.1134/S0869864312040014>
5. Marenzi, E., Ricco, P.: Growth and wall-transpiration control of nonlinear unsteady Görtler vortices forced by free-stream vortical disturbances. *Phys. Fluids* **29**, 114106 (2017). <https://doi.org/10.1063/1.4999993>
6. Sescu, A., Taoudi, L., Afsar, M.: Iterative control of Görtler vortices via local wall deformations. *Theor. Comput. Fluid Dyn.* **32**(1), 63–72 (2018). <https://doi.org/10.1007/s00162-017-0440-2>

Transitional Intermittency in a Flat Plate Boundary Layer Subjected to Elevated Free-Stream Turbulence



Nguyen Thanh Tung and Dmitry Sboev

Abstract The results are presented of experiments on verification of the recently proposed statistical model of laminar-turbulent transition in a boundary layer subjected to elevated free-stream turbulence. It turned out to be that not all of the assumptions in this theory were completely justified. However, the most important proposition on the threshold character of the turbulent spots' generation after the streamwise streaks reached certain amplitude was confirmed in all tests.

Keywords Boundary layer · Free stream turbulence · Streamwise streaks · Intermittency

1 Introduction

A transition prediction remains one of the main problems in the physics of turbulence. It is even truer for transition under influence of elevated free-stream turbulence (FST). The empirical correlations [1] are commonly used for predictions until now. Recently Ustinov suggested [2] a new statistical theory of intermittency in a transitional boundary layer under influence of elevated FST. The present contribution is aiming to an experimental validation of this theory.

The theory is based on the assumption of Poisson process of turbulent spots generation due to a secondary instability of streamwise streaks. The laminar streaks growth is assumed as algebraic $u_{rms}^2 = cX$, where the u_{rms} is root-mean-square velocity fluctuations, the X is streamwise coordinate and c is some constant of proportionality. The streaks development is represented as the one-dimensional Gaussian random process. The streaks breakdown starts as their instant amplitude rises above some

N. T. Tung · D. Sboev (✉)
Moscow Institute of Physics and Technology (MIPT), Moscow, Russia
e-mail: t124@inbox.ru

N. T. Tung
e-mail: thanh tung.tccn@gmail.com

D. Sboev
Central Aerohydrodynamic Institute, Zhukovsky, Russia

critical value a_c . With help of the well-known result of theory of random processes for the frequency of the outliers above a_c the following relation for the intermittency function F is obtained

$$F(\gamma) = -\ln(1 - \gamma) = A Re^n \left(\frac{u_{rms}}{a_c} \right)^4 \exp \left(-\frac{a_c^2}{2u_{rms}^2} \right), \quad (1)$$

where γ is intermittency, Re is the Reynolds number based on X . The meaning of the exponent n is explained below. In this formula the u_{rms} is taken on the laminar parts of flow. The kinematic parameter A depends only on kinematic parameters of spots propagation as well as on the streak's longitudinal length scale L . In the flat plate experiment [3] it was found that L grows as square root of X

$$L = a^* X^{1/2}, \quad (2)$$

where the a^* is constant of proportionality. The theory of optimal disturbances and the linear theory of receptivity predict the linear growth of L

$$L = aX. \quad (3)$$

In the experiments [4] it was shown that the streaks' longitudinal scales evolves from the linear dependence (3) at the early stages of their development to the nonlinear one (2) at the late stages. An exponent n at the Reynolds number Re in (1) is also depends on the law of streamwise scale L , $n = 1/2$ is for the linear law and $n = 1$ for the nonlinear one.

It is useful to represent the intermittency function as

$$G = \ln \left(-\frac{F(\gamma)}{u_{rms}^4 Re^n} \right) = -\frac{1}{2} a_c^2 \left(\frac{1}{u_{rms}^2} \right) + A \frac{1}{a_c^4} \quad (4)$$

In the following the notation G will be used for the linear normalization of (4) with $n = 1/2$ and G^* for the $n = 1$ case. The constant a_c is the same for both cases. The parameters a_c , A and A^* should be determined from experiment. M.V. Ustinov has obtained the values $a_c = 0.31$ and $A = 10.4$ for the linear normalization of (3), (4) after processing of flat plate experimental data available to him.

The theory described is semi-empirical by its nature and based on the following main assumptions: the algebraic growth of streaks, their gaussianity, a definitive law of the streak's longitudinal scales and the threshold character of breakdown. All of them were checked in some details in the course of present experiments.

2 Experimental Setup

The experiments were conducted in the MIPT open return wind tunnel AT-3 at free stream velocities $U_0 = 4\text{--}14 \text{ m/s}$. The test section has octagonal cross-section, the width 800 mm and length 1200 mm. Now the wind tunnel is about 80 years old. The model was a 1.2 m long, 10 mm thick flat plate with the semicylindrical (diameter 4 mm) leading edge. The leading edge arrangement was taken from [5] due to its technological simplicity. The coordinate system used has its origin on the leading edge, X is streamwise axis, and the Y is wall-normal coordinate. The hot-wire measurements were performed with single-wire probe mounted on traverse. The movement of the wire was carried out manually along the X axis and by means of PC-controlled linear stage along Y axis.

A FST was generated by the several two-plane and woven grids installed in the slot at the beginning of the test section at the distance 200 mm from the leading edge. The grids' wire diameters d and mesh sizes M are given in the Table 1. The FST levels Tu at the leading edge ranges from 1.7–4.9%. The FST decayed downstream as X^{-b} with $b = 0.50\text{--}0.87$. The turbulence integral scale Λ was 4.9–5.9 mm in all regimes. It turned out to be difficult in this set-up to get a broad variation in Λ as it was intended initially. By the choosing of U_0 and Tu values it was possible to adjust a transition zone position over the flat plate length.

A flat plate has a flap to adjust a stagnation line on its upper side. To avoid a leading edge separation a flap was so positioned that slightly accelerated boundary layer was created with a Hartree parameter $\beta = 0.03\text{--}0.05$. This boundary layer is still close to the Blasius solution. The velocity distribution over the model was close controlled in the each regime. In Fig. 1 an example of the mean flow evolution from the laminar to turbulent state is shown. A good agreement between the measured profiles and the Falkner-Skan solution in laminar parts of flow is obvious.

Table 1 Parameters of the experiments

Regime	Grid, $d \times M$ (mm)	U_0 (m/s)	Tu (%)	β	a_c	A
R1	G1, 0.5 × 9.8	10.47	1.84	0.035	0.32	12.01
R2		11.40	1.86	0.029	0.31	12.71
R3		13.96	1.88	0.026	0.28	13.06
R4	G2, 1.7 × 14	5.70	4.00	0.032	0.35	0.89
R5		6.67	4.02	0.046	0.35	1.45
R6		10.84	3.34	0.410	0.33	5.56
R7	G3, 0.75 × 6.75	11.15	1.69	0.032	0.29	60.76
R8	G6, 1.2 × 16	3.85	3.16	0.035	0.37	14.07
R9		7.64	4.19	0.054	0.36	2.48
R10		9.74	4.55	0.028	0.35	1.02
R11		12.71	4.91	0.044	0.33	3.08

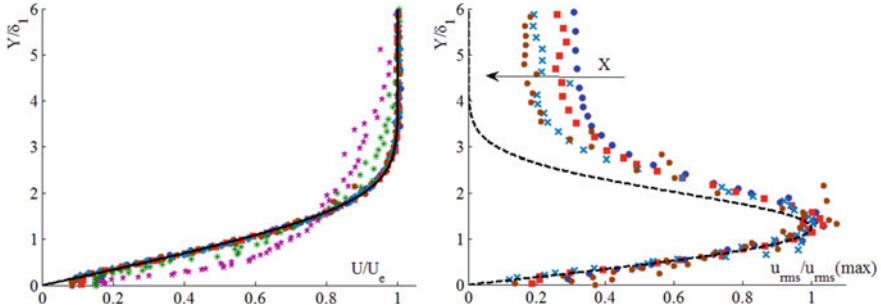


Fig. 1 The mean velocity profiles (left) and u_{rms} profiles (right) in the R2 regime. The solid and dashed lines is the Falkner-Skan solution for U and $U(dU/dY)$ respectively, $\beta = 0.029$, U_e is external velocity and δ_1 is the displacement thickness

A streaks formation is demonstrated in Fig. 1, where the profiles of the u_{rms} for the laminar parts of flow are plotted. The experimental points were smoothed by a spline and normalized with the maxima of smoothed curves. The profiles have a very characteristic bell-like shape with a single maximum in the middle part of the boundary layer. Also the curve of so called “breathing mode” $U(dU/dY)$ is plotted, which is a good representation of the theoretical streak profile. As it was expected, the agreement between the “breathing mode” and experimental profiles is good in the lower half of the boundary layer. In the upper half the influence of decaying external turbulence is seen.

For intermittency measurements a detector function was chosen in form of the envelopes of first and second derivatives of band-pass filtered signal u . Using of envelopes allows to dismiss a holding time parameter in the computations of the indicator functions. The cumulative intermittency distributions as functions of the threshold value were constructed. To choose the threshold level a method of [6] was implied. In some regimes, when it was difficult to fit a straight line to a cumulative intermittency distribution, the original method [7] of finding of the region of maximum curvature as threshold value was used. The examples of intermittency profiles through the boundary layer are plotted in Fig. 2.

3 Results

The algebraic growth of streaks. The some examples of u_{rms} development over streamwise coordinate are shown in Fig. 3. The data was taken from the positions of maxima in wall-normal profiles. In all regimes shown the transition onset is located at the middle or downstream part of the plate. The cases R2 and R7 at high velocities with moderate Tu demonstrates the well-known linear growth of u_{rms}^2

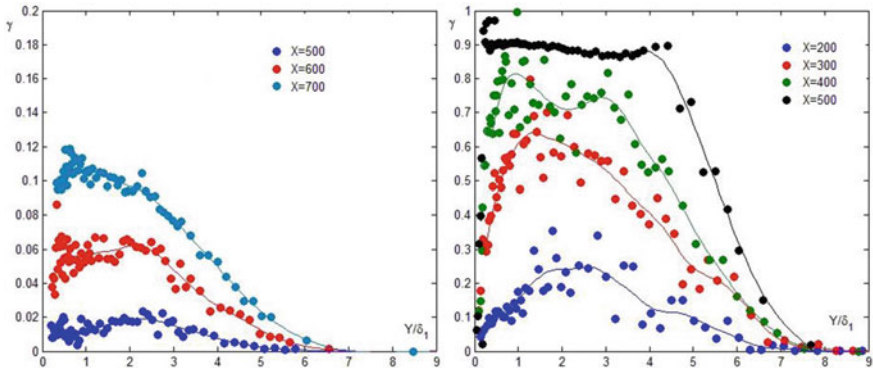
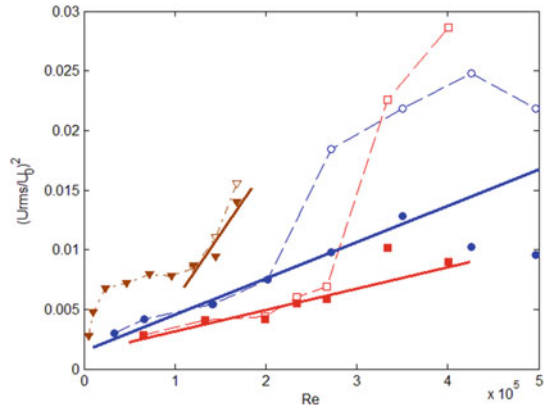


Fig. 2 The profiles of intermittency in the regimes R8 (left) and R5 (right), X is in mm

Fig. 3 Downstream evolution of u_{rms}^2 in the regimes R2 (blue), R7 (red) and R8 (brown). Open symbols corresponds to a full signal, the solid ones to laminar parts of a signal. The solid lines are the linear approximations of fluctuations on the laminar parts



with Reynolds number $Re = U_0 X / \nu$. Also on the laminar parts of the intermittent signal the fluctuations seems to be follow this tendency at least at the early stages of transition.

The regime R8 is somewhat anomalous. In all others regimes with this grid G6 a transition starts very close to the leading edge within a distance of first 100 mm. Because of the low Re , the growth of u_{rms}^2 in case R8, after a brief rapid amplification near the leading edge, is slowed down and starts again very close to the transition onset. It is possible that in R8-R11 cases the nonlinear receptivity (e.g. a vorticity stretching mechanism by the blunt leading edge) had a strong influence on disturbances development.

In some cases the fluctuations of laminar parts of flow begins to decay inside of zone of laminar flow destruction. For evaluation of functions G in these transitional regions the extrapolations of u_{rms}^2 dependencies from the laminar boundary layer were used just like it was done in [2] (see Fig. 3, R2 and R7). For the aforementioned regimes R8-R11 the data from the early stages of turbulent spots development were

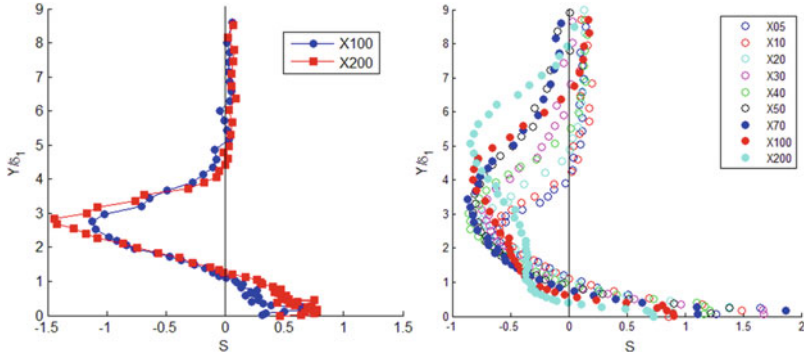


Fig. 4 The profiles of skewness S of the velocity fluctuations' probability density functions for the regimes R1 (laminar boundary layer, left) and R11 (transitional, right). X is in mm

fitted with cX (Fig. 3, R8) and extrapolated downstream if needed. So in some cases the prehistory of the disturbances development was ignored.

Gaussianity of fluctuations. It is known (e.g. [8, 9]) that the fluctuations' field in a boundary layer subjected to moderate FST is far from the gaussian one. The gaussianity of probability density function can be evaluated with the help of skewness S . The Gauss distribution has zero skewness. The profiles of S for the nonlinear cases R8 and R11 are given in Fig. 4. At the upstream positions (for example in the case R1) they are typical for all regimes. The S is positive near the wall and has a negative minimum near the edge of a boundary layer. The position of zero-crossings located at $Y/\delta_1 = 1.2\text{--}1.5$, almost at the same height as the maxima in Y -profiles of u_{rms} . Thus only near the middle part of laminar boundary layer and at the early stage of transition the fluctuations u could be approximately considered as gaussian. The beginning of turbulent spots generation leads to severe deformations of Y -profiles of S , zero-crossing points moves closer to the wall and assumption of gaussianity in [2] becomes no more valid at all.

The streak's longitudinal scale. Introducing the wave number $\alpha = 2\pi f/U_0$ and normalizing the power spectral density in the manner of [3] it is possible to show that nondimensional wavenumber spectra E should collapse if the α and E scaled with the δ_1 for nonlinear law (2) or with X for the linear one (3). The nonlinear scaling was for the first time demonstrated in the experiments [3]. In present study, as well as in [4], it was found that in general a change from the linear to nonlinear evolution of L occurs. Such example is shown in Fig. 5. The spectra of E while nondimensionalized with δ_1 does not collapse at the upstream stations, on another hand the spectra normalized with X collapses. At the $X = 400$ mm in the case R1 the first turbulent spots appears. In some regimes, just like in the aforementioned case R8, the nonlinear development of L starts from the very beginning of the streaks development. This diversity is not accounted for in the theory [2]. However, it only will affect the kinematic parameter A .

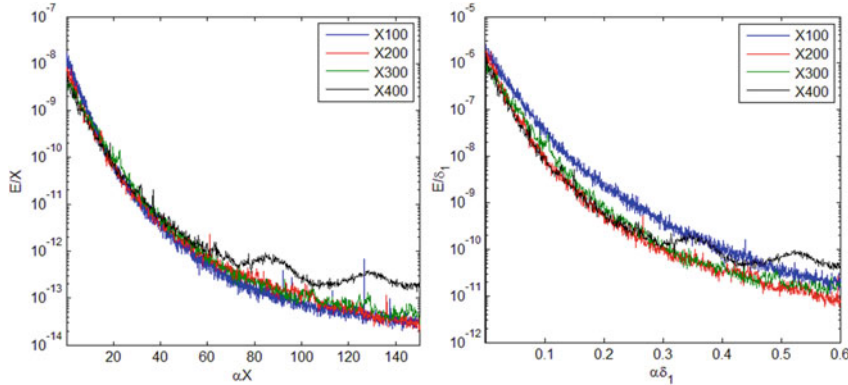


Fig. 5 Wavenumber spectra E nondimensionalized using the linear law (3) (left) and the nonlinear law (2) (right), regime R1, X is in mm

The intermittency functions G , G^* and F . The linear G and nonlinear G^* functions evaluated with the Eq. (4) is plotted in Fig. 6 for the regimes with the late transition onset. As predicted the linear fits agrees very well with the experimental points. However nor G functions, nor G^* functions do not collapses into a single straight line as it was proposed in [2]. Meanwhile, for the all regimes the negative slopes of the linear fits are very close to each other. The values of threshold constant a_c for the linear function G is given in the Table 1. The mean value of a_c in the Table 1 is 0.33 that is close to the value 0.31 obtained in [2] from the experiments [3]. For the nonlinear normalization G^* the values of a_c lays between 0.27 and 0.32 with the mean 0.30. It follows from these data that for whole range of regimes covered, the streaks' instance threshold amplitude to produce a turbulent spot is nearly the same.

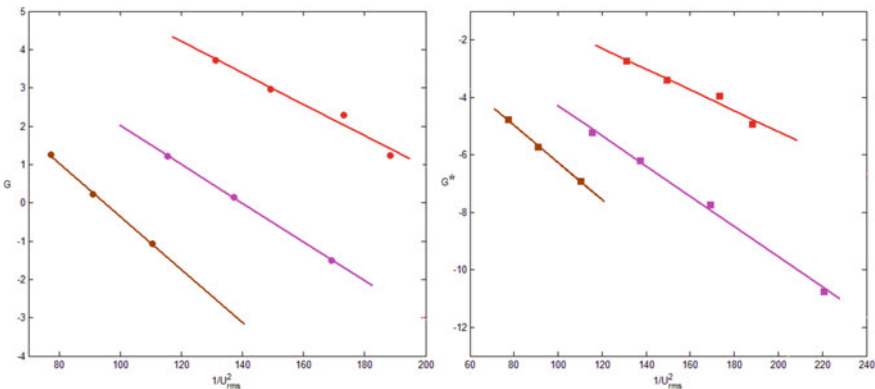


Fig. 6 The intermittency functions $G(1/u_{rms}^2)$ (left) and $G^*(1/u_{rms}^2)$ (right) for the regimes R1 (magenta), R7 (red) and R8 (brown)

Its value is about 30–35% of free-stream velocity and independent of longitudinal scales of streaks.

It should be noted that the theory under consideration does not specify an exact mechanism of spot formation. The theory only states that in the stationary random process of spots' birth and development the streak's instant amplitude required for new spot formation should be above a certain threshold. The first ever spot that needed to start this random process in the given region of flow could be produced by completely different means.

The fact that nor G nor G^* functions do not collapses into a single straight line is explained by the variations in kinematic parameter A . Because the turbulent spot's propagations velocities do not depend on the way of its birth, these variations are mainly could be explained by the aforementioned variations in the development of longitudinal scales of streaks. The values of A obtained for the linear normalization G are given in the Table 1. The scatter of A for nonlinear normalization is almost the same.

Because it is impossible from the data obtained to choose between two functions G and G^* it was decided to use the linear normalization to obtain the intermittency functions F from the Eq. (1). Due to the scatter in A the Eq. (1) was applied to the each set of data separately. In calculations of F the a_c and A values from the Table 1 for the each regime were used respectively. The results are shown in the Fig. 7. In most cases the agreement between the experiments and Eq. (1) is reasonably good. It is worth to mention, that the agreement is unexpectedly good for the nonlinear regimes R6, R10 and R11, when the transition starts in immediate vicinity of the blunt leading edge and regions of pure laminar streaks development is almost absent.

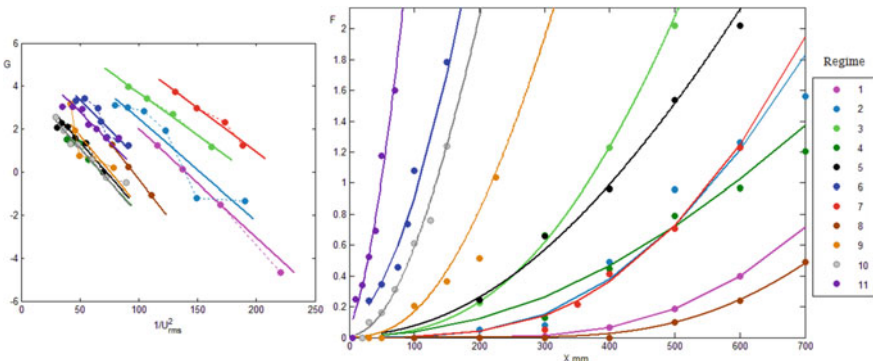


Fig. 7 The intermittency functions G (left) and the measured (points) and calculated (curves) intermittency functions F (right) obtained for all regimes

4 Conclusions

The statistically stationary process of the streaks transformation into the spots has a threshold character. The streak threshold level a_c for the birth of a turbulent spot in the present setup does not depend on a test regime and is about 30–35%.

When appropriately calibrated, the Ustinov's semiempirical statistical model of transition at high FST level gives the reasonable predictions. It performed well even in the cases of transition onset at the leading edge despite the fact that one of the main assumptions of gaussianity of the streaks development was not always hold.

Some of the assumptions behind the model weren't being justified in these experiments. In particular, the kinematic parameter A was found to be dependent on a test regime. To obtain a prediction method on basis of the model, the kinematic parameter needs to be calibrated in a more accurate manner.

References

1. Suzen, Y.B., Xiong, G., Huang, P.G.: Predictions of transitional flows in low-pressure turbines using an intermittency transport equation. In: AIAA Paper AIAA-2000-2654 (2000). <https://doi.org/10.2514/6.2000-2654>
2. Ustinov, M.V.: Statistical description of laminar-turbulent transition in a boundary layer at high freestream turbulence degree. *Fluid Dyn.* **48**, 192–200 (2013). <https://doi.org/10.1134/S001562813020063>
3. Matsubara, M., Alfredsson, P.H.: Disturbance growth in boundary layers subjected to free-stream turbulence. *J. Fluid Mech.* **430**, 149–168 (2001). <https://doi.org/10.1017/S0022112000002810>
4. Sboev, D.S.: Nonlinear interactions during early stages of boundary layer transition induced by free-stream turbulence. In: Paper Presented at the 15th European Turbulence Conference (ETC15), Delft, Netherlands, 25–28 August 2015. <http://resolver.tudelft.nl/uuid:b11cb911-4ce6-4941-ad14-489a169b26e5>. Accessed 12 July 2020
5. Kosorygin, V.S., et al: Development of disturbances in the laminar boundary layer on a plate at a high level of free stream turbulence. In: Levchenko, V.Y. (ed.) *Instability of Subsonic and Supersonic Flows*, pp. 85–92. Institute of Theoretical and Applied Mechanics, Siberian Branch of USSR Academy of Sciences, Novosibirsk (1982) (in Russian)
6. Fransson, J.H.M., Matsubara, M., Alfredsson, P.H.: Transition induced by free-stream turbulence. *J. Fluid Mech.* **527**, 1–25 (2005). <https://doi.org/10.1017/S0022112004002770>
7. Hedley, T.B., Keffer, J.F.: Turbulent/non-turbulent decisions in an intermittent flow. *J. Fluid Mech.* **64**(4), 625–644 (1974). <https://doi.org/10.1017/S0022112074001832>
8. Sboev, D.S.: The statistical properties of disturbances in a boundary layer under influence of elevated free-stream turbulence. In: 3rd All-Russian Conference of Young Scientists, p. 48. Institute of Theoretical and Applied Mechanics, Siberian Branch of Russian Academy of Sciences, Novosibirsk (2003) (in Russian)
9. Hernon, D., Walsh, E.J., McEligot, D.M.: Experimental investigation into the routes to bypass transition and the shear-sheltering phenomenon. *J. Fluid Mech.* **591**, 461–479 (2007). <https://doi.org/10.1017/S0022112007008336>

Response of NLF Airfoils to Small Scale Turbulence



Jonas Romblad, Duncan Ohno, Amandine Guissart, Werner Würz,
and Ewald Krämer

Abstract The effect of inflow turbulence level on the boundary layer transition on a Natural Laminar Flow (NLF) airfoil is investigated through detailed wind tunnel measurements. The free-stream turbulence level (Tu) is varied in the range $0.01\% \leq Tu \leq 0.11\%$ by employing an active grid. Within the range of amplified TS-frequencies the spectral distribution of the u' -component could be matched to free flight measurements obtained for a glider at low to moderately turbulent conditions. Transition locations as function of turbulence level are determined for three airfoils with fundamentally different baseflows and the results are compared to the modified e^9 method of Mack [6].

1 Introduction

The use of Natural Laminar Flow (NLF) airfoils with extended regions of laminar boundary layer is a way to significant reduction of friction drag. NLF airfoils are currently well established on glider aircraft and wind turbines while the application to commercial aircraft is being investigated [1].

An essential part of NLF airfoil design is the prediction of the transition from laminar to turbulent boundary layer. One of the most employed methods is the e^n method [2] developed by van Ingen [3]. The e^n method is based on amplification rates of Tollmien-Schlichting (TS) waves determined by Linear Stability Theory (LST) and assumes steady boundary conditions. However, flight through the convective part of the atmosphere causes unsteady inflow of a wide range of length scales [4], leading to significant variations of the critical n-factor. In the airfoil design process the choice of n_{crit} has a strong influence on the resulting airfoil and its performance.

J. Romblad (✉) · D. Ohno · W. Würz · E. Krämer
Institute of Aerodynamics and Gasdynamics, University of Stuttgart, 70550 Stuttgart, Germany
e-mail: jonas.romblad@iag.uni-stuttgart.de

A. Guissart
Institute for Fluid Mechanics and Aerodynamics, TU Darmstadt, 64347 Griesheim, Germany

Mack [6] used measurements on flat plates to derive a modified method where the n_{crit} is expressed as a function of the free-stream turbulence level.

1.1 Atmospheric Turbulence

The characteristic spectrum of atmospheric turbulence is well described by the Kolmogorov hypothesis [4] and can be divided in an energy containing range, an inertial subrange and a dissipative subrange, see Pope [5]. Glider airfoils with TS driven transition scenarios are expected to be most sensitive to initial disturbances in the range of wavelengths corresponding to the onset of the dissipative subrange. Detailed measurements of atmospheric turbulence influenced by convection in the Ekman layer were performed by Shei et al. [7], Li et al. [8] and Bodini et al. [9]. Otten et al. [10] performed measurements of inflow turbulence in flight at altitudes between 3.7 and 20 km while Zanin [11] used a glider aircraft for measurements at 1200 m, documenting turbulence levels in the order of 0.02% and 0.2% ($1 \leq f \leq 5000$ Hz) respectively. At low altitudes Riedel and Sitzmann [12] report $Tu \leq 0.04\%$ in “still air”, $Tu \leq 0.09\%$ in “weak, uniform turbulence” while in “strong, abrupt turbulence” $0.1\% \leq Tu \leq 1.0\%$ was measured, the latter likely in thermals. Nitsche et al. [13], Peltzer [14] and Seitz and Horstmann [15] all observed “orderly” transition dominated by the amplification of Tollmien-Schlichting (TS) waves in flight at especially low disturbance conditions. Reeh [16] performed measurements of transition in flight at turbulence levels up to $Tu = 0.11\%$ and found significant movement of transition position due to low frequency fluctuations with large amplitude. Reeh proposed a separation of the length scales in the turbulent inflow in “small” and “large” scales depending on their effect on the boundary layer. Large scale turbulence acts as variations of the inflow angle, creating unsteady variations of the pressure distribution to which the boundary layer responds. For the small scale free-stream turbulence, receptivity [17] provides a wavelength adaptation and seeds disturbances which are amplified and lead to transition.

1.2 Small Scale Turbulence and Its Effect on Transition

The effect of small scale turbulence on flat plate boundary layers has received a great deal of attention where for instance Kendall [18] used a large body of wind tunnel measurements to show that TS-waves being the dominant mechanism of transition for $0.1\% \leq Tu \leq 0.2\%$. At $Tu > 1.0\%$ streamwise vortices in the boundary caused by the free-stream turbulence trigger bypass transition, as described in the review paper by Durbin [19]. These streamwise vortices are often referred to as “streaky structures” or “Klebanoff modes”. In the published literature no threshold Tu -level can be found which separates the two transition scenarios. Arnal and Juillen [20] (see also Kendall [21] and [22], Matsubara and Alfredsson [23] and Fransson [24])

measured TS-waves at $Tu = 0.1\%$ which were barely observable at $Tu = 0.3\%$ and bypass transition was determined at $Tu = 1.0\%$. Similar results are reported by Suder et al. [25] who measured “classic” or “orderly” TS-transition at $Tu = 0.3\%$ and bypass transition already at $Tu = 0.65\%$. TS-waves and Klebanoff modes can co-exist as shown by Kendall [21] and others. The interaction between the two types of disturbances has been studied by several researchers including Kendall [18, 21, 26–29].

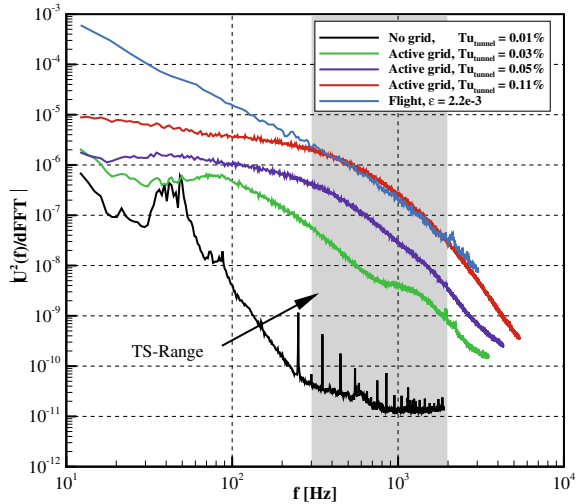
In summary, during flight in the convective part of the atmosphere, turbulence levels in the order of $Tu \leq 0.1\%$ can be expected in “calm” to “weak, uniform” [12] or “moderately turbulent” [32] regions outside thermals. In these conditions the transition tend to be TS-dominated. Nevertheless, in this range a solid relationship between the turbulence level and the critical n-factor for transition is not yet established. Due to the significant importance for the design of airfoils, the current paper focuses on the effect of small scale turbulence ($k \gtrsim 100 \text{ rad/m}$) on the transition on a NLF airfoil at $Tu \leq 0.11\%$.

2 Experimental Setup

The measurements were performed in the Laminar Wind Tunnel (LWT) of the Institute of Aerodynamics and Gas Dynamics (IAG) which is an open return tunnel with a test section of $0.73 \times 2.73 \text{ m}^2$ and 3.15 m length. The base turbulence level is $Tu \leq 0.01\%$ for a frequency range of $10 \leq f \leq 5000 \text{ Hz}$. The main investigation has been conducted on the pressure side of a MW-166-39-44-43 NLF airfoil with $c = 1.35 \text{ m}$ chord (a modified DU84-158 glider airfoil). The experimental parameters are matched with a corresponding free flight test case [30], i.e. $Re_{chord} = 3.4 \cdot 10^6$, $\alpha_{ref,tunnel} = -0.7^\circ$. The wind tunnel model is equipped with 42 pressure taps in streamwise direction, of which 21 are connected to SensorTechnics HCL0050 pressure transducers modified to reduce the internal volume and installed using the infinite line technique as described by Samuelson [31]. This allows measurements in the range $0 \leq f \leq 8000 \text{ Hz}$. An additional 16 unsteady pressure ports are located in a spanwise row at $x/c = 0.311$. CTA hot-wire anemometry is used for boundary layer traverses and free-stream turbulence measurements.

Additional inflow turbulence is generated using an active, pneumatic grid placed in the settling chamber (similar to Kendall [18]) resulting in $0.03\% \leq Tu \leq 0.11\%$ at $U_\infty = 38 \text{ m/s}$. This corresponds to flight conditions labelled as “still air” to “weak, uniform turbulence” [12] or “moderately turbulent” [32]. The spectrum matches glider flight measurements of Guissart et al. [32] well in the frequency range relevant for linear TS-transition in the current experiment, see Fig. 1. A direct comparison of turbulence levels in flight measurements and wind tunnel experiments is difficult due to the differences in spectral content at the low frequency range. A more consistent way is to fit a model spectrum (see Pope [5]) to the different datasets and use the dissipation rate ϵ for comparisons.

Fig. 1 Free-stream turbulence spectrum in the Laminar Wind Tunnel (with and without grid) and in flight at “moderately turbulent” conditions [32]



The LST calculations used for comparisons with the experimental results, and to deduce the critical n-factor in the experiments, follow a three step procedure. Based on viscous pressure distributions calculated with XFOIL V6.96 highly resolved boundary layer profiles are determined using a finite-difference scheme [33]. The results are used together with a shooting method [34] to solve the Orr-Sommerfeld equation.

3 Results, Baseflow Conditions

For the reference case the most amplified 2D TS-waves lie in the range 600 to 900 Hz as seen in the stability chart in Fig. 2. Figure 3a shows the streamwise development of surface pressure spectra at $Tu = 0.01\%$. The measurements show the expected features of TS-dominated transition and there is a good match with 2D Linear Stability Theory (LST) in both frequency and width of main TS-amplified region.

Good agreement is also found in amplification rates when comparing the hot-wire measurements of the wall near amplitude maxima with LST and 2D DNS, see Fig. 3b.

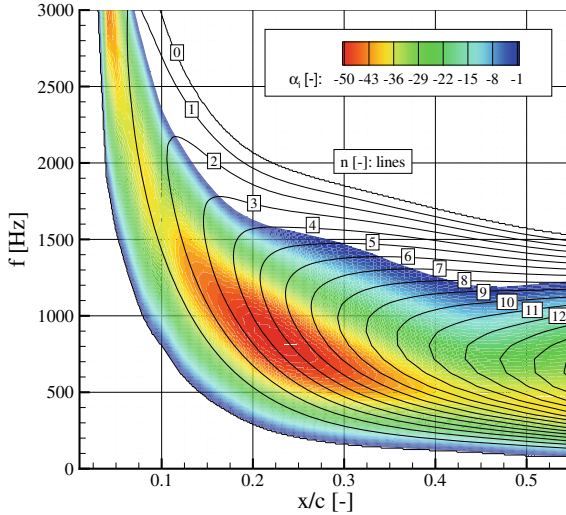


Fig. 2 2D stability chart from steady LST at α_{ref} , $Re = 3.4 \cdot 10^6$. Here α_i is non-dimensionalized by airfoil chord

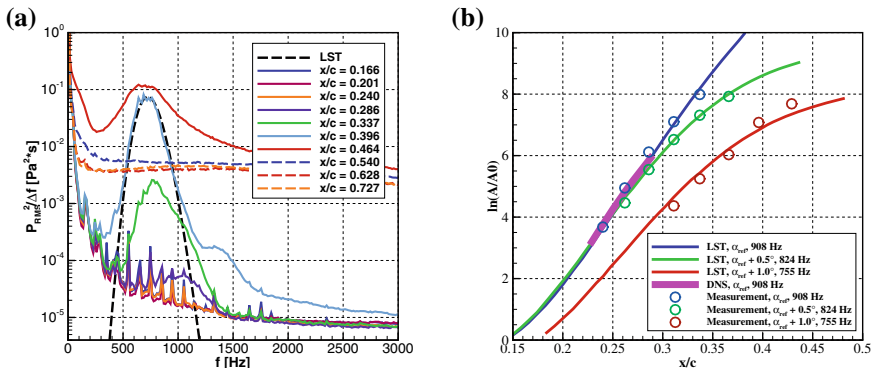


Fig. 3 Base flow at α_{ref} , $Re = 3.4 \cdot 10^6$ and $Tu = 0.01\%$. **a** Surface pressure spectra and **b** amplification rates from hot-wire (wall near amplitude maximum), 2D LST and 2D DNS

4 Results, Increased Turbulence Level

4.1 Spectral Development

As seen in Fig. 4, an increase of the free-stream turbulence from $Tu = 0.01\%$ to 0.11% leads to an upstream movement of the transition and a reduction of the peak TS-amplitude. There is a broadening of the amplified region and the TS-peak shifts to higher frequencies. The frequency shift of the TS-peak is at least partly due to the lin-

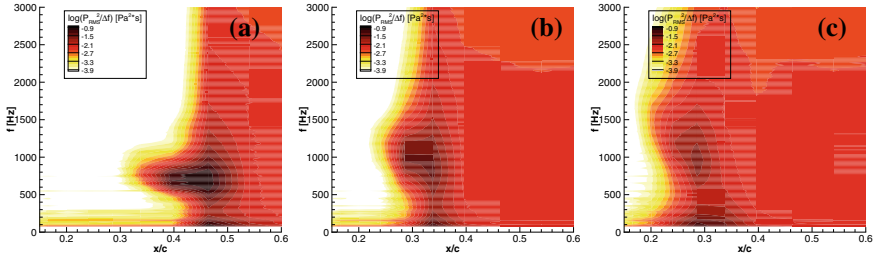


Fig. 4 PSD of wall pressure fluctuations at increased turbulence level. **a** $Tu = 0.01\%$, **b** $Tu = 0.05\%$ and **c** $Tu = 0.11\%$

ear stability characteristics emphasizing higher frequency disturbances at upstream locations.

4.2 Spanwise Wavenumber Spectrum

Frequency wavenumber spectra for different Tu are extracted from the pressure taps in the spanwise row at $x/c = 0.311$, see Fig. 5. The pressures fluctuation amplitudes have been transformed to u'_{max} based on LST calculations. The two angles of attack in Fig. 5 are chosen to have a comparable stage of the transition at the row of taps for both Tu . Increasing Tu from 0.01% to 0.08% reduces the amplitude of the TS peak and increases the energy at higher spanwise wavenumbers.

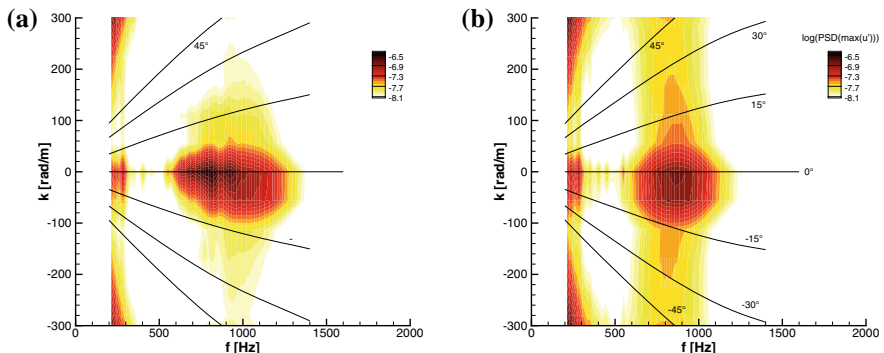


Fig. 5 Frequency wavenumber spectra at $x/c = 0.311$. **a** $Tu = 0.01\%$, $\alpha_{ref} = 0.2^\circ$ and **b** $Tu = 0.08\%$, $\alpha_{ref} + 1.0^\circ$

4.3 Temporal Development

The time traces of the unsteady pressure signals in streamwise direction reveal a change in the structure of the transition process with increasing turbulence level. The quasi-uniform nature at $Tu = 0.01\%$ is gradually replaced by a structure with formation of isolated wave packets which grow downstream and form turbulent spots, see Fig. 6a ($Tu = 0.01\%$) and b ($Tu = 0.11\%$). Similarly, Kendall [18] reports wave packets appearing in a flat plate boundary layer as Tu increases from 0.03% to $Tu \leq 0.1\%$. In flight measurements, Seitz and Horstmann [15] observed wave packets already at $Tu < 0.05\%$ and Peltzer [14] mentions local wave packets even in very calm air.

Fasel [29] as well as Wu and Choudhari [28] couples the occurrence of wave packets to the interaction between TS-waves and low frequency streamwise streaky structures (Klebanoff modes). According to Fasel [29] and Wu and Choudhari [28], the Klebanoff modes cause local and temporal variations in the stability characteristics of the boundary layer which can promote a significantly faster growth of disturbances than in the undisturbed boundary layer, leading to the formation of wave packets.

If the forming of wave packages is related to interaction between TS-waves and Klebanoff modes, some care should be taken when extrapolating wind tunnel results to flight conditions. The ratio between the energy at low and high frequencies in the spectrum of the inflow turbulence, relevant for Klebanoff modes and TS-amplification respectively, is significantly higher in the atmosphere than in most wind tunnel experiments, see Fig. 1.

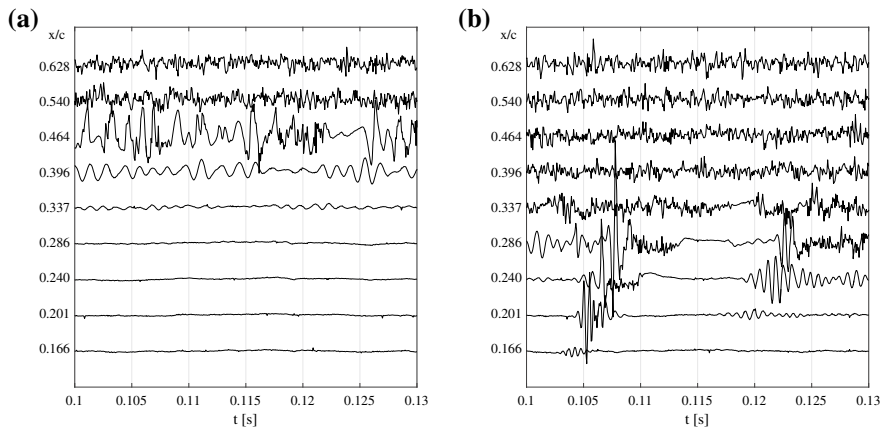


Fig. 6 Time traces of surface pressures at **a** $Tu = 0.01\%$ and **b** $Tu = 0.11\%$

4.4 Transition Prediction at Increased Turbulence Level

In the framework of transition prediction for NLF airfoil design it is essential to model the observed shift in transition position with increased turbulence level. Mack [6] proposed a modified e^9 method derived from measurements on flat plate boundary layers. In order to compare this approach to airfoil sections with considerably different base flow (comp. Fig. 7a), IR thermography is used to extract the transition location of three airfoil sections. In order to achieve consistent results a procedure based on the maximum local temperature gradient was applied [35]. The MW-166-39-44-43, XIS40mod and NACA64₃-418 airfoils show a large variation in the response of n_{crit} to Tu , see Fig. 7. The MW-166-39-44-43 follows the modified e^9 method of Mack [6] well while the two others show significantly smaller variations of n_{crit} in the same range of Tu as seen in Fig. 7b. The observed variation of n_{crit} over the investigated range of Tu is in the order of $\Delta n \geq 2$ which is significant in the context of NLF airfoil design. To investigate if a difference in the receptivity properties, which depend on local surface curvatures, non-dimensional frequencies and boundary layer parameters close to branch I, can explain this behaviour, a receptivity ratio k_r is defined as

$$k = \frac{G_{Mack}}{G_{Current}} \quad (1)$$

where G_{Mack} and $G_{Current}$ are the receptivity coefficients in the measurements used by Mack and in the current experiments respectively. This is a strong simplification as differences in the non-linear regime of the transition are also included in this ratio. The k_r is introduced in the expression of Mack

$$n_{tr} = -8.43 - 2.4 \cdot \ln(k_r \cdot Tu) \quad (2)$$

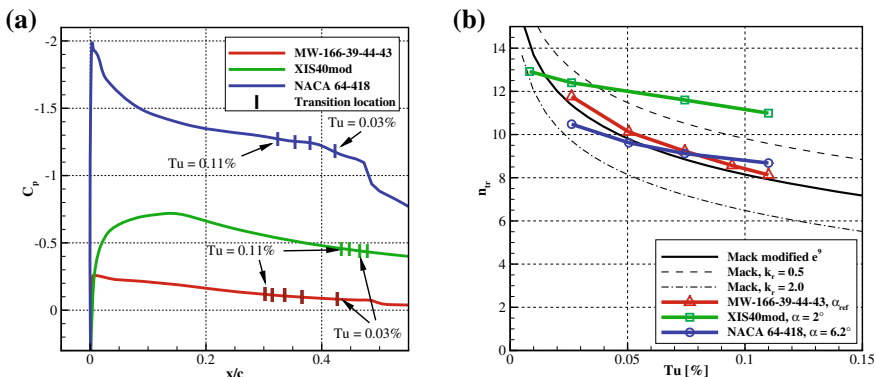


Fig. 7 For the three airfoils **a** steady pressure distributions and **b** n_{crit} as function of Tu

Varying k_r causes a vertical shift of the n_{crit} curve but does not change the gradient. Consequently the differences in airfoil response cannot be captured by a change in receptivity coefficient alone.

It is worth noting that in contrast to the “classical” measurements, e.g.. Schubauer and Skramstad [36], no lower Tu -limit for the influence of turbulence level on the transition location is found in the current measurements. Schubauer and Skramstad [36] found little influence on the transition below $Tu \approx 0.1\%$, an effect attributed to acoustic disturbances, see Arnal [37].

5 Conclusions

Detailed wind tunnel measurements of the transition behaviour of the NLF airfoil MW-166-39-44-43 have been performed at $0.01\% \leq Tu \leq 0.11\%$ inflow turbulence. The spectral distribution in the frequency range of the most amplified TS-waves was matched with glider free flight measurements.

As Tu increases, the transition on the MW-166-39-44-43 airfoil moves upstream while the TS frequency peak broadens and shifts to higher frequencies. A structure of isolated wave packets gradually replaces the quasi-uniform nature of the transition at low Tu and more energy is found at higher spanwise wavenumbers. The appearance of wave packets seems to be linked to an interaction between TS-waves and Klebanoff modes despite the low turbulence level.

Transition locations as function of turbulence level are detected for three airfoils with vastly different baseflow. The n_{crit} for the MW-166-39-44-43 follows the modified e^9 method of Mack [6] well while the XIS40mod and NACA 64₃-418 show significantly lower sensitivity to Tu in the investigated range. All three airfoils exhibited a variation of n_{crit} in the order of $\Delta n \geq 2$ which is significant for NLF airfoil design. The difference in response to Tu between the three airfoils is not captured by a possible difference in the receptivity coefficient due to free-stream turbulence alone.

Acknowledgements The reported work is part of the project “Laminar-turbulente Transition unter instationären Anströmbedingungen”, supported by the Luftfahrtforschungsprogramm (LuFo) of the Bundesministerium für Wirtschaft und Energie.

References

1. Airbus: Airbus’ ”BLADE” laminar flow wing demonstrator makes first flight, Airbus press release 26.09.2017 (2017) https://www.airbus.com/newsroom/press-releases/en/2017/09/airbus_-blade_-laminar-flow-wing-demonstrator-makes-first-fligh.html. Cited 2 Dec 2019
2. Crouch, J.: Boundary-layer transition prediction for laminar flow control. In: 45th AIAA Fluid Dynamics Conference, p.2472 (2015)

3. van Ingen, J.: A suggested semi-empirical method for the calculation of the boundary layer transition region. Report, TU Delft (1956)
4. Kolmogorov, A.N.: The local structure of turbulence in incompressible viscous fluid for very large Reynolds numbers. Dokl. Akad. Nauk SSSR **30**, 299–303 (1941)
5. Pope, S.: Turbulent flows. Cambridge University Press (2000)
6. Mack, L. M.: Transition and laminar instability. JPL Publ. 77-15, NASA-CP-153203 (1977)
7. Sheih, C.M., Tennekes, H., Lumley, J.L.: Airborne Hot-Wire Measurements of the Small-Scale Structure of Atmospheric Turbulence. The Physics of Fluids **14**(2), 201–215 (1995)
8. Li, S.W., Tse, K.T., Weerasuriya, A.U., Chan, P.W.: Estimation of turbulence intensities under strong wind conditions via turbulent kinetic energy dissipation rates. Journal of Wind Engineering and Industrial Aerodynamics **14**, 201–215 (1995)
9. Bodini, N., Lundquist, J.K., Newsom, R.K.: Estimation of turbulence dissipation rate and its variability from sonic anemometer and wind Doppler lidar during the XPIA field campaign. Atmospheric Measurement Techniques **11**(7), 4291–4308 (2018)
10. Otten, L.J., Pavel, A.L., Rose, W.C., Finley, W.E.: Atmospheric turbulence measurements from a subsonic aircraft. AIAA Journal **20**(5), 610–611 (1982)
11. Zanin, B. Y.: Transition at natural conditions and comparison with the results of wind tunnel studies. In Laminar-Turbulent Transition (pp.541-546). Springer, Berlin, Heidelberg (1985)
12. Riedel, H., Sitzmann, M.: In-flight investigations of atmospheric turbulence. Aerospace Science and technology **2**(5), 301–319 (1998)
13. Nitsche, W., Suttan, J., Becker, S., Erb, P., Kloker, M., Stemmer, C.: Experimental and numerical investigations of controlled transition in low-speed free flight. Aerospace science and technology **5**(4), 245–255 (2001)
14. Peltzer, I.: Comparative in-flight and wind tunnel investigation of the development of natural and controlled disturbances in the laminar boundary layer of an airfoil. Experiments in Fluids **44**(6), 961–972 (2008)
15. Seitz, A., Horstmann, K. H.: In-flight investigations of tollmien-schlichting waves. In IUTAM Symposium on One Hundred Years of Boundary Layer Research (pp. 115-124). Springer, Dordrecht (2006)
16. Reeh, A.D.: Natural laminar flow airfoil behavior in cruise flight through atmospheric turbulence. Ph.D. thesis, Technische Universität Darmstadt (2014)
17. Morkovin, M.V.: Critical evaluation of transition from laminar to turbulent shear layers with emphasis on hypersonically travelling bodies. Flight Dynamic Lab. Rep. AFFDL-TR-68-149, vol. 149 (1969)
18. Kendall, J.: Boundary layer receptivity to freestream turbulence. In 21st Fluid Dynamics, Plasma Dynamics and Lasers Conference p.1504 (1990)
19. Durbin, P.A.: Perspectives on the Phenomenology and Modeling of Boundary Layer Transition. Flow, Turbulence and Combustion **99**(1), 1–23 (2017)
20. Arnal, D., Juillen, J. C.: Contribution Experimentale a l'Etude de la Receptivite d'une Couche Limite Laminaire, a la Turbulence de l'Ecoulement General. ONERA, RT 1/5018 (1978)
21. Kendall, J.: Experimental study of disturbances produced in a pre-transitional laminar boundary layer by weak freestream turbulence. In 18th Fluid Dynamics and Plasmadynamics and Lasers Conference p.1695 (1985)
22. Kendall, J.: Experiments on boundary-layer receptivity to freestream turbulence. In 36th AIAA Aerospace Sciences Meeting and Exhibit p.530 (1998)
23. Matsubara, M., Alfredsson, P.H.: Disturbance growth in boundary layers subjected to free-stream turbulence. Journal of fluid mechanics **430**, 149–168 (2001)
24. Fransson, J. H.: Free-stream turbulence and its influence on boundary-layer transition. In 10th International Symposium on Turbulence and Shear Flow Phenomena, TSFP 2017, Chicago, United States, 6 July 2017 through 9 July 2017 (Vol. 2). International Symposium on Turbulence and Shear Flow Phenomena, TSFP10 (2017)
25. Suder, K.L., Obrien, J.E. and Reshotko, E.: Experimental study of bypass transition in a boundary layer. NASA-TM-100913 (1998)

26. Kendall, J.: Studies on laminar boundary-layer receptivity to freestream turbulence near a leading edge. In Boundary layer stability and transition to turbulence pp 23-30 (1991)
27. Boiko, A.V., Westin, K.J.A., Klingmann, B.G.B., Kozlov, V.V. and Alfredsson, P.H.: Experiments in a boundary layer subjected to free stream turbulence. Part 2. The role of TS-waves in the transition process. *Journal of Fluid Mechanics* **281**, 219–245 (1994)
28. Wu, X. and Choudhari J. M.: Effects of long-wavelength Klebanoff modes on boundary-layer instability. *Annual Research Briefs-2001*, p.305 (2001)
29. Fasel, H.F.: Numerical investigation of the interaction of the Klebanoff-mode with a Tollmien-Schlichting wave. *Journal of Fluid Mechanics* **450**, 1–33 (2002)
30. Romblad, J., Ohno, D., Nemitz, T., Würz, W., Krämer, E.: Laminar to Turbulent Transition due to unsteady Inflow Conditions: Wind Tunnel Experiments at increased Turbulence Levels. Deutsche Gesellschaft für Luft-und Raumfahrt-Lilienthal-Oberth eV (2018)
31. Samuelson, R.D.: Pneumatic instrumentation lines and their use in measuring rocket nozzle pressure. *Aerojet-General Corp. Rep. RN-DR-0124* (1967)
32. Guissart, A., Nemitz, T., Tropea, C.: Laminar to Turbulent Transition at Unsteady Inflow Conditions: Flight Experiments Under Calm and Moderately Turbulent Conditions. *Symposium der Deutsche Gesellschaft für Luft-und Raumfahrt* **185–194**, (2018)
33. Cebeci, T., Smith, A. M. O.: Analysis of Turbulent Boundary Layers. ISBN 0-12-164650-5, Academic Press (1974)
34. Conte, S.D.: The numerical solution of linear boundary value problems. *Siam Review* **8**(3), 309–321 (1966)
35. Joseph, Liselle A., Aurelien Borgoltz, and William J. Devenport: Transition detection for low speed wind tunnel testing using infrared thermography. In 30th AIAA Aerodynamic Measurement Technology and Ground Testing Conference, p. 2939. 2014
36. Schubauer, G.B., Skramstad, H.K.: Laminar Boundary-Layer Oscillations and Transition on a Flat Plate. *Journal of research of the National Bureau of Standards* **38**, 251–292 (1947)
37. Arnal, D. Description and prediction of transition in two-dimensional, incompressible flow. In AGARD Spec. Course on Stability and Transition of Laminar Flow 71 p (SEE N84-33757 23-34), scst (1984)

Disturbances in a Three Dimensional Boundary Layer at Elevated Free Stream Turbulence



Dmitry Sboev and Stepan Tolkachev

Abstract The experiments were devoted to the measurements in a three-dimensional boundary layer with negative streamwise pressure gradient at free-stream turbulence level 0.93%. The primary instability modes were identified as travelling cross-flow disturbances. Their initial growth was in accordance with the linear stability theory. The nonlinear interactions in the course of transition were studied.

Keywords Three-dimensional boundary layer · Cross-flow instability · Transient growth · Free stream turbulence

1 Introduction

The boundary layer flow over a swept wing is of obvious interest in practical applications. In the quiet external conditions the laminar-turbulent transition in this 3D flow is triggered by the modal inflection-type instability. However, similarly to a 2D boundary layer, the transient growth can be important in a 3D boundary layer transition under influence of elevated free-stream turbulence (FST). The theoretical studies [1, 2] shows that the transient growth per se can affect the disturbance development in a 3D boundary layer or it can set paths of the receptivity process.

The previous experimental investigations of transition in a 3D boundary layer had been conducted at moderate FST levels up to $Tu = 0.6\%$ [3–6]. It was shown in [3] that at $Tu = 0.57\%$ in their set-up the stationary cross-flow disturbances decreases with streamwise direction, while travelling modes shows the immense amplitudes from the first measurements station at 40% of chord. No data from upstream positions were presented. The pressure distribution over a flat plate in the DLR experiments was corresponded to rather strong downstream acceleration. In [6, 7] at $Tu = 0.61\%$ and 0.91% some signs of non-modal amplification were observed in a 3D boundary

D. Sboev (✉) · S. Tolkachev
Central Aerohydrodynamic Institute, Zhukovsky, Russia
e-mail: t124@inbox.ru

S. Tolkachev
e-mail: tolkachevst@gmail.com

layer with a flat-top pressure distribution that is typical of a laminarized airfoil at low incidence. So the question about the actual possibility of transient growth in a 3D boundary layer remains open.

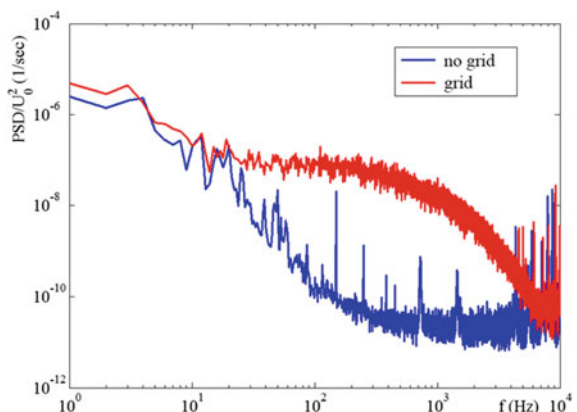
Difficulty arises as to distinguish between the possible non-modal perturbations and the cross-flow instability modes [6, 7]. The former bear a strong similarity to the cross-flow instability in their appearance, e.g. in bell-like shapes of wall-normal profiles of the streamwise oriented low-frequency disturbances. However their streamwise growth is different, as both stationary and travelling instability waves show the exponential growth. So the careful measurements of the disturbances amplification in a streamwise direction as well as the measurements of spanwise correlations were chosen as the primary means in the present experiments.

2 Experimental Setup

The experiments were conducted in the TsAGI low-turbulence wind tunnel T-124 at free stream velocities $U_0 = 6\text{--}24 \text{ m/s}$. The coordinate system used has the chordwise axis X normal to the leading edge and the spanwise axis Z parallel to it, the Y is wall-normal coordinate. The basic regime was $U_0 = 22.2 \text{ m/s}$. The model was a swept flat plate with imposed negative streamwise pressure gradient. The sweep angle of the leading edge is 35° . The conditions of spanwise-independent accelerated 3D boundary layer were achieved by means of properly streamlined inserts into the test section. The more detailed description of the model is given in our accompanying paper in this Proceeding.

The FST was generated by the two-plane $1.5 \times 25 \text{ mm}$ grid installed at the beginning of the test section. The FST level was $Tu = 0.93\%$ and the FST power spectral density is shown in Fig. 1. The examples of pressure distributions in our configuration are given in the accompanying paper. The accelerated boundary layer with an almost constant negative pressure gradient was created over the flat plate.

Fig. 1 Spectra of free-stream turbulence



The hot-wire measurements were performed. The probe was mounted in the PC-controlled 3D traverse. In the low FST case it was confirmed by means of V-shape double-wire probe that in this set-up the unstable 3D boundary layer was developing. The values of the cross-flow mean velocity component were about 2–3% of U_0 . The stationary streamwise vortices were the primary instability modes in this case. Due to the relatively large measurements volume of V-shape probe in present experiments a single-wire was used. The calibrations of hot-wire were performed *in situ* in the 3D external flow by common 5-hole probe that was installed at the traverse 40 mm above hot-wire. The 5-hole probe gives a direction and absolute value of flow velocity at the point of wire calibration. The AD converter was set to 25 kHz and typically 10 s traces were recorded, except the measurements of bispectra where 600 s traces were sampled at 5 kHz.

3 Results

The flow structure inside the boundary layer is shown in Figs. 2 and 3 at $U_0 = 22.2$ m/s. As it seen from these data, there are no significant deviations from the spanwise averaged values in the mean velocity (U) field. At these streamwise positions the linear stability theory (LST) gives for spanwise wavelengths of most amplified stationary disturbances values about 8–10 mm. As is shown in Fig. 3, the local deviations ΔU of the mean streamwise velocity from its spanwise averaged value with the similar wavelengths does not exceed 2%. The maxima in wall-normal profiles of ΔU_{rms} do not exceed 1% and no significant growth of this quantity was observed at

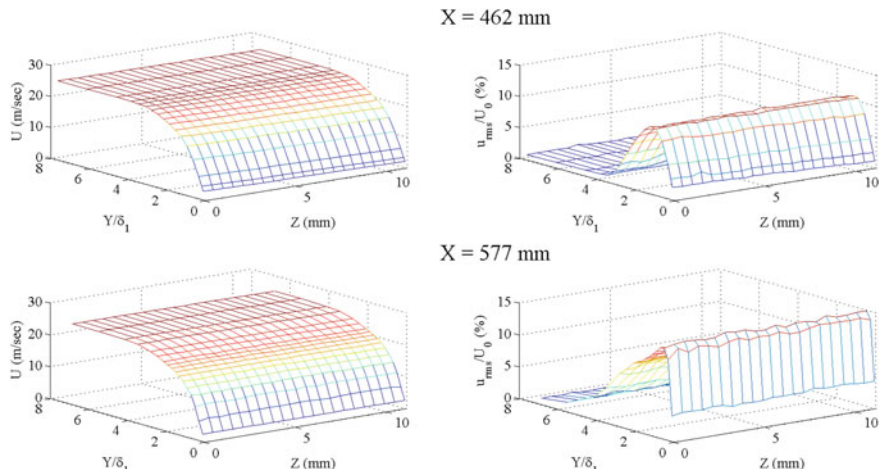


Fig. 2 The flow field at the start of transition ($X = 462$ mm) and in the transition region ($X = 577$ mm, intermittency $\gamma = 0.53$), δ_1 is displacement thickness

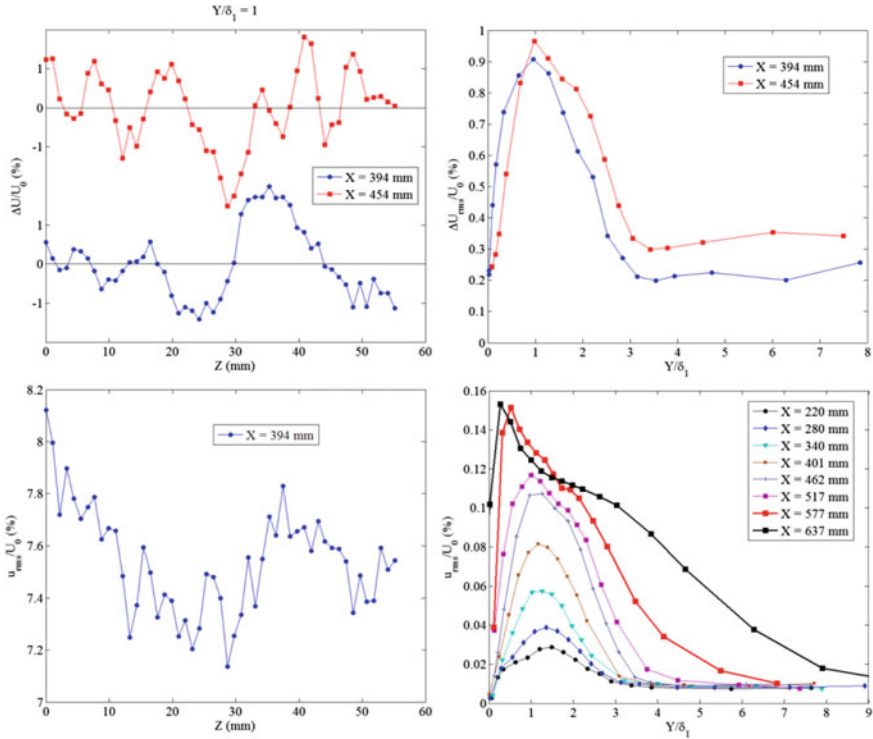


Fig. 3 The distributions of stationary ΔU and traveling disturbances u_{rms} over spanwise coordinate at $Y/\delta_1 = 1.2$ (left) and the wall-normal profiles of these disturbances (right)

the upstream stations. The stationary cross-flow vortices do not play any appreciable role in our experiments.

It is well-known from a number of experiments (e.g. [3]) that at low FST the unsteady modes show spanwise modulation due to nonlinear interactions prior to the transition. This was not the case in the present experiments. As it can be seen in Figs. 2 and 3, the u_{rms} fluctuations are almost constant in the spanwise direction. Variations of u_{rms} lies within 1% over 57 mm distance at $X = 394$ mm (Fig. 3). The uniformity of u_{rms} distributions also is clear from the (Y, Z) plots in Fig. 2. The wall-normal profiles for both stationary and normal modes until transition onset shows single maxima located just below the middle of the boundary layer. These profiles are quite similar to the typical profiles of the cross-flow instability, but also similarity with the optimal perturbations calculated in [2] exists. After transition starts the near-wall maximum appears in the u_{rms} profiles that corresponds to turbulent spots production and development.

In a 2D boundary layer subjected to the elevated FST the high-frequency components of fluctuations decay to the wall and their maxima located near the boundary layer edge (e.g. [8] and Refs. cited therein). Usually at rather high FST levels no

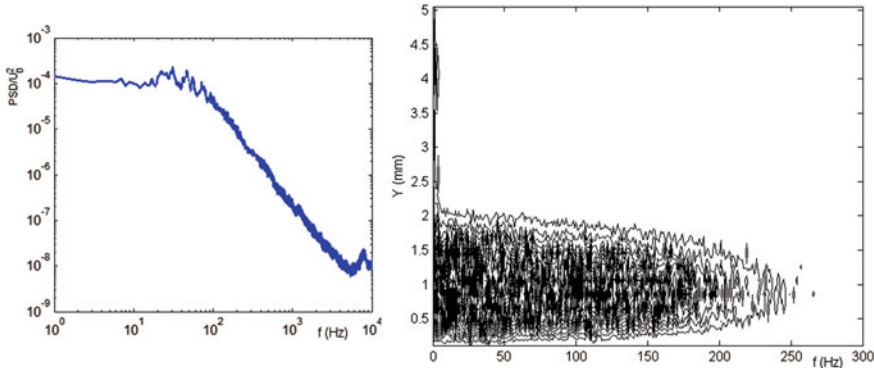


Fig. 4 The power spectral density at $Y/\delta_1 = 1.2$, (left) and the power spectral density contour plot (right), $X = 462$ mm

wave packets of TS-instability range (i.e. the modal instability) are observed in 2D case. Only low-frequency fluctuations that correspond to the developing streamwise streaks grow inside the boundary layer. On the other hand, in the 3D boundary layer at low FST level in the present set-up the pronounced fluctuations in the frequency range 100–500 Hz as predicted by the LST were clearly seen as packets in spectra. The example of frequency spectrum of travelling modes in 3D boundary layer at high FST level is given in Fig. 4. In this case no wave packets are seen, the energy is concentrated in a low-frequency range up to 100 Hz and smoothly decays at the higher frequencies. However, the wall-normal distribution of power spectral density shows that the higher frequencies don't decay to the wall. The disturbances up to 250 Hz amplified inside the boundary layer. In the middle part of boundary layer the energy of high-frequency fluctuations several times higher than in external flow. As it can be seen from the contour plot in Fig. 4, the frequency range of amplification compares well with the LST predicted range. This is in striking contrast with a 2D case. The optimal perturbations theories [1, 2] for a 3D boundary layer give a preferred transient amplification of low-frequency long-wave disturbances.

The measured growth curve for unsteady modes is plotted in Fig. 5. Because of their importance, the data obtained during nearly three week from the different test runs are given in a dimensional form to show a good repeatability and controllability of the experiment. The growth is not algebraic, but exponential. The comparison with the LST calculations performed for this set-up during the BUTERFLI project shows an excellent qualitative agreement. For instance, the positions of the growth curve's slope change are the same. In experiment the growth is slowed down after $X = 450$ mm with the start of turbulent spots generation. The experimental curve begins to saturate near the $X = 600$ mm, well downstream the transition onset.

To obtain a picture of disturbances' structure the cross-correlation measurements in the direction Z' normal to the outer streamline were performed. The results are plotted in Fig. 6. A single minimum is usually observed in a 2D boundary layer at a certain spanwise probe separation. That gives a spanwise scale of low-frequency streaks to be about twice local boundary layer thickness δ_{99} [8]. The

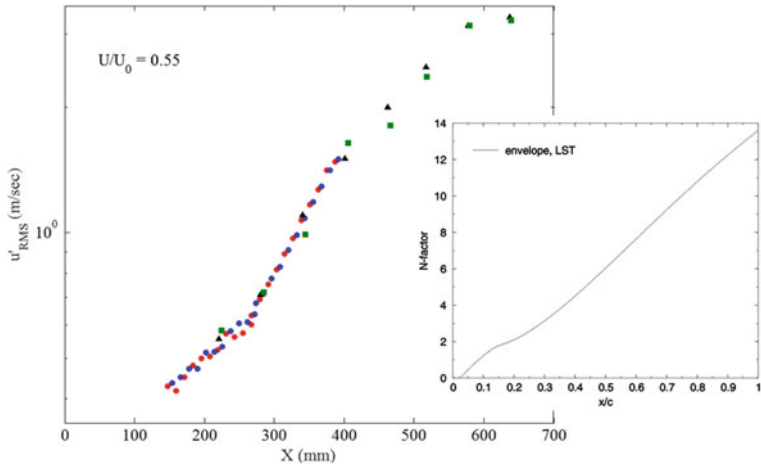


Fig. 5 The growth of unsteady disturbances at height $U/U_e = 0.55$. The different colors correspond to different test runs. In the insert the LST calculations of N -factor are shown (courtesy of and with permission of Stefan Hein, DLR), $X/c = 1$ corresponds to 1 m)

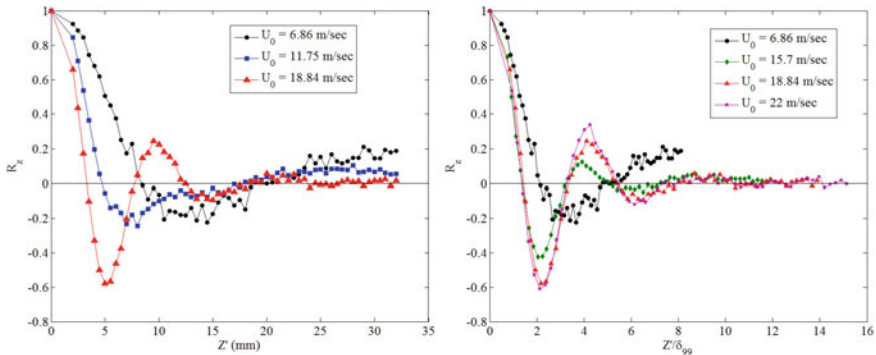


Fig. 6 The two-wire correlations in the middle of boundary layer at different free-stream velocities, $X = 381$ mm. In the right plot the coordinate Z' is normalized with the local boundary layer thickness

cross-correlations in 3D flow spread much further in spanwise direction and exhibit several maxima and minima. The number of these peaks increases with the velocity U_0 . All cross-correlations measured show a good coincidence when scaled with the local boundary layer thickness δ_{99} , except at the low velocity $U_0 = 6.86$ m/s. For instance, at $U_0 = 18.84$ and 22 m/s the anti-correlation about -0.1 is located near $6.5\delta_{99}$. So the spanwise scale is about $(10-15)\delta_{99}$, which is much higher than in a 2D case. The overall appearance of the cross-correlations corresponds rather to a wave-packet structure than to streaks. The evolution of cross-spectra (Fig. 7) is somewhat complicated as U_0 increases, but has several common features. The high degree of coherency is observed in frequency range up to 500 Hz at the spanwise distances

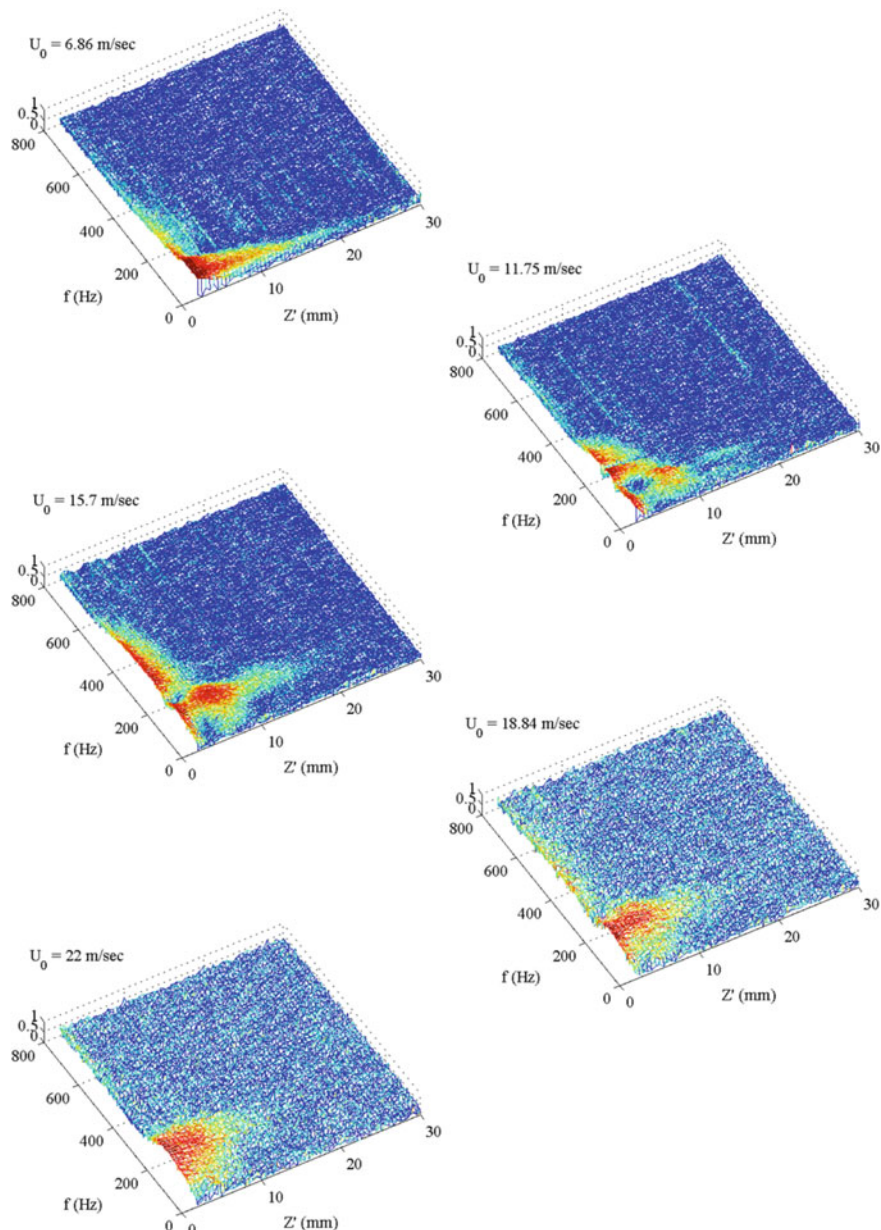


Fig. 7 The amplitude of cross-spectra of two-wire measurements

about several local thickness δ_{99} . In the low-frequency range 0–50 Hz at the distances about 10 mm the coherency gets worse as U_0 increases, while remains high at the range of hundreds Hz. In fact, only at $U_0 = 6.86$ m/s the cross-spectra as well as the cross-correlations have some signs of presence of transient disturbances. The dominant disturbances structures in the fluctuation field are the wave-packets of unstable cross-flow travelling modes. For example, the phase velocity in Z' direction in $U_0 = 22$ m/s regime for frequency 170 Hz that lies near the cross-spectrum maximum is equal to 1.7 m/s. This value is not uncommon to the cross-flow instability.

In order to gain some insight on nonlinear disturbances development the bispectral analysis was performed. It allows to identify the quadratic phase coupling in triads $f = f_1 + f_2$. In the processes with continuous spectrum such as transition under influence of FST this type of analysis requires very long realizations of signal to achieve statistically stable estimates. So the sampling length was increased to 600 s at 5 kHz during these measurements. Due to its symmetry properties the bispectrum, or its normalized variant called bicoherency, needs to be computed only in the triangle at the bifrequency plane (f_1, f_2). The vertices of the triangle is $(0, 0)$, $(0, f_n)$ and $(f_n/2, f_n/2)$, where f_n is the Nyquist frequency 2500 Hz. The bicoherency development is shown in Fig. 8. Only estimates with the 99% significance level are plotted. At the first station $X = 152$ mm the bispectrum is zero (with exception of some discrete noise). The disturbances are going through linear amplification. At $X = 272$ mm the high-frequency modes in the range of 1200–1500 Hz appears. The three types of nonlinear interactions are visible at this position. The first one is between the primary instability modes in the range of 0–200 Hz and the aforementioned high-frequency perturbations. The second is self-interacting high-frequency modes in the upper corner of bicoherency triangle ($f_1 = 1200$ –1400 Hz, $f_1 + f_2 = f_n$). The third type is interaction between fluctuations in the 300–700 Hz range and high-frequencies

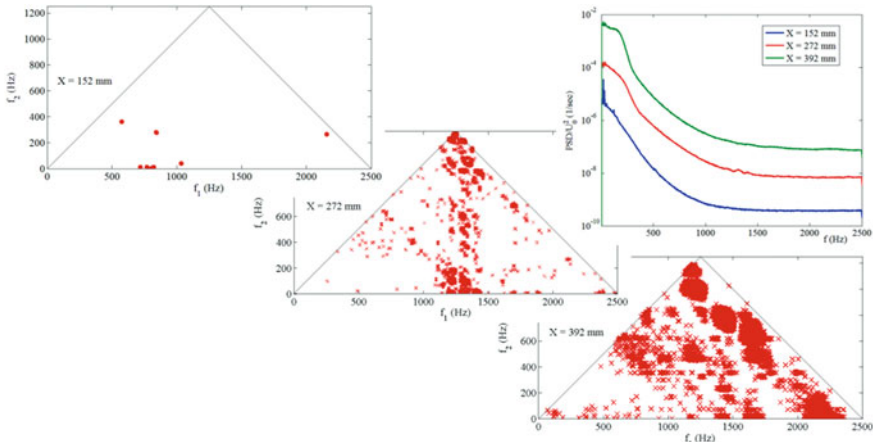


Fig. 8 The power spectral density and the bicoherency of boundary layer fluctuations at $Y/\delta_1 = 1.2$, $X = 152, 272$ and 392 mm. The consecutive PSD plots are shifted up by decade

about 1200–1400 Hz. This type results in the change of power spectrum slope that is clearly visible in Fig. 8 for frequencies above 300 Hz at $X = 272$ mm. At the position $X = 392$ mm, that is located about 60 mm upstream of transition onset, the whole strip between the lines $f_2 = f_n - f_1$ and $f_2 = 1200 - f_1$ shows the significant bicoherency levels. Also the low-frequency interactions appear in the $f_1 = 0$ –700, $f_2 = 0$ –200 Hz region. It corresponds to the non-linear development of the primary unsteady cross-flow instability modes. It is important to notice that despite the early start of nonlinear processes, the overall growth of u_{rms} fluctuations is still in good agreement with the LST at these stations as it seen from the Fig. 5.

As it was mentioned above, the transition itself is going through the turbulent spots development. The common representation of intermittency as function $F = \sqrt{-\ln(1 - \gamma)}$ shows that the straight line is very good approximation to the $F(X)$ dependence. It gives the transition onset located at $X = 452$ mm and transition end position ($\gamma = 0.99$) at $X = 767$ mm. The length of laminar flow destruction zone is very long, almost 40% of total distance from the leading edge to the well-developed turbulent flow.

4 Summary

The observations in the 3D accelerated boundary layer under influence of elevated FST about 1% can be summarized as follows:

- (i) The initial stages of transition are dominated by the wave packets of travelling cross-flow modes, the stationary modes are unimportant.
- (ii) Except the low Reynolds number regime, no traces of non-modal amplification were found; a possible transient growth has been overcome by the strong modal instability.
- (iii) The agreement between measured growth of unsteady cross-flow disturbances and the linear stability theory is good at the initial stages of the disturbance development.
- (iv) The laminar regime destruction manifests itself through high-frequency instability, followed by the turbulent spot development. The nonlinear interactions start well before the transition onset and cover the whole frequency range.
- (v) The streamwise length of the laminar flow destruction zone is rather long.

References

1. Breuer, K.S., Kuraishi, T.: Transient growth in two- and three-dimensional boundary layers. *Phys. Fluids.* **6**(6), 1983–1993 (1994). <https://doi.org/10.1063/1.868205>
2. Corbett, P., Bottaro, A.: Optimal linear growth in swept boundary layers. *J. Fluid Mech.* **435**, 1–23 (2001). <https://doi.org/10.1017/S0022112001003627>

3. Deyhle, H., Bippes, H.: Disturbance growth in an unstable three-dimensional boundary layer and its dependence on environmental conditions. *J. Fluid Mech.* **316**, 73-113 (1996). <https://doi.org/10.1017/S0022112096000456>
4. Kurian, T., Fransson, J.H.M., Alfredsson, P.H.: Boundary layer receptivity to free-stream turbulence and surface roughness over a swept flat plate. *Phys. Fluids* **23**(3), 034107 (2011). <https://doi.org/10.1063/1.3562843>
5. Borodulin, V.I., et al.: Laminar-turbulent transition delay on a swept wing. *AIP Conf. Proc.* **1770**, 030065 (2016). <https://doi.org/10.1063/1.4964007>
6. Kiselev, A.F., Sboev, D.S., Chernyshev, S.L.: Features of the laminar-turbulent transition in the three-dimensional boundary layer for increased external turbulence. *Dokl. Phys.* **59**, 107-110 (2014). <https://doi.org/10.1134/S1028335814020128>
7. Kiselev, A.P., et al.: The laminar-turbulent transition zone in 2D and 3D boundary layers with emphasis on effect of free stream turbulence. In: Paper Presented at the 29th ICAS Congress, St. Petersburg, Russia, 7-12 September 2014 (2014). https://www.icas.org/ICAS_ARCHIVE/ICA_S2014/data/papers/2014_0374_paper.pdf. Accessed 12 July 2020
8. Westin, K.J.A., Boiko, A.V., Klingmann, B.G.B., Kozlov, V.V., Alfredsson, P.H.: Experiments in a boundary layer subjected to free stream turbulence. Part 1. Boundary layer structure and receptivity. *J. Fluid Mech.* **281**, 193-218 (1994). <https://doi.org/10.1017/S0022112094003083>

Flow Control

Experimental Investigation of Spanwise-Periodic Surface Heating for Control of Crossflow-Dominated Laminar-Turbulent Transition



Hans Peter Barth[✉] and Stefan Hein

Abstract An actuation concept for control of crossflow-dominated laminar-turbulent transition is investigated which has not received much attention in this context so far: Spanwise-periodic surface heating. In a systematic variation of heating power, its ability to excite a stationary crossflow instability mode with well-defined wavelength and amplitude is investigated. In an actuated case with significantly high amplitude of this control mode, the effect of the actuation on the downstream evolution of the boundary-layer flow field is investigated in detail.

1 Introduction

Research into the control of laminar-turbulent transition is often motivated by the combined goals of saving fuel and reducing costs while also reducing climate gas emissions. The ability to actively delay transition on the external surfaces of an aeroplane could reduce skin friction drag and therefore achieve these goals. In a crossflow-dominated transition scenario, crossflow instability (CFI) occurs as both stationary and travelling modes, see e.g., [4]. As an alternative to transition control methods aiming at the direct stabilization of the boundary layer, e.g., the reduction of the crossflow component by suction, a nonlinear method has been first demonstrated experimentally by Saric et al. [8]. It involves the artificial excitation of a stationary CFI mode with a spanwise wavelength λ smaller than that of the naturally dominant mode. If excited with suitable wavelength and amplitude, this so-called *control mode* can generate a stabilizing deformation of the spanwise-averaged velocity profile in the nonlinear regime of the boundary layer, which consequently leads to delayed transition. In their DNS investigations on this effect, Wassermann and Kloker fur-

H. P. Barth (✉) · S. Hein
DLR, Institute of Aerodynamics and Flow Technology, Bunsenstr. 10, 37073 Göttingen, Germany
e-mail: peter.barth@dlr.de

S. Hein
e-mail: stefan.hein@dlr.de

thered the comprehension of it and introduced the name *Upstream Flow Deformation* (UFD) [10]. In order to artificially excite the stationary control mode, it is necessary to introduce a spanwise-periodic stationary disturbance with well-defined wavelength λ and amplitude into the boundary layer. In the investigations in [8], spanwise periodically applied discrete roughness elements were used to create this disturbance. Other methods for the same purpose, but with an easily adjustable excitation amplitude are called “*Active roughness*” -methods or methods of *active* actuation. Two such methods have already been investigated in the context of UFD: Spanwise periodic pneumatic blowing or suction and spanwise periodic plasma actuation. In the case of pneumatic actuation, the UFD effect has been successfully employed for transition delay in a cooperation of TU Berlin and DLR [7] in the same experimental setup as used in this investigation. In the case of plasma actuation, Serpieri et al. were not able to delay transition despite the successful excitation of the control mode with suitable wavelength and amplitude [9]. In their interpretation, the inadvertent excitation of travelling CFI by the plasma actuator was most probably responsible for this, despite the careful selection of the actuation frequency outside of the amplified frequency range. In a master thesis at DLR Göttingen, a student investigated spanwise periodic surface heating as a means of exciting stationary CFI and was successful [3]. The focus of his investigations lay in the comparison of experimentally observed instability mode growth with numerical results, not on the purposeful control of the transition scenario. This excitation method and its applicability in the context of UFD are the main topics of the present investigation.

2 Experimental Setup

The experimental investigations discussed in this publication take place in the DLR-SPECTRA (Swept flat PlatE Crossflow TRAnsition) B-configuration. It is based on the well-known experimental configuration used by Bippes et al. see [4].

2.1 DLR-SPECTRA Configuration

Both the original configuration and the redesigned SPECTRA configuration consist of a model plate with a displacement body together with a slat arranged above it, see Fig. 1a. The displacement body imprints a pressure distribution on the boundary layer on the upper side of the model plate where all experiments take place. The slat in front of the displacement body prevents separation on the upper side of the displacement body. The original displacement body used by Bippes et al. [4] featured an almost constant negative pressure gradient across the chord length of the model plate. The stability conditions of that boundary layer are not well suited for experiments on the UFD effect. Therefore, the experimental configuration was redesigned which consisted mainly of a new displacement body and an increase

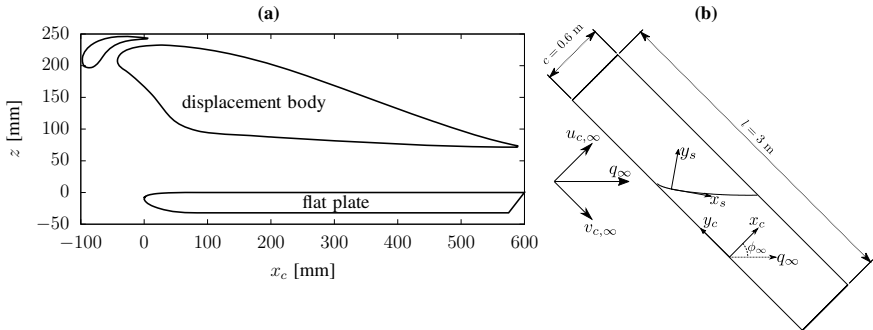


Fig. 1 **a** Cross-section sketch of the experimental configuration SPECTRA-B **b** Top-view sketch of the flat plate

in the chord length of the model plate, for details see [2]. The configuration used in the investigations discussed in this publication is shown in Fig. 1a and is called *SPECTRA-B*. Another displacement body has been designed, which nearly reproduces the characteristic features of the original configuration used by Bippes et al. in the current experimental setup. This configuration is designated *SPECTRA-A* in order to distinguish both configurations, their respective pressure distributions and base-flow features in future publications. The base flow and its stability conditions for SPECTRA-B are described in [2] in detail. The relevant coordinate systems are illustrated in Fig. 1b. The coordinate system fixed to the model plate bears the index “ c ”, while the coordinate system oriented along the curved potential streamline bears the index “ s ”.

2.2 Actuator: Spanwise Periodic Heating

In Sect. 1 the need for the introduction of a spanwise periodic initial disturbance into the boundary layer for exciting the stationary control mode was explained. This spanwise periodic disturbance is generated in the presently investigated actuation concept by introducing a defined periodicity into the spanwise distribution of the wall-temperature of the model surface. An increase in the wall-temperature is generated by a constant electrical current passing through a series connection of copper *heating elements* and *conductive elements*, called a “heating row”. These copper structures differ in their cross-sectional area and therefore their electrical resistance and are shown exemplarily in Fig. 2. Due to their higher electrical resistance, more heat is dissipated by heating elements than by conductive elements which creates a spanwise periodicity in the wall-temperature distribution. Its spanwise wavelength coincides with the wavelength $\lambda = 6 \text{ mm}$ of the selected control mode, see [2]. The copper structures are arranged on a flexible polyimide printed circuit board (PCB), which is fixed flush into a pocket of corresponding height in the surface of a nose insert for

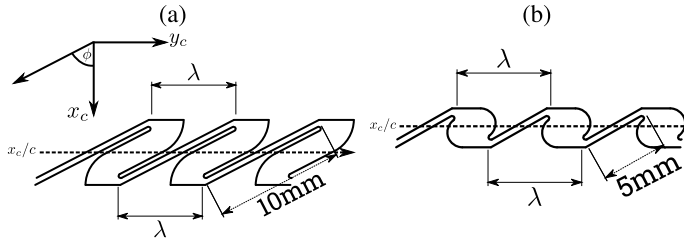


Fig. 2 Exemplary partial view of the series connection of **a** long heating elements and **b** short heating elements (three of each)

the model plate. The material selected for the nose insert is an epoxy block material with high temperature resistance and low heat conductivity.

In order to investigate the effect of the actuation location on the excitation of the control mode, eight of these heating rows are arranged on the PCB at successive chord locations. The local sweep angle of the heating elements is aligned with the angle of the control mode vortex axis at the respective average location of the heating row. This angle was obtained from LST analysis results. Two different types of heating elements were designed: Those with a length of 10 mm (see Fig. 2a) and those with a length of 5 mm (see Fig. 2b). Heating rows 1, 3, 5 and 7 feature long heating elements, heating rows 2, 4, 6 and 8 feature short heating elements. To reduce the surface inhomogeneity exposed to the boundary layer, the copper elements are covered with an epoxy resin surface, which is then polished to an average roughness of $R_a = 2.5 \mu\text{m}$.

2.3 Wind Tunnel Facility

The configuration is investigated in the open test section of the 1MG wind tunnel at DLR Göttingen, which is a closed-circuit wind tunnel of Göttingen type. The geometric sweep angle is $\phi_g = 45.0^\circ$ and the free-stream velocity is $q_\infty = 29.2 \text{ m/s}$. The relevant turbulence level of the free stream is determined to be $Tu = 0.18\%$ using a hot-wire probe upstream of the model, when integrating the spectrum of unsteady velocity fluctuations in the frequency range $2 \text{ Hz} < f < 2000 \text{ Hz}$ as e.g., Deyhle et al. described [5].

2.4 Measurement Techniques

The main measurement technique for the investigation of the boundary-layer flow field is constant-temperature hot-wire anemometry (CTA) using V-type boundary layer probes. For the investigation of the systematic variation of the heating power

of each heating row, spanwise scans at a constant chord location of $x_c/c = 0.35$ are conducted because this location coincides with the maximum amplitude of the control mode in its downstream development, see e.g., [7]. In these scans of spanwise length $l = 100$ mm, the hot-wire signals are sampled at 102 locations for a duration of 2 s each at a sampling rate of 32768 Hz. For the detailed investigation of the actuation effect, the boundary-layer flow field is sampled at $14 \cdot 61 \cdot 30$ locations distributed in chord-, spanwise and wall-normal direction respectively. The spanwise length covered is 60 mm with equidistant spacing and the wall-normal distance is adapted to the respective local boundary-layer thickness. At each location the hot-wire signals are sampled for a duration of 4 s at the same sampling rate as for the spanwise scans. In addition to hot-wire measurements, the surface-temperature distribution is characterized using an infrared camera.

3 Results

In the following, the immediate effect of the actuation on the surface-temperature distribution is characterized. Then, results from the systematic variation of heating power are shown after which the effect of the actuation is investigated in detail for a single set of actuation parameters.

3.1 Characterization of the Surface-Temperature Distribution

From infrared measurements during the hot-wire measurements in the 1MG wind tunnel, the two-dimensional surface-temperature distribution is observed. In this wind tunnel facility, the geometry of the setup dictates a minimum distance of the infrared camera to the model surface which limits the optical resolution. It is sufficient for evaluating the spanwise-averaged temperature distribution but not sufficient for determining the amplitude of the spanwise wall-temperature periodicity. Therefore, after the measurements in the 1MG wind tunnel, this amplitude is determined on the nose insert alone in a smaller wind tunnel at the same free-stream conditions. Apart from the intended spanwise periodicity of the wall-temperature distribution, an increase in the spanwise-averaged wall-temperature is observed. This elevation is shown in Fig. 3a for all heating rows operated individually at the maximum heating power used during its systematic variation.

The spanwise periodicity of the wall-temperature distribution is determined to have approximately sinusoidal shape and its amplitude is shown in Fig. 3b depending on the heating power for all heating rows. It depends linearly on the heating power for all rows and is used in the following as a measure for the actuation amplitude instead of heating power.

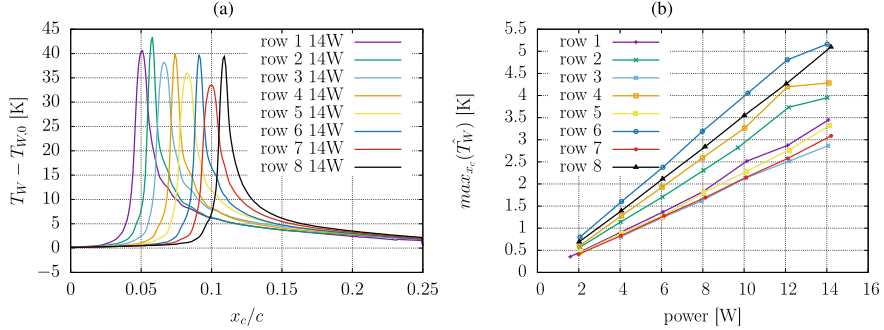


Fig. 3 **a** Spanwise-averaged wall-temperature distributions for all rows of heating elements at $P = 14$ W for $x_c/c \leq 0.25$ from infrared measurements. **b** Amplitude of spanwise sinusoidal wall-temperature periodicity depending on heating power for all heating rows

3.2 Impact of Surface Heating on Boundary-Layer Stability

The spanwise-averaged wall-temperature distributions shown in Fig. 3a are used as a boundary condition in solutions of the boundary-layer equations using COCO [1]. The wall-temperature distribution is only measured for $x_c/c < 0.25$. For $x_c/c \geq 0.25$, the model plate consists of Aluminium and it is assumed that its thermal conductivity is large enough that an unaffected wall-temperature distribution can be assumed. The stability of the resulting boundary-layer solutions with respect to stationary and travelling CFI is then analysed using NOLOT in LST mode [6].

Exemplary results are shown in Fig. 4 for the case of row 1 operated at the heating power $P = 14$ W with N-factors shown in coloured isocontours for the actuated case

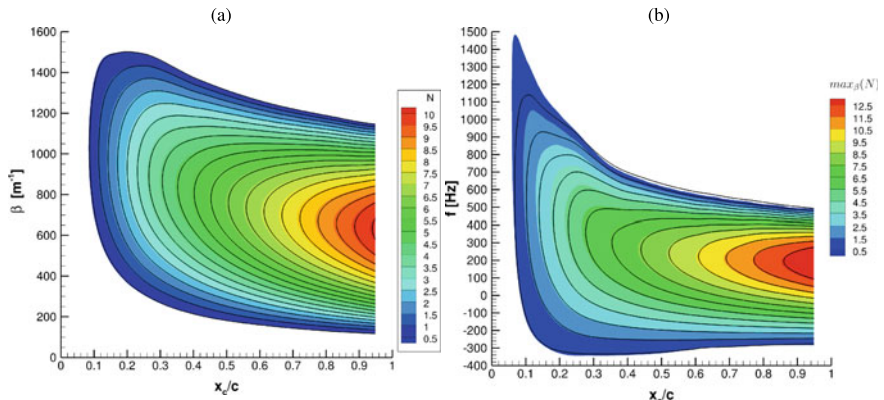


Fig. 4 **a** Comparison of N-factors of stationary CFI according to LST in the case of row 1 operated at $P = 14$ W, isocontours show N-factors for actuated case, isolines show N-factors for non-actuated case. **b** Comparison of N-factors of travelling CFI for the same case

and in isolines for the non-actuated case depending on the spanwise wavenumber $\beta = 2\pi/\lambda$ and chord location x_c/c . In Fig. 4a, N-factors for stationary CFI are shown. For travelling CFI, maximum N-factors with respect to spatial wavenumbers, are shown in Fig. 4b depending on frequency and chord location. In summary, only a small destabilization of the boundary layer is expected. For travelling modes, especially near the chord location of the highest wall-temperature elevation, previously stable modes at high frequencies are destabilized in a limited chord region.

3.3 Systematic Variation of Heating Power

For each individually operated row of heating elements, the heating power and with it the amplitude of the spanwise wall-temperature periodicity is varied systematically. For each heating power, an equilibrium state in terms of the surface temperature distribution is investigated, meaning that the wind tunnel is kept running for sufficient time after changing heating power before measurements in the boundary layer are conducted. The amplitude of the artificially excited control mode with spanwise wavelength $\lambda = 6 \text{ mm}$ ($\beta = 1047 \text{ 1/m}$) is determined from the spanwise hot-wire scans at $x_c/c = 0.35$. Exemplary results for row 1 are shown in Fig. 5a with the respective spanwise phase. In the non-actuated case, the amplitude of the control mode is already about 2% of the boundary-layer edge velocity q_e and is excited by the periodicity of the model surface at that wavelength. With increasing \hat{T}_W , the observed amplitude of the control mode at $x_c/c = 0.35$ decreases until a minimum value is reached and the amplitude then increases nearly linearly with \hat{T}_W . The phase of the control mode decreases with increasing \hat{T}_W which represents a shift of the CFI vortex axes in $+y_c$ -direction. This phase shift seems to asymptotically reach a value of $-\pi$ at high values of \hat{T}_W , representing a spanwise shift of $\lambda/2$.

The observed amplitude of the control mode at $x_c/c = 0.35$ in actuated cases is a result of the superposed excitation by the spanwise periodicity of the surface inhomogeneity with $\lambda = 6 \text{ mm}$ and the excitation by the surface heating with the same spanwise periodicity. Because the surface periodicity at that wavelength is mainly caused by the copper elements themselves and because row 1 is located near the neutral point of the control mode, it is reasonable to assume that both relevant excitations occur at the same chord location for this row. The decreasing amplitude and the phase shift can then be interpreted as symptoms of a partly destructive phase relationship of both fundamental excitation mechanisms. The spanwise distribution of the velocity component $u_{s,0}(y_c)$ at $x_c/c = 0.35$ in the non-actuated case contains the boundary-layer deformation caused by the surface inhomogeneity of the model surface, including the spectral contribution at $\lambda = 6 \text{ mm}$ of heating row 1 and the rows downstream. Subtracting this spanwise distribution from the spanwise distribution $u_s(y_c)$ in actuated cases represents a linear separation of the two excitation effects. The resulting velocity component $a_s(y_c) := u_s(y_c) - u_{s,0}(y_c)$ therefore ideally contains only the boundary-layer deformation introduced by the surface heating of the respective individually operated heating row for each value of \hat{T}_W . From $a_s(y_c)$, the

amplitude of its spanwise periodicity is determined for each heating row and each value of \hat{T}_W and results are shown in Fig. 5b. The amplitude \hat{a}_s of the periodicity with $\lambda = 6$ mm in this isolated spanwise distribution increases monotonously with increasing \hat{T}_W for all heating rows. This supports the interpretation of a destructive superposition of an excitation by surface inhomogeneities and surface heating at the same chord location causing the decreasing amplitude \hat{u}_s at low actuation amplitude in Fig. 5a. Analysis of the maximum slope $\frac{\partial \hat{a}_s}{\partial \hat{T}_W}$ for each heating row shows that at a similar actuation location, long heating elements are more efficient in exciting the control mode than short heating elements.

3.4 Effect on the Scenario of Laminar-Turbulent Transition

For a single set of actuation parameters, row 3 operated at $P = 18$ W with $\hat{T}_W = 3.7$ K, the effect of the actuation on the development of the boundary-layer flow field is investigated in more detail, see Sect. 2.4. This set of parameters was selected because the amplitude of the artificially excited control mode coincides nearly with that of cases of successful transition delay employing the UFD method in the same setup, see [7]. Three-dimensionally distributed hot-wire measurements are performed for both the actuated and the non-actuated case.

The boundary-layer flow field for both cases is visualized by the time-averaged velocity component u_s in isocontours in Fig. 6a, b. In contrast to the non-actuated case, where long-wavelength content dominates the spanwise spectrum of stationary CFI, a spanwise periodicity with $\lambda = 6$ mm is clearly visible in the actuated case because of the successfully excited control mode. The actuation clearly manages to significantly rearrange the stationary flow field.

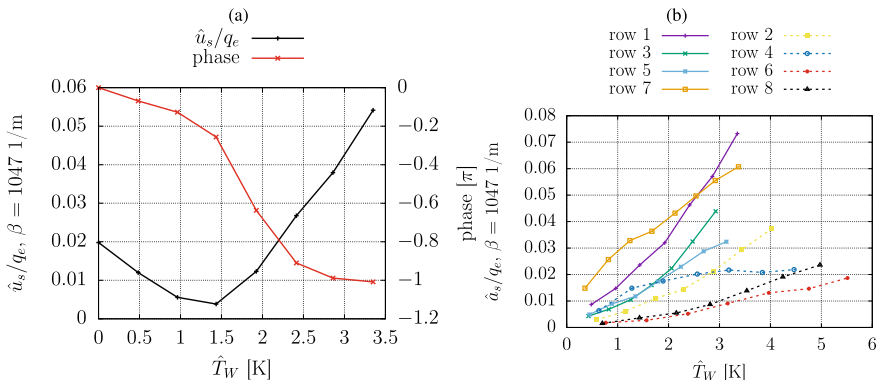


Fig. 5 **a** Amplitude and phase of the artificially excited stationary CFI mode with wavelength $\lambda = 6$ mm in the boundary layer at $x_c/c = 0.35$ for row 1 depending on \hat{T}_W **b** the amplitude \hat{a}_s of the spanwise periodicity with $\lambda = 6$ mm in the isolated effect of the actuation a_s for all rows

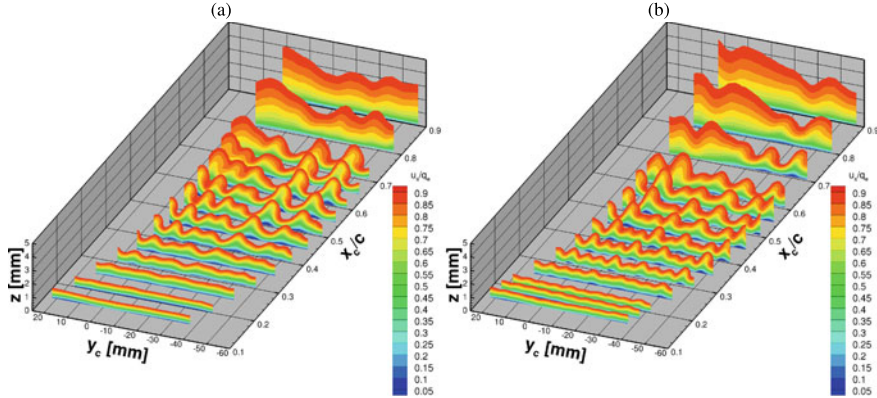


Fig. 6 Three-dimensional visualization of the boundary-layer flow field with the non-dimensional u_s velocity component shown in isocontours for **a** the non-actuated case and **b** the actuated case

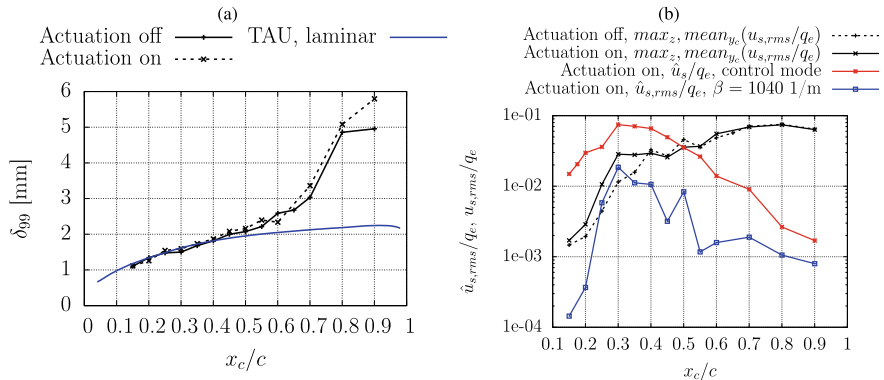


Fig. 7 **a** Boundary-layer thickness from spanwise-averaged velocity profile visualizing the spanwise-averaged transition location. **b** RMS values of unsteady velocity fluctuations and the amplitude of the artificially excited control mode

In Fig. 7a, the boundary-layer thickness, derived from the respective spanwise-averaged velocity profile in the non-actuated and actuated case is shown in comparison with the boundary-layer thickness in a laminar CFD simulation with DLR-TAU in order to visualize the spanwise-averaged transition location. The sudden increase of the boundary-layer thickness due to the turbulent breakdown occurs for both cases in parallel at nearly the same chord location. This means that despite the successful excitation of the control mode, the attempt at employing the UFD method for transition delay was unsuccessful in this case.

From LST results and from experimental spectra, it is known that in this experiment velocity fluctuations in the frequency range $100 \text{ Hz} < f < 600 \text{ Hz}$ can be associated with travelling CFIs. The wall-normal maximum of the spanwise-averaged RMS values of the streamwise velocity fluctuations in this frequency range are shown

in Fig. 7b for the non-actuated and the actuated case. These RMS values are elevated for the actuated case in a limited chord region $0.15 < x_c/c < 0.4$. The observed elevation is larger than the expected destabilization of travelling CFIs discussed in Sect. 3.2. Contrary to plasma actuation, where the excitation mechanism inherently possesses an unsteady contribution, surface heating is only stationary and the elevation of unsteady velocity fluctuations can either be a symptom of an increased receptivity or an indirect effect of the actuated stationary flow field. The observed elevated RMS values occur mostly at locations close to the wall and possess the same spanwise periodicity as the stationary control mode. From the spanwise distribution of the wall-normal maximum of the RMS value of velocity fluctuations in the frequency range $100 \text{ Hz} < f < 600 \text{ Hz}$, the amplitude of the spanwise periodicity of $\beta = 1040 \text{ 1/m}$ is determined, which corresponds nearly to the spanwise wavelength $\lambda = 6 \text{ mm}$. This amplitude is also shown in Fig. 7b and shows stronger growth than the wall-normally maximum of the spanwise-averaged RMS value of velocity fluctuations in the same frequency range. This is interpreted as evidence that the elevated velocity fluctuations are caused by a secondary instability of the stationary control mode and are not an inherent feature of actuation by spanwise-periodic surface heating.

In Fig. 8a, b, the wall-normal maximum of stationary CFI amplitudes is shown depending on the spanwise wavenumber β and chord location x_c/c . In the non-actuated case, spectral content with low wavenumbers around $\beta_1 \approx 420 \text{ 1/m}$ dominates the spectrum even though these wavenumbers are lower than those of the integrally most amplified modes, see Fig. 4a. This is most probably due to a waviness in the epoxy cover surface described in Sect. 2.2. In the actuated case, the successfully excited control mode is clearly visible as a local maximum around $\beta_2 = 1047 \text{ 1/m}$. The previously dominant low-wavenumber content at or above $\beta_1 = 420 \text{ 1/m}$ is significantly decreased in amplitude. But another local maximum appears in the spectrum at a wavenumber which corresponds roughly with the difference $\beta_2 - \beta_1$

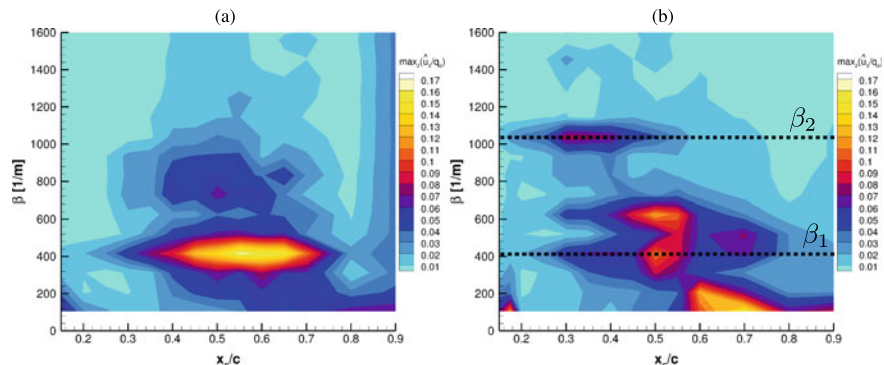


Fig. 8 Spanwise spectrum of stationary CFI depending on the spanwise wavenumber β and the chord location x_c/c , with the wall-normal amplitude maximum shown in colours for **a** the non-actuated case and **b** the actuated case

and which is close to the integrally most amplified wavenumber. This points to an undesired nonlinear interaction between the control mode and the low-wavenumber content excited by the waviness of the surface. It offers an explanation for the lack of transition delay: Instead of a nonlinear mean-flow distortion with stabilizing effect, the excitation of the control mode only led to a spectral redistribution of stationary CFIs and left the transition location nearly unaffected.

4 Conclusion

In the context of transition delay using the *Upstream Flow Deformation* method [8, 10], active actuation concepts for exciting stationary CFIs are of interest. One of these actuation concepts which has not been investigated in this context is investigated in this publication: spanwise periodic surface heating. It is shown that the amplitude of a stationary control mode can be easily controlled using spanwise periodic surface heating by varying the heating power. The observed characteristic phase difference between excitation by surface inhomogeneity and surface heating contains information on the relevant receptivity mechanism. Evidence is presented that the failure to employ the UFD method for transition delay is caused by a waviness of the model surface which disadvantageously alters the instability spectrum in the non-actuated case compared to the scenario for which the actuator was designed. It is shown that the observed elevation of unsteady velocity fluctuations is not mainly due to a thermal destabilization of the boundary-layer but due to a secondary instability of the control mode itself. Therefore it is concluded that the actuation concept is in principle suitable for Upstream Flow Deformation.

References

1. COCO – a program to compute velocity and temperature profiles for local and nonlocal stability analysis of compressible, conical boundary layers with suction. Tech. rep., ZARM (1998)
2. Barth, H.P., Hein, S., Rosemann, H.: Redesigned swept flat-plate experiment for crossflow-induced transition studies. In: Notes on Numerical Fluid Mechanics and Multidisciplinary Design, pp. 155–165. Springer International Publishing (2017)
3. Berger, C.: Einführung von künstlichen Störungen in die instabile, dreidimensionale, beschleunigte Grenzschichtströmung. Master's thesis, Universität Göttingen (1990)
4. Bippes, H.: Basic experiments on transition in three-dimensional boundary layers dominated by crossflow instability. *Prog. Aerosp. Sci.* **35**(4), 363–412 (1999)
5. Deyhle, H., Bippes, H.: Disturbance growth in an unstable three-dimensional boundary layer and its dependence on environmental conditions. *J. Fluid Mech.* **316**, 73–113 (1996)
6. Hein, S., Bertolotti, F.P., Simen, M., Hanifi, A., Hemmingson, D.: Linear nonlocal instability analysis - the linear NOLOT code. DLR-JB 223-94 A 56 (1995)
7. Lohse, J., Barth, H.P., Nitsche, W.: Active control of crossflow-induced transition by means of in-line pneumatic actuator orifices. *Exp. Fluids* **57**(8), 1–10 (2016)
8. Saric, W., Carrillo, R.J., Reibert, M.: Leading-edge roughness as a transition control mechanism. In: 36th AIAA Aerospace Sciences Meeting and Exhibit (1998)

9. Serpieri, J., Venkata, S.Y., Kotsonis, M.: Towards laminar flow control on swept wings with AC-DBD plasma actuators as active roughness. In: 55th AIAA Aerospace Sciences Meeting (2017)
10. Wassermann, P., Kloker, M.: Mechanisms and passive control of crossflow-vortex-induced transition in a three-dimensional boundary layer. *J. Fluid Mech.* **456**, 49–84 (2002)

Nonlinear Optimal Control Using Deep Reinforcement Learning



Michele Alessandro Bucci, Onofrio Semeraro, Alexandre Allauzen,
Laurent Cordier, and Lionel Mathelin

Abstract We propose a shift of paradigm for the control of fluid flows based on the application of deep reinforcement learning (DRL). This strategy is quickly spreading in the machine learning community and it is known for its connection with nonlinear control theory. The origin of DRL can be traced back to the generalization of the optimal control to nonlinear problems, leading—in the continuous formulation—to the Hamilton-Jacobi-Bellman (HJB) equation, of which DRL aims at providing a discrete, data-driven approximation. The only a priori requirement in DRL is the definition of an instantaneous reward as measure of the relevance of an action when the system is in a given state. The value function is then defined as the expected cumulative rewards and it is the objective to be maximized. The control action and the value function are approximated by means of neural networks. In this work, we clarify the connection between DRL and rediscuss our recent results for the control of the Kuramoto-Sivashinsky (KS) equation in one-dimension [4] by means of a parametric analysis.

M. A. Bucci

Université Paris-Saclay, INRIA Saclay, Laboratoire Interdisciplinaire des Sciences du Numérique (TAU-Team), 91190 Gif-sur-Yvette, France

e-mail: michele-alessandro.bucci@inria.fr

O. Semeraro (✉) · L. Mathelin

Université Paris-Saclay, CNRS, Laboratoire Interdisciplinaire des Sciences du Numérique, 91400 Orsay, France

e-mail: semeraro@limsi.fr

L. Mathelin

e-mail: mathelin@limsi.fr

A. Allauzen

LAMSADE, Université Paris Dauphine, Place du Maréchal de Lattre de Tassigny, 75016 Paris, France

e-mail: alexandre.allauzen@dauphine.fr

L. Cordier

Institut Pprime, CNRS, Université de Poitiers, ENSMA, 11 Boulevard Marie et Pierre Curie, Futuroscope Chasseneuil, France

e-mail: Laurent.Cordier@univ-poitiers.fr

1 Introduction

Control theory methods have attracted research in fluid dynamics due to the scientific challenges and the potential impact that such a technology might have in several engineering sectors, ranging from aeronautics to naval and road transport. Further impulse to these developments is undoubtedly due to the current environmental needs. Carbon dioxide emissions are considered among the causes of global warming and any reduction of these emissions can be beneficial in this regard. In this work, we focus on active control based on reinforcement learning (RL) algorithms, one of the main sub-fields of machine learning [3, 7]; RL is mainly used in robotics and has gained popularity in the last years for the super-human performance achieved in solving tasks as complex as solving games such as go, [14]. A possible definition can be given by quoting a recent work by [11]: “*RL [...] studies how to use past data to enhance the future manipulation of a dynamical system*”. Not surprisingly, this definition could also apply to control theory algorithms: RL is deeply rooted into optimal control theory [9, 11, 12] as it relies on data-driven based solutions to the Bellman equation [2]. Indeed, while sharing the theoretical ground of the optimal control, RL is fully data-driven and, as such, is characterized by the applicability of data-based approaches, like the ability of using only a limited amount of sensor measurements for determining an optimal control policy.

Following this rationale, we aim at leveraging RL strategies for the closed-loop nonlinear control. We have demonstrated in our recent work [4] that a nonlinear, chaotic system governed by the Kuramoto-Sivashinsky (KS) equations can be controlled without relying on a priori knowledge of the dynamics of the system, but solely on localized measurements of the system. Effective policies were computed, capable of driving the system to the vicinity of the unstable, non-trivial solutions of the KS in a chaotic regime [5]. Here, we further extend these results; we briefly introduce the basics of nonlinear optimal control theory and RL in §2; a parametric analysis is proposed in §3 aiming at discussing the robustness of the computed controllers.

2 Reinforcement Learning: Introductory Elements

In this section, we briefly introduce the main elements for comparing control theory and the fundamentals of RL. We refer the interested reader to the literature in optimal control [9], including the fluid mechanics applications [6, 8, 13], and RL for deeper insights [7, 10, 14].

2.1 Bellman's Optimality Condition

First of all, we introduce the state-space model

$$\frac{d\mathbf{v}}{dt} = \mathcal{F}(\mathbf{v}(t), \mathbf{u}(t), t), \quad (1a)$$

$$\mathbf{x}(t) = \mathcal{G}(\mathbf{v}(t)), \quad (1b)$$

describing a dynamical system governed by the nonlinear map \mathcal{F} and propagating the state $\mathbf{v} \in \mathbb{R}^N$. The model is forced by an input vector $\mathbf{u} \in \mathbb{R}^m$, with m being the number of inputs. In the second relation, the map \mathcal{G} associates the observed state \mathbf{v} to the observable $\mathbf{x} \in \mathbb{R}^p$, function of time t , recorded as outputs by p sensors. In the following, we will generally define the observables \mathbf{x} and the input vector \mathbf{u} as *signals*. The control signal \mathbf{u} corresponds to the amplitude in time of localized forcing introduced in the system, typically as actuators.

The optimal control problem applied to the dynamical system in Eq. 1 can be stated as follows:

To compute the control signal $\mathbf{u} \in \mathbb{R}^m$ using the sensor measurements $\mathbf{x} \in \mathbb{R}^p$, such that an objective function \mathcal{J} is minimized.

A general expression of the objective function is given by

$$\mathcal{J}(\mathbf{v}_t, t, \mathbf{u}(\tau)) = h(\mathbf{v}(T), T) + \int_t^T r(\mathbf{v}(\tau), \mathbf{u}(\tau), \tau) d\tau, \quad (2)$$

where h provides the terminal condition at time T , the optimization horizon, and r is the reward associated with the state \mathbf{v} and the action \mathbf{u} . Note that t can be any value less than or equal to T . As previously stated, the objective of the controller is to provide a mapping between the sensor signal \mathbf{x} and the control actions \mathbf{u} ; this mapping is usually called *policy* and will be indicated as π such that unknown optimal signal is obtained as

$$\mathbf{u}^*(t) = \pi^*(\mathbf{x}(t), t). \quad (3)$$

Hereafter, optimal solutions will be indicated with a (*). When the system in Eq. 1 is known, linear (or linearizable) and time-invariant, a classic approach to optimal control is the linear quadratic regulator (LQR), obtained when the reward r is quadratic; in that case, it is possible to resolve the associated Riccati equation and compute the corresponding policy [9]. Here, we keep the formulation as general as possible and proceed by maximizing the value of the objective function in Eq. 2 on the right-hand side (RHS) as

$$\mathcal{J}^*(\mathbf{v}(t), t) = \max_{\substack{\pi(\tau) \\ t \leq \tau \leq T}} \left[\int_t^T r(\mathbf{v}(\tau), \mathbf{u}(\tau), \tau) d\tau + h(\mathbf{v}(T), T) \right]. \quad (4)$$

The RHS can be further manipulated by splitting the integral in two contributions

$$\mathcal{J}^*(\mathbf{v}(t), t) = \max_{\substack{\pi(\tau) \\ t \leq \tau \leq t + \Delta t}} \left[\int_t^{t + \Delta t} r d\tau + \mathcal{J}^*(\mathbf{v}(t + \Delta t), t + \Delta t) \right], \quad (5)$$

where the first term defined in the interval $[t, t + \Delta t]$ and corresponds to an *immediate reward* while the remaining terms are now replaced by the optimal *value function*. The term $\mathcal{J}^*(\mathbf{v}(t + \Delta t), t + \Delta t)$ can be developed in Taylor series about $\mathbf{v}(t)$ and, in the limit for $\Delta t \rightarrow 0$, it leads to the well known Hamilton-Jacobi-Bellman (HJB)

$$-\dot{\mathcal{J}}^*(\mathbf{v}(t), t) = \max_{\pi(t)} [r(\mathbf{v}(t), \mathbf{u}(t), t) + \mathcal{J}_v^*(\mathbf{v}(t), t) \mathcal{F}(\mathbf{v}(t), \mathbf{u}(t), t)], \quad (6)$$

with \mathcal{J}_v^* being the derivative with respect to the state, and the terminal condition $\mathcal{J}^*(\mathbf{v}(T), T) = h(\mathbf{v}(T), T)$. This functional equation is continuous in time and defined backward. If the HJB is solved on the whole state-space and its value function is differentiable, the equation provides a necessary and sufficient condition for the optimum. More interestingly for what it follows, it can be shown that the discrete counterpart of the HJB equation is given by the Bellman equation

$$\mathcal{J}^*(\mathbf{v}_t) = \max_{\mathbf{u}} [\Delta t r(\mathbf{v}_t, \mathbf{u}_t) + \gamma \mathcal{J}^*(\mathbf{v}_{t + \Delta t})], \quad (7)$$

where $\gamma = \exp(-\Delta t \rho)$ is the discount factor and Δt the time step. This equation is applied using the Markov decision process (MDP) framework, where the probability of evolving from the present state to the future one under the action \mathbf{u} is expressed by transition matrices. Due to the probabilistic framework, the value function is reformulated in terms of expectation of the cumulative discounted reward defined by

$$\mathcal{J}^\pi(\mathbf{v}_t) = \mathbb{E} \left[\sum_{l=0}^{\infty} \gamma^l r(\mathbf{v}_{t+l \Delta t}) \right]. \quad (8)$$

The Bellman equation in (7) is central in dynamic programming, discrete optimal control and RL. We can observe an important property: the discounted infinite-horizon optimal problem is decomposed in a series of local optimal problems; more precisely, by quoting [2]

“An optimal policy has the property that whatever the initial state and initial decision are, the remaining decisions must constitute an optimal policy with regard to the state resulting from the first decision.”

This property is the *Bellman's principle of optimality* and allows to solve the optimization problem by breaking it in a sequence of simpler problems.

2.2 Reinforcement Learning

One of the assumptions in the previous section was the knowledge of the whole action-state space: when considering nonlinear maps \mathcal{F} of large dimensions, the computational costs would be prohibitive. As an alternative, we can observe that, in the Bellman equation, the model does not appear explicitly: it suffices to observe the state \mathbf{v}_t and measure the reward r for recovering $\mathcal{J}^\pi(\mathbf{v}_t)$ from the interaction of the system with the environment under the policy. If $\mathcal{J}^\pi(\mathbf{v}_t)$ is a solution of Eq. 7, we get a data-driven approximation of the optimal solution of the nonlinear control problem. This idea leads to the *reinforcement learning* (RL) framework; in the specific case of the *deep reinforcement learning* (DRL), the policy and the value function are represented by neural networks (NN).

2.3 General Classification for RL Algorithms

A rather general way to classify the RL algorithms can be made by identifying three main classes of techniques: (i) *Actor-only*, (ii) *Critic-only* and (iii) *Actor-Critic*. The word *actor* is synonym of policy, while *critic* indicates the value function.

1. **Actor-only** methods consist of evaluating parametric policies. In this procedure, each policy is evaluated by recording the system for a long time and computing the cumulative discounted reward; the optimization is performed by means of stochastic gradient-descent algorithms for the update of the policy. These algorithms are usually referred to as REINFORCE algorithms. From the mathematical viewpoint, the actor-only method satisfies the Pontryagin's maximum principle, a necessary condition for the optimality, where the system is optimized in the vicinity of only one trajectory.
2. **Critic-only** methods are based on the value function approximation; a general expression of the Bellman equation associated with this class of algorithm is given by

$$Q^\pi(\mathbf{v}_t, \mathbf{u}_t) = r(\mathbf{v}_t, \mathbf{u}_t) + \gamma Q^\pi(\mathbf{v}_{t+\Delta t}, \mathbf{u}_{t+\Delta t}). \quad (9)$$

In this way, the state-action value function, or *Q-function*, is written as solution of the Bellman equation and measures the long-term reward of a system evolving along a trajectory emanating from \mathbf{v}_t under an action \mathbf{u}_t , and subsequently driven by a policy π . *Q*-learning algorithms are aimed at approximating the optimal action-value function.

3. **Actor-critic** algorithms combine the two techniques, by providing an approximation for the policy and guaranteeing that the *Q-function* is a solution of the Bellman equation; this condition is satisfied when the analyzed system is Markovian and fully known from the observables.

2.4 Deep Deterministic Policy Gradient as an Actor-Critic Algorithm for DRL

In this application, we opted for an actor-critic strategy, the Deep Deterministic Policy Gradient (DDPG) [10], capable of handling continuous actions. First of all, we define the so-called *tuple*, composed by the current state \mathbf{x}_t , the associated reward r_t , and the state \mathbf{x}_{t+1} obtained under the action \mathbf{u}_t . The tuples are iteratively stacked in memory, and define the MDP. Note that in the most general case, we do not consider the full state, but only local measurements such that $\mathbf{x} = \mathcal{G}(\mathbf{v})$: in this case, the observability of the MDP can be limited, so typically we refer to as partial observability (PO)-MDP. This aspect is crucial as it can lead to non-Markovian representations of the system and, as consequence, non-optimal solutions.

The approximations of policy π and value function Q are obtained by NN. In particular, each element of the i -th layer of the NN approximation can be written as

$$x_j^i = f_j(\psi \mathbf{x}^{i-1} + \mathbf{b}), \quad (10)$$

where $\{f_j\}$ represents the basis of nonlinear functions (`swish` or `tanh` in the present work) selected for the approximation, with $j = 1, \dots, h$ and h the dimension of the hidden layer. The argument of these functions is given as a linear combination of each nodes at each layer x_j^i and the coefficients $\theta = \{\psi, \mathbf{b}\}$; the expansion coefficients θ are the unknowns and are computed using a stochastic, gradient-based optimization. In particular, by following the sketch in Fig. 1, the update of the value function Q , the *critic part*, is obtained by temporal difference TD as

$$TD = Q^\pi(\mathbf{x}_t, \mathbf{u}_t | \theta) - [r(\mathbf{x}_t, \mathbf{u}_t) + \gamma Q^\pi(\mathbf{x}_{t+1}, \mathbf{u}_{t+1} | \theta)]. \quad (11)$$

The gradient $\nabla_\theta TD$ allows to update the coefficients of the NN approximating the value function. By feeding back into the system the signal \mathbf{u} , based on the sensor measurements \mathbf{x} , we are able to close the loop and control the system, as sketched in Fig. 1. More in detail, the *Q*-function allows the update of the *actor part* providing the policy π

$$\mathbf{u}_t = \pi(\mathbf{x}_t | \omega) + \mathcal{N}, \quad (12)$$

and the action \mathbf{u}_t . The coefficients ω of the NN approximating π are updated via the gradient $\nabla_\omega Q$. A crucial aspect is the *exploration*: the optimality of the control is guaranteed by the hypothesis that the state-action space is known. To this end,

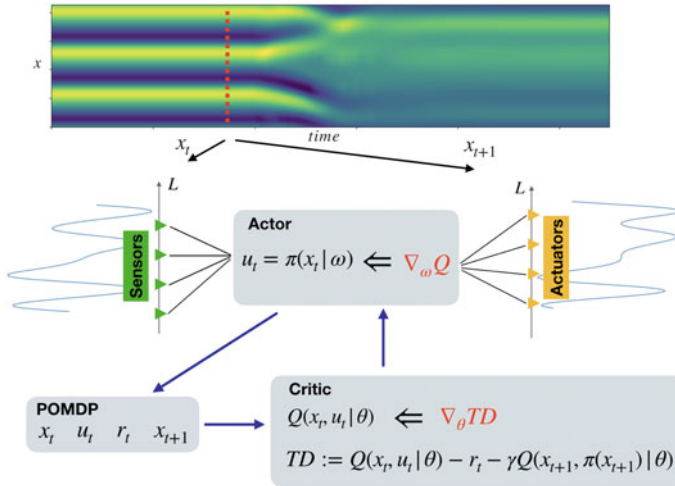


Fig. 1 Sketch of the DDPG algorithm applied for the control of the KS system. The system is detected by means of localized sensors; the current state of the system \mathbf{x} is recorded from these measurements. Based on the action \mathbf{u} and the scalar reward r , the updates of the Q -function and the policy π are performed. More details are provided in the text

the parameters ω of the NN describing the policy are perturbed and noise \mathcal{N} is introduced on the action; both the noise processes vary over time and are damped as the solution converges. As last note, we stress that one of the main features of DRL is the continuous learning in real time of the optimal policy.

3 Control of Chaotic Regimes: The Kuramoto-Sivashinsky System

In this section, we discuss the control of the one-dimensional Kuramoto–Sivashinsky (KS) equation using DRL. The KS system exhibits a rather rich dynamics, ranging from the steady solution to chaotic regimes. The critical parameter is the domain extent, here indicated with L . In particular, it can be shown that for $L < L_c = 2\pi$, the dynamics is stable and converges towards $\mathbf{E}_0 = \mathbf{0}$, while chaotic dynamics emerges for $L > L_c$. We consider the solutions obtained for $L = 22$, corresponding to a regime characterized by maximum Lyapunov exponent $\lambda_1 \approx 0.043$ and Kaplan–Yorke dimension $D_{KY} \approx 5.2$; for this case, the dynamics is low-dimensional and lies in a space characterized by three non-trivial equilibria and two traveling waves [5]. In Fig. 2, we show the null solution \mathbf{E}_0 and the three non-trivial solutions labelled \mathbf{E}_i , with $i = 1, 2, 3$; each of these solutions is unstable: the dynamics of the system becomes chaotic after a short transient. When increasing the domain extension, the number of positive Lyapunov exponents increases and the dynamics exhibits spatio-

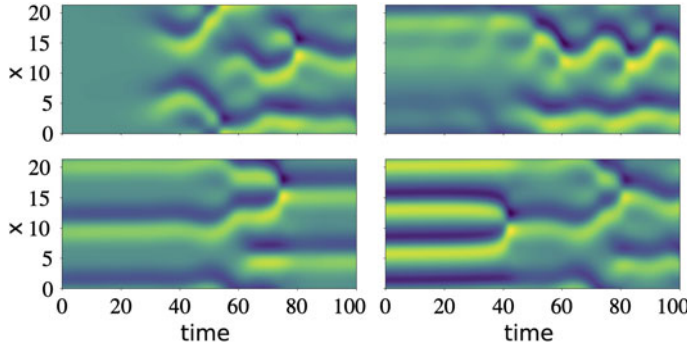


Fig. 2 When the domain is $L = 22$, the KS system exhibits 4 equilibria: the null solution E_0 (top-left), and the non-trivial solutions labelled with E_i and $i = 1, 2, 3$ (top-right, bottom-left and bottom-right, respectively). All of them are unstable, as shown by the dynamics of the system in the spatio-temporal plots

temporal chaos. The dynamics in time of the velocity $\mathbf{v} \in \mathbb{R}^N$ is governed by the equation

$$\frac{\partial \mathbf{v}}{\partial t} + \mathbf{v} \frac{\partial \mathbf{v}}{\partial x} = -\frac{\partial^2 \mathbf{v}}{\partial x^2} - \frac{\partial^4 \mathbf{v}}{\partial x^4} + \mathbf{g}(t), \quad (13)$$

here discretized with a resolution of $N = 64$ grid points on a periodic domain. The periodic domain allows for a Fourier mode expansion for the numerical resolution. Time marching was performed by 3rd-order Runge-Kutta scheme; the nonlinear terms are solved explicitly, while the linear terms are implicit. For all numerical simulations, a time step of 0.05 was adopted.

The control forcing is introduced by the term $\mathbf{g}(t) = \mathbf{B}\mathbf{u}(t)$, where $\mathbf{B} \in \mathbb{R}^{N \times m}$ is the spatial distribution of $m = 4$ localized, Gaussian shaped actuators

$$\mathbf{B}(x_a) = (2\pi\sigma)^{-1/2} \exp\left(-\frac{(x - x_a)^2}{2\sigma^2}\right), \quad (14)$$

placed at $x_a \in \{0, L/4, L/2, 3L/4\}$ and amplitude modulated in time by the forcing in time $\mathbf{u} \in \mathbb{R}^m$, computed by the DDPG and based on $p = 8$ localized sensor measurements, staggered with respect to the actuators location and equidistant. It can be shown that the KS equation can be controlled using linear controllers in combination with localized actuation [1]; however, the scope of this investigation is to demonstrate the feasibility of a purely model-free approach to the control of nonlinear flows.

3.1 Implementation of DDPG

We choose as objective for our controller to drive the system towards the solution \mathbf{E}_2 such that the distance $\|\mathbf{E}_2 - \mathbf{v}\|_2 := -r$ is minimized. As mentioned before, the DDPG policy is based on NN and its structure is as follows:

1. The actor part, representing the mapping between sensors and actuators, has $m = 4$ inputs and $p = 8$ outputs. Two hidden layers are considered, of respective dimensions 128 and 64, with activation functions `swish` and `tanh`.
2. The critic part, representing the value function, consists of an input of dimension $m + p = 12$, and a scalar output. Two hidden layers are introduced of 256 and 128 nodes, both with `swish` activation functions.

Adam optimization is applied for the update.

3.2 Results

We extend the results of [4] by considering a parametric analysis on the values of the discount factor γ and maximum amplitude of the outputs. In particular, we consider three policies with $\gamma = \{0.95, 0.97, 0.99\}$ and $|\mathbf{u}| < 1.0$, and two other policies with $\gamma = 0.99$ and maximum output amplitude set as $|\mathbf{u}| < \{0.5, 1.5\}$. The policy with $|\mathbf{u}| < 1.0$ and $\gamma = 0.99$ is the same as analysed in [4]. Due to the Markovianity of the system, the controllers are capable of driving the system to the target state \mathbf{E}_2 regardless of the initial conditions; here, for sake of conciseness and to make the comparison possible, we choose \mathbf{E}_1 as initial condition of all the test-cases.

In Fig. 3a-b, we show the trajectory in the phase-space (obtained by projecting the dynamics on the first three Fourier modes) and the reward, respectively, for $\gamma = 0.95$ (blue-dashed), $\gamma = 0.97$ (blue-dotted) and $\gamma = 0.99$ (green). The output is bounded as $|\mathbf{u}| < 1.0$. Surprisingly, despite the three controllers are always capable to drive the dynamics of the system towards \mathbf{E}_2 , the case with $\gamma = 0.99$ is also the one which exhibits smaller excursions in the phase-space before converging, with a higher reward. This behaviour resembles what is observed in model predictive control when longer time-horizon are chosen. In the second set of results, we show how with $\gamma = 0.99$, a different behaviour appears when changing the amplitudes $|\mathbf{u}| < \{0.5, 1, 1.5\}$, respectively depicted with a blue-dashed, red-dotted and green curve in Fig. 3c-d. In this case, as one would expect, in presence of greater control authority the policies are capable of converging rapidly towards the vicinity of \mathbf{E}_2 ; although the case with $|\mathbf{u}| < 1.5$ is the one showing higher reward, it is also characterized by a behaviour less clear than the case with $|\mathbf{u}| < 1.0$ when considering the phase-space (Fig. 3c).

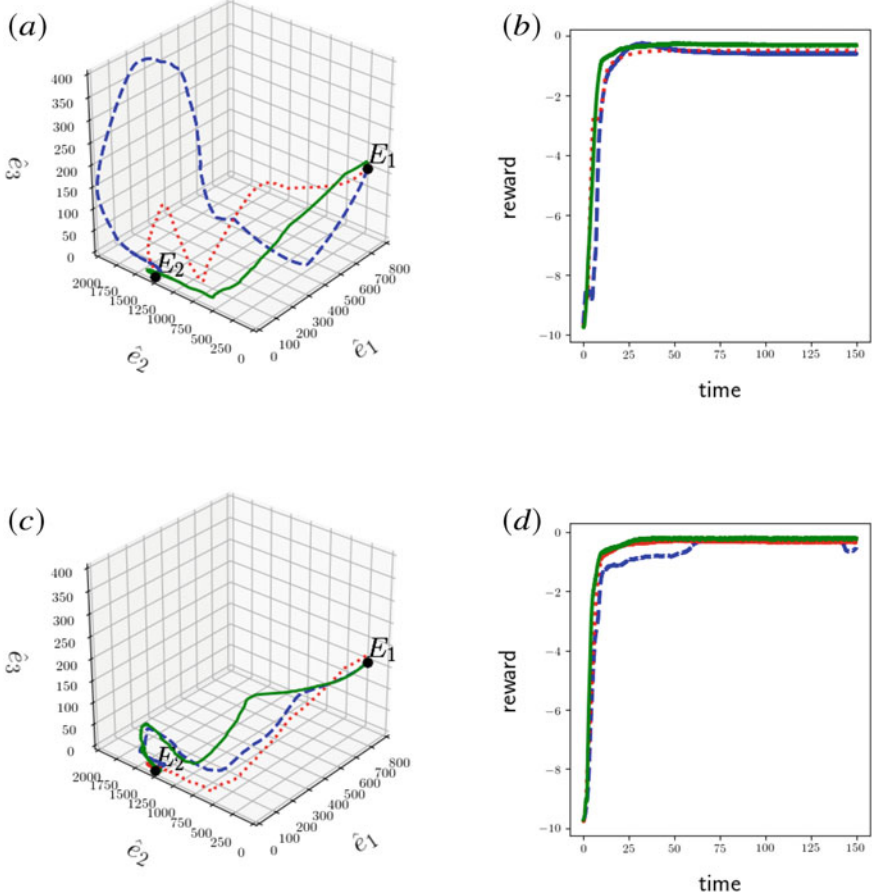


Fig. 3 Five policies for the control of the dynamics of the KS are compared for the same objective function: driving the system to the vicinity of E_2 . For simplicity of the discussion, the initial condition is set to be the invariant solution E_1 . The insets (a-b) show the behaviour of the system for $|\mathbf{u}| < 1$ and $\gamma = 0.95$ (blue-dashed), $\gamma = 0.97$ (red-dotted), $\gamma = 0.99$ (green); the trajectory is shown in phase space (a), while the corresponding reward is in (b). In the plots (c-d), we fix $\gamma = 0.99$ and consider three amplitudes: $|\mathbf{u}| < 0.5$ (blue-dashed), $|\mathbf{u}| < 1.0$ (red-dotted), $|\mathbf{u}| < 1.5$ (green); the corresponding trajectories (c) and rewards (d) are shown

4 Conclusions and Perspectives

This proceeding is part of a larger research effort aimed at applying reinforcement learning strategies to Navier-Stokes systems. Without any a-priori knowledge of the system, it is possible, by using localized sensors and actuators, to drive the dynamics of the chaotic KS system towards target states, here represented by unstable solutions of the system. The results are encouraging, although there are still numerous

questions to be addressed. From the application point of view, the control signals (not-shown here) are highly non-trivial; in this sense, we are currently analysing the extent to which we are capable of reproducing an action comparable to a linearized, optimal control in the vicinity of the unstable state and the associated energy budget. A challenging aspect of this work is represented by the extension to Navier-Stokes systems of this control strategy. A well-known limitation is represented, for instance, by the presence of time-delays in convective systems [6, 13]; this problem “translates” in RL into the so called credit-assignment problem. Also, it is important to keep a reasonable and realistic set-up, i.e. by limiting the number of sensors and actuators; these choices require a trade-off between the engineering needs and the low-observability, leading to the loss of Markovianity of the system, and low control-authority.

A future path is represented by the re-interpretation of RL from a control-oriented viewpoint: tools in standard, model-based control theory, such as model predictive control and adaptive algorithms [6, 15], rely on the Bellman formalism. The interplay between tools from optimal control theory and RL could help the development of reliable tools for the control of fluid systems.

Acknowledgements The authors gratefully acknowledge Sylvain Caillou for the support in the numerical implementation and Guillaume Wisniewski for interesting discussions. This project was funded by the French *Agence Nationale pour la Recherche* (ANR) and *Direction Générale de l'Armement* (DGA) via the FlowCon project (ANR-17-ASTR-0022).

References

1. Armaou, A., Christofides, P.D.: Feedback control of the Kuramoto-Sivashinsky equation. *Physica D* **137**, 49–61 (2000)
2. Bellman, R.: Dynamic programming and stochastic control processes. *Information and control* **1**(3), (1958)
3. Brunton, S.L., Noack, B.R., Koumoutsakos, P.: Machine learning for fluid mechanics. *Ann. Rev. Fluid Mech.* **52**, (2019)
4. Bucci, M.A., Semeraro, O., Allauzen, A., Wisniewski, G., Cordier, L., Mathelin, L.: Control of chaotic systems by deep reinforcement learning. *Proc. Royal Soc. A* **475–2231**, (2019)
5. Cvitanović, P., Davidchack, R.L., Siminos, E.: On the state space geometry of the Kuramoto-Sivashinsky flow in a periodic domain. *SIAM J. Appl. Dyn. Syst.* **9**1, 1–33 (2010)
6. Fabbiane, N., Semeraro, O., Bagheri, S., Henningson, D.S.: Adaptive and model-based control theory applied to convectively unstable flows. *App. Mech. Rev.* **66**(6), 060801 (2014)
7. Goodfellow, I., Bengio, Y., Courville, A.: Deep learning. MIT Press, Boston (2016)
8. Kim, J., Bewley, T.R.: A linear systems approach to flow control. *Annu. Rev. Fluid Mech.* **39**, 383–417 (2007)
9. Lewis, F.L., Vrabie, D., Syrmos, V.L.: Optimal control. John Wiley & Sons (2012)
10. Lillicrap, T.P., Hunt, J.J., Pritzel, A., Heess, N., Erez, T., Tassa, Y., Silver, D., Wierstra, D.: Continuous control with deep reinforcement learning, arXiv preprint 1509.02971 (2015)
11. Matni, N., Proutiere, A., Rantzer, A., Tu, S.: From self-tuning regulators to reinforcement learning and back again, arXiv preprint 1906.11392 (2019)
12. Recht, B.: A tour of reinforcement learning: The view from continuous control. *Annu. Rev. of Control, Robotics, and Autonomous Systems*, **2** (2019)

13. Schmid, P.J., Sipp, D.: Linear control of oscillator and amplifier flows. *Phys. Rev. Fluids*, **1**(4)-040501 (2016)
14. Silver, D., Schrittwieser, J., Simonyan, K., Antonoglou, I., Huang, A., Guez, A., Hubert, T., Baker, L., Lai, M., Bolton, A., Chen, Y.: Mastering the game of go without human knowledge. *Nature* **550–7676**, 354 (2017)
15. Xiao, D., Papadakis, G.: Nonlinear optimal control of bypass transition in a boundary layer flow. *Phys. Fluids* **29**, 054103 (2017)

Linear Impulse Response of a Plasma Jet



S. Demange, U. Ali Qadri, and F. Pinna

Abstract The full linear impulse response of the VKI plasma wind tunnel jet is investigated by solving a numerical spatio-temporal linear stability problem. A DNS code from literature is modified by including high temperature effects and compared to the finite-volume solver CoolFluid-ICP. High order schemes employed in the DNS code allow us to obtain radial derivatives of flow quantities needed by stability computations without relying analytical interpolations used with CoolFluid-ICP base flow. Simulations consider an axisymmetric jet described by the low Eckert number approximation of the Navier Stokes equations, for a mixture of perfect gases in local thermo-chemical equilibrium including ionization effects. The new steady state obtained through selective frequency damping is compared against CoolFluid-ICP simulations and the impact on stability features is assessed. Although an overall good agreement is found between the base states, DNS results yield a slightly thicker shear layer than previous simulations. Our analysis suggests that instability modes with pressure perturbations peaking in the shear are strongly affected by the change of base state, while jet-column modes with a maximum pressure perturbation around the centerline are hardly affected.

S. Demange (✉) · F. Pinna

Von Karman Institute for fluid dynamics, Chaussée de Waterloo 72, 1640 Rhode-Saint-Genese, France

e-mail: simon.demange@vki.ac.be

F. Pinna

e-mail: fabio.pinna@vki.ac.be

U. A. Qadri

Department of Engineering, University of Cambridge, Trumpington Street, Cambridge, UK
e-mail: uaq20@eng.cam.ac.uk

1 Introduction

Upon entering a planet's atmosphere, spacecrafts and their payloads must be shielded from extreme heat fluxes by a Thermal Protection System (TPS). Materials composing TPS are therefore tested in ground facilities tailored to reproduce boundary layer conditions met during entry flights. To this end, the Von Karman Institute (VKI) operates the largest Inductively Coupled Plasma (ICP) wind tunnel in the world, the Plasmatron [4], able to create and sustain a high enthalpy axisymmetric jet aimed at material samples or probes for long duration tests. However, experimental observations [6] have shown the presence of oscillations in the flow, which are believed to be caused in part by hydrodynamic instabilities of the heated jet and may disturb the phenomena studied in the facility.

Jets are flow structures known to exhibit self-sustained regular oscillations that are relatively insensitive to low amplitude perturbations when featuring a lower density or higher temperature than their ambient medium. The development of these non-linear *global* modes has been correlated to the concept of absolute instability developed by Briggs [5] and Bers [3], and applied to the local Linear Stability Theory (LST) by Huerre and Monkewitz [11] for shear flows. The theoretical work of Monkewitz and Sohn in [22] and experimental study of Monkewitz [23] showed that self-sustained oscillations appeared in round jets with jet-to-ambient density ratios below $S = 0.72$ due to the presence of an absolute instability region in the jet. More recently, several studies [7, 15, 16, 25] have shown that a region of absolute instability must exist in order to excite a global non-linear mode. Such a region should display a length of the order of the absolute wavelength and causes the global mode to beat at a distinct frequency close to the local absolute one found at the upstream boundary of the absolute pocket. Previous studies [1, 12, 14] have also focused on the parameters influencing the transition from convective to absolute instabilities by considering top hat jet profiles introduced by Michalke in [19] to approach the shape of the core region in turbulent jets. A particularly interesting result from [14] is the identification of the baroclinic torque as the main mechanism behind absolute instabilities. However, additional studies [8, 17] have also shown that studying top-hat profiles with independent flow parameters was not always representative of physical situations, and that the profile shape played an important role in jet stability. In particular, asymmetric velocity profiles with a maximum shear in the low-velocity region and steep density gradients near this region were found to promote absolute instabilities. Previous work [9] showed that Plasmatron jet contains a large region of absolute instability for axisymmetric mixed modes. However, the base state used in this work relied on second order spatial accurate simulations, and an analytical interpolation of the profiles was necessary to compute radial derivatives of the flow quantities. However, it appears clearly from the previous observations that jet profile shapes are a decisive factor to precisely identify stability features, therefore a high order DNS code is adapted to reproduce Plasmatron jet base state, and carry out its stability study without relying on analytical interpolation of the profiles.

2 Problem Formulation

Simulations of the axisymmetric plasma jet found in the Plasmatron facility are carried out using the cylindrical co-ordinates (r, θ, z) for the radial, azimuthal and stream-wise directions respectively. The setup used here is the one presented in previous Plasmatron study [9]. Thermodynamic and transport properties are shared between the stability study and simulations of the jet, assuming an 11-species air mixture in Local Thermo-chemical Equilibrium (LTE), accounting for ionization effects under the ambipolar assumption. Properties are computed within the VKI Extensible Stability and Transition Analysis toolkit, based on equilibrium compositions provided by the DEKAF boundary layer solver [10] for local values of pressure and temperature; more details on the models are available in the work of Miro Miro [20]. For the present study, a single electric power $P_{el} = 100$ kW and static pressure in the chamber $P_s = 150$ mbar are considered.

2.1 Jet Simulations

Jet simulations are carried out in the DNS code solving the low Mach number approximation of Navier Stokes equations developed by Nichols in [24] and used more recently by Qadri [28]. Within the LTE assumption, chemistry effects are fully contained within variations of the flow properties according to pressure and temperature changes, thus dimensional Navier-Stokes equations in LTE are identical to their low temperature counterparts.

Reference quantities are taken at the inlet centerline of the jet denoted by the subscript " j ", with the exception of the reference density ρ and pressure p taken in the outer flow, denoted by the subscript " ∞ ". Non-dimensional equations in LTE are however given in terms of Eckert number $Ec = (\rho_\infty u_{z,j}^2)/p_\infty$ - where u_z is the stream-wise velocity - instead of Mach number due to the non-trivial definition of the equilibrium speed of sound at high temperatures. The following non-dimensional numbers are then obtained:

$$S_1 = \frac{\rho_\infty}{\rho_j}, \quad Re = \frac{\rho_j u_j d}{\mu_j}, \quad Pr = \frac{\mu_j}{\lambda_j T_j} \frac{p_\infty}{\rho_\infty}. \quad (1)$$

where d is the jet diameter used as reference length, S_1 is the density ratio appearing in equations from the original DNS code [24], T denotes the temperature, μ the viscosity and λ the thermal conductivity. Similarly to Nichols with the Mach number, flow quantities are expanded around a small Eckert number $Ec = \epsilon$ as $p(\mathbf{x}, t) = p^{(0)}(\mathbf{x}, t) + \epsilon p^{(1)}(\mathbf{x}, t) + \dots$, which yields the following low Eckert number equations when retaining the lowest order terms:

$$\frac{\partial \rho}{\partial t} + \nabla(\rho u) = 0, \quad (2a)$$

$$\nabla p^{(0)} = 0, \quad (2b)$$

$$\frac{\partial(\rho u)}{\partial t} + \nabla(\rho uu) = \nabla p^{(1)} - \frac{1}{S_1 Re} \nabla(\tau), \quad (2c)$$

$$\rho \frac{Dh}{Dt} = \frac{1}{S_1 Re Pr} \nabla(\lambda \nabla T). \quad (2d)$$

Where τ is the viscous stress tensor and the energy equation is given in terms of static enthalpy h . Coupling of Eq. 2b with constant pressure boundary conditions introduced by Nichols [24] imply a constant zeroth order pressure $p^{(0)}$. Therefore, transport and thermodynamic properties are computed by neglecting their pressure dependence and are interpolated with respect to the temperature field from pre-computed tables at $p_\infty = P_s$ using a cubic Hermite interpolant method [13]. Additionally, the temperature dependence of μ and λ introduces new terms to the equations of Nichols [24] implemented in our code. When needed, the temperature field is deduced from the static enthalpy, using a similar table of properties.

The evaluation of term $\partial\rho/\partial t$ used in the pressure correction method of Nichols [24] is modified for our LTE implementation to:

$$\frac{\partial\rho}{\partial t} = \frac{1}{cp} \frac{\partial\rho}{\partial T} \frac{\partial h}{\partial t}. \quad (3)$$

where $cp = \partial h / \partial T$ is the constant pressure specific heat capacity and derivatives of h and ρ with respect to temperature are added to the interpolation tables exploiting the capacities of the VESTA toolkit property module described in [21].

All the boundary conditions used in the present work are similar to the ones described by Qadri in [28]. A viscous traction free lateral condition on momentum associated with Dirichlet conditions on the temperature and pressure mimic an infinite domain in the radial direction. A semi-infinite domain is also assumed in the axial direction by imposing a convective condition at the outlet. At the inlet, static enthalpy, streamwise and radial velocity profiles are prescribed along with a Neumann condition on the pressure. Inlet profiles are directly exported from CoolFluid-ICP simulations presented in [9].

The code uses a fourth order Runge-Kutta method to march forward in time, while spatial derivatives are computed using a finite difference sixth order compact scheme on a collocated mesh. The current domain extends to 4 and 20 diameters, and is discretized using 313×513 mesh points. Finally, the symmetry of the solution is enforced at each time step and the steady state is reached using a Selective Frequency Damping (SFD) method [28].

2.2 Linear Stability Theory

The stability analysis is carried out in the VESTA toolkit [26]. Stability equations are automatically derived from the compressible Navier-Stokes equations in the Automatic Derivation and Implementation Tool (ADIT) [27]. Additional terms F , G , ζ specific to high temperatures and described by [18] are used in our derivation. Stability equations consider the (u , v , w , p , T) variables, respectively the components of the velocity along (r , θ , z), pressure and temperature. The classical LST ansatz is used, substituting flow quantities q by:

$$q = \bar{q} + q' \quad , \quad q'(r, \theta, z, t) = \tilde{q}(r)e^{i(\alpha z + m\theta - \omega t)} + c.c. \quad (4)$$

where \bar{q} is the base state and q' a small perturbation around \bar{q} ; α and m denote the stream-wise and integral azimuthal wavenumbers, while ω denotes the angular frequency. Perturbations of the transport properties are considered by expanding their dependence on pressure and temperature as described by [26]. A set of compatibility conditions used in [9] is imposed at the centerline depending on the value of m , while homogeneous Dirichlet conditions are imposed in the outer flow. Stability equations and boundary conditions are reduced to a generalized eigenvalue problem, solved by imposing a value for α . The domain is described with $N = 201$ Chebyshev collocation points and the tangential mapping technique developed by Bayliss and Turkel [2]. The spatio-temporal formulation of the LST problem is assumed by imposing both α and ω complex.

3 Results

Results of jet simulations with $P_{el} = 100$ kW and $P_s = 150$ mbar in DNS and CoolFluid-ICP are compared and used to perform a stability analysis similar to previous Plasmatron analyses [9]. The spatio-temporal problem is solved across the complex wavenumber plane for $m = 0$ and $m = 1$ to display contours of constant growth-rate: $\sigma = \text{Imag}(\omega)$. Valid saddles are identified with the Briggs-Bers criterion and then tracked along the stream-wise direction to reveal the absolute pocket. The full impulse response of axisymmetric modes is then investigated by varying the group velocity vg [14] and tracking the saddles.

3.1 Comparison of Base States

Base states from DNS and CoolFluid-ICP are compared in terms of stream-wise velocity, temperature and density fields, as displayed in Fig. 1. We find an overall good agreement between the two solutions, our implementation is able to retrieve

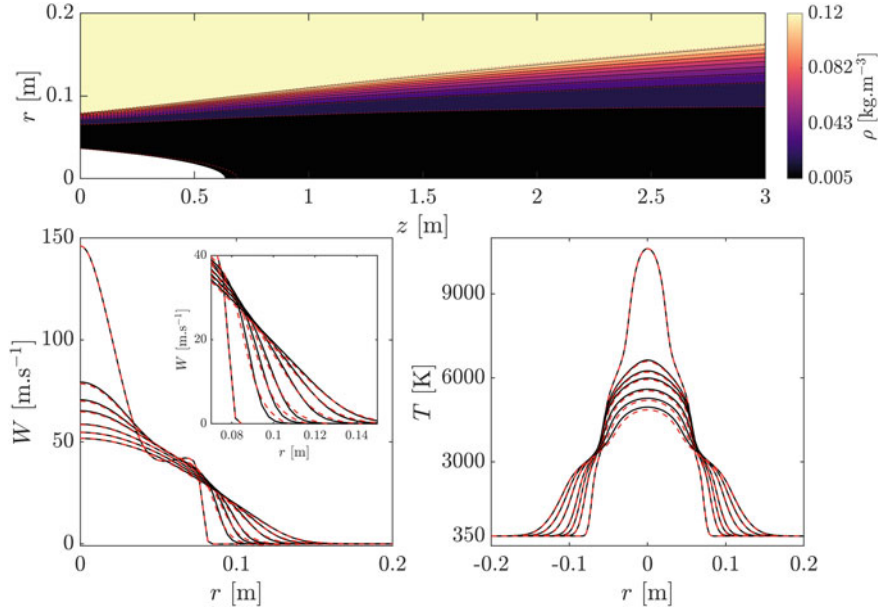


Fig. 1 Comparison of density (top), stream-wise velocity (bottom left) and temperature (bottom right) fields from the two codes for $P_{el} = 100$ kW and $P_s = 150$ mbar. Profiles are given at $z = [0; 0.5; 0.75; 1; 1.5; 2; 2.5]$ m, for CoolFluid-ICP (black) and LMaNS (red dashed). Contours of ρ are given for LMaNS (filled) and CoolFluid-ICP (red dotted)

the humps in the temperature profiles due to the different species dissociation, and the velocity profiles evolve from a co-axial jet to a single jet with thick shear layer in agreement with the finite-volume solver.

However, the region extending from the inlet to around half of the jet in our DNS presents a thicker shear layer with weaker maximum radial velocity gradients than the simulations in CoolFluid-ICP in. Differences between the shears decay rapidly after $z = 1$ m. A region of mismatch in temperature is observed around the iso-line: $T \approx 4000$ K, which correspond to the end of the O₂ dissociation in our mixture at 150 mbar. This error is believed to be caused by differences in the evaluation of the thermal conductivity by VESTA and MUTATION⁺⁺ which are non-negligible at this temperature. The DNS also under-predict the overall temperature field around the centerline when compared to CoolFluid-ICP in the second half of the jet. On the other hand, differences in the density fields are confined to the low temperatures shear layer area displayed in the contour plot of Fig. 1. Similarly to the velocity, the density shear is thicker in the DNS with respect to CoolFluid-ICP.

Nevertheless, the implementation of high temperature effects in the DNS is judged satisfactory as the maximum error between the codes is limited to respectively 3, 2%, 2.15% and 7.5% of the maximum stream-wise velocity, temperature and density fields.

3.2 Absolute Instabilities

The spatio-temporal stability analysis of axisymmetric perturbations around the DNS base flow yields similar results to the previous analysis on CoolFluid-ICP base state [9]. A large absolute region starting at the inlet is found in the flow for perturbations akin to the jet-column modes observed in top-hat jets [14]. The evolution of absolute growth-rate and dimensional frequency $f = \text{Real}(\omega)W_c/(2\pi R)$ along the chamber is plotted in Fig. 2 for both base states.

Despite a slight stream-wise offset for $z < 1$ m, the absolute jet-column mode is rather insensitive to the differences of shear layer thickness, with a discrepancy on the maximum growth-rate limited to 0.5% of the one found with the DNS base state. Results from the two simulations start to diverge downstream of the maximum growth-rate station, which is believed to be caused by the overall difference of temperature between DNS and CoolFluid-ICP observed near the centerline.

A similar analysis is carried out for the first azimuthal mode ($m = 1$), yielding a similar saddle point. In this case, the pressure perturbations reach their maximum value in the shear layer. The absolute region for $m = 1$ is confined inside the domain for both base states, with a lower growth-rate than for $m = 0$. We find that differences in base state have a stronger impact on these modes than on the axisymmetric ones, with a 27% difference on the maximum growth-rate value. In the downstream region, differences in the shear from the two simulations are decaying, accordingly, differences in the growth-rates decrease in this region. We also observe strong variations in the dimensional frequencies of $m = 0$ and $m = 1$ modes, which is believed to be linked to the adjustment of DNS simulations after the injection of profiles from CoolFluid-ICP. One can also note that stream-wise discontinuities due to the analytical interpolation of profiles [9] are no longer present with the DNS base state.

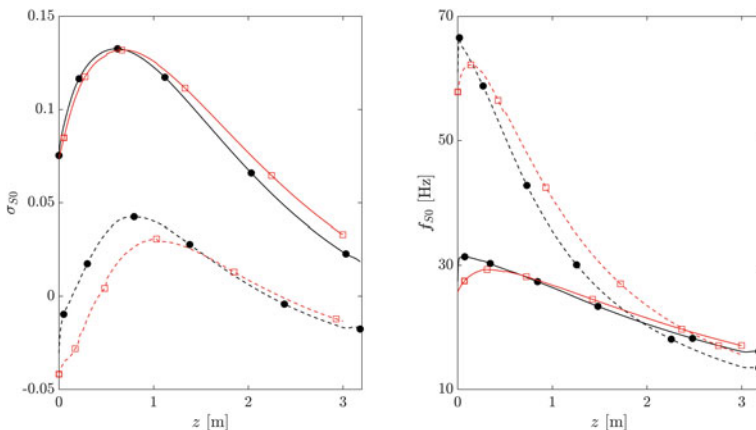


Fig. 2 Absolute growth-rate (left) and absolute frequency (right) as function of z for $m = 0$ (—) and $m = 1$ (- -) computed on LMaNS base state (black) against CoolFluid-ICP (red)

3.3 Full Impulse Response

The full impulse response is computed for axisymmetric perturbations on the two base states. Non-zero values of the group velocity are imposed by shifting the reference frame of the study, and stability results are shifted back to the static referential using standard techniques [14]. Results for the CoolFluid-ICP base state are already presented in a previous analysis [9], and compared to the present ones on the DNS base state in Fig. 3 in terms of temporal growth-rate and real frequency. Similarly to previous results, the analysis on the new base state reveals that absolute jet-column modes dominate the response at low group velocities, while the convective shear layer modes dominate the rest of the response for $z < 1.6$ m. Downstream, only mixed-modes with pressure perturbations amplified both in the shear and at the centerline are relevant to the full impulse response. Mixed modes present a strong amplification at the centerline for $vg = 0$, which decreases as vg is increased while the amplification at the shear layer becomes more important.

In agreement with results of the previous section, we observe a low impact of the base flow change on the jet-column modes at low group velocity, while shear layer modes at higher group velocities are strongly altered. However, unlike the absolute first azimuthal modes, the maximum growth-rate and real frequency of the convective shear layer mode are now under-estimated with the DNS base flow. Differences in maximum ω_i are of the same order of magnitude than for the first azimuthal mode at $vg = 0$.

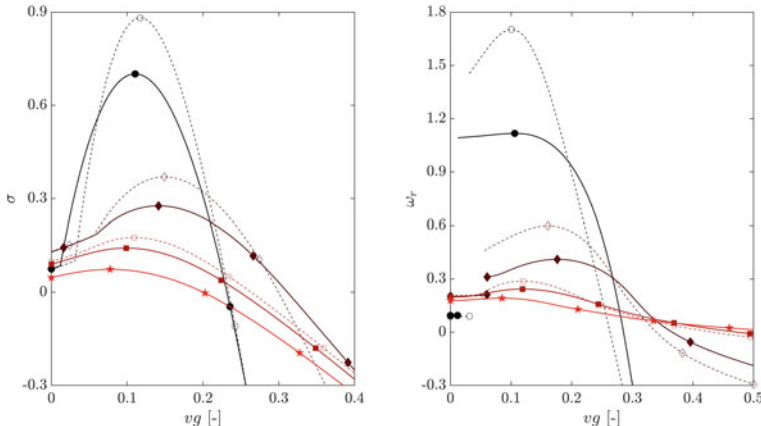


Fig. 3 Temporal growth-rate (left) and real frequency (right) as function of vg for $m = 0$ at $z = [0; 0.8; 1.6; 2.4]$ m (black to red); computed on LMaNS base state (—) against CoolFluid-ICP (···)

3.4 Conclusions

Modifications have been introduced in a literature DNS code to reproduce simulations of the VKI Plasmatron high enthalpy jet considering a mixture of gases in Local Thermo-chemical equilibrium. New simulations are in good agreement with results from the finite-volume solver CoolFluid-ICP commonly used at VKI, and the high order numerical scheme allows to perform stability studies without resorting to the analytical interpolation of profiles used with CoolFluid-ICP. However, our DNS code retrieves a slightly thicker shear layer than the finite volume solver. Our observations suggest that modes are most sensitive to changes in the base state located near the maximum of their pressure eigenfunctions. Consequently, we observe that axisymmetric shear layer modes and the absolute first azimuthal mode exhibiting a pressure perturbation with a maximum in the shear layer are strongly affected by the change of base state. On the other hand, jet-column modes with a maximum pressure perturbation around the centerline remain less sensitive to this change.

Acknowledgements This work benefited from the support of the Fonds de la Recherche Scientifique - FNRS under the FRIA Grant. U.A.Q. acknowledges support from the Leverhulme Trust and Isaac Newton Trust, through an Early Career Fellowship.

References

1. Balestra, G., Gloor, M., Kleiser, L.: Absolute and convective instabilities of heated coaxial jet flow. *Physics of Fluids* **27**(5), 054101 (2015)
2. Bayliss, A., Turkel, E.: Mappings and accuracy for Chebyshev pseudo-spectral approximations. *Journal of Computational Physics* **101**(2), 349–359 (1992)
3. A. Bers. Space-time evolution of plasma instabilities-absolute and convective. *Basic plasma physics*, page 451, 1984
4. B. Bottin, M. Carbonaro, V. Van Der Haegen, A. Novelli, and D. Vennemann. The VKI 1.2 MW Plasmatron facility for the thermal testing of TPS materials. *3 rd European Workshop on Thermal Protection Systems, ESTEC*, , 1998
5. R. J. Briggs. *Electron-stream interaction with plasmas*. M.I.T. Press, Cambridge, 1964. OCLC: 537479
6. Cipullo, A., Helber, B., Panerai, F., Zeni, F., Chazot, O.: Investigation of freestream plasma flow produced by inductively coupled plasma wind tunnel. *Journal of Thermophysics and Heat Transfer* **28**(3), 381–393 (2014)
7. Coenen, W., Sevilla, A.: The structure of the absolutely unstable regions in the near field of low-density jets. *Journal of Fluid Mechanics* **713**, 123–149 (2012)
8. Coenen, W., Sevilla, A., Sanchez, A.L.: Absolute instability of light jets emerging from circular injector tubes. *Physics of Fluids* **20**, (2008)
9. S. Demange and F. Pinna. Absolute and convective instabilities in high enthalpy jets. *8th European Conference for Aeronautics and aeroSpace Sciences (EUCASS)*, 2019
10. K. J. Groot, F. Miro Miro, E. S. Beyak, A.J. Moyes, F. Pinna, and H. L. Reed. Dekaf: Spectral multi-regime basic-state solver for boundary-layer stability. *2018 Fluid Dynamics, Conference, AIAA AVIATION Forum, (AIAA 2018-3380)*, 2018
11. Huerre, P., Monkewitz, P.A.: Absolute and convective instabilities in free shear layers. *Journal of Fluid Mechanics* **159**, 151–168 (1985)

12. Juniper, M.P.: The effect of confinement on the stability of non-swirling round jet/wake flows. *Journal of Fluid Mechanics* **605**, 227–252 (2008)
13. Kahaner, D., Moler, C., Nash, S.: Numerical methods and software. Prentice-Hall Inc, Upper Saddle River, NJ, USA (1989)
14. Lesshafft, L., Huerre, P.: Linear impulse response in hot round jets. *Physics of Fluids* **19**(2), 024102 (2007)
15. Lesshafft, L., Huerre, P., Sagaut, P.: Frequency selection in globally unstable round jets. *Physics of Fluids* **19**, 054108 (2007)
16. Lesshafft, L., Huerre, P., Sagaut, P., Terracol, M.: Nonlinear global modes in hot jets. *Journal of Fluid Mechanics* **554**, 393–409 (2006)
17. Lesshafft, L., Marquet, O.: Optimal velocity and density profiles for the onset of absolute instability in jets. *Journal of Fluid Mechanics* **662**, 398–408 (2010)
18. Malik, M.R., Anderson, E.C.: Real gas effects on hypersonic boundary-layer stability. *Physics of Fluids* **3**, (1991)
19. Michalke, A.: Survey on jet instability theory. *Progress in Aerospace Sciences* **21**, 159–199 (1984)
20. F. Miro Miro, E. S. Beyak, D. Mullen, F. Pinna, and H. L. Reed. Ionization and dissociation effects on hypersonic boundary-layer stability. *31st Congress of the International Council of the Aeronautical Sciences, Belo Horizonte, Brazil*, 2018
21. F. Miro Miro, E. S. Beyak, F. Pinna, and H. L. Reed. High-enthalpy models for boundary-layer stability and transition. *Physics of Fluids*, 31(4):044101, 2018
22. P. Monkewitz and K. Sohn. Absolute instability in hot jets and their control. In *10th Aero-acoustics Conference*, Seattle, WA, U.S.A., 1986
23. Monkewitz, P.A., Bechert, D.W., Barsikow, B., Lehmann, B.: Self-excited oscillations and mixing in a heated round jet. *Journal of Fluid Mechanics* **213**, 611–639 (1990)
24. J. Nichols. *Simulation and stability analysis of jet diffusion flames*. PhD thesis, University of Washington, 2005
25. Nichols, J., Schmid, P., Riley, J.: Self-sustained oscillations in variable-density round jets. *Journal of Fluid Mechanics* **582**, 341–376 (2007)
26. F. Pinna. *Numerical Study of Stability for Flows from Low to High Mach Number*. Von Karman Institute for fluid dynamics, 2012
27. F. Pinna and K. Groot. Automatic derivation of stability equations in arbitrary coordinates and for different flow regimes. In *44th AIAA Fluid Dynamics Conference*, AIAA AVIATION Forum. American Institute of Aeronautics and Astronautics, 2014
28. origin and control: U. Ali Qadri, G. Chandler, and M. Juniper. Self-sustained hydrodynamic oscillations in lifted jet diffusion flames. *Journal of Fluid Mechanics* **775**, 201–222 (2015)

Control of Travelling Crossflow Vortices Using Volume Forcing



Zhengfei Guo, Philipp C. Dörr, and Markus J. Kloker

Abstract In the present DNS work we focus on the most unstable travelling crossflow vortex (CFV) mode in a 3-d boundary layer, and examine the applicability of unsteady volume-force actuation to directly tackle the invoked nonlinear state. The actuators with forcing nearly in or against the crossflow direction are arranged in a spanwise row and operated with the same frequency as that of the oncoming mode. The unsteady volume forcing is designed as a model for actuation by plasma actuators. It is shown that unsteady forcing with a suitable phase can efficiently counteract the vortical motion of the nonlinear travelling CFVs, and hence delay the onset of secondary instabilities. However, a detrimental steady mode is also excited. The superposition of the steady and travelling modes renders some parts of the mean CFVs more unstable. By employing two additional actuator rows downstream with combined steady and unsteady forcing, the growing steady and travelling modes can be further attenuated, respectively, yielding enhanced delay of the complex transition with travelling primary 3-d structures.

1 Introduction

In swept-wing-type boundary layers the crossflow (CF) instability is the dominant mechanism of the laminar-turbulent transition. At high free-stream turbulence levels or with distributed roughness elements (DREs) on the wing in free flight with its attachment-line fluctuations, travelling crossflow vortex (CFV) modes may prevail over steady modes due to their higher growth rate. The resulting travelling CFVs quickly reach the nonlinear stage, leading to explosive secondary instabilities.

Z. Guo (✉) · P. C. Dörr · M. J. Kloker

Institute for Aerodynamics and Gas Dynamics, University of Stuttgart, Pfaffenwaldring 21, 70550 Stuttgart, Germany

e-mail: guo@iag.uni-stuttgart.de

M. J. Kloker

e-mail: kloker@iag.uni-stuttgart.de

Whereas the mechanism of travelling CFV dominated transition is well understood [2, 7, 11–13], only a small number of investigations on its control has been conducted.

In the present work we focus on the nonlinear disturbance state of travelling CFVs. Unsteady volume forcing actuators are employed to directly counteract the vortical motion of the primary CFVs and, hence, delay the onset of secondary instabilities. The volume-force distribution mimics that of an alternating-current dielectric-barrier-discharge (AC DBD) plasma actuator. The base-flow setup corresponds to the newly designed swept flat plate experiment at DLR Göttingen [1]. This study supplements a previous DNS investigation on lowering the growth rate of travelling CFVs by unsteady (upstream-flow-deformation) control vortices [8].

2 Numerical Method

2.1 Basic Setup

The compressible, high-order finite-difference code NS3D is used for the simulations presented in this work, see, e.g., Ref. [4] for details. The rectangular integration domain consists of block-structured Cartesian grids, see Fig. 1. We summarize the relevant parameters for the numerical discretization in Table 1. The inflow and outflow are treated with characteristic boundary conditions to minimize disturbance reflection. In addition, sponge zones based on a volume-forcing term and a spatial compact tenth-order low-pass filter are used. At the upper boundary, the base-flow values for ρ and T are kept, and $\partial u / \partial y|_e = \partial w / \partial y|_e = 0$ is prescribed for u and w to allow additional mass flow through the free-stream boundary; v is then calculated using the continuity equation, assuming $\partial \rho / \partial y|_e = 0$. At the isothermal wall, the no-slip condition with $\partial p / \partial y|_{\text{wall}} = 0$ is employed.

To allow computation at a non-prohibitive time step, the chordwise Mach number $Ma_\infty = 0.2$ ($Ma_{\infty,\text{exp}} = 0.066$) is chosen for the simulations. The ambient conditions and the Reynolds number are kept identical to those in the underlying experi-

Fig. 1 Integration domain and coordinate systems

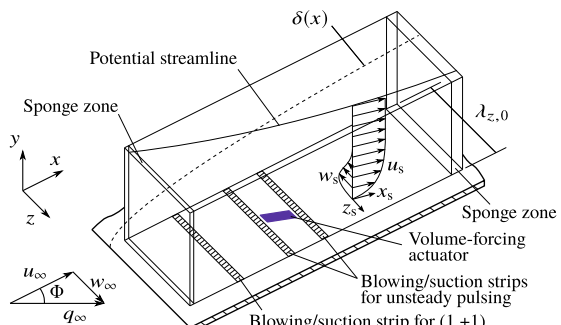


Table 1 Numerical discretization

x	Explicit O8	$0.173 \leq x \leq 4.078$, 2604 equidistant points, $\Delta x = 1.5 \cdot 10^{-3}$
y	Explicit O8	$0.000 \leq y \leq 0.121$, 152 points with stretching, $\Delta y_{\text{wall}} = 1.251 \cdot 10^{-4}$, $\Delta y_{\text{max}}/\Delta y_{\text{wall}} = 17$
z	Fourier spectral	fundamental wave number $\gamma_0 = 2\pi/\lambda_{z,0} = 70$, 10 de-aliased modes, 32 equidistant points, $\Delta z = 2.805 \cdot 10^{-3}$
t	Runge-Kutta O4	fundamental angular frequency $\omega_0 = 2\pi/T_0 = 6.0$, $\Delta t = 8.727 \cdot 10^{-6}$

ment for similarity. The chordwise reference velocity $\bar{U}_\infty = 68.87 \text{ m s}^{-1}$ ($\bar{U}_{\infty,\text{exp}} = 22.66 \text{ m s}^{-1}$), the reference length $\bar{L} = 0.033 \text{ m}$ ($\bar{L}_{\text{exp}} = 0.1 \text{ m}$), the reference density $\bar{\rho}_\infty = 1.181 \text{ kg m}^{-3}$ and the reference temperature $\bar{T}_\infty = \bar{T}_{\text{wall}} = 295.0 \text{ K}$ are used for normalization, with overbar denoting dimensional values. Note that \bar{L} is not the plate length $\bar{c}_{\text{exp}} = 0.6 \text{ m}$. The Reynolds number based on the plate length and the chord velocity is $Re_{\text{chord}} = 8.81 \times 10^5$. For details on the base-flow generation see Ref. [6].

Controlled disturbances are introduced at the wall using (synthetic) blowing/suction strips. At $0.766 \leq x \leq 0.835$ the integrally most amplified unsteady CFV test mode with spanwise wavenumber $\gamma = 70$ and angular frequency $\omega = 6$ is excited. It corresponds to the disturbance mode with a spanwise wavelength of 9 mm and a frequency of 217 Hz in the experiment. This mode is denoted in the following as $(1, +1)$ in a double-spectral notation $(h\omega_0, k\gamma_0)$. To test the onset of secondary instability and initiate controlled laminar breakdown, two additional disturbance strips with a strip extension of 0.045 each are employed at $x = 2.0$ and $x = 2.5$ to excite pulse-like (background) disturbances $(h, \pm 1)$, with $h = 1 - 50$. Note that the modes $|k| \geq 2$ not directly forced by the strips are nonlinearly generated at once by the (large) primary vortex modes already present in the flow.

2.2 Localized Volume Forcing

A non-dimensional wall-parallel volume-force distribution $\hat{f}(\hat{x}, \hat{y})$ in the \hat{x} - \hat{y} -plane perpendicular to the electrode axis of a virtual plasma actuator is prescribed. The three-dimensional distribution $f(x, y, z)$ produced in a discharge area with the length l_{PA} is then modeled by extrusion of $\hat{f}(\hat{x}, \hat{y})$ along the electrode edge, as sketched in Fig. 2. At the lateral edges a 5th-order polynomial is imposed over a range of 10% electrode length to smooth the changeover from zero to maximum forcing. The angle β_{PA} defines the clockwise rotation of the electrodes about the wall-normal axis through $(x_{\text{PA}}, z_{\text{PA}})$. According to previous investigations by Dörr and Kloker [4], the effect of the wall-normal force component is negligible. The unsteadiness of the

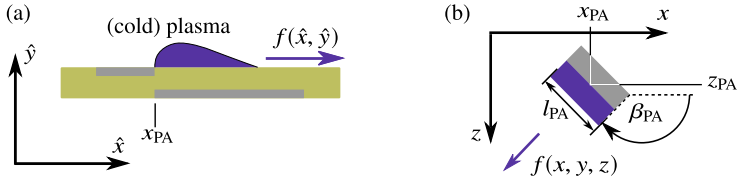


Fig. 2 (a) Plasma-actuator schematic and planar volume-force distribution. (b) Rotation about the wall-normal axis

Table 2 Actuator parameters; f , $c_{\mu, L_{\text{exp}}}$ and c_{μ, θ_s} correspond to the time-averaged values;

$$\bar{f} = f \frac{\bar{\rho}_{\infty} \bar{U}_{\infty}^2}{\bar{L}} = f \frac{\bar{\rho}_{\infty}^2 \bar{U}_{\infty}^3}{Re \bar{\mu}_{\infty}}, \max\{|\bar{f}|\} = \max\{[\bar{f}_x^2 + \bar{f}_z^2]^{1/2}\}$$

Actuator	x_{PA}	l_{PA}	z_{PA}	β_{PA}	$\max\{ \bar{f} \}$	$c_{\mu, L_{\text{exp}}}$	c_{μ, θ_s}	c_s	c_u	ϕ_{PA}
Row 1	2.25	0.60	0.025	130.2	0.38 kN m ⁻³	$5.1 \cdot 10^{-6}$	$2.2 \cdot 10^{-3}$	1	6.67	$7\pi/4$
Row 2	2.75	0.25	0.070	130.2	0.38 kN m ⁻³	$5.1 \cdot 10^{-6}$	$2.0 \cdot 10^{-3}$	1	6.67	$\pi/4$
Row 3	3.40	0.25	0.025	133.0	3.39 kN m ⁻³	$4.5 \cdot 10^{-5}$	$1.6 \cdot 10^{-2}$	1	0	-

forcing is taken into account by a sinusoidal time signal:

$$f(x, y, z, t) = f(x, y, z)Z(t), \quad Z(t) = c_s + c_u \sin(\omega_{\text{PA}}t + \phi_{\text{PA}}). \quad (1)$$

With $c_s/c_u = 0.15$, the oscillating volume force with a non-zero (temporal) mean mimics the asymmetric push and pull events of the plasma actuation with low frequency, resembling the direct-frequency mode for active wave cancellation investigated by Kurz et al. [10]. To provide additional information on the forcing strength, the actuation momentum coefficient $c_{\mu, \bar{L}_{\text{exp}}}$ based on the reference length \bar{L}_{exp} is calculated using equations (2) and (3) in Ref. [9]; c_{μ, θ_s} based on the local momentum thickness $\bar{\theta}_s$ in the streamline-oriented system is calculated as $c_{\mu, \theta_s} = c_{\mu, L_{\text{exp}}} \bar{L}_{\text{exp}} / \bar{\theta}_s$. The actuator parameters for the simulations presented in this paper are summarized in Table 2.

3 Base-Flow Characteristics and Reference Case

The simulations presented in this paper refer to the redesigned swept flat-plate experiment of DLR-Göttingen [1]. The flow is strongly accelerated in the leading edge region, followed by a weak but continuous acceleration over the whole plate length. An overview of the boundary-layer parameters is given by Dörr and Kloker [6]. The stability diagram for the travelling modes with $\omega = 6$ are shown in Fig. 3(a). The investigated mode (1, +1) with $\gamma = 70$ is one of the integrally most amplified travelling modes. We note that the wave vector of the most amplified steady CFV mode (0, 1) is nearly perpendicular to the local potential streamlines [6]. For the travelling

mode $(1, +1)$, the wave-vector angle ϕ_α , spanned by the x -axis and the wave vector $(\alpha_r, 0, \gamma)^T$, is about 5° smaller than that of the steady counterpart $(0, 1)$.

In the reference case REF without control, only the test mode $(1, +1)$ and background pulsing as described in Sect. 2.1 are activated. In Fig. 3(b), the modal amplitude development of the normalized disturbance velocity component \tilde{u}'_s is shown. It is calculated as $\tilde{u}'_s = u'_s / u_{s,e,\text{baseflow}} = (u_s - u_{s,\text{baseflow}}) / u_{s,e,\text{baseflow}}$, where the subscripts s and e denote the value in the streamline-oriented system and at the boundary-layer edge, respectively. The amplitude of the test mode $(1, +1)$ rises continuously to 10% at $x \approx 2.2$. The superharmonics $(k, +k)$, $k \geq 2$, are nonlinearly generated and saturate progressively with the generating mode $(1, +1)$. At $x \approx 2.5$, an explosive secondary instability is triggered. The high-frequency mode $\omega = 90$ is the most strongly amplified secondary mode, and laminar breakdown sets in slightly downstream. In Fig. 4(a-d), snapshots of the vortical structures at four time instances within a fundamental period T_0 are presented. The co-rotating CFVs appearing in the visualized region travel in the positive z -direction while convecting downstream. The orientation of the vortex axis is perpendicular to the wave-vector of the mode $(1, +1)$, therefore misaligned with the local potential streamlines. The finger-like structures emerging on the main CFVs correspond to the secondarily amplified high-frequency modes, finally developing into turbulence spots.

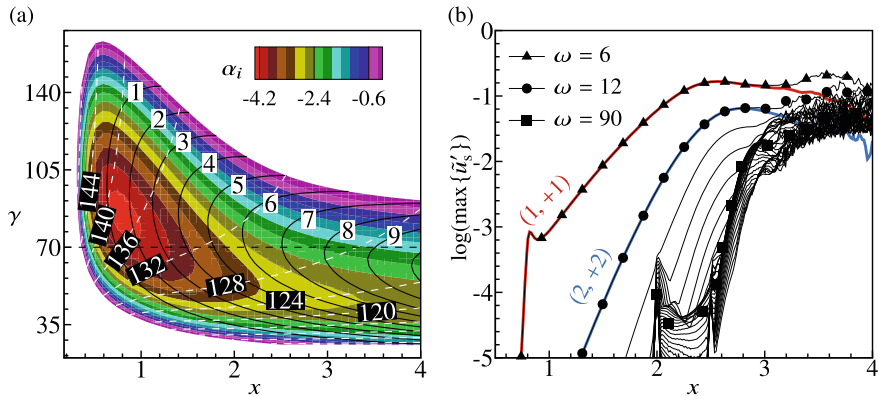


Fig. 3 (a) Spatial amplification rate $-\alpha_i$ (colour), n -factor (solid lines) and wave-vector angle ϕ_α (white dashed lines) of unstable CFV modes with $\omega = 6$. (b) Development of modal disturbance amplitudes $\tilde{u}'_{s,(h,k)}$ and $\tilde{u}'_{s,(h)}$ (maximum over y or y and z , $6 \leq \omega \leq 180$, $\Delta\omega = 6$) for case REF

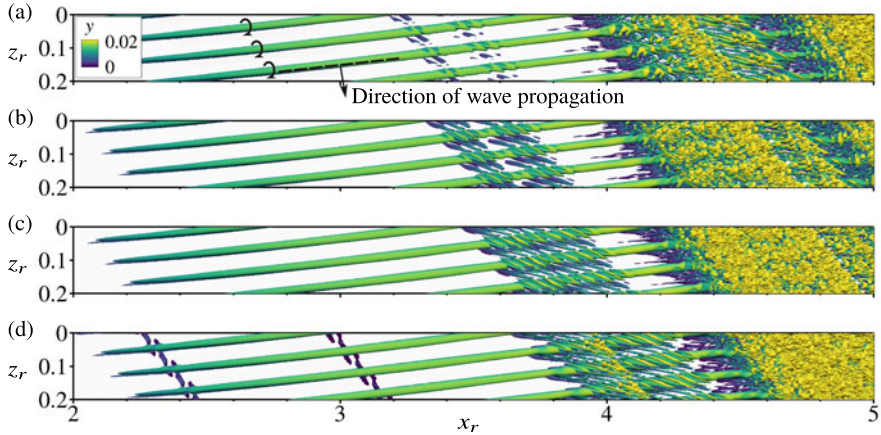


Fig. 4 Vortex visualization (snapshots, $\lambda_2 = -4$) for case REF at (a) $t/T_0 = 13.25$, (b) 13.5, (c) 13.75, (d) 13. Rotated reference system used. Not to scale

4 Investigations of Control

4.1 Single Row of Actuators

A spanwise row of volume-forcing actuators as described in Sect. 2.2 is now employed to control the transition induced by travelling CFVs. In Fig. 5, the (inactive) volume-forcing setup for case DA-1 is shown in a top view and a crosscut. The spanwise spacing of the actuators corresponds to the spanwise wavelength of the targeted travelling mode ($1, +1$). To ensure an effective wave cancellation, the actuators are aligned with the wave crests of $(1, +1)$. The induced unsteady volume force is then perpendicular to the axes of the oncoming CFVs, aimed at counteracting the rotational motion in the near wall region. The forcing towards the wave-vector direction is defined as positive. The spanwise position of the localized forcing is

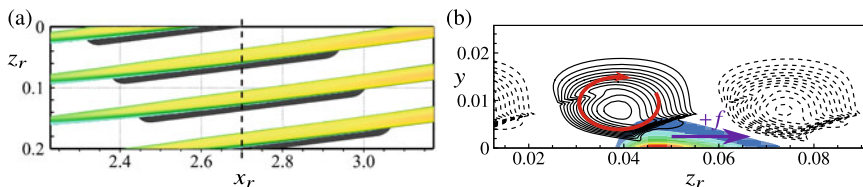


Fig. 5 (a) Travelling CFVs to be controlled ($\lambda = -4$, coloured) and volume-force distribution ($f_{10\%}$ -isosurface, black) for case DA-1. (b) Crosscut along the dashed line in ((a)). Colour indicates $|f|$ (levels 0.05 to 0.75, $\Delta = 0.10$). Solid and dashed lines show λ_2 -isocontours (levels -12 to -1 , $\Delta = 1$) of the travelling CFVs at the time of maximum positive and negative forcing, respectively

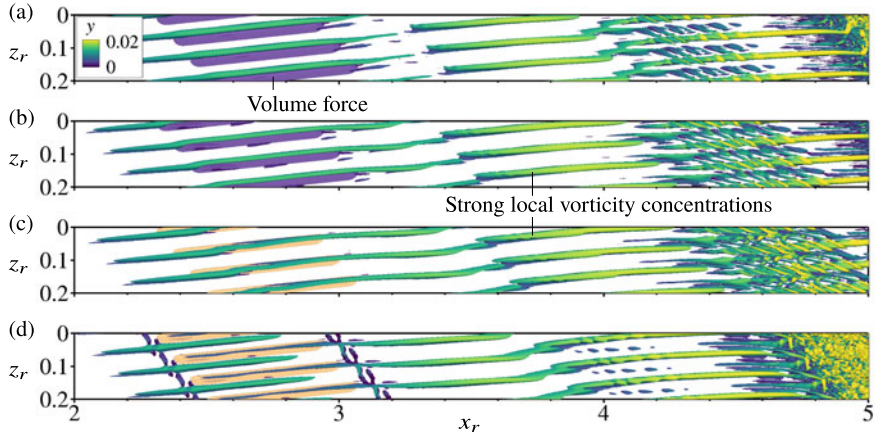


Fig. 6 Vortex visualization (snapshots, $\lambda_2 = -4$) and volume-force distribution ($f_{10\%}$ -isosurface, purple: positive; orange: negative) for case DA-1 at (a) $t/T_0 = 13.25$, (b) 13.5, (c) 13.75, (d) 13. Rotated reference system used. Not to scale

arbitrarily chosen while the forcing strength $\max|f|$ and the phase of the time signal $Z(t)$ are varied until the most delayed transition is found.

The vortical structures arising from the actuation during one fundamental period are shown in Fig. 6. The oncoming CFVs are clearly affected while travelling over the actuators. Farther downstream, their strength is decreased and their shape is strongly modulated in streamwise direction. Thanks to the attenuation of the primary vortices, the first secondary structures appear only at $x_r > 4.0$, and the transition is delayed compared to the reference case.

In Fig. 7(a), the downstream development of modal disturbance amplitudes for case DA-1 is shown. As expected, the oncoming CFV mode $(1, +1)$ is clearly attenuated in the vicinity of the actuators. Consequently, the onset of the secondary growth of high-frequency modes is delayed from $x \approx 2.5$ to $x \approx 3.0$. It is noteworthy that a steady mode $(0, 1)$ is also excited by the volume forcing due to the non-zero steady mean. This mode undergoes a continuous amplification farther downstream, and attains a nonlinear amplitude comparable with the travelling mode $(1, +1)$. The streamwise modulation of the main CFVs in the physical space can be explained as a result of the superposition of the modes $(0, 1)$ and $(1, +1)$. The constructive interference between both misaligned modes leads to emergence of some travelling 3-d structures associated with strong local vorticity concentrations, where the secondary finger-structures first appear. It is justified to say that the modes $(1, +1)$ and $(0, 1)$ are jointly responsible for the final breakdown. See Ref. [3] for a more detailed discussion on the laminar breakdown initiated by superposed steady and travelling modes.

To minimize the detrimental effect of the actuation induced steady mode $(0, 1)$, an additional simulation with purely sinusoidal forcing, i.e. $c_s = 0$, is performed. As shown by the dashed line in Fig. 7(a), the amplitude of $(0, 1)$ is indeed reduced

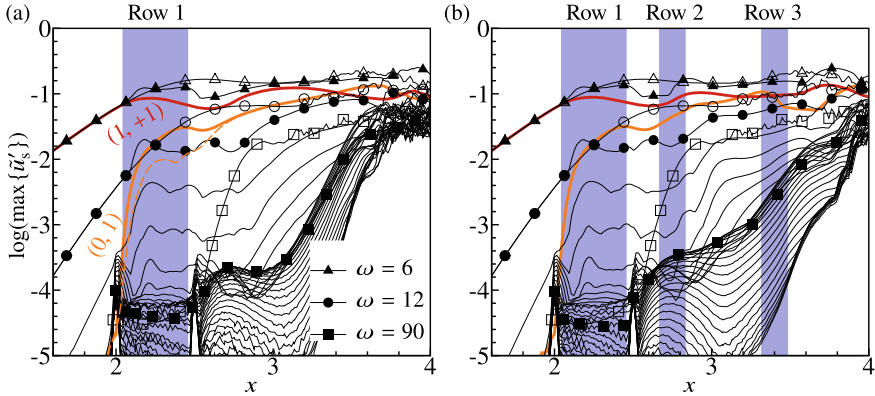


Fig. 7 Downstream development of modal disturbance amplitudes $\tilde{u}'_{s,(h,k)}$ and $\tilde{u}'_{s,(h)}$ (maximum over y or y and z , $6 \leq \omega \leq 180$, $\Delta\omega = 6$) for case (a) DA-1 and (b) DA-3. The dashed line in (a) shows the mode $(0,1)$ for case DA-1- $(c_s = 0)$. Open symbols denote the reference case REF. Blue rectangles mark the locations of volume forcing

in the vicinity of the actuator row. However, it grows to the same level as in case DA-1 farther downstream, and the control performance is virtually the same. We note that the unsteady force component excites the modal spectral contents $(1, \pm k)$ simultaneously. Even when the steady force component is absent, the steady mode $(0, 1)$ can still be generated by nonlinear interaction between travelling modes, e.g., by $(1, +1)$ and $(1, +2)$.

Preliminary investigations have shown that employing shorter actuators leads to a higher initial amplitude of the unwanted steady mode $(0, 1)$. Transition delay is only achievable by using actuators with a sufficient length l_{PA} . In fact, the actuators favour only wave structures aligned with their spatial arrangement, i.e. the misaligned steady mode $(0, 1)$ is hindered. Extending the actuator's length along the wave crests of the target mode helps intensify this receptivity selection effect.

4.2 Multiple Rows of Actuators

For case DA-3, we add two additional actuator rows downstream to attenuate the remaining CFVs for improvement of the transition delay. The second and third row are aimed at breaking the downstream growth of the mode $(1, +1)$ and $(0, 1)$, respectively. Since the main CFVs downstream of the first actuator row are strongly deformed, it is not possible to use elongated actuators along the CFVs. Instead, shorter actuators with more localized forcing are employed. The second row is centered at $x = 2.75$, before the travelling mode $(1, +1)$ attains an amplitude of 10%. The orientation and the time signal of the actuators are identical to those used for the first row. The spanwise location and the phase of the time signal is adapted to delay the transition as far as possible. For the third row, steady forcing is employed at

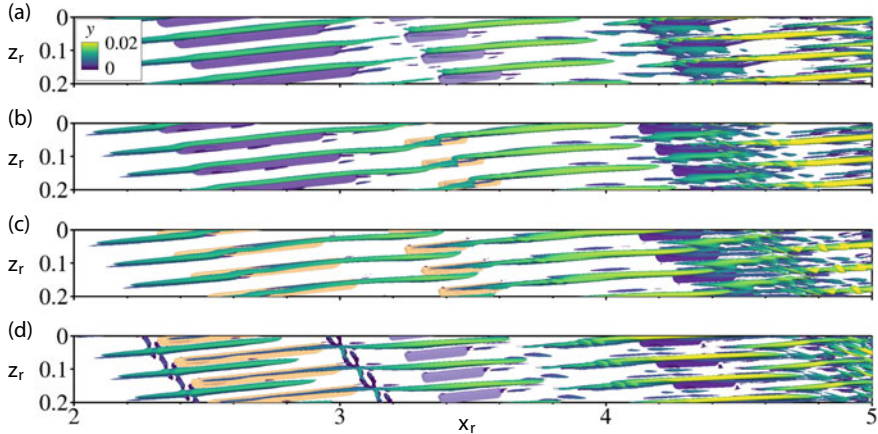
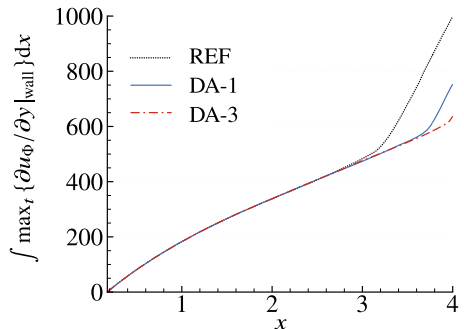


Fig. 8 Vortex visualization (snapshots, $\lambda_2 = -4$) and volume-force distribution ($f_{10\%}$ -isosurface, purple: positive; orange: negative) for case DA-3 at (a) $t/T_0 = 13.25$, (b) 13.5, (c) 13.75, (d) 13. Rotated reference system used. Not to scale

$x = 3.4$ to kill the steady CFV mode dominating farther downstream. The actuators are aligned with the orientation of the steady mode (0, 1). Note that this strategy is based on knowledge of previous [5] and the current investigations, and on educated intuition; prospectively the use of a controller would secure the control efficiency at varied conditions.

As shown in Fig. 7(b), the modes (1, +1) and (0, 1) are locally attenuated by the second and third actuator row, respectively. However, it seems that weakening one of both modes promotes the downstream growth of the other. The secondary growth of the high-frequency modes is only slightly slowed down. Vortex visualization in Fig. 8 shows that the strength of the main CFVs is further reduced by the additional actuator rows. The first turbulence spots appear at the end of the visualized region. It also makes clear that a perfect wave cancellation using localized forcing is hardly attainable in such a complex scenario. A rigorous real-time and in-situ optimization of the forcing configuration is necessary in practice.

Fig. 9 In the x -direction integrated wall-normal gradient of the spanwise mean velocity u_Φ . The maximum arising over one fundamental period is used to account for a fully turbulent flow



The effect of the wave attenuation on the skin-friction drag is compared in Fig. 9. The spanwise averaged wall-normal gradient $\partial u_\Phi / \partial y$ is integrated in the x -direction to indicate the skin-friction development, where u_Φ is the velocity component in the direction of the oncoming flow. The sudden slope change of the curves implies the location of the transition front. It is shown that the total skin-friction drag is successively reduced by three actuator rows due to the delayed transition.

5 Conclusions

The applicability of volume-forcing actuators to control large-amplitude travelling crossflow vortices has been explored. The localized, unsteady volume force mimics the effect of plasma actuators operated at low-frequency. The unsteady forcing (with alternating direction) is aimed at counteracting the rotational motion of the travelling CFVs in the nonlinear state. The actuators are arranged in a spanwise row and oriented parallel to the wave crests of the oncoming travelling CFVs. It is shown that the onset of secondary instabilities can be delayed by attenuating the primary vortices using unsteady volume forcing. However, it is found that a detrimental steady mode is also excited. It grows in amplitude and modulates the primary vortical structures, leading to an emergence of isolated structures associated with strong local vorticity concentrations, rendering some parts of the main CFVs more unstable. By employing two additional actuator rows downstream with combined steady and unsteady forcing, the growing steady and travelling modes can be further attenuated, respectively, yielding enhanced delay of the complex transition scenario with travelling primary 3-d structures. Therefore it is proven that a control is principally feasible. However, if broadband primary disturbances are present, modulating the travelling vortices in space and time, a fast controller scheme is necessary with more actuators. This may also be accomplished by the methodology of machine learning.

References

1. Barth, H., Hein, S., Rosemann, H.: Redesigned swept flat-plate experiment for crossflow-induced transition studies. In: New Results in Numerical and Experimental Fluid Dynamics XI, Notes on Numerical Fluid Mechanics and Multidisciplinary Design. Springer Berlin (2017)
2. Bippes, H.: Basic experiments on transition in three-dimensional boundary layers dominated by crossflow instability. *Prog. Aerosp. Sci.* **35**, 363–412 (1999)
3. Bonfigli, G., Kloker, M.: Numerical investigation of transition caused by superposed steady and travelling crossflow vortices. Tech. Rep. IAG-TR-2005-CFTRANS, Univ. of Stuttgart (2005)
4. Dörr, P.C., Kloker, M.J.: Stabilisation of a three-dimensional boundary layer by base-flow manipulation using plasma actuators. *J. Phys. D: Appl. Phys.* **48**, 285205 (2015)
5. Dörr, P.C., Kloker, M.J.: Transition control in a three-dimensional boundary layer by direct attenuation of nonlinear crossflow vortices using plasma actuators. *Int. J. Heat Fluid Flow* **61**, 449–465 (2016)

6. Dörr, P.C., Kloker, M.J.: Crossflow transition control by upstream flow deformation using plasma actuators. *J. Appl. Phys.* **121**, 063303 (2017)
7. Downs, R.S., White, E.B.: Free-stream turbulence and the development of cross-flow disturbances. *J. Fluid Mech.* **735**, 347–380 (2013)
8. Guo, Z., Kloker, M.J.: Control of crossflow-vortex-induced transition by unsteady control vortices. *Journal of Fluid Mechanics* **871**, 427–449 (2019)
9. Guo, Z., Kloker, M.J.: Effects of low-frequency noise in crossflow transition control. *AIAA J.* **58**(3), 1068–1078 (2020)
10. Kurz, A., Tropea, C., Grundmann, S., Forte, M., Vermeersch, O., Seraudie, A., Arnal, D., Goldin, N., King, R.: Transition delay using DBD plasma actuators in direct frequency mode. *AIAA Paper* (2012). 2012-2945
11. Li, F., Choudhari, M.M., Duan, L., Chang, C.L.: Nonlinear development and secondary instability of traveling crossflow vortices. *Phys. Fluids* **26**, 064104 (2014)
12. Saric, W.S., Reed, H.L., White, E.B.: Stability and transition of three-dimensional boundary layers. *Ann. Rev. Fluid Mech.* **35**, 413–440 (2003)
13. Wassermann, P., Kloker, M.: Transition mechanisms induced by travelling crossflow vortices in a three-dimensional boundary layer. *J. Fluid Mech.* **483**, 67–89 (2003)

Experimental Attenuation of a Trailing Vortex Inspired by Stability Analysis



Ross Richardson, Brian Eckert, Yang Zhang, Louis N. Cattafesta III,
Adam Edstrand, Yiyang Sun, Peter Schmid, and Kunihiko Taira

Abstract Inspired by a parabolized stability analysis [1], higher-order wake instability modes are targeted via the actuation of a tensioned string in the mean-chord-plane just aft of the trailing edge of a NACA0012 half-wing at 5° angle of attack and a chord based Reynolds number (Re_c) of 1.32×10^5 . Stereoscopic Particle Image Velocimetry (SPIV) and a load cell are used to assess the effects of the control just downstream of the trailing edge and 6.5 chords downstream. The results reveal increased turbulence intensity in the wake that is engulfed into the vortex during its formation, and a reduction in the time-averaged streamwise vorticity downstream with minimal loss of lift, providing evidence of the possibility of exciting instability modes for subsequent attenuation of the vortex farther downstream.

1 Introduction

A trailing vortex is formed at the tip of a finite-span wing that produces lift. The tip vortex causes adverse effects such as hazardous wake conditions for trailing vehicles in flight and a vortex wake in maritime applications [2, 3]. Furthermore, the persistence and strength of trailing vortices degrade the efficiency of airport opera-

R. Richardson (✉) · B. Eckert · Y. Zhang · L. N. Cattafesta III
Florida State University, Tallahassee, FL 32310, USA
e-mail: rbr11@my.fsu.edu

A. Edstrand
Sandia National Laboratories, Albuquerque, NM 87185, USA

Y. Sun
University of Minnesota, Minneapolis, MN 55455, USA

P. Schmid
Imperial College, London SW7 2AZ, UK

K. Taira
University of California, Los Angeles, CA 90095, USA

tions across the globe, requiring aircraft spacing guidelines [3] to limit the effects of induced rolling moments on smaller trailing aircraft [4]. Hence, attenuation of tip vortices represents a research area with significant practical impact. The challenge in addressing this issue stems from the inherent persistence of tip vortices and their resistance to control efforts.

The development and structure of trailing vortex flow physics have been extensively studied [3, 5, 6]. A well-known feature of the trailing vortices is their ability to “wander” or “meander”. This has been observed in numerous wind tunnel experiments, and the potential causes are attributed to the wind tunnel unsteadiness or instabilities associated to the vortex or vortices [5, 7, 8]. In the case of two trailing vortices generated at the two tips of a wing, the vortices persist for long distances and ultimately interact and are destroyed via the long wavelength Crow instability [9, 10].

Most efforts to attenuate trailing vortices typically aim to excite instabilities or to directly modify the vortical structure [6] with either passive or active flow control strategies. Passive efforts involve the addition of various kinds of appendages to the lifting surface predominately located at the tip of the wing. One of the most efficient end-plate designs known as a winglet has been implemented on modern aircraft due to its ability to improve cruise efficiency and reduce the rolling moment on a trailing wing [11]. Also, segmented gurney flaps along the trailing edge have been explored [12, 13]. Some active control schemes focus on steady spanwise blowing [14, 15]. Others have used unsteady forcing via synthetic jet actuators [16].

Previous research efforts by our group first consisted of a parallel stability analysis performed on the trailing vortex wake of a NACA0012 half-wing at a low Reynolds number, where multiple unstable modes were identified [17]. A follow-up linear parabolized stability analysis (PSE) was conducted on the same flow field revealing marginally stable wake modes that, when targeted through actuation, lead to an instability in the wingtip vortex further downstream. Direct numerical simulations (DNS) leveraging the findings of the stability analysis were performed where unstable modes were excited via a localized body force as a means of vortex wake control. The modal control scheme showed substantial reduction in the circulation and peak vorticity compared to when a higher-order wake mode was excited, providing evidence for a pathway to attenuate a trailing vortex [1]. Inspired by these findings, the current work seeks to explore the concept by actuating a tensioned string across the trailing edge of a NACA0012 half-wing in order to excite the desired wake modes leading to vortex attenuation in an experimental setup.

The rest of the paper is outlined as follows. Section 2 consists of a detailed description of the methodology and experimental setup. Section 3 includes quantitative comparisons of several candidate control cases to the baseline uncontrolled vortex. Section 4 offers preliminary conclusions and future work.

2 Methodology

2.1 Experimental Setup

Experiments are performed in the Florida State Aeroacoustic Tunnel (FSAT). This facility is an open circuit wind tunnel capable of freestream velocities (U_∞) from 2 to 75 m/s with a turbulence intensity level of less than 0.1%. The test section has dimensions of 0.91 m (height) by 1.21 m (width) by 3.05 m (length), and the standard test section used in these experiments permits optical access via two sidewall glass panels. A schematic of the experimental setup is shown in Fig. 1. A trailing vortex is generated by a 30.48 cm chord (c) NACA0012 airfoil with a half-aspect-ratio (b/c) of 1.29 at an angle of attack of 5°. All measurements are made at $U_\infty = 7$ m/s, corresponding to $Re_c = 132000$. The model is mounted vertically in the FSAT. The half-wing is attached to a sting mount that is fed through a clearance hole in the floor of the wind tunnel and is rigidly attached to a load cell located outside of the test section. The through hole has ample clearance to ensure the aerodynamic forces are felt solely by the load cell to maintain accurate force measurements. Also, there is a 6.35 mm gap between the base of the model and the tunnel floor to protrude the model outside of the tunnel wall boundary layer and to allow tolerance for potential structural deflection. The coordinate system origin is located at the trailing edge of the model.

Motivated by the parabolized stability analysis and direct numerical simulations in [1], the objective of the control experiments is to generate various spanwise wavelength sinusoidal disturbances in the near wake of the airfoil. Since independent control of the spanwise wavelength λ and frequency f_0 is desired, a tensioned string is selected to generate a standing wave pattern subject to $\lambda f_0 = \sqrt{T/\rho_L}$, where T is the string tension and ρ_L is the linear string density. The string is a Pasco SE-9409 elastic wave cord. It is attached inside one rectangular wingtip of the model and passed out through eyelets in adjustable length pins located at the two ends of the airfoil and ultimately through a small opening in the wind tunnel floor. The string is located as close as possible to the trailing edge, such that it did not touch the trailing

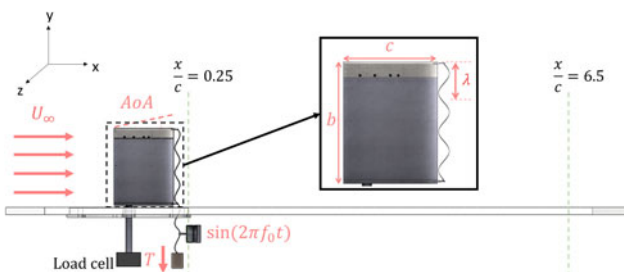


Fig. 1 Schematic of the experimental setup (not to scale). A tensioned string placed just downstream of the airfoil trailing edge is actuated to produce a standing wave pattern in the $x-y$ plane

edge of the model when actuated. The string is connected at an anti-node to a Pasco mechanical wave driver (SF-9324) to produce a sinusoidal standing wave pattern with a prescribed wavelength in the mean-chord-plane ($x - y$). The tension in the string is adjusted by attaching different masses to its end, thus permitting adjustment of the phase speed in the vibrating string. Only slight adjustments of the amplitude of the standing wave pattern are possible via the gain of the SF-9324.

2.2 Actuation Modes

Attempts are made to match the wake actuation modes explored in Edstrand et al. [1] with the elastic wave cord. However, due to limitations related to the linear density (4.28 g/m) of the SE-9409, low-frequency modes cannot be replicated with reasonable amplitude due to the small tension required. Table 1 summarizes the cases explored in this paper using a fixed mass of 265 g. Exploratory experiments indicated that an increase in the driving frequency of actuation resulted in a decreased amplitude. For the control cases tested, long exposure photographs of the actuated string are provided in Fig. 2 where the mode shapes of the standing wave patterns can be visualized without flow. Case 4, corresponding to $\lambda/b = 1/3$, is chosen to approximately match the wavelength of the 5th wake mode discussed in [1]. The actuation frequency is nondimensionalized as $\omega^* = 2\pi f_0 c/U_\infty$. Here we also note the baseline case is with the elastic wave cord affixed aft of the trailing edge without any actuation.

2.2.1 Stereo Particle Image Velocimetry (SPIV)

A schematic of the SPIV setup is illustrated in Fig. 3. A 200 mJ Evergreen Nd:YAG laser and optics creates a planar light sheet with a thickness of approximately 2 mm thick. The data are acquired at two $y-z$ planes downstream of the wing, namely at $x/c = 0.25$ and 6.5 to quantify the control input and response at the end of the test section. The particle images are captured using a pair of LaVision Imager sCMOS cameras. The angle between the two cameras in both cases is approximately 80°. The flow is seeded with propylene glycol from a Rosco VAPOUR, which produces

Table 1 Test case frequencies, wavelengths, and peak-to-peak amplitude of standing wave patterns

Cases	f_0 (Hz)	ω^*	λ/b	Amplitude (mm)
1	Baseline	—	—	—
2	68	18.6	1	23
3	137	37.5	1/2	13
4	200	54.7	1/3	6

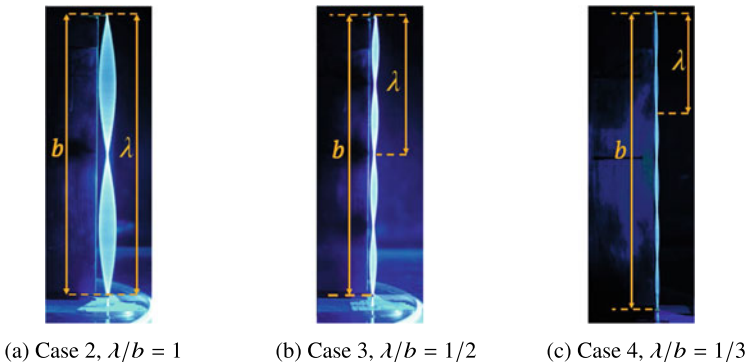
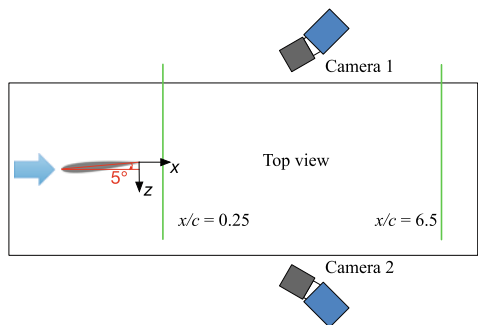


Fig. 2 Long exposure photographs of the actuation cases

Fig. 3 Schematic of the SPIV setup (not to scale)



approximately $2 \mu\text{m}$ diameter particles. The particles are introduced into the flow field through an ‘H’ shaped PVC pipe of 31.8 mm internal diameter connected to a settling chamber through a small access port just upstream of the tunnel contraction. For each test case, a total of 500 image pairs are acquired at a rate 15 Hz with a time delay of $\Delta t = 100 \mu\text{s}$ between image pairs. This time delay is optimized for the particle displacements with reduced out-of-plane particles in the SPIV measurement. Camera calibrations are performed using a LaVision Type 22 calibration plate. This is followed by a self-calibration step to correct the potential misalignment between the calibration plate and the laser sheet.

Displacement vectors between image pairs are calculated with the use of a spatial cross-correlation algorithm using LaVision DaVis 8.4.0 software. Image pre-processing is done using a time series filter to subtract the minimum pixel intensity to abate high intensity reflections in the images. A spatial intensity filter is used to mask regions with sub-optimal seeding density. Moreover, a multi-pass scheme is performed, reducing the interrogation window size from an initial 64 by 64 pixels to 32 by 32 pixels for the final pass, with a 75% overlap between windows. Post-processing using universal outlier detection [18] is performed to remove spurious vectors. Multivariate-outlier-detection [19] is applied to further remove statistical

outliers. The processing results in a vector resolution of 2.5 vectors/mm in the $x/c = 0.25$ plane and 2.2 vectors/mm in the $x/c = 6.5$ plane, respectively.

2.3 Lift and Drag Measurements

An ATI Industrial Automation six-axis Mini-40 load cell is employed to capture aerodynamic force measurements for the baseline and actuated cases, both with and without flow. The differences between these quantities result in a measure of the aerodynamic forces on the half-wing at testing conditions. Data are acquired for 30 s in order to provide statistically converged time-averaged lift and drag forces. The full scale range of the F_x and F_y axes of the load cell is 40 N with a resolution of 0.01 N. The F_x axis of the load cell is aligned with the chord of the NACA0012 model and thus a rotation to the tunnel's coordinates are required to obtain final lift and drag values.

3 Results

Results are provided to assess the effects of the control strategy at two streamwise locations of $x/c = 0.25$ and 6.5, which will be referred to as the near and intermediate fields of the trailing vortex wake. We note that the velocity fields are not corrected for vortex wandering in these results.

3.1 Near Field: Disturbance Characterization

Contour plots of the TKE at $x/c = 0.25$ for each case in Table 1 are shown in Fig. 4. The field of view at this location encompasses the vortex and approximately the top 1/3 of the airfoil span. At this streamwise location, the nascent vortex is still rolling up, manifesting as a wake spiral [5]. Compared to the baseline case (Fig. 4a), it is observed that each of the control cases possess an increase in TKE in the wake region of the airfoil due to the vibrating string. This clearly shows that the actuator has added disturbances which act to increase turbulence levels in the near field. The controlled flow with actuator frequency 68 Hz and wavelength of $\lambda/b = 1$, seen in Fig. 4b, provides substantially larger velocity fluctuations due to the larger actuation amplitude of the string, which can be seen in Fig. 2. Focusing on this case, one can also notice from the contour plot that higher turbulence levels are not restricted to only the wake but are also being entrained into the outer region of the developing vortex.

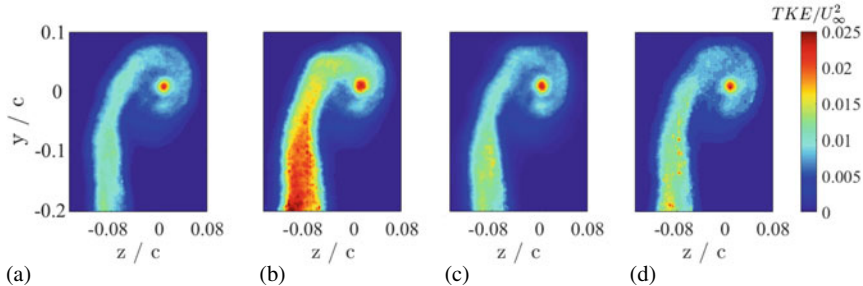


Fig. 4 TKE in the $y - z$ plane at $x/c = 0.25$. **a** Baseline; **b** Case 2, 68 Hz, $\lambda/b = 1$; **c** Case 3, 137 Hz, $\lambda/b = 1/2$; **d** Case 4, 200 Hz, $\lambda/b = 1/3$

3.2 Intermediate Field: Time-Averaged Quantities

In the intermediate field of the trailing vortex, the time-averaged streamwise vorticity and TKE are computed using the 500 image pairs for each of the cases. Contour plots of these cases are provided in Figs. 5 and 6. All of the control cases exhibit lower levels of vorticity in comparison with the baseline case. This is verified in Fig. 7, which depicts a slice across the vortex core in the z -direction, passing through the axis of the vortex. Note that a moving average of 7 points for the normalized vorticity values along the slice is computed to smooth the data. The observed decrease in the vorticity magnitude is localized to the core region. This decrease is quantified as a reduction of 21%, 16%, and 17% for cases 2, 3, and 4 respectively. Despite the larger amplitude disturbance introduced by case 2, the attenuation achieved in the other higher wavelength cases are comparable, suggesting that excitation of higher-order spanwise wake modes are indeed more effective for control as postulated in [1]. In addition, Fig. 6 shows that each of the control cases exhibit slightly lower TKE in the vortex core region.

Of particular interest to any wingtip vortex control scheme is its effect on the aerodynamic forces provided by the finite-span wing. The ideal goal is to reduce the strength or destabilize the wingtip vortex without negatively affecting the aerodynamic forces. Force measurements are presented to assess the impact of the control scheme on the aerodynamic loads compared to the baseline. The time-averaged lift and drag forces are quantified via the load cell measurements and normalized by the product of the free stream dynamic pressure and planform area of the half-wing to

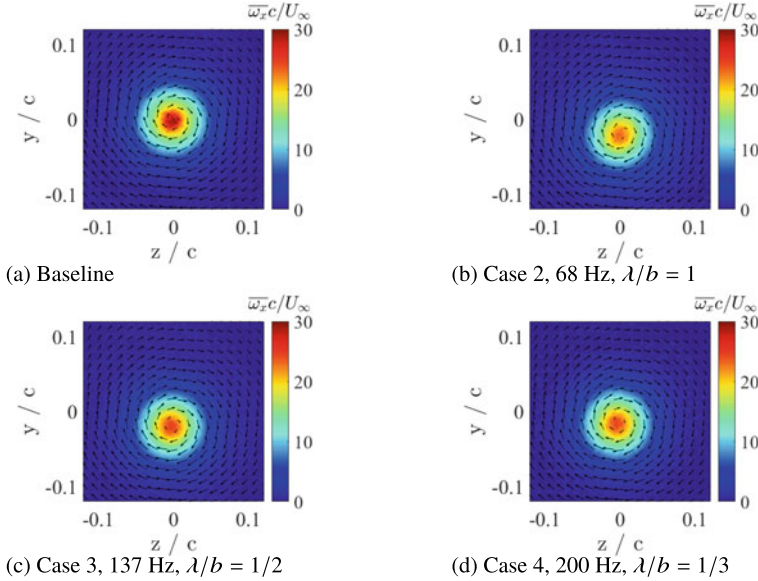


Fig. 5 Time-averaged streamwise vorticity in the $y - z$ plane at $x/c = 6.5$. Transverse velocity vectors are superimposed (only every 9th vector is shown for clarity)

Table 2 Lift and drag coefficients for different test cases

Cases	f_0 (Hz)	C_L	C_D
1	Baseline	0.359	0.059
2	68	0.333	0.070
3	137	0.351	0.064
4	200	0.349	0.066

determine the lift (C_L) and drag (C_D) coefficients. The resulting coefficients from the baseline and controlled cases are shown in Table 2 above with nominal uncertainties of ± 0.003 based on the resolution of the instrumentation. Minimal losses in lift and an associated increase in drag are observed for the actuated cases compared to the baseline. Further effort was also taken to quantify the drag created by the wave chord itself. Taking the difference between the drag associated with the baseline case and a bare NACA0012 half-wing (without the elastic wave cord) at test conditions, we find the C_D of the string to be 0.009 ± 0.003 .

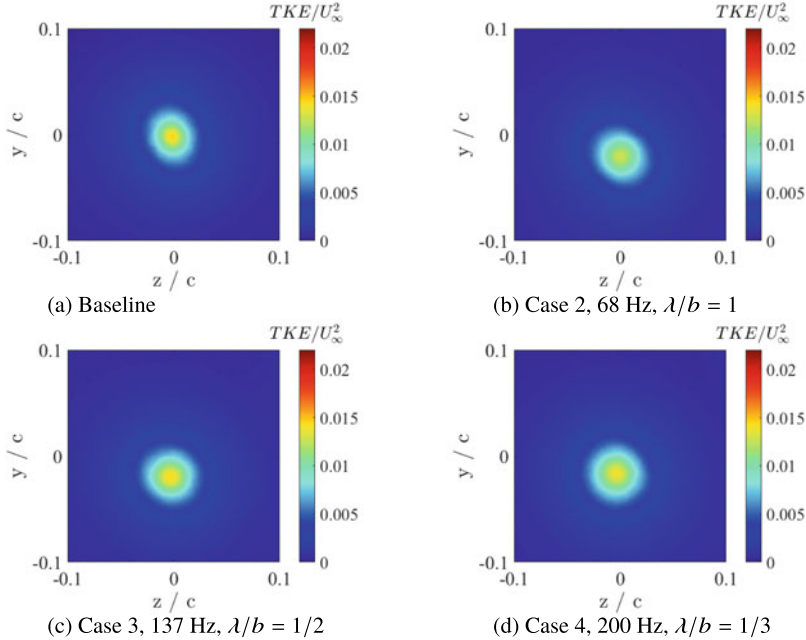
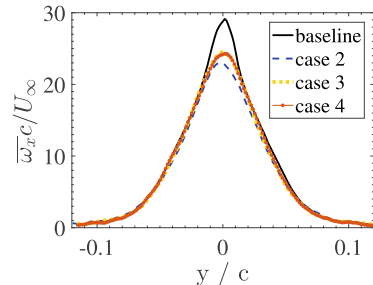


Fig. 6 Time-averaged streamwise vorticity in the $y - z$ plane at $x/c = 6.5$

Fig. 7 Streamwise vorticity slice across the vortex core at $x/c = 6.5$



4 Conclusions and Future Work

A stability-inspired modal control strategy is determined to have an impact on the time-averaged trailing vortex wake produced by a NACA0012 half-wing at 5° angle of attack and a chord based Reynolds number of 1.32×10^5 . The effects on the velocity fields are measured at streamwise locations of $x/c = 0.25$ and 6.5 , respectively. Controlled cases display an increase in TKE in the near field wake region due to the perturbations introduced by the actuation. The controlled disturbance is effectively wrapped into the vortex core during formation. Reductions in the peak magnitude of the normalized streamwise vorticity are observed in the intermediate field 6.5 chords

downstream of the trailing edge. In particular, reductions of 21%, 16%, and 17% for the control cases of $\lambda/b = 1, 1/2$ and $1/3$, respectively, are obtained. Despite having significantly lower amplitude in case 4, the $\lambda/b = 1/3$ perturbation, analogous to the effective higher-order wake mode identified in [1] at much lower Reynolds number, has comparable control performance compared to other cases.

The analysis of the effectiveness of the control scheme on the trailing vortex continues. To better interpret the effect the control has on the trailing vortex wake, a more thorough understanding of the fluidic perturbation being produced is necessary. SPIV at the streamwise distance of $x/c = 0.25$ will be undertaken across the entirety of the airfoil span to quantify the perturbation produced by the string. Phase-locked and/or time-resolved SPIV will also permit modal decomposition in the frequency domain, thus enabling analysis of modal growth rates. Another parameter of interest that will be investigated is the wandering of the vortex, a measure of which may be indicative of a vortex instability [8].

References

- Edstrand, A.M., Sun, Y., Schmid, P.J., Taira, K., Cattafesta, L.: Active attenuation of a trailing vortex inspired by a parabolized stability analysis. *J. Fluid Mech.* **855**, R2 (2018). <https://doi.org/10.1017/jfm.2018.701>
- May, D., Wren, Graeme G., et al.: Detection of submerged vessels using remote sensing techniques. *Australian Defence Force J.* **127**, 9–15 (1997)
- Spalart, P.R.: Airplane Trailing Vortices. *Annu. Rev. Fluid Mech.* **30**(1), 107–138 (1998). <https://doi.org/10.1146/annurev.fluid.30.1.107>
- Stickle, Joseph W and Kelly, Mark W (1977). Ground-based facilities for evaluating vortex minimization concepts. NASA-SP-409, pp. 129-156
- Devenport, William J., Rife, Michael C., Liapis, Stergios I., and Follin, Gordon J. (1996). The structure and development of a wing-tip vortex. Volume 312, pp. 17–106
- Crouch, J.: Airplane trailing vortices and their control. *C.R. Phys.* **6**(4–5), 487–499 (2005). <https://doi.org/10.1016/j.crhy.2005.05.006>
- Bilanin, A., and Widnall, S. (1973). Aircraft wake dissipation by sinusoidal instability and vortex breakdown. 11th Aerospace Sciences Meeting. AIAA 1973-107. <https://doi.org/10.2514/6.1973-107>
- Edstrand, A.M., Davis, T.B., Schmid, P.J., Taira, K., Cattafesta, L.: On the mechanism of trailing vortex wandering. *J. Fluid Mech.* **801**, R1 (2016). <https://doi.org/10.1017/jfm.2016.440>
- Crow, S.C.: Stability theory for a pair of trailing vortices. *AIAA Journal* **8**(12), 2172–2179 (1970). <https://doi.org/10.2514/3.6083>
- Rokhsaz, K., Foster, S., and Miller, L. (1999). Exploratory study of aircraft wake vortex filaments in a water tunnel. 17th Applied Aerodynamics Conference. AIAA 1999-3199. <https://doi.org/10.2514/6.1999-3199>
- Dunham Jr, R Earl (1977). Unsuccessful concepts for aircraft wake vortex minimization. NASA-SP-409, pp. 221-250
- Nikolic, V.R.: Effect of Full-Span Gurney Flap Height on Wing Wake Vortex Alleviation. *Journal of Aircraft* **43**(5), 1555–1558 (2006). <https://doi.org/10.2514/1.19369>
- Matalanis, C.G., Eaton, J.K.: Wake Vortex Control Using Static Segmented Gurney Flaps. *AIAA Journal* **45**(2), 321–328 (2007). <https://doi.org/10.2514/1.25956>

14. Edstrand, A., and Cattafesta, L. (2015). Topology of a Trailing Vortex Flow Field with Steady Circulation Control Blowing. 53rd AIAA Aerospace Sciences Meeting. AIAA 2015-1706. <https://doi.org/10.2514/6.2015-1706>
15. Duraisamy, K., Baeder, J.D.: Numerical Simulation of the Effects of Spanwise Blowing on Wing-tip Vortex Formation and Evolution. *Journal of Aircraft* **43**(4), 996–1006 (2006). <https://doi.org/10.2514/1.19746>
16. Margaris, P., Gursul, I.: Wing tip vortex control using synthetic jets. *The Aeronautical Journal* **110**(1112), 673–681 (2006). <https://doi.org/10.1017/s000192400001536>
17. Edstrand, A.M., Schmid, P.J., Taira, K., Cattafesta, L.: A parallel stability analysis of a trailing vortex wake. *J. Fluid Mech.* **837**, 858–895 (2018). <https://doi.org/10.1017/jfm.2017.866>
18. Westerweel, J., Scarano, F.: Universal outlier detection for PIV data. *Exp. Fluids* **39**(6), 1096–1100 (2005). <https://doi.org/10.1007/s00348-005-0016-6>
19. Griffin, J., Schultz, T., Holman, R., Ukeiley, L.S., Cattafesta, L.: Application of multivariate outlier detection to fluid velocity measurements. *Exp. Fluids* **49**(1), 305–317 (2010). <https://doi.org/10.1007/s00348-010-0875-3>

General Stability Analysis

Distributed Excitation of Crossflow Waves Due to Scattering of Freestream Vortices by Surface Waviness



V. I. Borodulin, A. V. Ivanov, and Y. S. Kachanov

Abstract The amount of quantitative experimental data, devoted to mechanisms of transformation of vortical free-stream disturbances into cross-flow (CF) instability modes is very restricted. The present experimental investigation is a continuation and subsequent development of studies [1, 2, 5, 6]. Problems of the *localized* vortical receptivity of a swept-wing boundary layer were examined previously for cases of scattering of freestream vortices by surface nonuniformities [5] and surface vibrations [6]. The *distributed* vortical receptivity concerning excitation of the CF-waves by streamwise freestream vortices on a smooth surface was investigated in [1, 2]. In the present study, the surface was not smooth but had controlled spanwise-uniform long-wavelength roughness (waviness). Based on a developed technique, values of coefficients of the distributed vortex-roughness receptivity are obtained experimentally for the first time. Dependences of these coefficients on parameters of the base flow instability, freestream vortices, and surface waviness have been investigated.

1 Introduction

Rather detailed introductions to the investigations of the localized and distributed mechanisms of swept-wing boundary-layer receptivity, including vortex receptivity ones, are given in our recent works devoted to excitation of CF-instability modes due to scattering of freestream vortices by localized surface roughness [5], localized surface vibrations [6], and distributed natural baseflow nonuniformity [1, 2]. The

V. I. Borodulin · A. V. Ivanov · Y. S. Kachanov (✉)

Khristianovich Institute of Theoretical and Applied Mechanics, Novosibirsk 630090, Russia

e-mail: kachanov@itam.nsc.ru

V. I. Borodulin

e-mail: Bo@itam.nsc.ru

A. V. Ivanov

e-mail: aniva101010@gmail.com

present paper is devoted to the experimental study of a mechanism of distributed excitation of nonstationary CF-instability modes in a swept-wing boundary layer due to scattering of freestream vortices by small-amplitude spanwise-uniform surface waviness.

The problem under study is of great fundamental interest and is important for various practical applications. Meanwhile, an analysis of literature has shown that quantitative investigations of the *distributed* swept-wing boundary-layer receptivity to *unsteady* freestream vortices (leading to excitation of unsteady CF-instability modes) have not been performed *experimentally* except for those carried out by the authors in [1, 2]. In contrast to [1, 2], the main goal of the present experiments was to investigate quantitatively the problem of excitation of unsteady cross-flow instability modes due to scattering of unsteady streamwise elongated freestream vortices by *small-amplitude surface waviness* (which was uniform in the spanwise direction). In particular, this goal includes estimation of the corresponding *distributed vortex-roughness receptivity coefficients*.

Prior to starting the measurements, a theoretical analysis of the corresponding distributed-receptivity problem was performed based on experience obtained in our previous experiments carried out for distributed excitation of Tollmien-Schlichting (TS-) and CF-waves by freestream vortices in 2D and 3D boundary layers. The main goal of this analysis was to find a proper definition of the distributed receptivity coefficients (functions) and to develop a procedure of determination of these functions based purely on the experimental data.

In particular, similar to [1, 2], the theoretical analysis has shown that in every regime of measurements it is necessary to perform two experiments simultaneously:

1. A *Distributed Receptivity (DR) experiment* itself with the distributed excitation of the CF-waves by freestream vortices. In contrast to previous studies [1, 2], the *DR*-experiments were performed both in presence of the controlled surface nonuniformities (experiments *DRSR*) and on smooth surface (experiments *DRSS*) in order to provide a better accuracy of obtaining the distributed receptivity coefficients.
2. A complementary *Stability (S) experiment* on development of pure CF-waves in absence of their distributed excitation. The *S*-experiments were also performed both in presence of the waviness (experiments *SSR*) and on smooth surface (experiments *SSS*) to check the dependence on (or independence of) the stability characteristics on the presence of those types of specific surface waviness, which were used in this study.

All experiments were carried out at fully controlled disturbance conditions. In the *DR*-experiments (the distributed receptivity measurements themselves), the free-stream vortices were generated by means of a technique, which was similar to that used in experiments [1, 2]: a vibrating wire with a spanwise non-uniformity (a swelling) on it. In the *S*-experiments (the stability measurements), the CF-wave trains were excited by a point source mounted on the same experimental model.

The main goal of the present study was to obtain (for the first time) quantitative experimental information about the distributed vortex-roughness receptivity coef-

ficients for a swept wing boundary layer at excitation of unsteady CF-instability modes.

To achieve this goal, our experiments consisted of the following most important stages: (i) measurements of shapes and wavenumber spectra of all studied kinds of the surface roughness (waviness), (ii) detailed investigation of the base flow. Then the *S*-experiments included: (iii) excitation of wave-trains of “pure” CF-instability modes by a point source mounted on the experimental model surface and performing detailed measurements of amplitudes and phases of the excited CF-instability waves both in absence and in presence of each studied surface waviness, (iv) performing Fourier decomposition of the excited CF-wave-trains into oblique (in general) modes of the frequency-spanwise-wavenumber spectrum, (v) obtaining all main stability characteristics of the boundary layer under study with respect to the excited unsteady CF-modes. The third stage of the experiments called the *DR*-one included: (vi) excitation in the incident flow of fully controlled time-periodic, streamwise-elongated (and spanwise-localized) vortices and examination of their characteristics, (vii) performing measurements of amplitudes and phases of CF-instability waves excited in the boundary-layer due to streamwise distributed scattering of the controlled freestream vortices by both the natural spatial nonuniformity of the growing boundary layer and by various kinds of surface waviness, (viii) performing Fourier decomposition of both freestream vortices and excited CF-waves into oblique (in general) modes of the frequency-spanwise-wavenumber spectrum, (ix) approximation of streamwise distributions of spectral amplitudes and phases of the excited CF-modes by analytical solutions of an evolution equation describing their distributed excitation, and (x) estimation of the corresponding distributed *vortex-roughness receptivity coefficients*.

The experiments discussed in the present paper were carried out as early as in 2003 within the framework of a research contract between the Khristianovich Institute of Theoretical and Applied Mechanics (ITAM) and the Boeing Operations International, Inc., but were published previously only in technical reports.

2 Theoretical Analysis

A deep theoretical analysis of the obtained experimental data was performed in the framework of the present study prior to the beginning of the experiments. The main goal of the analysis was to separate the effects of the flow instability and receptivity, which are present in the distributed receptivity problems in some overlapping spatial domains. In order to extract pure characteristics of the boundary-layer distributed receptivity and to estimate quantitatively the corresponding receptivity coefficients, a special technique has been developed and applied. The technique is based on approximation of experimentally measured streamwise distributions of the amplitudes and phases of the boundary-layer disturbances by analytical solutions of the corresponding evolution equation.

Following a phenomenological physical model [3, 4] and, especially, [1, 2] let us consider the distributed generation of CF-waves in a swept-wing boundary layer by 3D (in general) freestream vortices, which are periodic in time and represent a kind of a 3D vortex street. Both the CF-wave and the vortex street have a certain fixed real frequency $\omega = 2\pi f$ and a certain fixed real spanwise wavenumber β' . It was shown in [3, 4] that the streamwise evolution of boundary-layer disturbances excited in a distributed way can be described by equation

$$\begin{aligned} \frac{d\bar{B}^d(x', y_m)}{dx'} &= i\bar{\alpha}'(x')\bar{B}^d(x', y_m) + \bar{B}_v(x', y) |_{y=\delta} \bar{G}_v^d(x') + \\ &\quad + \bar{B}_v(x', y) |_{y=\delta} \bar{G}_{vs}^d(x')H(x'). \end{aligned} \quad (1)$$

where $\bar{B}^d(x', y)$ is the complex-valued CF-wave amplitude, $\bar{B}_v(x', y)$ is the complex-valued freestream vortex amplitude, δ is the boundary layer thickness, $\bar{G}_v^d(x')$ is the complex-valued distributed *vortex receptivity function*, $\bar{G}_{vs}^d(x')$ is the complex-valued distributed *vortex-roughness receptivity function*, $H(x') = \bar{H}(x') + \bar{\bar{H}}(x')$ is *real* roughness shape function, where $\bar{H}(x')$ is *complex-valued* roughness shape function, $\bar{\bar{H}}(x')$ is the *complex conjugate* roughness shape function and $\bar{\alpha}'(x') = \alpha'_r(x') + i\alpha'_i(x')$ is a *complex-valued* streamwise wavenumber of ‘pure’ CF-instability modes, i.e. the eigenvalues of the corresponding linear stability problem. (All complex-valued functions are marked with bars on the top, as vectors.) Formula (1) can be regarded as one of possible definitions of the distributed *vortex receptivity function* $\bar{G}_v^d(x')$ and of the distributed *vortex-roughness receptivity function* $\bar{G}_{vs}^d(x')$.

Let us assume that we know from experiment all functions included into (1) except the receptivity functions $\bar{G}_v^d(x')$ and $\bar{G}_{vs}^d(x')$, which have to be found. These functions can be expressed explicitly in the following way. If the surface roughness is absent or, alternatively, $\bar{G}_{vs}^d(x') = 0$, then the distributed *vortex receptivity function* can be defined as

$$\bar{G}_v^d(x') = \frac{\mathbf{L}\{\bar{B}^d(x', y_m)\}}{\bar{B}_v(x', y) |_{y=\delta}}. \quad (2)$$

where

$$\mathbf{L} = \frac{d}{dx'} - i\bar{\alpha}'(x') \quad (3)$$

is a linear differential operator. In presence of the two receptivity mechanisms, the *vortex-roughness receptivity function* can be expressed as

$$\bar{G}_{vs}^d(x') = \frac{\mathbf{L}\{\bar{B}^d(x', y_m)\}}{\bar{B}_v(x', y) |_{y=\delta} H(x')} - \frac{\bar{G}_v^d(x')}{H(x')}, \quad (4)$$

Formulas (2) and (4) can be also regarded as definitions of the distributed vortex receptivity function $\overline{G}_v^d(x')$ and the distributed vortex-roughness receptivity function $\overline{G}_{vs}^d(x')$.

The determination of the receptivity coefficients amounts to solving an inverse problem. Namely, a method of approximation of streamwise distributions of the measured normal-mode amplitudes and phases by analytical solutions of equation (1) is convenient to use. For the case of smooth surface this method was briefly described in [1, 2].

For simplicity let us consider a particular case, which correspond approximately to the experimental conditions, when $\bar{\alpha}'(x') = \alpha'_r + i\alpha'_i = \text{const.}$ and functions $\overline{B}_v(x')$, $\overline{G}_v^d(x')$, $\overline{G}_{vs}^d(x')$, and $\overline{H}(x')$ are the following: $\overline{B}_v(x') = \overline{B}_{vo}e^{i\bar{\alpha}'_v x'} = B_{vo}e^{i\phi_{vo}}e^{-\alpha'_{vi}x'}e^{i\alpha'_{vr}x'}$, $\overline{G}_v^d(x') = \overline{G}_{vo}^d e^{i\bar{\alpha}'_g x'} = G_{vo}^d e^{i\lambda_{vo}^d}e^{-\alpha'_{gi}x'}e^{i\alpha'_{gr}x'}$, $\overline{G}_{vs}^d(x') = \overline{G}_{vso}^d e^{i\bar{\alpha}'_g x'} = G_{vso}^d e^{i\lambda_{vso}^d}e^{-\alpha'_{gsi}x'}e^{i\alpha'_{gsr}x'}$, and $\overline{H}(x') = \overline{h}_{1o}e^{i\bar{\alpha}'_s x'} = h_{1o}e^{i\varphi_{1o}}e^{-\alpha'_{si}x'}e^{i\alpha'_{sr}x'}$.

Under such assumption, the general analytical solution of equation (1) is:

$$\begin{aligned} \overline{B}^d(x') &= \underbrace{\overline{B}_{vo}\overline{G}_{vo}^d e^{i\bar{\alpha}' x'}}_{A} \int_0^{x'} e^{i\bar{\sigma}' s} ds + \\ &\quad \underbrace{\frac{1}{2}\overline{B}_{vo}\overline{G}_{vso}^d e^{i\bar{\alpha}' x'} \left[\overline{h}_{1o} \int_0^{x'} e^{-i\bar{\sigma}'_s s} ds + \overline{\bar{h}}_{1o} \int_0^{x'} e^{-i\bar{\sigma}'_{s1} s} ds \right]}_{B+B1} + \underbrace{\overline{B}_o^d e^{i\bar{\alpha}' x'}}_C \end{aligned} \quad (5)$$

where $\bar{\sigma}' = \sigma'_r + i\sigma'_i = \bar{\alpha}'_v + \bar{\alpha}'_g - \bar{\alpha}'$, $\bar{\sigma}'_s = \sigma'_{sr} + i\sigma'_{si} = \bar{\alpha}'_v + \bar{\alpha}'_{gs} + \bar{\alpha}'_s - \bar{\alpha}'$, and $\bar{\sigma}'_{s1} = \sigma'_{s1r} + i\sigma'_{s1i} = \bar{\alpha}'_v + \bar{\alpha}'_{gs} - \bar{\alpha}'_s - \bar{\alpha}'$. Complex-valued parameters $\bar{\sigma}'$, $\bar{\sigma}'_s$, and $\bar{\sigma}'_{s1}$ represent the resonant detunings for the distributed vortex receptivity in absence ($\bar{\sigma}'$) and in presence ($\bar{\sigma}'_s$ and $\bar{\sigma}'_{s1}$) of surface roughness. Detunings $\bar{\sigma}'_s$ and $\bar{\sigma}'_{s1}$ are related to the *first* and *second* excited combination CF-modes. The cases $\bar{\sigma}' = 0$, $\bar{\sigma}'_s = 0$, or $\bar{\sigma}'_{s1} = 0$ correspond to various full-resonant versions of solution (5).

Term C in solution (5) corresponds to a pure CF-wave (in absence of the distributed excitation). Term A is associated with the distributed vortex receptivity on smooth surface and corresponds, in general, to a wave with another chordwise wavenumber, which gives spatial beatings in superposition with term C in non-resonant cases with $\bar{\sigma}' \neq 0$. Terms B and $B1$ correspond to the vortex-roughness distributed receptivity. In cases of absence of resonances with $\bar{\sigma}'_s = 0$ and $\bar{\sigma}'_{s1} = 0$, they also have streamwise wavenumbers different from those of term C , as well as of term A and lead to additional spatial beatings of the excited boundary-layer disturbances.

Various versions of the analytical solution (5) were derived and used for approximations of the experimental streamwise distributions of amplitudes and phases of the boundary-layer disturbances excited by freestream vortices in various regimes of measurements. As a result of such approximations, the distributed receptivity functions were obtained.

3 Experimental Setup and Base Flow

The experiments were conducted in a low-turbulence subsonic wind tunnel T-324 of the ITAM (Novosibirsk) in a swept-wing boundary layer that was simulated on a swept flat plate having elliptic leading edge (see Fig. 1a). The chordwise pressure gradient was induced by a swept contoured wall bump (uniform in the spanwise direction) mounted on the test-section ceiling just above the swept plate. Both the plate and the bump had the same sweep angle $\chi = 25^\circ$. The experimental model was equipped with two contoured sidewalls in order to diminish the influence of the wind-tunnel test-section walls and to provide better satisfaction of the sweep condition. The freestream turbulence level (in the frequency range higher 1 Hz) was about 0.06% at the present experimental conditions. All main measurements were carried out by means of a hot-wire anemometer at free-stream speed from 11.9 to 13.1 m/s (in the beginning and in the end of the region of main measurements, respectively).

A sketch of three sources of controlled perturbations is shown in Fig. 1b. They are: (a) a generator of freestream vortices by a vibrating wire with non-uniformity in DR-experiments, (b) a point source for excitation of pure CF-waves in S-experiments, and (c) an applique with surface roughness (waviness).

The characteristics of the 3D mean flow field over the present experimental model were measured in detail in both the potential flow and the boundary layer using, in particular, V-shaped hot-wire probes. These measurements were carried out in previous experiments. The results of these measurements are described in detail in [5, 6]. Additional information about the mean flow characteristics observed under the conditions of the present set of measurements is presented below.

Show in Fig. 2a are streamwise distributions of chordwise and spanwise potential-flow mean-velocity components measured at $y = 18$ mm, $z = 0$. It is seen, in particular, that the flow accelerates in the chordwise direction, while the spanwise velocity component W' is independent practically of the chordwise coordinate in agreement with the sweep condition $W' = \text{const}$.

Wall-normal profiles of streamwise and cross-flow mean velocity components measured inside the boundary layer are presented in Fig. 2b for several chordwise

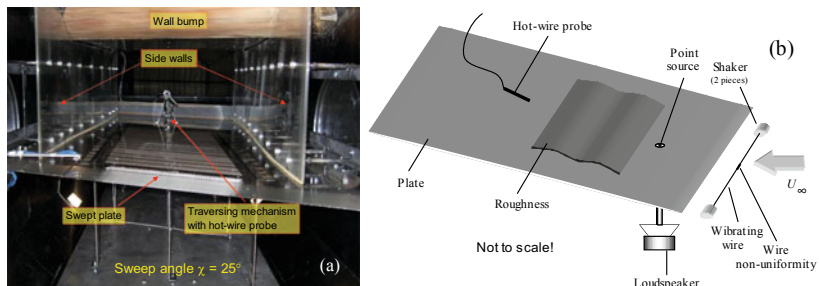


Fig. 1 Experimental model (a) and three sources of controlled perturbations (b)

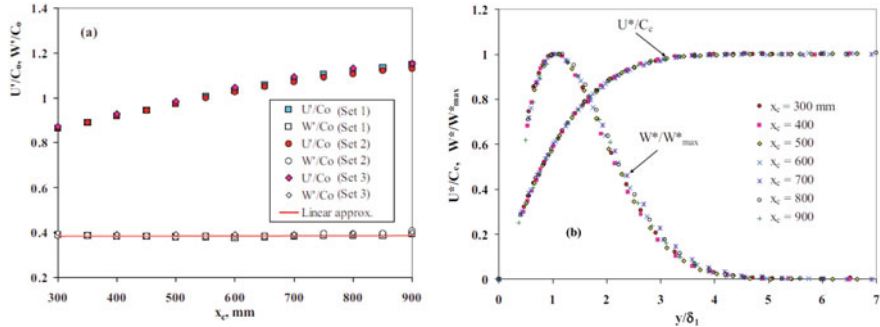


Fig. 2 Streamwise distributions of chordwise and spanwise potential-flow mean-velocity components (a) measured at $y = 18$ mm, $z = 0$ and wall-normal profiles of streamwise and cross-flow mean velocity components inside boundary layer normalized by streamwise edge velocity C_e and maximum cross-flow velocity W_{max}^* , respectively (b)

locations (the x_c -coordinate is the streamwise one but always has its origin at the swept-plate leading edge). These profiles are close to self-similar ones but not exactly. The absolute values of the cross-flow velocity (at their maxima in the wall-normal profiles) are of about 4% of the incident flow velocity C_o .

4 Most Important Results

Comparison of the obtained results with those obtained in the previous investigations [1, 2] has shown that the surface waviness is able to change significantly the character of both the excitation and development of the CF-modes compared to the case of smoothed surface. The most radical changes are found for the CF-modes having positive spanwise wavenumbers, which are the most dangerous from the viewpoint of the instability characteristics. For these modes, a resonant excitation becomes possible at satisfaction of conditions of the resonance of real streamwise wavenumbers ($\sigma_{s1r} = 0$, see section 2). Such resonances are found to be possible for both first, and second combination modes of the excited CF-waves (see Fig. 3 obtained under assumption that $\bar{\alpha}'_{gr} = \bar{\alpha}'_{gsr} = 0$, i.e. that the receptivity coefficients are constant within the region of measurements).

It is found that the influence of various kinds of surface waviness on the development of the CF-modes, excited distributedly by the free-stream vortices, can be both destabilizing and stabilizing depending on relationships between the streamwise wavenumbers of: (i) surface waviness, (ii) free-stream vortices, and (iii) CF-modes. In particular, Fig. 4a shows difference of the spectral amplitudes ΔB^d measured in two DR-regimes at frequency $f = 24.6$ Hz: DR12 (in presence of roughness # 2) and DRSS1 (in absence of controlled roughness). The strongest modifications of amplitudes of the excited CF-waves occurred due to presence of the surface rough-

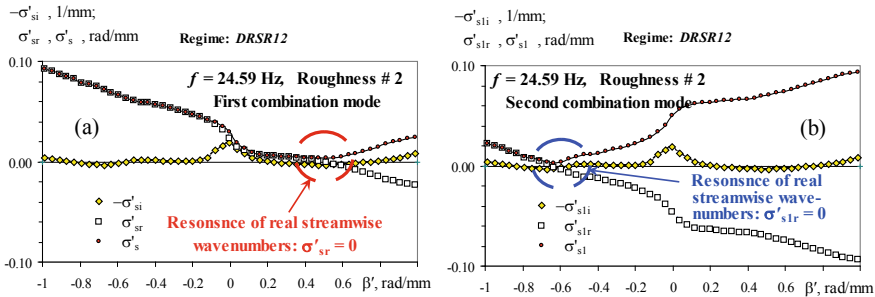


Fig. 3 Resonances of real streamwise wavenumbers observed in presence of waviness for first (a) and second (b) combination modes

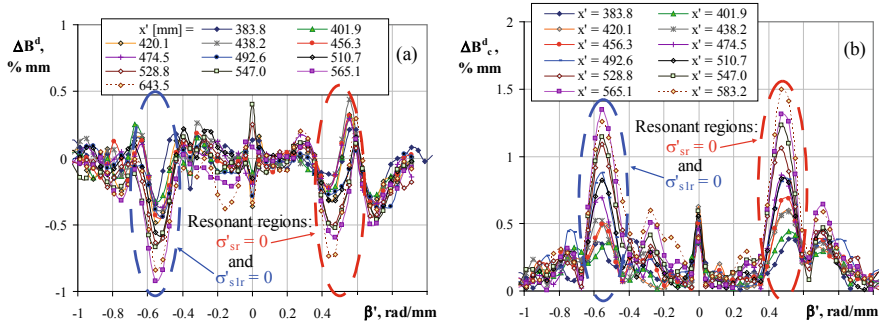


Fig. 4 Modifications of spanwise-wavenumber spectra of distributedly excited boundary-layer disturbances due to presence of surface roughness illustrating: a change of spectral amplitudes and b strength of joint effect of terms B and $B1$. $f = 24.6 \text{ Hz}$

ness are observed in the vicinities of the two combination resonances discussed above (see Fig. 3). This modification is associated with terms B and $B1$ in the evolution equation solution (5).

The strength of joint effects of terms B and $B1$ of the evolution equation solution (5) is characterized by amplitudes ΔB_c^d of complex-valued difference of spectral amplitudes measured in regimes: *DRSR12* (in presence of roughness # 2) and *DRSS1* (in absence of controlled roughness) shown in Fig. 4b versus the spanwise wavenumber. It is clearly seen again that the strongest impact of the surface roughness is present in the regions of resonances of the real streamwise wavenumbers shown in Fig. 3.

Shown in Fig. 5a is an example of approximation of the measured streamwise distributions of disturbance spectral amplitudes and phases by a non-resonant version of the analytical solution (5). The approximation is shown in plane of complex-valued spectral amplitudes (top) and for streamwise distributions of spectral amplitudes and phases (bottom). After performing such approximations for every studied disturbance frequency and spanwise wavenumber, the values of the distributed vortex-roughness

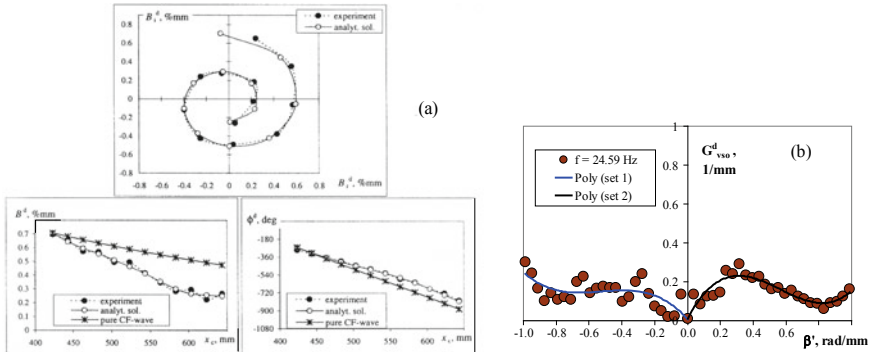


Fig. 5 Example of approximation of measured streamwise distributions by analytical solution (5) for $\beta' = 0.554$ rad/mm (a) and estimated amplitudes of the distributed vortex-roughness receptivity coefficients (b) $f = 24.6$ Hz

receptivity coefficients were estimated. The amplitudes of this coefficients are shown in Fig. 5b versus spanwise wavenumber for frequency $f = 24.6$ Hz. Similar results were obtained for two other studied frequencies (of $f = 34.9$ and 44.8 Hz). It is seen that the spanwise-wavenumber dependence of the distributed vortex-roughness receptivity coefficients is rather complicated. It is important to note that this distribution does not have any peculiarities in the vicinity of the streamwise-wavenumber resonances (see Fig. 3). This fact corresponds to the physical sense and means that the distributed vortex-roughness receptivity coefficients are essentially local characteristics responsible for efficiency of excitation of CF-wave by freestream vortices. However, these coefficients “do not know” about presence or absence of the streamwise-wavenumber resonances, which are essentially non-local characteristics of the flow. These characteristics manifest themselves only over rather long distances, which are comparable with the disturbance streamwise wavelengths.

Altogether, the obtained results testify that the actual amplitudes of the excited CF-instability waves represent a result of joint influence of two factors: (i) the localized efficiency of excitation, characterizing by the receptivity coefficients, and (ii) the presence or absence of the streamwise-wavenumber resonance. In other words, the receptivity coefficients and the wavenumber resonance are equally important for effective excitation of large-amplitude instability waves. Indeed, if the receptivity coefficients are large but the wavenumber detuning parameters are large as well, the excited CF-waves will display only high-amplitude spatial beatings with alternating quick growth and quick attenuation without permanent amplification. Only in cases of closeness of one of wavenumber detuning parameters to zero the period of beating tends to infinity and long-term amplification can be observed and is able to lead to the laminar-turbulent transition.

The most important conclusions of the present study are the following: (1) The distributed vortex-roughness receptivity coefficients are estimated experimentally for the first time. (2) It is shown that resonant distributed excitation of CF-waves is

very important in swept-wing boundary layers at interaction of freestream vortices with surface waviness. (3) The resonances are able either to enhance or to suppress growth of CF-waves. (4) The distributed receptivity coefficients are insensitive to the presence of resonances.

Acknowledgements This study is supported by the Boeing Operations International, Inc. and the Program of Fundamental Scientific Research of the Russian state academies of sciences in 2013–2020 (Project No. AAAA-A17-117030610128-8).

References

1. Borodulin, V., Ivanov, A., Kachanov, Y.: Distributed receptivity of swept-wing boundary layer to streamwise vortices. Part 1. Experimental approach. In: V. Fomin (ed.) Proc. 15th Int. Conf. Methods of Aerophysical Research. ITAM SB RAS, Novosibirsk (2010)
2. Borodulin, V., Ivanov, A., Kachanov, Y.: Distributed receptivity of swept-wing boundary layer to streamwise vortices. Part 2. Receptivity characteristics. In: V. Fomin (ed.) Proc. 15th Int. Conf. Methods of Aerophysical Research. ITAM SB RAS, Novosibirsk (2010)
3. Borodulin, V.I., Ivanov, A.V., Kachanov, Y.S., Komarova, V.Y.: Distributed two-dimensional boundary-layer receptivity to non-stationary vortical disturbances in the presence of surface roughness. Thermophysics and Aeromechanics **13**(2), 183–208 (2006)
4. Borodulin, V.I., Ivanov, A.V., Kachanov, Y.S., Mischenko, D.A., Fedenkova, A.A.: Comparison of distributed vortex receptivity coefficients at excitation of 3D TS-waves in presence and absence of surface waviness and pressure gradient. AIP Conf. Proc. **1770**, 030041–1–030041–7 (2016)
5. Borodulin, V.I., Ivanov, A.V., Kachanov, Y.S., Roschektayev, A.P.: Receptivity coefficients at excitation of cross-flow waves by free-stream vortices in the presence of surface roughness. J. Fluid Mech. **716**, 487–527 (2013). <https://doi.org/10.1017/jfm.2012.555>
6. Borodulin, V.I., Ivanov, A.V., Kachanov, Y.S., Roschektayev, A.P.: Receptivity coefficients at excitation of cross-flow waves due to scattering of free-stream vortices on surface vibrations. J. Fluid Mech. **793**, 162–208 (2016). <https://doi.org/10.1017/jfm.2016.129>

Overview of the AFT Model for Transition Prediction in Complex Aerodynamic Flows



James G. Coder

Abstract For many aerodynamic flows of practical interest, prediction of laminar-turbulent transition from first principles is a difficult, if not impossible, undertaking. These flows are often characterized by high Reynolds numbers, geometric complexities, and inherent unsteadiness, which limits the ability to perform direct numerical simulation of the transition processes or to perform detailed stability calculations against a base flow. In response to this and other flow simulation needs, there has been increased interest by the aerodynamics community in PDE-based transition models. Such models are generally phenomenological in nature and designed to estimate the path to transition using single-point correlations. The practical benefits of such models are that they can be fully integrated within a flow solver without an excessive increase in grid resolution requirements or sacrificing parallelization, and they can be applied to general three-dimensional configurations with minimal user intervention. An overview of these PDE-based models is provided, and, in particular, the amplification factor transport (AFT) model developed by the author. The AFT model is rooted in linear stability theory and it has been successfully applied to a wide range of engineering applications. The model formulation is discussed, and key results are included highlighting the model's predictive capabilities.

1 Introduction

Laminar-turbulent transition is a critical flow phenomenon in almost all aspects of aeronautics and aerodynamics, and is a performance driver in many practical aircraft systems spanning a wide range of Reynolds and Mach numbers. For low-speed systems, this comes through as a drag benefit due to the lower skin friction of a laminar boundary-layer, and for high-speed systems, it has a direct impact on the surface heating. Extensive runs of laminar flow may be achieved through passive

J. G. Coder (✉)
University of Tennessee, Knoxville, TN 37996, USA
e-mail: jcoder@utk.edu

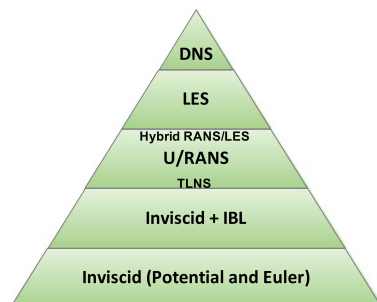
shaping, which is known as natural laminar flow (NLF), or through flow control, e.g. boundary-layer suction.

Controlling laminar-turbulent transition and exploiting laminar flow on commercial transports has a substantial economic and environmental impact, and is an enabling technology on ultra-efficient vehicle concepts [1, 2]. For example, the Boeing Transonic Truss-Braced Wing (TTBW) concept, which is similar in size and range to the Boeing 737 [1], anticipates over 10% reduction in drag due to boundary-layer control and other advanced airfoil design concepts. This contributes to a fuel-burn reduction exceeding 50% compared to a 2008 baseline.

Beyond transonic passenger aircraft, transition plays a major role in both rotorcraft and hypersonic flight vehicles. For a conventional helicopter, premature transition on the main rotor can increase the required power and degrade maximum-lift capabilities [3]. For hypersonic vehicles, laminar-turbulent transition has a leading-order impact on surface heating and design of thermal-protection systems [4]. Transitional boundary layers may also accentuate unsteady flow features in shockwave/boundary-layer interactions, leading to very large unsteady pressure loads compared to fully laminar or fully turbulent interactions [5].

A balance must be achieved between geometric fidelity and fluid physics fidelity in the aircraft design workflow, and a qualitative taxonomy of analysis methods is shown in Fig. 1. At the simplest level are fully inviscid analyses, such as linearized potential, full potential, and Euler methods. These methods run very quickly, allowing rapid exploration of a design space with reasonable accuracy for lift and compressibility effects (where applicable) for full vehicle configurations. These methods may be augmented by including a boundary-layer solver, such as an integral boundary-layer (IBL) method, which may or may not include transition-prediction models. If allowed to be fully interactive with the inviscid solver, accurate drag predictions may be obtained very quickly. Unfortunately, these methods are not well extensible to cases with moderate-to-large levels of geometric complexity. This deficiency is remedied through solving the Reynolds-averaged Navier-Stokes (RANS) equations with a turbulence closure model. It is commonplace for full aircraft configurations to be designed based on RANS predictions, and a single analysis point may completed in a matter of hours. Further increasing the physics fidelity requires that the fluid-dynamic turbulence be resolved, rather than modeled, in the flow field. Large-eddy

Fig. 1 Taxonomy of modeling approach for computational aerodynamics analyses. Computational cost increases for higher levels, driving simultaneous decreases in geometric fidelity



simulations (LES) capture the largest, energy-containing scales of turbulence while modeling the smaller, dissipative scales, while direct numerical simulation (DNS) resolves all scales without modeling. Unfortunately, the cost of resolving these scales increases strongly with Reynolds number, and the cost of a resolved transitional simulation usually exceeds that of a fully turbulent simulation [6]. The outcome of this is that LES and DNS may only be employed for sub-scale Reynolds numbers on highly simplified geometries, and even then the computational cost is excessively large to be used in the design loop.

Consequently, RANS-based computational fluid dynamics (CFD) methods are the standard tool for aerodynamic design and analysis, due largely to the balance between cost and accuracy for on-design predictions. In the maturation of these methods, much emphasis was placed on modeling the Reynolds stresses under the assumption of the flow being fully turbulent. Until recently, however, little attention has been given to the transition closure problem in RANS CFD. This may be attributed to a wide variety of reasons, such as the lack of appreciable laminar flow on most extant swept-wing commercial transports. By contrast, there is a rich history of transition modeling and prediction outside of the RANS CFD paradigm. Lower-order, correlation-based models may be traced back to the early 1950s, and prescribe that transition occurs once a predefined criterion is met [7–9]. In 1956, Smith and Gamberoni of Douglas Aircraft [10] and van Ingen of TU Delft [11] independently, and nearly simultaneously, discovered that linear stability theory (LST) may be used to predict transition through tracking the envelope of instability growth. This strategy may be simplified using databases constructed under the assumption of locally self-similar velocity profiles or through approximating the envelope growth rate based on self-similar profiles (cf. [12]). The boundary-layer stability approach was further extended by Herbert to yield the Parabolized Stability Equations (PSE) [13], which are widely used across all sectors of aerospace. Unfortunately, these are global in nature rather than being single-point closure, inhibiting their use in RANS CFD analyses. The correlation and database methods require integral boundary-layer properties to be readily available, which in turn requires non-local operations that are not aligned with the grid and may cross domain decomposition boundaries. Full solution of LST and PSE are non-local eigenvalue problems that require grid resolutions far exceeding those of RANS, and they are limited in the presence of geometric complexity.

The end result is a technology gap that exists between the current paradigm of production-quality CFD analyses and the current state of the art in transition modeling, including leading reduced-order models. Directly combining the two presents numerous technical challenges, including workflow, solution parallelization, and generalizability to arbitrarily complex geometries. In response to this, a new class of reduced-order model has arisen based on single-point, advection-diffusion PDEs. While these methods may not be as accurate as non-local transition models, they are fully compatible with modern RANS-based solvers.

2 Transition Prediction in General CFD Applications

Including laminar-turbulent transition modeling in RANS CFD requires consideration of the desired qualities of the model. Following Langtry and Menter [14], and based on the author's experiences, these qualities may be summarized as follows:

- Accurate prediction of transition onset location due to a variety of instability mechanisms
- General 3D formulation, applicable to arbitrarily complex geometries
- Amenability to massive parallelization without being a bottleneck
- Care-free application with minimal additional user intervention

In essence, the desired outcome of CFD transition modeling is to know whether the flow should be laminar or turbulent at a given point in the flow field. Fine-grain details, such as the critical frequency or mode shapes, are unnecessary in this endeavor.

From a physics-modeling perspective, the most straightforward approach is to apply a non-CFD transition model (such as local-correlation or stability-based methods) as an in-situ post-processing step between solver iterations. In this context, the CFD solution is taken to be quasi-converged after a specified number of iterations, and the transition front is predicted based on the full flow solution. The transition locations are then (re)-imposed, and the CFD solution continued. This process repeats until the coupled system converges.

Various strategies may be used to extract the necessary information from the CFD solution to feed the transition prediction routines. One possibility is to very fine wall-normal grid resolution and use the laminar regime as a base state for high-fidelity stability calculations [15–17]. Another option is to use the surface pressure distribution as inputs into an external boundary-layer solver [16, 18], at which point any transition prediction method may be used.

While this framework combines the best available knowledge of the transition phenomenon with a CFD solution, there remain shortcomings. For example, there is ambiguity in application of this method to general configurations where there are regions where it is difficult to infer a boundary layer in the classical sense. Additionally, the manner in which transition is imposed can have an unintentionally adverse impact on the solution. For example, laminar separation bubbles are often mis-predicted, or omitted entirely, when these methods are used [15, 19]. This not only adversely affects drag predictions, but can have a significant impact on the predicted maximum lift.

An alternative strategy that has gained much traction in the past few years is to use models based on the solution of advection-diffusion PDEs, which take the form,

$$\frac{\partial \rho\phi}{\partial t} + \frac{\partial \rho u_j \phi}{\partial x_j} = P_\phi - E_\phi + \frac{\partial}{\partial x_j} \left[\sigma (\mu + \mu_t) \frac{\partial \phi}{\partial x_j} \right] \quad (1)$$

where P_ϕ and E_ϕ may be fully evaluated using the local computational stencil. Various transition models have been developed following this form, and they may be

broadly grouped into two major categories: physics-based models and phenomenological models.

Physics-based models track single-point quantities that may be directly derived from the governing flow equations, akin to many turbulence models. An example of this is the laminar kinetic energy model proposed by Walters [20]. In this framework, laminar kinetic energy is the pre-transitional analog to turbulent kinetic energy, enabling the use of a similar transport equation. The use of the disturbance energy results in a stronger emphasis being placed on the non-linear aspects of transition, and anecdotal evidence shows that these models perform better for bypass transition than for natural transition. While the actual physicality of the predictions is debatable, this framework is no more or less physics-based than the $k - \epsilon$ class of turbulence models.

Phenomenological models take a different approach to predicting transition. Rather than tracking a single-point physical quantity, they track surrogate quantities that reflect the margin to transition. All models known to the author in this category are built on the comparison of a boundary-layer "age" parameter, such as a characteristic Reynolds number, with a "health" parameter, generally in the form of a pressure-gradient parameter. In essence, if the boundary layer is too "unhealthy" for its age, then transition will occur.

In current practice, developing these models is a two-step process. First, one-or-more suitable surrogate parameters must be identified. This may draw on the wealth of existing transition models, which use integral boundary-layer quantities as their surrogates. Next, the non-local surrogates need to be estimated using entirely local quantities, and therein lies the crux of the modeling challenge.

The widely used $\gamma - Re_{\theta t}$ of Langtry and Menter [14] is the most prominent phenomenological model. At its core, it is a local-correlation model that uses the Thwaites-Walz Λ_2 pressure-gradient parameter to calculate a limiting value of the momentum-thickness Reynolds number, Re_{θ} , which itself is estimated using the local vorticity-based Reynolds number. The development of this model was a major leap forward in CFD-based transition modeling; however, it is fundamentally limited by the underlying correlations that do not account for upstream boundary-layer history.

3 Amplification Factor Transport Transition Model

Based on the successes and limitations of the Langtry-Menter model [14], the author has developed a PDE-based transition model, known as the Amplification Factor Transport (AFT) model [21, 22]. The AFT model is rooted in linear stability theory, and is based heavily on the approximate-envelope method of Drela and Giles [12] for modeling the growth of Tollmien-Schlichting instabilities. This formulation reduces the infinite-dimensional linear stability problem to a single scalar integrated along the surface streamline (as seen by the outer, inviscid flow),

$$\tilde{n} = \int_{s_0}^s \frac{d\tilde{n}}{dRe_\theta} \frac{dRe_\theta}{ds} ds \quad (2)$$

The quantity \tilde{n} represents the amplification factor along the envelope of instabilities, and transition is taken to occur when \tilde{n} exceeds a pre-defined critical value, N_{crit} . The boundary-layer quantities necessary to evaluate this integral are the H_{12} shape factor (as a pressure-gradient parameter) and the momentum thickness (to provide a length scale). The integral along the surface streamline may be rewritten, without loss of generality, as an advection PDE for the amplification factor,

$$\frac{\partial \tilde{n}}{\partial t} + u_j \frac{\partial \tilde{n}}{\partial x_j} = U_e \frac{d\tilde{n}}{ds} \quad (3)$$

where U_e is the boundary-layer edge velocity. The term on the right-hand side is a production term; however, it is defined in terms of integral boundary-layer quantities. Rather than performing the wall-normal integrations, these quantities are estimated locally. This allows the governing equation to be rewritten as,

$$\frac{\partial \rho \tilde{n}}{\partial t} + \frac{\partial \rho u_j \tilde{n}}{\partial x_j} = \rho \Omega F_{crit} F_{growth} \frac{d\tilde{n}}{dRe_\theta} + \frac{\partial}{\partial x_j} \left[\sigma_n (\mu + \mu_t) \frac{\partial \tilde{n}}{\partial x_j} \right] \quad (4)$$

The left-hand side has been modified to be conservative (for consistency with the mean-flow equations), and a diffusion term has been added to the right-hand side for numerical reasons. The edge velocity is combined with other terms characterizing the boundary-layer growth to form the dimensionally correct grouping ΩF_{growth} , where F_{growth} is a non-dimensional function that depends only on the H_{12} shape factor. The F_{crit} function accounts for the critical Reynolds number as it depends on shape factor, and $d\tilde{n}/dRe_\theta$ describes the envelope growth rate, also as a function of H_{12} . Although H_{12} is integral in nature, it is locally estimated in the AFT model using a *local* shape factor, H_L (based on the work of Menter et al. [23]),

$$H_L = \frac{\rho d^2}{\mu} \nabla (\vec{u} \cdot \hat{n}) \cdot \hat{n} \quad (5)$$

such that $H_{12} \sim f(H_L)$. A detailed description of AFT model correlations may be found in Ref. [22].

The AFT model has been implemented in multiple production-level CFD flow solvers, including NASA OVERFLOW 2.2 [24] and the US Department of Defense HPCMP CREATETM-AV Kestrel component COFFE [25]. The model fully integrates with the widely used Spalart-Allmaras eddy-viscosity turbulence model [26]. Users need only specify the desired critical amplification factor, N_{crit} , often taken to be 9, and provide a grid with sufficient resolution to capture the relevant flow features. Experience has shown that RANS-quality grids are often sufficient for accurate calculations; however, the rapid change in boundary layer properties through the tran-

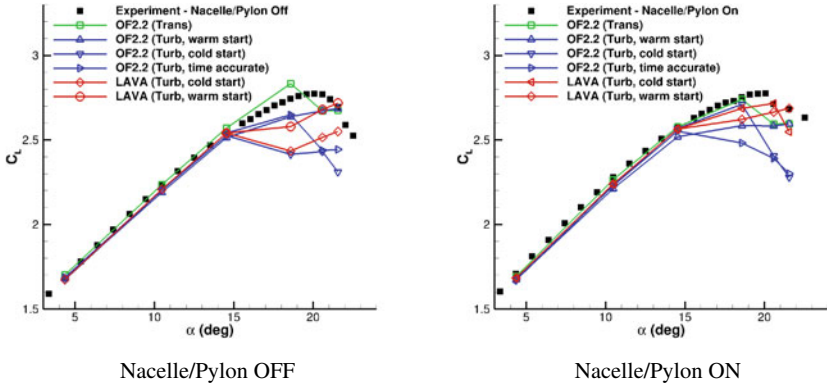


Fig. 2 Comparison of high-lift predictions for the JAXA Standard Model using transitional and fully turbulent methods (originally from Ref. [27])

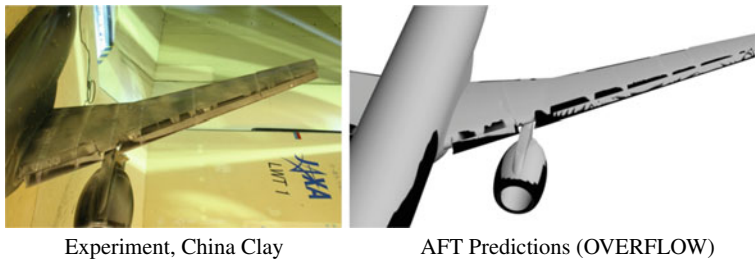


Fig. 3 Upper-surface main-element and slat transition patterns on the JAXA Standard Model for $\alpha = 18.58^\circ$ (originally from Ref. [27])

sition region sometimes necessitates finer streamwise spacing than a fully turbulent calculation.

Considerable benefit has been realized in using the AFT model for high-lift predictions, such as shown for the JAXA Standard Model high-lift configuration [27]. This configuration features a three-element high-lift system (slat, main element, and flap) along with the mounting brackets, and it was simulated both with and without a nacelle and pylon mounted to the wing. Representative lift curves from Ref. [27] are included as Fig. 2. Lift predictions using the AFT model are more consistent with experiment than fully turbulent results, obtained using two different solvers with multiple solution strategies, for both the nacelle/pylon on and off. Predicted surface transition patterns for a near-stall angle of attack are compared with experimentally observed patterns in Fig. 3, which highlights the predictive accuracy of the AFT model.

The AFT model is also fully applicable to unsteady flow fields such as those experienced by helicopters and other rotorcraft. A detailed example of this may be found in Ref. [28]. In Fig. 4 (from Ref. [28]), the surface transition patterns for a rotor/fuselage combination in hover are depicted using contours of turbulence index



Fig. 4 Predicted transition patterns (inferred from the turbulence index) on the surface of a rotor/fuselage configuration in hover (originally from Ref. [28])

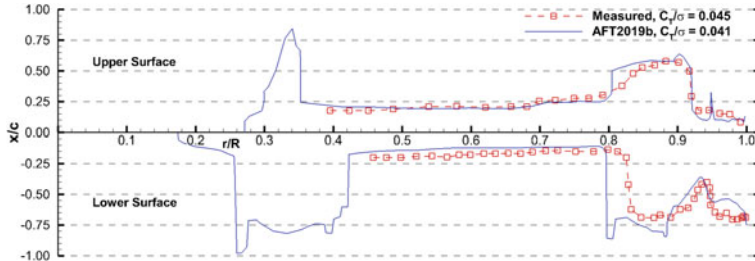


Fig. 5 Comparison of predicted and measured transition locations on the PSP rotor blade in hover with a 6° collective pitch (courtesy of Jared Carnes, University of Tennessee)

[26]. The blue regions correspond to laminar flow, while the red regions are laminar. Even with three-dimensional, moving bodies, the AFT model provides physically reasonable predictions. A more detailed quantitative comparison is included as Fig. 5, which compares experimentally measured transition lines with those predicted using the AFT model. The AFT model does very well to capture the transition front over the portion of the blade where measured data are available.

Lastly, the AFT model has also been successfully applied to predicting transitional shockwave/boundary-layer interactions in the supersonic regime [29]. Experimental observations of the phenomenon reveal salient flow features not observed for fully turbulent interactions, such as a weak shock upstream of the primary shockwave. Fully turbulent CFD predictions are unable to capture this feature, whereas the AFT model was able to pick up its influence on the resulting interaction. While the underlying flow physics are still being investigated, RANS calculations using the AFT model have provided key insights into the origins and behaviors of the interaction [29].

4 Conclusion and Outlook

The Amplification Factor Transport transition modeling framework is based on the solution of a locally defined, advection-diffusion PDE. It is fully compatible with modern RANS-based computational fluid dynamics solvers, and may be readily used

in an industrial design and analysis setting. The model is based on an approximate-envelope approach to linear stability theory, and represents an improvement over other CFD-compatible, PDE-based transition models. Its predictive capabilities have been demonstrated in the literature for complex aircraft configurations, including transport-type aircraft in a high-lift configuration, unsteady rotorcraft flows, and supersonic shockwave/boundary-layer interactions. The cost of including the AFT model in a simulation is relatively small, as it requires grid resolutions comparable to those needed for fully turbulent RANS simulations, and the solution may be parallelized in the same manner as the mean-flow equations.

Improvements and further developments of the AFT model are ongoing. Particular focus is being placed on modeling crossflow mechanisms in a Galilean invariant formulation, which will improve the predictive capabilities across all flight regimes. Future efforts are anticipated for hypersonic conditions and for noisy environments in which linear growth is bypassed.

Acknowledgements The development and maturation of the amplification factor transport model framework has been financially supported through a variety of sources, including the United States Department of Defense NDSEG program, the Office of Naval Research, the US Army Vertical Lift Research Centers of Excellence, and NASA. Any opinions, findings, and conclusions or recommendations expressed in this material are those of the author and do not necessarily reflect the views of the funding agencies.

Special thanks is extended to Dr. Mark D. Maughmer of the Pennsylvania State University for encouraging and advising the original development of the AFT model.

References

- Bradley, M. K. and Droney, C. K., "Subsonic Ultra Green Aircraft Research," NASA CR-2011-216847, 2011
- Greitzer, E. M. et al., "N+3 Aircraft Concept Designs and Trade Studies," NASA CR-2010-216794, 2010
- Overmeyer, A.D., Martin, P.B.: "Measured Boundary Layer Transition and Rotor Hover Performance at Model Scale," 55th AIAA Aerospace Sciences Meeting, AIAA Paper 2017-1872. Grapevine, TX (2017)
- Bertin, J.J., Cummings, R.M.: Fifty years of hypersonics research: where we've been, where we're going. *Progress in Aerospace Sciences* **39**, 511–536 (2003)
- Combs, C.S., Lash, E.L., Kreth, P.A.: Investigating Unsteady Dynamics of Cylinder-Induced Shock-Wave/Transitional Boundary-Layer Interactions. *AIAA Journal* **56**(4), 1588–1599 (2018)
- Slotnick, J. et al., "CFD Vision 2030 Study: A Path to Revolutionary Computational Aero-sciences," NASA/CR-2014-218178, 2014
- Michel, R., Etude de la Transition et Calcul de la Trainee des Profiles d'aile en Incompressible, ONERA Publ. 58, 1951
- Eppler, R. and Somers, D. M., "A Computer Program for the Design and Analysis of Low-Speed Airfoils," NASA TM-80210, 1980
- Abu-Ghannam, B.J., Shaw, R.: Natural Transition of Boundary Layers: The Effects of Turbulence, Pressure Gradient, and Flow History. *Journal of Mechanical Engineering Science* **22**(5), 213–228 (1980)

10. Smith, A. M. O. and Gamberoni, N., "Transition, Pressure Gradient and Stability Theory," Douglas Aircraft Rept. ES-26388, 1956
11. van Ingen, J. L., "Suggested Semi-Empirical Method for the Calculation of the Boundary Layer Transition Region," Rept. VTH-74, 1956
12. Drela, M., Giles, M.B.: Viscous-Inviscid Analysis of Transonic and Low-Reynolds Number Airfoils. *AIAA Journal* **25**(10), 1347–1355 (1987)
13. Herbert, T.: Parabolized Stability Equations. *Annual Review of Fluid Mechanics* **29**, 245–283 (1997)
14. Langtry, R.B., Menter, F.R.: Correlation-Based Transition Modeling for Unstructured Parallelized Computational Fluid Dynamics Codes. *AIAA Journal* **47**(12), 2894–2906 (2009)
15. Tufts, M.W., Kimmel, R.L.: "Stability Equation Based Transition Prediction," 2018 AIAA Aerospace Sciences Meeting, AIAA Paper 2018-0031. Kissimmee, FL (2018)
16. Krimmelbein, N., Krumbein, A.: Automatic Transition Prediction for Three-Dimensional Configurations with Focus on Industrial Application. *Journal of Aircraft* **48**(6), 1878–1887 (2011)
17. Lozano-Duran, A., Hack, P., Moin, P.: "Using parabolized stability equations to model boundary-layer transition in direct and large-eddy simulations," 2018 AIAA Fluid Dynamics Conference, AIAA Paper 2018-3698. Atlanta, GA (2018)
18. Groot, K.J., Miró Miró, F., Beyak, E.S., Moyes, A.J., Pinna, F., Reed, F.L.: "DEKAF: Spectral Multi-Regime Basic-State Solver for Boundary-Layer Stability," 2018 AIAA Fluid Dynamics Conference, AIAA Paper 2018-3380. Atlanta, GA (2018)
19. Yeh, D.T., Slotnick, J.P.: "Development of Trip Line Sub-Region Approach for Flow Transition Modeling," 55th AIAA Aerospace Sciences Meeting, AIAA Paper 2017-1457. Grapevine, TX (2017)
20. Walters, D.K., Leylek, J.H.: A New Model for Boundary Layer Transition Using a Single-Point RANS Approach. *Journal of Turbomachinery* **126**, 193–202 (2004)
21. Coder, J.G., Maughmer, M.D.: Computational Fluid Dynamics Compatible Transition Modeling Using an Amplification Factor Transport Equation. *AIAA Journal* **52**(11), 2506–2512 (2014)
22. Coder, J.G.: "Further Development of the Amplification Factor Transport Transition Model for Aerodynamic Flows," 2019 AIAA Aerospace Sciences Meeting, AIAA Paper 2019-0039. San Diego, CA (2019)
23. Menter, F.R., Smirnov, P.E., Liu, T., Avancha, R.: A One-Equation Local Correlation-Based Transition Model. *Flow, Turbulence and Combustion* **95**(4), 583–619 (2015)
24. Nichols, R. H. and Buning, P. G., "User's Manual for OVERFLOW 2.2," NASA Langley Research Center, August 2010
25. Stefanski, D.L., Glasby, R.S., Erwin, J.T., Coder, J.G.: "Development of a Predictive Capability for Laminar-Turbulent Transition in HPCMP CREATETM-AV Kestrel Component COFFE using the Amplification Factor Transport Model," 2018 AIAA Aerospace Sciences Meeting, AIAA Paper 2018-1041. Kissimmee, FL (2018)
26. Spalart, P.R., Allmaras, S.R.: A One-Equation Turbulence Model for Aerodynamic Flows. *Recherche Aerospatiale* **1**, 5–21 (1994)
27. Coder, J.G., Pulliam, T.H., Jensen, J.C.: High-Lift Simulations of the Japan Aerospace Exploration Agency Standard Model. *Journal of Aircraft* **56**(5), 1822–1832 (2019)
28. Parwani, A., Coder, J.G.: "CFD Predictions of Rotor-Fuselage Interactions Using Laminar-Turbulent Transition Modeling," American Helicopter Society 74th Annual Forum, Paper 1302., Phoenix AZ (2018)
29. Tester, B.W., Coder, J.G., Combs, C.S., Schmisser, J.D.: "Hybrid RANS/LES Simulation of Transitional Shockwave/Boundary-Layer Interaction" 2018 AIAA Fluid Dynamics Conference, AIAA Paper 2018-3224. Atlanta, GA (2018)

BiGlobal Stability Analysis of Swept-Wing Boundary Layers with Forward and Backward Facing Steps



Thibaut Appel, Emma Cooke, Shahid Mughal, and Richard Ashworth

1 Introduction

Quantitative knowledge about the effect of wing surface irregularity on laminar-turbulent transition remains deficient, forcing aircraft manufacturers to opt for overly conservative design margins. Improved confidence in accurate analysis tools able to correlate flow conditions, transition location as well as the geometry of surface irregularities should naturally lead to a drag count reduction and should also provide guidance on manufacturing tolerances required for sustaining laminarity in the presence of steps and gaps. Thus far, the vast majority of literature contributions have focused on the effect of steps, gaps, distributed roughness and surface waviness on the destabilisation of Tollmien-Schlichting (TS) waves, primarily on flat-plate geometries. However, studies involving ‘two-and-a-half-dimensional’ (2.5D) surface features and in particular their effect on crossflow (CF) instabilities on swept-boundary-layer flow geometries are scarce.

Steps, commonly encountered in the aeronautical field, are known to trigger an early transition to turbulence. Two-dimensional experiments on a flat plate suggested that, under similar free-stream parameters and absolute step height, the forward movement of transition is larger for a backward-facing step (BFS) than for a forward-

T. Appel (✉) · E. Cooke · S. Mughal
Imperial College London, 180 Queen's Gate, London SW7 2AZ, UK
e-mail: t.appel17@imperial.ac.uk

E. Cooke
e-mail: emma.cooke13@imperial.ac.uk

S. Mughal
e-mail: s.mughal@imperial.ac.uk

R. Ashworth
Airbus Central R & T, Aerospace Avenue, Filton, Bristol BS34 7PA, UK
e-mail: richard.ashworth@airbus.com

facing step (FFS), and that the decrease in the transition N-factor correlated with the relative step height [1]. Similar conclusions were reached in another flat-plate experiment [2] where the transition N-factor was found to vary linearly with the step height relative to the boundary-layer displacement thickness at the step location. For equal step heights, the N-factor reduction was greater for BFSs compared to FFSs. More recent swept-wing contributions nuance these observations, as [3] suggested a physics-based correlation between the critical FFS height and the height of the core of the stationary crossflow vortex. This height was associated with a sharp amplification of stationary crossflow modes as well as an upstream movement of the transition front towards the step. No stationary mode amplification was identified in the presence of BFSs. The swept-wing experimental study of [4] distinguished three regimes in terms of transition location and transition front pattern with an FFS. The authors also noted reasonable agreement with the criterion of [3] to estimate the critical step height.

The preliminary results reported in this paper intend to shed light on temporal instability mechanisms potentially arising due to a BFS/FFS located on a 2.5D wing profile. The novelty of this contribution lies in the application of the ‘BiGlobal’ methodology, an eigenvalue-based approach, to a curved body on which surface steps are present. While the above-cited contributions focused on sharp-edged steps, the step geometry considered in this work is slightly rounded. This introduces an additional curvature parameter and modifies the physics of the flow in the vicinity of the step edges. The presence of a recirculation bubble on the top of the FFS is generally reported in the few earlier computational studies, however in this work no such reversed flow region is found. The absence of the bubble on top of the FFS might well be due to the slight rounding of the step corners and to the fact that the steps are located in an overall favourable-pressure-gradient section of the aerofoil. On the other hand, a tiny recirculation bubble exists near the concave corner in front of the step.

2 Mathematical Approach

The linear evolution of incompressible flow perturbations in the unsteady Navier-Stokes equations can be described by decomposing the instantaneous flow variables $\mathbf{q} = (p, u, v, w)^T$ into

$$\mathbf{q}(\mathbf{x}, t) = \bar{\mathbf{q}}(\mathbf{x}) + \varepsilon \tilde{\mathbf{q}}(\mathbf{x}, t) \quad (1)$$

where the base flow $\bar{\mathbf{q}}$ represents a steady-state solution of the Navier-Stokes equations on which the infinitesimal perturbation $\varepsilon \tilde{\mathbf{q}}(\mathbf{x}, t)$ is introduced. The infinitesimal assumption ($\varepsilon \ll 1$) allows to linearise the equations and to retain the leading-order terms $O(\varepsilon)$, thus giving the Linearised Navier-Stokes (LNS) equations, which read in non-dimensional form

$$\Delta \tilde{p} + \nabla \cdot ((\bar{\mathbf{u}} \cdot \nabla) \tilde{\mathbf{u}}) + \nabla \cdot ((\tilde{\mathbf{u}} \cdot \nabla) \bar{\mathbf{u}}) = 0 \quad (2a)$$

$$\frac{\partial \tilde{\mathbf{u}}}{\partial t} + (\bar{\mathbf{u}} \cdot \nabla) \tilde{\mathbf{u}} + (\tilde{\mathbf{u}} \cdot \nabla) \bar{\mathbf{u}} + \nabla \tilde{p} - \frac{1}{Re} \Delta \tilde{\mathbf{u}} = \mathbf{0} \quad (2b)$$

The time coordinate is t , p is the pressure, $\mathbf{u} = (u, v, w)^T$ represents the velocity field components and $Re = UL/v$ is the Reynolds number quantifying the relative importance of viscous effects compared to inertial effects. In its definition, U is a velocity scale, L a length scale and v is the kinematic viscosity. The relevant quantities are non-dimensionalised by these scales, the time coordinate by L/U and the pressure by ϱU^2 where ϱ is the density. As discussed in [5, 6], the Linearised Pressure Poisson Equation (LPPE) formulation of the LNS equations is employed thanks to its well-posedness character when a discretisation on a collocated grid is used.

The temporal stability of swept-wing base flows subjected to streamwise geometry deformation is investigated with a BiGlobal analysis, as coined by [7] where perturbations that are a solution to the LNS Eqs. (2) are sought with a wave-like form,

$$\tilde{\mathbf{q}}(\mathbf{x}, t) = \tilde{\mathbf{q}}(x, y, z, t) = \hat{\mathbf{q}}(x, y) e^{i\beta z - i\omega t} + \text{c.c.} \quad (3)$$

A Fourier decomposition is used for the time and spanwise coordinates, assuming periodicity while the shape function $\hat{\mathbf{q}}(x, y)$ depends on the streamwise and wall-normal coordinate. The complex conjugate ('c.c.') is added to remind that they remain a real quantity. The angular frequency ω is an unknown complex eigenvalue; its real part ω_r represents a frequency while its imaginary part ω_i is the growth rate of the perturbation. Temporal instability is characterised by the existence of at least one eigenvalue with a positive growth rate, $\omega_i > 0$. The corresponding eigenfunction, or shape function $\hat{\mathbf{q}}$, describes the flow state that is preferentially amplified in time. Moreover, β is a real and prescribed spanwise wavenumber which is related to a periodicity wavelength $L_z = 2\pi/\beta$.

In this study, orthogonal body-fitted coordinates (x, y, z) are conveniently used to analyse curved-wing geometries and to align the grid with the local flow direction within the realms of possibility. Figure 1 represents a schematic view of the geometry and illustrates the concept of body-fitted coordinates. The corresponding Lamé coefficients are $(1 - \kappa(x)y, 1, 1)$ where κ is the local body surface curvature. In addition, the effect of the relatively smaller surface irregularity embodied by the BFS/FFS is modelled through an additional transformation of the wall-normal coordinate, $\check{y} = y - h(x)$ in which h is the surface height as a function of the chordwise coordinate x . The Jacobian of the mapping between the physical domain and the computational domain is modified accordingly.

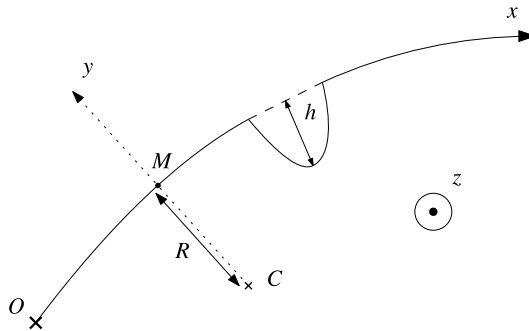


Fig. 1 Body-fitted orthogonal coordinates (x, y, z) with incorporation of deformation $h(x)$ normal to the surface. $R(x)$ represents the local radius of the body contour, linked to the local body curvature $\kappa(x) = 1/R(x)$. The streamwise position of any point M is measured by the distance along the body contour from the coordinate origin O . C is the local centre of curvature

3 Base Flow Computations

Following an experimental campaign on swept-wing crossflow transition due to roughness effects [8], a numerical investigation was undertaken to study 2.5D step destabilisation of travelling and stationary crossflow disturbances [9]. The geometry is a wing section with a chord $c = 0.8$ m and a span $b = 1.2$ m. Crossflow instability was promoted with a large sweep angle $\Lambda = 40^\circ$ together with the placement of periodically-aligned roughness elements shaped as circular disks. These were placed at the neutral stability point and forwards of the location of the steps. The numerical study [9] aimed at replicating experimental flow conditions of [10] by setting a Reynolds number based on chord $Re_c = 10^6$. The Mach number is $Ma = 0.3$ which corresponds to the upper limit of the incompressibility assumption regime. The effect of BFSs and FFSs located at either 10 % or 20 % chord was not measured in the experimental test campaign [10]. As such, the purely numerical BFSs and FFSs investigations were undertaken in [9] to provide guidelines for possible future experiments aimed at further clarifying the impact of surface steps on laminar flow destabilisation.

Four roughness heights were chosen: 413 μm , 619 μm , 825 μm and $h_0 = 893 \mu\text{m}$, which correspond to a certain fraction of boundary layer parameters on the clean geometry as detailed in Table 1. The aforementioned absence of recirculation bubble just downstream of the FFS can be observed in Fig. 2 which is also the case for smaller heights. A large reverse flow region of length $\approx 2h_0$ is located after the BFS location, whereas a much smaller one exists at the base of the FFS.

The base flow generation followed a hybrid approach, in that the overall, steady flow regime for the complete aerofoil was first computed with a Reynolds-Averaged Navier-Stokes (RANS) approach by means of the flow solver TAU [11]. A transition switch was set beyond 60 % of the chord length, ensuring steady laminar flow in the region of interest. Then, using ‘far-field’ boundary conditions provided by

Table 1 Step height h compared to boundary layer thickness δ and displacement thickness δ^*

Parameter	Boundary layer thickness (δ)				Displacement thickness (δ^*)			
	413	619	825	893	413	619	825	893
Step height (μm)	25	37	49	53	98	147	129	212
10 % chord (%)	18	27	36	38	68	102	136	148

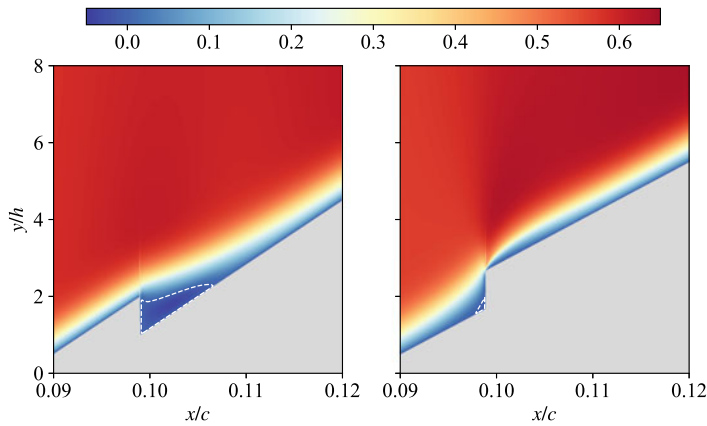


Fig. 2 Contours of non-dimensional steady streamwise velocity \bar{u} for the BFS (left) and the FFS (right) in the greatest height case $h_0 = 893 \mu\text{m}$. The white dashed line delimits the region of reverse flow. For viewing purposes, the wall-normal coordinate is distorted and not aligned with the normal to surface direction. The vertical artefact extending above the step location is a feature of the spline interpolation used for visualisation, due to the sharp gradients

the RANS solution, an embedded steady Direct Numerical Simulation (DNS) was computed with a spectral/ hp element discretisation within the Nektar++ software [12] to accurately capture any modifications arising in the laminar boundary layer region on introduction of the step features. A stiffly stable splitting scheme which decouples the velocity and pressure fields was employed, and time integration was achieved by a second-order accurate implicit-explicit (IMEX) scheme. A combination of triangular and quadrilateral elements formed the mesh with low-order and higher-order polynomial expansions, besides a Fourier expansion in the spanwise direction to define a 2.5D solution. Mesh independence was assessed, and steady laminar solutions were assumed to be reached once the relative error in the ℓ_2 -norm of velocity fields was less than 10^{-5} on the entire domain.

4 Numerical Strategy

In this numerical study, the velocity scale is the streamwise component of the free-stream velocity, $U = U_\infty$ and the greatest step height, $L = h_0 = 893 \text{ um}$ is used as the length scale of the problem.

After substituting the ansatz (3) in the LNS Eq. (2), the streamwise BiGlobal equations are spatially discretised in both streamwise and wall-normal directions with a high-order finite difference method based on piecewise polynomial interpolations on non-uniform grids [13]. After discretisation, the numerical solution of a generalised eigenvalue problem (GEVP) is sought as

$$\mathbf{A}\mathbf{Q} = \omega\mathbf{B}\hat{\mathbf{q}} \quad (4)$$

in which the matrix operator \mathbf{A} contains the linearised convective terms, the pressure gradient as well as the diffusion terms of Eq. (2). The time-harmonic coefficients are included in \mathbf{B} .

To close the BiGlobal problem, a set of homogeneous boundary conditions must be provided on the truncated computational domain. At the wall, the streamwise and spanwise perturbation velocities vanish, $\hat{u} = \hat{w} = 0$. The wall-normal perturbation velocity satisfies $\partial\hat{v}/\partial y = 0$ to ensure the divergence-free velocity field condition ($\nabla \cdot \hat{\mathbf{u}} = 0$) at the boundary, which is required for the LPPE formulation to be equivalent to the primitive formulation of the LNS Eqs. For the pressure, a compatibility equation is employed, which is a usual practice in LNS-based studies. At the far-field boundary, the perturbation field is forced to decay exponentially and then vanishes, $\hat{p} = \hat{u} = \hat{v} = \hat{w} = 0$. There is no optimal choice of inflow and outflow boundary condition in the context of streamwise BiGlobal analyses, the numerical spectrum being usually sensitive to how the domain is truncated in that direction. For this reason, a variety of them is tested and briefly mentioned in Sect. 5. Both operators \mathbf{A} and \mathbf{B} include degrees of freedom subjected to boundary conditions.

In the streamwise direction, the grid formed of 4,000 points is clustered near the step location ($x = 0.1$ or $x = 0.2$) by means of an interior contraction mapping coupled with the function $\tan(\gamma\pi x)/\tan(\gamma\pi)$, where the parameter γ is set to 0.48. A 6th-order finite difference method is used and the domain extends over a length of approximately $145h_0$, that is $x \in [0.05, 0.18]$ for the 10 % case and $x \in [0.15, 0.28]$ for the 20 % case.

In the wall-normal direction, a mapping introduced by [14] where the domain is divided into two separate regions with an equal number of grid points is employed to reach sufficient accuracy in the boundary-layer region. $y = 1.8h_0$ is the coordinate delimitating the two regions, whereas the wall-normal domain is truncated at $y_\infty = 100h_0$, yielding a sufficiently large extent to minimise the influence of the far-field boundary condition previously mentioned. A total of 150 grid points form the discretised wall-normal domain together with an 8th-order finite difference.

In the analysis, the non-dimensional spanwise wavenumber β spans a range of values which are logarithmically spaced from 0 to 10. Lastly, the base flow $\hat{\mathbf{q}}$ computed with Nektar++ is interpolated on the regular grid using B-splines.

Parallel matrix and vector assemblies are performed with the suite of data structures and routines PETSc [15]. The GEVP (4) is solved iteratively with a Krylov-Schur method encompassed in the parallel library SLEPc [16], in which a portion of interest of the eigenvalue spectrum is computed. This is achieved through a shift-and-invert spectral transformation in order to accelerate the convergence of the eigenpairs near the origin of the complex plane, where the physically relevant information is located. In this approach, the shift-and-invert operator requires the inversion of a matrix which is handled with the multifrontal solver MUMPS [17] performing sparse LU factorisation. For each value of the shift, a total of 20 eigenvalues are requested in the upper half of the (ω_r, ω_i) plane, that is the temporally unstable region of the spectrum. The corresponding dimension of the Krylov subspace is $\dim(\mathcal{K}^m) = 100$. Due to the intrinsic ill-conditioned character of the finite difference method with fine spatial resolution, a balancing technique is applied during the Krylov-Schur iterations in order to appropriately rescale the matrix rows and columns and hence improve the accuracy of the retrieved eigenpairs. Finally, the convergence of the eigenvalues is monitored with a prescribed tolerance of 10^{-11} below which the absolute error estimate on the associated eigenvalues should fall.

5 Results and Discussion

In this section, the temporal stability of the boundary-layer flows subjected to BFS/FFSs presented in Sect. 3 is recapitulated. A well-known feature of BiGlobal analyses conducted in the streamwise/wall-normal plane is the sensitivity of eigenvalues to the streamwise length of the computational domain as well as to the choice of inflow and outflow boundary conditions. Therefore, some numerical precautions have been deployed. For the different height and chord location cases, it has been verified that physically relevant eigenvalues do not undergo significant value changes when the streamwise length of the computational domain is varied, namely that the modulus of unstable eigenvalues of interest have been modified by no more than a relative 6 %. Furthermore, a very slight eigenvalue magnitude change has been observed when inflow and outflow boundary conditions have been varied. Inflow/outflow conditions included zero-Dirichlet/‘do-nothing’, zero-Dirichlet/Robin, Robin/‘do-nothing’ and Robin/linear extrapolation. This is a noteworthy feature, given the well-known issues of spectrum convergence with respect to inflow/outflow boundary conditions discussed in several literature contributions. In addition, mesh independence has also been assessed.

The existence of temporally unstable modes for the four height cases and two alternate chordwise step locations is presented in Table 2. No temporal instability is found for the smallest step heights for both the FFS and BFS cases at the two chordwise positions, while the highest step features unstable modes for solely the

Table 2 Presence of temporal instabilities for the step feature, height and chord location cases

Step height (μm)	BFS 10 %	BFS 20 %	FFS 10 %	FFS 20 %
413	No	No	No	No
619	Yes	No	Yes	Yes
825	Yes	Yes	Yes	No
893	Yes	Yes	No	No

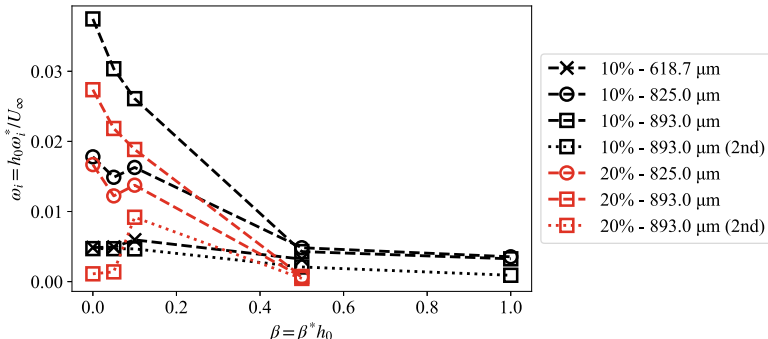


Fig. 3 Evolution of growth rates ω_i for the unstable eigenvalues as a function of the spanwise wavenumber β . Cases correspond to the BFS. When applicable, the second most unstable modes (2nd) are included. Symbols with an asterisk denote a dimensional quantity

BFS. The slightly rounded character of the step seems detrimental for the FFS; the absence of a recirculation region just downstream of the FFS in the steady solutions may be heavily impacting the stability characteristics. In comparison, [3] found evidence of a reasonably large recirculating laminar bubble on the top of the FFS, however their step was sharp. In the experiment of [4], the infrared thermography technique used to identify the transition front did not allow to determine its presence. Temporal instabilities are predicted to arise with current computations in the two intermediate height cases for both step configurations, although little correlation with the chordwise location of the step may be established.

Figure 3 compares growth rates of unstable eigenvalues found for the BFSs on varying the spanwise wavenumber β . Most eigenvalues are found to degenerate or become stable beyond $\beta = 1$. For the greatest height, two unstable eigenvalues are found. The variation of β turns out to not be necessarily discriminating between the different cases as most unstable modes are monotonically stabilised up to $\beta = 1$ except in the 0.0 – 0.1 region. A general trend is how higher BFSs appear to be associated with larger growth rates. At a glance, the 10% chord BFS yields more unstable eigenvalues than its 20% chord counterpart. Moreover, the second-most unstable eigenvalues in the greatest height cases have a much lower growth rate than the primary instability modes.

Remarkably, the growth rate of the three unstable eigenmodes retrieved for the FFSs seems independent of the spanwise wavenumber β as can be seen in Fig. 4. This

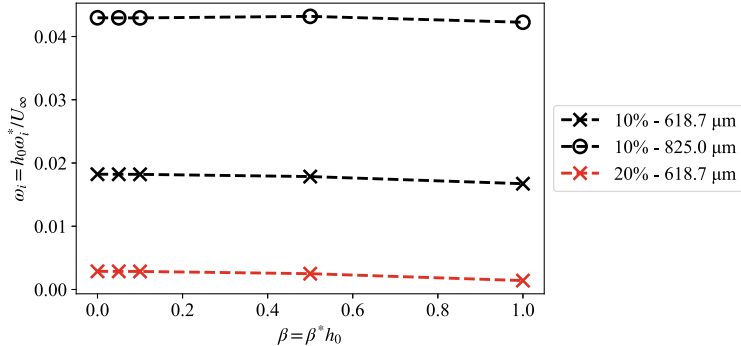


Fig. 4 Evolution of growth rates ω_i for the unstable eigenvalues as a function of the spanwise wavenumber β . Cases correspond to the FFS. Symbols with an asterisk denote a dimensional quantity

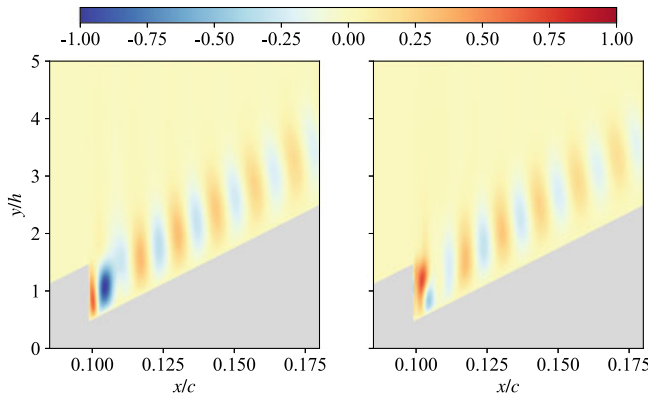


Fig. 5 Contours of non-dimensional streamwise perturbation velocity \hat{u}_i (left) and spanwise perturbation velocity \hat{w}_i (right) for the most unstable mode in the greatest height case $h_0 = 893 \mu m$ of the BFS and $\beta = 0.5$

remains to be explained. Regardless, the higher step possesses a larger growth rate in a similar manner to the BFS case. For equal step heights, the 20 % chord location does not seem as temporally destabilising as the 10 % chord location. A plausible explanation may be the thicker boundary layer at 20 % chord, where h/δ is smaller than at 10 % chord according to Table 1.

For both step types, the existing unstable eigenmodes are stationary ($\omega_r \approx 0$) except in a narrow band of spanwise wavenumbers comprised between 0.01 and 0.1. Two kinds of mode structure have been classified in the case of BFSs, namely localised regions of large streamwise and spanwise velocity magnitude as well as wave-like structures extending from the step height down to the lower BFS corner and convected further downstream as in Fig. 5. For the FFSs, the eigenfunctions fea-

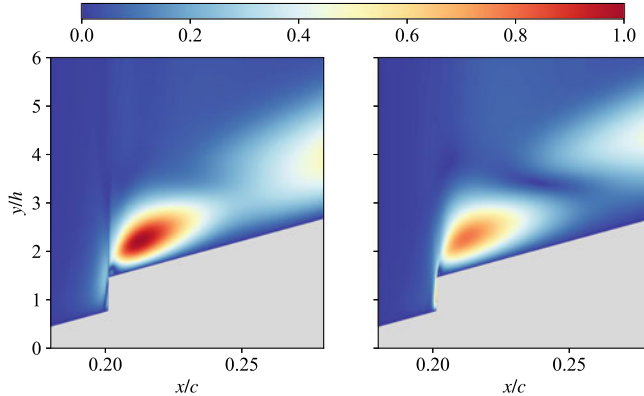


Fig. 6 Contours of non-dimensional streamwise perturbation velocity $|\hat{u}|$ (**left**) and spanwise perturbation velocity $|\hat{w}|$ (**right**) for the most unstable mode in the second-greatest height case $h = 613\text{ }\mu\text{m}$ of the FFS and $\beta = 0.1$

ture regions of relatively high streamwise and spanwise velocity magnitudes located above the step, just downstream as can be seen in Fig. 6.

6 Conclusions

The temporal stability of a boundary layer developing on a swept wing and undergoing destabilisation due to steps has been investigated. Preliminary results have been provided on moderately smooth backward- and forward-facing steps by means of streamwise BiGlobal analysis. Unstable modes have been found for step heights exceeding the clean geometry local boundary layer displacement thickness. Nevertheless, the highest forward-facing step has not been found to display instability, with only the intermediate step heights yielding unstable modes; the concept of critical step height discussed in previous works might not be applicable in this context due to the roundness of the steps considered. Owing to limited dataset availability, the analysis at the two step locations was insufficient in scope to allow any conclusions to be drawn on the instability behaviour. Further and more exhaustive investigation on larger datasets and conditions is required for the elucidation of the various instability mechanisms arising in swept-wing boundary layers. The results presented in this paper shed a first light on the usage of BiGlobal analysis on a numerically challenging swept-wing problem.

Acknowledgements This work was supported by the SSeMID Innovative Training Network, which has received funding from the European Union's Horizon 2020 research and innovation programme under the Marie Skłodowska-Curie grant agreement No. 675008.

References

1. Wang, Y.X., Gaster, M.: Effect of surface steps on boundary layer transition. *Exp. Fluids* **39**(4), 679–686 (2005). <https://doi.org/10.1007/s00348-005-1011-7>
2. Crouch, J.D., Kosorygin, V.S., Ng, L.L.: Modeling the effects of steps on boundary-layer transition. In: R. Govindarajan (ed.) IUTAM Symposium on Laminar-Turbulent Transition, *Fluid Mechanics and Its Applications*, vol. 78, pp. 37–44. Springer (2006). https://doi.org/10.1007/1-4020-4159-4_4
3. Tufts, M.W., Reed, H.L., Crawford, B.K., Duncan, G.T., Saric, W.S.: Computational investigation of step excrescence sensitivity in a swept-wing boundary layer. *J. Aircr.* **54**(2), 602–626 (2017). <https://doi.org/10.2514/1.C033892>
4. Rius Vidales, A.F., Kotsonis, M., Antunes, A.P., Cosin, R.: Effect of two-dimensional surface irregularities on swept wing transition: forward facing steps (2018). <https://doi.org/10.2514/6.2018-3075>. AIAA Paper 2018-3075 presented at the 2018 Fluid Dynamics Conference, Atlanta, 25–29 June 2018
5. Dellar, O.J., Jones, B.L.: Dynamically correct formulations of the linearised Navier-Stokes equations. *Int. J. Numer. Methods Fluids* **85**(1), 3–29 (2017). <https://doi.org/10.1002/fld.4370>
6. Appel, T., Mughal, S., Ashworth, R.: Global stability analysis of a boundary layer with surface indentations (2019). <https://doi.org/10.2514/6.2019-3537>. AIAA Paper 2019-3537 presented at the AIAA Aviation 2019 Forum, Dallas, 17–21 June 2019
7. Theofilis, V.: Advances in global linear instability analysis of nonparallel and three-dimensional flows. *Prog. Aerosp. Sci.* **39**(4), 249–315 (2003). [https://doi.org/10.1016/S0376-0421\(02\)00030-1](https://doi.org/10.1016/S0376-0421(02)00030-1)
8. Sunderland, R., Sawyers, D.: Evaluation of AERAST large scale wind-tunnel test results. *Tech. Rep. RP0905747*, Airbus (2009)
9. Cooke, E., Mughal, S., Sherwin, S., Ashworth, R., Rolston, S.: Destabilisation of stationary and travelling crossflow disturbances due to steps over a swept wing (2019). <https://doi.org/10.2514/6.2019-3533>. AIAA Paper 2019-3533 presented at the AIAA Aviation 2019 Forum, Dallas, 17–21 June 2019
10. Saeed, T.I., Mughal, M.S., Morrison, J.: The interaction of a swept-wing boundary layer with surface excrescences (2016). <https://doi.org/10.2514/6.2016-2065>. AIAA Paper 2016-2065 presented at the 54th AIAA Aerospace Sciences Meeting, San Diego, 4–8 January 2016
11. Kroll, N., Langer, S., Schwöppé, A.: The DLR flow solver TAU - status and recent algorithmic developments (2014). <https://doi.org/10.2514/6.2014-0080>. AIAA Paper 2014-0080 presented at the 52nd Aerospace Sciences Meeting, National Harbor, 13–17 January 2014
12. Cantwell, C.D., Moxey, D., Comerford, A., Bolis, A., Rocco, G., Mengaldo, G., De Grazia, D., Yakovlev, S., Lombard, J.E., Ekelschot, D., Jordi, B., Xu, H., Mohamied, Y., Eskilsson, C., Nelson, B., Vos, P., Biotto, C., Kirby, R.M., Sherwin, S.J.: Nektar++: An open-source spectral/hp element framework. *Comput. Phys. Commun.* **192**, 205–219 (2015). <https://doi.org/10.1016/j.cpc.2015.02.008>
13. Hermanns, M., Hernández, J.A.: Stable high-order finite-difference methods based on non-uniform grid point distributions. *Int. J. Numer. Methods Fluids* **56**(3), 233–255 (2007). <https://doi.org/10.1002/fld.1510>
14. Malik, M.R.: Numerical methods for hypersonic boundary layer stability. *J. Comput. Phys.* **86**(2), 376–413 (1990). [https://doi.org/10.1016/0021-9991\(90\)90106-B](https://doi.org/10.1016/0021-9991(90)90106-B)
15. Balay, S., Abhyankar, S., Adams, M.F., Brown, J., Brune, P., Buschelman, K., Dalcin, L., Dener, A., Eijkhout, V., Gropp, W.D., Karpeyev, D., Kaushik, D., Knepley, M.G., May, D.A., McInnes, L.C., Mills, R.T., Munson, T., Rupp, K., Saman, P., Smith, B.F., Zampini, S., Zhang, H., Zhang, H.: PETSc users manual. *Tech. Rep. ANL-95/11 - Revision 3.13*, Argonne National Laboratory, Lemont, IL, USA (2020)
16. Roman, J.E., Campos, C., Romero, E., Tomás, A.: SLEPc users manual. *Tech. Rep. DSIC-II/24/02 - Revision 3.13*, D. Sistemes Informàtics i Computació, Universitat Politècnica de València, Spain (2020)

17. Amestoy, P.R., Duff, I.S., L'Excellent, J.Y., Koster, J.: A fully asynchronous multifrontal solver using distributed dynamic scheduling. *SIAM J. Matrix Anal. Appl.* **23**(1), 15–41 (2001). <https://doi.org/10.1137/s0895479899358194>

Effect of Discrete Widely Spaced Suction on a Transitioning Flow at High Suction Rates



B. Crowley and C. Atkin

Abstract An experiment was performed on boundary layer suction, on a flat plate in a low turbulence wind-tunnel. This work focused on the process of ‘over-suction’ where at high suction rates, local flow structures around the suction perforations precipitate a premature laminar-to-turbulent transition instead of delaying the process. The historical ‘over-suction’ mechanism associated with widely spaced perforations, i.e. sufficiently widely spaced for local flow structures to act in isolation was studied. This high-frequency ($St \sim 30\text{--}90$) mechanism was identified and found to dominate in the absence of a pre-established transition front; however, where the natural transition front is pre-located close to the suction array (in the absence of suction): it was found that the dominant mechanism of ‘over-suction’ changed. The dominant modes during this new process was found to be at low frequency ($St \sim 0.3\text{--}6$). These low frequency modes appeared to be associated with inflectional instability, being sensitive to inflection points in wall normal profile of the span-wise mean velocity. The implications of this work is that the natural transition front location will need to be accounted for in the avoidance of ‘over-suction’ in the design of boundary layer suction systems.

1 Introduction

Wall-suction is a well-known method of controlling of the laminar-to-turbulent transition process. It serves to delay transition by creating the effect of a favourable pressure gradient, by accelerating the flow towards the wall: this creates more stable wall-normal ('y') profiles of mean stream-wise velocity 'u'. It also delays transition by reducing the boundary layer thickness, which reduces the local Reynolds number.

B. Crowley (✉)
University of Cambridge, Cambridge, UK
e-mail: barry.crowley.1@city.ac.uk

C. Atkin
City, University of London, London, UK
e-mail: C.Atkin@uea.ac.uk

However, wall-suction is commonly modelled as being uniformly distributed across the wall. In practice, the suction must permeate through pores in the wall, which creates local maxima and minima in the suction distribution. The resulting non-uniformity has been known to cause a premature transition at high suction rates for certain perforation array geometries [1, 2]. This type of transition scenario has been termed ‘over-suction’, and is the subject of this work.

In much of the literature this problem has primarily been investigated with the objective of predicting the conditions for over-suction. This has been commonly done through parametric studies in which dependent over-suction parameters are varied systematically [3, 4]. In these types of experiments, the effect of the suction on transition front location is often used to determine if the suction is stabilising or destabilising: it moves down-stream for the former, and upstream for the latter case [3, 5].

These dependent parameters are based on experimental investigations into the physical mechanisms for over-suction. Studies such as MacManus and Eaton [1, 6] and Goldsmith [7] identified what were believed to be the dominant flow structures for suction arrays where the individual perforations are sufficiently widely spaced to be seen as isolated. Here it was found that two counter rotating vortices are shed from each individual suction perforation: in early studies these vortices were described as simply growing unstable and inducing transition to a turbulent state [7]. Later studies by MacManus and Eaton [1, 6] found mean stream-wise velocity (u) profiles that were inflectional across the wall-normal (y). These inflectional profiles were attributed to be the source of transition for ‘over-suction’ in configurations with widely spaced perforations.

In our study these inflectional stream-wise velocity profiles ‘ $u(y)$ ’ were investigated and some spectral analysis of the associated fluctuating velocity fields ‘ $uf(x, y)$ ’ was performed.

2 Experimental Setup

This study was conducted at the Gaster Wind-tunnel facility at City, University of London. With the flat plate mounted in the tunnel, a free-stream turbulence level of 0.014% was measured between 2 and 5000 Hz for a unit Reynolds number ‘ $R1$ ’ of 0.9E6.

As shown in Fig. 1, a flat-plate model was used with a 6:1 asymmetrical leading edge, and a chord length ‘ C ’ of 2250 mm, including the flap. This model was designed to allow 296 mm (length in x -direction) suction array panels to be mounted 500 mm from the leading edge of the flat plate. Additionally, the suction array began 85 mm down-stream of the suction panel start, and ended 61 mm from the suction panel end. Behind the suction array was a single sealed suction plenum, used to apply a uniform pressure drop across the suction perforations. This plenum then connected to an Aalborg GFC mass flow controller, to measure the suction rate, which was then connected to the suction pump.

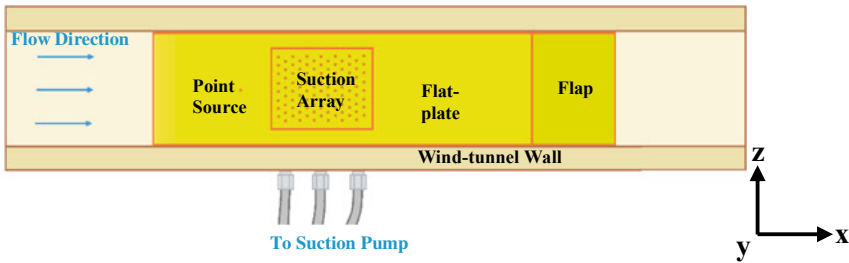


Fig. 1 Diagram showing elevation view of flat-plate model test arrangement

The suction array was composed of 1313 0.6 mm diameter suction perforations. These perforations were arrayed in a triangular pattern, with the base of the triangles equal to the height. The Perforations were spaced at 10 diameters, as suggested by Reneaux and Blanchard [4] and by Ellis and Poll [3].

A point source was located 375 mm (in x-direction) from the leading edge in line with the centre-line of the span of the plate (in z-direction). This point source consisted of a loudspeaker mounted behind the plate which was used to generate and inject sinusoidal disturbances into the boundary layer through a single small perforation.

In the experiments the exciter was used to study the effect of suction on the growth of linear travelling modes, as well as pre-locating a transition front that has developed from a clearly defined linear regime (where linear stability theory applies) upstream.

Steady and unsteady measurements were taken using a DISA type M hot-wire anemometry system. The hot-wire probe was mounted on a three-dimensional traverse system, with only the probe arm protruding inside the tunnel.

3 Results

Spectral energy distributions are shown for a set of different suction rates (0, 7E-6, 6.2E-5, 7.3E-5) at a fixed unit Reynolds number (0.9E6). A baseline case is shown in Fig. 2a. For this case, there were no perforations and therefore no suction. The exciter was used to force an unstable frequency in the boundary layer. A frequency of $St = 23$ ($f = 145$ Hz) was used with an amplitude of $\psi/u_{rms,e} = 1.64$. This amplitude was sufficient to cause transition to occur within the area of measurement. This amplitude was based on unsteady hot-wire signal at the intersection of the exciter near and far fields. This appears as the minimum value in amplitude over the plate length.

Figure 2 shows contour maps of spectral root mean square velocity ' ψ ' normalised by the total root mean square velocity at the boundary layer edge ' $u_{rms,e}$ '. This plotted against Strouhal number (St) on the y-axis where, ' f ' is frequency, ' C ' is chord length of the plate, and ' u_e ' is the stream-wise boundary layer edge mean velocity. On the x-axis is the distance from the leading edge ' x ' normalized by chord ' C '. Each data

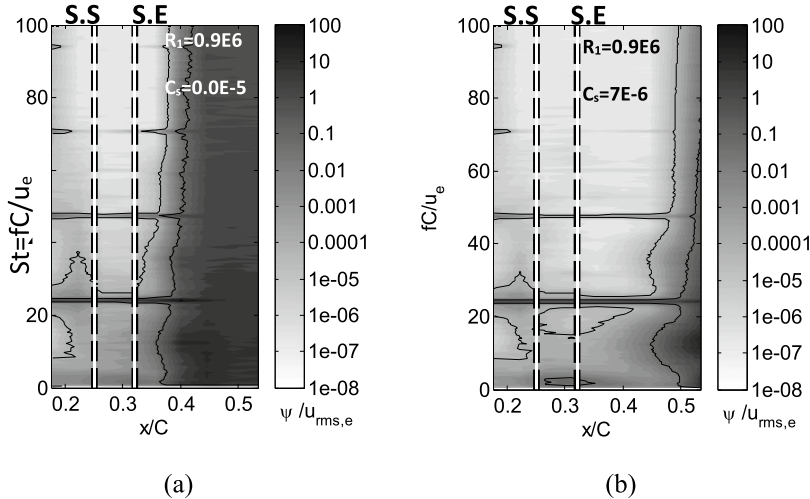


Fig. 2 Spectral energy across frequency domain at different stream-wise stations. S.S. and S.E. denote the beginning and end of the suction array. $z/d = -3.33$

point in the contour map corresponds to the maximum energy across the wall normal for a given x -location and Strouhal number (St). Suction Coefficient ' C_s ' is simply the ratio of volume flow rate through the suction panel ' Q_h ' to the volume flow rate through the test section ' $A_T u_{mean,e}$ '. R_1 is unit Reynolds number based on edge velocity ' u_e ' and a unit length scale.

Here, the transition front is taken to be where the spectrum energy spreads across the frequency axis (i.e. $x/C > 0.36$ in Fig. 2a). It can be seen that this spread of spectral energy originates at $St = 11$ ($x/C \sim 0.35$). This is a sub-harmonic of the forced mode, at $St = 22$: this spectral spread is characteristic of N-type transition and compares well with spectral energy plots presented by Kachanov and Levechenko [8].

It can be seen from Fig. 2b that on the application of some suction ($C_s = 7E-6$): the transition front moves down-stream (from $x/C > 0.36$ to $x/C 0.45$). It can also be seen that $St = 11$ is still the frequency, from which the spectral energy spreads. Additionally, a region of high energy has appeared at low frequency ($St \sim 3$) across the suction array (between S.S and S.E.).

Figure 3 shows the same test case as in Fig. 2, however, the suction rate has been increased ($C_s = 6.2E-5$ and $7.3E-5$ for (a) and (b) respectively). In Fig. 3a the transition front has moved sufficiently far down-stream that it is no longer visible in the region of measurement. It can also be seen that the low frequency disturbance has spread to neighbouring frequencies ($St < 10$) and increased in amplitude. The low frequency also now persists to some extent down-stream of the end of the suction array, denoted by S.E.

Figure 3b shows a case with an even higher suction rate ($C_s = 7.3E-5$). Here it can be seen that the transition front has returned to the region of measurement and is spreading from the low frequency disturbance ($St < 10$). Here it appears as though

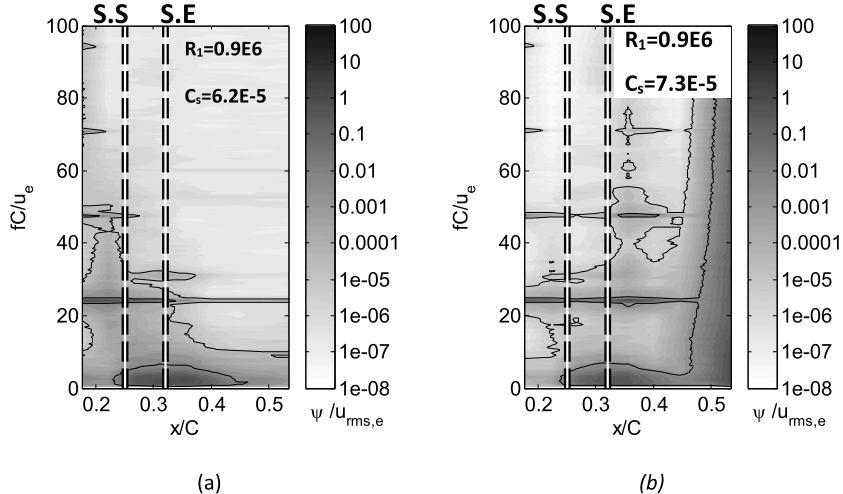


Fig. 3 Spectral energy across frequency domain at different stream-wise stations. S.S. and S.E. denote the beginning and end of the suction array. $z/d = -3.33$

it is causing transition, perhaps due to interactions with the low frequency oblique modes present in N-type transition [8].

Figure 4 shows the effect of removing the boundary layer forcing on the transition behaviour. The low frequency disturbance ($0 < St < 5$) is still present however, the transition behaviour now seems to be governed by high frequency disturbances ($60 <$

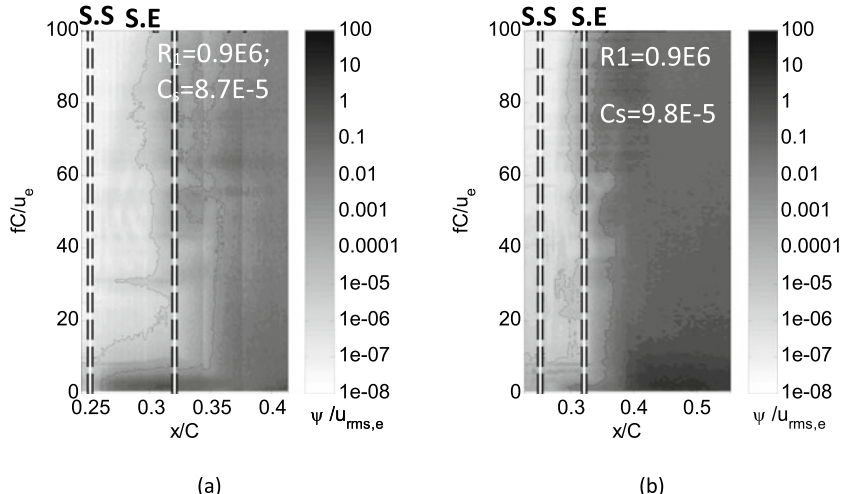


Fig. 4 Spectral energy across frequency domain at different stream-wise stations. S.S. and S.E. denote the beginning and end of the suction array. $z/d = -3.33$

$St < 100$). This is inferred from the beginning of the dark high amplitude regions of the spectrum which then spread across the frequency domain downstream approximately $x/C = 0.33$.

Figure 4 shows two sets of data: one where the suction rate has been maintained at $C_s = 8.7\text{E-}5$, and another where it been increased to $C_s = 9.8\text{E-}5$. The second case is provided as there are some discontinuities in the spectrum ($x/C = 0.34, 0.37$) shown in Fig. 4a due to pauses in the experiment, with insufficient settling time before resuming. These issues were resolved before taking the measurements shown in Fig. 4b.

Figure 5 shows the mean velocity profiles associated with the spectrum shown in Fig. 4a. In this plot, contours of normalised mean velocity are shown plotted against the non-dimensional wall-normal ‘ η ’ on the y-axis and, on the x-axis, stream-wise distance from the leading edge ‘ x ’ normalised by chord length ‘ C ’. Some velocity profile shapes are super-imposed on the contour map: these are profiles of $u(\eta)$. They are denoted by white on black lines, with their origins indicated by the white on black dashed lines. The start and end of the suction array are marked by the thicker black lines denoted with ‘S.S.’ and ‘S.E.’ respectively. ‘ η ’ is simply defined as the ratio Reynolds number based on ‘ y ’ to the square root of Reynolds number based on the plate length ‘ C ’.

It can be seen in Fig. 5 that the velocity profiles are inflectional down-stream of $x/C = 0.33$. The presence of inflectional velocity profiles on prior to an ‘oversuction’ induced transition is consistent with work done by MacManus and Eaton [1]. Comparing Figs. 4 and 5 it appears as though the inflectional profiles may be amplifying the high frequency ($40 < St < 100$) seen in the spectral contour plot. In prior work by MacManus and Eaton [1] the only the mean velocity was studied. No prior studies where the spectra associated with these inflectional profiles was found in the literature by the authors.

Figure 6a, b show the growth rates of the low and high frequency disturbances respectively for a set of different suction rates, but for a fixed unit Reynolds number of $R_1 = 0.9\text{E}6$. Here, the x-axis of the figure is the non-dimensional suction rate, defined as the ratio of volume flow rate through the suction array to the volume flow

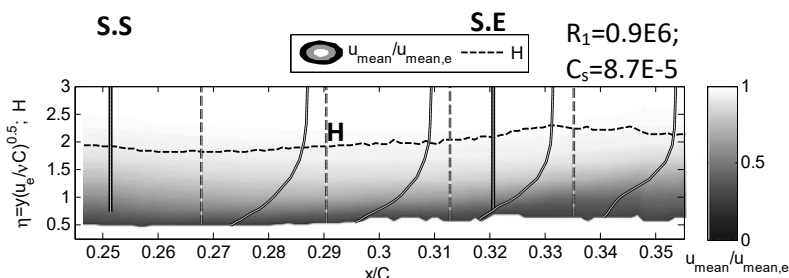


Fig. 5 Development of inflectional stream-wise velocity profiles $u_{\text{mean}}(\eta)$. Profile shapes of $u_{\text{mean}}(\eta)$ are shown super-imposed upon contours of the same quantity normalised by the mean boundary layer edge velocity $u_{\text{mean},e}$. H is the shape factor. $z/d = -3.33$

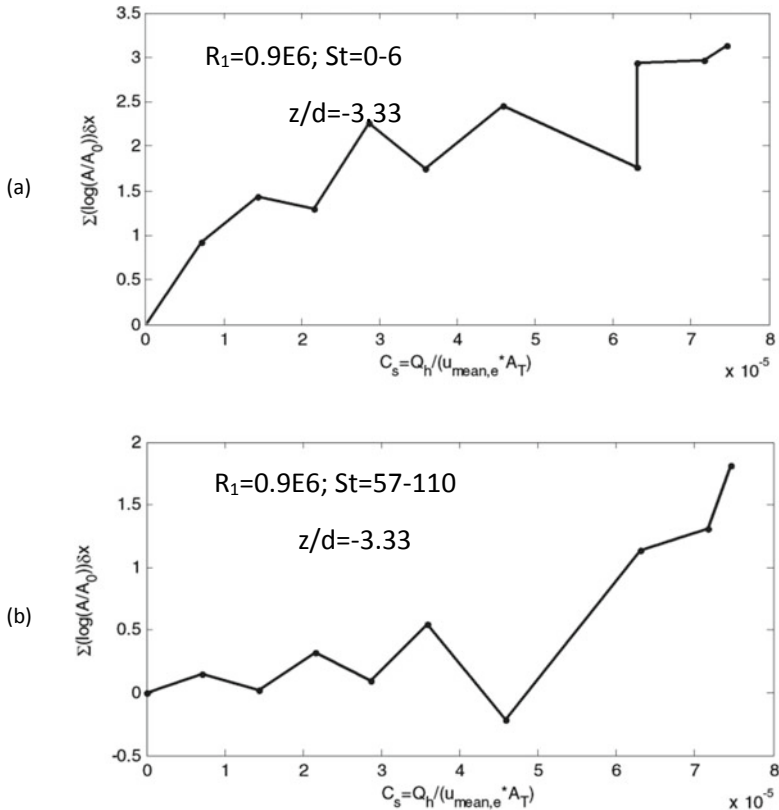


Fig. 6 Change in integrated amplitude of the low frequency disturbance (a) and the high frequency disturbance (b) for different suction rates at a prescribed Reynolds number

rate through the working section of the wind-tunnel. The y-axis shows the integrated growth of the disturbance field amplitudes ‘A’, taken across the suction panel only. This amplitude ‘A’ is normalised by the amplitude at the minimum suction rate ‘ A_0 ’.

Here it appears as though the low-frequency disturbance (shown in Fig. 6a) grows log-linearly with increasing suction. In contrast the high frequency disturbance (shown in Fig. 6b) only appears to start growing after reaching some threshold (here it is $C_s = 4.5E-5$), after which it grows log-linearly.

Figure 7 shows the growth rate of just the low frequency disturbance ($0.3 < St < 6$), here multiple curves are shown for different free-stream Reynolds numbers (R_1). The x-axis again shows non-dimensional suction rate ‘ C_s ’, and the y-axis again shows the normalised growth of the low frequency amplitude ‘A’, normalised by the amplitude in the no-suction case ‘ A_0 ’.

Here it can be seen that the curves showing the different Reynolds number cases collapse, suggesting that the growth of the low frequency disturbance might be

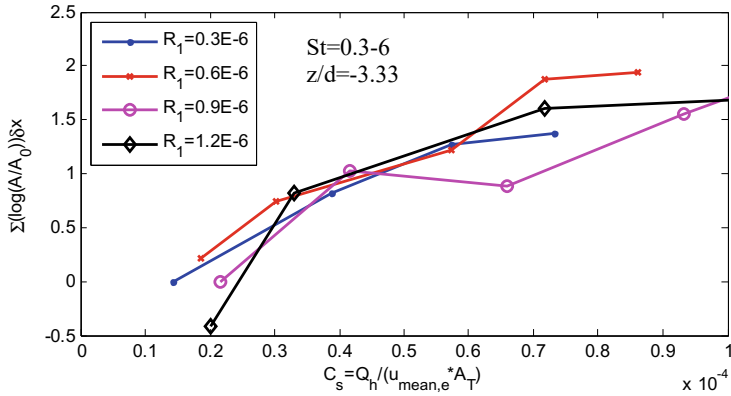


Fig. 7 Growth rate of low frequency disturbance at different Reynolds numbers

Reynolds number independent. This may suggest that it is some form of inflectional instability.

Figure 8 shows the spatial variation of the dimensionless gradient of the span-wise velocity ‘w’ with respect to ‘ η ’. It can be seen in Fig. 8 that there are regions of strong positive span-wise velocity gradient ‘ $dw/d\eta$ ’ over the suction panel, whose extent is denoted by S.S and S.E.

Down-stream of the end of the suction array ‘S.E’, it can be seen a region of strong negative gradient appears underneath the region of positive gradient. This might indicate the development of a vortex, which is expected in ‘over-suction’ transition from the literature [2].

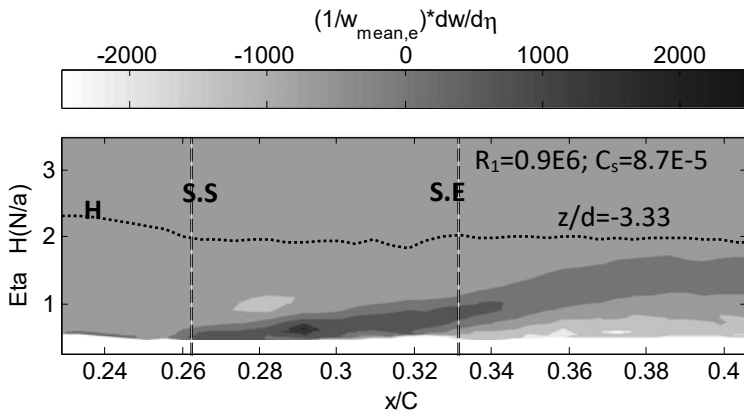


Fig. 8 Gradient of span-wise velocity ‘w’ component across the wall-normal ‘ η ’. S.S and S.E denote the beginning and end of the suction array respectively, while H is the shape factor

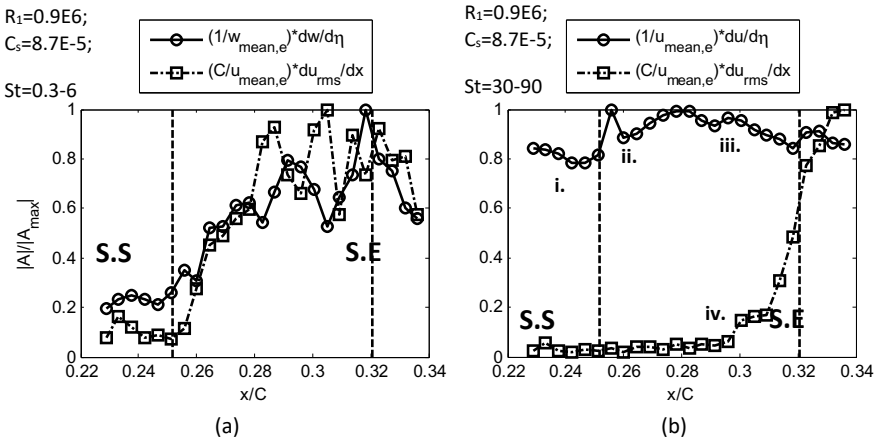


Fig. 9 **a** Shows the correlation between the stream-wise growth rate of the low frequency disturbance ($0.3 < St < 6$) and the span-wise velocity gradient across the wall-normal (dw/dy). **b** Shows the correlation between the high frequency disturbance ($30 < St < 90$) and the stream-wise velocity gradient across the wall normal (du/dy). Both quantities are normalised to provide an easier comparison. $z/d = -3.33$

Figure 9a shows the correlation between the growth rate of the low frequency disturbance ($0.3 < St < 6$) in the stream-wise direction (du_{rms}/dx); and the wall-normal ‘ η ’ gradient of the span-wise velocity component ‘ w ’. $dw/d\eta$ should have local maxima in regions of inflectional $w(\eta)$ profiles. Here the sum of the gradient is taken (across the wall) to produce a single value; similarly, the sum of (du_{rms}/dx) is also taken across the wall normal ‘ η ’ for each point on the plot. Here the amplitude ‘ A ’ for each of the two curves is normalised by their maximum value ‘ A_{\max} ’.

It can be seen that there is some agreement between the two curves, suggesting that the growth rate of the low frequency (du_{rms}/dx) is correlated with inflectional $w(\eta)$ profiles, which is consistent with the hypothesis that the low frequency disturbance may be an inflectional instability.

Figure 9b applies the same methodology but for the high frequency disturbance ($St = 30-90$) correlated with the wall-normal gradient of stream-wise velocity component ‘ $du/d\eta$ ’. Here, when looking for correlation between the disturbance field and the high frequency, the effect of velocity gradient must be considered as a deviation from the Blasius solution.

That is to say the gradient shown in Fig. 9b has a value of about 0.8 before reaching the suction array (see marker i.), after this it increases to 1.0 due to the accelerating effect of the suction (see marker ii.). At $x/C = 0.28$ the gradient starts to drop (see marker iii.), this has been linked to the onset of inflectional mean velocity profiles ‘ $u(\eta)$ ’ across the wall normal ‘ η ’. When this gradient drops, and the profile becomes inflectional it can be seen that the spatial growth rate of the high frequency starts to increase exponentially (see marker iv.) as a function of stream-wise displacement ‘ x ’.

In conclusion, it was found that the dominant mode during ‘over-suction’ transition was caused by high frequency modes ($St \sim 30\text{--}90$, $f \sim 200\text{--}600$ Hz) correlated with the inflectional $u(y)$ velocity profiles. In these test cases no natural transition front was pre-established on the flat-plate model (i.e. laminar flow was found across the entirety of the plate in the absence suction).

However, in other test cases were explored where a transition front was pre-established through forcing of linear modes using a pulsating jet (or point exciter): in these cases, a different (previously unreported) mechanism of ‘over-suction’ transition was found.

This ‘over-suction’ mechanism is governed by the growth of low frequency disturbances ($St \sim 0.3\text{--}6$, $f \sim 2\text{--}40$ Hz) that appear benign in the absence of the pre-established transition front. With a pre-established N-type transition front [8], it was found that the low-frequency disturbance could interact with the N-type transition front and move it forward. The only mention of potentially similar low frequency disturbances found in a survey of the literature was in a wall-suction study by [9] and arguably a cross-flow study by [10] where, in both studies, these disturbances were believed to be unimportant in the transition process.

Acknowledgments The Authors would like to thank Prof. Michael Gaster for his advice and support throughout this project. Gratitude is also extended to innova-teUK and ESPRC for funding this project under the ALFET (grant ref. 113022, coordinated by Airbus) and LFC-UK (grant ref. EP/I037946/1, led by Imperial College) and NWTF (grant ref. EP/L024888/1, led by Imperial College) programs respectively.

References

1. MacManus, D., Eaton, J.: Flow physics of discrete boundary layer suction-measurements and predictions. *J. Fluid Mech.* **417**, 47–75 (2000)
2. Gregory, N.: Research on suction surfaces for laminar flow. In: Lachmann, G. (ed.) *Boundary Layer and Flow Control*, vol. 2, pp. 924–960 (1961)
3. Ellis, E., Poll, D.: Laminar and laminarizing boundary layers by suction through perforated plates. 2nd European Forum on Laminar Flow Technology, Bordeaux (1996)
4. Renaux, J., Blanchard, A.: The design and testing of an airfoil with hybrid laminar flow control, 16–18 March 1992, Office National d’Etudes et de Recherches Aerospatiales. 1st European Forum on Laminar Flow Technology, Hamburg (1992)
5. Saric, W., Reed, H.: Effect of suction and weak mass injection on boundary-layer transition. *AIAA J.* **34**(3), 383–389 (1986)
6. MacManus, D., Eaton, J.: Predictions and observations of the flow field induced by laminar flow control microperforations. *Exp. Therm. Fluid. Sci.* **13**, 395–407 (1996)
7. Goldsmith, J.: Investigation of the flow in a tube with laminar suction through 80 rows of closely-spaced holes. *Northrop Aircraft. Rep. BLC-86* (1956)
8. Kachanov, Y., Levchenko, V.: The resonant interaction of disturbances at laminar-turbulent transition in a boundary layer. *J. Fluid Mech.* **138**, 209–247 (1983)
9. Sattarzadeh, S., Fransson, M.: Spanwise boundary layer modulations using finite discrete suction for transition delay. *Exp. Fluids* **58**(14), 1–14 (2017)
10. Serpieri, J., Kotsonis, M.: Three-dimensional organisation of primary and secondary crossflow instability. *J. Fluid Mech.* **799**, 200–245 (2016)

Global Stability Analysis and DNS of a Swept Airfoil Section in Subsonic Flow



N. De Tullio and N. D. Sandham

Abstract Direct numerical simulations are run for a NACA0012 airfoil at Mach 0.4 and Reynolds number 50,000. The flow fields are characterised by transitional separation bubbles that occupy 50–60% of the suction surface and are followed by a region of attached turbulent flow. At 20° sweep the dominant structures are oblique relative to the leading edge, while at 40° they are parallel to the leading edge. The latter case is also characterised by the emergence of a broadband peak in the energy spectrum. The changes in the flow are further studied by a global stability analysis based on the time and span-averaged flowfields. At the largest sweep angle a strongly unstable global mode emerges, peaking at a Strouhal number $St = 3$ and with a range $1 < St < 5$ that is in good agreement with the DNS spectra. From the global eigenmode it is possible to discover the mechanism responsible for the mode, which involves a combination of shear layer convective instability, leading-edge receptivity and trailing edge sound radiation. The consistency of the global analysis and the DNS is notable, considering that the base flow is not a steady solution of the governing equations.

1 Introduction and Methodology

Most previous work on transitional separation bubbles (TSBs) on airfoils has been conducted for unswept configurations. The structure and dynamics of TSBs, including their bursting behaviour, are greatly influenced by the underlying laminar-turbulent transition process that shapes them. Experiments [19] and numerical simulations [13] have highlighted the importance of the Kelvin-Helmholtz (K-H) instability of the separated shear layer, so that separation bubbles strongly amplify incoming distur-

N. De Tullio (✉) · N. D. Sandham
University of Southampton, Southampton SO16 7QF, United Kingdom
e-mail: nico.detullio.meana@gmail.com

N. D. Sandham
e-mail: n.sandham@soton.ac.uk

bances. However, self-sustained flow unsteadiness and laminar-turbulent transition in separation bubbles have also been observed in various numerical investigations, such as [14], indicating that the portrayal of TSBs as disturbance amplifiers does not always suffice. The resonator character of TSBs has been investigated in the context of absolute and global stability analyses [1], suggesting that a reversed flow magnitude of at least 15–30% of the free stream is needed before an absolutely unstable mode associated with the K-H instability of the separated shear layer appears. Such a mode appears to lead to self-sustained two-dimensional vortex shedding, over which an additional self-excited three-dimensional (3D) instability may evolve [6, 11], driving the flow to a turbulent state. This additional 3D mode may be viewed as an instability of the unsteady periodic flow induced by the saturated K-H instability. The global stability of nominally two-dimensional (2D) separation bubbles has been investigated for a variety of different flow configurations, including flat plate boundary layers [15]. In the absence of external disturbances, the primary instability of the separation bubble is a steady three-dimensional global centrifugal mode [18] that becomes unstable for a reverse flow of about 7%; well below the values reported for the onset of the unsteady, absolutely unstable K-H mode.

The effects of sweep on the TSB behaviour have received little attention. Experimental investigations [10, 20] concentrated on relating the mean flow properties of swept separation bubbles to the corresponding unswept configuration, thereby exploring the applicability of the so-called *independence principle*, according to which the introduction of infinite sweep does not affect the flow characteristics in the chordwise direction. Hetsch and Rist [9] also investigated the linear stability of laminar swept separation bubbles induced over a flat plate by an adverse pressure gradient. Using local linear stability analysis (LST) and solutions of the parabolised stability equation (PSE) they showed that the linear stability results for swept separation bubbles are not independent of sweep angle. In particular, the primary instability of the separation bubble was found to shift towards higher frequencies and spanwise wavenumbers with increasing sweep angle, while the dominant Tollmien-Schlichting wave in the attached boundary layer was only slightly affected by sweep. In this work we study how sweep affects the laminar-turbulent transition of the separation bubbles developing over a NACA-0012 airfoil in the compressible subsonic regime at moderate Reynolds numbers. The investigation is carried out using DNS and global linear stability analysis.

1.1 DNS and Global Stability Methods

Direct numerical simulations are carried out using the SBLI code; a high-order, multi-block, finite-difference solver developed at the University of Southampton. The code solves both the non-linear and the linearised compressible Navier-Stokes equations. The SBLI code uses a standard fourth-order central difference scheme to calculate derivatives at internal points and a stable treatment [4] developed for the calculation of derivatives at domain boundaries. Time integration is based on a third-

order compact Runge-Kutta method. In its non-linear variant, the code employs an entropy splitting approach, whereby the inviscid flux derivatives are split into conservative and non-conservative parts. The entropy splitting scheme, together with a Laplacian formulation of the heat transfer and viscous dissipation terms in the momentum and energy equations (which prevents the odd-even decoupling typical of central differences), helps improve the stability of the low dissipative spatial discretisation scheme used. More details of the basic scheme are given in [17]. Code parallelisation is achieved using the Message Passing Interface (MPI) library.

An investigation of the importance of linear dynamics in the laminar-turbulent transition process is carried out through global linear stability analysis of the time- and span-averaged flows. The global eigenvalue problem is solved in matrix-free mode [2, 3, 7], using the Implicitly Restarted Arnoldi Method provided by the parallel ARPACK library [12], with SBLI's linearised compressible Navier-Stokes solver as a timestepper. The timestepper advances the solution vector from a time $t = t_0$ to a time $t = t_0 + \tau$; where τ should be small enough to avoid aliasing (Nyquist sampling theorem) but large enough for the Arnoldi procedure to converge.

Direct numerical simulations have been performed for the flow over an infinitely swept wing with a NACA-0012 profile at an incidence $\alpha = 5^\circ$, Reynolds number based on the airfoil chord $Re = 5 \times 10^4$, Mach number $M = 0.4$, Prandtl number $Pr = 0.72$, with Sutherland's law for viscosity. The investigation is carried out for two sweep angles $\Lambda = 20^\circ$ (cases S20A and S20B) and 40° (case S40A and S40B), and an unswept wing case ($\Lambda = 0^\circ$, denoted S0) is also considered for comparisons. The A and B cases are run for different methods of implementing sweep and correspond to two different Reynolds numbers based on the flow perpendicular to the wing section, as discussed in [5]. Figure 1 shows the computational domain. The domain is divided into three blocks, with interface boundary conditions between neighbouring blocks, and its dimensions are $R = 7.3$, $W = 5$ and $S = 0.4$ for all the simulations. The NACA-0012 airfoil profile has a sharp trailing edge imposed by extending and rescaling the profile slightly. A zonal characteristic boundary condition [16] is applied over a distance $L_{zonal} \approx 0.85c$ near the outflow boundary of blocks 1 and 3, using 61 grid points. A standard characteristic condition is applied at the rest of the boundaries, where, in addition, outgoing characteristics are integrated over time and superimposed on the fixed free stream condition. The airfoil is modelled using a no-slip, isothermal boundary condition, with the wall temperature equal to the free stream temperature. Table 1 gives details of the computational domain and grid. The computations use 565 million grid cells and resolve the transitional and turbulent region with $\Delta y_{min}^+ = 0.92$, $\Delta x_{max}^+ = 3.46$ and $\Delta z_{max}^+ = 4.97$. Further details of the method are included in [5].

Fig. 1 Sketch of the computational domain used. Block 2 contains the NACA-0012 aerofoil, while blocks 1 and 3 meet at the wake plane

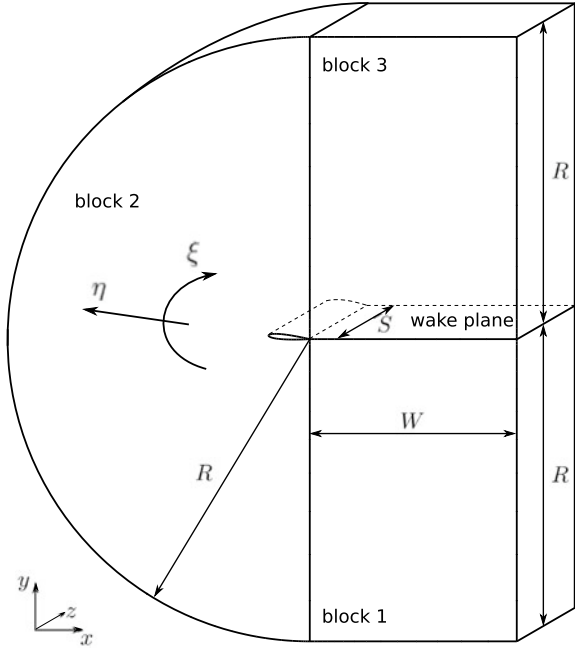


Table 1 Details of the computational study

Case	R/c	W/c	S/c	N _{foil}	N _{wake}	N _ξ	N _η	N _z	Δy _{min} ⁺	Δx _{max} ⁺	Δz _{max} ⁺
S0	7.3	5.0	0.4	1799	1602	3401	692	240	0.92	3.46	4.92
Jones et al.[11]	7.3	5.0	0.2	1066	1506	2570	692	96	1.0	3.36	6.49
S20A	7.3	5.0	0.4	1799	1602	3401	692	240	0.92	3.45	4.92
S20B	7.3	5.0	0.4	1799	1602	3401	692	240	0.84	2.80	4.48
S40A	7.3	5.0	0.4	1799	1602	3401	692	240	0.92	3.43	4.97
S40B	7.3	5.0	0.4	1799	1602	3401	692	240	–	–	–

2 Results

Figure 2 shows the flow structures in the transitional flow over the suction side of the airfoil through iso-surfaces of the second invariant of the velocity gradient tensor (Q-criterion) for all the cases considered, including two spans of the computational domain (0.8c in total) to help interpret the flow features. The dominant flow structures in the transitional separation bubble for case S0, shown in Fig. 2a, indicate that instabilities of the detached shear layer drive the initial stages of the laminar-turbulent transition process. Similar features can be observed for the cases S20A and S40A in Fig. 2b, and d, respectively, but with some significant changes in the coherence

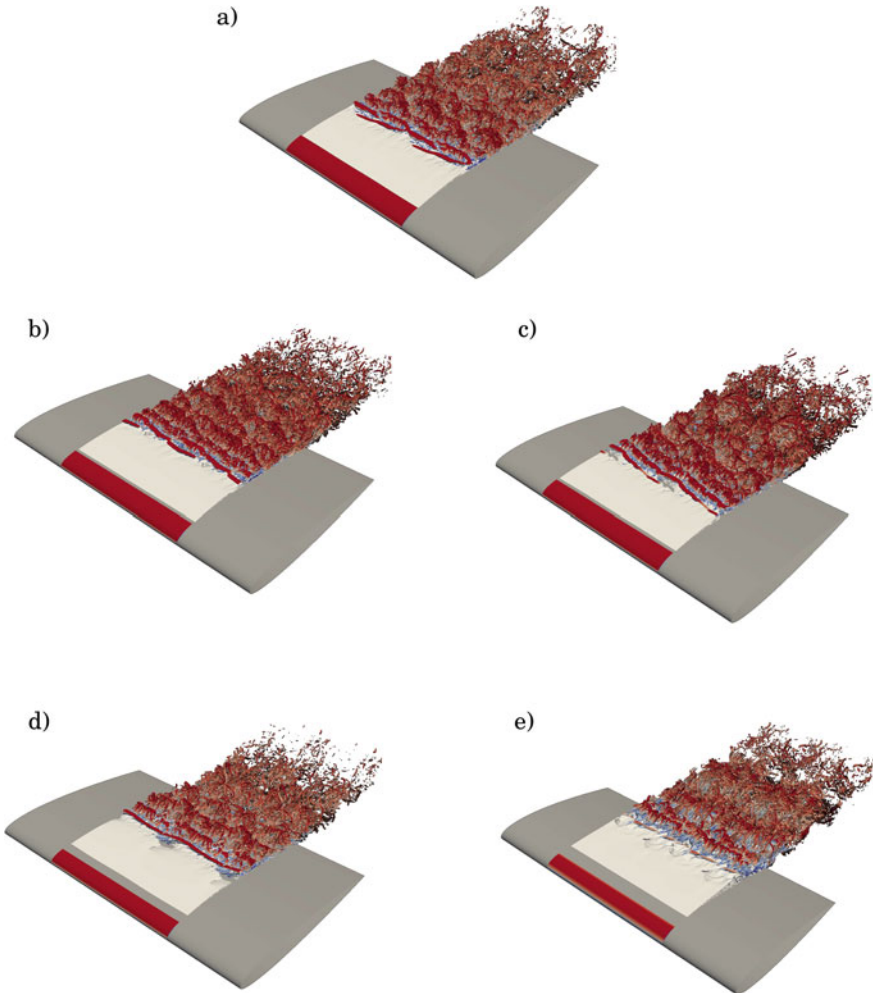


Fig. 2 Iso-surfaces of the second invariant of the velocity gradient tensor ($Q = 200$) showing the dominant vortical structures in the transitional and turbulent regions of the flow. **a** case S0, **b** case S20A, **c** case S20B, **d** case S40A and **e** case S40B. Two spans of the computational domain are shown

and organisation of the transitional structures, as discussed below. For case S20B (Fig. 2c), and in particular for case S40B (Fig. 2e), the transition process is delayed, consistent with the reduction in Reynolds number normal to the leading edge for these cases.

Several changes in flow structure are observed with the introduction of sweep. Firstly, comparing Figs. 2b and c with a we see that the introduction of modest sweep leads to structures that are more coherent and more two-dimensional, with the

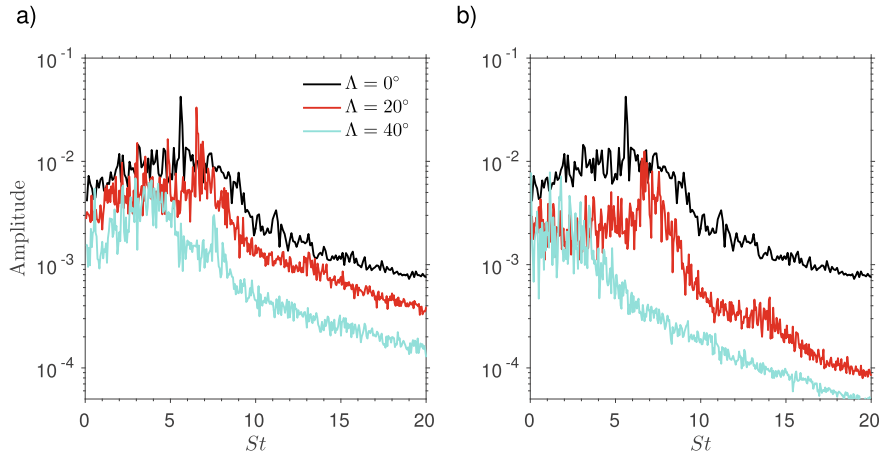


Fig. 3 Span-averaged temporal Fourier spectra for the wall pressure at the location of the initial vortex shedding location. **a** configuration A, **b** configuration B

orientation being perpendicular to the freestream direction and oblique to the leading edge. The increased coherence is maintained at the higher sweep angle (Figs. 2d, and e), but in these cases the orientation of the structures is parallel to the leading edge, with a dominant mode of $k_z = 0$. The zero spanwise wavenumber for cases S40A and S40B means that the wave vector forms a 40° angle with the free-stream flow direction. In the remainder of the paper, modes with zero spanwise wavenumber will be referred to as two-dimensional modes, while modes with non-zero spanwise wavenumber will be referred to as three-dimensional modes. It should be noted that no external disturbances have been imposed in the numerical simulations carried out in this work, so that the laminar-turbulent transition is self-sustained and cannot be attributed solely to the development of convective instabilities.

The dominant flow structures can also be identified from their wall pressure imprint. Pressure time series were accumulated for all spanwise positions over the whole surface of the wing. Span-averaged spectra are shown on Fig. 3, at a wall position under the initial vortex shedding location in each case. For $\Lambda = 20^\circ$ the Strouhal number of the highest amplitude mode is $St \approx 6.53$ for case S20A and $St \approx 6.7$ for case S20B. For case S40A, the most important 2D vortex shedding mode has a frequency of $St \approx 3.0$. The initial stages of laminar-turbulent transition are also driven by a range of 2D modes for case S40B, with peaks at $St = 1.15$ and $St = 1.8$.

In addition to a dynamic mode decomposition of the DNS results [5], a global linear stability analysis of the time- and span-averaged flow fields was performed in order to further investigate the origin of the self-sustained vortex shedding cycle. The focus of this section is to understand the underlying mechanisms that select the dominant modes that drive the vortex shedding at high sweep angles, hence the analysis will be limited here to the two-dimensional global stability problem. Extensions to three-dimensional modes are possible, but our experience to date is

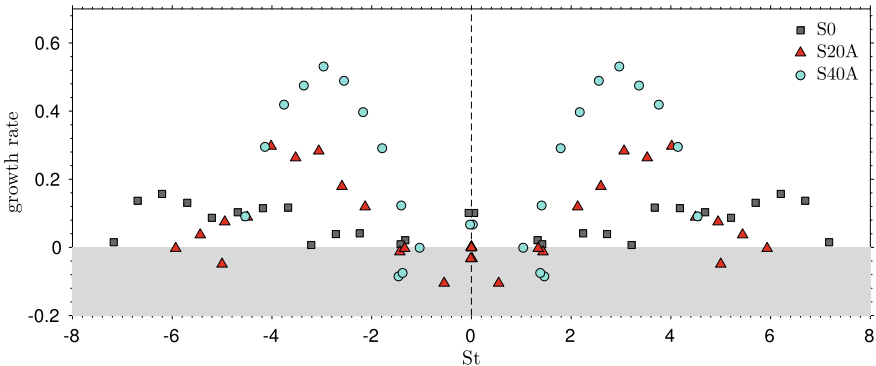


Fig. 4 Global 2D spectra for cases S0, S20A and S40A

that such modes are more susceptible to numerical issues in converging the global mode spectrum, whereas the two-dimensional modes shown here are fully converged.

Figure 4 shows the 2D ($k_z = 0$) global spectra for the different degrees of sweep. The mean flows obtained for all the different sweep angles are able to sustain the growth of 2D globally unstable modes. Increasing the sweep angle leads to the emergence of a strong global instability for the S40A case. A wider range of more weakly unstable modes is present for the lower sweep cases. The emergence of the strong global instability is a key result that explains the earlier observations of coherent structures preferentially aligned with the spanwise direction.

For case S0, Fig. 4 suggests that there are three underlying branches of instability, peaking at $St = 2.24$, $St = 3.67$ and $St = 6.20$. The second peak ($St = 3.67$) agrees well with the frequency of the strongest 2D DMD mode for this case [5]. For case S20A, the most unstable 2D global modes occur for frequencies in the range $St = 3.0 - 4.0$. The agreement between global linear stability and Fourier analyses is good in this case, with the dominant 2D DMD and Fourier modes found for frequencies $St = 2.74$ and $St = 3.0$, respectively. For case S40A a single branch of highly unstable modes can be observed, centred at $St = 2.96$. This corresponds closely to the DNS data, where the dominant Fourier modes were also found for a band of frequencies near $St = 3.0$. The consistency between the Fourier analysis of the DNS and the global stability analysis is a key finding of the present investigation.

Figure 5 shows the structure of the emerging global mode in the case with 40° sweep. Parts (a) and (b) of the figure show respectively the spanwise vorticity and velocity divergence, using the real part of the global mode eigenfunction. It can be seen that the global mode is characterised by vorticity fluctuations in the separation bubble and sound radiation from the trailing edge. Previous global stability studies [8] have also highlighted the importance of an acoustic feedback loop originating at the trailing edge as a source of disturbances for the excitation of shear layer modes in the separation bubble. In order to shed some light on the mechanisms leading to the selection of the most unstable frequencies for each case, a closer inspection of the global mode eigenfunctions is provided in Fig. 5 c and d, where the amplitude of

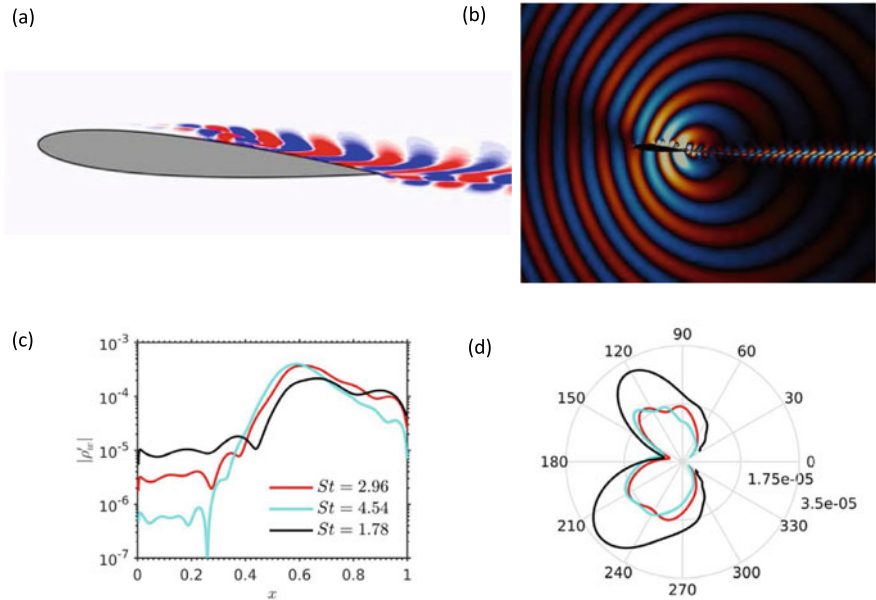


Fig. 5 Global 2D mode for case S40A: **a** real part of the spanwise vorticity at $St = 2.96$, **b** real part of the velocity divergence field at $St = 2.96$, **c** amplitude of wall density fluctuations over the suction side for various St , and **d** polar plot of the amplitude of velocity divergence fluctuations in the freestream for the same St as in (c)

the wall density over the suction side of the airfoil is plotted, together with a polar plot of the amplitude of the velocity divergence in the free stream, for a selection of Strouhal numbers. From the spatial structure of the global modes, shown on Fig. 5c, we can clearly identify regions of local spatial amplification of disturbances. The most globally unstable mode at $St = 2.96$ does not coincide with the mode showing the largest amplification across the separation bubble. Instead, the selection of the most globally amplified frequencies appears to occur via a trade off between the effectiveness of the trailing edge sound radiation, the disturbance receptivity, for example near the leading edge, as well as the strong amplitude growth in the separated shear layer.

3 Conclusion

Direct numerical simulations have been carried out to investigate the effect of sweep on the transitional separation bubbles forming on the suction side of a NACA-0012 airfoil. Laminar-turbulent transition of the separation bubble leads to the shedding of vortices at the back of the bubble, which is associated with a K-H instability of the

detached shear layer induced by the bubble. Interestingly, even for the largest sweep angle investigated ($\Lambda = 40^\circ$) no sign of crossflow instabilities were observed. The DNS data and a two-dimensional global stability analysis of the mean flows confirms that the convective instability of the shear layer is coupled with acoustic feedback originating at the airfoil's trailing edge, consistent with previous global stability studies of flows around unswept airfoils [8]. Here it was found that this is also true in the swept-wing case. The results of the global stability analysis were found to be in good agreement with the DNS data, despite the base flow for the global mode analysis being taken as the time average of the unsteady flow. Analysis of the global stability eigenmodes confirms that the selection of the most globally unstable frequencies is based on a trade-off between the convective instability of the separated shear layer and the acoustic receptivity near the leading edge of the airfoil.

Acknowledgements The authors would like to acknowledge support from EPSRC under grants EP/M822692/1 and EP/L000261/1. An extended version of this paper is available on arXiv as <https://arxiv.org/abs/1901.04727>.

References

1. Alam, M., Sandham, N.D.: Direct numerical simulation of short laminar separation bubbles with turbulent reattachment. *J. Fluid Mech.* **410**, 1–28 (2000)
2. Bagheri, S., Schlatter, P., Schmid, P.J., Henningson, D.S.: Global stability of a jet in crossflow. *J. Fluid Mech.* **624**, 33–44 (2009)
3. Barkley, D., Gomes, M.G., Henderson, R.: Three-dimensional instability in flow over a backward-facing step. *J. Fluid Mech.* **473**, 167–190 (2002)
4. Carpenter, M.H., Nordstrom, J., Gottlieb, D.: A stable and conservative interface treatment of arbitrary spatial accuracy. *J. Comput. Phys.* **148**, 341–365 (1999)
5. De Tullio, N., Sandham, N.: Direct numerical simulations and modal analysis of subsonic flow over swept airfoil sections, [arxiv:1901.04727](https://arxiv.org/abs/1901.04727) (2019)
6. Embacher, M., Fasel, H.F.: Direct numerical simulations of laminar separation bubbles: investigation of absolute instability and active flow control of transition to turbulence. *J. Fluid Mech.* **747**, 141–185 (2014)
7. Eriksson, L.E., Rizzi, A.: Computer-aided analysis of the convergence to steady state of discrete approximations to the euler equations. *J. Comput. Phys.* **57**, 90 (1985)
8. Fosas de Pando, M., Schmid, P.J., Sipp, D.: A global analysis of tonal noise in flows around aerofoils. *J. Fluid Mech.* **754**, 5–38 (2014)
9. Hetsch, T., Rist, U.: The influence of sweep on the linear stability of a series of swept laminar separation bubbles. *Eur. J. Mech. B/Fluids* **28**(4), 494–505 (2009)
10. Horton, H.P.: Laminar separation bubbles in two and three dimensional incompressible flows. PhD thesis, Queen Mary College, University of London, UK (1968)
11. Jones, L.E., Sandberg, R.D., Sandham, N.D.: Direct numerical simulations of forced and unforced separation bubbles on an airfoil at incidence. *J. Fluid Mech.* **602**, 175–207 (2008)
12. Lehoucq, R., Sorensen, D., Yang, C.: Arpack users' guide: Solution of large scale eigenvalue problems with implicitly restarted Arnoldi methods (1997)
13. Marxen, O., Lang, M., Rist, U.: Vortex formation and vortex breakup in a laminar separation bubble. *J. Fluid Mech.* **728**, 58–90 (2013)
14. Postl, D., Balzer, W., Fasel, H.F.: Control of laminar separation using pulsed vortex generator jets: direct numerical simulations. *J. Fluid Mech.* **676**, 81–109 (2011)

15. Rodriguez, D., Gennaro, E.M., Juniper, M.P.: The two classes of primary modal instability in laminar separation bubbles. *J. Fluid Mech.* **734**, R4 (2013)
16. Sandberg, R., Sandham, N.: Nonreflecting zonal characteristic boundary condition for direct numerical simulation of aerodynamic sound. *AIAA J.* **44**(2), 402–405 (2006)
17. Sandham, N.D., Li, Q., Yee, H.C.: Entropy splitting for high-order numerical simulation of compressible turbulence. *J. Comput. Phys.* **178**, 307–322 (2002)
18. Theofilis, V., Hein, S., Dallmann, U.: On the origins of unsteadiness and three-dimensionality in a laminar separation bubble. *Philos. Trans. R. Soc. Lond. A* **358**, 3229–3246 (2000)
19. Watmuff, J.H.: Evolution of a wave packet into vortex loops in a laminar separation bubble. *J. Fluid Mech.* **397**, 119–169 (1999)
20. Young, A.D., Horton, H.P.: Some results of investigations of separation bubbles. AGARD CP **4**, 780–811 (1966)

Instability of Tilted Shear Flow in a Strongly Stratified and Viscous Medium



Lloyd Fung and Yongyun Hwang

Abstract It is well known that stratification can stabilise shear flow. In a vertical shear flow, the Miles-Howard's criterion firmly indicates that flow should be stable if the local Richardson number is greater than one fourth. However, if shear is tilted with a non-zero angle from vertical, an instability can arise even under very strong stratification, and such an instability was recently observed in a titled wake flow at low Reynolds number (Meunier 2012, *J. Fluid Mech.*, 699:174). In the present study, we showed that in the limit of low Froude number and low Reynolds number, the linearised equations of motion could be reduced to the Orr-Sommerfeld equation on the horizontal plane, except the viscous term that contains vertical dissipation. Based on this equation, it is demonstrated that the low-Froude-number mode would be a horizontal inflectional instability, and should remain two dimensional at small tilting angles. It is further shown that the emergence of small vertical velocity at finite Froude number modifies the horizontal inflectional instability and leads to paradoxically stabilising buoyancy force on increasing Froude number. Finally, an absolute instability analysis is performed, revealing qualitatively good agreement with the experimental result.

1 Introduction

It is known that stratification tends to stabilise instabilities. Howard's theorem [1, 2] stated that in a stable stratification, a vertical shearing flow is always stable if the local Richardson number everywhere is greater than or equal to $1/4$. The implication is that the buoyancy force would stabilise the flow, while the shear would

L. Fung · Y. Hwang (✉)
Imperial College London Exhibition Road, London SW7 2AZ, UK
e-mail: y.hwang@imperial.ac.uk

L. Fung
e-mail: lloyd.fung@imperial.ac.uk

destabilise it, such that there exists a critical Ri that determines the necessary (but not sufficient) condition for flow instability.

However, in the recent experiment of [3], the wake behind a tilted cylinder destabilise even when the local Richardson number everywhere is greater than or equal to 1/4. Counter-intuitively, after the flow stabilised at $Ri \sim 1/4$, a further increase in stratification strength destabilises the wake into the vortex shedding again (as shown by Fig. 2 of [3]). Furthermore, the von Kármán-vortex street arises from the instability in the low Froude number (strong stratification) regime remained two-dimensional in the experiment. This is unlike the previous experiment by [4], who showed that vertical vortex columns in a strongly stratified fluid are prone to three-dimensional instability. The so-called ‘zigzag’ instability is the result of vertical lengthscale decreasing with the Froude number [5].

This work aims to understand better the instability found in the low Froude number and low Reynolds number regime and try to explain this seemingly contradicting experimental results. To this end, we perform a linear stability analysis of viscous parallel wake flow under strong stratification. A particular emphasis is given to the scaling and emergence of the low-Froude-number instability. Through the analysis, we will identify the origin of this instability and provide a theoretical justification as to why the onset remained two dimensional. Finally, We will provide an explanation as to why this instability only exists in the strongly stratified regime.

2 Equations of Motion

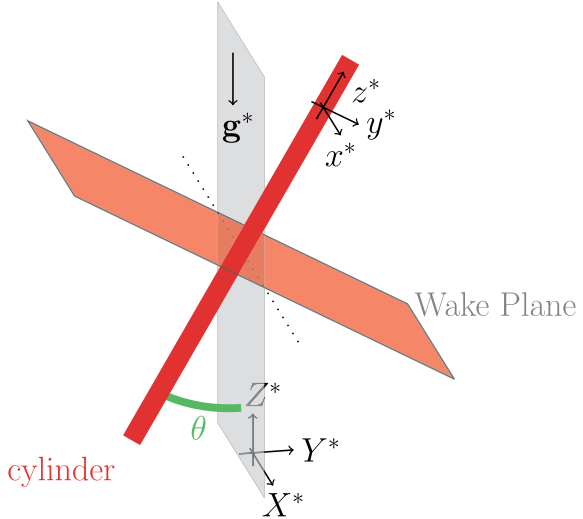
We will adopt the same Cartesian coordinate systems as those in [3], as is illustrated in Fig. 1. Note that, throughout the present study, the superscript * indicates dimensional quantities, while those without it are non-dimensionalised ones. Here, (x^*, y^*, z^*) are the coordinates aligned with a two-dimensional bluff body (i.e. cylinder), and is set to be tilted against the laboratory one defined by (X^*, Y^*, Z^*) coordinates with an angle θ . We shall assume that the base-flow (i.e. wake) profile remains to be unchanged in the (x^*, y^*, z^*) coordinates. In the (x^*, y^*, z^*) coordinate, velocity is denoted by $\mathbf{u}^* = (u^*, v^*, w^*)$ and pressure by p^* . Similarly, in the (X^*, Y^*, Z^*) coordinates, velocity is denoted by $\mathbf{U}^* = (U^*, V^*, W^*)$. Finally, the gravity is acting in the negative Z^* direction, such that the density variation is imposed along the same direction.

Under the Boussinesq approximation, the dimensionless equations of motion, defined in the (x, y, z) coordinate system, are given as follows:

$$\frac{\partial \mathbf{u}}{\partial t} + (\mathbf{u} \cdot \nabla) \mathbf{u} = -\nabla p + \frac{1}{Re} \nabla^2 \mathbf{u} + b \hat{\mathbf{g}}; \quad (1a)$$

$$\frac{\partial b}{\partial t} + (\mathbf{u} \cdot \nabla) b = \frac{1}{ReSc} \nabla^2 b, \quad (1b)$$

Fig. 1 Sketch of the flow configuration and the coordinate systems



in which $Re = U_{ref}^* D^*/\nu^*$ is the Reynolds number, $Sc = \nu^*/\kappa^*$ the Schmidt number and $\hat{\mathbf{g}}$ the unit vector representing the direction of gravity. For the density fluctuation, we consider the dimensionless buoyancy b , defined as $(g^* D^* / U_{ref}^{*2})(\rho/\rho_0)$.

Now, we consider a small perturbation around the basic state, which gives the linearised equations of motion as:

$$\frac{\partial \mathbf{u}'}{\partial t} + (\mathbf{u}_0 \cdot \nabla) \mathbf{u}' + (\mathbf{u}' \cdot \nabla) \mathbf{u}_0 = -\nabla p' + \frac{1}{Re} \nabla^2 \mathbf{u}' + b' \hat{\mathbf{g}}; \quad (2a)$$

$$\frac{\partial b'}{\partial t} + (\mathbf{u}_0 \cdot \nabla) b' + (\mathbf{u}' \cdot \nabla) (b_0/Fr^2) = \frac{1}{ReSc} \nabla^2 b', \quad (2b)$$

where ' represents the perturbation variables and $Fr = U_{ref}^* / (N^* D^*)$ with N^* being the constant Brunt-Väisälä frequency.

3 The Origin of the Instabilities in Strong Stratification

In this section, we try to identify the origin of the instability observed in the low Froude number regime. The Eq. (2b), containing Fr , can be written as

$$W' \frac{\partial b_0}{\partial Z} = Fr^2 \left[\frac{\partial}{\partial t} + u_0 \frac{\partial}{\partial X} - \frac{\nabla^2}{ReSc} \right] b'. \quad (3)$$

Now, it is not difficult to realise that the left-hand side of (3) is simply the vertical velocity fluctuation W' in the (X, Y, Z) coordinates, while $\partial b_0 / \partial Z$ is simply unity because of how we non-dimensionalised b .

Given the scope of the present study, $Fr \rightarrow 0$ will be taken, but special attention needs to be paid to the appropriate vertical lengthscale and Reynolds number in this limit. The first plausible scaling is according to [5], who proposed $W'_v = W'/Fr$ and $Z_v = ZFr$ in the limit of $Fr \rightarrow 0$, $Re \rightarrow \infty$ and $ReFr^2 \rightarrow \infty$. In this limit, (3) is given by

$$W'_v \frac{\partial b_0}{\partial Z_v} = \left[\frac{\partial}{\partial t} + u_0 \frac{\partial}{\partial X} - \frac{\nabla^2}{ReSc} \right] b'. \quad (4)$$

It is evident that this scaling is relevant to geophysical flow, as is valid at $Re \rightarrow \infty$.

However, at the onset of inflectional-type instability like the von Kármán-vortex street, the typical Reynolds number is only $Re \sim O(10)$, despite $Fr \rightarrow 0$ as in the experiment of [3]. In such a case, (3) needs to be scaled in the limit of $Fr \rightarrow 0$ and $ReFr^2 \rightarrow 0$ given the finite Reynolds number [6]. In this limit, (3) gives $W' = 0$, implying the suppression of the vertical velocity by the strong buoyancy force such that the perturbation velocity field lies only on the horizontal plane. We note that this is the same scaling as [7], but is fundamentally different to it from a physical viewpoint: in the scaling proposed here, it is the finite Reynolds number which ultimately results in $W' = 0$.

Here, it is important to emphasise that the choice between either scaling fundamentally depends on the parameter $ReFr^2$. The importance of this parameter, often called the buoyancy Reynolds number, is highlighted in Table 1, where the flow regimes of previous investigations are summarised. It is indeed seen that the experiment of [3] falls into the latter scaling featured by $ReFr^2 \rightarrow 0$. Therefore, we shall focus on studying the nature of instabilities in this regime from now on.

Now we proceed to identify the nature of the instability in the viscous and strongly stratified regime. With (3), (2) can be written as the following single equation for V' :

$$\left[\left(\frac{\partial}{\partial t} + U_0 \frac{\partial}{\partial X} - \frac{1}{Re} \left(\frac{\partial^2}{\partial X^2} + \frac{\partial^2}{\partial Y^2} + \frac{\partial^2}{\partial Z^2} \right) \right) \left(\frac{\partial^2}{\partial X^2} + \frac{\partial^2}{\partial Y^2} \right) - \frac{\partial^2 U_0}{\partial Y^2} \frac{\partial}{\partial X} \right] V' = 0. \quad (5)$$

From (5), we can make several important observations on the nature of instabilities arising in (2) when $Fr \rightarrow 0$:

1. Equation (5) is no more dependent of Fr and b' , implying that the density stratification cannot affect any instability arising from (5). Furthermore, (5) only contains the horizontal shear $\partial U_0 / \partial Y$, suggesting the barotropic nature of the possible instability at $Fr \rightarrow 0$ (i.e. instability in the horizontal plane).
2. The form of (5) is very similar to the physical-space Orr-Sommerfeld equation in the $X-Y$ plane: in fact, it is identical to the Orr-Sommerfeld equation, except the term with $\partial^2 / \partial Z^2$ in (5). Such a similarity strongly suggests that the given horizontal shear would admit an inflectional instability if $\partial^2 U_0 / \partial Y^2$ is not zero for some Y .

Table 1 A summary of two- and three-dimensional nature of primary instabilities observed in strongly stratified shear flows. Here, the acronyms indicate: H, horizontal; H/T, horizontal and tilted; 2D, two-dimensional; 3D, three-dimensional; EXP, experiment; NS, numerical simulation, LT, linear theory; NT, nonlinear theory; ST, Squire-like theorem. For the instabilities marked as ‘2D/3D’, the most unstable mode remains two dimensional, although the three-dimensional modes have growth rate close to that of two-dimensional one. For the instabilities marked as ‘2D*’, the nature of three-dimensional modes was not fully explored, despite the potential importance of this mode due to high buoyancy Reynolds number

References	Shear	$ReFr^2$	Primary instability	Approaches
[4, 8]	H	$O(10)$	3D	EXP/LT
[9]	H	∞	2D/3D	LT
[10]	H	$O(1 - 10^2)$	2D/3D	LT/NT
[11]	H	$O(10^2 - 10^4)$	3D	EXP/NS/LT
[12]	H/T	∞	2D*	LT
[3]	H/T	$O(10^{-1} - 10)$	2D	EXP/NS
Present study	H/T	$O(10^{-4} - 10)$	2D	LT with ST

3. In (5), $\partial^2/\partial Z^2$ emerges in the viscous term, implying that any vertical variation in the velocity perturbation might be stabilising via viscous dissipation. Indeed, as discussed, it is this term that prevented the scaling of [5]. We shall also see how this purely stabilising effect of the $\partial^2/\partial Z^2$ term enforced the dimensionality of the instability in Sect. 3.1.

Therefore, from (5), we can conclude that the low Fr instability observed in [3] is likely an inflectional instability on the barotropic plane, similar to the barotropic instability documented by [13, 14].

3.1 Squire’s Theorem for Weakly Tilted Shear Flows

As suggested by [9, 12], there is no Squire’s theorem stating that the most unstable mode is two dimensional in horizontal and tilted shear flows. However, the numerical results of [9] for horizontal shear flows and [12] for tilted Bickley jets showed that the most unstable mode arises when spanwise wavenumber is zero (i.e. when the mode is two-dimensional). The same is numerically true in the present case.

To demonstrate that the two-dimensional instability mode is always the most unstable one, the main technical difficulty is that the spanwise direction in the (x, y, z)

coordinates (where the base flow is defined) is not orthogonal to the direction of gravity. However, the low Froude number approximation of the equation of motion (5) relieves this difficulty. Let us consider a spanwise uniform mode in the (x, y, z) coordinates. This mode may then be interpreted as a tilted stack of horizontal modes in the (X, Y, Z) coordinates. If the given mode is uniform in the z -direction, each of these horizontal modes should have exactly the same spatial shape, but with a Y -direction shift depending on the vertical location Z . In other words, the perturbation velocity homogeneous in the z -direction should satisfy the following relation:

$$V'(t, X, Y, Z) = V'(t, X, Y - Z \tan \theta, 0). \quad (6a)$$

The same is true for the base flow $U_0(Y, Z)(= u_0(y))$ as it is uniform in the z -direction: i.e.

$$U_0(Y, Z) = U_0(Y - Z \tan \theta, 0). \quad (6b)$$

We assume that the base flow is weakly tilted (i.e. $\theta \ll 1$), so that we can introduce $\epsilon_\theta = \tan \theta$ and $Z_0 = \epsilon_\theta Z$. We take a Laplace transform to (5) in time, and apply WKBJ approximation in space, such that

$$\hat{V}(\omega, X, Y, Z) = \tilde{V}(\omega, Y; k_X, Z_0) \exp \left[\frac{i}{\epsilon_\theta} \int^{Z_0} k_Z(Z_0) dZ_0 - i\omega t + ik_X X \right], \quad (7)$$

where \hat{V} is the transformed V' , ω the frequency, $k_Z(Z_0)$ the local wavenumber in the Z -direction and k_X the streamwise wavenumber. At the leading order, (5) becomes

$$\left[\left(-i\omega + ik_X U_0 - \frac{\nabla^2}{Re} \right) (D_Y^2 - k_X^2) - ik_X D_Y^2 U_0 \right] \tilde{V}(\omega, Y; Z_0) = G(t = 0, Y; k_X, Z_0) \quad (8)$$

where $D_Y = \partial/\partial Y$ and $G(t = 0, Y; k_X, Z_0)$ is the $e^{ik_X X}$ harmonic component of initial condition, $V'(t = 0, X, Y, Z)$. Also, $\nabla^2 = D_Y^2 - k_X^2 - k_Z^2(Z_0)$ in (8). Here, it is important to note that, if $k_z(Z_0) = 0$, the stability property of (8) does not change with Z_0 due to the nature of the base flow in (6b). This then leads the following local dispersion for ω :

$$\omega = \omega_{2D} - \frac{ik_z(Z_0)^2}{Re}, \quad (9)$$

where ω_{2D} is the eigenfrequency obtained from (8) by setting $k_z(Z_0) = 0$. Using (9) and the well-known method of steepest descent used to study global instability [15], the following is obtained for the leading linear instability:

$$V(t, X, Y, Z) \sim \tilde{V}(\omega_{2D}, Y; Z_0) e^{-i\omega_{2D} t + ik_X X}, \quad (10)$$

where $\tilde{V}(\omega_{2D}, Y; Z_0)$ is the eigenmode of (8) when $k_z(Z_0) = 0$. We note that the linear operator in (8) is invariant under the transformation of $(Y; Z_0) \rightarrow (Y - Z_0 \tan \theta, 0)$ for $k_z(Z_0) = 0$. In other words, $\tilde{V}(\omega_{2D}, Y; Z_0)$ should satisfy (6a), indicating that the two-dimensional mode in the (x, y, z) coordinate should be most unstable in a slightly tilted horizontal shear flow.

4 Stabilisation of the Low Fr Instability $Fr \rightarrow \infty$

While taking $Fr \rightarrow 0$ allows us to understand the instability at low Fr as a barotropic instability, we have not explained how it stabilizes as Fr increases [3]. Here we start our analysis by extending it to the next order of Fr . We note that, from (3), $W' \sim Fr^2$. If we take $Fr^2 = \epsilon \ll 1$, the following asymptotic expansion can be written:

$$U' = U'_1 + \epsilon U'_2 + O(\epsilon^2), \quad (11)$$

$$V' = V'_1 + \epsilon V'_2 + O(\epsilon^2), \quad (12)$$

$$W' = W'_1 + \epsilon W'_2 + \epsilon^2 W'_3 + O(\epsilon^3), \quad (13)$$

$$b' = b'_1 + \epsilon b'_2 + O(\epsilon^2), \quad (14)$$

$$p' = p'_1 + \epsilon p'_2 + O(\epsilon^2). \quad (15)$$

At $O(\epsilon^{-1})$, (1b) then yields $W'_1 = 0$, retrieving (3). At $O(1)$, (1a), (1b) and the continuity equation in the (X, Y, Z) coordinates can be written as

$$\left[\frac{\partial}{\partial t} + U_0 \frac{\partial}{\partial X} - \frac{\nabla^2}{Re} \right] U'_1 + V'_1 \frac{dU_0}{dY} = - \frac{\partial p'_1}{\partial X}, \quad (16a)$$

$$\left[\frac{\partial}{\partial t} + U_0 \frac{\partial}{\partial X} - \frac{\nabla^2}{Re} \right] V'_1 = - \frac{\partial p'_1}{\partial Y}, \quad (16b)$$

$$b'_1 + \frac{\partial p'_1}{\partial Z} = 0, \quad (16c)$$

$$\frac{\partial U'_1}{\partial X} + \frac{\partial V'_1}{\partial Y} = 0, \quad (16d)$$

$$\left[\frac{\partial}{\partial t} + U_0 \frac{\partial}{\partial X} - \frac{\nabla^2}{ReSc} \right] b'_1 = W'_2. \quad (16e)$$

Here, we note that (16a, 16b, 16d) are decoupled with (16c, 16e). They can be combined to recover (5), indicating that this is merely a different derivation of (5) obtained in the (X, Y, Z) coordinates. Also, (16c) indicates the hydrostatic balance of b'_1 caused by the vertical velocity perturbation at $O(\epsilon)$ (i.e. W'_2).

Since (16) is identical to the low-Froude-number approximation of (5) given in Sect. 3, we further proceed to the next order. At $O(\epsilon)$, the equations of motion are

$$\left[\frac{\partial}{\partial t} + U_0 \frac{\partial}{\partial X} - \frac{\nabla^2}{Re} \right] U'_2 + V'_2 \frac{dU_0}{dY} + W'_2 \frac{dU_0}{dZ} = - \frac{\partial p'_2}{\partial X}, \quad (17a)$$

$$\left[\frac{\partial}{\partial t} + U_0 \frac{\partial}{\partial X} - \frac{\nabla^2}{Re} \right] V'_2 = - \frac{\partial p'_2}{\partial Y}, \quad (17b)$$

$$\left[\frac{\partial}{\partial t} + U_0 \frac{\partial}{\partial X} - \frac{\nabla^2}{Re} \right] W'_2 = - \frac{\partial p'_2}{\partial Z} - b'_2, \quad (17c)$$

$$\frac{\partial U'_2}{\partial X} + \frac{\partial V'_2}{\partial Y} + \frac{\partial W'_2}{\partial Z} = 0, \quad (17d)$$

$$\left[\frac{\partial}{\partial t} + U_0 \frac{\partial}{\partial X} - \frac{\nabla^2}{ReSc} \right] b'_2 = W'_3. \quad (17e)$$

Now, it becomes evident that the key structural difference between (16) and (17) is the presence of W'_2 in (17) – indeed, if $W'_2 = 0$, the form of (16) is identical to that of (17). This implies that the presence of the non-zero vertical velocity (i.e. W'_2) is the key player for the stabilisation mechanism of the low-Froude-number mode on increasing Fr from a very small value. Furthermore, the form of (17) suggests that there may be two possible stabilisation mechanisms played by W'_2 : one is modification of the shear instability through an interaction with the vertical shear (i.e. $W'_2(dU_0/dZ)$ in (17a)), and the other is coupling with the stabilising buoyancy through (17c). Despite the useful physical insight gained here, it is difficult to solve (17) even numerically. This is because of the unknown W'_3 in (17e), which will have to be obtained from the equations at $O(\epsilon^2)$. Unfortunately, the form of the equations at $O(\epsilon^2)$ is exactly identical to that of (17), requiring the vertical velocity perturbation at $O(\epsilon^3)$. In fact, this pattern repeats in the equations at any subsequent orders, creating a closure problem that makes it difficult to proceed any further.

5 Numerical Results

The Eq. (2) can be numerically solved as a standard stability problem, by assuming a parallel wake on the $x - y$ plane as the base flow. Here we, use the two-parameter wake profile suggested by [16] with $a = 1.34$ and $R = -1.105$ although the results presented in this section qualitatively remain the same with the change of a and R . The wake profile width and velocity also define the reference length scale D^* and the velocity scale U_{ref}^* , respectively. For the linear stability analysis, the following normal-mode solution to (2) is considered:

$$(u, v, w, b, p)^T = (\tilde{u}(y), \tilde{v}(y), \tilde{w}(y), \tilde{b}(y), \tilde{p}(y))^T \exp\{i(\alpha x + \beta z - \omega t)\}, \quad (18)$$

where α and β are given real wavenumbers in the x and z directions, and ω the complex frequency. An eigenvalue problem is then formed, in which $i\omega$ becomes the eigenvalue and $(\tilde{u}, \tilde{v}, \tilde{w}, \tilde{b}, \tilde{p})^T$ is the corresponding eigenfunction. We discretise

y using a Chebyshev collocation method [17], and solve the resulting eigenvalue problem numerically. All of the following results are computed with 300 mesh points with the wall-normal domain size of $y \in [-60.6, 60.6]$. The numerical solver is also validated by comparing with the results of [12, 18].

5.1 Numerical Analysis for Highly Tilted Shear Flows

We note that the theoretical argument in Sect. 3.1 is valid only for small θ (i.e. slightly tilted case). For a strongly tilted case where the cylinder is close to horizontal, it does not guarantee the slowly varying assumption of the base flow in the Z-direction. However, the numerical result, as shown in Fig. 2, reveals that the two-dimensional mode indeed remains to be most unstable even at tilting angle as high as $\theta = 85^\circ$. Therefore, the numerical result extends the theoretical argument for weakly tilted flow made in the previous section to the strongly tilted one. This observation is also consistent with [3], who experimentally showed that the horizontal vortex shedding emerges as the primary instability for any titling angles.

5.2 Absolute Instability

We have also computed the neutral curve for the absolute instability. Given the Squire's theorem shown in Sect. 3.1, we will focus on $\beta = 0$. In particular, we will fix θ and vary Fr progressively to find the critical Reynolds number for absolute stability Re_c for a given set of θ and Fr . To efficiently find absolute instability, the secant method is used to seek for the pinching point in the complex planes (i.e. $d\omega/d\alpha = 0$), which provides the absolute frequency $\omega_0 = \omega(\alpha_0)$ where α_0 is the absolute streamwise wavenumber.

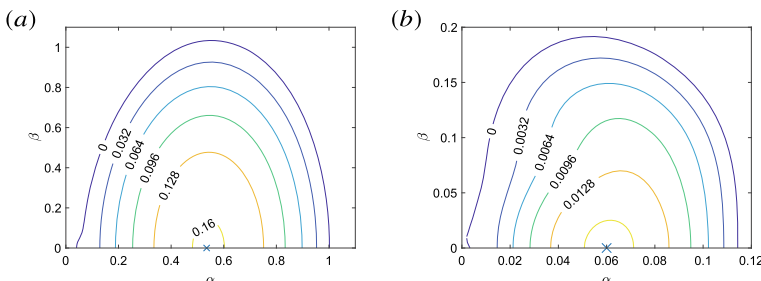


Fig. 2 Contour of the temporal growth rate ($\omega_{i,\max}$) of the most unstable mode in the real $\alpha - \beta$ plane at $Fr = 0.01$, with **a** $Re = 7.8, \theta = 30^\circ$ and **b** $Re = 50, \theta = 85^\circ$. Here, the wavenumber of the most unstable mode is indicated with the cross symbol, and it is always given for $\beta = 0$

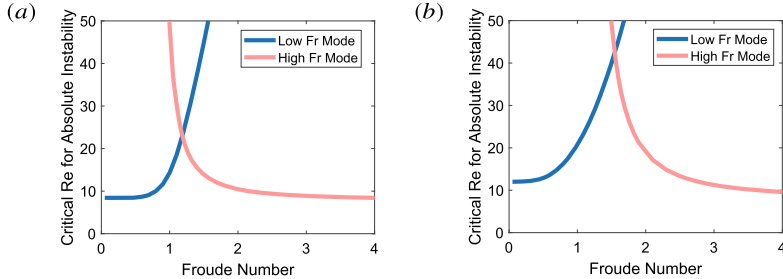


Fig. 3 The critical Reynolds number for absolute instability with respect to Froude number at **a** $\theta = 30^\circ$ and **b** $\theta = 60^\circ$

Two modes are found to be most absolutely unstable at a high and a low Froude number respectively, as shown in Fig. 3. The behaviour of the neutral stability curve is found to be very similar to that of Fig. 10 in [3]. They both show that as the Froude number decreases from the high *Fr* regime (say $Fr > 1$), the stratification tends to stabilise the flow. At some low *Fr*, the low-Froude-number mode becomes important. As its consequence, a sharp cusp emerges in the neutral Reynolds number curve (i.e. the point where the blue (dark) and pink (light) lines meet each other in Fig. 3). With a further decrease of *Fr*, the flow is more destabilised with a decrease of the critical Reynolds number. This destabilising behaviour with increasing stratification strength (decreasing Fr^2) is also consistent with the experiment. The shape and branch switching in Fig. 3 is qualitatively similar to Fig. 6 of [3], giving us good confidence that the stability analysis is a correct interpretation of the experimental result.

6 Conclusion

In the present study, we have explained the observation in [3] at low *Fr* and *Re* as a two-dimensional instability on the barotropic plane, and resolved the potential discrepancy with [4, 8, 19] by the difference in $ReFr^2$ [6]. By deriving (5) after taking $Fr \rightarrow 0$ with a suitable vertical length scale, we have also demonstrated why the instability remains two-dimensional, and proposed the potential mechanisms for stabilisation when *Fr* increases. The theoretical development proposed here is supported by the good agreement between the numerical stability analysis and the experimental result.

References

1. Howard, L.N.: *J. Fluid Mech.* **10**(4), 509 (1961)
2. Miles, J.W.: *J. Fluid Mech.* **10**(4), 496 (1961)
3. Meunier, P.: *J. Fluid Mech.* **699**, 174 (2012)
4. Billant, P., Chomaz, J.M.: *J. Fluid Mech.* **418**, 167 (2000)
5. Billant, P., Chomaz, J.M.: *Phys. Fluids* **13**(6), 1645 (2001)
6. Brethouwer, G., Billant, P., Lindborg, E., Chomaz, J.M.: *J. Fluid Mech.* **585**, 343 (2007)
7. Lilly, D.K.: *J. Atmos. Sci.* **40**(3), 749 (1983)
8. Billant, P., Chomaz, J.M.: *J. Fluid Mech.* **419**, 29 (2000)
9. Deloncle, A., Chomaz, J.M., Billant, P.: *J. Fluid Mech.* **570**, 297 (2007)
10. Lucas, D., Caulfield, C.P., Kerswell, R.R.: *J. Fluid Mech.* **832**, 409 (2017)
11. Facchini, G., Favier, B., Le Gal, P., Wang, M., Le Bars, M.: *J. Fluid Mech.* **853**, 205 (2018)
12. Candelier, J., Le Dizès, S., Millet, C.: *J. Fluid Mech.* **685**, 191 (2011)
13. Blumen, W.: *J. Atmos. Sci.* **28**(3), 340 (1971)
14. Blumen, W.: *J. Fluid Mech.* **68**(1), 177 (1975)
15. Huerre, P.; Rossi, M. In: Godreche, C., Manneville, P. (eds.) *Hydrodynamics and Nonlinear Instabilities*, pp. 81–294. Cambridge University Press, Cambridge (1998)
16. Monkewitz, P.A.: *Phys. Fluids* **31**(5), 999 (1988)
17. Weideman, J.A.C., Reddy, S.C., Trans, A.C.M.: *Math. Softw.* **26**(4), 465 (2000)
18. Hazel, P.: *J. Fluid Mech.* **51**(1), 39 (1972)
19. Billant, P., Chomaz, J.M.: *J. Fluid Mech.* **419**, 65 (2000)

Towards Understanding of Natural Boundary-Layer Transition for Low-Speed Flows via Random Excitation



Shirzad HosseiniVerdi and Hermann F. Fasel

Abstract The objective of this research is to contribute towards the understanding of ‘natural’ laminar-turbulent transition in low-speed zero-pressure-gradient boundary layers, where transition is initiated by random excitation. Toward this end, linear Secondary Instability Analysis (SIA) and Direct Numerical Simulations (DNS) are employed to investigate the effects of randomized external disturbances with a broad range of frequencies and wavenumbers on the linear and nonlinear stages of boundary-layer transition. In the present study, very low level vortical free-stream turbulence (FST) fluctuations are introduced at the inflow boundary. Since the leading-edge is not included in our simulations, the receptivity process to the FST is replaced by introducing small amplitude random disturbances generated by specifying a wall-normal velocity component across a narrow slot at the wall. This approach will allow the flow to naturally ‘select’ the relevant frequencies and wavenumbers from the broadband free-stream disturbances, which can then amplify and interact nonlinearly, and then ultimately lead to transition. The SIA results indicate that the random excitation creates randomized Tollmien-Schlichting (T-S) waves, reminiscent of the “modulated wave-trains” observed by Schubauer and Skramstad (Laminar-boundary-layer oscillations and transition on a flat plate :909, 1948 [1]) in their ‘natural’ transition experiments. Both the linear SIA and the DNS results indicate that subharmonic resonance is the dominant secondary instability mechanism. An unexpected finding from the DNS data is that in the nonlinear stages of the transition process tertiary vortices appear which are attached to the legs of the lambda structures. These tertiary structures seem to be linked to the disturbances with a frequency range that is orders of magnitude higher than the one associated with T-S waves. These preliminary results may hint that an inviscid instability mechanism may play a role in the development of these tertiary structures.

S. HosseiniVerdi (✉) · H. F. Fasel

Department of Aerospace and Mechanical Engineering, The University of Arizona,
Tucson, AZ 85721, USA

e-mail: shirzadh@email.arizona.edu

H. F. Fasel

e-mail: faselh@email.arizona.edu

1 Introduction

The landmark experiments by Schubauer and Skramstad [1] provided the first experimental evidence of the existence of instability waves (“oscillations”) inside the laminar boundary layer. Their experimental findings removed the earlier doubts [2] regarding the usefulness of the linear instability theory by Tollmien [3] and Schlichting [4] for capturing the early stage of the transition process. By reducing the free-stream turbulence level in their wind tunnel to a very low values, Schubauer and Skramstad [1] were able to observe and measure the “naturally” occurring oscillations, the so-called Tollmien-Schlichting (T-S) waves.

Schubauer and Skramstad [1] soon realized that a study of boundary-layer instability and transition could be carried with higher scientific rigor if “controlled” disturbances of known amplitude and frequency were introduced in the boundary-layer, rather than being caused by uncontrolled “natural” disturbances due to free-stream turbulence in their wind tunnel. In their “controlled” transition experiments a vibrating ribbon was placed inside the boundary layer to generate periodic two-dimensional disturbance waves. They concluded that the previously identified amplitude-modulated velocity fluctuations in their ‘natural’ (uncontrolled) experiments were linked to the T-S waves as predicted by the linear stability analysis. These controlled experiments provided strong evidence that the breakdown to turbulence is indeed a consequence of local disturbance input. Subsequently, ‘controlled’ experiments, and later direct numerical simulations based on the full Navier-Stokes equations, have been successfully employed for investigating various aspects of laminar-turbulent transition in boundary layer flows, both for low speed [5–10] and high speed [11–13].

From such detailed experimental and numerical investigations, for low-speed flows that are the focus of this paper, two markedly different arrangements of the Λ -shaped structures, which arise in the region where the disturbances become three-dimensional due to secondary instability mechanisms, were found, namely so-called aligned and staggered patterns [14]. The development of these two distinct patterns was later attributed to the two basic secondary instability mechanisms, namely (i) the so-called fundamental breakdown [5], and (ii) the subharmonic breakdown [7] based on the secondary instability theory [15].

In “controlled” transition investigations, the experimental and/or numerical conditions are tuned to produce a particular outcome by perturbing the boundary layer with only a limited number of disturbance waves. However, in a ‘natural’ transition scenario where disturbances with a broad spectrum of frequencies and a wide range of spanwise wavenumbers are present, complex interactions between all disturbance waves are possible. This was realized by Gaster and Grant [16], who introduced a new approach to model a ‘natural’ transition scenario by employing a short duration localized pulse (which generated a wave-packet) that contains a broad spectrum of wavenumbers and frequencies. In subsequent experimental and numerical studies of broad band “natural” transition by various researchers [17–19], it was found that

the weakly nonlinear stage of transition is characterized by the growth of oblique subharmonic waves.

A different approach to investigate transition was taken by Borodulin et al. [21, 22] where they carried out a set of experimental measurements for a self-similar adverse pressure gradient boundary-layer. In their experiments the transition was initiated by introducing a combination of predominantly 2-D T-S waves at a single frequency and small-amplitude, random broadband 3-D disturbances. They noted that the Λ -structures were not quite symmetrical, and they appeared in a random manner in time and space. Moreover, it was shown whereas the variation in the initial disturbance conditions led to significant changes in the instantaneous vortical structures in the late nonlinear stages of transition, the main statistical characteristics of all measured flow realizations in the post-transitional flow turned out to remain the same [23].

Investigations with both, “controlled” and wave-packet disturbances, have provided extensive and valuable knowledge regarding the linear and nonlinear stages of transition. While wave-packet investigations are more appropriate for ‘natural’ transition compared using controlled disturbances, wave-packets still lack an important characteristic of a truly ‘natural’ transition scenario, i.e. randomness of all the disturbances relative to each other. Therefore, the effect of randomness on the nonlinear stages of transition prior to the breakdown to turbulence remains an open question. The present research is aimed at providing a physics-based understanding of the breakdown mechanisms in a ‘natural’ transition scenario for zero-pressure-gradient boundary layers, when transition is initiated by random excitation. In particular, the main focus is on the effects of randomized external disturbances (with a broad spectrum of frequencies and wavenumbers) on the nonlinear stage of transition.

2 Approach

This research is motivated by the experiments of Schubauer and Skramstad [1] and Kendall [20] who investigated ‘natural’ transition for a flat-plate boundary layer. In these experiments, broadband modulated T-S waves were detected, the generation of which was attributed to free-stream turbulence (FST) via a receptivity mechanism at the leading-edge of the flat-plate. In the present study, very low level vortical FST fluctuations with an intensity of 0.05 % are introduced at the inflow boundary of the computational domain (see Fig. 1). Since the leading-edge is not included in our simulations, the receptivity process to the FST is modeled by introducing small amplitude 2-D random disturbances generated at a narrow strip at the wall (see Fig. 1) by specifying a wall-normal velocity component across a narrow slot at the wall. This approach will allow the flow to naturally ‘select’ the relevant frequencies and wavenumbers from the broadband free-stream disturbances.

It is worth noting that it is reasonable to assume that FST also generates high frequency (i.e. on the order of T-S wave frequency) oblique modes by virtue of some leading-edge receptivity mechanisms, which means that such waves should also be included in the computation. Since 2-D modes are more likely than 3-D modes to

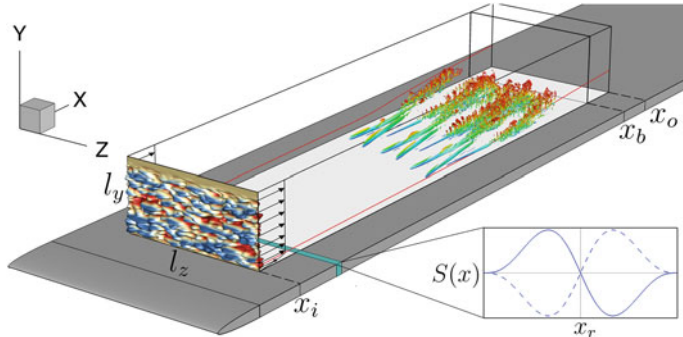


Fig. 1 Schematic of the computational set-up. Inflow/outflow locations, (x_i, x_o), and an onset of the buffer zone, x_b , are indicated in this figure as well. Random 2-D disturbances were introduced at strip (shown with green) using wall blowing/suction centered at $x_r = 1.6$. Vortical free-stream perturbations with an intensity of $Tu = 0.05\%$ are introduced at the inflow boundary

reach the first branch with small but nonzero amplitude, the present work is limited to 2-D random disturbances.

2.1 Computational Framework

Direct Numerical Simulation (DNS) of transition requires numerical methods with low numerical dispersion and dissipation errors. Therefore, an extensively validated high-order accurate Navier-Stokes solver developed in our CFD Laboratory was employed for the present numerical simulations [24]. The simulation code solves the three-dimensional, unsteady incompressible Navier-Stokes equations in vorticity-velocity formulation

$$\begin{aligned} \frac{\partial \boldsymbol{\omega}}{\partial t} &= \nabla \times (\mathbf{u} \times \boldsymbol{\omega}) + \frac{1}{Re} \nabla^2 \boldsymbol{\omega}, \\ \nabla^2 \mathbf{u} &= \nabla \times \boldsymbol{\omega}, \end{aligned} \quad (1)$$

where the vorticity, $\boldsymbol{\omega}$, is defined as the negative curl of the velocity $\boldsymbol{\omega} = -\nabla \times \mathbf{u}$. In the above equation, the global Reynolds number is defined as $Re = U_\infty^* L_\infty^*/\nu^*$, where U_∞^* and L_∞^* are reference velocity and length scales, respectively, and ν^* is the kinematic viscosity. The asterisk is used to denote dimensional quantities. Coordinates and velocities were made dimensionless with L_∞^* and U_∞^* , respectively.

The governing equations are solved in a three-dimensional Cartesian coordinate system where the streamwise, wall-normal and spanwise directions are denoted by x , y , and z , respectively, and the corresponding velocity and vorticity components are denoted by (u, v, w) and $(\omega_x, \omega_y, \omega_z)$. The governing equations are integrated in time using an explicit fourth-order Runge-Kutta scheme. All derivatives in

streamwise and wall-normal directions are approximated with fourth-order accurate compact finite differences. The flow field is assumed to be periodic in the spanwise direction. Therefore, the flow field can be expanded in Fourier cosine and sine series with a pseudo-spectral treatment of the nonlinear terms. For details of the numerical method see [24].

The computational domain for the present work is defined as $1.25 \leq x \leq 11.25$, $0 \leq y \leq 0.4$ and the domain width in the spanwise direction is $l_z = 1$. All the DNS presented in this work are carried out using the same computational grid with a resolution of $(n_x, n_y, n_z) = (2501, 160, 512)$ grid points. A Blasius profile with the displacement thickness Reynolds number of $Re_{\delta_1} = 660$ is specified at the inflow boundary of the computational domain. Near the outflow boundary, a buffer domain in region $10.4 < x < 11.25$ is employed in order to smoothly dampen out the fluctuations generated inside the domain.

2.2 Vortical Free-Stream Turbulence Generation

At the inflow boundary, the velocity and vorticity components of a Blasius profile are superimposed with velocity and vorticity fluctuations from a very low-level FST disturbances. The methodology adopted here to generate free-stream disturbances at the inflow boundary is based on a superposition of eigenmodes from the continuous spectra of the Orr-Sommerfeld (OS) and homogeneous Squire (SQ) operators [25, 26]

$$\mathbf{u}'(x_i, y, z, t) = \sum_{\omega} \sum_{k_z} A(k) \boldsymbol{\phi}(y; \omega, \gamma, \beta) e^{i(\beta z - \omega t)}. \quad (2)$$

Here, ω is the angular disturbance frequency, γ and β are the wall-normal and spanwise wavenumbers, respectively with $k = (\omega^2 + \gamma^2 + \beta^2)^{0.5}$. The dispersion relation $\alpha = \omega/U_\infty$ was used in Eq. 2 to express the streamwise wavenumber (α) in terms of the angular frequency. In the same manner, the inflow disturbance vorticity field is calculated from the disturbance velocity field as $\boldsymbol{\omega}' = -\nabla \times \mathbf{u}'$.

The eigenfunction $\boldsymbol{\phi}$ is a normalized, randomized weighted superposition of OS and SQ eigenmodes. The normalization is such that the energy of each disturbance mode is unity. Therefore, the coefficients $A(k)$ are used to determine the contribution of the eigenfunctions to the total turbulent kinetic energy. For the simulations presented in this work, the amplitudes of the individual inlet perturbations are assigned such that a von Kármán energy spectrum is obtained in the free stream. A detailed description of the implementation and validation results are provided in [27, 28].

2.3 Random Excitation Using a 2-D Blowing and Suction Slot

In the present simulations, 2-D random disturbances are introduced into the flow by specifying a wall-normal velocity component across a narrow blowing and suction slot at the wall. The forcing function has the following form

$$v_r(x, t) = A_r S(x) G(t), \quad (3)$$

where A_r is the maximum forcing amplitude and was set to $A_r = 0.0002$ for the results discussed in this paper. The shape function, $S(x)$, is a polynomial which is zero outside the suction/blowing slot (see Fig. 1, lower-right plot) and guarantees zero net volume flux over the disturbance slot at any time instant [29].

The randomness is realized through the temporal function $G(t)$, where a time signal is produced by specifying the desired Fourier spectrum of the signal and then performing an inverse FFT to generate a time series. Figure 2 shows such a signal and its corresponding frequency spectrum which exhibits a wide range of frequencies. It should be noted that the average and rms values of $G(t)$ are 0 and 1, respectively.

3 Secondary Instability Investigation

When the amplitude of a T-S wave has reached a sufficiently high level, the T-S wave and the steady mean flow together can be thought of as a new time- and streamwise-periodic base (or basic) flow that can be investigated using a Floquet-type secondary instability theory [15]. Since secondary instability (SI) is a linear mechanism, it can be studied using the linearized Navier-Stokes equations (LNSE) in the framework of a Floquet-type analysis. In the present work, the boundary-layer is perturbed by 2-D random disturbances with a broad band range of frequencies. This makes the use of the standard SI analysis [15] impractical. Our original in-house developed LNSE-based SI solver [27], which does not use any additional assumptions as required by standard SI analysis, was therefore not suitable to handle this task. Hence, we have devised a new and efficient approach for investigating spatial secondary instability for 2-D boundary layers in the presence of random excitations. The LNSE in the velocity-vorticity formulation are given by,

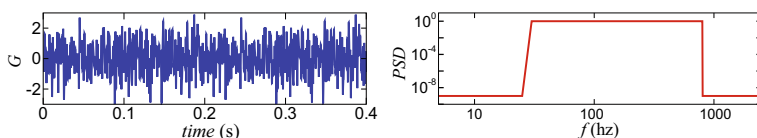


Fig. 2 Time signal of the random forcing (left) and the corresponding frequency spectrum (right)

$$\begin{aligned}\frac{\partial \boldsymbol{\omega}'}{\partial t} &= \nabla \times (\mathbf{U} \times \boldsymbol{\omega}' + \mathbf{u}' \times \boldsymbol{\Omega}) + \frac{1}{Re} \nabla^2 \boldsymbol{\omega}', \\ \nabla^2 \mathbf{u}' &= \nabla \times \boldsymbol{\omega}',\end{aligned}\quad (4)$$

where $\mathbf{U}(x, y, t)$ & $\boldsymbol{\Omega}(x, y, t)$ represent the velocity and vorticity vectors of the known baseflow and $\mathbf{u}'(x, t)$ & $\boldsymbol{\omega}'(x, t)$ are the velocity and vorticity disturbance vectors, respectively [30]. Since the baseflow is 2-D, oblique modes (3-D disturbance waves) can be decomposed as

$$\begin{aligned} [u', v', \omega_z']^T(x, y, z, t) &= [u, v, \omega_z]^T(x, y, t) \cos(\beta z), \\ [w', \omega_x', \omega_y']^T(x, y, z, t) &= [w, \omega_x, \omega_y]^T(x, y, t) \sin(\beta z),\end{aligned}\quad (5)$$

where β is the spanwise wavenumber. If a re-converged Blasius solution is used as baseflow, the solution of Eq. 4 leads to the full linear stability (including non-parallel effects) characteristics of the flat plate boundary-layer. Linear response of the boundary-layer to the 2-D disturbances introduced in the flow via random excitations are computed by solving

$$\frac{\partial \omega_z^{2D}}{\partial t} = -\frac{\partial (u_B \omega_z^{2D} + \omega_{z,B} u^{2D})}{\partial x} - \frac{\partial (v_B \omega_z^{2D} + \omega_{z,B} v^{2D})}{\partial y} + \frac{1}{Re} \nabla_{2D} \omega_z^{2D}, \quad (6)$$

where $\nabla_{2D} = \partial^2/\partial x^2 + \partial^2/\partial y^2$. In the above equation, u_B , v_B and $\omega_{z,B}$ are the (converged) Blasius solution and u^{2D} , v^{2D} and ω_z^{2D} represent the solution of LNSE for $\beta = 0$. For oblique modes ($\beta \neq 0$), which are susceptible to secondary instability, the following equation is solved

$$\frac{\partial \boldsymbol{\omega}'}{\partial t} = \nabla \times [(\mathbf{u}_B + \mathbf{u}^{2D}) \times \boldsymbol{\omega}' + \mathbf{u}' \times (\omega_{z,B} + \omega_z^{2D}) e_z] + \frac{1}{Re} \nabla^2 \boldsymbol{\omega}'. \quad (7)$$

The key aspect of the new method is that the Blasius solution is now supplemented by disturbances obtained from the solution of the 2-D modes (Eq. 6) and serves as a time-dependent baseflow for 3-D modes. It is important to note that the equations for 2-D and 3-D modes, Eqs. 6 and 7, are solved simultaneously with an explicit Runge-Kutta scheme, wherein at every sub-step the solution for 2-D modes is known and can be used to compute 3-D modes (Eq. 7).

Results from the linear SI investigation are presented in Figs. 3, 4 and 5. The solution was obtained by solving Eqs. 7 and 6 together for 13 individual 3-D spanwise wavenumbers based on the fundamental wavenumber $\beta_1 = 2\pi$. For $\beta = 0$, the random excitation introduces 2-D disturbances in the flow which superimposed on the Blasius solution constitute the baseflow for oblique modes. For nonzero β , free-stream disturbances (FSD) are introduced at the inflow boundary of the computational domain and their subsequent downstream development in the presence of the unsteady baseflow is evaluated. This is accomplished by first computing the

Fig. 3 Time signals of the disturbance u -velocity at $z = 0$ and $y = 0.009$ for various streamwise locations. Curves from top to bottom: $x_n = 3.2 + 0.8n$ for $1 \leq n \leq 7$

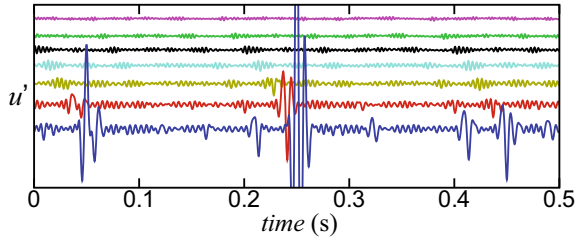


Fig. 4 Instantaneous contours of streamwise disturbance velocity in the $x - z$ plane inside the boundary-layer at $y = 0.009$

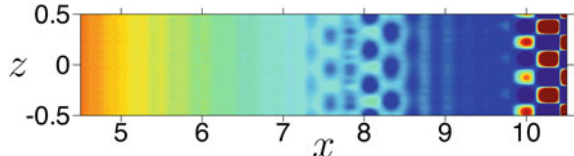
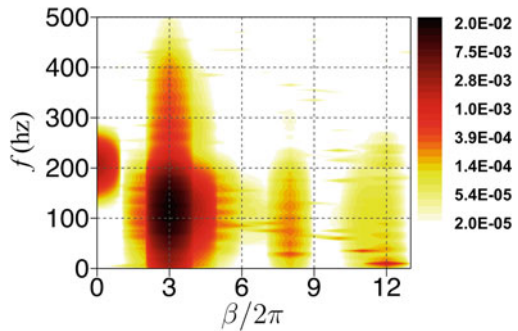


Fig. 5 Fourier spectra of the streamwise disturbance velocity in the frequency-spanwise-wavenumber plane at $x = 8.8$. Plotted are the maximum amplitudes inside the boundary layer



isotropic FST velocity and vorticity perturbations with an intensity of $Tu = 0.05\%$. Then, all the perturbations that share a similar β are grouped and introduced at the inflow boundary when solving Eq. 7 for the corresponding β . This approach leads to a realistic initial amplitude for each 3-D disturbance and allows a direct comparison with DNS. It should be noted that since FST perturbations are not symmetric, both positive and negative wavenumbers are computed for each β .

Time traces of the streamwise disturbance velocity are presented in Fig. 3 for several streamwise locations at a fixed distance from the wall in the mid-plane ($z = 0$). The solution in the physical domain is reconstructed using

$$u'(x, t) = U(x, y, t) + \sum_{m=1}^{13} u^c(x, y, t) \cos(\beta_m z) - \sum_{m=1}^{13} u^s(x, y, t) \sin(-\beta_m z), \quad (8)$$

where $U = u_B + u^{2D}$ and $\beta_m = m\beta_1$. The results indicate that the random excitation creates ‘packet’ of T-S waves. The time signals are reminiscent of ‘modulated wave-trains’ that are qualitatively similar to those observed by Schubauer & Skramstad [1]

in their ‘natural’ transition experiments, i.e. without the ‘controlled’ disturbance input using their vibrating ribbon technique. The spectral composition of these disturbances is consistent with predictions from linear stability analysis.

Traveling farther in the downstream direction at, $x = 7.2$, however, the u -velocity signal is characterized by isolated departures from the ‘linear’ pattern. These localized ‘events’ grow rapidly in amplitude with increasing streamwise distance from the leading-edge. This behaviour is an indication of a secondary instability mechanism and marks the onset of three-dimensionality.

Figure 4 displays the downstream evolution of the instantaneous u -velocity disturbance at $y = 0.009$ in the $x - z$ plane. The flow structures in the region $7.5 < x < 8.5$ appear to be linked to the onset of three-dimensionality caused by a subharmonic resonance mechanism. This conjecture is further corroborated by contours of Fourier amplitude of the disturbance u -velocity in the frequency-spanwise wavenumber ($f - \beta$) plane at $x = 8.8$ as shown in Fig. 5. In particular, the frequency range associated with the dominant oblique disturbance waves ($\beta = 3$) is about half the frequency of the dominant 2-D waves.

4 Direct Numerical Simulations

Although linear secondary instability accurately captures the onset of three-dimensionality, when the disturbance waves reach finite amplitudes, they start interacting with each other in a nonlinear fashion, which is beyond the scope of secondary instability theory. Therefore, DNS was employed for understanding the underlying nonlinear physics of transition initiated by random excitations. In particular, the focus is on the late, nonlinear stages of the transition process and on understanding if/how the flow structures evolving in that region are different from those observed in our previous transition simulations, when initiated by ‘controlled’ disturbance input or by 3-D wave-packets. It should be noted that vortical FST perturbations with an intensity of $Tu = 0.05\%$ are seeded at the inflow boundary of the computational domain while low-amplitude two-dimensional randomized disturbances are introduced in the flow at the wall (see Sects. 2.2 and 2.3).

To gain some insight into the nature and the evolution of the vortical structures in the nonlinear regime, instantaneous iso-surfaces of the λ_2 -criterion colored by u -velocity are provided in Fig. 6. The figure exhibits the formation of classical Λ -vortices with an open head, labeled 1 in Fig. 6a. These structures have counter-rotating legs that generate low-speed zones in between, with a shear-layer instability that leads to the formation of hair-pin eddies and later vortex rings, labeled 2 in Fig. 6a. A close inspection of the instantaneous flow field supports the findings obtained from the SI analysis, i.e., the development of lambda vortices in a staggered pattern.

A striking new observation is the formation of tertiary vortices (TVs) that are attached to the legs of the lambda structures in the nonlinear stages of the transition process as visualized in a close up, top-down view in Fig. 6b. The TVs have much smaller wavelength than the Λ -structure. Flow structures associated with the TVs are

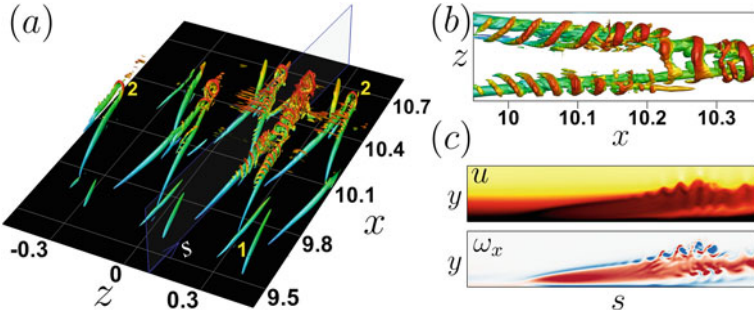


Fig. 6 **a** Instantaneous iso-surfaces of λ_2 -criterion colored by u -velocity, showing the development of staggered Δ -vortices prior to breakdown. **b** Close up top-down view of Δ -vortex exhibiting the appearance of tertiary vortices on the main vortex legs. **c** contours of streamwise velocity and vorticity along the plane passing through the left leg of the Δ -structure in (b)

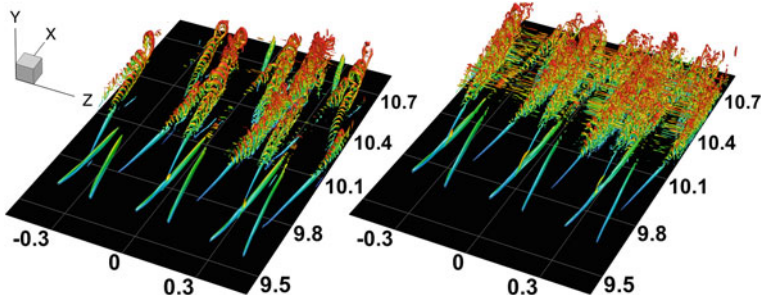


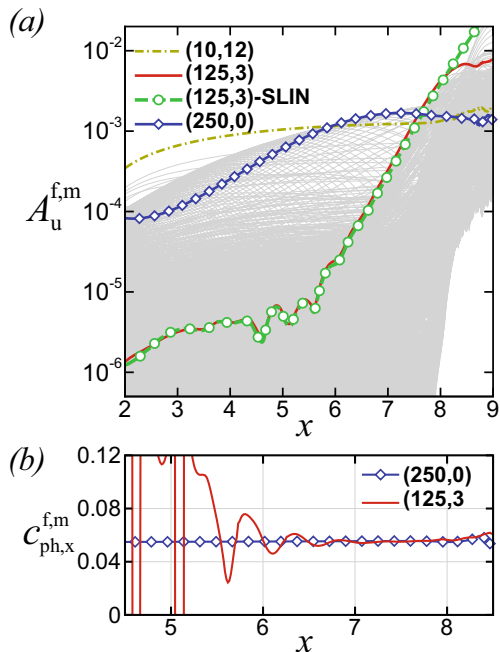
Fig. 7 Streamwise development of vortical structures shown in Fig. 6 at later time instants. Shown are perspective views of instantaneous iso-surfaces of λ_2 -criterion colored by u -velocity

further inspected by the contours of the streamwise velocity and vorticity in Fig. 6c, where they are projected onto the plane passing through one of the legs of the same vortex structure. It appears that the shear-layer adjacent to the leg exhibits a transient roll-up process, reminiscent of ‘roll-up’ of vorticity from the separated shear layer. In turn, this waviness generates inflectional velocity profiles which are highly unstable (cf. inviscid instability mechanism). It appears that a Kelvin-Helmholtz instability may be responsible for the formation of such TVs. Further, contours of ω_x -vorticity in the same plane (Fig. 6c, bottom) demonstrate that the TVs have the opposite sign compared with the vorticity of the leg. Note that red/blue contours in Fig. 6c, bottom plot, represent positive/negative values, respectively.

Figure 7 illustrates the subsequent streamwise evolution of the vortical structures presented in Fig. 6 at two later time instants. It clearly shows the generation of large numbers of TVs that are wrapped around the Δ -vortices.

Based on the results presented so far, it is conjectured that the nonlinear laminar-turbulent transition process is initiated by a “subharmonic” breakdown mechanism. By tracking the downstream development of the disturbance waves, both amplitude

Fig. 8 **a** Downstream development of Fourier amplitudes in (f, m) notation, where f is the frequency of the disturbances and $2\pi m$ is the spanwise wavenumber. Mode $(125, 3)$ -SLIN corresponds to an oblique mode obtained by the linear secondary instability analysis. **b** Phase speed development in the x -direction indicating the “phase lock-in” process between the primary 2D mode $(250, 3)$ and the dominant secondary oblique disturbance, mode $(125, 3)$



and phase speed, information can be gained regarding the nature of the instability mechanism. Toward this end, the flow data was Fourier decomposed in the spanwise direction as well as in time. The notation (f, m) is used, where f is the frequency and $2\pi m$ is the spanwise wavenumber of a disturbance wave (e.g. $m = 1$ indicates that the spanwise width of the disturbances is $\lambda_z = 1$ and for $m = 2$, $\lambda_z = 0.5$ and so on). The downstream development of the maximum u -velocity disturbance Fourier amplitude for various disturbance waves is presented in Fig. 8; note, however, that only the modes that reached high nonlinear amplitudes and relevant to the transition process are highlighted.

When isotropic FST is introduced at the inflow boundary, it generates disturbances with a wide range of frequencies and wavenumbers. However, it is well known that the boundary layer acts as a low-pass filter, allowing predominantly low-frequency modes to penetrate into the boundary layer and sheltering the high-frequency disturbances [28, 31–33]. This phenomenon is highlighted in Fig. 8a by the downstream development of mode $(10, 12)$ which attains the largest maximum amplitude for $x < 6$, although it plays no significant role in the transition process further downstream. In fact, this mode corresponds to the low-frequency, 3-D streamwise oriented disturbances, the so-called Klebanoff modes.

With the random excitation, two-dimensional disturbance modes with a wide range of frequencies are introduced at approximately the same amplitude level and develop individually in the downstream direction. When the broadband 2-D travelling waves are superimposed onto the steady mean baseflow, it forms a new baseflow,

which is time- and (approximately) streamwise-periodic and is secondarily unstable with respect to 3-D disturbances with a broad range of frequencies but a narrow range of spanwise wavenumbers. Consistent with the linear secondary stability analysis, Fig. 8a clearly shows that the strongest unsteady 3-D disturbance wave is mode (125, 3). The spanwise wavelength associated with this mode, $\lambda_z = l_z/3$, was found earlier to correspond to the spacing of the Λ -vortices (see Figs. 4, 6 and 7). The streamwise evolution of the same mode computed with our linear secondary instability solver is also included in Fig. 8a, see mode ‘(125, 3)-SLIN’, and compares very well with the results from DNS. This comparison confirms the proper implementation and accuracy of our new method for secondary instability investigations of two-dimensional boundary-layers perturbed by a wide range of frequencies. It also highlights the importance of implementing FST in the linear code, which gives correct initial amplitudes for individual 3-D waves.

The strong growth of mode (125, 3) alone does not reveal the nature of the secondary instability mechanism. In fact, the phase speed development of mode (125, 3) and the primary wave with twice the frequency, mode (250, 0), plotted in Fig. 8b provides strong evidence that the onset of transition is governed by a subharmonic resonance scenario. Once the “phase lock-in” process occurs around $x = 6$, mode (125, 3) exhibits strong streamwise exponential growth.

While the Fourier transform is a suitable tool for the linear and weakly nonlinear stages of transition, it cannot provide useful information about the localized events in the strongly nonlinear region of the transition process. Therefore, a local analysis technique, namely the Wavelet Transform (WT), is employed to extract information about large amplitude localized regions found in the time signals in the late stages of transition.

Figure 9 displays u -velocity time-signals and their respective WTs obtained for three streamwise locations at a constant distance from the wall and a fixed spanwise position. At $x = 9.65$, the signal contains two close and narrow frequency bands, centered around $f = 175$ hz and $f = 140$ hz. The first frequency band corresponds to the appearance of the 2-D T-S waves in the nonlinear regime when the boundary layer is in the ‘calmed’ period. The second band is linked to the generation of Λ -vortices which contain much higher energy than the T-S waves.

Moving further downstream at $x = 10.15$, the velocity time-signal shows the first indications of the development of higher-frequency oscillations. A close inspection of the wavelet plane shows that the frequency range of these fluctuations cover $1\text{ khz} < f < 10\text{ khz}$, which is orders of magnitude higher than the frequencies of the T-S waves and Λ -vortices. Correlating the flow structures in the same region and time period with these time signals, it was found that these high frequency oscillations are associated with the generation of the small-scale tertiary vortices. The high-frequency oscillations are even more pronounced further downstream at $x = 10.65$.

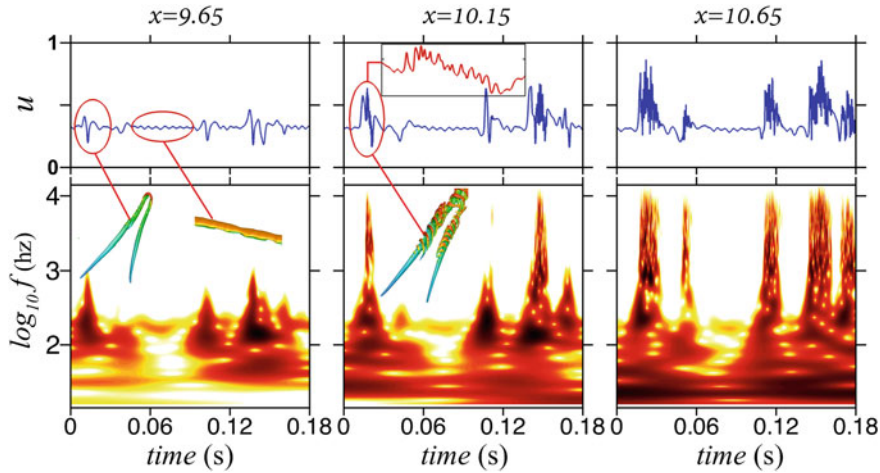


Fig. 9 Time-signals of u -velocity at $z = 0$ and $y = 0.009$ (top) and the corresponding wavelet transforms (bottom) in the nonlinear stages of the transition region

5 Conclusion

The objective of this research is to provide a physics-based understanding of the nonlinear stages and breakdown mechanisms of the transition process for a ‘natural’ transition scenario in low-speed ZPG boundary layers. This research was motivated by the experiments of Schubauer and Skramstad [1] and Kendall [20] who investigated ‘natural’ transition for a plat-plate boundary layer. In their experiments, broadband modulated T-S waves were detected, the generation of which was attributed to FST via a receptivity mechanism at the leading-edge of the flat plate. In the present study, very low level vortical FST fluctuations were introduced at the inflow boundary of the computational domain. Since the leading-edge was not included in the present simulations, its receptivity process with respect to the FST is replaced by introducing small amplitude 2-D random disturbances generated by specifying a wall-normal velocity component across a narrow slot at the wall.

The effects of randomized external disturbances on the linear and nonlinear stages of boundary-layer transition were investigated by both linear secondary instability analysis and high-fidelity DNS. The results indicate that the random excitation creates packets of amplitude-modulated T-S waves. The broadband 2-D travelling T-S waves superimposed on the Blasius solution form a new time-periodic and approximately streamwise-periodic baseflow, which is secondarily unstable to a broad range of frequencies but only to a narrowband of spanwise wavelengths, favoring a subharmonic resonance mechanism. The findings from the secondary instability analysis were corroborated by comparison with DNS results, which indicated the development of lambda vortices in a staggered pattern before the final breakdown.

Close examination of the instantaneous flow structures revealed a striking observation in the late nonlinear stage of transition, i.e. the formation of tertiary vortices embedded on the legs of the lambda vortices. These structures have much smaller wavelength than the Λ -vortices. Such structures were not observed in our previous transition simulations, neither when initiated by ‘controlled’ disturbance input, nor by 3-D wave-packets. The streamwise velocity signals and their wavelet analysis exhibited large-amplitude localized events with a frequency range orders of magnitude higher than the one associated with T-S waves. It was conjectured that the generation of the TV is linked to the inviscid instability mechanism of the intense inflectional velocity profiles of the shear layers.

Acknowledgements This work was supported by the Air Force Office of Scientific Research (AFOSR) under grant numbers FA9550-14-1-0184 and FA9550-19-1-0174, with Drs. D. Smith and G. Abate serving as the program managers, respectively. Computer time was provided by the University of Arizona High Performance Computing center.

References

1. Schubauer, G.B., Skramstad, H.K.: Laminar-boundary-layer oscillations and transition on a flat plate. NACA Tech. Rep No. p. 909 (1948)
2. Taylor, G.I.: Statistical theory of turbulence part V. effect of turbulence on boundary layer theoretical discussion of relationship between scale of turbulence and critical resistance of spheres. Proc. R. Soc. Lond. A. **156**, 307–317 (1936)
3. Tollmien, W.:Über die Entstehung der Turbulenz; 1. Mitteilung. Nachr. Ges. Wiss. Göttingen, Math. Phys. Klasse, 21–44 (1929)
4. Schlichting, H.: Zur Entstehung der Turbulenz bei der Plattenströmung. Z. Angew. Math. Mech. **13**, 171–174 (1933)
5. Klebanoff, P.S., Tidstrom, K.D., Sargent, L.M.: The three-dimensional nature of boundary-layer instability. J. Fluid Mech. **12**, 1–34 (1962)
6. Fasel, H.F.: Investigation of the stability of boundary layers by a finite-difference model of the Navier-Stokes equations. J. Fluid Mech. **18**, 355–383 (1976)
7. Kachanov, Y.S., Kozlov, V.V., Levchenko, V.Y.: Nonlinear development of a wave in a boundary layer. Izv. Akad. Nauk, SSSR Mech. Zhid Gaza 3:49–53 (1977) (in Russian); (transl. Fluid Dyn. 1987, 12:383–390)
8. Kachanov, Y.S., Levchenko, V.Y.: The resonant interaction of disturbances at laminar-turbulent transition in a boundary layer. J. Fluid Mech. **138**, 209–247 (1984)
9. Fasel, H.F., Konzelmann, U.: Non-parallel stability of a flat plate boundary layer using the complete Navier-Stokes equations. J. Fluid Mech. **221**, 311–347 (1990)
10. Fasel, H.F., Rist, U., Konzelmann, U.: Numerical investigation of the three-dimensional development in boundary-layer transition. AIAA J. **28**, 29–37 (1990)
11. Mayer, C., Wernz, S., Fasel, H.F.: Numerical investigation of the nonlinear transition regime in a Mach 2 boundary layer. J. Fluid Mech. **668**, 113–149 (2011)
12. Sivasubramanian, J., Fasel, H.F.: Direct numerical simulation of transition in a sharp cone boundary layer at Mach 6: fundamental breakdown. J. Fluid Mech. **768**, 175–218 (2015)
13. Hader, C., Fasel, H.F.: Direct numerical simulations of hypersonic boundary-layer transition for a flared cone: fundamental breakdown. J. Fluid Mech. **869**, 341–384 (2019)
14. Saric, W.S., Thomas, A.S.W.: Experiments on the subharmonic route to turbulence in boundary layers. In: Tatsumi, T. (ed.) *Turbulence and Chaotic Phenomena in Fluids*, pp. 117–22. Amsterdam, North-Holland (1984)

15. Herbert, T.: Secondary instability of boundary layers. *Annu. Rev. Fluid Mech.* **20**, 487–526 (1988)
16. Gaster, M., Grant, I.: An experimental investigation of the formation and development of a wave packet in a laminar boundary layer. *Proc. R. Soc. Lond. A.* **341**, 253–269 (1975)
17. Cohen, J., Breuer, K.S., Haritonidis, J.H.: On the evolution of a wave packet in a laminar boundary layer. *J. Fluid Mech.* **225**, 575–606 (1991)
18. Konzelmann, U., Fasel, H.F.: Numerical simulation of a three-dimensional wavepacket in a growing flat-plate boundary layer. In: *Boundary Layer Transition and Control*, pp. 1–24. The Royal Aeronautical Society (1991)
19. Yeo, K., Zhao, X., Wang, Z., Ng, K.: DNS of wavepacket evolution in a Blasius boundary layer. *J. Fluid Mech.* **652**, 333–372 (2010)
20. Kendall, J.M.: Boundary layer receptivity to freestream turbulence. In: *21st Fluid Dynamics, Plasma Dynamics and Lasers Conference*, AIAA Paper 1990–1504 (1990)
21. Borodulin, V.I., Kachanov, Y.S., Roschektayev, A.P.: Turbulence production in an APG-boundary-layer transition induced by randomized perturbations. *J. Turbul.* **7**(8), 1–30 (2006)
22. Borodulin, V.I., Kachanov, Y.S., Roschektayev, A.P.: Experimental detection of deterministic turbulence. *J. Turbul.* **12**(23), 1–34 (2011)
23. Borodulin, V.I., Kachanov, Y.S.: On properties of the deterministic turbulence and reproducibility of its instantaneous and statistical characteristics. *Theor. Appl. Mech. Lett.* **4**(6), 062004–062004–19 (2014)
24. Meitz, H.L., Fasel, H.F.: A compact-difference scheme for the Navier-Stokes equations in vorticity-velocity formulation. *J. Comput. Phys.* **157**, 371–403 (2000)
25. Jacobs, R.G., Durbin, P.A.: Simulations of bypass transition. *J. Fluid Mech.* **428**, 185–212 (2001)
26. Brandt, L., Schlatter, P., Henningson, D.S.: Transition in boundary layers subject to free-stream turbulence. *J. Fluid Mech.* **517**, 167–198 (2004)
27. Hosseinvandi, S., Fasel, H.F.: Role of Klebanoff modes in active flow control of separation: direct numerical simulations. *J. Fluid Mech.* **850**, 954–983 (2018)
28. Hosseinvandi, S., Fasel, H.F.: Numerical investigation of laminar-turbulent transition in laminar separation bubbles: the effect of free-stream turbulence. *J. Fluid Mech.* **858**, 714–759 (2019)
29. Hosseinvandi, S., Fasel, H.F.: Numerical investigation of the interaction of active flow control and Klebanoff modes. In: *47th AIAA Fluid Dynamics Conference*, AIAA 2017–4419 (2017)
30. Hosseinvandi, S., Fasel, H.F.: Onset of three-dimensionality and transition in controlled separation bubbles: secondary instability analysis and direct numerical simulations. In: *AIAA Scitech 2020 Forum*, AIAA 2020–0831 (2020)
31. Klebanoff, P.S., Tidstrom, K.D.: Evolution of amplified waves leading to transition in a boundary layer with zero pressure gradient. *NASA Tech. Note D-195* (1959)
32. Klebanoff, P.S.: Effect of free-stream turbulence on a laminar boundary layer. *Bull. Am. Phys. Soc.* **16**, 1323 (1971)
33. Hosseinvandi, S., Fasel, H.F.: Laminar-turbulent transition in a laminar separation bubble in the presence of free-stream turbulence. *Proc. IUTAM* **14**, 570–579 (2015)

On the Propagation of Two Types of Disturbances Through a Laminar Boundary Layer Subjected to Separation and Transition



Thomas J. B. Irps and Vasudevan Kanjirakkad

Abstract The propagation of two types of artificial disturbances within a boundary layer is discussed. The boundary layer is initially laminar but later transitions to become turbulent through the formation of a separation bubble under the influence of an imposed adverse pressure gradient. The growth of the boundary layer and that of the disturbances within it are tracked experimentally using hotwire anemometry measurements. The effects of the interaction of the disturbances with the separation bubble are captured using both hotwire and particle image velocimetry measurements. For a chord based Reynolds number of 210 k it is shown that Kelvin–Helmholtz shedding frequencies over the bubble are unchanged in the presence of either of the disturbances and are comparable to the steady flow case with no disturbances present. Both disturbances produced an extensive calmed region on interacting with the bubble. The calmed region due to the bar wake is relatively longer and persistent. The upstream location of the separation bubble formation is unaffected by the disturbances, however the average size of the bubble is shown to be sensitive to the type of disturbance with the bar wake producing a thinner and shorter bubble.

1 Introduction

The ability to understand, predict and control laminar separated flow transition on axial compressor and fan blades is of increasing importance to turbomachinery designers as higher efficiencies and lower emissions are continually sought. Separated boundary layer transition of flow under low Reynolds number and low free-stream turbulence conditions is particularly relevant in the front stages of aero-engine compressors operating at high altitudes and low speeds [7]. It was noted that the

T. J. B. Irps · V. Kanjirakkad (✉)

School of Engineering and Informatics, University of Sussex, Brighton, UK
e-mail: v.kanjirakkad@sussex.ac.uk

T. J. B. Irps
e-mail: T.Irps@sussex.ac.uk

Reynolds number of a compressor stator blade could reduce from a value of 1 million at sea level to nearly 200 k at an altitude of 15,000 m. The aerodynamic losses and the operability range of such compressor stages are dependent on the state of the boundary layer formed over the blades. It is of importance, therefore, that a reasonable knowledge of the transition mechanisms over such blade surfaces is available where propagation of unsteady disturbances are prevalent.

This paper discusses the propagation characteristics of two types of artificially introduced disturbances over a boundary layer subjected to laminar separation and subsequent transition to turbulent flow. The base boundary layer is formed over a flat plate subjected to a compressor blade like pressure field (over the suction side) using symmetrically contoured top and bottom walls within a wind tunnel test section. The boundary layer is initially laminar, in the accelerating part of the simulated blade profile, before undergoing deceleration within the adverse pressure gradient (APG) region resulting in separation and subsequent reattachment as turbulent boundary layer further downstream. The first of the disturbances studied is a synthetic puff introduced into the upstream laminar boundary layer using a loudspeaker (hereafter referred to as LSP). The LSP was used in the past by various researchers to generate and study the development of turbulent spots within boundary layers (e.g., [12]). The second type of disturbance studied is a propagating wake originating from a passing cylindrical bar situated upstream of the plate leading edge (hereafter referred to as BAR). Such wake-like disturbances have been used in many studies to simulate rotor–stator interaction in axial turbine and compressor research (e.g., [3]). Although the LSP is a 1-D disturbance and the BAR is a 2-D disturbance, Gostelow et al. [4] showed that there are strong similarities between their transitional breakdown processes in a turbomachinery context. Many researchers have studied the effect of APG on propagation of turbulent spots produced using triggered LSP (e.g., [11]). It was shown that the APG accelerated the growth rate of the turbulent spot compared to when no pressure gradient was present. However, the interaction of the disturbance with the separation bubble is not well understood. The effect of turbine like wakes on boundary layers with laminar separation bubble and subsequent transition was studied experimentally by Coull and Hodson [1]. It was shown that the wake induces amplified Klebanoff streaks (or K-modes) prior to the separation point and these then further destabilise the K-H instability over the separated shear layer to produce short span K-H structures. Both these phenomena have been reported to encourage early transition. The propagation of the LSP and BAR perturbations over a boundary layer subjected to a compressor like pressure field is the subject of the present investigation. The propagation and their interaction with the separation bubble and the subsequent transition process is studied using surface pressure measurements, hotwire (CTA) traverses and instantaneous PIV (particle image velocimetry). In the first part of the paper the experimental facility and methods are explained. The steady flow measurements are then compared to those from the reference geometry used in this study. The final part will illustrate the changes to the flow in the presence of both LSP and BAR.

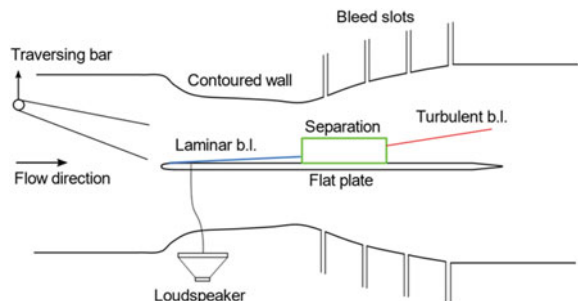
2 Experimental Setup

The experiments are conducted in a low speed blower type wind tunnel at the University of Sussex. The flow through the centrifugal blower is controlled via a variable frequency drive unit. The test section with a square cross section at its inlet features a 16.56 mm thick and 700 mm long flat plate with a super-elliptical leading edge [9]. The walls on either side of the plate are made of Perspex in order to facilitate optical access. The top and bottom walls of the test section are symmetrically curved in order to impose a pressure gradient on the plate mimicking that over a compressor blade. The compressor pressure profile selected for this study is that of the highly loaded Stator 67B that has been tested extensively within the large scale cascade at the Naval Postgraduate Research Laboratory, Monterey. A profile that matches the non-dimensional surface static pressure (C_p) distribution for the 640 k Reynolds number case as documented by Hobson et al. [7] was designed. In order to avoid separation along the profiled walls at the top and bottom, the test section was pressurised using perforated plates installed at the exit that forced air to be vented through four bleed slots located in the diverging part of the profiled wall. The trailing edge of the flat plate features a symmetric wedge. The test section layout is shown pictorially in Fig. 1.

The LSP is introduced through a small hole on the plate top surface located at 16% axial chord ($0.16 C_x$) downstream of the plate leading edge. The perturbation is triggered by a LabVIEW based code using a Farnell PG102 pulse generator connected to a loudspeaker amplifier (TDA7498). The loudspeaker used is a 150 W SoundLAB speaker with 12-inch woofer and 8Ω impedance. The loudspeaker was mounted outside of the test section and pneumatically connected to the plate using a nylon tube with 1 mm internal diameter.

The BAR disturbance has been produced using a cylindrical bar that is traversed normal to the flow direction 60% axial chord ($0.6 C_x$) upstream of the plate leading edge. The bar is 12 mm in diameter and is attached to a moving belt that passes vertically through a gap that is purposely created between the test section and the upstream duct. This method has been used by many authors, including Coull and Hodson [1] for flat plate measurements and Halstead et al. [5] as a replacement for rotor blades inside a multi-stage axial compressor. The linear speed of the bar in

Fig. 1 Test section layout



relation to the flow velocity produced a flow coefficient (ratio of air velocity to bar speed) of approximately 2.8. This is a rather large value compared to what would be the typical flow coefficient in an axial turbine or compressor in that the wake inclination to the plate surface would make a rather large foot print.

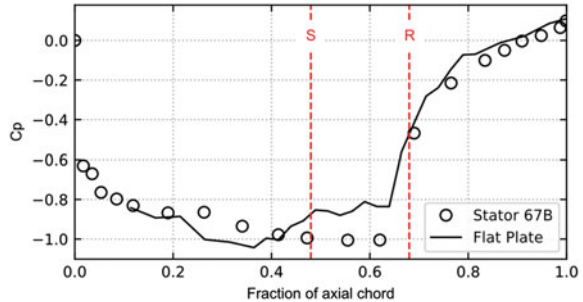
There was an intention to keep the amplitude of the velocity fluctuations within the LSP immediately downstream of its introduction to be similar to that of the BAR at the same streamwise position. However this was not successful due to attenuation within the nylon tubing. To enable ensemble measurements, both LSP and BAR disturbances were introduced at a low but regular frequency of 0.15 Hz. This ensured that the separation bubble that formed over the plate had plenty of time to fully recover after its interaction with each one of the successive disturbances. For all test cases the inlet freestream turbulence level was fixed at 0.75%. This is much lower than the turbulence contained within the wake which was measured to be in the 4–6% range during a previous commissioning study.

All the measurement reported in this paper correspond to a plate chord based Reynolds number of 210 k. For flow monitoring purposes pitot static tubes were installed to measure the flow velocity both upstream and downstream of the axial gap (as needed for the bar passing) between the test section and the upstream section. At the rear of the tunnel, static pressure measurements are taken to verify the symmetry of the flow above and below the plate. Surface static pressure was measured at a number of streamwise locations along the top surface of the plate. These are measured along a line offset from the plate centreline where PIV and CTA measurements were conducted. The surface pressures are measured using a custom-built array of pressure sensors in the range ± 2000 Pa. The flow velocity measurements within the boundary layer at selected streamwise locations were performed using both CTA traverses and PIV in the plate normal-streamwise plane. All CTA signals are obtained at a frequency of 20 kHz after analogue filtering at 10 kHz. The PIV images were processed using 32×32 cross correlation with 50% overlap. The results are then range validated and a moving average window is then applied.

3 Flow Development Under Steady Conditions

The non-dimensional pressure distribution measured under steady conditions with no artificial disturbances (hereafter referred to as ND) over the top surface of the flat plate is shown in Fig. 2. The non-dimensional pressure coefficient (C_p) is defined as: $(p_x - p_{ref})/(p_{0,ref} - p_{ref})$. Here, p_x is the local surface static pressure and $p_{0,ref}$ and p_{ref} are the reference total and static pressures respectively measured at the inlet. The measured data is compared with the Stator 67B pressure profile as described in Hobson et al. [7] for a Reynolds number of 210 k. The dotted lines annotated S and R represent the approximate location of separation ($0.49 C_x$) and reattachment ($0.69 C_x$) of the laminar separation bubble from the current experiments. These are well in agreement with the experimental observations reported by Hobson et al. [7] for 210 k Reynolds number. On comparing the two pressure distributions

Fig. 2 C_p distribution (S and R represent approximate locations of bubble separation and re-attachment)



one can see that although the pressure variation that was achieved across the bubble is lower, the rate of change of pressure and hence the level of diffusion is correctly captured. Thus, although the profiled walls in the test section were shaped to match the pressure distribution corresponding to the 640 k Reynolds number case, the above result confirms that, it can also replicate well the pressure field at 210 k Reynolds number.

For the ND case, boundary layer traverses using CTA were performed at 16 streamwise locations from immediately after the plate leading edge curvature to well beyond the bubble reattachment location. Figure 3 shows the wall normal velocity profiles at selected streamwise locations around the separation bubble. The profiles can be seen to turn from laminar to inflectional upstream of the leading edge of the bubble ($\sim 0.49 C_x$) until the re-attachment point ($\sim 0.69 C_x$). The dotted line indicates the locus of maximum u_{rms} intensity, which is measured to be very close to the point of inflection. This is similar to that reported in [2] who reasoned that this behaviour is expected as the shear present at the inflexion enhances transfer of energy from mean flow to the fluctuations.

Contours of the normalised u_{rms} intensity for the ND case is shown in Fig. 4. The intensity of fluctuations steadily increase starting from the leading edge of the separation bubble before rapidly growing to a maximum at a location very close to the re-attachment point. The rapid change in intensity near the maximum height of the bubble ($\sim 0.62 C_x$) can be identified from the bunched-up contour lines around this

Fig. 3 Boundary layer velocity profiles. S and R denote approximate locations of bubble separation and re-attachment. The red dotted line is the locus of maximum u_{rms} intensity

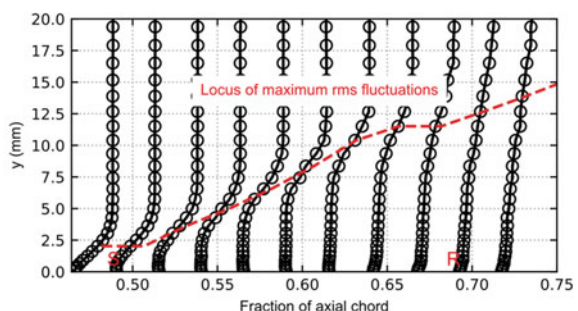
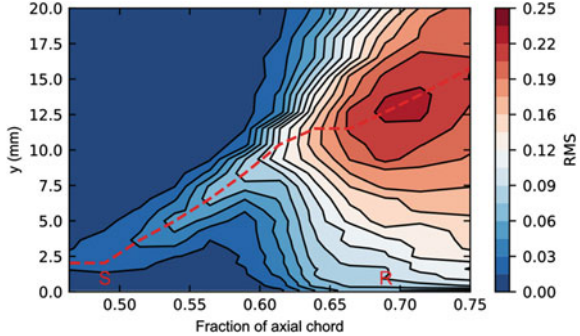


Fig. 4 Normalised u_{rms} contour plot. S and R represent approximate locations of bubble separation and re-attachment. The red dotted line is the locus of maximum u_{rms} intensity



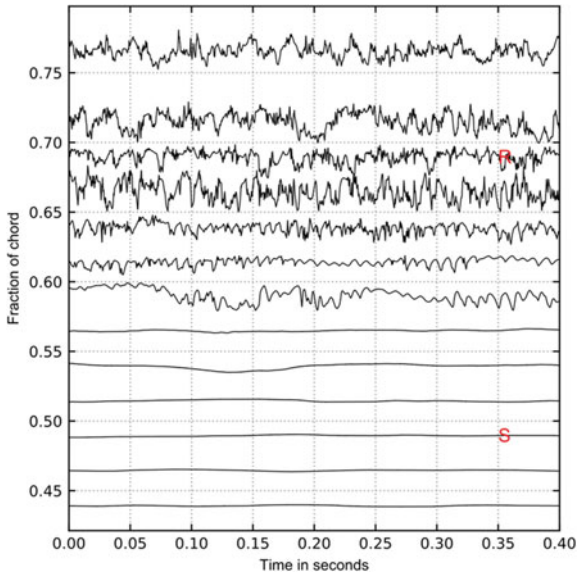
region. This pattern is consistent with that reported by Diwan and Ramesh [2] who identified an exponential growth in the u_{rms} intensity from relatively low amplitudes within the ‘dead air region’ (in the front portion of the bubble) to high values close to the maximum height location of the bubble. Such exponential growth is thought to be typical of a linear instability mechanism. Watmuff [14] and Marxen et al. [8] also observed the persistence of linear stability (exponential growth) behaviour up to streamwise locations where the normalised u_{rms} intensity has grown to 0.2 and 0.1 respectively. It is notable that in the present case the u_{rms} intensity measured near the maximum bubble height location is about 0.15. Significant amplification upstream of the reattachment indicate the growth of inherent disturbances within the rear of the bubble and in the separated shear layer. The growth pattern of these inherent disturbances is quantified and compared with that in the presence of artificially induced upstream disturbances later in the paper.

Figure 5 shows the streamwise evolution of velocity traces within the boundary layer measured along the locus of maximum u_{rms} intensity as identified in Fig. 3. The CTA signals corresponding to each streamwise location are plotted for a duration of 0.4 s. In the laminar attached region up to $0.4 C_x$ the signal is devoid of any disturbances. Low amplitude and low frequency fluctuations start to appear immediately upstream of the separation bubble at $0.49 C_x$, consistent with the u_{rms} intensity data presented in Fig. 4. At the location close $0.6 C_x$ a very clear periodic pattern starts to appear that becomes unstable downstream and eventually breaks down to a turbulent pattern close to the bubble re-attachment location. It will be shown later that the periodic pattern is a result of the K-H instability originating in the separated shear layer close to its maximum height.

4 Flow Development Under the Effect of Disturbances

This section describes the boundary layer development under the influence of the two separate artificial disturbances in the form of LSP introduced on the plate surface at $0.16 C_x$ downstream of the plate leading edge and the BAR introduced using

Fig. 5 CTA time traces showing the streamwise evolution of boundary layer for the ND case. S and R represent approximate locations of bubble separation and re-attachment



moving bars located at $0.6 C_x$ upstream of the plate leading edge. Comparison is made against the results from the ND case in order to understand the propagation of the artificially introduced disturbances and the effect of their interaction with the separation bubble. Figure 6 shows ensemble averaged velocity traces due to the LSP and BAR at a number of streamwise locations measured along the locus of maximum u_{rms} intensity. At each location, phase locked ensemble-averaging over 128 samples is carried out to make the propagating disturbances or wave-packets distinct from the random background flow. In the case of LSP, since the perturbation was introduced within the accelerating part of the boundary layer, the amplitude is low and is barely visible until amplification occurs above the front part of the bubble. This region of mild growth and low dispersion is annotated as region-I in Fig. 6a. This is followed by a region of rapid growth and dispersion, shown as region-II, where increased number of oscillations appear. Beyond $0.62 C_x$, there appears to be a different type of growth with no new oscillations but some dispersion (region-III). This may be a region of non-linear instability. Similar observations of propagating wave packets were made by Diwan and Ramesh [2]. Outside of the wave packet itself, periodic oscillations appear close to $0.6 C_x$ in a similar manner to the ND case. The periodic oscillations are therefore formed independently of the propagating artificial disturbances.

An important feature identified around $0.5 C_x$ is the appearance of a low frequency hump that resembles the ‘calmed region’ behind a turbulent spot where the boundary layer relaxes from turbulent to laminar state. The calmed regions are known to be resilient to fluctuations, resist separation and delay transition. It is clear that the periodic fluctuations that starts to appear at $0.6 C_x$ cannot penetrate into the calmed region. The extent of the ‘calming’ effect reduces further downstream.

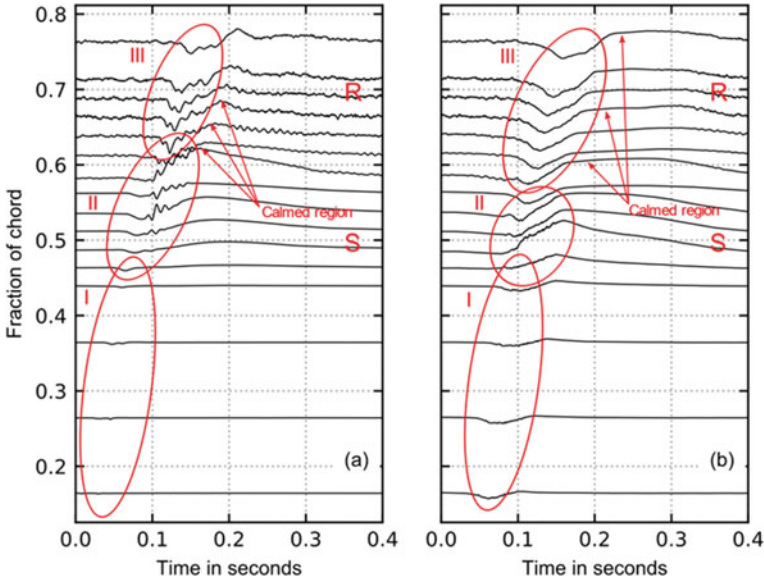


Fig. 6 Evolution of the velocity traces of the disturbances along the locus of maximum u_{rms} intensity: **a** LSP case and **b** BAR case

For the BAR case, Fig. 6b, the velocity traces exhibit three distinct regions of growth. However the signature of the mean wake is much stronger in region-I. Region-II is distinct where there is a sudden growth in the hump that follows the wake and this may be a region of linear instability, as in the LSP case, although with a shorter streamwise extent. In region-III there is further dispersion but it is mild and there are no change in the oscillation pattern. Interestingly, the low frequency hump, or calmed regions, originate almost at the same streamwise location as in the LSP case, but last for a longer duration and persist further downstream. The periodic fluctuations, although present, are not pronounced as the calmed regions associated with the wake (in this experiment) extend over a longer duration.

The rate of growth of the disturbances could be further analysed using a semi-log plot of the streamwise variation of the ensemble averaged streamwise velocity fluctuations as shown in Fig. 7. The values plotted are those measured along the locus of the maximum u_{rms} intensity as measured for the undisturbed case. The three distinct growth regions as identified while discussing the velocity traces are also seen in Fig. 7. The ND and LSP follow a similar growth pattern with a linear instability region that extends from upstream of the separation point to upstream of the maximum bubble height location. This is followed by a region of nonlinear growth. On re-attachment the fluctuations for all cases become nearly identical as the flow turns turbulent. For the BAR case, the linear instability part at the front of the bubble is much shorter. The higher u_{rms} intensity of the wake in the flow upstream is presumably due to the velocity deficit and turbulence levels within it.

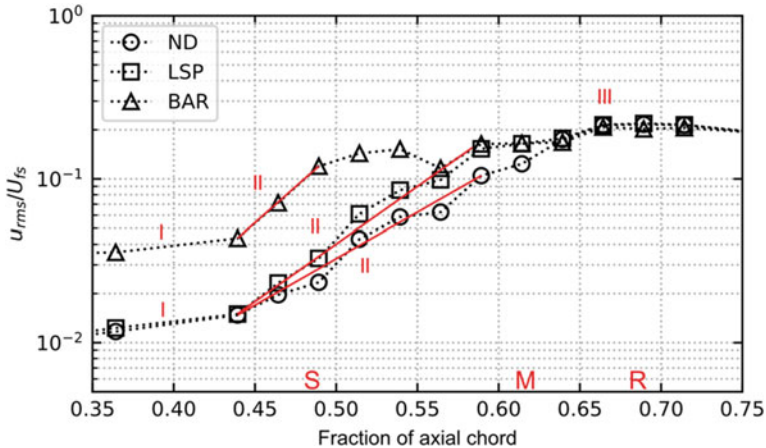
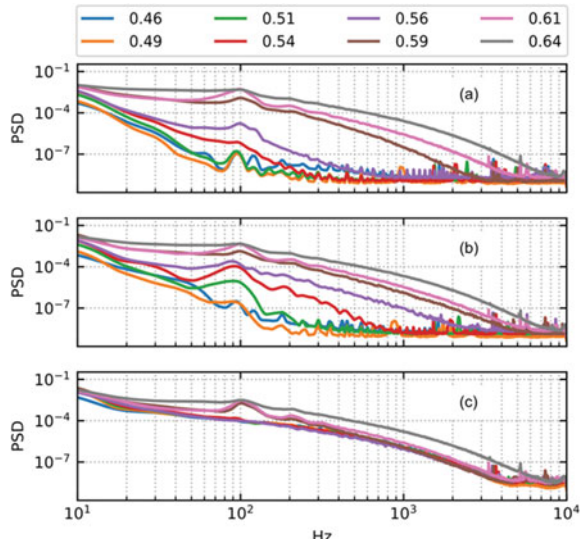


Fig. 7 Semi-log plot of ensemble averaged u_{rms} intensity. S, M and R show the approximate streamwise locations for separation, maximum bubble height and re-attachment respectively. Red lines represent the linear instability regions

Power spectra (PSD) associated with velocity traces measured along the locus of maximum u_{rms} are shown in Fig. 8 for selected streamwise locations around the separation bubble. These are calculated using the Welch periodogram technique that reduces noise in the estimated power spectra at the expense of frequency resolution. For all three disturbance scenarios (ND, LSP and BAR) a hump in frequency is visible peaking around 100 Hz. Various authors have observed such a frequency hump but some have attributed it to an amplification of T-S waves whereas others attributed

Fig. 8 Power spectral density surrounding the separation bubble: **a** ND case
b LSP case and **c** BAR case



it to K-H instability. To identify the source of the hump in the present case, the most amplified T-S wave frequency was evaluated using the correlation suggested by Walker [13]. The probable K-H instability frequency was also evaluated using a model put forward by Simoni et al. [10]. This when evaluated immediately before and after the separation bubble, the T-S frequency correlation gave values of 300 and 30 Hz respectively whereas the K-H frequency model gave values of 130 and 95 Hz respectively. It is, therefore, concluded that the hump in the present study is due to K-H instability. Moreover, no T-S activity was visible upstream of the bubble in the velocity traces for any of the disturbance scenarios.

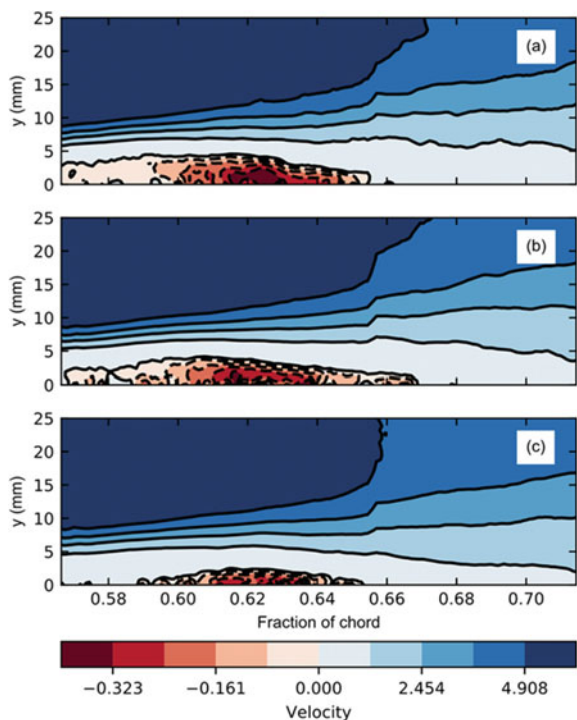
As noted previously, the turbulence level within the wake is (4–6%) higher than that in the freestream (0.75%). This can be noticed by comparing the PSD plots in Fig. 8 for the ND, LSP and BAR cases. For all streamwise locations upstream of 0.59 C_x it can be seen that the energy levels at most frequencies (except that corresponding to the periodic vortex shedding from the K-H instability) are considerably lower for both ND and LSP cases compared to the BAR case. While at high frequencies in the BAR case, the high-energy content is a result of increased turbulence levels within the wake, at low frequencies it is due to the fluctuation corresponding to the mean velocity deficit within the wake. Although not explicitly shown here, the slope of the PSD for streamwise locations $\geq 0.6 C_x$ agree with Kolmogorov's -5/3rd power law behaviour for inertial subrange for the range frequencies from 100 to 1000 Hz.

PIV measurements were carried out to visualise the development of the separation bubble under the influence of the three disturbance scenarios. Figure 9 shows bubble formation between streamwise locations 0.57 C_x and 0.71 C_x . The images shown are time averaged over a 1.0 s interval using 15 PIV realisations. This interval corresponds to double the duration for the longest disturbance due to the wake to convect through an otherwise ‘undisturbed’ flow field. The longest disturbance due to the wake corresponds to the streamwise location of 0.6 C_x as seen in Fig. 6. Although not shown here, the inception point of the ‘average bubble’ remained unchanged at $\sim 0.49 C_x$ for all three disturbance cases. However, the length, height and the size of the reverse flow region was found to vary from case to case. The reverse flow region appears to be thinner but longer in the presence of the LSP. The effect of the wake is to substantially reduce the reverse flow region both in height and length. This is understood to be the effect of the calmed region that follows the turbulent wake which can suppress separation from occurring for extended periods while the boundary layer relaxes from a fully turbulent to laminar state. Although there is a calmed region present in the LSP case, as noted before, it is much shorter in duration and is less persistent in its streamwise extent.

5 Conclusions

Wind tunnel experiments have been conducted over a flat plate subjected to flow with an adverse pressure gradient simulating the suction side of a highly loaded axial compressor blade. Under steady inlet flow conditions, without the presence of

Fig. 9 Time averaged PIV realisations showing the ‘average separation bubble’ over a 1.0 s period. **a** ND case **b** LSP case **c** BAR case



any artificial disturbances in the upstream flow, the initially laminar boundary layer undergoes separation at approximately $0.49 C_x$ and then transitions to turbulent flow on re-attachment at approximately $0.69 C_x$. After a quiescent period early on, the ‘steady flow’ boundary layer develops inherent fluctuations in the upstream part of the separation bubble that then exponentially grows suggesting the presence of a linear stability mechanism. Beyond the maximum height region of the bubble at approximately $0.62 C_x$ the growth of the fluctuation seems to be nonlinear with the maximum u_{rms} intensity found above the bubble re-attachment location. Frequencies corresponding to K-H instability in the separated shear layer over the bubble appear around $0.59 C_x$. Fluctuations under the presence of the LSP tend to grow in a very similar fashion to the ‘steady flow’ until the inception point of the bubble. Beyond this, the LSP disturbances are relatively amplified in the linear stability region. BAR produces much higher disturbance levels throughout the boundary layer until the flow becomes turbulent at which point disturbance levels for all cases become nearly identical. The presence of a calmed region is identified following both the LSP and BAR induced disturbances. The wake is seen to produce a temporarily longer and spatially (streamwise) persistent calmed region in comparison. In both cases the calmed region is shown to affect the size of the time averaged bubble.

Acknowledgements The authors would like to express their sincere gratitude to the Sussex Research Development Fund (RDF) for funding this research activity.

References

1. Coull, J.D., Hodson, H.P.: Unsteady boundary-layer transition in low-pressure turbines. *J. Fluid Mech.* **681**, 370–410 (2011)
2. Diwan, S.S., Ramesh, O.N.: On the origin of the inflectional instability of a laminar separation bubble. *J. Fluid Mech.* **629**, 263–298 (2009)
3. Gostelow, J.P., Walker, G.J., Solomon, W.J., Hong, G., Melwani, N.: Investigation of the calmed region behind a turbulent spot. *J. Turbomach.* **119**(4), 802–809 (1997)
4. Gostelow, J.P., Hodson, H.P., Walker, G.J.: Comparisons between triggered turbulent spots and unsteady transition phenomena on compressor and turbine blading. In: Fasel, H.F., Saric, W.S. (eds) Laminar-Turbulent Transition. IUTAM Symposia (International Union of Theoretical and Applied Mechanics). Springer, Berlin, Heidelberg (2000)
5. Halstead, D.E., Wisler, D.C., Okiishi, T.H., Walker, G.J., Hodson, H.P., Shin, H.: Boundary layer development in axial compressors and turbines: Part 1 of 4—composite picture. *J. Turbomach.* **119**(1), pp. 114–127 (1997)
6. Halstead, D.E., Wisler, D.C., Okiishi, T.H., Walker, G.J., Hodson, H.P., Shin, H.: Boundary layer development in axial compressors and turbines: part 2 of 4—Compressors. *J. Turbomach.* **119**(3), 426–444 (1997)
7. Hobson, G.V., Hansen, D.J., Schnorenberg, D.G., Grove, D.V.: Effect of reynolds number on separation bubbles on compressor blades in cascade. *J. Propul. Power* **17**(1), 154–162 (2001)
8. Marxen, O., Lang, M., Rist, U., Wagner, S.: A combined experimental/numerical study of unsteady phenomena in a laminar separation bubble. *Flow, Turbulence and Combustion* **71**(1), 133–146 (2003)
9. Narasimha, R., Prasad, S.N.: Leading edge shape for flat plate boundary layer studies. *Exp. Fluids* **17**(5), 358–360 (1994)
10. Simoni, D., Ubaldi, M., Zunino, P.: A simplified model predicting the Kelvin-Helmholtz instability frequency for laminar separated flows. *J. Turbomach.* **138**(044501), 1–6 (2015)
11. Van Hest, B.F.A.: Laminar-turbulent transition in boundary layers with adverse pressure gradient, PhD Thesis: TU Delft (1996)
12. Vasudevan, K.P., Dey, J., Prabhu, A.: Spot propagation characteristics in laterally strained boundary layers. *Exp. Fluids* **30**(5), 488–491 (2001)
13. Walker, G.J.: Transitional flow on axial turbomachine blading. *AIAA J.* **27**(5), 595–602 (1989)
14. Watmuff, J.H.: Evolution of a wave packet into vortex loops in a laminar separation bubble. *J. Fluid Mech.* **397**, 119–169 (1999)

Stability and Control of the Flow in a Porous Channel



Ravi Kant, Narayanan Vinod, and Uddipta Ghosh

Abstract In this article, optimally amplified growth of instabilities have been attenuated in porous channel flow through the standard wall transpiration technique (stability modifier). We have numerically investigated both modal and non-modal stability of the flow with underlying boundary condition as constant suction or injection through porous walls. The motivation behind this work is to delay the transition process in the porous channel flow. We formulate the state space model which includes control actuation as periodic suction/blowing of fluid through walls (wall transpiration). Variational method is used to compute the optimal growth of the system in the non-modal stability framework. We apply controls for both symmetric and non-symmetric base flow solutions (namely type I, type II and type III). Assuming the knowledge of full state, a linear quadratic regulator (LQR) is synthesized and an appropriate gain is feed-backed to the system to suppress the maximum amplification of optimal growth of the instabilities in the porous channel flow, which could be beneficial delaying the transition process in the flow.

Keywords Active flow control · Jeffery-Hamel flow · Optimal growth · Non-modal stability · Wall transpiration · Optimal control

1 Introduction

The flow through a channel with porous walls under the conditions of constant suction or injection is an idealization of the flow through porous medium that occurs in the real situations. It has acquired focus in recent years, owing its application

R. Kant (✉)

Pandit Deendayal Petroleum University, Gandhinagar, Gujarat 382007, India
e-mail: ravi.kant@sot.pdpu.ac.in

N. Vinod · U. Ghosh

IIT Gandhinagar, Gandhinagar, Gujarat 382355, India
e-mail: vinod@iitgn.ac.in

U. Ghosh

e-mail: uddipta.ghosh@iitgn.ac.in

in biological and engineering problems [1, 2]. It is used to model the system for flow past a biological membrane/filter. It is also useful in the modeling process of transpiration chilling/cooling, in which the boundaries of a channel carrying the overheated fluid is insulated from over-warming by transiting the cold fluid upon the outside region of the channel. The control of boundary layer flow over aircraft wings by withdrawal/pumping of fluid through the surface are few other utilizations of the porous flows. It is also useful to model the situation in the detachment of Uranium-235 and Uranium-238 isotopes by vaporised diffusion to create nuclear reactor fuel [2]. It is preferred in these situations that the flow is prohibited to prompt transition, otherwise this results in inessential flow circumstances. In order to tackle this situation, flow control is needed. It is desirable that these flow situations should not undergo quick transition otherwise it may lead to unnecessary flow conditions. In order to overcome this, flow control is required, and this will be the primary theme of this paper.

1.1 Motivation and Our Contribution

The significance of control of fluid flows are to hold back the transition processes, which results in drag reduction and flow-induced noise suppression [3]. Linear stability in flow through elementary geometries such as plane channel, converging/diverging and porous channels are well studied [4–19]. Furthermore the control of instabilities in plane Poiseuille flow [9–14, 19] and converging/diverging Jeffery-Hammel flows [20] in both modal and non-modal frameworks have also been studied, but the instability control in porous channel has not been examined previously to the best of our knowledge. It is evident that the active control of instabilities in porous channel flow has not been studied before to the best of our knowledge. In this article, we attempt a numerical study to control the non-modal optimal growth in porous channel flow.

1.2 Related Work

We now present a brief overview of the literature on stability of porous channel flows. The similarity solution of the porous channel flow with uniform suction/injection velocity through the porous walls was first studied by Berman [21] at very low Reynolds numbers ($|Re| < 1$). Similarity solutions were also validated experimentally on laminar flows in channels with wall injection [22]. Sellars [23] and Yuan [24, 25] extended the study for relatively higher positive and negative Reynolds numbers respectively. Later researchers deduced the bifurcation solution of the base flow for varying Reynolds numbers. For $0 < Re < 12.165$ there exist a unique solution of the base flow but, for $Re > 12.165$, three simultaneous solutions exist for each value of Reynolds numbers. The solutions are categorized as Type I solution, for

which the velocity profile has no inflection point. The Type II and Type III solution has inflection points in the velocity profiles. Recently, Tilton [15, 26] did the linear stability analysis (modal) for the pressure driven porous channel and concluded that the small amount of wall porosity significantly affect the Orr-Sommerfeld spectrum and can substantially decrease the stability of the porous channel flow.

2 Flow Setup and System Formulation

We now discuss the flow setup, governing equations and system formulation of the flow dynamics in state space control framework in subsequent sections. We consider the flow in the channel with porous walls with constant withdrawal or injection of fluid. The flow domain is also considered periodic in both spanwise and streamwise directions.

Figure 1 shows the graphical representation of a porous channel under constant suction velocity at walls. A linear stability analysis is carried out and will be the foundation of the subsequent state space model. The state space model comprises of a state and a measurement equation. An optimal control is synthesized on the basis of assumption that we know the full states a priori. We could also estimate the states through the measurement of wall shear stress, but to design a simplistic control model, we will confine ourself to synthesize a linear quadratic regulator (LQR) only. It is advantageous to express the disturbed flow variables in the form of wall normal vorticity and wall normal velocity. The reason being, we need to actuate the flow through mass injection at the boundaries along the wall normal direction. It has also been assumed that the actuations and sensing are to be equipped at wall boundaries in collocated manner. Here, the micro-electro mechanical systems (MEMS) jointly triggers a temporal withdrawal/pumping of fluid as a control input

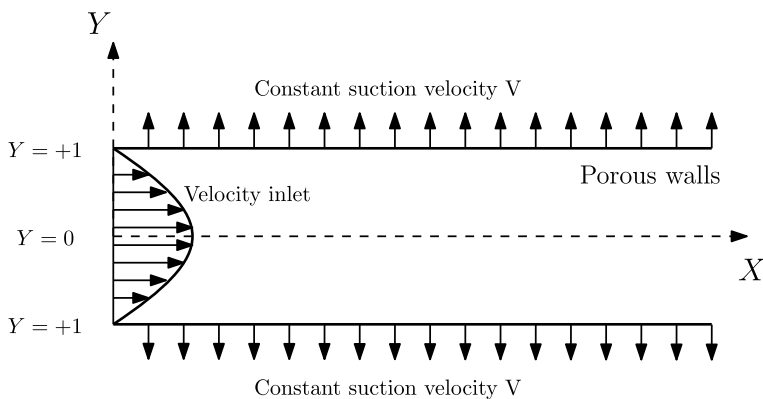


Fig. 1 Schematic of a porous channel flow

in sinusoidal [27] (also known as wall transpiration). Sinusoidal profile of actuation is supplied on top of the constant suction through walls due to the porosity. This also ensures that at any point of time, the overall mass of fluid is conserved in the domain. The measurement signals in reality may be interpreted by wall shear stress sensors. A fast Fourier transform is carried out in space (not in time) to recognize the spatial modes/frequencies (wavenumbers) constituted in the system. An appropriate controller is designed based in the aforementioned wavenumber pairs and is ready to actuate the signal. These signals are further decoupled at selected wavenumber pairs and an iFFT (inverse fast Fourier transform) is executed to produce the control actuation in actual physical domain and is provided through collocated actuators [13]. Velocity-vorticity equation is modified to include the controls, where the wall-normal velocity through the boundary is the control actuation to the model. The variational method [28] is adopted in contrast to the matrix exponential method to find the optimal growth [29]. However, both these methods ensure the accurately same solutions, we choose the variational method since it can effortlessly be unified with the state space control framework. We further preferred to select the total perturbation kinetic energy as the cost functional, for an optimal controller synthesis. A linear quadratic regulator (LQR) is synthesized in order to prevent the growth of the optimal growth function. It has been mentioned before that the optimal growth mechanism is often assumed to have non-linear triggering effects towards the system, which is responsible for prompt transition in the flow. Thus by limiting the optimal growth, we may achieve delay in the transition process.

We construct a state space model through linearly perturbed Navier-Stokes equations which include base flow variables. In this regard, the solution to the base flow equation of the porous channel flow is first obtained in the following subsection.

2.1 Base Flow Solution

We consider the flow in a porous channel with the characteristic length scale as channel half width h and characteristic velocity scale as the constant suction velocity at porous walls V . We define the Reynolds number (R_e) based on the above characteristics variables [21]. The width of the porous channel assumed to be large as compared to height of the channel. Thus for the base flow calculations, the flow is approximated to be two dimensional. We prefer to choose streamwise and wall normal dimensional co-ordinates as \bar{x} and \bar{y} respectively. The non-dimensional co-ordinates are based on local channel half width h , are $x = \bar{x}/y$ and $y = \bar{y}/y$. We may write the stream function (ψ) equation as follows,

$$\psi = h(\bar{U} - Vx)f(y) \quad (1)$$

where \bar{U} is an arbitrary velocity. The scale for non-dimensionalized pressure in the streamwise Navier-Stokes momentum equation is $\mu V/h$. We have,

$$p = f'(y) - \frac{R_e f^2(y)}{2} - \frac{\lambda x^2}{2} + Kx \quad (2)$$

where $R_e = Vh/\mu$, $K = \bar{U}\lambda/V$ and λ is the arbitrary constant 0.02 is known parameter depends on the suction or injection of fluid from porous walls. For numerical computation, let the air (kinematic viscosity $\mu = 15.06 \times 10^{-6} \frac{m^2}{s}$) injection velocity $V = 0.021 m/s$ from the duct of half width 0.01m. We eliminate p and write the equation for $f(y)$ as,

$$f'''(y) + R_e(f'^2(y) - f(y)f''(y)) - \lambda = 0 \quad (3)$$

We also consider the flow is symmetrical through the centreline of the channel. The flow is said to symmetric/asymmetric based on the bifurcation points [30]. The existence of asymmetric solutions is found in the neighbourhood of each bifurcation points. Based on bifurcation point we categories symmetric and asymmetric solutions. Thus the boundary conditions are written as, $f(0) = 0$, $f''(0) = 0$, $f(1) = 1$ and $f'(1) = 0$. For the solution for above ODE, we again differentiate with y which gives us the following form,

$$f''''(y) + R_e(f'(y)f''(y) - f(y)f'''(y)) = 0 \quad (4)$$

The modified governing equation is easy to solve since we have got rid with the constant of integration i.e. λ . We solve the above simplified governing equation by a shooting method with following initial conditions, $f(0) = 0$, $f'(0) = \text{guess1}$, $f''(0) = 0$ and $f'''(0) = \text{guess2}$ and these guess values are iteratively corrected to satisfy the leftover conditions $f(1) = 1$ and $f'(1) = 0$. It has been observed that there are three solutions to the ODE if the Reynolds number is higher than 12.165. The solutions at $Re = 14$ are categorized as type I, II and III solutions which are plotted in the Fig. 2a. The gradient of all the three base solutions are also shown in the Fig. 2b at $Re = 14$. We aim to analyze and control the non-modal optimal growth at various Reynolds numbers, wavenumbers and various base flows (Type I, II and III).

2.2 Linear Stability

We first establish the standard linear stability equation in primitive perturbations variables which include base flow solutions obtained in the previous subsection. Further, we formulate the governing equations in terms of wall normal velocity and wall normal vorticity variables as follows,

$$\frac{\partial \nabla^2 v'}{\partial t} + U \frac{\partial \nabla^2 v'}{\partial x} - \frac{d^2 U}{dy^2} \frac{\partial v'}{\partial x} - \frac{1}{Re} \nabla^2 (\nabla^2 v') = 0 \quad (5)$$

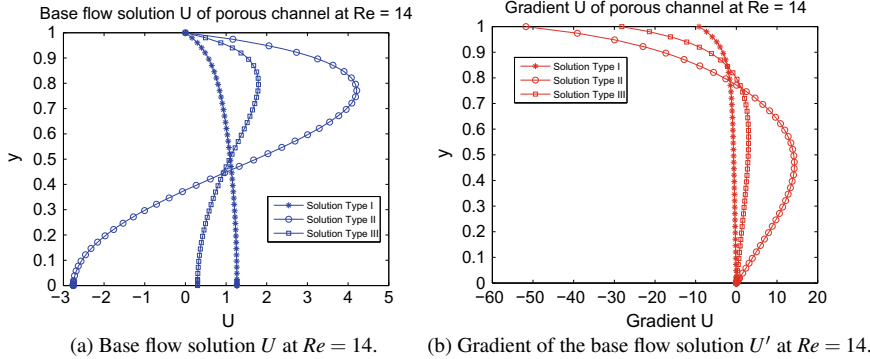


Fig. 2 Base flow solution U and gradient of the base flow solution U' at $Re = 14$

$$\frac{\partial \eta'}{\partial t} + \frac{\partial U}{\partial y} \frac{\partial v'}{\partial z} + U \frac{\partial \eta'}{\partial x} - \frac{1}{Re} \nabla^2 \eta' = 0 \quad (6)$$

We assume that the disturbance quantities can be written as a Fourier sum for all range of wavenumbers. Here each wavenumber pair can be treated independently for analysis also known as normal mode analysis. The disturbance quantities can be written in terms of its corresponding combination of all the spatial frequencies it possess. We use normal mode analysis at particular real wavenumber pairs (k_x, k_z) as,

$$v'(x, y, z, t) = \tilde{v}(y, t) e^{j(k_x x + k_z z)} \quad (7)$$

$$\eta'(x, y, z, t) = \tilde{\eta}(y, t) e^{j(k_x x + k_z z)} \quad (8)$$

where k_x and k_z are wavenumbers in streamwise x direction and spanwise z direction respectively. $\tilde{v}(y, t)$ and $\tilde{\eta}(y, t)$ are Fourier coefficients. These coefficients are function of space in general, but in the control framework, these coefficients are written by absorbing the temporal variation as well, since we require the flexibility of evolution of variables in time. The Fourier coefficients are further written as separation of variables,

$$\tilde{v}(y, t) = \sum_{n=1}^N a_{v,n}(t) \Gamma_n(y) \quad (9)$$

$$\tilde{\eta}(y, t) = \sum_{n=1}^N a_{\eta,n}(t) \Gamma_n(y) \quad (10)$$

where $a_{v,n}(t)$ and $a_{\eta,n}(t)$ are unknown coefficients which make state vector for our state space model. We substitute the perturbed velocities and vorticities in Eqs. (5) and (6) and obtain algebraic equations by discretization at finite number of Chebyshev

points. These equations are assembled in compact state space form and is the basis for our subsequent control model. Orr-Sommerfeld form [29],

$$\begin{aligned} & \left(-Uk^2 - \frac{\partial^2 U}{\partial y^2} - \frac{k^4}{jk_x Re} \right) \sum_{n=1}^N a_{v,n}(t) \Gamma_n(y) + \\ & \left(U + \frac{2k^2}{jk_x Re} \right) \sum_{n=1}^N a_{v,n}(t) \Gamma_n''(y) - \frac{1}{jk_x Re} \sum_{n=1}^N a_{v,n}(t) \Gamma_n'''(y) = \\ & \frac{j}{k_x} \left(-k^2 \sum_{n=1}^N \dot{a}_{v,n}(t) \Gamma_n(y) + \sum_{n=1}^N \dot{a}_{v,n}(t) \Gamma_n''(y) \right) \end{aligned} \quad (11)$$

$$\begin{aligned} & \left(jk_x U + \frac{k^2}{Re} \right) \sum_{n=1}^N a_{\eta,n}(t) \Gamma_n(y) - \frac{1}{Re} \sum_{n=1}^N a_{\eta,n}(t) \Gamma_n''(y) \\ & + jk_z \frac{\partial U}{\partial y} \sum_{n=1}^N a_{v,n}(t) \Gamma_n(y) = - \sum_{n=1}^N \dot{a}_{\eta,n}(t) \Gamma_n(y) \end{aligned} \quad (12)$$

where $k^2 = k_x^2 + k_z^2$, $\Gamma_n'(y)$, $\Gamma_n''(y)$, $\Gamma_n'''(y)$ are spatial derivatives of Chebyshev basis polynomials respectively. $\dot{a}_{v,n}(t)$ and $\dot{a}_{\eta,n}(t)$ are temporal derivatives of the unknown coefficients. U , U' , U'' are base velocity and its gradients, which we have already obtained by solving Eq.(2).

The Eqs.(11) and (12) assembled in the following matrix form,

$$\begin{pmatrix} \mathbf{L}_{11} & \mathbf{L}_{12} \\ \mathbf{L}_{21} & \mathbf{L}_{22} \end{pmatrix} \dot{\mathbf{X}} = \begin{pmatrix} \mathbf{A}_{11} & \mathbf{A}_{12} \\ \mathbf{A}_{21} & \mathbf{A}_{22} \end{pmatrix} \mathbf{X} \quad (13)$$

Standard open loop state space model takes the form as,

$$\dot{\mathbf{X}} = (\mathbf{L}^{-1} \mathbf{A}) \mathbf{X} \quad (14)$$

where

$$\mathbf{L} = \begin{pmatrix} \mathbf{L}_{11} & \mathbf{L}_{12} \\ \mathbf{L}_{21} & \mathbf{L}_{22} \end{pmatrix}, \mathbf{A} = \begin{pmatrix} \mathbf{A}_{11} & \mathbf{A}_{12} \\ \mathbf{A}_{21} & \mathbf{A}_{22} \end{pmatrix} \quad (15)$$

\mathbf{L} is an invertible matrix and the state vector constitutes unknown Chebyshev coefficients as,

$$\mathbf{X} = \begin{pmatrix} a_{v,1} \\ a_{v,2} \\ \vdots \\ a_{v,N} \\ a_{\eta,1} \\ a_{\eta,2} \\ \vdots \\ a_{\eta,N} \end{pmatrix} \quad (16)$$

and sub-matrices are,

$$\begin{aligned} \mathbf{A}_{11} &= \left(-k_x \mathbf{U} k^2 - k_x \mathbf{U}'' - \frac{\mathbf{I} k^4}{j Re} \right) \mathbf{D0}^{DN} \\ &\quad + \left(k_x \mathbf{U} + \frac{2 \mathbf{I} k^2}{j Re} \right) \mathbf{D2}^{DN} - \frac{\mathbf{D4}^{DN}}{j Re}; \end{aligned} \quad (17)$$

$$\mathbf{A}_{12} = [\mathbf{0}]; \quad (18)$$

$$\mathbf{A}_{21} = k_z \mathbf{U}' \mathbf{D0}^{DN}; \quad (19)$$

$$\mathbf{A}_{22} = \left(k_x \mathbf{U} + \frac{\mathbf{I} k^2}{j Re} \right) \mathbf{D0}^D - \frac{\mathbf{D2}^D}{j Re}; \quad (20)$$

$$\mathbf{L}_{11} = j(-k^2 \mathbf{D0}^{DN} + \mathbf{D2}^{DN}); \quad (21)$$

$$\mathbf{L}_{12} = [\mathbf{0}]; \quad (22)$$

$$\mathbf{L}_{21} = [\mathbf{0}]; \quad (23)$$

$$\mathbf{L}_{22} = j \mathbf{D0}^D; \quad (24)$$

where \mathbf{I} is identity matrix. $\Gamma_n(y)$, $\Gamma'_n(y)$, $\Gamma''_n(y)$, $\Gamma'''_n(y)$ are transformed into the modified Chebyshev differentiation matrices as $\mathbf{D0}^{DN}$, $\mathbf{D0}^D$, $\mathbf{D1}^{DN}$, $\mathbf{D1}^D$, $\mathbf{D2}^D$, $\mathbf{D2}^{DN}$, $\mathbf{D4}^{DN}$ to satisfy both Dirichlet and Neumann conditions (denoted by superscript DN) and only Dirichlet conditions (denoted by superscript D) also discussed in [10]. Base flow solution \mathbf{U} of porous channel flow and its derivatives \mathbf{U}' and \mathbf{U}'' have already been calculated in the previous subsection.

3 Control Framework

The linear stability equations are first integrated with that of the control, by mathematically introducing a forcing function as wall transpiration into the system. It has also previously mentioned that physically, the actuations and sensing are to be equipped at wall boundaries in collocated manner as shown in the Fig. 3. Here, the micro-electro mechanical systems (MEMS) jointly triggers a temporal withdrawal/pumping of fluid as a control input in sinusoidal [27] (also known as wall transpiration). Sinusoidal profile of actuation is supplied on top of the constant suction through walls due to

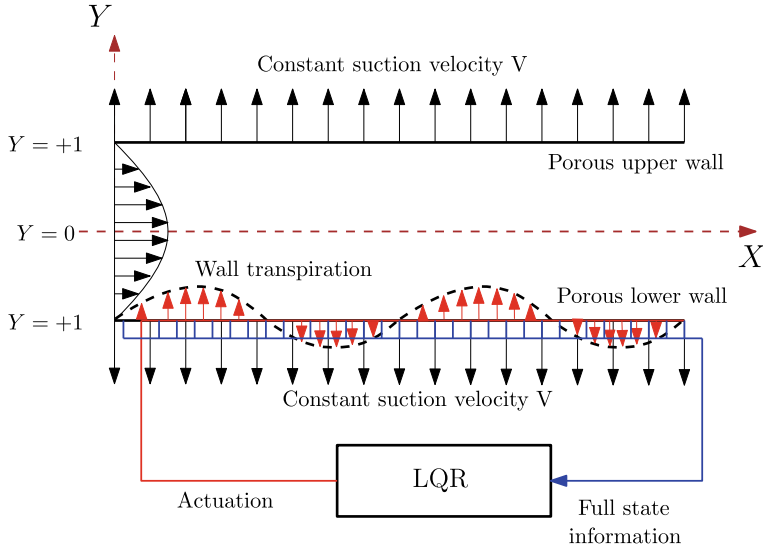


Fig. 3 Control block diagram for porous channel flow. The wall transpiration is applied on top of the suction profile

the porosity. This also ensures that at any point of time, the overall mass of fluid is conserved in the domain. The control integrated state space model is further formed. So far, the model is an open loop model. We have not included any control input \mathbf{q} as wall transpiration. Next step is to construct a state equation incorporating control as follows,

$$\dot{\mathbf{X}} = \mathbf{A}\mathbf{X} + \mathbf{B}\mathbf{q} \quad (25)$$

Similar to the Eqs. (7) and (8), we assume control input variable as,

$$q'(x, y, t) = \tilde{q}(y, t)e^{j(k_x x + k_z z)} \quad (26)$$

where $\tilde{q}(y, t)$ can be written as $\tilde{q}(y, t) = f(y)q(t)$. where $f(y)$ is taken as a known polynomial in y that satisfies a prescribed boundary conditions and $q(t)$ is the control input which is yet unknown and to be actuated through wall boundaries. Moreover the upper and lower walls are subjected to $q_u(t)$ and $q_l(t)$ respectively. Both upper and lower boundary walls are subjected to sinusoidal blowing and suction of fluid (this automatically satisfies zero net mass inflow to the system as well). For lower wall and upper walls, $\tilde{q}_l(y, t) = f_l(y)q_l(t)$ and $\tilde{q}_u(y, t) = f_u(y)q_u(t)$ expressions are used respectively. For $f_u(y)$ and $f_l(y)$, Mckernan [10] preferred to use,

$$f_l(y) = \left(\frac{y^3 - 3y + 2}{4} \right) \quad (27)$$

$$f_u(y) = \left(\frac{-y^3 + 3y + 2}{4} \right) \quad (28)$$

With the introduction of wall transpiration the regular no slip and no penetration boundary conditions of velocity-vorticity Eqs.(5) and (6) become non-homogeneous,

$$\tilde{v}(y = 1, t) = \tilde{q}_u \quad (29)$$

$$\tilde{v}(y = -1, t) = \tilde{q}_l \quad (30)$$

$$\frac{\partial \tilde{v}}{\partial y}(y = \pm 1, t) = 0 \quad (31)$$

To obtain the homogeneous form again, the following transformation can be done as described by Boyd [31],

$$\tilde{v}(y, t) = \tilde{v}_h(y, t) + f_u(y)q_u(t) + f_l(y)q_l(t) \quad (32)$$

where $\tilde{v}_h(y, t)$ is the homogeneous solution and then $f_u(y)$ and $f_l(y)$ is chosen in such a way, that

$$f_u(1) = f_l(-1) = 1 \quad (33)$$

$$f_u(-1) = f_l(1) = 0 \quad (34)$$

$$f'_u(\pm 1) = f'_l(\pm 1) = 0 \quad (35)$$

Substituting back, we get inhomogeneous equations with homogeneous boundary conditions as follows,

$$\tilde{v}(y, t) = \sum_{n=1}^N a_{v,n}(t)\Gamma_n(y) + f_u(y)q_u(t) + f_l(y)q_l(t) \quad (36)$$

$$\tilde{\eta}(y, t) = \sum_{n=1}^N a_{\eta,n}(t)\Gamma_n(y) \quad (37)$$

above equation is substituted in the Eqs.(11) and (12) and then can be assembled as,

$$\begin{aligned} & \begin{pmatrix} \mathbf{A}_{11} & \mathbf{A}_{12} \\ \mathbf{A}_{21} & \mathbf{A}_{22} \end{pmatrix} \mathbf{X} + \begin{pmatrix} \mathbf{E}_{11} & \mathbf{E}_{12} \\ \mathbf{E}_{21} & \mathbf{E}_{22} \end{pmatrix} \begin{pmatrix} q_u \\ q_l \end{pmatrix} \\ &= \begin{pmatrix} \mathbf{L}_{11} & \mathbf{L}_{12} \\ \mathbf{L}_{21} & \mathbf{L}_{22} \end{pmatrix} \dot{\mathbf{X}} + \begin{pmatrix} \mathbf{F}_{11} & \mathbf{F}_{12} \\ \mathbf{F}_{21} & \mathbf{F}_{22} \end{pmatrix} \begin{pmatrix} \dot{q}_u \\ \dot{q}_l \end{pmatrix} \end{aligned} \quad (38)$$

In compact form we may write as,

$$\mathbf{AX} + \mathbf{Eq} = \mathbf{L}\dot{\mathbf{X}} + \mathbf{F}\dot{\mathbf{q}} \quad (39)$$

where

$$\begin{aligned} \mathbf{L} &= \begin{pmatrix} \mathbf{L}_{11} & \mathbf{L}_{12} \\ \mathbf{L}_{21} & \mathbf{L}_{22} \end{pmatrix}, \mathbf{A} = \begin{pmatrix} \mathbf{A}_{11} & \mathbf{A}_{12} \\ \mathbf{A}_{21} & \mathbf{A}_{22} \end{pmatrix}, \\ \mathbf{E} &= \begin{pmatrix} \mathbf{E}_{11} & \mathbf{E}_{12} \\ \mathbf{E}_{21} & \mathbf{E}_{22} \end{pmatrix}, \mathbf{F} = \begin{pmatrix} \mathbf{F}_{11} & \mathbf{F}_{12} \\ \mathbf{F}_{21} & \mathbf{F}_{22} \end{pmatrix} \end{aligned} \quad (40)$$

and the sub-matrices $\mathbf{A}_{11}, \mathbf{A}_{12}, \mathbf{A}_{21}, \mathbf{A}_{22}$ and $\mathbf{L}_{11}, \mathbf{L}_{12}, \mathbf{L}_{21}, \mathbf{L}_{22}$ are same as depicted in Eqs. (29–36). Other sub-matrices are,

$$\mathbf{E}_{11} = \left(-k_x \mathbf{U} k^2 - k_x \mathbf{U}'' - \frac{\mathbf{I} k^4}{j Re} \right) \mathbf{f}_u + \left(-k_x \mathbf{U} + \frac{2\mathbf{I} k^2}{j Re} \right) \mathbf{f}_u''; \quad (41)$$

$$\mathbf{E}_{12} = \left(-k_x \mathbf{U} k^2 - k_x \mathbf{U}'' - \frac{\mathbf{I} k^4}{j Re} \right) \mathbf{f}_l + \left(k_x \mathbf{I} + \frac{2\mathbf{I} k^2}{j Re} \right) \mathbf{f}_l''; \quad (42)$$

$$\mathbf{E}_{21} = k_z \mathbf{U}' \mathbf{f}_u; \quad (43)$$

$$\mathbf{E}_{22} = k_z \mathbf{U}' \mathbf{f}_l; \quad (44)$$

$$\mathbf{F}_{11} = j(-k^2 \mathbf{f}_u + \mathbf{f}_u''); \quad (45)$$

$$\mathbf{F}_{12} = j(-k^2 \mathbf{f}_l + \mathbf{f}_l''); \quad (46)$$

$$\mathbf{F}_{21} = [\mathbf{0}]; \quad (47)$$

$$\mathbf{F}_{22} = [\mathbf{0}]; \quad (48)$$

where \mathbf{f}_u and \mathbf{f}_l are $diag(f_u)$ and $diag(f_l)$. In order to study the effect of lower wall boundary transpiration alone, we need to modify the Eq. (38) in such a way that we keep the upper wall as no slip boundary condition, and transpiration is only allowed through lower wall alone. To do so, all the terms associated with upper wall boundaries $f_u, f'_u, f''_u, q_u, \dot{q}_u$ are discarded. Modified form is,

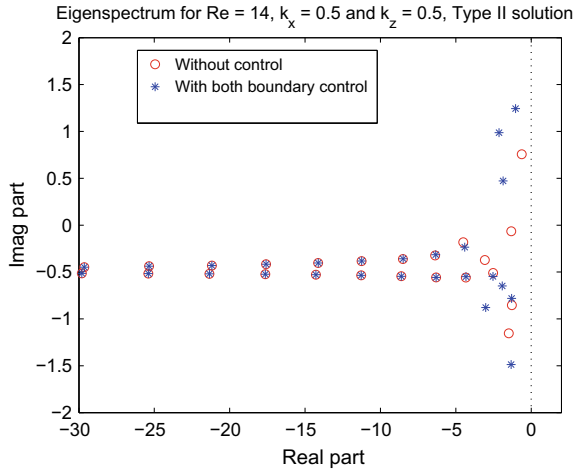
$$\begin{pmatrix} \mathbf{A}_{11} & \mathbf{A}_{12} \\ \mathbf{A}_{21} & \mathbf{A}_{22} \end{pmatrix} \mathbf{X} + \begin{pmatrix} \mathbf{E}_{12} \\ \mathbf{E}_{22} \end{pmatrix} (q_l) \quad (49)$$

$$= \begin{pmatrix} \mathbf{L}_{11} & \mathbf{L}_{12} \\ \mathbf{L}_{21} & \mathbf{L}_{22} \end{pmatrix} \dot{\mathbf{X}} + \begin{pmatrix} \mathbf{F}_{12} \\ \mathbf{F}_{22} \end{pmatrix} (\dot{q}_l) \quad (50)$$

In order to design the LQR controller, we need to augment the matrices so that the D matrix becomes null. Final state space form is augmented in following manner,

$$\dot{\mathbf{X}}_f = \mathbf{A}_f \mathbf{X}_f + \mathbf{B}_f \mathbf{u}_f \quad (51)$$

Fig. 4 Eigenspectrum of system matrix at $Re = 14$, $k_x = 0.5$ and $k_z = 0.5$ for type II solution



$$\text{where } \mathbf{A}_f = \begin{pmatrix} \mathbf{L}^{-1} \mathbf{A} & \mathbf{L}^{-1} \mathbf{E} \\ \mathbf{0} & \mathbf{0} \end{pmatrix}$$

$$\mathbf{B}_f = \begin{pmatrix} \mathbf{L}^{-1} \mathbf{F} \\ \mathbf{I} \end{pmatrix}; \mathbf{u}_f = \begin{pmatrix} \dot{q}_u \\ \dot{q}_l \end{pmatrix};$$

$$\mathbf{X}_f = (a_{v,1} a_{v,2} \dots a_{v,N} \dots a_{\eta,1} a_{\eta,2} \dots a_{\eta,N} \dots q_u q_l)^T.$$

Till this end, we can analyze the system by assessing the eigenvalues of the final system matrix \mathbf{A}_f by plotting the real and imaginary part of the eigenvalues of the system matrix, which is also known as modal analysis. In the Fig. 4, the red markers are the open loop uncontrolled eigenvalues of the system matrix for $Re = 14$, $k_x = 0.5$, $k_z = 0.5$ for type II base flow solution case.

Now we will discuss synthesis of the controller in the next subsection.

4 Control Synthesis—Linear Quadratic Regulator (LQR)

We now employ the actuated system with appropriate control strategies. One strategy would be to apply Linear quadratic regulator (LQR), if it is assumed that the full state information is available. Another way is to first estimate the states and then apply the output feedback (Linear Quadratic Gaussian LQG) to the system. In the Linear quadratic regulator (LQR) control strategy, it is assumed that the full state information of the system is available in advance. Before synthesizing controller, we need to define a cost function, which needs to be minimized. Perturbation kinetic energy would be the best candidate for this. perturbation Kinetic energy per unit volume of the system is defined in [5, 33] as,

$$E = \frac{1}{\tilde{V}} \int_{y=-1}^{y=1} \int_{x=0}^{\frac{2\pi}{k_x}} \int_{z=0}^{\frac{2\pi}{k_z}} \left(\frac{u'^2 + v'^2 + w'^2}{2} \right) dx dy dz \quad (52)$$

where $\tilde{V} = \frac{8\pi^2}{k_x k_z}$ is the volume of the domain. using Eqs.(7), (8), the Eq. 52 can be rewritten as,

$$E = \frac{1}{8k^2} \int_{-1}^1 \left(k^2 \tilde{\mathbf{v}}^T \tilde{\mathbf{v}} + \frac{\partial \tilde{\mathbf{v}}^T}{\partial y} \frac{\partial \tilde{\mathbf{v}}}{\partial y} + \tilde{\boldsymbol{\eta}}^T \tilde{\boldsymbol{\eta}} \right) dy \quad (53)$$

Discrete form is written as,

$$E = \frac{1}{8k^2} \left(\tilde{\mathbf{v}}^T \mathbf{Q}' \tilde{\mathbf{v}} + \frac{\partial \tilde{\mathbf{v}}^T}{\partial y} \mathbf{Q}' \frac{\partial \tilde{\mathbf{v}}}{\partial y} + \tilde{\boldsymbol{\eta}}^T \mathbf{Q}' \tilde{\boldsymbol{\eta}} \right) \quad (54)$$

where \mathbf{Q}' is quadrature weight matrix, $\tilde{\mathbf{v}}$ is Fourier velocity coefficient vector and $\tilde{\boldsymbol{\eta}}$ is Fourier vorticity coefficient vector also discussed in [10, 34]. The relation between velocity and state variable is given by a transformation matrix $[\mathbf{T}]$ also discussed in [10, 34]. Using transformation matrix above expressions in Eq. (57) we get,

$$E = \mathbf{X}_f^T \mathbf{Q}_f \mathbf{X}_f \quad (55)$$

where

$$\mathbf{Q}_f = \frac{1}{8k^2} \left(\mathbf{T}^T \begin{bmatrix} \mathbf{Q}' & \mathbf{0} \\ \mathbf{0} & \mathbf{Q}' \end{bmatrix} \mathbf{T} + \frac{\partial \mathbf{T}^T}{\partial y} \begin{bmatrix} \mathbf{Q}' & \mathbf{0} \\ \mathbf{0} & \mathbf{0} \end{bmatrix} \frac{\partial \mathbf{T}}{\partial y} \right) \quad (56)$$

The cost functional J is build as an integral sum of disturbance kinetic energy and a function that minimizes the control effort. An optimal feedback control gain (K) is to be obtained (in the view of control law $\mathbf{u}_f = -K \mathbf{X}_f$), such that the J is minimized, which is written as,

$$J = \int_0^\infty (\mathbf{X}_f^T \mathbf{Q}_f \mathbf{X}_f + \mathbf{u}_f^T \mathbf{R} \mathbf{u}_f) dt \quad (57)$$

subjected to the dynamic constraint as final state equation, where \mathbf{Q}_f is described through the Eq.(56) and \mathbf{R} is a weighted matrix (generally an positive definite identity matrix) in order to minimize the control effort. We then find an optimal gain \mathbf{K} upon solving algebraic Riccati equation [32]. Subsequently we acquire the feedback control law $\mathbf{u}_f = -K \mathbf{X}_f$ to obtain the closed loop dynamical evolution of the plant. Once the optimal gain \mathbf{K} is found out, the eigenvalues of closed loop system ($\mathbf{A}_f - \mathbf{B}_f \mathbf{K}$) is obtained in the view of modal analysis and it is shown in the Fig. 4 with closed loop plants eigenspectrum (with blue marker) along with open

loop eigenspectrum (red marker). We see the most unstable eigenmodes are pulled back in stable half plane with application of control inputs.

4.1 Non-modal Stability

Modal analysis characterizes the system at larger times only, it doesn't provide the details at transient times. In view of this, a non-modal stability approach is adopted for better characterizing the stability at transient times [29]. Optimal growth $G(t)$ is defined in [5], as a measure of greatest possible growth in energy with any initial perturbation at time t as,

$$G(t) = \max_{X_f(0)} \frac{||E(X_f(t))||}{||E(X_f(0))||} \quad (58)$$

Also maximum growth function G_{max} is defined as,

$$G_{max} = \max_{t>0} G(t) \quad (59)$$

Unlike the method adopted by Henningson [5] to calculate optimal growth, we will use variational method approach as described by Butler et al. [28]. Time evolution of state with any initial state is found out using,

$$\mathbf{X}_f^T = \boldsymbol{\psi} e^{\Lambda t} \mathbf{X}_{f,0}^T \quad (60)$$

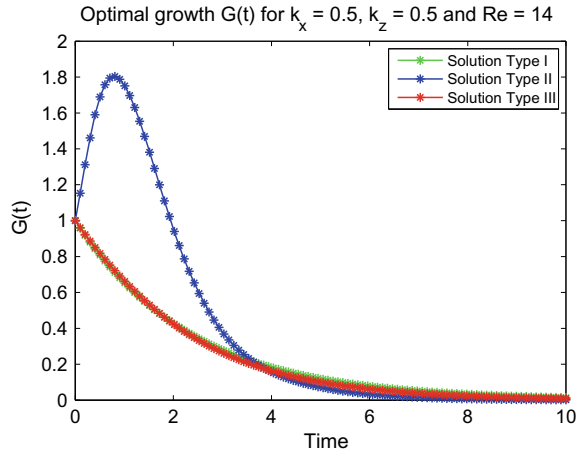
where $\boldsymbol{\psi}$ and Λ are eigenvectors and diagonal eigenvalue matrix associated with \mathbf{A}_f respectively and $\mathbf{X}_{f,0}$ is unknown initial state of the system. The worst initial state influences the system undergo the most unstable transient growth. Another way to define the quantity $G(t)$ as the largest possible value of $E(X_f(t))$ from unit initial condition ($E(X_{f,0}) = 1$) [34] as,

$$G(t) = \max_{E(X_{f,0})=1} ||E(X_f(t))|| \quad (61)$$

$$G(t) = \max_{\mathbf{X}_{f,0}^T \boldsymbol{\psi}^T \mathbf{Q}_f \boldsymbol{\psi} \mathbf{X}_{f,0}=1} \mathbf{X}_{f,0}^T e^{\Lambda^T t} \boldsymbol{\psi}^T \mathbf{Q}_f \boldsymbol{\psi} e^{\Lambda^T t} \mathbf{X}_{f,0} \quad (62)$$

This is a variational problem, which is used to get the solution of above optimization problem. A Lagrange multiplier (ζ) is chosen for above optimization problem such that,

Fig. 5 Optimal growth $G(t)$ at $Re = 14$, $k_x = 0.5$ and $k_z = 0.5$ for all the three Solution Types I, II and III



$$\frac{\partial}{\partial X_0} [\mathbf{X}_{f,0}^T e^{\Lambda^T t} \boldsymbol{\psi}^T \mathbf{Q}_f \boldsymbol{\psi} e^{\Lambda^T t} \mathbf{X}_{f,0} - \zeta (\mathbf{X}_{f,0}^T \mathbf{Q}_f \mathbf{X}_{f,0}^T - 1)] = 0 \quad (63)$$

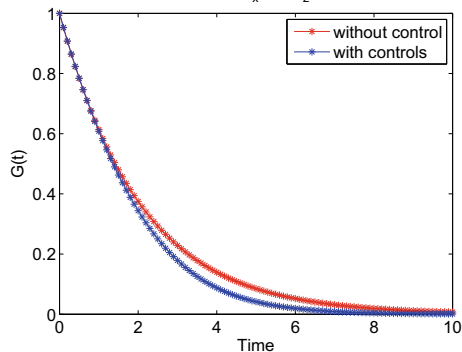
we get,

$$e^{\Lambda^T t} \boldsymbol{\psi}^T \mathbf{Q}_f \boldsymbol{\psi} e^{\Lambda^T t} \mathbf{X}_{f,0} = \zeta \boldsymbol{\psi}^T \mathbf{Q}_f \boldsymbol{\psi} \mathbf{X}_{f,0} \quad (64)$$

Above Eq. (64) is pre-multiplied with $\mathbf{X}_{f,0}^T$. we then get the form of a generalized eigenvalue problem. Maximum value of E is associated with the maximum chosen eigenvalue of the generalized eigenvalue problem. Consequently the corresponding eigenvector gives the worst initial state of the system that leads the system to undergo most unstable transient growth. We have plotted the open loop optimal growth function $G(t)$ at $Re = 14$, $k_x = 0.5$ and $k_z = 0.5$ for all the base flow solutions (Type I, II and III) as shown in the Fig. 2. We observe that only solution type II shows the transient jump in the growth function, which may be the result of non-normality present in the system when included with base flow solution type II. These transient peaks are often responsible for triggering the non-linear effects in the system, thus in turn leading to early transition in the flow (Fig. 5). We can suppress these transient peaks through the previously discussed LQR controller control gains synthesized. We apply similar strategy to find the optimal gain \mathbf{K} in the view of feedback control law $\mathbf{u}_f = -\mathbf{K}\mathbf{X}_f$. The closed loop system's optimal growth is also obtained and it is shown in the Fig. 6 with closed loop plants $G(t)$ (with blue marker) along with open loop $G(t)$ (red marker) for all the three base flow solutions for $Re = 14$, $k_x = 0$ and $k_z = 1$.

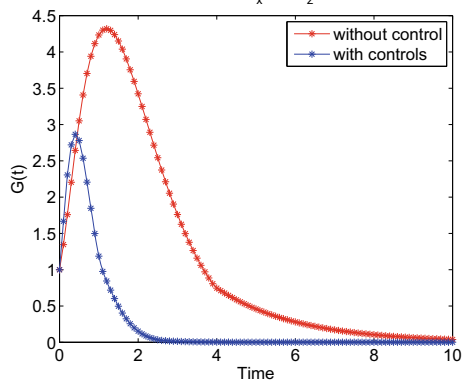
Fig. 6 Optimal growth $G(t)$ at $Re = 14$, $k_x = 0$ and $k_z = 1$ for Solution Type I, II and III for open and closed loop plants

$G(t)$ for porous channel, $Re = 14$, $k_x = 0$, $k_z = 0$, Type I base solution



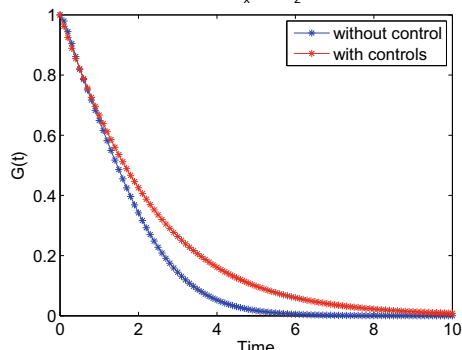
(a) Optimal growth $G(t)$ at $Re = 14$, $k_x = 0$ and $k_z = 1$ for Solution Type I.

$G(t)$ for porous channel $Re = 14$, $k_x = 0$, $k_z = 1$ for Type II base flow



(b) Optimal growth $G(t)$ at $Re = 14$, $k_x = 0$ and $k_z = 1$ for Solution Type II.

$G(t)$ for porous channel, $Re = 14$, $k_x = 0$, $k_z = 1$, Type III base solution



(c) Optimal growth $G(t)$ at $Re = 14$, $k_x = 0$ and $k_z = 1$ for Solution Type III.

5 Results and Discussions

We have formulated the state space control model utilizing the the porous channel flow linear stability equations. The state space model is integrated with that of control framework in both modal and non-modal perspective. We have computed the eigenspectrum along with the optimal growth of the open loop and closed loop plant at $Re = 14$ for several k_x and k_z values. The eigenspectrum for $Re = 14$, $k_x = 0.5$ and $k_z = 0.5$ for type II solution is shown in the Fig. 4. This shows that the most unstable eigenvalues all poorly pulled to the left of the stability plane. The reason we have chosen the particular Reynolds number $Re = 14$ is that, at this Reynolds number we get three distinct solutions of base flows because of the non-linear nature of the governing base flow equation. We have already seen that, at $Re < 12.65$, only one solution exist, whereas for Re much great than 12.65, there the two solutions merge. We get the evolution of optimal growth function through non-modal analysis at $Re = 14$, $k_x = 0.5$ and $k_z = 0.5$ for all the three base flow solutions and shown in the figure ???. We observer that the solution say Type I and III do not undergo transient growth, where as solution Type II shows transient growth, which may be associated with the non-normality of the system. We also did the simulation for several other modes but none of the modes are responsible for transient growth in solution Type I and III. We also observe that the attenuation is not effective as compared to the attenuation in the plane Poiseuille flows. The reason being, control actuation is struggling on top of the suction/injection of the fluid on both the walls. This could be the physical reason, the controller didn't work well as compared to the plane Poiseuille flow case [10].

6 Conclusion

In this article, We have numerically investigated the effect of the stability modifier (wall transpiration) on control of optimally amplified disturbances in porous channel flow with constant suction of the fluid at walls. We have adopted the similar systems approach to design the optimal feedback control strategy. We have adopted the non-modal analysis and associated control framework and used variational method to formulate the stability integrated control model. A standard state space form using linearized perturbed Navier-Stokes equation is constructed in this regard. Further, we have synthesized the linear quadratic regulator assuming that we have the knowledge of full state of the system. Based on the optimal control gain, we have supplied the wall transpiration at boundaries to stabilize the maximum of optimal growth and associated temporal growth of instabilities. The control action suppressed the growth function for all the base flow solutions. The attenuation of the growth function may leave behind the triggering of non-linear effects in the system, in turn delaying the transition process in the porous channel flow.

References

1. Ashwini, B., Katagi, N.N., Rai, A.S.: Analysis of laminar flow through a porous channel with velocity slip. *Malays. J. Math. Sci.* **11**(3)
2. Harwin, D.A.: Flows in porous channels. PhD thesis, University of Bath (2007)
3. Gad-el Hak, M.: *Flow Control: Passive, Active, and Reactive Flow Management*. Cambridge University Press (2007)
4. Schmid, P.L., Brandt, L.: Analysis of fluid systems: stability, receptivity, sensitivitylecture notes from the flow-nordita summer school on advanced instability methods for complex flows, stockholm, sweden, 2013. *Appl. Mech. Rev.* **66**(2), 024803 (2014)
5. Reddy, S.C., Henningson, D.S.: Energy growth in viscous channel flows. *J. Fluid Mech.* **252**, 209–238 (1993)
6. Huerre, P., Monkewitz, P.A.: Local and global instabilities in spatially developing flows. *Ann. Rev. Fluid Mech.* **22**(1), 473–537 (1990)
7. Swaminathan, G.: Global stability analysis of non-parallel flows. PhD thesis, JNCASR (2010)
8. Jotkar, M.R., Govindarajan, R.: Non-modal stability of jeffery-hamel flow. *Phys. Fluids* **29**(6), 064107 (2017)
9. Bewley, T.R., Liu, S.: Optimal and robust control and estimation of linear paths to transition. *J. Fluid Mech.* **365**, 305–349 (1998)
10. McKernan, J., Papadakis, G., Whidborne, J.F.: A linear state-space representation of plane poiseuille flow for control design: a tutorial. *Int. J. Model. Ident. Control* **1**(4), 272–280 (2006)
11. Höglberg, M., Bewley, T.R., Henningson, D.S.: Linear feedback control and estimation of transition in plane channel flow. *J. Fluid Mech.* **481**, 149–175 (2003)
12. Kim, J., Bewley, T.R.: A linear systems approach to flow control. *Annu. Rev. Fluid Mech.* **39**, 383–417 (2007)
13. Bewley, T.R.: Flow control: new challenges for a new renaissance. *Prog. Aerosp. Sci.* **37**(1), 21–58 (2001)
14. Joshi, S.S., Speyer, J.L., Kim, J.: A systems theory approach to the feedback stabilization of infinitesimal and finite-amplitude disturbances in plane poiseuille flow. *J. Fluid Mech.* **332**, 157–184 (1997)
15. Tilton, N., Cortelezzi, L.: Linear stability analysis of pressure-driven flows in channels with porous walls. *J. Fluid Mech.* **604**, 411–445 (2008)
16. Ferro, S., Gnani, G.: Spatial stability of similarity solutions for viscous flows in channels with porous walls. *Phys. Fluids* **12**(4), 797–802 (2000)
17. Chang, M.H., Chen, F., Straughan, B.: Instability of poiseuille flow in a fluid overlying a porous layer. *J. Fluid Mech.* **564**, 287–303 (2006)
18. Liu, Q., Prosperetti, A.: Pressure-driven flow in a channel with porous walls. *J. Fluid Mech.* **679**, 77–100 (2011)
19. Höglberg, M., Bewley, T.R., Henningson, D.S.: Relaminarization of $Re = 100$ turbulence using gain scheduling and linear state-feedback control. *Phys. Fluids* **15**(11), 3572–3575 (2003)
20. Kant, R., Vinod, N.: Control of optimal growth of instabilities in jeffery-hamel flow. *AIP Adv.* **9**(3), 035307 (2019)
21. Berman, A.S.: Laminar flow in channels with porous walls. *J. Appl. Phys.* **24**(9), 1232–1235 (1953)
22. Bundy, R.D., Weissberg, H.L.: Experimental study of fully developed laminar flow in a porous pipe with wall injection. *Phys. Fluids* **13**(10), 2613–2615 (1970)
23. Sellars, J.R.: Laminar flow in channels with porous walls at high suction reynolds numbers. *J. Appl. Phys.* **26**(4), 489–490 (1955)
24. Yuan, S.W.: Laminar pipe flow with injection and suction through a porous wall. Technical report, PRINCETON UNIV NJ JAMES FORRESTAL RESEARCH CENTER (1955)
25. Yuan, S.W.: Further investigation of laminar flow in channels with porous walls. *J. Appl. Phys.* **27**(3), 267–269 (1956)
26. Tilton, N., Cortelezzi, L.: The destabilizing effects of wall permeability in channel flows: A linear stability analysis. *Phys. Fluids* **18**(5), 051702 (2006)

27. Bamieh, B.: The structure of optimal controllers of spatially-invariant distributed parameter systems. In: Proceedings of the 36th IEEE Conference on Decision and Control, vol. 2, pp. 1056–1061. IEEE (1997)
28. Butler, K.M., Farrell, B.F.: Three-dimensional optimal perturbations in viscous shear flow. *Phys. Fluids A Fluid Dyn.* **4**(8), 1637–1650 (1992)
29. Schmid, P.J., Henningson, D.S.: Stability and Transition in Shear Flows, vol. 142. Springer Science & Business Media (2012)
30. Drazin, P.G., Riley, N.: The Navier-Stokes Equations: A Classification of Flows and Exact Solutions, No. 334. Cambridge University Press (2006)
31. Boyd, J.P.: Chebyshev and Fourier spectral methods. Courier Corporation (2001)
32. Ogata, K., Yang, Y.: Modern Control Engineering. Prentice-Hall Englewood Cliffs (1970)
33. Gustavsson, L.H.: Energy growth of three-dimensional disturbances in plane poiseuille flow. *J. Fluid Mech.* **224**, 241–260 (1991)
34. McKernan, J.: Control of plane Poiseuille flow: a theoretical and computational investigation. PhD thesis, Cranfield University (2006)

Use of Instabilities for Optimal Laminar Separation Delay



Michael Karp and M. J. Philipp Hack

Abstract The velocity disturbances at a given upstream position, which counteract laminar separation downstream, are sought by means of nonlinear optimization. For steady disturbances, an informed guess based on linear analysis of transient perturbation growth leads to significant delay of separation and serves as a starting point for the nonlinear optimization algorithm. Nonlinear optimal perturbations enable further delay of the separation location, with moderate improvements relative to the linear analysis. The mechanism of separation delay is the generation of a mean flow distortion by nonlinear interactions during perturbation growth. The mean flow distortion enhances the momentum close to the wall, and thus counteracts the deceleration of the flow in that region. For unsteady disturbances, it is found that Tollmien-Schlichting waves obtained by local stability theory provide very good estimates of the nonlinearly optimal disturbances. The mechanism that counteracts separation is the enhancement of the wall-normal momentum transfer in the separated shear layer. Comparison of optimal steady and unsteady perturbations reveals that the latter are able to obtain a higher time-averaged peak wall pressure.

1 Introduction

Boundary layers are prone to separation when subjected to adverse pressure gradients. Flow separation often leads to increased pressure drag and decreased lift, resulting in reduced performance of aerodynamic and hydrodynamic vehicles. Separation is particularly relevant for low-Reynolds-number aerodynamics of small unmanned air vehicles, for which laminar flow is the rule rather than the exception. Downstream of the separation point, the inflectional shear layer often triggers early breakdown

M. Karp (✉) · M. J. P. Hack
Center for Turbulence Research, Stanford, CA 94305, USA
e-mail: mkarp@stanford.edu

M. J. P. Hack
e-mail: mjph@stanford.edu

to turbulence. Although transition to turbulence induces flow reattachment, thereby reducing the size of the separated region, its adverse effects are increased friction and heat transfer.

Vortex generators have been proposed as a possible passive control device for mitigating flow separation, owing to their ability to generate counter-rotating streamwise vortices that often trigger transition to turbulence, thus enabling a delay or even prevention of separation (e.g. Ref. [1]). Significant reduction of airfoil drag, associated with laminar separation bubbles, has been demonstrated by using vortex generators completely submerged in the boundary layer (e.g. Ref. [2]). In fact, vortex generators have been shown to delay separation even in fully turbulent flows (e.g. Ref. [3]). In addition to passive approaches, active control has been successful in mitigating separation as well (see e.g. Ref. [4], for a review). Several studies explored the relevance of linear stability theory to active separation control (e.g. Refs. [5, 6]). In the current study, both passive and active approaches are considered, represented by steady and unsteady perturbations, respectively. The passive generation of steady perturbations avoids the requirement for a power source associated with unsteady perturbations.

The choice of parameters of vortex generators aimed at delaying separation is often based on trial and error, in particular their spanwise spacing. Moreover, the mechanism for optimal separation delay is poorly understood. To shed light on the underlying flow physics, we focus on the velocity field upstream of the point of separation. Our aim is to find the optimal perturbation, in a sense that the pressure recovery on the wall is maximized. Both steady and unsteady disturbances are considered and their performance is compared.

2 Methodology

2.1 Computational Setup

We consider the incompressible three-dimensional Navier-Stokes equations. All variables are non-dimensionalized by the free-stream velocity and boundary layer thickness at the inlet. The velocity components u , v and w correspond to velocities along x , y and z , the streamwise, wall-normal and spanwise dimensions, respectively. Note that throughout this work, the term “mean” is consistently used to indicate averaging in the spanwise dimension.

Our setting of triggering separation in the flow over a flat plate is similar to that utilized by [7] and is shown in Fig. 1. A suction-injection velocity distribution is prescribed along the upper boundary of the computational domain to create an adverse-to-favorable pressure gradient that produces a closed separation bubble. The vertical velocity distribution at the top boundary is given by

$$v_s(x) = -v_0 \bar{x} \exp\left(\frac{1}{2} - \frac{1}{2} \bar{x}^2\right), \quad \bar{x} = \frac{x - x_s}{\Delta x_s e^{-1/2}}, \quad (1)$$

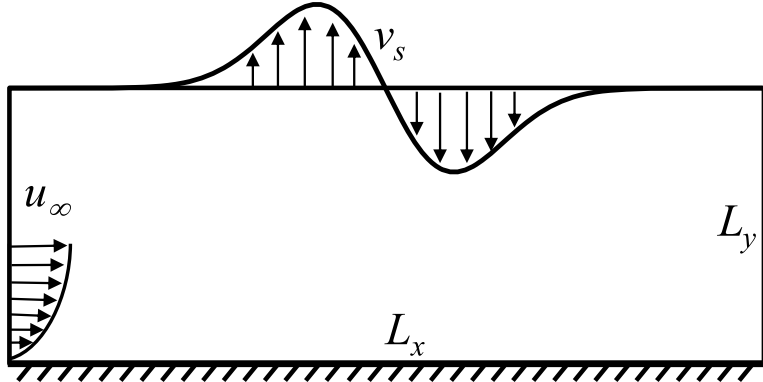


Fig. 1 Problem setup considered within this work

with x_s the location where the wall-normal velocity changes sign, Δx_s a representative width of the suction-injection region and v_0 the maximal amplitude. The amount of fluid removed ($x < x_s$) and injected ($x > x_s$) is equal to $v_0 \Delta x_s$.

2.2 Direct Numerical Simulations

The flow field is computed in direct numerical simulations using a second-order finite-volume formulation. At the inlet, a Blasius profile is superimposed with a disturbance, whose specific details are provided below. The size of the computational domain is $L_x = 200$ in the streamwise dimension and $L_y = 30$ in the wall-normal dimension. The domain is assumed periodic in the spanwise dimension and extends over one disturbance wavelength, $L_z = 2\pi/\beta$, where β is the spanwise wavenumber. An equidistant grid is used in x and z , and a hyperbolic tangent clustering with a ratio of $\Delta y_{\text{top}}/\Delta y_{\text{wall}} = 50$ is employed in the wall-normal dimension, leading to a spacing of $\Delta x = 0.1953$, $\Delta z = 0.0982/\beta$ and $\Delta y_{\text{wall}} = 0.0084$ for the high-resolution case ($N_x, N_y, N_z = (1024, 192, 64)$) and a spacing of $\Delta x = 0.3906$, $\Delta z = 0.1963/\beta$ and $\Delta y_{\text{wall}} = 0.0126$ for the low-resolution case ($N_x, N_y, N_z = (512, 128, 32)$). The effect of the resolution is limited to a change of the mean separation location of less than one boundary layer thickness in all considered cases. Two-dimensional simulations are performed with $N_z = 2$. Along the top boundary, a superposition of the Blasius solution and v_s is enforced and a convective condition is prescribed at the outlet. The finite-volume algorithm is based on [8], with the velocities stored on a staggered grid at the faces of the computational volumes and the pressure stored at their centers. The convective term is integrated in time using a second-order Adams-Bashforth scheme while a second-order Crank-Nicolson scheme is used for the diffusion term. Mass conservation is enforced through the fractional step method

[9]. For steady inflow perturbations, the convergence to steady state was accelerated by the application of selective frequency damping [10].

3 Steady Separation Delay

3.1 Maximal Transient Perturbation Growth

Our analysis begins by considering steady perturbations which can be implemented using a passive device and do not require an actuator. In a first step, the steady three-dimensional perturbations are obtained from linear transient growth analysis and their effect on the laminar separation bubble is analyzed. We employ local spatial stability analysis to calculate the linearly most highly amplified perturbations.

The procedure for finding the optimal solutions which maximizes the linear spatial transient energy growth is based on a singular value decomposition of the matrix exponential as described in [11] for the temporal setting. The analysis below assumes a spanwise wavenumber of 1.85, for which maximal linear energy growth is obtained (see e.g. Ref. [12]). The disturbance inflow kinetic energy is set to 10^{-4} .

A comparison between the optimized case and the base state is shown in Fig. 2. The wall shear is presented in Fig. 2a, the base state is indicated by the red dash-dotted line, the optimized case based on linear transient growth is given by the solid black line and the Blasius solution is indicated by the blue dashed line. A significant delay of the mean separation location is observed, from $x \approx 63$ to $x \approx 84$, accompanied by upstream shift of the mean reattachment from $x \approx 124$ to $x \approx 108$, reducing the

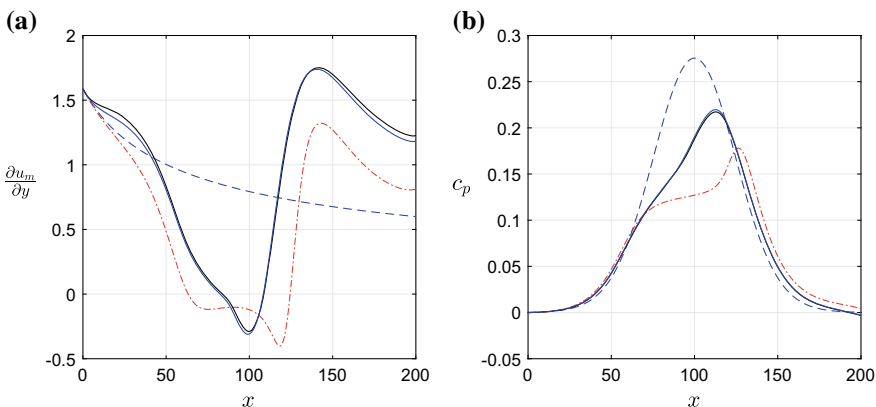


Fig. 2 Comparison of base (red dash-dotted line) and optimized (solid lines) states. In the optimized cases the inflow perturbation is obtained by local linear transient growth analysis (black line) and nonlinear optimization (blue line). **a** Mean wall shear. Dashed blue line corresponds to the Blasius solution. **b** Mean wall pressure coefficient. Dashed blue line corresponds to the inviscid solution

mean bubble size by approximately 60%. The wall shear in the optimized case (solid black line) is enhanced compared to the base state (red dash-dotted line). This effect is attributed to the mean flow distortion caused by the growth of the perturbations, which augments the streamwise momentum close to the wall (see also Ref. [13]). The wall pressure coefficient, $c_p = (p_w - p_\infty)/(0.5\rho_\infty u_\infty^2)$, is presented in figure 2(b). The blue dashed line corresponds to the inviscid solution obtained analytically by defining a flow potential (see [14] for details). The inviscid solution sets an upper bound for the pressure rise at the wall, which can be attained without separation. Initially, the viscous (red dash-dotted line) and inviscid (blue dashed line) curves rise together; however, upon separation the pressure flattens and remains below the level observed for the inviscid solution. The pressure coefficient attains a maximum of $c_p \approx 0.18$ close to the reattachment location, followed by a slow decay, as in the inviscid solution. In the optimized case (solid black line), the pressure continues to rise in the separated region and is appreciably closer to the inviscid distribution with a peak of $c_p \approx 0.22$.

3.2 Nonlinear Optimization

The perturbations obtained from the linear transient growth analysis serve as the starting point for nonlinear optimization. The optimization objective in the current work is set to maximal peak wall pressure, as maximizing c_p is desirable for reducing form drag in aeronautical applications. Analysis of additional possible optimization objectives is reported in [14].

The optimization procedure seeks the disturbance shape at the inlet such that the objective functional is maximized. For steady disturbances, the velocity field at the inflow can be written as

$$u(x = 0, y, z) = \hat{u}(s) \cos(\beta z), \quad (2a)$$

$$v(x = 0, y, z) = \hat{v}(s) \cos(\beta z), \quad (2b)$$

$$w(x = 0, y, z) = -\hat{w}(s) \sin(\beta z), \quad (2c)$$

where $s = (s_1, s_2, \dots, s_N)^T$ is a vector of the degrees of freedom in the problem and \hat{u} , \hat{v} and \hat{w} are real functions. The kinetic energy of the disturbance at the inlet, E_0 , is enforced by normalizing the disturbance kinetic energy to E_0 for each guess. Consistent with the investigation of inflow disturbances computed in the linear analysis, the kinetic energy of the disturbance at the inflow is maintained at $E_0 = 10^{-4}$. The objective functional is set to the peak wall pressure, defined as

$$c_{p_{\max}} = \max_x \{c_p(x)\}, \quad (3)$$

where c_p is the spanwise-averaged pressure coefficient at the wall.

A complete description of the optimization procedure is given in [14], with only the major features described below. Nonlinear optimization based on the full Navier-Stokes equations is often implemented through a variational formulation (e.g. Refs. [15, 16]). In the present study, we apply the conjugate gradient algorithm, in conjunction with the Polak-Ribière formula [17] and the degrees of freedom were selected as the values of the velocity components at several wall-normal locations. For optimal disturbances maximizing transient growth in a boundary layer, it is known that the streamwise component is marginal at the initial position, with most of the energy concentrated in the cross-stream components (see e.g. Ref. [18]). Therefore, in this work only v and w are considered in the optimization procedure.

The nonlinear optimization algorithm is initialized by an initial guess based on linear transient growth, with the aim of finding the perturbations which maximize the mean peak wall pressure. The resulting wall shear and wall pressure coefficient are indicated by the solid blue lines in Fig. 2. Very good agreement is observed when comparing the curves to the results obtained for linear transient growth, with marginal differences in the wall shear upstream of the separation and downstream of the reattachment.

A three-dimensional visualization of the separation bubble for the optimized case is shown in Fig. 3. The separation bubble is represented by a dark isosurface at $u = 0$, which provides a qualitative description of the bubble. Separation is delayed significantly at the locations of the high-speed streaks, indicated by the red isosurfaces, whereas the delay in separation is negligible in the low-speed streak region, indicated

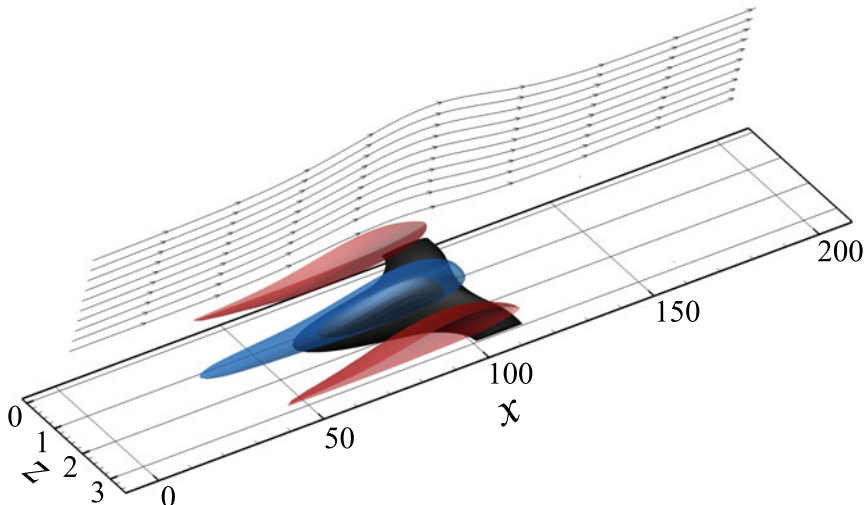


Fig. 3 Separation bubble for the nonlinear optimal for maximal peak wall pressure and $\beta = 1.85$ represented by an isosurface of $u = 0$ (dark color). Streamwise velocity streaks are shown by isosurfaces of ± 0.25 streamwise velocity fluctuations, positive (red) and negative (blue)

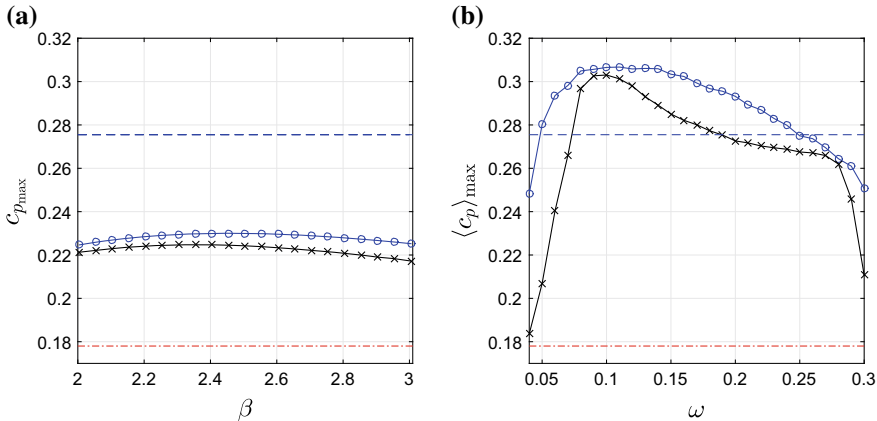


Fig. 4 Optimal peak wall pressure corresponding to nonlinear optimal perturbations (blue circles) and linear analysis (black crosses). **a** Steady perturbations, the linear analysis is based on transient growth, spanwise-averaged values are shown. **b** Unsteady perturbations, the linear analysis corresponds to Tollmien-Schlichting waves, time-averaged values are shown. The base state is indicated by the red dash-dotted lines and the inviscid peak is given by the blue dashed line

by the blue isosurface. Nevertheless, the mean separation location is delayed appreciably due to the mean flow distortion as detailed above. We note that downstream of the separation bubble, streaks with opposite sign are generated owing to the convex streamlines of the flow above the separation bubble, as detailed in Ref. [19].

3.3 Effect of Spanwise Wavenumber

So far, the optimization has been performed only for the single spanwise wavenumber which is known to maximize linear perturbation growth. The effect of varying this parameter is analyzed in the following.

The nonlinear optimization of the peak wall pressure is performed for each of the spanwise wavenumbers within the region $2.0 \leq \beta \leq 3.0$, and the resulting optimal peak wall pressure coefficient is indicated by blue circles in Fig. 4a. The peak wall pressure coefficients based on perturbations obtained from linear transient growth are indicated by black crosses. The optimum is found for $\beta = 2.45$ and reaches $c_{p_{\max}} = 0.23$, more than 80% of the inviscid pressure peak, indicated by the blue dashed line. The results based on linear transient growth show a similar trend. Although the optimum is reached for a lower spanwise wavenumber, the difference in $c_{p_{\max}}$ is approximately 2%. Moreover, the overall change in $c_{p_{\max}}$ is less than 3% within the range of examined spanwise wavenumbers, suggesting a weak sensitivity to the spanwise length scale of the disturbances.

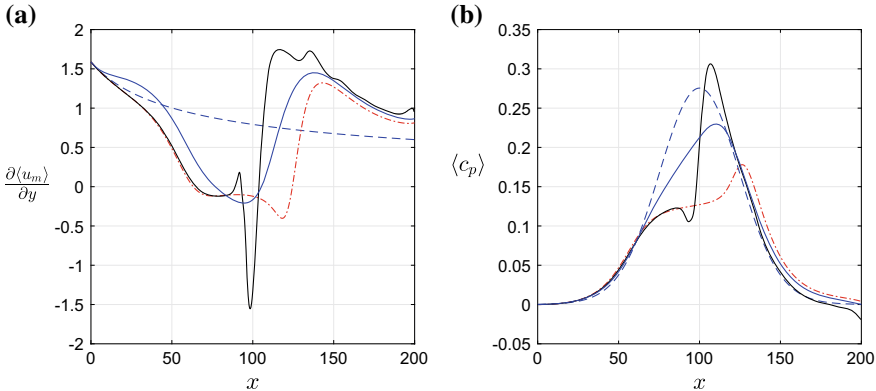


Fig. 5 Comparison between the time- and spanwise-averaged wall shear (a) and wall pressure coefficient (b) obtained for nonlinear optimal disturbances maximizing the peak pressure coefficient. Blue solid lines correspond to optimal steady perturbations ($\beta = 2.45$) and black solid lines to unsteady perturbations ($\omega = 0.1$). The base state is given for reference by the red dash-dotted line and the dashed blue line corresponds to the Blasius solution in (a) and the inviscid solution in (b)

The mean wall shear and wall pressure coefficient for the optimal steady perturbation are indicated by the blue solid lines in Fig. 5. Overall, the curves show similar trends to the ones observed for the initial results shown in Fig. 2. The most notable differences between Figs. 5 and 2 are the decreased wall shear downstream of the separation bubble in the optimal case shown in Fig. 5 which is only slightly above the base state.

4 Unsteady Separation Delay

In the previous section, our focus has been on the delay of flow separation by steady perturbations which can be generated passively without the need of an actuator or power source. Nevertheless, it is of interest to compare the outcome with results obtained for unsteady perturbations. The mechanism of separation delay based on unsteady disturbances relies on enhancing the wall-normal momentum transfer by triggering instabilities of the separated inflectional shear layer. The disturbances are expected to amplify significantly in the shear layer, promoting reattachment and altering the pressure distribution at the wall. We focus on the effect of unsteady two-dimensional, spanwise-homogenous, disturbances as they are expected to gain the highest growth rates. Optimization is performed to find the maximal time-averaged peak wall pressure coefficient. The velocity field at the inlet is written as

$$u(t, x = 0, y) = \hat{u}(s)e^{-i\omega t} + \text{c.c.}, \quad (4a)$$

$$v(t, x = 0, y) = \hat{v}(s)e^{-i\omega t} + \text{c.c.}, \quad (4b)$$

where ω is the frequency, \hat{u} and \hat{v} are complex functions and $s = (s_1, s_2, \dots, s_N)^T$ is a vector of the degrees of freedom in the problem. The time-averaged kinetic energy of the disturbance at the inflow is again chosen as $E_0 = 10^{-4}$. The objective functionals are modified to include averaging with respect to time, which is given by

$$\langle . \rangle = \frac{1}{T_s} \int_{t_0}^{t_0+T_s} (.) dt, \quad (5)$$

with averaging beginning at t_0 , over a time T_s . The sampling begins at $t_0 > 0$ to allow the transient responses, arising due to the change in inflow, convect out of the computational domain. Here t_0 is set to 5 flow-through times and T_s to 15 flow-through times, chosen such that further increase of the values results in minor changes in the optimums. The time-averaging horizon covers approximately 19 periods of the lowest considered disturbance frequency ($\omega = 0.04$). The initial guess for the unsteady optimization is obtained from a local linear stability analysis of the inflow Blasius profile. The least stable discrete (Tollmien-Schlichting) mode is chosen as the initial guess. Further details on the optimization algorithm are given in [14].

Nonlinear optimization of unsteady two-dimensional perturbations is conducted, with the aim of maximizing the time-averaged peak wall pressure coefficient, $\langle c_p \rangle_{\max}$. In a step towards the optimization, the performance of the initial guesses, i.e. Tollmien-Schlichting waves, is evaluated in the frequency range $0.04 \leq \omega \leq 0.3$. The resulting $\langle c_p \rangle_{\max}$ is indicated by the black crosses in Fig. 4b. An improvement is observed relative to the base state ($c_{p_{\max}} \approx 0.18$) for all considered frequencies, with the best frequency corresponding to $\omega \approx 0.10$. In fact, $\langle c_p \rangle_{\max}$ even exceeds the inviscid peak obtained assuming steady flow, indicated by the blue dashed line. We proceed by performing nonlinear optimization for each of the frequencies, resulting in the line indicated by the blue circles in Fig. 4b. The optimal $\langle c_p \rangle_{\max}$ is obtained for a range of frequencies centered around $\omega \approx 0.10$, with only slight improvements with respect to the initial guess calculated by linear stability theory. Tollmien-Schlichting waves can thus be seen as a good estimate of the optimal disturbances. The normalized optimal frequency $\omega L / U_\infty \approx 6$ is in good agreement with the results by Rist and Augustin [5] who showed considerable separation delay for a frequency of $\omega L / U_\infty = 5$, where L is the uncontrolled bubble length. Comparing the performance of steady and unsteady perturbations, the maximum wall pressure coefficient increases by more than 30% from approximately 0.23 in the steady case, to approximately 0.31 in the unsteady case.

The time-averaged wall shear and wall pressure coefficient for the optimal unsteady perturbation are indicated by the black solid lines in Fig. 5. Comparison of the results for optimal steady perturbations with the ones for unsteady disturbances emphasizes the different mechanisms leading to elevated peak wall pressure in the two cases. For the steady disturbance, the preeminent effect is a heightened mean flow distortion, which leads to an increase in the wall shear upstream of the separa-

tion bubble. For the unsteady disturbance, the main mechanism is the enhancement of the wall-normal momentum transfer in the separated shear layer, which affects the wall shear and wall pressure coefficient in that region.

5 Conclusions

The potential of steady and unsteady perturbations to delay laminar flow separation is examined by means of nonlinear optimization.

For steady perturbations, linear analysis of transient perturbation growth leads to significant delay of the onset of flow separation due to the generation of a mean flow distortion by nonlinear interactions during the amplification of the disturbances. The mean flow distortion augments the streamwise momentum close to the wall and counteracts the deceleration of the flow in that region. The linear transient growth serves as a starting point for a nonlinear optimization algorithm, however the nonlinearly optimal perturbations offer only marginal improvements compared to the linear transient growth. Nevertheless, the linear analysis is unable to predict the optimal spanwise wavenumber.

For unsteady perturbations, it is found that Tollmien-Schlichting waves, obtained by performing a local stability analysis of the inflow Blasius profile, serve as good estimates of the nonlinearly optimal disturbances. The underlying mechanism for counteracting separation is the enhancement of the wall-normal momentum transfer in the separated shear layer. Comparison between the optimal steady and unsteady disturbances reveals that the latter attain a 30% higher peak pressure coefficient.

Acknowledgements This investigation was funded by the Air Force Office of Scientific Research under grant FA9550-16-1-0319 and the Office of Naval Research under grant N00014-17-1-2341.

References

1. Pearcey, H.H.: Shock-induced separation and its prevention. In: Lachmann, G.V. (ed.) *Boundary Layer and Flow Control, Its Principle and Applications*. Pergamon Press (1961)
2. Kerho, M., Hutcherson, S., Blackwelder, R.F., Liebeck, R.H.: *J. Aircr.* **30**, 315 (1993)
3. Schubauer, G.B., Spangenberg, W.G.: *J. Fluid Mech.* **8**, 10 (1960)
4. Greenblatt, D., Wygnanski, I.J.: *Prog. Aerosp. Sci.* **36**, 487 (2000)
5. Rist, U., Augustin, K.: *AIAA J.* **44**, 2217 (2006)
6. Marxen, O., Kotapati, R.B., Mittal, R., Zaki, T.: *Phys. Fluids* **27**, 024107 (2015)
7. Na, Y., Moin, P.: *J. Fluid Mech.* **374**, 379 (1998)
8. Rosenfeld, M., Kwak, D., Vinokur, M.: *J. Comput. Phys.* **94**, 102 (1991)
9. Kim, J., Moin, P.: *J. Comput. Phys.* **59**, 308 (1985)
10. Åkervik, E., Brandt, L., Henningson, D.S., Høeppfner, J., Marxen, O., Schlatter, P.: *Phys. Fluids* **18**, 068102 (2006)
11. Schmid, P.J., Henningson, D.S.: *Stability and Transition in Shear Flows*. Springer-Verlag (2001)
12. Butler, K.M., Farrell, B.F.: *Phys. Fluids A* **4**, 1637 (1992)
13. Ran, W., Zare, A., Hack, M.J.P., Jovanovic, M.R.: *Phys. Rev. Fluids* **4**, 023901 (2019)

14. Karp, M., Hack, M.J.P.: *J. Fluid Mech.* **892**, A23 (2020)
15. Pringle, C.C.T., Kerswell, R.R.: *Phys. Rev. Lett.* **105**, 154502 (2010)
16. Huang, Z., Hack, M.J.P.: *J. Fluid Mech.* **894**, A5 (2020)
17. Polak, E., Ribi  re, G.: *Rev. Fr. Inform. Rech. O.* **16**, 35 (1969)
18. Hack, M.J.P., Zaki, T.A.: *J. Fluid Mech.* **778**, 389 (2015)
19. Karp, M., Hack, M.J.P.: *J. Fluid Mech.* **855**, 1208 (2018)

Wave Packet Dispersion in Inflectional and Non-inflectional Flows



Kirthy K. Srinivas, Sourabh S. Diwan, and O. N. Ramesh

Abstract We study the linear spatio-temporal stability characteristics of inflectional and non-inflectional parallel flows and towards this consider separated boundary layer flow (SBLF), plane Couette-Poiseuille flow (CPF) and Falkner Skan flow with Favourable Pressure Gradient (FSFPG) with the boundary moving opposite to bulk fluid motion. We compute the temporal growth rate ($\omega_{o,i}$) at the saddle point of the dispersion relation in a frame of reference moving in the streamwise direction at a constant speed V , and locate the leading and trailing edge velocities (V_{LE} , V_{TE}) of the unstable wave packet for each of these flows. We show that their difference $\Delta V = V_{LE} - V_{TE}$, taken as a measure of dispersion of the unstable wave packet and its dependence on Reynolds number (Re) show important features that differentiate spatio-temporal instability dynamics of inflectional and non-inflectional flows.

1 Introduction

Among the prototypical problems in hydrodynamic stability, incompressible one-dimensional parallel flows have been among the first to be investigated mathematically. From the classical studies of Rayleigh [1], Taylor [2], Squire [3], Schubauer and Skramstad [4] and several others, it has been shown that linear modal analysis lends itself suitable to linear stability investigations of parallel base flows. These studies have also revealed a dual role of viscosity in fluid flows—of promoting instability for non-inflectional profiles at moderate Reynolds numbers (Re) while damping it at sufficiently low and sufficiently high Reynolds numbers.

Examining long time asymptotic response of a flow to an impulse perturbation [5, 6] has led to significant proportion of studies in hydrodynamic stability being dedicated to understanding instability of flows as convective or absolute. These techniques can also provide further understanding of instability dynamics in terms of the

K. K. Srinivas · S. S. Diwan (✉) · O. N. Ramesh

Department of Aerospace Engineering, Indian Institute of Science, Bangalore 560012, India
e-mail: sdiwan@iisc.ac.in

dispersion of disturbance wave packet in space, which hasn't received appreciable attention in the stability literature thus far. In this regard, it is instructive to revisit the stability properties of candidate profiles for inflectional and non-inflectional parallel flows, and seek common and contrasting features in the nature of the instability dynamics. In the present work, we show that the extent of dispersion of an unstable wave packet and its dependence on viscosity in non-inflectional flows is markedly different from that in inflectional flows, providing an additional insight on the fundamental role that viscosity plays in the stability of fluid flows.

The structure of the paper is as follows. Section 2 introduces the flows we've considered in our present investigation, gives an overview of the problem and our analysis methods. Section 3 presents the results and Sect. 4 presents the conclusions.

2 Problem Formulation

In the present work, we study the linear spatio-temporal instability dynamics of three parallel base flows, namely—non-inflectional Couette-Poiseuille flow (CPF) and Falkner Skan flow with Favourable Pressure Gradient (FSFPG) with wall moving opposite to the bulk flow, and inflectional separated boundary layer flow (SBLF).

2.1 Base Flows

The CPF velocity profile [7], as shown in Fig. 1 is bounded between $y \in [-1, 1]$ and obtained as an exact solution to the Navier-Stokes equations with the boundary conditions of $U(-1) = 0$ and $U(1) = \lambda$ in the presence of a favourable pressure gradient ($dp/dx < 0$), where p denotes pressure, x the streamwise coordinate and y is the wall-normal coordinate. The analytical expression for $U(y)$ is given by

$$U(y) = \frac{\lambda}{2}(1 + y) + (1 - y^2) \quad (1)$$

Figure 2 shows the semi-bounded FSFPG velocity profile, which is obtained numerically using the shooting technique for the third order nonlinear Falkner Skan differential equation [8]

$$f''' + \frac{1}{2}(m + 1)ff'' + m(1 - f'^2) = 0 \quad (2)$$

where $f' = U(y)$, with the boundary conditions

$$U(0) = \gamma \quad \text{and} \quad U(\infty) = 1 \quad (3)$$

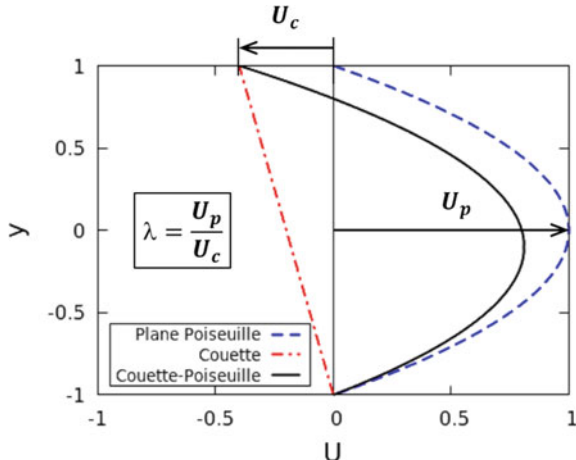
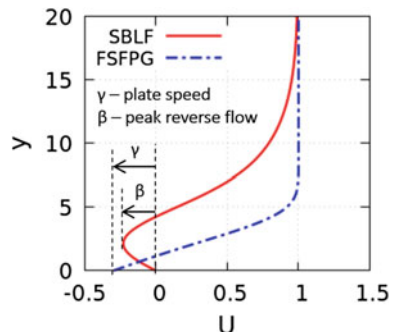


Fig. 1 The base flow velocity profile for CPF, $U(y)$, is shown by the solid line. The dash-dotted and dashed lines show the Couette and Poiseuille components of the flow respectively. U_c denotes the upper plate speed and U_p the Poiseuille component of the centerline velocity, determined by b —half channel width, μ —dynamic viscosity of the fluid, $d\mu/dx$ —streamwise pressure gradient imposed on the flow

Fig. 2 The SBLF and FSFPG base velocity profiles are shown by solid and dash-dotted lines respectively. For FSFPG γ denotes the plate speed and for SBLF β denotes the peak reverse flow



where γ is the plate speed and $U_\infty = Cx^m$. It turns out that for negative plate speeds, the resultant Falkner Skan velocity profile under zero pressure gradient is inflectional, and in order to force the inflection point back into the solid boundary, the parameter m has been set to a small positive value i.e., a slight favourable pressure gradient for each of the negative γ cases, making the FSFPG velocity profile non-inflectional.

The semi-bounded inflectional SBLF velocity profile is shown in Fig. 2. Here, we use an analytical expression for SBLF given by [9]

$$U(y) = \frac{\tanh[a(y-d)] + \tanh(ad)}{1 + \tanh(ad)} + (b\sqrt{3})\eta e^{(-1.5\eta^2+0.5)} \quad (4)$$

where $\eta = \gamma/d$, b is a measure of the magnitude of reversed flow, d is the non-dimensional distance of the inflection point from the wall normalized by the momentum thickness, and a is a constant chosen to satisfy

$$\int_0^\infty U(y)[1 - U(y)]dy = 1 \quad (5)$$

With $d = 5$ for all the cases and $b = -0.2, -0.4, -0.6$, the resultant velocity profile is captured by a single parameter - peak reverse flow β (see Fig. 2).

2.2 Numerical Solution of the Orr-Sommerfeld Equation

The linear viscous spatio-temporal problem for a parallel base flow with streamwise velocity component $U(y)$ is governed by the Orr-Sommerfeld equation [10]

$$\left[(-i\omega + i\alpha U)(D^2 - \alpha^2) - i\alpha U'' - \frac{1}{Re}(D^2 - \alpha^2)^2 \right] \hat{v} = 0 \quad (6)$$

where α and ω are complex streamwise wavenumber and frequency resulting from wavelike form of wall-normal velocity $v = \hat{v}(y)e^{i(\alpha x - \omega t)}$ and \hat{v} is the complex magnitude, U'' is the curvature of the base flow velocity profile $U(y)$ and the $D \equiv d/dy$ denotes derivative with respect to the inhomogeneous coordinate y .

Equation 6 is an eigenvalue problem which we solve numerically using Chebyshev pseudospectral method [11, 12]. Points in the physical space - $y \in [-1, 1]$ for CPF, and $y \in [0, \infty)$ for FSFPG and SBLF (which after mapping to a finite domain $[-1, 1]$ for applying Chebyshev polynomials [12]) are mapped to Chebyshev collocation points in the computational space, $\eta \in [-1, 1]$. This results in a generalized eigenvalue problem in a discrete form

$$A\hat{v} = -i\omega B\hat{v} \quad (7)$$

where A and B are the discrete Orr-Sommerfeld operators with the boundary conditions

$$\hat{v} = 0 \quad \text{at} \quad \eta = -1, 1 \quad (8)$$

The eigenvalue problem is linear in ω , while α appears to the fourth and second power in A and B matrices respectively. Hence, computing ω for a given α (temporal analysis) is relatively easier, compared to computing α for a given ω (spatial analysis), which requires reduction in the order of the equation in α through suitable transformations [13].

Equation 7 with the boundary conditions in Eq. 8 implemented by suitably modifying the rows of A and B operator matrices serves as the dispersion relation governing the spatio-temporal stability characteristics of the flow [5, 14]. This necessitates locating the saddle point of the dispersion relation which is done numerically using an iterative procedure suggested by Deissler [15]. The algorithm involves starting with an initial guess (α_o, ω_o) for the saddle point and fitting a complex quadratic to the function $\omega(\alpha)$ using the points $[\omega(\alpha_o), \omega(\alpha_o + \Delta\alpha_o), \omega(\alpha_o - \Delta\alpha_o)]$. By enforcing $(d\omega/d\alpha) = 0$, we obtain a new value for α_o which serves as the next guess for the saddle point. This iteration is carried out till the location of the saddle point is calculated to a desired degree of accuracy.

3 Results

We study the long time asymptotic response of each of the present flows—CPF, FSFPG and SBLF to a spatially and temporally localized impulse perturbation, by computing the temporal growth rate at the pinch point $(\omega_{o,i})$ of the dispersion relation in a frame of reference moving in the streamwise direction x with a velocity V as shown in Fig. 3 [15].

By varying the observer speed V and tracking the location of the pinch point singularity in the complex ω plane, we obtain a range of V where $\omega_{o,i} > 0$ and therefore, the points where $\omega_{o,i} = 0$ correspond to the leading and trailing edge velocities of the unstable wave packet - V_{LE} and V_{TE} . The difference between them, $\Delta V = V_{LE} - V_{TE}$ can be seen as a measure of the dispersion of the wave packet in the fluid medium. Figure 4 shows the dependence of ΔV on Re for each of the three flows. In Fig. 4a, b corresponding to CPF and FSFPG respectively, we see that the dispersion of the wave packet depends on viscosity in an interesting non-monotonic manner for all plate speeds, including the stationary case. At lower Re , closer to the critical values of their corresponding cases ($\sim 10^4$ for CPF and $\sim 10^2$ for FSFPG), the wave packet tends to be less dispersive, and the dispersion gradually increases with increase in Re . This behaviour continues upto an Re where the dispersion is highest,

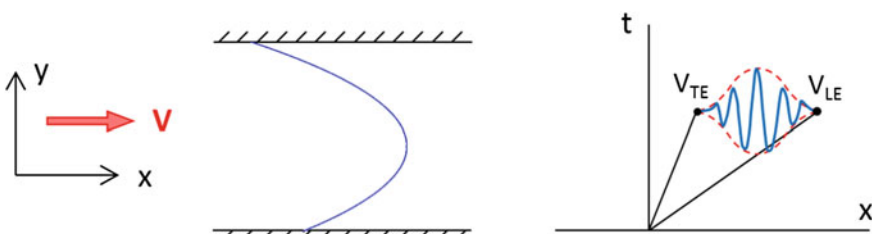


Fig. 3 Schematic showing the spatio-temporal evolution of an unstable wave packet in an observer frame of reference moving at a speed V . Here V_{LE} and V_{TE} are the leading and trailing edge velocities of the wave packet

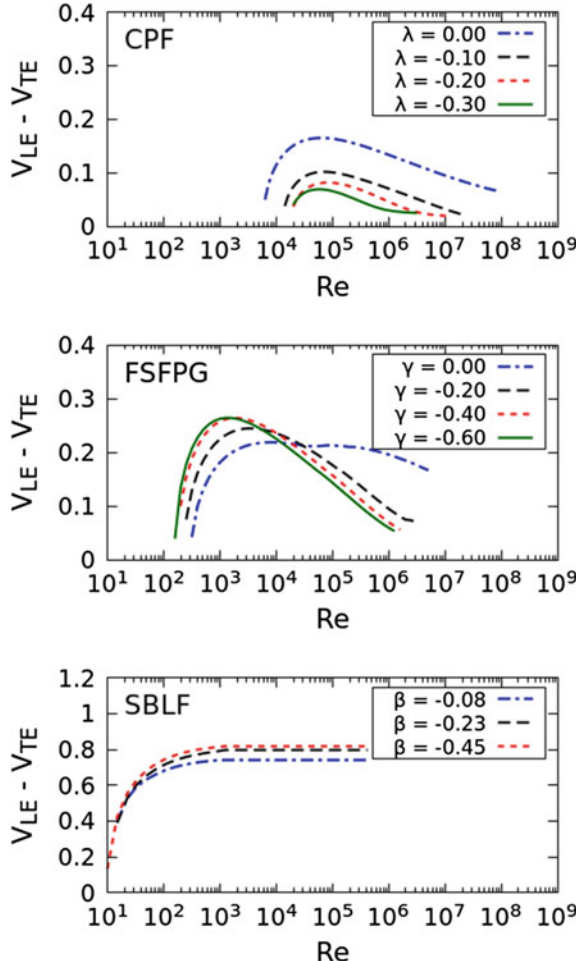


Fig. 4 $\Delta V = V_{LE} - V_{TE}$, a measure of the dispersion of the unstable wave packet as a function of Re for **a** CPF for a range of λ , **b** FSFPG for a range of γ and **c** SBLF for a range of β . Non-inflectional flows show a non-monotonic dependence of wave packet dispersion on viscosity as evident from (a) and (b). Inflectional flows such as SBLF (c) show weak dependence of dispersion on viscosity at high Re

which reduces again with further increase in Re . This means that the growth in spatial extent of instability is highest in the intermediate range of Re which promotes the spread of spatial envelope of the instability the most. This suggests that viscosity could be playing a role in this behaviour.

In the case of the inflectional SBLF shown in Fig. 4c however, the degree of dispersion does show a strong dependence on Re at very low Re ($\sim 10^2$) but quickly saturates to a constant value with increasing Re ($> 10^3$). This is reminiscent of the

neutral curves of a typical inflectional flow, where weak dependence on viscosity at higher values of Re is seen as a characteristic feature of the inviscid instability. Thus viscosity here plays its normal role—suppress the spread of disturbance in space when the flow is more viscous in character.

4 Conclusions

We have performed spatio-temporal analyses of both inflectional and non-inflectional parallel base flows for a range of plate speeds and Reynolds numbers (Re) in a moving frame of reference to identify the leading (V_{LE}) and trailing edge (V_{TE}) velocities of the unstable wave packet. The difference between them, $\Delta V = V_{LE} - V_{TE}$, can be seen as a measure of dispersion of the unstable wave packet which shows a non-monotonic dependence on viscosity for non-inflectional flows. In contrast, such dependence is weak in the case of inflectional flows except for a narrow range in Re sufficiently small in magnitude where the flow shows appreciable viscous character. This suggests that the difference in the dispersion characteristics of the unstable wave packet in inflectional and non-inflectional profiles could be due to a subtle role viscosity plays for the former, while the latter is dominated by inviscid dynamics. These results could provide an additional insight in understanding the dynamics and evolution of instability in inflectional and non-inflectional flows.

Acknowledgements The authors would like to thank Dr. Abhijith Mitra for lending the Chebyshev pseudospectral code used in the present work and for his help with numerical issues.

References

1. Rayleigh, L.: On the stability, or instability, of certain fluid motions. Ann. Mat. Pura. Appl. **169**, 321–354 (1995)
2. Taylor, G.I.: VIII Stability of a viscous liquid contained between two rotating cylinders. Phil. Trans. R. Soc. Lond. A **223**, 289–343 (1923)
3. Squire, H.B.: On the stability for three-dimensional disturbances of viscous fluid flow between parallel walls. Proc. R. Soc. Lond. A **142**, 621–628 (1933)
4. Schubauer, G.B., Skramstad, H.K.: Laminar-boundary-layer oscillations and transition on a flat plate. NACA **909** (1948)
5. Huerre, P., Monkewitz, P.A.: Absolute and convective instabilities in free shear layers. J. Fluid Mech. **159**, 151–168 (1985)
6. Huerre, P., Monkewitz, P.A.: Local and global instabilities in spatially developing flows. Ann. Rev. Fluid Mech. **22**, 473–537 (1990)
7. Potter, M.C.: Stability of plane Couette-Poiseuille flow. J. Fluid Mech. **24**, 609–619 (1966)
8. Schlichting, H., Gersten, K.: Boundary Layer Theory. Springer (2016)
9. Dovgal, A.V., Kozlov, V.V., Michalke, A.: Laminar boundary layer separation: instability and associated phenomena. Prog. Aerosp. Sci. **30**, 61–94 (1994)
10. Drazin, P.G., Reid, W.H.: Hydrodynamic Stability. Cambridge University Press (2004)
11. Boyd, J.P.: Chebyshev and Fourier Spectral Methods. Courier Corporation (2001)

12. Schmid, P.J., Henningson, D.S.: Stability and Transition in Shear Flows. Springer (2001)
13. Briggs, R.J.: Electron-Stream Interaction With Plasmas. MIT Press (1964)
14. Haj-Hariri, H.: Transformations reducing the order of the parameter in differential eigenvalue problems. *J. Comput. Phys.* **77**, 472–484 (1988)
15. Deissler, R.J.: The convective nature of instability in plane Poiseuille flow. *Phys. Fluids* **30**, 2303–2305 (1987)

Linearized Formulation for Fluid-Structure-Interaction for Rigid-Body Motion



Prabal S. Negi, Ardeshir Hanifi, and Dan S. Henningson

Abstract A linearized formulation for fluid-structure-interaction problems exhibiting rigid-body-motion is presented. The linearized equations are evaluated on a stationary grid and require no mesh motion. Numerical tests are performed to validate the derived formulation by comparing the time evolution between the linear and non-linear equations. In all cases both the growth rate and angular frequency of the instability matches to within 0.1% accuracy. The derived formulation is used to predict the phenomenon of symmetry breaking for a rotating cylinder with an attached splitter-plate, the onset of aeroelastic pitch-oscillations for a NACA0012 airfoil at transitional Reynolds numbers, and investigate the structural sensitivity of the least stable eigenvalue for an oscillating cylinder.

1 Introduction

Fluid-structure interaction (FSI) studies span a vast and diverse range of applications—from natural phenomenon such as the blood flow in arteries [1], to the more engineering applications of aircraft stability [2] and compliant surfaces [3]. The phenomena that emerge out of an FSI problem often exhibit complex, highly non-linear behavior with different flow regimes and state transitions. However, the initial transitions from one state to another may often be governed by a linear instability mechanism. Early investigations on the linear stability analysis of FSI problems can be traced to the investigations of the effect of compliance on boundary layer sta-

P. S. Negi (✉) · A. Hanifi · D. S. Henningson

Department of Engineering Mechanics, Linné Flow Centre and Swedish e-Science Research Centre (SeRC) KTH Royal Institute of Technology, Stockholm, Sweden

e-mail: negi@mech.kth.se

A. Hanifi

e-mail: ardeshir@mech.kth.se

D. S. Henningson

e-mail: henning@mech.kth.se

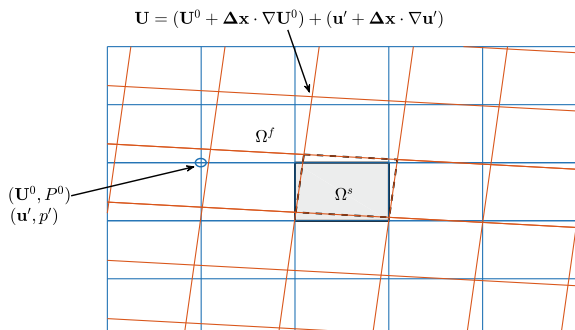
bility [4–6]. The formulation for the linear stability analysis has subsequently been used by many authors, see [3]. For problems requiring a more global approach, the first linear stability analysis of an oscillating cylinder was reported by [7], where the authors formulated the problem in a non-inertial frame of reference attached to the cylinder. Similar investigations for rigid-body motion have since followed [8–12].

In general linear global stability analysis for FSI problems have largely relied on relative frames of reference attached to the moving body. There have been a few investigations where the authors have attempted a general approach. Reference [13] have studied the linear stability of flapping of flags using an immersed boundary method. References [14, 15] use the Arbitrary-Lagrangian-Eulerian (ALE) formulation treating the grid velocity as a pseudo variable. References [16–18] formulate the linear equations independent of the grid velocity but require the evaluation of higher order derivatives for the interface stresses. In the current work, we derive and validate the linear stability equations for rigid-body-motion FSI problems. The methodology is similar to that of [16], however we approach the problem in its strong form as opposed to the weak formulation used by [16]. In addition no higher-order derivative terms for the interface stresses arise in the linear formulation.

2 Linearization of FSI

The typical linear stability analysis of a particular time-independent base flow state (\mathbf{U}^0, P^0) , involves the investigation of the behavior of small-perturbations (\mathbf{u}', p') , that are linearly super-imposed over this base state. For FSI problems, the requirement of moving interfaces poses a unique challenge when performing the linear analysis. The domain occupied by the fluid in the equilibrium position (base state) remains fixed in space however, for the time-evolving perturbations the FSI interface moves and thus the fluid domain varies with time. The issue is illustrated from a computational perspective in Fig. 1, where the blue lines are the equilibrium grid on which the base flow state is evaluated, and the red lines are the perturbed grid points due to the motion of the body, on which the linearly imposed small-perturbations evolve.

Fig. 1 Domain for a fluid-structure interaction problem showing the equilibrium grid (blue lines) and perturbed grid (red lines)



The challenge of linear FSI problems lies in the consistent treatment of the base flow and perturbation variables which may be defined on different fluid domains.

In the current work, the approach has been to define both the base flow as well as the perturbation variables on the equilibrium grid, and use a first-order Taylor expansion of the flow variables at the perturbed grid for the evaluation of the quantities in the Navier–Stokes equations. The definitions and Taylor expansions on the perturbed grid points is also illustrated in Fig. 1. In order to evaluate the derivatives of the quantities at the perturbed grid, information of the domain deformation is required. For a linear analysis, one may assume an affine mapping between the equilibrium and time-dependent grid as $\mathbf{x} = [\mathcal{I} + \mathcal{R}']\mathbf{x}^0 + \mathbf{b}$, where \mathcal{I} is the identity matrix, \mathcal{R}' is a perturbation matrix and \mathbf{b} is a translation vector. For small amplitude perturbations $\|\mathcal{R}'\| \ll 1$, and the inverse Jacobian may be conveniently expressed as

$$\frac{\partial \mathbf{x}^0}{\partial \mathbf{x}} = \left(\frac{\partial \mathbf{x}}{\partial \mathbf{x}^0} \right)^{-1} = [\mathcal{I} + \mathcal{R}']^{-1} \approx [\mathcal{I} - \mathcal{R}']. \quad (1)$$

We refer to this as the *geometric linearization* of the problem. Substitution of the Taylor expansion terms into the ALE form of the Navier–Stokes and use of geometric linearization for the evaluation of derivatives, one obtains again the standard linearized Navier–Stokes

$$\frac{\partial u'_i}{\partial t} + U_j^0 \frac{\partial u'_i}{\partial x_j^0} + u'_j \frac{\partial U_i^0}{\partial x_j^0} + \frac{\partial p'}{\partial x_i^0} - \frac{1}{Re} \frac{\partial^2 u'_i}{\partial x_j^0 \partial x_j^0} = 0. \quad (2)$$

$\partial/\partial x_j^0$ represents derivatives evaluated at the equilibrium grid. A similar procedure may be performed for the mass conservation equation to obtain the divergence free constraint as $\partial u'_i/\partial x_i^0 = 0$. Thus the final equations are evaluated completely on the equilibrium grid and no additional considerations of mesh movement are necessary. In the current work we only consider rigid-body motion and therefore the structural equations are modeled using a linear spring-mass-damper system. The linearized form of structural equations may be written as

$$\mathcal{M} \frac{\partial^2 \eta'_i}{\partial t^2} + \mathcal{D} \frac{\partial \eta'_i}{\partial t} + \mathcal{K} \eta'_i = \mathcal{F}'_i, \quad (3)$$

where η'_i is the perturbation in the position of solid body, \mathcal{M} , \mathcal{D} and \mathcal{K} represent the inertia, damping and stiffness of the structural system. \mathcal{F}'_i is the perturbation stress acting on the body due to the the perturbation field (\mathbf{u}', p') . For rotational motion η'_i represents the perturbation of the angular position while \mathcal{F}'_i represents the perturbation moment about the rotational axis. Due to the Taylor expansion asatz the velocity continuity boundary condition on the moving interface is modified as

$$\Delta x_j \frac{\partial U_i^0}{\partial x_j} + u'_i = \frac{d \Delta x_i}{dt}, \quad (4)$$

where $\Delta \mathbf{x}$ is the displacement of the interface point. Thus the perturbation velocities must account for the Taylor expansion term of the base flow at the perturbed boundary. The linear FSI problem for the perturbations is turned into a standard linear perturbation problem with the exception of the modified boundary conditions (transpiration instead of no-slip). The complete derivation of the linear equations, boundary conditions and discussion of the high-order terms may be found in [19].

3 Linear Results

3.1 Oscillating Cylinder

Numerical tests are performed to validate the linear equations for FSI derived in the previous section. All computations were performed using a high-order spectral-element method (SEM) code [20]. Moving boundaries are treated using the ALE formulation and the fluid and structural equations are coupled using the Green's function decomposition approach of [21].

A 2D circular cylinder free to oscillate in the cross-stream direction subject to the action of a spring-damper system is investigated. η in Eq. 3 represents the vertical position of the cylinder. The Reynolds number of the flow based on the cylinder diameter is $Re = 23.512$. The inlet of the computational domain is 25 diameters upstream of the cylinder while the outflow boundary is 60 diameters downstream of the cylinder. The lateral boundaries are 50 diameters away on either side. A uniform inflow Dirichlet boundary condition is applied on the inflow and the lateral boundaries while the stress-free boundary condition is applied on the outflow boundary. The base flow for all cases was calculated by keeping structure fixed at its initial position. Convergence to steady state is accelerated by using BoostConv [22]. The structural parameters are set to $\mathcal{M} = 5.4977$, $\mathcal{K} = 3.4802$ and $\mathcal{D} = 6.597 \times 10^{-2}$.

Pseudo-random perturbations of order $O(10^{-6})$ are added to the base flow field and the evolution of the coupled FSI system is tracked. Figure 2 (left) shows the variation of η with time during the initial stages of the evolution. The growth rate and frequency is determined by tracking the peak amplitudes of the oscillations, denoted as η^{pks} . Figure 2 (right) shows the time evolution of η^{pks} which traces a straight line in the semi-log plot, signifying exponentially growing instability. Figure 3 shows the one-sided eigenspectra obtained using the implicitly restarted Arnoldi method [23]. λ_r represents the real part of the eigenvalue (growth rate) and λ_i represents the imaginary part of the eigenvalue (angular frequency). In Table 1 the estimates of the unstable eigenvalue are reported for the non-linear simulations, linear simulations and the Arnoldi method. All three methods have a very good agreement with each other, with the relative difference in the growth rate being less than 0.1%.

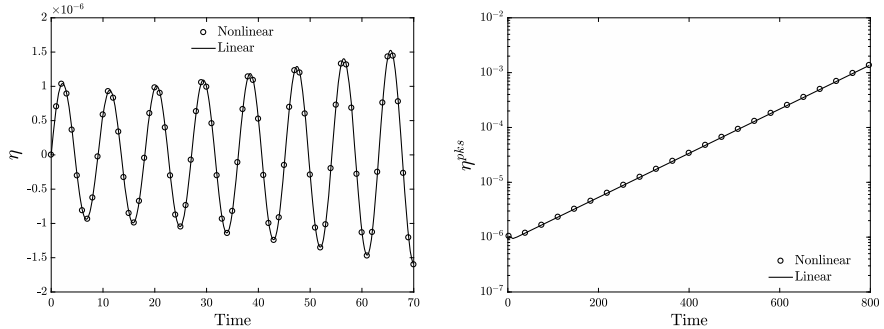


Fig. 2 Comparison of linear and non-linear evolution of cylinder position η for identical small amplitude disturbance. **a** shows the time evolution of η in the first few cycles of the oscillation. **b** shows the evolution of peak amplitudes of the oscillation in a semi-log scale

Fig. 3 One-sided eigenspectrum for a cylinder in cross-flow at $Re = 23.512$

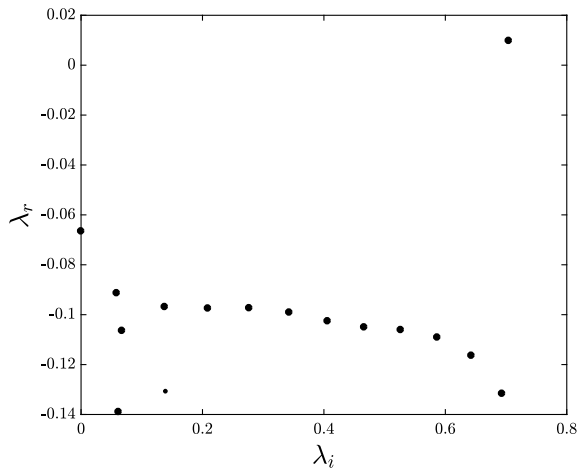


Table 1 Unstable eigenvalue estimates for an oscillating cylinder

Case	Eigenvalue
Non-linear	$9.86 \times 10^{-3} \pm 0.704i$
Linear	$9.85 \times 10^{-3} \pm 0.704i$
Arnoldi	$9.86 \times 10^{-3} \pm 0.704i$

3.2 Rotating Cylinder with Splitter-Plate

The derived linear formulation is used to investigate the case of a circular cylinder with an attached splitter-plate, free to rotate about its center. The structural equations take the same form as in Eq. 3. The rotational stiffness \mathcal{K} and damping \mathcal{D} are both set to zero. For certain lengths of the cylinder-splitter body, the system is known to exhibit spontaneous symmetry breaking and splitter-plate settles at a new equilibrium

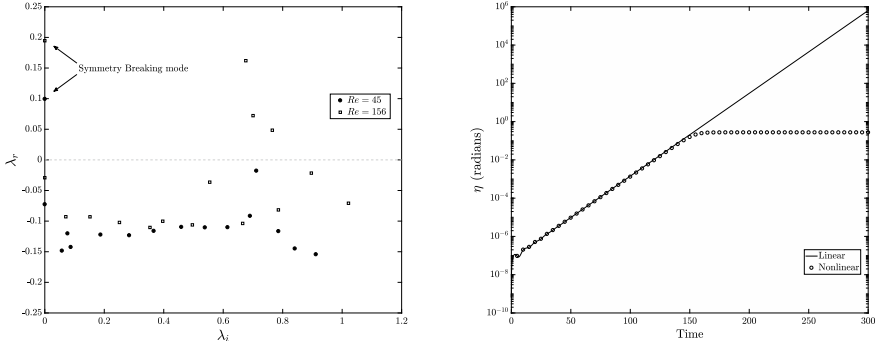


Fig. 4 (Left) One-sided spectra for the cases exhibiting spontaneous symmetry breaking at $Re = 45$ and $Re = 156$ for a rotatable cylinder with splitter-plate. (Right) Linear and non-linear evolution of η at $Re = 45$

position [24, 25]. The symmetry breaking effect is investigated through our linear FSI framework. In accordance with the results of [26], symmetry breaking is expected to occur for splitter-plate lengths of less than $2D$. The plate length is set to $1D$ and a thickness of $0.02D$. Following [26] we use a solid to fluid density ratio of 1.001 for $Re = 45$ and 1.01 for $Re = 156$. BoostConv is used to obtain the steady state solutions when the splitter-plate is at a zero angle of incidence to the oncoming flow.

Figure 4 (left) shows the spectra for the two different Reynolds numbers. Both cases have an eigenvalue lying on the positive y -axis ($\lambda = 0.10 + 0i$ for $Re = 45$ and $\lambda = 0.19 + 0i$ for $Re = 156$). This represents the symmetry-breaking eigenmode of the system since it does not oscillate about a zero mean but rather leads to a monotonic growth in the rotational angle. For the final symmetry breaking a non-linear mechanism is required since the flow must equilibrate at the new position. However the onset is governed by the zero frequency instability. For $Re = 45$, linear and non-linear evolution of the rotational angle is compared in Fig. 4 (right). Both the simulations undergo the same exponential growth of about five orders of magnitude before the non-linear case saturates, while the linear case continues its exponential growth. The saturation of the non-linear simulations occur at $\eta \approx 15.5^\circ$, which is the same turn angle reported by [26].

3.3 Aeroelastic Instability of NACA0012

The experimental investigation of [27] has brought to light the failure of classical aerodynamic models in predicting loss of aeroelastic stability at low-to-moderate transitional Reynolds numbers. In the aeroelasticity experiments the airfoil was free to rotate in the pitch degree-of-freedom while being constrained by a spring-damper system. The authors have reported aeroelastic instabilities for different spring stiffness values. We utilize the FSI global stability analysis framework to investigate onset

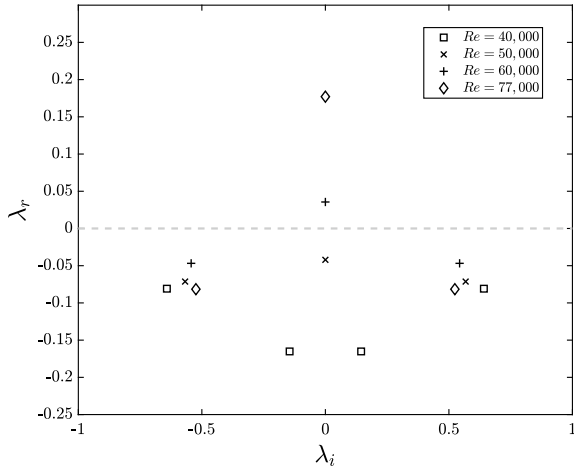


Fig. 5 Eigenvalue spectra for a NACA0012 airfoil at different Reynolds numbers. The zero frequency mode crosses the stability boundary somewhere between $Re = 50,000$ and $Re = 60,000$

of spontaneous pitch oscillations for a NACA0012 airfoil at transitional Reynolds numbers. The stability analysis is performed for the highest spring stiffness case of the experiments ($K_s = 0.30 \text{ Nm/rad}$) at different chord based Reynolds numbers. The stability analysis reveals the presence of an unstable (zero frequency) eigenvalue for the coupled aeroelastic system for a certain range of Reynolds numbers, with the onset of instability somewhere between $Re = 50,000$ and $Re = 60,000$. The results matches well with the experimental results of [27], which report the onset at $Re = 55,000$. The aeroelastic eigen-spectra for different Reynolds numbers is shown in Fig. 5 and the zero frequency unstable mode for $Re = 77,000$ is shown in Fig. 6.

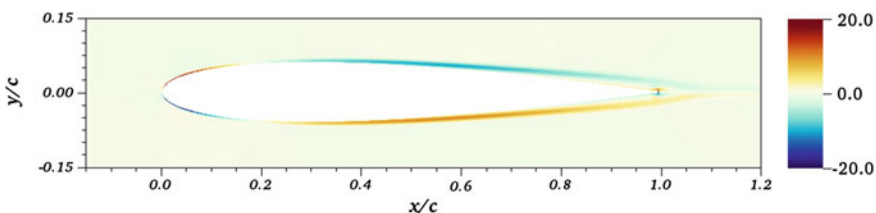


Fig. 6 Eigen-mode corresponding to the zero frequency unstable eigenvalue for the NACA0012 airfoil at $Re = 77,000$

3.4 Structural Sensitivity of the Eigenvalue

Finally, we investigate the changes in the structural sensitivity of the unstable eigenvalue, when the structural degrees of freedom are introduced into a purely fluid system. The eigenvalue sensitivity is typically studied through the use of adjoint Eqs. [28, 29] where, for any linear operator \mathcal{L} with an eigenpair (λ, q) , a first-order approximation to the perturbed eigenvalue problem $(\mathcal{L} + \Delta\mathcal{L})(q + \Delta q) = (\lambda + \Delta\lambda)(q + \Delta q)$ can be obtained by making use of the corresponding adjoint eigenvector [28]. To estimate the drift in eigenvalue, knowledge of the specific operator perturbation $\Delta\mathcal{L}$ is required. However, as shown by [28], if the structural perturbation is assumed to be of the form of a local feedback, a spatial sensitivity map for the eigenvalue perturbation can be found. The upper bound for the eigenvalue drift may be found as [28]

$$|\Delta\lambda| \leq ||C_0||\Theta(x_0, y_0),$$

$$\Theta(x, y) = \frac{||q^\dagger(x, y)|| \cdot ||q(x, y)||}{||\langle q^\dagger, q \rangle||}, \quad (5)$$

where C_0 is a matrix that defines the feedback due to the localized operator perturbation and the local coupling between different velocity components. q^\dagger represents the right eigenvector of the adjoint operator \mathcal{L}^\dagger with the eigenvalue of λ^* . The quantity $\Theta(x, y)$ gives an indication of regions where the localized feedback will produce a large drift in the eigenvalue, thus representing the sensitivity of the eigenvalue to structural perturbations.

We perform the structural sensitivity analysis for a spring-mounted cylinder oscillating in cross-flow at $Re = 50$. The density ratio of the cylinder is set to 10 and structural damping is set to zero ($\mathcal{D} = 0$). The quantity $\Theta(x, y)$ is evaluated for the unstable eigenvalue with varying natural frequencies $\omega_n = \sqrt{\mathcal{K}/\mathcal{M}}$ of the spring-mass system. The derivation of the adjoint FSI equations can be found in [19]. The obtained sensitivity map of the FSI system is compared to the case of a stationary cylinder at $Re = 50$ obtained by [28]. The unstable eigenvalue obtained for the stationary case is $\lambda = 1.3325 \times 10^{-2} \pm 0.74189i$. For the oscillating cases where the natural frequency ω_n is far away from the unstable frequency of the FSI system, the sensitivity map resembles that of stationary cylinder. However, as ω_n is brought close to the unstable frequency, the sensitivity map changes with regions very close to the cylinder becoming more sensitive. Very close to resonance, the sensitivity map changes quite radically and most of the sensitivity lies in two small lobes, above and below the cylinder. Figure 7 shows a comparison of the sensitivity maps for a stationary cylinder and the oscillating cylinder. The natural frequency of the spring-mass system is $\omega_n = 0.7665$ and the unstable eigenvalue for the coupled system is $\lambda = 7.2151 \times 10^{-2} \pm 0.74010i$.

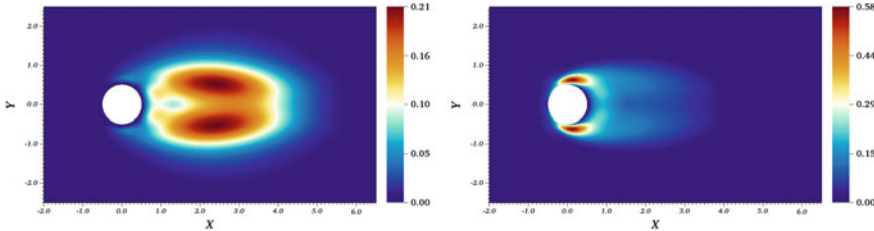


Fig. 7 Structural sensitivity map for the least stable eigenvalue for a stationary and oscillating cylinder. (Left) Θ for the stationary cylinder case and (right) Θ for the oscillating cylinder close to resonance

4 Conclusions

A formulation for the linear stability analysis of rigid-body-motion fluid-structure-interaction problems is presented. The final form of the linear equations reduces to the standard linearized Navier–Stokes with the exception of the velocity continuity boundary condition which transforms to a transpiration boundary condition. Numerical results comparing the linear and non-linear evolution show a very good agreement with each other. The FSI linear framework is used to analyze the case of symmetry breaking for a rotating cylinder with a rigid splitter-plate where a zero frequency unstable mode is identified as the cause of symmetry breaking. Performing the stability analysis for a NACA0012 airfoil at transitional Reynolds numbers also provides good agreement with the earlier experimental investigation on the onset of aeroelastic instability. Finally, the eigenvalue sensitivity to structural perturbations is investigated using the adjoint equations for FSI, for a 2D cylinder oscillating in the cross-stream direction. Close to resonance, the sensitivity map changes completely and the dominant region of sensitivity lies close to the cylinder, located symmetrically above and below.

Acknowledgements Financial support for this work was provided by the European Research Council under grant agreement 694452-TRANSEP-ERC-2015-AdG. The computations were performed on resources provided by the Swedish National Infrastructure for Computing (SNIC) at the PDC Center for High Performance Computing at the Royal Institute of Technology (KTH).

References

1. Freund, J.B.: *Annu. Rev. Fluid Mech.* **46**(1), 67 (2014)
2. Dowell, E.H., Hall, K.C.: *Annu. Rev. Fluid Mech.* **33**(1), 445 (2001)
3. Riley, J.J., Gad-el Hak, M., Metcalfe, R.W.: *Ann. Rev. Fluid Mech.* **20**(1), 393 (1988)
4. Benjamin, T.B.: *J. Fluid Mech.* **6**(2), 161–205 (1959)
5. Benjamin, T.B.: *J. Fluid Mech.* **9**(4), 513–532 (1960)
6. Landahl, M.T.: *J. Fluid Mech.* **13**(4), 609–632 (1962)
7. Cossu, C., Morino, L.: *J. Fluids Struct.* **14**(2), 183 (2000)

8. Mittal, S., Singh, S.: *J. Fluid Mech.* **534**, 185–194 (2005)
9. Assemat, P., Fabre, D., Magnaudet, J.: *J. Fluid Mech.* **690**, 173–202 (2012)
10. Tchoufag, J., Fabre, D., Magnaudet, J.: *J. Fluid Mech.* **740**, 278–311 (2014)
11. Cano-Lozano, J.C., Tchoufag, J., Magnaudet, J., Martínez-Bazán, C.: *Phys. Fluids* **28**(1), 014102 (2016)
12. Navrose, S., Mittal: *J. Fluid Mech.* **794**, 565–594 (2016)
13. Goza, A., Colonius, T., Sader, J.E.: *J. Fluid Mech.* **857**, 312–344 (2018)
14. Lesoinne, M., Sarkis, M., Hetmaniuk, U., Farhat, C.: Computer methods in applied mechanics and engineering. *Adv. Comput. Meth. Fluid Struct. Interact.* **190**(24), 3121 (2001)
15. Pfister, J.L., Marquet, O., Carini, M.: *Comput. Meth. Appl. Mech. Eng.* **355**, 663 (2019)
16. Fanion, T., Fernández, A.M., Le Tallec, P.: *Revue Européenne des Éléments Finis* **9**(6–7), 681 (2000)
17. Fernández, M.A., Le Tallec, P.: *Comput. Meth. Appl. Mech. Eng.* **192**(43), 4805 (2003)
18. Fernández, M.A., Le Tallec, P.: *Comput. Meth. Appl. Mech. Eng.* **192**(43), 4837 (2003)
19. Negi, P.: Stability and transition in pitching wings. Ph.D. thesis, KTH Royal Institute of Technology (2019). <http://kth.diva-portal.org/smash/record.jsf?pid=diva2>
20. Fischer, P.F., Lottes, J.W., Kerkemeier, S.G.: Nek5000 web page (2008). <http://nek5000.mcs.anl.gov>
21. Fischer, P., Schmitt, M., Tomboulides, A.: Recent Developments in Spectral Element Simulations of Moving-Domain Problems, pp. 213–244. Springer, New York, NY (2017)
22. Citro, V., Luchini, P., Giannetti, F., Auteri, F.: *J. Comput. Phys.* **344**, 234 (2017)
23. Sorensen, D.: *SIAM J. Matrix Anal. Appl.* **13**(1), 357 (1992)
24. Xu, J.C., Sen, M., Gad-el Hak, M.: *Phys. Fluids A Fluid Dyn.* **2**(11), 1925 (1990)
25. Bagheri, S., Mazzino, A., Bottaro, A.: *Phys. Rev. Lett.* **109**(15), 154502 (2012)
26. Lācis, U., Brosse, N., Ingremoine, F., Mazzino, A., Lundell, F., Kellay, H., Bagheri, S.: *Nat. Commun.* **5**, 5310 (2014)
27. Poirel, D., Harris, Y., Benaissa, A.: *J. Fluids Struct.* **24**(5), 700 (2008)
28. Gianetti, F., Luchini, P.: *J. Fluid Mech.* **581**, 167–197 (2007)
29. Luchini, P., Bottaro, A.: *Annu. Rev. Fluid Mech.* **46**(1), 493 (2014)

Investigations of Laminar to Turbulent Transition in an Oscillating Airfoil Boundary Layer



Duncan Ohno, Jonas Romblad, Marwan Khaled, and Ulrich Rist

Abstract Linear stability analysis and wind tunnel measurements are performed to investigate the behavior of laminar to turbulent transition in an oscillating airfoil boundary layer. A varying pressure gradient is induced by periodically changing the inflow angle to a natural laminar flow airfoil, simulating large-scale free-stream turbulence. In a quasi-steady approach, linear stability analysis is utilized based on flow field solutions acquired with RANS simulations for the periodic problem. The time-dependent growth rates of the “Tollmien-Schlichting” (TS) modes are computed along wave trajectories which predict a periodically moving transition location. Experimental results, obtained with time signals of wall pressures in streamwise direction in the wind tunnel, show a good agreement with numerical results. At high frequencies and amplitudes of the inflow oscillation, the downstream moving transition front is slower than the upstream moving transition front. Based on the results, there is evidence for an important linear contribution to the character of transition movement before the occurrence of the non-linear “convective transition mode”. A characterization of the unsteadiness of the transition movement with a new dimensionless quantity—taking the trajectory of TS-waves and the moving transition front into account—is discussed.

1 Introduction

The reduction of friction drag plays a crucial role in the design of future commercial aircraft and wind turbines, which is why the use of natural laminar flow (NLF) airfoils is gaining interest [1]. NLF airfoils feature a delayed laminar to turbulent transition and are generally designed using linear stability theory (LST) with the e^N -method [2]. Like most other transition prediction methods, this approach is based on the

D. Ohno (✉) · J. Romblad · M. Khaled · U. Rist

Institute of Aerodynamics and Gasdynamics, University of Stuttgart, 70550, Stuttgart, Germany
e-mail: ohno@iag.uni-stuttgart.de

assumption of a steady baseflow. However, atmospheric turbulence in realistic flight conditions causes an unsteady inflow to the airfoil with a wide range of length scales.

Based on the Kolmogorov hypothesis [3], free-stream turbulence spectra can be modelled covering the energy containing range, the inertial subrange as well as the dissipation range, see Pope [4]. Reeh [5] proposed a separation of the inflow turbulence in two ranges of length scales according to their influence on the boundary layer transition: small-scale disturbances with frequencies corresponding to Tollmien-Schlichting waves and large-scale, gust-like disturbances, which can be regarded as variations of the inflow angle. Small-scale turbulence generates initial perturbations in the boundary layer which ultimately lead to transition [6, 7]. On the other hand, large-scale disturbances lead to an unsteady pressure gradient, which strongly influences the amplification rates of boundary layer instabilities. The present work focuses on the latter disturbances, therefore on flows with oscillating free-stream.

Miller and Fejer [8] and Obremski and Fejer [9] conducted the first investigations of transition in oscillating flows on a flat plate boundary layer, where they observed the formation of turbulent spots at the oscillation frequency. Obremski and Fejer [9] classified the unsteady process into two periodic phases: an initial “creative mode”, where flow instabilities (e.g. TS-waves) lead to transition and a “convective mode”, where the created turbulent spot travels downstream. A similar behavior of transition was observed in further experimental investigations which were carried out by Studer et al. [10] on a NACA0015 airfoil for two unsteady cases. The work included the application of a wavelet transform to obtain time dependent frequency spectra. Romblad et al. [11] continued the research for a NLF airfoil by using a gust generator to create inflow variations in a wind tunnel. His work is part of the project of the present paper and will be briefly explained in Sect. 2.

For a theoretical understanding of the physical process with linear stability analysis, Obremski and Morkovin [12] utilized a quasi-steady trajectory-following method for wave packets, based on previous measurements by Obremski and Fejer [9]. This approach was again applied by Studer et al. [10] to compare unsteady amplification rates of TS-waves with corresponding measurements. Radespiel et al. [13] added an unsteady transition prediction scheme to URANS simulations for moving airfoils with laminar separation bubbles, based on LST with temporal theory.

This paper covers investigations with linear stability theory with an extended trajectory-following method for TS-waves including validation with wind tunnel measurements.

2 Investigated Case

The investigations were carried out on the pressure side of the “MW-166-39-44-43” NLF airfoil—depicted in Fig. 1a—which was designed for gliders and modified for free-flight experiments. The chord Reynolds number $Re = 3.4 \cdot 10^6$, with a Mach number of $Ma = 0.11$ and a negative angle of attack $AoA_{ref} = -1.4^\circ$ were selected as a reference case. As shown in the stability diagram in Fig. 1b, the amplification of

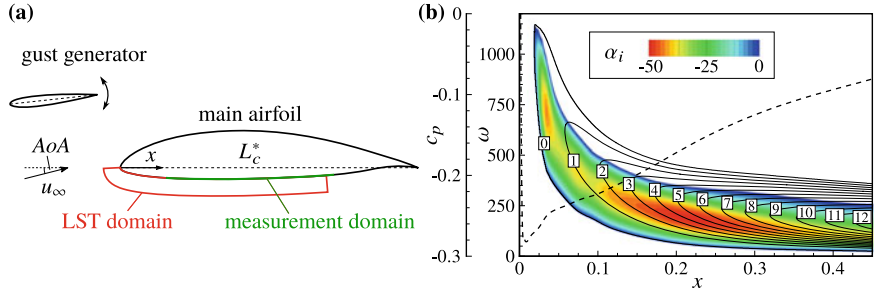


Fig. 1 **a** Experimental setup of gust generator airfoil and main airfoil with LST domain. **b** Stability diagram with α_i for AoA_{ref} ; solid lines: n -factors; dashed line: pressure distribution c_p

TS-waves is increased due to the adverse pressure gradient. Dimensional quantities are denoted with $*$, whereas the chord-length L_c^* and the free-stream velocity u_∞^* are used for nondimensionalization.

In the wind tunnel measurements [11], an additional airfoil (gust generator) is oscillating upstream, leading to 2D inflow angle fluctuations on the main airfoil, see Fig. 1a. For the numerical investigations, angle of attack fluctuations are realized with steady baseflows acquired with RANS simulations. In the current work, the definition of the reduced frequency

$$\kappa = \frac{\pi \cdot f_{osc}^* \cdot L_c^*}{u_\infty^*}, \quad (1)$$

where f_{osc}^* denotes the dimensional oscillation frequency, is used to describe the investigated cases, see Leishman [14]. The amplitude of the periodic gusts is expressed in angle of attack variations ΔAoA with respect to the reference angle of attack AoA_{ref} , leading to the formulation

$$AoA(t) = AoA_{ref} + \Delta AoA \cdot \sin(2\kappa \cdot t). \quad (2)$$

The range of investigated frequencies in the wind tunnel experiments is $\kappa \in [0.22, 1.67]$ at the amplitude of $\Delta AoA = 0.5^\circ$, whereas linear stability analysis is performed at $\Delta AoA \in [0.25^\circ, 1.25^\circ]$ for $\kappa \in [0.56, 1.67]$.

3 Experimental Results

Figure 2 shows broadband RMS values of unsteady pressure signals overlaid with the C_3 parameter of an adaption of the M-TERA intermittency method by Zhang et al. [15] in a space-time plot for two cases. Despite the oscillation, the characteristics of transition—including the amplification of TS-waves and the RMS peak—are clearly

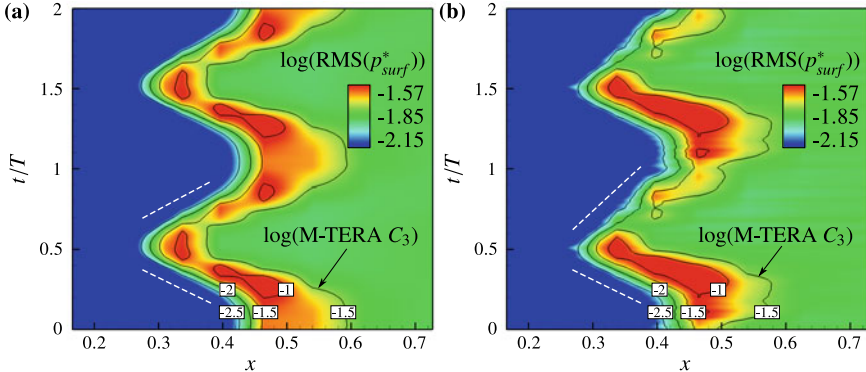


Fig. 2 Experimental results of Romblad et al. [11]: cycle averaged broadband RMS of unsteady surface pressure signals; lines: C_3 M-TERA intermittency method. **a** $\kappa = 0.22$ **b** $\kappa = 1.12$

visible at the frequency $\kappa = 0.22$ (Fig. 2a). The upstream and downstream movement of the transition front is symmetric with respect to time and exhibits the same velocities. In contrast, at the higher frequency of $\kappa = 1.12$ (Fig. 2b), the transition fronts appear asymmetrically with respect to time. In addition, the RMS peak is more pronounced for the upstream moving transition but almost disappears for the downstream moving transition. Studer et al. [10] interpreted this behavior as an indication of a “convective transition mode”, where the downstream moving transition front is slowed down due to the required time for the convection of the already turbulent flow. However, the present results show a downstream transition velocity maximum of $0.1 \cdot u_\infty$, which is much slower than observed in measurements by Studer et al. [10] with $0.4 \cdot u_\infty$ or by Obremski and Fejer [9] with $> 0.5 \cdot u_\infty$. Since the phase velocities of TS-waves are usually about $\approx 0.33 \cdot u_\infty$ —and therefore higher than the velocity of the downstream moving transition front—it must be assumed, however, that linear effects also play a role in the selected case. Therefore, the following sections deal with the analysis of the flow using LST. For detailed information on the setup and results of the measurements, see Romblad et al. [11].

4 Linear Stability Analysis

Linear stability calculations are carried out with an in-house solver for compressible flows on previously acquired baseflows from steady RANS simulations.

The case for gusts with $\kappa \rightarrow 0$ (very large wavelengths) can be investigated fully steady with “classical” LST and the e^N -method of van Ingen [16] by separately analyzing baseflows at different angles of attack AoA . The calculated envelopes of TS-wave amplification rates for each case can be assembled in a space-time plot, see Fig. 3 for $\Delta AoA = 0.5^\circ$. The colored lines are denoting the N -factors which are oscillating

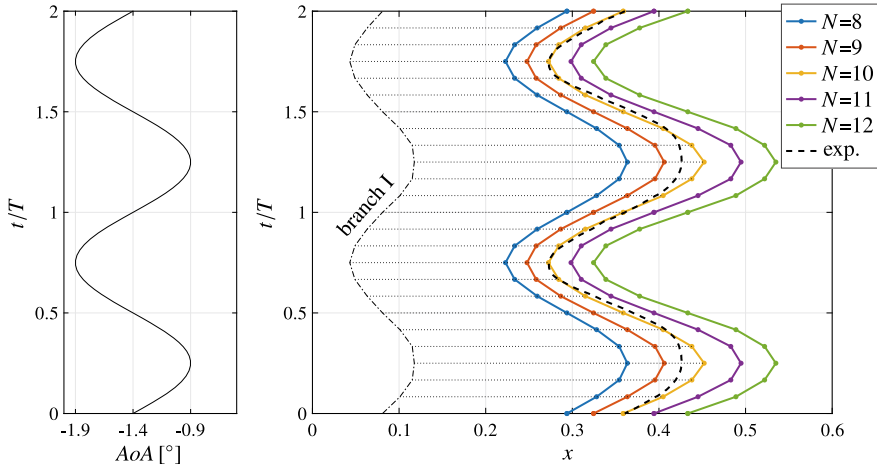


Fig. 3 Variation of the inflow angle AoA (left) with resulting transition prediction based on classical e^N -method for steady case ($\kappa \rightarrow 0$) with amplitude $\Delta AoA = 0.5^\circ$; experimental results (dashed line): $C_3 = 10^{-2.5}$ at $\kappa = 0.22$

versus time (normalized by the period) in x -direction. Branch I oscillates between $0.04 \leq x \leq 0.12$. For most of the period, there is a good agreement of the transition location for $N = 10$ with the quasi-steady case $\kappa = 0.22$ in the experiments. Since the oscillation is infinitely slow, the trajectories of the TS-waves run horizontally. In the following, the properties of this case are referred to as “quasi-steady”.

In order to calculate N -factors for higher oscillation frequencies (e.g. Fig. 2 with $\kappa = 1.12$), the amplification rate of TS-waves need to be integrated along their spatio-temporal trajectories. For the current work, 72 snapshots represent the “unsteady baseflow”, covering one cycle of the oscillation. While the time intervals Δt are thereby defined equidistantly, the intervals in space Δx can be determined using the phase velocity of the TS-waves c_{TS} , which is part of the stability solution of the spatial approach:

$$\Delta x = c_{TS} \cdot \Delta t = \frac{\omega}{\alpha_r} \cdot \Delta t. \quad (3)$$

A correlation of the stability solution is performed along the trajectories, in order to track the same perturbation. The n -factors are integrated for each combination of frequency ω and phase of the oscillation ϕ , starting from the respective point of neutral stability x_0 (branch I):

$$n_{\omega,\phi}(x) = - \int_{x_0(\omega,\phi)}^x \alpha_{i;\omega,\phi}(x) dx. \quad (4)$$

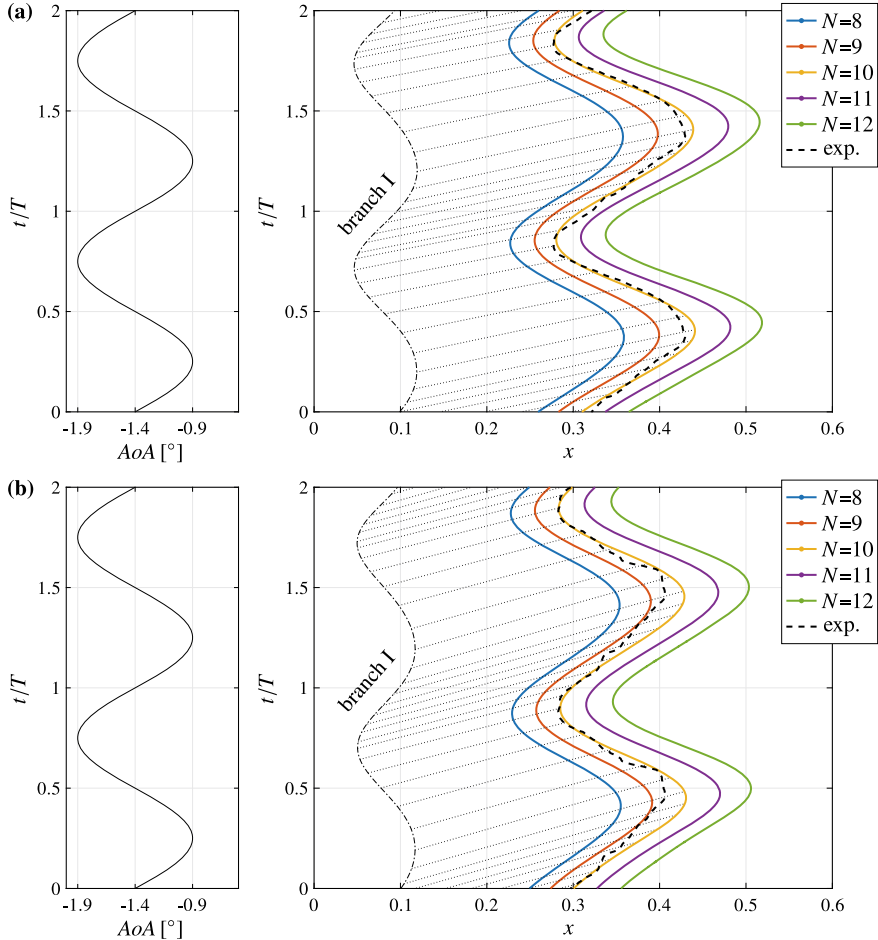


Fig. 4 Variation of the inflow angle AoA (left) with resulting transition prediction based on modified e^N -method with TS-wave trajectory-following with amplitude $\Delta AoA = 0.5^\circ$; experimental results (dashed line): $C_3 = 10^{-2.5}$. **a** $\kappa = 1.0$ **b** $\kappa = 1.34$

Analogous to the classic e^N -method, the envelope $N(x, t)$ can now be obtained by the maximum of all $n_{\omega, \phi}(x)$ in space and also in time. This method can also be applied using interpolation in postprocessing, without correlation along the trajectories. However, this may lead to a poor resolution. Other authors [10, 12] presumably shifted the amplitudes of the LST to the levels of experimental results instead of selecting branch I as the initial point of integration. Furthermore, they used the group velocity instead of the individual phase velocities of the modes.

The results of the aforementioned method for frequency $\kappa = 1.0$ and amplitude $\Delta AoA = 0.5^\circ$ can be found in the x/t -plot in Fig. 4a. Here, branch I is defined by the point of neutral stability of the first mode reaching $N = 10$. In contrast to the

quasi-steady case, the trajectories exhibit a gradient in the x/t -plot and the predicted transition position oscillates asymmetrically in time. Again, a very good accordance with the experimental results for $N = 10$ can be observed, suggesting that the transition can be described with the linear theory for this case. By increasing the frequency to $\kappa = 1.34$ the asymmetry becomes even more pronounced, see Fig. 4b. However, there is a slight discrepancy at maximum of the transition position and the downstream transition front is somewhat slower in the experiments. A possible reason for this might be the onset of the “convective transition mode”, hence non-linear effects. On the other hand, the quasi-steady approach—especially with regard to the baseflows—might already lose its validity at this frequency.

5 Analysis and Discussion

The properties of the measured and numerically predicted ($N = 10$) oscillating transition location can now be investigated with respect to the frequency. Figure 5a depicts the velocities v_{tr} of the upstream (blue) and downstream (red) transition fronts versus κ . The black line represents the theoretical, quasi-steady velocity for the case of the temporally symmetrical transition motion shown in Fig. 3a. While the upstream travelling transition front largely corresponds to the quasi-steady case, the downstream travelling transition front is significantly slower for higher frequencies, in both, experiments and LST. However, as already mentioned above, the measured downstream velocity is slightly lower than in theory. For increasing frequencies, the minimum and maximum transition locations move towards each other, which is depicted in Fig. 5b.

The theoretical velocities of the transition fronts for different amplitudes ΔAoA can likewise be calculated with the LST, see Fig. 6. The y-axis is scaled differently in each case. It becomes clear that the discrepancy between the upstream and downstream speed widens not only with the increase in frequency but also with the increase

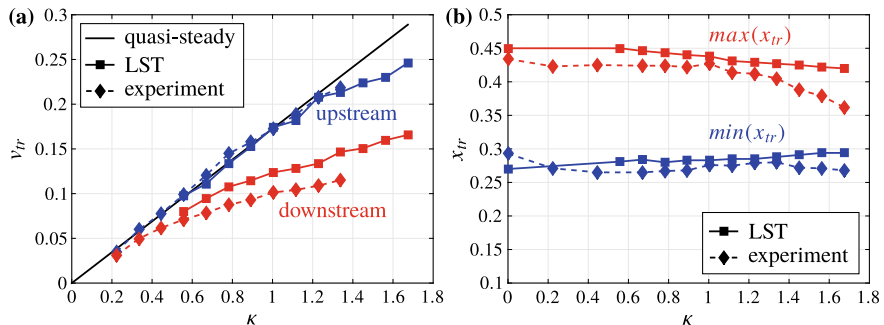


Fig. 5 $\Delta AoA = 0.5^\circ$, $N = 10$: **a** Velocity of the transition front v_{tr} versus κ for upstream and downstream movement. **b** Transition location x_{tr} versus κ

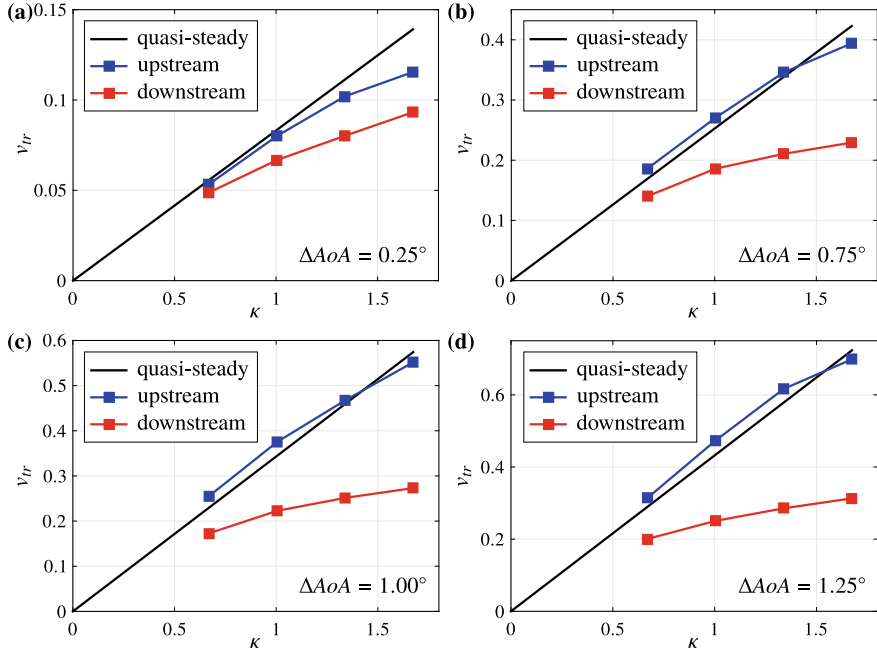


Fig. 6 Velocity of the transition front v_{tr} versus κ for upstream and downstream movement from LST with $N = 10$. **a** $\Delta AoA = 0.25^\circ$ **b** $\Delta AoA = 0.75^\circ$ **c** $\Delta AoA = 1.00^\circ$ **d** $\Delta AoA = 1.25^\circ$

in amplitude. Therefore, it must be noted that amplitude also plays an important role in the characterization of the physical problem.

The reduced frequency κ (see Eq. (1)) is defined with the chord length L_c^* , which has no direct relation to the unsteady transition behavior and is therefore questionable as a characterization measure. Hence, a new dimensionless quantity or reduced frequency

$$\kappa_{trans} = \frac{\omega_{osc}^* \cdot \Delta L_{tr}^*|_{steady}}{u_\infty^*} \quad (5)$$

is proposed, taking the length $\Delta L_{tr}^*|_{steady}$ into account, which represents the maximum length of the transition movement for the quasi-steady case, see depiction in Fig. 7 (inlay). This definition implicitly takes into account the amplitude ΔAoA , making it a suitable measure of the unsteadiness of oscillating transition locations. Since the numerator of Eq. (5) is proportional to the theoretical quasi-steady transition velocity and the phase velocities of the TS-waves are always coupled to the denominator u_∞^* , $\kappa_{trans} \sim v_{tr}/c_{TS}$ applies. Therefore, this quantity also describes the ratio of two gradients in the x/t -plot, where the velocities c_{TS} and v_{tr} (steady) are about the same for $\kappa_{trans} \approx 1$.

Using this definition, the results of the performed stability analyses (all combinations of amplitude and frequency) can now be adequately compared, see Fig. 7. The

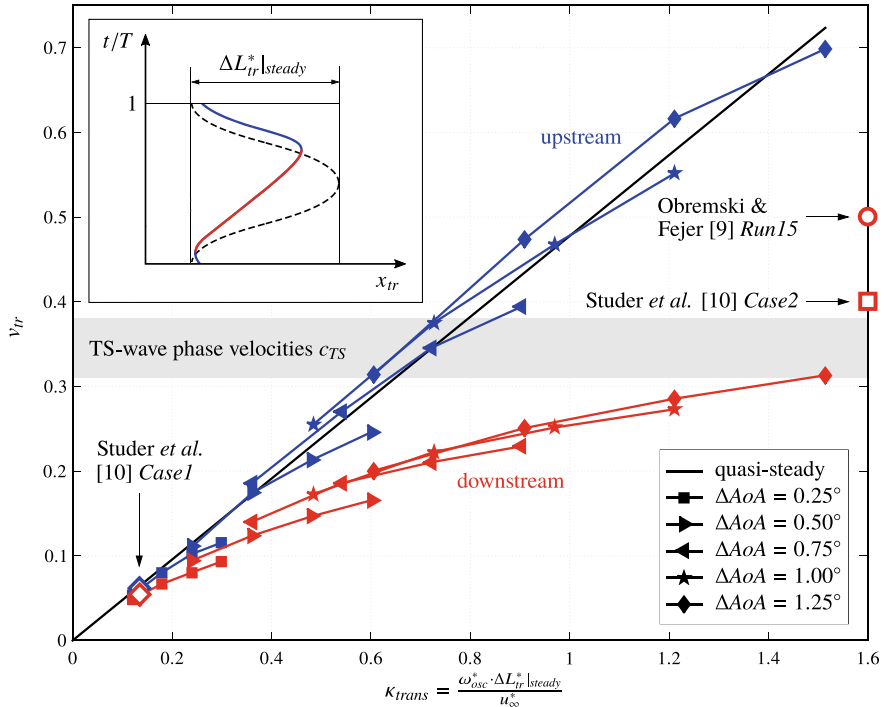


Fig. 7 Velocity of the transition front v_{tr} for upstream and downstream movement (LST with $N = 10$) as a function of a new dimensionless quantity, including references from Studer et al. [10] and Obremski and Fejer [9]. Inlay picture: depiction of transition fronts with TS-wave trajectory

upstream and downstream transition velocities are thereby grouped, respectively, along the quasi-steady line and in a flattening trend below the phase velocity of the TS-waves. While the quasi-steady case of Studer et al. [10] (Case1) can be inserted in the diagram, the unsteady cases of Studer et al. [10] (Case2) and Obremski and Fejer [9] (Run15) with the “convective transition” cannot be plotted versus κ_{trans} , since there is no quasi-steady reference case. With the inclusion of results from the literature in Fig. 7, it is stressed that there is a large range in which the “convective transition” does not yet occur, but an unsteady behavior that can be described by linear theory.

6 Conclusions

In a quasi-steady approach, the e^N -method based on linear stability analysis was extended for periodically oscillating boundary layer flows. A good agreement of the predicted transition locations with experimental results for the application case of a laminar profile was found. As in the experiments, a slower velocity of the downstream moving transition front compared to the upstream moving one was

observed for the cases with high amplitudes and/or high frequencies. However, this behavior cannot be classified as a fully (non-linear) “convective transition mode”, since it can be described with linear theory and downstream transition velocities are below the phase velocity of TS-waves. In addition, a suitable dimensionless quantity was found, by which different cases with different amplitudes, frequencies and boundary layer properties can be compared.

Acknowledgements The current work is part of the project “Laminar-turbulente Transition unter instationären Anströmbedingungen”, supported by the Luftfahrtforschungsprogramm (LuFo) of the Bundesministerium für Wirtschaft und Energie.

References

1. Airbus: Airbus’ “BLADE” laminar flow wing demonstrator makes first flight, Airbus press release 26.09.2017 (2017), https://www.airbus.com/newsroom/press-releases/en/2017/09/airbus_-_blade_laminar-flow-wing-demonstrator-makes-first-fligh.html. Accessed 2 Dec 2019
2. Crouch, J.: Boundary-layer transition prediction for laminar flow control. In: 45th AIAA Fluid Dynamics Conference, p. 2472 (2015)
3. Kolmogorov, A.N.: The local structure of turbulence in incompressible viscous fluid for very large Reynolds numbers. Dokl. Akad. Nauk SSSR **30**, 299–303 (1941)
4. Pope, S.: Turbulent Flows. Cambridge University Press (2000)
5. Reeh, A.D.: Natural laminar flow airfoil behavior in cruise flight through atmospheric turbulence. Ph.D. thesis, Technische Universität Darmstadt (2014)
6. Morkovin, M.V.: Critical evaluation of transition from laminar to turbulent shear layers with emphasis on hypersonically travelling bodies. Flight Dynamic Lab. Rep. AFFDL-TR-68-149, vol. 149 (1969)
7. Ohno, D., Romblad, J., Rist, U.: Laminar to turbulent transition at unsteady inflow conditions: direct numerical simulations with small scale free-stream turbulence. In: New Results in Numerical and Experimental Fluid Mechanics XII (2020)
8. Miller, J., Fejer, A.: Transition phenomena in oscillating boundary-layer flows. J. Fluid Mech. **18**(3), 438–448 (1964)
9. Obremski, H., Fejer, A.: Transition in oscillating boundary layer flows. J. Fluid Mech. **29**(1), 93–111 (1967)
10. Studer, G., Arnal, D., Houdeville, R., Seraudie, A.: Laminar-turbulent transition in oscillating boundary layer: experimental and numerical analysis using continuous wavelet transform. Exp. Fluids **41**(5), 685–698 (2006)
11. Romblad, J., Ohno, D., Würz, W., Krämer, E.: Laminar to turbulent transition at unsteady inflow conditions: wind tunnel measurements at oscillating inflow angle. In: New Results in Numerical and Experimental Fluid Mechanics XII (2020)
12. Obremski, H., Morkovin, M.: Application of a quasi-steady stability model to periodic boundary-layer flows. AIAA J. **7**(7), 1298–1301 (1969)
13. Radespiel, R.E., Windte, J., Scholz, U.: Numerical and experimental flow analysis of moving airfoils with laminar separation bubbles: AIAA J. **45**(6), 1346–1356 (2007)
14. Leishman, G.J.: Principles of Helicopter Aerodynamics. Cambridge University Press (2006)
15. Zhang, D., Chew, Y., Winoto, S.: Investigation of intermittency measurement methods for transitional boundary layer flows. Exp. Thermal Fluid Sci. **12**(4), 433–443 (1996)
16. van Ingen, J.: A suggested semi-empirical method for the calculation of the boundary layer transition region. Report, TU Delft (1956)

Global Stability Analysis of JAXA H-II Transfer Vehicle Re-entry Capsule



Andrea Sansica, Atsushi Hashimoto, and Yuya Ohmichi

Abstract The Japan Aerospace Exploration Agency (JAXA) conducted experimental and numerical investigations on the H-II Transfer Vehicle Re-entry (HTV-R) capsule and showed the existence of strong self-excited oscillations at an angle of attack of 20° and Mach 0.4. The present work aims at performing fully three-dimensional global stability analysis on the HTV-R capsule to characterize its wake dynamic instabilities. An implicit pseudo-unsteady approach at high Courant-Friedrichs-Lowy (CFL) number is used to obtain a Reynolds-Averaged-Navier-Stokes (RANS) solution. Separation occurs on the capsule shoulder and a large steady planar-symmetric recirculation bubble appears. The RANS solution is used as baseflow for the global stability and the leading eigen-modes are calculated by coupling a time-stepper technique to an Arnoldi algorithm. A globally unstable mode is found at a non-dimensional frequency of 0.161. Both frequency and spatial structure of the global mode correspond to the dominant hairpin-like vortex shedding mode found by Ohmichi et al. [1] using Dynamic Mode Decomposition (DMD). No evidence of the other two dominant DMD modes, associated with helical vortex shedding and low-frequency recirculation bubble breathing, was found by the global stability analysis.

1 Introduction

After the retirement of the Space Shuttle, the Japan Aerospace Exploration Agency's (JAXA's) H-II Transfer Vehicle (HTV) was selected for the re-supply of the International Space Station (ISS) [2, 3]. The HTV has a cargo capacity of 6,000 kg (4,500 kg pressurized and 1,500 kg unpressurized), a wide hatch that allows the transport of

A. Sansica (✉) · A. Hashimoto · Y. Ohmichi
Japan Aerospace Exploration Agency, Chofu 182-8522, Japan
e-mail: sansica.andrea@jaxa.jp

A. Hashimoto
e-mail: hashimoto.atsushi@jaxa.jp

Y. Ohmichi
e-mail: ohmichi.yuya@jaxa.jp

large experimental racks and a special rendezvous/berthing technology to dock the ISS using the ISS robotic arm. After resupply, the vehicle is destroyed upon re-entry [4]. Since 2009, the HTV completed several successful missions and encouraged JAXA to develop the concept for a new spacecraft called HTV-R [5, 6]. The HTV-R is conceived for the re-entry to Earth and recovery of materials/samples from the ISS. The HTV-R is equipped with a blunt-body re-entry vehicle called HTV Return Vehicle (HRV), designed for autonomous flight and lifting atmospheric re-entry.

Blunt-body re-entry capsules are well known to be subject to dynamic instabilities at transonic speeds that cause the capsule to oscillate in angular motions [7]. To tackle this critical re-entry phase, JAXA conducted single degree-of-freedom free-rotation tests in the JAXA 2m × 2m Transonic Wind Tunnel (JTWT) to investigate the effects of Mach (M) and Reynolds (Re) numbers for the design angle of attack (AoA) of 20° [8]. In support to the experimental campaign, the improved detached eddy simulations carried out by Hashimoto et al. [9] showed that strong angular motions occur at $M = 0.4$ and $M = 1.1$. The $M = 0.4$ case was later selected to perform a dynamic mode decomposition (DMD) analysis [10] combined to compressive sensing [11] to clarify the three-dimensional (3D) mechanisms that govern the wake instabilities for a stationary capsule [1]. It was found that while most of the dominant modes are associated with either hairpin-like or helical vortex shedding in the non-dimensional frequency range $St = 0.17 - 0.20$ (with St , Strouhal number), a recirculation bubble pulsation motion at a frequency $St = O(0.01)$ seems to be responsible for large drag fluctuations. These self-sustained phenomena are suspected to be globally unstable modes. The objective of the present study is therefore to perform a 3D global stability analysis on the fully-turbulent flow configuration around the re-entry capsule at AoA = 20° and $M = 0.4$. Being a relatively simple geometry, this study offers opportunities to compare the capsule wake dynamics with other simple compressible flow configurations, like spheres [12, 13] and elongated bluff bodies [14, 15], and further elucidate the mechanisms driving the capsule dynamic instabilities.

2 Numerical Method

The compressible 3D Reynolds-Averaged-Navier–Stokes (RANS) equations for a perfect gas can be written using Boussinesq hypothesis in the non-dimensional form as:

$$\frac{\partial \mathbf{q}}{\partial t} = \mathcal{N}(\mathbf{q}), \quad (1)$$

where $\mathbf{q} = [\rho, \rho\mathbf{u}, \rho E, \rho v_t]^T$ is the state vector in the conservative form (with ρ , \mathbf{u} , E and v_t being fluid density, velocity vector, total energy, and kinematic turbulent viscosity, respectively) and t is the time. The non-dimensional scheme is based on free-stream quantities and capsule diameter.

The differential nonlinear RANS operator \mathcal{N} can be explicitly expanded as

$$\mathcal{N}(\mathbf{q}) = - \begin{pmatrix} \rho \mathbf{u} \\ \rho \mathbf{u} \otimes \mathbf{u} + p \mathbf{I} - \boldsymbol{\tau} - \boldsymbol{\tau}_R \\ \rho E \mathbf{u} + p \mathbf{u} - \boldsymbol{\tau} \mathbf{u} - \boldsymbol{\tau}_R \mathbf{u} + \mathbf{q}_h + \mathbf{q}_R \\ \rho v_t \mathbf{u} - \frac{\mu + \rho v_t}{\sigma_M} \nabla v_t + \mathcal{S}_M \end{pmatrix} \quad (2)$$

with

$$\begin{aligned} p &= (\gamma - 1) \rho E - \frac{1}{2} \mathbf{u} \cdot \mathbf{u} \\ \boldsymbol{\tau} &= \mu [(\nabla \otimes \mathbf{u} + \nabla \otimes \mathbf{u}^T) - \frac{2}{3} (\nabla \cdot \mathbf{u}) \mathbf{I}] \\ \boldsymbol{\tau}_R &= \mu_t [(\nabla \otimes \mathbf{u} + \nabla \otimes \mathbf{u}^T) - \frac{2}{3} (\nabla \cdot \mathbf{u}) \mathbf{I}] \\ \mathbf{q}_h &= -\frac{\mu C_p}{Pr} \nabla T \\ \mathbf{q}_R &= -\frac{\mu_t C_p}{Pr_t} \nabla T \end{aligned} \quad (3)$$

being p the pressure, $\boldsymbol{\tau}$ the stress tensor, $\boldsymbol{\tau}_R$ the Reynolds stress tensor, C_p the heat capacity at constant pressure, μ the dynamic viscosity, μ_t the eddy viscosity, Pr and Pr_t the classical and turbulent Prandtl numbers, T the temperature, \mathbf{q}_h the heat flux and \mathbf{q}_R the flux of diffusion of turbulent enthalpy. The Prandtl numbers are considered constant and equal to $Pr = 0.72$ and $Pr_t = 0.90$. The dynamic viscosity is assumed to follow Sutherland's law as

$$\mu = T^{3/2} \frac{1 + T_s}{T + T_s} \quad (4)$$

where $T_s = 110.4 K / T_\infty^*$, with T_∞^* the dimensional free-stream temperature (the superscript * indicates dimensional quantities). The array of the streamwise, vertical and transverse directions is indicated by $\mathbf{x} = [x, y, z]^T$. Note that all variables are Reynolds averaged, except for \mathbf{u} and E that are Favre (density-weighted) averaged. The formulations of the coefficient σ_M and the turbulent source terms \mathcal{S}_M depend on the turbulence model.

2.1 Stability Problem

The stability problem is based upon the use of the linearized RANS equations. The first step to obtain this linearized set of equations is to assume that the nonlinear system in Eq. (1) admits an equilibrium solution, \mathbf{q}_b , defined by $\mathcal{N}(\mathbf{q}_b) = 0$ and referred to as fixed point or baseflow. In this case, the steady RANS solution corresponds to the baseflow. The standard small perturbation technique is used to decompose the instantaneous flow into baseflow and small disturbances $\mathbf{q}(\mathbf{x}, t) = \mathbf{q}_b(\mathbf{x}) + \varepsilon \mathbf{q}'(\mathbf{x}, t)$, with $\varepsilon \ll 1$. By assuming that the perturbations are infinitesimal, all nonlinear fluctuating terms are ignored and the linearized RANS equations can be written as

$$\frac{\partial \mathbf{q}'}{\partial t} = \mathcal{L} \mathbf{q}', \quad (5)$$

where $\mathbf{q}' = [\rho', \rho' \mathbf{u}_b + \rho_b \mathbf{u}', \rho' E_b + \rho_b E', \rho' v_{t,b} + \rho_b v_t']^T$ is the state vector of conservative perturbation variables and $\mathcal{L} = \partial \mathcal{N} / \partial \mathbf{q}|_{\mathbf{q}_b}$ is the Jacobian operator obtained by linearizing the RANS operator \mathcal{N} around the baseflow \mathbf{q}_b . By choosing the wave solution $\mathbf{q}'(\mathbf{x}, t) = \hat{\mathbf{q}}(\mathbf{x}) \exp(\lambda t) + c.c.$ (with *c.c.* indicating the complex conjugate), the eigenproblem $\mathcal{L}\hat{\mathbf{q}} = \lambda\hat{\mathbf{q}}$ is obtained. The complex eigenvalue can be split in its real and imaginary parts $\lambda = \sigma + i\omega$, where σ is the temporal growth rate and ω the pulsation. While the pulsation characterizes the oscillatory behavior, the temporal growth rate indicates whether the equilibrium state bifurcates to another solution. This bifurcation is expressed in a linear framework by the existence of eigenmodes with a corresponding positive growth rate.

2.2 Code Features

An in-house solver is used to compute the compressible RANS equations, both nonlinear and linearized formulations, on multi-block structured grids with a finite-volume approach. While the mean convective fluxes are calculated by means of a Jameson-Schmidt-Turkel third-order scheme with artificial dissipation, a second-order scheme with Harten's correction is used for the turbulent ones. All viscous terms are instead differentiated by a second-order centered scheme. The temporal discretization is based on a dual time-stepping method [16], where a second-order backward difference scheme is used for the derivatives with respect to the physical time. The boundary conditions used for both the steady and unsteady calculations in nonlinear and linearized forms are: no-slip velocity, adiabatic temperature and pressure extrapolation on the profile and side-walls; the AoA is applied on the imposed uniform velocity at the inflow of the numerical domain; characteristic boundary conditions are set at the domain lateral boundaries and outflow to minimize wave reflections. It is important to emphasize that, although the same discretization schemes and boundary conditions are used for both nonlinear and linear calculations, some adaptations to comply to the linearization procedure had to be taken into account. The boundary conditions are also linearized and modified: zero-velocity perturbations are enforced on the walls and domain inlet and the characteristic boundary conditions are evaluated on the baseflow solution. The Spalart-Allmaras turbulence model [17] with Edwards modification [18] and quadratic constitutive relation 2000 version [19] is used to close the averaged Reynolds stresses. A linearized version of the transport equation allows temporal evolution of the eddy viscosity perturbations in a “non-frozen turbulence” fashion. All steady solutions are computed by using a large Courant-Friedrichs-Lowy (CFL) number, allowing the filtering of possible unsteadiness and obtaining converged steady fixed points until the residuals of the state variables in the L_2 -norm are at least lower than 10^{-6} . A matrix-free method [20, 21] is used to solve the eigenproblem $\mathcal{L}\hat{\mathbf{q}} = \lambda\hat{\mathbf{q}}$. Being \mathbf{L} the discrete form of \mathcal{L} , it is possible to introduce the exponential propagator $\mathbf{M} = \exp(\mathbf{L}\Delta T)$ that linearly advances the perturbation solution in time as $\mathbf{q}'(t^{n+1}) = \mathbf{M}\mathbf{q}'(t^n)$, with $t^{n+1} = t^n + \Delta T$. An

Arnoldi algorithm [22–24] is coupled to the linear solver [12, 25, 26] to extract the leading eigenmodes of \mathbf{M} . A validation of both nonlinear and linear solvers for a turbulent compressible flow configuration is given in the Appendix.

3 Global Stability Analysis of JAXA's HTV-R Capsule

The numerical setup is based on the experimental flow conditions by Koga et al. [8]. An inflow Mach number is set to $M = 0.4$ and the Reynolds number based on freestream velocity and capsule diameter D is $Re = 1.9 \times 10^6$. The AoA is applied to the incoming flow and it is fixed to $AoA = 20^\circ$. In order to simplify the grid generation, the disk behind the original capsule geometry is removed, as sketched in Fig. 1 (left figure). A 13 blocks structured grid is used in a combination of “butterfly” and O-grid configurations, as schematically represented in Fig. 1 (middle and right figures). The domain extends $25 \times D$ in all directions, both upstream and downstream of the capsule. A grid of about 40 million cells is used and clustered in the near-wall vicinity ($y_w^+ < 50$ for all first points off the capsule walls) and wake region.

3.1 RANS Baseflow Solution

A fully-3D RANS simulation is carried out and a steady solution is obtained by using the pseudo-unsteady temporal integration with a CFL number equal to 5 to filter the unsteadiness. The steady solution is converged until the residuals of the state variables in the ℓ_2 -norm are lower than 10^{-6} . To first assess the quality of the result, the present RANS solution is compared with the results independently obtained with JAXA's unstructured CFD code, named FaSTAR. The separation regions behind the capsule obtained with the present code (black line) and FaSTAR (red line) are indicated by the zero-streamwise velocity iso-line and reported in Fig. 2 (left plot). Although some dis-

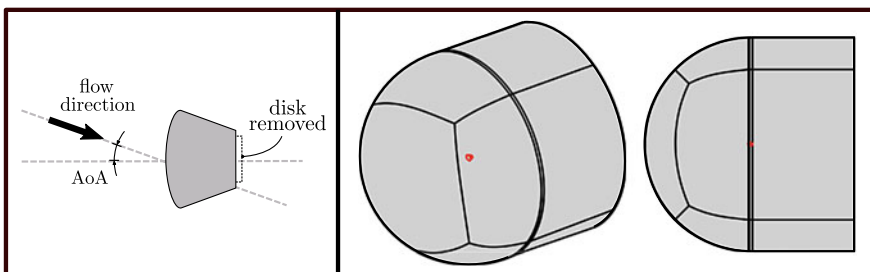


Fig. 1 Schematic representations of (left) capsule geometry and incoming flow direction and (middle and right) numerical domain in both 3D and lateral views, respectively

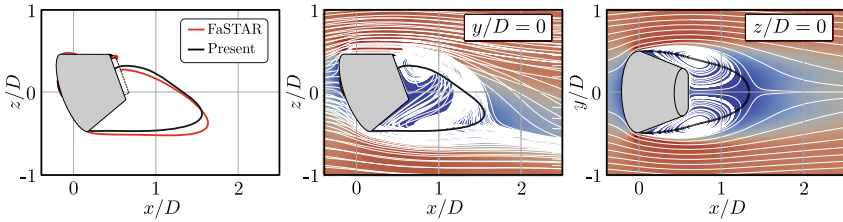


Fig. 2 RANS baseflow solution. Left plot: comparison between JAXA's FaSTAR code (red) and the present results (black) on the zero-streamwise velocity iso-line; Middle and right plots: Zero-streamwise velocity iso-line (black) and streamlines (white) over the streamwise velocity contours

crepancies exist due to the different numerical setups, a satisfactory qualitative agreement is achieved. The separation region (black line) and streamlines (white lines) are superimposed to the contours of the streamwise velocity in Fig. 2 (middle and right plots) for two perpendicular planes at $y/D = 0$ and $z/D = 0$, respectively. Due to a relatively sharp edge, the flow separates on the capsule shoulder and a large recirculation region of about $1.5 \times D$ is formed. The RANS solution presents planar-symmetry, as the axi-symmetry is broken in the plane where the AoA is applied. Although the capsule is tilted by an AoA, this feature links this turbulent configuration to other laminar compressible wakes around axi-symmetric bodies at zero-AoA [12, 13, 15] and provides an opportunity to further explain the capsule wake dynamics.

3.2 Global Stability Results

The RANS solution is used as baseflow for the global stability analysis. An unsteady linearized RANS calculation has been run with a physical time step fixed to $\Delta t = 4.25 \times 10^{-6}$ s. For the Arnoldi algorithm, the Krylov time step is set to sample 8 snapshots during one period of the shedding frequency and the dimension of the Krylov subspace is 128. The left plot in Fig. 3, reporting the eigen-spectrum obtained by global stability, indicates the existence of an unstable global mode at $(\sigma, St) = (0.017, 0.161)$. The corresponding real part of the eigen-velocities is reported in the middle and right plots of Fig. 3. As for the baseflow solution, the eigen-solution is planar-symmetric. Its spatial structure closely recalls the unstable eigen-mode of the compressible laminar sphere flow above the supercritical Hopf bifurcation, responsible of the unsteady periodic hairpin vortex shedding [12, 13].

The globally unstable mode is compared with the dominant hairpin-like vortex shedding DMD mode at $St = 0.189$ obtained by Ohmichi et al. [1] in Fig. 4. The spatial distribution and wavelength of the velocity packets and a higher amplitude in the lower part of the wake (corresponding to the region where a larger separation region is present) are in very good agreement between the two independent analyses. Interest-

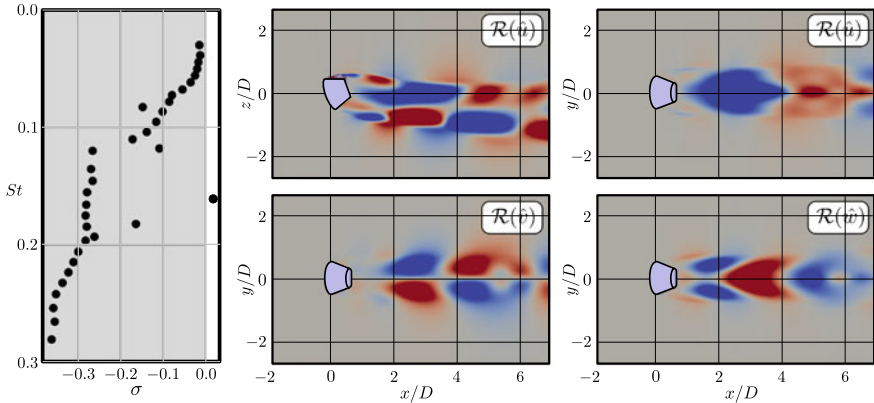


Fig. 3 Eigen-spectrum (left plot) and real part of the eigen-velocities (middle and right plots) for the unstable global mode at $(\sigma, St) = (0.017, 0.161)$

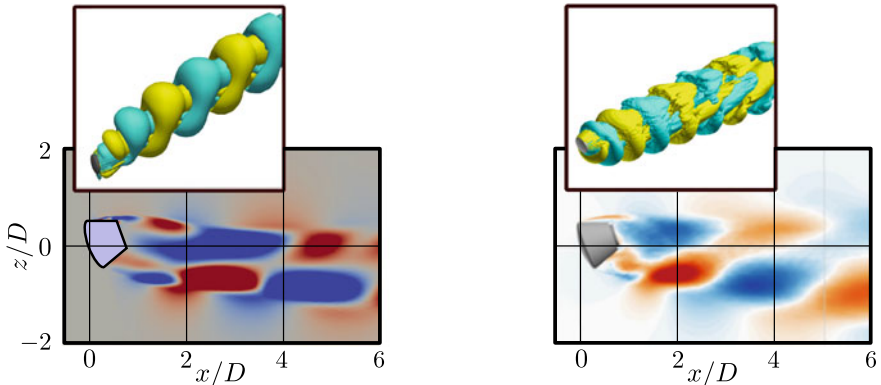


Fig. 4 Comparison between the contours (in the plots) and iso-surfaces (insets) of the real part of the streamwise eigen-velocity for the global stability (left) and DMD [1] (right) modes

ingly, the global stability analysis has not found any evidence of the existence of the helical and low-frequency bubble breathing modes that were found dominant in the DMD analysis, indicating that these modes may be related to nonlinear effects and/or convective instabilities.

4 Conclusions

A RANS-based fully-3D global stability analysis has been performed on JAXA's HTV-R capsule to characterize its unsteady wake dynamics, that both experiments and numerical simulations found to be responsible for strong self-sustained angular oscillations at $M = 0.4$ and $\text{AoA} = 20^\circ$. Although some differences exist between the

current numerical setup and that of the simulations carried out by Ohmichi et al. [1], the RANS solution is in qualitative good agreement with the results independently obtained with JAXA's code, FaSTAR. The wake behind the capsule predicted by the RANS calculation presents planar-symmetry, making this flow configuration of great interest due to the similarities with other simple geometries (like spheres, elongated bluff bodies, etc.). The flow separates at the capsule shoulder and a large recirculation bubble of about $1.5 \times D$ is formed. Global stability analysis is performed by using the RANS solution as baseflow and a globally unstable mode is found at a Strouhal number of $St = 0.161$. Frequency and eigen-function spatial distributions indicate that the globally unstable mode corresponds to the dominant DMD mode associated with the high-frequency hairpin-like vortex shedding. However, the other two dominant DMD modes, associated with the helical vortex shedding and the low-frequency recirculation bubble breathing, are not detected by the global stability analysis. These results suggest that both helical vortex shedding and separation bubble breathing may be related to nonlinear effects and/or be convective instabilities.

Appendix

While both nonlinear and linearized solvers have been already successfully verified for 3D compressible laminar flows [13], a validation for a turbulent transonic buffet case on the 2D OAT15A is here given. The flow conditions and geometry correspond to those in [27], for which the Mach number is $M = 0.73$ and the Reynolds number based on the chord length (c) is $Re = 3.2 \times 10^6$. The same 2D C-type structured grid obtained by normal extrusion around the airfoil has been used for all AoA. The numerical domain extends $30 \times c$ upstream of the profile and $40 \times c$ above, below and downstream. The grid counts about 149,000 cells: 160 in the profile-normal direction (about 60 cells in the boundary-layer and a $y_w^+ < 5$ for all first points off the profile), 300 along the suction side, 165 along the pressure side and 232 in the horizontal wake direction. The grid has been refined in the shock region between $x/c = 0.25$ and $x/c = 0.55$ where the grid spacing is about $\Delta_x/c = 0.002$. The pressure coefficient, C_p , distributions of the converged RANS solutions corresponding to the AoA = 3.50, 4.50 and 5.50° are compared against those of [27, 28] in Fig. 5 (left plot) and show good agreement on both airfoil sides and in terms of shock positions. Contours of the dimensional streamwise velocity for the steady solution at AoA = 4.50° are plotted in Fig. 5 (right plot) along with the sonic (black) and zero-streamwise velocity (white) iso-lines, showing the supersonic flow region/shock position and separation, respectively. The steady RANS solutions are selected as baseflows for the global stability analysis. For each AoA, an unsteady linearized RANS calculation has been run with a physical time step fixed to $\Delta t = 6.85 \times 10^{-7}$ s, a Krylov time step of $\Delta T_{Kr} = 2500 \times \Delta t$ and maximum Krylov dimension of 80 for all cases. The evolution of the growth rate of the least stable/most unstable mode as a function of the AoA is reported in Fig. 6 (left plot). The parabolic trend indicates buffet onset and offset at AoA $\approx 3.40^\circ$ and AoA $\approx 5.05^\circ$, respectively. For the AoA = 4.50° case, the eigen-

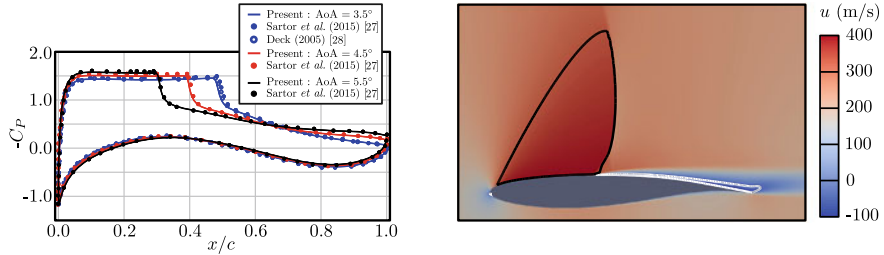


Fig. 5 Left plot: Pressure coefficient for the $\text{AoA} = 3.50^\circ$ (blue), $\text{AoA} = 4.50^\circ$ (red) and $\text{AoA} = 5.50^\circ$ (black). Present results (solid lines) are compared against those in [28] (empty circle symbols) and [27] (full circle symbols). Right plot: Streamwise velocity contours of the steady solution at $\text{AoA} = 4.50^\circ$ with sonic (black) and zero-streamwise velocity (white) iso-lines

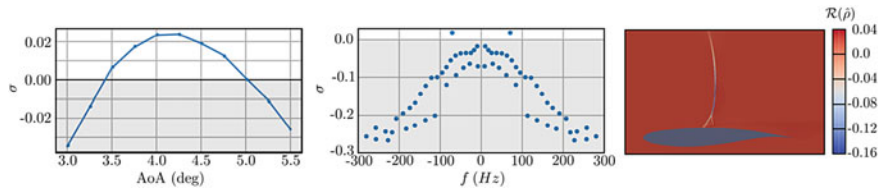


Fig. 6 Left plot: Growth rate of the least stable/most unstable mode as a function of the AoA . Middle plot: $\text{AoA} = 4.50^\circ$ case eigenspectrum. Right plot: $\text{AoA} = 4.50^\circ$ case contours of the real part of the eigen-density corresponding to the unstable (buffet) mode

spectrum is reported in Fig. 6 (middle plot) and shows the existence of an unstable mode at $f \approx 75 \text{ Hz}$. The contours of the real part of the eigen-density corresponding to this unstable mode are plotted in Fig. 6 (right plot). Similarly to [27, 29], this eigenmode corresponds to the buffet instability and is localized on the shock, shock foot and in minorly in the mixing layer.

References

1. Ohmichi, Y., Kobayashi, K., Kanazaki, M.: Numerical investigation of wake structures of an atmospheric entry capsule by modal analysis. *Phys. Fluids* **31**, 074105 (2019)
2. Pursuant to the authorization act of 2005, NASA provided congress with the human space flight transition plan, July 2006 (2006)
3. Foster, M.A., Sirk, R.J.: Leveraging existing space assets for delivery of cargo to the international space station. In: Space 2006, AIAA Paper 2006-7267 (2006)
4. Chullen, C., Blome, E., Tetsuya, S.: H-II transfer vehicle and the operations concept for extravehicular activity hardware. In: 41st International Conference on Environmental Systems, AIAA Paper 2011-5275 (2011)
5. Suzuki, Y., Imada, T.: Concept and technology of HTV-R: an advanced type of h-ii transfer vehicle. *Trans. JSASS Aerosp. Tech. Jpn.* **10**, Tg9–Tg18 (2012)
6. Imada, T.: Concept study of HTV-R (HTV-Return). *J. Space Technol. Sci.* **27**(2), 21–28 (2013)

7. Kazembla, C.D., Braun, R.D., Clark, I.G., Schoenenberger, M.: Survey of blunt body dynamic stability in supersonic flow. In: AIAA Atmospheric Flight Mechanics Conference, AIAA paper 2012-4509 (2012)
8. Koga, S., Hidaka, A., Tagai, R., Kimura, T., Yoshinaga, T., Nagai, S.: Dynamic stability testing of a reentry lifting capsule in a transonic wind tunnel. In: 52nd Aerospace Sciences Meeting, AIAA SciTech Forum, AIAA Paper 2014-1119 (2014)
9. Hashimoto, A., Murakami, K., Aoyama, T., Tagai, R., Koga, S., Nagai, S.: Dynamic stability analysis of a reentry lifting capsule with detached eddy simulation. In: 54th AIAA Aerospace Sciences Meeting, AIAA 2016-0552 (2016)
10. Schmid, P.J.: Dynamic mode decomposition of numerical and experimental data. *J. Fluid Mech.* **656**, 5–28 (2010)
11. Ohmichi, Y.: Preconditioned dynamic mode decomposition and mode selection algorithms for large datasets using incremental proper orthogonal decomposition. *AIP Adv.* **7**(075318) (2017)
12. Sansica, A., Robinet, J.-C., Alizard, F., Goncalvez, E.: Three-dimensional instability of a flow past a sphere: Mach evolution of the regular and HOPF bifurcations. *J. Fluid Mech.* **855**, 1088–1115 (2018)
13. Sansica, A., Robinet, J.-C., Hashimoto, A.: Supersonic sphere flow unstable bifurcations. In: 32nd International Symposium on Shock, Singapore (2019)
14. Meliga, P., Sipp, D., Chomaz, J.-M.: Effect of compressibility on the global stability of axisymmetric wake flows. *J. Fluid Mech.* **660**, 499–526 (2010)
15. Rigas, G., Esclapez, L., Magri, L.: Symmetry breaking in a 3d bluff-body wake. In: Proceedings of the Summer Program 2016. Center for Turbulence Research (2017)
16. Jameson, A.: Time-dependent calculations using multigrid with applications to unsteady flows past airfoils and wings. In: 10th Computational Fluid Dynamics Conference, Honolulu, HI, USA, AIAA Paper (1991)
17. Spalart, P.R., Allmaras, S.R.: A one-equation turbulence model for aerodynamic flows. In: 30th Aerospace Sciences Meeting and Exhibit, Aerospace Sciences Meetings, AIAA Paper (1992)
18. Edwards, J.R., Chandra, S.: Comparison of eddy viscosity-transport turbulence models for three-dimensional, shock-separated flowfields. *AIAA J.* **34**(4), 756–763 (1996)
19. Spalart, P.R.: Strategies for turbulence modelling and simulation. *Int. J. Heat Fluid Flow* **21**, 252–263 (2000)
20. Edwards, W.S., Tuckerman, L.S., Friesner, R.A., Sorensen, D.: Krylov methods for the incompressible Navier-Stokes equations. *J. Comput. Phys.* **110**, 82–101 (1994)
21. Bagheri, S., Åkervik, E., Brandt, L., Henningsson, D.S.: Matrix-free methods for the stability and control of boundary layers. *AIAA J.* **45** (2009)
22. Arnoldi, W.E.: The principle of minimized iterations in the solution of the matrix eigenvalue problem. *Q. Appl. Math.* **9** (1951)
23. Lehoucq, R.B., Sorensen, D.C., Yang, C.: Arpack user's guide: solution of large scale eigenvalue problems with implicitly restarted Arnoldi methods. Technical Note (1997)
24. Barkley, D., Blackburn, H.M., Sherwin, S.J.: Direct optimal growth analysis for timesteppers. *Int. Numer. Methods Fluids* **57**, 1435–1458 (2008)
25. Loiseau, J.-C., Robinet, J.-C., Cherubini, S., Leriche, E.: Investigation of the roughness-induced transition: global stability analyses and direct numerical simulations. *J. Fluid Mech.* **760**, 175–211 (2014)
26. Guiho, F., Alizard, F., Robinet, J.-C.: Instabilities in oblique shock wave/laminar boundary-layer interactions. *J. Fluid Mech.* **789**, 1–35 (2016)
27. Sartor, F., Mettot, C., Sipp, D.: Stability, receptivity, and sensitivity analyses of buffeting transonic flow over a profile. *AIAA J.* **53**(7), 1980–1993 (2015)
28. Deck, S.: Numerical simulation of transonic buffet over a supercritical airfoil. *AIAA J.* **43**(7), 1556–1566 (2005)
29. Crouch, J.D., Garbaruk, A., Magidov, D., Travlin, A.: Origin of transonic buffet on aerofoils. *J. Fluid Mech.* **628**, 357–369 (2009)

Global Linear Stability and Sensitivity of Hypersonic Shock-Boundary Layer Interactions



G. S. Sidharth, A. Dwivedi, J. W. Nichols, M. Jovanović, and G. V. Candler

Abstract Understanding physical mechanisms that cause transition of laminar boundary layers to turbulent state in hypersonic flows is important for vehicle design and analysis. Mechanisms of linear perturbation growth in high speed boundary layers subjected to abrupt inviscid pressure jumps have been relatively less studied. Inviscid pressure jumps are associated with geometry effects and impinging shocks. They cause the boundary layer to separate, forming a separation-reattachment shock system. In the present study, we investigate small perturbation growth in a nominally two-dimensional interaction on a slender double wedge. We report and discuss intrinsic instabilities as well as amplification of external perturbations in the setup, both of which result in streamwise heat flux streaks near and post-reattachment.

1 Introduction

High speed flow over a double-wedge is a canonical case of shock boundary layer interaction [1, 2]. Experiments of hypersonic flow on compression ramps and double wedges exhibit three-dimensionality in the form of streamwise striations or streaks in wall temperature near reattachment, that persist downstream. Vortical structures associated with these streaks result in heat transfer with large local peaks in span and have a destabilizing effect on the boundary layer, playing a role in the transition process [3, 4].

The present work aims to understand the structure of these three-dimensional perturbations that amplify in the presence of high speed boundary layers with a separation bubble. Knowledge of the structure will help construct a physics-based mechanistic picture of the early stage of the transition process in this class of flows.

G. S. Sidharth (✉) · A. Dwivedi · J. W. Nichols · G. V. Candler
University of Minnesota, Minneapolis, USA
e-mail: sidharth_gs@hotmail.com

G. S. Sidharth
Los Alamos National Laboratory, Los Alamos, USA

M. Jovanović
University of Southern California, Los Angeles, USA

A secondary objective of the paper is to demonstrate the use of global system matrix [5–9] to develop predictive tools in high speed boundary layer transition. These tools are necessitated due to breakdown of conventional high-speed transition analysis tools such as those involving parabolized governing equations [10]. While direct numerical simulations (DNS) are useful to analyze perturbation development, they are too expensive and do not isolate the relevant physics for inference.

The paper is organized as follows. The physical setup of the slender double wedge under consideration is first described. The formulation of the global linear system is presented next, followed by results on global instability and sensitivity of the flow configuration.

2 Physical Problem Setup

In this work, we study the flow dynamics on the slender double wedge geometry that corresponds to the experiments of Yang et al. [11]. Figure 1a shows the geometry and the free-stream conditions. The turn angle at the second ramp controls the strength of the separation. Direct numerical simulations beyond a critical turn angle obtained from this study point to the three-dimensional flow in the separation bubble and presence of reattachment streaks downstream (Fig. 1b).

The solutions are time-marched to steady state implicitly using the finite volume compressible flow solver US3D [12]. Due to low free-stream enthalpy and temperature, we model the flow by considering a calorically perfect gas that follows the ideal gas law. The viscosity of air is computed using the Sutherland's law. We assume an adiabatic wall in accordance with the relatively long test time (7 s) of the experiment.

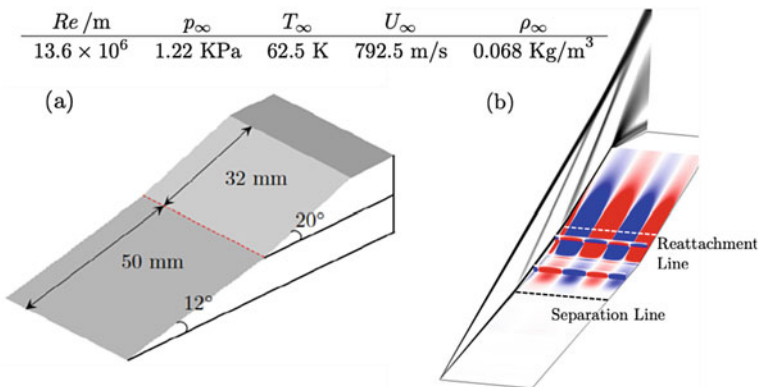


Fig. 1 **a** Slender double wedge geometry [6, 11]. **b** DNS: contours of spanwise velocity in color and contours of $|\nabla \rho|$ shown in grayscale

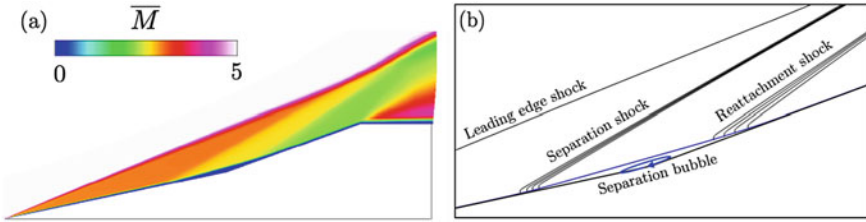


Fig. 2 **a** Mach number contours for the 2D steady state flow and **b** schematic of the associated shock/boundary layer interaction

The grid resolutions are dictated by the spatial resolution of the unstable eigenmodes. More details on grid resolution requirements are discussed in Sidharth et al. [6].

Figure 2a shows the Mach contours and the recirculation bubble streamlines at the compression corner in the 2D steady state base flow. The boundary layer separates upstream of the corner, forming a separation shock. The separated shear layer reattaches downstream of the corner and is associated with a reattachment shock. The schematic for the 2D base state is shown in Fig. 2b.

3 Linear System Formulation

The stability and sensitivity of the 2D slender double wedge flow is analyzed by studying the small perturbation dynamics which obey the linearized governing equations. We linearize the equations in the conserved variable set and use an unstructured finite volume discretization for the linear governing equations.

The Navier–Stokes equations for compressible flow are

$$\frac{\partial \mathbf{U}}{\partial t} + \frac{\partial \mathbf{F}_j}{\partial x_j} + \frac{\partial \mathbf{F}^v_j}{\partial x_j} = 0 \quad (1)$$

where \mathbf{U} is the vector of conserved solution variables, $\mathbf{F}_j = \mathbf{F}_j(\mathbf{U})$ is the inviscid flux vector and \mathbf{F}^v_j is the viscous flux vector. The viscosity of air is computed using the Sutherland's law of viscosity $\mu = \mu(T)$. Conductivity κ for air is evaluated corresponding to a Prandtl number $Pr \simeq 0.72$.

The conserved flow variables are decomposed into the base and small fluctuation components, $\mathbf{U} = \bar{\mathbf{U}} + \mathbf{U}'$ such that $\|\mathbf{U}'\| \ll \|\bar{\mathbf{U}}\|$. The superscript ‘‘’ denotes the perturbation quantities and the overbar denotes the base flow variables. The governing equations for small compressible perturbation (Eq. 2) can be expressed in the form

$$\begin{aligned} \frac{\partial \mathbf{U}'}{\partial t} + \frac{\partial}{\partial x_j} (\bar{\mathbf{A}}_j + \bar{\mathbf{A}}_j^v) \mathbf{U}' &= 0 \\ \bar{\mathbf{A}}_j = \frac{\partial \mathbf{F}_j}{\partial \mathbf{U}} \Big|_{\bar{\mathbf{U}}} &, \quad \bar{\mathbf{A}}_j^v = \left(\bar{\mathbf{M}}_{jk} \frac{\partial}{\partial x_k} + \bar{\mathbf{M}}_j^{VD} \right) \bar{\mathbf{N}} \end{aligned} \quad (2)$$

Here, the matrix $\bar{\mathbf{N}}$ is the transformation matrix from conserved to primitive variables such that, $\mathbf{V}' = \bar{\mathbf{N}} \mathbf{U}'$, the matrix \mathbf{M}_{ij} contains the transport coefficients, and the rank-1 tensor $\bar{\mathbf{M}}_j^{VD}$ arising from linearization of the viscous dissipation term. More details can be found in the Ref. [6]. The use of conserved perturbation variables results in a conserved form of linear governing equations.

The conserved form of linearized Navier–Stokes equations can be discretized spatially using a finite volume framework. The semi-discrete form of Eq. 2 can be expressed as

$$\frac{\partial \mathbf{U}'_c}{\partial t} + \frac{1}{V_c} \sum_f \left((\bar{\mathbf{A}}_j + \bar{\mathbf{A}}_j^v) S_j \mathbf{U}' \right)_f = 0 \quad (3)$$

where the subscript ‘*c*’ refers to the cell and ‘*f*’ refers to the face. S_k is the face normal vector scaled with the face area. The inviscid linearized flux is split into its central and dissipative components, and the dissipative term can be selectively activated at shocks and contact discontinuities by convolving the expression with an appropriate sensor. High order polynomial interpolation for the face-reconstructed perturbation variables is employed using neighboring cell and gradient stencils to increase the spatial order of accuracy. In this work, we restrict our results to second-order accurate central fluxes. Note that in our approach we linearize the equations first, followed by their discretization. No limiters are employed on the face reconstructions to minimize numerical dissipation. This allows us to employ zero numerical dissipation, avoiding nonphysical dampening of the eigenvalues and corresponding normal perturbation modes, thereby ensuring a physically accurate asymptotic temporal behavior.

To compute the solutions to span-homogeneous global system, we assume perturbations of the form

$$\mathbf{U}'(x, y, z, t) = \mathbf{U}'_{2D}(x, y) \exp(-i(\omega_r + i\omega_i)t + i2\pi z/\lambda_z) \quad (4)$$

where λ_z is the spanwise wavelength of the perturbation mode and ω_i is the growth rate. Substituting this perturbation form in the linear system of equation 3 results in a generalized eigenvalue problem for \mathbf{U}'_{2D} , which we solve using the shift-invert approach with the software PARPACK [13] and SuperLU [14]. The linear perturbations are forced to decay at the downstream end of the computational domain using a numerical sponge/buffer zone. The results presented in this work are found to be insensitive to the location and strength of this zone provided it is downstream of the separation bubble.

4 Global Linear Stability

In this section, we compute the global linear stability of the 2D flow on the slender double wedge with respect to three-dimensional perturbations. A range of wedge turn angles and free-stream Reynolds numbers are considered as control parameters. For all interactions, the 2D flow is globally stable to two dimensional perturbations. Beyond a certain turn angle or a free-stream Reynolds number, the two-dimensional steady state becomes unstable to three-dimensional perturbations.

4.1 The Onset of Linear Instability

The two control parameters in our setup are the turn angle and the free-stream Reynolds numbers. When the turn angle is varied, we fix the free-stream Reynolds number at $\text{Re}/m = 13.6 \times 10^6$ and when the Reynolds number is increased, the turn angle is fixed at 10° . The Reynolds number is varied using the free-stream density and pressure. Increase in both parameters destabilizes the flow. The spanwise wavelength of the perturbation λ_z is a free parameter in Eq. 4. A sweep of λ_z parameter space is carried out for the two control parameters θ and Re/m to search for the most unstable perturbation.

Figure 3a, b show the variation of the growth-rate of the least stable modes with λ_z for different turn angles and free-stream Reynolds numbers respectively. For this specific geometry, the critical turn angle is found to be 8° , while the critical free-stream Reynolds number for a 10° turn angle is found to be approximately $\text{Re}/m = 4 \times 10^6$. In both cases, non-oscillatory perturbations with a specific spanwise wavelength of $\lambda_z/L \approx \mathcal{O}(10)$ are found to be the least stable. The non-dimensional length scale L

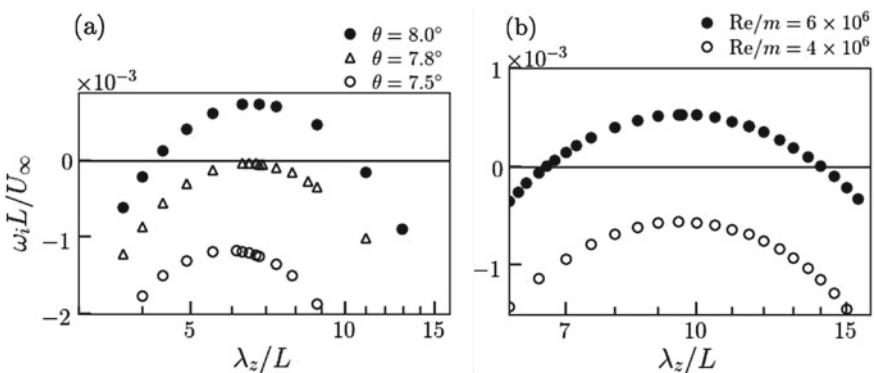


Fig. 3 Bifurcation of the 2D steady flow on the slender double wedge with increase in **a** turn angle and **b** free-stream Reynolds number

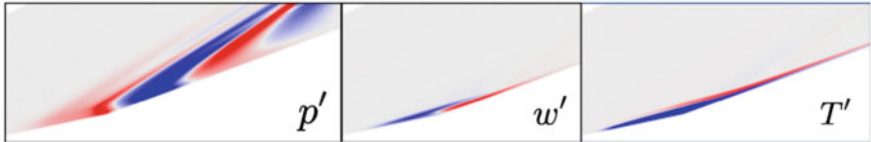


Fig. 4 Unstable eigenmode at $\lambda_z/L = 6.28$: various perturbation quantities

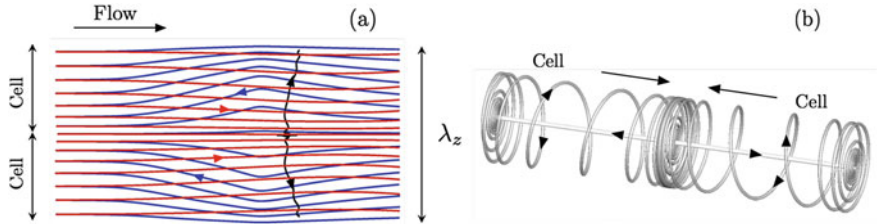


Fig. 5 **a** Streamlines in 3D bubble, red $u_i > 0$ and blue $u_i < 0$, **b** simplified model of the 3D bubble topology

corresponds to the boundary layer thickness prior to separation. This spanwise wavelength approximately scales with the streamwise extent of the separation bubble.

The spatial structure of the unstable global mode is visualized in Fig. 4. The perturbation components corresponding to pressure, spanwise-velocity and temperature are plotted on z-planes where they attain their maximum. Note that w' is 90° out of phase with the other perturbation components. Unlike other components that are localized in the separation bubble and streaks in the reattached boundary layer, the pressure component has a standing acoustic wave character and is associated with spanwise oscillations in the shock system, particularly the reattachment shock. The temperature perturbation has different signs in a single z-plane, which is an outcome of an out-of-plane three-dimensional recirculation. The spanwise velocity perturbation shows the direction of the crossflow in the front and rear parts of the bubble.

The three-dimensional recirculation resulting from the growth of the unstable mode is shown in Fig. 5. In the 3D bubble, there are two independent flow cells per wavelength in span. While the outer streamlines move from the unstable to the stable focii, the inner streamlines move in the opposite direction. As the perturbations grow exponentially towards non-linear saturation, the stable focii descend to the wall, resulting in tornado-type flow structures at the wall. This phenomenon is confirmed with direct numerical simulations [6].

4.2 Beyond the Critical Parameters: A Small λ_z Instability

In the experiments of [11], the turn angle and the free-stream parameters are beyond their critical values as predicted by the linear stability analysis. But the wavelength of the streaks in the experiments is much smaller than that predicted at the critical

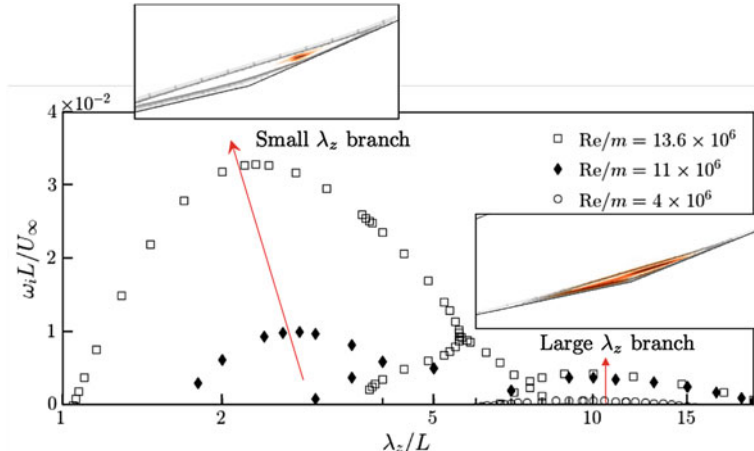


Fig. 6 Growth rate versus spanwise wavelength λ_z/L with increasing Re . Insets show contours of the wavemaker superimposed on the separation bubble streamlines

turn angle (or Re). Therefore, we carry out the stability analysis of the 2D steady state at the experimental conditions. The analysis is valid because the 2D steady state flow is still stable to 2D perturbations at these conditions. It is also relevant because the flow that sets up in the experiment is initially 2D with eventual appearance of 3D streaks.

Using the global stability analysis at these conditions, we discover an alternate unstable mode branch with much smaller spanwise wavelength. This is shown in Fig. 6. The wavelength of the most unstable mode from the small λ_z branch matches well with the experimental observations [6, 11]. As the free-stream Re is increased from its critical value to the experimental value, the small λ_z unstable branch shoots up, while the growth rate of the large λ_z mode branch, discussed in the previous subsection, saturates.

The small and the large λ_z unstable mode branches have different spatial structures in their respective perturbations.

While the large λ_z mode exists in the entirety of the bubble, the small λ_z mode exist in a small region near the rear end of the separation bubble. The wave-makers [15, 16] for these modes are shown as insets in Fig. 6 and indicate differences in spatial origin of the two unstable global modes.

5 Sensitivity to External Perturbations : Input-Output Analysis

Recent analysis by Dwivedi et al. [7, 8] has shown that globally stable compression ramp flow configurations are extremely sensitive to upstream disturbances. These disturbances are spatially amplified by the base flow and can result in formation of

streaks near reattachment [17, 18]. In the presence of physical uncertainties such as leading edge roughness, free-stream disturbance environment, additional sources of persistent external disturbances exist. We carry out a global input-output (I/O) analysis to quantify the amplification of perturbations from such exogenous excitation. We augment the evolution model (3) with external excitation sources in the semi-discrete form,

$$\frac{d}{dt} \mathbf{q} = \mathbf{A}\mathbf{q} + \mathbf{B}\mathbf{d}, \quad \boldsymbol{\phi} = \mathbf{C}\mathbf{q}, \quad (5)$$

Here, \mathbf{q} denotes the perturbation vector, $\mathbf{d}(x_i, t)$ is a disturbance source (input) and $\boldsymbol{\phi}$ is the output. In Eq. (5) the matrix \mathbf{B} specifies how the input enters the state equation, while the matrix \mathbf{C} extracts the output from the state \mathbf{q} . In this work, \mathbf{B} is used to constrain the inputs to be far upstream of the interaction, but no *a priori* restriction on wall-normal distribution is imposed. The inputs can exist in the freestream or at the wall. However, any realizability constraints or semblance to physical perturbations is not imposed in this study. For a globally stable fluid flow system, a time-periodic input with frequency ω , $\mathbf{d}(t) = \hat{\mathbf{d}}(\omega)e^{i\omega t}$ results in a steady-state output $\boldsymbol{\phi}(t) = \hat{\boldsymbol{\phi}}(\omega)e^{i\omega t}$, where $\hat{\boldsymbol{\phi}}(\omega) = \mathbf{H}(i\omega)\hat{\mathbf{d}}(\omega)$ and $\mathbf{H}(i\omega)$ is the frequency response [19–21],

$$\mathbf{H}(i\omega) = \mathbf{C}(i\omega\mathbf{I} - \mathbf{A})^{-1}\mathbf{B}. \quad (6)$$

For a given temporal frequency ω , we use a matrix-free approach [7] to compute the largest singular value $\sigma_1(\omega)$ of $\mathbf{H}(i\omega)$ and the corresponding input forcing direction \mathbf{d}_1 which leads to the output $\boldsymbol{\phi}_1$. Note that, at any ω ,

$$G(\omega) := \sigma_1(\omega) = \frac{\|\mathbf{H}(i\omega)\mathbf{d}_1(\omega)\|_E}{\|\mathbf{d}_1(\omega)\|_E} = \frac{\|\boldsymbol{\phi}_1(\omega)\|_E}{\|\mathbf{d}_1(\omega)\|_E}, \quad (7)$$

denotes the largest induced gain with respect to Chu's compressible energy norm [22].

Using this framework, we evaluate the response of the 2D steady state slender double wedge geometry flow. The free-stream conditions are the same as in the previous section and the turn angle is 7.5° , below its critical value. We observe two peaks in the amplification contours which correspond to (i) unsteady disturbances at $\omega = 0.4$, $\lambda_z = 3$ with the dominant output $\boldsymbol{\phi}_1$ being oblique waves in the reattaching shear layer, (ii) $\omega = 0$, $\lambda_z = 1.5$ with dominant output $\boldsymbol{\phi}_1$ being streak-like perturbations resulting from upstream streamwise vortical disturbances \mathbf{d}_1 .

Figure 7a shows the I/O amplification $G(\omega)$, defined in Eq. (7) over a range of λ_z and ω (non-dimensionalized with $\delta_{\text{reattachment}}$ and U_∞).

The second peak corresponds to a steady input and is the global maximum of the amplification contours in Fig. 7. This region in the gain map points to a low-pass filter characteristic of the amplification mechanism: G achieves its largest value at $\omega = 0$, decreases slowly for low frequencies, and experiences a rapid decay after

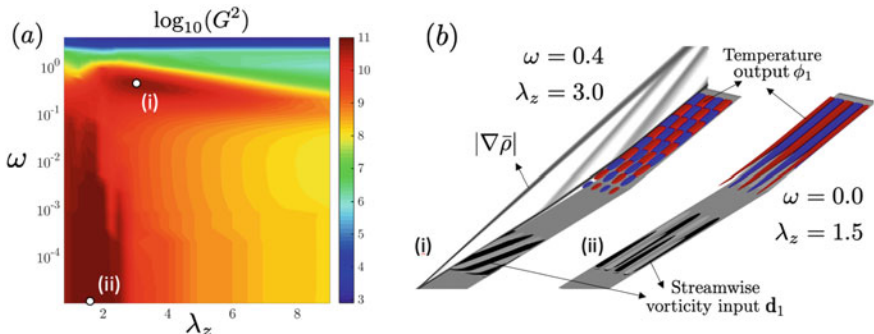


Fig. 7 **a** $G_{\max}(\omega, \lambda_z)$ for ω and λ_z . **b** Isosurfaces of streamwise vorticity input \mathbf{d}_1 and T' output(ϕ_1) for the local maxima at $(\omega, \lambda_z) =$ (i) $(0, 1.5)$ and (ii) $(0.4, 3.0)$

the roll-off frequency ($\omega \approx 0.1$). The base flow preferentially amplifies upstream perturbations with a specific spanwise wavelength resulting in reattachment streaks in experiments despite the absence of a global linear instability.

6 Conclusions and Future Work

We analysed the global stability and sensitivity of the 2D high speed boundary layer on a slender double-wedge. The base state involves a recirculation bubble with a separation-reattachment shock. Increase in free-stream Reynolds number or the turn angle at the compression corner destabilizes the flow to three-dimensional perturbations. Beyond the critical parameters, the recirculation region is three-dimensional and results in streak-like flow structures downstream. Separately, input-output analysis at stable turn angles reveals that the flow can selectively amplify upstream streamwise vortical perturbations in the boundary layer, which also results in reattachment temperature streaks. Therefore, nominally 2D interactions can exhibit streamwise reattachment streaks from both, modal and non-modal mechanisms.

The physical results from this study are also relevant to other shock-boundary layer interaction configurations such as separation in presence of impinging oblique shocks. More generally, global system tools are expected to play an important role in discovery and control of transition mechanisms in 3D boundary layers on geometries of engineering relevance. However, more work is required to better interpret the convoluted structures from global ‘modes’ and use it for physics-aided design. Prior physics from these models in conjunction with high-fidelity data from targeted direct simulations will help transition prediction on complex hypersonic flow-fields.

Acknowledgements This work was presented by Dr. N. Hildebrand with support from NASA. Financial support from the AFOSR (award FA9550-18-1-0422) and ONR (awards N00014-17-1-2496 and N00014-19-1-2037) is gratefully acknowledged by AD, JWN, MRJ and GVC.

References

1. Olejniczak, J., Wright, M.J., Candler, G.V.: Numerical study of inviscid shock interactions on double-wedge geometries. *J. Fluid Mech.* **352**, 1 (1997)
2. Sidharth, G.S., Dwivedi, A., Nichols, J., Jovanovic, M., Candler, G.: Emergence of three-dimensional flow structures in shock boundary layer interactions. *Bull. Am. Phys. Soc.* **62** (2017)
3. Ginoux, J.: On some properties of reattaching laminar and transitional high speed flows, Note 53, Von Karman Institute (1969)
4. Simeonides, G., Haase, W.: Experimental and computational investigations of hypersonic flow about compression ramps. *J. Fluid Mech.* **283**, 17 (1995)
5. Sidharth, G.S., Dwivedi, A., Candler, G.V., Nichols, J.W.: Global linear stability analysis of high speed flows on compression ramps. In: 47th AIAA Fluid Dynamics Conference (2017)
6. Sidharth, G.S., Dwivedi, A., Candler, G.V., Nichols, J.W.: Onset of three-dimensionality in supersonic flow over a slender double wedge. *Phys. Rev. Fluids* **3**(9), 093901 (2018)
7. Dwivedi, A., Sidharth, G.S., Candler, G.V., Nichols, J.W., Jovanović, M.R.: Input-output analysis of shock boundary layer interaction. In: 48th AIAA Fluid Dynamics Conference, p. 3220 (2018)
8. Dwivedi, A., Sidharth, G.S., Nichols, J.W., Candler, G.V., Jovanović, M.R.: Reattachment vortices in hypersonic compression ramp flow: an input-output analysis. *J. Fluid Mech.* **880**, 113 (2019)
9. Mittal, S., Sidharth, G.S.: Steady forces on a cylinder with oblique vortex shedding. *J. Fluids Struct.* **44**, 310 (2014)
10. Paredes, P., Hanifi, A., Theofilis, V., Henningson, D.S.: The nonlinear PSE-3D concept for transition prediction in flows with a single slowly-varying spatial direction. *Proc. IUTAM* **14**, 36 (2015)
11. Yang, L., Zare-Behtash, H., Erdem, E., Kontis, K.: Investigation of the double ramp in hypersonic flow using luminescent measurement systems. *Exp. Therm. Fluid Sci.* **40**, 50 (2012)
12. Candler, G.V., Barnhardt, M.D., Drayna, T.W., Nompelis, I., Peterson, D.M., Subbareddy, P.: Unstructured grid approaches for accurate aeroheating simulations. In: AIAA paper 3959 (2007)
13. Lehoucq, R.B., Sorensen, D.C., Yang, C.: Arpack users' guide: solution of large-scale eigenvalue problems with implicitly restarted Arnoldi methods (1998)
14. Li, X.S., Demmel, J.W.: Superlu-dist: A scalable distributed-memory sparse direct solver for unsymmetric linear systems. *ACM Trans. Math. Softw.* **29**(2), 110 (2003)
15. Hildebrand, N., Dwivedi, A., Nichols, J.W., Jovanović, M.R., Candler, G.V.: Simulation and stability analysis of oblique shock-wave/boundary-layer interactions at Mach 5.92. *Phys. Rev. Fluids* **3**, 013906 (2018)
16. Giannetti, F., Luchini, P.: Structural sensitivity of the first instability of the cylinder wake. *J. Fluid Mech.* **581**, 167 (2007)
17. Dwivedi, A., Nichols, J.W., Jovanovic, M.R., Candler, G.V.: Optimal spatial growth of streaks in oblique shock/boundary layer interaction. In: 8th AIAA Theoretical Fluid Mechanics Conference, p. 4163 (2017)
18. Chuvakhov, P.V., Borovoy, V.Y., Egorov, I.V., Radchenko, V.N., Olivier, H., Roghelia, A.: Effect of small bluntness on formation of Görtler vortices in a supersonic compression corner flow. *J. Appl. Mech. Tech. Phys.* **58**(6), 975 (2017)
19. Jovanović, M.R., Bamieh, B.: Componentwise energy amplification in channel flows. *J. Fluid Mech.* **534**, 145 (2005)
20. Schmid, P.J.: Nonmodal stability theory. *Annu. Rev. Fluid Mech.* **39**, 129 (2007)
21. Dwivedi, A., Sidharth, G.S., Hollender, C., Candler, G.: Linear analysis of high-speed axisymmetric flows. In: AIAA Aviation 2020, p. 2987 (2020)
22. Hanifi, A., Schmid, P.J., Henningson, D.S.: Transient growth in compressible boundary layer flow. *Phys. Fluids* **8**(3), 826 (1996)

On the Influence of Frequency and Spanwise Wavelength on the Formation of Görtler Vortices



Adriano Sueke Takata and Leandro Franco de Souza

Abstract The first feature of the laminar-turbulent transition process in boundary layers over concave surfaces is often the emergence of the streamwise-oriented counter-rotating vortices, known as Görtler Vortices. The generation of these vortices occurs due to the imbalance of centrifugal and inertial forces, and the understanding of these vortices is of extreme importance in the industry because it can delay or anticipate the laminar-turbulent transition process. Some recent studies focus on unsteady disturbances to generate steady or unsteady Görtler vortices. This problem is studied here by high-order numerical simulations to verify the evolution and the structure of the steady and unsteady Görtler vortices for different values of spanwise wavelength and disturbance frequencies. The results show that when the spanwise wavelength and time-frequency increase, the flow is not dominated by mode (1, 1) but by (0, 2) and this implies that unsteady disturbances can generate steady Görtler Vortices.

1 Introduction

In fluid mechanics, instability studies have as objective to understand the behavior of the perturbations in the flow. In general, the amplitude of these perturbations may decrease (stable), be constant (neutral), or grow (unstable). One type of instability of great importance and applicability in the industry is centrifugal instability [1, 2], and usually, three different domains are used to study this instability which depends on whether the system is open or closed and whether the base state is parallel or nonparallel [3]. In a boundary layer flow over a concave surface (open system and weakly nonparallel base state), the streamwise-oriented counter-rotation vortices

A. Sueke Takata · L. Franco de Souza (✉)

University of São Paulo, 400 Trabalhador São-carlense, Avenue São Carlos, São Paulo 13566-590, Brazil

e-mail: lefraso@gmail.com

A. Sueke Takata

e-mail: adrianostakata@gmail.com

may occur due to the imbalance between the centrifugal and inertial forces [4]. These vortices were studied initially by Görtler [5], which bears his name.

The model used to study the Görtler vortices may be the incompressible or compressible Navier-Stokes equations, and in the flow may introduce the steady or unsteady disturbances. Boiko et al. [6] were the first to publish the experimental and theoretical study considering incompressible fluid and unsteady disturbances, and their article boosted and opened a new branch in the study of Görtler vortices, and works about the receptivity problem [7–10], weakly nonlinear effect [11], wall-transpiration [12], and secondary instability [13] are already found in the literature.

In the present study, it is adopted a high-order numerical simulation (DNS) to study and understand the evolution and the structure when unsteady disturbances are introduced in a flow over a concave wall. Two spanwise wavelengths and five frequencies were considered.

The mathematical formulation and the numerical procedure is the same adopted in [14–16]. The only difference between the simulations carried out here from the previous works is that an unsteady disturbance is introduced at the suction and blowing strip with a given frequency.

2 Results

The physical parameters adopted in the simulations are the same of [17]: the radius of curvature is $R^* = 3.2$ m, the freestream velocity is $U_\infty^* = 5.0$ m/s, and $\nu^* = 1.509 \times 10^{-5}$ m/s². The reference length adopted was $L^* = 0.1$ m, giving Reynolds number and Görtler number equal $Re = ((L^* U_\infty^*) / \nu^*) = 33124.0$ and $Go = ((L^* / R^*) \sqrt{Re})^{1/2} = 2.385$, respectively. The spanwise wavelengths studied here are $\lambda_z^* = 9.0$, and 18.0 mm, and the respective values for the wavelength parameter of the fundamental Fourier mode are $\Lambda = ((U_\infty^* \lambda_z^*) / \nu^*) \sqrt{(\lambda_z^* / R^*)} = 158.099$ and 447.173.

The distance of two consecutive points in the streamwise direction is $dx = 2.0 \times 10^{-2}$, the first distance of two consecutive points in the wall-normal direction is $dy = 5.0 \times 10^{-4}$ with a stretching of 1%, and, the time step is $dt = 1.0 \times 10^{-3}$. In the spanwise direction it was adopted 21 Fourier modes with 64 collocation points in physical space, to avoid aliasing. The disturbances were introduced between $x_2 = 1.2$ and $x_3 = 1.52$ at the wall by a suction and blowing technique. The parameter that adjust the disturbance amplitudes was $A = 3.5 \times 10^{-3}$ and 1.08×10^{-3} , for $\lambda_z^* = 9.0$ and 18.0 mm, respectively. For the steady disturbance ($f_{gv} = 0$ Hz), the results obtained using these values for A are in agreement with the article [14], where the metric used is the disturbance energy [18].

For the simulations where unsteady disturbances were introduced, five frequencies are considered: 3, 6, 9, 12, and 15 Hz. The results are presented in the frequency–spanwise wavenumber spectrum (m, k). The Fourier analysis in time is applied to analyze the evolution of these disturbances and the maximum amplitude is calculated by:

$$U_{max,m,k} = \max_y |U_{m,k}(x, y)|. \quad (1)$$

Figure 1 shows the maximum amplitude of the modes $(0, 0)$, $(1, 1)$, $(0, 2)$, $(2, 0)$, $(2, 2)$, $(1, 3)$, and $(3, 1)$ for $\lambda_z^* = 9.0$ mm. The results for the five frequencies simulations are shown. According to [11], the shown modes are the most relevant in these studies because they reach higher amplitudes than the others. It can be observed that, as the frequency of the disturbances increases, the magnitude of the modes decreases. With the adopted spanwise wavelength ($\lambda_z^* = 9.0$ mm) the first spanwise harmonic is $\lambda_z^* = 4.5$ mm—mode $(0, 2)$, and this mode is stable, therefore, as the disturbance frequency increases, the flow becomes stable. Initially, the $(1, 1)$ mode dominates the flow until $x = 8.4$, 9.2 , and 11.0 for $f_{gv}^* = 3$, 6 , and 9 Hz, respectively, where the intersection of $(1, 1)$ and $(0, 0)$ occurs. After this intersection a saturation region is obtained. The results for $f_{gv}^* = 12$ and 15 Hz show that the mode $(1, 1)$ does not achieve enough amplitude to reach a saturation region. Therefore the flow becomes stable to the disturbances introduced in the flow field.

The isosurfaces, shown by Q criterion [19] with $Q = 0.01$, and crosscuts showing the streamwise velocity isocontours in the (y, z) -plan are shown in Fig. 2. The graphics shown correspond to the five frequency simulations shown in Fig. 1. The flow direction is from bottom left to right top. The structures obtained show a Λ shape, with a shift in spanwise direction. The number of structures increase with the frequency, as expected. The streamwise velocity isocontours cuts for $f_{gv}^* = 3$, 6 and 9 Hz simulations show the mushroom shape of the streamwise velocity, characteristic of flows with Görtler Vortices. A weak undulation of the streamwise velocity can be seen in the crosscuts of the $f_{gv}^* = 12$ and 15 Hz simulations. This shows that high frequency disturbances to generate Görtler Vortices are stable for this spanwise wavelength.

The streamwise velocity maximum amplitude $U_{m,k}(x, y)$ for spanwise wavelength $\lambda_z^* = 18.0$ mm are shown in Fig. 3. The same frequencies adopted in the previous case are shown here: $f_{gv}^* = 3, 6, 9, 12$ and 15 Hz. In all cases the excited mode $(1, 1)$ initially dominate the scenario, but in the present simulations the first harmonic—mode $(0, 2)$, that correspond to spanwise wavelength of $\lambda_z^* = 9.0$ mm is also unstable. Therefore, mode $(0, 2)$ dominate the transition scenarium as the disturbance frequency increases. The results obtained for the cases with $f_{gv}^* = 3$ and 6 Hz show that the analyzed modes achieve high amplitudes near the end of the domain. This is compatible with the last stages of laminar-turbulent transition process. The results for $f_{gv}^* = 9$ Hz shows a competition between mode $(1, 1)$ and mode $(0, 2)$ until the saturation region, where the mode $(0, 2)$ starts to dominate the transition process. The results of the higher frequency simulations— $f_{gv}^* = 12$ and 15 Hz, shows that mode $(0, 2)$ dominate the transition process.

Figure 4 shows the isosurfaces ($Q = 0.01$) and streamwise velocity crosscuts for the simulations shown in Fig. 3.

Three different behavior can be observed, for the cases with frequencies $f_{gv}^* = 3$ and 6 Hz, secondary instabilities arises and the varicose mode dominates the transition

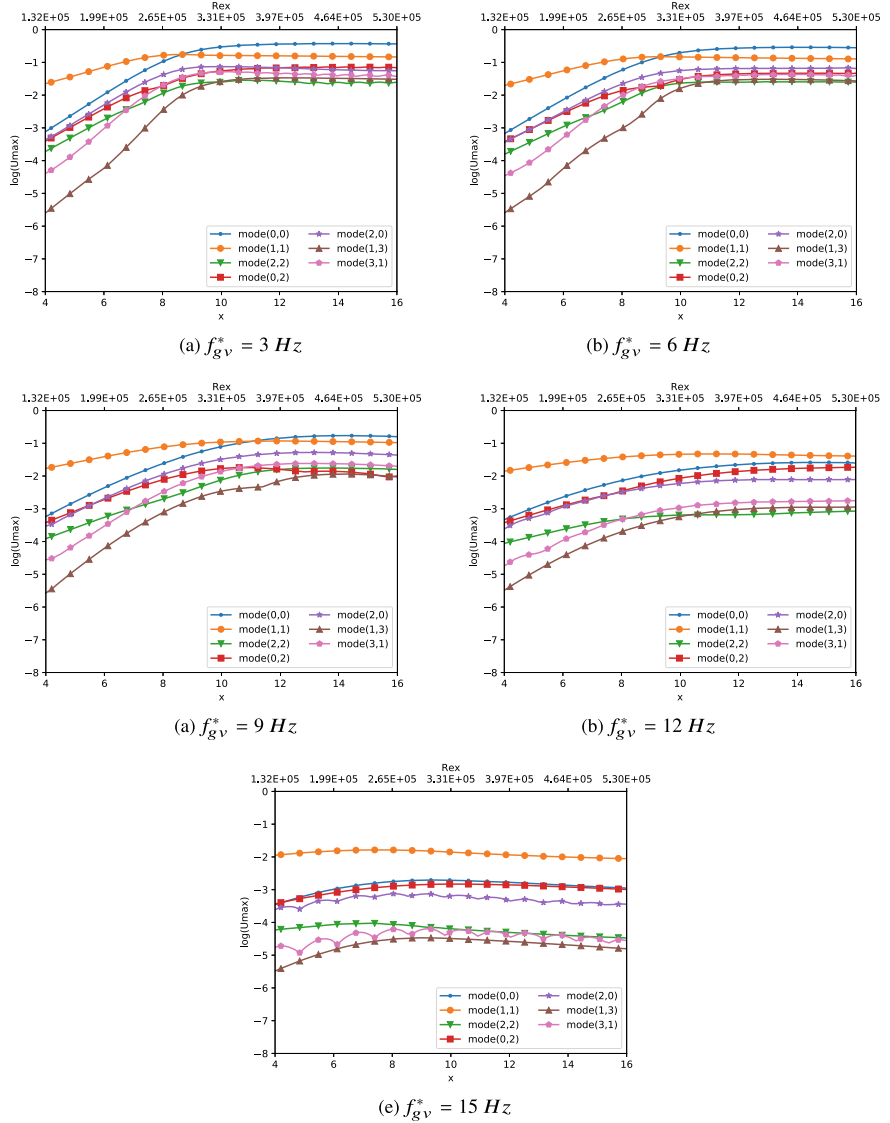


Fig. 1 The maximum streamwise velocity amplitude with spanwise wavelength $\lambda_z^* = 9.0 \text{ mm}$ for the following frequencies: **a** $f_{gv}^* = 3 \text{ Hz}$, **b** $f_{gv}^* = 6 \text{ Hz}$, **c** $f_{gv}^* = 9 \text{ Hz}$, **d** $f_{gv}^* = 12 \text{ Hz}$, and **e** $f_{gv}^* = 15 \text{ Hz}$

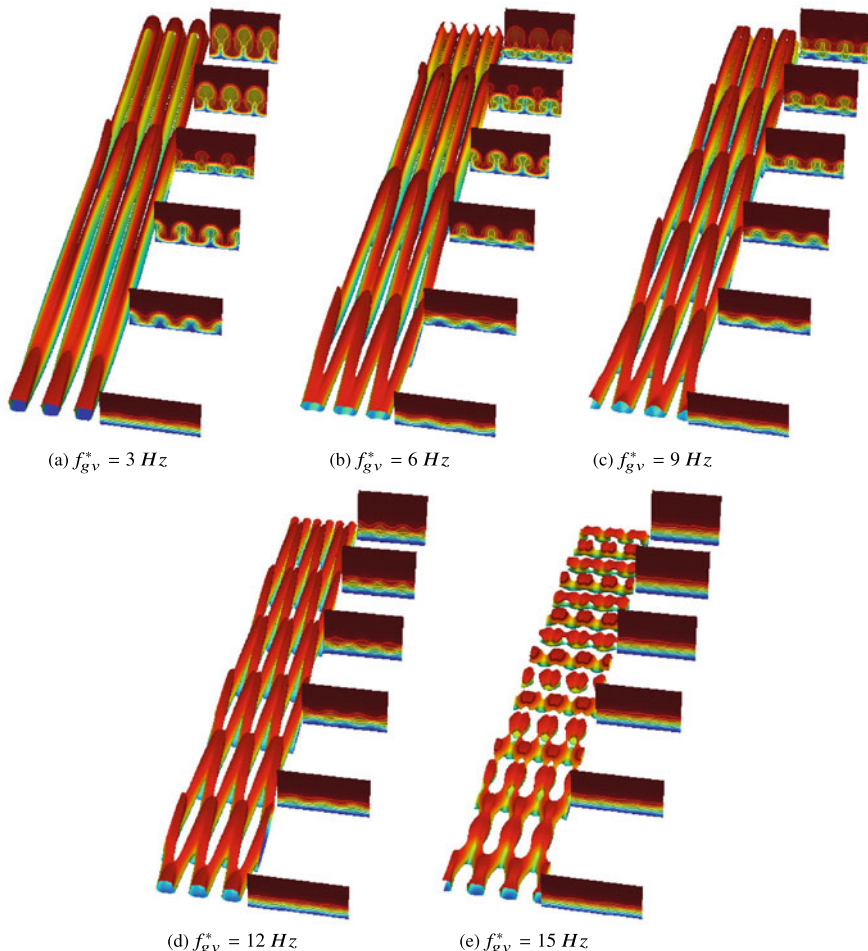


Fig. 2 The isosurface $Q = 0.01$ and the isocontours of the velocity profile \tilde{u} in the (z, y) -plan for $\lambda_z^* = 9.0 \text{ mm}$ with $\cos(\omega_{gv}t) = 0.0$ for: **a** $f_{gv}^* = 3 \text{ Hz}$, **b** $f_{gv}^* = 6 \text{ Hz}$, **c** $f_{gv}^* = 9 \text{ Hz}$, **d** $f_{gv}^* = 12 \text{ Hz}$, and **e** $f_{gv}^* = 15 \text{ Hz}$

near the end of the domain. The cases with frequencies $f_{gv}^* = 9$ and 12 Hz show that although a competition between unsteady mode $(1, 1)$ and stationary mode $(0, 2)$ exists, the unsteady mode is more pronounced in the flow field. For the case with $f_{gv}^* = 15 \text{ Hz}$ it is clear that mode $(0, 2)$ dominate the transition process.

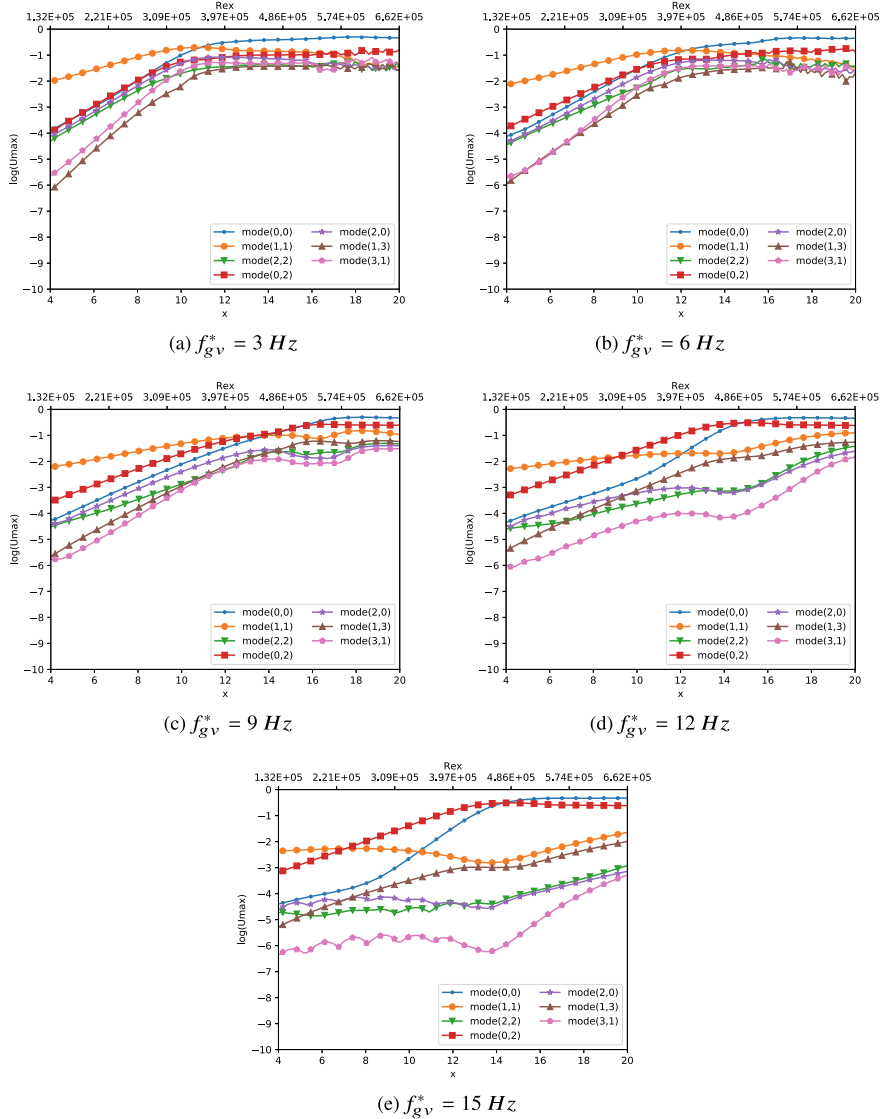


Fig. 3 The maximum streamwise velocity amplitude with the spanwise wavelength $\lambda_z^* = 18.0 \text{ mm}$ for the following frequencies: **a** $f_{gv}^* = 3 \text{ Hz}$, **b** $f_{gv}^* = 6 \text{ Hz}$, **c** $f_{gv}^* = 9 \text{ Hz}$, **d** $f_{gv}^* = 12 \text{ Hz}$, and **e** $f_{gv}^* = 15 \text{ Hz}$

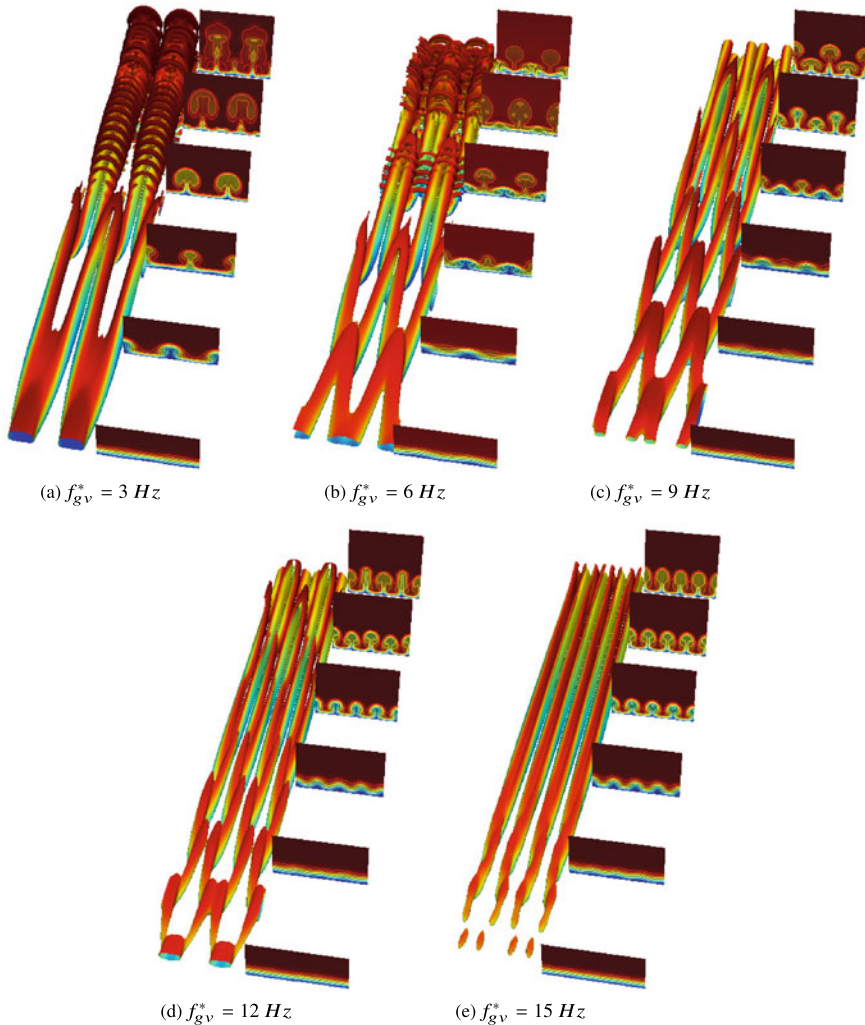


Fig. 4 The isosurface $Q = 0.01$ and the isocontours of the velocity profile \tilde{u} in the (z, y) -plan for $\lambda_z^* = 18.0 \text{ mm}$ with $\cos(\omega_{gv}t) = 0.0$ for: **a** $f_{gv}^* = 3 \text{ Hz}$, **b** $f_{gv}^* = 6 \text{ Hz}$, **c** $f_{gv}^* = 9 \text{ Hz}$, **d** $f_{gv}^* = 12 \text{ Hz}$, and **e** $f_{gv}^* = 15 \text{ Hz}$

3 Conclusions

In the present work a high-order numerical simulation of low frequency unsteady disturbances in a flow over a concave wall was carried out. Two spanwise wavelengths and five frequencies were investigated. The results show that for the smaller wavelength investigated ($\lambda_z^* = 9.0 \text{ mm}$) the unsteady excited disturbance mode $(1, 1)$ dominates the transition process, and that the flow becomes stable to higher fre-

quencies disturbances. This behavior can be explained by the fact that the steady harmonic spanwise mode (0, 2) is stable for this spanwise wavelength. The results obtained with the simulations for $\lambda_z^* = 18.0$ mm show that as the disturbance frequency increases the steady harmonic spanwise mode (0, 2) increases and dominate the transition process. The lower frequencies simulation for this spanwise wavelength $f_{gv}^* = 3$ and 6 Hz showed that the secondary instability modes arises with the appearance of varicose mode in the late stages of transition.

Acknowledgements This work was supported by the CAPES and ICMC-USP. Research carried out using the computational resource of the Center for Mathematical Applied to Industry (CeMEAI) funded by FAPESP (Process Number 2013/07375-0).

References

1. Brown, A., Martin, B.: Flow transition phenomena and heat transfer over the pressure surfaces of gas turbine blades. In: ASME 1981 International Gas Turbine Conference and Products Show. American Society of Mechanical Engineers (1981)
2. Wang, J.-S., Feng, L.-H., Wang, J.-J., Li, T.: Görtler vortices in low-reynolds-number flow over multi-element airfoil. *J. Fluid Mech.* **835**, 898–935 (2018)
3. Drazin, P.G., Reid, W.H.: *Hydrodynamic Stability*. Cambridge University Press, Cambridge (2004)
4. Saric, W.S.: Görtler vortices. *Annu. Rev. Fluid Mech.* **26**(1), 379–409 (1994)
5. Görtler, H.: Instabilität laminarer grenzschichten an konkaven wänden gegenüber gewissen dreidimensionalen störungen. *ZAMM-J. Appl. Math. Mech./Z. für Angew. Math. und Mech.* **21**(4), 250–252 (1941)
6. Boiko, A., Ivanov, A., Kachanov, Y.S., Mischenko, D.: Steady and unsteady görtler boundary-layer instability on concave wall. *Eur. J. Mech.-B/Fluids* **29**(2), 61–83 (2010)
7. Schrader, L.-U., Brandt, L., Zaki, T.A.: Receptivity, instability and breakdown of görtler flow. *J. Fluid Mech.* **682**, 362–396 (2011)
8. Ivanov, A., Kachanov, Y., Mischenko, D.: Generation of nonstationary görtler vortices by localized surface nonuniformities. Receptivity coefficients. *Thermophys. Aeromech.* **19**(4), 523–539 (2012)
9. Borodulin, V.I., Ivanov, A.V., Kachanov, Y.S., Mischenko, D.A.: Systematic study of distributed excitation of unsteady görtler modes by freestream vortices. *Eur. J. Mech.-B/Fluids* **68**, 167–183 (2018)
10. Vairo, S., Ricco, P.: Neutral stability curves of low-frequency görtler flow generated by free-stream vortical disturbances. *J. Fluid Mech.* **845** (2018)
11. Boiko, A., Ivanov, A., Kachanov, Y.S., Mischenko, D.: Investigation of weakly-nonlinear development of unsteady görtler vortices. *Thermophys. Aeromech.* **17**(4), 455 (2010)
12. Marensi, E., Ricco, P.: Growth and wall-transpiration control of nonlinear unsteady görtler vortices forced by free-stream vortical disturbances. *Phys. Fluids* **29**(11), 114106 (2017)
13. Xu, D., Zhang, Y., Wu, X.: Nonlinear evolution and secondary instability of steady and unsteady görtler vorwatices induced by free-stream vortical disturbances. *J. Fluid Mech.* **829**, 681–730 (2017)
14. Souza, L.F.: On the odd and even secondary instabilities of görtler vortices. *Theor. Comput. Fluid Dyn.* **31**(4), 405–425 (2017)
15. Rogenski, J.K., de Souza, L.F., Floryan, J.M.: Influence of pressure gradients on the evolution of the görtler instability. *AIAA J.* **54**(9), 2916–2921 (2016)
16. Rogenski, J.K., de Souza, L.F., Floryan, J.M.: Non-linear aspects of görtler instability in boundary layers with pressure gradient. *Phys. Fluids* **28**(12), 124107 (2016)

17. Swearingen, J.D., Blackwelder, R.F.: The growth and breakdown of streamwise vortices in the presence of a wall. *J. Fluid Mech.* **182**, 255–290 (1987)
18. Li, F., Malik, M.R.: Fundamental and subharmonic secondary instabilities of görler vortices. *J. Fluid Mech.* **297**, 77–100 (1995)
19. Dubief, Y., Delcayre, F.: On coherent-vortex identification in turbulence. *J. Turbul.* **1**(1), 011–011 (2000)

Non-modal Linear Stability Analysis of Ablation Flows Relative to Inertial Confinement Fusion



G. Varillon, J.-M. Clarisse, and A. Couairon

1 Introduction

Inertial confinement fusion (ICF) aims at achieving controlled thermonuclear burn by means of a sufficiently symmetric implosion of a spherical pellet, under the action of an external radiation flux [1]. Such implosions are triggered and driven by the deflagration, or *ablation*, heat wave that thrusts inwardly the pellet outer shell, the *ablator*, chosen to be opaque to the incoming irradiation. The associated flow consists of a subsonic heat front, or *ablation front*, coinciding with the leading edge of the heated material expansion wave, that penetrates into the ablator, preceded by a fore-running shock wave [1, Chap. 2], [2, vol. 2, Chap. 10, Sect. 8]. Inherently unsteady, these ablation flows which undergo different regimes of acceleration during the implosion, are compressible and highly nonuniform with a steep heat front, owing to the strong nonlinearity of the heat transport and the intense incident heating.

Right from the beginning of research on the subject back in the 1970s, the hydrodynamic stability of ablation fronts has been identified as one of the most critical issues to the success of ICF. Since then, an impressive amount of efforts, in terms of modeling, numerical simulations, reduced- and full-scale laboratory experiments, has been devoted to the prediction, measurement and mitigation of hydrodynamic instabilities

G. Varillon · J.-M. Clarisse
CEA, DAM, DIF, 91297 Arpajon, France
e-mail: jean-marie.clarisse@cea.fr

J.-M. Clarisse
Université Paris-Saclay, CEA, LMCE, 91680 Bruyères-le-Châtel, France

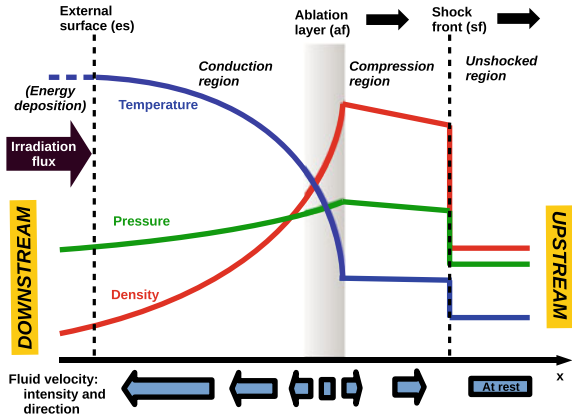
G. Varillon (✉) · A. Couairon
CPHT, CNRS, École Polytechnique, Institut Polytechnique de Paris, 91128 Palaiseau, France
e-mail: gregoire.varillon@polytechnique.edu

A. Couairon
e-mail: arnaud.couairon@polytechnique.edu

in ICF implosions and, in particular, in ICF ablation flows. Despite these efforts, thermonuclear ignition experiments carried out on the largest existing ICF facility have not been yet conclusive [3]. Theoretical investigations of ablation flow stability have relied on simplifying assumptions that are not necessarily met in actual cases: e.g. mean-flow steadiness, low Mach-number approximation, unbounded domains, discontinuous ablation front, flow region uniformity of some sort [4]. In addition, these works have exclusively employed the method of normal modes, focusing on the least stable eigensolutions and thus only furnishing asymptotic stability results. More realistic configurations are classically handled by means of multidimensional numerical simulations carried out with ICF hydrodynamics codes which incorporate the most relevant physical phenomena. These “full-physics” simulations which are computationally very demanding, are necessarily of limited accuracy for decreasing perturbation scales and also suffer from overly dissipative and dispersive numerical schemes used in such hydrocodes. Such simulations consist in computing perturbation amplifications from selected perturbed initial or boundary conditions that are considered to be the “most dangerous” for a given mean-flow configuration. Comparisons with theoretical results and specifically designed experiments where a dominant most dangerous perturbation source is selected by a careful control of experimental conditions, have helped building confidence in the ability of ICF hydrocodes to reproduce instability dynamics [5, 6]. However, this approach faces a major difficulty in having to deal, in actual ICF implosions, with multiple perturbation sources whose contributions remain, for some of them, unsufficiently known and controlled. This fact is substantiated by recent successively targeted series of experiments which have revealed the detrimental effects of perturbation sources previously held to be minor, thus questioning the common acceptation of most dangerous perturbation sources for ICF pellet implosions.

In this context, methods of non-modal stability theory [7], being capable of identifying the most dangerous perturbations in time-dependent flows of finite durations, not only appear to be most valuable but also to be a necessity. Since the current cost of full-physics simulations forbids the implementation of such methods with existing ICF hydrocodes, we have recourse to a simplified modeling of unsteady ablation waves provided by self-similar solutions to the Euler equations with nonlinear heat conduction [8]. Some of these solutions are representative of the first stage of a pellet implosion, or *shock transit phase*, during which the fore-running shock wave is still traveling inside the ablator [9, 10]. In particular these self-similar flows present the complete structure of an ablation wave: a leading shock front, a quasi-isentropic compression (*post-shock*) region, an ablation layer and an expansion wave where heat conduction dominates (the *conduction region*): cf. Fig. 1. This modeling which does not give up essential features of ICF ablation waves (unsteadiness, compressibility, stratification and confinement) has previously been used to obtain linear perturbation responses for configurations of ICF commonly held as most dangerous [11, 12]. Here we perform a non-modal stability analysis that consists in finding *optimal initial perturbations* (OIPs), i.e. initial perturbations that maximize a semi-norm of the flow perturbations at a given time horizon. Having to deal with time-dependent and non-uniform base flows, these OIPs are obtained by means of a direct-adjoint method

Fig. 1 Structure of an ablation wave



that we have developed based on our previous experience with linear perturbation computations in such flows.

2 Model

The chosen ablation wave modeling considers a semi-infinite slab of a polytropic gas subject to an incident radiation flux and a material pressure exerted at its external boundary. The gas is assumed to remain at local thermodynamic equilibrium and optically thick to the incoming radiation, allowing us to use a fluid model and the radiation heat-conduction approximation of radiative transfer to describe its motion. Under the conditions of ICF pellet irradiation, the external radiation flux is sufficiently high so that radiation heat conduction dominates any other diffusive effect within the fluid (e.g. viscosity) while the fluid temperature remains sufficiently low for radiation pressure and radiation energy to be negligible compared to material pressure and internal energy. Consequently, the equations of motion come down to the Euler equations with nonlinear heat conduction [2].

2.1 Base Flow

Assuming that the flow is along the x direction of a Cartesian system of coordinates (O, x, y, z), the equations of motion come, in dimensionless form and in the Lagrangian coordinate m such that $dm = \rho dx$, as [9]

$$\partial_t 1/\rho - \partial_m v = 0, \quad \partial_t v + \partial_m p = 0, \quad \partial_t(e + v^2/2) + \partial_m(pv + \varphi) = 0, \quad (1)$$

where ρ , v , p , e and φ denote, respectively, the fluid density, velocity, pressure, specific internal energy, and radiation heat flux of expression

$$\varphi = -\rho^{-\mu} T^\nu \rho \partial_m T \equiv \Psi(\rho, T, \partial_x T), \quad \text{with } \mu = 2, \nu = 13/2, \quad (2)$$

according to a radiation conduction model for a fully-ionized gas [2]. These equations are closed by the dimensionless equation of state

$$p = \rho T, \quad e = C_v T, \quad C_v = 1/(\gamma - 1), \quad (3)$$

where γ is the adiabatic gas exponent. Self-similar reduction of (1)–(3) arises if the incident heat flux and pressure at the external surface follow specific power laws [8, 13], namely

$$\varphi(0, t) = \mathcal{B}_\phi \square^{\exists \alpha - \exists}, \quad \sqrt{(t, \square)} = \mathcal{B} \square^{\epsilon \alpha - \epsilon}, \quad \text{for } \square > t, \text{ with } \alpha = \frac{\epsilon \nu - \infty}{\epsilon \nu - \epsilon}, \quad (4)$$

and for an initial state given by $(\rho, v, T) = (1, 0, 0)$ for $m \geq 0$. For certain values of the boundary parameters $(\mathcal{B}_p, \mathcal{B}_\varphi)$, these self-similar solutions reproduce the features of ICF ablation waves [9, 10]. Highly accurate solutions to (1)–(4) are obtained by means of an adaptive multidomain Chebyshev spectral method [14].

2.2 Linear Perturbations

Three-dimensional linear perturbations of the above self-similar ablative waves are considered using an Eulerian description in the coordinate system (m, y, z) . The resulting system of partial differential equations (PDEs) in physical space is replaced by a system of one-dimensional PDEs in the yz -Fourier space. With the notation \hat{f} for the yz -Fourier component of the base flow quantity f of transverse wavenumber $k_\perp = \sqrt{k_y^2 + k_z^2}$, this system amounts to

$$\partial_t \hat{\mathbf{U}} = \mathbf{L} \hat{\mathbf{U}} \equiv -\mathbf{A} \partial_{m^2}^2 \hat{\mathbf{U}} - \mathbf{B} \partial_m \hat{\mathbf{U}} - \mathbf{C} \hat{\mathbf{U}}, \quad (5)$$

with $\hat{\mathbf{U}} = [\hat{\rho} \hat{v} \hat{d}_\perp \hat{T}]^\top$, where \hat{d}_\perp denotes the Fourier component of the transverse divergence of the transverse velocity. The matrix \mathbf{A} comprises a single non-zero coefficient, $A_{44} = C_v^{-1} \rho \Psi_{T'}$, while the expressions of \mathbf{B} and \mathbf{C} are given by

$$\mathbf{B} = \begin{pmatrix} 0 & \rho^2 & 0 & 0 \\ T & 0 & 0 & \rho \\ 0 & 0 & 0 & 0 \\ C_v^{-1} \Psi_\rho & C_v^{-1} p & 0 & B_{44} \end{pmatrix}, \quad \mathbf{C} = \begin{pmatrix} \rho \partial_m v & \rho \partial_m \rho & \rho & 0 \\ T \partial_m \rho / \rho & \rho \partial_m v & 0 & \partial_m \rho \\ k_\perp^2 T / \rho & 0 & 0 & -k_\perp^2 \\ C_{41} & \rho \partial_m T' & C_v^{-1} T & C_{44} \end{pmatrix},$$

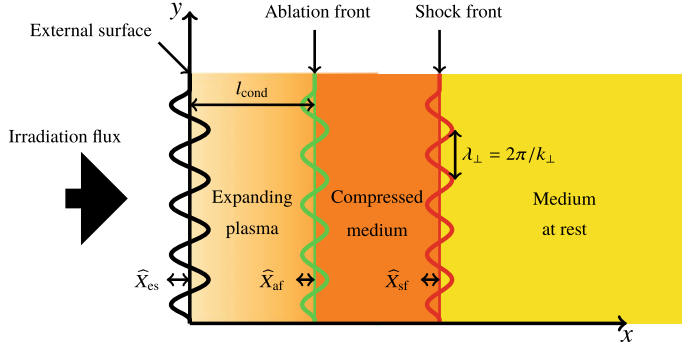


Fig. 2 Two-dimensional schematic view of a perturbed planar ablation wave. The length of the conduction region is denoted by l_{cond} while \hat{X}_a , $a = \text{es}, \text{af}$ or sf , denote the Fourier components, of transverse wavenumber $k_{\perp} = 2\pi/\lambda_{\perp}$, of the linear deformations of, respectively, the external surface, ablation front and shock front

where

$$\begin{aligned} B_{44} &= C_v^{-1} [\partial_m(\rho\Psi_{T'}) + \Psi_T], \quad C_{41} = C_v^{-1} (\partial_m\Psi_\rho - \rho^{-1} \partial_m\varphi), \\ C_{44} &= C_v^{-1} [\rho\partial_m v + \partial_m\Psi_T - k_{\perp}^2\rho^{-1}\Psi_{T'}]. \end{aligned}$$

In these expressions Ψ_ρ , Ψ_T and $\Psi_{T'}$ stand for, respectively, the partial derivatives of the function Ψ of (2) with respect to the density, temperature and temperature gradient. System (5) is of the incompletely parabolic type [15] since it comprises a parabolic subequation for the variable \widehat{T} and a hyperbolic subsystem for the complementary variable vector $[\widehat{\rho} \widehat{v} \widehat{d}_{\perp}]^\top$. Boundary conditions are provided by the linearization (i), at the external surface of linear deformation \widehat{X}_{es} (Fig. 2), of the continuity equations for the pressure and heat flux, and of the kinematic relation at a material surface, and (ii), at the shock front of linear deformation \widehat{X}_{sf} , of the Rankine–Hugoniot jump relations [11]. From these boundary conditions, we infer, at any of the two boundaries $a = \text{es}$ or sf , the proper set of boundary conditions that defines a well-posed boundary value problem (BVP) for (5), namely: a scalar boundary condition for the parabolic subequation in \widehat{T} , say

$$\widehat{\mathbf{B}}_a^p(\partial_m \widehat{\mathbf{U}}|_a, \widehat{\mathbf{U}}|_a, \widehat{X}_a, d_t \widehat{X}_a) = 0, \quad (6)$$

as many boundary conditions as there are incoming waves of the hyperbolic subsystem at the boundary, or the system

$$\widehat{\mathbf{B}}_a^h(\widehat{\mathbf{U}}|_a, \widehat{X}_a, d_t \widehat{X}_a) = \mathbf{0}, \quad (7)$$

and an evolution equation for the boundary surface deformation \widehat{X}_a written as

$$f_a(\mathbf{d}_t \hat{X}_a, \hat{X}_a, \hat{\mathbf{U}}|_a) = 0. \quad (8)$$

3 Optimal Perturbation

The present non-modal stability analysis consists in finding the initial perturbation states $(\hat{\mathbf{U}}, \hat{X}_{\text{es}}, \hat{X}_{\text{sf}})|_{t_0}$ that maximize an objective functional \mathcal{J} depending only on the final states $(\hat{\mathbf{U}}, \hat{X}_{\text{es}}, \hat{X}_{\text{sf}})|_{\mathcal{T}}$ where $(\hat{\mathbf{U}}, \hat{X}_{\text{es}}, \hat{X}_{\text{sf}})$ are solutions to (5)–(8) for zero external forcing and zero perturbations upstream to the shock front.

3.1 Direct-Adjoint Method

The optimization problem to be solved is presently formulated using the Lagrange multiplier technique [16]. In effect a Lagrange functional is defined from \mathcal{J} augmented by constraints enforcing the evolution equation (5), *the sets of boundary conditions defining a well-posed BVP for (5)*, i.e. (6)–(8), and a normalization of the initial conditions, $\mathcal{I}(t_0) = K_0$, namely

$$\begin{aligned} \mathcal{L} = \mathcal{J} - \int_0^{m_{\text{sf}}} \int_{t_0}^{\mathcal{T}} \hat{\mathbf{U}}^{\dagger \top} (\partial_t \hat{\mathbf{U}} - \mathbf{L} \hat{\mathbf{U}}) dt dm \\ - \sum_{a=\text{es,sf}} \int_{t_0}^{\mathcal{T}} \left(\hat{\mathbf{v}}_a^{\dagger \top} \hat{\mathbf{B}}^{h_a} + \hat{\eta}_a^{\dagger} \hat{\mathbf{B}}^{p_a} + \hat{\mu}_a^{\dagger f_a} \right) dt - \beta^{\dagger} (\mathcal{I}(t_0) - K_0). \end{aligned} \quad (9)$$

The optimum lies in the stationary points of \mathcal{L} . Differentiating with respect to the state variables yields the adjoint equation

$$\partial_t \hat{\mathbf{U}}^{\dagger} = \mathbf{L}^{\dagger} \hat{\mathbf{U}}^{\dagger} \equiv \mathbf{A}^{\top} \partial_m^2 \hat{\mathbf{U}}^{\dagger} + (2 \partial_m \mathbf{A} - \mathbf{B})^{\top} \partial_m \hat{\mathbf{U}}^{\dagger} + (\partial_m^2 \mathbf{A} - \partial_m \mathbf{B} + \mathbf{C})^{\top} \hat{\mathbf{U}}^{\dagger}, \quad (10a)$$

$$\hat{\mathbf{B}}_a^{h^{\dagger}} = \mathbf{0}, \quad \hat{\mathbf{B}}_a^{p^{\dagger}} = 0, \quad \mathbf{d}_t \hat{X}_a^{\dagger} = \hat{X}_a^{\dagger}, \quad (10b)$$

where $\hat{\mathbf{B}}_a^{h^{\dagger}}$ and $\hat{\mathbf{B}}_a^{p^{\dagger}}$ represent the boundary condition operators for, respectively, the hyperbolic subsystem and parabolic subequation of (10a), \hat{X}_a^{\dagger} and \hat{X}_a^{\dagger} are scalar linear combinations of $\hat{\mathbf{v}}_a^{\dagger}$, $\hat{\eta}_a^{\dagger}$ and $\hat{\mu}_a^{\dagger}$. The adjoint equation (10a) is well-posed for backward time integration from $t = \mathcal{T}$ to $t = t_0$ with terminal conditions

$$\hat{\mathbf{U}}^{\dagger}|_{\mathcal{T}} = \nabla_{\hat{\mathbf{U}}|_{\mathcal{T}}} \mathcal{J}, \quad \hat{X}_a^{\dagger}|_{\mathcal{T}} = \nabla_{\hat{X}_a|_{\mathcal{T}}} \mathcal{J}. \quad (11)$$

Differentiation with respect to the control parameters, $\widehat{\mathbf{U}}|_{t_0}$, $\widehat{X}_a|_{t_0}$, yields the optimality conditions

$$\nabla_{\widehat{\mathbf{U}}|_{t_0}} \mathcal{L} = \widehat{\mathbf{U}}^\dagger|_{t_0}, \quad \nabla_{\widehat{X}_a|_{t_0}} \mathcal{L} = \widehat{X}_a^\dagger|_{t_0}. \quad (12)$$

where the right-hand-sides vanish at an optimum.

Perturbation measure

The functional \mathcal{J} to be optimized is chosen to be defined after the energy of Chu [17], namely

$$\mathcal{J} = \int_0^{m_{sf}} \frac{j}{\rho} dm, \quad \text{with } j = \frac{1}{2} \left(\frac{T \widehat{\rho}^2}{\rho} + \rho \widehat{v}_x^2 + \frac{\rho \widehat{d}_\perp^2}{k_\perp^2} + \frac{C_v \rho \widehat{T}^2}{T} \right), \quad (13)$$

for $k_\perp > 0$. This functional, being a semi-norm of the state variables, has to be supplemented by a complementary semi-norm which must be a norm for the kernel of \mathcal{J} [18] and which we take to be

$$\mathcal{J}^* = (X_{es}^2 + \widehat{X}_{sf}^2)/2, \quad (14)$$

so that $\mathcal{J} + \mathcal{J}^*$ is a full norm. Since our problem is linear, it is sufficient to restrict ourselves to the case $K_0 = \mathcal{J}(t_0) + \mathcal{J}^*(t_0) = 1$ in (9) and to vary the initial distribution of energy $r_c = \mathcal{J}(t_0)/(\mathcal{J}(t_0) + \mathcal{J}^*(t_0))$ between 0 and 1.

Optimization and numerical methods

The direct and adjoint problems, (5) and (10), are solved iteratively using forward and backward temporal integrations, from a given starting initial condition. The terminal condition (11) is used to initialize the adjoint integration. Successive initial conditions of the direct problem are obtained from (12) by power iterations (e.g. see [19]). Numerical solutions to the direct system (5)–(8) and to the adjoint system (10), are obtained, in the space variable, using the same multidomain pseudospectral method as for the base flow and, in time, with a three-step implicit-explicit Runge–Kutta scheme. Boundary conditions are handled using a penalty method while matching conditions at subdomain interfaces are enforced exactly. The numerical codes for the direct and adjoint problems perform computations over each subdomain in parallel using the MPI paradigm with a single process per subdomain.

3.2 Optimal Initial Perturbations

The present analysis is performed for the self-similar ablative wave defined by the boundary parameters $(\mathcal{B}_\vee, \mathcal{B}_\phi) = (\infty, \infty \triangleright, \exists, \exists \exists)$ in (4). Optimization results have been computed with a spatial grid made of 189 subdomains with 50 collocation points each.

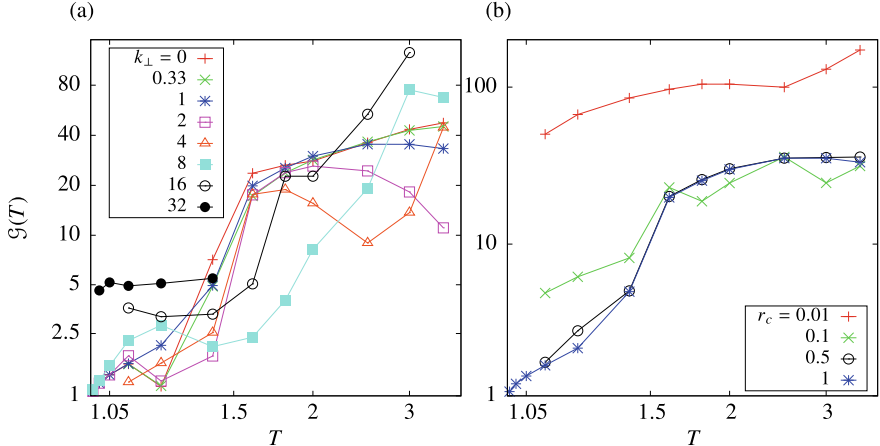


Fig. 3 Curves of the gain $\mathcal{G}(T)$ for (a) $r_c = 1$ and several values of k_{\perp} , (b) $k_{\perp} = 1$ and several values of r_c

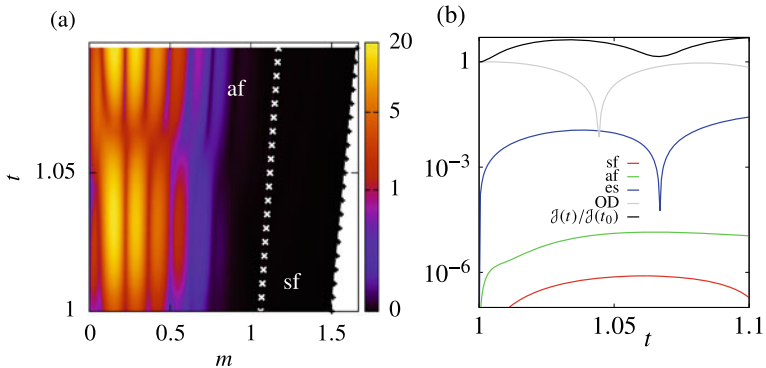


Fig. 4 Optimal gain for $(k_{\perp}, T) = (32, 1.1)$, $r_c = 1$. (a) Chu's energy density j in the variables (m, t) . (b) Deformations X_a of the shock front (sf), ablation layer (af) and external surface (es), Chu's energy amplification ($\mathcal{J}(t)/\mathcal{J}(t_0)$) and optical depth perturbation (OD) as functions of time

Optimal gains $\mathcal{G}(T) = \mathcal{J}(T)/\mathcal{J}(t_0)$ larger than one have been obtained for all the transverse wavenumbers k_{\perp} , initial energy distributions r_c , and terminal times T that have been explored (Fig. 3). This fact denotes an inclination of the present ablation flow to significantly amplify perturbations. This amplification increases with k_{\perp} for small terminal times, evidencing fast transient growth at small wavelengths (Fig. 3a). The initial distribution of perturbations in the deformations of the external surface and shock front, i.e. low values of r_c , leads to the strongest amplifications within the flow (Fig. 3b).

Two optimal growth mechanisms have been identified. For short final times ($1.01 \leq T \leq 1.5$), the OIP is concentrated within the tail of the conduction region

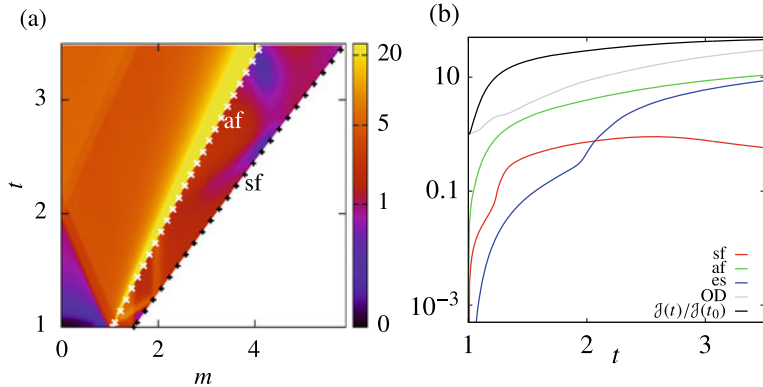


Fig. 5 Optimal gain for $(k_{\perp}, T) = (0.33, 3.5)$, $r_c = 1$. (a) Chu's energy density j in the variables (m, t) . (b) Deformations \hat{X}_a of the shock front (sf), ablation layer (af) and external surface (es), Chu's energy amplification ($J(t)/J(t_0)$) and optical depth perturbation (OD) as functions of time

and develops from local constructive interactions between acoustic and vorticity waves (Fig. 4a). The ablation layer and shock front are not involved in this mechanism as the terminal time T is shorter than the acoustic crossing time between these two locations (Fig. 4b). For larger terminal times, the OIP takes the form of forward acoustic and entropy signals in the post-shock region and perturbation energy grows from the interactions between the shock front and ablation layer resulting from the propagation of acoustic, entropy and vorticity waves across this region (Fig. 5). This mechanism is made possible since T exceeds several times the travel times of these waves across the post-shock region. At such terminal times, Chu's energy density is mostly located in the ablation layer (Fig. 5a). Temporal responses of optical depth perturbations, a quantity usually measured in experiments, appear to be uncorrelated to Chu's energy evolution (Figs. 4b, 5b) implying that experimental observation of perturbation amplification would require some other means of detection.

4 Discussion and Conclusion

The first non-modal stability analysis of an ablation flow reported in this paper shows that ablation waves are susceptible to present transient perturbation growth for a wide range of perturbation characteristic lengths and time horizons. For the present self-similar ablation wave representative of the shock transit phase of an ICF pellet implosion, perturbation transient growths are found at all tested wavelengths and time horizons. Physical mechanisms responsible for such transient growths have been identified to be local constructive interactions between acoustic and vorticity waves within the flow conduction region at short time horizon, and interactions between the ablation layer and shock front for long terminal times. These findings contrast with

previously known results established from normal mode analysis, simulations and dedicated experiments of selected “most dangerous” configurations, for which only large wavelengths are subject to a possible amplification whereas small wavelengths undergo damped oscillations [5, 20]. This confirms the interest and the necessity of non-modal stability analysis for ICF related flows. The present stability analyses has focused on the optimal perturbation problem. Optimal perturbations are found upon solving an optimization problem by means of a direct-adjoint method derived from the Lagrange multiplier technique. In the process, we identified the principle leading to a proper formulation of a Lagrange functional with boundary condition constrains for an incompletely parabolic system of equations with perturbed dynamical boundaries. This framework could easily be applied to receptivity problems and should stimulate the undertaking of non-modal analyses using ICF hydrocodes with “full physics”.

References

1. Atzeni, S., Meyer-ter-Vehn, J.: *The Physics of Inertial Fusion*. Oxford University Press, Oxford (2004)
2. Zel'dovich, Y.B., Raizer, Y.P.: *Physics of Shock Waves and High-temperature Hydrodynamic Phenomena*. Academic, New York (1967)
3. Lindl, J., et al.: Review of the National Ignition Campaign 2009–2012. *Phys. Plasmas* **21**, 020501 (2014)
4. Bychkov, V., Modestov, M., Law, C.K.: Combustion phenomena in modern physics: I. Inertial confinement fusion. *Prog. Energy Combust. Sci.* **47**, 32–59 (2015)
5. Aglitskiy, Y., et al.: Basic hyrdodynamics of Richtmyer-Meshkov-type growth and oscillations in the inertial confinement fusion-relevant conditions. *Philos. Trans. R. Soc. A* **368**, 1739–1768 (2010)
6. Raman, K.S., et al.: An in-flight radiography platform to measure hydrodynamic instability growth in inertial confinement fusion capsules at the National Ignition facility. *Phys. Plasmas* **21**, 072710 (2014)
7. Schmid, P.J.: Nonmodal stability theory. *Annu. Rev. Fluid Mech.* **39**, 129–162 (2007)
8. Marshak, R.: Effect of radiation on shock wave behavior. *Phys. Fluids* **1**(1), 24–29 (1958)
9. Boudesocque-Dubois, C., Gauthier, S., Clarisse, J.-M.: Self-similar solutions of unsteady ablation flows in inertial confinement fusion. *J. Fluid Mech.* **603**, 151–178 (2008)
10. Clarisse, J.-M., et al.: A hydrodynamic analysis of self-similar radiative ablation flows. *J. Fluid Mech.* **848**, 219–255 (2018)
11. Clarisse, J.-M., Boudesocque-Dubois, C., Gauthier, S.: Linear perturbation response of self-similar ablative flows relevant to inertial confinement fusion. *J. Fluid Mech.* **609**, 1–48 (2008)
12. Clarisse, J.-M., et al.: Transient effects in unstable ablation fronts and mixing layers in HEDP. *Phys. Scr.* **91**, 074005 (2016)
13. Abéguilé, F., Boudesocque-Dubois, C., Clarisse, J.-M., Gauthier, S., Saillard, Y.: Linear perturbation amplification in self-similar ablation flows of inertial confinement fusion. *Phys. Rev. Lett.* **97**, 035002 (2006)
14. Boudesocque-Dubois, C., Lombard, V., Gauthier, S., Clarisse, J.-M.: An adaptive multidomain Chebyshev method for nonlinear eigenvalue problems: application to self-similar solutions of gas dynamics equations with nonlinear heat conduction. *J. Comput. Phys.* **235**, 723–741 (2013)
15. Strikwerda, J.C.: Initial boundary value problems for incompletely parabolic systems. *Commun. Pure Appl. Math.* **XXX**, 797–822 (1977)

16. Gunzburger, M.D.: Introduction into mathematical aspect of flow control and optimization. In: von Karman Institute for Fluid Dynamics (ed.) Lecture Series 1997-05 on Inverse Design and Optimisation Methods, April 1997 (1997)
17. Chu, B.-T.: On the energy transfer to small disturbances in fluid flow (Part II). *Acta Mech.* **1**, 215–234 (1965)
18. Foures, D.P.G., Caulfield, C.P., Schmid, P.J.: Variational framework for flow optimization using seminorm constraints. *Phys. Rev. E* **86**(2), 026306 (2012)
19. Corbett, P., Bottaro, A.: Optimal perturbations for boundary layers subject to stream-wise pressure gradient. *Phys. Fluids* **12**(1), 120–130 (2000)
20. Goncharov, V.N., et al.: A model of laser imprinting. *Phys. Plasmas* **7**(5), 2062–2068 (2000)

Transition Due to Aerofoil-Wake Boundary Layer Interaction



Dhamotharan Veerasamy and Chris Atkin

Abstract The laminar-turbulent transition due to the interaction of an upstream aerofoil wake on a downstream flat plate boundary layer is studied experimentally. Measurements conducted on the flat plate boundary layer for four different aerofoil heights (h_w) above the flat plate demonstrate the evolution of both a non-modal disturbance profile and a longitudinal streaky structure in the pre-transition region. Sensitivity to aerofoil height suggests that this experimental arrangement would enable more systematic investigations of the receptivity mechanisms in multi-element configurations than possible using grid turbulence-induced transition.

1 Introduction

Wake-boundary layer (WBL) interactions are common in multi-element aerofoils and turbomachines. Several experimental and numerical investigations have been reported in the literature on the WBL interaction to look into the laminar-turbulent transition mechanisms. Nevertheless, most of the research carried out in the literature has employed a circular cylinder as the upstream wake generating body [3, 8, 10, 11], while most practical applications experience upstream disturbances originating from an aerofoil or blade wake. Furthermore, cylinder wake characteristics are quite different from those of an aerofoil wake, despite the global wake characteristics (mean velocity profile, [13]) are similar; a cylinder wake sheds large scale vortices, an aerofoil wake is fully turbulent, with no vortex shedding at higher Reynolds number. Particularly in multi-element high-lift systems and turbomachinery blades, chord Reynolds numbers are in the order of 10^6 [4, 12]. At such high Reynolds number it is anticipated that the vortex shedding will only occurs at small scales or that the wake will be fully turbulent, with no large scale unsteadiness. This difference in

D. Veerasamy (✉) · C. Atkin
City, University of London, London EC1V 0HB, UK
e-mail: dhamotharan.veerasamy.1@city.ac.uk

C. Atkin
e-mail: chris.atkin.1@city.ac.uk

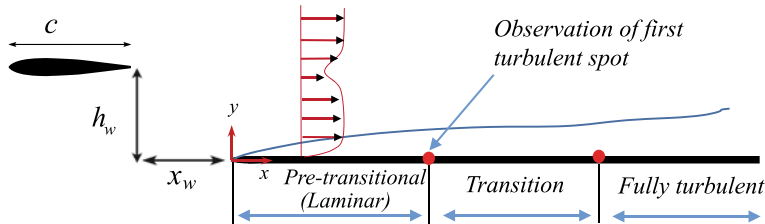


Fig. 1 Schematic representation of the experimental setup

wake characteristics will probably result in different transitional characteristics in the downstream boundary layer. Thus, to reveal the mechanisms in WBL interactions in multi-element aerofoils, the flow field characteristics should be reproduced as faithfully as possible. In this context, the present research addresses the interaction problem considering a simplified but realistic system involving an aerofoil and a flat plate. It is believed to be the first kind of study focusing on the transition mechanisms for such a configuration.

2 Experimental Setup

All the experiments reported in this paper were performed in the low-turbulence wind tunnel at City, University of London. This is a closed-circuit wind tunnel with test section dimensions $0.924 \times 0.915 \times 3.66$ m. The operating velocity inside the test section can vary from 0.5 to 25 m/s; for the present experiment, a free-stream velocity (U_0) of 20 m/s was considered. The flat plate used in the experiment was mounted vertically along the centre line of the test section. Ahead of and above the leading edge of the flat plate, a NACA 0014 aerofoil, with a chord length (c) of 253 mm, was placed at zero angle of attack, shown schematically in Fig. 1.

The vertical separation between the aerofoil and the flat plate is denoted as the ‘height’ (h_w) and the horizontal separation is denoted as the ‘overlap’ (x_w). The streamwise and wall-normal measurement stations are defined using a coordinate system shown in Fig. 1 with origin at the leading edge of the flat plate. The aerofoil spanned the entire test section and was tripped at around 25% chord using a sandpaper roughness strip (average roughness height = 425 μm) to avoid the vortex shedding. With the flat plate and aerofoil mounted in the tunnel, the free-stream turbulence intensity in the streamwise direction, at 20 m/s, was measured as 0.015% (in the frequency range 5 Hz to 5 kHz). This compares with 0.007% when the tunnel is empty. All velocity measurements were carried out using a Dantec DISA 55M01, Constant Temperature Anemometry (CTA) unit.

The aerofoil wake profile followed the plane wake distribution of [13] shown in Fig. 2a. The wake turbulence contained a broad bandwidth of disturbances, dominated by a mid-range frequencies (Fig. 2b), which then interact with the downstream

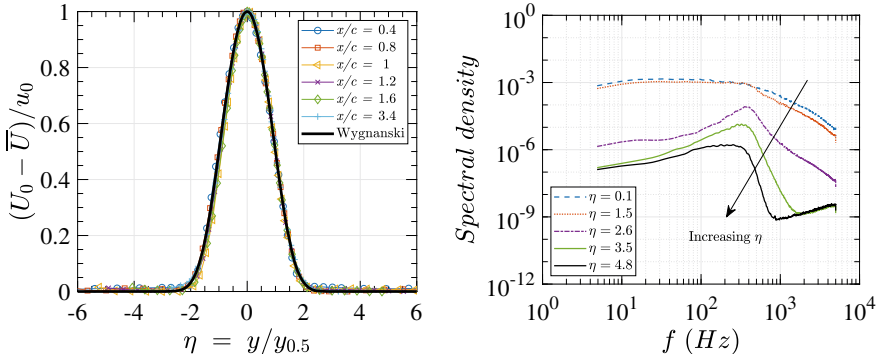


Fig. 2 **a** Mean velocity profile of the present wake follows the plane wake self-similar solution obtained by [13]. U_0 —free-stream velocity, \bar{U} —mean free-stream velocity, u_0 —maximum defect velocity, $y_{0.5}$ —wall-normal location of $0.5 u_0$. **b** Power spectral density of the aerofoil wake, at $x/c = 0.8$. For both **a** and **b** $Re_c = 3.4 \times 10^5$

boundary layer and accelerated the laminar-turbulent transition process. To ascertain the transitional characteristics, measurements were conducted on the pre-transitional region (between the leading edge and the appearance of the first turbulent spot) for three different aerofoil heights, $h_w = 40, 60$ and 80 mm, at a fixed Reynolds number of $Re_c = 3.4 \times 10^5$ and at $x_w = 0.25c$.

3 Disturbance Profile

The disturbance profiles obtained at the pre-transition region for the $h_w = 40, 60$ and 80 mm are shown in Fig. 3. It can be noticed that for $h_w = 40$ mm, disturbance profile in the pre-transitional region is self-similar and follows the transient growth theory (black solid line) developed by [1, 7]. However, if the aerofoil height increases, $h_w = 60$ and 80 mm, the disturbances in the upstream stations (at $x/l = 0.09$ for $h_w = 60$ mm and $0.09 \leq x/l \leq 0.22$ for $h_w = 80$ mm) initially display modal characteristics (where the location of maximum disturbance occurs close to the wall) before displaying non-modal characteristics further downstream. For a given geometric condition, this interesting transformation of the disturbance profile from modal to non-modal type has not been previously reported in the literature and this arrangement should prove useful for studying the receptivity mechanisms for such borderline test cases in detail.

In free-stream turbulence (FST) induced transition studies, whether the disturbance profile is modal (natural transition) or non-modal (bypass transition) is determined by the turbulence intensity level measured in front of the leading edge, since the disturbances propagate through the leading edge of the flat plate. In contrast, for the present study, the wake disturbance enters boundary layer further downstream. As

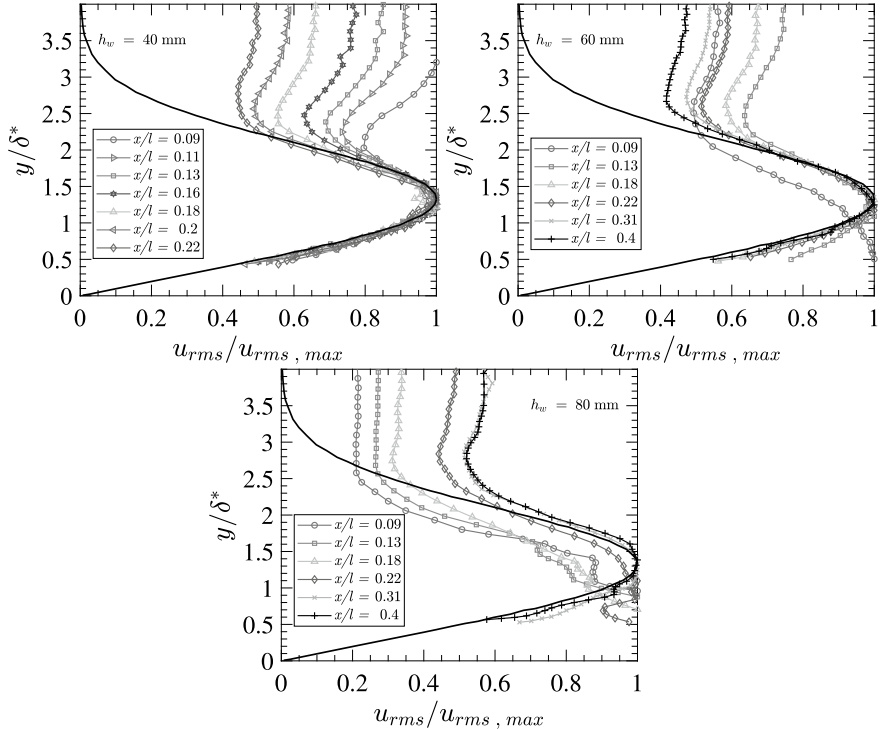
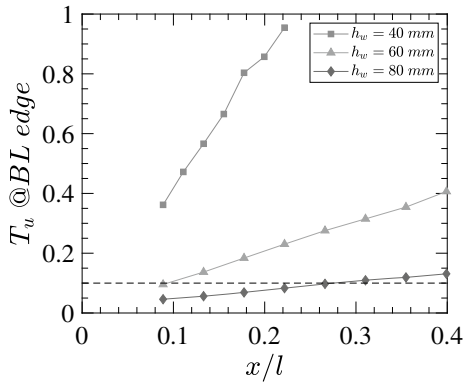


Fig. 3 Normalised u_{rms} profiles for the three aerofoil heights considered. Black line represents u_{rms} distributions from the transient growth theory, [7]

Fig. 4 T_u measured at the local edge of the boundary layer for the different aerofoil heights



a consequence, the turbulence intensity measured at the local edge of the boundary layer is here considered the important parameter. The streamwise turbulent intensity (T_u) of the forcing disturbance, obtained at the local edge of the boundary layer ($T_u @ BL \text{ edge}$) is plotted in Fig. 4.

By comparing the turbulent intensities in Fig. 4 with the corresponding disturbance profiles in Fig. 3, it is inferred that, for $T_u @ BL \text{ edge} > 0.1\%$, the disturbance profile displays non-modal characteristics, whereas if $T_u @ BL \text{ edge} < 0.1\%$ then the disturbance profile is of the modal type. It is interesting that this criterion for local T_u at the boundary layer edge matches that used for the case of FST induced transition [2, 6] where $T_u = 0.1\%$ is generally defined as the threshold separating natural and bypass transition.

4 Streaky Structure

Figure 5 shows the contour of the streamwise correlation function obtained for the case $h_w = 40 \text{ mm}$. For this particular measurement, one hot-wire probe was fixed at $x/l = 0.13$, $y/\delta^* = 1.3$ and $z = 0$. Another hot-wire probe was positioned at the same wall-normal location but the streamwise and the spanwise locations were varied within the domain of the $x - z$ plane shown in Fig. 5. It is well established that in the presence of streamwise streaks a strong negative correlation occurs at certain spanwise probe spacing [5, 9]. Figure 5 reveals, presence of negative correlation (dashed line) in both the spanwise and streamwise distance, supports the existence of a longitudinal streaky structure in the present experiment.

In Fig. 6, for $h_w = 40 \text{ mm}$, negative correlation exist throughout the transitional region. On the other hand, if the aerofoil height increases, weak or positive correlations can be seen at the upstream stations, for example in the case of $h_w = 60 \text{ mm}$, at $x/l = 0.09$, and $h_w = 80 \text{ mm}$, at $x/l = 0.09$ and 0.13 . These trends are consistent with the u_{rms} profiles shown in Fig. 3, where the disturbance profiles are of a non-modal type for strong negative correlation and of modal type for weak or positive correlation. These trends indicates that the origin of the streaky structure

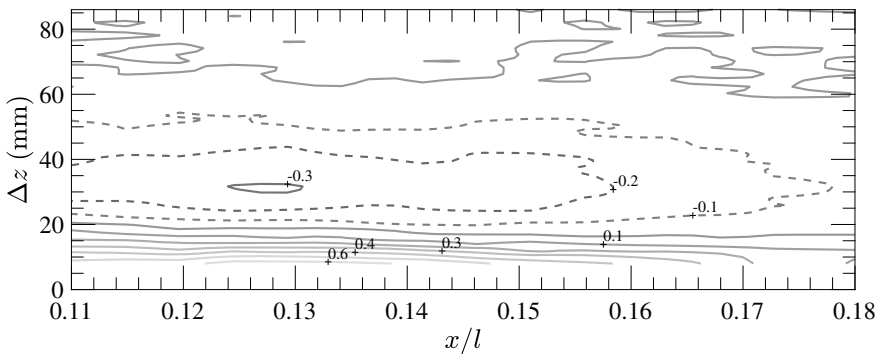


Fig. 5 Streamwise contour of the correlation function, and its values are marked within the figure. Dashed line represents negative correlation

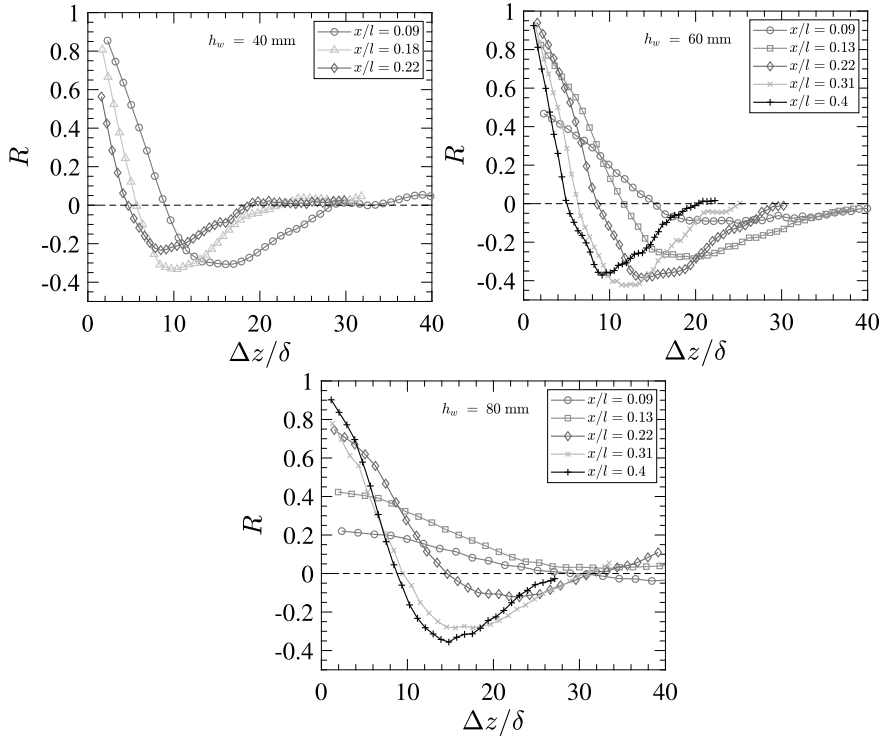


Fig. 6 Spanwise correlation function (R) measured at the wall-normal position close to $u_{rms,max}$ in the pre-transitional zone. The spanwise distance (Δz) is normalised with the boundary layer thickness (δ)

can be pinpointed and that it shifts downstream with an increase in aerofoil height and corresponding reduction in forcing intensity.

5 Conclusion

A novel experimental arrangement has been implemented whereby the level of turbulence intensity and the nature of disturbance interacting the downstream boundary layer can be altered by adjusting the height (h_w) between an upstream aerofoil and a downstream flat plate.

Varying h_w produced interesting laminar-turbulent transitional characteristics, such as the evolution from modal to non-modal disturbance profiles and the variable development of a longitudinal streaky structure in the pre-transitional zone. Such characteristics offer the prospect of exploring the receptivity mechanisms in

multiple-element flows in greater detail than possible with FST-induced transition arrangements.

In the case of cylinder wake-induced transition, it seems that the initial disturbance growth is dominated by secondary spanwise vortices and that the later stage is dominated by FST-induced bypass transition characteristics [8, 11]. In contrast, in the present study the initial disturbance region was dominated by the streaky structure and its origin varies with the position of the aerofoil. Thus we also conclude that aerofoil wake-induced transition differs significantly from cylinder wake-induced transition.

Acknowledgements The Authors would like to thank Prof. Michael Gaster for his advice and support. Gratitude is also extended to InnovateUK and ESPRC respectively for funding this project under the Enhanced Fidelity Transonic Wing project (InnovateUK grant ref. 113024, coordinated by Airbus) and the National Wind Tunnel Facility project (EPSRC grant ref. EP/L024888/1, led by Imperial College).

References

1. Andersson, P., Berggren, M., Henningson, D.S.: Optimal disturbances and bypass transition in boundary layers. *Phys. Fluids* **11**(1), 134–150 (1999)
2. Fasel, H.F.: Numerical investigation of the interaction of the Klebanoff-mode with a Tollmien-Schlichting wave. *J. Fluid Mech.* **450**, 1–33 (2002)
3. He, G., Wang, J., Pan, C.: Initial growth of a disturbance in a boundary layer influenced by a circular cylinder wake. *J. Fluid Mech.* **718**, 116–130 (2013)
4. Hourmouziadis, J.: Aerodynamic design of low pressure turbines. In: AGARD, Blading Design for Axial Turbomachines (SEE N 89-27661 22-07), 40p. (1989)
5. Kendall, J.: Experimental study of disturbances produced in a pre-transitional laminar boundary layer by weak freestream turbulence. In: 18th Fluid Dynamics and Plasma dynamics and Lasers Conference, p. 1695 (1985)
6. Kosorygin, V., Polyakov, N.P.: Laminar boundary layers in turbulent flows. In: Laminar-Turbulent Transition, pp. 573–578. Springer, Berlin (1990)
7. Luchini, P.: Reynolds-number-independent instability of the boundary layer over a flat surface. *J. Fluid Mech.* **327**, 101–115 (1996)
8. Mandal, A., Dey, J.: An experimental study of boundary layer transition induced by a cylinder wake. *J. Fluid Mech.* **684**, 60–84 (2011)
9. Matsubara, M., Alfredsson, P.H.: Disturbance growth in boundary layers subjected to free-stream turbulence. *J. Fluid Mech.* **430**, 149–168 (2001)
10. Ovchinnikov, V., Piomelli, U., Choudhari, M.M.: Numerical simulations of boundary-layer transition induced by a cylinder wake. *J. Fluid Mech.* **547**, 413–441 (2006)
11. Pan, C., Wang, J.J., Zhang, P.F., Feng, L.H.: Coherent structures in bypass transition induced by a cylinder wake. *J. Fluid Mech.* **603**, 367–389 (2008)
12. Spaid, F.: High reynolds number, multielement airfoil flowfield measurements. *J. Aircr.* **37**(3), 499–507 (2000)
13. Wygnanski, I., Champagne, F., Marasli, B.: On the large-scale structures in two-dimensional, small-deficit, turbulent wakes. *J. Fluid Mech.* **168**, 31–71 (1986)

High Speed and Hypersonics

Roughness-Induced Laminar-Turbulent Transition in the Boundary Layer of a Capsule-Like Geometry at Mach 20 Including Non-equilibrium



Antonio Di Giovanni and Christian Stemmer

Abstract Direct Numerical Simulations are performed to investigate the instability mechanisms in a capsule-like configuration with a rough wall under typical re-entry conditions. The growth of unstable crossflow-type modes induced by a patch of randomly distributed roughness is analyzed in both the linear and non-linear stages up to laminar-turbulent breakdown. At the considered conditions, molecular dissociation and non-equilibrium effects significantly change the temperature profiles of the capsule boundary layer and have a non-negligible effect on the stability properties of the roughness wake.

1 Introduction

At hypersonic speeds, the wall heat transfer in the case of a turbulent boundary layer is considerably larger than in the laminar case. Therefore, the prediction of the transition location is an important issue in the design of re-entry vehicles. For blunt re-entry capsules with a smooth surface, the accelerated boundary layer is modally stable. However, roughness is always present on the capsule wall due to thermal ablation and manufacturing uncertainties.

In numerous experimental and numerical investigations on roughness-induced transition on capsule-like spherical forebodies [1–6], the roughness Reynolds number,

$$Re_{kk} = \frac{\rho_k u_k k}{\mu_k}, \quad (1)$$

defined with the flow properties at the roughness height for the corresponding smooth configuration, is regarded as the parameter of greatest relevance. For a given configuration, the roughness can trigger different instability mechanisms, depending on

A. Di Giovanni · C. Stemmer (✉)

Chair of Aerodynamics and Fluid Mechanics, Technical University of Munich, Boltzmannstr. 15, 85748 Garching, Germany

e-mail: christian.stemmer@tum.de

the values of the roughness Reynolds number. As already observed for the case of flat-plate boundary layers, other parameters, such as the shape of the roughness, can greatly influence the stability properties of the roughness wake [7]. Previous investigations on hemispherical geometries with a rough wall under cold wind-tunnel conditions ($M = 5.9$) showed that skewed roughness geometries can generate crossflow-type vortices similar to the ones known for subsonic three-dimensional boundary layers [8]. These roughness-induced crossflow-type vortices can support the presence of highly unstable modes.

In the altitudes where laminar-turbulent transition occurs, chemical reactions and non-equilibrium significantly affect the state of the boundary layer and can destabilize the flow in the roughness wake. Stability investigations, including high-temperature gas effects, have been performed, among others, by Malik and Anderson [9] and Hudson et al. [10] for the case of a smooth flat plate. Chemical dissociation was found to have broadly similar effects as cooling at the wall, stabilizing the first-mode instability and destabilizing the second-mode instability. Stemmer et al. [11, 12] analyzed the three-dimensional reacting boundary layer of the HyBoLT geometry ($M = 8.5$) in the presence of a cuboid roughness element and showed that incorporation of finite-rate chemistry results in a larger disturbance amplification rate in the roughness wake compared to the case of a gas in chemical equilibrium. The influence of chemical dissociation and non-equilibrium on the base flow of a smooth capsule geometry under re-entry conditions ($M = 20$) was investigated by the authors in Di Giovanni and Stemmer [13], whereas stability analyses of linear disturbances for a capsule-like hemispherical geometry in the presence of a patch of randomly distributed roughness were presented in Di Giovanni and Stemmer [14]. It was shown that chemical and thermal non-equilibrium significantly change the temperature profiles of the capsule boundary layer and have a non-negligible influence on the stability properties of the roughness wake.

In this study, we numerically investigate the laminar-turbulent transition of the boundary layer on a capsule-like geometry with distributed roughness in a typical re-entry scenario ($M = 20$). By means of Direct Numerical Simulations (DNS), unsteady disturbances are forced in the roughness wake, revealing the presence of different instability modes in correspondence with roughness-induced crossflow-type vortices. Both the linear and non-linear growth of the unstable modes are considered, including laminar-turbulent breakdown. The various non-equilibrium effects on the (non-)linear growth of the unsteady disturbances are compared based on different simulations conducted with gas models of increasing complexity, i.e. equilibrium air, chemical non-equilibrium and thermochemical non-equilibrium.

2 Numerical Setup

The freestream conditions are chosen to match realistic re-entry conditions at $M = 20$ and are summarized in Table 1. At these conditions, high-temperature gas effects have a significant influence on temperature and velocity profiles of the base flow and on

Table 1 Freestream conditions for the present simulations

$M (-)$	$Re_\infty (\text{m}^{-1})$	$p_\infty (\text{Pa})$	$T_\infty (\text{K})$	$T_w (\text{K})$
20	$1.97 \cdot 10^6$	30	253	1800

the stability properties of the boundary layer. In order to highlight the effects of finite-rate chemistry and thermal non-equilibrium, simulations are performed with three different gas models: gas in chemical and thermal equilibrium (CEQ), gas in chemical non-equilibrium (CNEQ) and gas in thermochemical non-equilibrium (CTNEQ). Park's two-temperature model for air consisting of five species (O_2 , N_2 , NO , O , N) was employed. In the case of CEQ, the concentration of the different species is solved using algebraic equations for the dissociation of molecular species and for the conservation of the atomic species O and N. In the case of CNEQ, the Navier-Stokes equations are solved together with a continuity equation for each one of the five species. In the case of CTNEQ, an additional vibrational-energy equation is included for each molecular species. Further details on the governing equations and on the modeling of the physical and thermal coefficients as applied in this work are given in [14, 15].

The considered geometry is a capsule-like hemispherical forebody (Fig. 1 top-left). The domain ends in a shoulder resembling the one of a generic Apollo capsule. Hereafter, results are presented with reference to a curvilinear coordinate system with x the wall-parallel streamwise coordinate, y the wall-normal coordinate and z the spanwise coordinate. The origin of the coordinate system $(x, y, z) = (0, 0, 0)$ is located on the stagnation point of the hemisphere. To ease the computational cost, simulations are sequentially performed on two different geometries, zooming in on the roughness position. In particular, simulations on a full two-dimensional hemispherical domain with a smooth wall are used to generate the boundary conditions for a restricted, azimuthally periodic three-dimensional domain with a highly-resolved rough wall. The restricted domain has a spanwise angular extension of $[-2\pi/65, 2\pi/65]$ and is extracted for $x \in [3.682, 4.843]$. Here, the boundary layer is transonic to supersonic and the local values of the Reynolds number are large enough for the roughness wake to become modally unstable for roughness heights smaller than the boundary-layer thickness. The restricted domain is azimuthally periodic in spanwise direction, whereas Dirichlet conditions are applied at the inflow boundaries and Riemann invariants are used at the outflow at the shoulder. The wall is modeled as non-catalytic and with a constant temperature of $T_w = 1800$ K. The restricted domain does not comprehend the bow shock ahead of the capsule and is resolved with about 100 million grid points. Details on the grid resolution as well as the validation of the numerical approach can be found in [8, 14].

The focus of this work is on the instability mechanisms in the wake of a patch of randomly distributed roughness. The roughness patch, shown in Fig. 1 (bottom-right), is obtained by superposing different sinusoidal waves with pseudo-random amplitudes and phases. Details on the shape and on the parameters defining the

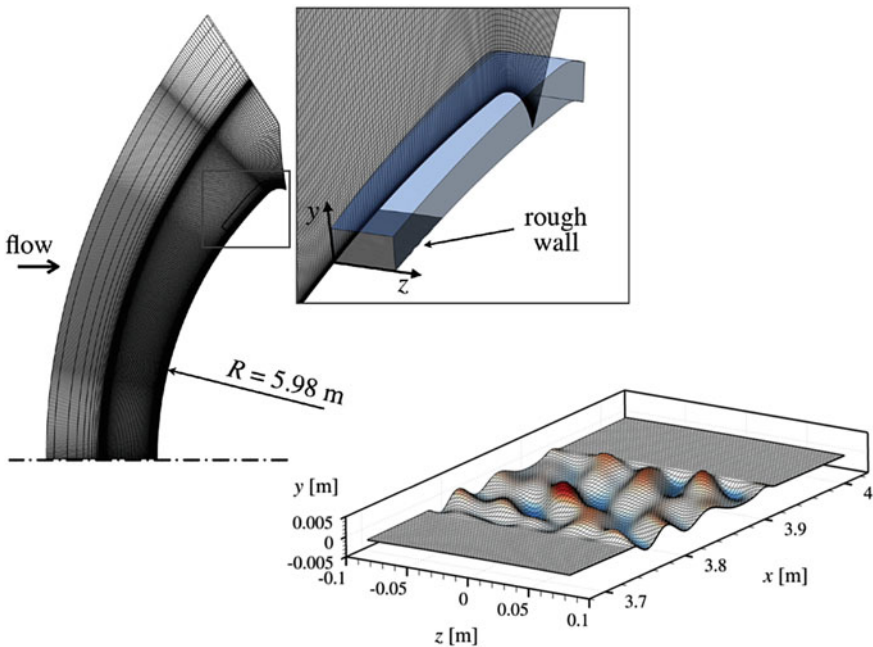


Fig. 1 Full and restricted computational domains (top-left) and grid points on the wall at the roughness location (bottom-right) from [15]

roughness geometry are given in [14]. The roughness height (i.e., the maximal surface height with respect to the smooth-wall configuration) is $k = 4.6 \text{ mm}$, corresponding to a roughness Reynolds numbers of 226 for CEQ, 244 for CNEQ and 221 for CTNEQ. The roughness is modelled to resemble a realistic sand-grain roughened wall where the distance between a roughness peak and the successive cavity is of the same order of magnitude of the roughness height (see also [2]). The height of the roughness has been chosen such that the roughness generates a wake where modal growth of small disturbances can be observed.

Stability investigations of the roughness wake are performed with DNS by introducing pressure disturbances at an inflow boundary located immediately downstream of the roughness wake ($x = 3.935 \text{ m}$). The evolution of the unsteady disturbances in the roughness wake is analyzed by means of temporal Fourier analysis. Based on preliminary stability investigations, six relevant frequencies are considered, corresponding to the first six harmonics of the base frequency 8.33 kHz ($f_n = n \cdot 8.33 \text{ kHz}$, with $n = 1, 2, \dots, 6$). The disturbance amplitude at the inflow is kept at a level of 0.1% with reference to the values of the boundary-layer edge variables, such that linear growth is observed in the near field downstream of the roughness, whereas strong non-linear interactions and laminar-turbulent breakdown occur further downstream, before the corresponding growth rate becomes negative in the damped region of the roughness wake.

Parallel Direct Numerical Simulations are performed with the Navier Stokes Multi Block (NSM) solver (Vos et al. [16]), a semi-commercial, finite-volume code already tested in the computations of hypersonic flows (see, e.g., [8, 12]). Simulations in the restricted domain are performed with a fourth-order central discretization scheme and a fourth-order Runge-Kutta method for time integration.

3 Results

Figure 2 shows the velocity distribution of the flow on a longitudinal section downstream of the roughness wake ($x = 3.935$ m). Several longitudinal vortices are present in the roughness wake as a result of the different protuberances and cavities in the roughness patch. In particular, in correspondence to roughness protuberances with a skewed profile with respect to the flow direction, the streamlines of the steady base flow are deviated such that a spanwise velocity component is locally induced downstream of the roughness. As a result, the roughness wake is characterized by the presence of crossflow-type vortices that are similar to crossflow vortices known from three-dimensional boundary layers (see, e.g., [17]). Contrary to the case of crossflow vortices in three-dimensional boundary layers, which are subject to the presence of a spanwise velocity in the base flow, the flow in the present smooth-wall configuration is two-dimensional. These roughness-induced crossflow-type vortices form because of the asymmetry of the roughness distribution and are not the result of an instability mechanism. The main roughness-induced crossflow-type vortex (Fig. 2 at $z \approx -0.03$ m) originates at the largest roughness protuberance and is very persistent in the accelerated boundary layer of this blunt-capsule configuration. Accordingly, this crossflow-type vortex turns out to be the most unstable region in the roughness wake.

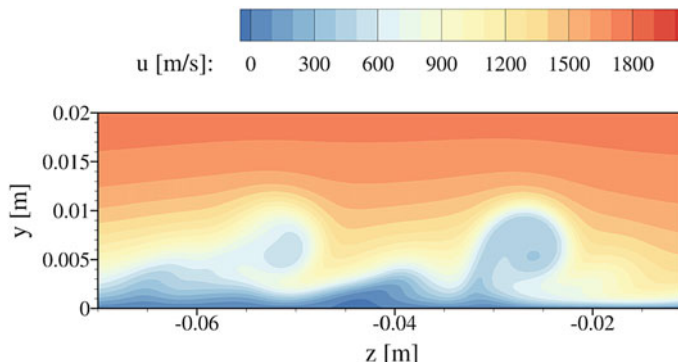
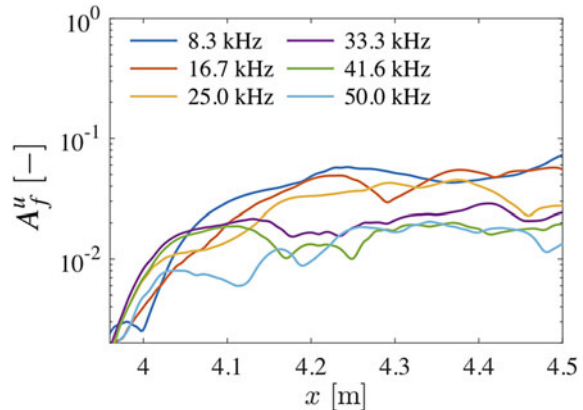


Fig. 2 Streamwise velocity for CEQ in a cross-section of the roughness wake at $x = 3.935$ m

Fig. 3 Amplitude of the temporal Fourier modes for chemical non-equilibrium air normalized with the boundary-layer edge velocity at the roughness location (case CNEQ)



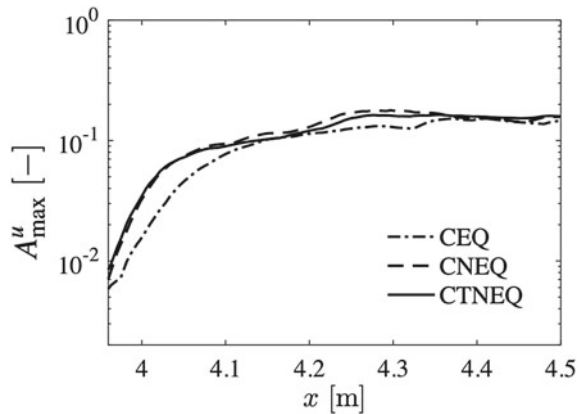
The development of unsteady disturbances forced in the roughness wake is investigated by means of temporal Fourier analysis. The general variable q is decomposed into a frequency spectrum $\hat{q}_f(x, y, z)$ and the amplitude of the Fourier mode is defined at each x as the maximum of the absolute value of \hat{q}_f found in the $y - z$ plane,

$$A_{\max}^q = \max_{y,z} |\hat{q}_f(x, y, z)|. \quad (2)$$

The amplitude of the temporal Fourier modes for the streamwise velocity are shown in Fig. 3 for the case of gas in chemical non-equilibrium, as in this case the largest disturbance amplification was observed. The mode amplitudes are normalized with the boundary-layer edge velocity at the roughness location ($U = 1800$ m/s). The Fourier amplitude curves for the other gas models are qualitatively similar and are not discussed in detail here (see [15] for more details). In the near field region close to the roughness location ($x < 4.05$ m), the mode amplitudes are smaller than 1% and the perturbed modes are linearly amplified downstream of the inflow boundary. The most amplified modes in the linear range have frequencies $f_4 = 33.3$ kHz and $f_5 = 41.7$ kHz. In particular, stability analyses of small disturbances in the linear range showed that the largest N -factor is reached at $f_4 = 33.3$ kHz for all gas cases. The gas in chemical non-equilibrium shows the largest linear amplification ($N = 5.3$), followed by the gas in thermochemical non-equilibrium ($N = 4.6$) and, finally, by the gas in equilibrium ($N = 4.3$). Once the modes enter the non-linear range of growth ($x > 4.05$ m), the modes amplitude tends to saturate and a strong non-linear interaction of the disturbed modes is observed, leading to strong oscillations in the Fourier amplitude curves. Furthermore, the modes at lower frequencies (i.e., f_1 and f_3) become dominant because of the thickening of the roughness wake as it diffuses downstream and their amplitudes reach and exceed the ones of f_4 and f_5 .

A direct comparison among the three gas models is presented in Fig. 4, which shows the amplitude of the total disturbance for the three gas models, obtained as a sum of the amplitudes of the temporal Fourier modes. Little difference is present

Fig. 4 Amplitude of the total disturbance for the three gas models normalized with the boundary-layer edge velocity at the roughness location



between CNEQ and CTNEQ, with the saturation of disturbance growth reached at about $x = 4.08$ m in both cases, corresponding to 145 mm downstream of the inflow boundary. Instead, the case of equilibrium air shows the smallest linear amplification. This was expected, as the case of CEQ presented the smallest value of the roughness Reynolds number. Accordingly, in this case the saturation of disturbance growth is observed further downstream (at about $x = 4.105$ m), with a delay of about 20% compared to the non-equilibrium cases.

Similarly to the case of crossflow vortices in three-dimensional boundary layers, two different instability modes are found for the roughness-induced crossflow-type vortex. Stability results are shown exemplarily for case CNEQ. At lower frequencies (i.e. between 8.3 and 16.7 kHz), the main instability mode is driven by the spanwise gradients of the velocity (z -mode), as confirmed by the overlapping of the regions of high spanwise shear stress and the disturbance mode in Fig. 5 (left). At higher frequencies (i.e. between 33.3 and 50.0 kHz), the main instability mode is driven

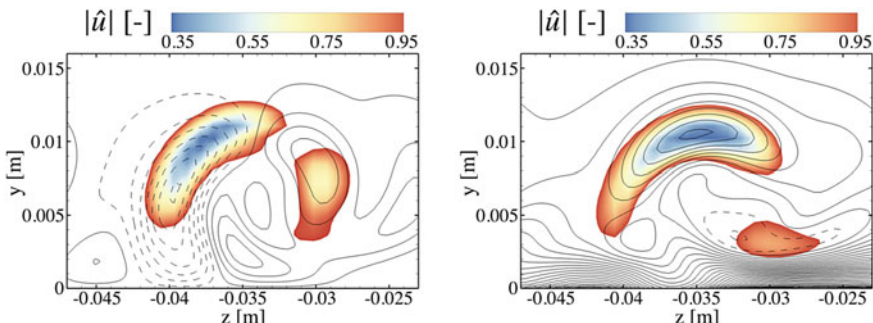


Fig. 5 Disturbance modes at 16.7 kHz with isolines of spanwise shear stress (left) and at 41.7 kHz with isolines of wall-normal shear stress (right). (case CNEQ)

by the wall-normal gradients of the velocity (y -mode) and the disturbance mode correlates with the regions of high wall-normal shear stress, as shown in Fig. 5 (right).

As the amplitudes of the instability modes grow further downstream ($x > 4.1$ m), the mutual interaction between modes at different frequencies becomes significant, eventually leading to the laminar-turbulent breakdown. The crossflow-type vortices break up and smaller structures appear which are not fully resolved as described in detail in [15]. The analyses revealed that the onset of instabilities in the non-linear range is associated with a significant increase of the heat flux at the wall in the unsteady flow compared to the steady laminar flow (not shown here). During transition, the wall heat flux increases by a factor of about 2 compared to the laminar case, with the strongest wall heat-flux augmentation observed in the case of CNEQ. The gas in thermochemical non-equilibrium, which is the most complex gas model considered in the current analysis, exhibits the lowest peak values of wall heat flux in the region of laminar-turbulent transition.

4 Conclusions

In the absence of modal instability mechanisms in the boundary layer of blunt capsule geometries with a smooth wall, the crossflow-type vortex induced by randomly distributed roughness provides a possible explanation for laminar-turbulent transition at hypersonic speeds. At these altitudes, chemical dissociation and non-equilibrium effects are non-negligible. Chemical non-equilibrium can significantly destabilize the roughness wake. These results highlight the importance of including non-equilibrium effects in the stability analysis of high-enthalpy boundary layers on rough walls as well as the detailed consideration of the roughness shape.

Acknowledgements The authors gratefully acknowledge the financial support of the German Research Foundation (DFG) under contract STE 1454/8-2 and the provision of the computing resources by the Leibniz Supercomputing Centre (LRZ) on SuperMUC.

References

1. Hollis, B.R.: Distributed roughness effects on blunt-body transition and turbulent heating. In: AIAA Paper 2014-0238 (2014)
2. Hollis, B.R.: Experimental investigation of roughness effects on transition onset and turbulent heating augmentation on a hemisphere at Mach 6 and Mach 10. NASA Technical Report, NASA/TM-2017-219613 (2017)
3. Reda, D.C.: Review and synthesis of roughness-dominated transition correlations for reentry applications. *J. Spacecr. Rocket.* **39**(2), 161–167 (2002)
4. Reda, D.C., Wilder, M.C., Bogdanoff, D.W., Prabhu, D.K.: Transition experiments on blunt bodies with distributed roughness in hypersonic free flight. *J. Spacecr. Rocket.* **45**(2), 210–215 (2008)

5. Chang, C.-L., Choudhari, M., Venkatachari, B.S., Li, F.: Effects of cavities and protuberances on transition over hypersonic vehicles. In: AIAA Paper 2011-3245 (2011)
6. Theiss, A., Hein, S., Ali, S.R.C., Radespiel, R.: Wake flow instability studies behind discrete roughness elements on a generic re-entry capsule. In: AIAA Paper 2016-4382 (2016)
7. Van den Eynde, J.P.J.P., Sandham, N.D.: Numerical simulations of transition due to isolated roughness elements at Mach 6. *AIAA J.* **54**(1), 53–65 (2016)
8. Di Giovanni, A., Stemmer, C.: Crossflow-type breakdown induced by distributed roughness in the boundary layer of a hypersonic capsule configuration. *J. Fluid Mech.* **856**, 470–503 (2018)
9. Malik, M.R., Anderson, E.C.: Real gas effects on hypersonic boundary layer stability. *Phys. Fluids* **3**, 803 (1991)
10. Hudson, M.L., Chokani, N., Candler, G.: Linear stability of hypersonic flow in thermochemical nonequilibrium. In: AIAA Paper 1996-0671 (1996)
11. Stemmer, C., Birrer, M., Adams, N.A.: Hypersonic boundary-layer flow with an obstacle in thermochemical equilibrium and nonequilibrium. *J. Spacecr. Rocket.* **54**(4), 899–915 (2017)
12. Stemmer, C., Birrer, M., Adams, N.A.: Disturbance development in an obstacle wake in a reacting hypersonic boundary layer. *J. Spacecr. Rocket.* **54**(4), 945–960 (2017)
13. Di Giovanni, A., Stemmer, C.: Numerical simulations of the high-enthalpy boundary layer on a generic capsule geometry with roughness. In: New Results in Numerical and Experimental Fluid Mechanics XI, STAB/DGLR Symposium, pp. 189–198. Springer, Berlin (2017)
14. Di Giovanni, A., Stemmer, C.: Roughness-induced crossflow-type instabilities in a hypersonic capsule boundary layer including nonequilibrium. *J. Spacecr. Rocket.* (2019). <https://doi.org/10.2514/1.A34404>. Published online on 27 Mar 2019
15. Di Giovanni, A., Stemmer, C.: Roughness-induced boundary-layer transition on a hypersonic capsule-like forebody including nonequilibrium. *J. Spacecr. Rocket.* (2019). <https://doi.org/10.2514/1.A34488>. Published online 26 Aug 2019
16. Vos, J., Duquesne, N., Lee, H.: Shock wave boundary layer interaction studies using the NSMB flow solver. In: Proceedings of the 3rd European Symposium on Aerothermodynamics for Space and Vehicles, ESA SP-426, ESTEC, pp. 229–236. European Space Agency (1999)
17. Malik, M.R., Li, F., Choudhari, M.M., Chang, C.-L.: Secondary instability of crossflow vortices and swept-wing boundary-layer transition. *J. Fluid Mech.* **399**, 85–115 (1999)

The Role of Receptivity in Prediction of High-Speed Laminar-Turbulent Transition



I. V. Egorov, A. V. Fedorov, A. V. Novikov, and P. V. Chuvakhov

Abstract Receptivity plays a crucial role in the physics-base methodology for prediction of the transition onset location in the boundary-layer flows. A major stumbling block for developing of this methodology is sensitivity of transition to the initial and boundary conditions. In the case of relatively small free-stream and body-induced disturbances, the transition onset can be predicted by the amplitude method, where receptivity and instability growth stages are simulated using the linear theory. In this framework, receptivity affects the instability amplitude at the transition onset via the three major factors: the location of receptivity region, the coherence of external forcing and the spectral content of external disturbances. The role of these factors in the transition prediction methodology is estimated for the boundary-layer flows past a supersonic compression corner and a flat plate in supersonic and hypersonic free streams. In particular, it is shown that large uncertainty in atmospheric turbulence gives marginal error in the transition onset location. This finding encourages further developments of the physics-based amplitude method for transition prediction.

1 Introduction

Laminar-turbulent transition (LTT) evolves in different ways depending on the mean flow and external disturbances [1–3]. Even for relatively simple two-dimensional or axisymmetric boundary layers on a flat plate or a sharp cone at zero angle of attack, there are several paths to turbulence associated with different physical mechanisms [2]. This study focuses on the path relevant to small external forcing. It consists of the three major stages: receptivity to external disturbances, exponential growth of unstable normal modes in accord with the linear stability theory (LST), and nonlinear breakdown. This path is typical for configurations, which are designed to get maximal

I. V. Egorov · A. V. Fedorov · A. V. Novikov (✉) · P. V. Chuvakhov
Central Aerohydrodynamic Institute, 1 Zhukovsky Street, Zhukovsky, Russia
e-mail: AndrewNovikov@yandex.ru

Moscow Institute of Physics and Technology (National Research University), 9 Institutsky per., Dolgoprudny, Russia

laminar runs in the low disturbance environment. A good example is the X-43A vehicle flying at Mach numbers from 7 to 10 and altitude about 30 km [4].

A physics-based transition prediction methodology assumes adequate modeling of the mentioned above stages of transition. This can be done using direct numerical simulations (DNS) [5], which provide holistic modeling of the transition process. However, DNS are time consuming and need enormous computational resources, which are not affordable for engineering applications. This approach is currently used for fundamental studies of transition mechanisms on simple configurations.

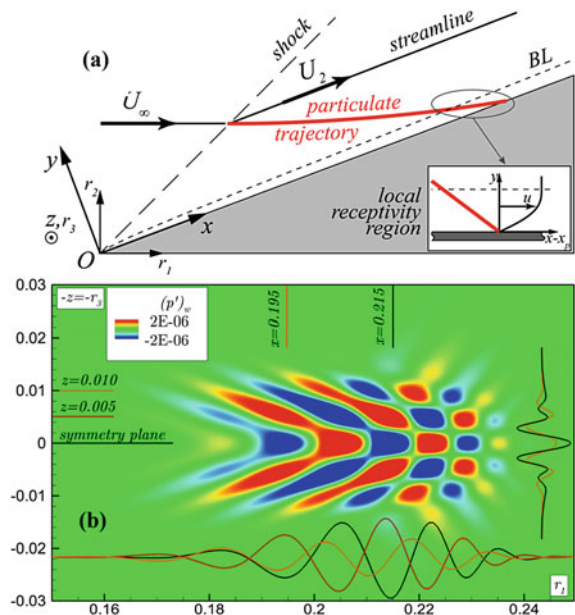
More practical is the amplitude method suggested by Mack [6], where receptivity and amplification stages are simulated using the linear theory. The transition onset is predicted using an amplitude criterion, where the critical amplitude of instability is determined using empirical data and/or theoretical models of nonlinear interactions. The amplitude method can be implemented on economical basis with keeping the numerical requirements nearly the same as for the e^N method. Implementations of the amplitude method to predictions of the transition onset in high-speed flows are discussed in [7, 8].

A major stumbling block for developing of the foregoing approaches is sensitivity of LTT to the initial and boundary conditions for disturbances. Mack [6] noted: “A good deal must be known about the disturbance source, but this is only a reflection of the physical situation that transition is dependent on the type, intensity and spectrum of the disturbance source, and not just on the boundary layer.” Stetson [9] pointed out: “...even if we could perform a miracle and obtain an analytical method to calculate exactly the stability characteristics of the boundary layer and the breakdown to turbulence, we would still have to somehow prescribe the external disturbances.” For these reasons, it is believed that transition is not predictable with sufficiently high accuracy because of uncertainties in the disturbance environment. In this paper, we try to explore to what extent this negative viewpoint is justified for natural transition in high-altitude supersonic flights. Namely, we evaluate the role of receptivity in prediction of the transition onset by estimating effects associated with the location of receptive region, the coherence of external forcing and the spectrum of environmental disturbances.

2 Wave Packets Excited by Coherent and Incoherent Disturbances

The external forcing may be deterministic (expressed as a group of coherent waves) or random (expressed as a group of incoherent waves). As an example, coherent wave packets are induced by solid particulates present in atmosphere. Following Ref. [10] consider a sharp wedge flying at the altitude $H^* = 20$ km, zero angle of attack and Mach number $M_\infty = 4$. The particle has spherical shape of radius $r_p^* = 10$ mcm, and density $\rho_p^* = 1$ g/cm about water density. Hereafter the upper asterisk denotes dimensional quantities. The particle penetrates into the shock layer, crosses a thin

Fig. 1 Schematics of the particle impact (a), and the wall pressure disturbance $p'_w(x, z) = p'_\infty / (\rho_\infty^* U_\infty^{*2})$ (b) at $t = t^* U_\infty^*/L^* = 0.24$, excited by the particle, which collides with the wall at $t = 0.009$ and $x_0 = x_0^*/L^* = 0.067$, the Reynolds number $Re_\infty = U_\infty^* L^* / \nu_\infty^* = 7.381 \times 10^6$



laminar boundary layer and hits the wall at a point (x_0, z_0) as schematically shown in Fig. 1a. The numerical simulation [10] of this process shows that far downstream of the collision point the particle-induced wave packet consists mainly of coherent oblique waves related to the first mode. Its instantaneous wall-pressure footprint is shown in Fig. 1b.

Assuming that the nonparallel effect is weak, this disturbance at an observation point (x, z) is expressed as.

$$p'_w(x, z) = \int_{-\infty}^{+\infty} d\omega \int_{-\infty}^{+\infty} a(x_0, z_0, \omega, \beta) \exp(S + i\beta(z - z_0) - i\omega t) d\beta \quad (1)$$

$$S(\omega, \beta, x) = i \int_{x_0}^x \alpha(\omega, \beta, x) dx \quad (2)$$

where $\alpha(\omega, \beta, x)$ is complex eigenvalue of the first mode; a is the corresponding initial spectral density, which is a product of the external-forcing spectral density and the receptivity coefficient, $a = a_{ext} c_{rec}$, if the receptivity mechanism is linear. Assuming that the eikonal is large, $|S| \gg 1$, we can evaluate the double integral (1) using the steepest descent method and express a hump amplitude for the wall-pressure wave packet as.

$$p'_w(x) \approx |a(\omega_s, \beta_s, x_0, z_0)| D_S(x, \omega_s, \beta_s) e^{N(\omega_s, \beta_s, x_0, x)} \quad (3)$$

$$D_S(x, \omega_s, \beta_s) = 2\pi \left| \left[\frac{\partial^2 S}{\partial \omega^2} \frac{\partial^2 S}{\partial \beta^2} - \left(\frac{\partial^2 S}{\partial \omega \partial \beta} \right)^2 \right]^{-1/2} \right| \quad (4)$$

$$D_S(x, \omega_s, \beta_s) = 2\pi \left| \left[\frac{\partial^2 S}{\partial \omega^2} \frac{\partial^2 S}{\partial \beta^2} - \left(\frac{\partial^2 S}{\partial \omega \partial \beta} \right)^2 \right]^{-1/2} \right| \quad (5)$$

where ω_s and β_s correspond to the dominant wave, the dispersion factor D_S is proportional to the wave-packet spectral width $\Delta\omega\Delta\beta$, the N factor characterizes an exponential growth of the wave-packet hump amplitude.

In natural transition, the external forcing is, as a rule, random. It consists of incoherent waves having random initial phases. Good examples are second-mode dominated transition triggered by thermal fluctuations [11–13], or cross-flow dominated transition triggered by random micro-roughness [14]. In these and similar cases we should perform statistical analysis and consider RMS quantities of the excited disturbances. The far field asymptotic is different from the case of coherent forcing. The RMS wall-pressure disturbance is expressed as.

$$p'_{w,RMS} \equiv \langle p_w^2(x) \rangle^{1/2} \approx |\Phi(x_0, \omega_s, \beta_s)|^{1/2} D_N(x, \omega_s, \beta_s) e^{N_S(x_0, x)} \quad (6)$$

$$D_N(x, \omega_s, \beta_s) = 2\pi \left| \left[\frac{\partial^2 N}{\partial \omega^2} \frac{\partial^2 N}{\partial \beta^2} - \left(\frac{\partial^2 N}{\partial \omega \partial \beta} \right)^2 \right]^{-\frac{1}{4}} \right|_{\omega_s, \beta_s} \quad (7)$$

$$N_S(x_0, x) = N(\omega_s, \beta_s, x_0, x) \quad (8)$$

where $\Phi(\omega_s, \beta_s)$ is the initial power spectral density (PSD), which is a product of the external-forcing PSD and the receptivity coefficient: $\Phi = \Phi_{ext} c_{rec}$, if the receptivity mechanism is linear; D_N characterizes the selective amplification of the wave components, which is proportional to the square root of the PSD width, $\Delta\omega\Delta\beta$.

In accord with the amplitude method, the transition onset point x_{tr} is determined by the amplitude criterion $p'_{w,RMS}(x_{tr}) = p'^{(tr)}_w(x_{tr})$ in the case of deterministic (or coherent) external forcing, or by the RMS criterion $p'_{w,RMS}(x_{tr}) = p'^{(tr)}_{w,RMS}$ in the case of random (or incoherent) forcing.

Equations (3)–(5) and (6)–(8) indicate that the transition onset depends on:

1. The location of receptivity region, which is characterized by the point (x_0, z_0) in the case of coherent forcing or the station x_0 in the case of incoherent forcing.
2. The initial spectral density $|a(\omega_s, \beta_s, x_0, z_0)|$ in the case of coherent forcing and the initial power spectral density $\Phi(x_0, \omega_s, \beta_s)$ in the case of incoherent forcing.

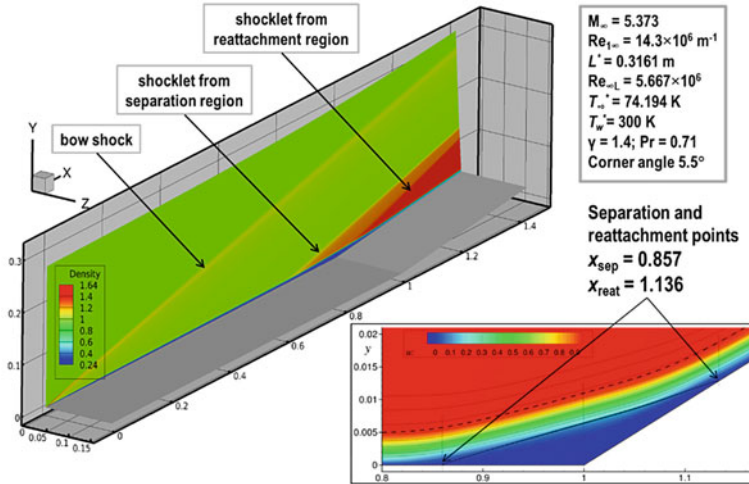


Fig. 2 The undisturbed laminar flow on the compression corner configuration

3. The dispersion factor $D_S(x, \omega_s, \beta_s)$ in the case of coherent forcing and the selective amplification factor $D_N(x, \omega_s, \beta_s)$ in the case of incoherent forcing.
4. The amplification factor $N(x, \omega_s, \beta_s)$ in the both cases.

According to Eq. (5) the location of receptivity region directly affects the N-factor. Therefore the transition onset point, x_{tr} , where the disturbance amplitude reaches a critical level, strongly depends on x_0 . Hereafter this statement is illustrated by few examples.

Consider 3D disturbances propagating in the near-wall flow over a 5.5° compression corner at the Mach number $M_\infty = 5.373$. The free-stream parameters shown in Fig. 2 are the same as in the 2D numerical study [15]. A wave packet is excited by a suction-blowing actuator, which is located upstream from the corner and consists of the two holes of rectangular cross-section.

First, we compute a steady (undisturbed) laminar flow field, which serves as a base flow for further computations of unsteady disturbances. This flow has a shallow separation bubble formed near the corner line. The suction-blowing actuator is modelled with boundary condition on mass flow

$$q_w(x, z, t) \equiv (\rho v)_w = \varepsilon \sin\left(\pi \frac{x - x_0 + d}{d}\right) \sin\left(\pi \frac{z - d/2}{d}\right) \sin(\omega_0 t),$$

$$x_0 - d < x < x_0 + d; -d/2 < z < d/2; 0 < t < t_1.$$

Here $d = 0.00815$ is the hole size, $\omega_0 = 225$ is the carrier frequency; $t_1 = \pi/\omega_0$ is operating time of the actuator, the forcing amplitude $\varepsilon = 10^3$ is small to avoid nonlinear effects. The spatial and temporal spectra of q_w are shown in Fig. 3. Both low and high frequencies associated with first and second modes are present. The

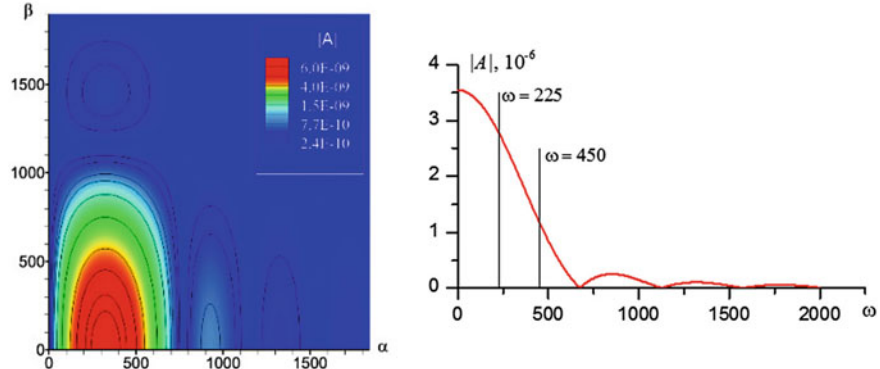


Fig. 3 The spatial (left) and temporal (right) spectra of $q_w(x, z, t)$

two locations of the actuator are considered: the central point $x_0 = 0.044$ that is close to the plate leading edge, and 0.6 that is far downstream from the leading edge.

Preliminary computations using the local-parallel LST showed that in the boundary layer upstream of the separation point there are unstable waves of both first and second mode. Their exponential growth strongly depends on the initial point x_0 . In the case of $x_0 = 0.044$, the first mode is dominant in the pre-separation region $x < x_{sep}$. It consists of oblique waves having relatively low frequency $\omega \approx 100$. In the case of $x_0 = 0.6$, the second mode is dominant. It consists of predominantly plane waves having relatively high frequency $\omega \approx 450$. Thus, it is natural to assume that in these two cases the wave packets propagating in the boundary layer should be very different.

Consider the wall-pressure disturbance excited by the actuator of $x_0 = 0.044$. Figure 4 shows that the wave-packet consists of mostly oblique waves. Their interference leads to a staggered 3D pattern having a V-shaped tail. Plane waves associated with the second mode of small amplitude are noticeable near the center line $z = 0$. Circular fronts propagating ahead of the wave-packet are relevant to fast acoustic waves.

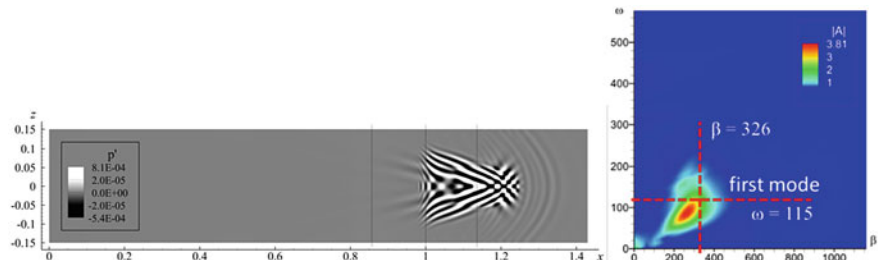


Fig. 4 An instantaneous pattern of the wall pressure disturbance at $t = 1.4$ in the case of $x_0 = 0.044$ and the β - ω spectrum at $x = 1.3$

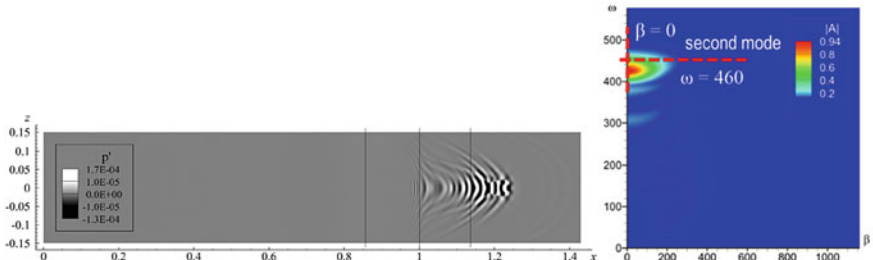


Fig. 5 An instantaneous pattern of the wall-pressure disturbance at $t = 0.7$ in the case of $x_0 = 0.6$ and the $\beta\text{-}\omega$ spectrum at $x = 1.3$

It should be noted that the animation of DNS solution clearly shows that even within the separation region all waves propagate downstream.

Now consider a wave-packet excited far downstream of the leading edge, $x_0 = 0.6$. Its behavior is quite different (Fig. 5): the dominant waves are plane, while oblique waves have relatively small amplitude. The pressure footprint is typical for the second-mode dominated wave packets (for example, see DNS [16]).

In the both cases, the (β, ω) spectrum at the observation point $x = 1.3$ is consistent with the LST prediction—frequency and wavenumber of the dominant wave predicted by LST is close to the spectral peak predicted by DNS.

3 Effect of the External Forcing Coherence

Consider the two cases: a flat plate with adiabatic wall in a supersonic stream of Mach number $M_\infty = 3.5$ and temperature $T_\infty^* = 300$ K; a flat plate with surface temperature $T_w^* = 1200$ K in a hypersonic stream of Mach number $M_\infty = 7.9$ and temperature $T_\infty^* = 327$ K. The local-parallel LST computations were performed starting from the neutral points $x_0 = x_{neut}(\omega, \beta)$. In Fig. 6 the blue line shows the dependency of the N-factor envelope N_S on the Reynolds number $R = \sqrt{U_e^* x^* / \nu_e^*}$; the black line shows the distribution of the selective amplification factor $D_N(R)$ (see Eq. (7)); the red line shows the distribution of the dispersion factor $D_S(R)$ (see Eq. (4)); the green line shows the error $\Delta N_S = \ln(D_N/D_S)$ associated with uncertainty of coherence. Since the selective amplification factor D_N is much larger than the dispersion factor D_S , the random (incoherent) forcing is much more effective than the deterministic (or coherent) forcing, and the corresponding value of ΔN_S is quite large: $\Delta N_S \approx 5$ in the case of $M_\infty = 3.5$ (Fig. 6a), and $\Delta N_S \approx 4$ in the case of $M_\infty = 7.9$ (Fig. 6b).

Similar results were obtained by Fedorov [14] for the cross-flow dominated transition on a supersonic swept wing having a thin parabolic arc-shape airfoil. It was shown that randomly distributed roughness, which produces the incoherent forcing, leads to about two order of magnitude reduction of the critical roughness height

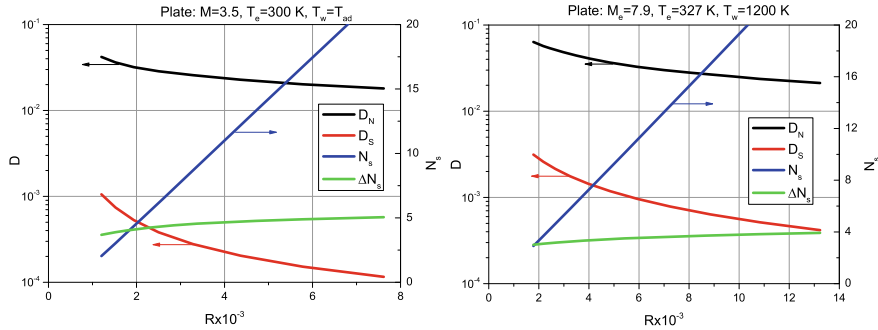


Fig. 6 The effect of coherence on N-factors in the cases: $M_e = 3.5$, $T_e = 300 \text{ K}$, $T_w = T_{\text{ad}}$ (left), and $M_e = 7.9$, $T_e = 300 \text{ K}$, $T_w = 1200 \text{ K}$ (right)

compared with to the case of rarely distributed local roughness elements producing the coherent forcing. Here the critical roughness height provides the transition onset at a certain observation point $x = x_{tr}$. This difference translates to $\Delta N_s \approx 4.6$ that is consistent with distributions shown in Fig. 6.

4 Uncertainty in the External Disturbance Environment

The next factor is associated with uncertainty in the external disturbance environment. Possible sources of external disturbances were identified by Bushnell [17] for supersonic and hypersonic flights. Besides the body-induced disturbances there are indispensable free-stream disturbances, which include atmospheric turbulence, particulates, and thermal noise associated with the Browning motion. The role of particulates and thermal noise has been discussed in [10–13, 18, 19]. Herein we try to estimate to what extent the uncertainty in atmospheric turbulence affects the transition prediction.

Frequencies f^* of the first-mode or second-mode waves are estimated using the e^N method assuming that $N = 10$ at the transition onset for various configurations. If receptivity is linear, the unstable waves are excited by atmospheric disturbances of the same frequency. In Fig. 7, the instability wave length, $\lambda^* = U_\infty^*/f^*$, is compared with the length scales of atmospheric turbulence reported in [20]. In the all cases considered, the instability length-scale lies in the inertial interval or in the viscous dissipation interval. The spectrum of such small-scale fluctuations in atmospheric turbulence can be predicted using the theory of locally homogeneous and isotropic turbulence. It is determined by the two parameters only: kinematic viscosity ν_∞^* , which can be taken from the standard atmosphere, and the dissipation rate of turbulent energy ε^* , which is documented for various weather conditions. There are different analytical approximations of this spectrum. All of them gives the $-5/3$ power law of Kholmogorov and Obukhov in the inertial interval and the exponential drop in the

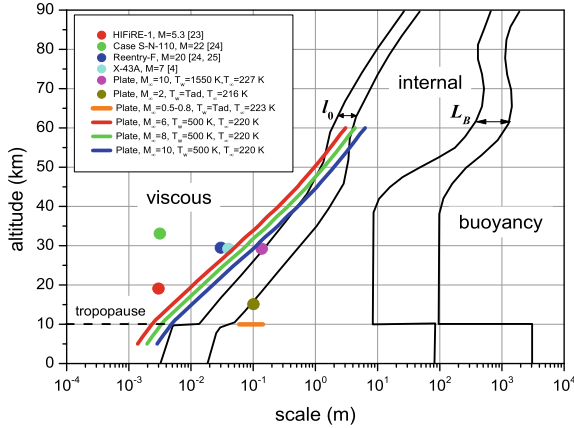


Fig. 7 Comparison of the instability wave length $\lambda^* = U_\infty^*/f^*$ with atmospheric turbulence scales: $l_0^* \approx 7.4\eta^*$ – scale determining the transition region between the dissipative and inertial ranges; L_B^* – scale determining the transition region between the inertial and buoyancy ranges; here $\eta^* = (v_\infty^{*3}/\varepsilon^*)^{1/4}$ – Kolmogorov length-scale, ε^* – dissipation rate of turbulent energy

viscous dissipation interval. For further estimates, we use the approximation of Pao [21] for the streamwise velocity fluctuation

$$\begin{aligned} u'^*_{RMS} &\approx \sqrt{\phi^*(k_1^*) \Delta k_1^*}, \quad \phi^*(k_1^*) = \int_{k_1^*}^{\infty} \left(1 - \frac{k_1^{*2}}{k^*{^2}}\right) \frac{E^*(k^*)}{k^*} dk^*, \\ E^*(k^*) &= (\varepsilon^* v_\infty^{*5})^{\frac{1}{4}} \cdot \alpha (k^* \eta^*)^{-\frac{5}{3}} \exp\left(-\frac{3}{2}\alpha (k^* \eta^*)^{\frac{4}{3}}\right), \\ \eta^* &= (v_\infty^{*3}/\varepsilon^*)^{1/4}, \quad \alpha = 1.7, \end{aligned} \quad (9)$$

where $E^*(k^*)$ is 3D spectrum of turbulent energy and k^* is modulus of the wave-number vector (k_1^*, k_2^*, k_3^*).

To proceed further we need distributions of the dissipation rate versus altitude $\varepsilon^*(H^*)$. However, this distribution is quite uncertain (Fig. 8). The hot-wire measurements [22] showed that values of ε^* scatter from $\varepsilon_{min}^* = 0.1\varepsilon_{av}^*$ to $\varepsilon_{max}^* = 10\varepsilon_{av}^*$ (see the blue box in Fig. 8). To understand if this uncertainty acceptable for transition prediction, we performed estimates using the following procedure: by the e^N method with $N = 10$, estimate frequency f^* of the dominant instability; estimate wavenumber $k_1^* = f^*/U_\infty^*$ for atmospheric fluctuations; evaluate $\varepsilon_{av}^*(H^*)$, and the spectral density $\phi^*(k_1^*)$ in the range of $\varepsilon_{min}^* < \varepsilon^* < \varepsilon_{max}^*$; evaluate the RMS of velocity fluctuations u'^*_{RMS} ; evaluate uncertainty as $\Delta N_+ = \ln(u'^*_{RMS}(\varepsilon_{max}^*)/u'^*_{RMS}(\varepsilon_{av}^*))$ and $\Delta N_- = \ln(u'^*_{RMS}(\varepsilon_{min}^*)/u'^*_{RMS}(\varepsilon_{av}^*))$.

For the cases of $\lambda^* \geq l_0^*$ (see the corresponding points in Fig. 7), results of these estimates are shown in Table 1. It is seen that large uncertainty in ε^* gives a marginal

Fig. 8 Distribution of the turbulence energy ε^* versus altitude and its scatter relative to the average value ε_{av}^*

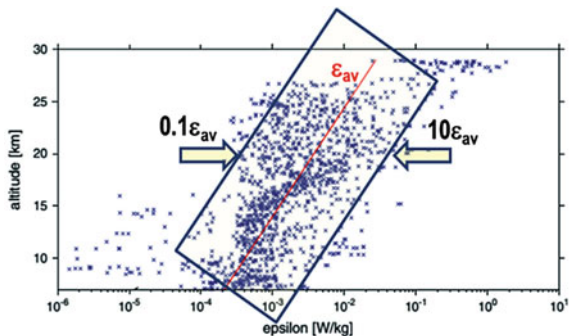


Table 1 Estimates for the uncertainties of N-factor and transition onset

Case	H*, km	ε_{av}^* , m ² /s ³	ΔN_+	ΔN_-	$(\Delta x_+/x)_{tr}$	$(\Delta x_-/x)_{tr}$
Plate, M = 0.5	10	8.E-2	0.86	-0.86	0.14	-0.12
Plate, M = 2	15	5.E-2	0.87	-0.95	0.17	-0.17
Plate, M = 10	30	2.E-2	0.87	-1.00	0.16	-0.17

error in the transition onset. Thus, it is reasonable to apply the amplitude method to these and similar cases.

5 Conclusions

In the case of relatively small free-stream and body-induced disturbances, the transition onset can be predicted by the amplitude method, where receptivity and instability growth stages are simulated using the linear theory. In this framework, receptivity affects the instability amplitude at the transition onset via the three major factors: the location of the receptivity region, the coherence of external forcing and the spectral content of external disturbance field.

On the example of the flow past a hypersonic (Mach 5.373) compression corner, it is shown that the location of receptivity region, x_0 , strongly affects the instability growth stage. Namely, excited wave-packets can be first-mode or second-mode dominated depending on x_0 . This leads to qualitative changes of the spectral content and spatial structure of the disturbance field. Since the location of receptivity region directly affects the N factor, the transition onset location strongly depends on x_0 .

Considering the boundary-layer flow on a flat plate in supersonic (Mach 3.5) and hypersonic (Mach 7.9) free streams, we found that the coherence of external forcing strongly affects the instability amplitude. Namely the random (incoherent) forcing is much more effective than the deterministic (coherent) forcing that leads to the quite large difference in the amplification factor ($\Delta N_S \approx 4 - 5$) and, thereby, in the transition onset location. Similar results were obtained by Fedorov [14] for the

cross-flow dominated transition on a supersonic swept wing having a thin parabolic arc-shape airfoil.

It was shown that for many practical cases, the instability length-scale lies in the inertial interval or the viscous dissipation interval (Fig. 7), where the turbulence spectrum depends on the two parameters only: kinematic viscosity ν_∞^* , which can be taken from the standard atmosphere, and the dissipation rate of turbulent energy ε^* , which was documented for various weather conditions. For the boundary-layer flows on a flat plate in the free stream corresponding to flights at Mach number 0.5, 2 and 10 and altitudes 10, 15 and 30 km, respectively, it was shown that a large uncertainty in the dissipation rate of turbulent energy, $0.1\varepsilon_{av}^* < \varepsilon^* < 10\varepsilon_{av}^*$, gives a marginal error in the transition onset ($\Delta x/x)_{tr} < \pm 17\%$ (see Table 1). Note that in the flat-plate boundary layer, the envelope of N-factors, $N_S(x)$, has a relatively small slope; i.e., the uncertainty $\Delta N_S(x_{tr})$ leads to a significant error of x_{tr} . In more practical cases, the pressure gradient leads, as a rule, to steeper distributions of $N_S(x)$ that reduces the transition locus sensitivity to variations of $N_S(x_{tr})$.

Thus, the physics-based amplitude method can be robust in the cases where transition is induced by atmospheric turbulence. This encourages further developments of the amplitude method for transition prediction.

In some practical cases, such as HIFI-RE-1, Reentry F and X-43A flights, the instability wavelength is much smaller than the scale l_0^* (see Fig. 7). In these and similar situations, the atmospheric turbulence is negligible and transition is triggered by some other source of external disturbances. This could be body-induced disturbances, solid particles (or aerosols) present in atmosphere, or even thermal noise associated with Brownian motion.

Acknowledgements This work has been carried out at Moscow Institute of Physics and Technology (National Research University) with financial support of the Russian Science Foundation (project No. 19-19-00470 – section 2; project No. 19-79-10132 – section 4).

References

1. Reshotko, E.: Transition issues for atmospheric entry. *J. Spacecraft Rockets* **45**(2), 161–164 (2008)
2. Morkovin, M.V., Reshotko, E., Herbert, T.: Transition in open flow systems: a reassessment. *Bull. APS* **39**(9), 1–31 (1994)
3. Fedorov, A.: Transition and stability of high-speed boundary layers. *Annu. Rev. Fluid Mech.* **43**, 79–95 (2011)
4. Berry, S., Daryabeigi, K., Wurster, K., Bittner, R.: Boundary layer transition on X-43A. *AIAA Pap.* 2008–3736 (2008)
5. Zhong, X., Wang, X.: Direct numerical simulation on the receptivity, instability, and transition of hypersonic boundary layers. *Annu. Rev. Fluid Mech.* **44**, 527–561 (2012)
6. Mack, L.M.: Transition and laminar instability. *NASA-CP-153203*, Jet Propulsion Lab., Pasadena, California (1977)
7. Fedorov, A.V.: Applications of the mack amplitude method to transition predictions in high-speed flows. *NATO RTO-MP-AVT-200* (2012)

8. Balakumar, P., Chou, A.: Transition prediction in hypersonic boundary layers using receptivity and freestream spectra. *AIAA J.* **56**(1), 1–16 (2017)
9. Stetson, K.F.: Comments on hypersonic boundary-layer transition. WRDC-TR-90-3057, Wright Research and Development Center (1990)
10. Chuvakhov, P.V., Fedorov, A.V., Obraz, A.O.: Numerical modelling of supersonic boundary-layer receptivity to solid particulates. *J. Fluid Mech.* **859**, 949–971 (2019)
11. Fedorov, A.V., Averkin, A.N.: Receptivity of a compressible boundary layer to kinetic fluctuations. In: Schlatter, P., Henningson, D.S. (eds.) In: Proceedings of the Seventh IUTAM Symposium on Laminar-Turbulent Transition. IUTAM Bookseries, vol. 18, pp. 485–488 (2010)
12. Fedorov, A.V.: Prediction and control of laminar-turbulent transition in high-speed boundary-layer flows. IUTAM ABCM Symposium on Laminar-Turbulent Transition, Procedia IUTAM **14**, 3–14 (2015)
13. Fedorov, A., Tumin, A.: Receptivity of high-speed boundary layers to kinetic fluctuations. *AIAA J.* **55**(7), 2335–2348 (2017)
14. Fedorov, A.V.: Prediction of cross-flow dominated transition on a supersonic swept wing. *AIAA Pap.* 2012–0920 (2012)
15. Balakumar, P., Zhao, H., Atkins, H.: Stability of hypersonic boundary layers over a compression corner. *AIAA Pap.* 2002–2848 (2002)
16. Sivasubramanian, J., Fasel, H.: Transition initiated by a localized disturbance in a hypersonic flat-plate boundary layer. *AIAA Paper* 2011–374 (2011)
17. Bushnell, D.: Notes on initial disturbances fields for the transition problem. In: Hussaini, M.Y., Voigt, R.G. (eds.) *Instability and Transition*, vol. 1, pp. 217–232. Springer-Verlag, Berlin (1990)
18. Fedorov, A.V.: Receptivity of a supersonic boundary layer to solid particulates. *J. Fluid Mech.* **737**, 105–131 (2013)
19. Pugach, M.A., Ryzhov, A.A., Fedorov, A.V.: Estimation of the effect of free-stream turbulence and solid particulates on the laminar-turbulent transition at hypersonic speeds. *TsAGI Science J.* **47**(1), 15–28 (2016)
20. Hocking, W.K.: Measurement of turbulent energy dissipation rates in the middle atmosphere by radar techniques: A review. *Radio Science* **20**(6), 1403–1422 (1985)
21. Pao, Y.H.: Structure of turbulent velocity and scalar fields at large wavenumbers. *Phys. Fluids* **8**, 1063–1075 (1965)
22. Haak, A., Gerdin, M., Lübken, F.-J.: Characteristics of stratospheric turbulent layers measured by LITOS and their relation to the Richardson number. *J. Geophys. Res. Atmos.* **119**, 605–618 (2014)
23. Li, F., Choudhari, M., Chang, C.L., Kimmel, R., Adamczak, D., Smith, M.: Transition analysis for the HIFiRE-1 flight experiment. *AIAA Pap.* 2011–3414 (2011)
24. Johnson, H.B., Candler, G.V.: Hypersonic boundary layer stability analysis using PSE-Chem. *AIAA Paper* 2005–5023 (2005)
25. Malik, M.R.: Hypersonic flight transition data analysis using parabolized stability equations with chemistry effects. *J. Spacecraft Rockets* **40**(3), 332–344 (2003)

Numerical Investigation of the Nonlinear Transition Stages in a High-Enthalpy Hypersonic Boundary Layer on a Right Cone



Michelle Bailey, Christoph Hader, and Hermann F. Fasel

Abstract Direct Numerical Simulations (DNS) were used to investigate the laminar-turbulent transition process for a straight (right) cone for the high enthalpy conditions of the Caltech T5 hypersonic tunnel. Preliminary results of a three-dimensional wave packet simulation indicated that the so-called “fundamental breakdown” is most likely the dominant nonlinear mechanism for these conditions and geometry. Contours of the time-averaged Stanton number obtained from a preliminary “controlled” fundamental breakdown DNS exhibited the formation of “hot” streaks on the cone surface. “Hot” streak patterns have also been observed for low enthalpy experiments in the Boeing/AFOSR Mach 6 Quiet Tunnel (BAM6QT) at Purdue and in investigations using DNS for these conditions.

1 Introduction

The laminar-turbulent transition process in high speed boundary layers is affected by a multitude of factors. A key parameter is the wall to recovery temperature ratio (T_w/T_r). The effect of this parameter, in particular on the nonlinear transition mechanisms, is not very well understood. Recent numerical investigations have shown that for highly cooled walls ($T_w/T_r \approx 0.1$) spontaneous acoustic-like emissions can occur when the disturbance waves synchronize with the slow acoustic mode [1–3]. Additionally the linear instability regime was found to be affected by this parameter [4]. In ground-based experiments low values of T_w/T_r are generated in high-enthalpy facilities (e.g. the T5 Reflected Shock Tunnel at the California Institute of Technol-

M. Bailey (✉) · C. Hader · H. F. Fasel

Department of Aerospace and Mechanical Engineering, The University of Arizona, Tucson, AZ, USA

e-mail: mlevbailey@email.arizona.edu

C. Hader

e-mail: chader@email.arizona.edu

H. F. Fasel

e-mail: faselh@email.arizona.edu

ogy (Caltech T5)). Experiments in such facilities are difficult and expensive. On the other hand, numerical investigations using direct numerical simulations (DNS) are challenging due to the resolution requirements caused by the large temperature gradients near the wall as well as due to real gas effects. Consequently, detailed numerical investigations that include the effects of high enthalpy on the nonlinear transition stages are currently not yet available.

The preliminary numerical investigations presented here were motivated by the experiments conducted in the Caltech T5 tunnel for a right cone (length $L_{\text{cone}} = 1$ m, nose half angle $\theta_{\text{cone}} = 5^\circ$, nose radius $r_{\text{nose}} = 0.1778$ mm) at zero angle of attack. For experimental Test Shot 2718, see [5], the test gas was air with the following flow conditions: $M = 5.32$, $Re_1 = 5.42 \cdot 10^6 \text{ m}^{-1}$, $p_0 = 37.50 \text{ MPa}$, $T_0 = 8367.50 \text{ K}$, $h_0 \approx 10 \text{ MJ/kg}$. Despite the high free-stream temperature ($T_\infty = 1530 \text{ K}$), the wall of the cone remained at room temperature ($T_w = 297 \text{ K}$) due to the short duration of the experiments. This resulted in a “cooled” wall with a very low $T_w/T_r = 0.04$. The results presented in this paper are a continuation of the numerical investigations by Salemi and Fasel [1, 3]. Following their effort [3], the effect of the composition of the test gas was modelled with an effective constant Prandtl number, $Pr = 0.7692$ and a constant ratio of specific heats, $\gamma = 1.3158$. Chemical reactions were omitted to first understand how a strongly cooled wall affects the relevant nonlinear mechanisms. This limits the validity of the results to flows having peak temperatures below approximately 2600 K but is still applicable to the experimental conditions of the T5 facility as reported by [4]. Furthermore, in a first go around, it can be assumed that including chemical reactions would not qualitatively affect the relevant nonlinear transition mechanisms.

2 Numerical Approach

The coordinate system used in the investigations discussed below is shown in Fig. 1. In order to conduct stability investigations using DNS, a laminar base flow for the given geometry and flow conditions is required. Towards this end, first, a precursor calculation was carried out for the base flow around the entire geometry using an in-house finite volume code [6]. This solution was then used to extract initial and boundary conditions to obtain a re-converged base flow solution in a smaller sub-domain also using an in-house developed, high-order accurate, finite-difference solver [7]. For details explaining this approach and the numerical schemes used refer to [7]. The sub-domain starts downstream of the nose of the cone in order to focus all computational resources on parts of the cone that will be relevant in the transition process. This re-converged solution serves as the steady, undisturbed laminar base flow for the stability and transition simulations discussed below. Dirichlet conditions were prescribed at the inflow and at the free-stream boundary that are obtained from the precursor calculation. At the wall of the cone, no-slip, no-penetration and isothermal conditions were assumed (except at the downstream locations where disturbances are introduced in the flow as discussed in Sects. 3 and 4). At the outflow

Fig. 1 Schematic of the cone geometry and the reference coordinate systems

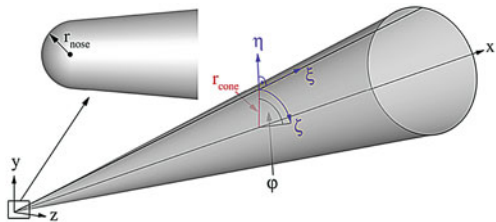
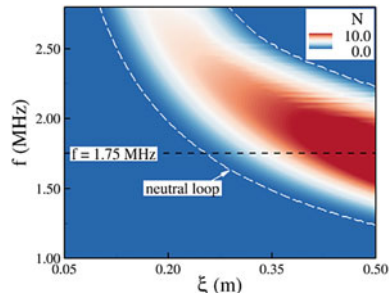


Fig. 2 Contours of N-factor in a plane of frequency (f) versus downstream direction (ξ) for axisymmetric disturbances ($k_c = 0$) obtained from LST [9]



boundary, second derivatives of the primitive variables were set to zero. In addition, a buffer zone was employed at the downstream end of the computational domain, using a ramp that forces the disturbances to vanish in order to avoid reflections from the outflow boundary. Symmetry conditions were employed at the azimuthal boundaries.

3 Three-Dimensional Wave Packet

Before investigating the nonlinear transition stages, the linear stability regime had to be explored. Towards this end, an in-house developed compressible Linear Stability Theory (LST) code was employed. Figure 2 shows an N-factor map (see [8] for definition) as obtained by Haas [9], which indicates that second mode waves in the frequency range $1.5 \text{ MHz} \leq f \leq 2.0 \text{ MHz}$ result in the largest N-factors. Knowing *a priori* which frequencies result in the largest N-factors is helpful in setting up the pulse forcing needed for the wave packet investigations to ensure that the most amplified second mode frequency band is contained in the initial disturbance spectrum.

To explore which nonlinear mechanisms may be relevant for the T5 conditions, a wave packet was generated using a short-duration pulse disturbance through a blowing and suction hole at the wall (see Table 1 for details). The selected forcing interval ensured that the linearly most amplified waves (see Fig. 2) are contained in the initial disturbance spectrum (centered around $f = 1.75 \text{ MHz}$). The pulse amplitude $A_{pulse} = 10^{-3}$ was chosen so that all relevant stages from linear instability to the strongly nonlinear stages can be observed in the computational domain. The inflow location of the computational domain was chosen based on LST results (Fig. 2) so

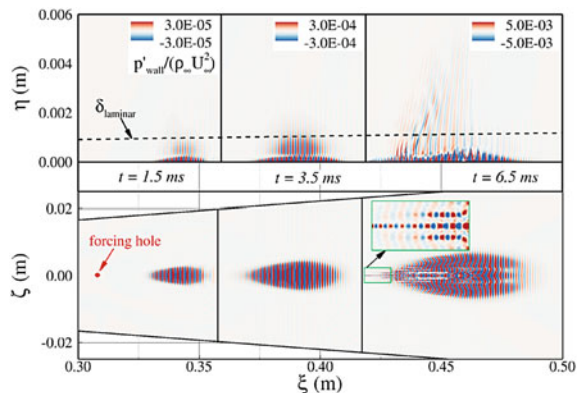
Table 1 Simulation setup for the three-dimensional wave packet

Parameter	Wave packet
Forcing type	3D pulse
Forcing amplitude	$A_{\text{pulse}} = 10^{-3}$
Forcing duration	$\approx 0.57 \mu\text{s}$
Forcing ξ -extent (m)	$0.308 \leq \xi \leq 0.310$
Forcing ϕ -extent (rad)	$-0.09 \leq \phi \leq 0.09$
Grid, $n_\xi \times n_\eta$	6500×400
Grid, n_ζ (Fourier modes)	299 (150 modes)
Wall units from turbulent estimates [10]	$\Delta x^+ \approx 37, \Delta y^+ \approx 9$
ξ -domain extent (m)	$0.30 \leq \xi \leq 0.50$
η -domain extent (m)	$0.00 \leq \eta \leq 0.10$
ϕ -domain extent (rad)	$0.00 \leq \phi \leq \pi/5$

that, at that location a wide range of frequencies are already linearly unstable. The azimuthal extent of the domain is a fifth of the cone to allow for a wide range of azimuthal wavenumbers ($k_c = 2\pi\lambda_\zeta$, where $\lambda_\zeta = r\lambda_\varphi$). Note that due to the symmetry condition in the azimuthal direction, nonsymmetric effects are neglected and that the extent of the azimuthal domain limits the resolution of the azimuthal wavenumbers to integer multiples of $k_c = 5$.

The propagation of the wave packet in the downstream direction is shown in Fig. 3. The contours of the pressure disturbance on the unrolled cone surface shown in Fig. 3 (bottom) indicate that the wave fronts are predominantly two dimensional, implying that at these instances the wave packet is dominated by axisymmetric second mode disturbance waves. The wave packet rapidly elongates in the downstream direction as it propagates, which suggests that a wide range of frequencies (wide range of phase speeds) are amplified. Once the flow enters the nonlinear regime, the wave fronts

Fig. 3 Contours of the pressure disturbance, from preliminary DNS, at different time instances in the symmetry plane (top) and on the unrolled surface of the cone (bottom). Contour levels are adjusted at each time instance to account for the increase in pressure disturbance as the wave packet propagates downstream



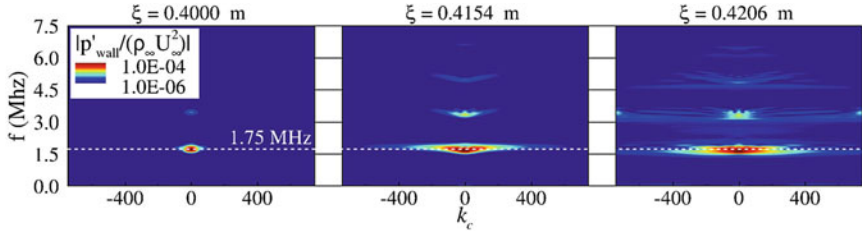


Fig. 4 Contours of the pressure disturbance amplitude extracted at the wall, from preliminary DNS, for select downstream locations (ξ) in a plane of azimuthal wavenumber (k_c) versus frequency (f)

become distorted in the azimuthal direction, which is an indication that nonlinear interactions with oblique waves occur. The contour plot of the disturbance pressure in the symmetry plane ($\phi = 0$ rad) in Fig. 3 (top) clearly shows that the disturbances penetrate far into the freestream when the wave packet has moved far downstream.

To analyze which disturbance waves dominate the various stages of the wave packet development, the amplitude spectra of frequency versus azimuthal wavenumber at various downstream locations are consulted (see Fig. 4). At $\xi = 0.4000$ m, a clear maximum is observed for $f = 1.75$ MHz, consistent with the most amplified frequency band obtained from LST (Fig. 2). A weak nonlinearly generated higher harmonic at $f = 3.50$ MHz is observed, as well as nonlinearly generated shallow oblique waves (small k_c) with $f = 1.75$ MHz. Farther downstream, at $\xi = 0.4154$ m (Fig. 4), a third higher harmonic is visible and the further broadening of the k_c range for $f = 1.75$ MHz suggests that fundamental resonance is a likely relevant secondary instability mechanism. At $\xi = 0.4206$ m (Fig. 4), in addition to the broadening of the k_c range, which is now observed even for the higher harmonics, the accumulation of energy (large amplitude) at the highest k_c values at $f = 3.5$ MHz points to the fact that further resolution in the azimuthal direction is required to allow the breakdown of the wave packet to a turbulent spot, which however, was not part of this investigation.

The preliminary wave packet results show that for the Caltech T5 flow conditions and geometry, fundamental breakdown will likely be the relevant nonlinear mechanism. The spectra in Fig. 4 provide no indication that subharmonic breakdown could be relevant. Therefore a subsequent detailed investigation of secondary instability was performed for fundamental resonance only.

4 Controlled Fundamental Breakdown

In (Sect. 3) fundamental resonance was identified as the dominant nonlinear mechanism. Therefore, a so called “controlled” fundamental breakdown simulation was carried out, by disturbing the flow with a large amplitude axisymmetric primary wave and a pair of low amplitude oblique secondary waves of the same frequency.

To narrow the parameter space for the disturbance wave frequency and azimuthal wavenumber, each of the relevant stages (primary and secondary instability) preceding the strongly nonlinear stages were investigated separately. The underlying assumption is that disturbances which dominate the primary instability regime will most likely become relevant for secondary instability onset, and that secondary disturbances with azimuthal wave numbers with the strongest secondary growth (here for fundamental resonance) will “win the race” to the nonlinear stages. For convenience, a mode terminology (n, m) , shorthand for $(n \cdot f_{\text{primary}}, m \cdot k_c, \text{secondary})$ was adopted here. Thus prior to performing a preliminary DNS of a “controlled” fundamental breakdown, first the frequency of the primary wave (mode $(1, 0)$) and the k_c of the secondary wave (mode $(1, 1)$) have to be determined.

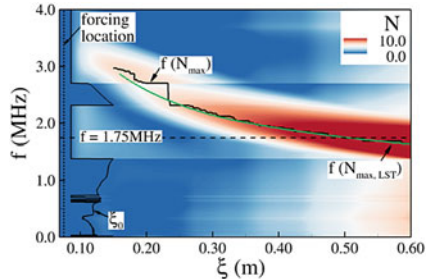
4.1 Primary and Secondary Instability Regime

A high speed boundary layer for the flow conditions of the T5 facility, is assumed to be most unstable with respect to axisymmetric second mode waves based on primary (linear) instability theory [11]. Therefore to explore the primary instability regime using DNS, an axisymmetric wave packet was generated by introducing a short-duration, low amplitude (wall normal) velocity perturbation through a blowing and suction slot at the wall (see Table 2). Due to the very low amplitude of the pulse, the disturbance development can be considered to be linear. The size of the computational domain is the same as in [3]. By tracking all disturbance frequency components of the

Table 2 Simulation setup for the different stages investigated

Parameter	Primary instability	Secondary instability	Controlled breakdown
Forcing type	2D Pulse	Continuous	Continuous
Forcing amplitude	$A_{\text{pulse}} = 10^{-6}$	$A_{1,0} = 10^{-5}$	$A_{1,0} = 5 \times 10^{-4}$
		$A_{1,1} = 10^{-6}$	$A_{1,1} = 10^{-6}$
Forcing ξ -extent (m)	$0.079 \leq \xi \leq 0.082$	$0.300 \leq \xi \leq 0.301$	Time Dependent Inflow
Forcing ϕ -extent (rad)	N/A	$-\pi/k_c \leq \phi \leq \pi/k_c$	Time Dependent Inflow
Grid, $n_\xi \times n_\eta$	4703×464	1620×464	6500×400
Grid, n_ζ (Fourier modes)	N/A	9 (5 modes)	119 (60 modes)
Wall units from turbulent estimates [10]	NA	NA	$\Delta x^+ \approx 18, \Delta y^+ \approx 9$
ξ -domain extent (m)	$0.06 \leq \xi \leq 0.62$	$0.29 \leq \xi \leq 0.48$	$0.30 \leq x \leq 0.50$
η -domain extent (m)	$0.00 \leq \eta \leq 0.25$	$0.00 \leq \eta \leq 0.25$	$0.00 \leq \eta \leq 0.10$
ϕ -domain extent (rad)	N/A	$0.00 \leq \phi \leq \pi/k_c$	$0.00 \leq \phi \leq \pi/300$

Fig. 5 N-factor contours of the disturbance wall pressure in a plane of frequency (f) versus downstream direction (ξ). The reference location (ξ_0) was used to normalize the amplitude development to obtain the N-factors



wave packet as it propagates downstream the N-factors can be extracted (for details, see [12]) and an N-factor map is obtained as shown in Fig. 5. Comparison of the N-factor map with that from LST (in Fig. 2) confirms the presence of a dominant second mode frequency in the range of 1.50 MHz – 2.00 MHz. Therefore, a primary wave with frequency, $f_{\text{primary}} = 1.75$ MHz was selected for the “controlled” breakdown simulation.

Since fundamental resonance was found to be the most likely relevant nonlinear mechanism (see Sect. 3) a parameter study was carried out to determine which azimuthal wave number of the secondary wave ($k_{c,\text{secondary}}$) leads to the largest N-factor. Towards this end, primary and secondary disturbance waves of the same frequency ($f_{\text{primary}} = 1.75$ MHz) but varying azimuthal wavenumbers (k_c) were continuously forced using wall-normal velocity perturbations through a blowing and suction slot at the wall (see Table 2). The location of the inflow boundary of the computational domain was chosen such that the primary wave frequency is already amplified in order to avoid having to compute through a large stable portion of the boundary layer (see Sect. 3). The forcing amplitude of the primary wave was based on test calculations (not shown here) to ensure that the primary wave exhibits linear growth before saturating. This part of the calculation setup was kept the same for the subsequent controlled fundamental breakdown DNS with the only differences being that the primary and secondary wave was forced as a time-dependent inflow using eigenfunctions from the LST results [9] and the forcing amplitude of the primary wave was increased (see Table 2).

A typical development of the primary wave (1, 0) and secondary wave (1, 1) amplitude as obtained from the secondary instability investigation using DNS is shown in Fig. 6 (a, top). Note that the amplitude of the primary wave can still be growing in ξ even after onset of nonlinear saturation. This is in contrast to the original secondary instability theory where the amplitude of the primary wave is fixed and the secondary wave is growing in time (see [13]). The primary wave (1, 0) grows exponentially until it saturates, while the secondary wave (1, 1) at first exhibits a downstream behavior that matches that of a “linear” calculation (without the primary wave) until a clear departure occurs at $\xi \approx 0.40$ m indicating resonance onset between the primary and secondary disturbance waves. This is confirmed by the “phase-speed locking” between the primary and secondary disturbance waves (Fig. 6

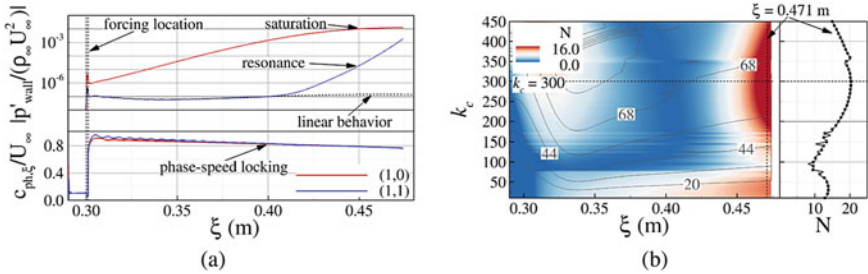


Fig. 6 Secondary instability investigations for fundamental resonance: **a** fundamental resonance onset for $k_c = 100$; amplitude development in downstream direction (ξ) for disturbance pressure at the wall (top) dashed line indicates linear behavior of the secondary wave. Normalized phase speed versus downstream direction (ξ) (bottom). **b** N-factor contours for the secondary wave in a plane of azimuthal wavenumber (k_c) versus the downstream direction (ξ)

(a, bottom)) at the location of the resonance onset ($\xi \approx 0.40$ m). These calculations were carried out for a wide range of azimuthal wavenumbers and the results are shown in Fig. 6b as contours of the N-factors for the secondary waves. Figure 6b shows that strong secondary disturbance growth occurs for a very broad range of azimuthal wavenumbers and that a secondary wave with $k_{c,\text{secondary}} = 300$ has the largest N-factor, which was selected for the “controlled” fundamental breakdown simulation (see Sect. 4.2).

4.2 Controlled Fundamental Breakdown

With the frequency of the primary wave (mode (1, 0)) and the k_c of the secondary wave (mode (1, 1)) determined, a preliminary DNS of a “controlled” fundamental breakdown, including all stages from the linear regime to the late nonlinear stages was carried out. The “controlled” breakdown was initiated with the primary and secondary disturbance wave parameters as determined in Sect. 4.1 with details of the computational setup provided in Table 2.

In experiments for a flared cone in the BAM6QT at Purdue University [14] as well as in DNS investigations for the same geometry and flow conditions [12], patterns of “hot” streaks were observed on the surface of the cone. From the DNS investigations it was found that the streak formation resulted from the nonlinear generation of streamwise modes (counter-rotating vortices) when fundamental breakdown was the dominant nonlinear mechanism [12]. This was confirmed by DNS investigations for a 7° right cone for the same experimental (BAM6QT) conditions [15]. In order to determine if a similar streak development could be observed for the high enthalpy Caltech T5 conditions, contours of the time averaged Stanton number (C_h) on the surface of the cone were computed from the preliminary DNS results and are shown in Fig. 7a. The contours of the Stanton number show a clear development of azimuthally

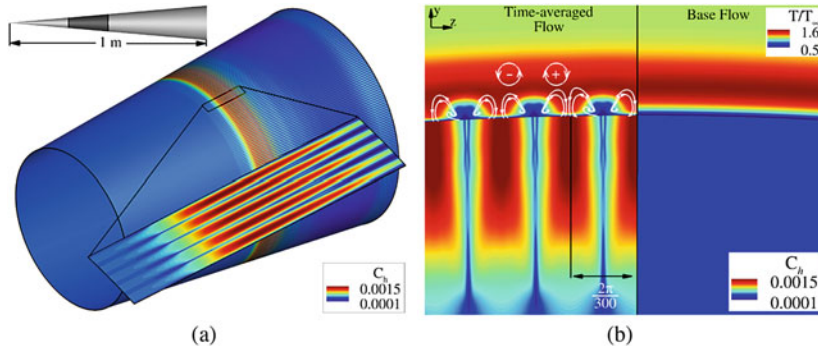
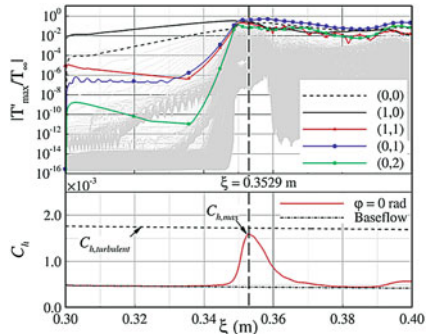


Fig. 7 Contours of the time averaged Stanton number on the surface of the cone: **a** the dark shaded area of the cone in the top left corner is the computational domain used for the preliminary fundamental breakdown DNS. **b** Contours of the time averaged total temperature (left) and the base flow temperature (right) extracted in a plane normal to the surface of the cone at a location where the streaks are present ($\xi = 0.3529$ m), together with the contours of the time averaged Stanton number (left) and the Stanton number of the base flow (right). Streamlines on the left were obtained from the time-averaged disturbance flow field

very closely spaced streamwise “hot” streaks. A close up of the streak region in Fig. 7a provides a more detailed view of these streaks. Following the analysis in [12], the time-averaged temperature contours in a plane normal to the surface at a location where the streaks appear ($\xi = 0.3529$ m) are shown in Fig. 7b. The streamlines from the time-averaged disturbance flow field show that counter-rotating vortical structures are present that appear to push the hot fluid from the freestream towards the wall where the streaks are formed, while displacing the cooler fluid into “pockets” between the streaks. For comparison the laminar base flow is provided in the right half of Fig. 7b showing the unperturbed temperature contours for reference. The streak spacing corresponds directly to the azimuthal wavenumber of the secondary disturbance wave ($k_{c,\text{secondary}} = 300$) which results in 300 streaks around the circumference of the cone.

To determine which disturbance waves are responsible for the streak development, the downstream development of the maximum temperature disturbance amplitudes for various disturbance components is shown in Fig. 8 (top) together with the time-averaged Stanton number development (Fig. 8, bottom). The preliminary results show that the sudden rise in the Stanton number is linked to the nonlinearly generated steady streamwise mode (0, 1), which becomes dominant at the location where the Stanton number reaches its maximum. This is consistent with the observations for a straight and flared cone geometry for the low enthalpy (BAM6QT) conditions [12, 15, 16].

Fig. 8 Development of the maximum temperature disturbance (T'_{\max}) (top) and Stanton number (C_h) (bottom) in the downstream direction obtained from preliminary DNS. At $\xi = 0.3529$ m, a maximum in C_h is observed corresponding to when mode (0, 1) dominates in amplitude



5 Conclusions

Preliminary numerical investigations of the nonlinear boundary layer transition for the high enthalpy conditions of the Caltech T5 tunnel showed that fundamental resonance is the likely relevant nonlinear breakdown mechanism. Investigations of the primary instability regime exhibited a wide band of growing second mode frequencies, while secondary instability investigations indicated that a wide range of azimuthal wavenumbers yield large N-factors. This is in contrast to DNS results obtained for the low enthalpy (BAM6QT) conditions [12, 15]. From DNS results of a “controlled” fundamental breakdown, a similar pattern of “hot” streaks was found. Such hot streak patterns were previously observed in the BAM6QT experiments [14] and in DNS for the BAM6QT conditions [12, 15]. The underlying mechanisms of the streak development appear to be consistent with those found for the low enthalpy (BAM6QT) conditions, however the streak topology for the high enthalpy Caltech T5 conditions is different. Understanding this difference will require DNS with improved spatial resolution, that will be carried out in future investigations.

Acknowledgements This work was supported by AFOSR Grant FA9550-15-1-0265, with Dr. Ivett Leyva serving as the program manager. Computer time was provided by the Department of Defense (DoD) High Performance Computing Modernization Program (HPCMP). The views and conclusions contained herein are those of the authors and should not be interpreted as necessarily representing the official policies or endorsements, either expressed or implied, of the Air Force Office of Scientific Research or the U. S. Government. The authors would like to thank Anthony Haas for providing compressible LST calculations.

References

1. Salemi, L., Fasel, H.F., Wernz, S.H., Marquart, E.: AIAA 2014-2775 (2014)
2. Chuvakhov, P.V., Fedorov, A.V.: J. Fluid Mech. **805**, 188 (2016)
3. Salemi, L.C., Fasel, H.F.: J. Fluid Mech. **838**, R2 (2018)
4. Bitter, N., Shepherd, J.: J. Fluid Mech. **778**, 586 (2015)

5. Jewell, J.S.: Boundary-layer transition on a slender cone in hypervelocity flow with real gas effects. Ph.D. thesis, California Institute of Technology (2014)
6. Gross, A., Fasel, H.: AIAA J. **46**(1), 204 (2008)
7. Laible, A.C.: Numerical investigation of boundary layer transition for cones at Mach 3.5 and 6.0. Ph.D. thesis, The University of Arizona (2011)
8. van Ingen, J.: AIAA 2008-3830 (2008)
9. Haas, A.: Private communication (2018)
10. White, F.: Viscous Fluid Flow, International edn. McGraw-Hill (2006)
11. Mack, L.M.: Jet Propulsion Laboratory (1969)
12. Hader, C., Fasel, H.F.: J. Fluid Mech. **869**, 341 (2019)
13. Herbert, T.: Ann. Rev. Fluid Mech. **20**, 487 (1988)
14. Chynoweth, B., Schneider, S., Hader, C., Fasel, H., Batista, A., Kuehl, J., Juliano, T., Wheaton, B.: J. Spacecr. Rocket. **56**(2), 333 (2019)
15. Meersman, J., Hader, C., Fasel, H.: AIAA 2018-3851 (2018)
16. Hader, C., Fasel, H.F.: AIAA 2016-3344 (2016)

Direct Numerical Simulations (DNS) of Natural Transition in High-Speed Boundary Layers Using a Broadband Random Forcing Approach



Christoph Hader and Hermann F. Fasel

Abstract A direct numerical simulation (DNS) was carried out for which random pressure fluctuations were forced at the inflow of the computational domain to initiate the laminar-turbulent transition process. The random forcing generated a broad spectrum of disturbances with respect to both frequency and azimuthal wavenumbers without any bias towards any of the known relevant nonlinear mechanisms (fundamental, subharmonic, oblique). The DNS results showed clear evidence that fundamental resonance is the dominant nonlinear mechanism. The time-averaged Stanton number contours indicated the formation of a pattern of streamwise “hot” streaks on the surface of the cone. Such hot streak patterns have previously been observed in experiments in the BAM6QT and in “controlled” breakdown DNS for flared and straight cones.

1 Introduction

To simulate the laminar to turbulent transition process in high-speed boundary layers using direct numerical simulations (DNS), disturbances have to be introduced into the computational domain. For many so-called quiet, high-speed experimental facilities (low levels of free-stream noise, [1]) reliable disturbance spectra are not yet available. Without meaningful experimental disturbance spectra to guide the simulation setup, selecting proper parameters for the disturbance waves (frequency and wavenumber) and choosing a suitable disturbance forcing method are non-trivial tasks. Inspired by the landmark experiments of Schubauer and Skramstad [2], Fasel [3] demonstrated the applicability and usefulness of so-called “controlled” transition simulations (using continuously forced disturbances) to reproduce the stability characteristics of Tollmien-Schlichting waves for a flat-plate boundary layer by solving the complete Navier-Stokes equations. Since then, the “controlled transition sim-

C. Hader (✉) · H. F. Fasel

University of Arizona, 1130 N Mountain Ave, Tucson, AZ, USA

e-mail: christoph.hader@gmail.com

H. F. Fasel

e-mail: faselh@email.arizona.edu

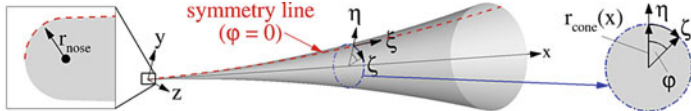


Fig. 1 Schematic of the flared cone geometry and the coordinate systems, and a cross section of the flared cone

ulation” approach has been successfully employed for investigations of transition for low and high-speed boundary layers (see for example [4, 5]). Setting up these “controlled” simulations for high-speed flows requires detailed knowledge of the relevant nonlinear mechanisms that will likely dominate the transition process. This, in turn, demands a careful investigation of all relevant instability stages preceding the nonlinear breakdown. “Controlled” transition simulations have shown good qualitative agreement with experimental measurements and had been instrumental for determining the dominant nonlinear mechanisms present in wind tunnel experiments. However, of course, no direct quantitative comparison is possible between a “controlled” transition DNS and experiments, where transition occurs “naturally” caused by the free-stream disturbances present in all wind tunnel experiments. Therefore, a random inflow forcing method was proposed in [6] as a model for “natural” transition.

2 Geometry and Flow Conditions

The transition simulation using the random forcing method was carried out for the Purdue flared cone geometry of the experiments performed in the BAM6QT [7]. A schematic of the flared cone and the reference coordinate systems are provided in Fig. 1. To facilitate a comparison with the “controlled” (fundamental) breakdown simulations, the flow conditions are identical to those used in [8], with the free-stream Mach number $M = 6$, a stagnation pressure $p_0 = 140\text{ psi}$, and a stagnation temperature of $T_0 = 420\text{ K}$. This results in a unit Reynolds number $Re_1 = 10.8 \cdot 10^6 \text{ 1/m}$. The fluid is treated as a perfect gas with $Pr = 0.71$ and $\gamma = 1.4$. The viscosity is calculated using Sutherland’s law. The wall was assumed to be isothermal with a wall temperature of $T_w = 300\text{ K}$. As a result, the wall to recovery temperature ratio in this case is $T_w/T_r \approx 0.83$, which is unrealistically high compared to values typically encountered in free-flight.

3 Random Forcing Approach

The random forcing approach proposed in [6] was used to initialize the disturbances in the computational domain and to initiate the laminar-turbulent transition process.

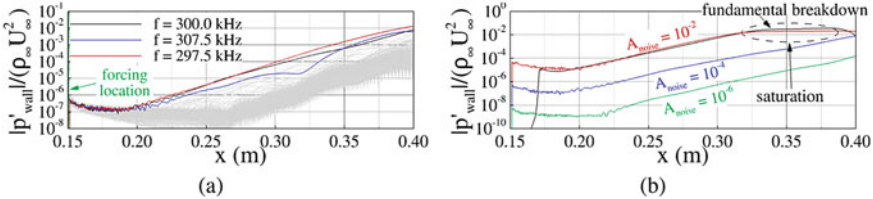


Fig. 2 Downstream development of the pressure disturbance amplitude at the wall for a wide range of frequencies obtained from an axisymmetric, randomly forced calculation with $A_{\text{noise}} = 10^{-4}$ (a), and the comparison of the $f = 300$ kHz disturbance wave for varying values of A_{noise} with the amplitude development obtained from a “controlled” fundamental breakdown simulation (b)

Random disturbances in space and in time were introduced as pressure fluctuations

$$p'_{i,j,k,n}/(\rho_\infty U_\infty^2) = A_{\text{noise}}(2r - 1), \quad (1)$$

where ρ_∞ and U_∞ are the freestream density and velocity, i, j, k are the grid line indices in the streamwise, the wall-normal and the azimuthal direction, n is the time step index, r is a random number generated with the compiler independent random_number() function, and A_{noise} is the amplitude of the random “noise”. As discussed above, the disturbance spectra for the BAM6QT facility when operated as a quiet tunnel were not available. Consequently, an ad hoc determination of the random noise amplitude based on axisymmetric calculations was necessary. The downstream development of the pressure disturbance amplitude at the wall in Fig. 2a for $A_{\text{noise}} = 10^{-4}$ confirms that random perturbations applied at the inflow generate a wide range of disturbance wave frequencies. One of the most rapidly amplified disturbance waves obtained from the random forcing is $f = 300$ kHz, which is consistent with primary instability investigations discussed in [8]. The comparison of the $f = 300$ kHz disturbance wave for an increasing random noise amplitude in Fig. 2b shows that the disturbance wave begins to saturate within the computational domain for sufficiently large values of A_{noise} . This provides a rough guideline for selecting the required noise amplitude to guarantee that the randomly forced disturbance waves will reach the late nonlinear stages upstream of the outflow boundary.

4 Results

A highly-resolved DNS was carried out with a high-order compressible Navier-Stokes code (for code details see [9]). The disturbances were generated at the inflow using the random forcing method described in Sect. 3 using a forcing amplitude of $A_{\text{noise}} = 10^{-2}$. Details of the simulation strategy, the employed numerical schemes and the boundary conditions used for this simulation are provided in [6]. The domain in the azimuthal direction extended from $\varphi = 0$ rad to $\varphi = \pi/40$ rad. With the

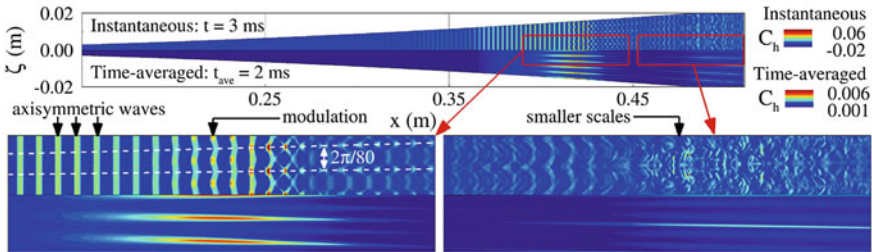


Fig. 3 Contours of the instantaneous and the time-averaged Stanton number on the unrolled surface of the cone close ups of the streak regions

employed symmetry condition at $\varphi = 0$, azimuthal wave numbers which are integer multiples of $k_c = 40$ were resolved in the simulation. First the random disturbances were advected through the computational domain for approximately 2.5 flow-through times ($t_{\text{adv}} = 1 \text{ ms}$). Then the flow field was sampled and averaged for a total of $t_{\text{ave}} = t - t_{\text{adv}} = 2 \text{ ms}$ (approximately 5 flow-through times).

Contours of the instantaneous and the time-averaged Stanton number (C_h) on the unrolled surface ($\zeta = r_{\text{cone}}(x)\varphi$) of the cone are provided in Fig. 3. The top half ($\zeta > 0$) shows the instantaneous values and the bottom half ($\zeta < 0$) the corresponding time average. Instantaneously, dominant axisymmetric waves (straight wave fronts) are visible starting at $x \approx 0.35 \text{ m}$. More details of these waves are visible in the close-up on the bottom left in Fig. 3. The axisymmetric waves become strongly modulated in the azimuthal direction with a wavelength corresponding to $k_c = 80$. These travelling waves eventually cause the development of streamwise “hot” streaks that are revealed by the contours of the time-averaged Stanton number ($\zeta < 0$, Fig. 3). These streaks disappear after a short downstream distance. Towards the end of the computational domain (see close-up, bottom right in Fig. 3) the azimuthal modulation of the instantaneous structures exhibits the generation of smaller scales. This is an indication that the flow has reached the late nonlinear stages of the breakdown process where a wide range of frequencies and azimuthal wavenumbers have been nonlinearly generated. Similar streak patterns as observed here have also been found in the flared cone experiments at Purdue University [7] and for DNS of “controlled” transition for the same experimental conditions [8]. A comparison with the experimental measurements will be provided below.

The instantaneous peak Stanton number values along the symmetry line of the cone ($\varphi = 0 \text{ rad}$) far exceed the maximum time-averaged values (see Fig. 4). Note that the scale for the instantaneous values (provided on the axis on the left) is much larger compared to the scale for the time-averaged C_h (displayed on the right side and highlighted with red). The development of C_h in the downstream direction at $t = 1.5 \text{ ms}$ ($t_{\text{ave}} = 0.5 \text{ ms}$, Fig. 4, top) shows that the amplitude of the Stanton number fluctuations continuously rises until $x \approx 0.419 \text{ m}$, followed by a sudden drop. Farther downstream, the Stanton number fluctuations appear to be random. The development of the time-averaged Stanton number (Fig. 4, top) monotonically increases

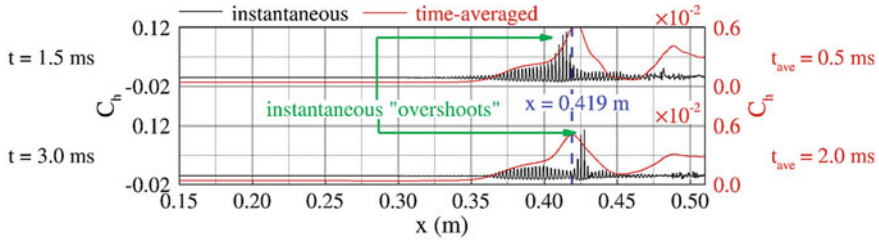


Fig. 4 Downstream development of the instantaneous Stanton number at two different time instances and the corresponding time-averaged Stanton number distribution

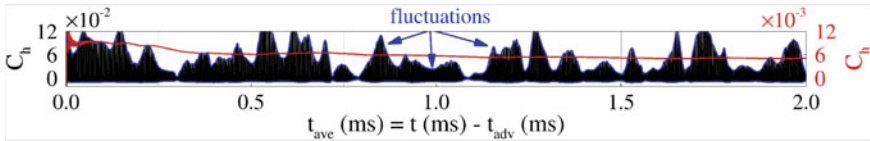


Fig. 5 Evolution of the instantaneous and the time-averaged Stanton number at $x = 0.419 \text{ m}$

until a maximum is reached at $x = 0.419 \text{ m}$. This maximum occurs at a downstream location where the “hot” streaks were observed in Fig. 3. Subsequently, the time-averaged Stanton number drops rapidly to a value that is comparable to the laminar Stanton number upstream of the streak location. Near the outflow of the computational domain, the Stanton number rises again and appears to approach the turbulent value. At a later time instant ($t = 3 \text{ ms}$, Fig. 4, bottom) the maximum oscillations of the instantaneous Stanton number shifted downstream compared to the previous time instant (Fig. 4, top). The time-averaged C_h at $t_{\text{ave}} = 2 \text{ ms}$ (Fig. 4, bottom) exhibits a slight adjustment of the maximum values compared to the previous time step. The downstream x -location of the instantaneous maxima is not fixed but rather shifts in either the upstream or downstream direction. Instantaneously, the maximum Stanton numbers can be in excess of 20 times the time-averaged values (instantaneous “overshoots”).

The evolution of the instantaneous and the time-averaged Stanton number at $x = 0.419 \text{ m}$ is shown in Fig. 5. As for the results in Fig. 4, the left ordinate provides the scale for the instantaneous C_h and the right ordinate shows the levels of the time-averaged values. Instantaneously, large fluctuations resulting in rapidly changing peak Stanton numbers are observed. The time-averages appear to be sufficiently converged after approximately $t_{\text{ave}} = 1.5 \text{ ms}$, after which the time-averaged C_h does no longer significantly change.

The contours of the time-averaged Stanton number on the surface of the cone in Fig. 6 again confirms that streamwise “hot” streaks appear, disappear and then farther downstream reappear. As mentioned above, this phenomenon has been observed in experiments in the BAM6QT at Purdue University [7] using temperature sensitive paint (TSP) and also in DNS of a “controlled” fundamental breakdown [8]. It was found that streaks are formed by nonlinearly generated steady streamwise vortical

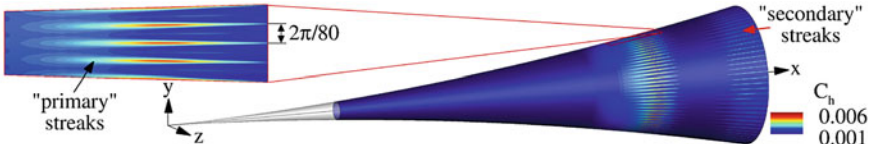


Fig. 6 Contours of the time-averaged Stanton number on the surface of the cone with a close up of the “primary” streak region

modes [8]. To distinguish the two streak patterns, the two regions are denoted as “primary” and “secondary” streaks (Fig. 6). The close up in Fig. 6 shows that the “primary” streaks are spaced $\Delta\varphi = 2\pi/80$ rad apart, which results in exactly 80 streaks around the circumference of the cone. The Stanton number contours obtained in the experiments for slightly different conditions ($p_0 = 131.9$ psi, $T_0 = 432.72$ K) using TSP [7] and the contours of the time-averaged Stanton number resulting from the “controlled” fundamental breakdown DNS [8] and the random forcing DNS [6] exhibit qualitatively similar patterns (see Fig. 7). To facilitate a better comparison, the same contour levels are used for all three cases in Fig. 7. The contours of the Stanton number of the “controlled” fundamental breakdown (Fig. 7, middle) appear to be oversaturated indicating that much larger Stanton number values are reached compared to the experiment (Fig. 7, left) or the random forcing DNS (Fig. 7, right). This is a consequence of the “controlled” disturbance input used for the fundamental breakdown DNS. While in the experiment “natural” transition occurs that involves many disturbance frequencies and spanwise wavenumbers, only one large amplitude axisymmetric (primary) disturbance wave and a pair of lower amplitude oblique (secondary) disturbances of the same frequency are forced to trigger a so-called “fundamental breakdown”. Thus, a bias towards these forced disturbance modes is introduced, which then consequently contain most of the disturbance energy for a large downstream portion of the computational domain. As discussed in Sect. 1, while yielding qualitatively similar results, a good quantitative comparison between the experimental measurements and the “controlled” fundamental breakdown cannot be expected. The random forcing approach (Fig. 7, right) shows a clear improvement towards a quantitative comparison with experimental measurements (Fig. 7, left).

The Stanton number development in the downstream direction along the symmetry line of the cone in Fig. 8a confirms that the fundamental breakdown leads to much larger peak values of C_h . The C_h values obtained from the random forcing DNS agree reasonably well with the experimental measurements. The Stanton number development in the unrolled cone coordinate ($\zeta = r_{\text{cone}}(x)\varphi$) normalized with the local cone circumference ($2\pi r_{\text{cone}}(x)$), at a location where the “primary” streaks are present (see Fig. 8b), allows for an accurate determination of the azimuthal spacing of the streaks. The “controlled” fundamental breakdown and the random forcing DNS resulted in exactly 80 streaks around the circumference of the cone. The measured streak spacing in the experiments is not constant (65–90 streaks), but falls within the same range of the azimuthal spacing obtained from DNS (“controlled” and random).

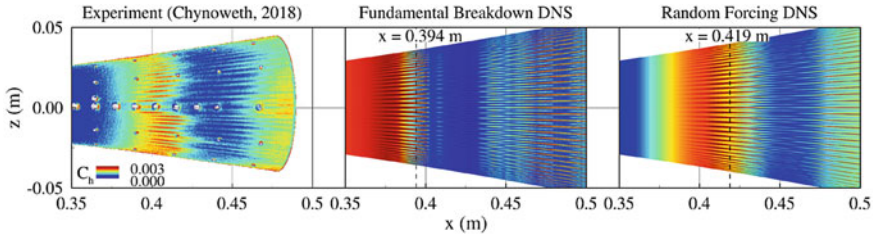


Fig. 7 Comparison of Stanton number contours obtained from experiments using temperature sensitive paint (left, $p_0 = 131.9$ psi, $T_0 = 432.72$ K, [7]), the time-averaged Stanton number for a “controlled” fundamental breakdown, (middle, $p_0 = 140$ psi, $T_0 = 420$ K, [8]) and the time-averaged Stanton number resulting from the random forcing DNS (right, $p_0 = 140$ psi, $T_0 = 420$ K)

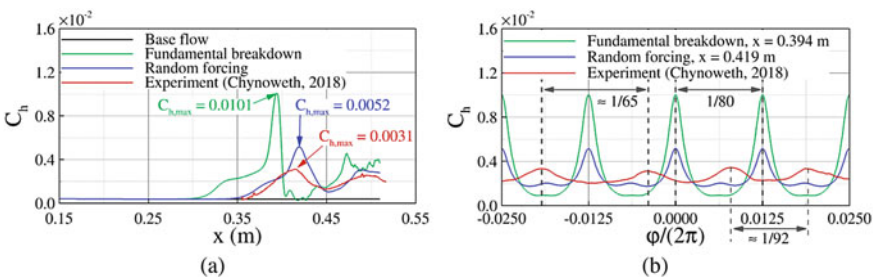


Fig. 8 Comparison of the Stanton number development in the streamwise direction (a), and in the azimuthal direction (b) between the values obtained from the experiments [7], a “controlled” fundamental breakdown DNS and the random forcing DNS

Time signals from the experimental measurements [7], from the “controlled” fundamental breakdown and the random forcing DNS at two different downstream locations are plotted in Fig. 9a. Note that the time signal of the “controlled” breakdown is periodically extended in time for visualization purposes. In the experimental data and the DNS using random forcing an intermittent wave-packet like character of the time signals can be observed while the “controlled” fundamental breakdown exhibits more regular time signals with a constant amplitude. Farther downstream at $x = 0.492$ m, the time signals from the experiments and the random forcing DNS appear to be random, indicating that the flow has progressed deep into the nonlinear regime. The shorter wavelengths observed at $x = 0.492$ m for the “controlled” transition DNS confirms that the time signal is composed of a wider range of frequencies and therefore has also reached the late nonlinear stages of the transition process. Compared to the random forcing DNS and the experimental measurements, however, the signals appears to be a lot more regular. The corresponding power spectral density (PSD) distributions in Fig. 9b indicate that the random forcing DNS produces the same amplitude for the same frequency bands at $x = 0.390$ m as measured in the experiments. While the “controlled” transition DNS also matches the same frequency bands, the disturbance energy is much more concentrated in the frequency range of

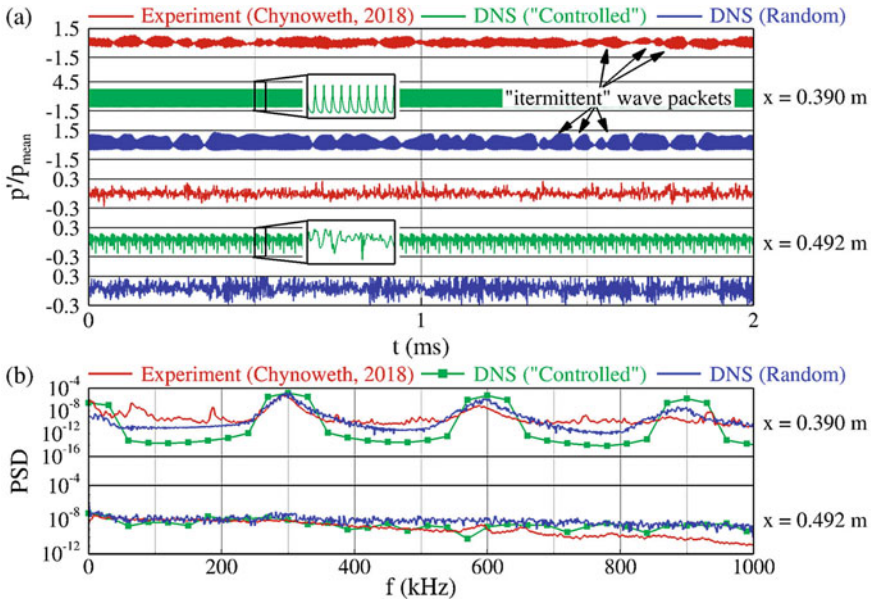


Fig. 9 Time signals extracted at two different downstream locations (a), and the corresponding power spectral density (PSD) distribution (b)

the forced disturbance wave ($f = 300 \text{ kHz}$) and its higher harmonics. Towards the downstream end of the computational domain (Fig. 9b, bottom) the spectra are much broader without any discernible dominant frequency.

The frequency-wavenumber amplitude spectra at two different downstream locations for the random forcing DNS are given in Fig. 10. The red circles on the surface of the cone on the left of Fig. 10 mark the locations at which the displayed spectra were extracted. The surface of the cone is colored with contours of the time-averaged Stanton number to provide a reference of where the spectra were extracted relative to the “primary” and the “secondary” streaks. When the “primary” streaks have developed ($x = 0.415 \text{ m}$, Fig. 10, middle), a wide range of frequencies and azimuthal wave numbers have reached large amplitudes. There is a dominant frequency band around $f = 295 \text{ kHz}$ and its higher harmonics. This is consistent with a fundamental breakdown scenario. Towards the downstream end of the computational domain ($x = 0.510 \text{ m}$, Fig. 10, right) the spectrum shows that the energy is distributed over a wide range of frequencies and azimuthal wavenumbers without any clearly dominant modes, providing evidence that the flow has progressed deep into the nonlinear breakdown regime towards fully turbulent flow. The peak observed at $f = 0 \text{ kHz}$ and $k_c = 0$ indicates that the base flow has been strongly modified. The instantaneous contours of the density gradient in the symmetry plane (Fig. 11) exhibit typical structures of a transitional boundary layer. So-called “rope-like” structures begin to develop around $x \approx 0.36 \text{ m}$. These structures intensify and large amplitude trapped

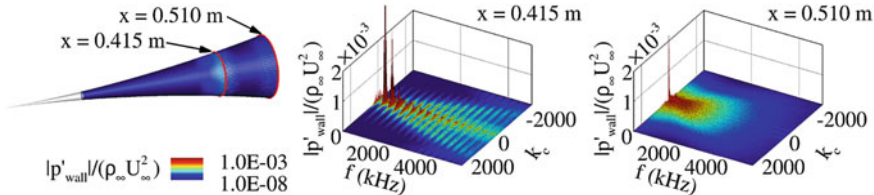


Fig. 10 Amplitude spectra of the wall pressure disturbance at three different downstream locations

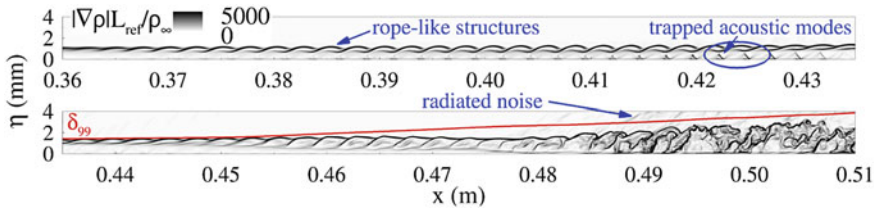


Fig. 11 Instantaneous contours of the magnitude of the density gradient ("pseudo-schlieren") in the symmetry plane

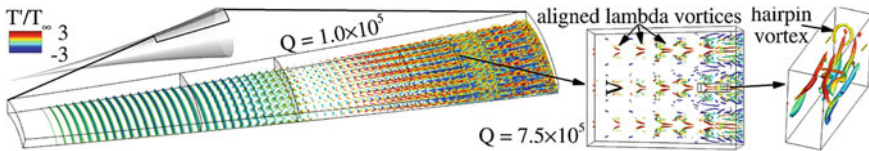


Fig. 12 Instantaneous flow structures visualized with isocontours of the Q criterion

acoustic waves can be observed. Around $x = 0.48$ m the boundary layer begins to thicken rapidly and noise is radiated from a boundary layer that has reached the late nonlinear stages of the laminar-turbulent transition process.

The flow structures of the transitional region in the boundary layer are visualized using the Q -criterion (Fig. 12). The approximate beginning and end of the "primary" streaks are marked for reference. The streak extent was determined based on the contours in Fig. 6 and is, therefore, only a qualitative approximation of the streak extent since it is dependent on the selected contour levels. The Q -isocontours are colored with the temperature disturbance values. Upstream of the "primary" streak development the flow is dominated by axisymmetric structures (large amplitude second mode waves). A deformation in the azimuthal direction corresponding to the azimuthal wavenumber of $k_c = 80$ is observed in the "primary" streak region. Downstream of the "primary" streaks the flow begins to break down to smaller scales. The close-up in the middle in Fig. 12 clearly displays aligned lambda vortices, which are typical for a fundamental (K-type) breakdown. A snapshot (close-up on the right of Fig. 12) of one of the structures in the late nonlinear stages reveals the formation of a hairpin vortex.

The results presented in this paper demonstrate the capability of the random forcing approach to reproduce many of the characteristics of “natural” transition observed in the experiments, which previously could not be captured by the “controlled transition” simulations.

5 Conclusions

A random forcing approach was used to initiate the laminar-turbulent breakdown in a flared cone boundary layer at Mach 6. A quantitative comparison to experimental measurements showed reasonable agreement. In addition, the random forcing approach resulted in the same “hot” streak patterns on the surface of the cone as previously observed in experiments and for “controlled” fundamental breakdown DNS. The results showed that, without any bias towards any particular frequency or azimuthal wavenumber, the random forcing resulted in a typical fundamental resonance/breakdown scenario. Thus, the random forcing seems to be a viable model for investigating “natural” transition.

Acknowledgements This work was supported by AFOSR Grant FA9550-15-1-0265, with Dr. Ivett Leyva serving as the program manager. Computer time was provided by the DoD HPCMP. The views and conclusions contained herein are those of the authors and should not be interpreted as necessarily representing the official policies or endorsements, either expressed or implied, of the AFOSR or the U. S. Government. The authors would like to thank Steve Schneider and Brandon Chynoweth for fruitful discussions and for making all the experimental data and PSD post processing scripts readily available.

References

1. Schneider, S.: *Prog. Aerosp. Sci.* **72**, 17 (2015)
2. Schubauer, G., Skramstad, H.: NASA Report No. 909 (1948)
3. Fasel, H.: *J. Fluid Mech.* **78**, 355 (1976)
4. Rist, U., Fasel, H.: *J. Fluid Mech.* **298**, 211 (1995)
5. Fasel, H.F., Thumm, A., Bestek, H.: Fluids Engineering Conference. ASME (1993)
6. Hader, C., Fasel, H.: *J. Fluid Mech.* **847** (2018)
7. Chynoweth, B.: Measurements of transition dominated by the second-mode instability at Mach 6. Ph.D. thesis, Purdue University (2018)
8. Hader, C., Fasel, H.F.: *J. Fluid Mech.* **869**, 341 (2019)
9. Laible, A.C.: Numerical investigation of boundary layer transition for cones at Mach 3.5 and 6.0. Ph.D. thesis, The University of Arizona (2011)

Sensitivity of Boundary-Layer Stability and Transition to Thermochemical Modeling



H. L. Kline, C.-L. Chang, and F. Li

Abstract The presence of transitional flow in the hypersonic regime, and the difficulty of accurately predicting the point of transition, is a major source of uncertainty, particularly for predicting wall heating. Potential applications of improved hypersonic boundary layer stability and transition prediction include reentry vehicles, hypersonic transports, and defense applications. Boundary layer transition in these applications particularly impacts heat transfer, affecting material compliance and ablation rates, and potentially leads to either failure of the vehicle or reduced performance due to overdesigned heat shielding. Chemical and thermal nonequilibrium effects are relevant to hypersonic boundary layer stability and transition, where molecular dissociation, chemical reactions, and thermal nonequilibrium may occur. To accurately model the aerothermodynamics and boundary layer stability of such boundary layer flows, the chemical and thermal nonequilibrium effects can be taken into account in the mean flow and in the stability equations. The LAngley Stability and TRansition Analysis Code (LASTRAC) version 3.0 accommodates a variety of models for thermochemical and transport properties, and the gas model can be varied to either include or neglect chemical reactions and thermal nonequilibrium, independent of the mean flow solution. These capabilities are used to investigate the sensitivity of boundary layer stability and transition location with respect to a selection of parameters controlling the gas model, freestream conditions, and fluid properties.

H. L. Kline
National Institute of Aerospace, Hampton, VA 23666, USA
e-mail: kline.hl@gmail.com

C.-L. Chang (✉) · F. Li
NASA Langley Research Center, Hampton, VA 23681, USA
e-mail: chau-lyan.chang@nasa.gov

F. Li
e-mail: fei.li@nasa.gov

1 Introduction

Hypersonic boundary layer transition is critically important to hypersonic vehicle design due to its influence on heat transfer rates, aerodynamic forces, and flow separation. Under hypersonic conditions the temperature within the boundary layer may rise to a point where dissociation and chemical reactions occur. The presence of transitional flow, and the difficulty of accurately predicting the point of transition, is a major source of uncertainty, particularly for predicting heating [1] for hypersonic vehicles. This uncertainty leads to vehicle designs assuming fully-turbulent [2] flow which may lead to overdesigned heat shielding.

Chemical and thermal nonequilibrium are relevant to hypersonic conditions where the temperature within the boundary layer and behind strong shocks can rise above the point where molecular dissociation and chemical reactions will occur. At high enough temperatures, ionization reactions are possible, and in the case of ablative Thermal Protection Systems (TPS), the ablating material may react with the surrounding atmosphere. In order to accurately model the aerodynamics and boundary layer stability of this system, the chemistry effects must be taken into account. A number of analytical studies focusing on hypersonic boundary layer transition neglecting chemistry effects are available in the literature [3–7]. Experimental results that include chemistry effects are also available [8–11]. Boundary layer stability with equilibrium, chemical nonequilibrium, and thermochemical nonequilibrium gas has been compared computationally as well [12–15]. Direct Numerical Simulations (DNS) have also been used to analyze these circumstances [9, 16].

STABL-3D and PSE-Chem addresses thermochemical nonequilibrium boundary layer stability with linear parabolized stability equations (PSE) [12, 17–19]. The Langley Stability and Transition Analysis Code (LASTRAC) [20] includes nonlinear PSE capabilities and other tools such as adjoint PSE-based receptivity modules for calorically perfect (CP) and thermally perfect (TP) gases, and LASTRAC version 3.0 allows chemical nonequilibrium in thermal equilibrium (CNE), chemical and thermal equilibrium (CTE), and thermochemical nonequilibrium (TNE) air gas chemistry for PSE and LST on axisymmetric and two-dimensional geometries [15, 21, 22]. In this work we investigate the sensitivity of LST results to thermochemical nonequilibrium (TNE) and to other modeling parameters such as the freestream conditions, transport model, and reaction rates. PSE results are also included for comparison to literature.

2 Methodology

The development and further details of the nonequilibrium linear PSE and LST functionality in LASTRAC have been discussed in previous work by the authors [14, 15, 20–22], and their description will be omitted from this work for brevity. Section 2.1 describes the chemistry modeling in this work, the simulation case definition is

presented in Sect. 2.2, and the process of selecting appropriate factors to vary and analysis of variation in Sect. 2.3.

2.1 Chemical Rates and Thermodynamic Properties

Species production rates $\dot{\omega}_s$, transport properties viscosity and thermal conductivity, and thermodynamic quantities of specific heats and enthalpy are required, and numerous options exist to model each of these. Viscosity is modeled with polynomial fits, with a small difference between the mean flow viscosity model [23] and that used in LASTRAC [24] due to what had been implemented at the time. Thermal conductivity is modeled either with the polynomial fits, using the Eucken relation or with a constant Prandtl number. The Park correction factor [25] is added at high temperatures. Thermodynamic curve fits used in this work follow the Chemical Equilibrium with Applications (CEA) format, with the equations for specific heat, enthalpy, and entropy for each species from McBride et al. [26]. The constants for this curve fit are available from Ref. [27]. The modified Arrhenius equations are used to calculate reaction rates used to produce the species production rate $\dot{\omega}$, with the rate-controlling temperature T_c determined by the type of reaction. $T_c = \sqrt{T T_V}$ as used by Park [28, 29] for dissociation reactions and $T_c = T$ for heavy molecule collision reactions. In this work, coefficients for the Arrhenius reaction rate equations are taken from Refs. [30] or [31].

The vibrational-translational energy relaxation time $\tau_{s,j}$ for diatomic molecules of species s is found using Landau-Teller [32] theory using the characteristic temperature θ_j of each molecular vibrational mode j , with a collision cross-section correction by Park [25]. This relaxation time is used in the vibrational-translational energy equation, in a source term. The vibrational energy term, $e_{v,s} = \int_0^{T_V} C_{v,V}^s dT$, and this same term taken if the vibrational-electronic temperature was set equal to the translational-rotational temperature, $e_{v,s}^*$, are also calculated using the characteristic vibrational temperature. The vibrational specific heat $C_{v,V}^s$ can be expressed in terms of the energy mode characteristic temperatures as:

$$C_{v,V}^s = \frac{R_u}{M_s} \left(\frac{\theta_j}{T} \right)^2 \frac{e^{(-\theta_j/T)}}{\left(1 - e^{(-\theta_j/T)} \right)^2}, \quad (1)$$

where R_u is the universal gas constant and M_s is the species mass. Taking the integral to find the internal energy, for N_v vibrational modes with degeneracy g_j ,

$$\frac{e_{v,s}^* - e_{v,s}}{\tau_s} = \sum_{j=1}^{N_v} \frac{g_j \theta_j}{\tau_{s,j}} \frac{R_u}{M_s} \left(\left(e^{\left(\frac{\theta_j}{T} \right)} - 1 \right)^{-1} - \left(e^{\left(\frac{\theta_j}{T_V} \right)} - 1 \right)^{-1} \right), \quad (2)$$

The effects of ablation, ionization, and the presence of electron species are neglected in this work.

2.2 Mean Flow Conditions

From Ref. [33], we have a high-enthalpy straight 7-degree half-angle cone case with a 2.5-mm blunt nose, 1-m length, in air, with experimental results from two tunnels and stability results using NOLOT, a PSE code using perfect gas assumptions, with TNE mean flow. Selected experiment conditions from the Japan Aerospace Exploration Agency High Enthalpy Shock Tunnel (HIEST) and the DLR High Enthalpy Shock Tunnel Göttingen (HEG) are summarized in Table 1.

Mean flow solutions were generated for the cone using VULCAN [34, 35]. Mean flow gas modeling options used in this work include one- or two-temperature thermodynamics, species conductivity modeled with a constant Prandtl number or using a ‘McBride’ option, and chemical reactions as input by the user. The reaction rate sets used in this work follow either Park [36], or Dunn and Kang [31]/Gupta and Yos [37] values. The freestream conditions, Schmidt number, and Prandtl number are also varied in this work. Additional options are available but were not varied in this work, such as modeling choice for viscosity, which was the ‘McBride’ option for all cases in this work, or the data used in relaxation time between the vibrational-electronic temperature and the translational-rotational temperature. The stability solutions with LASTRAC used similar settings, except where Blottner’s curve fits for viscosity and thermal conductivity are used in the stability model instead of McBride. Previous experience [22] indicated negligible changes in growth rates when changing the viscosity model.

2.3 Design of Experiments

A fractional factorial design of resolution IV with 7 factors and 16 cases was designed using MATLAB®. This allows an analysis of the variation of the output with main effects unaliased from 2-factor interactions. Including more varied factors would

Table 1 Experimental conditions from Ref. [33]

Experiment	T_{wall} (K)	T_∞ (K)	ρ_∞ (kg/m ³)	M_∞
HEG high-enthalpy	293	1268	0.0171	6.09
HIEST high-enthalpy	297.73	1310	0.0175	6.09

require twice evaluating as many boundary layer stability analyses. The fractional factorial design is shown in Table 2.

Variables representing a mixture of freestream conditions, model parameters, and model assumptions were chosen to allow qualitative comparison between these various sources of uncertainty in transition location. Based on the variability between wind tunnel tests conducted at different facilities shown in Table 1, freestream temperature and density were chosen as representing variation in freestream conditions. Species mass fractions are also included as these were not listed explicitly in the experimental conditions, and as their freestream values are sensitive to other quantities such as reaction rates and nozzle conditions. The wall temperature was not included as this has been addressed in previous work for other conditions [15]. Limiting this study to 16 cases, only two options are used for each factor, and these are shown in Table 3. Variation in the Schmidt number, the thermal conductivity model, and reaction rates, were included as representative of the many options available for modeling gas properties. Work in the literature thoroughly surveys a number of the gas modeling options that have been used in boundary layer stability analyses [38, 39]. The factors chosen are by no means an exhaustive list—a number of other possibilities, including the coefficient values within the reaction rate sets, within the polynomial fits for thermal conductivity and/or viscosity, and within the model for relaxation time, would be reasonable to include in future studies.

In order to quantify the effects of a number of different factors that may otherwise be difficult to separate, we use an analysis of variation technique more traditionally applied to experimental results. The theory behind Analysis of Variation with N factors (ANOVAN or N-way ANOVA), is described further in Matlab documentation [40], as well as in numerous statistics texts. Equation 3 defines the F -statistic for a set of observations y_{ij} varying two factors, where \bar{y}_j is the mean of all observations with setting j of the second factor, \bar{y} is the mean of all observations, and y_{ij} is an observation at setting i of the first factor and setting j of the second factor. The equation for two factors,

$$F = \frac{\text{sum of squares due to between-group effects}}{\text{sum of squared errors}} = \frac{\sum_j n_j (\bar{y}_j - \bar{y})^2}{\sum_i \sum_j (y_{ij} - \bar{y}_j)^2}, \quad (3)$$

can easily be extended to an arbitrary number of factors. The replication n_j is one in all cases.

3 Results

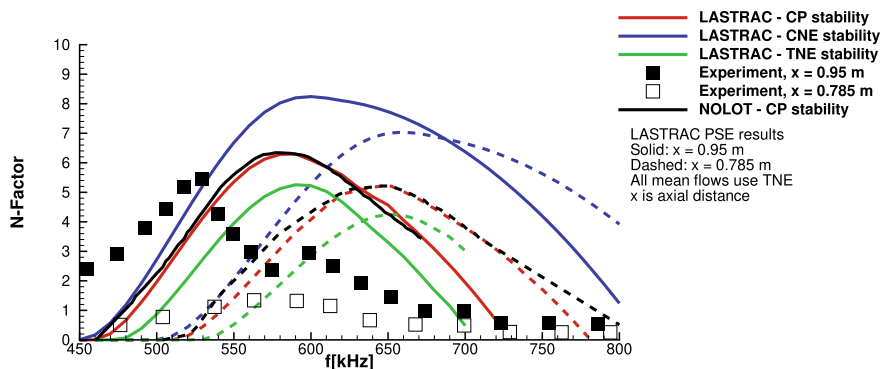
Mean flow solutions were generated using VULCAN [34, 35] at nominal conditions for the high-enthalpy HEG case using thermochemical nonequilibrium. PSE results using a mean flow at nominal HEG wind tunnel conditions as listed in Table 1, and LASTRAC settings of either CP, CNE, or TNE models, are shown in Fig. 1. Scanned

Table 2 Fractional factorial design, resolution IV with 7 factors and 16 experiments

Case #	00	01	02	03	04	05	06	07	08	09	10	11	12	13	14	15
T_∞	-1	-1	-1	-1	-1	-1	-1	-1	1	1	1	1	1	1	1	1
ρ_∞	-1	-1	-1	-1	1	1	1	-1	-1	-1	-1	1	1	1	1	1
Gas mix	-1	-1	1	1	-1	1	1	-1	-1	1	1	-1	-1	1	1	1
Schmidt #	-1	1	-1	1	-1	1	-1	1	-1	1	-1	1	-1	1	-1	1
Conductivity	-1	1	-1	1	-1	1	-1	1	-1	1	-1	1	-1	1	-1	1
TNE or CNE	-1	1	-1	-1	1	1	-1	1	-1	1	-1	1	-1	1	-1	1
Reaction rates	-1	1	-1	1	1	-1	1	-1	1	-1	1	-1	-1	-1	-1	-1

Table 3 Level settings for the 7 factors varied

Factor Level	T_∞ (K)	ρ_∞ (kg/m^3)	Gas Mixture	Schmidt #	Conductivity	TNE or CNE	Reaction rates
-1	1250	0.0171	0.78 N_2 0.22 O_2	0.7	McBride	CNE	[36]
+1	1350	0.0181	0.77 N_2 0.21 O_2 0.01 O 0.01 N	0.72	$\text{Pr} = 0.71$	TNE	[37]

**Fig. 1** Comparison of LASTRAC results with similar settings to NOLOT solution for HEG-High-E case

results from Ref. [33] are included for reference. As shown in this figure, the results using a CP model with LASTRAC match closely to the NOLOT results, which were also conducted with perfect gas assumptions. The difference between TNE and CP stability is larger in our work than shown in Ref. [33], which concluded that the TNE and CP results were close enough to reasonably use the CP stability equations.

Figure 2 illustrates the results of the cases with varied factor settings as described in Sect. 2.3, superimposed on the NOLOT and experimental results shown previously. None of the factor combinations align with the experimental results, although some show a shift in the peak frequency, which indicates that values outside of the tested range may result in matching the peak frequency value. Figure 3 illustrates the N-Factor envelopes for each case, as well as the maximum and minimum transition locations for the groups of cases using the CNE and the TNE models, respectively. We can see from these plots that the choice of thermochemical model has a strong effect on the transition location that outweighs the differences caused by changing other factors. The variation between the cases that used the CNE model is larger than that among the cases that used the TNE model. This indicates that the outcome is more sensitive to the other factors when using the CNE model.

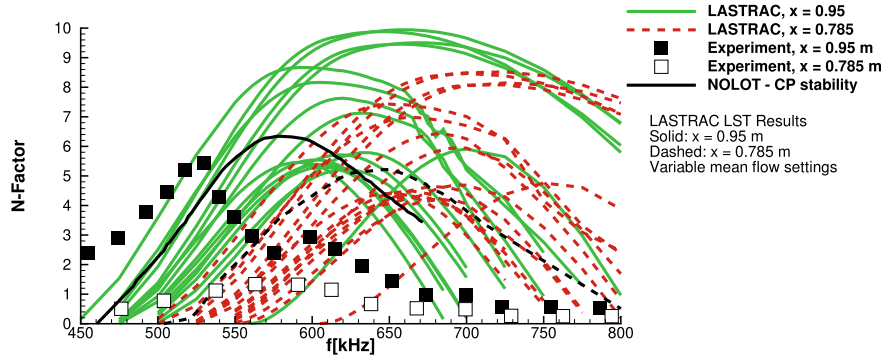


Fig. 2 Effect of varying mean flow inputs

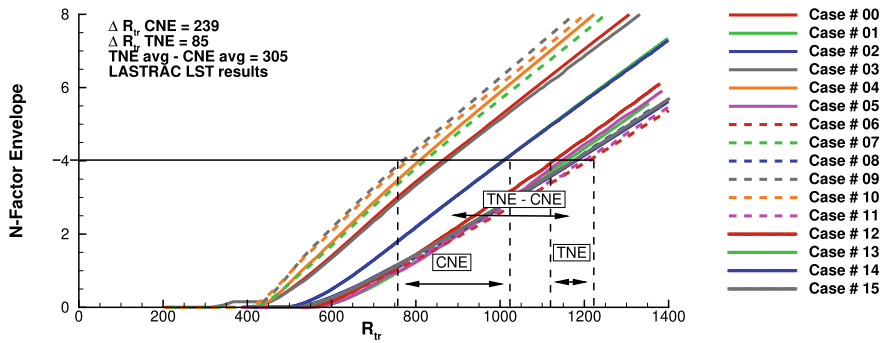


Fig. 3 The effect of varying mean flow inputs on the N-Factor envelopes and transition locations in terms of the Reynolds number based on characteristic boundary layer length, $\ell u_e / v_e = \sqrt{s u_e / v_e}$

3.1 Analysis of Variation

The transition locations illustrated in Fig. 3 were extracted and then processed along with the factor settings using MATLAB[®] ANOVAN analysis. The F -statistic, defined in Eq. 3, is used here to quantify the influence of the different factors varied. A larger F -statistic indicates a more significant factor, and the three most significant factors are highlighted in Table 4. The choice of TNE or CNE is the largest effect, confirming what we could observe visually in Fig. 3. The modeling parameters overall have a more significant effect than the freestream conditions, specifically through the conductivity model and the TNE/CNE choice. The freestream density, however, is not far behind in the third most significant factor. Both the Schmidt number and the reaction rate set show a less significant effect on the transition location, although there is an argument that both of these terms could have been varied more broadly—

Table 4 Factor ranges and F-Statistic output for R_{tr}

Variable	T_∞ (K)	ρ_∞ (kg/m ³)	Gas Mixture	Schmidt #	Conductivity	TNE or CNE	Reaction rates
F-Statistic	0.5283	1.607	0.6526	5.92E-04	7.386	100.6	0.0887

with a larger range of change in the Schmidt number as conducted by Ref. [8], or a variation in the reaction rate coefficients rather than a binary choice of the reaction rate sets.

4 Conclusions

In this work, we examined the sensitivity of a single case against several factors including modeling choices such as TNE or CNE, model parameters such as reaction rate coefficients, and freestream conditions such as temperature and density. Among the varied mean flow factors, the gas thermodynamic model (TNE or CNE) was the most significant, followed by the species thermal conductivity model, and the freestream density. Matching the gas model to capture appropriate physical phenomena, and modeling the thermodynamic coefficients such as conductivity accurately, are expected to have at least as significant an effect as matching the freestream conditions.

Acknowledgements This work was funded under NASA contract number NNL13A08B, task orders NNL17AA56T and 80LARC18F0084, supported by the Hypersonics Technology Project in the NASA Aeronautics Mission Directorate. I would also like to thank Pedro Paredes, Robert Baurle, Kyle Thompson, Elizabeth Lee-Rausch, and Jeff White for their input and fruitful discussions.

References

1. Bose, D., Brown, J.L., Prabhu, D.K., Gnoffo, P., Johnston, C.O., Hollis, B.: Uncertainty assessment of hypersonic aerothermodynamics prediction capability. *J. Spacecr. Rocket.* **50**(1), 12–18 (2013). <https://doi.org/10.2514/1.A32268>. January
2. Edquist, K.T., Hollis, B.R., Johnston, C.O., Bose, D., White, T.R., Mahzari, M.: Mars science laboratory heat shield aerothermodynamics: design and reconstruction. *J. Spacecr. Rocket.* **51**(4), 1106–1124 (2014). <https://doi.org/10.2514/1.A32749>. July
3. Zanù, L., Miró Miró, F., Pinna, F.: Nonlinear parabolized stability analysis of hypersonic flows in presence of curvature effects. In: 2018 AIAA Aerospace Sciences Meeting, AIAA SciTech Forum (AIAA Paper 2018-2087), January 2018 (2018). <https://doi.org/10.2514/6.2018-2087>
4. Unnikrishnan, S., Gaitonde, D.V.: Kovasznay-type analysis of transition modes in a hypersonic boundary layer. In: 2018 AIAA Aerospace Sciences Meeting, AIAA SciTech Forum (AIAA Paper 2018-2086), January 2018 (2018). <https://doi.org/10.2514/6.2018-2086>

5. Lakebrink, M.T., Paredes, P., Borg, M.P.: Toward robust prediction of crossflow-wave instability in hypersonic boundary layers. *Comput. Fluids* **144**, 1–9 (2017). <https://doi.org/10.1016/j.compfluid.2016.11.016>
6. Moyes, A.J., Paredes, P., Kocian, T.S., Reed, H.L.: Secondary instability analysis of crossflow on a hypersonic yawed straight circular cone. *J. Fluid Mech.* **812**, 370–397 (2017). <https://doi.org/10.1017/jfm.2016.793>
7. Chang, C.-L., Choudhari, M., Hollis, B., Li, F.: Transition analysis for the Mars Science Laboratory entry vehicle. In: 41st AIAA Thermophysics Conference (AIAA Paper 2009-4076) (2009). <https://doi.org/10.2514/6.2009-4076>
8. Miró Miró, F., Pinna, F., Beyak, E.S., Barbante, P., Reed, H.L.: Diffusion and chemical non-equilibrium effects on hypersonic boundary-layer stability. In: 2018 AIAA Aerospace Sciences Meeting, AIAA SciTech Forum (AIAA Paper 2018-1824), January 2018 (2018). <https://doi.org/10.2514/6.2018-1824>
9. Knisely, C.P., Zhong, X.: Supersonic modes in hot-wall hypersonic boundary layers with thermochemical nonequilibrium effects. In: 2018 AIAA Aerospace Sciences Meeting, AIAA SciTech Forum (AIAA Paper 2018-2085), January 2018 (2018). <https://doi.org/10.2514/6.2018-2085>
10. Wang, X.: Passive control of hypersonic non-equilibrium boundary layers using regular porous coating. In: 47th AIAA Fluid Dynamics Conference, AIAA AVIATION Forum (AIAA Paper 2017-4519), June 2017 (2017). <https://doi.org/10.2514/6.2017-4519>
11. Wang, X.: Non-equilibrium effects on the stability of a Mach 10 flat-plate boundary layer. In: 8th AIAA Theoretical Fluid Mechanics Conference, AIAA AVIATION Forum (AIAA Paper 2017-3162), June 2017 (2017). <https://doi.org/10.2514/6.2017-3162>
12. Johnson, H., Candler, G.: Hypersonic boundary layer stability analysis using PSE-Chem. In: 35th AIAA Fluid Dynamics Conference and Exhibit (AIAA Paper 2005-5023) (2005). <https://doi.org/10.2514/6.2005-5023>
13. Malik, M.R.: Hypersonic flight transition data analysis using parabolized stability equations with chemistry effects. *J. Spacecr. Rocket.* **40**(3), 332–344 (2003). <https://doi.org/10.2514/2.3968>
14. Chang, C.-L., Vinh, H., Malik, M.: Hypersonic boundary-layer stability with chemical reactions using PSE. In: 28th Fluid Dynamics Conference (AIAA Paper 1997-2012) (1997). <https://doi.org/10.2514/6.1997-2012>
15. Kline, H., Chang, C.-L., Li, F.: Hypersonic chemically reacting boundary-layer stability using LASTRAC. In: 2018 Fluid Dynamics Conference (AIAA Paper 2018-3699) (2018). <https://doi.org/10.2514/6.2018-3699>
16. Stemmer, C., Birrer, M., Adams, N.A.: Hypersonic boundary-layer flow with an obstacle in thermochemical equilibrium and nonequilibrium. *J. Spacecr. Rocket.* **54**(4), 899–915 (2017). <https://doi.org/10.2514/1.A32984>
17. Johnson, H., Candler, G.: PSE analysis of reacting hypersonic boundary layer transition. In: 30th Fluid Dynamics Conference (AIAA Paper 1999-3793) (1999). <https://doi.org/10.2514/6.1999-3793>
18. MacLean, M., Mundy, E., Wadhams, T., Holden, M., Johnson, H., Candler, G.: Comparisons of transition prediction using PSE-Chem to measurements for a shock tunnel environment. In: 37th AIAA Fluid Dynamics Conference and Exhibit (AIAA Paper 2007-4490) (2007). <https://doi.org/10.2514/6.2007-4490>
19. Johnson, H., Candler, G.: Analysis of laminar-turbulent transition in hypersonic flight using PSE-Chem. In: 36th AIAA Fluid Dynamics Conference and Exhibit (AIAA Paper 2006-3057), June 2006 (2006). <https://doi.org/10.2514/6.2006-3057>
20. Chang, C.-L.: Langley Stability and Transition Analysis Code (LASTRAC) Version 1.2 User Manual. NASA TM-2004-213233, NASA, June 2004 (2004). <https://ntrs.nasa.gov/search.jsp?R=20040082550>
21. Kline, H.L., Chang, C.-L., Li, F.: Boundary layer stability and transition in a chemically reacting martian atmosphere using lastrac. In: 22nd AIAA International Space Planes and Hypersonics Systems and Technologies Conference (AIAA Paper 2018-5206) (2018). <https://doi.org/10.2514/6.2018-5206>

22. Kline, H., Chang, C.-L., Li, F.: Multiple boundary layer instability modes with nonequilibrium and wall temperature effects using lastrac. In: AIAA Aviation 2019 Forum (AIAA Paper 2019-2850) (2019)
23. McBride, B.J., Gordon, S., Reno, M.A.: Coefficients for calculating thermodynamic and transport properties of individual species. NASA TM- 4513, NASA (1993)
24. Blottner, F.G., Johnson, M., Ellis, M.: Chemically reacting viscous flow program for multi-component gas mixtures. SC-RR- 70-754, Sandia Labs., Albuquerque, NM (1971). <https://doi.org/10.2172/4658539>
25. Park, C.: Problems of rate chemistry in the flight regimes of aeroassisted orbital transfer vehicles. In: AIAA, vol. 96, pp. 511–537 (1985). <https://ntrs.nasa.gov/search.jsp?R=19990067211>
26. McBride, B.J., Zehe, M.J., Gordon, S.: Nasa glenn coefficients for calculating thermodynamic properties of individual species. NASA TP- 2002-211556, NASA (2002). <https://ntrs.nasa.gov/search.jsp?R=20020085330>
27. Chemical equilibrium with applications (2016). <https://www.grc.nasa.gov/www/CEAWeb/>. Accessed 02 July 2018
28. Park, C.: Assessment of two-temperature kinetic model for ionizing air. *J. Thermophys. Heat Transf.* **3**(3), 233–244 (1989)
29. Park, C., Howe, J.T., Jaffe, R.L., Candler, G.V.: Review of chemical-kinetic problems of future NASA missions. II - Mars entries. *J. Thermophys. Heat Transf.* **8**(1), 9–23 (1994). <https://doi.org/10.2514/3.496>
30. Park, C., Howe, J., Jaffe, R., Candler, G.: Chemical-kinetic problems of future NASA missions. In: 29th Aerospace Sciences Meeting (AIAA Paper 1991-464) (1991)
31. Dunn, M.G., Kang, S.: Theoretical and experimental studies of reentry plasmas. NASA CR-2232, NASA, April 1973 (1973). <https://ntrs.nasa.gov/search.jsp?R=19730013358>
32. Millikan, R.C., White, D.R.: Systematics of vibrational relaxation. *J. Chem. Phys.* **39**(12), 3209–3213 (1963). <https://doi.org/10.1063/1.1734182>
33. Wartemann, V., Wagner, A., Wagnild, R., Pinna, F., Miró Miró, F., Tanno, H., Johnson, H.: High-enthalpy effects on hypersonic boundary-layer transition. *J. Spacecr. Rocket.* **56**(2), 347–356 (2018). <https://doi.org/10.2514/1.A34281>
34. White, J.A., Morrison, J.H.: Pseudo-temporal multi-grid relaxation scheme for solving the parabolized Navier-Stokes equations. In: 14th Computational Fluid Dynamics Conference (AIAA Paper 99-3360), June 1999 (1999). <https://doi.org/10.2514/6.1999-3360>
35. Baurle, R.A.: Analysis of facility thermodynamic non-equilibrium effects on HiFiRE ground tests. In: 2014 JANNAF CS/APS/PSHS Joint Meeting, December 2014 (2014)
36. Park, C.: Review of chemical-kinetic problems of future NASA missions. I-Earth entries. *J. Thermophys. Heat Transf.* **7**(3), 385–398 (1993). <https://doi.org/10.2514/3.431>
37. Gupta, R.N., Yos, J.M., Thompson, R.A., Lee, K.-P.: A review of reaction rates and thermodynamic and transport properties for an 11-species air model for chemical and thermal nonequilibrium calculations to 30000 K. NASA-RP- 1232, NASA (1990). <https://ntrs.nasa.gov/search.jsp?R=19900017748>
38. Miró Miró, F., Beyak, E.S., Mullen, D., Pinna, F., Reed, H.L.: Ionization and dissociation effects on hypersonic boundary-layer stability. In: 31st Congress of the International Council of the Aeronautical Sciences (2018)
39. Miró Miró, F., Beyak, E.S., Pinna, F., Reed, H.L.: High-enthalpy models for boundary-layer stability and transition. *Phys. Fluids* **31**(4), 044101 (2019). <https://doi.org/10.1063/1.5084235>
40. MATLAB. version 9.6.0 (R2019a). The MathWorks Inc., Natick, Massachusetts (2019)

Effects of Streaky Structures on the Instability of Supersonic Boundary Layers



Jianxin Liu, Elena Marensi, and Xuesong Wu

Abstract Streaky structures in the boundary layers are often generated by surface roughness elements and/or free-stream turbulence, and are known to have significant effects on boundary-layer instability. In this paper, we investigate the impact of two forms of streaks on the instability of supersonic boundary layers. The first concerns the streaks generated by an array of spanwise periodic and streamwise elongated surface roughness elements, and our interest is how these streaks influence the lower-branch viscous first modes, whose characteristic wavelength and frequency are on the classical triple-deck scales. By adapting the triple-deck theory in the incompressible regime to the supersonic one, we first derived a simplified system which allows for efficient calculation of the streaks. The asymptotic analysis simplifies a bi-global eigenvalue problem to a one-dimensional problem in the spanwise direction, showing that the instability is controlled at leading order solely by the spanwise-dependent wall shear. In the fundamental configuration, the streaks stabilize first modes at low frequencies but destabilize the high-frequency ones. In the subharmonic configuration, the streaks generally destabilize the first mode across the entire frequency band. Importantly, the spanwise even modes are of radiating nature, i.e. they emit acoustic waves spontaneously to the far field. Streaks of the second form are generated by low-frequency vortical disturbances representing free-stream turbulence. They alter the flow in the entire layer and their effects on instability are investigated by solving the inviscid bi-global eigenvalue problem. Different from the incompressible case, a multitude of compressible instability modes exists, of which the dominant mode is an inviscid instability associated with the spanwise shear. In

J. Liu

Department of Mechanics, Tianjin University, Tianjin, China
e-mail: shookware@tju.edu.cn

E. Marensi

Institute of Science and Technology (IST), Klosterneuburg, Austria
e-mail: elena.marensi@ist.ac.at

X. Wu (✉)

Department of Mathematics, Imperial College London, London, UK
e-mail: x.wu@ic.ac.uk

addition, there exists a separate branch of instability modes that have smaller growth rates but are spontaneously radiating.

1 Introduction

Instabilities of streaky boundary layers have been the focus of intense recent interest because of their important roles in laminar-turbulence transition. Depending on their strength and length scales, streaks may delay or promote the onset of transition by modifying the existing instability of the boundary layer or generating new instabilities. As a result, streaks may be deployed for flow control.

Streaky structures are often excited by physically realizable external disturbances, the most common of which are spanwise isolated or periodic surface roughness elements [1–3] and free-stream turbulence [4–6]. In response to these perturbations, streaks (i.e. regions of low and high speeds along the spanwise direction) arise in the boundary layer. In either case, the base flow then becomes three-dimensional. Typically, the streaks have a much longer lengthscale in the streamwise direction than those in the transverse directions so that the streamwise velocity dominates over the other two velocity components. The streamwise velocity is strongly sheared in both the wall-normal and spanwise directions, y and z . This characteristic makes the instability of the streaks bi-global, and thus the bi-global instability analysis methodology must be adopted in general.

Two related questions are of interest: how streaks influence existing instabilities in the original two-dimensional boundary layer, and whether or what new instability the streaks may induce. In the incompressible regime, experiments indicate that streaks tend to enhance the existing viscous Tollmien-Schlichting instability, and at a sufficiently large amplitude cause new inviscid instability [1, 3, 6].

Possible stabilizing effects of streaks have been reported, but the evidence had been rather limited and circumstantial until the detailed experimental investigations by Fransson et al. [7–9]. Using suitable forms of surface roughness elements, they managed to generate streaks of significant amplitude yet still below the threshold for causing inviscid secondary instability, and showed that such streaks can indeed stabilize the T-S waves appreciably. The possibility of stabilisation was confirmed by solving the finite-Reynolds-number version of the bi-global eigenvalue problem [10, 11]. Recently, Kaita and Wu [12] took a high-Reynolds-number asymptotic approach and investigated the generation of streaks by arrays of spanwise periodic, streamwise elongated roughness elements and their impact on the lower-branch T-S waves. The self-consistent asymptotic approximation simplified the bi-global stability problem to a one-dimensional eigenvalue problem in the spanwise direction, and showed that the instability of the streaky boundary layer was controlled at leading order by the spanwise-dependent wall shear. The theoretical result indicates that streaks inhibit planar and weakly oblique T-S modes in the typical frequency band of the lower-branch instability, but destabilize high-frequency modes as well as strongly oblique

modes. The first task of the present study is to extend the work of Kaita and Wu [12] to the supersonic regime.

The second problem to be investigated is concerned with the instability of the streaky boundary layer that forms under the influence of elevated level of low-frequency vortical disturbances, which represent the most relevant components in the free-stream turbulence [6]. The appropriate mathematical theory for predicting the streaks was formulated by Ricco et al. [13] for the incompressible case and that work was extended by Marensi et al. [14] to the compressible case including both sub- and super-sonic regimes. Ricco et al. [13] also showed that in the incompressible case, inviscid instability occurs when the free-stream disturbance intensity exceeds a certain threshold. The impact of such streaks on supersonic boundary layer instability remains unknown, and will be investigated in this paper. Specifically, the influence of streaks on the existing first mode in a two-dimensional boundary layer will be discussed. Furthermore, possible new instabilities will be sought.

2 Effect of Roughness-Induced Streaks on Viscous First-Mode Instability

In a supersonic boundary layer, a lower-branch viscous first mode can be viewed as a continuation of a T-S mode in the incompressible case, and like the latter, is also described by the triple deck theory, as was shown by Smith [15, 16]. In order to influence the first-mode instability effectively, the streaks and hence the roughness should have the spanwise lengthscale λ_z on the triple-deck scale. The streamwise lengthscale λ_x is taken to be elongated; this assumption is line with experiments but is invoked here so that the mathematical theories describing the streaks and their impact on instability become possible. The scalings are thus $\lambda_z = O(\text{Re}^{-3/8}L)$ and $\lambda_x \gg \lambda_z$, where L is the distance from the leading edge to the roughness centre, and Re the Reynolds number based on L . The additional parameter is the free-stream Mach number M , which is assumed to be greater than unity ($M > 1$). The shape of the roughness is expressed as $Y = hF(X, Z)$, where the coordinates X , Y and Z , and the roughness height h are suitably scaled in a similar manner as in Kaita and Wu [12]. The equations governing the streaky base flow read [12],

$$\frac{\partial U}{\partial X} + \frac{\partial V}{\partial Y} + \frac{\partial W}{\partial Z} = 0, \quad (1)$$

$$\left[U \frac{\partial}{\partial X} + V \frac{\partial}{\partial Y} + W \frac{\partial}{\partial Z} \right] U = \frac{\partial^2 U}{\partial Y^2}, \quad (2)$$

$$\left[U \frac{\partial}{\partial X} + V \frac{\partial}{\partial Y} + W \frac{\partial}{\partial Z} \right] W = - \frac{\partial P}{\partial Z} + \frac{\partial^2 W}{\partial Y^2}, \quad (3)$$

where

$$P(X, Z) = \frac{h}{\pi} \int_{-\infty}^{\infty} \frac{\partial^2 F(X, \zeta)}{\partial X^2} \ln |Z - \zeta| d\zeta. \quad (4)$$

Since the pressure is given by the roughness shape, this system of equations is parabolic and hence can be solved by a marching method with the appropriate boundary and matching conditions, which are, in terms of the rescaled variables, the same as in Kaita and Wu [12].

The lower-branch viscous first-mode instability in a compressible boundary layer is known to acquire the standard triple-deck structure, that is, with L and the oncoming velocity as reference length and speed respectively, the characteristic streamwise and spanwise wavelengths are both of $O(\text{Re}^{-3/8})$, the characteristic frequency is $O(\text{Re}^{2/8})$, and the width of the lower deck is of $O(\text{Re}^{-5/8})$ [16]. Despite the fact that the streaky base flow becomes three-dimensional in the wall layer, the transverse dependence of the instability mode can be treated analytically for the elongated roughness elements under consideration. In particular, because the lower deck of the instability is much thinner than the wall layer of the streaky base flow, the spanwise-dependent wall shear $\lambda_u(Z)$ is the only quantity controlling the instability. After following the procedure in Smith and Walton [17] and Walton and Patel [18], the analysis of the lower-deck dynamics gives

$$\left(\frac{\partial^2}{\partial Z^2} - \frac{\lambda_u Z}{\lambda_u} \mathcal{G}(\eta_0) \frac{\partial}{\partial Z} - \alpha^2 \right) \hat{P}_1 - \frac{(i\alpha\lambda_u)^{5/3} \text{Ai}'(\eta_0)}{\kappa(\eta_0)} \hat{A}_1 = 0, \quad (5)$$

where

$$\mathcal{G}(\eta_0) = \frac{3}{2} + \frac{\eta_0}{2 \text{Ai}(\eta_0)} \left[\eta_0 \kappa(\eta_0) + \text{Ai}'(\eta_0) \right], \quad \kappa(\eta_0) = \int_{\eta_0}^{\infty} \text{Ai}(t) dt. \quad (6)$$

Note that the equation involves only the derivatives with respect to Z , and the instability is controlled solely by the wall shear $\lambda_u(Z)$.

Because the wall shear $\lambda_u(Z)$ is periodic in the spanwise direction, the mode can be written in the Floquet form,

$$\hat{\phi} = e^{iq\beta Z} \sum_{-\infty}^{+\infty} \hat{\phi}_n(y) e^{in\beta Z}, \quad (7)$$

where $\hat{\phi}$ represents either \hat{P}_1 or \hat{A}_1 , and q is the Floquet exponent. The cases with $q = 0$ and $1/2$ correspond to the fundamental and subharmonic parametric resonance respectively. Accordingly, the pressure disturbance in the upper deck is governed by the equation

$$\bar{p}_{n\bar{y}\bar{y}} - \left[\beta^2(q+n)^2 - \alpha^2(M^2 - 1) \right] \bar{p}_n = 0, \quad (8)$$

which reduces to that in Kaita and Wu [12] when $M = 0$. The analysis of the upper deck yields the pressure-displacement (P-A) relation as

$$A_n = \frac{1}{\alpha^2} [\beta^2(q + n)^2 - \alpha^2(M^2 - 1)]^{\frac{1}{2}} P_n. \quad (9)$$

Equations (5) and (9) form an eigenvalue problem, which is obviously one-dimensional and describes the dispersion relation of the original bi-global instability of the streaky boundary layer.

The upper-deck pressure Eq. (8) indicates that the disturbance is oscillatory and radiating in the normal direction if $\beta^2(q + n)^2 - \alpha^2(M^2 - 1) < 0$. Physically, a radiating mode emit sound waves to the far field. In the absence of streaks, i.e. the base flow is two-dimensional, $\bar{p}_n = 0$ for $n \neq 1$, and the constraint $\beta > \sqrt{M^2 - 1}\alpha$ is required for first mode instability to exist [16]; the first mode in the flat-wall case is non-radiating in the wall-normal direction. On the contrary, in the presence of streaks, the Fourier components with a lower spanwise wavenumber $n\beta$ may be spontaneously radiating. In particular for $q = 0$, if $\bar{p}_0 \neq 0$, then \bar{p}_0 is definitely oscillatory in the far field and thus the mode as a whole is radiating. This is a significant difference from the instability of incompressible streaky boundary layers.

In order to solve the eigenvalue problem numerically, the wall shear $\lambda_u(Z)$ can be written as $\lambda_u(Z) = \sum A_n \cos nZ$. In the following, a spatial case with only one component will be discussed, and the Mach number is taken to be $M = 1.5$.

The streaks are symmetric in the spanwise direction. It follows that the eigenfunction can be classified into two types: even (symmetric) and odd (anti-symmetric) modes. Figure 1a–c show the eigenfunction of an odd mode, which is nearly neutral. This odd mode is non-radiating because the $n = 0$ Fourier component is zero and $\beta > \sqrt{M^2 - 1}\alpha_r$, which ensures exponential attenuation of the $n = 1$ component in the far field. Figure 1d–f display the eigenfunction of a nearly neutral even mode. This mode is spontaneously radiating because $\bar{p}_0 \neq 0$.

Next, we examine how the streaks affect the first modes. To answer this question, we calculate their growth rates in the presence of streaks of increasing amplitude $A \equiv A_1$. Three representative frequencies are selected in each case of odd and even modes. The results for the fundamental resonance are presented in Fig. 2, where we plot the growth rate of the first-mode instability versus the streak amplitude A . The streaks stabilize significantly the first modes with low frequencies within the unstable band, but destabilize those with high frequencies. The streaks also destabilize decaying odd modes (which have low frequencies; see Fig. 2a) and even render them unstable when A becomes sufficiently large, but have only moderate effect on the decaying even modes (Fig. 2b).

Figure 3 shows the variation of the growth rate with the streak amplitude A for the subharmonic resonance. The streaks generally destabilize odd modes, of which decaying modes with low frequencies become unstable when A is large enough. The growth rate of unstable even modes is slightly reduced as A increases, while the decaying mode is farther attenuated before the trend reverses. The growth rate of the mode with high frequency $\omega = 4$ is about 0.0002–0.0003.

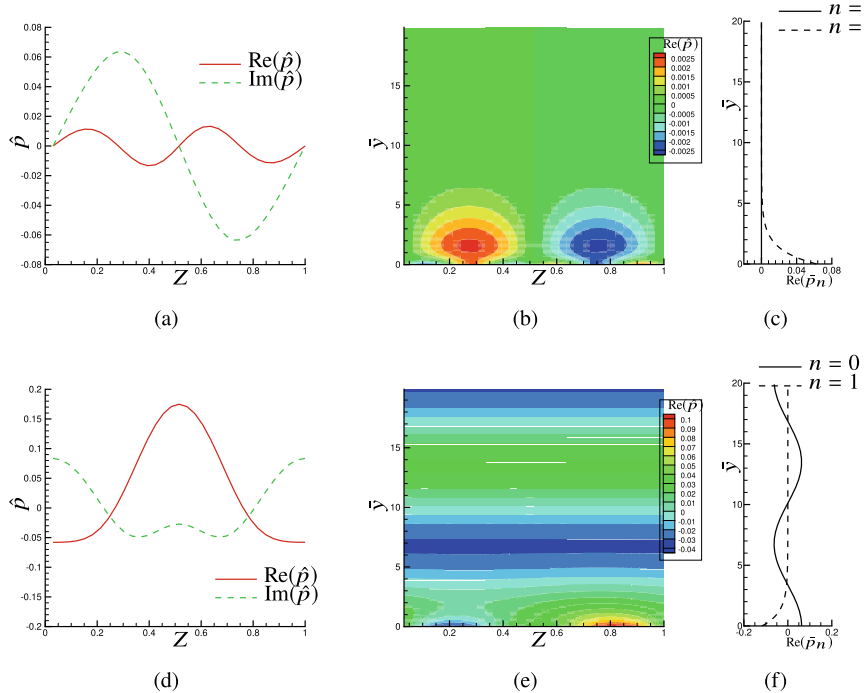


Fig. 1 The eigenfunctions of odd and even modes in the case of fundamental resonance. First row: odd mode with $\omega = 1.5$, $\beta = 1.0$, $\alpha = 0.497 + 0.0003i$; second row: even mode: $\omega = 1.32$, $\beta = 1.0$, $\alpha = 0.417 - 0.0001i$. Left column: spanwise distribution of the surface pressure; central column: contours of the upper-deck pressure in the (\bar{y}, Z) plane; right column: wall-normal profiles of the $n = 0, 1$ components in the upper-deck pressure

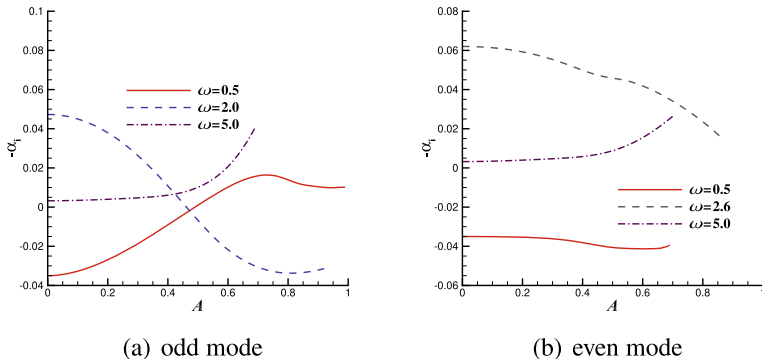


Fig. 2 The growth rate of first-mode instability versus the streak amplitude in the case of fundamental resonance ($\beta = 1.0$, $q = 0.0$)

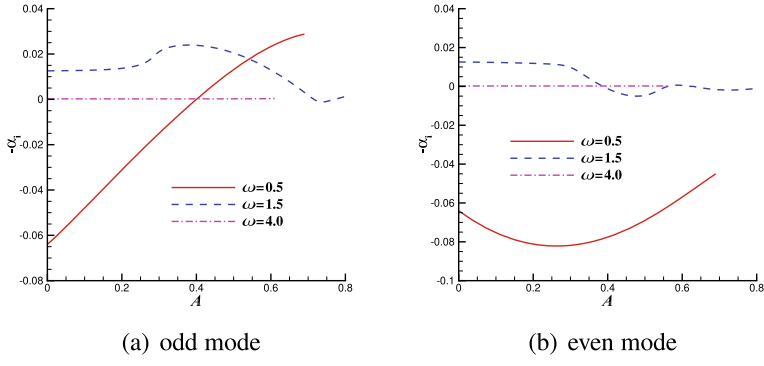


Fig. 3 The growth rate of first-mode instability versus the streak amplitude for subharmonic resonance ($\beta = 1.0$, $q = 0.5$)

3 Secondary Instability of Streaks Induced by Free-Stream Turbulence

We now consider the streaks induced by low-frequency (long-wavelength) free-stream vortical disturbances. As a simple representative, the latter are taken to be a pair of oblique components with the same frequency but opposite spanwise wavenumbers. The streaks are computed by solving the initial-boundary-value problem, consisting of the boundary-region equations and the appropriate initial and far-field conditions, which characterise properly the impact of free-stream disturbances on the boundary layer. The free-stream Mach number $M = 3$, and other parameters are chosen to mimic the flight conditions. The details can be found in Table 1 of Marenzi et al. [14]. Figure 4 displays the contours of the streamwise flux $\rho_b U_b$ and its wall-normal and spanwise gradients; here the streaks are slowly modulated in time, and a phase $\phi = \frac{4}{7}\pi$ is selected. It is clear that the streaky flow is strongly three dimensional and $\rho_b U_b$ have inflectional points in both the y and z directions, suggesting that inviscid bi-global instability may exist.

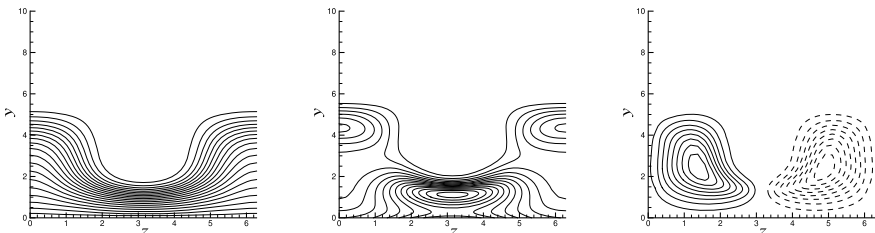


Fig. 4 Characteristics of the streaky boundary layer at $M = 3$ and $\phi = \frac{4}{7}\pi$. Left: streamwise flux $\rho_b U_b$; middle: wall-normal gradient $\partial(\rho_b U_b)/\partial y$; right: spanwise gradient $\partial(\rho_b U_b)/\partial z$

When the streaky base flow q_b is perturbed by disturbance q' , the total flow is $q_b + q'$. Since the streamwise variation and temporal modulation are both very slow, the streamwise and time variables in q_b can be treated as parameters. The disturbance in the bi-global instability of the streaks can be set as $q' = \hat{q}(y, z)e^{i(\alpha x - \omega t)} + c.c.$. After substituting into the N-S equations and simplifying, the inviscid bi-global instability equations can be written as:

$$[-\alpha^2(1 - \mathcal{M}^2) + \nabla_{yz}^2] \hat{p} - \frac{\partial}{\partial y} [\ln(\mathcal{M}^2)] \frac{\partial \hat{p}}{\partial y} - \frac{\partial}{\partial z} [\ln(\mathcal{M}^2)] \frac{\partial \hat{p}}{\partial z} = 0, \quad (10)$$

where $\mathcal{M} = M(U_b - c)/\sqrt{T_b}$ is the relative Mach number, with U_b and T_b being the streamwise velocity and temperature of the streaky base boundary layer. The quantity \mathcal{M} describes the compressibility of a disturbance relative to the local flow.

Inspecting the secondary instability Eq. (10), one may note two important characteristics. Firstly, when the local relative Mach number $|\mathcal{M}| > 1$, the disturbance is supersonic locally, and the inviscid Eq. (10) may admit compressible unstable modes, similar to the mechanism of the Mack modes in a two-dimensional supersonic flow. Secondly, when the relative Mach number in the free stream $|\mathcal{M}_\infty| = |M(1 - c)| > 1$, the disturbance is supersonic and oscillatory there, in which case the far-field boundary condition must be of $e^{-ik_y y}$ form instead of exponential attenuation, where $k_y = [\alpha^2(\mathcal{M}_\infty - 1)^2 - \beta^2]^{1/2}$. A new radiating instability mode may exist.

Discretisation of the inviscid bi-global instability Eq. (10) leads to a large scale eigenvalue problem in two dimensions. This equation is solved by START (stability and transition analysis and research toolkit), an in-house code developed at Tianjin University.

Numerical calculations indicate that there exist several families of bi-global instability modes. Figure 5 displays the instability characteristics of the four families, which are most unstable, and named modes 1, 2, 3 and 4.

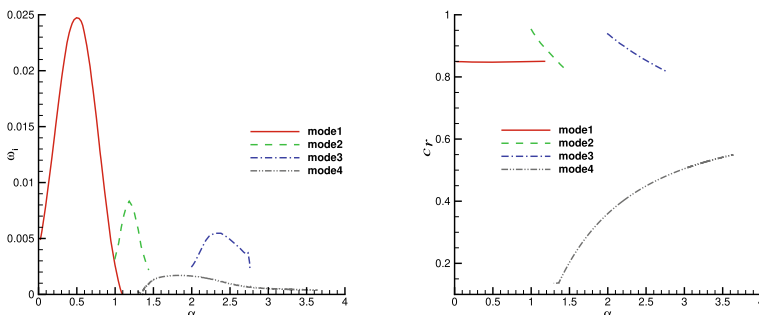


Fig. 5 Characteristics of inviscid bi-global instability. Left: temporal growth rate ω_i versus the wavenumber α ; right: phase velocity c_r versus the wavenumber α

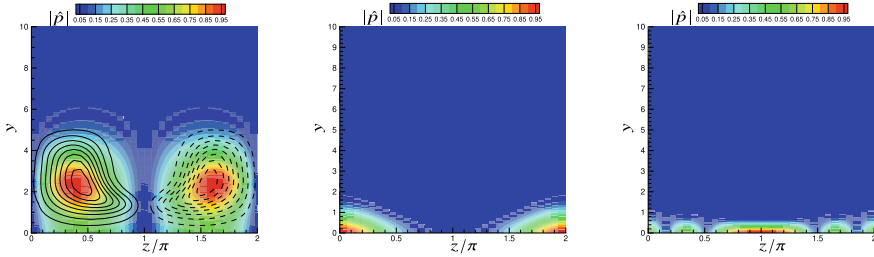


Fig. 6 Contours of the eigenfunctions $|\hat{p}|$ of mode 1 (left), mode 2 (middle) and mode 3 (right)

The mode-1 family consists of the most unstable modes, which have larger growth rates overall than other families. Interestingly, the phase velocities are almost constant, being approximately 0.85, which is close to the base-flow velocity at the point, where $\partial^2(\rho_b U_b)/\partial z^2 = 0$. Modes in this family are associated primarily with the shear whilst compressibility plays a secondary role. In order to trace the dominant mechanism of the instability, the contours of the eigenfunctions of a typical mode 1 (with wavenumber $\alpha = 0.5$ and the complex frequency $\omega = 0.4236 + 0.02479i$) are shown in the left panel of Fig. 6. The eigenfunction contours resemble those of the spanwise gradient of the streaky flow, $\partial(\rho_b U_b)/\partial z$, displayed in Fig. 4, suggesting that the spanwise shear is the dominant instability mechanism. Obviously, the mode is anti-symmetric mode. The peak value occurs near the location of $\partial^2(\rho_b U_b)/\partial z^2 = 0$.

The mode-2 and mode-3 families are similar to each other, but very different from the mode 1: their growth rates are lower compared to those in the mode-1 family, and their phase velocities exhibit significant variation with the frequency. Contours of the eigenfunctions $|\hat{p}|$ of the mode 2 and mode 3 are displayed in the middle and right panels of Fig. 6, respectively. Modes 2 and 3 concentrate in the near wall region, in stark contrast to mode 1, which resides close to the critical level. It thus appears that the instability of modes 2 and 3 is controlled by a rather different mechanism.

The difference between the mode 1 and mode 2 and mode 3 may be explained by inspecting the inviscid Eq. (10), the local property of which is determined by the coefficients of the second and zero-th order derivatives, which are in turn determined by the relative Mach number \mathcal{M} . The contours of the relative Mach number are displayed in Fig. 7. As is illustrated, there is a region near the wall where $\mathcal{M} < -1$, or in other words, the flow is relatively supersonic. The eigenfunction of the mode 2 (Fig. 6) concentrates in this region, suggesting that the mode 2 is caused by the compressible effect of the supersonic streaky flow, similar to the Mack mode in the two-dimensional case. Mode 3 is also trapped in this region, except that its eigenfunction changes its sign more than once within a spanwise period of the streaks. Both modes 2 and 3 represent a new instability which has no counterpart in incompressible streaky flows.

Finally, we consider mode 4, which has a considerably smaller growth rate than those of the other three families. Mode 4 stands as a separate branch, which can be traced neither to a counterpart in incompressible streaky flows, nor to that in

Fig. 7 Contours of \mathcal{M} for mode 2, where the dash lines represent the region where $\mathcal{M} < -1$

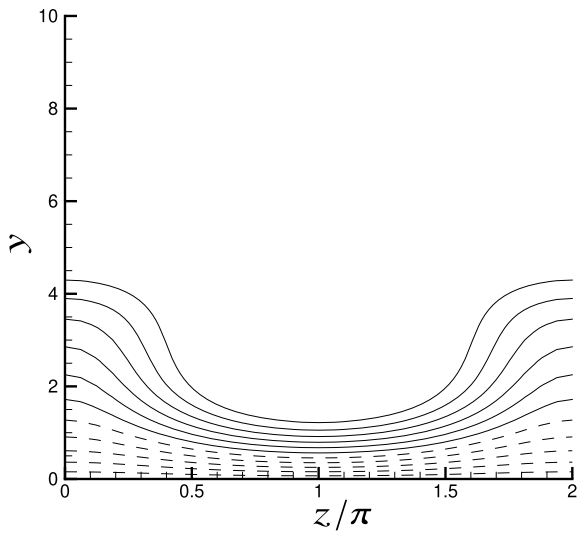
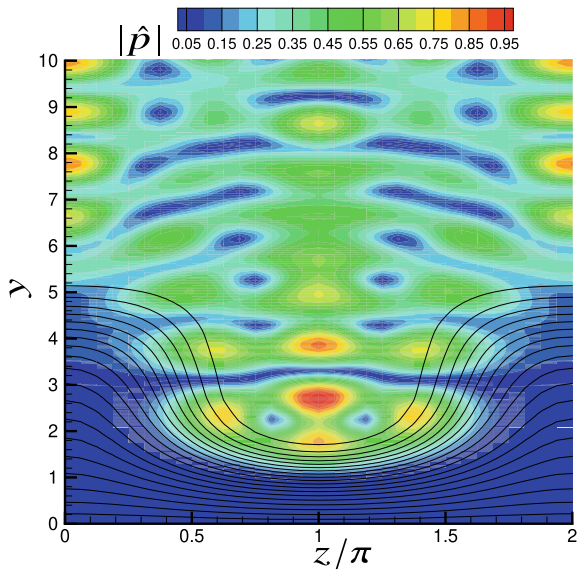


Fig. 8 Contours of the eigenfunction $|\hat{p}|$ of mode 4



the supersonic two-dimensional flow. Its eigenfunction contours are shown in Fig. 8, which indicates mode 4 is radiating spontaneously. This is consistent with the fact that at the onset of the instability its phase velocity is below $1 - 1/M$ (see Fig. 5), for which the relative Mach number $|\mathcal{M}| > 1$ in the free stream. Furthermore, the perturbation outside the boundary layer features ‘beating’ structures, caused by the superposition of components with different spanwise wavenumbers.

4 Summary and Conclusions

Streaks induced by surface roughness and free-stream turbulence play an important role in the laminar-turbulence transition of incompressible boundary layers. As streaks distort the original two-dimensional boundary layer into a three dimensional flow that is sheared in both the spanwise and wall-normal directions, the existing instability can be modified substantially and a new type of instability may arise. The present work investigated both scenarios in supersonic boundary layers. Specifically, we have demonstrated that the streaks induced by arrays of spanwise periodic and streamwise elongated surface roughness elements influence the lower-branch first mode through the fundamental and subharmonic parametric resonances. The streaks stabilize the low-frequency modes, but destabilize the high-frequency ones in the case of the fundamental resonance. A remarkable effect of streaks is that the even (symmetric) first mode is spontaneously radiating, i.e. it emits sound waves to the far field. In the subharmonic configuration, the streaks generally destabilize the first odd mode, but make the even mode slightly less unstable.

The streaks generated by low-frequency free-stream vortical disturbances were calculated by solving the appropriate initial-boundary-value problem, and their impact on instability was assessed by an inviscid bi-global instability analysis. Multiple families of unstable modes were found. The dominant mode is associated with the spanwise shear of the streaks. The second most unstable ones are two families of compressible modes, which are analogous to the Mack mode in a two-dimensional boundary layer. In addition, there exists a separate branch of modes, which have rather small growth rates but are of interest because they are spontaneously radiating.

Acknowledgements The work is supported by the National Key Research and Development Program of China (No. 2016YFA0401200), the National Natural Science Foundation of China (Grant Nos. 91952202 and 11402167).

References

1. Asai, M., Minagawa, M., Nishioka, M.: The instability and breakdown of a near-wall low-speed streak. *J. Fluid Mech.* **455**, 289–314 (2002)
2. White, E.B.: Transient growth of stationary disturbances in a flat plate boundary layer. *Phys. Fluids* **14**, 4429–4439 (2002)
3. Denissen, N.A., White, E.B.: Secondary instability of roughness-induced transient growth. *Phys. Fluids* **25**, 114108 (2013)
4. Klebanoff, P.S.: Effect of free-stream turbulence on a laminar boundary layer. *Bull. Am. Phys. Soc.* **16**, 1323 (1971)
5. Westin, K.J.A., Boiko, A.V., Klingmann, B.G.B., Kozlov, V.V., Alfredsson, P.H.: Experiments in a boundary layer subjected to free stream turbulence. Part 1. Boundary layer structure and receptivity. *J. Fluid Mech.* **281**, 193–218 (1994)
6. Matsubara, M., Alfredsson, P.H.: Disturbance growth in boundary layers subjected to free-stream turbulence. *J. Fluid Mech.* **430**, 149–168 (2001)

7. Fransson, J.H.M., Brandt, L., Talamelli, A., Cossu, C.: Experimental and theoretical investigation of the nonmodal growth of steady streaks in a flat plate boundary layer. *Phys. Fluids* **16**(10), 3627–3638 (2004)
8. Fransson, J.H.M., Brandt, L., Talamelli, A., Cossu, C.: Experimental study of the stabilization of Tollmien-Schlichting waves by finite amplitude streaks. *Phys. Fluids* **17**(5), 299–304 (2005)
9. Fransson, J.H.M., Talamelli, A., Brandt, L., Cossu, C.: Delaying transition to turbulence by a passive mechanism. *Phys. Rev. Lett.* **96**(6), 064501 (2006)
10. Piot, E., Casalis, G., Rist, U.: Stability of the laminar boundary layer flow encountering a row of roughness elements: biglobal stability approach and DNS. *Eur. J. Mech. B/Fluids* **27**, 684–706 (2008)
11. Siconolfi, L., Camarri, S., Fransson, J.H.M.: Stability analysis of boundary layers controlled by miniature vortex generators. *J. Fluid Mech.* **784**, 596–618 (2015)
12. Katai, C.B., Wu, X.: Effects of streamwise elongated and spanwise periodic surface roughness elements on boundary-layer instability. *J. Fluid Mech.* (2020). Accepted
13. Ricco, P., Luo, J., Wu, X.: Evolution and instability of unsteady nonlinear streaks generated by free-stream vortical disturbances. *J. Fluid Mech.* **677**, 1–38 (2011)
14. Maresni, E., Ricco, P., Wu, X.: Nonlinear unsteady streaks engendered by the interaction of free-stream vorticity with a compressible boundary layer. *J. Fluid Mech.* **817**, 80–121 (2017)
15. Smith, F.T.: On the non-parallel flow stability of the Blasius boundary layer. *Proc. R. Soc. Lond. A* **366**, 91–109 (1979)
16. Smith, F.T.: On the first-mode instability in subsonic, supersonic and hypersonic boundary layers. *J. Fluid Mech.* **198**, 127–153 (1989)
17. Smith, F.T., Walton, A.G.: Nonlinear interaction of near-planar TS waves and longitudinal vortices in boundary-layer transition. *J. Fluid Mech.* **36**, 262–289 (1989)
18. Walton, A.G., Patel, R.A.: On the neutral stability of spanwise-periodic boundary-layer and triple-deck flows. *Q. J. Mech. Appl. Math.* **51**(2), 311–328 (1998)

Sensitivity of Reacting Hypersonic Boundary Layers to n -periodic Surface Roughness



Athanasis T. Margaritis, Taraneh Sayadi, Olaf Marxen, and Peter J. Schmid

Abstract Successful design of aerospace missions requires accurate modelling of the physical phenomena in a hypersonic boundary layer. The behaviour of hypersonic boundary layers is strongly influenced by finite-rate thermochemical effects. These effects can be captured by including finite-rate thermochemistry models in computational tools. Such models are typically highly parametrised, introducing non-equilibrium features into the flow that generate significant uncertainty, which reflects on the output quantities of interest. The way such phenomena interact with solid boundaries and roughness is fundamentally unknown and the additional uncertainty is unquantifiable. In the present work, we propose the investigation of the linear response of n -periodic roughness arrays using an efficient mathematical framework. We extend an existing computational tool to investigate the effect of roughness, including real-gas and finite-rate chemistry effects by coupling with the Mutation++ library. The proposed framework allows to study efficiently and in parallel the linear flow response and wake synchronisation without the restricting idealised periodicity constraint. The results are extracted from reduced-order geometries using automatic linearisation tools. This framework can be potentially combined with sensitivity analysis tools to identify critical roughness configurations. In this paper, we provide the necessary background and present preliminary results for canonical flat plate hypersonic boundary layers.

A. T. Margaritis (✉) · P. J. Schmid
Imperial College London, London, UK
e-mail: a.margaritis@imperial.ac.uk

P. J. Schmid
e-mail: pjschmid@imperial.ac.uk

T. Sayadi
Sorbonne University, Paris, France
e-mail: taraneh.sayadi@upmc.fr

O. Marxen
University of Surrey, Guildford, UK
e-mail: o.marxen@surrey.ac.uk

1 Introduction

The evolution of aerospace missions has intensified the requirements for fundamental research in fluid dynamics at high speeds. In the hypersonic regime, multiple complexities arise in the physics of boundary layer transition. The effect of chemical reactions, especially near solid boundaries, has not yet been fundamentally explained [6, 10]. Two major objectives in hypersonics research [33] are the prediction of boundary layer stability and the description of flows in thermal and chemical non-equilibrium (TCNEQ).

Recent experimental progress is summarised in [34]. In the computational domain, to tackle this problem we need sophisticated numerical tools to extend common computational fluid dynamics (CFD) codes. Modelling TCNEQ effects is necessary, since the chemistry and energy exchange time scales become important. The importance of finite-rate phenomena in hypersonic flows has been reviewed by [2]. These phenomena are typically described by models that involve a large number of empirical parameters and significant uncertainty. Models based on first-principles are being developed and are expected to replace older models in the future [2]. Lower-fidelity models combined with sensitivity analysis may indicate parameters that need to be prioritised in further investigations.

Apart from finite-rate phenomena independently, additional complexity arises from the interaction of reacting flows with solid boundaries. Multiple gas-surface interaction phenomena occur, as described in [2, 4, 13], but they remain outside of the scope of this work. In this project, we investigate the behaviour of the developing boundary layer near a smooth or rough wall in the presence of hypersonic real-gas effects.

Even in the absence of roughness, transition in the hypersonic regime involves nonlinear mechanisms and includes strong 3D effects [30]. Extending concepts from subsonic and supersonic flow [11, 12] has proven partially successful. More recent work has looked into the chemistry and surface effects [20, 21, 21–23, 41, 42], in an effort to rank the significance of different physical phenomena for accurate flow simulations, concluding that many of these surface effects can be negligible under certain conditions compared to the chemical reactions in the fluid [21]. Similar work has been conducted by the group of Candler [7, 8, 26].

The majority of studies of roughness effects in hypersonic boundary layers treat the domains as periodic, investigating the effect of isolated roughness elements in the flow [14, 37, 38]. In this work, we attempt to extend existing direct numerical simulation (DNS) tools [24, 25] that have been used already to study hypersonic transition in the presence of chemical non-equilibrium (CNEQ) and roughness [15–18]. We couple our numerical solver with the Mutation++ library [36] to investigate reacting real-gas mixtures as well as traditional models. We verify our tests against previous results in the literature and present some preliminary results herein. The objective of this work is to provide a simple and efficient framework to investigate realistic types of roughness without the commonly used assumptions of single-unit periodicity, while maintaining accurate flow physics models. We present the background

for an efficient mathematical formulation to study n -periodic roughness arrays. We suggest an automated linearisation procedure that is independent of the thermophysical models and boundary conditions. To investigate the potential wake interaction and synchronisation behind roughness elements, we are able to decouple the system to smaller subsystems that can be studied in parallel. This framework has the potential to be combined with efficient adjoint-based sensitivity analysis and optimisation tools [3].

2 Theoretical Background

2.1 Governing Equations and Modelling Approaches

The nondimensional Navier–Stokes equations are modified as presented in Eqs. (1)–(4). For a non-reacting mixture, for example a calorically perfect gas (CPG) or thermally perfect gas (TPG) model, or a reacting mixture in local thermodynamic equilibrium (LTE), only the global mass conservation, Eq. (1), is needed; the species mass conservation, Eq. (2), is not necessary. In the case of a finite-rate reacting mixture, where the composition needs to be tracked, Eq. (1) is solved together with Eq. (2) for all but one species s . Another approach is to solve Eq. (2) for all species, and maintain the redundant Eq. (1) as a test to verify that global mass conservation is respected. The omitted species is selected based on numerical considerations, paying attention not to omit species with negligible concentrations or species that play a critical role in slow reactions. For gases in thermal non-equilibrium (TNEQ), additional energy conservation equations are needed; these cases are not investigated in the current research, since it is expected that CNEQ effects are dominant.

$$\frac{\partial \rho}{\partial t} + \nabla \cdot (\rho \mathbf{u}) = 0 \quad (1)$$

$$\frac{\partial \rho_s}{\partial t} + \nabla \cdot (\rho_s \mathbf{u} + \rho_s \mathbf{V}_s) = \omega_s, \quad \forall s \in \mathcal{S} \quad (2)$$

$$\frac{\partial \rho \mathbf{u}}{\partial t} + \nabla \cdot (\rho \mathbf{u} \otimes \mathbf{u}) = -\nabla p + \nabla \cdot \mathbf{T} \quad (3)$$

$$\frac{\partial \rho e_0}{\partial t} + \nabla \cdot (\rho h_0 \mathbf{u}) = \nabla \cdot (\mathbf{T} \cdot \mathbf{u}) - \nabla \cdot \mathbf{q} \quad (4)$$

In the above equations, the nondimensional quantities are the time, t , the density, ρ , the velocity, \mathbf{u} , the pressure, p , the stress tensor, \mathbf{T} , the total energy, e_0 , the total enthalpy, h_0 , the heat flux, \mathbf{q} , and the partial density, ρ_s , the net mass production rate, ω_s , and the diffusion velocity, \mathbf{V}_s , for the species s . More details regarding the derivation and the validity of the equations and the available modelling approaches are provided in the textbook by Anderson [1] and comprehensive reviews [5, 9].

The Eqs. (1)–(4) can be brought in the following compact form, seen in Eqs. (5) and (6).

$$\frac{\partial \mathbf{Q}}{\partial t} = \mathbf{F}(\mathbf{Q}) = -\nabla \cdot \mathbf{F}_C + \nabla \cdot \mathbf{F}_D + \mathbf{S} \quad (5)$$

$$\mathbf{Q} = \begin{bmatrix} \rho \\ \rho_s \\ \rho \mathbf{u} \\ \rho e_0 \end{bmatrix}, \quad \mathbf{F}_C = \begin{bmatrix} \rho \mathbf{u} \\ \rho_s \mathbf{u} \\ \rho \mathbf{u} \otimes \mathbf{u} + p \\ \rho h_0 \mathbf{u} \end{bmatrix}, \quad \mathbf{F}_D = \begin{bmatrix} 0 \\ -\rho_s \mathbf{V}_s \\ \mathbf{T} \\ \mathbf{T} \cdot \mathbf{u} - \mathbf{q} \end{bmatrix}, \quad \mathbf{S} = \begin{bmatrix} 0 \\ \omega_s \\ 0 \\ 0 \end{bmatrix} \quad (6)$$

In the following, the terms in their nondimensional notation are presented. The quantities are nondimensionalised using $\tilde{T}_{\text{ref}} = (\tilde{\gamma}_{\infty} - 1)\tilde{T}_{\infty}$ for temperature, $\tilde{\rho}_{\infty}$ for densities, $\tilde{\rho}_{\infty}\tilde{c}_{\infty}^2$ for the pressure, energy, and enthalpy where the speed of sound is denoted c , \tilde{k}_{∞} for thermal conductivity, $\tilde{\mu}_{\infty}$ for viscosity, $\tilde{\rho}_{\infty}\tilde{c}_{\infty}/\tilde{L}_{\text{ref}}$ for mass production rates, and $\tilde{\mathbf{c}}_{\infty}$ for velocities. The notation $(\tilde{\cdot})_{\infty}$ refers to free stream dimensional values.

We define the nondimensional total energy, $e_0 = \frac{e}{E_c} + \frac{1}{2}||\mathbf{u}||^2$, internal enthalpy, $h = e + \frac{p}{\rho}$, and total enthalpy, $h_0 = e_0 + \frac{p}{\rho}$, respectively. The nondimensional internal gas energy is denoted e . We also define here the viscous stress tensor, $\mathbf{T} = \frac{\mu}{Re}(\nabla \mathbf{u} + (\nabla \mathbf{u})^T - (\nabla \cdot \mathbf{u})\mathbb{I})$, and heat flux, $\mathbf{q} = -\frac{k}{RePrEc}\nabla T + \sum_{s \in S} \rho_s h_s \mathbf{V}_s$.

The nondimensional thermal conductivity, k , and viscosity, μ , are appropriately computed for different thermophysical models. For CPG, energy is proportional to temperature, the thermal conductivity is considered constant and the viscosity follows Sutherland's law [15]. For TPG, energy is a nonlinear function of temperature, the thermal conductivity follows Keyes' law and the viscosity follows Sutherland's law [15]. For LTE and CNEQ, we use the Mutation++ library to compute all properties using statistical mechanics and the kinetic theory of gases [35, 36]. The nondimensional numbers are defined in the free stream at the domain inlet. We define the nondimensional numbers Reynolds, $Re = \frac{\tilde{\rho}_{\infty}\tilde{c}_{\infty}\tilde{L}_{\text{ref}}}{\tilde{\mu}_{\infty}}$, Prandtl, $Pr = \frac{\tilde{\mu}_{\infty}\tilde{c}_{\infty}}{\tilde{k}_{\infty}}$, and

Eckert, $E_c = \frac{\tilde{c}_{\infty}^2}{\tilde{c}_{\rho \infty}\tilde{T}_{\text{ref}}} \equiv 1$. In the heat flux, the second term is included only in the case of CNEQ. Barodiffusion, thermodiffusion, and radiation are neglected in all cases. The nondimensional equation of state for non-reacting mixtures of fixed composition is $p = \rho \frac{\gamma-1}{\gamma E_c} T$, where the molar mass and the gas constant do not vary. This formulation is valid in this form for the CPG and TPG models. In the case of reacting mixtures, the right hand side needs to be scaled by a factor accounting for the change of gas constant. For CNEQ, the mass diffusion terms and the mass production terms are computed by Mutation++ using the Stefan-Maxwell diffusion equations and Arrhenius chemical kinetics rates equations [27, 28], respectively.

2.2 Linearised Analysis

We provide a short description of the methodology for linearisation. Linearisation of the flow around a base flow is used to study its stability behaviour. The flow quantities are separated to mean values and small perturbations around the mean, $\mathbf{Q} = \bar{\mathbf{Q}} + \mathbf{Q}'$. By substituting this into Eq. (5) and keeping only the first order terms, one gets the result in Eq. (7), where the Jacobian matrix is defined as $\mathbf{A} \equiv \left. \frac{\partial F}{\partial \mathbf{Q}} \right|_{\mathbf{Q}=\bar{\mathbf{Q}}}$.

$$\frac{\partial \mathbf{Q}'}{\partial t} \approx \mathbf{A} \cdot \mathbf{Q}' \quad (7)$$

There are various types of analysis appropriate for linearised systems in the form of Eq. (7). Due to the large size of the matrix \mathbf{A} in practical fluids problems, it is prohibitive to store and manipulate. It is preferable to manipulate the operation of \mathbf{A} on vectors, and reduce the Jacobian \mathbf{A} to a Hessenberg matrix \mathbf{H} , which approximates the linear behaviour of the original \mathbf{A} . This technique is possible using the Arnoldi iterative method [39] and will be discussed in Sect. 3.2. The eigenmode and input-output analysis presented below can equivalently be applied on the Hessenberg matrix \mathbf{H} instead of the Jacobian \mathbf{A} , in which case the results are approximations of the original spectrum or response of \mathbf{A} . Typical ways to investigate the linear dynamics of \mathbf{A} are the eigenmodal analysis, extracting the global modes, and the resolvent (or input-output) analysis, extracting the response to harmonic forcing.

Extension to n -periodic Systems

Using the described linearised analysis one can study the response of boundary layers, relevant to the transition to turbulence. This is valid in all regimes, including hypersonic boundary layers. One commonly neglected aspect is the influence of roughness on the stability of the boundary layer. In this work, our objective is to study the effect of roughness, in the form of n -periodic roughness arrays, on hypersonic boundary layers. This helps alleviate the typical restriction when the investigation is carried out on a single or limited number of units [37] and allows to study the linear interaction of an arbitrary number of units and potential wake synchronisation.

A relevant sketch of such a configuration is presented in Fig. 1a, with three of infinitely-many n roughness units are shown. The linear analysis described above is further simplified for n -periodic systems. This simplification is presented below, following the work by Schmid et al. [32].

The structure of the Jacobian \mathbf{A} in this particular case is block-circulant [19]. In Eq. (8), the operators \mathbf{A}_j for $j = 0, 1, \dots, n - 1$ describe the linear dynamics between units. The units in this formulation are considered identical and only interact with their nearest neighbours. Therefore, $\mathbf{A}_0 = \mathbf{A}_C$, $\mathbf{A}_1 = \mathbf{A}_R$, $\mathbf{A}_{n-1} = \mathbf{A}_L$, and $\mathbf{A}_j = 0$ for $j = 2, 3, \dots, n - 2$, and the system becomes banded block-circulant (see Sect. 3.3 for details). This is accurate for rotationally symmetric systems, as in Fig. 1b, and is approximate for a flat plate with a large number of units n , as in Fig. 1a.

$$\mathbf{A} = \begin{pmatrix} \mathbf{A}_0 & \mathbf{A}_1 & \cdots & \mathbf{A}_{n-2} & \mathbf{A}_{n-1} \\ \mathbf{A}_{n-1} & \mathbf{A}_0 & \cdots & \mathbf{A}_{n-3} & \mathbf{A}_{n-2} \\ \vdots & \vdots & \ddots & \vdots & \vdots \\ \mathbf{A}_2 & \mathbf{A}_3 & \cdots & \mathbf{A}_0 & \mathbf{A}_1 \\ \mathbf{A}_1 & \mathbf{A}_2 & \cdots & \mathbf{A}_{n-1} & \mathbf{A}_0 \end{pmatrix} \quad (8)$$

With the roots of unity $\rho_j = \exp(i\theta_j)$, where $\theta_j = 2\pi j/n$, the operator \mathbf{A} is transformed to a block-diagonal operator $\hat{\mathbf{A}} \equiv \mathbf{P}^H \mathbf{A} \mathbf{P} = \text{diag}(\hat{\mathbf{A}}_0 \hat{\mathbf{A}}_1 \cdots \hat{\mathbf{A}}_{n-1})$, where $\mathbf{P} = \mathbf{J} \otimes \mathbb{I}$ where \mathbb{I} is the identity matrix of the same dimensions as each unit operator \mathbf{A}_j , and $\mathbf{J}_{j+1,k+1} = \rho_j^k / \sqrt{n}$, for $j = 0, 1, \dots, n-1$ and $k = 0, 1, \dots, n-1$.

Therefore, instead of the large full system, only n smaller systems $\hat{\mathbf{A}}_j$ need to be manipulated. These subsystems are fully independent and decoupled, and can be computed in parallel. Any type of linear analysis on each of them, such as eigenmodal or resolvent analysis, can provide information for the global linear dynamics of the system.

The reader is referred to the work by [32] for details. Further information about the implementation of this approach is given in Sect. 3.3.

3 Methods

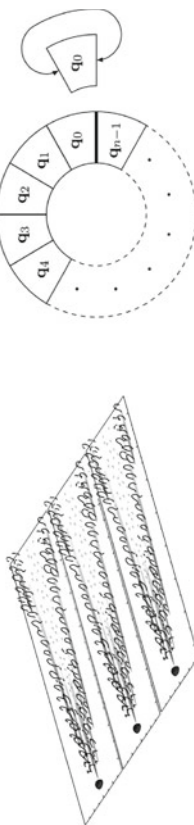
3.1 Computational Setup and Tools

Direct numerical simulations (DNSs) are carried out using the numerical code developed by Nagarajan [24, 24, 25]. The domain investigated is a flat plate boundary layer without a leading edge, as seen in Fig. 2. Perturbations can be included using blowing and suction strips, as well as roughness elements on the surface of the flat plate.

The Eqs. (1)–(4), are solved in curvilinear coordinates on a staggered grid, as presented in [24]. Space discretisation is done using a fourth-order accurate Padé compact finite-difference scheme [24], with a compact fourth-order one-sided scheme at the boundaries. High-order high-wavenumber filtering is implemented to avoid numerical instabilities, although it was not necessary to activate it in the simulations presented below, due to sufficient spatial resolution. For time integration we use a third-order accurate Runge–Kutta scheme. More details regarding the numerical methods can be found in the original work by [24].

On wall surfaces, isothermal or adiabatic boundary conditions are imposed. No-slip boundary conditions are enforced for momentum, and a non-catalytic surface is imposed for CNEQ, with vanishing gradients of Y_s in the wall-normal direction.

In other regions of the flow (inlet, outlet, free stream), numerical damping is enforced, using $\frac{\partial \mathbf{Q}}{\partial t} = \mathbf{F}(\mathbf{Q}) - \sigma(\mathbf{x})(\mathbf{Q} - \mathbf{Q}_{\text{ref}})$, a method known as sponge [24, 25], illustrated in Fig. 2. The sponge strength, $\sigma(\mathbf{x})$, is a third-order smooth poly-



(a) An array of three roughness elements on a flat plate. Each roughness element and the region around it is considered a single unit in the n -periodic analysis. Adapted from [40].
 (b) A system of n -periodic units, interacting only with their nearest neighbours, and the approximation of a unit as periodic. Adapted from [32].

Fig. 1 A sketch of three of infinitely many n -periodic roughness units on a flat plate boundary layer (**a**) and a theoretical rotationally symmetric system (**b**)

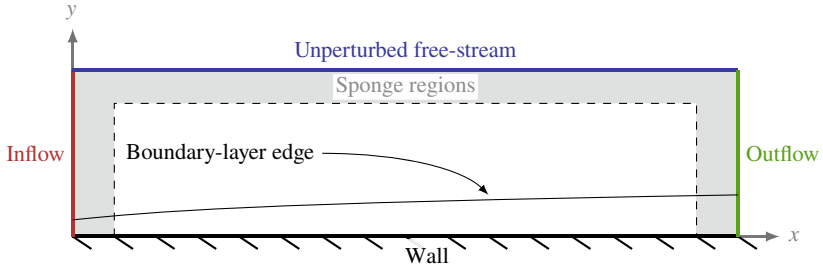


Fig. 2 A sketch of the computational domain for a flat plate boundary layer. A strip is used to force perturbations into the flow

nomial function of space, vanishing in the inner flow and approaching a high value, empirically adjusted, towards the boundaries. Inside the sponge, the flow is forced toward a self-similar reference solution, \mathbf{Q}_{ref} .

3.2 Automatic Linearised Stability Analysis of Large Nonlinear Systems

We propose an efficient linearisation of Eq. (5), as seen in Eq. (9). This approach is implicit and matrix-free, avoiding the need to compute and store the full Jacobian operator \mathbf{A} . Only the operation of the Jacobian \mathbf{A} on the vector \mathbf{Q}' is computed indirectly by two evaluations of the nonlinear right-hand-side function \mathbf{F} . This decouples the linearisation process from the underlying thermophysical models, and the linear analysis tools are universal, independent of the underlying thermochemical model.

$$\mathbf{A} \cdot \mathbf{Q}' \approx \lim_{\epsilon \rightarrow 0} \frac{\mathbf{F}(\bar{\mathbf{Q}} + \epsilon \mathbf{Q}') - \mathbf{F}(\bar{\mathbf{Q}})}{\epsilon} \quad (9)$$

The parameter ϵ is small enough to provide an accurate first-order approximation of the linearised system, but not too small, to avoid numerical instabilities. A similar approach, with different implementation is presented by [29], using the (MFP) method. The methods are practically equivalent, with the latter providing higher-order accuracy in time and allowing easier implementation.

After linearisation, the Arnoldi iterative method [39] or the DMD method [31] can be used to project the Jacobian operator \mathbf{A} onto a Krylov subspace of manageable dimensions where the linear analysis can be applied easily. This way we can extract the global stability modes without explicitly forming the operator.

3.3 Extension to N-Periodic Systems of Roughness Units

Based on the description in Sect. 2.2, we simplify the case of a flat plate, spanned by n identical roughness elements, defining n identical units in the spanwise direction. For sufficiently large n , the n -periodicity assumption is reasonable. This limitation is dropped in the case of rotationally symmetric geometries. Limiting the investigation to direct neighbour interactions, the system is transformed to a tridiagonal (banded) block-circulant system.

Based on the work by Schmid et al. [32], each unit of the transformed block-diagonal operator $\hat{\mathbf{A}}$ will be given by $\hat{\mathbf{A}}_j = \rho_j \mathbf{A}_L + \mathbf{A}_C + \rho_j^{-1} \mathbf{A}_R$, for $j = 0, 1, \dots, n - 1$. A simulation of only a triplet of units is enough to extract the global dynamics of a system of an arbitrary number of units n . Any linear analysis can be then applied to the decoupled units $\hat{\mathbf{A}}_j$, allowing for massive parallelisation.

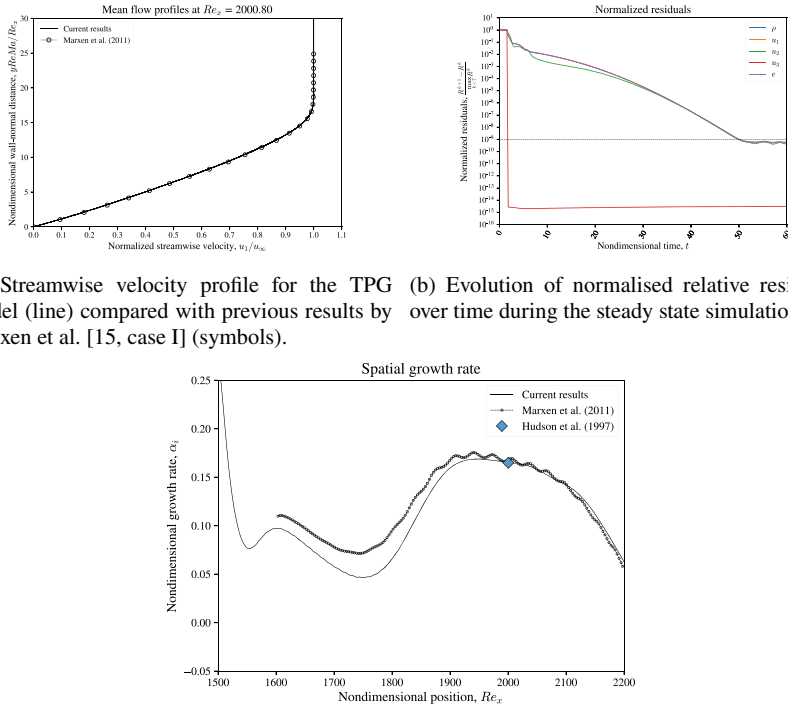
4 Preliminary Results and Discussion

Code verification is achieved by comparing to previous results using similar tools. We present some initial findings herein. A two-dimensional (2D) Tollmien-Schlichting instability is investigated, introduced by a blowing and suction strip, similar to [15–18]. A hypersonic flat plate boundary layer is selected. The base flow is extracted by converging to the steady state, without perturbations. The detailed setup is found in [15, caseI], following [7]. The Reynolds number is $Re = 1 \times 10^4$, the Mach number is $Ma = 10.0$, the forcing is located between $x_1 = 19.3$ and $x_2 = 20.7$ in nondimensional units and a frequency $\omega \equiv F Ma^2 Re = 45.0$ is selected, with an amplitude $A = 0.001 Ma$. A higher-resolution discretisation is achieved, with a nondimensional streamwise grid size of $\Delta x \approx 0.075$, simulating the domain from $x \approx 3.36$, using 960 streamwise grid points, with sponge regions extending for 5.00 and 15.0 nondimensional units at the inflow and outflow, respectively. In the wall-normal direction, 211 grid points are used, clustered near the wall, with the last 26 points near the free stream used as a sponge region.

We present some early results for the TPG model. More accurate, CNEQ results are part of ongoing work.

The mean flow streamwise velocity profile for the steady state simulation is compared with the results by Marxen et al. [15] in Fig. 3a. The agreement is perfect as expected. The relative residuals convergence is shown in Fig. 3b, reaching almost machine precision for all equations. The linear growth rate of the small amplitude perturbation is computed and presented in Fig. 3c. A grid convergence study has been carried out, verifying the independence of our results to the grid. Very good agreement is found with the results by Marxen et al. [15] and Hudson et al. [7].

The results included herein verify the numerical tools used. Further studies of different cases, wall roughness effects, and different thermophysical models are part of ongoing work. Additionally, linearised analysis, as presented in Sects. 2.2 and 3.2,



(a) Streamwise velocity profile for the TPG model (line) compared with previous results by Marxen et al. [15, case I] (symbols). (b) Evolution of normalised relative residuals over time during the steady state simulation.

(c) Streamwise growth rate of the perturbation. Results are presented for the TPG model (solid line), compared with previous results by Marxen et al. [15, case I] using the same models, and by Hudson et al. [7] (symbol) using linear stability theory (LST).

Fig. 3 Summary of results for the hypersonic boundary layer simulation at Mach 10 in TPG. Comparison of mean flow profiles (a), evolution of simulation residuals (b), and comparison of streamwise growth rate (c)

can be applied around the base flows computed using the nonlinear DNS solver, with minimal extra computational cost. This allows to investigate the stability of hypersonic boundary layers for different thermophysical models and with parametrised roughness configurations. The results can be extracted in a straightforward manner, without adapting the tools. Further investigations will follow.

5 Conclusions and Future Work

Aerospace mission design requires accurate and reliable predictions of the hypersonic boundary layer around atmospheric entry vehicles. In this work, we propose an approach to investigate the influence of n -periodic roughness arrays to the stability of the boundary layer with complex thermodynamic and chemical models. The cou-

pling of our nonlinear DNS code with the Mutation++ library to extend the solver's thermochemical modelling capabilities has been discussed. Preliminary verification results have been presented in this paper. Our tools have been verified on canonical flat plate hypersonic boundary layers for a range of Mach numbers. The agreement with past results is excellent. Simulations using finite-rate chemistry for various gas mixtures are part of ongoing work.

We propose an efficient framework for the investigation of n -periodic systems with nearest-neighbour coupling. The benefit of this approach is that it is independent of the underlying nonlinear model, since the linearisation is done automatically. Additionally, the system is decoupled into n smaller systems that can be treated in parallel.

Linearised analysis, eigenmodal or resolvent, can complement our nonlinear solver tools. The efficient automatic linearisation allows to carry out analysis for various models and large systems without modifications. There is potential for coupling with adjoint-based sensitivity and optimisation tools in future steps.

Acknowledgements The authors wish to acknowledge the support of the US Air Force Office for Scientific Research (AFOSR) and the European Office of Aerospace Research and Development (EOARD) through the grant FA9550-18-1-0127, managed by Dr. Ivett Leyva and Dr. Douglas Smith. The views and conclusions presented herein are those of the authors and should not be considered representing the AFOSR or the U.S. Government. The computational time allocation by the UK Turbulence Consortium (UKTC) is also acknowledged.

References

1. Anderson, J.D.: Hypersonic and High-Temperature Gas Dynamics, 3 edn. American Institute of Aeronautics and Astronautics (AIAA), Washington, DC (2019). <https://doi.org/10.2514/4.105142>, ISBN 978-1-62410-514-2
2. Candler, G.V.: Rate effects in hypersonic flows. *Annu. Rev. Fluid Mech.* **51**(1), 379–402 (2019). <https://doi.org/10.1146/annurev-fluid-010518-040258>, ISSN 0066-4189
3. Fosas de Pando, M., Sipp, D., Schmid, P.J.: Efficient evaluation of the direct and adjoint linearized dynamics from compressible flow solvers. *J. Comput. Phys.* **231**(23), 7739–7755 (2012)
4. Gnoffo, P.A.: Planetary-entry gas dynamics. *Annu. Rev. Fluid Mech.* **31**(1), 459–494 (1999). <https://doi.org/10.1146/annurev.fluid.31.1.459>, ISSN 0066-4189
5. Gnoffo, P.A., Gupta, R.N., Shinn, J.L.: Conservation equations and physical models for hypersonic air flows in thermal and chemical nonequilibrium. Technical report 2867, NASA (1989)
6. Holden, M.S.: Review of aerothermal problems associated with hypersonic flight. In: AIAA Paper, Reston, Virginia, pp. 1–40. American Institute of Aeronautics and Astronautics (AIAA) (1986). <https://doi.org/10.2514/6.1986-267>
7. Hudson, M.L., Chokani, N., Candler, G.V.: Linear stability of hypersonic flow in thermochemical nonequilibrium. *AIAA J.* **35**(6), 958–964 (1997). <https://doi.org/10.2514/2.204>, ISSN 0001-1452
8. Johnson, H.B., Seipp, T.G., Candler, G.V.: Numerical study of hypersonic reacting boundary layer transition on cones. *Phys. Fluids* **10**(10), 2676–2685 (1998). <https://doi.org/10.1063/1.869781>, ISSN 1070-6631
9. Josyula, E., Vedula, P.: Fundamental fluid transport equations for hypersonic nonequilibrium flows. In: Josyula E. (ed.) *Hypersonic Nonequilibrium Flows: Fundamentals and Recent*

- Advances, pp. 1–43. American Institute of Aeronautics and Astronautics (AIAA) (2015). <https://doi.org/10.2514/5.9781624103292.0001.0044>
- 10. Leyva, I.A.: The relentless pursuit of hypersonic flight. *Phys. Today* **70**(11), 30–36 (2017). <https://doi.org/10.1063/PT.3.3762>, ISSN 00319228
 - 11. Malik, M.R.: Prediction and control of transition in supersonic and hypersonic boundary layers. *AIAA J.* **27**(11), 1487–1493 (1989). <https://doi.org/10.2514/3.10292>, ISSN 00011452
 - 12. Malik, M.R., Anderson, E.C.: Real gas effects on hypersonic boundary-layer stability. *Phys. Fluids A: Fluid Dyn.* **3**(5), 803–821 (1991). <https://doi.org/10.1063/1.858012>, ISSN 0899-8213
 - 13. Marschall, J., MacLean, M., Norman, P.E., Schwartzenruber, T.E.: Surface chemistry in non-equilibrium flows. In: Josyula E. (ed.) *Hypersonic Nonequilibrium Flows: Fundamentals and Recent Advances*, pp. 239–327. American Institute of Aeronautics and Astronautics (AIAA) (2015). <https://doi.org/10.2514/5.9781624103292.0239.0328>
 - 14. Marxen, O., Iaccarino, G., Shaqfeh, E.S.G.: Disturbance evolution in a mach 4.8 boundary layer with two-dimensional roughness-induced separation and shock. *J. Fluid Mech.* **648**, 435–469 (2010). <https://doi.org/10.1017/S0022112009992758>, ISSN 00221120
 - 15. Marxen, O., Magin, T.E., Iaccarino, G., Shaqfeh, E.S.G.: A high-order numerical method to study hypersonic boundary-layer instability including high-temperature gas effects. *Phys. Fluids* **23**(8), 084108 (2011). <https://doi.org/10.1063/1.3614526>, ISSN 10706631
 - 16. Marxen, O., Magin, T.E., Shaqfeh, E.S.G., Iaccarino, G.: A method for the direct numerical simulation of hypersonic boundary-layer instability with finite-rate chemistry. *J. Comput. Phys.* **255**, 572–589 (2013). <https://doi.org/10.1016/j.jcp.2013.07.029>, ISSN 10902716
 - 17. Marxen, O., Iaccarino, G., Magin, T.E.: Direct numerical simulations of hypersonic boundary-layer transition with finite-rate chemistry. *J. Fluid Mech.* **755**, 35–49 (2014). <https://doi.org/10.1017/jfm.2014.344>, ISSN 14697645
 - 18. Marxen, O., Iaccarino, G., Shaqfeh, E.S.G.: Nonlinear instability of a supersonic boundary layer with two-dimensional roughness. *J. Fluid Mech.* **752**(4), 497–520 (2014). <https://doi.org/10.1017/jfm.2014.266>, ISSN 14697645
 - 19. Mensah, G.A., Moeck, J.P.: Efficient computation of thermoacoustic modes in annular combustion chambers based on bloch-wave theory. In: ASME Turbo Expo 2015: Turbine Technical Conference and Exposition, Volume 4B: Combustion, Fuels and Emissions of *Turbo Expo: Power for Land, Sea, and Air*, pp. 1–11 (2015). <https://doi.org/10.1115/GT2015-43476>. V04BT04A036
 - 20. Miró Miró, F., Pinna, F.: Effect of uneven wall blowing on hypersonic boundary-layer stability and transition. *Phys. Fluids* **30**(8) (2018). <https://doi.org/10.1063/1.5043353>, ISSN 10897666
 - 21. Miró Miró, F., Pinna, F.: On decoupling ablation effects on boundary-layer stability and transition. In: AIAA Aviation 2019 Forum, Reston, Virginia. American Institute of Aeronautics and Astronautics (AIAA) (2019). <https://doi.org/10.2514/6.2019-2854>, ISBN 978-1-62410-589-0
 - 22. Miró Miró, F., Beyak, E.S., Mullen, D., Pinna, F., Reed, H.L.: Ionization and dissociation effects on hypersonic boundary-layer stability. In: 31st Congress of the International Council of the Aeronautical Sciences (ICAS) 2018 (2018)
 - 23. Miró Miró, F., Dehairs, P., Pinna, F., Gkolia, M., Masutti, D., Regert, T., Chazot, O.: Effect of wall blowing on hypersonic boundary-layer transition. *AIAA J.* **57**(4), 1567–1578 (2019). <https://doi.org/10.2514/1.J057604>, ISSN 0001-1452
 - 24. Nagarajan, S.: Leading edge effects in bypass transition. Ph.D. thesis, Stanford University (2004)
 - 25. Nagarajan, S., Lele, S.K., Ferziger, J.H.: A robust high-order compact method for large eddy simulation. *J. Comput. Phys.* **191**(2), 392–419 (2003)
 - 26. Nichols, J.W., Candler, G.V.: Input-output analysis of complex hypersonic boundary layers. In: AIAA Scitech 2019 Forum, Reston, Virginia, pp. 1–11. American Institute of Aeronautics and Astronautics (AIAA) (2019). <https://doi.org/10.2514/6.2019-1383>, ISBN 978-1-62410-578-4
 - 27. Park, C.: Review of chemical-kinetic problems of future NASA missions, I: Earth entries. *J. Thermophys. Heat Transf.* **7**(3), 385–398 (1993). <https://doi.org/10.2514/3.431>, ISSN 0887-8722

28. Park, C., Howe, J.T., Jaffe, R.L., Candler, G.V.: Review of chemical-kinetic problems of future NASA missions, II: Mars entries. *J. Thermophys. Heat Transf.* **8**(1), 9–23 (1994). <https://doi.org/10.2514/3.496>, ISSN 08878722
29. Ranjan, R., Unnikrishnan, S., Gaitonde, D.V.: A robust approach for stability analysis of complex flows using Navier-Stokes solvers (2019). [arXiv:1906.06466](https://arxiv.org/abs/1906.06466)
30. Reshotko, E.: Transition issues for atmospheric entry. *J. Spacecr. Rocket.* **45**(2), 161–164 (2008). <https://doi.org/10.2514/1.29777>, ISSN 00224650
31. Schmid, P.J.: Dynamic mode decomposition of numerical and experimental data. *J. Fluid Mech.* **656**, 5–28 (2010). ISSN 14697645
32. Schmid, P.J., Fosas de Pando, M., Peake, N.: Stability analysis for n -periodic arrays of fluid systems. *Phys. Rev. Fluids* **2**(11), 7739–7755 (2017)
33. Schmisseur, J.D.: Hypersonics into the 21st century: a perspective on AFOSR-sponsored research in aerothermodynamics. *Prog. Aerosp. Sci.* **72**, 3–16 (2015). <https://doi.org/10.1016/j.paerosci.2014.09.009>, ISSN 03760421
34. Schneider, S.P.: Summary of hypersonic boundary-layer transition experiments on blunt bodies with roughness. *J. Spacecr. Rocket.* **45**(6), 1090–1105 (2008). <https://doi.org/10.2514/1.37431>, ISSN 00224650
35. Scoggins, J.B.: Development of numerical methods and study of coupled flow, radiation, and ablation phenomena for atmospheric entry. Ph.D. thesis, Université Paris-Saclay and von Karman Institute for Fluid Dynamics (2017)
36. Scoggins, J.B., Magin, T.E.: Development of mutation++: multicomponent thermodynamic and transport properties for ionized plasmas written in C++. In: 11th AIAA/ASME Joint Thermophysics and Heat Transfer Conference. American Institute of Aeronautics and Astronautics (AIAA) (2014). ID: AIAA 2014-2966
37. Shrestha, P., Candler, G.V.: Direct numerical simulation of high-speed transition due to roughness elements. *J. Fluid Mech.* **868**, 762–788 (2019). <https://doi.org/10.1017/jfm.2019.179>, ISSN 0022-1120
38. Subbareddy, P.K., Bartkowicz, M.D., Candler, G.V.: Direct numerical simulation of high-speed transition due to an isolated roughness element. *J. Fluid Mech.* **748**, 848–878 (2014). <https://doi.org/10.1017/jfm.2014.204>, ISSN 0022-1120
39. Trefethen, L.N.: Numerical linear algebra. Society for Industrial and Applied Mathematics, Philadelphia (1997). ISBN 9780898713619
40. Ye, Q., Schrijer, F.F., Scarano, F.: Geometry effect of isolated roughness on boundary layer transition investigated by tomographic PIV. *Int. J. Heat Fluid Flow* **61**, 31–44 (2016). <https://doi.org/10.1016/J.IJHEATFLUIDFLOW.2016.05.016>, ISSN 0142-727X

41. Zanus, L., Miró Miró, F., Pinna, F.: Nonlinear parabolized stability analysis of hypersonic flows in presence of curvature effects. In: 2018 AIAA Aerospace Sciences Meeting, Reston, Virginia. American Institute of Aeronautics and Astronautics (AIAA) (2018). <https://doi.org/10.2514/6.2018-2087>, ISBN 978-1-62410-524-1
42. Zanus, L., Miró Miró, F., Pinna, F.: Weak non-parallel effects on chemically reacting hypersonic boundary layer stability. In: AIAA Aviation 2019 Forum, Reston, Virginia, pp. 1–20. American Institute of Aeronautics and Astronautics (AIAA) (2019). <https://doi.org/10.2514/6.2019-2853>, ISBN 978-1-62410-589-0

Hypersonic Boundary Layer Instability and Control by Passive Porous Coatings



S. O. Morozov, S. V. Lukashevich, and A. N. Shiplyuk

Experimental studies have been performed to understand the influence of the small angle of attack on the effective stabilization of a hypersonic boundary layer on the cone with a passive porous coating at Mach number $M = 5.8$. The 7° half-angle cone with different nose tip bluntness is used. The passive porous coating presents a three-layer mesh with the porosity of 44%. One half of the cone along its generatrix is partly covered with the passive porous coating, while the other side is solid. Wall-pressure disturbances and surface heat fluxes are measured at two unit Reynolds numbers: $Re_1 = 6.8 \cdot 10^6$ and $20 \cdot 10^6 \text{ m}^{-1}$. It is shown that the boundary layer becomes more stable on the windward side and less stable on the leeward side against the case of the zero angle of attack. The passive porous coating effectively suppresses the most unstable second-mode disturbances in the hypersonic boundary layer both on the leeward and windward sides of the cone. It is found that the passive porous coating delays the laminar-turbulent transition both on the windward and leeward sides of the cone with bluntness radii of 0.03 and 0.5 mm.

S. O. Morozov (✉) · S. V. Lukashevich · A. N. Shiplyuk
Khristianovich Institute of Theoretical and Applied Mechanics, SB RAS, Novosibirsk, Russia
e-mail: morozov@itam.nsc.ru

S. O. Morozov
Novosibirsk State University, Novosibirsk, Russia

A. N. Shiplyuk
Novosibirsk State Technical University, Novosibirsk, Russia

1 Introduction

The mechanism of the laminar-turbulent transition in the general case is the loss of the laminar flow steadiness under the action of the growing disturbances. As certain amplitudes are reached, non-linear interactions between disturbances begin, they lead to the turbulence.

The method of hypersonic boundary layer stabilization by a passive porous coating was proved theoretically and experimentally [3, 4]. This method does not require energy supply therefore it is a promising way of laminar-turbulent transition control in zero-pressure gradient boundary layers on the surface of hypersonic vehicles. Stabilization involving passive porous coatings results from the reducing energy of the most unstable high-frequency disturbances in a hypersonic boundary layer (second-mode disturbances). The most evident effect takes place on the cold wall which corresponds to hypersonic flight conditions. The stabilizing effect is already reachable at the small thickness of the porous coating, about 30% of the boundary layer thickness. It was shown that the passive porous coatings suppressed successfully the second-mode disturbances and delayed the laminar-turbulent transition at certain conditions [5, 6, 9]. Hypersonic boundary layer stability strongly depends on the angle of attack and bluntness [1, 7, 8], therefore it is important to investigate the influence of small angles of attack and bluntness on the effective stabilization of a hypersonic boundary layer on a cone by means of the passive porous coating.

2 Experimental Setup

Experiments are performed in hypersonic short-duration wind tunnel Transit-M in ITAM SB RAS. Free stream Mach number is 5.8. The 7° half-angle cone with different bluntness is used Fig. 1. The nose tip radius is 0.03 mm and 0.5 mm. The

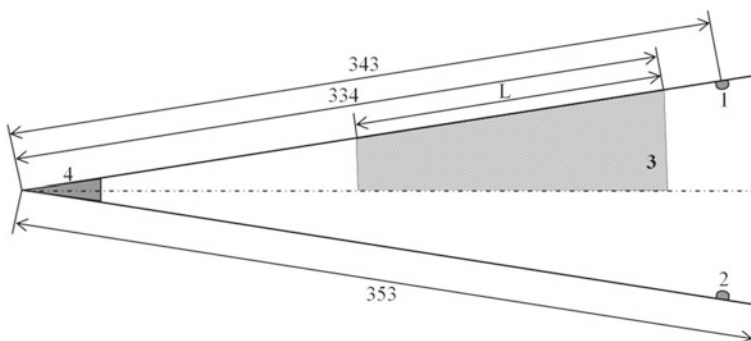


Fig. 1 Cone model; dimensions are in mm. 1, 2—high-frequency pressure gages; 3—section with a passive porous coating; 4—interchangeable nose tip

cone length is 353 mm. The passive porous coating presents a three-layer nylon woven mesh with the porosity of 44% and total thickness of 0.18 mm. One half of the cone, along its generatrix, is partly covered with the passive porous coating with length L , while the other side is solid. The coating length of the varies along the cone generatrix from the point $x_0 = 334$ mm toward the cone nose tip. Two high-frequency pressure gages (PCB132A31) are mounted on the cone surface Fig. 1. The laminar-turbulent transition place is determined by the heat flux variation on the cone surface. The cone is made of polyoxymethylene (POM) «Tecaform AH» and is covered with a black-deadening paint. The heat flux is calculated by the Cook–Felderman technique [2]. The surface temperature is measured by an infrared camera (FLIR SC7750L) at 200 fps. This method allows to obtain only qualitative dependence of the heat flux on the cone surface with the porous coating, but it is good enough for transition location measurements.

3 Results

Measurements of the laminar boundary layer stability are carried out at free stream unit Reynolds number $Re_1 = 6.8 \cdot 10^6 \text{ m}^{-1}$ with the porous coating length $L = 64 \text{ mm}$. Figures 2 and 3 show the pressure fluctuations spectra on the cone solid surface (solid line) and on the surface with porous coating (dashed lines), the nose bluntness radius $R = 0.03 \text{ mm}$ and 0.5 mm , respectively. Different colors show the angles of attack. The second mode disturbances are clearly visible at the frequency peak about 200 kHz on the cone solid surface at the zero angle of attack for two bluntnesses. The dependence of the maximum frequency on the angle of attack proves that these

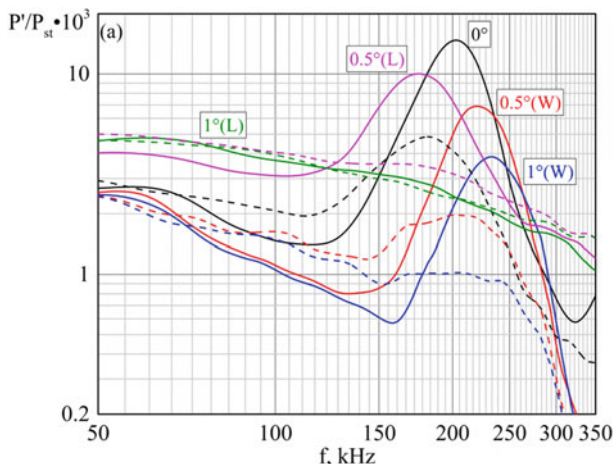


Fig. 2 Pressure fluctuations spectra at $Re_1 = 6.8 \cdot 10^6 \text{ m}^{-1}$ on the cone with bluntness $R = 0.03 \text{ mm}$ at different angles of attack. Solid line—solid surface; dashed line—porous surface

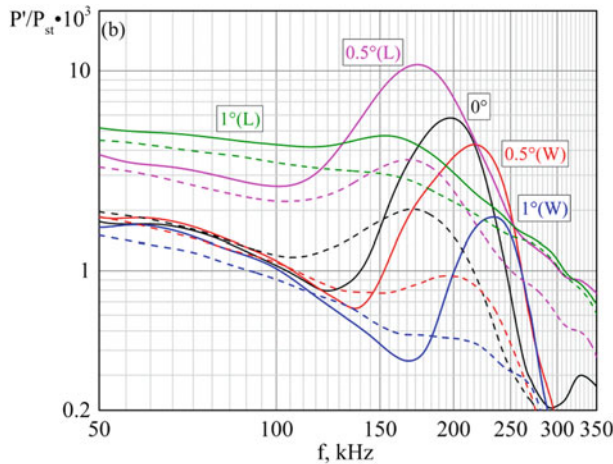


Fig. 3 Pressure fluctuations spectra at $Re_1 = 6.8 \cdot 10^6 \text{ m}^{-1}$ on the cone with bluntness $R = 0.5 \text{ mm}$ at different angles of attack. Solid line—solid surface; dashed line—porous surface

are the second-mode disturbances. On the cone with the bluntness $R = 0.5 \text{ mm}$, the disturbance amplitude within the studied frequency range is much lower than in the case of $R = 0.03 \text{ mm}$. The second-mode amplitude decreases with increasing angle of attack on the leeward and windward side for the bluntness $R = 0.03 \text{ mm}$ Fig. 2. But the amplitude of other disturbances decreases on the windward side and increases on the leeward side with increasing angle of attack. It means that the laminar boundary layer becomes more stable on the windward side and less stable on the leeward side, and at this unit Reynolds number is in the transition state on the leeward side. The frequency of the second mode decreases with increasing angle of attack on the leeward side because the boundary layer thickness rises. On the windward side, as the angle of attack increases, the boundary layer becomes thinner and the second mode frequency increases. The second-mode amplitude on the porous coating is smaller than on the solid surface under the relevant angles of attack. However, lower frequency disturbances relative to the second mode are destabilized by the porous coating. These disturbances are associated with the first Mack mode.

On the cone with bluntness $R = 0.5 \text{ mm}$, the effect of the angle of attack and porous coating on the boundary layer stability is the same as with bluntness $R = 0.03 \text{ mm}$ on the windward side Fig. 3. The second-mode and other disturbances are much higher on the leeward side at the angle of attack 0.5° than for the zero angle of attack. Further increase of the angle of attack to 1° makes the second-mode amplitude decrease, the other disturbances rise, which means the start of the transition mode for the boundary layer. On the porous surface, the second-mode amplitude is lower than it is on the solid surface for every studied angle of attack at $R = 0.5 \text{ mm}$.

Figure 4 demonstrates the effective damping of the second-mode disturbances by the porous coating on the cone at different angles of attack. $P'_{\max,p}$ and $P'_{\max,s}$ are the maximum amplitudes of the second mode on the porous and solid surfaces,

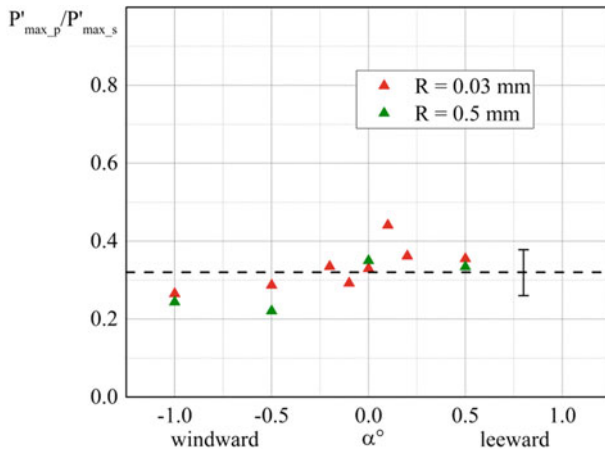


Fig. 4 Ratios of maximum amplitudes of second-mode disturbances on the porous and solid surfaces at $Re_1 = 6.8 \cdot 10^6 \text{ m}^{-1}$

respectively. Evident that the second-mode disturbance amplitude on the porous surface is 0.35 on the average on the solid surface for both radii $R_b = 0.03 \text{ mm}$ and 0.5 mm . At the angle of attack $\alpha = 1^\circ$ (the leeward side), the boundary layer is in the transitional mode and there are no corresponding points on the graph.

The places of the laminar-turbulent transition are measured at free stream unit Reynolds number $Re_1 = 20 \cdot 10^6 \text{ m}^{-1}$ with the porous coating length $L = 210 \text{ mm}$. Figure 5 presents the heat flux distributions on solid and porous surfaces for the cone with two bluntnesses at the zero angle of attack. St is the Stanton number

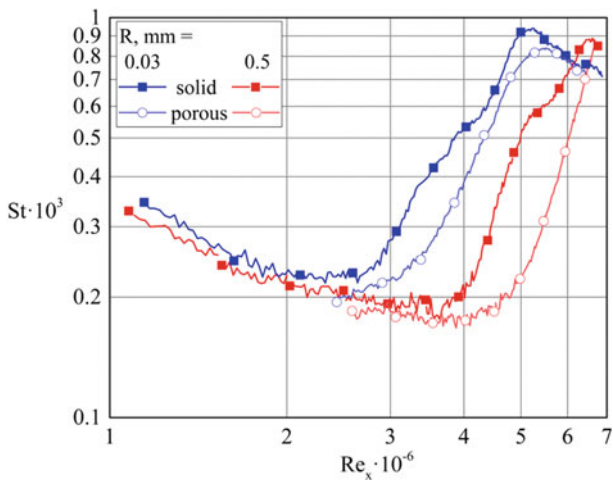


Fig. 5 Heat flux distribution on the cone at the zero angle of attack at $Re_1 = 20 \cdot 10^6 \text{ m}^{-1}$

defined by free-stream parameters, and Re_x is the Reynolds number defined by free-stream unit Reynolds number (Re_1) and distance from the nose tip (x). Note that on the porous surface, the heat flux magnitude cannot be determined by Cook–Felderman technique used here, but the qualitative behavior of heat flux distributions is determined successfully. On the solid surface, the heat flux decreases from the nose tip to Reynolds numbers $Re_x = 2 \cdot 10^6$ and $3.7 \cdot 10^6$ (points of the transition onset) for $R = 0.03$ mm and 0.5 mm, respectively. This region corresponds to the laminar boundary layer. Downstream of this region, the heat flux increases until $Re_x = 5.1 \cdot 10^6$ and $6.5 \cdot 10^6$ (points of the transition end) for $R = 0.03$ mm and 0.5 mm, respectively, which corresponds to the transitional mode of the boundary layer. Further decreasing of the heat flux indicates a turbulent boundary layer. On the porous section, the laminar region rises, and the transition end shifts downstream for both bluntness radii.

Figure 6 shows the location of the laminar-turbulent transition on solid and porous surfaces as the function of the angle of attack for $R = 0.03$ mm and 0.5 mm. It is clear that on the cone with bluntness $R = 0.5$ mm, the laminar-turbulent transition occurs later downstream than on the cone with $R = 0.03$ mm, and it is valid for every considered angle of attack. The passive porous coating increases the laminar boundary layer region and delays the end of the transitional region in every case but one. In the case $R = 0.03$ mm and $\alpha = 1^\circ$, the porous coating shears the transition end slightly upstream, because the porous coating located downstream of the transition onset and does not influence the boundary layer stability.

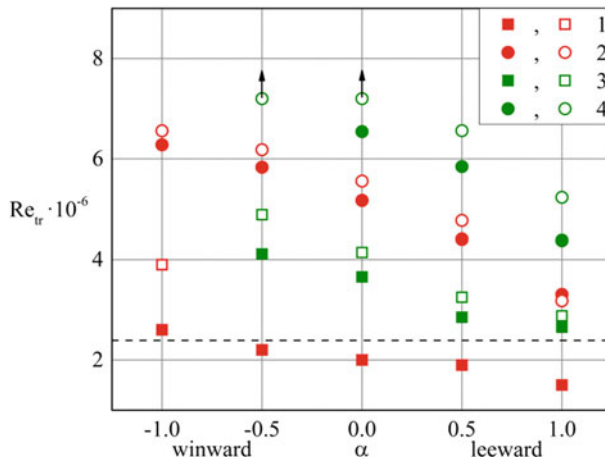


Fig. 6 Location of the laminar-turbulent transition on the cone versus the angle of attack at $Re_1 = 20 \cdot 10^6 \text{ m}^{-1}$. Horizontal dashed line—porous coating onset. Solid symbols—solid surface; open symbols—porous surface. 1—transition onset, $R = 0.03$ mm; 2—transition end, $R = 0.03$ mm; 3—transition onset, $R = 0.5$ mm; 4—transition end, $R = 0.5$ mm

4 Conclusions

Stability and laminar turbulent transition of the hypersonic boundary layer have been studied experimentally at Mach number $M = 5.8$. Under study is the influence of the small angle of attack on the effective stabilization of the hypersonic boundary layer on a cone by the passive porous coating (the 7° half-angle cone with bluntness radii $R = 0.03$ mm and 0.5 mm). It is shown that the boundary layer becomes more stable on the windward side and less stable on the leeward side comparing with the zero angle of attack. The amplitude of the most unstable second-mode disturbances in the hypersonic boundary layer, both on the leeward and windward sides of the cone, is lower on the porous coating than on the solid surface. It is found that the passive porous coating delays the laminar-turbulent transition both on the windward and leeward sides.

References

1. Buntin, D.A., Lukashevich, S.V., Maslov, A.A., Shiplyuk, A.N.: Effect of the cone nose bluntness and the ultrasonically absorptive coating on transition in a hypersonic boundary layer. *Fluid Dyn.* **45**(6), 898–904 (2010). <https://doi.org/10.1134/S0015462810060074>
2. Cook, W.J., Felderman, E.J.: Reduction of data from thin-film heat-transfer gages: a concise numerical technique. *AIAA J* **4**(3), 561–562 (1966). <https://doi.org/10.2514/3.3486>
3. Fedorov, A.V., Malmuth, N.D., Rasheed, A., Hornung, H.G.: Stabilization of hypersonic boundary layers by porous coatings. *AIAA J.* **39**(4), 605–610 (2001). <https://doi.org/10.2514/2.1382>
4. Fedorov, A.V., Shiplyuk, A.N., Maslov, A.A., Burov, E.V., Malmuth, N.D.: Stabilization of a hypersonic boundary layer using an ultrasonically absorptive coating. *J. Fluid Mech.* **479**, 99–124 (2003). <https://doi.org/10.1017/S0022112002003440>
5. Lukashevich, S.V., Morozov, S.O., Shiplyuk, A.N.: Experimental study of the effect of a passive porous coating on disturbances in a hypersonic boundary layer. 1. Effect of the porous coating length. *J. App. Mech. Tech. Phys.* **54**(4):572–577. <https://doi.org/10.1134/S002189441304007X>
6. Lukashevich, S.V., Morozov, S.O., Shiplyuk, A.N.: Experimental study of the effect of a passive porous coating on disturbances in a hypersonic boundary layer 2. Effect of the porous coating location. *J. App. Mech. Tech. Phys.* **57**(5):873–878. (2016) <https://doi.org/10.1134/S002189441605014X>
7. Maslov, A.A., Bountin, D.A., Shiplyuk, A.N., SidorenkoAA, S.Q., Bi, Z.: Experimental study of compressible boundary layer on a cone at angles of attack // *Acta Mech. Sinica.* **25**(3), 325–333 (2009). <https://doi.org/10.1007/s10409-009-0228-8>
8. Stetson, K.F.: Mach 6 experiments of transition on a cone at angle of attack. *J Spacecraft and Rockets* **19**(5), 397–440 (1982). <https://doi.org/10.2514/3.62276>
9. Wagner, A., Hannemann, K., Wartemann, V., Giese, T.: Hypersonic boundary-layer stabilization by means of ultrasonically absorptive carbon-carbon material Part 1: Experimental results. In: 51st AIAA Aerospace Sciences Meeting. AIAA Paper 2013–270 (2013)

Numerical Study of Crossflow Jet Generated Instabilities in a High-Speed Boundary Layer



Andrey V. Novikov and Alexander V. Fedorov

Abstract Numerical simulations of 3-D disturbances induced by an underexpanded jet in supersonic crossflow (JISC) in the Mach 5.4 flat-plate boundary layer (BL) are carried out. The Navier–Stokes equations for compressible perfect gas are integrated using the in-house solver implementing an implicit finite-volume shock-capturing scheme with the second-order approximation in space and time. The numerical solutions indicate that the wall normal injection through a circular hole forms an underexpanded jet of barrel shape, which induces a system of vortices propagating downstream. These vortices are destabilized at a short distance that leads to rapid nonlinear breakdown and formation of a turbulent wedge. The vortex structure, its instability and breakdown to turbulence resemble those induced by an isolated roughness element. It is shown that the normal wall injection effectively trips the BL flow. This encourages further numerical studies of active tripping of high-speed BL flows using rows of JISC.

1 Introduction

A turbulent BL flow has a much greater resistance to separation than laminar BL. As such, turbulent BL is desirable, for example, to mitigate separations in the flow approaching an inlet of ramjet engine. To promote early transition to turbulence in high-speed BL, passive or active devices are needed [2] known as tripping devices. For the experimental sub-scale vehicle Hyper-X, a wind tunnel program was implemented to screen and downselect several passive discrete trip configurations, resulting in an array of swept ramp vortex generators [1, 3]. More recently, tests have

A. V. Novikov (✉)
Central Aerohydrodynamic Institute, 1 Zhukovsky Street, Zhukovsky, Russia
e-mail: AndrewNovikov@yandex.ru

A. V. Novikov · A. V. Fedorov
Moscow Institute of Physics and Technology (National Research University), 9 Institutskiy per.,
Dolgoprudny, Russia
e-mail: afedorov55@gmail.com

been performed to investigate the feasibility of active trips via gas blowing into the BL [1, 3]. Such an active system is able to control the tripping effect, allowing for system shut-off when not needed. However, physical mechanisms of passive and active tripping are still not clear. This gap can be bridged by numerical simulations providing details of the tripping process which are not accessible in experiments. In connection with this, the passive tripping via roughness elements has been studied using direct numerical simulations [6, 15]. Active devices, based on the wall injection, have received less attention. We found only one paper [14], where numerical simulations were performed for laminar-turbulent transition induced by the wall injection.

In this paper, we consider tripping of a high-speed BL flow by a microjet in crossflow. Propagation of 3-D disturbances induced by an isolated underexpanded jet injected into the BL on a flat plate at the free-stream Mach number 5.4 is studied numerically. Since computations are performed without artificial sources of disturbances, instabilities are excited by numerical noise that mimics low-disturbance environment typical for free flights. The in-house code HSFlow++ [9] is used to solve the Navier–Stokes equations for viscous compressible perfect gas. The mean flow and the disturbance field are analyzed using 3-D visualization of the vortical structures, the spatial-temporal spectra of disturbances and distributions of the friction coefficient.

2 Problem Formulation and Numerical Method

The considered 3-D unsteady flows are described by the Navier–Stokes equations for a perfect gas (air) with the specific heat ratio $\gamma = 1.4$ and Prandtl number $\text{Pr} = 0.72$. Herein, the equations are employed in conservative dimensionless form. The coordinates and time are scaled using a reference length L^* and time L^*/U_∞^* ; the dependent variables are scaled using the corresponding freestream quantities, and pressure is scaled by the doubled dynamic pressure $\rho_\infty^* U_\infty^{*2}$. Hereafter asterisks denote dimensional quantities. The dynamic viscosity is calculated using the Sutherland’s law $\mu = T^{3/2}(S + 1)/(S + T)$, where $S = 100K/T_\infty^*$. Details of the governing equations may be found in [9].

The Navier–Stokes equations are integrated using the in-house solver HSFlow++ (High Speed Flow) [9], which implements an implicit finite-volume shock-capturing method with effectively the third-order approximation in space and second-order in time. Godunov-type TVD scheme with Roe approximate Riemann solver is used. Reconstruction of the dependent variables at the grid cell edges is performed using van Leer slope limiter. The system of nonlinear algebraic discrete equations is solved using the Newton iteration method. At every iteration step, the corresponding linear system is solved using the GMRes method. The HSFlow++ solver employs MPI technology and PETSc framework for distributed calculations. Note that this implicit shock-capturing numerical technique is robust and most efficient if the flow field contains shock waves, separation bubbles and other spatial inhomogeneities.

Despite dissipative nature of the TVD scheme, the HSFlow++ solver allows simulations of instabilities including their nonlinear breakdown and fնjectionregionis showormation of turbulent spots [5, 7, 12].

Considered is a supersonic flow past a sharp flat plate at zero angle of attack with an isolated crossflow jet injection. The free stream parameters correspond to the transition measurements on a Hyper-X model in the NASA LaRC 20-Inch Mach 6 Air Tunnel [4]: the Mach number $M_\infty = 5.373$, the unit Reynolds number $Re_{\infty,1} = 1.7927 \times 10^6$ 1/m, temperature $T_\infty^* = 74.194$ K. The wall temperature is $T_w^* = 300$ K. The earlier stability and numerical studies under these free-stream conditions were performed on a 5.5 degree compression corner [8, 12, 13, 17]. The reference length scale is $L^* = 0.3161$ m is the distance from the plate leading edge to the corner point [4], and the corresponding Reynolds number is $Re_{\infty,L} = 5.667 \times 10^6$.

The problem is solved in two steps. First, a steady laminar flow field (base flow) is computed using the time-dependent method. Then, gas injection through a circular hole is turned on that forms a JISC. The injection hole diameter is $d^* = 1$ mm ($d = 0.00316$), which is typical for practice. The injected gas is air – the same as in the free stream. The injection port is located in the $z = 0$ symmetry plane at $x_{inj} = 0.2$ where the unperturbed BL thickness is $\delta \approx 3.8$ mm ($\delta_{0.99} \approx 0.012$). A similar jet was considered in [14], where hypersonic BL transition forced by the wall injection was investigated numerically.

The main parameter driving the jet is the total pressure $p_{0,inj}$ in an injection supply channel. Further consideration is focused on the case of sufficiently high injection pressure providing the choked flow with the injection Mach number $M_{inj} = 1$. In this case, static temperature and pressure of the injected gas at the channel exit are expressed as $T_{inj}^s = T_{0,inj}^{2/\gamma(\gamma+1)}$, $p_{inj}^s = p_{0,inj}^{(2/\gamma(\gamma+1))^{1/\gamma-1}}$, where the superscript “s” denotes sonic conditions and subscript “0” – total value. The choked injection regime sets in, if p_{inj}^s exceeds the wall static pressure p_w in the unperturbed BL: $p_{inj}^s \geq p_w$. In this case, an underexpanded supersonic jet is formed and its mass flow rate does not depend on pressure perturbations in the supply channel.

The jet can penetrate into the BL and produce the tripping effect at sufficiently high values of p_{inj}^s . Hereafter $p_{inj}^s = 10.19 p_w$, where $p_w = 1.037 p_\infty$ is wall static pressure at the injection port location $x_{inj} = 0.2$ in the unperturbed BL. The injection temperature is chosen to be equal to the plate surface temperature, $T_{inj}^s = T_w = 4.04$. The other injection parameters are deduced from these predefined values: $p_{0,inj} = 20 p_\infty$, $T_{0,inj} = 4.852$, and $v_{inj}^s = 0.374$. The wall injection through a circular hole is modeled by the local boundary condition imposed on the hole exit

$$\{\rho u, \rho v, \rho w, p, T\}_{w,inj} = \{0, \rho_{inj} v_{inj}^s, 0, p_{inj}^s, T_{inj}^s\}. \quad (1)$$

This allows us to omit simulations inside the supply channel and, thereby, simplify the grid topology. The validity of this simplification was confirmed by additional computations that did include the flow inside the supply channel of conical shape.

The core part of the computational domain is a box with $[0, 1.4] \times [0, y_{max}(x)] \times [0, 0.014]$ extents in x , y and z directions. The top domain edge $y_{max}(x)$ is a piecewise constant function chosen to be below the bow shock. Appended to the core domain

are buffer (sponge) regions $1.4 \lesssim x \leq 2$ and $0.014 \lesssim z \leq 0.15$ with large grid cells where disturbances should dissipate due to increased numerical viscosity.

The boundary conditions are: no-slip and isothermal $T = T_w$ on the wall $y = 0$; the free-stream conditions on the $x = 0$ (left) and $y = y_{max}$ (top) boundaries; the linear extrapolation from the interior for the dependent variables on the outflow boundaries $x = x_{max} = 2$ (right) and $z = z_{max}$ (front); the symmetry condition on the $z = 0$ plane. The local boundary condition (1) is imposed on the hole outlet to simulate the injection.

Computations are performed on an orthogonal grid of $2801 \times \{84.221\} \times 141$ size totaling 74.2×10^6 nodes. The grid step in the streamwise direction is $\Delta x \approx 5 \times 10^{-4}$ with clustering near the injection hole to $\Delta x = 2 \times 10^{-4}$. In the wall normal direction, the grid step is $\Delta y = 1 \times 10^{-4}$ within the BL (about 120 grid lines) and gradually increases towards the top boundary. The spanwise grid step is $\Delta z \approx 2 \times 10^{-4}$. Note, that the grid steps are significantly larger than the Kolmogorov length scale $l_K \sim Re_{\infty,L}^{-3/4} = 0.086 \times 10^{-4}$. Therefore, this numerical study falls within the ILES (implicit large-eddy simulation) approach, which is presumably valid because relatively large eddies dominate in the considered flow fields.

To check that the flow features are resolved well enough, an additional grid was built to provide doubled resolution in the y direction ($\Delta y = 0.5 \times 10^{-4}$ within the BL). The flow fields computed on that y -refined grid exhibited more fine vortical structures (not shown here) than on the original grid. Nevertheless, the main horseshoe-shaped vortex (HSV) had a similar location and size. This behavior is inherent to the ILES approach. Also, by analogy with [14] it is expected that time-averaged flow quantities should hardly be influenced by further grid refining. Hence, the base grid is assumed to be appropriate for numerical simulations of the present work.

The time step for simulations of the disturbance evolution is $\Delta t = 0.0001$. Computations were carried out using multiprocessor high-performance computing cluster with distributed memory. Up to 302 CPU cores were employed simultaneously for a single case.

3 Results

The computed instantaneous flow field in the injection region is shown in Figs. 1 and 2. Hereafter the vortices are identified by Q-criterion, where Q is the second invariant of the velocity gradient tensor. For convenience, the patterns shown hereafter are obtained by mirroring of the computed flow field relative the $z = 0$ symmetry plane. This field contains well-known structures of the jet in supersonic crossflow (JISC): the main bow shock due to the jet, the barrel shape of the under-expanded jet ending with a Mach disk, the separation zone ahead of the jet, the horseshoe vortices (HSV), and the primary counter-rotating longitudinal vortices (CRV).

Visual inspection of the near-jet flow structures, which are similar to those shown in Fig. 2, at different time instants reveals the following features: the separation

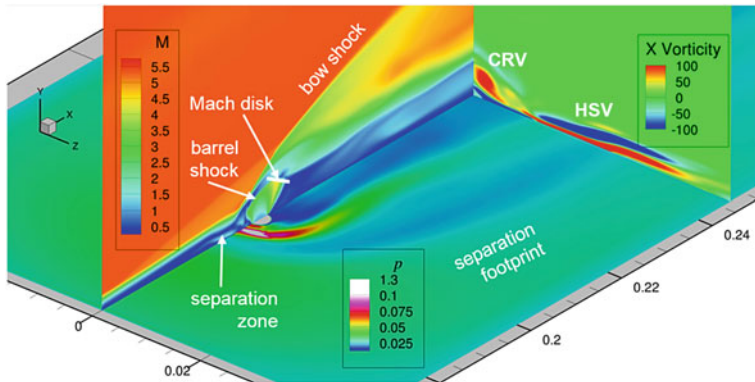


Fig. 1 Flow structure in the injection region visualized with the Mach number field in the symmetry plane, wall pressure and x-vorticity at $x = 0.247$

zone ahead of the jet pulsates with relatively low frequency; these pulsations induce perturbations of the primary counter-rotating longitudinal vortices (2 in Fig. 2) moving downstream; both HSV and CRV quickly exhibit secondary instabilities in the form of small-sacle vortices wrapped around the primary vortices (3 in Fig. 2); the small-scale vortices quickly evolves to hairpin vortices, which are main drivers of turbulence in the BL flow; some vortical structures emits acoustic waves into the outer flow, because these vortices move downstream with so slow speed that the outer flow is supersonic with respect to them. Similar features are observed in an instantaneous flow field including the far-field region (Fig. 3). The initial HSV and CRV structures quickly breakdown into small-scale vortices typical for a turbulent wedge flow. Note, that the vortical structure in Fig. 3 is very similar to that induced by an isolated cylindrical effective roughness (e.g. see the DNS solution of Chaudhry et al. in Fig. 15 of Ref. [6]).

It should be noted that in our simulations the breakdown process is not initialized by any artificial unsteady forcing. It occurs naturally due to numerical noise of very low intensity. This allows us to assume that the injection jet forms a near-field flow which is absolutely unstable; i.e., numerical perturbations of very small level are amplified in the injection region to appreciable amplitudes and feed the breakdown process.

The wave content of unsteady disturbance field is characterized by the spatial-temporal spectra. Figure 4 shows (β, ω) spectra (absolute values of 2-D Fourier transform vs. z and t) of the wall pressure disturbances in various x -stations. Here, the wavenumber β and frequency ω are associated with a wave $\sim q(x, y) \exp(i\beta z - i\omega t)$. In the local-parallel approximation, the amplitude function can be expressed as $q(x, y) \approx \hat{q}(y) \exp(i\alpha x)$, where $\alpha = \alpha(\beta, \omega) = \alpha_r + i\alpha_i$ is a complex eigenvalue and $\theta = \tan^{-1}(\beta/\alpha_r)$ is a wave-front angle. The spectrum is rather broad in the station $x = 0.3$ located near the jet ($x_{inj} = 0.2$). As x increases the spectrum broadens further and starts to resemble a spectrum of equilibrium turbulence. In the all x -

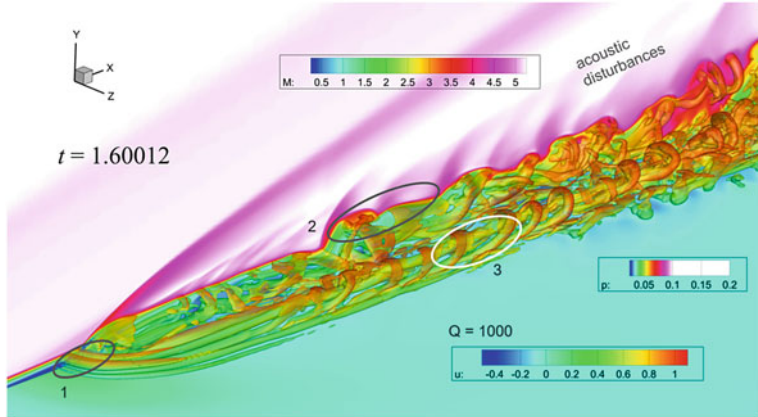


Fig. 2 Flow structure in the injection region. Shown are semitransparent isosurface of Q-criterion colored by x-velocity, Mach number field in the symmetry plane and wall pressure. 1—separation zone ahead of the jet, 2—perturbation of CRV moving downstream, 3—secondary instability of HSV

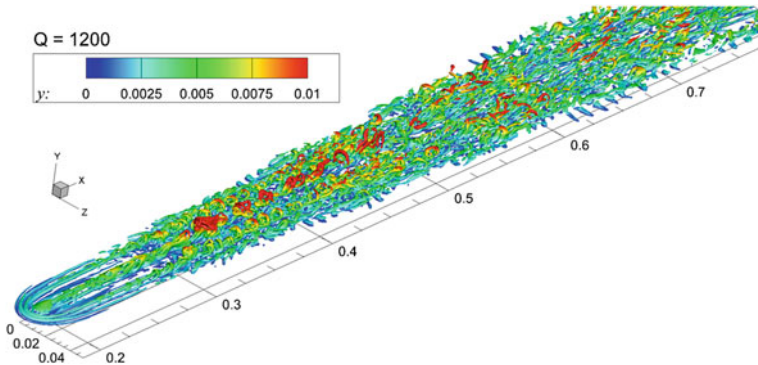


Fig. 3 Instantaneous vortex structure downstream the injection visualized with isosurface of Q-criterion colored by the distance from the wall

stations considered, the dominant are harmonics of zero frequency associated to the mean flow distortions, and waves of low frequency $\omega \approx 45$. The $\omega = 0, \beta = 0$ component represents the mean BL flow distortion in the near-field of injection, and the far-field distortion due to laminar-turbulent transition. Waves of $\omega = 0, \beta > 0$ correspond to longitudinal vortices—near-wall streaks. The waves of $\omega \approx 45$ are presumably related to the low-frequency pulsation of the separation zone ahead the jet. Starting from the station $x \approx 1.0$ there are high-frequency peaks of $\omega \approx 350$ associated with the secondary instability of HSV and CRV. These small-scale structures are modulated with frequency $\omega \approx 45$ corresponding to the low-frequency oscillations of the primary vortices.

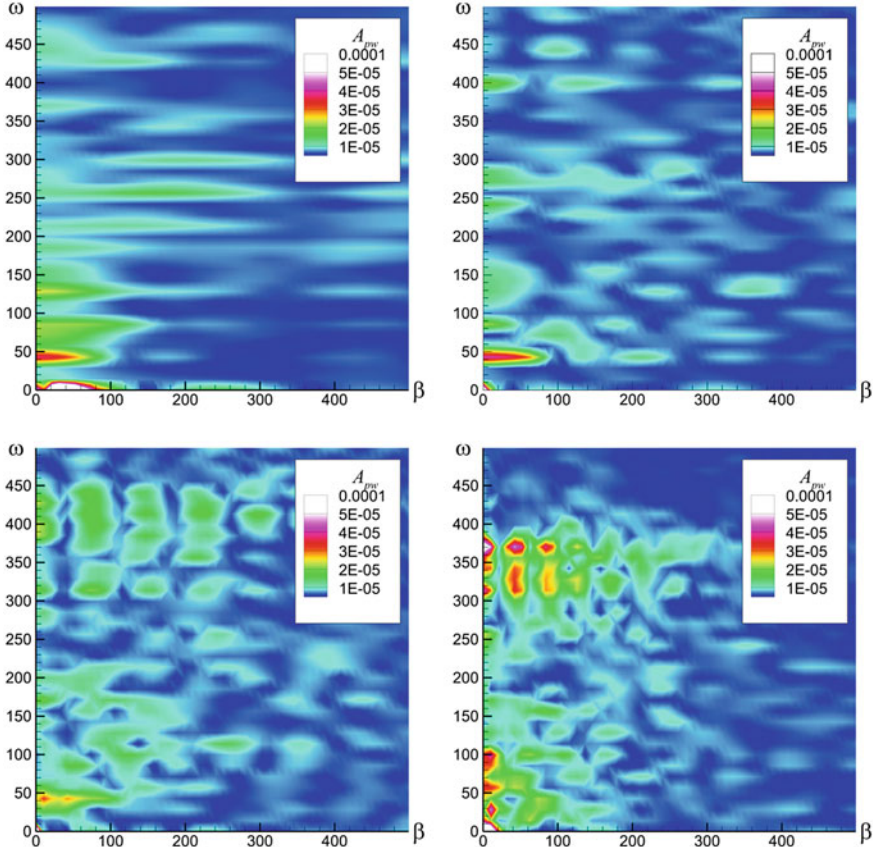


Fig. 4 Wall pressure disturbance spectra at x -stations $x = 0.3, 0.5, 0.8, 1.35$ respectively

The transition onset and the streamwise length of transitional region can be evaluated using distributions of the skin friction coefficient $c_{fx} = \frac{\tau_w^*}{\frac{1}{2}\rho^*V_\infty^*} = \left[\mu \frac{\partial u}{\partial n} \right]_w / \frac{1}{2} Re_\infty$. Figure 5 shows time-averaged pattern of $c_{fx}(x, z)$ on the plate surface. It reveals streaks typical for the flow within young turbulent wedge. The visual assessment of the lateral spread angle of this wedge gives $\phi \approx 2.3^\circ$. This value agrees well with the lateral spread angles of turbulent spots obtained experimentally [11] and numerically [10].

Distributions of skin friction coefficient $c_{fx}(x)$ along the center line $z = 0$ are shown in Fig. 6 together with distributions for laminar and fully turbulent BL. The skin friction approaches the turbulent level over a short distance from the jet. Significant overshoots of the turbulent level indicates the presence of highly nonlinear

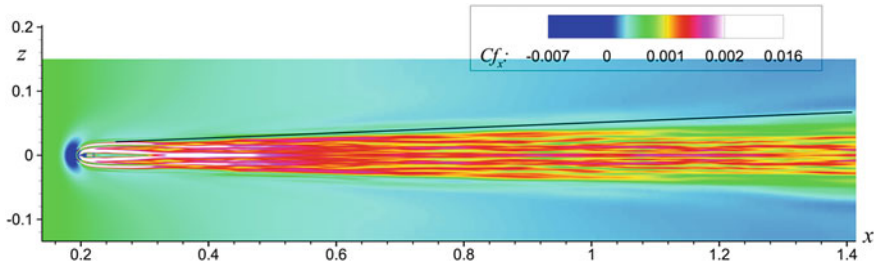


Fig. 5 Time-averaged skin friction coefficient $c_{fx}(x, z)$. The black inclined lines indicate the core part of the turbulent wedge

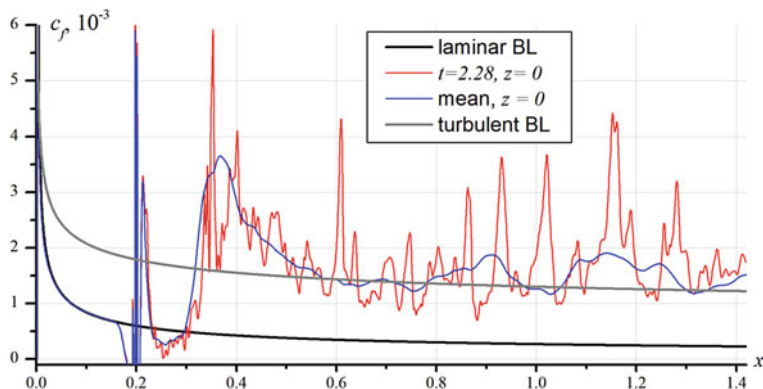


Fig. 6 Instantaneous (red line) and time-averaged (blue line) distributions of the skin friction coefficient along the center line $z = 0$; “laminar BL”—steady unperturbed BL flow without injection; “turbulent BL”—Van Driest II correlation [16] for turbulent BL

transitional flow which has not achieve the equilibrium turbulent state yet. Large oscillations of the time-averaged distribution (blue line) are due to a relatively short time interval in the averaging procedure.

4 Conclusions

Implicit large-eddy simulations have been performed to investigate 3-D disturbances propagating over a flat plate at the free-stream Mach number $M_\infty = 5.373$ with wall injection through a circular hole. The computations have been conducted using the in-house Navier-Stokes solver HSFlow implementing an implicit finite-volume shock-capturing method with the second-order approximation in space and time. It was shown that this code is able to simulate highly nonlinear dynamics of disturbances induced by the jet in supersonic crossflow (JISC) up to the stage of “young” turbulent wedge. The numerical solutions show that the injection produces a barrel-

shaped JISC and a system of unstable vortices evolving downstream. The nonlinear breakdown of these vortices leads to laminar-turbulent transition.

The computed JISC induced flow is very similar to that past an isolated roughness element of effective height. In the both cases, the observed flow structures include: bow shock, upstream separation zone, horseshoe vortices (HSV), primary counter-rotating longitudinal vortices (CRV), and small-scale structures associated with secondary instability of the primary HSV and CRV.

The injection jet leads to very quick laminar-turbulent transition without artificial unsteady forcing. Since the flow instability is excited by numerical noise of very low intensity, the flow field near JISC seems to be absolutely unstable. The near-field disturbances are amplified to appreciable amplitudes and feed the breakdown process downstream from the JISC.

The wall pressure disturbance spectra exhibit low-frequency harmonics associated with pulsations in the separation zone ahead the JISC, as well as high-frequency harmonics associated with the secondary instability of HSV and CRV. The latter quickly evolve to hairpin vortices, which drive a self-sustaining process of turbulence production in the BL flow. Ultimately a “young” turbulent wedge is formed at a relatively short distance from the jet. Its lateral spreading angle is estimated as 2.3° , that fall within the scatter range of experimental and DNS data for turbulent spots in high-speed BL.

The numerically predicted skin friction coefficient exhibits a rapid increase with significant overshoot of the turbulent level. Similar to the flow past an effective roughness element, the transitional region is short and it is located at a small distance downstream the jet.

Thus, this numerical study confirms that JISC is very effective in tripping of high-speed BL flows. As contrasted to roughness elements, the injection jets are adjustable to a broad range of flow conditions. Moreover, the injection of relatively cold gas reduces thermal loads that is of critical importance for high-speed applications. This encourages further numerical studies of active tripping of high-speed BL flows using rows of JISC.

Acknowledgements This work was supported by the Russian Foundation for Basic Research (project 18-08-01295 – calculations) and Russian Science Foundation (project 19-19-00470 – development of the model for flow in a channel) and has been carried out using computing resources of the federal collective usage center Complex for Simulation and Data Processing for Mega-science Facilities at NRC “Kurchatov Institute”, <http://ckp.nrcki.ru/>.

References

1. Bathel, B., Danehy, P., Inman, J., Alderfer, D., Berry, S.: PLIF visualization of active control of hypersonic boundary layers using blowing. In: AIAA paper 2008–4266 (2008). <https://doi.org/10.2514/6.2008-4266>
2. Berry, S., Horvath, T.: Discrete roughness transition for hypersonic flight vehicles. In: AIAA paper 2007–307 (2007). <https://doi.org/10.2514/6.2007-307>

3. Berry, S., Nowak, R., Horvath, T.: Boundary layer control for hypersonic airbreathing vehicles. In: AIAA paper 2004-2246 (2004). <https://doi.org/10.2514/6.2004-2246>
4. Berry, S.A., DiFulvio, M., Kowalkowski, M.K.: Forced boundary-layer transition on X-43 (hyper-X) in NASA LaRC 20-inch mach 6 air tunnel. NASA/TM 2000-210316, NASA Langley Research Center (2000)
5. Bountin, D., Chimitov, T., Maslov, A., Novikov, A., Egorov, I., Fedorov, A., Utyuzhnikov, S.: Stabilization of a hypersonic boundary layer using a wavy surface. AIAA J. **51**(5), 1203–1210 (2013). <https://doi.org/10.2514/1.j052044>
6. Chaudhry, R.S., Subbareddy, P.K., Nompelis, I., Candler, G.V.: Direct numerical simulation of roughness-induced transition in the VKI mach 6 tunnel. In: AIAA paper 2015-0274 (2015). <https://doi.org/10.2514/6.2015-0274>
7. Chuvakhov, P.V., Fedorov, A.V.: Spontaneous radiation of sound by instability of a highly cooled hypersonic boundary layer. J. Fluid Mech. **805**, 188–206 (2016). <https://doi.org/10.1017/jfm.2016.560>
8. Egorov, I.V., Novikov, A.V., Fedorov, A.V.: Numerical modeling of the disturbances of the separated flow in a rounded compression corner. Fluid Dyn. **41**(4), 521–530 (2006). <https://doi.org/10.1007/s10697-006-0070-7>
9. Egorov, I.V., Novikov, A.V., Fedorov, A.V.: Direct numerical simulation of the laminar-turbulent transition at hypersonic flow speeds on a supercomputer. Comput. Math. Math. Phys. **57**(8), 1335–1359 (2017). <https://doi.org/10.1134/s0965542517080061>
10. den Eynde, J.V., Steelant, J.: Compressibility and temperature effects on turbulent spot growth. In: HiSST: International Conference on High-Speed Vehicle Science Technology, 26–29 November 2018, Moscow (2018)
11. Fischer, M.C.: Spreading of a turbulent disturbance. AIAA J. **10**(7), 957–959 (1972). <https://doi.org/10.2514/3.50265>
12. Novikov, A., Egorov, I., Fedorov, A.: Direct numerical simulation of wave packets in hypersonic compression-corner flow. AIAA J. **54**(7), 2034–2050 (2016). <https://doi.org/10.2514/1.J054665>
13. Novikov, A.V.: Transition induced by a wave train in a supersonic boundary layer over a compression ramp. In: AIAA paper 2017-4517 (2017). <https://doi.org/10.2514/6.2017-4517>
14. Orlik, E., Fedioun, I., Lardjane, N.: Hypersonic boundary-layer transition forced by wall injection: a numerical study. J. Spacecr. Rocket. **51**(4), 1306–1318 (2014). <https://doi.org/10.2514/1.a32645>
15. Shrestha, P., Candler, G.V.: Direct numerical simulation of high-speed transition due to roughness elements. J. Fluid Mech. **868**, 762–788 (2019). <https://doi.org/10.1017/jfm.2019.179>
16. Van Driest, E.R.: The problem of aerodynamic heating. Aeronaut. Eng. Rev. **15**(8), 26–41 (1956)
17. Zhao, H., Balakumar, P.: Nonlinear disturbance evolution across a hypersonic compression corner. AIAA J. **43**(5), 1034–1041 (2005). <https://doi.org/10.2514/1.2244>

Influence of High-Temperature Effects on the Stability of the Wake Behind an Isolated Roughness Element in Hypersonic Flow



Iván Padilla Montero, Fernando Miró Miró, and Fabio Pinna

Abstract The influence of high-temperature effects on the stability of the wake behind a cuboidal roughness element is presented. Different flow assumptions are considered, including a calorically perfect gas, a thermally perfect gas and a mixture of gases in chemical non-equilibrium. Two-dimensional linear stability (2D-LST) computations are performed along the roughness wake for each of the different flow models and compared. The results show that, in the vicinity of the roughness element, the sinuous perturbation is stabilized by the excitation of the vibrational energy mode, whereas the varicose disturbance presents a strong destabilization. Further downstream, the sinuous instability is found to decay at a slower rate when accounting for vibrational excitation in its modeling, yielding a higher integrated amplification factor than with a calorically perfect gas assumption.

1 Introduction

Boundary-layer transition is a critical design driver for vehicles capable of hypersonic flight. Turbulent high-speed boundary layers are characterized by large heat fluxes that lead to challenging aerothermodynamic loads. The transition process at hypersonic speeds is known to be strongly influenced by the presence of isolated roughness elements on the surface. Examples include damaged heat-shield tiles, rivets or protruding gap fillers, among many others. Such three-dimensional elements with heights comparable to the local boundary-layer thickness generally induce counter-

I. Padilla Montero (✉) · F. Miró Miró · F. Pinna
von Karman Institute for Fluid Dynamics, Chaussée de Waterloo 72, 1640 Rhode-Saint-Genèse,
Belgium
e-mail: ivan.padilla@vki.ac.be

F. Miró Miró
e-mail: fernando.miro.miro@vki.ac.be

F. Pinna
e-mail: fabio.pinna@vki.ac.be

rotating streamwise vortices in the flow [1], giving rise to a low-velocity streak that is surrounded by regions of high shear.

In recent years, several researchers have studied the stability characteristics of the wake induced by isolated roughness elements, both experimentally and numerically, and mainly at calorically perfect gas conditions (see [2–7]). Their analyses revealed that the roughness wake supports the growth of sinuous and varicose instability modes that develop in the high-shear regions introduced by the counter-rotating vortex pair, and that these modes can undergo a substantial growth during the linear stages of the transition process.

High-temperature effects on the stability of hypersonic boundary layers were first studied by Malik and Anderson [8], who considered self-similar boundary layer profiles in local thermodynamic equilibrium (LTE). Next, Stuckert and Reed [9] extended this analysis to boundary layers in chemical non-equilibrium and Hudson et al. [10] included also thermal non-equilibrium effects. The main findings show a destabilization of the second Mack mode instability in the presence of internal-energy-mode-excitation and dissociation-driven base-flow cooling as well as a shift towards lower frequencies. Many authors have since investigated high-enthalpy effects on various configurations and test conditions, with different stability theories [11–17]. However, the studies were restricted to second-mode instabilities.

Regarding the role of isolated roughness elements in boundary-layer transition for high-enthalpy flows, very few studies are available. Groskopf et al. [18] analyzed the instability introduced by a discrete oblique roughness element in cold and hot flow conditions. For the hot case, the base-flow solutions were obtained in chemical non-equilibrium, while a thermally perfect gas model was implemented for the stability computations. The results showed a significant destabilizing influence of high-temperature effects on the stability behavior of the modes developing in the roughness wake. Very recently, Di Giovanni and Stemmer [19] performed direct numerical simulations on a hemispherical capsule-like geometry, finding that the inclusion of chemical non-equilibrium has a destabilizing effect on the evolution of unstable modes in the roughness wake.

This work investigates the influence of high-temperature effects on the instability of the wake induced by a cuboidal roughness element mounted on top of a flat plate at freestream conditions that are representative of the Space Shuttle reentry trajectory. Two-dimensional linear stability theory (2D-LST) is employed together with base flows obtained from laminar and steady Navier–Stokes simulations accounting for high-enthalpy effects. The formulation of the linear perturbation equations used for the stability analysis is made fully consistent with the base-flow solutions by including the appropriate thermodynamic and transport modeling in the derivation of the stability equations.

2 Theoretical Framework

The accurate reproduction of the physical features of high-enthalpy flows requires appropriate sets of modeling hypotheses. The excitation of internal energy modes and the subsequent departure of the gas' thermal law from a linear one (constant specific heat), as well as the dissociation of molecules, must be accounted for. To that end, three different flow assumptions are introduced [20]. The first is a mixture of perfect gases in chemical non-equilibrium (CNE) with five species, N, O, NO, N₂ and O₂, in which reactions are allowed to occur at a finite rate (see Park et al. [21]). The second is a thermally perfect gas (TPG) with frozen chemistry, in which the excitation of internal energy modes is considered but the flow time scale is assumed to be much smaller than that of chemical reactions. The third is a calorically perfect gas (CPG), which establishes a constant value of the heat capacity, thus assuming the enthalpy to be a linear function of temperature.

For the CNE and TPG assumptions, the thermal properties of the mixture are obtained employing the polynomial expressions for each species provided by Thompson et al. [22].

Regarding the transport properties, two different sets of models are compared for the CPG assumption. The first is Sutherland's law (with the coefficients reported by White [23]) to obtain the dynamic viscosity (μ), combined with a constant Prandtl number of 0.7 to retrieve the thermal conductivity (κ). The second employs Gupta et al.'s [24] polynomial-logarithmic curve fits to retrieve the species viscosities and thermal conductivities. These are then mixed with Wilke's mixing rule [25]. It is therefore referred to as the Gupta-Wilke (GW) model, and it is also the one used for the other flow assumptions (TPG and CNE). The use of the CPG assumption, together with the two mentioned sets of models is distinguished by denoting them as CPGS (Sutherland) and CPGGW (Gupta-Wilke).

Concerning the stability analysis, the flow is decomposed into steady (\bar{q}) and perturbation (\hat{q}) components. Linear stability theory (LST) assumes a locally-parallel base flow and wave-like perturbations that are periodic in time (t), in the streamwise (x) and in the spanwise (z) directions:

$$q(x, y, z, t) = \bar{q}(y) + \hat{q}(y) \exp[i(\alpha x + \beta z - \omega t)] + c.c.. \quad (1)$$

Similarly, 2D-LST (also referred to as BiGlobal [26] stability theory) relaxes the periodicity assumption in the spanwise direction of both the base-flow and perturbation quantities:

$$q(x, y, z, t) = \bar{q}(y, z) + \hat{q}(y, z) \exp[i(\alpha x - \omega t)] + c.c.. \quad (2)$$

The deployment of Eqs. 1 or 2 on the Navier-Stokes equations, leads to the LST or the 2D-LST eigenvalue problem (see Pinna and Groot [27] or Pinna et al. [28]). The treatment is analogous for all flow assumptions described before, varying only the set of equations that must actually be solved (see Miró Miró et al. [17]).

3 Numerical Methodology

The problem studied in this work consists of a wedge inside a hypersonic freestream with a cuboidal roughness element mounted on top (see Fig. 1). The wedge has a half-angle of $\theta = 20^\circ$ and it is infinitely sharp. The freestream conditions are Mach number $M_\infty = 18$, static temperature $T_\infty = 231.45$ K and static pressure $p_\infty = 10$ Pa, representative of a point in the reentry trajectory of the Space Shuttle Orbiter. The leading edge of the roughness element is located inside the laminar boundary layer at a streamwise distance of $x_r = 1.2$ m from the wedge leading edge and is centered at the spanwise symmetry plane. The roughness is $h_r = 1.62$ cm high and has a square planform that is $6h_r$ long. These dimensions were chosen to yield a ratio of roughness height to the local unperturbed boundary layer thickness (δ_{99}) of $h_r/\delta_{99} \approx 0.6$ and a roughness Reynolds number of $Re_r = u_r h_r / v_r \approx 400$. Here, δ_{99} is estimated using the total enthalpy (h_0) criterion defined as $h_0/h_{0,e} = 0.995$, with $h_{0,e}$ being the total enthalpy at the boundary layer edge. The quantities u_r and v_r are respectively the streamwise velocity and kinematic viscosity at the roughness height and at x_r in the same unperturbed boundary layer used to estimate δ_{99} .

The computational domain employed for the base-flow calculations is also represented in Fig. 1, where the inflow plane is located at $x_{in} = 0.5$ m from the wedge leading edge and it is $y_{in} = 0.49$ m tall. The outlet plane is located at $x_{out} = 60$ m with maximum $y_{out} = 1.87$ m. The spanwise size of the domain is $z_\infty = 0.65$ m. The domain is located inside the shock layer established between the shock wave induced at the wedge leading edge and the wedge surface. In this approach, a boundary-layer profile is prescribed at the inflow boundary of the domain, similarly to [3, 5, 6, 29].

The computation of the steady base-flow solutions is performed by means of the software package CFD++® using a block-structured grid with a resolution of $N_x \times N_y \times N_z = 830 \times 320 \times 190$.

The base-flow boundary conditions are labeled in Fig. 1. At the inflow, a boundary-layer profile obtained with the flow solver DEKAF [16, 30] is prescribed. Similarly,

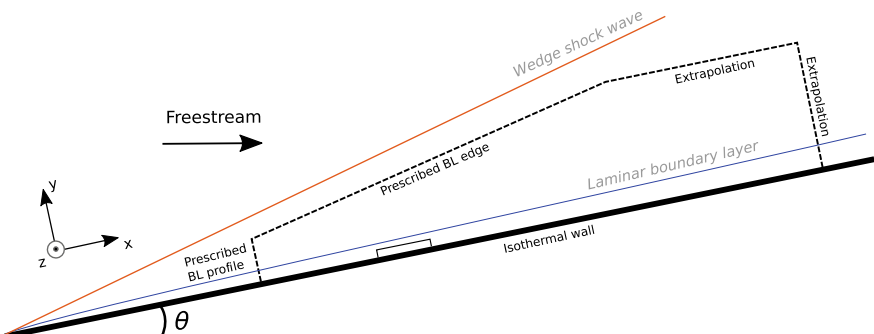


Fig. 1 Representation of the geometrical configuration of the problem under study and the computational domain employed for the base-flow calculations (not to scale)

at the initial (inclined) part of the top boundary, the boundary-layer edge conditions are prescribed, which are identical to the post-shock conditions obtained from inviscid theory through the Rankine-Hugoniot relationships [20]. Additionally, the wall-normal velocity component is set to zero. At the second (wall-parallel) portion of the top boundary and at the outflow, the primitive flow variables are extrapolated from the interior of the domain. At the spanwise boundaries ($z = 0$ and $z = z_\infty$), symmetry conditions are specified. Finally, at the wall, a no-slip isothermal condition is enforced with a wall temperature of $T_w = 1900$ K, similar to the thermal limit of the Space Shuttle's thermal protection system [31].

The numerical solution of the stability problem is carried out using the von Karman Institute Extensible Stability and Transition Analysis (VESTA) toolkit [32]. The generalized eigenvalue problem is assembled and discretized using the high-order finite-difference scheme known as FD- q (Hermanns and Hernández [33]). The mapping originally introduced by Malik [34] is applied in the wall-normal direction. In the spanwise direction, a BiQuadratic mapping [35] concentrates one-third of the grid points in the region of interest.

The boundary conditions for 2D-LST enforce a homogeneous Dirichlet condition on the velocity and temperature perturbations at the wall and at the wall-normal far-field boundary. The density fluctuation is determined by means of a compatibility condition satisfying the wall-normal momentum equation at both wall-normal boundaries. For the case of CNE, four of the five species are forced to obey the species wall-normal momentum equation (see Miró Miró and Pinna [36]). At the spanwise boundaries, periodic boundary conditions are specified for all the variables.

The eigenvalue problem is solved by means of an implicitly-restarted Arnoldi algorithm [37].

4 Stability Analysis of the Smooth Wedge Configuration

The effect of the different flow assumptions on the stability of the smooth wedge boundary layer is illustrated in Fig. 2, which shows N -factor envelope curves obtained with LST. The second Mack mode is destabilized when accounting for internal-energy-mode excitation and dissociation, as a consequence of the smaller predicted boundary-layer thickness.

The comparison between the N -factors predicted by the CPGS and the CPGGW flow assumptions provides a measure of the error associated to an inaccurate modeling of the transport properties. The validity of Sutherland's law is restricted to temperatures below 2000 K, underpredicting the dissipation beyond this threshold [17]. An appropriate evaluation of internal-energy-excitation and dissociation effects on the instabilities can only be performed between flow assumptions with an equivalent set of transport models, that is, CPGGW, TPG and CNE.

Additional N -factor envelopes have also been computed using base flows obtained by solving the full Navier-Stokes equations, in order to assess the appropriateness of the boundary-layer assumptions under the conditions considered. The resulting

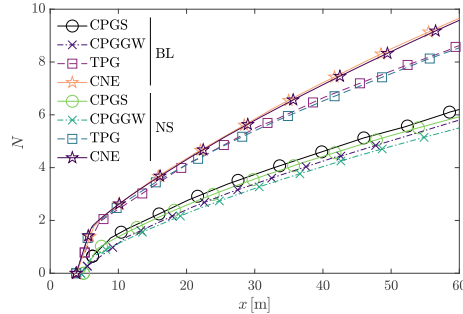


Fig. 2 Second Mack mode N -factor envelope curves for the various flow assumptions, using boundary-layer (BL) and Navier–Stokes (NS) base flows

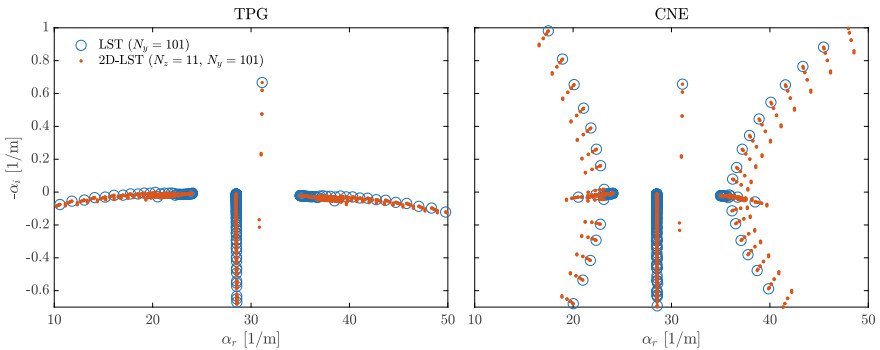


Fig. 3 Comparison between the spatial stability spectrum obtained by means of LST and 2D-LST for a fixed location and frequency in the smooth wedge boundary layer

curves are also shown in Fig. 2, labeled as NS. The fact of using the boundary-layer equations does not lead to important differences in the current case.

The smooth wedge case is ideal to verify the implementation of the 2D-LST equations for the TPG and CNE flow assumptions. Since LST and 2D-LST are based on the same assumptions, except that in the 2D-LST case there is an additional non-homogeneous direction, all the instability modes that are solution to the LST eigenvalue problem must also be a solution to the 2D-LST one. For verification purposes, a location of $x = 5.06 \text{ m}$ and a frequency of 22.85 kHz are considered. The results of the comparison are presented in Fig. 3, illustrating that for each LST mode there is a corresponding family of 2D-LST modes. More specifically, $N_z - 2$ modes are obtained from the 2D-LST problem for each respective mode of the LST one, with N_z being the number of grid points in the spanwise direction. All the possible spanwise wavenumbers (β) that can be resolved by the discretization along z become part of the solution as well. The verification is certified by the excellent agreement of the first 2D-LST mode of each family ($\beta = 0$) with the LST one, where $\beta = 0$ is explicitly imposed.

The LST solver inside VESTA has been successfully verified against other authors in the past for base flows including high-temperature phenomena [17].

5 Stability Analysis in the Roughness Wake

The main features of the computed base-flow solutions with roughness are presented in Fig. 4, which displays the streamwise velocity and temperature contours obtained for the CPGGW and the CNE cases. The streamwise velocity results are presented on the spanwise symmetry plane, including the regions of separated flow. The temperature field is illustrated on a plane located at a height equal to half of the roughness element height. Focusing on the streamwise velocity plots, it can be observed that the roughness element generates two small regions of separated flow, located immediately upstream and downstream of the roughness leading and trailing edges, respectively.

By looking at the streamwise flow structure, given by the temperature contour plots, a pair of strong counter-rotating vortices can be identified, which form at the edges of the roughness element. These streamwise structures lift-up low-momentum fluid adjacent to the wedge surface and give rise to a low-velocity streak, which is surrounded by regions of high streamwise shear and large shear gradients in the wall-normal and spanwise directions (see [3, 4]).

The most notable difference between the two base-flow solutions presented lies in the temperature values obtained for each of the flow assumptions. The excitation of the vibrational energy mode, the presence of chemical reactions and the molecular diffusion accounted for in the CNE case yield a significantly lower temperature field than for the CPG assumption. Such a lower temperature, in turn, leads to a decrease in the boundary layer thickness. The TPG temperature field (not presented) is very similar to the CNE one, as a consequence of the low level of dissociation attained at the streamwise location of the roughness element.

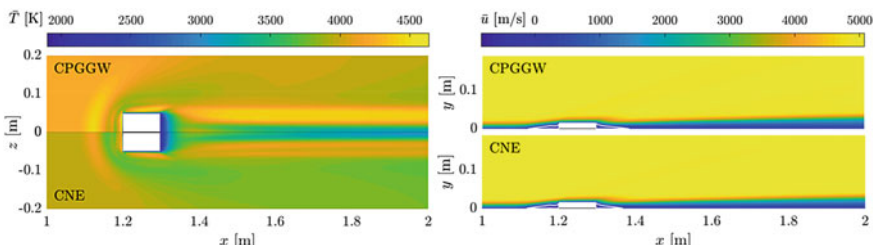


Fig. 4 Comparison of the base-flow solutions obtained for the CPGGW and the CNE flow assumptions. Streamwise velocity contours are shown on the spanwise symmetry plane ($z = 0$). The white solid lines represent isolines of $\bar{u} = 0$. Temperature contours are depicted on an xz plane located at half of the roughness element height

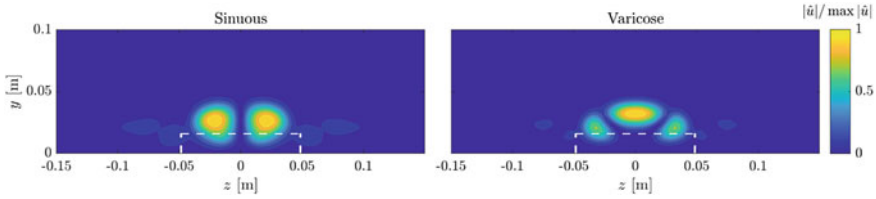


Fig. 5 Normalized magnitude of the streamwise velocity amplitude function of the two most unstable modes for CNE at $x = 2$ m. Sinuous mode at a frequency $f = 3$ kHz and varicose mode at $f = 9$ kHz

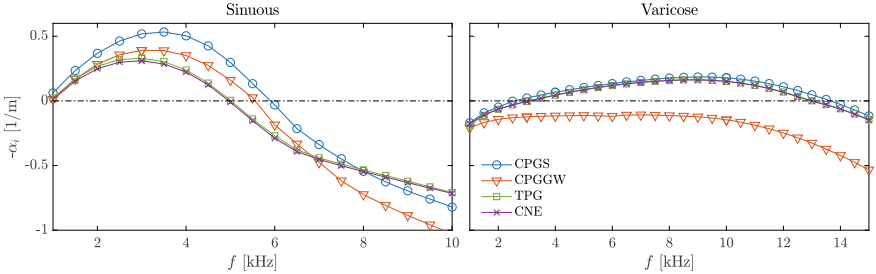


Fig. 6 Evolution of the growth rate of the most unstable sinuous and varicose instabilities as a function of frequency for the various flow assumptions at $x = 2$ m

Spatial 2D-LST computations have been performed in the wake behind the roughness element for the four different flow assumptions under study. All the calculations have been carried out using an order of $q = 8$ and setting the wall-normal base-flow velocity to zero. Figure 5 displays contour plots of the streamwise velocity amplitude function of the two most unstable modes obtained for CNE at $x = 2$ m downstream of the wedge leading edge. These two instabilities are, respectively, the sinuous (odd) and varicose (even) modes that develop in the wake behind the roughness element. Their regions of development are concentrated inside and around the low-velocity streak that characterizes the wake flow structure. The sinuous mode features a zero amplitude at the spanwise symmetry plane, which reflects its antisymmetric character. These modes are found to dominate the wake instability for all the various flow assumptions investigated.

Figure 6 represents the evolution of the growth rate of the two most unstable wake modes as a function of frequency for each flow assumption at $x = 2$ m. At their unstable frequency range, the sinuous and varicose instabilities follow opposite trends when the excitation of the vibrational energy mode is taken into account. While the sinuous mode is more stable for TPG/CNE than for CPGGW, the varicose mode is strongly destabilized. It can also be observed that the growth rate of both the sinuous and varicose instabilities is higher for CPGS than for CPGGW for all the frequencies analyzed. This is the same behavior observed for the second Mack mode results reported in Sect. 4. The evolution of the varicose mode growth rate

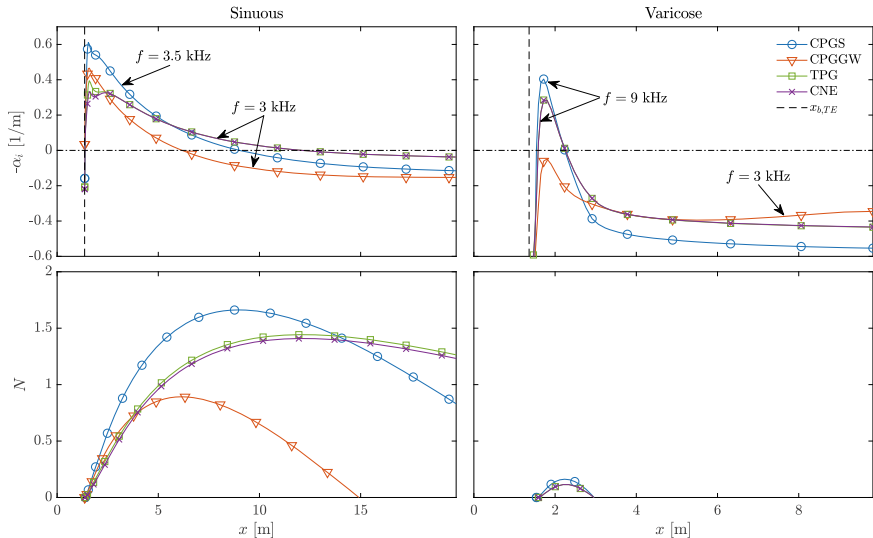


Fig. 7 Evolution of the growth rate and associated N -factor curves of the most unstable sinuous and varicose instabilities as a function of the streamwise coordinate for the different flow assumptions

with frequency for CPGS happens to be in agreement with that of the TPG and CNE cases. Nevertheless, this is a mere coincidence rather than a behavior attributed to a sound modeling of the vibrational excitation.

Figure 7 displays the streamwise evolution of the sinuous and varicose instabilities for the different flow assumptions, both in terms of growth rate and N -factor. The frequency associated to each curve corresponds to the respective most unstable frequency retrieved from the results shown in Fig. 6. The vertical dashed line labeled $x_{b,TE}$ denotes the streamwise coordinate of the end of the separation bubble induced at the trailing edge of the roughness element. Close to the roughness element, the growth rate of the sinuous mode is smaller for CNE than for TPG, which is likewise smaller than for CPGGW. However, this trend is inverted further downstream, and the mode is significantly destabilized for approximately $x > 2.5$ m. This is strongly reflected in the N -factor evolution for each of these cases.

Once again, the varicose mode features an opposed behavior, as it is destabilized near the roughness element for the TPG or the CNE assumptions. When accounting for vibrational excitation, the varicose mode follows a similar trend to the second Mack mode. Similarities between the second Mack mode and the varicose mode instabilities have been already recognized by previous authors. For the wake behind a cuboidal roughness element in CPG at Mach 6, De Tullio and Sandham [5] found a varicose instability tuned with the boundary-layer thickness, similarly to what is observed for the second Mack mode with LST. Nevertheless, in their case they found the varicose disturbance to be stabilized by wall cooling, as opposed to what is retrieved in this analysis for boundary-layer cooling.

The discrepancies between the behavior of the two modes could be related to differences in the disturbance energy extraction mechanisms between the two types of instabilities. The similarities between the varicose mode and the Mack mode suggest that the energy of the varicose instability is dominated by the interaction between the perturbation quantities and the wall-normal base flow gradients over the spanwise ones. This is argued to make the varicose mode more sensitive to changes in the boundary-layer thickness than the sinuous one, which would explain its strong destabilization in the presence of boundary-layer cooling.

Since the geometrical configuration considered in this work does not feature a stagnation point, no chemical reactions take place at the wedge leading edge. The dissociation of O₂, for instance, which is the most relevant reaction at the temperature range obtained for the CNE case [20], starts to occur downstream of the leading edge. Because of this configuration, the flow did not have enough time to undergo a sufficient amount of dissociation at the location of the roughness element. For this reason, the wake instability results obtained for TPG and CNE are very close to each other. Chemistry effects are more noticeable for instabilities developing further downstream, as it is the case for the second Mack mode (see Fig. 2).

It is also worth emphasizing that, for the conditions under investigation, the maximum N -factor values obtained for both wake instability modes are still far from being relevant for triggering boundary-layer transition.

6 Conclusions

To the best of the authors' knowledge, this work constitutes the first 2D-LST implementation that incorporates a modeling of chemical non-equilibrium effects into the perturbation equations. This capability is of paramount importance for the study of roughness-induced transition on hypersonic vehicles. Stability computations have allowed the identification of the well-known varicose and sinuous instabilities also in the presence of vibrational-energy-mode excitation and chemical reactions. The investigation has shown that, in the vicinity of the roughness element, the two types of disturbances feature an opposite behavior. While the sinuous mode is stabilized when vibrational excitation and molecular dissociation are taken into account, the varicose perturbation undergoes a significant destabilization. The varicose mode is then found to behave in the same way as the second Mack mode in the presence of base-flow cooling. Further away from the roughness element, however, the sinuous instability decays at a slower rate when modeling the excitation of the vibrational energy mode and molecular dissociation, reaching a higher integrated amplification factor for the TPG and CNE flow assumptions than for CPGGW. Despite the sinuous disturbance undergoing a much higher amplification than the varicose one, both modes are still far from reaching N -factor values that are relevant for triggering transition.

On the other hand, only small differences in the instability of the wake modes have been obtained between the TPG and the CNE flow assumptions, revealing that

the influence of chemical reactions is not relevant at the conditions investigated. This is due to the lack of a stagnation point in the problem geometry, such that chemical reactions are not active at the wedge leading edge. At the streamwise position of the roughness element, the flow has not yet undergone sufficient dissociation so as to affect the propagation of instabilities.

Acknowledgements This work is part of a project that has received funding from the European Union's Horizon 2020 research and innovation programme under the Marie Skłodowska-Curie grant agreement No 675008. It was also partially funded by the Belgian National Fund for Scientific Research (FNRS) through the FRIA fellowship.

References

1. Ruban, A.I., Kravtsova, M.A.: Generation of steady longitudinal vortices in hypersonic boundary layer. *J. Fluid Mech.* **729**, 702–731 (2013)
2. Kegerise, M., King, R., Owens, L., Choudhari, M., Norris, A., Li, F., Chang, C.-L.: An experimental and numerical study of roughness-induced instabilities in a Mach 3.5 boundary layer. *RTO-AVT-200/RSM-030 29*, NATO (2012)
3. De Tullio, N., Paredes, P., Sandham, N.D., Theofilis, V.: Laminar-turbulent transition induced by a discrete roughness element in a supersonic boundary layer. *J. Fluid Mech.* **735**, 613–646 (2013)
4. Choudhari, M., Chang, C.L., Norris, A., Edwards, J.: Wake instabilities behind discrete roughness elements in high speed boundary layers. In: 51st AIAA Aerospace Sciences Meeting Including the New Horizons Forum and Aerospace Exposition, Grapevine, Dallas/Ft. Worth Region, USA, 7–10 January 2013, AIAA 2013-0081 (2013)
5. De Tullio, N., Sandham, N.D.: Influence of boundary-layer disturbances on the instability of a roughness wake in a high-speed boundary layer. *J. Fluid Mech.* **763**, 136–165 (2015)
6. Theiss, A., Hein, S.: Investigation on the wake flow instability behind isolated roughness elements on the forebody of a blunt generic re-entry capsule. *EUCASS Book Ser. - Adv. Aerosp. Sci.* **9**, 451–480 (2017)
7. Groskopf, G., Kloker, M.J.: Instability and transition mechanisms induced by skewed roughness elements in a high-speed laminar boundary layer. *J. Fluid Mech.* **805**, 262–302 (2016)
8. Malik, M.R., Anderson, E.C.: Real gas effects on hypersonic boundary-layer stability. *Phys. Fluids* **803**(3), 803–821 (1991)
9. Stuckert, G., Reed, H.L.: Linear disturbances in hypersonic, chemically reacting shock layers. *AIAA J.* **32**(7), 1384–1393 (1994)
10. Hudson, M.L., Chokani, N., Candler, G.V.: Linear stability of hypersonic flow in thermochemical non-equilibrium. *AIAA J.* **35**(6), 958–964 (1997)
11. Johnson, H.B., Seipp, T.G., Candler, G.V.: Numerical study of hypersonic reacting boundary layer transition on cones. *Phys. Fluids* **10**(10), 2676–2685 (1998)
12. Malik, M.R.: Hypersonic flight transition data analysis using parabolized stability equations with chemistry effects. *J. Spacecr. Rocket.* **40**(3), 332–344 (2003)
13. Marxen, O., Iaccarino, G., Magin, T.E.: Direct numerical simulations of hypersonic boundary-layer transition with finite-rate chemistry. *J. Fluid Mech.* **755**, 35–49 (2014)
14. Bitter, N.P., Shepherd, J.E.: Stability of highly cooled hypervelocity boundary layers. *J. Fluid Mech.* **778**, 586–620 (2015)
15. Mortensen, C., Zhong, X.: Real-gas and surface-ablation effects on hypersonic boundary-layer instability over a blunt cone. *AIAA J.* **54**(3), 980–998 (2016)
16. Miró Miró, F., Beyak, E.S., Mullen, D., Pinna, F., Reed, H.L.: Ionization and dissociation effects on hypersonic boundary-layer stability. In: 31st Congress of the International Council of the Aeronautical Sciences, Belo Horizonte, Brazil (2018)

17. Miró Miró, F., Beyak, E.S., Pinna, F., Reed, H.L.: High-enthalpy models for boundary-layer stability and transition. *Phys. Fluids* **31**(044101) (2019)
18. Groskopf, G., Kloker, M.J., Stephani, K.A., Marxen, O., Iaccarino, G.: Hypersonic flows with discrete oblique surface roughness and their stability properties. In: Proceedings of the Summer Program 2010. Center for Turbulence Research, Stanford, CA, USA (2010)
19. Di Giovanni, A., Stemmer, C.: Roughness-induced crossflow-type instabilities in a hypersonic capsule boundary layer including nonequilibrium. *J. Spacecr. Rocket.* **56**(5), 1409–1423 (2019)
20. Anderson Jr., J.D.: Hypersonic and High Temperature Gas Dynamics, 2nd edn. American Institute of Aeronautics and Astronautics, Reston VA (2006)
21. Park, C., Jaffe, R.L., Partridge, H.: Chemical-kinetic parameters of hyperbolic earth entry. *J. Thermophys. Heat Transf.* **15**(1), 76–90 (2001)
22. Thompson, R.A., Lee, K.-P., Gupta, R.N.: Computer codes for the evaluation of thermodynamic properties, transport properties, and equilibrium constants of an 11-species air model. Technical report TM-102602, NASA (1990)
23. White, F.M.: Viscous Fluid Flow. McGraw-Hill (1991)
24. Gupta, R.N., Yos, J.M., Thompson, R.A., Lee, K.-P.: A review of reaction rates and thermodynamic and transport properties for an 11-species air model for chemical and thermal nonequilibrium calculations to 30000K. Technical report RP-1232, NASA (1990)
25. Wilke, C.R.: A viscosity equation for gas mixtures. *J. Chem. Phys.* **18**(4), 517–519 (1950)
26. Theofilis, V.: Advances in global linear instability analysis of nonparallel and three-dimensional flows. *Prog. Aerosp. Sci.* **39**(4), 249–315 (2003)
27. Pinna, F., Groot, K.J.: Automatic derivation of stability equations in arbitrary coordinates and different flow regimes. In: AIAA paper, vol. 2014-2634 (2014)
28. Pinna, F., Miró Miró, F., Zanus, L., Padilla Montero, I., Demange, S.: Automatic derivation of stability equations and their application to hypersonic and high-enthalpy shear flows. In: International Conference for Flight Vehicles, Aerothermodynamics and Re-entry Missions & Engineering, Monopoli, Italy (2019)
29. Di Giovanni, A., Stemmer, C.: Cross-flow-type breakdown induced by distributed roughness in the boundary layer of a hypersonic capsule configuration. *J. Fluid Mech.* **856**, 470–503 (2018)
30. Groot, K.J., Miró Miró, F., Beyak, E.S., Moyes, A.J., Pinna, F., Reed, H.L.: DEKAF: spectral multi-regime basic-state solver for boundary layer stability. In: AIAA paper, vol. 2018-3380 (2018)
31. Williams, S.D., Curry, D.M., Chao, D.C., Pham, V.T.: Ablation analysis of the shuttle orbiter oxidation protected reinforced carbon-carbon. *J. Thermophys. Heat Transf.* **9**(3), 478–485 (1995)
32. Pinna, F.: VESTA toolkit: a software to compute transition and stability of boundary layers. In: 43rd Fluid Dynamics Conference, San Diego, CA, USA, 24–27 June 2013, AIAA 2013-2616 (2013)
33. Hermanns, M., Hernández, J.A.: Stable high-order finite-difference methods based on non-uniform grid point distributions. *Int. J. Numer. Meth. Fluids* **56**, 233–255 (2008)
34. Malik, M.R.: Numerical methods for hypersonic boundary layer stability. *J. Comput. Phys.* **86**(2), 376–413 (1990)
35. Esposito, A.: Development and analysis of mapping and domain decomposition techniques for compressible shear flow stability calculations. Technical report, VKI SR 2016-16, von Karman Institute for Fluid Dynamics (2016)
36. Miró Miró, F., Pinna, F.: Linear stability analysis of a hypersonic boundary layer in equilibrium and non-equilibrium. In: AIAA paper, vol. 2017-4518 (2017)
37. Lehoucq, R.B., Sorensen, D.C.: Deflation techniques for an implicitly restarted Arnoldi iteration. *SIAM J. Matrix Anal. A* **17**(4), 789–821 (1996)

Effect of the Single Roughness on Shock Wave/Laminar Boundary Layer Interaction



Pavel A. Polivanov and Andrey A. Sidorenko

Abstract The paper deals with an experimental study of the wake behind a single roughness on the shock wave/laminar boundary layer interactions (SWBLI) for the flow Mach number $M = 1.45$. Incident shock wave was generated by a wedge inducing the separation of the boundary layer developed on the flat plate. 2D PIV measurements were carried out in 10–15 sections to study 3D flow structure. The effect of roughness height and its location was studied. It was found that a pair vortices is generated as a result of interaction of the shock wave and the turbulent wake. This flow pattern is significantly different from the case of turbulent incoming boundary layer.

1 Introduction

Using of laminar airfoils in transonic flow can improve the performance of turbojet compressors and reduce aerodynamic drag of an aircraft [1, 2]. An important feature of transonic flows is the shock wave/laminar boundary layer interaction (SWBLI) which can lead to the flow separation. At some regimes the strong unsteady processes in separation region can be found (including transonic buffet) [3, 4]. The turbulent boundary layer is more resistant to an adverse pressure gradient. Therefore turbulizers can be used to suppress the laminar bubble. The effect of two-dimensional roughness on SWBLI at small supersonic Mach numbers was studied in the preceding research [5]. The interaction of the single roughness wake with zone of SWBLI was not studied in detail.

In addition, experimental data on the effect of a single roughness on areas with an unfavorable pressure gradient are necessary for validation of numerical simulation. Modern CFD RANS models taking into account the laminar-turbulent transition

P. A. Polivanov (✉) · A. A. Sidorenko

Khristianovich Institute of Theoretical and Applied Mechanics, SB RAS, Novosibirsk, Russia
e-mail: polivanov@itam.nsc.ru

P. A. Polivanov
Novosibirsk State Technical University, Novosibirsk, Russia

have not been developed to simulate the effect of a single roughness, which are often found in practical tasks. Therefore the development of numerical models allowing to take into account an effect of single roughness for compressible flows is necessary. The SWBLI is a complex flow including various phenomena (laminar-turbulent transition, nonstationarity, supersonic and subsonic regions and etc.) and therefore is a “good case” for the validation of numerical models.

The main goal of this work is to obtain experimental data suitable for verification of numerical codes aimed at modeling the effect of a turbulent wake behind single roughnesses at Mach numbers close to transonic. The problem of interaction of a shock wave with a laminar boundary layer was chosen as the base flow.

2 Experimental Setup

The experiments were performed in wind tunnel T-325 (ITAM SB RAS) for Mach number $M_\infty = 1.45$, total temperature 291 K and total pressure $P_0 = 0.7$ bar. The test section of the wind tunnel has a rectangular cross section of 160×200 mm. The configuration of the experimental model is presented in Fig. 1. The experimental model consisted of a plate with a sharp leading edge occupying full span of the test section and a wedge generating a shock wave. In this series of experiments, the wedge angle was 4° . This corresponds to regular reflection of a shock wave from a model for the inviscid case. The blockage ratio of the test section was relatively high therefore the flow start was provided by extended cavities above the wedge and below the plate. The coordinate of the intersection of the incident oblique shock wave with the plate was $X_{imp} = 134$ mm.

The single roughness was a cylinder with a diameter of 0.5 mm. During the experiments the height ($h = 0.04, 0.08, 0.12, 0.5$ mm) and position ($X_s = 50, 70$,

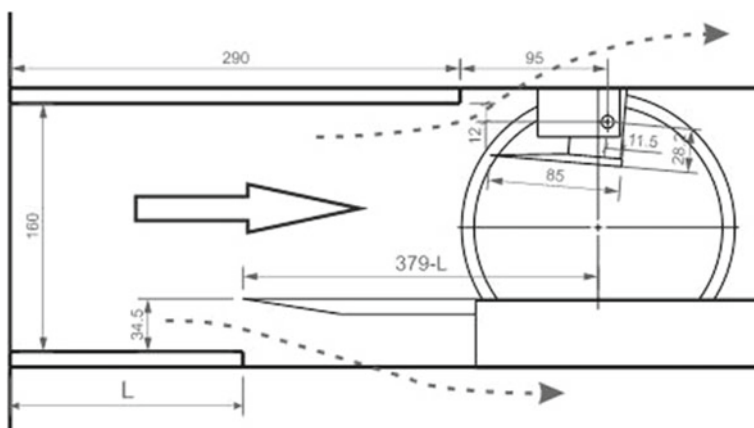


Fig. 1 The draft and photo of experimental model ($L = 250$ mm)

100 mm) of the cylindrical roughness were varied. In addition cases with two single roughnesses were considered.

The main measurement techniques were 2D PIV and oil flow visualization. DEHS microparticles with an average size of 1μ were used for PIV measurement. The velocity field was reconstructed from tracer images by means of the cross-correlation adaptive algorithms with continuous sliding of interrogation window and grid refinement of the interrogation cells. Mean velocity distributions and distributions of unsteady characteristics were obtained on the basis of 2000 instant velocity fields. The width of the laser beam in measurement region did not exceed 0.5 mm. For each case several (5–15) velocity fields in XY plane were measured at different transverse coordinates. This method did not allow to determine the transverse component of the velocity, but the wind tunnel design prevented the use of the stereo PIV. Nevertheless, the flow fields obtained during the experiments are sufficient to analyze the 3D flow characteristics.

3 Results

The most detailed 3D fields were measured for cases of single roughness with a height of $h = 0.5$ mm located at $X_r = 70, 100$ mm from the leading edge of the model. The roughness height was approximately equal to the thickness of the laminar boundary layer, therefore the boundary layer was turbulized almost immediately after the roughness.

In Fig. 2 shows an oil flow visualization of a turbulent wedge generated behind a single roughness. Note that the resulting oil flow visualization is the result of using oil tracers in the PIV measurement. In the zone of the laminar boundary layer convective flows are insignificant and the oil particles move parallel to the surface and do not collide with it. At the beginning of the laminar-turbulent transition region convective flows arise with significant values of the normal component of velocity. Due to the

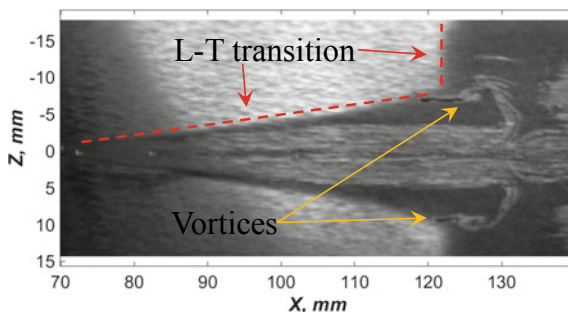


Fig. 2 Oil flow visualization after PIV measurement

inertia of the oil particles some of them collide with the surface, which leads to the appearance of an oil film in the region of turbulent flow.

From the figure is clearly to see that the wake of single roughness leads to change of the flow pattern in zone of SWBLI. The presence of a pair of vortices in the interaction zone at the edge of the turbulent wedge is clearly seen. Moreover in the region outside the turbulent wedge the location of transition does not shift and corresponds to the laminar case (turbulization begin in the region of the laminar separation).

In Fig. 3 shows the mean velocity fields in the plane of symmetry of the model ($Z = 0$ mm) for different cases. In all the figures the incident shock wave (which generates

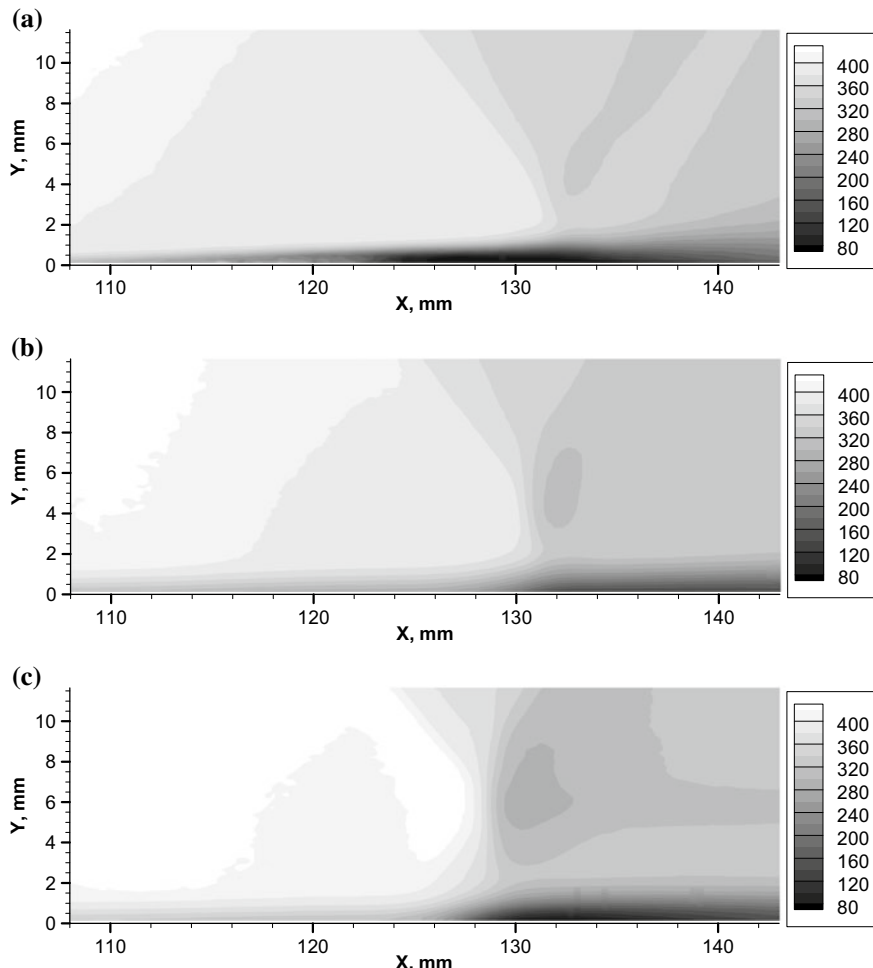


Fig. 3 Example of velocity fields (a—Laminar case, b—Single roughness ($X_r = 70$ mm) plane of symmetry ($Z = 0$ mm), c—Turbulent case)

an unfavorable pressure gradient) is well detected. But the position of the incident shock wave varies slightly for different cases due to the influence of compression waves/shock waves generated due to the separation zone. For the laminar case a long and thin separation zone was found. An increase in the displacement thickness in the separation region leads to the generation of a compression wave from a longitudinal coordinate of approximately 100 mm. For the turbulent case, the size of the separation region decreases substantially, but the growth of the displacement thickness in the interaction zone occurs more intensively.

For a single roughness case the velocity distribution in section after the roughness is basically similar to the turbulent case. But in the zone of incoming flow the compression waves are clearly visible. These waves are generated by a laminar separation located outside the turbulent wedge. Thus it can be assumed that the main difference between a turbulent case (Fig. 3c) and a single roughness case (Fig. 3b) is the 3D distortion of the shape of compression wave.

The three-dimensionality of the flow formed behind a single roughness can be found in Fig. 4. Deformation of the laminar-turbulent transition line due to the roughness leads to a distortion of the two-dimensional flow in the separation zone. As a result the shape of the shock wave arising due to the flow displacement is changed. It generates two counter-rotating vortices, which lead to a significant increase of displacement thickness downstream of SWBLI zone, in the lateral regions behind the vortices.

The difference of the velocity distribution between the laminar and the a single roughness cases is shown in Fig. 5a. It is clearly seen that the main distortion of the flow occurs in the zone of the turbulent wedge. It is interesting to note that a slight distortion of the flow was found outside the turbulent wedge ($Z > 10$ mm), which appears as an increase of the fullness of the velocity profiles in the interaction zone. At the edge of the turbulent wedge region the elongation of isolines in upstream direction is visible due to the generation of the vortex ($Z = 5-10$ mm). Vortex motion

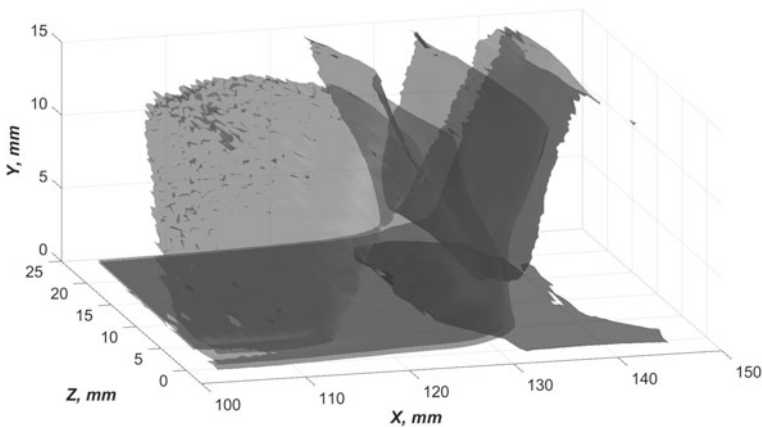
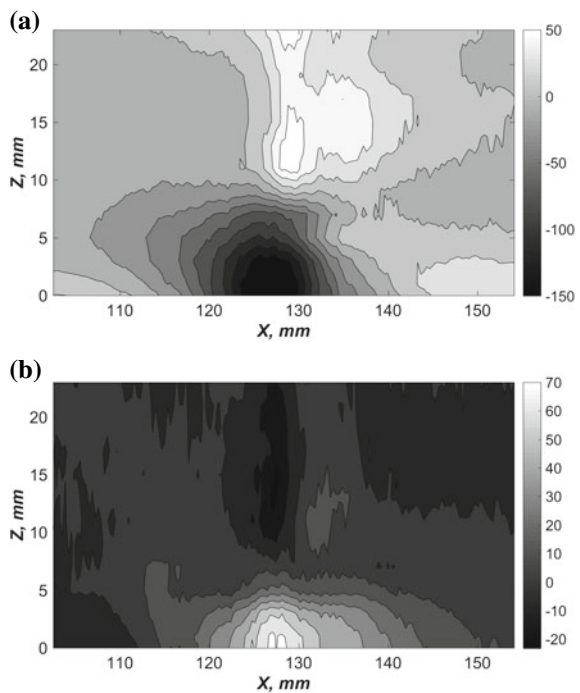


Fig. 4 Isosurfaces of velocity ($U = 150, 340, 370, 405$ m/s) for single roughness case ($X_r = 70$ mm)

Fig. 5 **a** Velocity and **b** RMS of velocity difference between laminar and roughness cases (XZ plane at $Y = 0.5$ mm)



leads to a more intensive increase of the boundary layer thickness in the wake behind the zone of SWBLI in comparison with the symmetry section ($Z = 0$ mm).

The difference in the distribution of RMS of velocity (Fig. 5b) demonstrates a decrease the level of pulsations in the zone behind the turbulent wedge, but in the remaining region an increase in pulsations was found.

Note that for other roughness positions the flow pattern remained qualitatively the same.

In Fig. 6 shows the effect of the roughness height (located at $X_r = 70$ mm) on the velocity in the plane of symmetry at a height of $Y = 0.5$ mm. Five cases were

Fig. 6 Velocity at $Y = 0.5$ mm in plane of symmetry (The effect of roughness height)

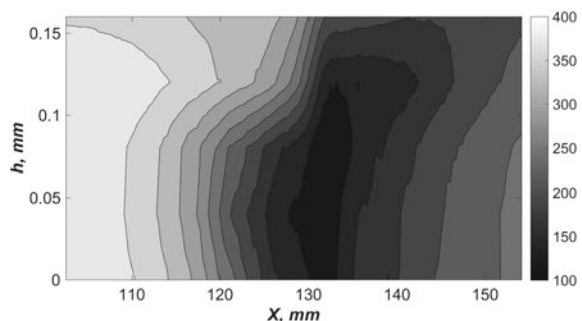
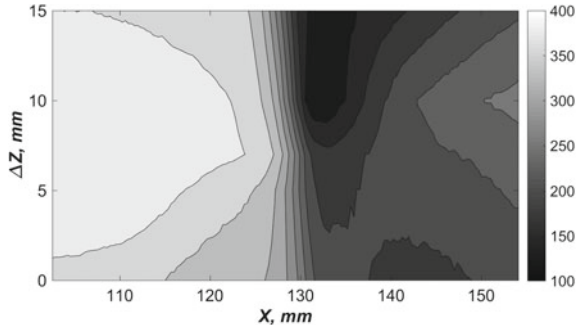


Fig. 7 Velocity at $Y = 0.5$ mm in plane of symmetry (The effect of double roughness)



investigated: without roughness ($h = 0$ mm); $h = 0.04$ mm; $h = 0.08$ mm; $h = 0.12$; $h = 0.5$ mm. The difference between the roughness heights for the last two cases ($\Delta h = 0.38$ mm) is significantly higher than for other neighboring cases ($\Delta h = 0.04$ mm). A sharp change of the step of changing the roughness height could lead to the complexity of the data analysis at low roughness heights. Therefore it was decided to label in Fig. 6 the data found for the roughness height $h = 0.5$ mm as $h = 0.16$ mm. The figure shows a weak effect of roughness on the flow for heights of 0.04 and 0.08 mm. No turbulent wedge was found for these roughnesses. For a height $h = 0.12$ mm the zone of interaction is decreases in comparison with the laminar case. For this roughness height a turbulent wedge arises at a distance of 20 mm downstream from the roughness. A further increase in the roughness height up to 0.5 mm leads to a decrease in the thickness of the boundary layer in the wake of the SWBLI zone ($X > 135$ mm). The decrease the velocity in the incoming region ($X < 130$ mm) is associated with an increase of the boundary layer thickness.

In Fig. 7 shows the data obtained for case of two single roughnesses. Double roughness was placed at a distance of $X_r = 70$ mm from the leading edge. Two identical roughnesses with a height of $h = 0.5$ mm were used. The measurements were performed in the plane of symmetry between the roughnesses. The value ΔZ corresponds to the distance from the plane of symmetry to the roughness. The case $\Delta Z = 15$ mm corresponds to a turbulent flow and is not a case of double roughness (is shown as an example).

At the beginning an increase of the distance Z leads to an increase of velocity (the interaction region is decreased). But for the case $\Delta Z = 10$ mm a sharp decrease of velocity occurs in the zone of interaction, which is due to the generation of a new vortex between roughnesses. The reason for this is the division of turbulent wedges in transverse direction for this case.

4 Conclusions

Detailed experimental data were obtained for different cases of a single roughness. These data are planned to be made publicly available for validation of the numerical models.

The flow pattern for a single roughness case is significantly different from the fully turbulent case. The main difference is the generation of a pair of vortices.

A weak effect of roughness on the flow in the zone of SWBLI outside the turbulent wedge was found.

The effect of the position and height of a single roughness has been studied. If the roughness does not generate a turbulent wedge then the flow distortion is not significant.

Acknowledgements The work was supported by grant of RSF 18-19-00547. The data processing algorithms were developed in framework of the Program of Fundamental Scientific Research of the state academies of sciences in 2013–2020 (project No. AAAA-A17-117030610126-4). The study was conducted at the Joint Access Center «Mechanics» of ITAM SB RAS.

References

1. Allison, E., Kroo, I., Sturdza, P., Suzuki, Y., Martins-Rivas, H.: Aircraft conceptual design with natural laminar flow. In: 27th International Congress of the Aeronautical Sciences, France, Nice (2010)
2. Green, J.E.: Laminar flow control - back to the future? In: AIAA Paper 2008-3738 (2008). <https://doi.org/10.2514/6.2008-3738>
3. Lee, B.H.K.: Self-sustained shock oscillations on airfoils at transonic speeds. Prog. Aerosp. Sci. **37**, 147–196 (2001). [https://doi.org/10.1016/S0376-0421\(01\)00003-3](https://doi.org/10.1016/S0376-0421(01)00003-3)
4. Dussage, J.P., Dupont, P., Debieve, J.F.: Unsteadiness in shock wave boundary layer interactions with separation. Aerosp. Sci. Technol. **10**, 85–91 (2006). <https://doi.org/10.1016/j.ast.2005.09.006>
5. Polivanov, P.A., Sidorenko, A.A., Maslov, A.A.: Transition effect on shock wave/boundary layer interaction at $M = 1.47$. In: AIAA Paper 2015-1974 (2015). <https://doi.org/10.2514/6.2015-1974>

Linear Instability of Shock-Dominated Laminar Hypersonic Separated Flows



Saurabh S. Sawant, Ozgur Tumuklu, Vassilis Theofilis, and Deborah A. Levin

Abstract The self-excited spanwise homogeneous perturbations arising in shock-wave/boundary-layer interaction (SWBLI) system formed in a hypersonic flow of molecular nitrogen over a double wedge are investigated using the kinetic Direct Simulation Monte Carlo (DSMC) method. The flow has transitional Knudsen and unit Reynolds numbers of 3.4×10^{-3} and $5.2 \times 10^5 \text{ m}^{-1}$, respectively. Strong thermal nonequilibrium exists downstream of the Mach 7.2 detached (bow) shock generated due to the upper wedge surface. A linear instability mechanism is expected to make the pre-computed 2-D base flow potentially unstable under spanwise perturbations. The specific intent is to assess the growth rates of unstable modes, the wavelength, location, and origin of spanwise periodic flow structures, and the characteristic frequencies present in this interaction.

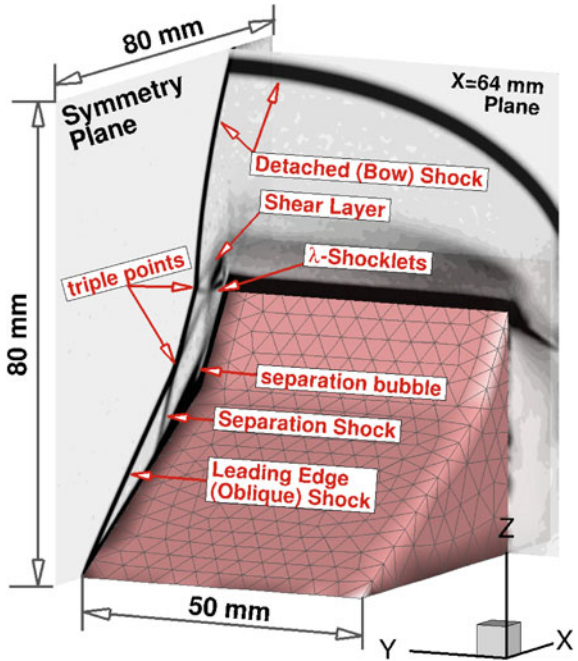
1 Introduction

The identification and analysis of potential growing modes in unsteady, laminar hypersonic flows is essential to predict the possible transition to turbulence, which in turn affects the aerothermodynamic loads on the surface of an embedded body. This work concerns an Edney type-IV/V SWBLI system [1] in a molecular nitrogen flow over a double wedge which exhibits complex flow dynamics characterized by thermal nonequilibrium, a flow recirculation zone near the hinge of the two angular surfaces, shear layers downstream of the triple point and above the recirculation zone, and λ -shocklets [2]. In particular, understanding of these phenomena at unit Reynolds number, Re_1 , on the order of 10^5 m^{-1} using the stochastic DSMC method [3] provides highest fidelity for shock dominated flows. The DSMC method is valid for a broader range of Knudsen numbers than Navier-Stokes equations; as a result, the critical treatment of strong shocks ($M \gg 1.6$) [4–6], the rarefaction effects such

S. S. Sawant (✉) · V. Theofilis · D. A. Levin
University of Illinois at Urbana-Champaign, Champaign, USA
e-mail: ssawan2@illinois.edu

O. Tumuklu
NASA Jet Propulsion Laboratory, Pasadena, CA, USA

Fig. 1 SWBLI interactions for the previous, three dimensional (3-D), symmetry-imposed, hypersonic flow of nitrogen over the double wedge [14] at 0.4 ms [7]



as the velocity and temperature slip [7–10], thermal nonequilibrium [3, 7], and the temporal evolution of self-excited perturbations are natural outcomes of the DSMC approach [11–13].

Tumuklu et al. [13] studied a 2-D (spanwise independent) flow over a double wedge and demonstrated decaying modes using proper orthogonal decomposition (POD). The flow took 0.9 ms to reach steady-state and the recirculation zone of 36 mm length was developed at the hinge. Previously, the authors studied a three dimensional (3-D) flow over a double wedge with a finite half-span of 50.8 mm [7] by imposing a symmetry plane at the center of the span, as shown in Fig. 1. The flow was found to be unsteady for 0.57 ms of simulation and started to exhibit 3-D structures inside the separation bubble and at the reattachment point. Figure 2 shows the third spatial mode obtained from a POD analysis of 0.4 to 0.57 ms DSMC data of streamwise velocity. Spanwise striations are less prominent towards the free edge of the wedge because of the spanwise acceleration of the gas. It is challenging to understand the origin of such striations and to determine their characteristic wavelength in the presence of flow pressure relief induced by the finite span. Therefore, to understand the unsteady dynamics of this SWBLI system, a simpler, spanwise periodic case has been undertaken [15], as shown in Fig. 3 describing the simulation setup.

The specific goal of this work is first to understand whether the 2-D base flow remains stable under spanwise homogeneous, self-excited perturbations. The presence of strong recirculation zones and shear layers is a recipe for generation and/or amplification of self-excited spanwise perturbations through linear instability mecha-

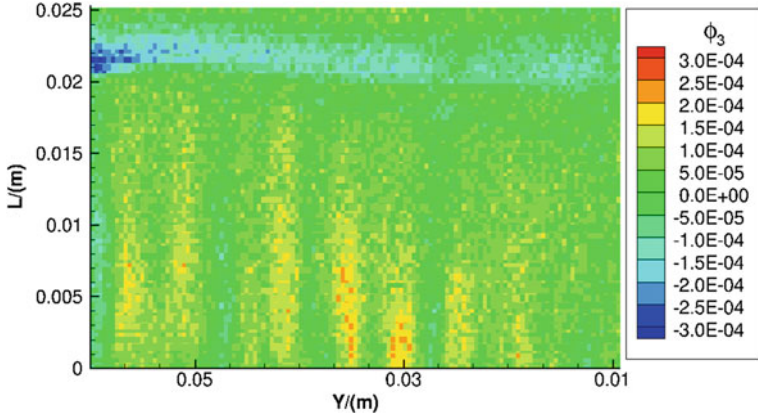


Fig. 2 The contours show the third spatial mode on a slant plane 3.44 mm above and parallel to the upper wedge and between the boundary and shear layers. Along the span, the symmetry plane and spanwise opposite edge are at $Y = 60$ and at 9.2 mm, respectively

nisms [16–22]. If these perturbations do not damped out, naturally, then the amplitude of the disturbance characteristic wavelength is amplified in the SWBLI system and resulting spanwise periodic flow structures form with a periodicity of this wavelength [17, 19, 23, 24]. If this occurs, the spatial and temporal characteristics of such structures, their origin, and growth rate will be investigated in this work.

DSMC performs advection of simulated particles, each of which represents a large number of real molecules, for a duration of a discrete timestep [3]. Then the particles are mapped on to discrete cells of the collision mesh encompassing the flow domain. From each cell, particle pairs are selected using appropriate collision cross-sections, and post-collisional instantaneous velocities are computed. Note that the particles also reflect from embedded surfaces using gas-surface collision models and are introduced, removed, or reflected from the domain boundaries. The macroscopic flow parameters such as velocity and temperatures are extracted from particles' instantaneous velocities using statistical relations of kinetic theory [3, 25, 26]. In complex 3-D flows, billions of computational particles are simulated to satisfy the numerical requirements. This is achieved by the Scalable Unstructured Gas-dynamics Adaptive mesh-Refinement (SUGAR-3D) code that has been demonstrated to scale well on many thousands of CPU-cores [7]. By using SUGAR-3D, a preliminary spanwise periodic case was simulated [15] for 0.25 ms with a span length of 72 mm, (twice the size of the separation length), which revealed 7.2 mm long spanwise periodic structures downstream of reattachment. With this estimate, a 28.8 mm span case was simulated using 19,200 processors with ~ 60 billion particles and ~ 4.5 billions collision cells in a $(400 \times 144 \times 400)$ octree grid. The input parameters are given in Table 1, whereas the convergence and span independence is demonstrated in Appendix.

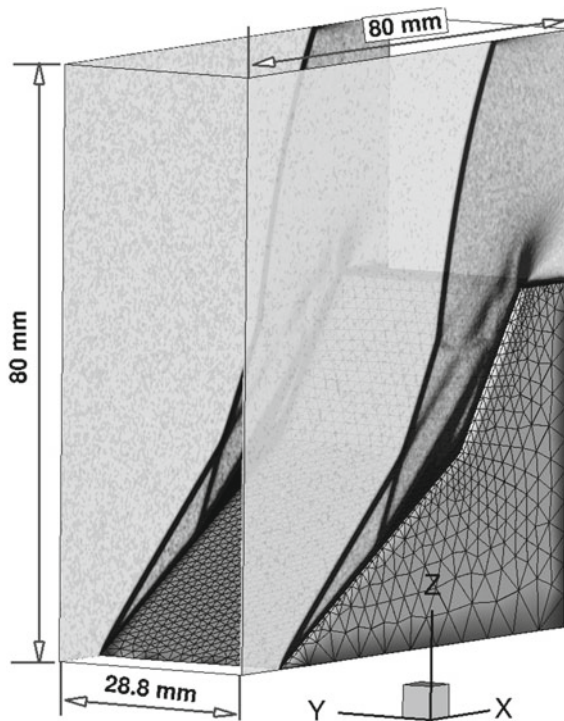


Fig. 3 New, span-periodic setup

Table 1 Simulation parameters for a flow of molecular nitrogen over a double wedge

Parameters	Values
Mach number, M	7.2
Unit Reynolds number	52,200
Freestream Knudsen number	0.0034
Freestream number density, $n/(m^3)$	1×10^{22}
Freestream gas temperatures ^a /(K)	710
Surface ^b temperature, $T_s/(K)$	298.5
Timestep, $\Delta t/(ns)$	5
Mesh refinement interval/(\(\mu s\))	5

^aTranslational, rotational, and vibrational temperatures are denoted as T_{tr} , T_{rot} , and T_{vib} , respectively. For thermal relaxation Larsen-Borgnakke model with Millikan-White expression for vibrational probability is used ^bThe surface is fully accommodated

2 Small-Amplitude Disturbances

The small amplitude disturbances are seen to grow in the recirculation region and the shear layer above it. Figure 4a shows the iso-contours of residual kinetic energy defined by,

$$|KE|_2 = \sqrt{(U - U_b)^2 + V^2 + (W - W_b)^2} \quad (1)$$

where U , V , and W are bulk velocities in the streamwise (X), spanwise (Y), and streamwise-normal (Z) directions, respectively, whereas U_b and W_b are respective 2-D base flow values at a given $X - Z$ location. Six spanwise periodic structures can be identified in the shear layer above the separation bubble. Note that to plot the iso-contours, the velocities in Eq. 1 are sampled only for 200 timesteps ($1\mu s$) from the time instant of $t = 0.06$ ms and as a result, suffer from statistical scatter. The time instant $t = 0.06$ ms is roughly the end of transient period, as seen from Fig. 4b, which shows the temporal history of residual kinetic energy. These structures change dynamically on the same time scale; therefore, they cannot be sampled for a longer duration. Later, as the disturbance amplitude increases, such structures are expected to become more prominent. Furthermore, from Fig. 4b, a low frequency sinusoidal variation is observed from 0.13 ms. Such variation is also seen at probes located at the separation point, which is analyzed in Sect. 3.

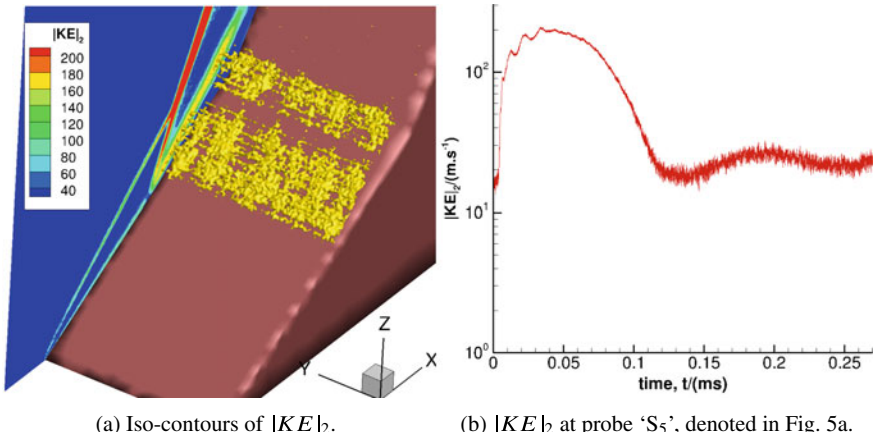


Fig. 4 **a** Spanwise periodic structures in the shear layer above the separation bubble at time $t = 0.06$ ms and **b** temporal history of spanwise averaged residual kinetic energy

3 Frequency Analysis

Spanwise averaged pressure residual at the reattachment location, shear layer downstream of the triple point, and inside the separation region is shown in Fig. 5b. It is seen that flow is unsteady, and the case needs to be run further to understand the long-time behavior of flow evolution. Notice a dip in the residuals at nearly 0.135 ms in the shear layer and the separation indicating that these dynamics are coupled. Such a decrease is also seen at reattachment at 0.16 ms, indicating a delayed response to the region of reattachment. Inside the separation region, a low-frequency wave is seen to originate after the decrease at 0.135 ms. An 8.5 kHz of frequency oscillation is seen at probe S_2 at the foot of separation in Fig. 5c. Later, because the separa-

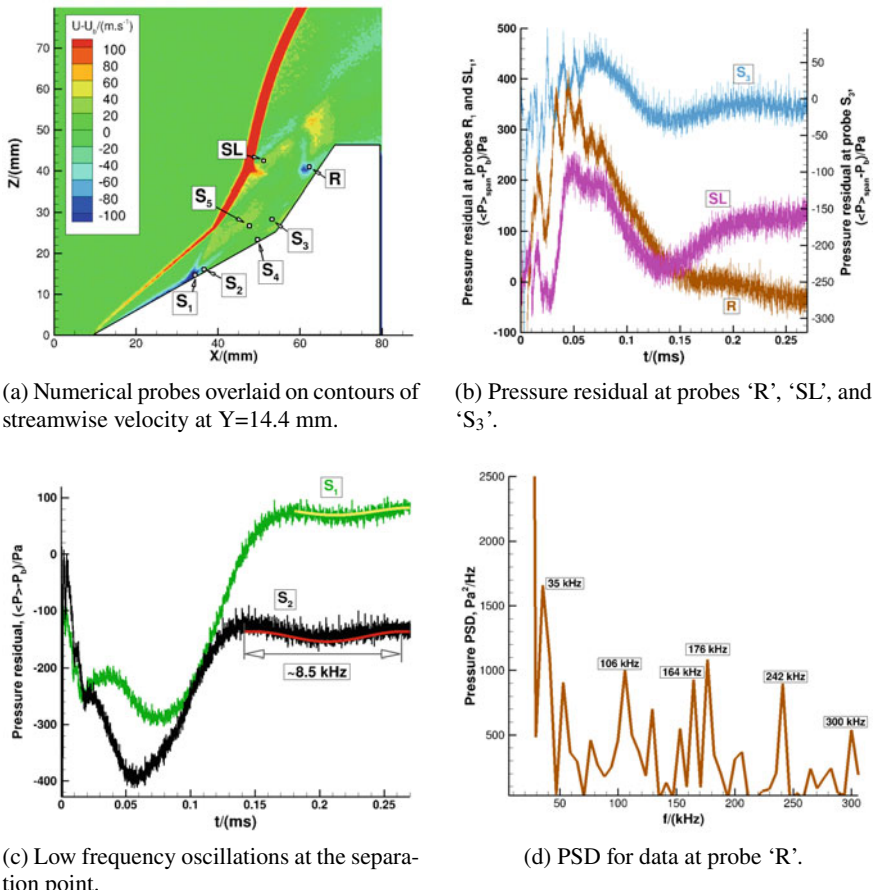


Fig. 5 Underlying frequencies in the temporal history of spanwise averaged pressure residual at numerical probe locations, denoted in a, inside and at the foot of separation bubble, at reattachment, and inside shear layer downstream of the triple point

tion shock moved upstream, the delayed frequency oscillation is seen to develop in probe S₁. Furthermore, to understand the high frequencies present in residuals, the power spectral density (PSD) of the pressure spectra from 0.1 ms to 0.27 ms was computed. At the reattachment and shear layer, many high frequencies ranging from 30 to 300 kHz are observed. Figure 5d shows a dominant frequency of 35 kHz at reattachment, whereas, in the shear layer, it is 46 kHz (not shown). These frequencies also exist inside the separation bubble (not shown). Note that the frequency resolution for the current analysis is 6 kHz. Further analyses performed with a finer resolution on probe data obtained at longer times (0.9 ms) will be described in a journal paper [27].

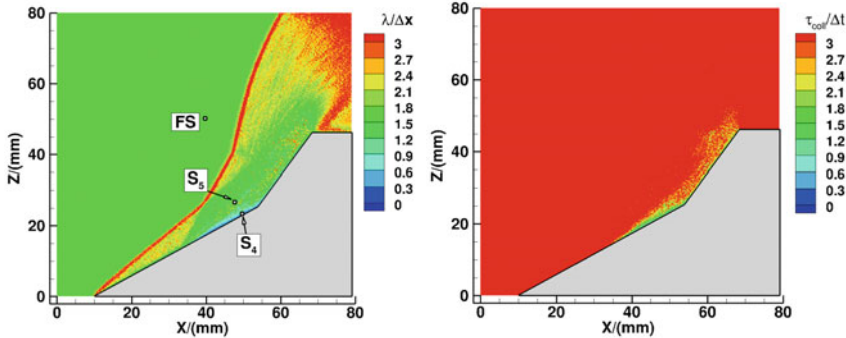
4 Conclusion

In summary, the self-excited spanwise perturbations are formed in the shear layer above the separation bubble, and its imprint is noticeable in spite of the statistical scatter present in the stochastic DSMC method. Spanwise periodic structures appear intermittently but are prominent in the shear layer above the separation bubble. A presence of 8.5 kHz low frequency is observed in residuals of streamwise velocity and pressure at the location of the shear layer above and inside the separation bubble. Besides, a range of high frequencies between 30 and 300 kHz are present in the shear layer downstream of triple point, at reattachment, and inside the separation bubble. In particular, 35 ± 6 and 46 ± 6 kHz dominant frequencies are observed in the PSD of pressure spectra at reattachment and shear layer downstream of the triple point. A detailed analysis confirming the prediction of the linear nature of instability will be presented in a journal paper, shortly. In addition, the identification of the nature of such disturbances (acoustic, vorticity waves, entropy waves) [28] will be studied in future.

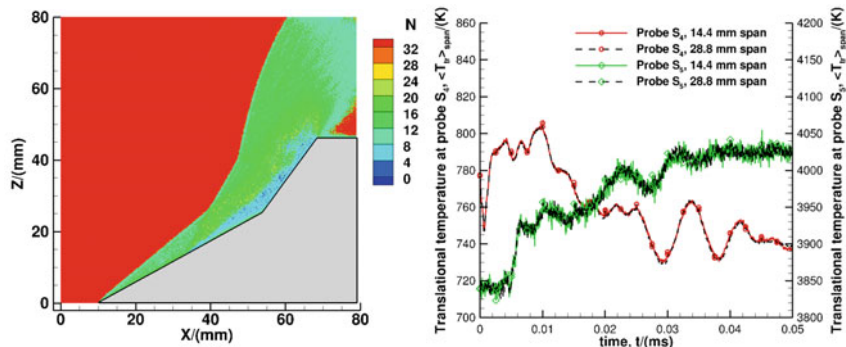
Acknowledgements This research is part of the Blue Waters sustained-petascale computing project, which is supported by the National Science Foundation (awards OCI-0725070 and ACI-1238993) and the state of Illinois. Blue Waters is a joint effort of the University of Illinois at Urbana-Champaign and its National Center for Supercomputing Applications.

Appendix

Figure 6a shows that local mean-free-path is comparable to the collision cell size in the vicinity of the wedge surface inside the recirculation region and is greater than one everywhere else, including the strong shocks. To ensure the decoupling of collisions and movement of particles, the ratio of mean-collision-time to timestep is much higher than one, as shown in Fig. 6b. To ensure unbiased collisions, the number of computational particles per collision cell are at least eight in the recir-



(a) Ratio of local mean-free-path to the collision cell size.
(b) Ratio of local mean-collision-time to the timestep.



(c) Number of computational particles per collision cell.
(d) Spanwise independence in spanwise averaged translational temperature.

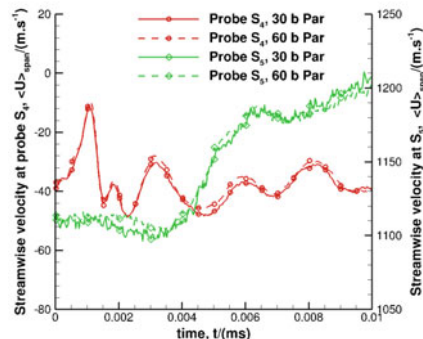


Fig. 6 Convergence and spanwise independence of the spanwise periodic simulation. The X-Z Contours in **a**, **b**, **c** are shown at $Y = 14.4$ mm for the 28.8 mm span case with 60 billion particles. **e** Spanwise independence between the 28.8 and 14.4 mm span cases with 60 and 30 billion particles, respectively. **d** Convergence in terms of the number of particles for the 14.4 mm span case

culation region, as shown in Fig. 6c, where the cell size is 1.25×10^{-5} (fourth level of refinement). To ensure that the numerical results are independent of the chosen span length of 28.8 mm (60 billion particles), another case with 14.4 mm span length (30 billion particles) was run, and the comparison is shown in Fig. 6d. The comparison of spanwise averaged translational temperature as a function of time is excellent at probe locations S₄ and S₅ in the vicinity of surface and further away in the shear layer above the separation bubble. Furthermore, a stringent test of convergence is performed on a 14.4 mm span case (30 billion particles), where the effect of doubling the number of particles is compared in Fig. 6e. It is seen that the spanwise averaged velocity follows the same temporal trend during the initial transient phase, where severe changes in macroscopic flow parameters are seen. Close to the surface where the Knudsen number is 0.9, the maximum difference in spanwise averaged velocity is 5 to 7% at the peaks, whereas away from the surface, the difference is within 1.5%.

References

1. Edney, B.: Anomalous heat transfer and pressure distributions on blunt bodies at hypersonic speeds in the presence of an impinging shock. Tech. rep, Flygtekniska Forsoksanstalten, Stockholm (Sweden) (1968)
2. Délery J.: Physical Introduction. Cambridge University Press, 2011, pp. 5–86. Cambridge Aerospace Series. <https://doi.org/10.1017/CBO9780511842757.002>
3. Bird, G.A.: Molecular Gas Dynamics and the Direct Simulation of Gas Flows, 2nd edn. Oxford Engineering Science Series. Clarendon Press, 1994
4. Bird, G.A.: The Phy. Fluids **13**(5), 1172 (1970). <https://doi.org/10.1063/1.1693047>
5. Ohwada, T.: Phys. Fluids A **5**(1), 217 (1993). <https://doi.org/10.1063/1.858777>
6. Cercignani, C., Frezzotti, A., Grosfils, P.: Phys. Fluids **11**(9), 2757 (1999). <https://doi.org/10.1063/1.870134>
7. Sawant, S.S., Tumuklu, O., Jambunathan, R., Levin, D.A.: Comput. Fluids **170**, 197 (2018). <https://doi.org/10.1016/j.compfluid.2018.04.026>
8. Tumuklu, O., Levin, D.A., Gimelshein, S.F., Austin, J.M.: AIP Conference Proceedings, vol. 1786 (AIP Publishing, 2016), vol. 1786, p. 050005. <https://doi.org/10.1063/1.4967555>
9. Moss, J.N., Bird, G.A.: AIAA J. **43**(12), 2565 (2005). <https://doi.org/10.2514/1.12532>
10. Chambre, P.A., Schaaf, S.A.: Flow of rarefied gases, vol. 4971. Princeton University Press (2017)
11. Tumuklu, O., Levin, D.A., Theofilis, V.: Phys. Fluids **30**(4), 046103 (2018). <https://doi.org/10.1063/1.5022598>
12. Tumuklu, O., Theofilis, V., Levin, D.A.: Phys. Fluids **30**(10), 106111 (2018). <https://doi.org/10.1063/1.5047791>
13. Tumuklu, O., Levin, D.A., Theofilis, V.: Phys. Rev. Fluids **4**(3), 033403 (2019). <https://doi.org/10.1103/PhysRevFluids.4.033403>
14. Swantek, A., Austin, J.: AIAA J. **53**(2), 311 (2014)
15. Sawant, S.S., Tumuklu, O., Theofilis, V., Levin, D.A.: AIAA Aviation 2019 Forum (2019), pp. 3442–c1. <https://doi.org/10.2514/6.2019-3442.c1>
16. Theofilis, V., Hein, S., Dallmann, U.: Philosophical transactions of the royal society of London. Ser. A: Math., Phys. Eng. Sci. **358**(1777), 3229 (2000). <https://doi.org/10.1098/rsta.2000.0706>
17. Theofilis, V.: Annu. Rev. Fluid Mech. **43**, 319 (2011). <https://doi.org/10.1146/annurev-fluid-122109-160705>
18. Pagella, A., Rist, U.: in Meeting Proceedings RTO-MP-AVT-111, Prague. Czech Republic (2004). <https://doi.org/10.1007/BF00311809>

19. Sidharth, G., Dwivedi, A., Candler, G.V., Nichols, J.W.: *Phys. Rev. Fluids* **3**(9), 093901 (2018). <https://doi.org/10.1103/PhysRevFluids.3.093901>
20. Dwivedi, A., Sidharth, G., Nichols, J.W., Candler, G.V., Jovanović, M.R.: *J. Fluid Mech.* **880**, 113 (2019). <https://doi.org/10.1017/jfm.2019.702>
21. Alves, L.S., Santos, R.D., Cerulus, N., Theofilis, V.: *AIAA Scitech 2019 Forum* (2019) p. 2321. <https://doi.org/10.2514/6.2019-2321>
22. Gai, S.L., Khraibut, A.: *J. Fluid Mech.* **877**, 471 (2019). <https://doi.org/10.1017/jfm.2019.599>
23. Chuvakhov, P.V., Borovoy, V.Y., Egorov, I.V., Radchenko, V.N., Olivier, H., Roghelia, A.: *J. Appl. Mech. Tech. Phys.* **58**(6), 975 (2017). <https://doi.org/10.1134/S0021894417060037>
24. Roghelia, A., Chuvakhov, P.V., Olivier, H., Egorov, I.V.: 47th AIAA Fluid Dynamics Conference (June), 1 (2017). <https://doi.org/10.2514/6.2017-3463>
25. Vincenti, W.G., Kruger, C.H.: *Introduction to physical gas dynamics*. Wiley, New York (1965)
26. Kogan, M.: *Rarefied Gas Dynamics*, 1st edn. Springer (1969)
27. Sawant, S.S., Theofilis, V., Levin, D.A.: *J. Fluid Mech.* (in preparation) (2020)
28. Duck, P.W., Lasseigne, D.G., Hussaini, M.: *Theoret. Comput. Fluid Dyn.* **7**(2), 119 (1995). <https://doi.org/10.1007/BF00311809>

Controlled Cross-Flow Mode Interaction in Mach 6 Boundary Layer



Alexander Arndt, Thomas Corke, Eric Matlis, and Michael Semper

Abstract Experiments were performed to investigate a quadratic interaction between stationary and traveling cross-flow modes in the boundary layer on a sharp right-circular cone at an angle of attack at Mach 6.0. Passive discrete roughness was applied near the cone tip, just upstream of Branch I of the linear stability neutral curve to excite stationary cross-flow modes. A plasma actuator was located just downstream of the discrete roughness array. This was designed to produce an azimuthally uniform unsteady disturbance with a frequency that was at the center of the band of most amplified traveling cross-flow modes. Measurements consisted of off-wall azimuthal profiles of mean and fluctuating total pressure at different axial locations. Spectra of total pressure fluctuations verified the receptivity of the boundary layer to the unsteady excitation. This affected the azimuthal and streamwise development of the stationary cross-flow modes, with a general effect to move the transition location upstream by 9%. The quadratic interaction between the stationary and traveling cross-flow modes was verified through cross-bicoherence analysis. This presents a scenario where traveling cross-flow modes whose initial amplitudes are sensitive to free-stream disturbance levels, can interact with stationary cross-flow modes to produce rapid spectral broadening and accelerated turbulent transition.

A. Arndt · T. Corke (✉) · E. Matlis
University of Notre Dame, Notre Dame, IN, USA
e-mail: tcorke@nd.edu

A. Arndt
e-mail: aarndt1@nd.edu

E. Matlis
e-mail: ematlis@nd.edu

M. Semper
U.S. Air Force Academy, Colorado Springs, CO, USA
e-mail: michael.semper.1@us.af.mil

1 Introduction

Turbulence transition on hypersonic **lifting** bodies is likely to be dominated by a mean cross-flow velocity component that is subject to a cross-flow instability. Based on linear stability theory, traveling cross-flow modes are more amplified than stationary cross-flow modes. However, the stationary modes are highly receptive to surface roughness which can provide higher initial amplitudes that compensate for their lower amplification rate. As a result, except in instances of higher free-stream turbulence levels, the stationary modes are the leading mechanism in cross-flow dominated transition.

The approach to control cross-flow transition stems from the extreme receptivity of the stationary modes to surface roughness. This feature was exploited by Corke and Knasiak [1] and Corke et al. [2] to excite selected wavenumbers of cross-flow modes in the boundary layer over a rotating disk, which is a canonical three-dimensional flow that exemplifies the cross-flow instability. Saric et al. [3] and Radeztsky et al. [4] exploited this property in their swept wing experiments to excite fixed spanwise wavenumber stationary cross-flow modes using arrays of micron-sized circular distributed roughness elements

The ability to excite specific wavenumbers of stationary cross-flow modes led to the concept for cross-flow transition control where discrete roughness is used to excite less amplified stationary cross-flow modes [3]. Schuele et al. [5] investigated this approach for transition control on a sharp-tipped right-circular cone at an angle of attack in a supersonic flow. The experiments were performed in the Mach 3.5 Supersonic Low Disturbance (“quiet”) Tunnel (SLDT) at NASA Langley Research Center that is specially designed to minimize acoustic disturbances. In these experiments, Schuele et al. [5] documented a 40% *increase* in the transition Reynolds number.

More recently Corke et al. [6] applied this approach on the same cone model in a Mach 6 flow. The model was placed at a 6° angle of attack so that the most amplified band of wavenumbers of stationary cross-flow modes, and Branch I location, were the same as that at the lower Mach number Schuele et al. [5] experiments. This allowed the same discrete roughness cone tips to be used. These experiments observed a 25% increase in the transition Reynolds number. In addition, evidence of an interaction between the stationary and traveling cross-flow modes was observed. A similar interaction was *not observed* by Schuele et al. [5], suggesting that it might be the result of the higher free-stream disturbance levels in the Mach 6 experiment, which was conducted in a conventional (“non-quiet”) tunnel. The speculation was that the higher free-stream disturbance levels resulted in higher initial amplitudes of traveling cross-flow modes that enhanced a nonlinear interaction with the stationary cross-flow modes, affecting transition.

This prompted a follow-on investigation in which the initial amplitude of traveling cross-flow modes would be directly controlled, while simultaneously using discrete roughness to excite fixed wavenumber stationary cross-flow modes. The experiment

would then document the effect this had on the nonlinear interaction between these modes, as well as its effect on turbulent transition.

2 Experimental Setup

The experiments were conducted in the Air Force Academy (AFA) Mach 6.0 Ludwieg Tube Facility. The facility is based on the design used in the Technical University at Braunschweig, Germany [7]. The inside diameter of the test section is 0.5 m, and its length is 0.98 m. For optical access, it has three 0.26 m flanged windows, two on opposite sides, and one on top. Further details of the facility are given by Cummings and McLaughlin [8]. A schematic of the facility is shown in Fig. 1 along with a photograph of the cone model in the tunnel test section.

The model is a hollow, thin-walled right-circular cone with a half angle of $\phi_c = 7^\circ$. The total length of the cone is 35.56 cm (14 in). The first 4.303 cm (1.694 in) (tip) of the cone is removable. The base of the cone mounted to a hollow sting that was connected to a vertical strut. The vertical strut bolted to a base plate that attached to the wind tunnel wall. An angled shim under the base plate was used to orient the cone at the $\alpha = 6^\circ$ angle of attack. This gave an $\alpha/\phi_c = 0.86$, which was in the range of dimensionless angles where King [9] had documented stationary cross-flow vortices.

A traversing mechanism moved a total-pressure Pitot probe in the wall-normal, axial and azimuthal directions within the boundary layer. The total pressure Pitot probe utilized a Kulite model XCE-062-1.7A (1.7 bar, 25 psi absolute) pressure transducer. The transducer was inserted into a circular sleeve whose inside diameter closely matched the outside diameter of the transducer body, and covered the diaphragm end. A series of three telescoping hypodermic tubes were then attached to the diaphragm end of the cylindrical sleeve, giving a final inside diameter of 0.43 mm, which was then the sensing diameter of the Pitot probe. This corresponded to 20% of

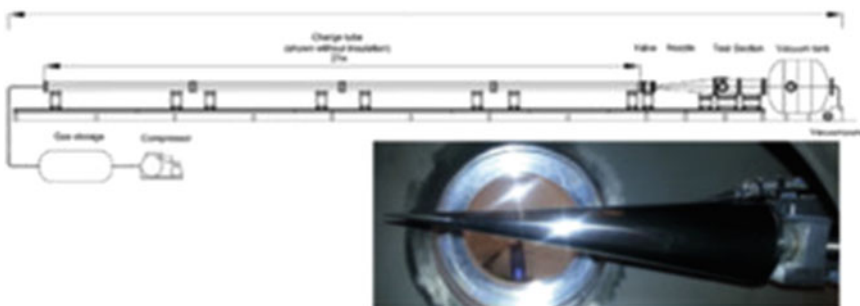


Fig. 1 Schematic of U.S. Air Force Academy Mach 6 Ludwieg Tube where the experiments were performed, and photograph of the cone model inside test section

Fig. 2 Photographs of discrete roughness “dimples” used to excite a $m = 45$ stationary mode (left), and fully assembled cone tip with exposed plasma actuator electrode for traveling mode excitation

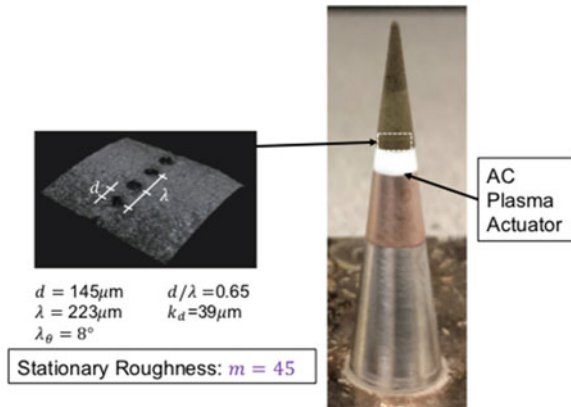
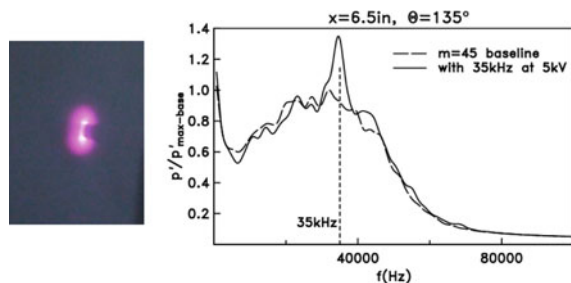


Fig. 3 Photograph of cone tip with plasma actuator operating in the Mach 6 flow, and spectra of total pressure fluctuations in the boundary layer with plasma off and on to produce 35 kHz excitation



the most amplified stationary mode azimuthal wavelength. The frequency response of the Pitot probes, determined in the previous work [6], was 50 kHz. This was sufficient to capture the traveling cross-flow modes whose band of most amplified frequencies was centered near 35 kHz.

The discrete roughness consisted of 45 “dimples” equally spaced azimuthally around the cone tip to excite an azimuthal wavenumber, $m = 45$, which is in the center of the most amplified band of stationary cross-flow modes based on linear stability theory [10]. An enlarged photograph of the roughness is shown in the left part of Fig. 2. The axial location of the roughness was $x_r = 1.27$ cm from the cone tip, which placed it slightly upstream of the lower linear stability neutral growth curve. The unsteady disturbances introduced into the boundary layer were produced by a plasma actuator that encircled the cone tip. It was located 3.5 mm downstream of the discrete roughness. The fully assembled cone tip is shown in the right part of Fig. 2.

Figure 3 shows the cone tip with the plasma actuator operating in the Air Force Academy Mach 6 Ludwieg tube during a data run. The plasma actuator frequency was 35 kHz, which is in the center of the most amplified band of traveling cross-flow modes [10]. The plasma (ionized air) appears as a purple ring around the cone tip. Included in the figure are spectra of the total pressure fluctuations in the boundary layer with the plasma actuator off, and operating to produce a 35 kHz excitation. The

baseline (plasma off) spectrum shows a broad peak centered around 35 kHz consistent with the most amplified traveling cross-flow modes [10]. With the plasma actuator operating, the total pressure spectrum shows a distinct peak above the baseline, at the 35 kHz excitation frequency. A vertical dashed line at 35 kHz is shown for reference.

3 Results

The experimental conditions are listed in Table 1. The measurements consisted of total-pressure time series taken at a fixed height above the surface of the cone. The azimuthal extent was $130^\circ \leq \theta \leq 140^\circ$ in increments of 1° , and an axial extent of $10.16\text{ cm} \leq x \leq 16.51\text{cm}$ (4.0 to 6.5 in.) in increments of 1.27 cm (0.5 in.).

The Pitot probe surveys were used to provide a direct measure of the mean flow distortion produced by the stationary cross-flow modes. This involved averaging the total pressure time series taken over the duration of a run at each (θ, x) location. The results are shown in Fig. 4. The color rendering of the total pressure is presented as the deviation about the local mean value, $P_0(\theta, x) - \bar{P}_0(\theta, x)$. This clearly reveals the azimuthal variation in the total pressure that is indicative of the mean flow distortion produced by the stationary cross-flow mode. The negative mean-removed pressures correspond to locally thickened portions of the boundary layer, and positive mean-removed pressures correspond to locally thinned portions. This is illustrated by the $\delta(\theta)$ dashed line that is included in both plots.

The stationary cross-flow mode that corresponds to the $m = 45$ roughness has an azimuthal wavelength of 8° , namely $360^\circ/45$. Its half-wavelength then corresponds to $\theta = 4^\circ$, which has been denoted in Fig. 4 as $\lambda_{45}/2$. This appears to closely correspond to the spacing between the peak and valley in the azimuthal pressure distribution, and therefore is a good indication that the mean flow distortion is the result of the discrete roughness.

Table 1 Summary of Experimental Conditions and Measurement Locations

Mach no.	6.0
T_0 (K)	480
P_0 (bar)	11.5
Unit reynolds number (m^{-1})	10×10^6
Typical run time (ms)	80
Re_{x_r}	0.127×10^6
Roughness mode no.	45
Plasma actuator frequency (kHz)	35
Axial location (cm)	$10.2 \leq x \leq 16.5$
Azimuthal location (de.g.)	$130 \leq \theta \leq 140$
Wall normal location	$\sim y @ p'_{max}$

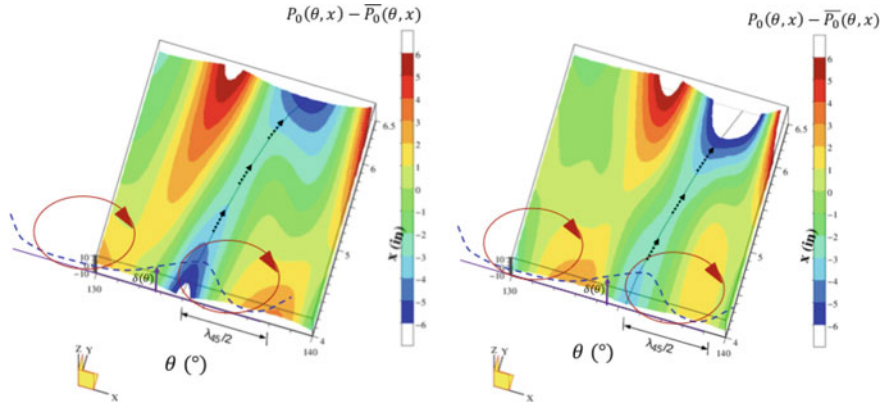
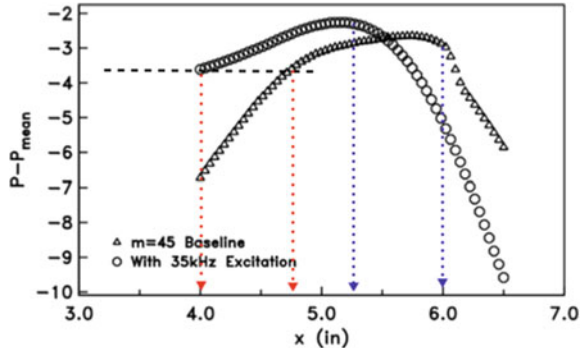


Fig. 4 Mean total pressure distributions at a constant height above the surface with plasma actuator off (left) and operating to produce a 35 kHz excitation (right)

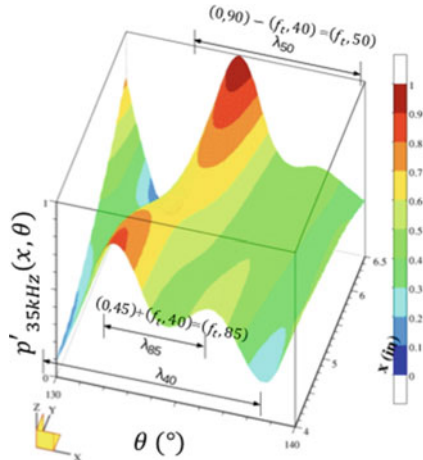
Fig. 5 Axial distributions following the pressure minima denoted by the dotted curve in the total pressure distributions in Fig. 4



The location of turbulent transition in each case was found by measuring the streamwise development of the total pressure along a trajectory that followed the locally thickened boundary layer. Such regions are known to develop an off-wall inflectional shear layer and subsequent inviscid instability that quickly leads to turbulence [11]. These trajectories are shown by the dotted curves with arrows pointing in the downstream direction. The results are shown in Fig. 5.

At a fixed height above the surface, the streamwise development of the local total pressure is an indication of the wall shear stress [12]. The *onset* of transition is normally observed as a rise in the shear stress (total pressure) above a common reference. A reference that can apply to the two cases is shown by the horizontal dashed line. The x -locations of the intersection of the reference line with the total pressure distribution represents the respective transition locations. These are shown by the red dotted vertical lines. This indicates that the onset of transition moved upstream by about 9% with the addition of the 35 kHz excitation.

Fig. 6 Spatial amplitude distribution of the 35 kHz spectral peak with 35 kHz excitation of the $m = 45$ roughness tip



An indication of the *last* stage of turbulent transition is evident by a rapid reduction of the total pressure, signifying a rapid thickening of the boundary layer. The blue dotted vertical lines provide estimates of the beginning of that process for the two cases. The change in the late-stage transition location resulting from the 35 kHz excitation is consistent with the 9% reduction based on transition onset.

The total pressure Pitot probe had a frequency response that was capable of detecting the traveling cross-flow modes. One representation of spectra of total pressure fluctuations at one azimuthal location in the boundary layer with and without 35 kHz excitation was shown in Fig. 3. Similar spectra were compiled at all of the measured (θ, x) locations for these two cases. These took on a distinctive spatial distribution that reflected the linear and nonlinear interaction of the excited traveling and stationary cross-flow modes. An example of the spatial amplitude distribution of the 35 kHz spectral peak for the 35 kHz excitation of the $m = 45$ roughness tip is shown in Fig. 6.

Based on Li et al. [10], the 35 kHz traveling cross-flow mode has an azimuthal wavenumber of $m = 40$. This is observable in the spatial distribution in Fig. 6, where it is labeled λ_{40} . In addition to this, features with other azimuthal wavelengths are observable. One corresponds to a summing interaction between the stationary mode, $(0, 45)$, and the excited traveling mode, $(f_t, 40)$, to give a traveling mode, $(f_t, 85)$. The azimuthal wavelength of this mode is approximately 4° . Another corresponds to an azimuthal wavelength that is representative of a difference interaction between the harmonic stationary mode, $(0, 90)$, and the excited traveling mode, $(f_t, 40)$, to give a traveling mode, $(f_t, 50)$.

Proof that these features are a result of nonlinear interactions comes from cross-bicoherence (CBC) analysis. The CBC is a measure of triple phase locking between two modes in sum and difference interactions to produce a third mode. The CBC varies between 0 and 1, with 1 indicating perfect nonlinear phase locking. In applying this analysis, one data series corresponded to the mean flow distortion with the 35 kHz

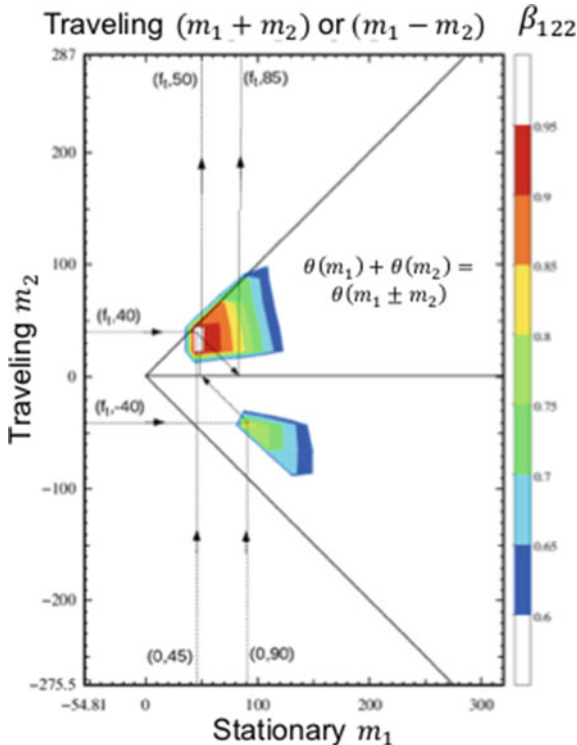


Fig. 7 Cross-bicoherence for stationary-traveling-traveling mode interaction at $x = 10.16$ cm (4.0 in.) and $\theta = 135^\circ$ with $m = 45$ roughness tip and excitation at 35 kHz

excitation at the most upstream location as shown in the right part of Fig. 4. The second data series corresponded to the total pressure fluctuation time series measured at the most upstream location at $\theta = 135^\circ$. With the pressure time series, frequency was converted to wavenumber using the theoretical wave speed. The resulting CBC is shown in Fig. 7.

For the CBC shown in Fig. 7, the data series corresponding to the stationary cross-flow modes is designated by subscript 1, with its wavenumber (m_1) read from the abscissa. The data series corresponding to the traveling cross-flow modes is designated by subscript 2, with its wavenumber (m_2) read from the ordinate. The ordinate wavenumbers are either added (top triangle) or subtracted (bottom triangle) from those read on the abscissa to give the third frequency which is read as the intercept of a -45° line to the abscissa. This method for reading the CBC is outlined by the arrows for either the summing interaction or the difference interaction. The CBC levels are shown as filled color contours. All of the levels indicate significant to perfect nonlinear phase locking.

The two interactions that appeared in the spatial amplitude distribution in Fig. 6 are highlighted by the arrows in the CBC. One is the summing interaction between

the stationary mode, (0, 45), and the traveling mode, (f_t , 40), to give the traveling mode, (f_t , 85). The other is the difference interaction between the stationary mode, (0, 90), and the traveling mode, (f_t , 40), to give the traveling mode, (f_t , 50). The nearly perfect CBC in these cases *confirms* that they are the result of a nonlinear interaction between the stationary and traveling cross-flow modes.

Although the focus has been on the modes that were prescribed in the experiment, the CBC indicates a significant nonlinear phase locking among wavenumbers that encompassed the most amplified linear stability band of traveling and stationary cross-flow modes. The importance of this on transition depends on the amplitudes of the respective modes. With the traveling modes, it is linked to the free-stream disturbance level. For the stationary modes, it is linked to the magnitude of surface roughness. For example, the amplitude of a $m = 90$ component in the discrete roughness was significant enough, upon interaction with the prescribed traveling mode, to produce a $m = 50$ traveling mode that was identifiable in Fig. 6. In this instance, it is conceivable that a broader wavenumber range of discrete roughness could have led to a more rapid spectral broadening and accelerated transition. This could also explain how random distributed roughness of sufficient amplitude could significantly impact transition in cross-flow dominated flows.

4 Summary

These experiments were designed to investigate if, through a nonlinear interaction with stationary cross-flow modes, the initial amplitude of the traveling modes could impact transition. In this case, the mode numbers and amplitudes of both the stationary and traveling cross-flow modes were directly introduced. In a natural scenario, the stationary modes would be initiated through surface roughness. If the roughness was uniformly distributed and produced linear disturbance levels, the excited stationary modes would be in the band of most amplified wavenumbers based on linear theory.

The growth of the stationary cross-flow mode is a powerful mechanism leading to a dominant mean flow distortion that produces elevated shear layers that break down rapidly to turbulence. Evidence suggests that the stationary cross-flow modes are insensitive to free-stream disturbance levels. In contrast, the traveling cross-flow modes, at least in subsonic Mach number experiments [13], are sensitive to free-stream disturbance levels. We speculate this is the case in higher Mach number flows. Such sensitivity, and the documented interaction between traveling and stationary cross-flow modes, provides a mechanism whereby free-stream disturbance levels can affect cross-flow transition.

References

1. Corke, T.C., Knasiak, K.F.: Stationary traveling cross-flow mode interactions on a rotating disk. *J. Fluid Mech.* **355**, 285–315 (1998)
2. Corke, T., Matlis, E., Othman, H.: Transition to turbulence in rotating-disk boundary layers—convective and absolute instabilities. *J. Eng. Math.* **57**, 253–272 (2007)
3. Saric, W., Carillo, R., Reibert, M.: Leading-edge roughness as a transition control mechanism. AIAA Paper AIAA-98-0781 (1998)
4. Radeztsky, R., Reibert, M., Saric, W.: Effect of isolated micron-sized roughness on transition in swept-wing flows. *AIAA J.* **37**(11), 1370–1377 (1999)
5. Schuele, C.-Y., Corke, T., Matlis, E.: Control of stationary cross-flow modes in a Mach 3.5 boundary layer using patterned passive and active roughness. *J. Fluid Mech.* **718**, 5–38 (2013)
6. Corke, T., Arndt, A., Matlis, E., Semper, M.: Control of stationary cross-flow modes in a Mach 6 boundary layer using patterned roughness. *J. Fluid Mech.* **856**, 822–849 (2018)
7. Estorf, M., Wolf, T., Radespiel, R.: Experimental and numerical investigations on the operation of the hypersonic Ludwieg tube Braunschweig. In: 5th European Symposium on Aerothermodynamics for Space Vehicles (2004)
8. Cummings, R., McLaughlin, T.: Hypersonic Ludwieg tube design and future usage at the U.S. Air Force Academy. In: 50th AIAA Aerospace Sciences Meeting, Paper AIAA 2012-0734 (2012)
9. King, R.A.: Three-dimensional boundary-layer transition on a cone at Mach 3.5. *Exp. Fluids* **13**, 305–314 (1992)
10. Li, F., Choudhari, M., Chang, C.-L., White, J.: Analysis of instabilities in non-axisymmetric hypersonic boundary layers over cones. In: 10th AIAA/ASME Joint Thermophysics and Heat Transfer Conference, Paper AIAA 2010-4643 (2010)
11. Saric, W., Reed, H., White, E.: Stability and transition of three-dimensional boundary layers. *Ann. Rev. Fluid Mech.* **35**, 413–440 (2003)
12. Preston, J.H.: The determination of turbulent skin friction by means of Pitot tubes. *J. R. Aero-naut. Soc.* **58**, 109–121 (1954)
13. Bippes, H.: Basic experiments on transition in three-dimensional boundary layers dominated by crossflow instability. *Prog. Aerosp. Sci.* **35**, 363–412 (1999)

Stability Analyses of Hypersonic, Conical Flows with Transpiration Cooling



Viola Wartemann, Giannino Ponchio Camillo, Jens Neumann,
Alexander Weber, and Alexander Wagner

Abstract The influence of transpiration cooling on second modes is analyzed in the present study. The investigations are carried out on a 7° half angle, blunted cone with a nose radius of 5 mm. At a free stream Mach number of 7, various gas injection mass flow rates are applied. The goal is to have the cooling effect, without triggering the transition. Thus the investigations focused on low mass fluxes. As injection gas nitrogen is used. At the considered free stream conditions second modes are the dominant boundary-layer instabilities, which are consequently the focus of this study. The stability analyses are performed by the stability code NOLOT, NOnLOcal Transition analysis, of the German Aerospace Center (DLR). Beside the analyses of the influence of different mass injection on the frequencies and growth rates of the second modes and finally on the transition onset itself, different stability approaches are applied: Calculations based on Linear Stability Theory (LST) are compared against Parabolized-Stability-Equations (PSE) results. The numerical predictions are compared with experimental data, which were obtained in the DLR High Enthalpy Shock Tunnel Göttingen (HEG).

Keywords Transpiration cooling · Conical · Hypersonic boundary-layer transition · Second mode instability · Stability analysis · Linear Stability Theory (LST) · Parabolized Stability Equations (PSE) · High Enthalpy Shock Tunnel Göttingen (HEG)

V. Wartemann (✉) · J. Neumann · A. Weber
German Aerospace Center, Lilienthalplatz 7, 38108 Braunschweig, Germany
e-mail: Viola.Wartemann@dlr.de

G. P. Camillo · A. Wagner
German Aerospace Center, Bunsenstraße 10, 37073 Göttingen, Germany
e-mail: Giannino.PonchioCamillo@dlr.de

A. Wagner
e-mail: Alexander.Wagner@dlr.de

1 Introduction

During re-entry, extreme heat loads occurs and the temperatures often exceed the melting point of conventional materials. Hence one of the dominant design factor and cost-driver for re-entry vehicles is the thermal protection system (TPS). Mostly, passive systems are applied, which, consequently, can not be adjusted during the flight. Thus, in general, the peak heat load is the design criterion for the entire flight path. One material strategy for passive systems are Ceramic Matrix Composites (CMC). As one example, Carbon fiber based CMCs can be named. These carbon fiber ceramics have the potential to realize TPSs up to 1900K and were already flown on an experimental status, e.g. X-38 [40] or SHEFEX I and SHEFEX II [39]. Latest development of ultrahigh temperature ceramics promises to allow hot-structure designs over 2300K, see e.g. Savino et al. [29] or Kütemeyer et al. [18]. Thermal protection systems, based on ablation, see for example Kendall et al. [16], McManus [24] or Loehle et al. [21], are able to accommodate high heating rates for a short period. The limitation of the ablation approach lies in the total heat dissipation.

Another TPS approach is active cooling, which promises the possibility of both, high heat rates and large amounts of total heat dissipation, however requires more complex systems, see e.g. Kim et al. [17] (numerical investigations) or Börk et al. [3, 4] (SHEFEX II flight experiment with active cooling).

This paper is focused on the active cooling approach, applying different low mass fluxes. Low mass fluxes means, that the transition is not triggered. Since boundary-layer transition can increase the surface heating rates by a factor of 4 to 8 (see e.g.: Choudhari et al. [6]), the goal is to have the cooling effect, without triggering the transition. Because the transition would repeal the cooling effect.

For more than 50 years the importance of blowing to instability respectively, transition has been known (see for example the review of Morkovin [26], p. 66). A detailed summary of hypersonic boundary-layer transition experiments with blowing of the 1960s and 1970s is given by Schneider [31], who summarized, that experimental data is more generally available for blowing-induced transition for blunt bodies and models at large Angle of Attack (AOA) and slender cones near zero AoA. But, there are no quantitative measurements of the instabilities that lead to transition [31]. Further Schneider [31] described in his paper from 2010, that little has been done since the 1980s.

As example for hypersonic experiments with blowing in the 2010s can be named the work of Leyva et al. [19], which based on a 5° sharp cone using as injection gas carbon dioxide (CO_2). The experimental data was obtained at the Caltech T5 shock tunnel and demonstrated a delaying of the transition. This work was continued by experiments of Jewell et al. [13, 14] in the T5 tunnel and experiments of Schmidt et al. [30], which were performed in the Caltech Mach 4 Ludwieg tube using a scale model of the cone, which were used in the T5 study. They presented a significant increase in transition location compared to pure air. Further in Ref. [33] is described, an unstable shear layer downstream of the injector section occurs. The experiments were accompanied by PSE calculations from Jewell [13] and Wagnild et al. [35], which predict,

that transition will occur immediately following the injection [35]. Further Wagnild et al. [35] investigated the influence of non-equilibrium process in detail. Fedorov et al. [9] performed corresponding LST calculations with T5 conditions: These e^N computations of Fedorov showed, that the injection leads to destabilization of the near-field region, stabilization of the mid-field relaxation region, and destabilization of the far-field relaxation region where the basic flow is almost parallel. The width and location of these regions as well as the level of stabilization/destabilization effect essentially depend on the injected mass flow rate. The results of Fedorov et al. [9] are consistent with Wagnild et al. [35].

Li et al. [20] recalculated the experiments of Akin et al. [1], a 5° half angle cone at Mach 7.4. The numerical predicted stabilizing effect of the injection is contrary to the measured trend. For the discrepancy with the measured trend, as one possible explanation is mentioned, that the transition in the experiment could have been caused by an instability mechanism other than the second mode [20].

In a more recent paper from Miró Miró et al. [25], who performed effusion experiment with a 7° cone at Mach 6, a good agreement between the numerical predicted and measured transition Reynolds number $Re_{x,\text{tr}}$ were shown.

For the analyses of the present paper a 7° half-angle blunted cone with a nose radius of 5 mm and a total length of about 1 m at a Mach number of about 7 is used. For a cone with zero AoA with a hypersonic boundary-layer and a cold wall, as here, second mode instability are the dominate modes [23]. Hence these modes are in the focus of the present paper.

The main Sect. 4 is split into two parts: Sect. 4.1 summarizes the effect of small inaccuracy of the experimental sensor values, which are used for the base flow calculations, applying a non-effusion reference case. In Sect. 4.2 the influence of mass flux variations on the transition onset and in detail on the second modes itself is studied, using LST as well as PSE. The analyses of the current paper is focused on low effusion test cases. Low mass fluxes mean, that by injection of the cooling gas, no visible shock in the schlieren images is induced. The idea is to reduce the second modes, without triggering the transition, so that in consequence the transition onset shift further downstream. The transition prediction as well as the predicted second modes are compared with experimental results obtained in the High Enthalpy Shock Tunnel Göttingen (HEG). A good classification of the present study compared to some of the above mentioned preceding analyses/experiments, in relation to the mass flow rate and Renoldys number can be found in Camillo et al. [27]. In comparison to previous preceding studies, the recent paper includes a detailed comparison of the measured/predicted second modes, applying different mass fluxes.

2 Numeric Methods

2.1 Mean Flow Solver

For the base flows \bar{q} calculations the DLR TAU code is used. The code is a three-dimensional parallel hybrid multi-grid code and has been validated for hypersonic flows (see e.g. Mack et al. [22], Schwamborn et al. [32] or Reimann et al. [28]). The wall condition for the effusion section is described in Hannemann [11].

The laminar base flow calculations are based on non-equilibrium gas modelling with 5 species for air: N_2, O_2, NO, N, O , applying thermal equilibrium and chemical non-equilibrium (one temperature model), which is a suitable approach for the here investigated test conditions (see Wartemann et al. [38]). The transport coefficients are expressed in terms of the collision integrals, see Bottin [5]. The mixing rules are based on constant Schmidt numbers. Further lookup tables are used, see Esser [8]. The grid is axisymmetric. Previous analyses have shown, that the base flow simulations should include the nozzle, test chamber, and cone model [38], which is consequently applied. For all grids, grid clustering towards the walls as well as around the shock is applied. For the near-field cone a structured grid is used, with 654 grid points in streamwise direction and 350 grid points in wall normal direction. A grid study can be found for example in Wartemann et al. [38]. Based on the nozzle calibration of Wagner [34], the nozzle boundary-layer is set turbulent, which is modelled with the Spalart-Allmaras turbulence model. The model wall temperature for all tests is assumed to be isothermal at 293 K.

2.2 Stability Code

For the stability analyses the so called NOLOT code [12] (NOnLocal Transition analysis) is used. NOLOT was developed in cooperation between DLR and the Swedish Defence Research Agency (FOI). The code can be used with the local-parallel Linear Stability Theory approach (LST) as well as Parabolized Stability Equations (PSE), which are compared against each other in this paper. The equations are derived from the conservation equations of mass, momentum and energy, which govern the flow of a viscous, compressible, ideal gas. All flow and material quantities are decomposed into a steady laminar base flow \bar{q} and an unsteady disturbance flow \tilde{q}

$$q(x_c, y_c, z_c, t) = \bar{q}(x_c, y_c) + \tilde{q}(x_c, y_c, z_c, t). \quad (1)$$

As mentioned above, the laminar base-flow \bar{q} is calculated by the DLR TAU code. The disturbance \tilde{q} of Eq. 1 is represented as a harmonic wave

$$\tilde{q}(x_c, y_c, z_c, t) = \hat{q}(x_c, y_c, z_c) \exp[i(\alpha x_c + \beta z_c - \omega t)] \quad (2)$$

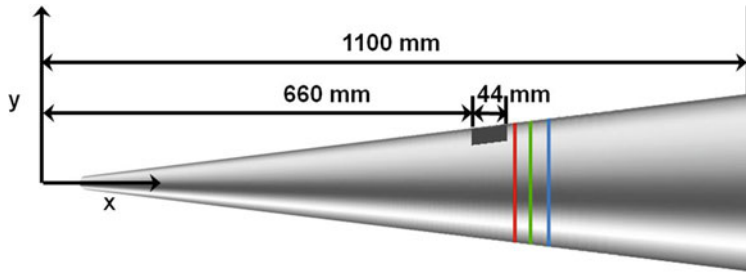


Fig. 1 7° half angle, blunted cone with effusion insert

with the complex-valued amplitude function \hat{q} . The three coordinate directions of the Eqs. 1 and 2 are denoted as x_c , y_c and z_c and describe a curvilinear surface-oriented orthogonal coordinate system.

3 Geometry and Test Matrix

The investigated model is a 7° half angle, blunted cone with a nose radius of 5 mm and a length of about 1 m. The transpiration cooling with nitrogen is done through a carbon ceramic (C/C) plate starting at $x = 0.66$ m, measured from the sharp tip, and having a length of $x = 0.044$ m in streamwise direction, while covering 60° of the model in circumferential direction; see also the schematic drawing in Fig. 1.

The experiments were performed in the DLR High Enthalpy Shock Tunnel Göttingen (HEG), which is a free driven shock tunnel. For further information about the HEG see e.g. Hannemann et al. [10]. The investigated test cases of this study have a free stream Mach number of about 7 at an unit Reynolds number of $Re_m = 2.4 \cdot 10^6 / \text{m}$. Beside the non-effusion reference case, four cases with different mass fluxes are analyzed in detail. Table 1 summarizes these chosen test cases. The cone model was supported by a sting at a nominal angle of attack of 0°. Further, the model was equipped with thermocouples and Atomic Layer Thermopile sensors, short ALTP sensors. The ALTP sensors were used to capture the second mode frequencies. On the model these sensors were placed at 0.725 m, 0.750 m and 0.780 m from the sharp tip, located downstream of the active cooling element.

4 Results

This chapter is split into two parts: starting with analyses of the non-effusion reference case (Sect. 4.1) and ending with the investigations of the effusion cases (Sect. 4.2).

Table 1 HEG test cases

Test case	Mass flux \dot{m}_{eff} (g/s)	Re_m (m^{-1})	$\text{Ma}_{\infty}(-)$	ρ_{∞} (g/m ³)
Non-eff1	0.000	2.41×10^6	7.14	17.97
eff1-0.084	0.084	2.45×10^6	7.15	18.15
eff2-0.098	0.098	2.41×10^6	7.14	17.97
eff3-0.142	0.142	2.45×10^6	7.16	18.11
eff4-0.154	0.154	2.42×10^6	7.15	17.94

Table 2 HEG test cases of Sect. 4.1.1

Test case	p_0 (MPa)	T_0 (K)	ρ_0 (g/m ³)	h_0 (MJ/kg)
Non-eff2-min	1.1386	2808	14.06	3.42
Non-eff2-mean	1.1904	2831	14.58	3.38
Non-eff2-max	1.2422	2853	15.10	3.41

4.1 Reference Test Cases Without Effusion

The first Sect. 4.1.1 summarizes the influence of small inaccuracy of the experimental sensor values, which are used for the base flow calculations. The second Sect. 4.1.2 shows the comparison of LST/PSE versus measurements.

4.1.1 Influence of Small Inaccuracies of the Free Stream Conditions

As already mentioned, previous analyses have demonstrated, that for the comparison with the experimental data, the base flow simulations should include the nozzle, test chamber and cone model [38], which is consequently applied in this paper. To analyze possible errors due to small measurement uncertainties, the input values for the mean flow calculation are examined. The essential reservoir quantity is the measured pressure p_0 , which is the measured pressure at the beginning of the nozzle. The Table 2 provides an upper (sensor 1) and a lower limit (sensor 2) of the reservoir pressure, spanning about 10% difference, and additional the averaged values. As reference test case for this investigation a case, which shows the maximal difference between these two sensors of the current test campaign, is chosen.

The resulting differences are summarized in Fig. 2 by LST calculations. The LST results show the second modes on the three sensor positions of the experiments. The comparison with the experimental data follows in the next Sect. 4.1.2. The different positions are marked by different colors: $x = 0.725 \text{ m} \Rightarrow$ red color, $0.750 \text{ m} \Rightarrow$ green color and $0.780 \text{ m} \Rightarrow$ blue color. The NOLOT results illustrates the typical, expected behaviour: the second mode is amplified in streamwise direction. Due to the increase of the boundary-layer thickness in the downstream direction and the relation between

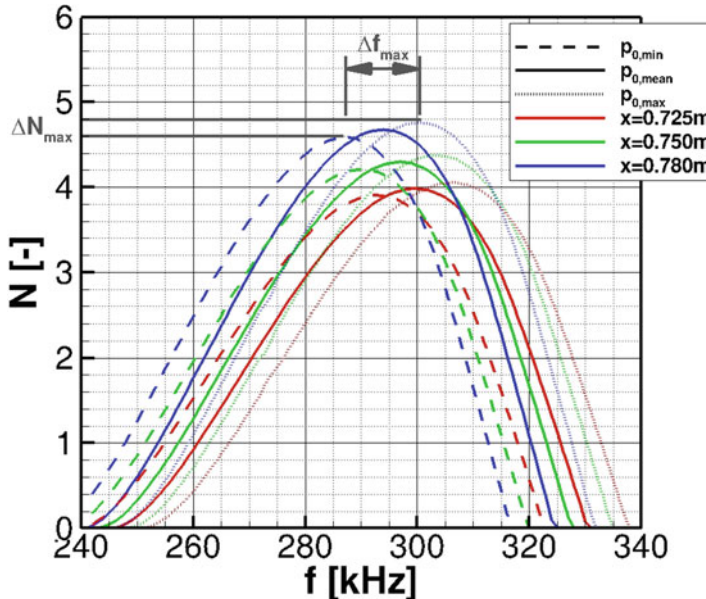


Fig. 2 Non-effusion: Influence of small inaccuracies of p_0 (LST)

the boundary-layer thickness δ and the second mode wavelength, $\lambda \approx 2\delta$, the typical shift towards lower frequencies can be observed. The distributions based on the minimal measured reservoir pressure $p_{0,\min}$ are depicted by dashed lines, the mean reservoir pressure $p_{0,\text{mean}}$ by solid lines and the maximal measured reservoir pressure $p_{0,\max}$ by dots. The differences at the maxima of the functions between the results of $p_{0,\min}$ and $p_{0,\max}$ are about 4% for the N-factors at the maximum ΔN_{\max} and for the corresponding frequencies Δf_{\max} about 5%, independent from the sensor position (in Fig. 2 these values are illustrated for the sensor position 0.780 m). Performed PSE investigations of this test case deliver the same differences (ΔN_{\max} 4% and Δf_{\max} 5%).

For all following results the $p_{0,\text{mean}}$ values are used for the base flow calculations.

4.1.2 Comparison LST/PSE Versus Experimental Data

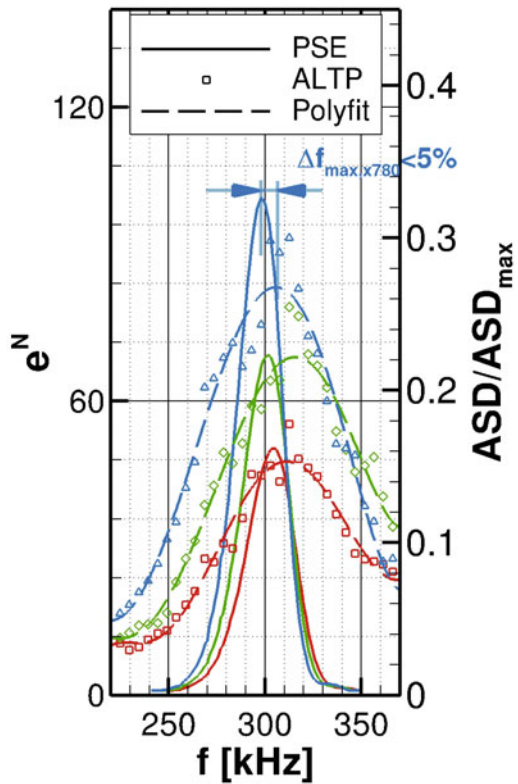
Previous investigations of the same geometry with similar free stream conditions, based on a comparison of the experimental/calculated growth rate of the second modes, show that it is possible to apply Linear Stability Theory (LST) instead of Parabolized Stability Equations (PSE) for test cases without active cooling, see e.g. Wartemann [36]. Nevertheless, one focal point of this paper is the comparison LST versus PSE for the test cases with effusion. Consequently, both approaches are also applied for the non-effusion reference case of this section. The free stream condition

Table 3 Percental error of LST and PSE compared to the measurements of the non-effusion reference test case

Approach	Δf_{\max}	$\Delta e_x^N / e_x^N$	$\Delta e_x^N / e_x^N$
	Compared to the experimental ASD data		
LST	<5%	<4%	$\approx 20\%$
PSE	<5%	<4%	$\approx 17\%$

of the selected test case is summarized in Table 1. The LST results of this reference test case in comparison with the measurements are already published in Wartemann et al. [38]. Thus Fig. 3 gives only the PSE results in comparison with the measurements for a better visibility. Both approaches PSE as well as LST are summarized in Table 3. In Fig. 3 the same colors as of the previous figure are applied. The normalized, measured amplitude spectral density (ASD) are shown as symbols. For the numerical PSE predictions, e^N is used (marked by lines), instead of N , to allow the comparison of the increase of the second modes. Additionally, polyfits for the measurements are added. Comparing the maxima of the polyfits/predicted curves, the corresponding frequencies deliver a good agreement: Δf_{\max} is less than 5% for all three sensor positions, remembering the differences of the previous section due to small inaccuracies. The measured ASD can only be compared indirectly with e^N . It is not possible to compare directly the values, but the increase from one to the next sensor position. From sensor position 1 to 2 an excellent agreement is presented: $e_x^N / e_x^N = 0.72 \approx \text{ASD}_{x725} / \text{ASD}_{x750} = 0.70$. But the agreement between position 2 and 3 is suboptimal: $e_x^N / e_x^N = 0.68$ and $\text{ASD}_{x750} / \text{ASD}_{x780} = 0.82$. NOLOT overpredicts the increase for the last sensor position. This was already discuss in Wartemann et al. [38] for the LST calculations of this reference test case. One, most likely explanation is that in the experiments the transition process already started at the last sensor position and thus the measured second mode already started decomposing at 0.780 m (see detailed analysis in: Wartemann et al. [38]). PSE as well as LST delivers for this reference case nearly the same trend, see Table 3, which summarizes the deviation of PSE and LST compared to the experiments. Beside the frequency comparison at the maxima of all sensor position, the percental deviation of e_x^N / e_x^N to $\text{ASD}_{x725} / \text{ASD}_{x750}$ and e_x^N / e_x^N to $\text{ASD}_{x750} / \text{ASD}_{x780}$ is given. Both approaches, PSE as well as LST delivers a good agreement to the experimental data, looking at the Δf_{\max} and also for the increase of the second modes between sensor positions $x = 0.725$ m and $x = 0.750$ m. Due to the consideration of non-linear/non-parallel effects with PSE, the difference to the experiment between sensor position $x = 0.750$ m and $x = 780$ m is still high with PSE, but less than as predicted with LST. Nevertheless, with exception of the overprediction at the last position, a good agreement of the frequency range as well as the increase between measured and calculated second modes are represented for the non-effusion test case for both approaches.

Fig. 3 Non-effusion reference case: Comparison PSE versus measurements



4.2 Effusion Test Cases

The first Sect. 4.2.1 summarizes the analysis of the general behaviour of the different mass fluxes. The second Sect. 4.2.2 shows the comparisons with the experimental data. The numerical results of both these subsections are based on the LST. The last Sect. 4.2.3 gives the comparisons LST/PSE approach versus experiments.

4.2.1 General Behavior

In this first subsection of the effusion chapter the general effect of the effusion is analyzed. As visible in Table 1, beside the reference test case without effusion, two cases with a mass flux of about $\dot{m}_{\text{eff}} = 0.1 \text{ g/s}$ and two cases with about $\dot{m}_{\text{eff}} = 0.15 \text{ g/s}$ are investigated. For a better visibility for the first diagrams (Fig. 4) only three test cases are chosen: the reference test case non-eff1 is depicted by black lines, eff2-0.098 by orange lines and eff4-0.154 by blue lines. The position of the effusion element is marked by grey colour. In Fig. 4a the N-factors as a function of the x-

coordinate are illustrated for the frequency range from 245 kHz up to 330 kHz. As expected, in the first region, from the starting point of the shown amplified frequencies to the beginning of the effusion element only small differences between the three test cases are visible. In principle, for all test cases the same HEG condition is used, but, as usual, small differences in the free stream conditions from shot to shot exist (see Table 1). This is the reason for these visible differences in the first region. At the start of the effusion element, the non-effusion case lies above the two test cases with effusion. Applying the transition N-factor of the non-effusion case (see more detail in Wartemann et al. [38]), the transition is predicted to be shifted downstream through the effusion. For the effusion case with higher mass flux eff4-0.154 a higher transition onset is predicted than for the eff2-0.098 case. The reason of this behaviour gets clear considering the growth rate over the surface length from Fig. 4b, which depicts the evaluation of the growth rates over the x-coordinate, exemplary for the frequencies 245 kHz and 325 kHz. For a descriptive qualitative comparison three characteristic regions are labeled in Fig. 4b by *I*, *II* and *III*. In the front cone section up to the effusion location, all growth rate are similar. As already mentioned, small differences caused by small differences in the free stream conditions. A previous pre-study using the exact same free stream condition showed in this section no differences (Wartemann et al. [37]). In region *I* the growth rate of the frequency 325 kHz, which was amplified before, falls abruptly to negative values. This is the result of a quickly changing boundary-layer thickness, whereby the amplified frequency spectrum shifts towards lower frequencies. The consequence is, that higher frequencies, like the exemplary shown 325 kHz, die out and lower frequencies, here shown at the example of 280 kHz, are almost suddenly amplified, so that a steep rise in the growth rates curve is present. Furthermore there are other frequencies, not shown here, that were strongly amplified only in this area, becoming immediately extinct elsewhere. Additional to the dominant effect of the quickly changing boundary-layer thickness, secondary, minor effects due to the change of the boundary-layer profiles, have also an influence. Region *II* shows the highest growth rates, which occur probably due to a number of trailing effects, such as the adverse pressure gradient present behind the effusion location. Remarkable in region *III* is that frequencies get amplified with large positive growth rates over a very long distance before they begin to decrease, which is due to the boundary-layer becoming more parallel behind the blowing region in case of active effusion. This is in contrast to the non-effusion case, where a constant frequency is excited most only over a short distance before the growth rates starts to decrease. This family of longer amplified frequencies may be present only in a specific mass flux range, which is applied here. Fedorov [9] showed for higher effusion rates, applying a total mass flow rate of $\dot{m} = 13.5$ g/s, that this effect begins to reverse. Hereby, at large mass fluxes, an enhanced boundary-layer thickening occurred that forms a local boundary-layer thickness peak, which then drops again, so the boundary-layer thickness changes strongly and therefore the amplified frequency range [9]. Due to the described behaviour in Fig. 4b, the corresponding N-factors in Fig. 4a for the higher frequencies start to get damped and die out and the second family of lower frequencies gets strongly excited, but first has to grow in downstream direction to

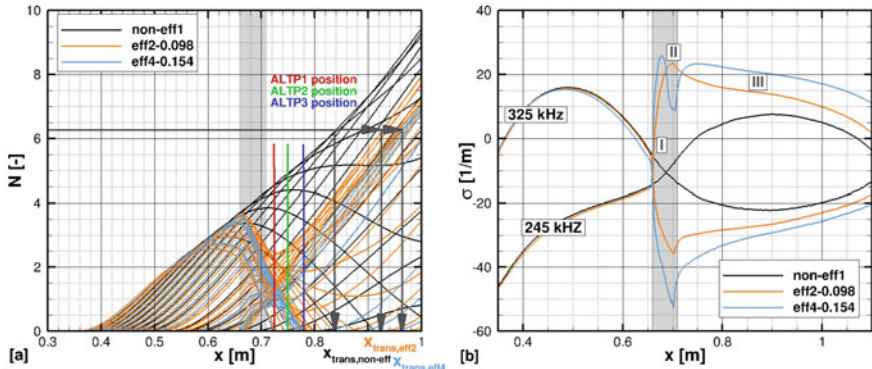
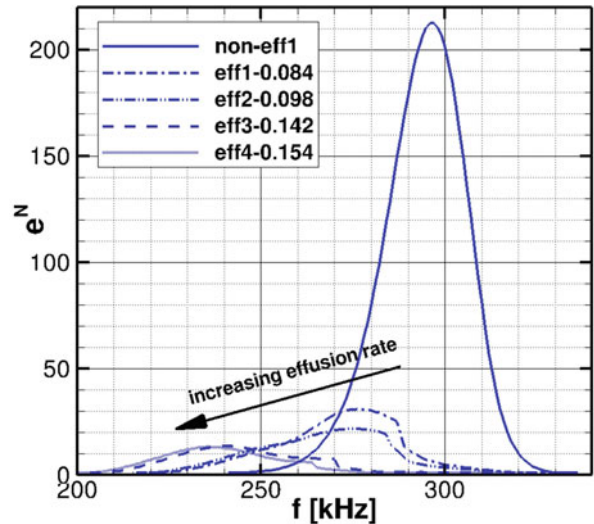


Fig. 4 LST effusion study: **a** $N = f(x)$ for 245 kHz–330 kHz, **b** $\sigma = f(x)$ for $f = 245$ kHz and 325 kHz

Fig. 5 LST effusion study:

a $e^N = f(f)$ for the position $x = 0.780$ m



reach high N -values. This result in a downstream transition shift, depending on the selected mass flux. This apparent downstream shift was also observed by Johnson et al. [15] for mass flux ratios of $F_{\text{avg}} = 0.005$, who analyzed the stability of hypersonic boundary-layer over flat plates and cones using linear stability analysis.

For a better visibility, from Fig. 4a the N -factors only at the ALTP sensor positions 0.780 m (blue color) are extracted and depict as $e^N = f(f)$ in Fig. 5 including all test cases. This diagram illustrates very clearly the already mentioned shift to lower frequencies due to the change of the boundary-layer thickness. The second visible effect is the damping of the second modes. An increase mass flux results in lower e^N maxima for all here investigated mass fluxes as well as for all sensor positions, which are demonstrated in the next subsection.

4.2.2 Comparison LST Versus Experimental Data

Figure 6 provides the second modes at all the three sensor positions (the same colours, as defined before, are applied: $x = 0.725 \text{ m} \Rightarrow$ red color, $0.750 \text{ m} \Rightarrow$ green color and $0.780 \text{ m} \Rightarrow$ blue color). The predicted LST results (lines) are compared with the measured ASD data (symbols). Clearly visible for all sensor positions is with increase of the mass flux (from Fig. 6a–d) the shift of the maxima to lower frequencies and the decrease of the second modes, as discussed in Sect. 4.2.1. Starting with the numerical results in Fig. 6a, additional second maxima are observable. The clearest second maximum is shown at the first sensor position (red line), which marks the position of the old, non-effusion maximum. Further downstream the second maxima vanish. For a better comparability, in Fig. 6a, b polynomial fits for the measured ALTP data are included. These second maxima are also visible in the experiments. With a further increase of the mass flux the functions of the LST calculations get three maxima, see Fig. 6c, d. Also more than two maxima can be interpreted in the functions of the experimental data, but through the decrease of the first maxima, polyfits would merge to just one broad function. For the comparison of the second mode increase from one sensor position to the next, the values at the first maxima are used. Please note, that for the experimental data the maximum values at the maxima are used, not the maxima from the polyfits. This results by trend in a higher deviation between the results of the numerical predictions and measurements. As one example, the test case eff1-0.084 is summarized here: $e_{x725}^N/e_{x750}^N = 0.93$, $\text{ASD}_{x725}/\text{ASD}_{x750} = 0.62$ and $e_{x750}^N/e_{x780}^N = 0.65$ and $\text{ASD}_{x750}/\text{ASD}_{x780} = 0.61$. This results in a numerical deviation compared to the experiments of $\Delta e_{x725}^N/e_{x750}^N = 50\%$ and $\Delta e_{x750}^N/e_{x780}^N = 6\%$. Using the values from the polyfits, the deviation can be reduced to 45% and 3%. Table 4 summarizes the deviation for all four test cases. In general, the prediction of the growth from the first to the second position is worse than from the second to third sensor position. It seems, for the first sensor position, which is the nearest to the effusion element, where the highest effects occur, the LST prediction is not accurate. Especially, for the test cases eff1-0.084 and eff2-0.098: with NOLOT more frequencies survive directly behind the cooling element ($x = 0.725 \text{ m}$). Further downstream, between position $x = 0.750 \text{ m}$ and $x = 0.780 \text{ m}$ again a good agreement is visible. Additional, Table 4 illustrates the good agreement of the corresponding frequency at the first maxima of all sensor positions for the test cases with the clear two maxima (eff1-0.084 and eff2-0.098): the percental deviation of the numerical predictions versus the experimental measurements is less than 5%.

Beside the second mode investigation, the transition prediction is analyzed. The N-factor diagrams, exemplary shown for eff2-0.098 and eff-0.154 in Fig. 4a, delivers the predicted transition N-factor $N_{\text{trans,LST}}$. The corresponding heat flux measurements are already published in Wartemann et al. [38]. Thus the results are just listed together with the numerical LST predictions in Table 5, without a corresponding heat flux diagram. NOLOT predicts a shift in downstream direction for all test cases, while the experimental data delivers a negligible change in transition location (see Table 5). Remembering Sect. 4.2.1, a group of low frequencies exists, which are strongly amplified downstream of the injection. Although the calculated N-factor

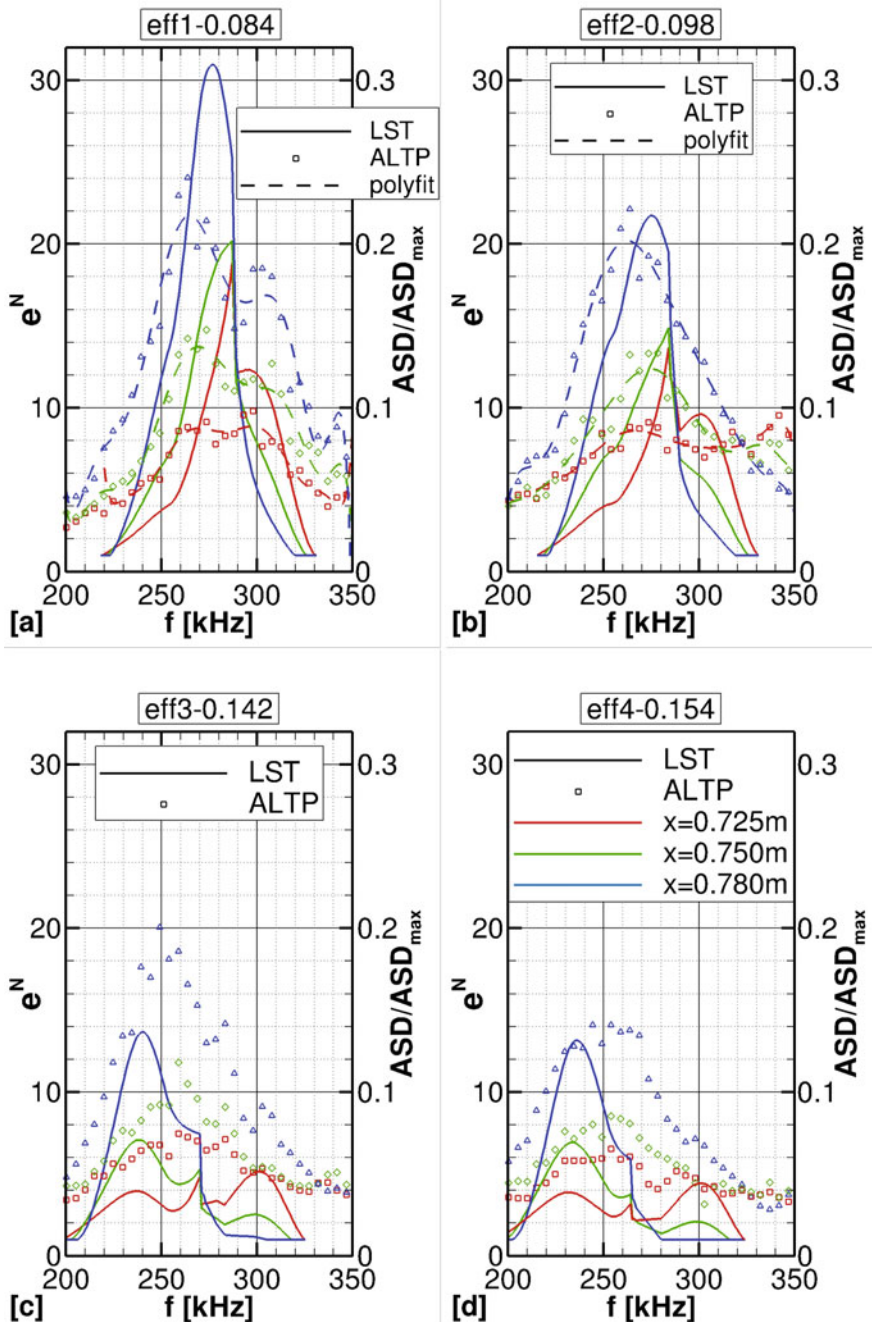


Fig. 6 LST versus experimental ASD-data for all three sensor positions: **a** eff1-0.084, **b** eff2-0.098, **c** eff3-0.142, **d** eff4-0.154

Table 4 Percental error of LST compared to the measurements growth of the second modes

Test case	Δf_{\max}	$\Delta e_x^N / e_x^N$	$\Delta e_x^N / e_x^N$
	Compared to experimental ASD data		
eff1-0.084	<5%	50%	7%
eff2-0.098	<5%	35%	13%
eff3-0.142	—	12%	12%
eff4-0.154	—	19%	12%

Table 5 LST compared to the measurements: transition onset

Test case	$x_{\text{trans, LST}}$ (m)	$x_{\text{trans, exp.}}$ (m)
eff1-0.084	0.91	0.84
eff2-0.098	0.92	0.84
eff3-0.142	0.95	0.84
eff4-0.154	0.96	0.84

trend with LST is correct, it seems, that the negligence of non-linear and/or non-parallel behaviour, results in an underprediction of this group of lower frequencies. Thus the next section includes PSE analyses.

4.2.3 Comparison LST/PSE Versus Experimental Data

In Fig. 7 the N -functions of PSE (blue lines) against LST (orange lines) are shown exemplary for the test cases eff2-0.098 (Fig. 7a) and eff4-0.154 (Fig. 7b). Corresponding to the previously shown results of Fig. 4a, for the lower mass flux cases (represented by eff2-0.098) PSE predicts a lightly higher shift of the transition onset, whereas for the higher mass flux cases (represented by eff4-0.154) no longer are differences visible in the prediction of the transition onset. Table 6 gives all transition onsets: PSE delivers the same trend for all investigated test cases as LST. The similar N-factors result in corresponding similar second modes and deliver the nearly the same precental deviations, compared to the experiments, as the LST predictions of Table 5. Against the expectation of the authors, PSE did not improve the transition onset predictions.

The initial idea of this paper was to reduce the second modes, without triggering the transition, so that finally the transition onset may shift further downstream for the test cases with effusion. Although the reduction of the second modes by effusion are shown for the numerical predictions as well as in the experiments, the shift of the transition onset are only predicted numerically (LST as well as PSE) and are not detectable in the experiments, which are investigated here. But please note, that with higher mass fluxes, which are not longer applicable for the selected numerical approaches, also in the experiments a transition shift in downstream direction was

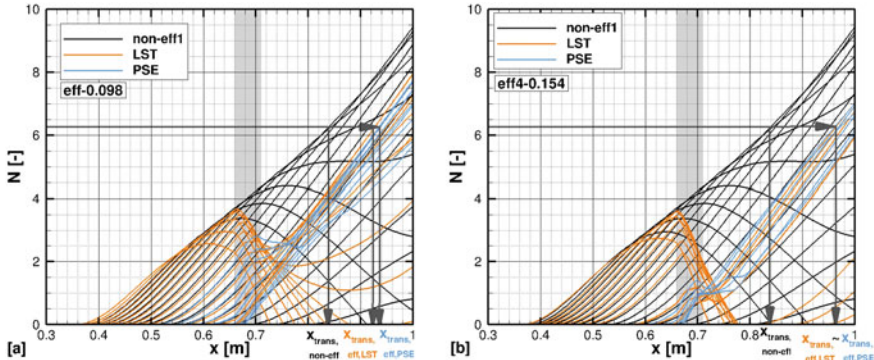


Fig. 7 LST versus PSE: $N = f(x)$ for **a** eff2-0.098 and **b** eff4-0.154

Table 6 PSE compared to the measurements: transition onset

Test case	$x_{\text{trans, PSE}}$ (m)	$x_{\text{trans, exp.}}$ (m)
eff1-0.084	0.93	0.84
eff2-0.098	0.94	0.84
eff3-0.142	0.95	0.84
eff4-0.154	0.96	0.84

demonstrated (see Camillo et al. [27]). One possible explanation is, that LST as well as PSE underpredicts the increase of the low frequency group, which results in the here shown transition shift; Presumably due to some additional effects induced by the effusion, which also can not be handled by the non-linear, non-parallel PSE approach, despite the low selected mass fluxes. Another explanation is, that is second mode is due to the damping no longer the dominating factor for the transition process. The third possible explanation is, just the here used approach (applying the non-effusion transition N-factor for the effusion test cases) is not applicable. E.g., for subsonic flow with suction the N-factors also decrease (see for example: Coustreix et al. [7] or Arnal et al. [2]) and one approach there is to adapt the transition N-factor between suction and non-suction cases.

5 Conclusion

In the current paper hypersonic boundary-layers of a 7° blunted cone with 5 mm nose radius are investigated.

The Sect. 4.1 contains the non-effusion reference case and demonstrates the importance of accurate free stream conditions. Beside this study a good agree-

ment between the second mode predictions and the measured data ($\Delta f_{\max} < 5\%$ and $e_{x725}^N/e_{x750}^N \approx \text{ASD}_{x725}/\text{ASD}_{x750}$) is shown for the non-effusion reference case.

The Sects. 4.2.1–4.2.3 summarize the investigations of the cases with effusion. These analyses are focused on low effusion test cases. Low mass fluxes mean, that by injection of the cooling gas, no visible shock in the schlieren images is induced. A strong indication that the effusion experiment also has a laminar boundary-layer flow at the ALTP sensor positions, are the clearly measurable second modes and the good agreement between the measured and predicted characteristics (LST as well as PSE): Δf_{\max} is less than 5% for the first maxima and the differences between the increase of e_{x750}^N/e_{x780}^N versus $\text{ASD}_{x750}/\text{ASD}_{x780}$ is less than 13% for all test cases. The only exception is the sensor position $x = 0.725$ m, which is the nearest sensor to the effusion element, where higher deviations occur. In the experiment as well as in the LST predictions second maxima appear, which vanish downstream for the lower investigated mass fluxes (eff1-0.084 and eff2-0.098). For higher mass fluxes eff3-0.142 and eff4-0.154 three maxima are predicted by LST, which are comparable with the functions of the measurements.

The idea was to reduce the second modes, without triggering the transition, so that finally the transition onset shift further downstream for the test cases with effusion. The reduction of the second modes by effusion are shown for the numerical predictions as well as in the experiments. The shift of the transition onset are only predicted numerically (LST as well as PSE), but are not detectable in the experiments, which are investigated here. Please note, that with higher mass fluxes, which are not longer applicable for the selected numerical approaches, also in the experiments a transition shift in downstream direction was demonstrated (see Camillo et al. [27]). One possible explanation is, that LST as well as PSE underpredicts the increase of the low frequency group, which results in the here shown transition shift; Presumable due to some additional effects induced by the effusion, which also can not be handled by the non-linear, non-parallel PSE approach, despite the low selected mass fluxes. Another explanation is, that the second mode is due to the damping not longer the dominate factor for the transition process. The third possible explanation is, just the here used approach (applying the non-effusion transition N-factor for the effusion test cases) is not applicable. E.g., for subsonic flow with suction it is also common to adapted the transition N-factor between suction and non-suction cases.

For the prediction of the second modes the selected numerical approaches are adequate. The differences between the LST and PSE are small. However, the transition location based on N-factor distribution was inaccurate indicating an underprediction of the instability growth rate. For the transition prediction of the effusion cases LST as well as PSE are not recommend for the here investigated mass fluxes and the here applied approach (using the non-effusion transition N-factor for the effusion cases).

Please note, that all described effects and the resulting conclusion are strongly dependent on the selected mass flux as well as on the investigated cone position.

References

1. Akin, C., Marvin, J.: Combined effects of mass addition and nose bluntness on boundary-layer transition. *AIAA J.* **8**(5), 857–863 (1970). <https://doi.org/10.2514/3.5778>
2. Arnal, D., Schrauf, G., de Bruin, A., Seitz, A., Cousteix, J., Smith, P.: Transition for airfoils and wings. Technical Report Final report of GARTEUR AD (AG14), GARTEUR (1994)
3. Böhrk, H.: Transpiration-cooled hypersonic flight experiment: setup, flight measurement, and reconstruction. *J. Spacecr. Rocket.* **52**(3), 674–683 (2015). <https://doi.org/10.2514/1.A33144>. ISSN 0022-4650 V
4. Böhrk, H., Wartemann, V., Eggers, T., Martinez Schramm, J., Wagner, A., Hannemann, K.: Shock tunnel testing of the transpiration-cooled heat shield experiment AKTIV. In: 18th AIAA/3AF International Space Planes and Hypersonic Systems and Technologies Conference, Tours, France (2012). AIAA-Paper 2012-5935
5. Bottin, B.: Aerothermodynamic model of an inductively-coupled plasma wind tunnel: numerical and experimental determination of the facility performance. Ph.D. thesis (1999)
6. Choudhari, M., Li, F., Paredes, P., Chang, C.L.: Boundary layer transition on hypersonic vehicles: effects of surface roughness and surface blowing (EN-AVT-289-04) (2017). <https://doi.org/10.14339/STO-EN-AVT-289>
7. Cousteix, J., Arnal, D., Aupoix, B., Gleyzes, C.: Recent studies on transition and turbulence at onera-cert. In: 29th Aerospace Science Meeting (1991). AIAA 91-0332
8. Esser, B.: Die Zustandsgrößen im Stoßwellenkanal als Ergebnisse eines exakten Riemannlösers. Ph.D. thesis, TH Aachen (1991)
9. Fedorov, A., Soudakov, V., Leyva, I.: Stability analysis of high-speed boundary-layer flow with gas injection. In: 7th AIAA Theoretical Fluid Mechanics Conference, AIAA AVIATION Forum (2014). <https://doi.org/10.2514/6.2014-2498>. AIAA 2014-2498
10. Hannemann, K., Martinez Schramm, J., Wagner, A., Ponchio Camillo, G.: The high enthalpy shock tunnel Göttingen (HEG) of the German aerospace center (DLR). *J. Large-Scale Res. Facil.* **4**(A133) (2018). <https://doi.org/10.17815/jlsrf-4-168>
11. Hannemann, V.: Numerical investigation of an effusion cooled thermal protection material. In: ICCFD4 (2006)
12. Hein, S., Bertolotti, F.P., Simen, M., Hanifi, A., Henningson, D.: Linear nonlocal instability analysis—the linear NOLOT code. Technical Report IB-223-94 A56, DLR (1994)
13. Jewell, J.: Boundary-Layer Transition on a Slender Cone in Hypervelocity Flow with Real Gas Effects. Ph.D. thesis, California Institute of Technology (2014)
14. Jewell, J., Leyva, I., Parziale, N., Shepherd, J.: Effect of gas injection on transition in hypervelocity boundary layers. In: 28th International Symposium on Shock Waves (2012). https://doi.org/10.1007/978-3-642-25688-2_111
15. Johnson, H., Gronvall, J., Candler, G.: Reacting hypersonic boundary layer stability with blowing and suction. In: 47th AIAA Aerospace Sciences Meeting including The New Horizons Forum and Aerospace Exposition, Aerospace Sciences Meetings (2009). <https://doi.org/10.2514/6.2009-938>. AIAA938-2009
16. Kendall, R., Rindal, R., Bartlett, E.: Thermochemical ablation. In: AIAA Thermophysics Specialist Conference (1965). AIAA-Paper1965-642
17. Kim, S., Hassan, I.: Numerical study of film cooling scheme on a blunt-nosed body in hypersonic flow. *J. Therm. Sci. Eng. Appl.* **3**(4), 1–7 (2011). <https://doi.org/10.1115/1.4005052>
18. Kütemeyer, M., Helmreich, T., Rosiwal, S., Koch, D.: Influence of zirconium-based alloys on manufacturing and mechanical properties of ultra high temperature ceramic matrix composites. *Adv. Appl. Ceram.* **117**(S1), 62–69 (2018). <https://doi.org/10.1080/17436753.2018.1509810>
19. Leyva, I., Laurence, S., Beierholm, A., Hornung, H., Wagnild, R., Candler, G.: Transition delay in hypervelocity boundary layers by means of CO₂/Acoustic instability interactions. In: 47th AIAA Aerospace Sciences Meeting including The New Horizons Forum and Aerospace Exposition (2009). <https://doi.org/10.2514/6.2009-1287>

20. Li, F., Choudhari, M., Chang, C., White, J.: Effects of injection on the instability of boundary layers over hypersonic configurations. *Phys. Fluids* **25**(10), 104107 (2013). <https://doi.org/10.1063/1.4825038>
21. Loehle, S., Staebler, T., Reimer, T., Cefalu, A.: Photogrammetric surface analysis of ablation processes in high-enthalpy air plasma flow. *AIAA J.* **53**(11), 3187–3195 (2015). <https://doi.org/10.2514/1.J053728>
22. Mack, A., Hannemann, V.: Validation of the unstructured DLR-TAU-Code for hypersonic flows. In: 32nd AIAA Fluid Dynamics Conference and Exhibit, St. Louis, Missouri (2002). AIAA 2002-3111
23. Mack, L.M.: Boundary layer linear stability theory. In: AGARD—Special Course on Stability and Transition of Laminar Flow, vol. R-709, pp. 2–1–2–71 (1984)
24. McManus, H.L., Springer, G.S.: High temperature thermomechanical behavior of carbon-phenolic and carbon-carbon composites, 1. analysis. *J. Compos. Mater.* **26**(2), 206–229 (1992). <https://doi.org/10.1177/002199839202600204>
25. Miró Miró, F., Dehairs, P., Pinna, F., Gkolia, M., Masutti, D., Regert, T., Chazot, O.: Effect of wall blowing on hypersonic boundary-layer transition. *AIAA J.* **57**(4), 1567–1578 (2018). <https://doi.org/10.2514/1.J057604>
26. Morkovin, M.V.: Critical evaluation of transition from laminar to turbulent shear layers with emphasis on hypersonically traveling bodies. techreport AFFDL-TR-68-149, Air Force Flight Dynamics Lab. DTIC citation AD-686178 (1969)
27. Ponchio Camillo, G., Wagner, A., Wartemann, V., Dittert, C., Leroy, B.: Experimental investigation of the effect of transpiration cooling on second mode instabilities in a hypersonic boundary layer. *Exp. Fluids* **61**, 162 (2019)
28. Reimann, B., Hannemann, V.: Numerical investigation of double-cone and cylinder experiments in high enthalpy flows using the dlr tau code. In: 48th AIAA Aerospace Sciences Meeting Including the New Horizons Forum and Aerospace Exposition (2010). <https://doi.org/10.2514/6.2010-1282>
29. Savino, R., Fumo, M., Silvestroni, L., Sciti, D.: Arc-Jet Testing on HfB2 and HfC-Based ultra-high temperature ceramic materials. *J. Eur. Ceram. Soc.* **28**(9), 1899–1907 (2008). <https://doi.org/10.1016/j.jeurceramsoc.2007.11.021>
30. Schmidt, B., Bitter, N., Hornung, H., Shepherd, J.: Experimental investigation of gas injection into the boundary layer on a slender body in supersonic flow. In: 7th AIAA Theoretical Fluid Mechanics Conference (2014). <https://doi.org/10.2514/6.2014-2496>
31. Schneider, S.P.: Hypersonic boundary-layer transition with ablation and blowing. *J. Spacecr. Rocket.* **47**(2), 225–237 (2010). <https://doi.org/10.2514/1.43926>
32. Schwamborn, D., Gerhold, T., Heinrich, R.: The dlr tau-code: Recent applications in research and industry. In: European Conference on Computational Fluid Dynamics ECCOMAS CFD (2006)
33. Shepherd, J.: Transition delay in hypervelocity boundary layers by means of co2/acoustic instability interaction. Technical Report, California Institute of Technology (2014)
34. Wagner, A.: Passive hypersonic boundary layer transition control using ultrasonically absorptive carbon-carbon ceramic with random microstructure. Ph.D. thesis, Katholieke Universiteit Leuven (2014)
35. Wagnild, R., Candler, G., Leyva, I., Jewell, J., Hornung, H.: Carbon dioxide injection for hypervelocity boundary layer stability. In: 48th AIAA Aerospace Sciences Meeting Including the New Horizons Forum and Aerospace Exposition, Aerospace Sciences Meetings (2010). <https://doi.org/10.2514/6.2010-1244>
36. Wartemann, V.: Mack-moden-dämpfung mittels mikroporöser oberflächen im hyperschall. Ph.D. thesis, Technische Universität Braunschweig (2014)
37. Wartemann, V., Ponchio Camillo, G., Reiter, P., Neumann, J., Wagner, A.: Influence of transpiration cooling on second mode instabilities investigated on hypersonic, conical flows. *CEAS* **11**(3), 341–350 (2019). <https://doi.org/10.1007/s12567-019-00249-9>
38. Wartemann, V., Wagner, A., Wagnild, R., Pinna, F., Miró, F.M., Tanno, H., Johnson, H.: High enthalpy effects on hypersonic boundary layer transition. *J. Spacecr. Rocket.* **56**(2), 347–356 (2019). <https://doi.org/10.2514/1.A34281>

39. Weihs, H.: Shefex ii mission overview and first results. In: 4th International ARA Days, Arca-chon, France (2013)
40. Weihs, H., Hald, H., Reimer, T., Fischer, I.: Development of a cmc nose cap for x-38. In: 52nd International Astronautical Congress (2001). IAF-01-I.3.01

Nonlinear PSE Transition Predictions in Hypersonic Boundary Layers with Finite-Rate Chemical Reactions



L. Zanus, F. Miró Miró, and F. Pinna

Abstract Transition on a Mach 10 adiabatic flat-plate boundary layer is analyzed by means of nonlinear parabolized stability equations (NPSE). To the best of authors' knowledge, for the first time NPSE are derived and applied to the study of a finite-rate chemically reacting flow. A fundamental breakdown transition mechanism is investigated within two flow assumptions: a frozen and a 5-species chemical nonequilibrium air mixture. The set of hypotheses deployed modifies the predicted perturbation-amplitude evolution, as well as the types of harmonics that are excited. This results in an earlier predicted transition onset in the case of a chemically reacting flow. The effect of chemical reactions is confirmed to be predominant in the base flow, while it is weak on the perturbation field. In particular, the chemically driven modification of the disturbance quantities shows a tendency to slightly increase perturbation amplitudes, contrary to what previous linear N-factor predictions revealed. Moreover, they lead to the appearance of a second distortion region of the boundary-layer temperature field, localized close the wall.

1 Introduction

Laminar-to-turbulent boundary-layer transition is a critical aspect to deal with during the design phase of a hypersonic vehicle [1]. In a turbulent flow, surface drag and heat transfer can increase several times, compared to the laminar values [2], with the risk of compromising not only spacecraft thermal protection systems (TPS), but the whole vehicle integrity. On the other hand, low turbulence levels can prevent

L. Zanus (✉) · F. Miró Miró · F. Pinna
von Karman Institute for Fluid Dynamics, Chaussée de Waterloo 72,
1640 Rhode-Saint-Genèse, Belgium
e-mail: ludovico.zanus@vki.ac.be

F. Miró Miró
e-mail: fernando.miro.miro@vki.ac.be

F. Pinna
e-mail: fabio.pinna@vki.ac.be

adequate air-fuel mixing at scramjets inlet, with consequent engines failure [3]. For these reasons, boundary-layer transition is often referred to as a potential *aerospace mission killer*, if not properly taken into account.

Whether the interest is in delaying or promoting transition, it is a fundamental requirement to understand the physical mechanisms involved in the entire process. Only then can one provide reliable transition-location predictions and eventually implement effective control strategies. In hypersonic regime, the description of the phenomenon increases in complexity compared to lower-speed flows, due to the amount of effects influencing it (see [4], Chap. 6). Moreover, experimental data are difficult to collect, because of the measurement techniques required and the infeasibility in reproducing simultaneously the whole flight-conditions in ground-test facilities. Hence, for these applications, numerical studies become a fundamental tool for investigation and validation purposes.

During the past thirty years, there have been continuous improvements to the modeling complexity deployed on both the thermophysical gas properties and the perturbation characteristics. Linear stability theory (LST) has been applied to flows in chemical nonequilibrium (CNE) [5], thermo-chemical nonequilibrium (TCNE) [6] and local thermodynamic equilibrium (LTE) [7] conditions. The same flow assumptions were also investigated by means of linear parabolized stability equations (LPSE), which include in the analysis also nonparallel effects. Examples are the works of Chang et al. [8], Kline et al. [9], Zanus et al. [10] and Johnson et al. [11]. Transition-location prediction based on these linear tools can be performed only through the correlations provided by the e^N method. Despite its successful application also to hypersonic flows [12, 13], no knowledge about the physical mechanisms developing in the transition nonlinear stages can be obtained from its employment.

Direct numerical simulations (DNS) can be used to investigate this transition region. Nevertheless, for hypersonic applications, especially in reacting flow regimes, the literature is very scarce, due to the computational effort in solving the size-increased system of equations and the grid resolution to capture the higher disturbance harmonics that generate from the perturbations nonlinear interactions. To authors' knowledge the only studies dealing with this type of analysis are the recent works of Marxen et al. [14] on a flat plate with finite-rate chemical reactions and Di Giovanni et al. [15] on a spherical forebody in TCNE conditions. Both investigations concluded about the importance in taking into account nonequilibrium phenomena when predicting transition in high-Mach scenarios.

Nonlinear PSE are a well-established tool to capture the relevant physics of perturbations evolution within a boundary layer [16, 17]. However, its application to hypersonic flows has been only restricted to frozen chemistry conditions, because of the difficulties in deriving the stability equations, handling the generated enormous amount of terms. To authors' knowledge, the only NPSE analyses of reacting flows are the preliminary simulations of Zanus et al. [18] for flows in equilibrium conditions, while they have never been applied to finite-rate chemically reacting flows.

In the present work, a Mach 10 boundary layer over an adiabatic flat plate is investigated by means of NPSE, both in frozen and chemical nonequilibrium con-

ditions, simulating a fundamental breakdown mechanism. A very hot flow with an edge-temperature of 600 K is chosen, in order to highlight the presence of chemical reactions. These flow conditions are not representative of any realistic application, but they define an ideal academic problem to test the new NPSE solver for reacting flows. Moreover, avoiding low T_w/T_{ad} ratios, usually encountered at these Mach conditions, allows to suppress the appearance of eventual supersonic modes, whose correct treatment in the PSE framework is still controversial [8, 19].

2 Problem Formulation

Stability equations are derived starting from the multi-species Navier–Stokes equations, here expressed in their dimensional invariant form. Superscripts q^i denote vectorial contravariant variables, whereas subscripts q_i denote vectorial covariant variables (see Pinna et al. [20]). Also, indices following a comma denote spatial derivatives (e.g. $u^i_{,j} = \partial u^i / \partial x^j$).

$$\frac{\partial \rho_s}{\partial t} + (u^j \rho_s)_{,j} = -J_{s,j}^j + \dot{\omega}_s, \quad (1a)$$

$$\rho \frac{\partial u^i}{\partial t} + \rho u^j u^i_{,j} = -g^{ij} p_{,j} + \mathbb{T}_{,j}^{ij}, \quad (1b)$$

$$\rho \frac{\partial h}{\partial t} + \rho u^j h_{,j} = \frac{\partial p}{\partial t} + u^j p_{,j} + (\kappa g^{ij} T_{,i})_{,j} - \mathcal{J}_{,j}^j + g_{ik} \mathbb{T}^{kj} u^i_{,j}, \quad (1c)$$

where g^{ij} is the metric tensor [21], u^j is the velocity, ρ_s the species density, $\dot{\omega}_s$ the chemical production term for the s -species, p the pressure, T temperature, h enthalpy and κ the thermal conductivity. J_s^j are the diffusion mass fluxes of each species, while the energy diffusion fluxes \mathcal{J}^j read:

$$\mathcal{J}^j = \sum_{s \in \mathcal{S}} h_s J_s^j. \quad (2)$$

The viscous stress tensor \mathbb{T}^{ij} is defined as:

$$\mathbb{T}^{ij} = \lambda g^{ij} u^k_{,k} + \mu (g^{jk} u^i_{,k} + g^{ik} u^j_{,k}), \quad (3)$$

where μ and λ are respectively the first and second viscosity coefficients. The numerical algorithm, on the other hand, solves the nondimensional version of the stability equations; details about how the nondimensionalization is performed can be found in Zanus et al. [10].

In perturbation theory, every flow quantity is decomposed into a base-flow and a perturbation component (i.e. $q = \bar{q} + \epsilon q'$, with $\epsilon \ll 1$). Inserting this decomposition into Eq. (1) and subtracting the equations satisfied by the laminar base flow, equations governing the physical-perturbations evolution are obtained. From here, nonlinear PSE can be derived by assuming every physical perturbation taking the form:

$$q'(x, y, z, t) = \sum_{n=-N}^N \sum_{m=-M}^M \tilde{q}_{(n,m)}(x, y) \exp(i\Theta) + c.c., \quad (4)$$

with the exponential argument reading:

$$\Theta = \int_{x_0}^x \alpha_{(n,m)}(\xi) d\xi + m \beta_0 z - n \omega_0 t, \quad (5)$$

where $\alpha_{(n,m)}$ is the streamwise wavenumber of mode (n, m) , while β_0 and ω_0 are respectively the spanwise wavenumbers and frequency of the fundamental harmonic.

Equation (4) states that every physical disturbance is considered as a sum of multiple wave-like harmonics, defined by the couple of coefficients (n, m) , indicating respectively the frequency and spanwise-wavenumber indices in the double Fourier expansion. Each mode¹ (n, m) has to satisfy the following system of equations, written in matrix form:

$$L \tilde{\mathbf{q}} + M \frac{\partial \tilde{\mathbf{q}}}{\partial x} + \frac{\partial \alpha}{\partial x} Na \tilde{\mathbf{q}} \Big|_{(n,m)} = \mathbf{F}_{(n,m)}, \quad (6)$$

where $\tilde{\mathbf{q}} = [\tilde{u}^i, \tilde{T}, \tilde{\rho}_s]$ is the vector of the perturbation variables, the L , M and Na matrices are functions of the mean-flow quantities and the stability parameters, and $\mathbf{F}_{(n,m)}$ is the forcing vector for mode (n, m) . The forcing vector includes the nonlinear terms in the perturbation equations, associated to the interactions between the different harmonics. It is important to mention that the results presented in this work were obtained considering only quadratic nonlinearities (i.e. after variables decomposition, terms of order ϵ^3 and higher were dropped). This represents an approximation to the more correct derivation of NPSE for chemically reacting flows, since in principle all orders of perturbations nonlinearities present in the equations should be kept.

Moreover, perturbations of the thermophysical gas properties are obtained by Taylor-expanding them, based on their functional dependency to the state quantities (ρ_s and T). For example perturbation viscosity is defined as:

$$\mu' = \sum_{s \in S} \frac{\partial \bar{\mu}}{\partial \bar{\rho}_s} \rho'_s + \frac{\partial \bar{\mu}}{\partial \bar{T}} T' + \dots \quad (7)$$

¹ Throughout this article the word *mode* is not used in its mathematical meaning, but as synonym of disturbance harmonic, as defined by Eq. (4).

Only linear terms were retained in this work, even if, to be theoretically consistent, the expansion should include terms up to the maximum perturbation equation nonlinear order kept (in this case second order).

These choices were made considering the large amount of equations terms already achieved despite these simplifications and the relative computational effort in building the forcing at every algorithm iteration. For this first attempt in applying NPSE to flows in CNE conditions, these decisions were found reasonable, but the effect of including higher-order nonlinearities in the perturbation dependent quantities description and in the governing equations themselves must be verified in the future.

State-of-the-art models are used to described thermal-transport properties, mixture and chemical reactions. Air is modeled with five species (N , O , NO , N_2 and O_2), and with the set of reactions and reaction-rate constants proposed by Park et al. [22]. The thermal state of the mixture is retrieved from assuming the particles behave like a rigid rotor and a harmonic oscillator (RRHO) [23]. The transport properties (μ and κ) are provided by Yos' approximation to Chapman and Enskog's theory [24, 25], and the diffusion fluxes by solving the Stefan-Maxwell equations [26, 27]. The collisional data required for these is obtained from fitting a polynomial-logarithmic expression [28] to Wright et al.'s data [29]. For a more detailed explanation of the models and relative references please refer to the work of Miró Miró et al.[28].

3 Numerical Tools

The NPSE solver is developed within the VKI Extensible Stability and Transition Analysis (VESTA) toolkit [30]. Stability equations are derived and implemented into matrix formulations in an automatic manner thanks to the VESTA Automatic Derivation and Implementation Toolkit (AD&IT) [20]. Within the NPSE theory, this approach allows, with a minimum effort, to generate equations by choosing the desired maximum order of nonlinearities to retain or the maximum Taylor-expansion order of the thermophysical gas properties perturbations. The VESTA PSE solver has been extensively verified to include flows in CNE conditions, in its linear version [10, 19] and flows in equilibrium conditions in its nonlinear one [18]. The present work is an extension of the solver to include nonlinearities in the analysis of CNE flows. Details about the general equations implementation, algorithm and numerical methods used can be found in Zanus et al. [18, 19]. Concerning the computation of the considered laminar base flows, the DEKAF [31, 32] boundary-layer code is used.

4 Results

The laminar base flow considered is a Mach 10 flat-plate boundary layer with a freestream temperature of 600 K and a unit-Reynolds number equal to $6.6 \times 10^6 \text{ m}^{-1}$.

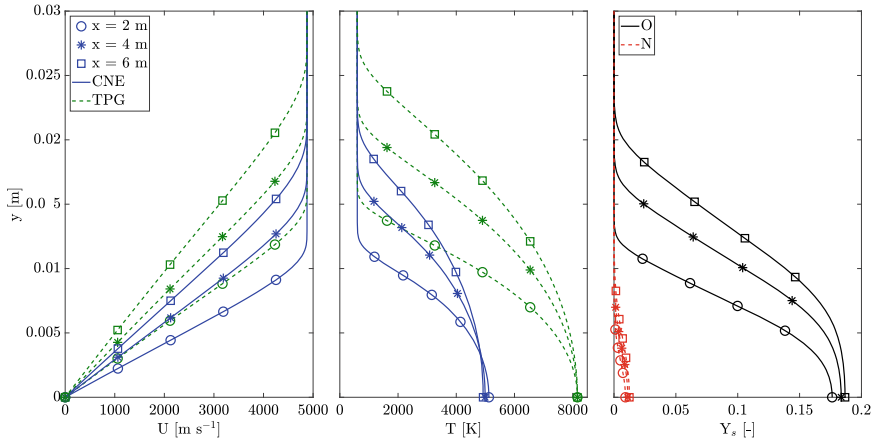


Fig. 1 Streamwise velocity, temperature and atomic species mass-fractions profiles at three different locations along the flat plate: comparison between TPG and CNE flow conditions

The freestream composition is 76.7% N₂ and 23.3% O₂ in mass. Two flow assumptions are taken into account: a thermally perfect gas (TPG) with frozen mixture composition and a gas in chemical nonequilibrium (CNE). Figure 1 displays the streamwise velocity, temperature and atomic species mass-fractions profiles at three different locations along the flat plate. The chemical activity cools down considerably the boundary layer, shrinking its size. Atomic oxygen is present with a relevant concentration, while the atomic nitrogen mass fraction is very small.

A fundamental breakdown transition mechanism is simulated, since for hypersonic Mack's second-mode instability it was found to be one of the most likely scenarios [33]. Within the NPSE framework, this type of breakdown is obtained by initializing the computation with a two-dimensional primary disturbance (i.e. mode (1, 0)) and a pair of oblique waves at the same frequency (i.e. modes (1, ±1)). An initial amplitude $A_{(1,0)} = 1\%$ of the freestream temperature was chosen for mode (1, 0), while for mode (1, 1) it was equal to $A_{(1,1)} = 0.01\%$. Results are displayed in terms of maximum physical perturbation amplitude. Hence,

$$A_{(n,m)} = r_n r_m |\tilde{q}_{(n,m)}|_{max} \exp \left(- \int_{x_0}^x \alpha_{\Im(n,m)} d\xi \right), \quad \text{with} \quad r_a = \begin{cases} 1 & \text{if } a = 0 \\ 2 & \text{if } a \neq 0 \end{cases}, \quad (8)$$

where α_{\Im} is the imaginary part of the streamwise wavenumber α . The most critical transition conditions are chosen for both flow assumptions. The frequency of the perturbations initially inserted into the boundary layer were obtained by performing e^N analyses by means of LST, selecting the disturbances expected to promote transition according to a certain N-factor value (in this case equal to 9). Figure 2 shows the N-factors envelopes, highlighting the N curves relative to the chosen frequencies. For the flow in CNE conditions a frequency around $f = 75$ kHz was found, while

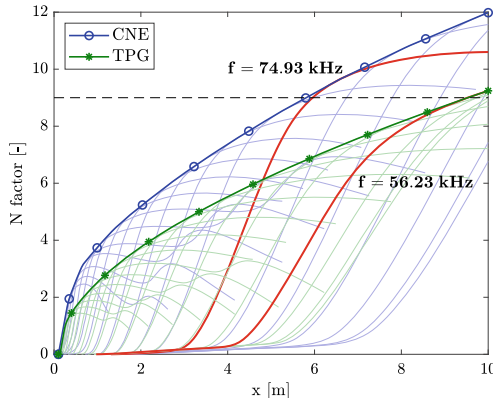


Fig. 2 N-factor evolution along the flat plate for TPG and CNE flow conditions, obtained from LST. N-factor curves of the selected instability frequencies used as initial conditions in the NPSE simulations are highlighted

for a TPG assumption a frequency around $f = 56$ kHz was retrieved. As expected, the boundary-layer cooling, in this case associated with the chemical activity, destabilizes the Mack's second mode, anticipating the predicted transition location.

The fundamental spanwise wavenumber, characterizing the initial conditions of the oblique modes, was chosen by taking the three-dimensional disturbance whose amplitude is mostly excited by the interaction with the primary two-dimensional mode. In order to select it, a series of low-resolved NPSE (i.e. $N = M = 1$ in the Eq. (4) Fourier decomposition) with different β were run. Figure 3 displays the modes amplitude evolutions for the tested spanwise wavenumbers. The oblique mode depending on β behaves quite differently according to the flow assumption considered. In particular, in CNE conditions it reaches the highest amplitude for the smallest β value (i.e. $\beta = 43.12 \text{ m}^{-1}$), while in TPG conditions the highest excitation is obtained for $\beta = 129.97 \text{ m}^{-1}$, which lies in between the tested β range. It has to be highlighted, that the interaction between the inserted modes is generally weak, only appreciable towards the end of the simulation, where the curves depart from their respective linear solutions. Increasing the initial amplitude of the three-dimensional disturbance would anticipate the appearance of the nonlinear interaction, but qualitatively the result is not expected to change.

With the defined initial conditions, NPSE were run with a maximum of $N = 6$ harmonics in frequency and $M = 4$ in spanwise wavenumber. Figure 4 shows the mode amplitudes evolutions for both flow assumptions considered, highlighting the most relevant modes. Depending on the aerothermodynamic model used, perturbations evolve relative to each other in different ways. Particularly, in CNE conditions the high harmonics of the Mack's mode reach higher amplitude levels at the end of the simulations, as well as the mean-flow distortion (MFD, i.e. mode $(0, 0)$). On the contrary, in frozen conditions the harmonics of the three-dimensional mode and the ones of the longitudinal vortex $(0, 1)$ are more excited. Especially the latter shows

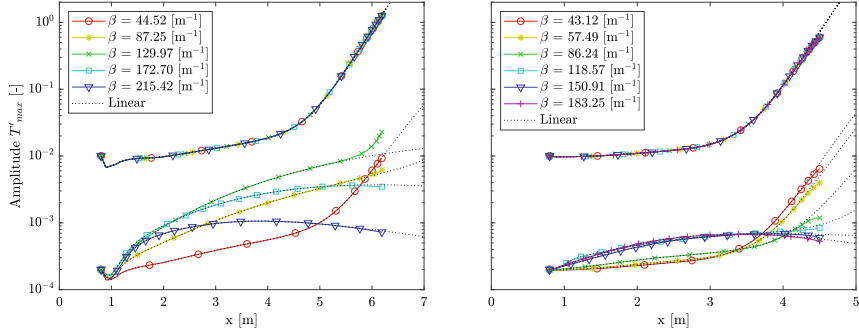


Fig. 3 Evolution of maximum temperature perturbation amplitude of modes $(1, 0)$ and $(1, 1)$, for different initial spanwise wavenumbers: comparison between TPG (left) and CNE (right) flow assumptions

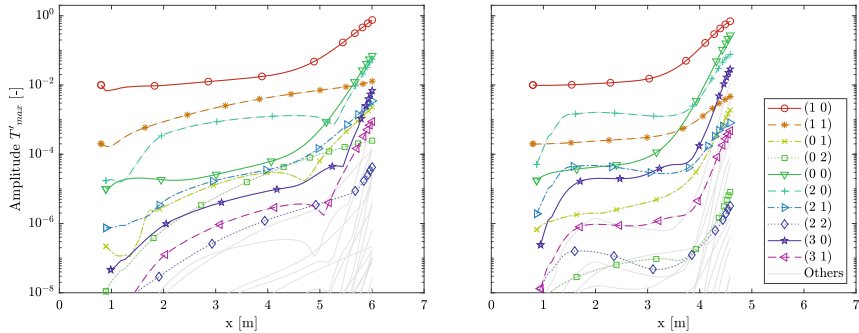
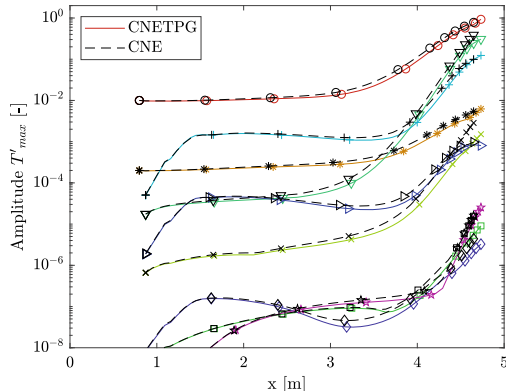


Fig. 4 Evolution of maximum temperature perturbation amplitude for different modes: comparison between TPG (left) and CNE (right) flow assumptions

a significant amplitude difference. As expected, the NPSE simulation stops earlier in CNE conditions than assuming a frozen flow, because of the high perturbations amplitude reached farther upstream.

The influence of chemical activity only on the perturbation field is analyzed by forcing to zero the chemical production terms in the stability equations, while considering as laminar base flow the solution in CNE conditions. This comparison was made reducing the simulations resolution, considering $N = M = 2$ for the maximum order of harmonics entering the computations. Figure 5 shows that the effect of perturbation chemical reactions on disturbance amplitudes is weak, confirming that it is much more important to properly model the chemistry in the base flow, rather than in the perturbation field. Assuming frozen perturbations tends to slightly decrease the harmonics amplitude, contrary to their destabilizing contribution found in N-factor linear predictions [10, 12, 32, 34]. This happens because the disturbance growth rate in the case of frozen perturbation chemistry (here not shown) is higher than the one in CNE conditions at the peak, but smaller in the ascending part of the growth-rate

Fig. 5 Effect of perturbation chemical reactions on disturbances amplitude: comparison between NPSE applied to CNE conditions both in base flow and perturbation field and CNE conditions in base flow while perturbations are frozen (CNETPG)



curve. The NPSE analysis highlights the amplitudes evolution only in the ascending part, which has a minor contribution in the linear N-factor computation. Moreover, it is worth pointing out that the chemistry effect on the perturbation field is not affected by nonlinearities, since it acts in the same way on the primary wave, which evolves mainly linearly, and on the higher harmonics, whose evolution is driven by nonlinear interactions.

Finally, the distortion of the boundary layer produced by the nonlinearities is compared for different quantities and flow assumptions. Figure 6 depicts the streamwise velocity, temperature and pressure amplitude profiles of mode $(0, 0)$, for TPG, CNETPG and CNE conditions. A position closer to the computational domain end is chosen, respectively at $x = 6$ m in case of TPG flow, and at $x = 4.6$ m for CNETPG e CNE conditions. Disturbance amplitudes are nondimensionalized dividing them by the local respective base-flow quantity, while the wall-normal spatial coordinate is made nondimensional using the local boundary-layer height δ , defined as the 99% of the streamwise velocity. Temperature and streamwise velocity deformations show overall the same qualitative features, regardless the flow assumption. The predominant distortion of the temperature field takes place at the boundary-layer edge. Nevertheless, when chemical reactions are taken into account in the base flow, a second deformation region starts to be noticed close to the wall, becoming more evident in the case reactions are introduced also in the perturbation field. Generally, considering a CNE flow assumption leads to the biggest distortion of the boundary layer, followed by CNETPG and frozen conditions. The deformation of the pressure field, on the other hand, is predominant and localized at the boundary-layer edge in the case of a frozen flow, while it is closer to the wall and smaller in amplitude, when reactions are introduced in the base flow.

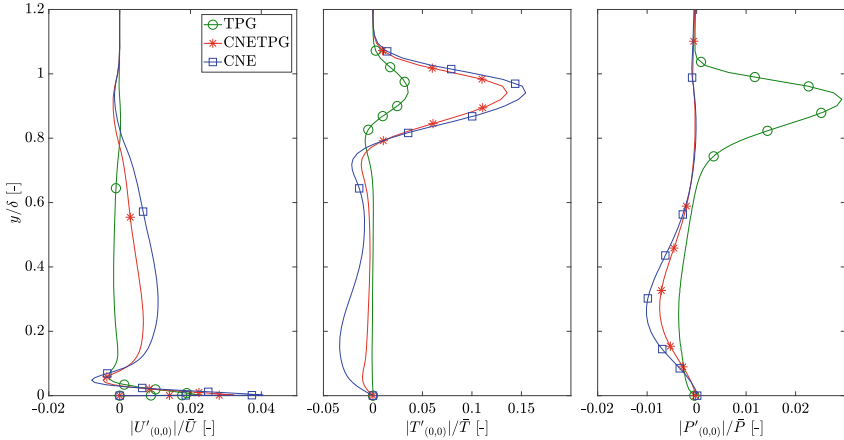


Fig. 6 Mean flow distortion, mode $(0, 0)$, nondimensional profiles of streamwise velocity, temperature and pressure: comparison between TPG, CNETPG and CNE flow assumptions

5 Conclusions

A fundamental breakdown transition mechanism is simulated by means of NPSE on an adiabatic Mach 10 flat-plate boundary layer. Two flow assumptions are investigated: a frozen and a chemical nonequilibrium one, with gas properties described by state-of-the-art models. After selection of initial conditions leading to the most critical transition scenarios, NPSE analyses revealed significant differences in the perturbation-amplitude evolution, both in terms of the magnitude and the type of harmonics excited. In particular, in frozen conditions these were the harmonics of the three-dimensional fundamental disturbance and the ones related to streamwise vortices, while in CNE conditions they were the higher-harmonics of the fundamental two-dimensional Mack's second mode. The effect of chemical reactions on perturbation is weak, confirming the major importance in properly modeling chemical activity in the base flow computation rather than in the stability problem. Considering the perturbations frozen has a tendency to decrease the disturbance amplitudes, contrary to the destabilizing contribution found in previous linear N-factor predictions [10, 12, 32, 34]. This was linked to the fact that the disturbance growth-rate curve in CNETPG conditions, compared to the one in CNE, is lower during the ascending part and greater at the peak. The distortion of the boundary-layer streamwise velocity and temperature fields shows qualitatively the same features, regardless the flow assumption considered. The biggest temperature deformation is localized at the boundary-layer edge. However, perturbations chemical reactions lead to the appearance of a second evident deformation region also close to the wall. Generally, chemical activity produces higher perturbation amplitudes. The pressure field distortion highlights differences in the perturbation-amplitude shape: it is predominant at the boundary-layer edge in case of a frozen flow, while concentrated closer

to the wall in the case of CNE and CNETPG conditions. The success in deriving and implementing nonlinear PSE for nonequilibrium chemically reacting flows is an important step for the development of a tool able to investigate the transition physics in hypersonic regime, with major computational savings with respect to DNS.

Acknowledgements This research was funded by the Belgian National Fund for Scientific Research (FNRS), through the FRIA fellowship (FNRS, dossier FC21045).

References

1. Kimmel, R.L.: Aspects of hypersonic boundary-layer transition control. In: 41st Aerospace Sciences Meeting and Exhibit, vol. 2003, p. 772 (2003)
2. Reed, H.L., Kimmel, R.L., Schneider, S.P., Arnal, D.: Drag prediction and transition in hypersonic flow. In: AIAA paper 1997-1818 (1997)
3. Lockwood, M.K., Petley, D.H., Martin, J.G., Hunt, J.L.: Airbreathing hypersonic vehicle design and analysis methods and interactions. *Prog. Aerosp. Sci.* **35** (1999)
4. Anderson Jr., J.D.: Hypersonic and High Temperature Gas Dynamics, 2nd edn. American Institute of Aeronautics and Astronautics, Reston (2006)
5. Stuckert, G., Reed, H.L.: Linear disturbances in hypersonic, chemically reacting shock layers. *AIAA J.* **32**(7), 1384–1393 (1994)
6. Hudson, M.L., Chokani, N., Candler, G.V.: Linear stability of hypersonic flow in thermochemical nonequilibrium. *AIAA J.* **35**(6), 958–964 (1997)
7. Malik, M.R., Anderson, E.C.: Real gas effects on hypersonic boundary-layer stability. *Phys. Fluids* **80**(3), 803–821 (1991)
8. Chang, C.-L., Vinh, H., Malik, M.R.: Hypersonic boundary-layer stability with chemical reactions using PSE. In: AIAA paper 1997-2012 (1997)
9. Kline, H.L., Chang, C.-L., Li, F.: Hypersonic chemically reacting boundary-layer stability using LASTRAC. In: AIAA paper 2018-3699 (2018)
10. Zanus, L., Miró Miró, F., Pinna, F.: Weak non-parallel effects on chemically reacting hypersonic boundary layer stability. In: AIAA paper 2019-2853 (2019)
11. Johnson, H.B., Candler, G.V.: PSE analysis of reacting hypersonic boundary layer transition. In: AIAA paper 99-3793 (1999)
12. Johnson, H.B., Seipp, T.G., Candler, G.V.: Numerical study of hypersonic reacting boundary layer transition on cones. *Phys. Fluids* **10**(10), 2676–2685 (1998)
13. Johnson, H.B., Candler, G.V.: Analysis of laminar-turbulent transition in hypersonic flight using PSE-Chem. In: AIAA paper 2006-3057 (2006)
14. Marxen, O., Iaccarino, G., Magin, T.E.: Direct numerical simulations of hypersonic boundary-layer transition with finite-rate chemistry. *J. Fluid Mech.* **755**, 35–49 (2014)
15. Di Giovanni, A., Stemmer, C.: Roughness-induced boundary-layer transition on a hypersonic capsule-like forebody including nonequilibrium. *J. Spacecr. Rocket.*, pp. 1–14 (2019)
16. Herbert, T.: Parabolized stability equations. In: AGARD 793 Progress in Transition Modelling, pp. 4.1–4.34 (1993)
17. Joslin, R.D., Streett, C.L., Chang, C.L.: Spatial direct numerical simulation of boundary-layer transition mechanisms: validation of PSE theory. *Theor. Comput. Fluid Dyn.* **4**(6), 271–288 (1993)
18. Zanus, L., Pinna, F.: Stability analysis of hypersonic flows in local thermodynamic equilibrium conditions by means of nonlinear PSE. In: AIAA paper 2018-3696 (2018)
19. Zanus, L., Miró Miró, F., Pinna, F.: Parabolized stability analysis of chemically reacting boundary layer flows in equilibrium conditions. *Proc. Inst. Mech. Eng., Part G: J. Aerosp. Eng.* **234**(1), 79–95 (2020)

20. Pinna, F., Groot, K.J.: Automatic derivation of stability equations in arbitrary coordinates and different flow regimes. In: AIAA paper 2014-2634 (2014)
21. Aris, R.: Vectors, Tensors, and the Basic Equations of Fluid Mechanics, 2nd edn. Dover - Prentice Hall, New York (1962)
22. Park, C., Jaffe, R.L., Partridge, H.: Chemical-kinetic parameters of hyperbolic earth entry. *J. Thermophys. Heat Transf.* **15**(1), 76–90 (2001)
23. Scoggins, J.B., Magin, T.E.: Development of mutation++: multicomponent thermodynamics and transport properties for IONized gases library in C++. In: AIAA paper, vol. 2014, p. 2966 (2014)
24. Yos, J.M.: Approximate equations for the viscosity and translational thermal conductivity of gas mixtures. Technical report AVSSD-0112-67-RM, Avco Corporation (1967)
25. Gupta, R.N., Yos, J.M., Thompson, R.A., Lee, K.-P.: A review of reaction rates and thermodynamic and transport properties for an 11-species air model for chemical and thermal nonequilibrium calculations to 30000 K. Technical report RP-1232, NASA (1990)
26. Hirschfelder, J.O., Curtiss, C.F., Bird, R.B.: Molecular Theory of Gases and Liquids, 2nd edn. Wiley, New York (1954)
27. Magin, T.E., Degrez, G.: Transport algorithms for partially ionized and unmagnetized plasmas. *J. Comput. Phys.* **198**(2), 424–449 (2004)
28. Miró Miró, F., Beyak, E.S., Pinna, F., Reed, H.L.: High-enthalpy models for boundary-layer stability and transition. *Phys. Fluids* **31**(044101) (2019)
29. Wright, M.J., Bose, D., Palmer, G.E., Levin, E.: Recommended collision integrals for transport property computations part I: air species. *AIAA J.* **43**(12), 2558–2564 (2005)
30. Pinna, F.: Numerical study of stability of flows from low to high Mach number. PhD thesis, Università degli Studi di Roma La Sapienza (2012)
31. Groot, K.J., Miró Miró, F., Beyak, E.S., Moyes, A.J., Pinna, F., Reed, H.L.: DEKAF: spectral multi-regime basic-state solver for boundary layer stability. In: AIAA paper 2018-3380 (2018)
32. Miró Miró, F., Beyak, E.S., Mullen, D., Pinna, F., Reed, H.L.: Ionization and dissociation effects on hypersonic boundary-layer stability. In: 31st ICAS Congress (Belo Horizonte, Brazil), International Council of the Aeronautical Sciences (2018)
33. Hader, C., Fasel, H.F.: Towards simulating natural transition in hypersonic boundary layers via random inflow disturbances. *J. Fluid Mech.* **847**(July) (2018)
34. Klentzman, J., Tumin, A.: Stability and receptivity of high speed boundary layers in oxygen. In: AIAA paper 2013-2882 (2013)

Roughness and Receptivity

Investigation of a Sectioned Boundary Layer Suction System in Case of Failure of One of Its Sections in Application to the Three-Dimensional Boundary Layer Laminarization on the Swept Wing



Sergey Baranov, Andrey Kiselev, Dmitry Sboev, and Stepan Tolkachev

Abstract The sectioned system of boundary layer suction was tested on the swept plate model, which simulates swept wing flow conditions. There were investigated the influence of one suction section failure on laminarization efficiency and strategies of its compensation by the increase of suction rate on remaining sections. Estimated the power requirements for the normal and emergency cases of suction system.

Keywords Swept wing · Laminar-turbulent transition · Boundary layer suction · Suction failure · Laminarization · Crossflow instability

1 Introduction

To protract the laminar-turbulent transition, it is possible to use active methods of flow laminarization, such as suction of the boundary layer, surface cooling, local heating, etc. The system of boundary layer laminarization by suction is one of the most effective [1], but it is not insured from the failure. One of the possible ways for the increase of suction efficiency and reliability is using of sectioned suction system. This work is aimed on the comparing the laminar-turbulent transition process in the normal regime of suction system, in the case of failure of one of four suction sections and in the emergency regime, when the suction rate increase in other sections. Another subject of research was the question of the possibility of extrapolating the experimental data on laminarization obtained in industrial wind tunnels (as a rule, with an increased level of freestream turbulence) to flight conditions.

S. Baranov · A. Kiselev · D. Sboev · S. Tolkachev (✉)
Central Aerohydrodynamic Institute, Zhukovsky, Russia
e-mail: tolkachevst@gmail.com

D. Sboev
e-mail: t124@inbox.ru

2 Experimental Setup

The experiments were carried out in the test section ($1000 \times 1000 \times 4000$ mm) of the low turbulent wind tunnel T-124 of Central Aerohydrodynamic Institute (TsAGI).

3D boundary layer was organized on a swept flat plate with curvilinear upper and side walls, imitating pressure gradient present on a swept wing (Fig. 1). This method of creating a three-dimensional boundary layer is widely used [2, 3]. The model with sweep angle 35° , 998 mm span, 2100 mm chord, 20 mm thickness was made of plexiglas. Leading edge of the model is ellipse shaped with a semi-major axis 80 mm. X distance is normal to the leading edge and counted from it.

The wind tunnel doesn't have a thermostatic system, thus the air heated up during the experiment. To neutralize its effect on the process of laminar-turbulent transition the freestream velocity was corrected during the experiment between the measurements to maintain the Reynolds number per unit length constant.

Two regimes of freestream turbulence were investigated.

Low freestream turbulence regime is close to the conditions of cruise flight of airplane. It was provided by the design of wind tunnel and the value was about 0.12%. The base regime for investigation was chosen: freestream velocity— $U_{fs} = 28.6$ m/s; air temperature $T_{air} = 303^\circ\text{K}$. Reynolds number per unit length was $\text{Re}_1 = 1.746 \times 10^6$ 1/m.

Elevated freestream turbulence regime refers to the industrial wind tunnels. The benefit of this regime for the experiment is independence on transversal position (Z —coordinate). It was provided by turbulizing grid, made of square braided wire with diameter 1.5 mm and size of cell 25 mm. The value of turbulence level was 0.93%. The base regime for investigation was chosen: freestream velocity— $U_{fs} = 31.3$ m/s; air temperature $T_{air} = 303^\circ\text{K}$. Reynolds number per unit length was $\text{Re}_1 = 1.911 \times 10^6$ 1/m.

The investigation of the boundary layer structure was carried out by single wire constant temperature anemometry.

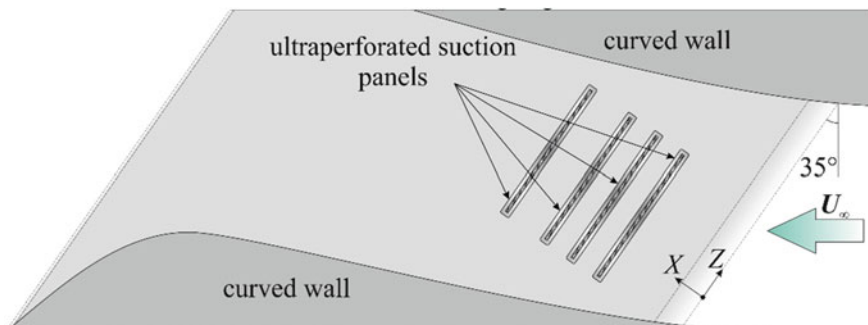
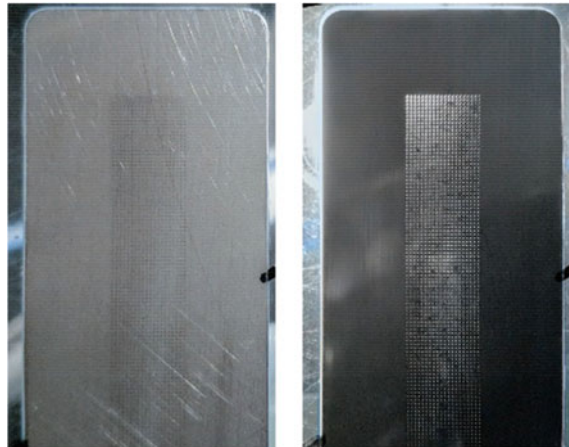


Fig. 1 Scheme of experiment

Fig. 2 The external view of ultraperforated panels in natural light (left picture) and in backlight (right picture)



The model is equipped with 4 perforated suction panels of $484 \times 32 \times 0.49$ mm (Fig. 2). The perforated area of the panel has a size of 460×9.5 mm. 20 rows of holes with a diameter of $80 \mu\text{m}$ are located in the nodes of a square grid with an edge of 0.5 mm. The porosity of perforated area is about 2%. The middle positions of suction panels were in $X = 304$ mm; 404 mm; 504 mm; 654 mm.

To protract the transition, the suction mode with a speed of 5.6 m/s in the holes of all suction panels was chosen as the base regime. There were investigated two emergency strategies, when the failure of one suction section modelled. The first one is based on increase of suction rate on the neighbour suction section, the second one—on the all remaining sections.

3 Results

To control the suction mass flow the pressure drop between chamber under the suction panel and surface on the model was measured. Thus, the calibration of ultraperforated suction panel was done using the vacuum chamber and orifice plate (Fig. 3). The dependence of pressure drop on the suction flow rate is linear. The divergence from the linear law on the flow rates higher, than 120 l/min caused by off-design behaviour of orifice plate.

The wing model has 2 lines of 11 pressure taps. Typical distribution of pressure coefficient over the model for wide interval of freestream velocity presented on the Fig. 4. Accelerated flow is implemented and it creates favorable conditions for cross-flow instability on our swept plate model.

Fig. 3 Calibration of ultraperforated panel

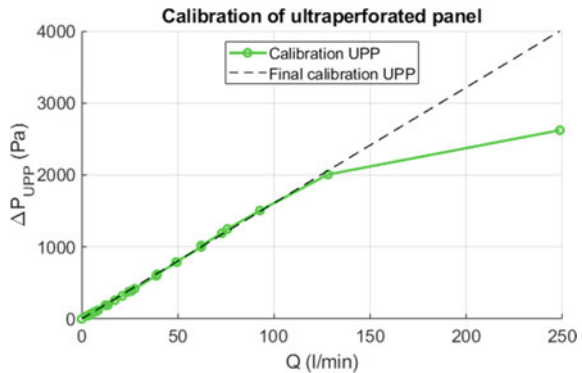
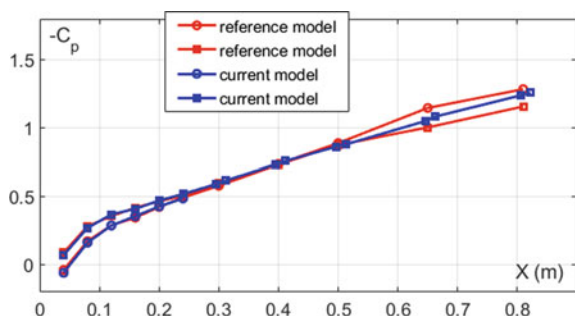


Fig. 4 The distribution of pressure coefficient on the model



3.1 Low Freestream Turbulence Regime

The main attention is paid to the study of the destruction zone of the laminar flow regime in the boundary layer. In order to characterize the flow, the parameter intermittency γ used—it shows the percentage of turbulent flow in the oscillogram of velocity, measured in boundary layer. Previously, this method was successfully used by the authors in investigations of the laminar-turbulent transition [4].

An analysis of data showed sufficiently different laminarization efficiency of suction panels (Fig. 5), it decays downstream. We can conclude, that fourth section has weak laminarization efficiency.

In the base regime, when all four suction sections were working, the intermittency was 23% (Fig. 6). The position of hot-wire measurements $X = 830$ mm was chosen to achieve this value, which allows to monitor both increase and decrease of intermittency.

According to the distribution of laminarization efficiency the disabling of the first section had the greatest impact on the flow—the intermittency increased up to 75–80%. To compensate this situation, it is necessary to increase suction rate on the second suction panel from standard 5.6 m/s up to 40 m/s. This is equivalent to an increase of power consuming by suction system from 1 W up to 13.8 W. The second

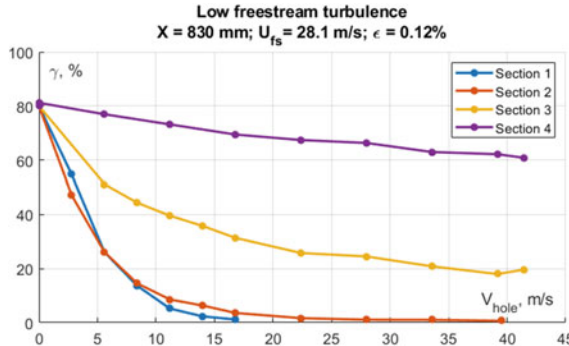


Fig. 5 The dependence of intermittency in $X = 830$ mm on suction speed for each section in low freestream turbulence regime

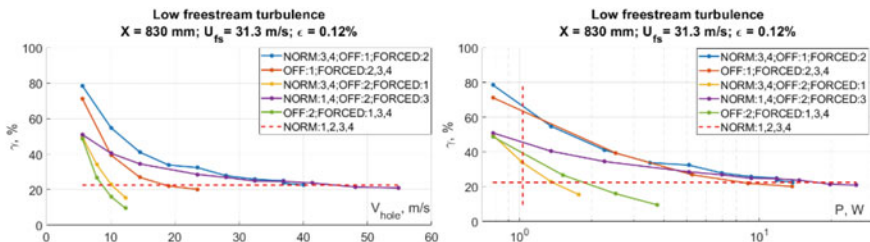


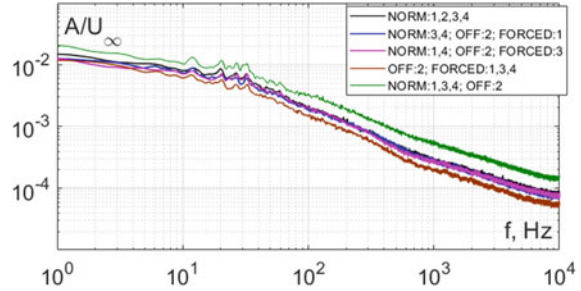
Fig. 6 The dependence of intermittency in $X = 830$ mm on suction speed in holes of perforation (left picture) and on power consumption of suction system (right picture) in different emergency regimes. NORM—sections with normal suction regime; OFF—disabled suction sections; FORCED—sections with increased suction rate

strategy need to increase the suction rate on all remaining suction sections up to 19 m/s or 9 W in power terms.

The disabling of the second section lead to increase of intermittency from 23 to 50%. Three strategies for compensating the loss of laminarization efficiency were investigated: by the first section, by the third section and by remaining suction sections. The first strategy needs to increase the suction rate on the first section from 5.6 m/s up to 10 m/s, which corresponds to the increase of required power from 1 W up to 1.3 W. The second strategy is less effective: suction rate needs to be increased up to 41 m/s, required power—up to 14 W. The third strategy is more attractive in comparison to the second—to compensate the loss of laminarization efficiency it is necessary to increase the suction rate on remaining suction sections up to 8.5 m/s. The required power increases up to 1.8 W.

The next question is the behavior of laminar-turbulent transition in three cases: working state, when all suction sections are involved; two emergency states, when the second section is disabled and the loss of laminarization efficiency is fully compensated by the increase of suction rate, using the first section or all remaining sections.

Fig. 7 Velocity pulsations spectra in normal suction regime and emergency regimes. NORM—sections with normal suction regime; OFF—disabled suction sections; FORCED—sections with increased suction rate



These conditions were found and the velocity pulsations spectra for these regimes are presented on Fig. 7. The level of pulsations for them and the shape of the spectra are the similar. From the figure it can be clearly seen, that level of pulsations in the case of disabled suction panel is higher in wide frequency band.

3.2 Elevated Freestream Turbulence Regime

In conditions of elevated freestream turbulence physics (Fig. 8) is qualitatively the same to the case of low turbulent regime (Fig. 6)—the disabling of the first section has the greatest impact on laminar-turbulent transition (intermittency increases from 23% up to 98%), but the specific values differ. To compensate this situation, it is necessary to increase suction rate on the second suction panel from standard 5.6 m/s up to 30 m/s. This is equivalent to an increase of power consuming by suction system from 1 W up to 7.8 W. The second strategy need to increase the suction rate on all remaining suction sections up to 21 m/s or 11.5 W in power terms.

The disabling of the second section lead to increase of intermittency from 23% to 84%. Three strategies for compensating the loss of laminarization efficiency were investigated: by the first section, by the third section and by remaining suction

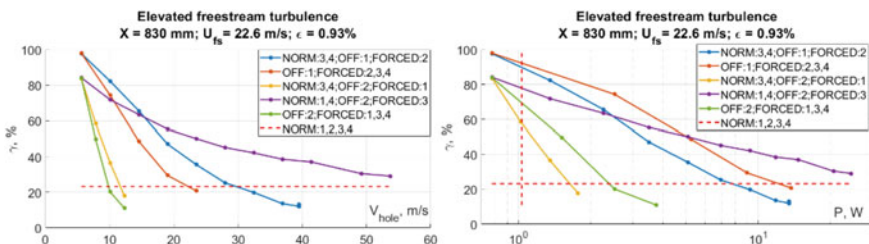


Fig. 8 The dependence of intermittency in $X = 830$ mm on suction speed in holes of perforation (left picture) and on power consumption of suction system (right picture) in different emergency regimes. NORM—sections with normal suction regime; OFF—disabled suction sections; FORCED—sections with increased suction rate

sections. The first strategy needs to increase the suction rate on the first section from 5.6 m/s up to 11.5 m/s, which corresponds to the increase of required power from 1 W up to 1.65 W. The second strategy is ineffective—full laminarization efficiency compensation wasn't reached. The third strategy is less effective in comparison to the first—to compensate the loss of laminarization efficiency it is necessary to increase the suction rate on remaining suction sections up to 10 m/s. The required power increases up to 2.5 W.

Like in the case of low turbulent regime there were selected three suction regimes: working state and two emergency regimes with disabled second section, which provide the same intermittency value. The velocity pulsations spectra for these regimes is presented in Fig. 9. The level of pulsations for them and the shape of the spectra are the similar. The level of pulsations in the case of disabled suction panel is higher in wide frequency band.

Comparison of rate of intermittency growing along the flow for three regimes (operating and 2 emergency) is given on Fig. 10. It turned out an amazing result—the identity of these three regimes. It speaks about the equivalence of suction impact on

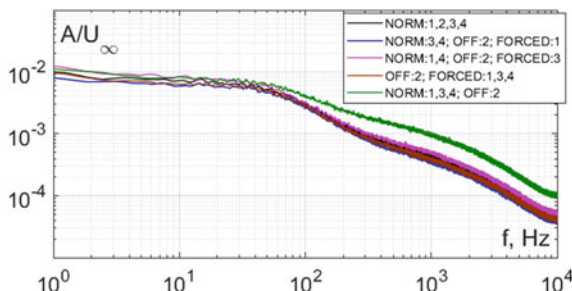


Fig. 9 Velocity pulsations spectra in normal suction regime and emergency regimes. NORM—sections with normal suction regime; OFF—disabled suction sections; FORCED—sections with increased suction rate

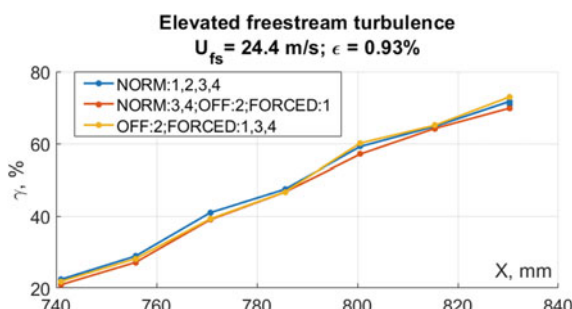


Fig. 10 The development of intermittency along the flow for normal and emergency suction regimes. NORM—sections with normal suction regime; OFF—disabled suction sections; FORCED—sections with increased suction rate

the boundary layer despite the different position and thus the different laminarization efficiency of suction sections.

4 Conclusion

The experiments carried out in conditions of low and elevated freestream turbulence showed the identical picture—the task of compensation of laminarization efficiency in the case of disabling of one of sections is a challenge, the difficulty level of which depends on the laminarization efficiency of this section. It can easily happen, when the multiple increase of the suction rate could be needed. In the real case, when the suction rate is distributed optimal to provide the maximal performance of boundary layer suction system, the shutdown of one section will displace the optimal point for the suction system and the overall laminarization efficiency inevitably will be decreased. So as to reduce losses it is logical to split the most efficient suction sections on smaller and place them closer.

The nice result of this investigation is the equivalence of laminar-turbulent transition processes for the operating and emergency regimes of suction system, which makes the task of selecting an emergency mode easier.

References

1. Chernyshev, S.L., Kiselev, A.Ph., Kuryachii, A.P.: Laminar flow control research at TsAGI: past and present. *Prog. Aerosp. Sci.* **47**, 3 (2011). <https://doi.org/10.1016/j.paerosci.2010.11.001>
2. Deyhle, H., Bippes, H.: Disturbance growth in an unstable three-dimensional boundary layer and its dependence on environmental conditions. *J. Fluid Mech.* **316**, 73 (1996). <https://doi.org/10.1017/S0022112096000456>
3. Gaponenko, V.R., Ivanov, A.V., Kachanov, Y.S., Crouch, J.D.: Swept-wing boundary-layer receptivity to surface non-uniformities. *J. Fluid Mech.* (2002). <https://doi.org/10.1017/S0022112002008297>
4. Kiselev, A.Ph., Shboev, D.S., Chernyshev, S.L.: Features of the laminar-turbulent transition in the three-dimensional boundary layer for increased external turbulence. *Dokl. Phys.* **59** (2014). <https://doi.org/10.1134/s1028335814020128>

Destabilisation of Stationary and Travelling Crossflow Disturbances Due to Forward and Backward Facing Steps over a Swept Wing



Emma E. Cooke, Shahid Mughal, Spencer Sherwin, Richard Ashworth, and Stephen Rolston

Abstract The destabilisation effects of forward and backward facing steps on cross-flow (CF) disturbances on an infinite swept wing is investigated. Stationary and travelling CF-wave instability modulations, as they convect over the abrupt surface features, are investigated computationally with step heights ranging from 18% to 53% of the boundary layer thickness at chordwise locations of 10% and 20%. An embedded mesh approach is used to compute boundary layer base flow profiles over the swept wing with the high order spectral/hp element solver, Nektar++. Linear Stability Theory (LST), Parabolised Stability Equations (PSE) and Linearised Harmonic Navier–Stokes (LHNS) models are used to investigate the development of the convecting CF disturbances. LST is used to understand the instability parameter space and map out neutral curves. PSE equations fail to correctly capture the effects of the steps due to the strong short scale variations introduced whereas, the LHNS provide a rapid and more physics correct technique to ascertain flow destabilisation effects.

E. E. Cooke (✉) · S. Mughal

Imperial College London, Huxley Building, 180 Queens Gate, London SW7 2AZ, UK
e-mail: emma.cooke13@imperial.ac.uk

S. Mughal

e-mail: s.mughal@imperial.ac.uk

S. Sherwin

Imperial College London, City and Guilds Building South Kensington, SW7 2AZ London, UK
e-mail: s.sherwin@imperial.ac.uk

R. Ashworth · S. Rolston

Airbus Group Central Research and Technology, Airbus Wing Integration Centre, Building 07Y,
Bristol BS34 7PA, UK
e-mail: rashworth@airbus.com

S. Rolston

e-mail: s.rolston@airbus.com

1 Introduction

Small-scale surface imperfections in the form of rivets or step features introduced, for example, by the joint between the leading edge to wing box junction on an aircraft wing can be a major impedance on achieving and maintaining a laminar boundary layer. Engineering imperfections, *ex crescences*, can act as sites for enhanced flow destabilisation and arise at their simplest in the form of steps or bumps. These excrescences cause any pre-existing convecting instabilities to modify their growth and/or immediately trip the laminar flow to a turbulent form through a variety of bypass or abrupt tripping mechanisms. The plethora of flow tripping pathways to turbulence are nicely summarised by Morkovin et al. [9], ranging from linear and non-linear mechanisms through local flow destabilisation and bypass phenomenon. The presence of steps may well bring into play any one of the aforementioned routes to flow destabilisation, depending upon the severity, type and form of the step feature.

Flow instabilities past a swept wing can be modelled with Direct Numerical Simulation (DNS) to gain greater flow physics insight but at considerable High Performance Computing (HPC) cost. Even today such simulations are limited to very simplistic and/or reduced-order geometries. This option is extremely impractical for industry. There is a need for rapid computational analyses tools to obtain solutions at lower Central Processing Unit (CPU) overhead. For many years industry has adopted the semi-empirical e^N method coupled with linear stability theory (LST) to predict the transition front location. LST however, makes gross oversimplifications for swept wing geometries due to neglect of non-parallel effects, surface curvature and non-linearity. These simplifications become even more ill-suited in the presence of highly localised step-type features due to the exacerbated local flow non-parallelism imposed in the near-field of the step. Parabolised stability equations [2, 7] (PSE) are today accepted to offer major enhancements in fidelity of flow modelling, but when the spatial scale of the step-like feature is of the same length scale or shorter than the convecting disturbances wavelength, PSE have been shown to be invalid [20], due to the step size restriction [8] required for the numerical stability of the PSE model. Moreover, their use in the presence of trapped laminar separation bubbles (LSBs) is also questionable, in view of the parabolic nature of the PSE model. In such scenarios, the linearised harmonic Navier Stokes (LHNS) model [10, 15] becomes an attractive tool, since it does not suffer from any step-size restriction. By its very nature it captures non-parallel effects, upstream and downstream propagation of all short scale processes, given sufficient resolution in the numerical discretisation.

Effects of two-dimensional (2D) steps on Tollmien-Schlichting waves in the presence of LSBs for flat plate problems have been studied widely in experimental, numerical and theoretical frameworks [11, 13, 18, 19]. These studies have shown that dependent upon the strength, the 2D-LSB can either act as an oscillator and amplifier to already convecting instabilities and/or give rise to bi-global modes. When the problem becomes an aerofoil with the additional complexity of curvature and sweep [1, 12] (the so-called 2.5D problem), and also features a localised step [5,

[16, 17], its modelling and understanding of the mechanisms involved in 2.5D LSB flow induced destabilisation are extremely limited.

Backward facing steps (BFSs) are generally perceived to be much more detrimental to a laminar boundary layer than forward facing steps (FFSs) in the 2D context. Literature on 2.5D boundary-layer flow with steps included (gathered primarily from experiments) tends to describe a sudden forward movement in the transition front for FFSs, implying there exists a critical step height. For BFSs the movement is rather gradual, making it difficult to characterise a critical step height. Tufts et al. [16] describe a destabilising interaction between the crossflow (CF) disturbance and the downstream helical flow located on top of the FFS when the step height is smaller than that of the clean CF vortex core. Eppink [4, 5] also investigated the effect of FFSs on CF instability and found that the Tufts et al. [16] criteria predicts a critical step height 15% larger than that in experiments. Eppink [5] reasons that the core of the primary CF vortex is lifted up from the wall sufficiently such that it should not interact with the step or helical flow. There exists a second set of vortices which could interact with the helical flow, but it is argued that this should not be destabilising. In the context of BFSs investigated, Eppink et al. [6] found that generally the stationary CF was affected quite weakly, if at all. Travelling CF modes appeared to be destabilised by the BFS more so, but the underpinning mechanisms are not clearly understood and are likely to be very different to those arising in FFS boundary layers.

Along with the above cited works, this work was motivated by the experimental work of Saeed et al. [14] who looked at varying bump shapes on a 40% swept wing model (AERAST). In experiments, varying bump heights were placed at about 3% (neutral point location), 10% and 20% chord. The forward movement of the laminar-turbulent transition front with increasing bump heights was observed with naphthalene. The computational work reported in this paper is concerned not only with examining bump like excrescences, but also its decomposition into forward and backward facing steps (not done in the experiments). This paper reports on some preliminary findings of our analysis. We firstly proceed by briefly describing the theoretical tools used in the modelling, and follow this with some initial findings from our analysis. Results are presented for four excrescence heights at two different locations along the swept wing geometry.

2 Methods

For more extensive information on the computational methods used in the study, the reader should refer to Cooke et al. [3]. Here we give only brief details. To summarise we use the high order spectral h/p element solver, Nektar++ to compute steady boundary layer flows over the step features, followed by the use of LST, PSE and the linear harmonic Navier–Stokes approach.

2.1 Base Flow Generation

Firstly, the entire AERAST aerofoil is computed with the Airbus RANS solver, TAU. Flow conditions are configured to match the experimental regime of Saeed et al. [14] as closely as possible. The Reynolds number is 1 million and Mach number 0.3. The clean (no excrescence present) embedded mesh is generated with AutoCAD Inventor and Nekmesh—a high order mesh generation software within the Nektar++ framework. Boundary and initial conditions are extracted from the full step-free RANS solution and interpolated to an embedded mesh where the step features are to be introduced. Nektar++ solutions with the step included features are thus only computed within the embedded mesh.

Nektar++ essentially discretises the domain into varying element sizes, h-type refinement, which are represented by piecewise polynomials, p-type refinement, and the solution is then represented through this polynomial basis. The incompressible Navier–Stokes solver applies a splitting scheme where the velocity fields are decoupled from the pressure field along with an implicit-explicit scheme for the time stepping. Fourier expansions are utilised in the span-wise direction to complete the 2.5D domain. Convergence is achieved by ramping up the polynomial order and time averaging the highest order solution. This is confirmed through application of a L^2 norm to ensure the error is less than 10^{-5} . Typically, the near wall quadrilateral elements are expanded with a polynomial order seven and a lower order is applied within the unstructured surrounding mesh. Meshes contain around 10,000 elements before polynomial expansion.

2.2 Boundary Layer Extraction

Boundary layer profiles extracted from the steady converged Nektar++ solution are then post-processed to be in the correct format for the subsequent analyses with the instability methods. Extracted data points are clustered around the leading edge flow attachment point and become more sparse moving downstream or away from the wall, with the exception of regions where the excrescence is placed, where the grid there is kept fine enough to capture the rapid changes in flow structure. The coordinate system is body fitted and the boundary layer field derivatives are calculated to second order accuracy. Obtaining smooth second order derivatives is non-trivial as Nektar++ only provides solution variables which are C_0 continuous. Cubic spline interpolation is applied in the normal and stream-wise directions with exception to the step locality. Here, finite differencing is applied to avoid spurious overshoots which would arise from spline fitting regions of drastic gradient changes.

Table 1 The various stability ansatz and assumptions; (α , β) denote chordwise and span-wise wave numbers and ω the temporal frequency

Stability method	Ansatz	Assumptions
LST	$\hat{\phi}(y)e^{i(\alpha x + \beta z - \omega t)} + c.c.$	$\bar{\phi}_x = \bar{\phi}_z = 0$
PSE	$\hat{\phi}(x, y)e^{i(\int \alpha(x)dx_1 + \beta z - \omega t)} + c.c.$	$\bar{\phi}_z = 0, \quad \bar{\phi}_x \ll \bar{\phi}_y$
LHNS	$\hat{\phi}(x, y)e^{i(\beta z - \omega t)} + c.c.$	$\bar{\phi}_z = 0$

2.3 Stability Tools

Derivation of the four linear instability models in this paper, begin by decomposing the flow field into a steady flow field, $\bar{\phi}$, and a perturbed field $\hat{\phi}$, such that, $\phi(x, y, z, t) = \bar{\phi}(x, y, z) + \epsilon\hat{\phi}(x, y, z, t)$, where ϵ is small and ϕ is a vector field of $[u, v, w, p]$. The incompressible Navier–Stokes equations are then linearised and the perturbed field is assumed to take a particular form dependent upon the physics modelling fidelity. The LST, PSE and LHNS techniques are well described in the cited references, and are summarised in Table 1.

Once the relevant ansatz has been substituted into the linearised equations a final further transformation is made to the PSE and LHNS equations in order to incorporate the excrescence. Without this step, the solvers will only have visibility of the roughness through the base flow components, the perturbed field is based upon the coordinate system of the clean geometry. In order to change this we propose the following transformation,

$$s = x, \quad Y = y - h(x), \quad z = z, \quad (1)$$

where $h(x)$ is a function describing the shape of the roughness and is dependent on the stream-wise location. Over the majority of the wing this will hold a zero value and, since the height of the roughness in question is of the order of hundreds of microns on a wing chord of the order of metres, the few non-zero values will be extremely small.

The space marching PSE have been shown to suffer a step-size limitation whereby the minimum step size, Δx , must satisfy, $\Delta x \geq 1/\alpha_r$, where α_r is the real part of the stream-wise wave number, in order to maintain numerical stability [8]. The LHNS equations do not space march, and so suffer no step size limitation. Instead the equations are discretised into a large matrix of knowns, \mathcal{L} , a vector of unknowns, $\hat{\phi}$, and a forcing vector, r , such that, $\mathcal{L}\hat{\phi} = \hat{r}$. The forcing vector r modifies the wall boundary condition to create a small actuator to initialise the CF instability (CFI) and is located at the neutral point. This work is less concerned with the receptivity of the problem, but more so with the way in which a pre-existing CFI is modified by the presence of a more large scale roughness. A large LU matrix factorisation is then performed to solve for $\hat{\phi}$. The computational grid applies fourth order finite

Table 2 Roughness height as a percentage of the local boundary layer thickness (based upon the clean, no step geometry) at each given location

	412.5 μm (%)	618.7 μm (%)	825 μm (%)	893 μm (%)
10% chord	24.43	36.65	48.86	52.93
20% chord	18.49	27.73	36.98	40.06

differencing in the stream-wise direction and a pseudo-spectral method is applied in the wall normal direction. The time-stepping Nektar++ Linearised Navier Stokes (LNS) has been used as a further independent check on the validity of the PSE and LHNS codes for the clean case [3].

3 Results

The AERAST geometry is simulated with a 0.3 Mach number, Reynolds number 1 million, negative 4.5% angle of attack and a wing sweep of 40% with the Nektar++ incompressible Navier–Stokes solver. The four varying heights of FFS, BFS and bump and locations are denoted in Table 2.

Firstly, we begin with elucidating the instability parameter space to understand the range over which CF disturbances arise, and secondly how this range is modified by the different forms of excrescences present. This is performed using LST to sweep though a range of CF wave numbers, β , for stationary and travelling CFI. Neutral curves depicting the unstable parameter space for the largest roughness height are given in Fig. 1 for 10% chord and Fig. 2 for 20% chord. The FFS 10% chord stationary case appears to have two closed destabilising regions which are quite distinct, and are separated by a small region in between, where a very localised and weak 2.5D LSB exists at the juncture between the FFS and surface. Just after the step location there is an increase in higher wave number destabilisation compared to the base case. The BFS stationary case features three unstable zones in which the parameter space comprising the bubble region has the most impact in extending the range of unstable wave numbers, i.e. $0 \leq \beta < 2500$. There is only a slight increase on this, to about $\beta = 2600$, for the bump case. Again, the region over the second separation bubble (BFS component) has the most impact. The separated unstable zones merge at the reattachment point of the second reverse LSB flow. Looking to the travelling scenarios of each of these cases we can see again that the unstable zones have begun to merge. There is now an unstable region present in the separated flow of the FFS and interestingly there is a small zone for the BFS and bump case which is stabilising, see around 11% chord between 500–1000 β . For the 20% chord cases, in Fig. 2, we can see that generally the same wave number ranges are destabilised, but that they are unstable for a longer extent of the chord. There also seem to be fewer closed unstable regions, instead they are merged. The FFS case is quite different to the equivalent

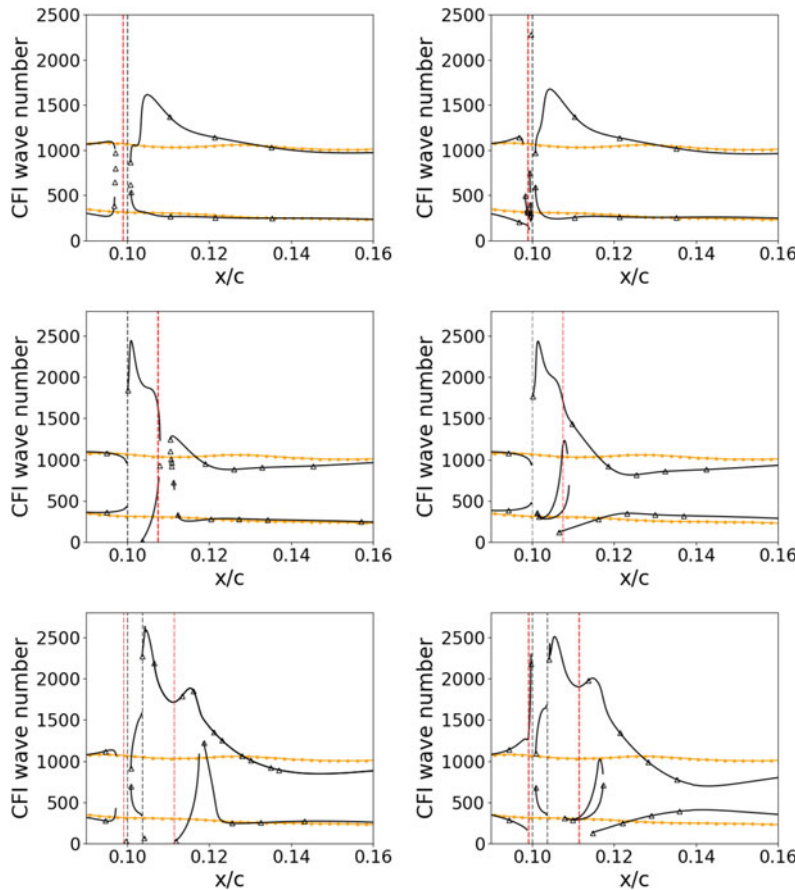


Fig. 1 Neutral stability curves computed with LST for 10% chord largest step height for FFS (top), BFS (centre) and bump (bottom) for stationary (left) and travelling (right) CFI. For the travelling waves neutral curves were computed at the most destabilising frequency 190 Hz for the FFS, 330 Hz for the BFS 340 Hz for the bump. Yellow denoted the neutral curve for the clean geometry and black for the excrescence case. The step location is marked with the black vertical dashed line; two to mark the beginning and end for the bump, and the red vertical lines denote the beginning or end of the separation bubble

10% chord FFS case, now featuring an unstable region in the small neighbourhood of the laminar separation bubble.

The PSE are used to sweep through the wave numbers and frequencies to find the single most destabilising stationary and travelling CFI combination for each roughness case. However, if the wavelength of the instability is greater than the roughness width the PSE will fail to compute a valid solution [20]. Unfortunately, this is the case here. There are extremely large velocity gradients local to the roughness meaning a number of stream-wise locations need to be stepped-over in order for the

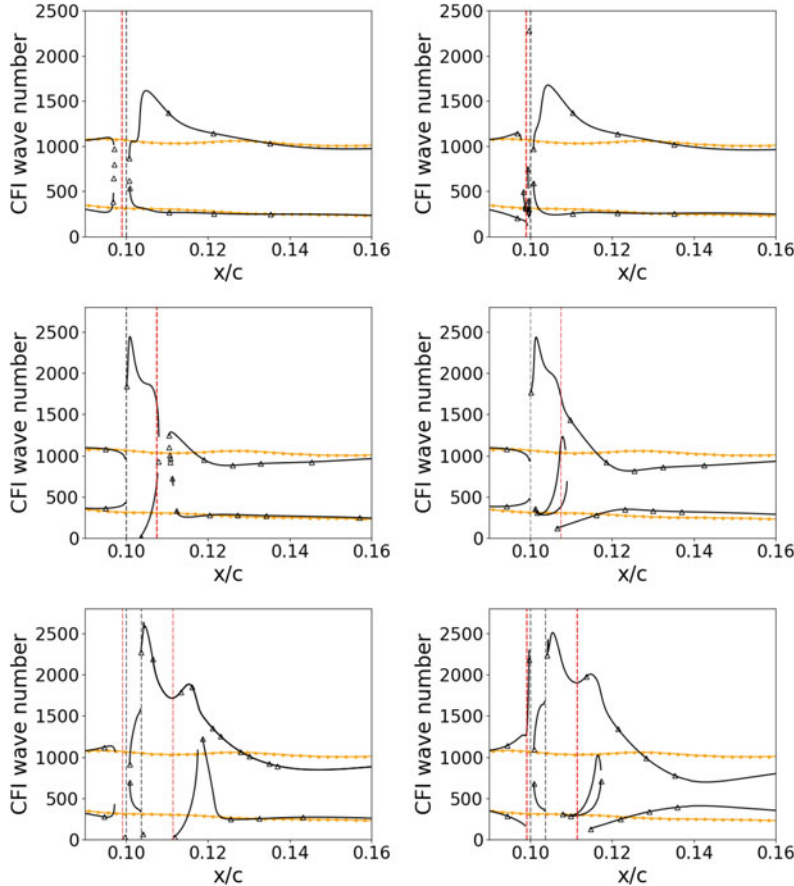


Fig. 2 Neutral stability curves computed with LST for 20% chord largest step height for FFS (top), BFS (centre) and bump (bottom) for stationary (left) and travelling (right) CFI. For the travelling waves neutral curves were computed at the most destabilising frequency 190 Hz for the FFS, 450 Hz for the BFS 540 Hz for the bump. Yellow denoted the neutral curve for the clean geometry and black for the excrescence case. The step location is marked with the black vertical dashed line; two to mark the beginning and end for the bump, and the red vertical lines denote the beginning or end of the separation bubble

PSE to converge. This could also be a consequence of the step size limitation of the PSE since, although we refer to this roughness as large scale, it is still extremely short in scale relative to the convecting disturbances wavelength. Due to the disputable result of the PSE, no results will be showcased for this method, as we have determined the reliability of the method is questionable for these harshly changing geometrical shapes.

The LHNS have been used to compute amplitude growth plots of the instability. The plot is generated by normalising each stream-wise location $\max|\hat{u}|$ with the local

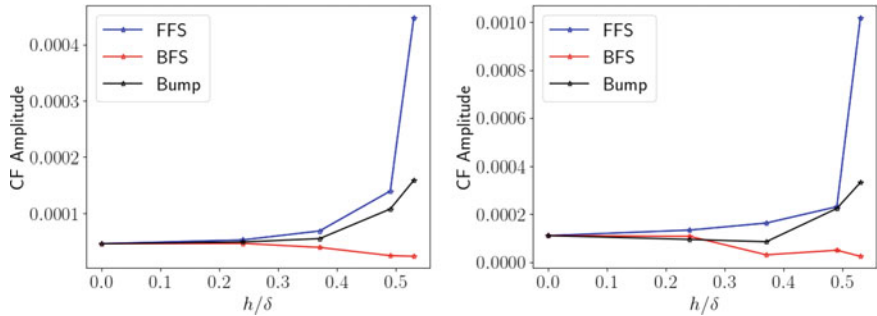


Fig. 3 Comparison of CFI amplitude at 20% chord for all roughness shapes and heights located at 10% chord. The x-axis is the roughness height normalised with boundary layer thickness, as in Table 2. Blue for FFS, red for BFS and black for bump. Left: Stationary CFI. Right: Travelling CFI

boundary layer edge velocity. The perturbation is generated at the neutral point and undergoes amplification when reaching the roughness. This amplification increases with an increase of bump height. Saeed et al. [14] found that for the stationary CF problem there was no overall amplification for the smallest bump height compared to the clean. Our results agree but also predict no additional amplification for the next bump height. The travelling CF growth is an order of magnitude more dangerous. These can be seen in Fig. 8 from the paper of Cooke et al. [3].

If we now focus on a particular location, a further 10% downstream of the roughness location, Fig. 3 shows the normalised amplitude growth against the height of the roughness, h , normalised with the boundary layer thickness δ .

Interestingly we can see that the FFS appears to be most detrimental to the flow field, with the BFS actually providing a stabilising effect with increased roughness height for both stationary and travelling CF disturbances. Due to the very sharp increase in amplitude growth between the 825 micron case and the 893 micron case, should a critical step height exist it should be somewhere within this range. For the BFS, Eppink et al. [6] observe little evidence of the stationary CF disturbance undergoing further destabilisation in their experiments, which is in-line with the results we see here. For travelling CF disturbance however, Eppink et al. found a destabilising interaction takes place between the travelling mode and the step: this is not reflected in our results. The reader should bear in mind that this finding is subject to the stream-wise location chosen for plotting and requires further numerical confirmatory investigations, however the general trend is the same for different x -locations. Finding the best way to display all the various data is still undergoing some iteration.

4 Conclusions

We have extended the work from Cooke et al. [3] to evaluate steps located at 20% and 10% chord cases based upon the experimental work of Saeed et al. [14]. Three types of roughness have been evaluated, FFS, BFS and bump at four different heights. LST has provided a good basic overview of the stability parameter space for the various FFS, BFS and bump shaped roughness and the PSE model is found to be impractical due to the very rapid changes in the local surface geometry. LHNS equations have been used to evaluate the effect of the roughness shape and height. We find that increasing the roughness height generally increases the amplification of the CFI, with travelling CF being much more detrimental to the flow than its stationary counterpart. The exception of this finding comes with the BFS, which seems to predict a slight stabilisation of both the stationary and travelling CF waves. The mechanisms involved with destabilising/stabilising the instability are clearly very different between the FFS and BFS. How much of this is a consequence of the laminar separation bubble present remains to be explored. Future work will involve using the time-stepping Linearised-Navier Stokes equations within Nektar++ to further investigate and validate the LHNS analysis.

References

1. Ashworth, R., Lawson, S., Lowry, R., Martinez-Cava, A., Mughal, S., Roland, H., Thomas, C.: Numerical and experimental study of the tolerance of natural laminar flow on a wing to its destabilisation at the leading edge /wing-box junction. Royal Aeronautical Society Applied Aerodynamics Paper, pp. 336–349 (2016)
2. Bertolotti, F.P.: Linear and nonlinear stability of boundary layers with streamwise varying properties. Ph.D. thesis, Ohio State University (1991)
3. Cooke, E.E., Mughal, M.S., Sherwin, S.J., Ashworth, R., Rolston, S.: Destabilization of stationary and traveling crossflow disturbances due to steps over a swept wing. AIAA Paper (3533) (2019). <https://doi.org/10.2514/6.2019-3533>
4. Eppink, J.: Stereo particle image velocimetry measurements of transition downstream of a forward-facing step in a swept-wing boundary layer. AIAA Paper (0306) (2017). <https://doi.org/10.2514/6.2017-0306>
5. Eppink, J.: The effect of forward-facing steps on stationary crossflow instability growth and breakdown. AIAA Paper (0817) (2018). <https://doi.org/10.2514/6.2018-0817>
6. Eppink, J., Wlezien, R.W., King, R.A., Choudhari, M.M.: Influence of a backward-facing step on swept-wing boundary-layer transition. AIAA J. **57**(1), 267–278 (2019). <https://doi.org/10.2514/1.J057437>
7. Herbert, T.: Parabolized stability equations. Ann. Rev. Fluid Mech. J. **29**, 245–283 (1997). <https://doi.org/10.1146/annurev.fluid.29.1.245>
8. Li, F., Malik, M.R.: On the nature of PSE approximation. Theor. Comput. Fluid Dyn. **8**(4), 253–273 (1996)
9. Morkovin, M.V., Reshotko, E., Herbert, T.: Transition in open flow systems—a reassessment. Bul. Smrt. Phys. Soc. **39**, 1882 (1994)
10. Mughal, S.M., Ashworth, R.: Uncertainty quantification based receptivity modelling of cross-flow instabilities induced by distributed surface roughness in swept wing boundary layers. AIAA Paper (3106) (2013). <https://doi.org/10.2514/6.2013-3106>

11. Park, D., Park, S.O.: Linear and non-linear stability analysis of incompressible boundary layer over a two-dimensional hump. *Comput. Fluids* **J.** *73*, 80–96 (2013). <https://doi.org/10.1016/j.compfluid.2012.12.007>
12. Reed, H.L., Saric, W.S.: Stability of three dimensional boundary layers. *Ann. Rev. Fluid Mech.* **J.** *21*, 235–284 (1989) <https://doi.org/10.1146/annurev.fl.21.010189.001315>
13. Rizzetta, D.P., Visbal, M.R.: Numerical simulation of excrescence generated transition. *AIAA J.* **52**(2), 385–397 (2014). <https://doi.org/10.2514/1.J052530>
14. Saeed, T.I., Mughal, S.M., Morrison, J.F.: The interaction of a swept-wing boundary layer with surface excrescences. *AIAA Paper* (2065) (2016). <https://doi.org/10.2514/6.2016-2065>
15. Thomas, C., Mughal, S., Roland, H., Ashworth, R., Martinez-Cava, A.: The effect of gap deformations on the stability of TS wave disturbances. *AIAA J.* **56**(6), 2157–2165. <https://doi.org/10.2514/1.J056821>
16. Tufts, M.W., Reed, H.L., K., C.B., Duncan Jr., G.T., Saric, W.S.: Computational investigation of step excrescence sensitivity in a swept-wing boundary layer. *AIAA J.* **54**(2), 602–626 (2017). <https://doi.org/10.2514/1.C033892>
17. Vidales, A.F.R., Kotsonis, M., Antunes, A., Cosin, R.: Effect of two-dimensional surface irregularities on swept wing transition: Forward facing steps. *AIAA Paper* (3075) (2018). <https://doi.org/10.2514/6.2018-3075>
18. Wang, Y., Gaster, M.: Effect of surface steps on boundary layer transition. *Exp. Fluids* **39**(4), 679–686 (2005)
19. Wörner, A., Rist, U., Wagner, S.: Humps/steps influence on stability characteristics of two-dimensional laminar boundary layer. *AIAA J.* **41**(2), 192–197. <https://doi.org/10.2514/2.1960>
20. Wu, X., Dong, M.: A local scattering theory for the effects of isolated roughness on boundary-layer instability and transition: transmission coefficient as an eigenvalue. *JFM* **794**, 68–108 (2016). <https://doi.org/10.1017/jfm.2016.125>

Deep Learning Based Transition Prediction for Aeronautical Applications



Renato Cosin, Marcio T. Mendonca, Ardeshir Hanifi, Dan S. Henningson, and Gilberto G. Becker

Abstract Drag reduction is vital for any new airplane design as the demand for a greener aviation is increasing. Wings and nacelles with laminar flow can reduce the total drag significantly and the backbone for designing laminar surfaces is the transition prediction. The highly complex physics of boundary-layer transition has led to the development of a wide range of prediction methods. Considering their good compromise between accuracy and computational cost, the standard prediction methods used by industry are based on the Linear Stability Theory (LST) and on the Parabolized Stability Equations (PSE). Although these methods have been successfully applied, it can be difficult to make them fully automated due to lack of robustness. Besides, tuning the model setups can be time-consuming. The inclusion of such methods in the aerodynamic design significantly increases the computational cost, especially in optimization loops. The present work proposes a solution for these disadvantages of LST and PSE using a metamodel based on deep learning. Complex Neural networks created using artificial intelligence concepts allows classification and regression of the large datasets necessary for transition analysis. The metamodel reproduces a local stability code and the results are promising both in terms of accuracy and processing speed.

R. Cosin
Embraer, São José dos Campos, Brazil
e-mail: renato.cosin@embraer.net.br

M. T. Mendonca (✉)
Instituto de Aeronáutica e Espaço, São José dos Campos, Brazil
e-mail: marciomtm@fab.mil.br

A. Hanifi · D. S. Henningson
Department of Mechanics, Linné FLOW Centre, KTH Royal Institute of Technology,
Stockholm, Sweden
e-mail: hanifi@kth.se

D. S. Henningson
e-mail: henning@emech.kth.se

G. G. Becker
Embraer, São José dos Campos, Brazil
e-mail: gilbertobecker@yahoo.com.br

1 Introduction

Laminar flow has been considered for many years as a way to reduce fuel consumption due to the reduced skin-friction drag. Besides the reduction in operational costs, it has the additional benefit of reducing carbon emissions. In order to design aerodynamic surfaces that maximizes laminar flow it is necessary to have reliable predictive tools for laminar to turbulent flow transition.

In the aeronautical industry the most accurate and accepted transition model is the N-factor method (e^N) [1], which is based on hydrodynamic stability theory and empirical correlations. Growth of Tollmien-Schlichting and cross-flow disturbances along the surface, predicted by linear stability theory, are correlated with transition location determined experimentally. This transition prediction methodology has been incorporated into aerodynamic analysis and design tools [2, 3].

The transition methodology based on LST is time-consuming and alternatives have been devised to retrieve the same information at a lower cost. One such method is the database method [4], which uses previously computed results stored in a database which provides growth rates for given boundary-layer conditions. The present work is somewhat similar to the database method. It proposes a method using a metamodel based on deep learning. Neural networks (NN) are one of the most powerful tools for machine learning and can handle multivariate classification and regression problems. Considering its great potential, deep neural networks were chosen to model the LST. Results show great improvements where the computation of the amplification factors is much faster, enabling new possibilities in terms of optimization.

2 Methodology

The development of the metamodel of a stability analysis was based on the high level requirements that enabled the most effective solution for the challenges on accuracy, validity range, robustness and computational cost. The set of requirements are: (i) surrogate of a complete stability analysis, (ii) per mode amplification, (iii) wave numbers and propagation direction, (iv) high accuracy on mode amplification, (v) accurate reproduction of stability behavior, (vi) single model for the whole design space and (vi) single model for Tollmien-Schlichting (TS) and cross flow (CF) instabilities. The stability analysis is based on LST which is a local stability method that allows simpler neural networks and simpler database generation.

The primary neural network option for this approach was the feed-forward neural network, also known as Multi Layer Perceptrons (MLP). This type of neural network has numerous variants with scalable complexity. Consequently, it provides a versatile baseline structure on top of which a good performance metamodel can be built.

The MLP take one dimensional inputs through successive layers of artificial neurons to compute the output. The first and last layers are respectively the input and output nodes. In between them there are the so called hidden layers that contain the

artificial neurons. On their simplest form, each neuron performs a linear combination of all the previous layers outputs and apply to that result a nonlinear function denoted activation function. The result is then broadcast to all neurons of the next layer. The coefficients of the linear combinations are called weights and consist of most of the trainable parameters.

Once the stability method to be modeled and the type of neural network were defined, the development took the following steps: database generation, problem statement and inputs definition, codes implementation, set-based MLP structure definition, final training, final validation and testing. These steps are discussed below.

2.1 Database Generation, Problem Statement and Input Definition

The database generation considers the stability analysis of a given aerodynamic configuration and corresponding boundary-layer characteristics. The geometry is a fully parameterized wing body configuration with several sweep-angles. The configuration was designed featuring a non-tapered wing and high aspect ratio to produce regions that adheres to the 2.5D infinite swept wing hypothesis.

The boundary-layer solutions were obtained using a proprietary code. The compressible boundary-layer equations are discretized using a second-order central-difference scheme in the wall-normal direction and a second-order backward Euler in stream-wise direction. The potential flow aerodynamic solution with pressure coefficient distribution necessary for the boundary-layer code was obtained using a full-potential compressible solver.

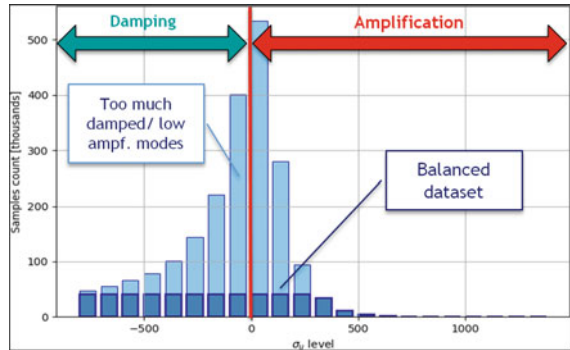
The LST stability analysis were performed using the proprietary stability code PSECOMP that solves both local and non-local stability equations for compressible flows. The equations were discretized using a fourth-order compact finite-difference scheme in the wall-normal direction. Although the code allows non-parallel solutions, for the present work parallel results were used.

The aerodynamic solution preprocessing, the boundary-layer and stability codes as well as the post-processing code were integrated in a fully automated framework that allows the whole process to be run for a large number of cases. The post-processing includes the filtering of results from the previous steps that did not meet a comprehensive set of quality criteria to eliminate spurious numerical solutions.

The following ranges defining the design space are considered: Reynolds number $5.0 \times 10^6 \leq Re \leq 26.0 \times 10^6$, leading edge sweep angle $0^\circ \leq \text{sweep} \leq 35^\circ$, Mach number $0.5 \leq Ma \leq 0.8$ and angle of attack between -2.5° and $\leq 2.5^\circ$. This design space was explored using a design-of-experiment based on SOBOL sequences. This technique aims at providing a low discrepancy quasi-random distribution of the multi-dimensional data parameters along their specified range.

During an exploratory data analysis of the generated dataset an excessive amount of damped samples was observed in comparison to positive amplification rates.

Fig. 1 Amplification rate histogram before and after dataset balance



Therefore, the dataset was balanced to provide a more even histogram of amplification rates during training. This procedure results are shown in Fig. 1.

Regarding the problem statement and input definition, the model surrogates the complete solution of a LST solver. The inputs for the metamodel are directly derived from those of the LST solver and represented by the functional relation below, where f is a regression neural network. The outputs are the amplification rate σ and streamwise wavenumber α . The amplification rate is used to compute the N-factor with the same scheme as the stability code. The streamwise wavenumber α is used to compute the propagation direction ψ for a given disturbance defined by a spanwise wavenumber β and frequency F .

$$\sigma, \alpha = f(\beta, F, C_p, x, z, MF, BL, FF, s), \quad \psi = \text{atan}(\beta/\alpha).$$

Where x and z are the streamwise and spanwise directions, C_p is the pressure coefficient, MF and BL correspond to the boundary-layer mean flow and boundary-layer properties, FF corresponds to the free flow conditions, s is the distance along the surface and ψ is the disturbance propagation direction. The boundary-layer parameters considered in the analysis are the streamwise and span velocity distributions, the density, the temperature, the first and second derivatives of these variables in the normal direction and first derivative in the streamwise direction. In order to generate the required column matrices for the inputs, the y -dependent variables at each wall-normal position are read as independent features.

The N -factor at the i th station for the j th mode defined by a pair (F, β) is:

$$N^{i,j} = \int_{s_{np}}^s \sigma^{i,j} ds.$$

Table 1 Initial hyperparameter search space

Hyperparameter	Max (approx.)	Min (approx.)
Number of hidden layers	6	12
Number of trainable hyperparameters*	2×10^6	40×10^6
Number of neurons**	1500	20500
Learning rate	0.0001	0.1
Learning rate decay	0.2/50	0.0
Batch size	256	16384
L2 regularization term	0.0	0.1
Dropout keep probability	0.8	1.0

* Consequence of the network structures

** Consequence of the number of neurons per layer

2.2 *Code Implementation and Set-Based MLP Structure Definition*

The machine learning tool used is an in-house Python 3 code with modules for developing, training, testing and deploying feed forward neural networks. The tool aims at classification and regression of multivariate problems with arbitrary input and output dimensions. The code includes several improvements to the classic MLP structure and several advanced training features in order to cope with the challenging training of deep neural network on regression problems of high dimensionality and with non-smooth or discontinuous data.

For the set-based MLP structure definition, considering the novelty of the approach and the size of the search space for the metamodel structure, a wide range for each hyperparameter was firstly defined, as presented in Table 1. Based on these ranges, a Latin Hypercube distribution of potential model structures was generated.

The time taken for a full dataset training was in the order of days. Thus, its usage for searching the optimal model would be unfeasible. In order to allow a more efficient model definition, a reduced dataset with a 1:10 down sampling was generated. Nevertheless, considering the modeled physics complexity and large input dimensionality, even the reduced dataset provided a training computational time prohibitive for a fully automated search. Therefore, the pseudo-random hyperparameters set was manually explored. Along the iterative process, the range of the hyperparameters was reduced following the gain of knowledge on the model behavior. Finally, a grid search on a very reduced parameters space was performed to fine tune the model structure after the optimal region on the hyperparameters was defined.

Apart from the numerical hyperparameters, the model structure is also defined by setup of flags, loss function, optimization algorithms and training schemes. The set of hyperparameters explored is described in Table 2.

In order to set the training process as an optimization problem a loss function is defined. The training goal is the minimization of the loss function using a gradient

Table 2 Hyperparameter search space

Activation function	tanh, RELU, leaky RELU*
Learning rate decay	Yes/No
Batch normalization	Yes/No
Gradient descent scheme	Mini-batch always
Optimizer**	ADAM always
Regularization	Yes/No
Dropout	Yes/No
Initializers***	Xavier/He
Loss functions	Mean quadratic error/Huber loss

* Maas et al. [5],

** As defined by Kingman and Ba [6],

*** As defined by He et al. [7]

descent algorithm or one of its variations. The gradient descent algorithm uses the loss function gradients in relation to the trainable parameters to update their own values. This process is called back propagation [8] and is performed on the opposite direction of the network graph, from the output to the input. Although the mean quadratic error is the standard loss function for regression models, the Huber loss function was also tested because of its smaller sensitivity to outliers on input data.

Given the network input parameters X and output parameters Y the mean quadratic error \mathcal{L} and the Huber loss function \mathcal{L}_δ are defined as:

$$\mathcal{L}(Y, \hat{Y}) = \sum_{j=1}^{n_{inp}} \sum_{k=1}^m (\hat{Y}_{jk} - Y_{jk})^2, \quad \mathcal{L}_\delta(Y, \hat{Y}) = \begin{cases} \frac{1}{2} (Y - \hat{Y})^2, & \text{for } |Y - \hat{Y}| \leq \delta \\ \delta (Y - \hat{Y})^2 - \frac{1}{2} \delta^2, & \text{otherwise} \end{cases}$$

Large differences on the inputs and outputs order of magnitudes can cause a series of numerical problems on the training and inference of the neural networks. The problems may result in overflow on the internal computation and unbalanced influence of large inputs. Vanishing or exploding gradients during the back propagation of the loss function derivatives can also be affected by the scale of the data values. In order to solve this potential problem, a normalization procedure is applied to both model inputs and outputs. This normalization procedure is the following:

$$X = \frac{X_{un} - \langle X_{un} \rangle}{std(X_{un})}, \quad Y = \frac{Y_{un} - \langle Y_{un} \rangle}{std(Y_{un})}, \quad \hat{Y} = \frac{\hat{Y}_{un} - \langle Y_{un} \rangle}{std(Y_{un})}.$$

Where $\langle X \rangle$ and $\langle Y \rangle$ represent mean values and std stands for standard deviation.

Considering the application on transition prediction and aerodynamic optimization, the model accuracy for the integrated N-factor was given higher priority on the performance criteria over the network size and complexity. This strategy was used

Table 3 Network structure and set of hyperparameters

Number of hidden layers	10
Neurons per layer	8 layers of 1024 + 2 layer of 512
Activation function	leaky RELU
Batch size	2048
Trainable parameters	11.5 millions
Batch normalization	ON
Optimizer	ADAM
Initial learning rate	0.002
Learning rate decay/decay steps/decay rate	exponential/200/0.9
L2 regularization/drop-off	0.01/no

to select the model among the many tested network configurations. Thus, the design space was first explored to find the best achievable accuracy. The minimal model size in terms on trainable parameters that keeps the optimal accuracy was selected.

2.3 Final Neural Network Setup and Training

The final network structure and set of parameters are given in Table 3. The final training was performed in two steps, the first 400 epochs without regularization to allow a faster convergence, and the last 100 epochs with regularization turned on. On the restart for the last one hundred epochs, the learning rate was reset to its initial value, following the same decay rule. The training took approximately 70 h on a Linux server with Intel ® Xeon ® CPU E5-2685 v3 @ 2.60GHz, 24 Cores, 128 GB RAM. No GPU was available.

Figure 2 shows that the coefficient of determination R^2 have values close to 1. Those values indicate that the network output accurately reproduces the physical model. The coefficient of determination for the final training are $\sigma_u R^2 = 0.996$ and $\alpha R^2 = 0.999$ for the training set, and $\sigma_u R^2 = 0.973$ and $\alpha R^2 = 0.998$ for the test set. The network results with respect to the physical model is also shown in Figs. 3 and 4 in a histogram. In Fig. 3 the distance from the diagonal is a measure of the error and the histogram height represents the density of points. The results show that a large number of points have a small error.

In Fig. 4 a relative change difference is used to provide a valid accuracy metric for modes with amplification close to zero. Plain relative error may result on division by zero or very small numbers. the relative change difference amplification rate $RCD(\sigma_u)$ and streamwise wavenumber $RCD(\alpha)$ are given below. The subscript u indicates that the amplification rate is computed based on the velocity disturbance streamwise component. The network predicted values are represented by $\hat{\sigma}$ and $\hat{\alpha}$.

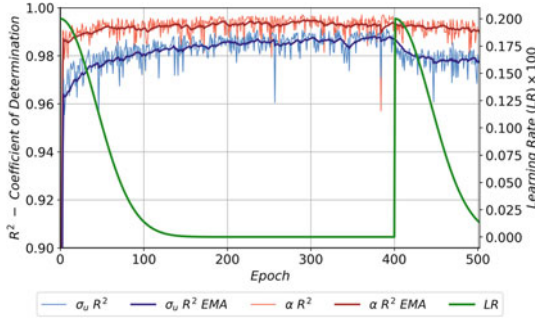


Fig. 2 Coefficient of determination R^2 and learning rate for the final training. EMA is the exponential moving average. The reset of the learning rate and the R^2 drop at the epoch 400 are consequences of the L_2 regularization being turned on

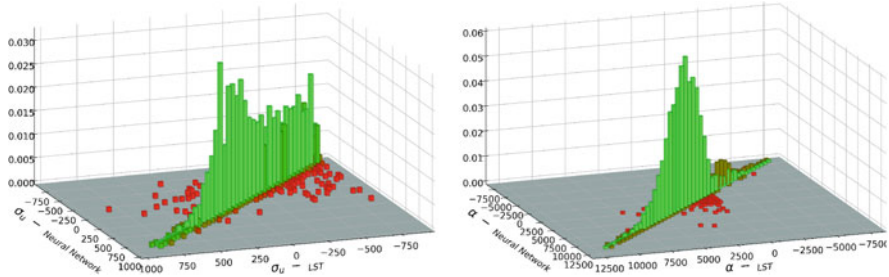


Fig. 3 Network versus physical model fitting for the growth rate and spanwise wavenumber. Error measured by the distance from the diagonal and density of points measured by the histogram height

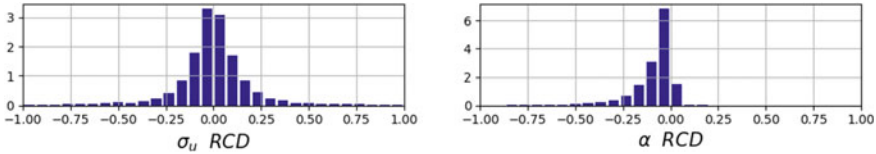


Fig. 4 Relative change difference (RCD) amplification rate and spanwise wavenumber histograms for the final training

$$RCD(\sigma_u) = \frac{2(\hat{\sigma}_u - \sigma_u)}{|\hat{\sigma}_u| - |\sigma_u|}, \quad RCD(\alpha) = \frac{2(\hat{\alpha} - \alpha)}{|\hat{\alpha}| - |\alpha|}.$$

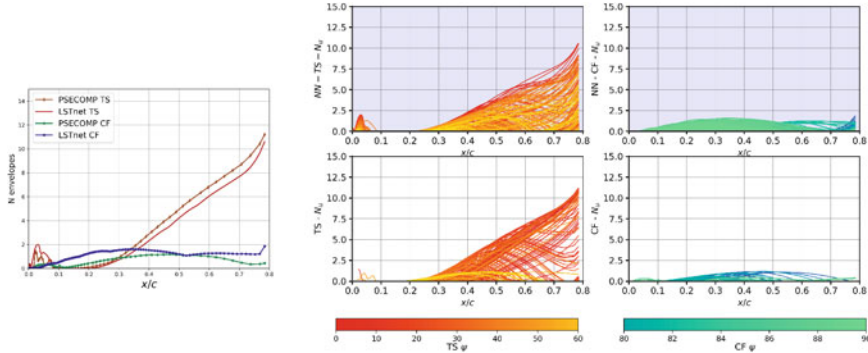


Fig. 5 Comparison between NN and LST N-factors, case 1. Envelope curves on the left plot

3 Validation and Testing

Full stability analyses were performed with both the physical and surrogate models to validate the surrogate model and check the accuracy. The results were compared in terms of amplification rate and integrated N-factors. The accuracy of the metamodel predicted σ_u , especially for the positive values that result in amplified regions, is high enough to result in an N-factor accuracy within the requirements.

One unexpected issue with the results was a significant noise upstream of the actual disturbances neutral points. This effect generated a spurious upward shift on the N-factor curves. The solution was to use the modified N-factor integration strategy shown below, which doesn't completely avoid bumpy amplification curves near the neutral points, but keeps the N-factor accurate downstream.

$$N_u^i = \max \left(0.0, \left(N_U^{i-1} + (s^i - s^{i-1}) \times \frac{\sigma_u^i + \sigma_u^{i-1}}{2} \right) \right); \quad i = 0, 1, \dots, n_x.$$

Figures 5 and 6 show comparisons between the N-factor computed by the neural network and by the LST approach for two different cases. The first case considers $Re = 11 \times 10^6$, $Ma = 0.58$ and leading edge sweep angle of 13.2° . The second case considers $Re = 18 \times 10^6$, $Ma = 0.7$ and leading edge sweep angle of 30.2° . Different disturbance propagation angles are indicated by the color code at the bottom. The disturbance type, TS or CF, are classified based on the propagation angle. The results shown in Fig. 5 for the first case are dominated by TS waves due to the low sweep angle. The second test case with a sweep angle of 30.2° shows much stronger cross-flow disturbances as expected. These features where correctly capture by the neural network.

The neural network captures a larger number of growing modes both for TS waves and cross-flow disturbances. This may be due to unrealistic modes that are not computed by the physical model, but are found by the neural-network. It may also be due to numerical issues on modes not found by the automatic initializing procedure

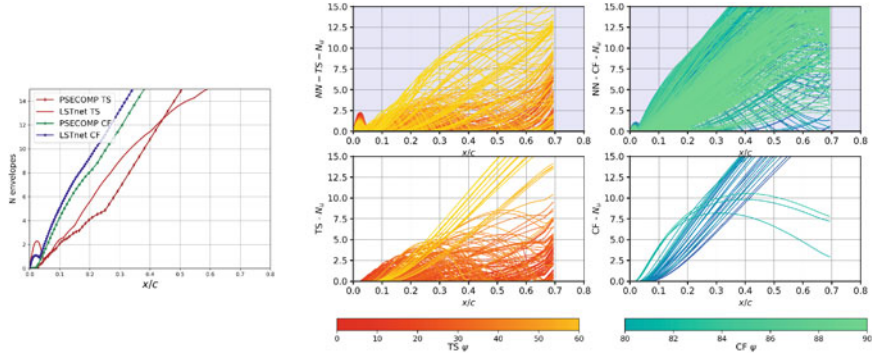


Fig. 6 Comparison between NN and LST N-factors, case 2. Envelope curves on the left plot

in the LST code, but are properly solved by the neural network. This topic, however, requires further investigation.

4 Conclusions

A transition prediction metamodel based on a deep learning neural network was developed and tested. The results present accurately amplified TS and CF modes. Oblique Cross-flow and TS modes are much more frequent on the metamodel than on the LST model, but the resulting N-factors are not significantly different.

Although the N-factor accuracy is harmed by integration errors, the overall accuracy of the metamodel fulfills the initial requirements. When σ_u is close to zero, large relative errors result in irregular N-factor amplification curves. The integration strategy, however, prevents this issue from jeopardizing the accuracy at higher N-factors. Positive σ_u are better reproduced than negative ones, what produce reasonably accurate disturbances growth prediction.

The neural network have shown to be large enough, showing a slight trend to overfitting the training data noise. This behavior was properly controlled by the use of L2 regularization. The metamodel has shown robustness similar to the LST and a dedicated set of automated checks and filters is necessary to improve the results and allow a fully automated stability analysis.

The complex stability behavior from LST is well reproduced and the NN is able to reproduce accurately the LST model. N-factor accuracy and the metamodel robustness are good enough for aerodynamic optimizations and analysis. Finally, the strong point of the neural network metamodel is the ability to surrogate the LST stability analysis approximately 40 times faster.

References

1. J.L. van Ingen, in *Proceedings of the Colloquium Transitional Boundary Layers in Aeronautics* (1996)
2. Bégou, G., Deniau, H., Vermeersch, O., Casalis, G.: AIAA J. **55**(11), 3648 (2017)
3. Halila, G.L.O., Chen, G., Shi, Y., Fidkowski, K.J., Martins, J.R.R.A., Mendonca, M.T.: Aerosp. Sci. Technol. **91**, 321 (2019)
4. Crouch, J.D., Crouch, I.W.M., Ng, L.L.: AIAA J. **40**, 1536 (2002)
5. A.L. Maas, A.Y. Hannun, A.Y. Ng, in *Proceedings of the 30th International Conference on Machine Learning* (2013)
6. D.P. Kingma, J.L. Ba, in *International Conference on Learning Representations* (2014)
7. K. He, X. Zhang, S. Ren, J. Sun, in *IEEE International Conference on Computer Vision (ICCV 2015)*, vol. 1502 (2015)
8. Rumelhart, D.E., Hinton, G.E., Williams, R.J.: Nature **323**, 533 (1986)

Numerical Studies on the Influence of Step-Like Surface Irregularities on the Development of Tollmien-Schlichting Waves



Juan Alberto Franco and Stefan Hein

Abstract The effect of a single step-like surface irregularity on the spatial development of Tollmien-Schlichting (TS) waves is investigated by the recently developed Adaptive Harmonic Linearized Navier-Stokes (AHLNS) methodology. The steps considered in the present work, forward- and backward-facing steps (FFS & BFS), are varied not only in height but also in shape (rectangular and rounded). This work is motivated by the growing interest in the aeronautical industry on the effect of surface irregularities on the location of laminar-turbulent transition. The main contribution of this paper is to present, for fixed flow conditions, the combined influence of the height and shape of step-like irregularities on the expected transition location. A second motivation of this paper is to demonstrate the AHLNS methodology used in the course of this investigation as a perfectly suited stability analysis tool for performing numerical studies on the effect of surface irregularities on the spatial development of traveling instabilities with a relatively moderate computational effort.

1 Introduction

One of the key areas for present and future aircraft design is to achieve a significant drag reduction by delaying the transition of the incoming free-stream air from laminar to turbulent state. The presence of surface irregularities like steps, gaps, humps, etc. introduces regions of localized strong streamwise gradients in the base flow quantities. TS waves may lead to the onset of laminar-turbulent transition and therefore, it becomes critical to correctly model their interaction with the above mentioned surface irregularities.

J. A. Franco (✉) · S. Hein
DLR - German Aerospace Center, Bunsenstrasse 10, 37073 Göttingen, Germany
e-mail: Juan.Franco@dlr.de

S. Hein
e-mail: Stefan.Hein@dlr.de

J. A. Franco
UPM - Universidad Politécnica de Madrid, Madrid, Spain

Techniques like Parabolized Stability Equations (PSE) are not suited for boundary-layer instability analysis in the vicinity of those surface irregularities: its formulation assumes that streamwise variations of base flow and disturbances quantities are small (compared to surface-normal variations), allowing a marching procedure for their resolution. Moreover, PSE is unable to resolve the very short-scale streamwise variations in the base flow due to its step size limitations. On the other hand, techniques like Linearized Navier-Stokes (LNS), Harmonic LNS (HLNS) and Direct Numerical Simulation (DNS) do not impose any assumption regarding the nature of the convective instabilities in streamwise direction. This fact implies that the required numerical resources increase significantly. Alternatively, the Adaptive Harmonic LNS (AHLNS) equations can also handle these large streamwise gradients by using a fully-elliptic system of equations (similar to DNS). The AHLNS formulation assumes a wave-like character of the instabilities (as in PSE), leading to a significant reduction in the number of streamwise grid points required compared with LNS, HLNS or DNS computations.

The effect of steps on the onset of laminar-turbulent transition has been extensively studied, both numerically and experimentally. One of the first attempts was done by Nenni and Gluyas [1], who provide a critical Reynolds number based on the step height (for rectangular FFS & BFS). Smooth BFS steps were considered by Ragab and Nayfeh [2] using LST (Local Stability Theory). Recently, Edelmann [3] studied the effect of rectangular FFS by means of DNS. He found that there was a good agreement between DNS and LST, assuming that a small region around the step is omitted from the LST computations.

The present paper provides a systematic study of the effect of a single step (FFS and BFS) on the spatial development of TS waves in a compressible subsonic flow. The height and shape have been varied in order to provide a clearer understanding how these parameters influence the base flow and the linear growth of the oncoming TS waves. A similar work about the effect of a single hump on laminar-turbulent transition has been recently published by Franco et al. [4]. To the authors' knowledge, there is no similar work published regarding the influence of a single step.

2 Problem Description

2.1 Setup

We study numerically the effect of a single step on boundary-layer transition of a two-dimensional laminar flow on a flat plate. Figure 1 shows schematically the computational domain used in the present study, including the type of boundary conditions imposed for computing the laminar base flow. All dimensional quantities are marked with an asterisk *. The free-stream Mach number Ma_∞ is set to 0.5 for all cases. The shape of the step is defined by the expression

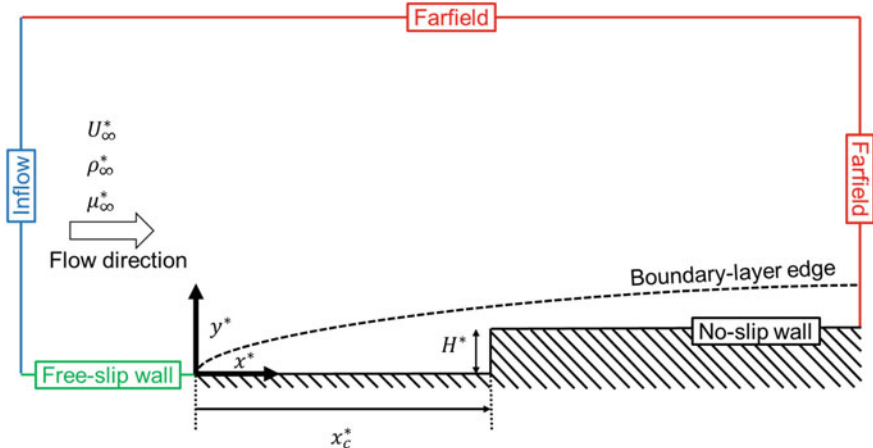


Fig. 1 Schematic representation of the computational domain defined for the present study. The labels at the edges of the domain indicate the type of boundary conditions used for the base flow computations

$$y^* = \frac{H^*}{2} \left(1 + \operatorname{erf} \left(\frac{1}{C} \frac{x^* - x_c^*}{\delta^*} \right) \right), \quad (1)$$

where the parameter H^* indicates the height of the step (positive for FFS and negative for BFS). The center of the step is placed at x_c^* . The geometrical parameter C defines the shape of the step. The rectangular shape can be considered the limiting case when $C \rightarrow 0$. Geometrical quantities are nondimensionalized with δ^* (the compressible boundary-layer displacement thickness at the x_c^* position for a flat plate at zero pressure gradient (ZPG)). The Reynolds number based on δ^* is defined as $Re_{\delta^*} = \frac{\rho_\infty^* U_\infty^* \delta^*}{\mu_\infty^*}$, where ρ_∞^* , U_∞^* and μ_∞^* denotes the density, velocity and dynamic viscosity at the boundary-layer edge, respectively. In the present study, the value of Re_{δ^*} at the step location x_c^* is fixed to 1823. We will consider three values for the geometric parameter C : 10, 50 and the rectangular-shaped case r , i.e. $C \rightarrow 0$. For the nondimensional height H , six values will be examined here: ± 0.4 (small), ± 0.8 (medium) and ± 1.2 (large). The combination of parameters H and C gives a total of 18 types of surface irregularities, which are summarized in Table 1.

2.2 AHLNS Equations

The boundary-layer instability analysis of the above mentioned configurations will be done using the Adaptive Harmonic Linearized Navier Stokes (AHLNS) equations [5] in combination with linear PSE [6], following a multi-zonal approach as described in Fig. 2. Here, a brief introduction to the AHLNS methodology is given. For a detailed

Table 1 Values of the nondimensional parameters H and C considered in the present study. The case $C = r$ refers to the rectangular-shaped step. The maximum slope of the wall is also included

Case name	H	C	Max. slope	Case name	H	C	Max. slope
FFS_H04_C50	0.4	50	0.26°	BFS_H04_C50	-0.4	50	-0.26°
FFS_H04_C10	0.4	10	1.29°	BFS_H04_C10	-0.4	10	-1.29°
FFS_H04_r	0.4	r	90°	BFS_H04_r	-0.4	r	-90°
FFS_H08_C50	0.8	50	0.52°	BFS_H08_C50	-0.8	50	-0.52°
FFS_H08_C10	0.8	10	2.58°	BFS_H08_C10	-0.8	10	-2.58°
FFS_H08_r	0.8	r	90°	BFS_H08_r	-0.8	r	-90°
FFS_H12_C50	1.2	50	0.78°	BFS_H12_C50	-1.2	50	-0.78°
FFS_H12_C10	1.2	10	3.87°	BFS_H12_C10	-1.2	10	-3.87°
FFS_H12_r	1.2	r	90°	BFS_H12_r	-1.2	r	-90°

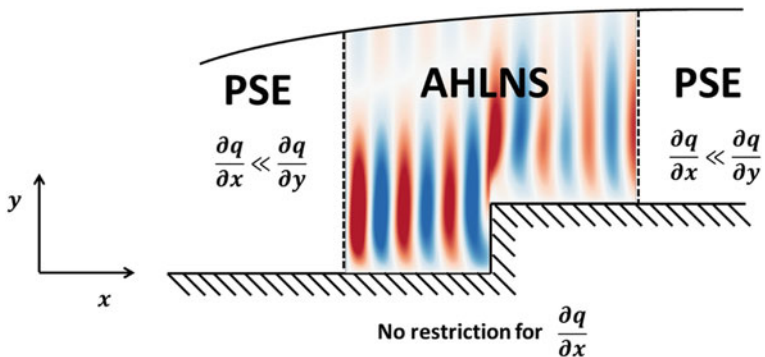


Fig. 2 Sketch of the multi-zonal technique for boundary-layer instability analysis in the presence of surface irregularities. The vertical dashed lines represent the inflow and outflow locations for AHLNS computations. A TS wave of reduced frequency $F = 20$ is depicted (case *FFS_H08_r*)

description of this methodology, the readers are referred to Franco and Hein [5]. For a complete explanation about the PSE methodology, the readers are referred to Hein et al. [6].

The AHLNS equations are obtained from the compressible Navier-Stokes (NS) equations linearized for small disturbances. All flow and material quantities \mathbf{q} are decomposed into a steady base flow $\bar{\mathbf{q}}$ plus an unsteady disturbance flow component $\tilde{\mathbf{q}}$, i.e. $\mathbf{q}(\mathbf{x}, t) = \bar{\mathbf{q}}(\mathbf{x}) + \varepsilon \tilde{\mathbf{q}}(\mathbf{x}, t)$, with $\varepsilon \ll 1$. Here, t represents time. This flow decomposition is introduced into the NS equations, then the base state solution is subtracted and products of disturbance quantities are neglected. To further simplify the analysis, it is assumed that the base flow is homogeneous in spanwise z direction. Moreover, disturbances are assumed to be periodic in time t and in spanwise z direction. The adaptive approach is introduced here: the disturbance flow variables are divided into an amplitude function and a suitable, iteratively updated

wave function, i.e. $\tilde{\mathbf{q}}(x, y, z, t) = \hat{\mathbf{q}}(x, y)e^{i\Theta}$, where the wave function is defined as $\Theta = \int \alpha(x)dx + \beta z - \omega t$. The major advantage of the adaptive approach is that it exploits the *wave-like* character of the convective instabilities in a similar fashion as in the PSE method. However, unlike to the PSE approach [6], the streamwise wavenumber α and the amplitude function $\hat{\mathbf{q}}$ are allowed to vary rapidly in streamwise direction.

2.3 N-factor envelope

The *n*-factor, which measures the accumulated growth of the disturbances, is computed as $n(x) = \ln(A(x)/A_0)$, where A_0 denotes the maximum amplitude, in normal direction, of the streamwise velocity component of the corresponding TS mode at the streamwise position where the disturbance starts to grow. The *n*-factor is set to zero if during the course of the calculation, the value of A becomes smaller than A_0 . Each *n*-factor curve is computed for a single TS wave defined by a particular nondimensional frequency F and spanwise wavenumber β . The nondimensional frequency F is defined as $F = 2\pi f^* \frac{\mu_\infty^*}{\rho_\infty^*(U_\infty^*)^2} \times 10^6$, where f^* is the physical frequency of the disturbances. The envelope of all *n*-factor curves considered is called the *N*-factor envelope, following the definition given by Arnal [7].

3 Numerical Results

3.1 Base Flow Computations

The laminar steady two-dimensional flow on a flat plate in the presence of a single step was computed numerically. We used the compressible Navier-Stokes solver TAU [8], developed at DLR. Grids were generated using the structured grid generator MEGACADS, also developed at DLR. A schematic representation of the computational domain and the boundary conditions imposed for computing the base flows is depicted in Fig. 1. Farfield boundary conditions were enforced sufficiently far from the surface irregularity (about 5000 δ^* in both streamwise and normal directions).

3.2 Base Flow Results

The base flow pressure \bar{p} is made nondimensional by twice the incoming dynamic pressure, i.e. $\rho_\infty^*(U_\infty^*)^2$. Figure 3 shows the contours of \bar{p} and streamlines for *large* steps. For FFS (Fig. 3-a), (c), (e)), the flow field remains attached for smooth steps, while for the rectangular-shaped case, a tiny recirculation area appears in front of the

step. For BFS (Fig. 3-b),-d),-f)), the parameter C has a crucial influence on the presence and size of the recirculation area. In particular, for very smooth steps ($C = 50$) the flow remains attached. If the shape parameter C is reduced (cases *BFS_H12_C10* and *BFS_H12_r*), a large bubble appears right after the step. The size of the bubble increases the more the shape of the step approaches the rectangular one.

In terms of pressure contours, it is interesting to notice that for BFS the pressure contours barely change with the shape of the step. However, for FFS the pressure gradients in the vicinity of the step become more intense as the step shape approaches that of a rectangular step.

3.3 Instability Analysis

The computation of the spatial development of a broadband spectrum of TS waves (each one computed individually as explained in Sect. 2.3) is described in this section. The spatial growth in amplitude of each TS wave is collected in the corresponding n -factor curve.

The instability analysis is performed in the domain $(x - x_c) \in [-500, 2000]$. An initial investigation done on a flat plate using PSE for several frequencies F and spanwise wavenumbers β revealed that two-dimensional ($\beta = 0$) TS waves of frequencies $F \in [20, 75]$ produce the highest n -factor curves in the domain mentioned above. When a surface irregularity is present, the multi-zonal approach described in Sect. 2.2 is applied. The interfaces between PSE and AHLNS are placed at $(x - x_c) = \pm 165$, sufficiently far away from the recirculation regions (see Fig. 3). The following results were obtained considering incoming two-dimensional TS waves ($\beta = 0$) with frequencies in the range $F \in [20, 75]$.

3.4 Effect of Step Height and Shape

3.4.1 Forward-Facing Steps

Figure 4 compares the N -factor envelope curves when *small* (-a)), *medium* (-c)) and *large* (-e)) FFS are considered. In the vicinity of the step, the development of the TS waves is driven by the pressure gradients that the presence of the step introduces into the flow field. It is well known (see Drazin and Reid [9]) that an acceleration in the flow usually has a stabilizing effect. Figure 5 shows the nondimensional pressure distribution at the wall \bar{p}_{wall} when *small* (-a)), *medium* (-c)) and *large* (-e)) FFS are considered. The flat plate case is also included for comparison. For all cases, there is an initial deceleration of the flow (adverse pressure gradient) followed by a very rapid acceleration. This effect explains why in the step region $x \approx x_c$ there is a small increase in the N -factor curves followed by a reduction. The favorable pressure gradient around x_c increases with the height of the step, but it is also very

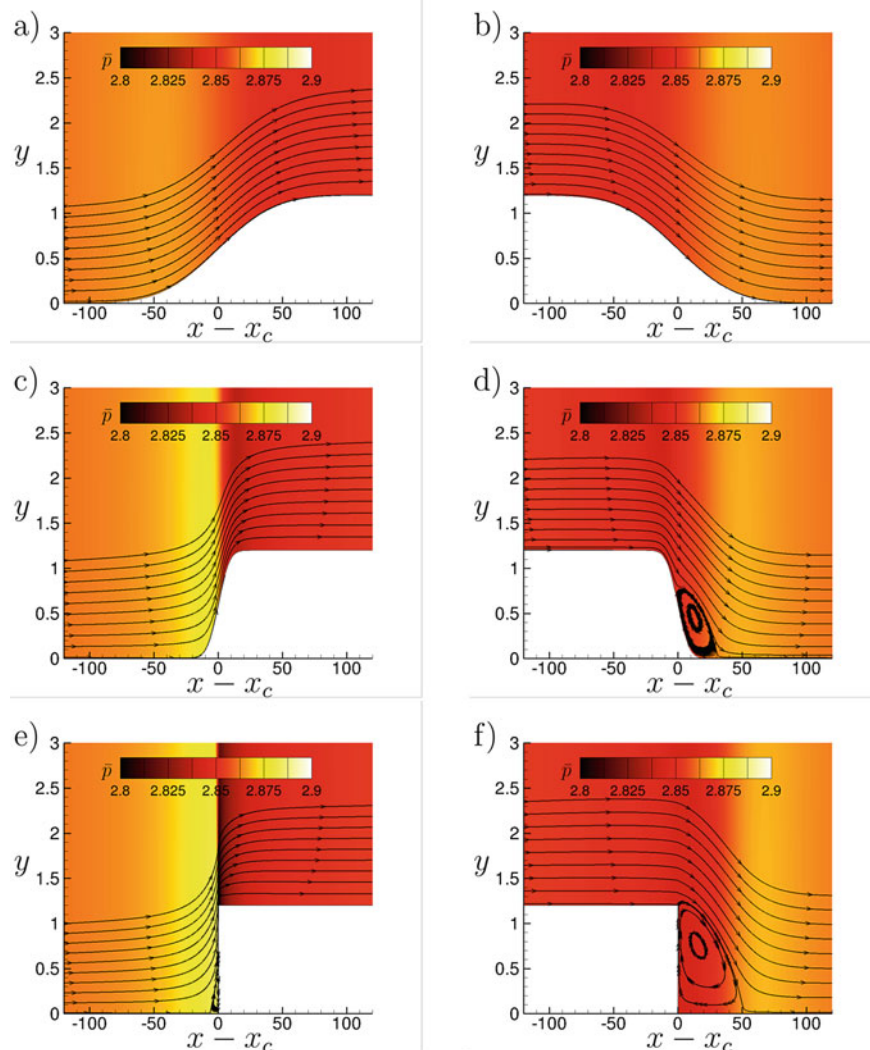


Fig. 3 Pressure \bar{p} contours and streamlines for cases **a** *FFS_H12_C50*; **b** *BFS_H12_C50*; **c** *FFS_H12_C10*; **d** *BFS_H12_C10*; **e** *FFS_H12_r*; **f** *BFS_H12_r*. Flow direction is from left to right. Axes are not to scale

dependent on the shape of the step. Downstream, around $(x - x_c) \approx 50$, the pressure distribution starts to recover the ZPG, and the N -factor curves grow nearly parallel to the flat plate case.

3.4.2 Backward-Facing Steps

Figure 4 compares the N -factor envelope curves when *small* (-b)), *medium* (-d)) and *large* (-f)) BFS are considered. Similar to the above mentioned FFS, the development of the TS waves is driven by the pressure gradients that the presence of the step introduces into the flow field. Figure 5 shows the nondimensional pressure distribution at the wall \bar{p}_{wall} when *small* (-b)), *medium* (-d)) and *large* (-f)) BFS are considered. For all cases, there is an initial acceleration of the flow (favorable pressure gradient) followed by a very rapid deceleration. This is the reason of the small reduction in the N -factor curves followed by a large increase in the vicinity of the step $x \approx x_c$. The adverse pressure gradient around x_c increases with the height of the step, but it is also very dependent on the shape of the step. Next, around $(x - x_c) \approx 50$, the pressure distribution starts to recover the ZPG, and the N -factor curves grow almost parallel to the flat plate case.

Although the pressure gradients around the step are less intense for BFS than for the corresponding FFS, the presence of a relatively large recirculation region, whose size depends strongly on the step shape as already described in Sect. 3.2, increases significantly the growth of the TS waves (see e.g. Hein [10]). Therefore, when a separation region is present in a BFS, the N -factors are considerably larger than for the FFS counterpart.

3.5 Prediction of Transition Location

The N -factor results of Fig. 4 can be used to assess the effects of the different surface irregularities on the transition location. Without having any further information, it is very common [11] to set the expected transition location x_{tr} as the closest point to the leading edge where the amplification curves reach the threshold value of $N_{tr} = 9$. The corresponding streamwise location is defined as the expected location where the transition to turbulence takes place. The resulting expected transition locations x_{tr} for the different cases are summarized in Fig. 6. In this figure, the expected transition location for a flat plate is named x_{tr0} . The abscissa $(x_{tr} - x_c)/(x_{tr0} - x_c)$ relates the downstream distance of the expected transition from the step position x_c to the downstream distance without any surface irregularity.

Costantini et al. [12] used the *loss of laminarity* Δs (%) as the counterpart of the parameter $(x_{tr} - x_c)/(x_{tr0} - x_c)$. In this sense, the maximum Δs for *small* steps is about 14% (i.e. $(x_{tr} - x_c)/(x_{tr0} - x_c) = 0.86$, case *BFS_H04_r*). However, for *large* steps the maximum Δs is about 94% (case *BFS_H12_r*), i.e. transition is expected to occur in the vicinity of the step. Interestingly, the effect of smoothing the step can reduce

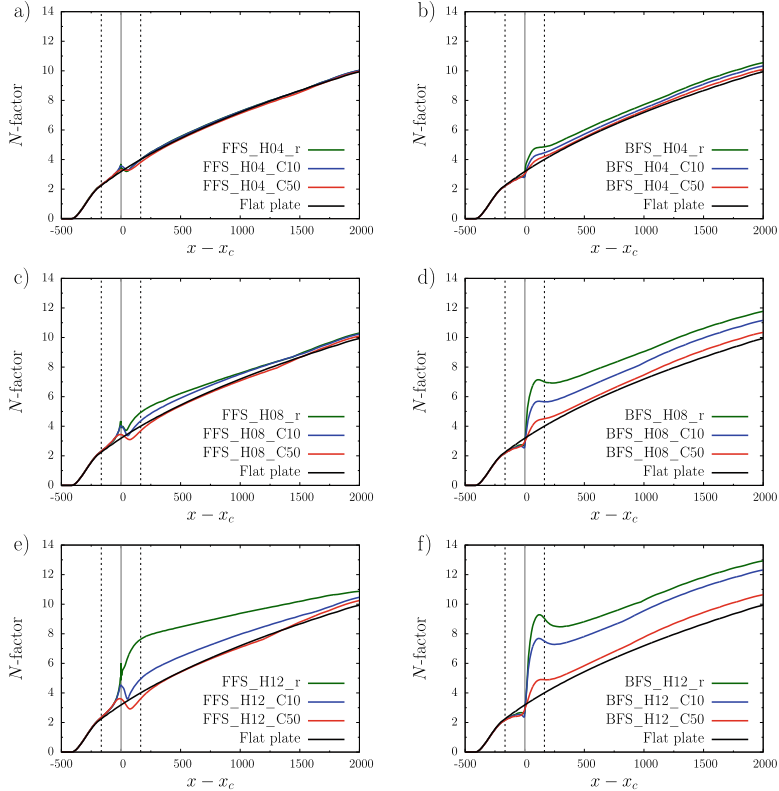


Fig. 4 Effect of shape parameter C on N -factor envelope curves for cases **a** FFS_H04 ; **b** BFS_H04 ; **c** FFS_H08 ; **d** BFS_H08 ; **e** FFS_H12 ; **f** BFS_H12 . Vertical dashed lines indicate the location of the interfaces between PSE and AHLNS methodologies. The grey line represents the position of the step. The N -factor envelope curve for a flat plate (black line) is included as reference

the *loss of laminarity* up to only 17% (case BFS_H12_C50). Clearly, for *large* steps the impact of smoothing the shape of the step has a much stronger influence on the expected transition location. For *medium* steps the situation depends on the type of the step: for FFS the expected transition location is relative unaffected by the shape of the step, while for BFS the *loss of laminarity* can be reduced from 39% (case BFS_H08_r) to 10% (case BFS_H08_C50).

4 Summary and Conclusions

The spatial linear stability analysis of Tollmien-Schlichting waves in the presence of a large variety of forward- and backward-facing steps on a flat plate in a compressible flow is presented here. In order to reduce the scope of all possible parameter com-

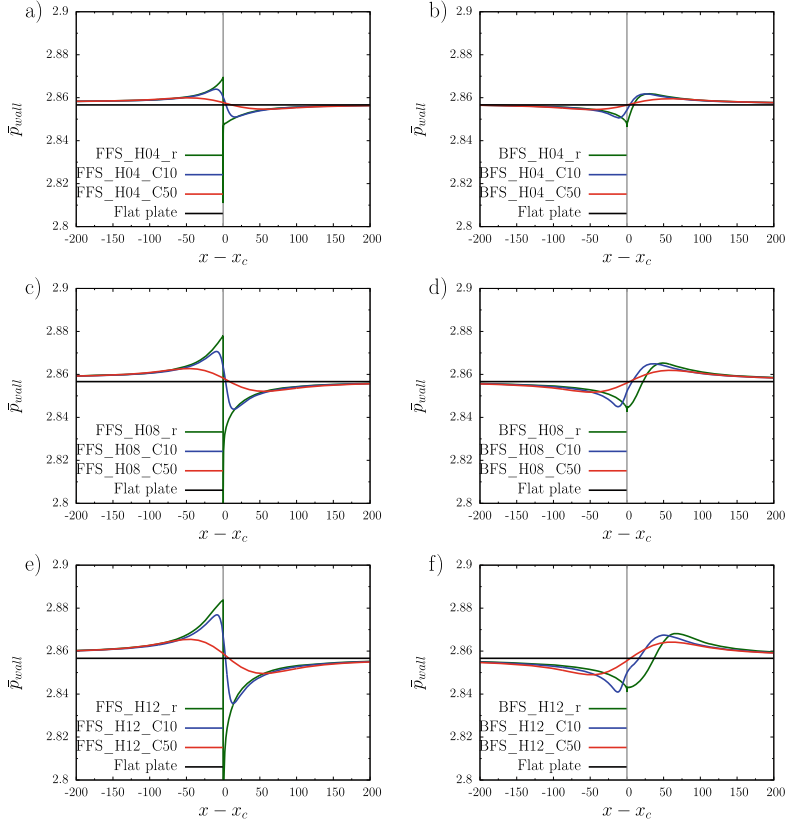
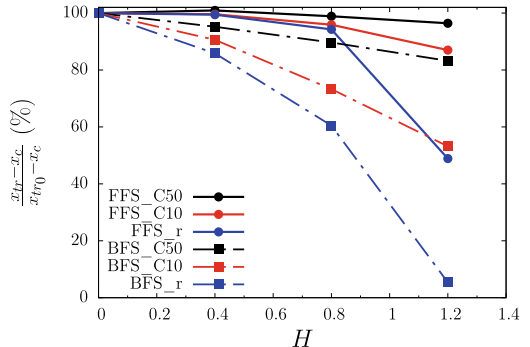


Fig. 5 Effect of shape parameter C on pressure distribution at the wall \bar{p}_{wall} for cases **a** FFS_H04; **b** BFS_H04; **c** FFS_H08; **d** BFS_H08; **e** FFS_H12; **f** BFS_H12. The grey line represents the position of the step. The pressure distribution for a flat plate (black line) is included as reference

Fig. 6 Expected transition location x_{tr} , referred to the expected transition location for a flat plate x_{tr0} , for all steps considered in the present work. The e^N methodology, with a transition N -factor of 9, is applied



binations, unit Reynolds number, Mach number and step location were kept fixed. The geometrical parameters which define the step (height and shape) were systematically varied. The recently developed AHLNS methodology was used to compute the N -factor envelope curve for each step.

A physical interpretation of the instability results, based on the changes in pressure distribution introduced by the presence of the step is also described in detail. The results of the stability analysis were related with an expected transition location via the e^N methodology, assuming that a value of $N_{tr}=9$ triggers the onset of transition to turbulence. It is shown that, for *small* steps (in terms of the displacement thickness at the step location x_c) the expected transition location is barely affected by the shape of the step (rounded or rectangular). However, for *large* steps the expected transition location for rectangular steps can be significantly delayed by smoothing the shape of the step. This effect was noticed for both forward- and backward-facing steps. However, further parametric studies which extend the scope of the present work are required in order to be able to describe completely all possible laminar-turbulent transition scenarios.

The AHLNS methodology presented here is very well suited for such parametric studies as it can be applied to other types of surface irregularities like humps, gaps, porous walls and suction slots, both in two-dimensional and quasi-three dimensional boundary layers. Quantifying the influence of such irregularities on the location of laminar-turbulent transition represents one of the major tasks in the design of laminar wings for future aircraft.

Acknowledgements Part of this work was supported by the European project NACOR (Grant Agreement no. CS2-AIR-GAM-2014-2015-01).

References

1. Nenni, J.P., Gluyas, G.L.: Aerodynamic design and analysis of an LFC surface. *Astron. & Aeronaut.* 52–57, (1966)
2. Ragab, S., Nayfeh, A.: Stability of compressible boundary layers over a smooth backward-facing step. *AIAA Paper* 1990–1449, (1990)
3. Edelmann, C.A.: Influence of forward-facing steps on laminar-turbulent transition. PhD Dissertation. Univ. Stuttgart (2014)
4. Franco, J.A., Hein, S., Valero, E.: On the influence of two-dimensional hump roughness on laminar-turbulent transition. *Phys. Fluids.* **32**, 034102 (2020)
5. Franco, J.A., Hein, S.: Adaptive Harmonic Linearized Navier-Stokes equations used for boundary-layer instability analysis in the presence of large streamwise gradients. *AIAA Paper* 2018–1548, (2018)
6. Hein, S., Bertolotti, F.P., Simen, M., Hanifi, A., Henningson, D.: Linear nonlocal instability analysis - the linear NOLOT code. *DLR IB* 223–94, A56 (1995)
7. Arnal, D.: Boundary layer transition: Predictions based on linear theory. In: *Progress in Transition Modelling*. AGARD report 793 (1994)
8. TAU-Code User Guide: DLR. v.2017.1.0. (2017)
9. Drazin, P.G., Reid, W.H.: *Hydrodynamic Stability*. Cambridge University Press (1981)
10. Hein, S.: Linear and nonlinear nonlocal instability analyses for two-dimensional laminar separation bubbles. *Laminar-Turbulent Transition. Proceedings of the IUTAM Symposium* (1999)

11. Masad, J.A., Iyer, V.: Transition prediction and control in subsonic flow over a hump. *Phys. Fluids.* **6**, 313–327 (1994)
12. Costantini, M., Risius, S., Klein, C.: Experimental investigation of the effect of forward-facing steps on boundary-layer transition. *Procedia IUTAM.* **14**, 152–162 (2015)

Receptivity to Surface Imperfections



Michael Gaster

Abstract The continued drive towards increased zones of laminar flow on aircraft flying surfaces requires the research community to improve its ability to understand and predict factors causing instability leading to transition and turbulent flow. One of the factors that arise in trying to develop laminar wings is surface finish and the influence played by various types of surface imperfections. It turns out that small protuberances, or depressions, on the surface can interact with either sound waves, or existing instability waves, to generate additional instability disturbances through the receptivity process. There are many possible ways of tackling this problem and predicting the disturbances created by the interaction of, say, a sound wave and a small surface bump. Colleagues who work with DNS methods assure me that this problem can be tackled effectively by DNS, but as we are mainly considering very small acoustic excitation so that linearised equations are appropriate. High order methods commonly employed can deal with very weak perturbations with adequate accuracy. Until these solutions are available for the parameters of the current project we cannot gauge the value of the method. It is also possible to further simplify the computing by linearising the boundary conditions on the excrescence to plate values on the bounding surface. This is certainly permissible for very shallow imperfections but may not be suitable for larger ones. Triple deck methods have also successfully solved these problems see [1].

1 Introduction

Here we report a somewhat different approach that uses further approximations, but can handle excrescences and depressions of small but finite size that were used in a series of wind tunnel experiments on the acoustic receptivity of a laminar boundary layer carried out at City University by Placidi et al. [2]. The set up is shown on Fig. 1. Small amplitude perturbations are only considered in the current approach so that the equations of motion can be linearised. The flow speed in the experiment was low

M. Gaster (✉)

University of London, Northampton Square, London EC1V0HB, UK

e-mail: Michael.Gaster.1@city.ac.uk

and incompressible flow was therefore assumed. As the receptivity process is a local phenomenon it is reasonable to ignore the slow boundary layer growth over the bump zone and to apply the parallel flow assumption. There will also be a local mean flow perturbations caused by the bump in the steady boundary layer and these are also ignored here. Then the governing equation in Fourier space is the Orr-Sommerfeld equation. For small, but not infinitesimal, bumps this is reasonable, but we do not know at what bump height this assumption becomes untenable. We will return to this topic in the discussion. The necessary boundary conditions that the sum of both fluctuating velocity perturbations, the sound field and the instability mode, are set to zero on the boundary of the excrescence was applied. The plane sound wave induced a fluctuating boundary layer over the plate, often called a Stokes Layer, that arises on an infinite plane. The experiment recorded the velocities generated by the sound field on the smooth plate and they were found to be linearly increasing from the surface. This model of the acoustic flow was taken as the excitation signal and provided the acoustic velocities on the boundary of the bump. The imposed boundary velocity on the bump was equated to minus that of the vortical component of the Orr-Sommerfeld solution set. Solutions were then calculated using an SVD technique from a set of base solutions of the governing equation.

An apology is offered to anyone who attended the conference where some rather strange behaviour was presented. In fact, there were some coding mistakes, but the major problems arose from the corners of the chosen bump, as I had suggested in the presentation—although I did not realise how significant they were then. The experiment carried out for Airbus used a sharp-edged rectangular form of bump. Unfortunately, without infinite resolution this cannot be modelled properly, and some rather artificial rounding of the corners was needed to obtain sensible results. The present set of data refers to this modified shape. With an increase in resolution the method will almost certainly be capable of dealing with higher bumps with sharper corners, but will take longer to evaluate solutions. Here we use a resolution of 1 mm that provides some useful solutions. The method can deal with changes in Reynolds number, bump height, excitation frequency and pressure gradient. Individual solutions can be found in roughly 2 min on a laptop.

2 Analysis

The most direct and simplest approximation involves a Taylor expansion about the boundary wall so that for very shallow bumps, the boundary condition on the upper surface can be transferred to the boundary surface on the plate so that the problem reduces to predicting the disturbance flow field created by a boundary value. In the parallel flow context this reduced to the evaluation of an integral expression for a point source with an excitation frequency of ω .

$$u(x, y, t) = \frac{\Delta u}{2\pi} \int \frac{\tilde{u}(y; \alpha, \omega)}{\tilde{u}(0; \alpha, \omega)} e^{i(\alpha x - \omega t)} d\alpha \quad (1)$$

This can then be integrated over the length of the excrescence, while the downstream asymptotic solution is given by the residue of the integral, again integrated over the length. This model is commonly used and can certainly provide useful results for shallow bumps, but it is not clear as to whether this model is adequate for larger ones [3]. It turns out that unless the excrescence is small, say less than 50 microns in the case studied, the boundary conditions on the surface of the bump are poorly met. In the current scheme the boundary conditions on the bump surface are properly represented.

The solutions of the linearised parallel flow equations are composed of sums of solutions of the Orr-Sommerfeld equation over a range of wavenumbers to match the acoustic velocity on the surface of the excrescence. The excited disturbance can then be defined as:

$$u(x, y, t) = \hat{u}(y)e^{-i(\omega t)} + \sum A_n e^{i(\alpha_n x - \omega t)} \hat{u}_A(y; \alpha_n, \omega) + \sum B_n e^{i(\alpha_n x - \omega t)} \hat{u}_B(y; \alpha_n, \omega), \quad (2)$$

where $\hat{u}(y)e^{-i(\omega t)}$ is the velocity imposed by the sound field.

These summations were carried out over all Fourier terms with α ranging from $-\pi$ to $+\pi$ typically using -150 to $+150$ steps. Similar expressions are defined for the normal velocity component.

The two fundamental solutions of the Orr-Sommerfeld equation that decay in the free-stream are:

$$\hat{u}_A(y; \alpha_n, \omega), \hat{v}_A(y; \alpha_n, \omega) \quad (3)$$

$$\hat{u}_B(y; \alpha_n, \omega), \hat{v}_B(y; \alpha_n, \omega) \quad (4)$$

With boundary conditions:

$$\hat{u}_A(0; \alpha_n, \omega) = 1.0, \hat{v}_A(0; \alpha_n, \omega) = 0 \quad (5)$$

$$\hat{u}_B(0; \alpha_n, \omega) = 0, \hat{v}_B(0; \alpha_n, \omega) = 1.0 \quad (6)$$

The large set of equations for the two velocity components satisfy the conditions of no slip and normal component on the boundaries. An SVD procedure is used to solve the set of equations and determine the magnitudes of the Fourier solutions as well as possible with the resolution employed. A finite number of Fourier components can only satisfy the boundary conditions approximately, but if the errors in the boundary values are small enough, the result provides a valid approximate solution to the problem.

3 Results

The experiments were carried out at City University in the low turbulence tunnel on the flow formed on a flat plate with a bump of 20mm in stream direction and 200mm across the span. The bump was mounted on a stepper motor driven mechanism that enabled the bump to be moved in and out of a slot when the tunnel was running. This enabled recordings to be made with the bump deployed and then again with it set flush with the surface, without moving the hot-wire probe, or having to re-start the tunnel. The difference between the two records taken was often small and without this device inaccuracies occurred in determining the component from the interaction. The centre of the bump was 0.57 m from the leading edge of the plate. The tunnel was run at 18.0 m/s and the sound excitation was provided by a large loud-speaker mounted on the wall of the wind tunnel contraction driven 90 Hz.

All calculations shown here were for the above conditions. The edges of the block were rounded so that 1 mm wavelength solutions would be adequate.

The particular geometry chosen for the experiment produced Tollmien–Schlichting waves that were slightly damped at the Reynolds numbers close to the bump but increased significantly downstream. Of course the parallel flow model can't deal with this behaviour, but the relative magnitudes of the response to different heights etc. can be gauged. It is not that difficult to make some allowance for boundary layer growth, but at this stage it was not considered necessary and comparison with the experiment can only be made in a qualitative way.

The contour plots of the u-component of the response for various bump heights are shown on Fig. 2 for almost rectangular bumps and depressions. The shape of the disturbed flow pattern slowly changes with bump height. But these calculations could not produce valid converged solutions for heights greater than 375 microns. We know from the experiments that the response increased considerably with height above 150 microns, but it is not clear whether the current calculations model that behaviour correctly, as the matching errors also increased with height.

The method used can also calculate the response to depressions, and these are also shown on Fig. 2. Finally, the response to various heights is shown for a range of displacements for which we have reasonably converged solution. No doubt these results could be improved with a narrower bandwidth decomposition and finer resolution.

4 Discussion and Conclusions

This project was carried in support of the experiments being made in the very low-turbulence wind tunnel at City. The experiments were made for Airbus to support the linearised approach in [3]. The author believed that the current method would not only model the flow processes more faithfully for shallow but finite bumps, but would also yield greater insight into the receptivity process. Since the methods can yield results rapidly it will be possible to explore the effects of various parameters, such as Reynolds number, excitation frequency and pressure gradient, on the response.

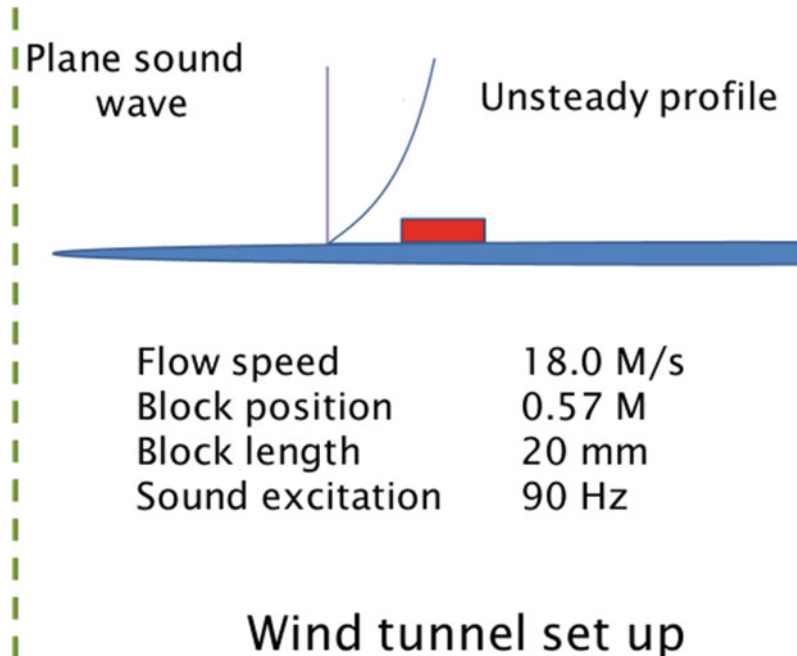


Fig. 1 Wind tunnel set up

The solutions of the Orr-Sommerfeld equation for all the wavenumbers were evaluated for the Blasius velocity profile. For the study of depressions it was necessary to know the mean velocity profile below the x-axis. This can be defined as a continuation of the boundary layer equations. The velocities in the cavity are very small and as an alternative model they could be assumed to be zero. In fact, the calculations showed negligible differences between these two models, suggesting that the relatively weak local distortions to the mean base may not make any significant effect in the response. This is clearly an important topic being currently researched. The simple method has been shown to be able to predict the unsteady travelling waves generated by the interaction of a plane acoustic wave and a shallow bump, albeit with rounded corners. The response turned out to be almost linear up to a bump height of 50 microns and it then increased above that of the linear behaviour. For negative displacements the response was again initially linear but below minus 50 microns showed a response below the linear trend (Fig. 3).

The method can obviously be extended so that it can handle sharper corners and larger displacements, but this will require solutions of the Orr-Sommerfeld to be stable at rather large values of the wavenumber that make the numerical integration inaccurate. It is planned to treat the large wavenumber solutions analytically as they are only required close to the boundary. We need also to explore finer resolution to see if that will enable larger bump heights to be treated.

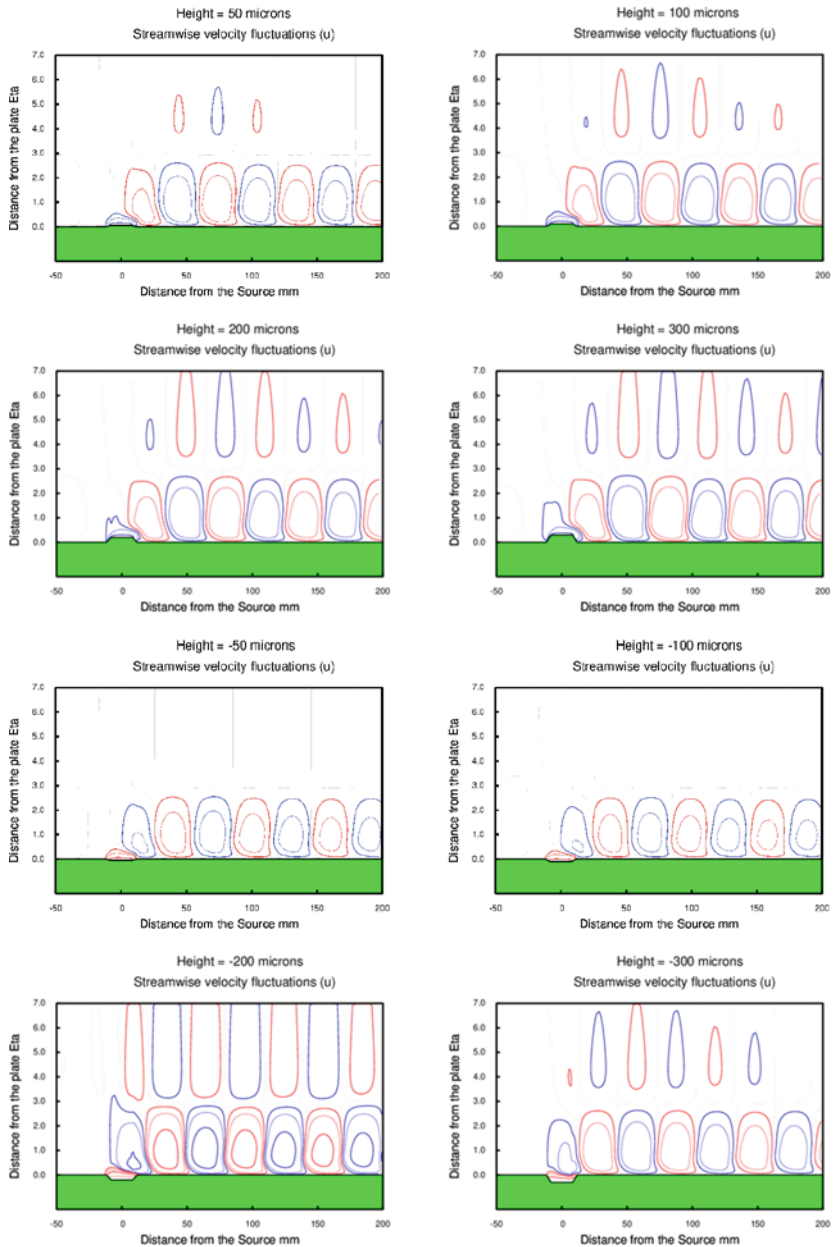


Fig. 2 Tollmien–Schlichting waves generated by a plane sound wave

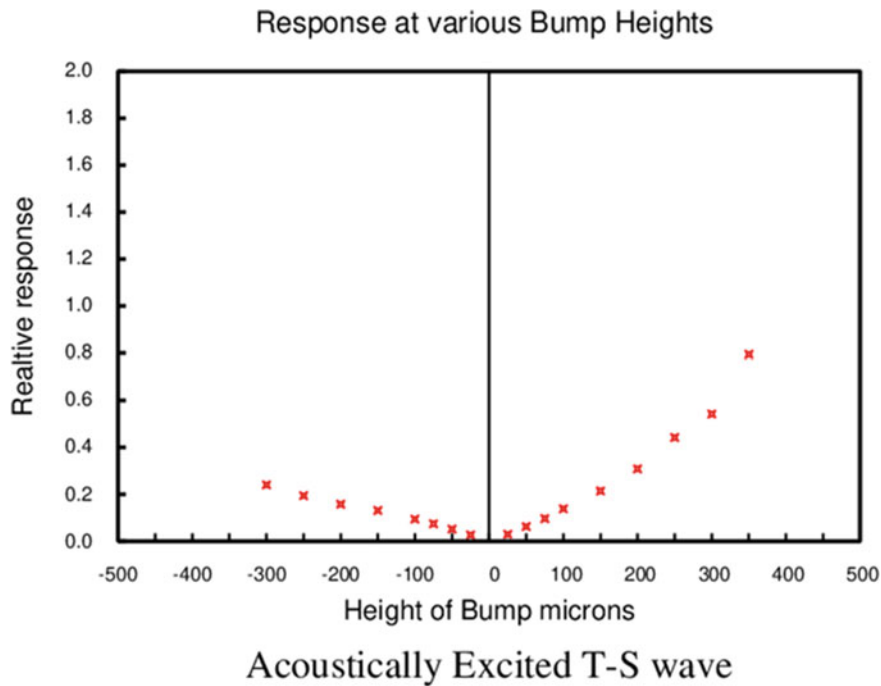


Fig. 3 Relative amplitudes of Tollmien-Schlichting waves generated by the acoustic interaction with excrescences of different heights

References

1. De Tullio, N., Ruban, A.I.: A numerical evaluation of the asymptotic theory of receptivity for subsonic compressible boundary layers. *J. Fluid Mech.* **771**, 520–546 (2015)
2. Placidi, M., Gaster M. Atkin, C.J.: Acoustic receptivity of Tollmien-Schlichting waves to localised surface roughness (to be published Journal Fluid Mechanics) (2020)
3. Raposo, H., Mughal, S.M., Ashworth, R.: Acoustic receptivity and transition modeling of Tollmien-Schlichting disturbances induced by distributed surface roughness. *Phys. Fluids* **30**(4), 044105 (2018)

Influence of Cylindrical and Two-Dimensional Roughness Elements on the Laminar-Turbulent Transition on Flying Wing Model



A. M. Pavlenko, V. S. Kaprilevskaya, V. V. Kozlov, and S. N. Tolkachev

Abstract In this work results of an experimental investigation of the flow over windward side of flying wing with generators of disturbances placed on its surface are presented. These generators were made as three-dimensional and two-dimensional roughness elements, their height matching the boundary layer thickness. Influence of three- and two-dimensional roughness elements on the flow structure was investigated and area of maximum receptivity to surface roughness was found.

Keywords Flying wing · Longitudinal structure · Cross-flow instability · Laminar-turbulent transition · Three-dimensional roughness · Two-dimensional roughness element · Liquid crystal thermography

1 Introduction

Drones are known mostly in military application but recently they are becoming popular with civil aviation and vastly used in various areas. Nowadays the most optimal conception of the drone aircraft is a flying wing. Rapid development of drone aircraft leads to the competition for improving characteristics of aircrafts. One of the parameters that can be improved is a drone aircraft drag. It can be reduced by laminarization of the flow over surface.

However, the flying wing construction has sweep shape. It gives the stability during the flight and allows shifting the impact point of the aerodynamic forces downstream. The boundary layer of this type of wing has three-dimensional structure and like for the swept one it leads to the appearance of many boundary layer instability mechanisms, such as instability near the attachment line, cross-flow instability, Tollmien-Schlichting instability and Görtler instability. Some of them can be

A. M. Pavlenko (✉) · V. S. Kaprilevskaya · V. V. Kozlov
Khristianovich Institute of Theoretical and Applied Mechanics SB RAS, Institutskaya Str. 4/1,
Novosibirsk 630090, Russia
e-mail: pavlenko@gmail.com

S. N. Tolkachev
Central Aerohydrodynamic Institute, Zhukovsky Str. 1, Zhukovsky, Moscow Region 140180,
Russia

efficiently suppressed by choosing the optimal airfoil design. The crossflow instability is connected to the sweep angle, thus it is quite hard to suppress by wing design only. It leads to the laminar-turbulent transition near the leading edge, so it is of interest of researchers.

It is known that the behavior of cross-flow instability depends on freestream turbulence level [1]. When turbulence level is low (less than 0.1%), laminar-turbulent transition is brought about by development of stationary disturbances excited by surface roughness. In case of elevated turbulence level, the origin of transition lies in traveling disturbances of cross-flow instability caused by freestream vortices.

Longitudinal vortices of crossflow instability don't lead to transition itself, but they modify boundary layer structure by adding inflection points in transverse and normal-to-wall of the model directions. It results in appearance of secondary disturbances which lead to the laminar-turbulent transition. More detailed description of characteristics and spatial structure of secondary disturbances are described by Kozlov et al. [7] and Chernoray et al. [3].

Turbulence level $Tu \approx 0.05\%$ is the most characteristic value for in-flight regimes [2]. It makes this regime the most valuable for experiments. But it is important to assess the influence of the roughness elements on the flow because even insects (good example of the localized three-dimensional roughness element) on the leading edge can cause rapid laminar-turbulent transition. Wing and leading edge slat junction can be considered as two-dimensional roughness element.

Main goal of the work is the investigation of physical mechanisms of laminar-turbulent transition on the flying wing. These effects are caused by localized three-dimensional and two-dimensional roughness elements placed in the area of favourable gradient. The investigation was made by liquid crystal thermography. This is a panoramic method that can make parametrical measurements easier.

This work is a continuation of the investigation of the flow over the flying wing model. First results were published by Pavlenko et al. [8].

2 Experimental Setup and Investigation Methods

The set of the experiments was carried out in the test section of the subsonic low turbulent wind tunnel T-324 ITAM SB RAS. Freestream turbulence level was less than 0.04%. Free-stream velocity was in range from 7.2 m/s to 20 m/s and was controlled by Pitot-Prandtl nozzle connected to micro manometer. Unit Reynolds number was in range from $Re_1 = 4.6 \times 10^5$ 1/m to 1.3×10^6 1/m.

Flying wing model. Use was made of flying wing model with smooth surface made of wood and coated with lacquer. Shape of the model and its parameters are shown in Fig. 1.

Wing profile is not categorized, so its form is represented on the Fig. 2.

Investigations were carried out on the windward side of the model. The wing was placed in the working part of the wind tunnel at angle of attack $\alpha = -5^\circ$ for creating favourable pressure gradient over windward side of the wing. This parameter was

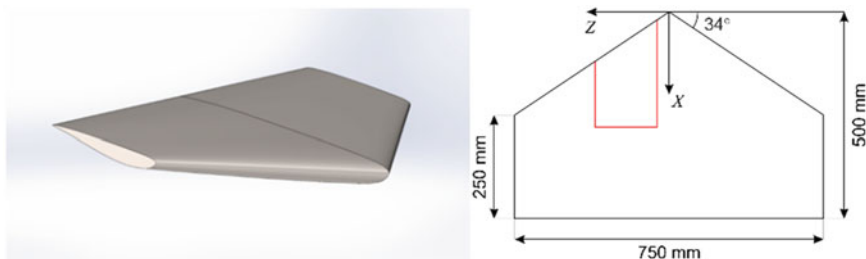


Fig. 1 Model of the flying wing (a) and its dimensions (b) in mm. Red line is a research area

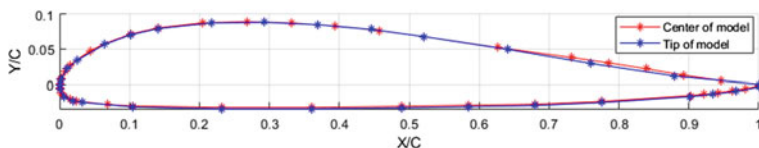


Fig. 2 Central and side section of the flying wing

constant during the experiment. It allowed us to suppress the Tollmien-Schlichting waves and build up appropriate conditions for cross-flow instability disturbances.

For the experiment orthogonal coordinate system was chosen (Fig. 1b). Coordinate X is along the free-stream flow, $X = 0$ is on the leading edge. Coordinate Z is orthogonal to coordinate X and $Z = 0$ is at centre of the wing model. Coordinate Y starts from wing surface and orthogonal to X and Z .

Also the following notation is used: C —local chord of the wing model for coordinate Z ; C_{loc} —projection of the local chord C onto X axis; $S = 750$ mm—wingspan; $Z_S = Z/S$.

Visualization techniques. In this experiment the main method of visualization was liquid crystal thermography. This method is based on the dependency relation between light wave-length selective reflection and the temperature of liquid crystal. Within working range the colour of the liquid crystal film being heated changes from dark red to deep blue. More conclusive description of liquid crystal thermography is presented by Zharkova and Kovrzhina [11, 12].

In the experiment visualization was made by thin-film liquid crystal coating placed in the research area. The working temperature range of the liquid crystal film used in the experiment was 30–32 °C. Model of the wing was heated by halogen lamps then was slowly cooled down by free-stream. This allowed to see the near-wall structure of the flow.

Liquid crystal thermography is a visual and informative technique proved to be useful for quick diagnostic operation and qualitative analysis of wall-adjacent flows [9].

Oil film technique was chosen as a second visualization method. Use was made of titanium dioxide mixed with kerosene. Having been covered in solution the wing was

placed in working part of the wind tunnel. Exposed to the free-stream the solution became dry and after the experiment pictures of the flow were taken. Visualization made by oil film technique gives an idea of limiting streamline on the wing surface.

Hot-wire measurements. Quantitative measurements of boundary layer structure and its characteristics were carried out by constant-temperature hot-wire anemometry. Conducting the experiment use was made of tungsten single-wire probe with diameter 5 μm and length 1.2 mm. Probe was connected to hot-wire anemometer AN-1003 A.A. Labs by coaxial cable. Hot-wire output signal was filtered by analog low-pass filter built into hot-wire anemometer. Then signal was digitalized by ADC National Instruments PCI-6023 with 16-bit capacity. Acquisition frequency was 20 kHz.

Carrying out the calibration test hot-wire was placed near Pitot-Prandtl nozzle connected to micro manometer Omega PX2650-10D5V. Accuracy of pressure measurements was $\pm 1\%$.

Probe movement was released by triaxial traversing system. Accuracy for axis Oy was $\pm 2.5 \mu\text{m}$, for Ox and Oz $\pm 10 \mu\text{m}$.

Excitation of stationary disturbances. Disturbances were excited by multi-layer cylindrical and two-dimensional roughness element, height is multiple of 0.14 mm. Multilayer structure was chosen to investigate the influence of roughness element height on the process of stationary disturbance excitation and development of these disturbances. Diameter of cylindrical three-dimensional roughness elements is 1.6 mm. Width of the two-dimensional roughness element is 15 mm. The leading edge of the two-dimensional roughness element was at $X/C_{loc} = 0.068$ and trailing edge was at $X/C_{loc} = 0.115$.

3 Results

The formation of favourable pressure gradient on the windward side of the flying wing was a crucial condition in the experiment, so it was checked firstly. For this measurement of velocity distribution was carried out chordwise and outside of boundary layer at the distance of 20 mm from the wing surface for different Z coordinate (Fig. 3). Free-stream velocity was $U_0 = 10 \text{ m/s}$. In Fig. 3 it can be seen that velocity grows from leading edge to $X/C_{loc} = 0.7$, velocity distributions for different Z coincide with each other rather good.

Flow deceleration takes place in the rear part of the wing after $X/C_{loc} = 0.7$. It results from mounting the wing at negative angle of attack and shifting the runoff line from leeward to windward side. This feature also can be seen then using oil film visualization (Fig. 4.a). This visualization was carried out at $U_0 = 25 \text{ m/s}$. It is seen that the flow is attached throughout most of the wing. Runoff line can be clearly distinguished near the trailing edge of the wing. Similar runoff line was observed by Kornilov [6].

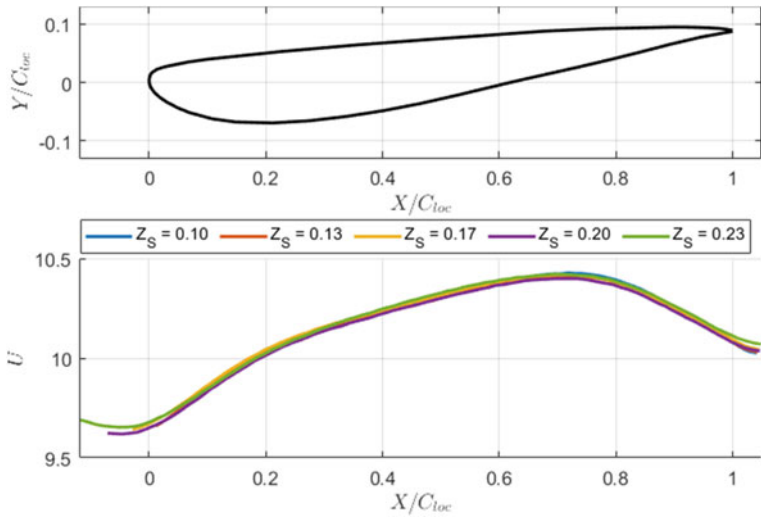


Fig. 3 Mean velocity distribution outside of boundary layer over the model's surface

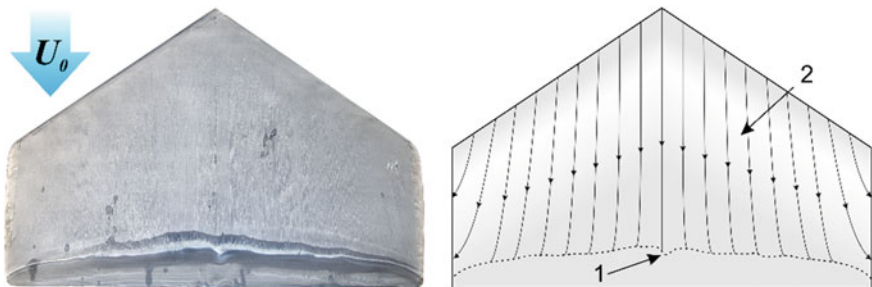


Fig. 4 Oil film visualization (a) and flow topology near wing surface (b). 1—Runoff line, 2—Area of the attached flow

3.1 Flow Structure Near the Wing Surface

Velocity profiles were measured by hot-wire anemometry for free-stream velocity range of $U_0 = 10\text{--}14.2 \text{ m/s}$ for $Z = 176 \text{ mm}$ ($0.23S$). For range of $X = 0.21\text{--}0.66C_{loc}$ nondimensionalized velocity profiles match well (Fig. 5). It is associated with approximately constant acceleration of the flow for this area (Fig. 3).

Figure 6 represents the growth of boundary layer in terms of displacement thickness δ^* and momentum thickness δ^{**} along the flow.

The data obtained allow calculating the change of form factor H along the stream (Fig. 7). In the beginning it takes sufficiently large values like 2.6–2.8. This is quite common for filled laminar velocity profile in the favourable pressure gradient region.

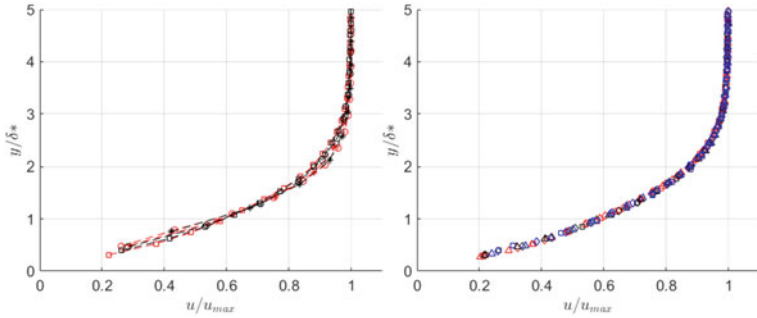


Fig. 5 Velocity profile for $X > 0.21C_{loc}$, $Z = 0.23S$ (176 mm). Red marks—10 m/s; black marks—12.4 m/s; blue marks—14.2 m/s. \square — $0.21C_{loc}$; \diamond — $0.4C_{loc}$; Δ — $0.66C_{loc}$

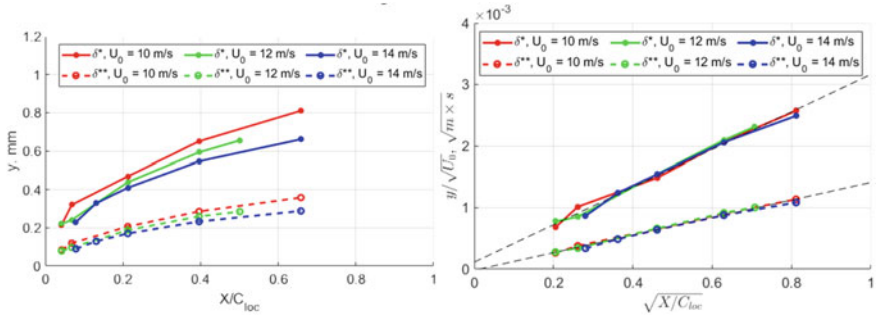


Fig. 6 Growing of the boundary layer thickness streamwise

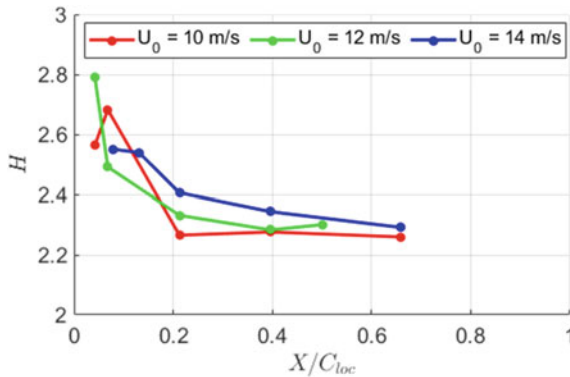


Fig. 7 Evolution of the form factor H downstream

In case of natural parameters boundary layer maintains laminar state at a minimum of $X/C_{loc} = 0.66$.

3.2 Boundary Layer Structure Depending on the Height of the Three-Dimensional Roughness Element

Next part of the experiment was devoted to the investigation of the roughness element influence on the boundary layer depending on the height of the roughness. At this point of the experiment use was made of the roughness element set with various heights. Near the leading edge of the wing four roughness elements were placed (Fig. 8 from left to right $h_{3D} = 0.44; 0.6; 0.73; 0.98$ mm). Diameter of cylindrical roughness elements was 1.6 mm. The set was placed along the leading edge at distance of 6 mm from it. The distance between elements was 7 mm. Free-stream velocity was varied from 7.2 to 20 m/s.

Roughness elements near the leading edge lead to the forming of the longitudinal structures (Fig. 8). The intensity of these structures depends on the height of the element and freestream velocity. Strong nonlinear effects leading to flow turbulization appear behind the highest roughness element $h_{3D} = 0.98$ mm when $U_0 = 15.1$ m/s. Roughness element $h_{3D} = 0.6$ mm causes appearance of these effect when $U_0 = 20$ m/s. All roughness elements studied were bigger than displacement thickness. Reynolds number $Re \approx 900$ leads to almost instant turbulization of the flow ($Re_k = \rho U_k h_{3D}/\mu$; U_k —velocity for upper bound of roughness element; ρ —air density; μ —air dynamical viscosity).

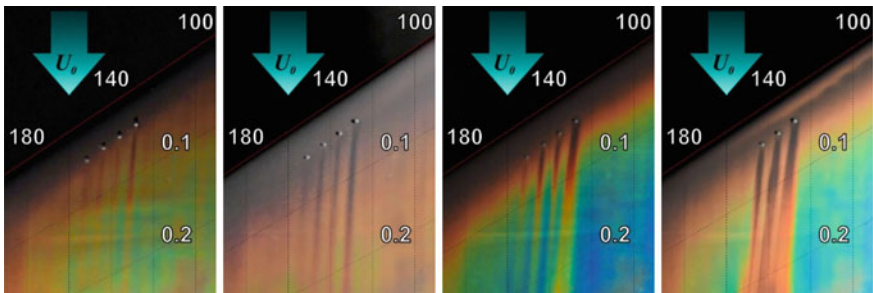


Fig. 8 Wall-adjacent flow visualization behind roughness element depending on free-stream velocity: **a** $U_0 = 7.2$ m/s; **b** $U_0 = 10.2$ m/s; **c** $U_0 = 15.1$ m/s; **d** $U_0 = 20$ m/s

3.3 Determining the Area of the Boundary Layer Maximum Receptivity

The set of nine cylindrical roughness elements ($h_{3D} = 0.98$ mm) was used for the determination of the area of the boundary layer maximum receptivity to disturbances forming behind roughness elements. The set was placed on wing surface at distance of 0; 1; 5.5; 12; 19; 30; 40; 50; 54 mm from the leading edge for X coordinate and at distance of 207.5; 194; 179.5; 159.5; 140; 119.5; 98.5; 76.5; 56.5 mm from central cross-section. All roughness elements were placed in such a way to not to influence on each other (Fig. 9).

Primarily 10.2 m/s and 20 free-stream velocity regimes were investigated (Fig. 10). For the first mode the most intensive longitudinal structure formed behind third roughness element placed at distance of 6 mm from leading edge (Figs. 9, 10a). When free-stream velocity is 20 m/s it can be seen that all roughness element influence massively on the flow (Fig. 10b) and lead to rapid turbulization of the flow. Thus, according to the experiment, the area of the boundary layer maximum receptivity to roughness receptivity was determined for flying wing model. This area is located between roughness element № 2 and 4, near $X/C_{loc} = 0.014$.

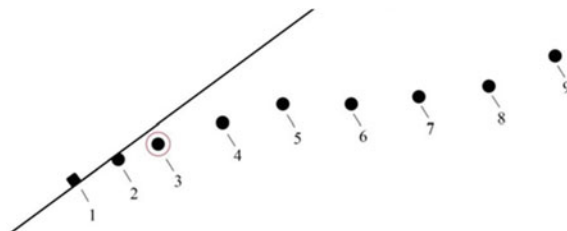


Fig. 9 Roughness set position near leading edge of the flying wing

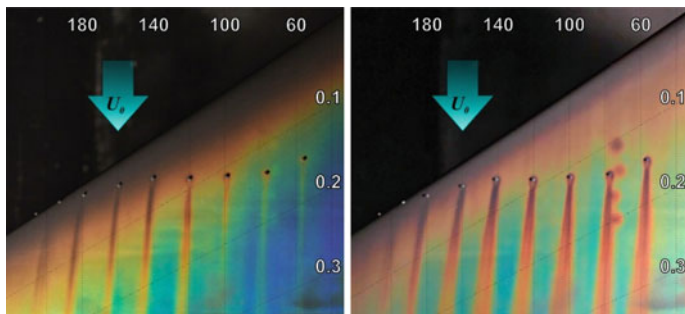


Fig. 10 Wall-adjacent flow visualization behind roughness element depending on free-stream velocity: **a** $U_0 = 10.2$ m/s; **b** $U_0 = 20$ m/s

It is known that large isolated roughness elements lead to formation of twain hairpin vortices [5] in the boundary layer of flat plane. These vortices mix layers and change the structure of the boundary layer. It is called lift-up effect. In Fig. 10 two distinct lines behind roughness elements can be seen.

3.4 Influence of 2d-Roughness Element

Investigation of the two-dimensional roughness element influence was firstly carried out on the swept wing model by Kaprilevskaya and Kozlov [4] and Tolkachev et al. [10]. Figure 11 represents influence of two-dimensional roughness element placed on the flying wing for free-stream velocity $U_0 = 10.2$ m/s. It can be seen that roughness element doesn't have any effects on the flow stability when its height up to $h_{2D} = 0.28$ mm. However when height of the two-dimensional roughness element is 0.84 mm, the stationary disturbance excited behind localized roughness element ($h_{3D} = 0.98$ mm) is destabilized. Increase of the two-dimensional roughness element height up to $h_{2D} = 1.4$ mm leads to excitation of the stationary disturbances unto itself. Thus it can be said that boundary layer is rather stable to the presence of two-dimensional roughness element, at least before height of the roughness reaches boundary layer displacement thickness.

It seems that main contribution to the boundary layer stability is made by local pressure gradient change. It leads to excitation of stationary disturbances by irregularities on the surface of the two-dimensional roughness element.

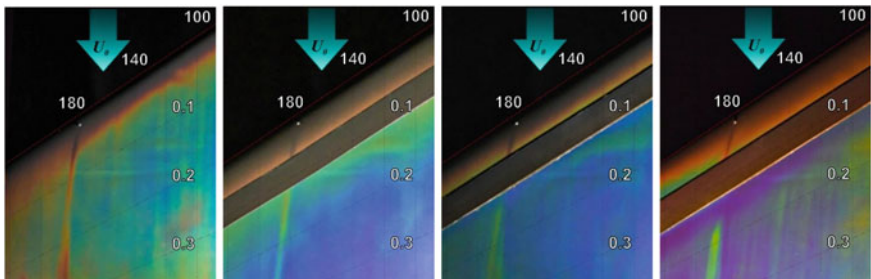


Fig. 11 Influence of two-dimensional roughness element height on the flow for $U_0 = 10.2$ m/s:
a $h_{2D} = 0$ mm; **b** $h_{2D} = 0.28$ mm; **c** $h_{2D} = 0.84$ mm; **d** $h_{2D} = 1.4$ mm

4 Conclusions

The investigation of the flow on the windward side was carried out for the flying wing model with disturbances generators placed on its surface. Large enough roughness elements were used as generators with height on the order of boundary layer thickness. It was found that when $Re_k > 900$, roughness element leads to turbulization of the flow.

The set of isolated roughness elements was used for determination of the maximum receptivity area of boundary layer to roughness. In this experiment this area was near $X/C_{loc} = 0.014$.

It was shown that boundary layer is rather stable to the presence of the two-dimensional roughness. First signs of the destabilization appeared when height of the roughness was bigger than boundary layer displacement thickness. It also was found that two-dimensional roughness element generates stationary disturbances itself when displacement thickness bigger than $4\delta^*$. It can be argued that the results of the work are in qualitative agreement with the results obtained by the authors earlier on the model of swept wing.

Acknowledgements The work was supported by the Russian Science Foundation (Project No. 18-79-00189).

References

1. Bippes, H.: Basic experiments on transition in three-dimensional boundary layers dominated by crossflow instability. *Prog. Aerosp. Sci.* **35**, 363–412 (1999)
2. Carpenter, A.L., Saric, W.S., Reed, H.L.: Roughness receptivity in swept-wing boundary layers experiments. *Int. J. Eng. Syst. Model. Simul.* **2**, 128 (2010)
3. Chernoray, V.G., Kozlov, V.V., Löfahl, L., Chun, H.H.: Visualization of sinusoidal and varicose instabilities of streaks in a boundary layer. *J. Vis.* **9**, 437–444 (2006)
4. Kaprilevskaya, V.S., Kozlov, V.V.: The investigation of influence of two-dimensional roughness element on the swept wing flow structure in favourable gradient region. In: AIP Conference Proceedings (2018). <https://doi.org/10.1063/1.5065338>
5. Klebanoff, P.S., Cleveland, W.G., Tidstrom, K.D.: On the evolution of a turbulent boundary layer induced by a three-dimensional roughness element. *J. Fluid Mech.* **237**, 101–187 (1992)
6. Kornilov, V.I.: Three-dimensional turbulent near-wall flows in streamwise corners (revised and completed), Second edn. Novosibirsk (2013)
7. Kozlov, V.V., Grek, G.R., Litvinenko, Y.A., Tolkachev, S.N., Chernoray, V.G.: Experimental studies of the localized disturbances and their secondary high-frequency instability in the flat plate, unswept and swept wing boundary layer (review). *Vestn. NSU Phys.* **9**, 39–64 (2014)
8. Pavlenko, A.M., Zanin, B.Y., Katasonov, M.M.: Flow around a small-sized UAV model in a turbulent trace. In: AIP Conference Proceedings (2018). <https://doi.org/10.1063/1.5065278>
9. Tolkachev, S.N., Kaprilevskaya, V.S., Kozlov, V.V.: The role of two-dimensional roughness element in the laminar-turbulent process in the favorable pressure gradient of the swept wing. *Vestn. NSU Phys.* **9**, 65–73 (2014)
10. Tolkachev, S.N., Kozlov, V.V., Kaprilevskaya, V.S.: Influence of two-dimensional roughness element on boundary layer structure in the favourable pressure gradient region of the swept wing. *J. Aerosp. Eng.: Part G* **234**, 20–27 (2020). <https://doi.org/10.1177/0954410019841776>

11. Zharkova, G.M., Kovrzhina, V.N., Hachaturyan, V.M.: Experimental study of subsonic flows by liquid-crystal thermography. *J. Appl. Mech. Tech. Phys.* **43**, 122–128 (2002)
12. Zharkova, G.M., Zanin, B.Y., Kovrzhina, V.N., Brylyakov, A.P.: Free stream turbulence effect on the flow structure over the finite span straight wing. *J. Vis.* **5**, 169–176 (2002)

On the Effects of Sound in Subsonic Boundary Layer Flows



Henrique Raposo, Shahid Mughal, and Richard Ashworth

Abstract The study of acoustic receptivity in quiet disturbance environments can be decomposed into several sub-problems. One such problem consists of determining the response of the unsteady boundary layer to acoustic forcing in the freestream. In this paper, we describe two methods to characterize the acoustic boundary layer response based on the linear stability equations. In their inviscid form, we first show how to determine the reflection coefficient. The sum of the incident and reflected waves then drives the unsteady Stokes motion within the boundary layer, for which a double-layer high Strouhal number asymptotic solution is obtained. The outer layer solution is calculated numerically whereas the inner layer solution, introduced to satisfy the no-slip condition, is determined analytically. The full linear stability equations can also be integrated numerically to directly obtain a complete disturbance profile accounting for the effects of viscosity. A comparison between these models and the linearised unsteady boundary layer equation (LUBLE) model shows good agreement at high Strouhal number, low Mach number and for downstream-travelling waves. However, for near sonic Mach numbers and for upstream-travelling waves, the LUBLE are shown to be not valid because the assumption that the acoustic wavelength is long compared to the boundary layer thickness no longer holds.

1 Introduction

At subsonic Mach numbers (i.e. $M_\infty < 1$), most acoustic receptivity studies are restricted to downstream travelling waves, together with the assumption that the acoustic wavelength remains large relative to the boundary layer thickness. Under

H. Raposo (✉) · S. Mughal

Department of Mathematics, Imperial College London, South Kensington Campus,
London SW7 2AZ, UK

e-mail: h.raposo17@imperial.ac.uk

S. Mughal

e-mail: s.mughal@imperial.ac.uk

R. Ashworth

Airbus Central Research and Technology, Bristol BS99 7AR, UK

e-mail: richard.ashworth@airbus.com

such conditions, the usual assumption of the pressure invariance through the viscous wall-normal layer can be introduced to model the forced response of the boundary layer to plane acoustic waves. This leads to a parabolic set of governing equations, the so-called linearised unsteady boundary layer equations (LUBLE) [11].

The LUBLE are a valid model of the boundary layer acoustic signature provided that the acoustic transverse unsteady pressure oscillations are negligible. If we choose the acoustic streamwise wavelength $1/\alpha_a^*$ and boundary layer thickness δ^* as the streamwise and transverse length scales respectively, scale analysis of the convective terms of the x-momentum equation indicates that the transverse velocity of the acoustic perturbation is of order

$$v_a^* = \mathcal{O}(\bar{U}_\infty \delta^* \alpha_a^*) , \quad (1)$$

where \bar{U}_∞ is the far-field uniform flow velocity. If we then balance the wall-normal pressure gradient and the convective terms in the y-momentum equation we obtain

$$\frac{\frac{\partial p_a^*}{\partial y^*}}{\bar{\rho}^* \bar{U}^* \frac{\partial v_a^*}{\partial x^*}} = \mathcal{O}\left(\frac{\bar{\rho}_\infty \bar{U}_\infty^2}{\delta^*}\right) = 1 , \quad (2)$$

where the over-bar denotes steady base flow quantities, the subscript “a” denotes acoustic quantities and the subscript ∞ is concerned with far-field quantities. This implies that

$$\delta^* = \mathcal{O}\left(\frac{1}{\alpha_a^*}\right) . \quad (3)$$

Therefore transverse pressure variations become significant when the streamwise wavelength of the acoustic wave is comparable to the boundary layer thickness. This also indicates that the streamwise diffusion terms are no longer negligible, invalidating another core premise of the boundary layer approximation.

Let us consider two-dimensional acoustic waves impinging on a flat plate. The acoustic wave dispersion relation suggests that the wavelength is shortened for upstream inclined waves and in near sonic flows. In such cases, the LUBLE should be replaced by a more accurate model of the acoustic signature within the boundary layer. References [8, 10] introduced forcing theory based on the compressible linear stability equations to predict the forced response of the boundary layer to external disturbances such as acoustic and vortical waves. Reference [7] also studied this topic in the high Reynolds number limit but he did not obtain quantitative agreement with the results of Mack. Other works based on forced linear stability equations are by [5] in the context of subsonic acoustic receptivity and [2] in the context of supersonic acoustic receptivity. On the one hand, the linear stability equations make no simplifying assumptions based on the order of magnitude of the disturbances, unlike the LUBLE. This ensures that the effects of wall-normal pressure gradients are fully accounted for. On the other hand, the main disadvantage of this method is

that it makes a parallel flow assumption and therefore it can not account for the slow variation of the basic flow nor for the upstream history of the acoustic disturbance.

In this paper we investigate two distinct models of the acoustic forcing based on the compressible linear stability equations. Firstly, we study the inviscid limit of the governing equations. This analysis is similar to that of [7], however the technique to derive the acoustic reflection coefficient is based on the work of [4]. A complete disturbance profile is obtained by introducing an inner viscous layer that satisfies the no-slip condition and deriving composite solutions. The second approach consists of numerically integrating the full linear stability equations. The essentials to perform such direct integration have been described by [8, 10, 13]. We remove the assumption that the acoustic wave travels in a single direction and proceed to investigate the validity of the LUBLE across the Mach number and angle of incidence parameter space. A study of the effects of these parameters on the boundary layer unsteady disturbance profiles and on the reflection coefficient is carried out. The limitations of each of the models based on their respective assumptions are then discussed.

2 Acoustic Boundary Layer Modelling

The forced response of the boundary layer to acoustic forcing is essential to quantifying acoustic receptivity. A model based on numerical solutions of the LUBLE was devised by [11] for three-dimensional incident acoustic waves. In this section, we present two alternative models based on the linear stability equations for two-dimensional (2D) carrier flows and 2D acoustic waves over a zero pressure gradient flat plate geometry.

2.1 Inviscid Reflection

Under a quasi-parallel flow assumption, the governing equations are the compressible linear stability equations [10]. In the inviscid limit [9], they reduce to the following system of first-order differential equations

$$\frac{\partial \hat{p}_a}{\partial y} = i \bar{\rho} (\omega - \bar{U} \alpha_a) \hat{v}_a , \quad (4a)$$

$$\frac{\partial \hat{v}_a}{\partial y} + \frac{\bar{U}_y}{c_a - \bar{U}} \hat{v}_a + \frac{i \alpha_a}{c_a - \bar{U}} \left[\bar{T} - M_\infty^2 (\bar{U} - c_a)^2 \right] \hat{p}_a = 0 , \quad (4b)$$

or a single second-order differential equation for the acoustic pressure \hat{p}_a

$$\frac{\partial^2 \hat{p}_a}{\partial y^2} - \left(\frac{\bar{\rho}_y}{\bar{\rho}} - \frac{2 \bar{U}_y}{c_a - \bar{U}} \right) \frac{\partial \hat{p}_a}{\partial y} - \bar{\rho} \alpha_a^2 \left[\bar{T} - M_\infty^2 (\bar{U} - c_a)^2 \right] \hat{p}_a = 0 , \quad (5)$$

where $c_a = \omega/\alpha_a$ is the phase speed. Acoustic quantities are decomposed according to a Fourier series and a single harmonic is analysed, e.g. $p_a(y) = \hat{p}_a(y) \exp(i(-\omega t + \alpha_a y))$. The reference scales are the usual far-field quantities while the reference length scale is the streamwise coordinate of the boundary layer profile.

Following [4], we consider the freestream acoustic pressure perturbation

$$\hat{p}_{a,\infty} = \hat{p}_{a,i} \exp(-i\lambda_1 \alpha_a y) + \hat{p}_{a,r} \exp(i\lambda_1 \alpha_a y) , \quad (6)$$

where $\hat{p}_{a,i}$ is the amplitude of the incident wave and $\hat{p}_{a,r}$ is the amplitude of the reflected wave. For this representation to be consistent, λ_1 is such that $\lambda_1 \alpha_a$ is always positive. We define the reflection coefficient $C_r = \hat{p}_{a,r}/\hat{p}_{a,i}$ and write the ratio of $\frac{\partial \hat{p}_{a,\infty}}{\partial y}$ to $\hat{p}_{a,\infty}$ as

$$Q(y) = i\lambda_1 \alpha_a \frac{\hat{p}_{a,r} \exp(i\lambda_1 \alpha_a y) - \hat{p}_{a,i} \exp(-i\lambda_1 \alpha_a y)}{\hat{p}_{a,r} \exp(i\lambda_1 \alpha_a y) + \hat{p}_{a,i} \exp(-i\lambda_1 \alpha_a y)} , \quad (7)$$

which can be rearranged as

$$C_r = \exp(-2i\lambda_1 \alpha_a y) \frac{i\lambda_1 \alpha_a + Q(y)}{i\lambda_1 \alpha_a - Q(y)} . \quad (8)$$

The problem of acoustic reflection in the presence of a boundary layer is thus reduced to calculating $Q(y)$ which, we will see shortly, is very advantageous. Dividing Eq. (5) by \hat{p}_a and introducing the change of variable $\frac{\partial \hat{p}_a}{\partial y}/\hat{p}_a = Q(y)$ yields

$$\frac{\partial Q}{\partial y} + Q^2 - \left(\frac{\bar{\rho}_y}{\bar{\rho}} - \frac{2\bar{U}_y}{c_a - \bar{U}} \right) Q - \bar{\rho} \alpha_a^2 \left[\bar{T} - M_\infty^2 (\bar{U} - c_a)^2 \right] = 0 . \quad (9)$$

Equation (9) is a nonlinear first-order differential equation, readily solved by numerical integration given an initial condition at the wall. Provided the perturbed flow satisfies the impermeability condition, it follows from Eq. (4a) that $Q(0) = 0$. We use a third-order implicit Adams method from the complex-valued variable-coefficient ordinary differential equation solver in the Python package *SciPy*. Special care performing the integration is required when a critical layer arises— $\bar{U}(y_c) = c_a$. However, our focus here is in subsonic flow conditions where the critical layer singularity issue does not arise. Furthermore, note that Eq. (9) must be integrated far into the freestream where solution (6) becomes valid and therefore Eq. (8) can be used to determine the reflection coefficient. After determining the reflection coefficient, Eqs. (4) can be solved subject to boundary conditions

$$\hat{v}_a(0) = 0 , \quad (10a)$$

$$\hat{p}_a(y_e) = \hat{p}_{a,i} [\exp(-i\lambda_1 \alpha_a y_e) + C_r \exp(i\lambda_1 \alpha_a y_e)] , \quad (10b)$$

where y_e defines the edge of the computational domain. In practice, these equations are amenable to a simple shooting method.

To obtain complete disturbance profiles across the boundary layer we must introduce an inner layer solution that satisfies the no-slip condition, violated by the inviscid solution. The y-momentum linear stability equation provides the matching condition, indicating that $\frac{\partial \hat{p}_a}{\partial y} = 0$ near the wall. Consequently, the LUBLE are a valid set of governing equations. Following a similar procedure to that of Sect. 2.2 of [11], we arrive at the following high Strouhal number solution

$$\hat{u}_a = \frac{S_o \hat{p}_a(0)}{c_a} \left(1 - \exp\left\{-\sqrt{-\frac{i\omega S_o}{\bar{\mu}_o}} Y\right\} \right), \quad (11a)$$

where $\hat{p}_a(0)$ is determined by the inviscid solution of Eq. (4), S_o is the adiabatic wall temperature and $\bar{\mu}_o$ is the dynamic viscosity at the wall. The wall-normal coordinate Y is defined in detail in [11]. Composite solutions can be obtained for each flow field variable following an identical procedure to the one used in [11].

2.2 Viscous Reflection

Let us now consider the full compressible linear stability equations (see [10]). Herein, we seek to solve these equations subject to inhomogeneous boundary conditions representing the forcing of the boundary layer by an incident plane acoustic wave from the far field. We choose to use a shooting method, following the work of [8, 10].

The compressible linear stability equations form a system of six first-order variable-coefficient linear ordinary differential equations. The coefficients become constant in the far-field limit $y \rightarrow \infty$, and the equations admit the solution

$$\begin{bmatrix} \hat{v}_a, \hat{u}_a, \hat{p}_a, \hat{\theta}_a, \frac{\partial \hat{u}_a}{\partial y}, \frac{\partial \hat{\theta}_a}{\partial y} \end{bmatrix}^T = c_1 \hat{\mathbf{q}}_1 e^{i\lambda_1 y} + c_2 \hat{\mathbf{q}}_2 e^{i\lambda_2 y} + c_3 \hat{\mathbf{q}}_3 e^{i\lambda_3 y} + c_4 \hat{\mathbf{q}}_4 e^{i\lambda_4 y} + c_5 \hat{\mathbf{q}}_5 e^{i\lambda_5 y} + c_6 \hat{\mathbf{q}}_6 e^{i\lambda_6 y}, \quad (12)$$

where c_i are constants determining the amplitude of each mode, λ_i are the eigenvalues and \mathbf{q}_i are the eigenvectors. Moreover, note that $\hat{\theta}_a$ denotes the temperature acoustic perturbation. In the limit of high Reynolds number, the eigenvalues simplify to [10]

$$\lambda_{1,2} = \pm i\alpha_a \sqrt{1 - M_\infty^2 (1 - c_a)^2}, \quad (13a)$$

$$\lambda_{3,4} = \pm i\sqrt{i\alpha_a R (1 - c_a)}, \quad (13b)$$

$$\lambda_{5,6} = \pm i\sqrt{i\alpha_a R \sigma (1 - c_a)}, \quad (13c)$$

where $R = x^* \bar{U}_\infty / \bar{v}_\infty$ is the Reynolds number based on the distance from the leading edge of the flat plate x^* , and σ is the Prandtl number. From the expression of $\lambda_{1,2}$ we can deduce that if

$$c_a > 1 + \frac{1}{M_\infty} \quad \text{or} \quad c_a < 1 - \frac{1}{M_\infty}, \quad (14)$$

then $\lambda_{1,2}$ is a purely real number and therefore the first and second eigenmodes are purely oscillatory and thus bounded. We recognize the lower and upper bounds of the acoustic phase velocity as being the phase velocities of the inviscid downstream and upstream acoustic wave solutions, respectively. The first and second eigenmodes are identified with incident and reflected acoustic waves, where the angle of incidence is controlled by the ratio $\lambda_{1,2}/\alpha_a$. The effects of viscosity are to weakly dampen the acoustic waves in their direction of propagation. This means that the incident wave violates the boundedness condition in the far field. However, in reality this wave is generated at a finite distance from the flat plate, thus bounding its amplitude to a finite value.

The eigensolutions 3 and 4 correspond to the first viscous velocity solution, whereas 5 and 6 correspond to a viscous temperature solution. These eigenmodes are highly amplified or damped. Modes 3 and 5 violate the boundedness condition and therefore must be excluded from a physical solution

$$\left[\hat{v}_a, \hat{u}_a, \hat{p}_a, \hat{\theta}_a, \frac{\partial \hat{u}_a}{\partial y}, \frac{\partial \hat{\theta}_a}{\partial y} \right]^T = c_1 \hat{\mathbf{q}}_1 e^{i\lambda_1 y} + c_2 \hat{\mathbf{q}}_2 e^{i\lambda_2 y} + c_4 \hat{\mathbf{q}}_4 e^{i\lambda_4 y} + c_6 \hat{\mathbf{q}}_6 e^{i\lambda_6 y}. \quad (15)$$

The eigenvectors and eigenvalues are obtained with the generalised eigenvalue problem solver *eig* from the Python package *SciPy*. The basic idea of the shooting method is to continue these freestream eigensolutions $\hat{\mathbf{q}}_i \exp(i\lambda_i y)$ into the boundary layer by direct numerical integration of the linear stability equations. The amplitude of the incident wave c_1 is considered known. The problem is then reduced to finding a linear combination of the four modes such that the boundary conditions are respected

$$\hat{v}_a = \hat{u}_a = \hat{\theta}_a = 0, \quad \text{at the wall}, \quad (16)$$

which is always possible. The viscous modes are highly amplified in the direction of numerical integration. Thus numerical round-off errors tend to be amplified accordingly until the solution is completely spoiled. This so-called parasitic error growth problem has been addressed by multiple authors and with a number of methods—see [1, 10]. Gram-Schmidt orthonormalization is one of the most popular and effective methods to overcome this issue. Reference [13] describes it comprehensively and discusses implementation issues in great detail. Numerical integration is performed with a fixed step-size fourth-order Runge-Kutta method.

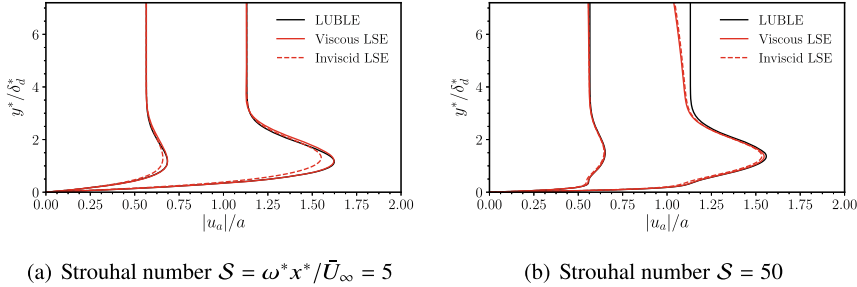


Fig. 1 Stokes layer streamwise velocity profile scaled by $a = 1/M_\infty$ (from left to right $M_\infty = \{0.4, 0.8\}$, $\Theta_i = 45^\circ$ and $R = \bar{U}_\infty x^* / \bar{v}_\infty = 0.5 \times 10^6$); δ_d^* represents the boundary layer displacement thickness. Comparison between the LUBLE and the LSE, in full viscous and inviscid limits

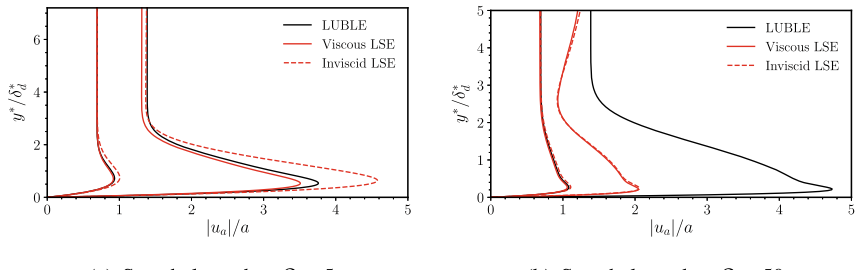


Fig. 2 Stokes layer streamwise velocity profile scaled by $a = 1/M_\infty$ (from left to right $M_\infty = \{0.4, 0.8\}$, $\Theta_i = 150^\circ$ and $R = 0.5 \times 10^6$). Comparison between the LUBLE and the LSE, in full viscous and inviscid limits

3 Acoustic Boundary Layer Profiles

The main objective of this section is to cross validate the three different models of the boundary layer acoustic signature and assess their domain of validity, recognising the underlying assumptions and limitations.

Firstly, in Figs. 1 and 2 we compare the acoustic streamwise velocity perturbation profile across the boundary layer for different conditions. The angle of incidence Θ_i is 0° for downstream-travelling waves and 180° for upstream-travelling waves. We denote the approaches described in Sects. 2.1 and 2.2 “Inviscid LSE” and “Viscous LSE” respectively, where LSE is an abbreviation for linear stability equations.

For an angle of incidence of 45° , we observe generally good agreement between the LUBLE and the “Viscous LSE” at all Mach and Strouhal numbers considered. Expectedly, the comparison between the “Inviscid LSE” and the other two approaches is dependent on the Strouhal number—excellent agreement is observed for $S = 50$, but it deteriorates for $S = 5$. This approach is only formally valid in the high Strouhal number limit, thus these computations confirm expected behaviour. For an angle of incidence of 150° the LUBLE no longer always agree with the profiles obtained

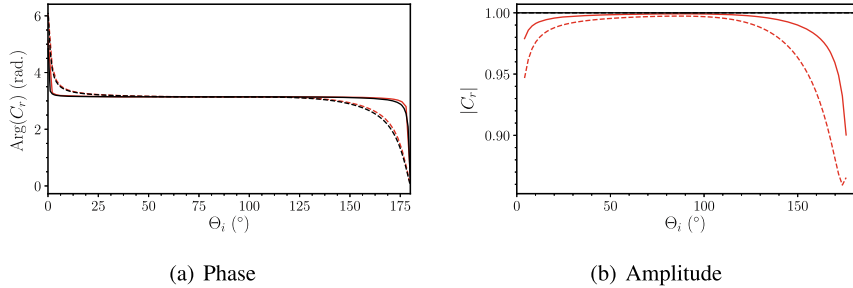


Fig. 3 Reflection coefficient variation with incident acoustic wave angle at fixed $M_\infty = 0.4$ and $R = 0.5 \times 10^6$. Solid lines— $S = 5$; Dashed lines— $S = 50$; Red lines—Viscous LSE; Black lines—Inviscid LSE

with the “Viscous LSE” approach. At $M_\infty = 0.4$ the differences are negligible at both Strouhal numbers, but at $M_\infty = 0.8$ and $S = 50$ the two solutions are not even comparable. The latter case corresponds to the lowest ratio between the acoustic wave streamwise wavelength and the boundary layer thickness among all the different conditions analysed in Figs. 1 and 2. Therefore it is abundantly clear that viscosity, i.e. the presence of the boundary layer, affects the acoustic wave reflection and boundary layer signature.

In Figs. 3 and 4 we show how the reflection coefficient C_r varies with the angle of incidence Θ_i of the acoustic wave for different combinations of Strouhal and Mach number, and using both the “Viscous LSE” and the “Inviscid LSE” models. Note that the reflection coefficient is based on the acoustic wall-normal velocity \hat{v}_a rather than pressure, and that it is measured at $y^* = 3\delta_{99}^*$, where δ_{99}^* is the boundary layer thickness such that $\bar{U}(y^* = \delta_{99}^*) = 0.99$.

When using the LUBLE model there is an assumption that the acoustic waves reflect off a solid wall in a purely inviscid process. Consequently, the reflection coefficient is $C_r = -1$ ($\text{Arg}(C_r) = \pi$ rad., $|C_r| = 1$), which follows immediately from its definition and the far-field acoustic wave solution. The corresponding wall-pressure perturbation is $|\hat{p}_a(0)| = 2/M_\infty$. In the discussion that follows we will refer to this result as the “baseline” case.

We note that the amplitude of the reflection coefficient according to the “Inviscid LSE” is constant and equal to $|C_r| = 1$. The sole effect of the boundary layer is to cause a phase shift of the outgoing acoustic wave. The effects of viscosity, as seen from the difference between “Viscous LSE” and “Inviscid LSE” result, are mostly felt at the amplitude level and thus the reflected waves magnitude is generally reduced. At $M_\infty = 0.4$, for both Strouhal numbers and a relatively large variation of the incident angle, the reflection coefficient is very similar to that of the baseline case. Deviations appear at shallow incidences with respect to both the directions of downstream and upstream-travelling waves. Moreover, higher Strouhal numbers are associated with larger deviations over wider ranges of acoustic wave incident angles. The increase in Mach number has a similar effect, most notably in the amplitude of the reflected

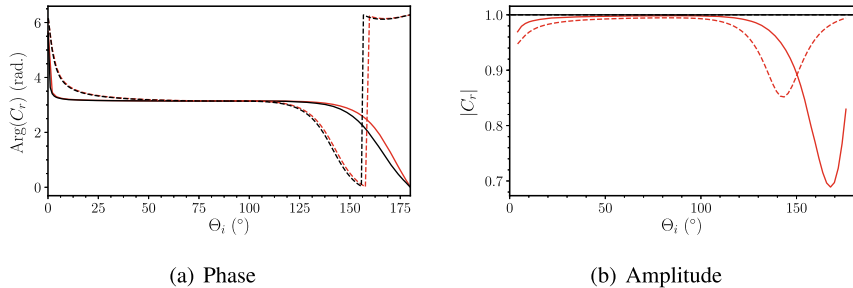


Fig. 4 Reflection coefficient variation with incident acoustic wave angle at fixed $M_\infty = 0.8$ and $R = 0.5 \times 10^6$. Solid lines— $S = 5$; Dashed lines— $S = 50$; Red lines—Viscous LSE; Black lines—Inviscid LSE

wave—which can be as low as approximately 70% of that of the incident wave for $M_\infty = 0.8$ and $S = 5$.

The approaches based on the LSE should be more accurate than the approach based on the LUBLE because they account for the boundary layer and for the effects of viscosity on the acoustic wave reflection. Mathematically, these models resolve the y -momentum equation, neglected in the boundary layer approach ($\partial \hat{p}_a / \partial y = 0$). On the other hand, we note that in the limits of $\Theta_i \rightarrow 0^\circ$ and $\Theta_i \rightarrow 180^\circ$ the predicted boundary layer acoustic signature by these models tends to vanish. This is most easily seen by considering the “Inviscid LSE” approach. The amplitude of the reflection coefficient is constant and equal to one and its phase tends towards zero in these limits. Meanwhile, the equivalent reflection coefficient based on the pressure perturbation is -1 which, through Eq. (10b), indicates that the total pressure perturbation in the far field is zero. Because the acoustic waves are then plane, the wall-normal velocity in the far field tends to vanish too. Consequently, the solution to the system of Eqs.(4) is the trivial solution. The decrease in the wall-pressure perturbation amplitude for large angles of incidence nearing 180° , as well as the corresponding trend of the reflection coefficient $C_r \rightarrow 1$, are in agreement with the theoretical study of [3], particularly with his Eqs. 3.55 and 3.56. It is also in agreement with the trends observed in the acoustic receptivity study of [5].

Nevertheless, these results seem to contradict the acoustic signature solution for downstream-travelling waves obtained by a number of other researchers through asymptotic methods, linear stability theory and DNS [3, 6, 12]. The reason Eqs. (4) do not support a non-trivial solution when forced by a plane acoustic wave ($\hat{v}_a(0) = 0$ and $\hat{v}_a(y_e) = 0$) is because the steady boundary layer forces a displacement effect causing a non-zero wall-normal velocity to appear which is incompatible with the plane acoustic wave solution in the far field. In general, the introduction of a reflected wave works to compensate for this effect which, in the particular case of $\Theta_i \rightarrow 0^\circ$ and $\Theta_i \rightarrow 180^\circ$, means that the “reflected” wave mirrors exactly the incident wave, resulting in zero total disturbances throughout the boundary layer. We would argue that this approach is invalid for very shallow angles of incidence with respect to

the upstream and downstream directions of propagation. This is essentially for two reasons: (i) in a finite-sized flat plate not all streamwise positions would “see” a reflected wave because the angle of incidence, and therefore of reflection, is too shallow; locally, the boundary layer is therefore not necessarily excited by the sum of these two waves; (ii) there is no guarantee that the parallel flow assumption holds when the incident acoustic wave travels within the boundary layer for a streamwise distance that is comparable with the characteristic boundary layer development length scale and with the acoustic waves streamwise wavelength; consequently, this undermines the assumption that the reflected wave exits the boundary layer at a **supplementary** angle (rather than “at a y angle”) (see Eq. (6)). A study of the domain of validity of the approaches based on the LSE would clearly be useful.

4 Conclusions

This research was motivated by the need to obtain accurate solutions of the acoustic boundary layer signature in order to predict acoustic receptivity in compressible boundary layer flows. The main limitation of the numerical LUBLE-based method in [11] is that it neglects wall-normal unsteady pressure variations which may be important when the acoustic wavelength is comparable to the boundary layer thickness. Such situations arise at near sonic Mach numbers, high frequencies and for near-upstream travelling waves. Consequently, an effort was made to assess limitations of the LUBLE-based approach and develop alternative models based on the forced linear stability equations (in the full viscous and inviscid limits). In their current form, the LSE-models are only applicable to flat plate geometries. The inviscid LSE-based method relies on a three-layer decomposition of the acoustic field that differs from the LUBLE-based method in that it accounts for the steady boundary layer effects over the inviscid wave-plate interaction. A comparison of the models showed that appreciable differences between the LSE-based and LUBLE-based results arise at high Mach numbers and for upstream-propagating waves. However, the fact that the LSE-based models breakdown for waves travelling parallel to the plate suggests that further investigations should be undertaken for shallow angles of incidence.

Acknowledgements This project has received funding from the European Union’s Horizon 2020 research and innovation programme under the Marie Skłodowska-Curie grant agreement no.675008.

References

1. Asfar, O.R., Masad, J.A., Nayfeh, A.H.: A method for calculating the stability of boundary layers. *Comput. Fluids* **18**(3), 305–315 (1990)
2. Balakumar, P., King, R.A., Chou, A., Owens, L.R., Kegerise, M.A.: Receptivity and forced response to acoustic disturbances in high-speed boundary layers. In: 46th AIAA Fluid Dynamics Conference. AIAA Paper 2016-3193 (2016)

3. Bernots, T.: Receptivity of the boundary layer in transonic flow past an aircraft wing. PhD thesis, Imperial College London (2014)
4. Brand, R.S., Nagel, R.T.: Reflection of sound by a boundary layer. *J. Sound Vib.* **85**(1), 31–38 (1982)
5. Choudhari, M.: Acoustic receptivity of compressible boundary layers: receptivity by way of surface-temperature variations. Technical Report NASA-CR-4599, NASA (1994)
6. De Tullio, N., Ruban, A.I.: A numerical evaluation of the asymptotic theory of receptivity for subsonic compressible boundary layers. *J. Fluid Mech.* **771**, 520–546 (2015)
7. Duck, P.W.: The response of a laminar boundary layer in supersonic flow to small-amplitude progressive waves. *J. Fluid Mech.* **219**, 423–448 (1990)
8. Gaponov, S.A.: Interaction between a supersonic boundary layer and acoustic disturbances. *Fluid Dynamics* **12**(6), 858–862 (1977)
9. Lees, L., Lin, C.C.: Investigation of the stability of the laminar boundary layer. Technical Report TN-1115, NACA (1946)
10. Mack, L.M.: Boundary layer linear stability theory. In: Special Course on Stability and Transition of Laminar Flow, number 709, pp. 3.1–3.81. AGARD Rep. 709 (1984)
11. Raposo, H., Mughal, S., Ashworth, R.: An adjoint compressible linearised Navier-Stokes approach to model generation of Tollmien-Schlichting waves by sound. *J. Fluid Mech.* **877**, 105–129 (2019)
12. Ruban, A.I.: On Tollmien-Schlichting wave generation by sound. In Kozlov, V.V. (Ed.) *Laminar-Turbulent Transition*, pp. 313–320. Springer, Berlin, Heidelberg (1985)
13. Scott, M.R., Watts, H.A.: Computational solution of linear two-point boundary value problems via orthonormalization. *SIAM J. Numer. Anal.* **14**(1), 40–70 (1977)

Receptivity of Unsteady Compressible Görtler Flows to Free-Stream Vortical Disturbances



Pierre Ricco and Samuele Viaro

Abstract The perturbations triggered by free-stream vortical disturbances in compressible boundary layers developing over concave surfaces are investigated by asymptotic methods and numerically. We utilize an asymptotic framework based on the limits of high Reynolds and Görtler numbers and solve the receptivity problem by integrating the initial-boundary value problem coupled with appropriate initial and boundary conditions, synthesizing the effect of the free-stream vortical disturbances. The conditions for which the Görtler vortices start to grow are revealed and we find that the Mach number is destabilizing when the spanwise diffusion is negligible and stabilizing when the boundary-layer thickness is comparable with the spanwise wavelength of the vortices. During the initial development of the vortices, only the receptivity calculations are accurate. At streamwise locations where the free-stream disturbances have fully decayed, the growth rate and wavelength are computed with sufficient accuracy by an eigenvalue method, although the correct amplitude and shape of the Görtler vortices can only be determined by the receptivity calculations. We find that Klebanoff modes always evolve from the leading edge, the Görtler vortices dominate when the influence of the curvature becomes significant, and highly-oblique Tollmien-Schlichting waves may precede the Görtler vortices for moderate Görtler numbers. We also obtain the neutral stability curves, i.e. curves that distinguish spatially growing from spatially decaying perturbations at different streamwise locations. For relatively high frequencies the triple-deck formalism allows us to confirm the numerical results of the negligible influence of the curvature on the Tollmien-Schlichting waves when the Görtler number is an order-one quantity. Experimental data for compressible Görtler flows are mapped onto our neutral-curve graphs and earlier theoretical results are compared with our predictions.

P. Ricco (✉) · S. Viaro

Department of Mechanical Engineering, The University of Sheffield, Sheffield, UK
e-mail: p.ricco@sheffield.ac.uk

S. Viaro

e-mail: samuele.viaro84@gmail.com

1 Introduction

In this paper we study compressible boundary layers that evolve over concave surfaces and are exposed to free-stream vortical disturbances. We focus on the importance of the receptivity approach for the computation of the boundary-layer disturbance dynamics and of the neutral stability curves, i.e. curves that distinguish the regions of growth and decay of the perturbations in the space of the flow parameters.

Unsteady Görtler (G) vortices are the main disturbances appearing within the boundary layer, although we also compute the evolution of thermal Klebanoff (K) modes and highly-oblique Tollmien-Schlichting (TS) waves. Görtler vortices are counter-rotating and streamwise-elongated disturbances, originating from an inviscid unbalance between pressure and centrifugal forces caused by the curvature of flow streamlines. Comprehensive reviews on Görtler flow have been published by [1] and [2]. Transition to turbulence caused by Görtler instability influences the performance of several technological applications, especially in the compressible regime. An important example is the high-speed flow in turbine engine intakes. It is therefore crucial to study the influence of free-stream disturbances to predict transition in these systems and to evince how the change of the flow regime from laminar to turbulent affects the performance of turbomachinery [3, 4]. Other examples of Görtler flows in the compressible regime include airfoils [5] and supersonic nozzles [6].

We combine the framework of [7] for incompressible flows over concave surfaces and the framework [8] for compressible Klebanoff modes over flat surfaces. We investigate the effect of the Görtler number, the frequency, and the Mach number, and the impact of the oblique Tollmien-Schlichting waves on the neutral curves. We confirm our numerical results by using the triple-deck theory to prove that the curvature does not influence the TS-wave instability at leading order and we conclude by mapping experimental data on our neutral-curve graphs and by comparing our predictions with earlier theoretical results. Further details can be found in our papers [9–11].

2 Mathematical and Numerical Procedures

2.1 Flow Definition, Scaling, and Equations of Motion

We consider a uniform compressible air flow of velocity U_∞^* and temperature T_∞^* past an adiabatic streamwise-concave plate with constant radius of curvature r^* . A kinematic and thermal boundary layer forms over the curved plate. Vortical disturbances are passively advected by the uniform free-stream flow and are modeled as three-dimensional gusts, which, away from the plate, have the form

$$\mathbf{u} - \mathbf{i} = \epsilon \hat{\mathbf{u}}^\infty e^{i(\mathbf{k} \cdot \mathbf{x} - k_x R t)} + \text{c.c.}, \quad (1)$$

where ϵ is a small parameter, $\mathbf{x} = \{x, y, z\}$ denotes the streamwise, wall-normal, and spanwise directions, $\mathbf{k} = \{k_x, k_y, k_z\}$ defines the wavenumber vector, $\hat{\mathbf{u}}^\infty = \{\hat{u}^\infty, \hat{v}^\infty, \hat{w}^\infty\}$ is the amplitude of the free-stream disturbance, c.c. indicates the complex conjugate, and \mathbf{i} is the unit vector of the streamwise direction. The vectors \mathbf{k} and $\hat{\mathbf{u}}^\infty$ satisfy the solenoidal condition $\mathbf{k} \cdot \hat{\mathbf{u}}^\infty = 0$. Lengths are scaled by $\Lambda_z^* = \lambda_z^*/2\pi$, where λ_z^* is the gust spanwise wavelength, velocities are scaled by U_∞^* , and the pressure is scaled by $\rho_\infty^* U_\infty^{*2}$, where ρ_∞^* is the free-stream air density. The Reynolds number is $R = U_\infty^* \Lambda_z^* / v_\infty^* \gg 1$, where v_∞^* is the kinematic viscosity of air in the free stream, the Görtler number is $G = R^2 \Lambda_z^* / r^* = \mathcal{O}(1)$, and the Mach number is $M = U_\infty^* / a_\infty^* = \mathcal{O}(1)$, where $a_\infty^* = (\gamma \mathcal{R}^* T_\infty^*)^{1/2}$ is the speed of sound in the free stream, $\mathcal{R}^* = 287.06 \text{ J kg}^{-1} \text{ K}^{-1}$ is the ideal gas constant for air, and $\gamma = 1.4$ is the ratio of specific heats. The scaled spanwise wavenumber is $k_z = 1$ and the frequency parameter is $\mathcal{F} = k_x R = 2\pi \Lambda_z^{*2} U_\infty^* / (\lambda_x^* v_\infty^*)$. We use the scaled streamwise coordinate $\hat{x} = x^* / (R \Lambda_z^*)$ and the scaled time variable $\hat{t} = U_\infty^* t^* / (R \Lambda_z^*)$ because low-frequency streamwise-elongated perturbations are dominant.

The boundary-layer velocity, pressure, and temperature $\mathbf{q}(\mathbf{x}, t) = \{u, v, w, p, \tau\}(\mathbf{x}, t)$ are decomposed into their mean $\mathbf{Q}(\mathbf{x})$ and perturbation $\mathbf{q}'(\mathbf{x}, t)$ as $\mathbf{q} = \mathbf{Q} + \epsilon \mathbf{q}'$. The mean flow $\mathbf{Q}(\mathbf{x})$ is the compressible Blasius boundary layer for which the Dorodnitsyn-Howarth transformation is used to scale its equations in similarity form. The independent variable is $\eta = \bar{Y} / (2\hat{x})^{1/2}$, where $\bar{Y}(\hat{x}, y) = \int_0^y [T(\hat{x}, \bar{y})]^{-1} d\bar{y}$ and the dynamic viscosity is $\mu(T) = T^\omega$, where $\omega = 0.76$. The constant Prandtl number is $Pr = 0.707$. In the limits $R \gg 1$, $\epsilon \ll R^{-1}$, and $k_x \ll 1$, the linearized unsteady boundary-region (LUBR) equations describe the perturbation flow when coupled with the initial and boundary conditions derived through asymptotic matching to synthesize the effect of the free-stream vortical disturbances [10, 12]. A second-order implicit finite-difference scheme is employed to solve the LUBR equations [8], which are parabolic along x . All the mathematical and numerical details can be found in [11]. The four flow parameters are M , G , k_y , and \mathcal{F} , accounting for the effects of compressibility, curvature, ratio of free-stream spanwise and wall-normal wavelengths, and frequency, respectively. As in [10] and [11], in low-frequency incompressible flows over concave surfaces and for realistic streamwise distances, TS-waves do not appear and the perturbations evolve as K-modes or G-vortices. However, for finite Mach number [8] showed that oblique first-mode TS-waves are triggered over a flat plate by a leading-edge receptivity mechanism. Therefore, in the presence of curvature, a low-frequency compressible boundary layer may be unstable due to K-modes, TS-waves, or G-vortices.

As in [9] and [11], the regions of instability are mapped by the parameters

$$\varsigma(\hat{x}) \equiv \frac{dE(\hat{x})}{d\hat{x}} \quad \text{and} \quad \beta(\hat{x}) \equiv \frac{d^2|\bar{u}(\hat{x})|_{\max}}{d\hat{x}^2}, \quad (2)$$

where $E(\hat{x}) \equiv \int_0^\infty |\bar{u}(\hat{x}, \eta)|^2 d\eta$ is the scaled perturbation energy divided by $(2\hat{x})^{1/2}$ [1] and $|\bar{u}(\hat{x})|_{\max} \equiv \max_\eta |\bar{u}(\hat{x}, \eta)|$ is the maximum along η of the streamwise-velocity amplitude as \bar{u} is dominant inside the boundary layer. The flow is unstable for $\varsigma > 0$

and stable for $\varsigma < 0$, with $\varsigma = 0$ defining the neutral points. The parameter β is instrumental in discriminating between perturbations that display an algebraic-type growth ($\beta < 0$, K-modes) and perturbations that display an exponential-type growth ($\beta > 0$, TS-waves or G-vortices). The condition $\beta < 0$ distinguishes the K-modes from the other perturbations only if it is used during the initial stage of the evolution because TS-waves and G-vortices may display a negative- β growth due to viscous attenuation, following an initial positive- β growth.

3 Results

3.1 Growth Rates

Figure 1 shows the comparison between the growth rate of a LUBR solution and an eigenvalue (EV) solution. The receptivity process selects the most unstable modes. The parallel and non-parallel EV formulations, studied in detail in [10], show the strongest disagreement with the receptivity LUBR solution closer to the leading edge, where the solution has not yet acquired a modal form. In this region, the non-parallel effects and the initial and free-stream boundary conditions therefore play a crucial role in the perturbation dynamics. In the limit $\hat{x} \rightarrow 0$ the EV solutions are invalid as the growth rate becomes negative. The agreement between the LUBR solution and the parallel EV solution is worse in the supersonic case than in the subsonic case. The use of the rigorous receptivity framework is thus essential to capture the correct

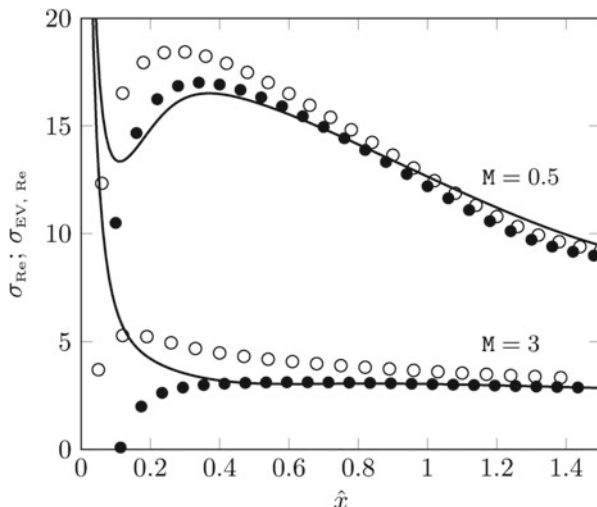


Fig. 1 Comparison between the LUBR $\sigma_{\text{Re}}(\hat{x}, \eta)$ (—) at $\eta = 2$, the non-parallel EV $\sigma_{\text{EV,Re}}(\hat{x})$ (●), and the parallel EV $\sigma_{\text{EV,Re}}(\hat{x})$ (○). Further discussion on the original figure can be found in [10]

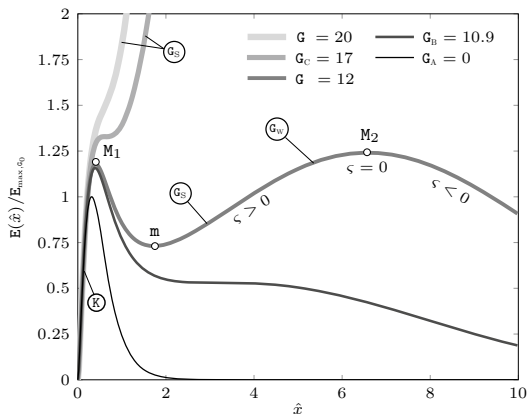
flow evolution. The disagreement is also documented by the velocity profiles, shown in Figs. 18 and 19 of [10]. Although the EV results match the receptivity results sufficiently downstream, the perturbation amplitude can only be computed through receptivity, while it has to be assigned arbitrarily in the EV cases.

3.2 Energy Growth

The energy $E(\hat{x})$ of incompressible K-vortices and Görtler vortices, normalized by the maximum value $E_{\max,G_0} \equiv \max_{\hat{x}} |E(\hat{x})|_{G=0}$ for $G = 0$, is shown in Fig. 2 as a function of \hat{x} for $\mathcal{F} = 0$ and $k_y = 2$.

Three critical Görtler numbers occur for this configuration, i.e., G_A , G_B , and G_C . In the flat-plate case, for which $G = G_A = 0$, only K-vortices are present. They start growing from the leading edge and then dissipate rapidly due to viscosity. As the curvature is introduced, the imbalance between pressure and centrifugal forces energizes the boundary-layer perturbation. Only for $G > G_B = 10.9$ the Görtler vortices become unstable as secondary growing disturbances after the viscous decay of the K-vortices and another maximum M_2 thus emerges. For $G = 12$, K-vortices represent the initial instability of the boundary layer and, after the viscous decay, the onset of the Görtler vortices causes the boundary layer to become unstable again at m . Their initial strong growth (G_S) shifts into a weak growth (G_W) at $\hat{x} = \hat{x}_G$ before ultimately stabilizing again at M_2 . In the range $G_B < G < G_C = 17$ both instabilities are thus present. For $G > G_C$ the K-vortices turn into Görtler vortices directly without the intermediate viscous decay. The neutral maps as functions of the flow parameters in the incompressible case are shown in Fig. 3 of [9].

Fig. 2 Perturbation energy $E(\hat{x})$ for $M = 0$ normalized by E_{\max,G_0} , the maximum value of E for $G = 0$, as a function of \hat{x} for $\mathcal{F} = 0$ and $k_y = 2$. Further discussion on the original figure can be found in [9]



3.3 Neutral Map

For $\mathcal{F} = 150$, $M = 3$, and $k_y = 1$, the neutral map shown in Fig. 3 reveals that the boundary layer can experience the three types of instability, i.e. the K-modes, the TS-waves, and the G-vortices. Since curvature effects are not at work near the leading edge [7] and \hat{x} is not large enough for the TS-wave receptivity mechanism studied by [8] to operate, only K-modes initially grow from the leading edge with $\beta < 0$ at any G due to the continuous free-stream forcing. The K-modes either stabilize downstream of the first encountered neutral line at $\hat{x} = \hat{x}_{s_0}$ or, for $G > G_{C_1} = 1792$, turn directly into G-vortices at $\hat{x} = \hat{x}_K$, indicated by the thick gray dotted line in Fig. 3. This zero- β line continues inside S_1 as G decreases (thin gray dotted line, $\hat{x} = \hat{x}_{\beta_0}$) and identifies the conditions for which the perturbation decay changes from strong to weak.

For the flat-plate case ($G = 0$), the only growing perturbations are the K-modes and the TS-waves. The K-modes start growing from the leading edge and dissipate rapidly due to viscous effects [12]. The combined influence of the frequency and the Mach number triggers the TS-waves at point A_1 , which display a second energy peak. For these flow conditions, the TS-waves are weaker than the K-modes and decay downstream of point A_2 , shown in Fig. 3. If the frequency or the Mach number increase, the oblique TS waves grow rapidly and the instability onset moves closer to the leading edge.

As the curvature is introduced, the imbalance between pressure and centrifugal forces energizes both the K-modes and the TS-waves, but for $G < G_B$ this is not sufficient to alter the zero-G pattern qualitatively, thus resulting in a boundary layer without G-vortices. The thin gray dashed line represents the zero- β streamwise location $\hat{x} = \hat{x}_{TS_s}$ where the TS_{CC} -waves shift from a strong growth ($TS_{CC,s}$, $\beta > 0$) to a weak growth ($TS_{CC,w}$, $\beta < 0$). The first growth with $\beta > 0$ downstream of S_1 has to be of the TS_{CC} -wave type because it evolves continuously from the flat plate scenario for which centrifugal effects are absent. The influence of G on the onset of the TS-waves is mild as the neutral lines are almost vertical.

For $G > G_B$, the centrifugal effects intensify and the perturbation starts growing again with $\beta > 0$ further downstream, i.e. the G-vortices appear. At $\hat{x} = \hat{x}_{TS_w}$ (thick gray dashed line), the strong-growth Görtler instability (G_s , $\beta > 0$) ensues from the weakly growing TS_{CC} -waves (TS_{CCw} , $\beta < 0$). Much further downstream at $\hat{x} = \hat{x}_G$ a weak G-vortex growth occurs (G_w , $\beta < 0$) and ultimately a stable boundary layer is computed downstream of $\hat{x} = \hat{x}_{s_0}$ (not shown). In the range $G_{C_2} < G < G_D$ the region of weak TS_{CC} -wave instability widens downstream. As the curvature increases, the G-vortices move closer to the leading edge and the region of weak TS_{CC} -waves shortens.

For $G > G_D = 1350$, the regime of weak TS_{CC} -wave growth disappears. The Görtler instability overcomes the weak negative- β TS_{CC} -wave growth and downstream of S_1 the perturbations always grow with $\beta > 0$. Therefore, for $G > G_D$ the pressure-centrifugal imbalance caused by the curvature is sufficiently intense for the perturbation to grow as G-vortices immediately downstream of the stable region. The three types of boundary-layer instability thus occur only in the range $G_B < G < G_D$.

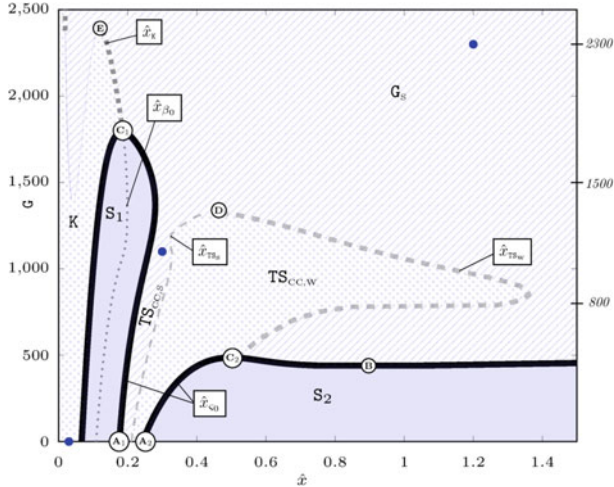


Fig. 3 Neutral stability curve, $\hat{x} = \hat{x}_{\zeta_0}$ (—), and regions of instability for $\mathcal{F} = 150$, $k_y = 1$, and $M = 3$. Further discussion on the original figure can be found in [11]

3.4 Asymptotic Analysis at Relatively High Frequency

We investigate the effect of curvature on the TS-waves generated by the receptivity mechanism first studied by [8]. We are motivated by the numerical result, shown in Fig. 3, of the negligible influence of curvature on stable region S_1 .

The Görtler terms, found in the y -momentum equation (2.11) of [10] and scaled here in the $(\bar{x} = k_x x, \eta)$ coordinate system for consistency with the receptivity analysis by [8], are

$$\frac{G}{(2\bar{x})^{1/2}} \left[2 F' \bar{u}(\bar{x}, \eta) - \frac{F'^2}{T} \bar{\tau}(\bar{x}, \eta) \right] \frac{\kappa}{k_z}, \quad (3)$$

where $G = \mathcal{O}(1)$, $\kappa = k_z \mathcal{F}^{-1/2}$, and $T(\eta)$ is the temperature of the mean flow. Extending [8]'s triple-deck analysis to flows over concave surfaces with $\kappa \ll 1$ and $G = \mathcal{O}(1)$, in the lower deck (subscript L) the Görtler terms (3) become

$$\frac{G}{(2\bar{x})^{1/2}} \left[2 F''(0) \eta_L \bar{u}_L - \frac{F''(0)^2}{T(0)} \eta_L^2 \bar{\tau}_L \kappa \right] \frac{\kappa^2}{k_z} \ll \frac{\partial \bar{p}_L}{\partial \eta_L} = \mathcal{O}(1), \quad (4)$$

in the main deck (subscript M) they become

$$\frac{G}{(2\bar{x})^{1/2}} \left(2 F' \bar{u}_M - \frac{F'^2}{T} \bar{\tau}_M \right) \frac{\kappa^{3/2}}{k_z} \ll \frac{\partial \bar{p}_M}{\partial \eta} = \mathcal{O}(1), \quad (5)$$

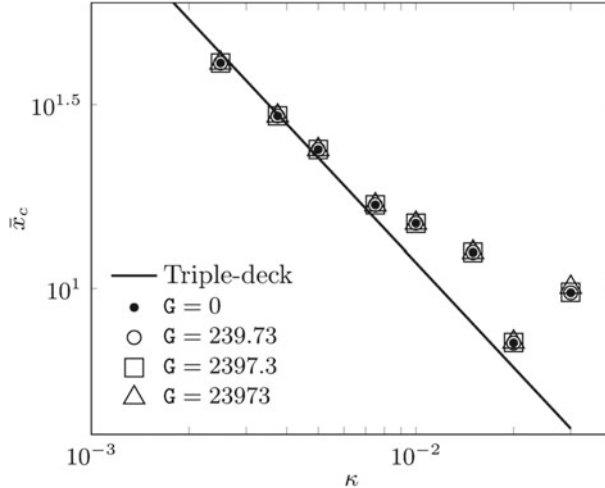


Fig. 4 Influence of the Görtler number on the streamwise location \bar{x}_c as a function κ for the triple-deck solution (continuous line) and the LUBR solution (symbols) for $M = 3$ and $k_y = 1$. Further discussion on the original figure can be found in [11]

and in the upper deck (subscript u) they are

$$\frac{2G\bar{u}_u}{(2\bar{x})^{1/2}} \frac{\kappa^2}{k_z} \ll \frac{\partial \bar{p}_u}{\partial \eta_u} = \mathcal{O}(1), \quad (6)$$

where the pressure terms in (4), (5), and (6) are of the same order of the other terms in the triple-deck y -momentum equations of [8]. The curvature terms can therefore be neglected at first order and the flat-plate dispersion relation for the streamwise wavenumber $\alpha_1(\bar{x})$ is recovered [8],

$$\int_{\eta_0}^{\infty} \text{Ai}(\check{\eta}) d\check{\eta} - (i\alpha_1)^{-1/3} \left[\frac{F''(0)}{(2x_1)^{1/2}} \right]^{5/3} \left[\frac{\mu(0)}{T(0)^7} \right]^{1/3} \text{Ai}'(\eta_0) = 0, \quad (7)$$

where $\text{Ai}(\eta)$ is the Airy function, $x_1 = \kappa\bar{x} = \mathcal{O}(1)$ is the scaled streamwise coordinate, and $\eta_0 = -[2iF''(0)\alpha_1 x_1 T(0)/\mu(0)]^{1/3}/[\alpha_1 F''(0)]$. Numerical integration of (7) gives the local growth rate, $\text{Im}(\alpha_1)$.

Figure 4 shows the critical streamwise location \bar{x}_c where the TS_{cc} -waves start to grow as a function of κ for different G values. Excellent agreement is obtained between the LUBR computation and the triple-deck theoretical solution, i.e. $\bar{x}_c = C\kappa^{-1}$. This comparison allows us to compute the proportionality constant, $C = 3.32$. The effect of the curvature only appears for $\kappa \geq 0.02$ and $G \geq 23973$, which is consistent with the analytical results valid for $\kappa \ll 1$ and $G = \mathcal{O}(1)$. This finding gives full support to the lines \hat{x}_{s_0} defining the stable region S_1 being nearly vertical

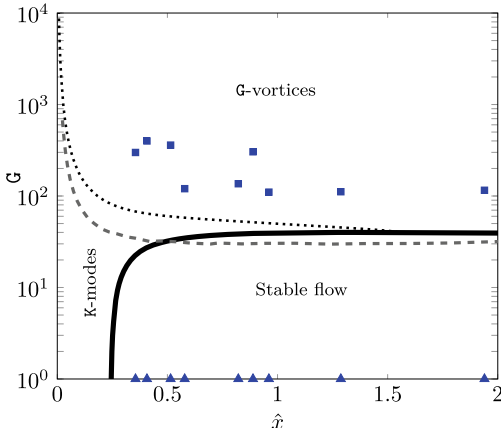


Fig. 5 Comparison of the LUBR neutral curve (—) at $\mathcal{F} = 0$, $k_y = 1$ with the neutral curves in [13] (---) for $M = 3$. Experimental data by [14] (■, ▲), and locations where the K-modes become G-vortices ($\hat{x} = \hat{x}_K$, ·····). Further discussion on the original figure can be found in [11]

for moderate G , as shown in Fig. 3. As the frequency increases, these lines become even more parallel to the ordinate axis and extend to higher G values, which confirms that TS-waves are not affected by the curvature when the frequency is sufficiently high. This also strengthens the argument that the perturbations downstream of the stable region S_1 can be classified as TS-waves for moderate G .

3.5 Comparison with Experimental and Theoretical Results

In Fig. 5, the neutral curves computed by the LUBR equations for $\mathcal{F} = 0$ and $k_y = 1$ are compared with neutral curves by other authors (dashed lines) for $M = 3$. The figure also shows the positions $\hat{x} = \hat{x}_K$ where the K-modes shift to G-vortices (dotted lines) and the streamwise locations and Görtler numbers of experimental data.

The neutral curve of [13] for $M = 3$ in Fig. 5 does not predict the algebraic growth from the leading edge, although the agreement with the LUBR solution improves as \hat{x} increases. The experimental data by [14] at supersonic conditions, corresponding to perturbations with a spanwise wavelength equal to 0.2 mm, fall in the unstable region and are thus classified as G-vortices. [14] also measured the perturbations at the same locations and flow conditions over a flat plate and no growing perturbations were detected. This also agrees with our calculations as these experimental points all lie in the stable zero-G region downstream of the K-mode growth.

4 Conclusions

The evolution of compressible Görtler vortices over streamwise-concave surfaces triggered by gust free-stream disturbances has been investigated. We have solved the boundary-region equations to study the receptivity of the base flow to free-stream vortical disturbances and have carried out a complete parametric study on the effects of frequency, Mach number, and Görtler number, focusing particularly on the growth rates and the neutral maps that identify the regions of disturbance growth and decay. Further details are found in our papers [9–11]. The key point is that both the initial conditions from the proximity of the leading edge and the outer free-stream boundary conditions are determined by the oncoming free-stream flow. Both conditions play a cardinal role in the development and growth of the Görtler vortices. The receptivity boundary-region solutions match the EV solutions sufficiently downstream, but it is only through the rigorous receptivity framework that the amplitude of the disturbances can be computed and linked to the amplitude of the free-stream perturbation. On the contrary, the EV formulation gives incorrect results not only near the leading edge, but also at locations comparable with the streamwise wavelength.

Acknowledgements We wish to acknowledge the financial support of the US Air Force through the AFOSR grant FA9550-15-1-0248 with Prof. Russell Cummings as the Program Officer. We also thank Dr Marvin E. Goldstein for the invaluable discussions about this research work.

References

1. Hall, P.: Görtler vortices in growing boundary layers: the leading edge receptivity problem, linear growth and the nonlinear breakdown stage. *Mathematika* **37**(74), 151–189 (1990)
2. Saric, W.: Görtler vortices. *Annu. Rev. Fluid Mech.* **26**(1), 379–409 (1994)
3. Mayle, R.: The role of laminar-turbulent transition in gas turbine engines. *J. Turbom.* **113**(4), 509–537 (1991)
4. Volino, R., Simon, T.: Bypass transition in boundary layers including curvature and favorable pressure gradient effects. *J. Turbomach.* **117**(1), 166–174 (1995)
5. Mangalam, S., Dagenhart, J., Hepner, T., Meyers, J.: The Görtler instability on an airfoil. AIAA Paper, pp. 85–0491 (1985)
6. Chen, F., Malik, M., Beckwith, I.: Görtler instability and supersonic quiet nozzle design. *AIAA J.* **30**(8), 2093–2094 (1992)
7. Wu, X., Zhao, D., Luo, J.: Excitation of steady and unsteady Görtler vortices by free-stream vortical disturbances. *J. Fluid Mech.* **682**, 66–100 (2011)
8. Ricco, P., Wu, X.: Response of a compressible laminar boundary layer to free-stream vortical disturbances. *J. Fluid Mech.* **587**, 97–138 (2007)
9. Viaro, S., Ricco, P.: Neutral stability curves of low-frequency Görtler flow generated by free-stream vortical disturbances. *J. Fluid Mech.* **845**, no. R1 (2018)
10. Viaro, S., Ricco, P.: Compressible unsteady Görtler vortices subject to free-stream vortical disturbances. *J. Fluid Mech.* **867**, 250–299 (2019)
11. Viaro, S., Ricco, P.: Neutral stability curves of compressible Görtler flow generated by low-frequency free-stream vortical disturbances. *J. Fluid Mech.* **876**, 1146–1157 (2019)

12. Leib, S., Wundrow, D., Goldstein, M.: Effect of free-stream turbulence and other vortical disturbances on a laminar boundary layer. *J. Fluid Mech.* **380**, 169–203 (1999)
13. El-Hady, N., Verma, A.: Growth of Görtler vortices in compressible boundary layers along curved surfaces. *J. Eng. Appl. Sci.* **2**(3), 213–238 (1983)
14. Ciolkosz, L., Spina, E.: An experimental study of Görtler vortices in compressible flow. AIAA Paper **4512**, 1–21 (2006)

Leading-Edge Receptivity of Moderately Supersonic Boundary Layers to Free-Stream Disturbances



Pierre Ricco and M. E. Goldstein

Abstract We study the receptivity and resulting global instability of boundary layers due to free-stream vortical and acoustic disturbances at moderately supersonic Mach numbers. The vortical disturbances produce an unsteady boundary layer flow that develops into oblique instability waves with a viscous triple-deck structure in the downstream region. The boundary layer fluctuations produced by the acoustic disturbances evolve into oblique normal modes in a region that lies downstream of the viscous triple-deck region but will still be fairly close to the leading edge when the phase speed of these disturbances is small compared to the free-stream velocity. We use asymptotic analysis to show that both the vortically and small phase speed acoustically-generated disturbances ultimately develop into modified Rayleigh modes that can exhibit spatial growth or decay depending on the nature of the receptivity process.

1 Introduction

We are concerned with the effect of unsteady free-stream disturbances on laminar to turbulent transition in supersonic boundary layer flows. For low free-stream disturbances levels (say less than 1%) the transition usually results from a series of events beginning with the so-called receptivity process that refers to the generation of spatially growing instability waves by acoustic and/or vortical disturbances in the free-stream. The most fundamental receptivity mechanism arguably results from the nonparallel leading edge flow and the focus here is, therefore, on that case.

For incompressible flows, Goldstein [1] showed that there is an overlap domain where appropriate asymptotic solutions to the forced boundary layer equations match onto the so-called Tollmien-Schlichting (TS) waves that satisfy the Orr-Sommerfeld

P. Ricco (✉) · M. E. Goldstein

Department of Mechanical Engineering, The University of Sheffield, Sheffield, UK
e-mail: p.ricco@sheffield.ac.uk

M. E. Goldstein

e-mail: m.e.g@oh.rr.com

equation further downstream. Ricco and Wu [2] extended the analysis of Goldstein [1] to subsonic and supersonic boundary layers and showed that the coupling is more intense in supersonic flows and that the instability can either be of the viscous TS type or of the purely inviscid Rayleigh type when the mean boundary layer flow has a generalized inflection point. The coupling mechanism can be of the viscous type considered in [3] or of the inviscid type considered by Fedorov and Khokhlov [4]. The latter mechanism tends to be dominant when the flow is hypersonic and the obliqueness angle θ of the disturbance differs from the critical angle $\theta_c = \cos^{-1}(M_\infty^{-1})$ by an $\mathcal{O}(1)$ amount [4] (M_∞ is the free-stream Mach number).

Reference [3] shows that the instability occurs too far downstream to be of practical interest at the moderately supersonic Mach numbers being considered here when $\Delta\theta = 0(1)$ but can occur much further upstream when $\Delta\theta$ is sufficiently small. Figure 1 shows that the theoretical results of Fedorov and Khokhlov [4] are in good agreement with experimental data when $\Delta\theta = \theta_c - \theta = \mathcal{O}(1)$ but the agreement breaks down when $\theta \rightarrow \theta_c$. Reference [3] extended that analysis to small values of $\Delta\theta$ and showed that the instability can occur much further upstream when $\Delta\theta$ is sufficiently small. But there is a smallest value of $\Delta\theta$ for which the instability wave coupling can occur.

Smith [5] showed that viscous instabilities exhibiting the same triple-deck structure as the subsonic TS waves can also occur at supersonic speeds when the obliqueness angle θ is larger than the critical angle θ_c . But their phase speeds are very small and they must therefore be produced by a viscous wall layer mechanism identified in [1]. It therefore makes sense to treat both the viscous and the small- $\Delta\theta$ inviscid mechanisms at the moderately supersonic Mach number considered here. Further details can be found in [3, 6].

2 Free-Stream Disturbances

Since the boundary layer is believed to be convectively unstable, the receptivity phenomena are best illustrated by considering a small amplitude harmonic distortion with angular frequency ω^* superimposed on a moderately supersonic Mach number flow of an ideal gas past an infinitely thin flat plate with uniform free-stream velocity U_∞^* , temperature T_∞^* , dynamic viscosity μ_∞^* and density ρ_∞^* . The velocities, pressure fluctuations, temperature and dynamic viscosity are normalized by U_∞^* , $\rho_\infty^* U_\infty^*$, T_∞^* , and μ_∞^* , respectively. The time t is scaled by ω^* and the Cartesian coordinates x , y , and z are scaled by $L = U_\infty^*/\omega$ with x being in the meanflow direction and y being normal to the plate.

We require that the Reynolds number $Re = \rho^* U_\infty^* L^* / \mu_\infty^*$ be large or, equivalently, that the frequency parameter $\mathcal{F} = Re^{-1}$ be small, and we use asymptotic theory to explain how the imposed harmonic distortion generates oblique instabilities at large downstream distances in the viscous boundary layer that forms on the surface of the flat plate. The expansion parameter is taken to be $\epsilon = \mathcal{F}^{-1/6}$. The free-stream disturbances will be inviscid at the lowest order of approximation and

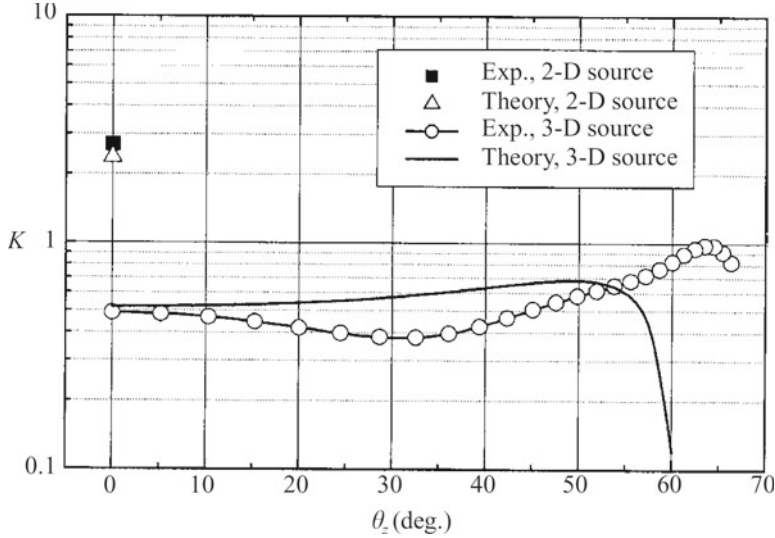


Fig. 1 Comparison of the Fedorov/Khokhlov solution with experimental data [7]

can be decomposed into an acoustic component that carries no vorticity, and vortical and entropic components that produce no pressure fluctuations. But only the first two will be considered here.

The vortical velocity \mathbf{u}_v is given by

$$\mathbf{u}_v = \{u_v, v_v, w_v\} = \hat{\delta}\{u_\infty, v_\infty, w_\infty\} \exp[i(x - t + \gamma y + \beta z)], \quad (1)$$

where $\hat{\delta} \ll 1$ and $u_\infty, v_\infty, w_\infty$ satisfy the continuity condition

$$u_\infty + \gamma v_\infty + \beta w_\infty = 0 \quad (2)$$

but are otherwise arbitrary constants while the acoustic component is governed by the linear wave equation which has a fundamental plane wave solution

$$\{\mathbf{u}_a, p_a\} = \{u_a, v_a, w_a, p_a\} = \frac{\hat{\delta} p_\infty}{1 - \alpha} \{\alpha, \gamma, \beta, 1 - \alpha\} \exp[i(\alpha x + \gamma y + \beta z - t)], \quad (3)$$

for the velocity and pressure perturbations. More details are found in §2 of [3].

3 Boundary Layer Disturbances Generated by Free-Stream Vorticity

We begin by considering the fluctuations imposed on the boundary layer by the free-stream vortical disturbance. These disturbances will generate oblique TS instability waves which are known to exhibit a triple-deck structure in the vicinity of their lower branch which lies at an $\mathcal{O}(\epsilon^{-2})$ distance downstream of the leading edge in the high Reynolds number flow being considered here. They will have $\mathcal{O}(\epsilon^{-1})$ spanwise wavenumbers and we therefore require that

$$\bar{\beta} \equiv \epsilon\beta = \mathcal{O}(1) \quad (4)$$

since the spanwise wavenumber is assumed to remain constant as the disturbances propagate downstream. The continuity condition (2) and the obliqueness restriction $v_\infty/w_\infty \ll 1$ will be satisfied if we put

$$\bar{w}_\infty \equiv \frac{w_\infty}{\epsilon} = \mathcal{O}(1), \bar{v}_\infty \equiv \frac{v_\infty}{\epsilon} = \mathcal{O}(1), \bar{\gamma} \equiv \epsilon\gamma = \mathcal{O}(1). \quad (5)$$

The vortical velocity (1) will then interact with the plate to produce an inviscid velocity field that generates a slip velocity at the surface of the plate which must be brought to zero in a thin viscous boundary layer whose temperature, density and streamwise velocity, say $T(\eta)$, $\rho(\eta)$, $U(\eta)$ respectively, are assumed to be functions of the Dorodnitsyn-Howarth variable

$$\eta \equiv \frac{1}{\epsilon^3 \sqrt{2x}} \int_0^y \rho(x, \tilde{y}) dy \quad (6)$$

and are determined from the similarity equations given in Stewartson [8].

We begin by considering the flow in the vicinity of the leading edge where the streamwise length scale corresponds to $x = \mathcal{O}(1)$. Since the inviscid velocity field can only depend on the streamwise coordinate through this relatively long streamwise length scale the solution for the velocity and temperature perturbation $\{u, v, w, \vartheta\}$ in this region of the boundary layer is given by [2]

$$\{u, v, w, \vartheta\} = \left\{ F'(\eta), \frac{\epsilon^3 T}{\sqrt{2x}} (\eta_c F' - F), 0, T \right\} + \tilde{\delta} \left\{ \bar{u}_0(x, \eta), \epsilon^3 \sqrt{2x} \bar{v}_0(x, \eta), \epsilon \bar{w}_0(x, \eta), \bar{\vartheta}_0(x, \eta) \right\} e^{i(\bar{\beta}z/\epsilon - t)}, \quad (7)$$

where $\eta_c \equiv T(\eta)^{-1} \int_0^\eta T(\tilde{\eta}) d\tilde{\eta}$.

The vector $\{\bar{u}_0(x, \eta), \epsilon^3 \sqrt{2x} \bar{v}_0(x, \eta), \epsilon \bar{w}_0(x, \eta), \bar{\vartheta}_0(x, \eta)\}$ is determined by the linearized boundary layer equations and $\{\bar{u}_0, \bar{v}_0, \bar{w}_0, \bar{\vartheta}_0\}$ can be divided into the following two components [9]

$$\{\bar{u}_0, \bar{v}_0, \bar{w}_0, \bar{\vartheta}_0\} = \bar{u}_\infty \{\bar{u}, \bar{v}, 0, \bar{\vartheta}\} + i\bar{\beta} (\bar{w}_\infty + i\bar{v}_\infty) \left\{ \bar{u}^{(0)}, \bar{v}^{(0)}, -i\bar{w}^{(0)}/\bar{\beta}, \bar{\vartheta}^{(0)} \right\}, \quad (8)$$

where $\{\bar{u}^{(0)}, \bar{v}^{(0)}, \bar{w}^{(0)}, \bar{\vartheta}^{(0)}\}$ satisfy the three-dimensional compressible linearized boundary layer equations subject to the boundary conditions [2]

$$\bar{u}^{(0)} \rightarrow 0, \quad \bar{w}^{(0)} \rightarrow e^{ix}, \quad \bar{\vartheta}^{(0)} \rightarrow 0 \quad \text{as } \eta \rightarrow \infty, \quad (9)$$

while the two-dimensional solution $\{\bar{u}, \bar{v}, 0, \bar{\vartheta}\}$ satisfies the two-dimensional linearized boundary layer equations. The downstream asymptotic solutions to the boundary-layer equations are discussed in detail in [3, 6]. A key point is that it is only necessary to consider the lowest-order asymptotic mode because that is the only one that matches onto a spatially growing oblique TS wave further downstream. The receptivity problem can then be solved by combining the numerical boundary layer solutions with appropriate matched asymptotic expansions to relate the instability wave amplitude to that of the free-stream disturbance.

4 Boundary Layer Disturbances Generated by the Fedorov/Khokhlov Mechanism at Near Critical Obliqueness Angles

Fedorov and Khokhlov [4], whose focus was on hypersonic flows, analyzed the generation of Mack mode instabilities in flat plate boundary layers by oblique acoustic waves of the form (3) where the incidence angle γ is equal to zero. They showed that diffraction of the slow acoustic wave by the nonparallel mean boundary layer flow can produce a first Mack mode instability in the downstream region where $x = \mathcal{O}(\epsilon^{-6})$ when its obliqueness angle θ is less than the critical angle $\cos^{-1}(M_\infty^{-1})$ and the deviation $\Delta\theta = \theta_c - \theta$ is $\mathcal{O}(1)$.

But as noted in the introduction the instability emerges too far downstream to be of practical interest when scaled up to actual flight conditions at the low supersonic Mach numbers being considered here. It will however emerge much further upstream when $\Delta\theta \ll 1$. Reference [3] extended the result of Fedorov and Khokhlov [4] to the small- $\Delta\theta$ regime and showed that

$$\beta = \beta_1 = \frac{\tilde{\beta}}{\Delta\theta}, \quad \alpha = \frac{\tilde{\alpha}}{\Delta\theta} + \tilde{\alpha}_1 + \dots, \quad (10)$$

where $\tilde{\alpha}, \tilde{\beta}, \tilde{\alpha}_1 = \mathcal{O}(1)$ and $\Delta\theta \ll 1$, which means that α and β become large when $\Delta\theta \rightarrow 0$. Reference [3] also shows that the relevant solution has a triple-deck structure: an outer diffraction region and a viscous wall layer in which the unsteady, convective and viscous terms all balance and a main boundary layer region where the solution is of the form

$$\{u, v, w, \vartheta, p\} = \{1, 0, 0, 1, 1\} + \hat{\delta} \left\{ u_2(x_2, y_2), \epsilon^{3/2} v_2(x_2, y_2), w_2(x_2, y_2), \vartheta_2(x_2, y_2), p_2(x_2) \right\} \exp \left\{ i \left[\left(\frac{\tilde{\alpha}}{\Delta\theta} + \tilde{\alpha}_1 \right) x + \frac{\tilde{\beta}z}{\Delta\theta} - t \right] \right\}, \quad (11)$$

where

$$x_2 \equiv x\epsilon^3 = \mathcal{O}(1), \quad y_2 \equiv y\epsilon^{3/2} = \mathcal{O}(1) \quad (12)$$

and the surface pressure $p_2(x_2)$ behaves like

$$p_2(\tilde{x}_2) \sim \exp \left[\gamma_0^2 \pi \left(\tilde{x}_2 \right)^2 \right] \quad \text{as } \tilde{x}_2 \rightarrow \infty, \quad (13)$$

where

$$\gamma_0 \equiv \frac{\tilde{x}_2 (\tilde{\alpha}^2 + \tilde{\beta}^2) \tilde{\alpha}^{1/2} T_w^2}{\lambda \sqrt{2\pi i (M_\infty^2 - 1)}}. \quad (14)$$

The acoustically and vortically generated boundary layer disturbance considered in this section eventually evolve into propagating eigensolutions in regions that lie further downstream. The resulting flow will have a triple-deck structure of the type considered in [2, 5, 10] in the former (i.e. vortically generated) case. But the acoustically generated disturbance will only develop an eigensolution structure in a region that lies much further downstream. This region will be closest to the leading edge when $\Delta\theta = \mathcal{O}(\epsilon^{2/3})$. We begin by considering the triple-deck region.

5 The Viscous Triple-Deck Region

As shown by [2, 5, 10] the linearized Navier-Stokes equations possess an eigensolution of the form

$$\{u, v, w, p\} = \hat{\delta} \Phi(y, \epsilon) \exp \left\{ i \left[\frac{1}{\epsilon^3} \int_0^{x_1} \kappa(x_1, \epsilon) dx_1 + \bar{\beta}\bar{z} - t \right] \right\} \quad (15)$$

in the triple-deck region where

$$x_1 \equiv \epsilon^2 x = \mathcal{O}(1) \quad (16)$$

and $\bar{z} \equiv z/\epsilon = z^* \omega^*/(\epsilon U_\infty^*)$ is a scaled transverse coordinate. As noted in [1], κ has the expansion $\kappa(x_1, \epsilon) = \kappa_0(x_1) + \epsilon \kappa_1(x_1) + \epsilon^2 \kappa_2(x_1) + \dots$, where the lowest order term in this expansion satisfies the following dispersion relation

$$\kappa_0^2 + \bar{\beta}^2 = \frac{1}{(i\kappa_0)^{1/3}} \left(\frac{\lambda}{\sqrt{2x_1}} \right)^{5/3} \left(\frac{\mu_w}{T_w^7} \right)^{1/3} \frac{\left[\bar{\beta}^2 - (M_\infty^2 - 1) \kappa_0^2 \right]^{1/2} \text{Ai}'(\xi_0)}{\int_{\xi_0}^\infty \text{Ai}(q) dq} \quad (17)$$

and

$$\xi_0 = -i^{1/3} \left(\frac{\sqrt{2x_1}}{\kappa_0 \lambda} \right)^{2/3} \left(\frac{T_w}{\mu_w} \right)^{1/3}, \quad (18)$$

which is easily obtained by rewriting Eq. (5.2) of [2] or Eq. (3.17) of [10] in the present notation. The solution must satisfy the inequality $\Re \left\{ \left[\bar{\beta}^2 - (M_\infty^2 - 1) \kappa_0^2 \right]^{1/2} \right\} \geq 0$ in order to exclude solutions exhibiting unphysical wall-normal exponential growth.

This requirement will be satisfied for all $M_\infty < 1$ but will only be satisfied at supersonic Mach numbers when the obliqueness angle θ is greater than the critical angle $\theta_c = \cos^{-1}(M_\infty^{-1})$. Equations (17) and (18) can be satisfied at small values of x_1 if $\kappa_0 \sim \sqrt{x_1}$ and $\xi_0 \rightarrow \zeta_n$ for $n = 0, 1, 2, \dots$ as $x_1 \rightarrow 0$ where ζ_n is the nth root of

$$\text{Ai}'(\zeta_n) = 0 \quad \text{for } n = 0, 1, 2, 3, \dots, \quad (19)$$

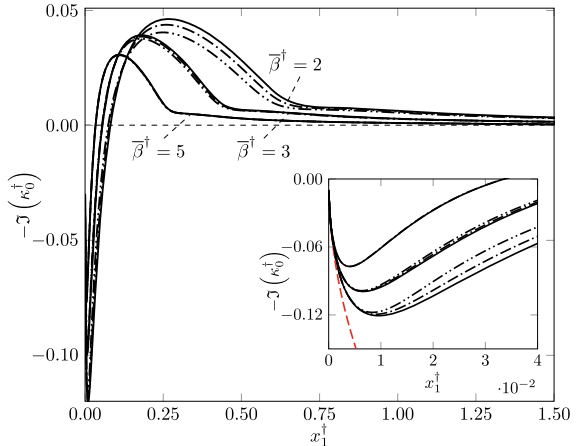
as discussed in [3]. Inserting these expressions of κ_0 and ξ_0 into (17) shows that $\kappa_0 \rightarrow (2T_w x_1 / i \mu_w)^{1/2} / \lambda \zeta_n^{3/2}$ as $x_1 \rightarrow 0$, which, as shown in [2, 3], matches onto the downstream asymptotic limit of the boundary layer solution.

5.1 Numerical Results

The dispersion relation (17), which determines the complex wavenumber of the triple-deck instabilities, is expected to have at least one root corresponding to each of the infinitely many roots of the Lam-Rott dispersion relation (19), as discussed in [3]. But only the lowest order $n = 0$ root can produce the spatially growing modes of (17). The wall temperature T_w and viscosity μ_w can be scaled out of this equation by introducing the rescaled variables $\kappa_0^\dagger = \kappa_0 T_w^{1/2} \mu_w^{1/6}$, $x_1^\dagger = x_1 T_w^2 / \mu_w^{2/3}$, $\bar{\beta}^\dagger = \bar{\beta} T_w^{1/2} \mu_w^{1/6}$.

Figure 2 are plots of the negative imaginary parts of the scaled wavenumber κ_0^\dagger as a function of the scaled streamwise coordinate \bar{x}_1^\dagger calculated from (17) for $M_\infty = 2, 3, 4$ and three values of the frequency scaled transverse wavenumber $\bar{\beta}^\dagger \geq 2$. The inset is included to more clearly show the changes at small \bar{x}_1^\dagger . The red dashed curves in the inset denote the imaginary parts of the small- \bar{x}_1^\dagger asymptotic formula found at the end of §5. The composite Lam-Rott triple-deck eigensolution can undergo a significant amount of damping before it turns into a spatially growing instability wave at the lower branch with the amount of damping determined by the upstream behavior of the triple-deck solution (15) since this solution actually contains the Lam-Rott solution as an upstream limit. The inset in Fig. 2 is particularly relevant because it shows that the length $\Delta x_1^\dagger = 0.01$ of this upstream region is very short and

Fig. 2 $-\Im(\kappa_0^\dagger)$ as a function of the scaled streamwise coordinate x_1^\dagger calculated from the dispersion relation (17) together with the asymptotic initial condition found at the end of §5 for $M_\infty = 2, 3, 4$ (double dot dashed, dot dashed, and solid lines, respectively) and three values of the scaled transverse wavenumber $\bar{\beta}^\dagger \geq 2$



therefore that the damping is relatively small in the supersonic case being considered here. The leading edge receptivity mechanism is therefore expected to be much more efficient than in the incompressible case considered in [1].

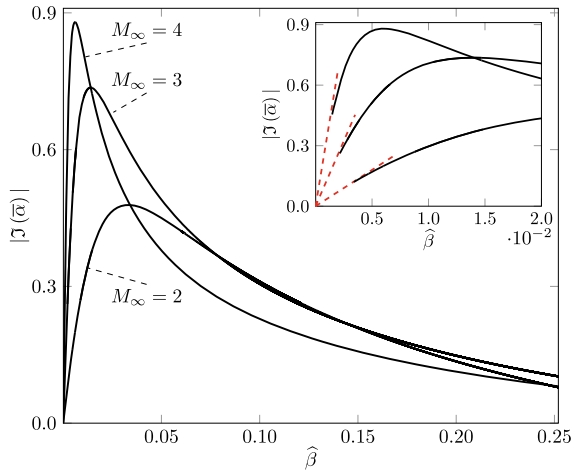
6 The Inviscid Triple-Deck Region

The acoustically driven solution will only match onto an eigensolution in a region that lies downstream of the viscous triple-deck region considered above and will have an inviscid structure. The relevant dispersion relation is given by

$$\bar{\kappa}_0^2 + \bar{\beta}^2 = \frac{\lambda \left[\bar{\beta}^2 - (M_\infty^2 - 1) \bar{\kappa}_0^2 \right]^{1/2}}{\bar{\kappa}_0 \sqrt{2\hat{x}_1} T_w^2} \quad (20)$$

where the square root $\left[\bar{\beta}^2 - (M_\infty^2 - 1) \bar{\kappa}_0^2 \right]^{1/2}$ is required to remain finite as $\epsilon \rightarrow 0$. Our papers [3, 6] show that the lowest order wave number κ_0 is purely real, which means that exponential growth (if it occurs) can only occur at higher order. The key result is that the acoustically generated instabilities will be less significant than the vortically-generated instabilities that are generated upstream.

Fig. 3 $|\Im(\bar{\alpha})|$ versus $\hat{\beta}$ calculated from the reduced Rayleigh solution. The dashed lines in the inset are $|\Im(\bar{\alpha})| = C\hat{\beta}$, where the following values for the scale factor C were obtained by optimizing the fit to the computations: $C=36$ for $M_\infty=2$, $C=129.4$ for $M_\infty=3$, and $C=340.1$ for $M_\infty=4$



7 Next Stage of Evolution

References [3, 6] also show that the viscous and the inviscid triple-deck solutions both evolve into reduced Rayleigh modes further downstream. The wall-normal velocity component satisfies the reduced Rayleigh equation

$$\frac{d}{d\eta} \left(\frac{1}{T^2} \frac{d\bar{v}}{d\eta} \right) + \left[\frac{\bar{\alpha}}{1 - \bar{\alpha}U} \left(\frac{U'}{T^2} \right)' - \left(\bar{\beta}\sqrt{2\bar{x}_1} \right)^2 \right] \bar{v} = \mathcal{O}(\epsilon^{2(1-r)}) , \quad (21)$$

and the following boundary conditions

$$\bar{v} \sim e^{-\bar{\beta}\bar{y}} \quad \text{for } \bar{y} \rightarrow \infty \quad \text{and} \quad \bar{v} = 0 \quad \text{at } \bar{y} = 0 . \quad (22)$$

Figure 3 shows the downstream evolution of the growth rate at different Mach numbers. The red dashed lines demonstrate how the Rayleigh solutions match the triple-deck solutions as the leading edge is approached.

8 Conclusions

This paper uses high Reynolds number asymptotics to study the nonlocal behavior of boundary layer instabilities generated by small amplitude free-stream disturbances at moderately supersonic Mach numbers. The appropriate small expansion parameter turns out to be $\epsilon = \mathcal{F}^{-1/6}$, where \mathcal{F} denotes the frequency parameter. The oblique first Mack mode instabilities generated by free-stream acoustic disturbances are compared with those generated by elongated vortical disturbances. The focus is on

explaining the relevant physics and not on obtaining accurate numerical predictions. The free-stream vortical disturbances generate unsteady flows in the leading edge region that produce short spanwise wavelength instabilities in a viscous triple-deck region which lies at an $\mathcal{O}(\epsilon^{-2})$ distance downstream from the leading edge. The mechanism was first considered for two-dimensional incompressible flows in reference [1], but the instability onset occurs much further upstream in the supersonic case and is, therefore, much more likely to be important at the higher Mach numbers considered in this paper. The lowest order triple-deck solution does not possess an upper branch and evolves into an inviscid first Mack mode instability with short spanwise wavelength at an $\mathcal{O}(\epsilon^{-4})$ distance downstream. Fedorov and Khokhlov [4] used asymptotic methods to study the generation of inviscid instabilities in supersonic boundary layers by fast and slow acoustic disturbances in the free stream whose obliqueness angle θ deviated from its critical value by an $\mathcal{O}(1)$ amount and showed that slow acoustic disturbances generate unsteady boundary layer disturbances that produce $\mathcal{O}(1)$ spanwise wavelength inviscid first Mack mode instabilities at a much larger $\mathcal{O}(\epsilon^{-6})$ distance downstream. But the calculations in our paper [3] show that the physical streamwise distance $x^*(U_\infty^*)^3/(\omega^*)^2 v_\infty^*$ corresponding to this scaled downstream location is at least equal to about 7 m for the typical supersonic flight conditions at $M_\infty = 3$ ($U_\infty^* = 800$, $v_\infty^* = 0.000264 \text{m}^2/\text{s}$) and an altitude of 20 km with an upper bound of 100 kHz for the characteristic frequency. This means that this instability occurs too far downstream to be of any practical interest at the moderately low supersonic Mach numbers considered here. But, the inviscid instability, which first appears at an $\mathcal{O}(\epsilon^{-(4+2/3)})$ distance downstream when $\Delta\theta$ is reduced to $\mathcal{O}(\epsilon^{-(4+2/3)})$ can be significant when scaled to flight conditions. We therefore compared the vortically-generated instabilities with the instabilities generated by oblique acoustic disturbances with obliqueness angles in this range.

Acknowledgements PR acknowledges the financial support by the Air Force Office of Scientific Research Grant FA9550-15-1-0248 with Prof. R. Cummings as Program Officer.

References

1. Goldstein, M.: The evolution of Tollmien-Schlichting waves near a leading edge. *J. Fluid Mech.* **127**, 59–81 (1983)
2. Ricco, P., Wu, X.: Response of a compressible laminar boundary layer to free-stream vortical disturbances. *J. Fluid Mech.* **587**, 97–138 (2007)
3. Goldstein, M., Ricco, P.: Non-localized instabilities resulting from leading-edge receptivity at moderate supersonic mach numbers. *J. Fluid Mech.* **838**, 435–477 (2018)
4. Fedorov, A., Khokhlov, A.: Excitation of unstable modes in a supersonic boundary layer by acoustic waves. *Fluid Dynamics* **26**(4), 531–537 (1991)
5. Smith, F.: On the first-mode instability in subsonic, supersonic or hypersonic boundary layers. *J. Fluid Mech.* **198**, 127–153 (1989)
6. Goldstein, M., Ricco, P.: Leading edge receptivity at subsonic and moderately supersonic mach numbers. In *Boundary Layer Flows-Theory. Applications and Numerical Methods*, IntechOpen (2019)

7. Fedorov, A.: Receptivity of a high-speed boundary layer to acoustic disturbances. *J. Fluid Mech.* **491**, 101–129 (2003)
8. Stewartson, K.: The theory of laminar boundary layers in compressible fluids. Clarendon Press, Oxford (1964)
9. Gulyaev, A., Kozlov, V., Kuzenetsov, V., Mineev, B., Sekundov, A.: Interaction of a laminar boundary layer with external turbulence. *Fluid Dynamics*. Translated from Izv, Akad. Nauk. SSSR Mekh. Zhid. Gaza 6, vol. 5, pp. 55–65., vol. 24, no. 5, pp. 700–710, 1989
10. Wu, X.: Generation of Tollmien-Schlichting waves by convecting gusts interacting with sound. *J. Fluid Mech.* **397**, 285–316 (1999)

Direct Numerical Simulations of Tollmien-Schlichting Disturbances in the Presence of Surface Irregularities



Francesco Tocci, Guillaume Chauvat, Stefan Hein, and Ardeshir Hanifi

Abstract A realistic aircraft wing is not expected to be an ideally smooth surface: the influence of junctions or wing panels must be taken into account in the laminar wing design. The presence of these spanwise invariant two-dimensional surface irregularities further amplifies the boundary-layer streamwise instabilities existing on a smooth surface, potentially causing an early transition to turbulence. In the present work, the effect of steps, gaps and humps on the development of Tollmien-Schlichting (TS) waves in an incompressible boundary layer is studied using direct numerical simulations (DNS). For a specific height we investigated several shapes of the geometric irregularity. Depending on their shape the surface imperfections give rise to a local separation bubble which interacts with the oncoming TS waves: for the frequency considered, all the surface irregularities have a destabilizing effect, with the rectangular hump case being the most dangerous one.

1 Introduction

Besides being a fundamental question of fluid mechanics, laminar-turbulent transition prediction has a wide range of engineering applications. Transition has a strong impact on skin-friction drag and heat transfer, therefore is of considerable interest in the aerodynamic design. Maintaining the laminar flow on wings at a chord Reynolds number beyond what is usually transitional or turbulent allows a strong decrease in friction drag. Laminar Flow Control (LFC), Natural Laminar Flow (NLF) design or a combination of both, Hybrid Laminar Flow Control (HLFC) are the possible approaches to achieving laminar flow over an aircraft surface. However, the effectiveness of these methods is sensitive to surface imperfections [1]. Aerodynamic surfaces

F. Tocci (✉) · S. Hein
German Aerospace Center (DLR), Bunsenstrasse 10, 37073 Göttingen, Germany
e-mail: francesco.tocci@dlr.de

G. Chauvat · A. Hanifi
FLOW, Department of Engineering Mechanics, KTH Royal Institute of Technology,
SE-100 44 Stockholm, Sweden

inevitably have geometric irregularities: manufacturing process leads to the creation of steps, gaps or humps, and additionally these can be inherent in the design of high-lift and anti-icing devices. The breakdown of laminar flow in 2-D boundary layers can be strongly influenced by these imperfections. From a practical point of view, it is of great importance to be able to provide an estimate for the surface irregularity sizes that can be tolerated without affecting transition. Tollmien-Schlichting (TS) waves dominate transition in 2-D. Wörner et al. [2] investigated the role of a rectangular hump on the oncoming TS waves in an incompressible 2-D boundary layer by direct numerical simulations (DNS). They found that the height of the roughness has a bigger influence, compared to the width, on the resulting amplitude of the TS waves far downstream. DNS were also performed by Edelmann et al. [3] to incorporate the impact of forward-facing steps in the e^N method and Xu et al. [4] studied the impact of 2-D and 3-D surface indentations on the destabilization of TS waves in an incompressible boundary layer. The present investigation represents a further contribution to the work of Wörner et al. [2], extending the analysis to different geometric irregularities for a fixed height.

2 Numerical Setup

In this work we investigate through DNS the development of TS waves encountering a forward-facing step, backward-facing step, rectangular or smooth hump and gap. The flow conditions were selected to match those used by Wörner et al. [2]. The surface irregularities were located on a flat plate without pressure gradient at Reynolds number based on the centre position of the irregularity $Re_{x_c} = 4 \times 10^5$. In the following, the coordinates are non-dimensionalized with the Blasius length scale $l_0 = x_c / \sqrt{Re_{x_c}}$ at this location. With this scaling, the center of the irregularities is located at $x_c = 632.46$. The non-dimensional height or depth of the geometric features was $h = 0.808$ ($Re_h = 511$). The non-dimensional width of the humps and gaps was $w = 31.62$ ($Re_w = 2 \times 10^4$). The calculations were performed with the incompressible spectral-element code Nek5000 [5] and consisted of a DNS of the steady laminar 2-D base flows and succeeding DNS for the disturbance propagation. A Blasius profile was specified at the inflow boundary and when the base flow reached its steady state, the TS waves were artificially excited. The disturbances were introduced by periodic blowing and suction through a narrow strip at the wall near the inflow boundary ($298 \leq x \leq 334$). The normal velocity v was prescribed across the strip:

$$v(x, y_{wall}, t) = A v_{B/S}(x) \sin(\omega t), \quad (1)$$

where A denotes the amplitude, ω the non-dimensional circular frequency of the disturbance and $v_{B/S}(x)$ is a shape function that guarantees zero net volume flow through the blowing-suction strip and smooth derivatives near the boundaries [6]. The non-dimensional reduced frequency for the TS waves was $F = \omega v / U_\infty^2 = 49.34 \times 10^{-6}$. Oblique 3-D TS waves can be generated as well with a given spanwise wavelength. In this case, Eq. 1 was replaced by:

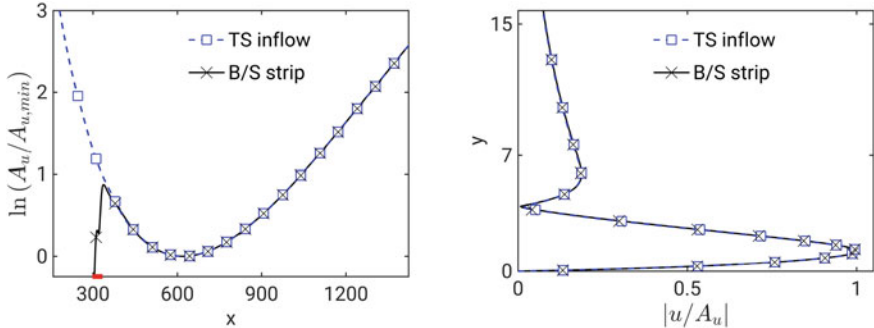


Fig. 1 Left: natural logarithm of the normalized disturbance amplitude ($A_u(x) = \max |u(x, y)|$) for 2-D TS at $F = 49.34 \times 10^{-6}$. The short red thick line indicates the location and the extent of the blowing/suction strip. Right: wall-normal amplitude distribution of the normalized streamwise disturbance velocity at $x = 632.46$

$$v(x, y_{wall}, z, t) = Av_{B/S}(x) \sin(\beta_0 z + \omega t), \quad (2)$$

where β_0 is the non-dimensional spanwise wavenumber. An alternative of introducing TS waves by blowing and suction is the superposition of the eigensolutions of the Orr-Sommerfeld equation to the Blasius inflow profile. Figure 1 shows excellent agreement between the two methods for the generation of 2-D TS waves on a smooth flat plate.

After a transient phase where the perturbations propagate through the entire domain, a time-periodic flow field in the unsteady DNS was reached. This enables a Fourier analysis in time of the streamwise component of the disturbance velocity to obtain the perturbation amplitudes at different streamwise locations. After the Fourier analysis, the maximum amplitude in the wall-normal direction was extracted at each position in streamwise direction: $A_u(x) = \max |u(x, y)|$. In this paper, $A_{u,min}$ represents the maximum amplitude along y at the streamwise position where the amplitude starts to grow.

As the disturbance velocities grow above a few percent of the base flow, non-linear effects usually become significant. However, the non-linear terms of the incompressible Navier-Stokes equations are conservative and therefore only redistribute energy between spatial scales. Thus, the growth of the total disturbance energy must originate from a linear mechanism [7]. The amplitudes of the introduced disturbances ($A = 10^{-6}$ in Eqs. 1, 2) were chosen to be small enough to grant a purely linear development throughout the domain.

For the rectangular hump, gap and steps the geometric irregularities were directly meshed. For the smooth cases the surface imperfection was instead defined by analytical mapping of the Gauss-Lobatto-Legendre (GLL) points used to build the velocity Lagrange polynomial interpolants in each spectral element. The latter procedure requires the irregularities to be localised and smooth. The smooth hump (+) and gap (-) were defined by:

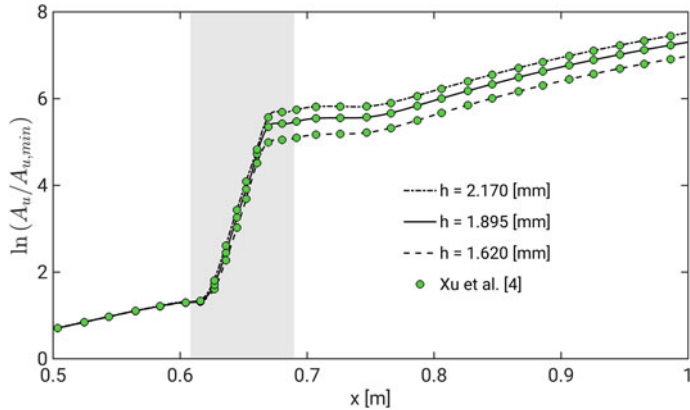


Fig. 2 Comparison with Fig. 15(a) of Ref. [4]. Natural logarithm of the normalized disturbance amplitude ($A_u(x) = \max |u(x, y)|$) for 2-D TS at $F = 50 \times 10^{-6}$. The grey area indicates the location of the indentation. The three depths of the indentation are: $h = 1.620$ mm, 1.895 mm and 2.170 mm

$$y = \pm \frac{h}{2} \left(\cos \left(2\pi \frac{r}{w} \right) + 1 \right), \quad r = \sqrt{(x - x_c)^2}, \quad x_c - \frac{w}{2} \leq x \leq x_c + \frac{w}{2}. \quad (3)$$

Since Nek5000 is designed to have a spectral element discretization in all directions, either 2-D or 3-D, it was not possible to exploit the spatial homogeneity in spanwise direction (e.g. using a more optimal Fourier expansion) for the oblique 3-D TS waves. In this case, the 2-D base flow was extruded in the spanwise direction over a spanwise width given by the spanwise wavelength of the introduced disturbance. The subsequent DNS for the disturbances was therefore 3-D and obviously computationally more expensive than the 2-D computations for the 2-D TS. Moreover, in incompressible flow it can be demonstrated that 2-D TS waves are the most unstable ones (see Mack et al. [8] and Fig. 8). Thus, only one irregularity, i.e. the smooth hump, was computed with oblique 3-D TS waves.

Grid convergence of the results was checked by increasing the polynomial order and the number of elements in both directions. The results presented here were obtained with a polynomial order of 9 within the spectral elements. A verification test was also conducted using results available in literature. As mentioned earlier in Sect. 1, Xu et al. [4] looked at the influence of 2-D and 3-D indentations on the instability of 2-D TS waves. In Fig. 2 we compare the streamwise disturbance development only for the 2-D indentation with three different depths, see Fig. 15(a) in Ref. [4]. If the same computational domain is used, the results agree very well.

3 Results and Discussion

First, steady laminar 2-D base flows were computed for the different surface irregularities. Secondly, disturbances were added to these base flows and unsteady calculations of the disturbance propagation were carried out.

3.1 Base Flow Calculations

An insight into the different steady flow fields is given in Fig. 5, where coloured contours and some iso-lines of the streamwise velocity in the vicinity of the irregularities are plotted. In the analysis of the flow topology the most evident phenomenon is the presence of separation bubbles. The region of reversed flow is indicated by the iso-line of zero streamwise velocity, marked in red in Fig. 5. For all the configurations, a separation bubble can be seen. However, in front of the forward-facing step, it is extremely small, due to the small step height. Moreover, there are no zones of separated flows on top of the steps or the rectangular hump. Figure 3 shows the wall pressure along the streamwise coordinate. Upstream and far downstream of the irregularities the wall pressure is the same as on the flat plate. In front of the forward-facing step, rectangular and smooth hump the pressure rises. Then, a sudden drop occurs followed by a steep increase. In the case of the forward-facing step this increase is monotonic and asymptotically reaches the flat plate level. For the hump cases, rectangular and smooth, this rise exceeds the flat plate value before recovering it as the flow is accelerated further downstream in a region of local favourable pressure gradient. For the rectangular hump, there is also a pressure decrease after the hump center followed by the aforementioned steep rise and slow decay given by the local favourable pressure gradient. Upstream of the backward-facing step, rectangular and smooth gap, the pressure decreases and then starts increasing at the step location and at the beginning of the gap. Further downstream the behaviour for the backward-facing step is similar to the hump case while the gap case shows some differences around its end, if compared to the forward-facing step. In fact, for the rectangular gap there is again a sudden pressure drop at the gap end, similar to the forward-facing step, however the succeeding rise is not monotonic: there is a steep increase followed by a small decrease and again a slow rise which approaches asymptotically the clean flat plate level. The smooth gap resembles the rectangular gap except around the gap end where it experiences a smaller pressure decay. As shown in Fig. 4, the skin friction around the surface imperfections deviates considerably from that over a smooth flat plate. For the humps and forward-facing step, there is a local adverse pressure gradient ahead of the surface imperfections, and therefore the skin friction drops below the smooth flat plate value. At the step and humps location the skin friction rises sharply. In the forward-facing step case, it then decreases to asymptotically reach the value of the clean flat plate, while for the humps it first decreases around the hump center and then increases again to match the value of the clean flat plate. On

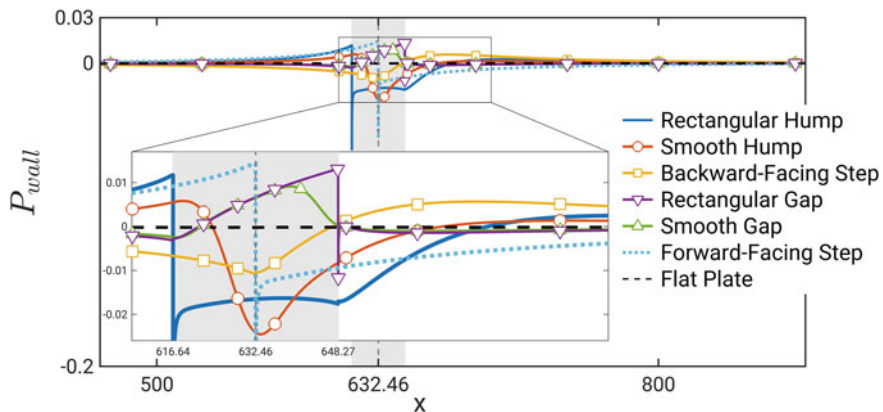


Fig. 3 The effect of the surface irregularities on the non-dimensional wall pressure distribution. The grey area indicates the location of the humps and gaps, while the dashed grey line shows the location of the steps

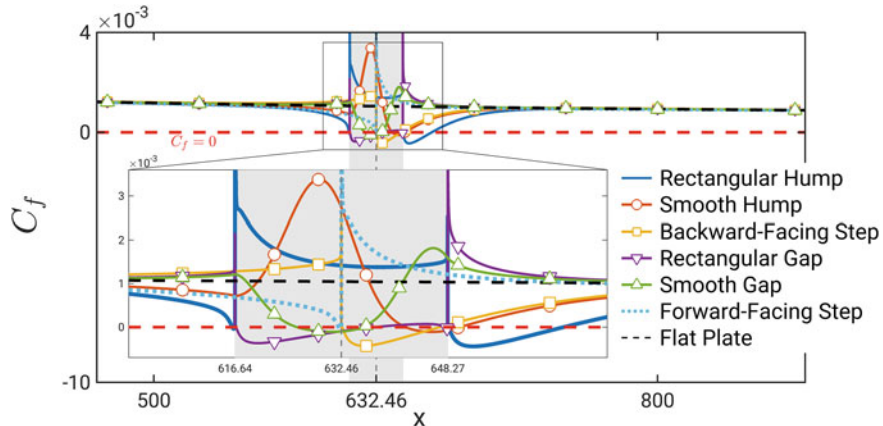


Fig. 4 The effect of the surface irregularities on the skin-friction coefficient C_f

the other hand, the backward-facing step and the gaps produce an adverse pressure gradient that leads to a separation zone immediately behind the irregularities. Inside the rectangular gap and downstream of the rectangular hump and backward-facing step there are the strongest regions of adverse pressure gradient, causing the longest separation bubbles.

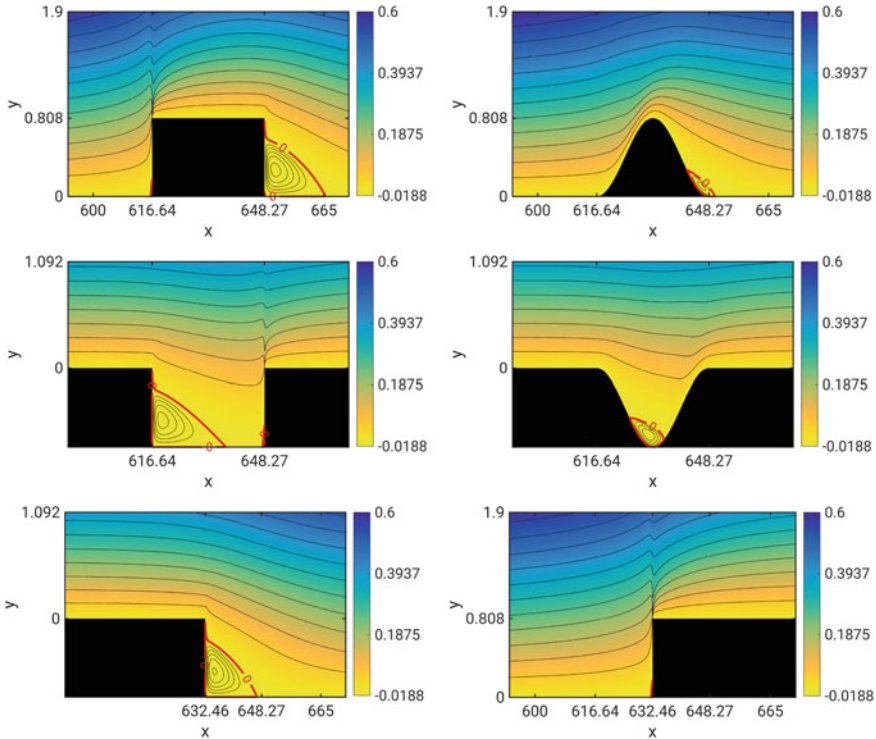


Fig. 5 Coloured contours and iso-lines (black line) of the non-dimensional streamwise velocity component for the base flows (the axes are not to scale). The red lines indicate the iso-lines of zero streamwise velocity. From top left to bottom right there are the six surface imperfections: rectangular hump, smooth hump, rectangular gap, smooth gap, backward-facing step and forward-facing step

3.2 Evolution of Tollmien-Schlichting Disturbances

The TS waves were extracted from the total solution of the second DNS by subtracting the base flow resulting from the first DNS. Typical results for the disturbances at an arbitrary instant of time are shown in Fig. 6, where the impact of the surface irregularities on the development of 2-D TS waves can be seen qualitatively. For a quantitative analysis the maximum amplitude $A_u(x) = \max |u(x, y)|$ along the wall normal coordinate was calculated (see Sect. 2) and its development for the different surface imperfections is shown in Fig. 7. For the selected frequency of $F = 49.34 \times 10^{-6}$ the location of the irregularities was close to the neutral point and all the surface deformations have a destabilising effect on the TS disturbances. At the very beginning, the amplitude development of the TS waves agrees with the clean flat plate result. However, the upstream influence of the surface imperfection causes soon a modification of the disturbances amplification. With the rectangular and smooth hump the TS waves are unstable in the adverse pressure gradient region, ahead of the

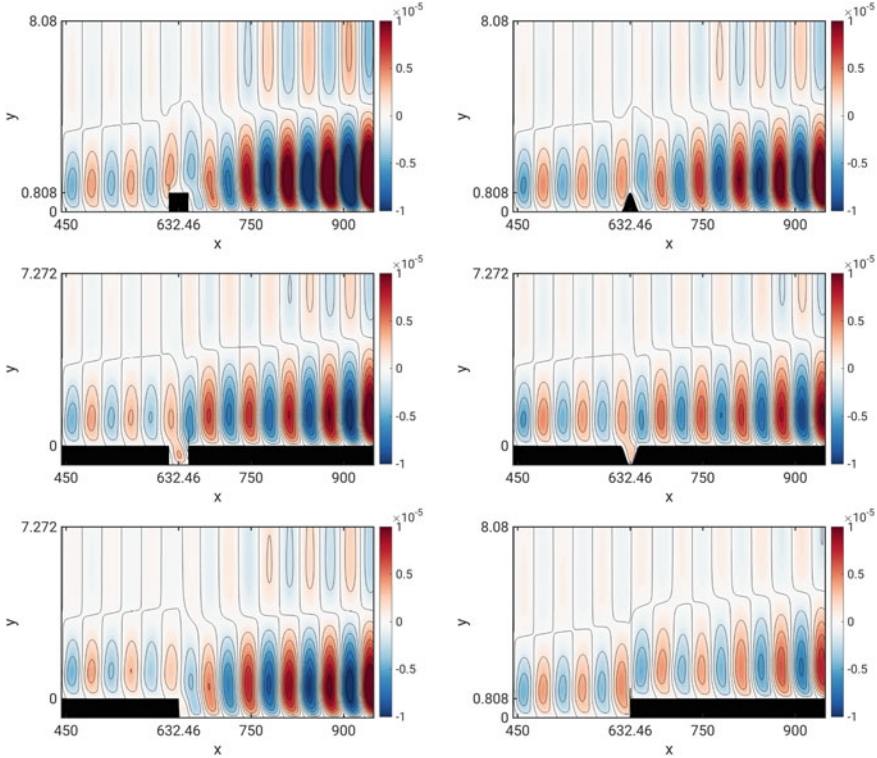


Fig. 6 Coloured contours of the non-dimensional streamwise velocity component for the disturbances (the axes are not to scale)

surface irregularity, become stable over the short favourable pressure gradient region and then turn unstable again in the separation region. The forward-facing step case shows a similar trend upstream, being above the smooth flat plate case. However, downstream of the step the amplitude is damped over a longer distance compared to the hump cases where the hump end immediately amplifies the disturbances. Further downstream the amplitudes start to grow again also for the forward-facing step. For the backward-facing step and both gap cases there is a localised favourable pressure gradient region in front of the imperfections which stabilizes the disturbances, but then the amplitudes grow again starting from the step location and the beginning of the gaps. The backward-facing step shows the largest upstream influence. Generally speaking all the imperfections act as stability modifiers and this is a direct consequence of the base flow modification owing to the surface irregularities. Far downstream of the surface imperfections the disturbance growth rates recover the flat plate solution, however the effect of the geometric features concern flow regions much larger than the geometric extent of the irregularities. Smoothing the imperfections affects the amplitudes in a similar way for both the hump and the gap: the

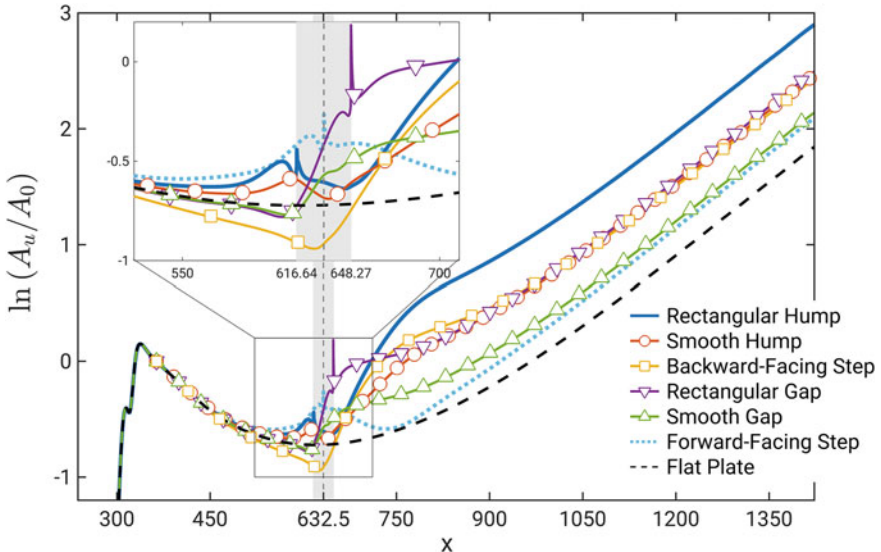
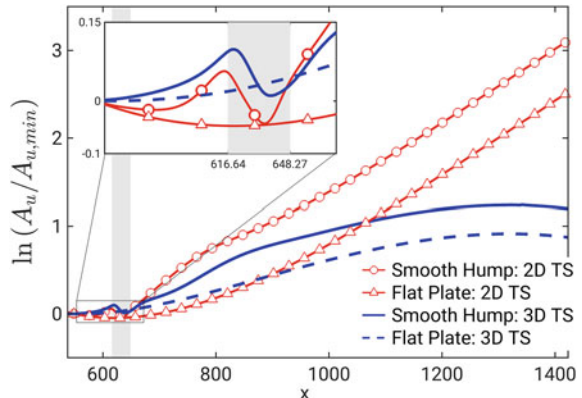


Fig. 7 Natural logarithm of the normalized disturbance amplitude ($A_u(x) = \max |u(x, y)|$) for 2-D TS at $F = 49.34 \times 10^{-6}$. A_0 represents the maximum amplitude along y at $x_0 = 363.66$. The grey area indicates the location of the humps and gaps, while the dashed grey line shows the location of the steps

Fig. 8 Natural logarithm of the normalized disturbance amplitude for 2-D and 3-D TS with $\beta_0 = 0.1265$ at $F = 49.34 \times 10^{-6}$.
 $A_u(x) = \max |u(x, y)|$ and $A_{u,min}$ represents the maximum amplitude along y at the streamwise position where the 3-D TS starts to grow. The grey area indicates the location of the smooth hump



rectangular cases, as could be expected, have a stronger destabilizing effect on the TS waves. The rectangular gap case reaches almost the same amplitude value of the backward-facing step case, indicating that for this width/height ratio ($w/h \approx 39$) the TS waves impact is dominated by the backward-facing step. Within the geometric shapes studied, the strongest destabilization is given by the rectangular hump. The smooth hump case approaches the amplification given by the backward-facing step or rectangular gap, even though the separation bubble is noticeably smaller: this can

be explained by the local adverse pressure gradient in front of the hump which leads to higher amplitudes before the separation region, compared to the gap or backward-facing step. A 3-D oblique TS wave was also considered in the presence of the smooth hump. Figure 8 shows the disturbance amplitude development for an oblique wave with $\beta_0 = 0.1265$ (wave angle $\psi \approx 55^\circ$). The smooth hump has a stronger destabilizing effect on the 2-D TS wave ($\psi = 0^\circ$) and far downstream the 2-D TS waves are the most unstable ones, as expected at low speed.

4 Conclusions

For a fixed height ($Re_h = 511$, $h = 0.808$, $w/h \approx 39$) and a selected frequency ($F = 49.34 \times 10^{-6}$) the influence of different surface irregularities, i.e. steps, humps and gaps, on the stability of TS disturbances in the linear regime has been investigated by means of DNS. The amplitude development of the disturbances undergoes a significant deviation from the clean flat plate level as they pass the imperfections, due to the base flow modification. All the irregularities are found to have an overall destabilizing effect with the larger amplification given by the rectangular hump. The surface imperfections are characterized by different flow topologies around their location as regards local regions of adverse and favourable pressure gradient and the backflow zone. The results presented can also be used to validate other approaches for the stability analysis in the presence of such irregularities.

Acknowledgements The authors acknowledge the financial support of SSeMID: Stability and Sensitivity Methods for Industrial Design funded by European Union's Horizon 2020 research and innovation program under the Marie Skłodowska-Curie Grant Agreement No. 675008. F.T. would also like to thank Dr. Hui Xu for providing the data used in the comparison of Fig. 2.

References

1. Crouch, J.D.: Modeling transition physics for laminar flow control. AIAA Pap. 2008–3832, (2008)
2. Wörner, A., Rist, U., Wagner, S.: Humps/steps influence on stability characteristics of two-dimensional laminar boundary layer. *AIAA J.* **41**(2), 192–197 (2003)
3. Edelmann, C.A., Rist, U.: Impact of forward-facing steps on laminar-turbulent transition in transonic flows. *AIAA J.* **53**(9), 2504–2511 (2015)
4. Xu, H., Mughal, S., Gowree, E., Atkin, C., Sherwin, S.: Destabilisation and modification of Tollmien-Schlichting disturbances by a three-dimensional surface indentation. *J. Fluid Mech.* **819**, 592–620 (2017)
5. Fischer, P.F., Lottes, J.W. and Kerkemeier, S.G.: Nek5000 web page. <http://nek5000.mcs.anl.gov> (2008)
6. Fasel, H., Konzelmann, U.: Non-parallel stability of a flat-plate boundary layer using the complete Navier-Stokes equations. *J. Fluid Mech.* **221**, 311–347 (1990)
7. Henningson, D.S., Reddy, S.C.: On the role of linear mechanisms in transition to turbulence. *Phys. Fluids* **6**(3), 1396–1398 (1994)
8. Mack, L.M.: Boundary-layer linear stability theory. In: Special course on stability and transition of laminar flow, AGARD report, vol. 709 (1984)

Stability Analysis of Boundary Layer Flow with Rotating Cylindrical Surface Roughness Elements



Yongxiang Wu and Ulrich Rist

Abstract A method by rotating the cylindrical surface roughness element is proposed, and its stability property is investigated by Bi-global linear stability theory. A high-velocity streak is obtained with this method. Linear stability analysis show that the viscous TS-like mode is attenuated in the induced streaky wake, however, the inflectional roughness mode is amplified in the downstream. The attenuation of the TS-like mode is attributed to the increase of dissipation and the amplification of the roughness mode is due to the increase of the wall-normal production.

1 Introduction

Surface roughness of either distributed or isolated type is ubiquitous and has a crucial influence on the boundary layer instability and laminar-turbulent transition. In the surface roughness element induced streaky boundary layer, the spanwise modulation of the base flow results in inflection points in both wall normal or spanwise directions. As the streak amplitude reaches 26% of the free-stream velocity, the inflectional instability is encountered [2]. On the other hand, circular roughness-element-induced streaky flows are also observed to stabilize and delay boundary layer transition [8]. The relevant stabilization mechanism is that the negative spanwise production energy together with viscous dissipation outweighs the remaining wall-normal production energy, thus creating an overall stabilizing effect [4]. However, this effect can only be expected with delicately designed streaky flow, which triggers a non-modal disturbance to attenuate the other modal disturbance [5] and at the same time avoid bypass transition. In addition, it has been confirmed that higher amplitude streaks have a greater stabilizing effect [6]. Therefore, miniature vortex generators (MVGs) with

Y. Wu (✉) · U. Rist
Institute of Aerodynamics and Gas Dynamics, University of Stuttgart,
Pfaffenwaldring 21, 70569 Stuttgart, Germany
e-mail: wu@iag.uni-stuttgart.de

U. Rist
e-mail: rist@iag.uni-stuttgart.de

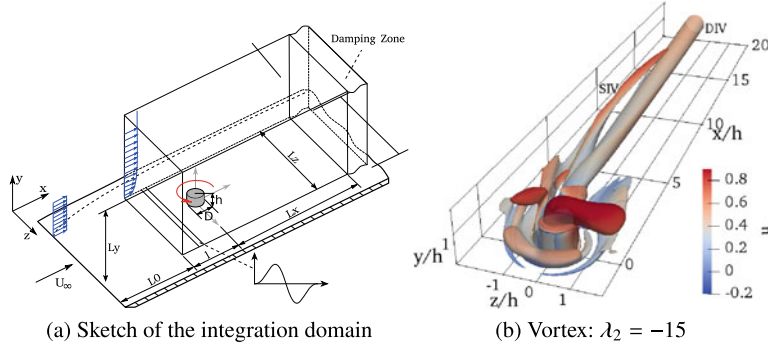


Fig. 1 Numerical model with the rotating cylindrical roughness element. DIV and SIV denote dominant inner vortex and secondary inner vortex. Vortex visualisation by means of λ_2 -criterion

a beneficial aerodynamic shape were proposed to generate more robust streamwise streaks, which produce preferable higher amplitude streaks and smaller recirculating zones. With MVGs, the streak amplitude limit with respect to stabilization effect is pushed up to 32% of the free stream velocity [7].

Based on the same thinking and with the purpose of obtaining higher streak amplitudes, the stability of a streaky boundary layer induced by a rotating cylindrical roughness element is studied, see Fig. 1. The rotation effect is measured by the relative tangential velocity at the top of the roughness to the incoming local velocity, defined as $Wu = \Omega D / 2u(h)$. Here Ω is the angular velocity, $u(h)$ is the velocity at the height of roughness h , and D is the roughness diameter. Since the roughness rotates at a constant angular speed, a local accelerated flow is generated close to the wall, which compresses the recirculation zone behind the roughness element and creates a dominating vortex in the downstream, see Fig. 1b. The stability property of this streaky flow is studied in this work with linear stability theory.

2 Numerical Methods

2.1 Baseflow Computation

In the study of hydrodynamic stability, flow quantities $\mathbf{q}(\mathbf{x}, t) = \{u, v, w, p\}$ are split into a steady base-flow part $\mathbf{q}_0(\mathbf{x})$ and an unsteady perturbation part $\mathbf{q}'(\mathbf{x}, t)$ according to the Reynolds decomposition. If the flow Reynolds number is higher than a certain critical value Re_{cr} , the flow will become unsteady and transitional. There are several methods to obtain a steady base flow for a physically unsteady flow. The selective frequency damping (SFD) [1] introduces a filtered state $\tilde{\mathbf{u}}$ and its evolution equation to dampen the unstable waves above the specified frequency, and has been widely used recently for computing steady baseflows. The governing equations are as followed:

Table 1 Parameters of simulation, dimensionless variables are referenced to roughness height h and freestream velocity u_0

Re_h	h	η	x_h/h	δ_h/h	Re_{kk}	$Re_{\delta 1}$	Wu
(-)	(m)	(-)	(-)	(-)	(-)	(-)	(-)
620	0.01	1	99.2	0.6883	465.8	426.7	0/0.46

$$\nabla \cdot \mathbf{u} = 0, \quad (1)$$

$$\frac{\partial \mathbf{u}}{\partial t} = \mathcal{N}(\mathbf{u}) - \chi(\mathbf{u} - \tilde{\mathbf{u}}), \quad (2)$$

$$\frac{\partial \tilde{\mathbf{u}}}{\partial t} = \omega_c(\mathbf{u} - \tilde{\mathbf{u}}), \quad (3)$$

where \mathcal{N} is the Navier-Stokes operator, ω_c is the filter cut-off circular frequency and χ is the feedback control coefficient. The open source OpenFOAM solver *icoFoam*, which solves the incompressible N-S equation by using the PISO algorithm, is used to implement the SFD solver for the current study. The simulation parameters are summarized in Table 1.

2.2 Bi-Global Linear Stability Analysis

The linear stability theory studies the asymptotic behaviour of infinitesimal perturbation superimposed on the base flow [13]. The perturbations $\mathbf{q}'(\mathbf{x}, t)$ are assumed to be small, i.e. $|q'_i| < 1$ and $|q'_i||q'_j| \ll 1$, and are modelled by the following temporal modal mode ansatz:

$$\mathbf{q}'(\mathbf{x}, y, z, t) = \hat{\mathbf{q}}(y, z)e^{i(\alpha x - \omega t)}, \quad (4)$$

where $\hat{\mathbf{q}}$ is the two-dimensional complex wave-like amplitude functions, α is the real streamwise wavenumber and $\omega = \omega_r + i\omega_i$ is complex frequency. The real part of the eigenvalue ω_r is related with the angular frequency of the eigenmode, while the imaginary part ω_i determines its temporal exponential growth or damping rate. Substituting the modelled perturbations $\mathbf{q}'(\mathbf{x}, t)$ into the linearized Navier-Stokes equation, the following general eigenvalue problem for temporal stability analysis is obtained:

$$L\hat{\mathbf{q}} = \omega M\hat{\mathbf{q}}, \quad (5)$$

where L and M are the coefficient matrices. The Fourier spectral method and summation-by-parts method [11] are used to discretize the above equation in spanwise and wall-normal directions, respectively. At the wall surface, the perturbations are assumed to zero, i.e. $\hat{\mathbf{q}} = 0$. The periodic boundary condition is specified for the spanwise boundary and a Neumann boundary condition $\partial\hat{\mathbf{q}}/\partial y = 0$ is used for the

top boundary. Equation (5) is then solved with the ARPACK functions which use an implicitly restarted Arnoldi method [10].

2.3 Linear Stability Mechanisms

In order to analyse the instability mechanisms, a perturbation kinetic energy analysis following Cossu and Brandt [4] is performed. In this method, by integrating the perturbation kinetic energy $e' = (u'^2 + v'^2 + w'^2)/2$ over a streamwise wavelength and spanwise extent, the following energy balance equation is obtained:

$$\frac{\partial E}{\partial t} = T_y + T_z - D, \quad (6)$$

where E is the total perturbation kinetic energy, and D the viscous dissipation energy. T_y and T_z are the production energy from the work of Reynolds stress $\hat{\tau}_{xy}$ and $\hat{\tau}_{xz}$ and wall-normal shear $\partial u / \partial y$ and spanwise shear $\partial u / \partial z$, respectively. Taking the normal mode ansatz of the perturbation \mathbf{q}' into account, the perturbation energy balance terms can be expressed in the form $(E, D, T_y, T_z) = (\hat{E}, \hat{D}, \hat{T}_y, \hat{T}_z)e^{2\omega_i t}$. Substituting this expression back into the energy balance equation, the following equation is obtained:

$$\omega_i = \frac{\hat{T}_y}{2\hat{E}} + \frac{\hat{T}_z}{2\hat{E}} - \frac{\hat{D}}{2\hat{E}}, \quad (7)$$

where ω_i is the temporal growth rate of the perturbation mode. A more detailed derivation can be found in [3, 4]. The above expression means that the temporal growth rate of the stability mode is composed of three parts, i.e. wall-normal and spanwise production in addition to dissipation.

3 Results

3.1 Base Flow

A schematic of the rotating roughness element and the laminar vortex structure are shown in Fig. 1. Vortices are visualised by the λ_2 -criterion. The dominating inner-vortex (DIV) surrounded by the secondary inner vortex (SIV) can be observed. The vortex rotating direction can be inferred from the velocity isolines in Fig. 2, where the low-momentum and high-momentum fluids induced by the so-called “lift-up effect” squeeze the velocity isolines and result in the high shear region (identified by the I_2 -criterion [12]). It’s typical of streaky flow to find the high shear region above the low speed fluid, which is normally composed of wall-normal ($\partial u / \partial y$) and spanwise

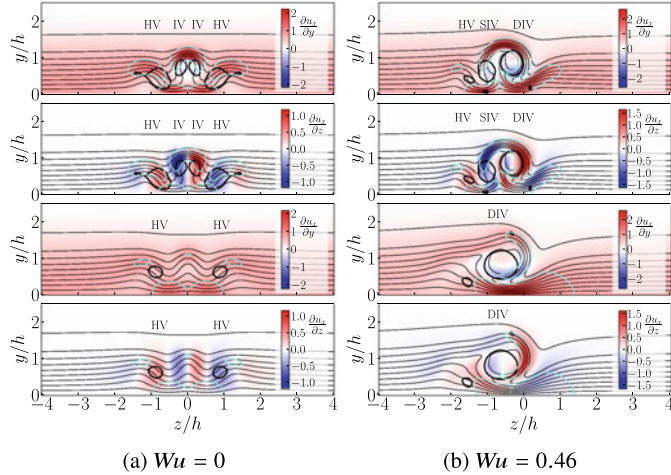


Fig. 2 Streamwise base flow comparison between static and rotating case. Thin solid lines are isolines of $u/u_0 = 0.1 \sim 0.95$. Thick black solid lines are $\lambda_2 = -8$. Thick cyan solid lines are shear regions by means of I_2 -criterion. In 1st and 2nd rows: $x/h = 5$, in 3rd and 4th rows: $x/h = 15$

$(\partial u / \partial z)$ terms. Different from the static case ($Wu = 0$), the shear for the rotating case is no longer symmetric with respect to the $z = 0$ axis, but rather rotates around the central DIV. For the rotating case ($Wu = 0.46$), the SIV is only evident in the near wake and decays quickly in the far wake, leaving the DIV the dominant flow structure.

Figure 3a shows the streamwise evolution of velocity gradients in a comparative way. Obviously, the $\partial u / \partial y$ and $\partial u / \partial z$ terms are the primary components of shear in both static and rotating cases. The rotation effect not only promotes the magnitude of the u -term related velocity gradients, but also slightly the $\partial v / \partial z$ and $\partial w / \partial y$ terms. In both cases, the streamwise gradient terms $\partial / \partial x$ remain negligibly low except for the short near wake region. Since the production of the perturbation is proportional to the shear magnitude, the associated instability mode is fundamentally determined by the component and distribution of the velocity gradients.

The strength of the velocity streak is evaluated with the following definition:

$$u_{st}(x) = \frac{1}{2}(\max_{yz}[u(x, y, z) - \langle u \rangle(x, y)] - \min_{yz}[u(x, y, z) - \langle u \rangle(x, y)]), \quad (8)$$

where $\langle u \rangle$ is the spanwise mean value, which represent the three-dimensional base-flow deformation caused by the low and high speed streaks. The influence of the rotation effect on the streak amplitude is then shown in Fig. 3b. Apparently the streak promotion effect is saturated at around $Wu = 0.46$, and the maximum streak amplitude reaches 40% of the free-stream velocity.

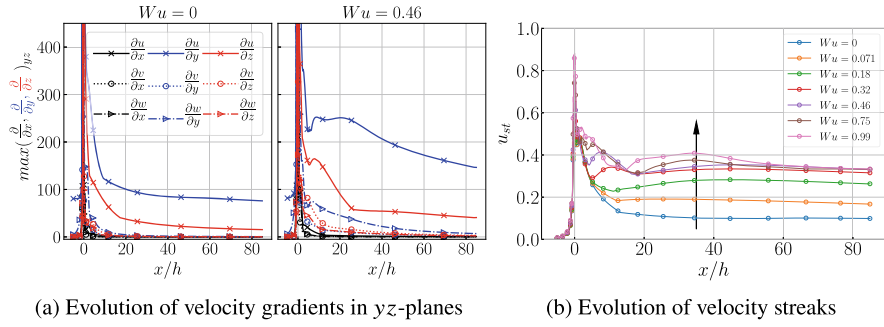


Fig. 3 Evolution of baseflow gradient and streak amplitude

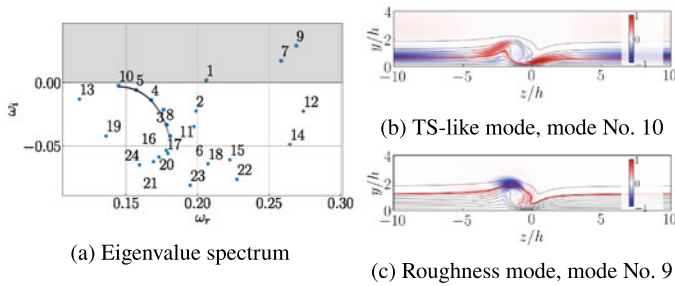


Fig. 4 Typical eigenvalue spectrum and eigenmodes (real part of \hat{u}) for the rotating case ($Wu = 0.46$) with wavenumber $\alpha = 0.35$ at location $x_p/h = 30$. The red solid lines mark the phase velocity c

3.2 Linear Stability

The bi-global linear stability analysis is performed on the yz -crosscut planes of consecutive streamwise positions, from which the most amplified eigenvalues and corresponding eigenmodes are identified. Figure 4a shows a typical eigenvalue spectrum at the position $x_p/h = 30$ with wavenumber $\alpha = 0.35$ for rotating case ($Wu = 0.46$), where the continuous viscous Tollmien-Schlichting (TS)-like mode branch can be identified on the left side and the isolated roughness modes are located on the upper right of the spectrum. The eigenfunctions of the most amplified viscous TS-like mode and the inflectional roughness mode are illustrated in Fig. 4b and Fig. 4b, respectively. The modes are normalized by the local mode maximum. The inflectional roughness mode is exclusively located around the DIV, whereas the viscous TS-like mode is in fact the insertion of an anti-phase structure into the TS mode due to the existence of the DIV.

The stability diagram for the TS-like mode and the roughness mode are shown in Fig. 5 with reference to that of TS mode obtained from the flat-plate boundary layer. The critical position for the TS mode is around $x_p/h = 45$, which correspond to $Re_{\delta^*} = 520$. With the existence of the static roughness element, the critical position

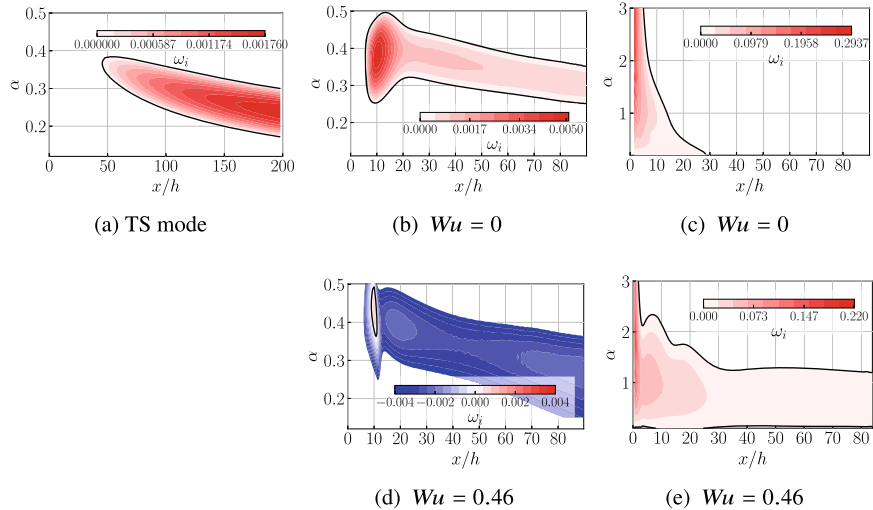


Fig. 5 Stability diagram for TS-like mode (sub-figure: (b) and (d)) and roughness mode (sub-figure: (c) and (e)) with reference to the TS mode. Blue color indicates negative ω_i . Thick black line marks the neutral curve

for TS-like mode is moved forward to $x_p/h = 8$, where a localized high amplification region provoked by the roughness near wake is identified, see Fig. 5b. However, the amplification rate ω_i just behind that region decays in the streamwise direction. This pattern is further enhanced in the case of a rotating roughness element (Fig. 5d), where the high ω_i region is largely reduced and the mode is fully damped (negative ω_i) in the downstream behind that near wake region. The preferred attenuation effect of the roughness element on the TS wave instability is reinforced by the rotation effect. Nevertheless, the instability property is deteriorated by the inflectional roughness mode, see Figs. 5c, e. The roughness mode is highly amplified directly behind the roughness element for both static and rotating cases, since the recirculation zone is a globally unstable region [9]. This unstable region is only restricted to the near wake region for the static case, whereas the rotation effect intensifies the inflectional roughness mode and extends the unstable region in the downstream. The amplification rate of the roughness mode (order 0.01 at $x_p/h = 70$) is one magnitude higher than that of the TS-like mode (order 0.001 at $x_p/h = 70$), making it the dominating instability mode. Note that the validity of the Bi-global LST in the very near wake region is questionable and should therefore not be stressed too much.

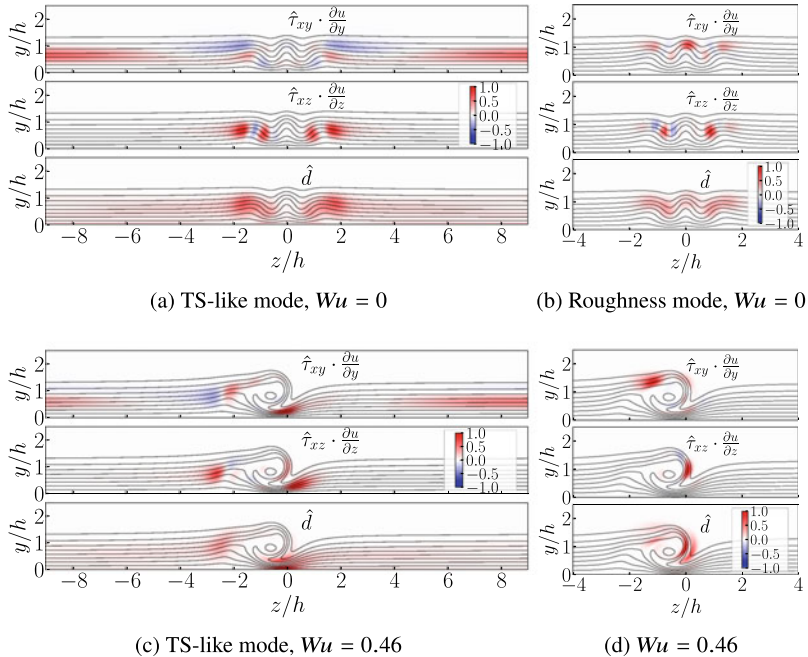


Fig. 6 Normalised production and dissipation of perturbation kinetic energy at $x_p/h = 15$. TS-like mode (sub-figure (a) and (c)) with $\alpha = 0.4$, roughness mode (sub-figure (b) and (d)) with $\alpha = 1.0$. Thin solid line are isolines of u/u_0

3.3 Instability Mechanisms

In order to get a physical insight into the mechanisms responsible for the above observed instability properties of the TS-like mode and roughness mode, the perturbation kinetic energy analysis is performed. Figure 6 shows the density of the production and dissipation perturbation kinetic energy evaluated at the wavenumber leading to the maximum growth, i.e. $\alpha = 0.4$ for the TS-like mode and $\alpha = 1$ for the roughness mode. Since the TS mode is two dimensional, only the wall-normal shear ($\partial u / \partial y$) contributes to the production perturbation kinetic energy. The TS-like mode exhibits a similar behaviour, except that in the streak region both wall-normal and spanwise shear contribute to the production energy, see Fig. 6a. Interestingly, the wall-normal production \hat{T}_y in the cylinder-induced streak region is mostly negative, meaning a stabilization effect. Together with the dissipation (\hat{D}), which is also distinct in the streak region, attenuation of the TS mode is obtained. The negative wall-normal production in the streak region is also observed for the rotating case, see Fig. 6c. It can also be noted that the production zone for the TS-like mode is mostly located around the side low speed streak, i.e. $z/h = \pm 1.5$ for case $Wu = 0$ and $z/h = -2.2$ for case $Wu = 0.46$, whereas the production zone for the rough-

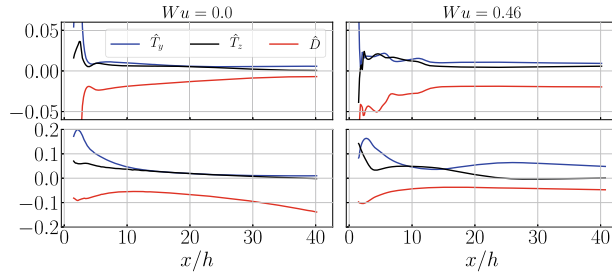


Fig. 7 Streamwise evolution of the perturbation kinetic energy. 1st row: TS-like mode, 2nd row: roughness mode

ness mode is mainly located around the central low speed streak for the static case and around the DIV for the rotating case. The viscous dissipation (\hat{D}) for roughness modes appears at the high shear region as identified by the I_2 -criterion shown in Fig. 2.

The streamwise evolution of the kinetic perturbation energy is shown in Fig. 7. The peak for all cases in the near wake region is due to the local high shear. Behind that region, both production and dissipation decay gradually in the case of the TS-like mode. The difference is that the dissipation \hat{D} for the rotational case increases significantly, whereas the spanwise production \hat{T}_z is slightly reduced. The overall attenuation of the TS-like mode is then attributed mainly to the increase of dissipation. As for the roughness mode, both production terms for the static case drop significantly after the near wake region, therefore an unstable region is only found close to the roughness, see Fig. 5c. For the rotational case, the wall-normal \hat{T}_y and spanwise \hat{T}_z production terms behave contrarily from position $x_p/h = 20$ on. While the wall-normal term \hat{T}_y is significantly increased, the spanwise term \hat{T}_z is almost decreased to zero. In the meantime, the dissipation \hat{D} is also weakened. The reduction of \hat{T}_z is not strong enough to compensate for the increase of \hat{T}_y and the decrease of \hat{D} . Consequently, the roughness mode is slightly amplified in the downstream, see Fig. 5e.

4 Conclusions

The linear stability of a boundary layer containing an isolated rotating cylindrical surface roughness element has been investigated comparatively with Bi-global linear stability theory. Due to constant rotation velocity along the height of the cylinder, a local accelerated flow close to the bottom wall is induced. This accelerated fluid compresses the recirculation zone behind the cylinder and produces a dominating vortex in the downstream. A high-amplitude streaky boundary layer with up to 40% streak amplitude is obtained. Two distinct types of instability modes are identified,

one is the viscous TS-like mode and the other is the inflectional roughness mode. The TS-like instability is found to be attenuated in the rotational roughness case, whereas the roughness mode is slightly amplified in the downstream. The perturbation kinetic energy analysis shows that the attenuation of the TS-like mode is mainly due to the strengthening of dissipation. Although the spanwise production energy is also slightly reduced, its contribution is minor. The amplification of the roughness mode is due to the increase of the wall-normal production energy.

Acknowledgements The authors gratefully acknowledge the financial support from the China Scholarship Council (No.201406280033) and Deutsche Forschungsgemeinschaft under project number RI680/39-1. Computational resources provided by the federal high-performance computing center Stuttgart (HLRS) is kindly acknowledged.

References

1. Åkervik, E., Brandt, L., Henningson D.S., Hoepffner, J., Marxen, O., Schlatter, P.: Steady solutions of the Navier-Stokes equations by selective frequency damping. *Phys. Fluids* **18**(6), 2006
2. Andersson , P., Brandt, L., Bottaro, A., Henningson, D.S.: On the breakdown of boundary layer streaks. *J. Fluid Mech.* **428**, 29–60 (2001)
3. Brandt, L.: Numerical studies of the instability and breakdown of a boundary-layer low-speed streak. *Eur. J. Mech.-B/Fluids* **26**(1), 64–82 (2007)
4. Cossu, C., Brandt, L.: On Tollmien-Schlichting-like waves in streaky boundary layers. *Eur. J. Mech.-B/Fluids* **23**(6), 815–833 (2004)
5. Fransson, J.H.M.: Transition to turbulence delay using a passive flow control strategy. *Procedia IUTAM* **14**, 385–393 (2015)
6. Fransson, J.H.M., Brandt, L., Talamelli, A., Cossu C.: Experimental study of the stabilization of tollmien–schlichting waves by finite amplitude streaks. *Phys. Fluids* **17**(5):054110 (2005)
7. Fransson, J.H.M., Talamelli, A.: On the generation of steady streamwise streaks in flat-plate boundary layers. *J. Fluid Mech.* **698**, 211–234 (2012)
8. Fransson, J.H.M., Talamelli, A., Brandt, L., Cossu, C.: Delaying transition to turbulence by a passive mechanism. *Phys. Rev. Lett.* **96**(6), 064501 (2006)
9. Loiseau, J.C., Robinet, J.C., Cherubini, S., Leriche, E.: Investigation of the roughness-induced transition: global stability analyses and direct numerical simulations. *J. Fluid Mech.* **760**, 175–211 (2014)
10. Lehoucq, R.B., Sorensen, D.C., Yang, C. (1998) ARPACK users' guide: solution of large-scale eigenvalue problems with implicitly restarted Arnoldi methods, Vol. 6. Siam (1998)
11. Mattsson, K., Nordström, J.: Summation by parts operators for finite difference approximations of second derivatives. *J. Comput. Phys.* **199**(2), 503–540 (2004)
12. Meyer, D.: Direkte numerische Simulation nichtlinearer Transitionsmechanismen in der Strömungsgrenzschicht einer ebenen Platte. Shaker (2003)
13. Theofilis, V.: Global linear instability. *Annu. Rev. Fluid Mech.* **43**, 319–352 (2011)

Triadic Resonance Analysis of Distributed Roughness Effects on Crossflow Instability in Swept-Wing Boundary Layers



Jiakuan Xu, Jiyang He, and Xuesong Wu

Abstract It is known that crossflow instability and transition can be influenced significantly by micron-sized surface roughness. He, Butler and Wu sought to explain such a sensitive effect from the standpoint of a generalized resonant triad interactions between crossflow instability modes and distributed roughness-induced perturbations. The mechanism was demonstrated for Falkner-Skan-Cooke similarity velocity profiles. In the present paper, we examine its role in destabilising stationary and travelling crossflow vortices in the boundary layers over the NLF(2)-0415 swept wing, for which Reibert & Saric's experiment found that micron-sized roughness caused much earlier transition. Our analysis shows that the generalized resonance mechanism operates in a swept-wing boundary layer and the resulting corrections to the growth rates of crossflow eigenmodes are proportional to the height of distributed surface roughness. The mechanism is highly effective when the roughness is near the leading edge. Importantly, it is found that the wavenumbers of the roughness spectra participating in the most effective resonant interactions with stationary and travelling-wave crossflow vortices are very close to the wavenumbers of the right-branch neutral stationary eigenmode. As a result, micron-sized distributed roughness generates a perturbation of much larger amplitude, which alters, through the resonant triad interactions, the growth rates of the crossflow vortices by an $O(1)$ amount.

1 Introduction

Surface roughness even of micron size can substantially influence crossflow instability and transition in three-dimensional boundary layers such as that over a swept wing, as has been demonstrated by a series of wind-tunnel experiments [1, 2]. Broadly speaking, an increase in roughness height enhances growth or amplitudes of crossflow vortices, and promotes earlier transition. However, this sensitive effect has not yet

J. Xu (✉) · X. Wu

Imperial College London, 180 Queen's Gate, London SW7 2AZ, UK
e-mail: jiakuan.xu@imperial.ac.uk

J. He
Tianjin University, Tianjin 300072, China

been fully explained, physically or mathematically, although it is known that depending on their location and characteristics (e.g.. height and length scales), roughness elements may affect transition through receptivity (especially of stationary vortices) [3–5], or through altering the base flow thereby changing the linear instability [6].

Recently, a possible new mechanism was proposed by He, Butler and Wu [7], which is the resonant-triad interactions among suitable crossflow modes and the perturbation induced by distributed roughness. Resonant-triad interaction is a rather general and well-known concept in nonlinear wave mechanics. It was applied to boundary-layer transition by Craik [8], who considered the evolution of a resonant triad consisting of a single planar and a pair of subharmonic oblique Tollmien-Schlichting (T-S) waves. Hall et al. [9] investigated the resonance among a pair of T-S waves and a Görtler mode, while El-Hady [10] considered triadic interactions of crossflow modes in three-dimensional boundary layers. Further theoretical and experimental studies of resonant modal interactions were reviewed by Wu in [11]. In almost all existing theories on resonant-triad interactions, the waves involved are all eigenmodes, which were all also required to be nearly neutral.

He, Butler and Wu [7] generalised the concept of triadic resonance to the case where two of the interacting waves are eigenmodes, which may have $O(1)$ growth rates and even be the most unstable, while the other is a roughness-generated perturbation, which is of course neutral but non-modal. Their calculations, performed for the Falkner-Skan-Cooke similarity solutions, showed that through such resonant interactions, distributed roughness of micron size may significantly enhance the growth rates of the crossflow instability modes.

Since the Falkner-Skan-Cooke solutions do not actually correspond to any physically realizable flow, in this paper we carry out the analysis and calculations of the type by He, Butler and Wu [7] for a swept-wing boundary layer and assess whether the resonance mechanism operates and remains quantitatively viable.

2 Mathematical Description

2.1 Perturbation Equations

In the body-fitted coordinate system, the base flow over an infinite swept wing has the velocity field $\vec{U} = (U, V, W)$, which is to be obtained by solving the boundary layer equations, and then used for stability analysis. Let $\vec{u}' = (u', v', w')$ and p' denote the velocity field and pressure of the disturbance. Substituting $(U + u', V + v', W + w', p + p')$ into the non-dimensional incompressible Navier-Stokes equations without curvature and subtracting out the governing equations of the base flow, we obtain the nonlinear disturbance equations,

$$\frac{\partial \vec{u}'}{\partial t} + (\vec{U} \cdot \nabla) \vec{u}' + (\vec{u}' \cdot \nabla) \vec{U} + \nabla p - \frac{1}{Re} \nabla^2 \vec{u}' = -(\vec{u}' \cdot \nabla) \vec{u}', \quad \nabla \cdot \vec{u}' = 0, \quad (1)$$

where $Re = U_\infty L_{ref}/\nu$, with L_{ref} being 1mm and U_∞ the oncoming mean speed respectively, which are taken to be the reference length and velocity respectively.

2.2 Crossflow Eigenmodes and Roughness Modes

In the linear stability theory, a crossflow eigenmode has the form,

$$(u', v', w', p') = \epsilon(\hat{u}, \hat{v}, \hat{w}, \hat{p})e^{i(\alpha x + \beta z - \omega t)} + c.c., \quad (2)$$

where $\epsilon \ll 1$ is a measure of the amplitude, α and β are chordwise and spanwise wavenumbers respectively, ω the frequency, and *c.c.* stands for the complex conjugate. A variable with hat (e.g.. \hat{u}) means the shape function of the disturbance. Substitution of Eq. (2) into Eqs. (1), followed by linearisation and making local parallel-flow approximation, yields the non-dimensional first-order disturbance equations, which form, along with the homogeneous boundary conditions, an eigenvalue problem describing the linear instability of the boundary layer.

In general, the surface roughness may be written as a sum of Fourier components with different wavenumbers. A typical Fourier component is

$$y_w = h e^{i(\alpha_w x + \beta_w z)} + c.c., \quad (3)$$

where α_w and β_w are the chordwise and spanwise roughness wavenumbers respectively, and h is the non-dimensional roughness height. We shall assume that $h \ll 1$ and so it suffices to consider each individual component, and moreover its interaction with crossflow modes could be analyzed through a perturbation scheme. Under the local parallel-flow assumption, the perturbation induced by roughness component takes the form,

$$[u'_w, v'_w, w'_w, p'_w] = h[\hat{u}_w(y), \hat{v}_w(y), \hat{w}_w(y), \hat{p}_w(y)]e^{i(\alpha_w x + \beta_w z)} + c.c., \quad (4)$$

where again a variable with a hat represents the shape function. Substituting Eq. (4) into Eq. (1), we can derive similar linearized perturbation equations for $\hat{u}_w(y)$, etc., which are however subjected to inhomogeneous boundary conditions: $(\hat{u}_w, \hat{w}_w) = -(\partial U/\partial y, \partial W/\partial y)|_0$. The boundary-value problem is solved to give the perturbation induced by the roughness, and each solution will be referred to as a ‘roughness mode’; the details can be found in Ref. [7].

Our calculations were performed for infinite swept-wing boundary layers, pertaining to the experiments of Ribert and Saric on the NLF(2)-0415 infinite aerofoil [1]. The Mach number is 0.063, swept angle 45 de.g., the angle of attack -4 de.g., and the Reynolds number is 2.4×10^6 based on the airfoil length 1.83m. Note that the chord length c perpendicular to the leading edge is 1.294m and x_c represents the chordwise coordinate.

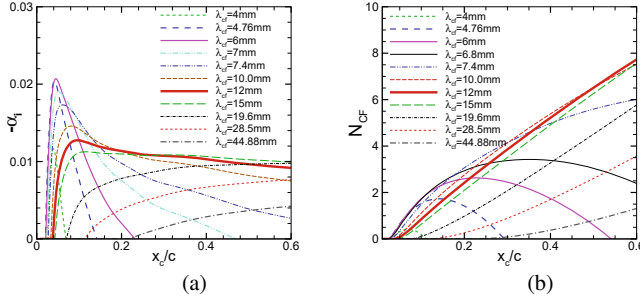


Fig. 1 Instability characteristics of stationary crossflow vortices: **a** local growth rate; **b** N factor

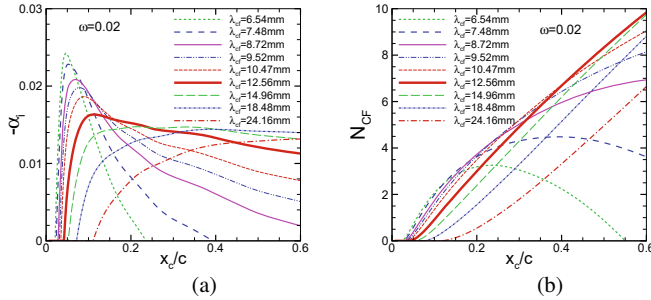


Fig. 2 Instability characteristics of travelling crossflow vortices with frequency $\omega = 0.02$: **a** local growth rate; **b** N factor

Figure 1a plots the spatial growth rates of stationary crossflow vortices for various spanwise wavenumbers. Integrating the local growth rates gives the corresponding values of the N-factor, N_{CF} , which measures the accumulated growth. These are displayed in Fig. 1b. The most unstable stationary vortices obtained in the present calculations have a spanwise wavelength of 12mm, which is in agreement with the measured data in experiments [1, 2]. The eigenvalues and N-factor N_{CF} of travelling crossflow vortices were calculated using a similar method, and the results for the vortices with frequency $\omega = 0.02$ are illustrated in Fig. 2. In order to compare the resonant interactions at different positions, the velocity profiles at $x_c/c = 0.05$ and $x_c/c = 0.2$ are selected to conduct the analysis of resonant interactions. The first one is at the position of the maximum growth rate of stationary crossflow vortices, and the latter is in the development region.

2.3 Generalized Resonance Mechanisms

We now consider possible resonant interactions at quadratic order between crossflow eigenmodes and roughness. Take two crossflow eigenmodes $E_1 = \exp[i(\alpha_1 x +$

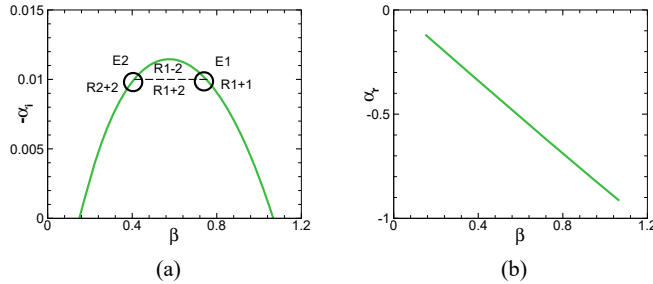


Fig. 3 Instability characteristics of stationary vortices at $x_c/c = 0.2$: **a** the variation of $-\alpha_i$ with β and the schematic of the resonances, where the letters ‘E’ and ‘R’ stand for eigenmode and roughness modes respectively; **b** the variation of α_r with β

$\beta_1 z - \omega_1 t)$ and $E_2 = \exp\{i(\alpha_2 x + \beta_2 z - \omega_2 t)\}$, and one roughness mode $E_w = \exp\{i(\alpha_w x + \beta_w z)\}$ into analysis. Of interest is the resonant triadic interaction: one of the eigenmodes interacts with the roughness mode to generate the other and vice versa. This may take place in the two forms:

$$E_1 = E_2 E_w \quad (5)$$

and

$$E_1 = E_2^* E_w, \quad (6)$$

where the superscript * denotes the complex conjugate. For these two equations, the corresponding wavenumbers and frequencies must satisfy the resonance conditions,

$$\begin{cases} \text{Im}\alpha_1 = \text{Im}\alpha_2, & \omega_1 = \omega_2, \\ \text{Re}\alpha_1 - \text{Re}\alpha_2 = \alpha_w, & \beta_1 - \beta_2 = \beta_w, \end{cases} \quad (7)$$

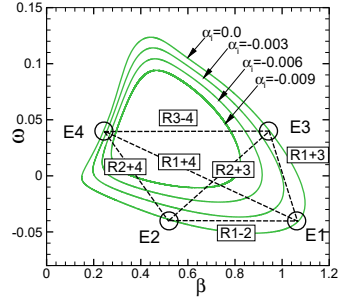
and

$$\begin{cases} \text{Im}\alpha_1 = \text{Im}\alpha_2, & \omega_1 = -\omega_2, \\ \text{Re}\alpha_1 + \text{Re}\alpha_2 = \alpha_w, & \beta_1 + \beta_2 = \beta_w, \end{cases} \quad (8)$$

respectively. These two forms of resonance will be referred to as triad difference and triad sum respectively. The constraint on the frequencies becomes irrelevant for stationary vortices. The special case of the form (8) with $\alpha_1 = \alpha_2$ and $\beta_1 = \beta_2$ will be referred to as generalized Bragg scattering.

Linear stability analysis gives the dependence of the growth rate $-\alpha_i$ and chordwise wavenumber α_r on the spanwise wavenumber β . The results for stationary modes at the position of $x_c/c = 0.2$ are illustrated in Fig. 3. The grow rate peaks at a finite β , which means that there exist two modes having the same growth rate ($-\alpha_i$), and they are denoted as E_1 and E_2 in the figure. A schematic of the resonance for stationary vortices is in shown in Fig. 3a. As is illustrated, E_1 and E_2 can interact with each other via roughness modes $R1 - 2$ and $R1 + 2$, which are termed triad

Fig. 4 Growth rate contours of travelling-wave vortices at $x_c/c = 0.2$, and the schematic of the resonances, where the letters ‘E’ and ‘R’ stand for eigenmode and roughness mode respectively



difference and triad sum, respectively. In addition, they also interact with $R1 + 1$ and $R2 + 2$ to influence their own growth, and the interaction is of Bragg scattering type. As with the Falkner-Skan-Cooke profiles, a remarkable result is that there is an almost perfect linear relationship between α_r and β , which means that if $(\beta_1 + \beta_2)$ is close to β_n , the spanwise wavenumber of the right-branch neutral mode, then $(\alpha_{1r} + \alpha_{2r})$ is close to α_n , the chordwise wavenumber of the neutral mode.

Figure 4 displays the contours of the growth rate of travelling vortices at $x_c/c = 0.2$. Four travelling eigenmodes with the same $|\omega|$ and $-\alpha_i$ can be found to satisfy the resonance conditions, and they are labelled as $E1$, $E2$, $E3$ and $E4$. These four modes can interact with six roughness components, namely $1 + 3$, $1 + 4$, $2 + 3$ and $2 + 4$ through triad sum, and $1 - 2$, $3 - 4$ through triad difference.

If a roughness component satisfies one of the resonant conditions Eqs. (7)–(8), the result quadratic interactions cause an $O(h)$ correction to the growth rate of the crossflow modes; otherwise, the interactions at cubic order produce a much smaller $O(h^2)$ correction. In order to account for the $O(h)$ correction, we introduce a slow variable $\bar{x} = hx$, and the amplitude of each eigenmode is a function of \bar{x} . Using a multi-scale method, the amplitude equations for the eigenmodes were derived in [7]. The analysis can easily be extended to interactions with multiple-wavenumber roughness. Stationary and travelling cases are considered separately due to different forms of resonance.

2.3.1 Stationary Crossflow Vortices

Two stationary modes (α_j, β_j) ($j = 1, 2$) with the same growth rate can, in general, interact with each other, through the triad sum and difference interactions with roughness modes $(\alpha_{w1\pm2}, \beta_{w1\pm2})$ (Fig. 3). Through Bragg scattering, each mode also interacts with roughness modes $(\alpha_{w1+1}, \beta_{w1+1})$ or $(\alpha_{w2+2}, \beta_{w2+2})$ respectively. These interactions can take place simultaneously in the presence of the four roughness components, and will be referred to as $1 - 2$, $1 + 2$, $1 + 1$ and $2 + 2$, respectively. The disturbance consisting of these modes takes the form,

$$\begin{aligned}\phi = & h(\hat{\phi}_{w_{1-2}} E_{w_{1-2}} + c.c.) + h(\hat{\phi}_{w_{1+2}} E_{w_{1+2}} + c.c.) + h(\hat{\phi}_{w_{1+1}} E_{w_{1+1}} + c.c.) \\ & + h(\hat{\phi}_{w_{2+2}} E_{w_{2+2}} + c.c.) + \epsilon[A_1(\bar{x})\hat{\phi}_{10}(y) + h\hat{\phi}_{11} + c.c.]E_1 \\ & + \epsilon[A_2(\bar{x})\hat{\phi}_{20}(y) + h\hat{\phi}_{21} + c.c.]E_2 + \dots\end{aligned}\quad (9)$$

Note that the amplitudes of the crossflow modes, A_1 and A_2 , are functions of the slow variable $\bar{x} = hx$: $A_1 = A_1(\bar{x})$ and $A_2 = A_2(\bar{x})$. Substituting Eq. (9) into Eq. (1) and the boundary conditions, we obtain at $O(\epsilon)$ and $O(h)$ the eigenvalue problem for the crossflow eigenmodes and the inhomogeneous boundary-value problem for the roughness modes, respectively. At $O(\epsilon h)$, the two linearly coupled amplitude equations are derived as

$$\frac{dA_1}{d\bar{x}} + F_{2-w_{1-2}} A_2(\bar{x}) + F_{2^*-w_{1+2}} A_2^*(\bar{x}) + F_{1^*-w_{1+1}} A_1^*(\bar{x}) = 0, \quad (10)$$

$$\frac{dA_2}{d\bar{x}} + F_{1-w_{1-2}} A_1(\bar{x}) + F_{1^*-w_{1+2}} A_1^*(\bar{x}) + F_{2^*-w_{2+2}} A_2^*(\bar{x}) = 0. \quad (11)$$

The solution for A_1 and A_2 is of the exponential form, and this leads to the eigenvalue problem, $\lambda \vec{a} = \mathbf{F} \vec{a}$, with \mathbf{F} being a 4×4 real-valued matrix.

2.3.2 Travelling-Wave Crossflow Vortices

Resonances can take place among four travelling eigenmodes (with the same α_i and $|\omega|$) and six roughness modes; see Fig. 4. The interactions are labelled as $1+3$, $1+4$, $2+3$ and $2+4$, which are of the triad sum type, and as $1-2$ and $3-4$, which are of triad difference type. The disturbance consisting of these components has the form,

$$\begin{aligned}\phi = & h(\hat{\phi}_{w_{1-2}} E_{w_{1-2}} + c.c.) + h(\hat{\phi}_{w_{1+3}} E_{w_{1+3}} + c.c.) + h(\hat{\phi}_{w_{1+4}} E_{w_{1+4}} + c.c.) \\ & + h(\hat{\phi}_{w_{2+3}} E_{w_{2+3}} + c.c.) + h(\hat{\phi}_{w_{2+4}} E_{w_{2+4}} + c.c.) + h(\hat{\phi}_{w_{3-4}} E_{w_{3-4}} + c.c.) \\ & + \epsilon[A_1(\bar{x})\hat{\phi}_{10} + h\hat{\phi}_{11} + c.c.]E_1 + \epsilon[A_2(\bar{x})\hat{\phi}_{20} + h\hat{\phi}_{21} + c.c.]E_2 \\ & + \epsilon[A_3(\bar{x})\hat{\phi}_{30} + h\hat{\phi}_{31} + c.c.]E_3 + \epsilon[A_4(\bar{x})\hat{\phi}_{40} + h\hat{\phi}_{41} + c.c.]E_4 + \dots\end{aligned}\quad (12)$$

The amplitudes of the crossflow vortices, A_1 , A_2 , A_3 and A_4 , are functions of the slow variable $\bar{x} = hx$: $A_j = A_j(\bar{x})$ ($j = 1, 2, 3$ and 4). By following similar steps as before, the four coupled amplitude equations were derived,

$$\frac{dA_1}{d\bar{x}} + F_{2-w_{1-2}} A_2 + F_{3^*-w_{1+3}} A_3^* + F_{4^*-w_{1+4}} A_4^* = 0, \quad (13)$$

$$\frac{dA_2}{d\bar{x}} + F_{1-w_{1-2}} A_1 + F_{3^*-w_{2+3}} A_3^* + F_{4^*-w_{2+4}} A_4^* = 0, \quad (14)$$

$$\frac{dA_3}{d\bar{x}} + F_{1^*-w_{1+3}} A_1^* + F_{2^*-w_{2+3}} A_2^* + F_{4-w_{3-4}} A_4 = 0, \quad (15)$$

$$\frac{dA_4}{dx} + F_{1^*-w_{1+4}} A_1^* + F_{2^*-w_{2+4}} A_2^* + F_{3-w_{3-4}^*} A_3 = 0. \quad (16)$$

As above, seeking exponential form of solutions leads to an eigenvalue problem, $\lambda \vec{a} = \mathbf{F} \vec{a}$, but now \mathbf{F} is an 8×8 real-valued matrix.

In both cases of stationary and travelling vortices, the eigenvalue $\lambda = \lambda_r + i\lambda_i$ is complex-valued, and its real part represents the growth-rate correction coefficient since it modifies the growth through the factor $e^{(\lambda_r h - \alpha_i)x}$. Hence, the value of λ_r is of primary interest, which indicates the correction to the growth rate is $\lambda_r h$.

3 Numerical Results on Effects of Roughness Through Resonant Interactions

3.1 Stationary Vortices

Stationary eigenmodes 1 and 2 interact resonantly with each or all of four Fourier components in the roughness. The values of the resulting growth-rate correction coefficient, λ_r , are displayed in Fig. 5 for two streamwise locations. Three main features can be observed. Firstly, the λ_r for the multiple-wavenumber interaction is similar to that for the single-wavenumber interaction that dominates among the four interactions with the dominant one being the triad sum 1 + 2 for the majority of $-\alpha_i$ and Bragg scattering 1 + 1 and 2 + 2 near the largest $-\alpha_i$. Secondly, the greater the growth rate is, the larger is the correction coefficient. Thirdly, λ_r in the near-leading region ($x_c/c = 0.05$) is overall significantly (about twice) greater than that in the downstream region ($x_c/c = 0.2$).

Typically, since the reference length is chosen as 1 mm, surface height (e.g., for a painted surface) is 10 μm , the non-dimensional height h is thus 0.01. The growth-rate correction coefficients at these locations are about 0.5 and 0.2 for the

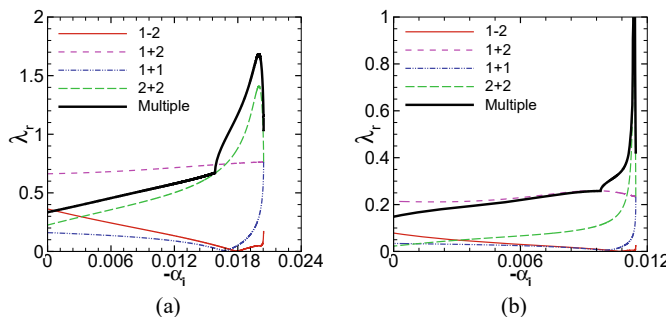


Fig. 5 Comparisons of λ_r for stationary vortices interacting with single and multiple roughness components at **a** $x_c/c = 0.05$; **b** $x_c/c = 0.2$

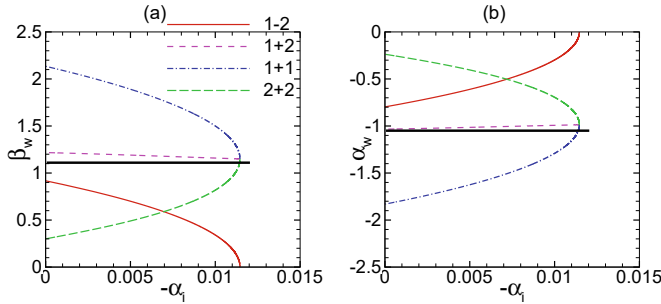


Fig. 6 The roughness wavenumbers satisfying the resonance conditions in the case of stationary vortices: triad sum ($1 + 2$), triad difference ($1 - 2$), and Bragg scattering ($1 + 1$) and ($2 + 2$). The bold solid lines stand for the wavenumbers of the right-branch neutral stationary eigenmodes (β_n , α_n). **a** β_w against $-\alpha_i$; **b** α_w against $-\alpha_i$

majority of the modes. The corrections to the growth rates, $\lambda_r h$, are roughly 0.005 and 0.002, which are comparable with the growth rates of the eigenmodes. It should be acknowledged that the maximum values of λ_r at $x_c/c = 0.05$ and 0.2 reach 1.74 and 2.35 respectively. With the roughness height of $10\mu\text{m}$, the growth-rate corrections amount to 0.0174 and 0.0235, both comparable with the leading-order growth rates of $O(10^{-2})$. In summary, our calculations indicate that the closer to the leading edge, the more sensitive to the roughness are the eigenmodes. Although roughness located at large distances produces much reduced corrections to the growth rates for the majority of vortices, the correction to the most unstable modes remains significant at all locations. This is probably the main reason that roughness triggers earlier transition.

In order to understand the reason behind the large effects, in Fig. 6 the roughness wavenumbers (β_w , α_w) satisfying the resonance conditions of the triad sum, triad difference as well as Bragg scattering for stationary vortices are compared with (β_n, α_n) , the spanwise and chordwise wavenumbers of the right-branch neutral stationary eigenmode in the swept-wing boundary layer. The results reveal that the wavenumbers of the roughness in the triad sum $1 + 2$ are close to (β_n, α_n) so that the roughness forcing is in near resonance with the neutral eigenmode, and consequently generates a large-amplitude perturbation. This is also true with the roughness in Bragg scattering when $-\alpha_i$ is near its maximum. These mathematical properties lead to the dominance of $1 + 2$ and Bragg scattering.

3.2 Travelling Vortices

Travelling eigenmodes 1, 2, 3 and 4 can interact with each or all of the six roughness components. At $x_c/c = 0.05$, the correction coefficients due to the resonances with the frequencies $\omega = 0.005$, $\omega = 0.01$ and $\omega = 0.03$ are displayed in Fig. 7a, c and e, respectively. Among six interactions, the triad sum $1 + 4$ and $2 + 3$ are the two dominant ones. For relatively low frequencies, the greater the growth rate is, the

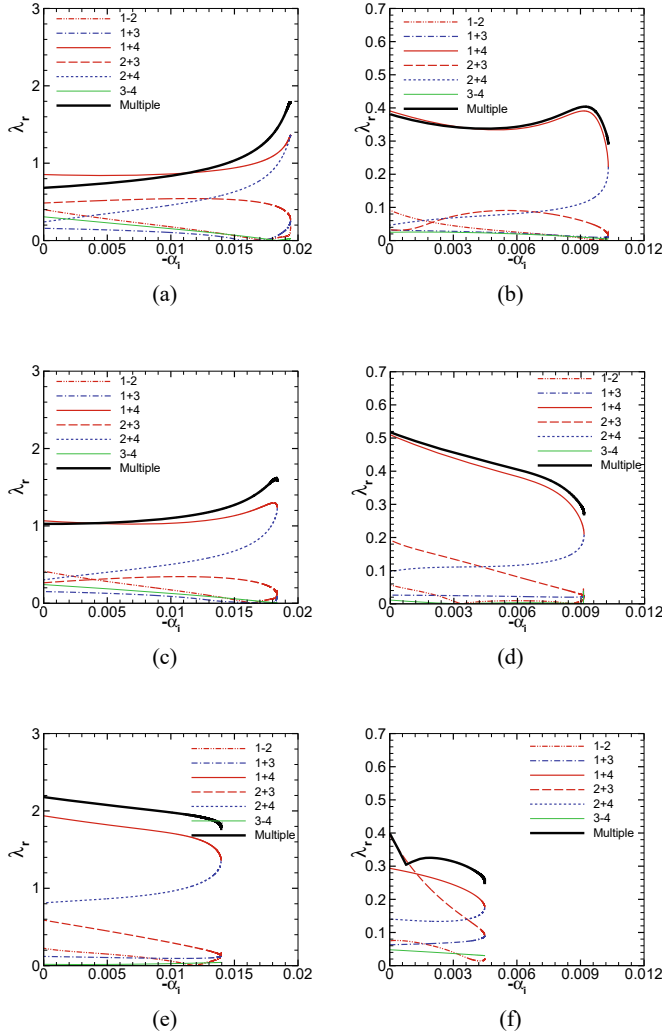


Fig. 7 Comparisons of λ_r for travelling vortices interacting with single and multiple roughness components at **a** $\omega = 0.005$ and $x_c/c = 0.05$; **b** $\omega = 0.005$ and $x_c/c = 0.2$; **c** $\omega = 0.01$ and $x_c/c = 0.05$; **d** $\omega = 0.01$ and $x_c/c = 0.2$; **e** $\omega = 0.03$ and $x_c/c = 0.05$; **f** $\omega = 0.03$ and $x_c/c = 0.2$

greater is the correction to it. For the higher frequency $\omega = 0.03$, the correction coefficient decreases very slightly with the growth rate. The growth-rate correction coefficient, λ_r , is significantly higher, being about twice of that in the stationary case. Roughness with $10\mu\text{m}$ height would produce corrections in the range of 0.01 to 0.015 to the growth rate, which are comparable with the growth rates in the flat-surface case.

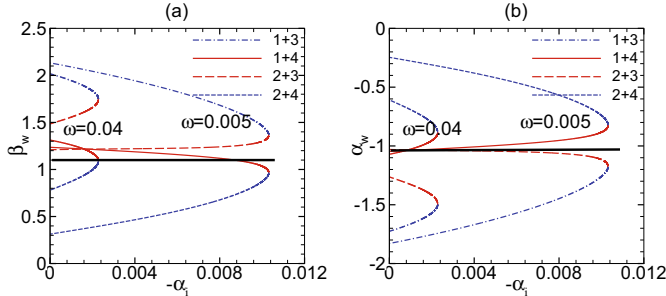


Fig. 8 The roughness wavenumbers satisfying the resonance conditions of the triad sum (1 + 3), (1 + 4), (2 + 3) and (2 + 4) in the case of travelling vortices. The bold solid lines stand for the wavenumbers of the right-branch neutral stationary eigenmodes (β_n, α_n). **a** β_w against $-\alpha_i$; **b** α_w against $-\alpha_i$

At $x_c/c = 0.2$, the correction coefficients due to the resonances with the frequency $\omega = 0.005$, $\omega = 0.01$ and $\omega = 0.03$ are displayed in Fig. 7b, d and f, respectively. For low frequencies, λ_r is larger both when the growth rate is near zero or the maximum. As the frequency increases, λ_r decreases. Compared with the results at the upstream position, the correction coefficients are overall much reduced to about 0.3, and a roughness with $10\mu\text{m}$ would cause a correction of 0.003 to the growth rate, which amounts to a 30% change for the majority of travelling modes.

Our results indicate that roughness near the leading edge can enhance remarkably the amplification of travelling vortices, whereas roughness located downstream has little effect.

As mentioned in Ref. [7] and shown in Fig. 7, the triad sum interactions, 1 + 4 and 2 + 3, appear to contribute the dominant corrections. Fig. 8 shows that the roughness wavenumbers (β_w, α_w) of the roughness components participated in triad sum, 1 + 4 and 2 + 3, are very close to the wavenumbers (β_n, α_n) of the right-branch neutral stationary eigenmode. As a result, there exists a near resonance with the right-branch neutral stationary eigenmode as in the stationary case. Such roughness components generate large response and hence large correction to the growth rate.

4 Conclusions

The present study shows that the resonant interactions between crossflow vortices and roughness modes, identified in Ref. [7] for the Falkner-Skan-Cooke profiles, operate in the swept-wing boundary layers. In the case of stationary vortices, the triad sum and Bragg scattering are found to be most effective in enhancing the growth of the vortices in the main unstable band and the vortices with nearly the maximum growth respectively. In the case of travelling vortices, the interactions of triad sum type are most effective. For both stationary and travelling cases, the high effectiveness can be

attributed to the fact that the wavenumbers of the roughness components participating in the resonant interactions turn out to be close to (β_n, α_n) of the right-branch neutral stationary eigenmode. Such roughness components can generate very large response due to the near resonance with the neutral eigenmode.

The destabilizing effect is remarkably sensitive when the roughness is located near the leading edge, but diminishes for roughness located downstream, except Bragg scattering, which appears to keep destabilizing the most unstable stationary vortices farther downstream. Distributed roughness destabilises low-frequency vortices even more significantly than their steady counterparts. Our calculations indicate that distributed roughness with $10\mu\text{m}$ height can cause corrections comparable with the growth rates of stationary and travelling vortices at $x_c/c = 0.05$, and continue to do so to the most unstable stationary vortices up to $x_c/c = 0.2$ and possible beyond.

Acknowledgements This work was supported by the Tianjin Natural Science Foundation (Grant No. 18JCZDJC38800)

References

- Reibert, M.S., Saric, W.S., Carrillo, R.B., Chapman, K.L.: Experiments in nonlinear saturation of stationary crossflow waves in a swept-wing boundary layer. AIAA Paper **1996-0184**, (1996)
- Radeztsky, R.H., Reibert, M.S., Saric, W.S.: Effect of isolated micron-sized roughness on transition in swept-wing flows. AIAA J. **37**, 1370–1377 (1999)
- Choudhari, M.: Roughness-induced generation of crossflow vortices in three-dimensional boundary layers. Theor. Comput. Fluid Dyn. **6**, 1–30 (1994)
- Kurz, H.B.E., Kloker, M.J.: Receptivity of a swept-wing boundary layer to micron-sized discrete roughness elements. J. Fluid Mech. **755**, 62–82 (2014)
- Butler, A., Wu, X.: Stationary crossflow vortices near the leading edge of three-dimensional boundary layers: the role of non-parallelism and excitation by surface roughness. J. Fluid Mech. **845**, 93–140 (2018)
- Thomas, C., Mughal, S.M., Gipon, M., Ashworth, R., Martinez-Cava, A.: Stability of an infinite swept wing boundary layer with surface waviness. AIAA J. **54**, 3024–3038 (2016)
- He, J., Butler, A., Wu, X.: Effects of distributed roughness on crossflow instability through generalized resonance mechanisms. J. Fluid Mech. **858**, 787–831 (2019)
- Craik, A.D.D.: Non-linear resonant instability in boundary layers. J. Fluid Mech. **50**, 393–413 (1971)
- Hall, P., Smith, F.T.: The nonlinear interaction of Tollmien-Schlichting waves and Taylor-Görtler vortices in curved channel flows. Proc. R. Soc. A. **2**, 255–282 (1988)
- El-hady, N.: Evolution of resonant wave triads in three-dimensional boundary layers. Phys. Fluids. **1**(3), 549–563 (1989)
- Wu, X.: Nonlinear theories for shear flow instabilities: Physical insights and practical implications. Annu. Rev. Fluid Mech. **51**, 451–485 (2019)